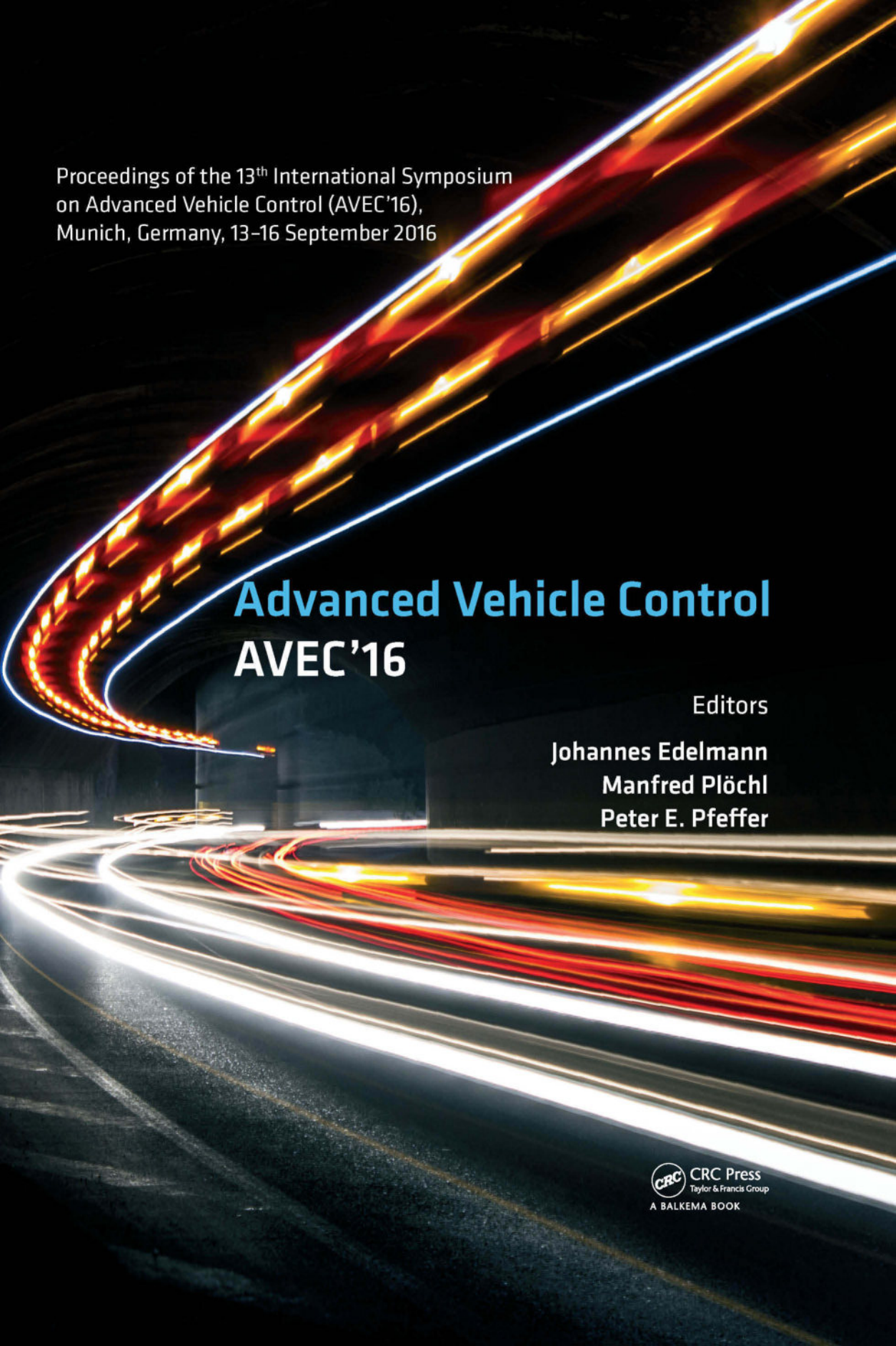

Proceedings of the 13th International Symposium
on Advanced Vehicle Control (AVEC'16),
Munich, Germany, 13–16 September 2016
Advanced Vehicle Control
AVEC'16
Editors
Johannes Edelmann
Manfred Plöchl
Peter E. Pfeffer
CRC Press
Taylor & Francis Group
A BALKEMA BOOK

ADVANCED VEHICLE CONTROL
AVEC'16

www.TechnicalBooksPDF.com

www.TechnicalBooksPDF.com

PROCEEDINGS OF THE 13TH INTERNATIONAL SYMPOSIUM ON ADVANCED VEHICLE CONTROL (AVEC'16), MUNICH, GERMANY, 13–16 SEPTEMBER 2016

Advanced Vehicle Control AVEC'16

Editors

Johannes Edelmann & Manfred Plöchl
TU Wien, Vienna, Austria

Peter E. Pfeffer
Munich University of Applied Sciences, Munich, Germany

CRC Press
Taylor & Francis Group
Boca Raton London New York Leiden

CRC Press is an imprint of the
Taylor & Francis Group, an **informa** business

A BALKEMA BOOK

www.TechnicalBooksPDF.com

Cover image: Source: Shutterstock by Nikifor Todorov/Shutterstock.com

CRC Press/Balkema is an imprint of the Taylor & Francis Group, an informa business

© 2017 Taylor & Francis Group, London, UK

Typeset by MPS Limited, Chennai, India

All rights reserved. No part of this publication or the information contained herein may be reproduced, stored in a retrieval system, or transmitted in any form or by any means, electronic, mechanical, by photocopying, recording or otherwise, without written prior permission from the publishers.

Although all care is taken to ensure integrity and the quality of this publication and the information herein, no responsibility is assumed by the publishers nor the author for any damage to the property or persons as a result of operation or use of this publication and/or the information contained herein.

Published by: CRC Press/Balkema
P.O. Box 11320, 2301 EH Leiden, The Netherlands
e-mail: Pub.NL@taylorandfrancis.com
www.crcpress.com – www.taylorandfrancis.com

ISBN: 978-1-138-02992-7 (Hardback)
ISBN: 978-1-315-26528-5 (eBook)

www.TechnicalBooksPDF.com

Advanced Vehicle Control – Edelmann, Plöchl & Pfeffer (Eds)
© 2017 Taylor & Francis Group, London, ISBN 978-1-138-02992-7

Table of contents

Preface XIII
AVEC'16 International Scientific Committee XV

Advanced concepts of integrated tyre force control

Development of vehicle dynamics characteristics using modern chassis systems for body control depending on the vehicle concept 3
G. Boisdequin, Th. Maulick & St. Sabath

Optimization-based analysis of active suspension authority within integrated vehicle dynamics control systems 9
J. Deur, M. Čorić, L. Xu, H.E. Tseng & D. Hrovat

Energy efficient torque vectoring control 17
P. Gruber, A. Sorniotti, B. Lenzo, G. De Filippis & S. Fallah

Steering redundancy for self-driving vehicles using differential braking 23
M. Jonasson & M. Thor

ADAS

Risk predictive safe speed control for collision avoidance in right turn dynamic environment situation 31
Y. Fujinami, P. Raksincharoensak, Y. Akamatsu, D. Ulbricht & R. Adomat

Speed control for reduced risk of collision with oncoming vehicles in obstacle avoidance scenarios 37
A. Arikere, M. Klomp & M. Lidberg

Torque-based steering assistance for collision avoidance during lane changes 43
Z. Ercan, A. Carvalho, S. Lefèvre, F. Borrelli, H.E. Tseng & M. Gokasan

Enhancing path tracking performance by using haptic shared steering control combined with DYC 49
S. Inoue, H. Inoue, T. Ozawa, P. Raksincharoensak & M. Nagai

Evaluation of an evasive manoeuvre assistance system at imminent side collisions 55
D. Yang, M. Jonasson, T. Halleröd & R. Johansson

Generalized predictive control based on vehicle path following strategy by using active steering system 61
Y. Cao & F. Yu

Target & control based lane keeping assistance system with center error correction algorithm 67
E. Wang, L.-W. Jeng, K. Li & C. Fan

Adaptation of ADAS-functions by identifying driver fingerprint 73
G. Büyükyildiz, A. Hafner, R. Henze, F. Küçükay & M. Vollrath

DrivingCube – A novel concept for validation of powertrain and steering systems with automated driving 79
C. Schyr & A. Brissard

Close to reality surrounding model for virtual testing of autonomous driving and ADAS 85
F. Chucholowski, C. Gnandt, C. Hepperle & S. Hafner

www.TechnicalBooksPDF.com

Vehicle following

Autonomous cruise control with cut-in target vehicle detection 93
A. Carvalho, A. Williams, S. Lefèvre & F. Borrelli

Padé approximation of delays in CACC-controlled string-stable platoons 99
H. Xing, J. Ploeg & H. Nijmeijer

A vehicle following controller for highly-actuated vehicles 105
R. de Castro, A. Schaub, C. Satzger & J. Brembeck

Distributed receding horizon control of a platoon of multiple CAVs with discontinuous-gear transmissions 111
S.E. Li, Y. Zheng, Y. Bian & K. Li

Obstacle avoidance control design: An experimental evaluation in vehicle platooning 119
M. Alirezaei, E. Semsar-Kazerooni & J. Ploeg

Automated driving

Collision avoidance system using state dependent Riccati equation technique: An experimental robustness evaluation 127
M. Alirezaei, S.T.H. Jansen, A.J.C. Schmeitz & A.K. Madhusudhanan

Autonomous drifting with onboard sensors 133
J. Gonzales, F. Zhang, K. Li & F. Borrelli

A new nonlinear model predictive control algorithm for vehicle path tracking 139
G. Schildbach

Real-time optimal obstacle avoidance of MGV using modified Carathéodory-π solutions 145
S. Watanabe & M. Harada

Control target algorithm for direction control of autonomous vehicles in consideration of mutual accordance in mixed traffic conditions 151
S. Kitazawa & T. Kaneko

Implementation of a modified Hamiltonian algorithm for control allocation 157
Y. Gao, T. Gordon & M. Lidberg

Design of an automated steering controller with steering actuator dynamics and adaptive preview time 163
B.-C. Chen, C.-T. Tsai, Y.-M. Lin & K. Lee

Motion sickness in automated vehicles 169
T. Wada

Path planning

Study on update method of avoidance trajectory for the autonomous frontal obstacle avoidance system 177
S. Fujimori, H. Iwata & R. Hayashi

Development of collision probability based motion planning algorithm for automated driving vehicles 183
J. Suh, B. Kim & K. Yi

Autonomous vehicle trajectory planning and control based on virtual disturbance compensation via simulation of feedback control systems 189
P. Raksincharoensak, T. Ehira, K. Shimono & Y. Tagawa

A hierarchical controller for path planning and path following based on model predictive control 195
Q. Wang & S. Müller

Roll-over prevention and risk assessment

A novel control mediation approach to active rollover prevention 203
D. Zhang, T. Gordon, Y. Gao, C. Zong & M. Lidberg

www.TechnicalBooksPDF.com

The noise of acceleration signal as an indicator of the loss of control risk 209
C. Naude, T. Serre, M. Dubois-Lounis, J.-Y. Fournier & V. Ledoux

Prediction based advanced emergency braking for vulnerable road users 215
T. Kim, K. Park, K. Yi & K. Min

Lateral dynamics and optimization

Torsional moment representation in lateral load transfer equations 223
D. Srivastava

Optimizing suspension systems for feasibility, performance and cost 229
J. Wimmler, M. Wahle, M. Zimmermann & D. Schramm

Multi-objective cooperative control of vehicle stability with electro hydraulic brake 235
Z. Jin, C. Wang, L. Zhang & A. Khajepour

Stability and modelling

Straight ahead running of a non linear car and driver model 243
F. Della Rossa, O. Sukharev & G. Mastinu

Handling and stability control for an in-wheel-motor-driven electric vehicle 249
Y. Shi, H. Lu & F. Yu

Real-time simulation of elasto-kinematic multi-body vehicle models 255
M. Klomp, P. Sundström & A. Johnsson

Control of a variable-geometry suspension as independent wheel steering 261
B. Németh, D. Fényes & P. Gáspár

Simulator and test-rig

Model-based steering ECU application using offline simulation (software in the loop) 269
M. Niegl, P.E. Pfeffer & A. Contini

Control system of a wheel-based “auto.mobile-driving simulator” 275
T. Tüschen, S. Ernst, D. Beitelschmidt, G. Prokop & W. Tischer

Tire-suspension hardware-in-the-loop simulation system compensating delay of testing machine 281
T. Hosono, Y. Udagawa, S. Kawaguchi & T. Shiiba

Evaluation of coupled suspension system using four electromagnetic dampers by motor HILS system 285
Y. Imai, Y. Fukumori, R. Hayashi, K. Nakano & Y. Suda

Driver

Investigation on the lane tracking steering control with two preview points to make preview time shorter 293
K. Nishizaki, H. Mouri, H. Furusho & P. Raksincharoensak

Bayesian network-based identification of driver lane-changing intents using eye tracking and vehicle-based data 299
X.H. Li, M. Rötting & W.S. Wang

Influence of different ground truth hypotheses on the quality of Bayesian networks for maneuver detection and prediction of driving behavior 305
T. Rehder, L. Louis, W. Muenst & D. Schramm

Driving behavior modeling for avoidance of road rushing out pedestrians in non-intersection areas 311
H. Imanaga, R. Iwaki, I. Yamaguchi & N. Uchida

Modelling the effect of sensory dynamics on a driver’s control of a nonlinear vehicle 317
C.J. Nash & D. Cole

Fundamental study on driver model for lateral and longitudinal control to advanced driver assistance systems 323
I. Kageyama, Y. Kuriyagawa & Y. Wang

www.TechnicalBooksPDF.com

Model predictive control to represent interaction of driver and active accelerator pedal 329
C.W. Rosier & D. Cole

Inferring driver's deceleration intent in vehicle platoon system by using feedback estimators 335
H. Suzuki, T. Ishikura & T. Nakatsuji

Driver's steering torque modeling based on lateral deviation and reaction torque 341
H. Yoshida, J. Yamakawa & T. Honjo

Modelling human steering behaviour at the limit of adhesion using robust nonlinear model predictive control 345
G. Braghieri & D. Cole

A skill learning process model for driving a car 351
K. Togai, A. Ohno, T. Matsumoto & H. Tamaki

Steering

In vehicle truck steering-system modeling and validation 359
J. Loof, I. Besselink & H. Nijmeijer

A design of the lead-steer in active front steering system using lead-lag compensator 365
J. Jung, R. Chung, J. Heo, J. Oh & J. Lee

The influence of time delay on stability of the steering simulator 371
Y. Jiang, W. Deng, J. Wu, S. Zhang & K. Zhang

Study on reactive steering torque control for bar type steering in high speed range 377
S. Tamakawa, H. Tanabe, K. Sato, H. Mouri & P. Raksincharoensak

Electric power steering

H_∞ filtering design for driver torque estimation in electric power steering system 385
K. Yamamoto, P. Moulaire, D. Koenig & O. Sename

Design of equivalent friction using a motor control for Electric Power Steering (EPS) 391
S. Ohno & A. Yoneda

The relationship between the resonance frequency of a steering system and the tire-road friction coefficient 397
L. Chen, Y. Luo, M. Bian, Z. Qin & K. Li

Steer-by-wire/ADAS

Upperbounds on the closed loop sensitivity for the control of a steer-by-wire vehicle 405
T. van der Sande, P. Zegelaar, I. Besselink & H. Nijmeijer

Evaluation of handling performance in steer-by-wire vehicle 411
F. Takagi, T. Shiiba, R. Ishizaki, K. Tamura & H. Hata

Fault detection scheme for a road vehicle with four independent single-wheel electric motors and steer-by-wire system 417
B. dos Santos, A. Lopes & R.E. Araújo

Study on active safety for aquaplaning assistance 423
T. Raste & D. Frerichs

Subjective evaluation and handling

Validation of a moving base driving simulator for subjective assessments of steering feel and handling 431
G.L. Gil Gómez, C. Andersson Eurenius, J. Donnay Cortiñas, E. Bakker, M. Nybacka, L. Drugge & B. Jacobson

Tire handling subjective evaluation related to model parameters of three driver models 437
S. Monsma, M. van Oort & P. Bremmer

www.TechnicalBooksPDF.com

Special vehicles

Intelligent based terrain preview controller for a 3-axle vehicle 445
J.T. Economou, D.J. Purdy, D. Galvão Wall, D. Diskett & D. Simner

Optimal control of lateral stability for articulated heavy vehicles based on adaptive dynamic programming approach 451
B. Li, S. Rakheja & Z. Fu

MiniMax – a situational and geometrical adaptive chassis: Driving safety and space efficiency 457
J. Kalbfleisch, P. Wagner & H. Winner

A cascaded model-predictive approach to motorcycle safety 463
S. Hans, M. Krehel, M. Köbe & G. Prokop

Database

Geostatistical meta-modeling for a model-based calibration of an adaptive shock absorber 471
S. Blume, S. Reicherts, H. Koegeler, N. Didcock & T. Henn

Predictive modeling for vehicle time-series data 477
J. Wallner, F. Diermeyer & S. Engel

Study on cooperative driving of automated driving vehicles via spatial information server 483
S. Okada, T. Hisamatsu & M. Omae

Database of relevant traffic scenarios as a tool for the development and validation of automated driving 489
P. Themann, A. Pütz, A. Zlocki & L. Eckstein

State estimation

Full vehicle and tyre identification using unscented and extended identifying Kalman filters 497
M.C. Best & K. Bogdanski

Model-based state estimator for an intelligent tire 503
J. Goos, A.P. Teerhuis, A.J.C. Schmeitz, I. Besselink & H. Nijmeijer

Nonlinear vehicle velocity estimation with friction adaption for four-wheel-independent-drive EVs 509
X. Xia, L. Xiong, B. Leng & Z. Yu

Unscented Kalman filter for combined longitudinal and lateral vehicle dynamics 515
M. Wielitzka, S. Eicke, A. Busch, M. Dagen & T. Ortmaier

Vehicle state estimation from a sports-car application point of view focusing on handling dynamics 521
M. Haudum, J. Edelmann, M. Plöchl & M. Höll

Exploring different vehicle model complexity for reference in a sensor signal processing model controller 527
I. Ramirez Ruiz, M. Alirand, F. Cheli & E. Sabbioni

Articulation angle estimation and control for reversing articulated vehicles 533
S. Kim, J. Yang & K. Huh

Tyre and friction

Friction utilization for tyre-road friction estimation on snow: An experimental study 541
A. Albinsson, F. Bruzelius & B. Jacobson

Wheel force measurement for vehicle dynamics control using an intelligent bearing 547
S.M.A.A. Kerst, B. Shyrokau & E.G.M. Holweg

The influence of tire transient property on vehicle behavior 553
T. Takahashi

www.TechnicalBooksPDF.com

Estimation of tire road friction during vehicle steering 559
L. Shao, C. Lex, A. Hackl & A. Eichberger

Longitudinal dynamics

Adaptive anti-slip regulation method for distributed drive electric vehicle 567
K. Sun, Z. Yu, L. Xiong & R. Zhang

Perceptible changes in driving dynamics due to regenerative braking: Analysis and reduction through active chassis systems 573
T. Helfrich & M. Lienkamp

A development of nonlinear adaptive ABS control using optimal slip tracker 579
S. Lee, B. Yang & J. Jeon

Integration of torque blending and slip control using real-time nonlinear model predictive control 585
M.S. Basrah, E. Siampis, E. Velenis, D. Cao & S. Longo

Torque/G-Vectoring

Study of mechanism improving target course traceability in G-Vectoring Control 593
M. Yamakado, M. Abe, Y. Kano, D. Umetsu & T. Yoshioka

Development of G-Vectoring Control system based on engine torque control 599
T. Yoshioka, Y. Takahara, F. Kato, O. Sunahara, T. Tsukano, Y. Takeda, K. Takemura, D. Umetsu, M. Yamakado, Y. Kano, M. Abe & J. Takahashi

Effect of yaw-moment control based on lateral jerk information on lane change task 605
J. Takahashi, M. Yamakado, K. Nagatsuka, S. Sato, N. Hiraga, D. Umetsu & Y. Takahara

Model predictive control for active drive-torque distribution during a slalom manouevre 611
J.S. Hellewell, A.A. Popov, G.E. Burnett & J.W. Griffin

Torque vectoring

Evaluation of optimal yaw rate reference for electric vehicle torque vectoring 619
E.N. Smith, E. Velenis, D. Cao & D. Tavernini

Inversion based feedforward design to improve the lateral dynamics of high performance sports cars 625
S. Rahimi Fetrati, C. Kandler, C. Kärcher & D. Schramm

Efficient direct yaw moment control of in-wheel motor vehicle 631
T. Kobayashi, H. Sugiura, E. Ono, E. Katsuyama & M. Yamamoto

Torque vectoring control for different powertrain layouts of hybrid and electric vehicles 637
M. Vignati & E. Sabbioni

Vertical dynamics

A study on invariant points of semi-active suspension 645
Y. Zhuang, S. Nie, F. Chen & J. Xie

Dynamic sensitivity analysis of a suspension model 651
S. Hamza, F. Anstett-Collin, Q. Li, L. Denis-Vidal, A. Birouche & M. Basset

Improvement of ride comfort by unsprung negative skyhook damper control using in-wheel motors 657
E. Katsuyama & A. Omae

Nonlinear $\mathcal{H}_2$ control of a low-bandwidth active vehicle suspension system using Takagi-Sugeno methods 663
N. Pletschen

Powertrain

Optimal design of hybrid track-type dozers with two-planetary gear sets and clutches 673
Z. Qin, Y. Luo, K. Li, Z. Pan & H. Peng

Upshift control strategy for dual clutch transmission with single clutch's slipping 679
J. Liu, B. Ma, H. Li & G. Li

www.TechnicalBooksPDF.com

Predictive energy management of hybrid powertrains using deterministic and Markov chain predictions 685
R.S. Vadamalu & C. Beidl

Adaptive power management strategy for a four-mode plug-in hybrid electric vehicle 691
J.-C. Guan, B.-C. Chen & L.-K. Chen

Reduced order propulsion models for vehicle control and energy management 697
K. Togai, N. Fujinaga & H. Yamaura

Modeling hydro mounts in vehicles for durability load analyses, ride comfort and vehicle dynamics simulation 703
C. Scheiblegger, N. Roy, P.E. Pfeffer & A. Hillis

Energy efficiency

Rolling loss analysis of combined camber and slip angle control 713
M.M. Davari, M. Jonasson, J. Jerrelind, A. Stensson Trigell & L. Drugge

Integrated traction control strategy for 4-motorized-wheels electric vehicles with improvement of economy and longitudinal driving stability 717
X. Zhang & D. Göhlich

Author index 723

www.TechnicalBooksPDF.com

www.TechnicalBooksPDF.com

Advanced Vehicle Control – Edelmann, Plöchl & Pfeffer (Eds)
© 2017 Taylor & Francis Group, London, ISBN 978-1-138-02992-7

Preface

The 13th International Symposium on Advanced Vehicle Control (AVEC'16) was held in Munich, Germany, from 13th to 16th September 2016. The symposium was hosted by the Munich University of Applied Sciences.

The AVEC symposium is a leading international conference in the fields of vehicle dynamics and advanced vehicle control, bringing together scientists and engineers from academia and automotive industry. The first symposium was held in 1992 in Yokohama, Japan. Since then, biennial AVEC symposia have been established internationally and have considerably contributed to the progress of technology in automotive research and development. In 1996, AVEC was hosted in Aachen, for the first time in Germany. 20 years later, AVEC returned to Germany.

AVEC'16 puts a special focus on automatic driving, autonomous driving functions and driver assist systems, integrated control of interacting control systems, controlled suspension systems, active wheel torque distribution, and vehicle state and parameter estimation.

Three keynote addresses were given by Henk Nijmeijer (Eindhoven University of Technology) on "Control of vehicles: cooperative and autonomous driving", David Cole (University of Cambridge) on "Understanding the human steering control task", and Marko Gustke (Verband der Automobilindustrie) on "Approaches for road safety and efficiency – opportunities and action fields" at plenary sessions of the symposium.

112 papers were presented at the symposium and are published in these proceedings. The papers review the latest research developments and practical applications in highly relevant areas of vehicle control, and may serve as a reference for researchers and engineers. Four contributions have been devoted to the special interest session "Advanced concepts of integrated tyre force control" and placed at the beginning of these proceedings.

Besides the paper presentations technical visits were offered to the participants to ADAC Technology Centre, Audi AG, BMW AG, IABG mbH, and MAN Truck & Bus AG.

We would like to thank the International Scientific Committee, the AVEC Board, the members of the AVEC'16 Secretariat as well as the sponsors of the symposium.

Peter E. Pfeffer
General Chairman

Manfred Plöchl
Chairman of ISC

www.TechnicalBooksPDF.com

www.TechnicalBooksPDF.com

Advanced Vehicle Control – Edelmann, Plöchl & Pfeffer (Eds)
© 2017 Taylor & Francis Group, London, ISBN 978-1-138-02992-7

AVEC'16 International Scientific Committee

Chairman: M. Plöchl (Austria)

M. Abe (Japan)
M. Basset (France)
B.-Ch. Chen (Taiwan)
D. Cole (UK)
J. Edelmann (Austria)
T. Gordon (UK)
S. Hecker (Germany)
D. Hrovat (USA)
K. Li (China)
M. Nagai (Japan)
H. Peng (USA)
A. Schmeitz (The Netherlands)
T. Takahashi (Japan)
M. Valášek (Czech Republic)
H. Winner (Germany)
D. Ammon (Germany)
M. Best (UK)
E. Coelingh (Sweden)
K. Deng (China)
Y. Furukawa (Japan)
P. Gruber (UK)
S. Horiuchi (Japan)
I. Kageyama (Japan)
G. Mastinu (Italy)
H. Nijmeijer (The Netherlands)
G. Rizzo (Italy)
A. Stensson Trigell (Sweden)
M. Tomizuka (USA)
H. Wallentowitz (Germany)
K. Yi (Korea)

www.TechnicalBooksPDF.com

www.TechnicalBooksPDF.com

Advanced concepts of integrated tyre force control

www.TechnicalBooksPDF.com

www.TechnicalBooksPDF.com

Advanced Vehicle Control – Edelmann, Plöchl & Pfeffer (Eds)
© 2017 Taylor & Francis Group, London, ISBN 978-1-138-02992-7

Development of vehicle dynamics characteristics using modern chassis systems for body control depending on the vehicle concept

G. Boisdequin, Th. Maulick & St. Sabath
Dr. Ing. h.c. F. Porsche AG, Weissach, Germany

ABSTRACT: This paper gives an overview over the complete range of chassis control systems offered by Porsche and their functional characteristics. It takes the active roll compensation system as an example to detail their main objectives regarding driving dynamics, their functions and their performances when combined with different vehicle concepts. The active roll compensation system is well-known for the main goal it is designed for: body roll reduction under lateral acceleration that enhances the sporty character of a vehicle and its driving experience. But there is more to it than that. The system influences driving dynamics much deeper. It also increases driving performance, agility, precision and the typical Porsche spread between handling and ride comfort. Those performances are objectively described in this paper by the corresponding driving dynamics criteria.

1 INTRODUCTION

The current chassis control systems are well-diversified. There are many different systems with different functions that directly and indirectly affect the driving behavior of a vehicle. This paper deals with their functional characteristics and their interactions with different Porsche vehicle concepts. The active roll compensation serves as an example to detail those characteristics.

2 DRIVING DYNAMICS

The driving dynamics of a vehicle describes how it reacts on the road to the driver inputs and to the road unevenness as well as the feedback from the vehicle to the driver. It includes handling, steering feel, braking, traction and ride comfort.

Those criteria, together with the suitability for daily use, are affected by the active chassis systems in a way that is described in the next paragraph.

2.1 *Handling*

Handling describes the driving behavior of a vehicle under steering inputs. It is characterized by:

- its roll compensation, the amplitude and damping of the body roll motions in curve
- its stability, the predictability of its yaw reactions and the possibility to modulate them
- its agility, the amplitude and responsiveness of its yaw reactions
- its maneuverability, the ability to direct the vehicle in city traffic under low dynamics
- its precision with which the vehicle responds to the driver inputs and follows the target line
- its lateral dynamics performance or the maximum reachable lateral acceleration

2.2 *Steering feel*

Steering feel includes:

- the steering moment characteristics, the amplitude and progression of the steering moment for the driver
- the steering feedback, the quantity and quality of vehicle and road information that are communicated through the steering wheel

2.3 *Braking and traction*

The driving behavior of a vehicle when braking and accelerating is characterized by:

- its pitch compensation, the amplitude and damping of the body pitch motions under longitudinal acceleration
- its traction, the ability to transfer the drive forces to the road
- its braking potential, the ability to transfer the braking forces to the road

2.4 *Ride comfort*

Ride comfort describes the vibrational comfort of the vehicle that is mainly influenced by the chassis and its systems. It includes:

- Primary ride, the level of vibrations with frequencies close to the body natural frequencies

www.TechnicalBooksPDF.com

– Secondary ride, the level of vibrations with frequencies close to the subsystem natural frequencies
– Impact, describing the vibration peaks when driving over a single obstacle or on stochastic road excitations
– Harshness, the level of vibrations at frequencies higher than the chassis subsystem natural frequencies

3 OBJECTIVES OF ACTIVE CHASSIS SYSTEMS

The active chassis systems have different objectives regarding driving behavior. First they offer additional functionalities and therefore enlarge the full driving dynamics potential of a vehicle. Then, and contrary to the passive systems, they have the possibility to adapt their characteristics to the driving situations. This leads to a better trade-off not only between the driving dynamics characteristics but also between them and the other vehicle characteristics like mileage and suitability for daily use. Finally, the driving behavior can be adapted to the instantaneous requirements of the vehicle occupants through the manual or automatic selection of predefined modi. While the active systems increase the overall performance potential of the vehicle, the modi shift the focus on one or the other characteristics.

Most chassis control systems feature several functionalities influencing the driving behavior characteristics directly or indirectly. The qualitative assessment of those effects is shown in Tables 1 to 4 for the chassis control systems available at Porsche.

The active chassis systems are linked via an internal communication network. It ensures the exploitation of the full potential of each single system and it avoids

Table 1. Active systems and handling.

	Roll compensation	Stability	Agility	Maneuverability	Precision	Performance
Controlled damper	++	+	+		+	+
Air spring/ride height and level control						+
Air spring/spring rate control	+					
Active roll compensation	++	+	+		++	++
Rear-wheel steering		++	++	++	+	
Torque vectoring			++		+	++
Limited slip differential		++				+
4-wheel-drive		++				+
Controlled drivetrain Mounts		+			+	
Lift system front axle						
Electro power steering					+	

+/++: big/very big effect of the control system on the considered criteria

Table 2. Active systems and steering feel.

	Steering moment	Steering feedback
Controlled damper		+
Air spring/ride height and level control		
Air spring/spring rate control		
Active roll compensation		
Rear-wheel steering		
Torque vectoring		
Limited slip differential		
4-wheel-drive		
Controlled drivetrain Mounts		
Lift system front axle		
Electro power steering	++	+

+/++: big/very big effect of the control system on the considered criteria

Table 3. Active systems and longitudinal dynamics.

	Pitch compensation	Traction	Braking potential
Controlled damper	++	+	+
Air spring/ride height and level control			
Air spring/spring rate control	+		
Active roll compensation			
Rear-wheel steering			
Torque vectoring			
Limited slip differential		+	
4-wheel-drive		++	
Controlled drivetrain Mounts			
Lift system front axle			
Electro power steering			

+/++: big/very big effect of the control system on the considered criteria

Table 4. Active systems and ride comfort.

	Primary ride	Secondary ride	Impact	Harshness	Daily Use
Controlled damper	++	+	++	+	
Air spring/ride height and level control			+	+	++
Air spring/spring rate control			++	+	
Active roll compensation	+		+		
Rear-wheel steering					
Torque vectoring					
Limited slip differential					
4-wheel-drive					
Controlled drivetrain Mounts		+			
Lift system front axle					++
Electro power steering		+	+	+	

+/++: big/very big effect of the control system on the considered criteria

www.TechnicalBooksPDF.com

negative interactions between them. It also reduces the complexity, for example during the tuning phases.

3.1 *Controlled damper*

The controlled damper system controls the damping force of the suspension dampers. It provides the optimal wheel and body damping depending on the driving situation and on the vibrational state of the vehicle.

It improves the following target conflicts:

1. Body roll and pitch compensation in handling which requires a high damping vs. isolation on uneven roads. The better roll compensation also reduces the inertia effects and therefore the vehicle response times. It increases the driving precision.
2. Isolation vs. traction, braking and lateral dynamics performance in handling on uneven roads by damping the wheel vibrations and optimizing the tire-road-contact
3. Isolation on uneven roads vs. reduction of body and wheel natural vibrations by adapting the damping depending on the vibration source
4. Stability vs. agility by adapting the dynamic roll moment distribution in handling
5. Road feedback vs. ride comfort

The manual selection of the controlled damper modus displaces the focus towards handling or ride comfort by changing the basic damping. It also influences the subjective impression given to the vehicle occupants.

3.2 *Air spring/ride height and level control*

The ride height is changed by increasing or decreasing the air spring volume and therefore the spring length. The body level is maintained constant by adapting the air spring pressure to the vehicle load state. It also optimizes the spring rate to the loading condition.

The air spring system improves the following target conflicts:

1. Higher ability to drive on bad road with high ride height vs. higher vehicle dynamics performance and reduced air resistance with low ride height
2. Optimized isolation in all loading conditions due to the air spring characteristics that offer the possibility to select a low spring rate for the unloaded state while adapting automatically to the actual vehicle weight
3. Higher ability to drive on bad road with high ride height vs. easy access in very low level – advantage specific to SUVs

The ride height can be changed manually in predefined speed areas.

3.3 *Air spring/spring rate control*

The spring rate is changed by modifying the active air volume. It is realized by connecting or disconnecting the different air spring chambers.

It improves isolation by allowing a low spring rate while keeping a good roll and pitch compensation through an increase of the spring rate depending on the lateral or longitudinal acceleration.

The manual selection of the air spring modus affects the basic spring rate for straight line driving.

3.4 *Active roll compensation*

The active roll compensation system adapts the static and dynamic stiffness of the front and rear anti-roll bars, possibly separately, depending on the driving situation. This affects the total roll rate, the roll damping and the roll moment distribution between the front and rear axles.

The active roll compensation system improves the following target conflicts:

1. High roll compensation in handling which positively affects passenger comfort and gives them an even sportier driving impression vs. roll isolation which requires a low roll rate. The better roll compensation in curve also reduces the inertia effects and therefore the vehicle response times. This increases the driving precision. Furthermore, it optimizes the contact patch between tire and road and therefore the lateral dynamics potential.
2. High damping of the body motions at the body roll natural frequency vs. roll isolation which requires a low roll damping.
3. Stability in combined dynamics maneuvers which requires a front-biased roll moment distribution vs. agility and high lateral dynamics potential which requires a rear-biased roll moment distribution

The manual selection of the Active Roll Compensation Modus affects the amount of roll compensation in curve and therefore the target conflict between handling and comfort in curve.

3.5 *Rear-wheel steering*

The system steers the rear wheels in the same or in the opposite direction compared to the front wheels depending on the driving situation.

It ensures an even higher stability at high speed and allows therefore a more direct front axle steering which increases the agility at lower speed. It improves the target conflict between stability on motorways and agility on country roads. In addition, it increases the driving precision by having a fast build-up of the rear axle side forces. It also significantly reduces the turning circle and increases the maneuverability.

3.6 *Torque vectoring*

The Porsche torque vectoring system brakes the curve-inside wheel of the rear axle to produce a yaw-in moment.

It reduces the understeering tendency of the vehicle and increases the lateral acceleration potential through the related side force release of the front axle. It also

www.TechnicalBooksPDF.com

increases the driving precision by fastening the vehicle reaction after the steering input.

3.7 *Limited slip differential*

The limited slip differential reduces the rotational speed difference between the wheels of an axle with a fixed or a controlled degree of maximum slip.

It offers the advantage of an open differential in terms of understeering while improving the stability when accelerating in a curve, the traction potential and the straight line driving abilities on uneven roads or roads with different surfaces. This is realized by automatically braking the fastest rotating wheel and therefore increasing the total side force potential in the first case, limiting the drive loss in the second case and generating a turning back yaw moment in the last one. Those advantages are even amplified with the controlled slip differential. In addition, the limited slip differential increases the drift abilities of a vehicle.

3.8 *All-wheel drive and drive torque management*

The drive torque management system distributes the drive torque between the front and rear axles through a controlled differential depending on the driving situation.

It improves the target conflict between agility and stability. An agile basic chassis setup ensures the agility in the steady-state driving phases while the stability under acceleration or power-off is obtained by transferring drive torque to the front axle and therefore increasing the side force potential of the rear axle. In addition, it increases the traction potential of the vehicle by making use of all four wheels to transfer the drive forces.

3.9 *Controlled engine mounts*

The engine mount stiffness and damping are adapted to the driving situation in order to optimally control the engine motions.

It improves the target conflicts between acoustic isolation – which requires a low mount damping and stiffness – and:

1. Stability and precision when steering in and in combined dynamics maneuvers like accelerating in a curve. In those driving situations, the engine motions are better controlled which reduces the inertia effects and the vehicle yaw motions.
2. Secondary ride by increasing the mount damping in case of natural vibrations of the engine.

The manual selection of the sport modus affects the basic mount damping and stiffness.

3.10 *Electric power steering*

The steering assist force and therefore the steering torque can be fully adapted to the driving situations and road conditions.

The electro power steering improves the target conflict between low steering torque for parking and higher steering torque for straight line ability at higher speeds. It also optimizes the feedback about the driving state of the vehicle and the road conditions. Finally, it can isolate the driver from disturbing road excitations and damp the natural vibrations of the steering system.

3.11 *Front axle lift system*

The front axle lift system changes the distance between body and wheel by shifting the spring foot plate vertically.

The system improves the target conflict between low ride height for handling and high ground clearance for passing higher obstacles.

4 CHASSIS SYSTEMS AND VEHICLE CONCEPT

The weight given to the different functions of an active system and their effects on the driving behavior of the vehicle depend on the vehicle concept, its targets and on the properties of its mechanical components such as tires and axles. This is illustrated in this paper by the active roll compensation system. The most relevant vehicle concept parameters for that system are the center of gravity height, the vehicle mass and the mass and drive torque distribution. The handling and ride comfort targets of a vehicle define among others whether the system is offered or not and how it is setup. The interrelationships between tire grip, camber and wheel load define the potential of the system to increase the lateral dynamics performance. Finally, the properties of the system hardware determine the quality of the control strategy realization. Figure 1 shows the effect of the active roll compensation on the target conflict between roll compensation in handling and roll isolation for ride comfort.

The system reduces the roll angle in curves and the roll vibrations of the vehicle body on uneven road. It therefore moves those vehicle properties on a better Pareto-optimum than with passive anti-roll bars. The compromise between vehicle dynamics and ride comfort can still be adapted by the driver along that Pareto

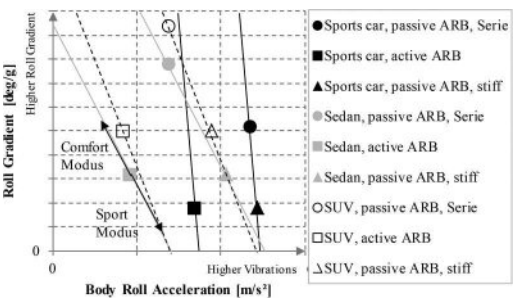


Figure 1. Roll compensation vs. roll isolation.

www.TechnicalBooksPDF.com

line by manually selecting different predefined system modi. The SUVs and Sedans show a very high potential for active roll compensation because of their higher center of gravity and mass. The reduction of the roll gradient leads to a higher handling potential which is shown on Figure 2.

The system increases the maximum lateral acceleration during the steady-state driving situations. In the SUV case, it also increases the steady-state stability reserve which is represented by the sideslip angle gradient at the same lateral acceleration. The higher side force potential results from two main effects. The lower vehicle roll angle reduces the lateral displacement of the body center of gravity and the total lateral load transfer but also the negative camber of the outside wheels relative to the road. It therefore optimizes the working conditions of the tires. The driving stability in combined dynamics maneuvers is improved for all three vehicle types by actively shifting the roll moment distribution frontwards depending on the driving situation. This is shown in Figure 3 for a power-on in a curve maneuver.

The compensation of the dynamic roll motions in handling also reduces the inertia effects and fastens the front and rear axle responses. Figure 4 shows the time delay between front and rear axles.

Regarding ride comfort, the active anti-roll bar system does not only improve roll isolation by actively reducing the global roll rate and damping on uneven road but it also damps the body roll natural mode when needed. This is shown in Figure 5.

This leads to a better Pareto-optimum for roll isolation and body roll damping.

Altogether, the active anti-roll bar system makes the vehicle tighter and even more precise. It gives it higher lateral dynamics performances without compromising driving stability, controllability and driver trust. This is realized with at least the same or even a better ride comfort level depending on the chosen system modus.

5 CONCLUSION

Porsche offers a wide range of chassis control systems with different functions that influence driving dynamics directly and indirectly. This paper describes how they add functionalities to the vehicle, how they better solve potential target conflicts and how they broaden the full driving experience. This is concretized for the active roll compensation system by objectively showing its effects on handling and ride comfort for different vehicle concepts. Furthermore, chassis control systems are introduced to solve potential target conflicts between driving behavior and other vehicle properties like mileage. The need for such systems will increase in the future with vehicle electrification and (partly-)automated driving. The quality of the input signals used by those systems will continue to improve not only with sensor development but also with the access to external data. This will further enhance the overall control quality. The vehicle will adapt itself even better to the driving situations. Together with the manual selection of suitable modi, it will turn the occupant requests into reality with even more reliability. This benefits the trend for individualization.

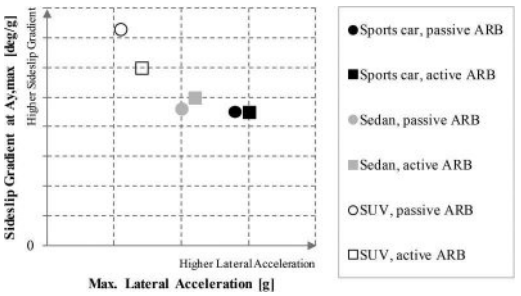


Figure 2. Handling potential.

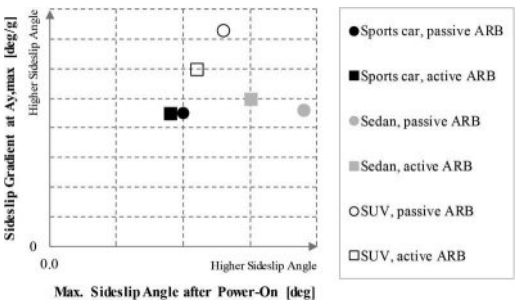


Figure 3. Driving stability.

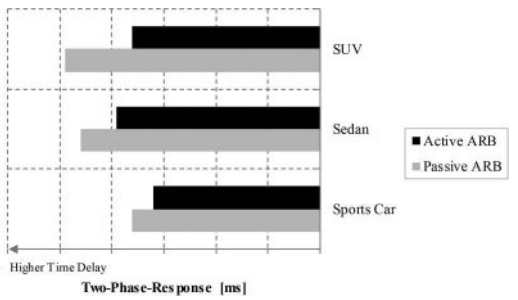


Figure 4. Time delay between front and rear axles.

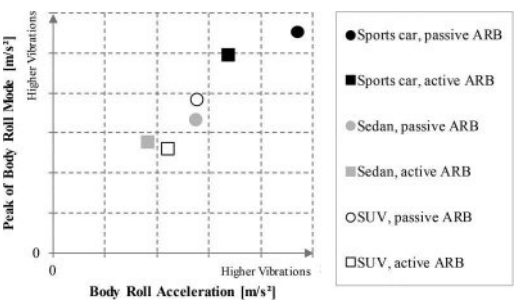


Figure 5. Roll isolation vs. roll damping.

www.TechnicalBooksPDF.com

www.TechnicalBooksPDF.com

Advanced Vehicle Control – Edelmann, Plöchl & Pfeffer (Eds)
© 2017 Taylor & Francis Group, London, ISBN 978-1-138-02992-7

Optimization-based analysis of active suspension authority within integrated vehicle dynamics control systems

J. Deur & M. Čorić
Faculty of Mechanical Engineering & Naval Architecture, University of Zagreb, Zagreb, Croatia

L. Xu, H.E. Tseng & D. Hrovat
Ford Research & Innovation Center, Ford Motor Co., Dearborn, MI, USA

ABSTRACT: Active suspension is commonly considered under the framework of vertical vehicle dynamics control aimed at improvements in ride comfort. This paper uses a collocation-type control variable optimization method to analyze to which extent the fully active suspension (FAS) application can be broaden to the tasks of vehicle handling/cornering control and braking distance reduction. The emphasis is on integrated control systems, where the FAS control action supports other actuators such as active brakes and active steering. The analysis is extended to the ride control task for the case of emphasized, discrete road disturbances such as high-magnitude bumps and potholes. The main control objective is to provide a favorable trade-off of ride comfort and road holding capability, as well as a robustness against wheel damage, e.g. at the pothole trailing edge. The optimization is based on a nonlinear 10-DOF vehicle dynamics model, including a combined-slip tire model, and it is subject to various, generally nonlinear equality and inequality constraints.

1 INTRODUCTION

Integrated vehicle dynamics control (VDC) systems utilize different types of actuators and complex control laws to improve the overall vehicle safety and comfort performance (Hrovat et al. 2011). Active suspension has a unique ability of controlling the vertical vehicle dynamics. As such, it has been mostly investigated and applied with the aim of improving the ride comfort performance, while preserving a high level of road holding ability (Hrovat 1997).

Owing to a large control authority over the tire normal load, fully active suspension (FAS) can indirectly control the tire longitudinal and lateral forces, thus assisting ABS and VDC systems for improved braking and handling performance. Based on the use of a control variable optimization method, Edren et al. (2015) reveal that the ABS performance can be improved by a properly managed FAS-based tire load boost action. Similarly, Edren et al. (2012) demonstrate that the FAS can provide a short-term boost of total tire load, and, thus, a boost of the vehicle lateral forces, which can improve the handling performance.

Čorić et al. (2016a, 2016b, 2017) present broad and systematic optimization-based studies aimed at revealing FAS control mechanisms and performance gains related to enhancement of vehicle handling, ride, and braking performance. Compared to (Edren 2012, 2015), where the focus is on braking distance reduction, these studies assess in detail the FAS-based handling control, and ride comfort control for the case of emphasized discrete road disturbances. Also, they are based on a full 10 DOF vehicle dynamics model with a combined-slip tire model, and a variety of vehicle maneuvers and control tasks.

This paper gives an overview of the main results from (Čorić 2016a, 2016b, 2017). The emphasis is on cooperative (integrated) control action of FAS and active steering/brake actuators. Details of the used TOMLAB-based pseudo-spectral collocation method of control trajectory optimization, VDC optimization problem formulation, vehicle dynamics model, and maneuvers' specification are given in the original papers.

2 VEHICLE MODEL

The conducted optimization studies are mostly based on the 10 DOF passenger vehicle dynamics model depicted in Figures 1a, b (Hancock 2006). The model state variables include longitudinal (U), lateral (V), and heave (W) velocities, and roll (p), pitch (q), and yaw (r) rates, as well as the four state variables related to the rotational speeds ω_i of each wheel, $i = 1, \ldots, 4$. For the ride control optimization task, the simple quarter-car vehicle model shown in Figure 1c (Hrovat 1997) is mostly used. The 10 DOF model is extended by the unsprung mass dynamics (dashed lines in Fig. 1b) when verifying the basic 10 DOF model-based optimization results, or when using the full vehicle model for ride control optimization.

www.TechnicalBooksPDF.com

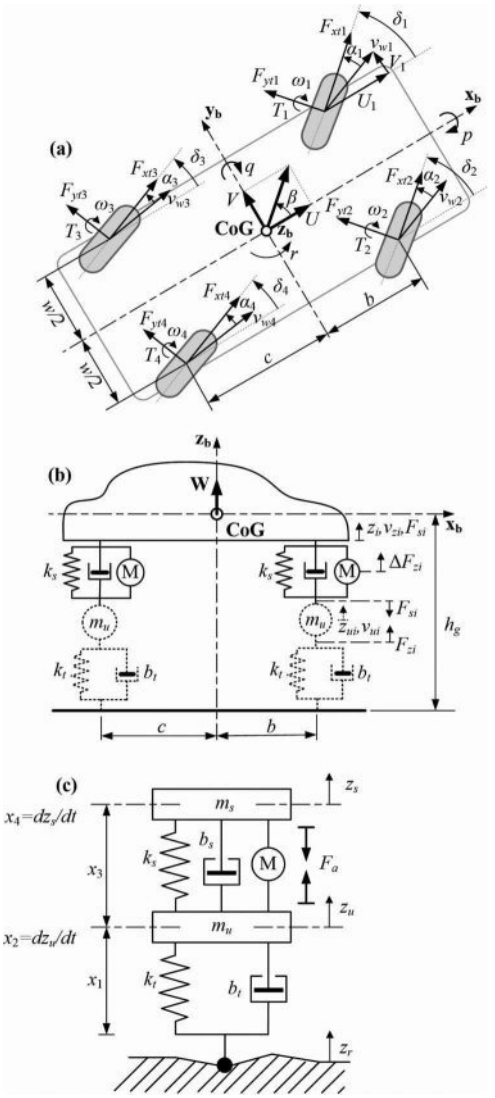


Figure 1. 10 DOF vehicle dynamics model (a, b) and quarter car model (c).

The variable ΔF_{zi} (or F_a in Fig. 1c) represents the FAS control input to be optimized along with other control inputs such as $\Delta\delta_1 = \Delta\delta_2$ (for active front steering, AFS) and T_i (for active brakes, ABS).

The tire is described by the 1994 Magic formula combined-slip model, including the relaxation length dynamics for the lateral DOF (Pacejka 2006). The longitudinal and lateral tire forces are scaled by the tire-road friction coefficient μ.

3 BRAKING DISTANCE REDUCTION

Figure 2 shows the vehicle response for a pulse-type μ-split scenario, where the FAS and brake control inputs ΔF_{zi} and $T_i, i = 1,\ldots,4$, are optimized. The FAS provides a load boost on those tires that experience the high-μ condition (first front, F_{zf}, and then rear tires, F_{zr}). This results in a boost of the longitudinal deceleration $-a_x$, and finally in reduction of the braking distance by 5.1% (on the given, fixed time horizon).

The side effects of FAS action include excitation of vehicle heave and pitch dynamics. This results in the long stroke of heave Z (approx. +/− 10 cm, which is closely related to the suspension stroke constraint of the same amount) and the heave acceleration peak of 0.69 g. The pitch angle response θ includes some more oscillatory content as the results of FAS action.

In order to produce a strong tire load boost during the high-μ period and at the same time satisfy the suspension stroke constraint, the FAS relaxes the tire load immediately before and after the high-μ interval (see F_{zf} and F_{zr}). These tire load holes have a weaker effect on the deceleration than the load boost, because they occur during the low-μ intervals.

The analysis is extended in (Čorić et al. 2017) for other μ-scenarios. The braking distance reduction is lower for the step-type μ-split case (around 2% for the same μ and time horizon values) and very low for the constant-μ scenario (0.5%). In the latter case, the performance gain is higher (around 2%) if the ABS actuator bandwidth is lower than the FAS bandwidth. This is because the FAS can boost the tire load when the braking torque is being settled, while preparing for the boost through generating the tire load hole in the early stage of braking torque transient.

In the split-μ scenario ($\mu_{1,3} = 10\mu_{2,4} = 1$ in the particular case), the FAS again transfers the load to the high-μ tires (left tires in this case), and the braking distance reduction is around 2%. To keep the vehicle moving straight, the optimized active steering input is such to counteract the yaw torque caused by unequal left and right braking forces. Consequently, the chassis roll is induced (towards the high-μ wheels), but, in turn, the heave and pitch motion excitation is minor. Between the high-μ tires, the load is transferred to the non-steered tire, because it has a larger longitudinal force potential according to the friction circle.

The constant-μ scenario has been extended by imposing oscillatory behavior of the longitudinal slip (through an equality constraint), in order to mimic the ABS-inherent limit-cycle behavior. The optimized FAS action is such to increase the tire load in the wheel torque peak periods, thus resulting in a higher tire friction potential in those periods, and finally boosted deceleration. This is in accordance with the FAS+ABS control strategy proposed by Alleyne (1997).

4 HANDLING CONTROL - STABILIZATION

Figure 3 shows the optimization results for the sine-with-dwell maneuver, where details of the optimization problem formulation are given in (Čorić et al. 2017). A typical, though, simplified feedback ESC strategy predominantly brakes the outer front wheel (F_{x1}) to generate an oversteer compensation (OSC)

www.TechnicalBooksPDF.com

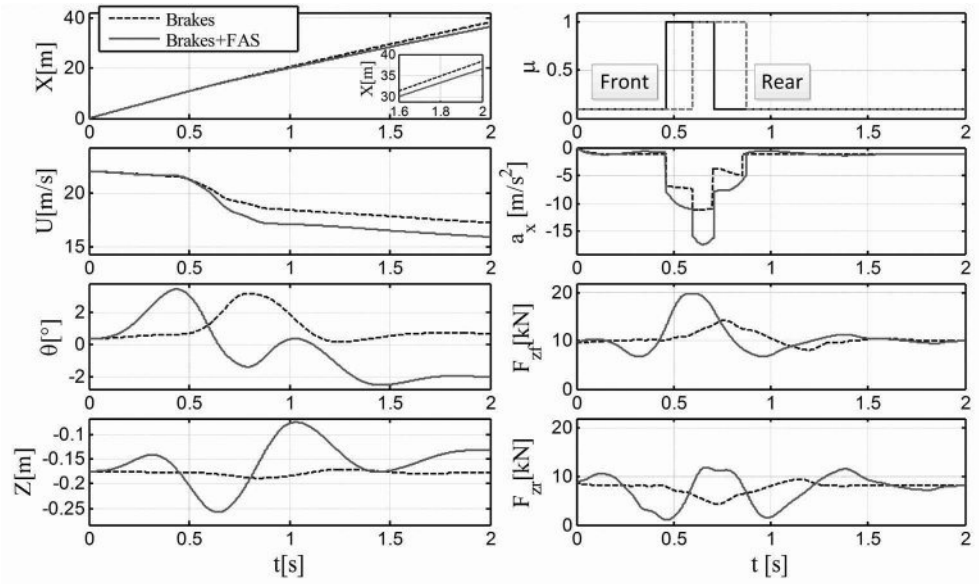


Figure 2. Comparative Brakes and FAS + Brakes optimisation results for pulse-type μ-split scenario.

component of the yaw torque M_z and stabilize the vehicle. The OSC action is emphasized in the interval around $t = 1$ s in order to suppress the excursion of sideslip angle β (stabilization effect), as well as around $t = 2$ s (but to a lower extent).

According to the sine-with-dwell ESC test formulation (FMVSS 2007), the FAS control action was optimized with the objective of minimizing the yaw rate error $r_{err} = r_R - r$ (r_R = reference model output), while maximizing the lateral displacement peak max(Y) for a favorable responsiveness. The ESC+FAS optimization results in Figure 3 point to a significant yaw rate error reduction (45% lower yaw rate RMS error) and also β-peak reduction (a wider stability margin). This is achieved by two distinct actions: (i) the total tire load boost (see ΣF_{zi} around $t = 0.7$ s and $t = 1.3$ s) that increases the lateral acceleration a_y over its saturation level for improved handling, and (ii) transfer of load from front to rear tires to generate OSC yaw torque (see F_{zf} and F_{zr} around $t =$ 0.65 s and $t = 1.9$ s). As side effects, the former excites significant heave motion (the heave acceleration peak of 0.38 g), while the latter causes notable pitch angle magnitudes (θ). The lateral displacement Y (i.e. the responsiveness) remains largely unaffected. However, the agility is notably improved in the case of integrated control ($U(t_f)$ is higher, $t_f = 4$ s), because the ESC system uses the brakes to a lower extent than in the ESC-only case (see $F_{x1}, \ldots, F_{x4}$).

Since the optimization is inherently conducted over the full time window (full-horizon preview is available), the comparison between the optimized FAS control action and the causal ESC action (no preview) is strictly speaking unfair. To provide a more faithful comparison between the FAS and ESC systems control authorities, the same optimization approach has been applied in the FAS-only case (ΔF_{zi} inputs are optimized) and active brake-only case (T_i inputs are optimized). The results given in (Čorić et al. 2017) show that the optimized FAS and active brake systems give comparable yaw rate RMS errors. The advantages of FAS control include improved responsiveness (by 17%) and agility (by 70%) since the brakes are not used, while the disadvantages are related to emphasized heave accelerations (0.5 g vs. 0.04 g) and also pitch angle magnitudes (3.4° vs. 2°).

5 HANDLING CONTROL – PATH FOLLOWING

A path following minimization objective has been used along a double lane change maneuver (DLC) to further investigate the FAS control authority, particularly under the conditions of understeer behavior (with respect to reference trajectory). The problem formulation and results for a wide range of actuator configurations and three maneuver types are described in detail in (Čorić 2016b).

Figure 4 shows the optimization results for the worst-case maneuver 3. The reference response corresponds to the passive vehicle for $\mu = 1$, zero driveline torque, and optimized driver steering input. The achieved vehicle path $Y(X)$ is used as the reference path for other cases presented in the same figure, where the same driver steering input is applied, but for the reduced tire-road friction coefficient $\mu = 0.6$ and the driveline torque of 250 Nm. Under these condition the passive vehicle ('No control' case) becomes unstable (see β). The optimized active front steering

www.TechnicalBooksPDF.com

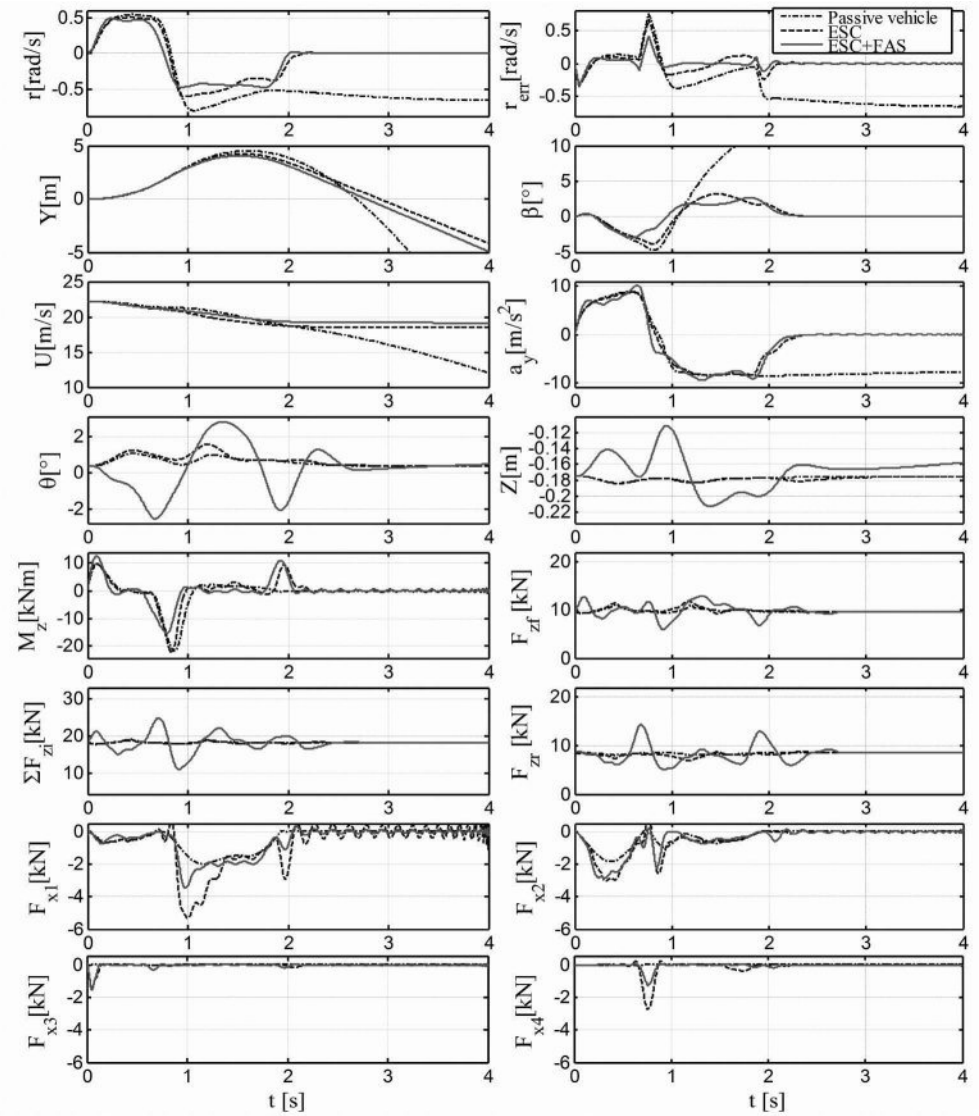


Figure 3. Comparative FAS + ESC optimization results for sine-with-dwell maneuver, including comparison with passive vehicle and ESC-only cases.

(AFS) control stabilizes the vehicle and provides an accurate path following.

The path following RMS error is further reduced (by 30%) when the integrated FAS + ARS control is applied. Since the AFS has a large control authority over the lateral vehicle dynamics, the FAS action is focused on the effect of boosting the total tire load (ΣF_{zi}) and, thus, the lateral acceleration a_y in the critical intervals (when the lateral acceleration is saturated, i.e. the friction potential limit is reached). The FAS, though, provides a certain front/rear tire load transfer by strongly unloading the rear axle for understeer compensation (USC) around the intervals of 0.3 s, 1.1 s, and 2.6 s. The side effects of FAS action are again related to excitation of heave and pitch dynamics: the heave acceleration peak is 0.6 g while the pitch angle amplitude is relatively modest (1°).

Table 1 shows the path following RMS errors [m] for various single- and multi-actuator configurations, and different DLC maneuver types. Maneuver 1 is similar to the already described Maneuver 3, but the driveline torque is set to zero. Maneuver 2 is executed for the non-reduced friction coefficient ($\mu = 1$) like in the reference case, but with a non-zero driveline torque (350 Nm).

The results in Table 1 indicate that the FAS-only control is inferior to the AFS/ARS control, which may appear to be in contrast with the handling control

www.TechnicalBooksPDF.com

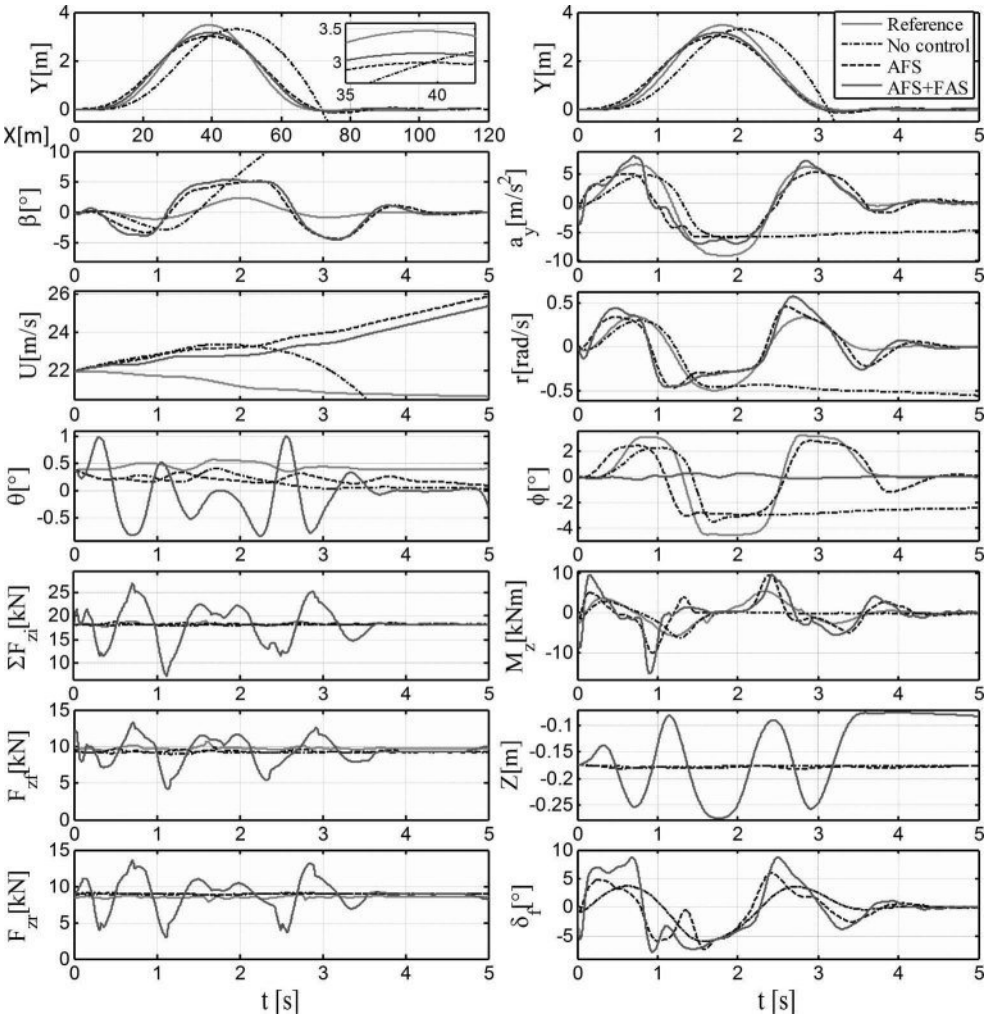


Figure 4. Comparative AFS and FAS + AFS optimization results for double lane change maneuver-type 3 and path following task.

Table 1. Comparative path following RMS error values [m] for different active steering and FAS configurations and different DLC maneuver types.

Maneuver	ARS	FAS	ARS + FAS	AFS	AFS + FAS	4WS	4WS + FAS
1	0.112	0.281	0.077	0.137	0.086	0.091	0.067
2	0.044	0.197	0.025	0.045	0.027	0.030	0.023
3	0.175	0.405	0.141	0.229	0.157	0.163	0.130

results from Section 4, where the FAS was very competitive to active brake control. This is because in the considered control task a strong USC action is required, including the preview action during the initial period when the vehicle moves straight (see $\delta_f = \delta_1 = \delta_2$ in the AFS case in Fig. 4). The fact that the FAS cannot generate lateral tire force in the absence of tire sideslip angle explains its inferiority compared to AFS. Nevertheless, it effectively stabilizes the vehicle and provides relatively accurate path following.

Table 1 further shows that the ARS is more effective then AFS, because it utilizes a driver-untapped lateral force potential of rear tires (Deur et al. 2014). The FAS action is, thus, less effective when integrated with ARS (than with AFS), and it is reduced solely to the unique ability of FAS to boost the total tire

www.TechnicalBooksPDF.com

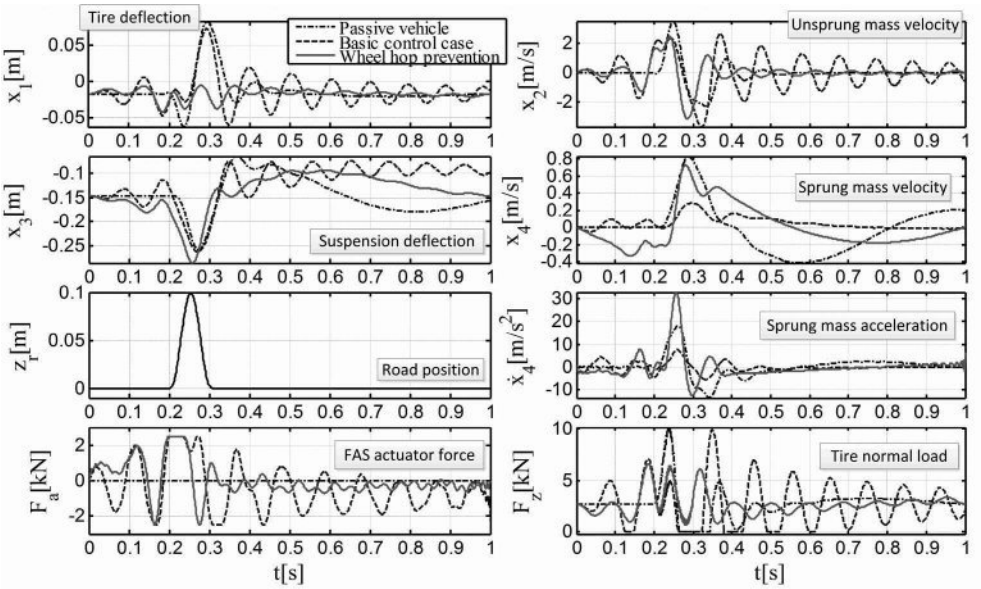


Figure 5. Optimization results for emphasized discrete bump-type road disturbance.

load and the lateral acceleration. This unique control authority explains why the FAS brings more significant improvement to the AFS (in the AFS + FAS configuration) than the ARS does (in the ARS + AFS = 4WS configuration).

There are several other, secondary mechanisms through which the FAS can improve the vehicle handling performance (Čorić 2016b). First, for a throttle-on maneuver and the example of rear-wheel-drive vehicle, the FAS unloads the inner driven tire to increase its longitudinal slip and, thus, weaken its lateral force to provide USC. Next, the FAS can increase the left-right tire load difference on the front axle and make the tire load more balanced on the rear axle, thus generating OSC yaw torque based on the convexity feature of tire lateral force vs. load static curve. Finally, the FAS can provide the vehicle tilting effect as an USC intervention acting through the front-axle bump steer component of the toe effect.

6 RIDE COMFORT CONTROL

This section presents the basic ride comfort optimization results from (Čorić 2016a), which relate to emphasized discrete road bumps and potholes.

The dashed-line blue curves in Figure 5 represent the basic optimization results for the case of high-amplitude bump (10 cm), bump length of 0.1 s, and the bump preview time of 0.2 s (see z_r response). Immediately before the bump occurrence, the FAS generates a positive force F_a, which tends to lift the tire (see x_1 and F_z in Fig. 1c), thus reducing the strong tire-bump impact. Consequently, the sprung mass acceleration dx_4/dt is suppressed when compared to the passive vehicle, thus resulting in better ride comfort. After the wheel hop peak, occurring around $t = 0.3$ s (see x_1), the FAS abruptly reverses its action ($F_a < 0$) to prevent the strong sprung mass (free) fall that would affect the ride comfort. However, such "bang-bang"-like FAS action excites strong oscillations of the system response, which results in residual wheel hops and the related temporary losses of road holding ability ($F_z = 0$). During the bump preview period ($t < 0.2$ s), the FAS prepares for the tire lift action at the leading bump edge by exciting the unsprung mass oscillations with a proper phase angle.

The solid-line red response in Figure 5 corresponds to the case of imposing the lower-limit constraint on the tire normal load ($F_z > 1000$ N). The wheel is prevented from hopping (see x_1 and F_z responses) by generating a strong negative FAS force F_a after the bump peak ($0.3 > t[\text{s}] > 0.25$), which presses the wheel to the ground. However, the reactive force of the same amount F_a acts on the sprung mass (see Fig. 1), thus causing a very strong peak of the sprung mass acceleration and affecting the ride comfort. Therefore, there is an evident trade-off between the ride comfort and road holding ability. It is shown in (Čorić 2016a) that the cost function weighting factor can be tuned so that both ride comfort and road holding indices are notably better than in the passive vehicle case.

The analysis has been extended to the case of full vehicle model (Fig. 1a,b with the unsprung mass dynamics included). It has been found out that there is an additional cross-axle FAS control mechanism, which reduces the total (four-quarter) sprung mass/chassis force variation for improved ride comfort. This mechanism counteracts the anti-wheel-hop peak of suspension force on the active axle (the one exposed to the bump) by means of suspension force reduction on the inactive axle.

www.TechnicalBooksPDF.com

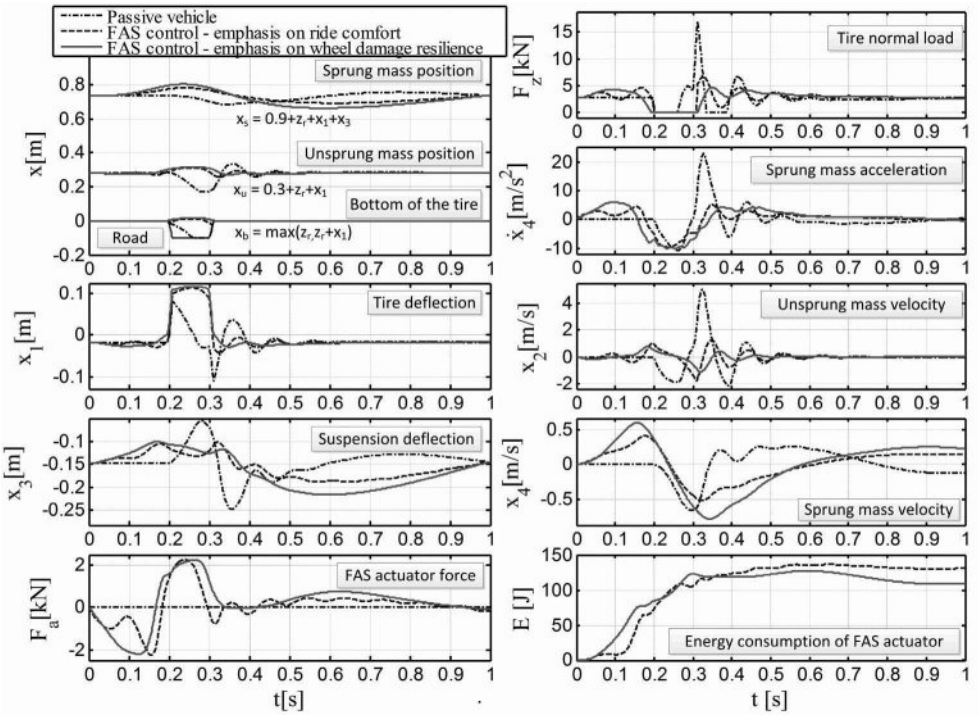


Figure 6. Optimization results for emphasized discrete pothole-type road disturbance of square shape.

Figure 6 shows the optimization results for the case of square-shape pothole with the depth of 0.1 m, length of 0.1 s, and the preview time of 0.2 s (see z_r trace). The cost function includes the terms that penalize ride discomfort, FAS actuator energy consumption, and wheel damage.

Regardless of the cost function tuning, the optimal system behavior is such that the wheel hops over the pothole (see x_b) to prevent the wheel damage on the pothole trailing edge (see x_1 and F_z immediately after $t = 0.3$ s). To effectively prepare for the wheel hop, the FAS first increases the (absolute value of) tire deflection x_1 immediately before the pothole ($F_a < 0$). It then quickly reverses its control action ($F_a > 0$) to lift the wheel near the pothole leading edge ($t \cong 0.2$ s) with some significant hop-off velocity x_2. The response of FAS energy consumption E indicates that the FAS predominantly generates active force ($dE/dt > 0$), where the power peaks equal around 1.5 kW.

The main difference between the two active control responses in Figure 6 is that the wheel entirely hops over the pothole when the emphasis is on damage prevention (solid red curves) compared to the case when the ride comfort is emphasized (dashed blue curves). In the former case, the FAS action F_a is stronger (longer) both in the preview phase ($t < 0.2$ s) and during the pothole period ($0.2 < t$ [s] < 0.3), in order to better prepare for the wheel hop and keep the wheel lifted action when hopping over. The post-pothole peak of the normal tire force F_z is not only lower in that case, but it occurs after the trailing edge, thus reducing further the possibility of wheel damage. However, the ride comfort is reduced (see dx_4/dt) due to the stronger FAS activity before and during the pothole period.

Another cost function tuning case is considered in (Čorić et al. 2016), where the emphasis is on energy consumption. In this case the FAS action is such that it keeps the suspension deflection x_3 constant during the pothole period (and longer), i.e. no power is consumed in that case (as the velocity dx_3/dt is then equal to 0). This results in halving the energy consumption compared to the previous two cases, but the ride comfort or damage resilience is compromised. The case of long pothole is analyzed therein, as well. In that case the optimal behavior includes the phases of (i) wheel landing and traveling over the pothole bottom, and (ii) hopping over the pothole trailing edge.

7 CONCLUSION

The presented control variable optimization study has pointed to the unique control authority of FAS, which relates to boosting the tire load for providing an increased tire friction potential and improved VDC performance. The tire load boost can be applied under conditions of non-uniform tire friction coefficient μ (the load is increased during the high-μ interval, e.g. for improved ABS performance) or during the critical handling/cornering maneuvers (to increase the

www.TechnicalBooksPDF.com

lateral acceleration over its μ-related saturation level and improve the VDC performance without affecting the agility). The VDC performance can also be enhanced by the FAS ability to generate the oversteer compensation- or understeer compensation-yaw torque (by transferring the load to rear or front tires, respectively). There are additional FAS control mechanisms for enhanced VDC, such as those relying on spinning a tire by reducing its load, balancing the left-right tire load on an axle to boost its lateral force, and increasing the steering effort through the bump steer component of the toe effect. Finally, in the case of emphasized discrete road disturbances such as high-amplitude bumps and potholes, a proper (optimal) FAS control action can improve both comfort and road holding performance. Moreover, in the pothole case, the wheel damage can be prevented by forcing it to hop over the pothole.

However, the FAS control action has certain side effect and limitations. The tire load boost and load transfer actions are directly associated with excitation of heave and pitch dynamics, respectively, thus affecting the driving comfort. Due to the limited suspension stroke, a particular FAS action can last only for a relatively short interval. To emphasize the FAS control effect (e.g. the tire load boost) and satisfy the suspension stroke constraint, the FAS action typically includes a preparatory phase during the preview period (e.g. a tire load hole), and is usually succeeded by a similar relaxation phase. This makes the control system development more challenging, as it would require some kind of on-line optimization (e.g. that included within the model predictive control framework), and a preview of critical period of maneuver and/or road disturbance. Another limitation relates to the fact that the FAS cannot influence the tire lateral forces unless the tire is subject of lateral sideslip angle. This affects the effectiveness of understeer compensation, particularly if it is a part of preview control action during the straight driving.

ACKNOWLEDGEMENT

It is gratefully acknowledged that this work has been supported by Ford Motor Company.

REFERENCES

Alleyne A. 1997. Improved vehicle performance using combined suspension and braking forces. *Vehicle System Dynamics* 27(4):235–265.

Čorić M., Deur J., Xu L., Tseng H.E. & Hrovat D. 2016a. Optimization of active suspension control inputs for improved vehicle ride performance. *Vehicle System Dynamics*. doi: 10.1080/00423114.2016.1177655.

Čorić M., Deur J., Kasać J., Tseng H.E. & Hrovat D. 2016b. Optimization of active suspension control inputs for improved vehicle handling performance. *Vehicle System Dynamics*. Accepted.

Čorić M., Deur J., Xu L., Tseng H.E. & Hrovat D. 2017. Optimisation of Active Suspension Control Inputs for Improved Active Safety Systems Performance. *Vehicle System Dynamics*. Submitted.

Deur J., Čorić M., Kasać J., Assadian F. & Hrovat D. 2014. Application of Computational Optimal Control to Vehicle Dynamics. In H. Waschl et. al. (eds.), *Optimization and Optimal Control in Automotive Systems*, pp. 131–145, Cham: Springer.

Edren J., Jonasson M., Jerrelind J. & Stensson Trigell A. 2012. Utilization of vertical loads by optimization for integrated vehicle control. *Proc. of 11th Symposium on Advanced Vehicle Control (AVEC12).* Seoul, Korea.

Edren J., Jonasson M. & Jerrelind J. 2015. Utilisation of optimisation solutions to control active suspension for decreased braking distance. *Vehicle System Dynamics* 53(2):256–273.

. . ., FMVSS No. 126, 2007. *Electronic Stability Control Systems.* National Center for Statistics and Analysis.

Hancock M. 2006. *Vehicle handling control using active differentials.* Ph.D. Thesis, University of Loughborough, UK.

Hrovat D. 1997. Survey of Advanced Suspension Developments and Related Optimal Control Applications. *Automatica* 33(10):1781–1817.

Hrovat D., Tseng H.E, Lu J., Deur J., Assadian F., Borrelli F. & Falcone P. 2011. Vehicle Control. In: Levine W.S. (ed) The Control Handbook: Control System Applications, 2nd edn. Boca Raton: CRC Press.

Pacejka H. B. 2006. *Tyre and vehicle dynamics.* Amsterdam: Elsevier.

www.TechnicalBooksPDF.com

Advanced Vehicle Control – Edelmann, Plöchl & Pfeffer (Eds)
© 2017 Taylor & Francis Group, London, ISBN 978-1-138-02992-7

Energy efficient torque vectoring control

P. Gruber, A. Sorniotti, B. Lenzo, G. De Filippis & S. Fallah
University of Surrey, Guildford, UK

ABSTRACT: Tire forces are at the heart of the dynamic qualities of vehicles. With the advent of electric vehicles the precise and accurate control of the traction and braking forces at the individual wheel becomes a possibility and a reality outside test labs and virtual proving grounds. Benefits of individual wheel torque control, or torque-vectoring, in terms of vehicle dynamics behavior have been well documented in the literature. However, very few studies exist which analyze the individual wheel torque control integrated with vehicle efficiency considerations. This paper focuses on this aspect and discusses the possibilities and benefits of integrated, energy efficient torque vectoring control. Experiments with a four-wheel-drive electric vehicle show that considerable energy savings can be achieved by considering drivetrain and tire power losses through energy efficient torque vectoring control.

1 INTRODUCTION

Typically, by generating different traction/braking forces on the left and right hand sides of a vehicle, a torque-vectoring (TV) controller induces a yaw moment that directly influences the vehicle handling qualities. With the introduction of electric vehicles with multiple motors, the tire forces can be controlled in a precise and accurate way and, importantly, at each wheel of the car. As a result, the system becomes overactuated and the asymmetric torque distribution between the vehicle sides can be achieved in infinite ways. This configuration opens up several development avenues to substantially alter the vehicle characteristics both in terms of cornering behavior and energy efficiency, without changing the mechanical setup. For instance, a large body of literature discusses the possible vehicle dynamics improvements, including active safety and fun-to-drive aspects, that can be achieved through TV control (e.g., Jonasson et al., 2011, Kang et al., 2011), see section 2.1. In recent years, research activities have been extended to explore individual wheel torque control integrated with vehicle efficiency considerations (e.g., Wang et al., 2011, De Novellis et al., 2013, Chen & Wang, 2014, Fujimoto & Harada, 2015), see section 2.2.

This article is an account of the possibilities and benefits of integrated, energy efficient torque vectoring control by presenting and discussing results obtained with the fully electric vehicle (EV) demonstrator of the European Union FP7 projects E-VECTOORC (www.e-vectoorc.eu) and iCOMPOSE (www.i-compose.eu). The EV is a prototype Range Rover Evoque equipped with four identical on-board electric drivetrains, each of them comprising a switched reluctance electric motor (75 kW peak power, 35 kW nominal power, and 80 Nm nominal torque), a single-speed transmission system (10.56:1 gear ratio), constant velocity joints, and a half-shaft (Figs. 1, 2).

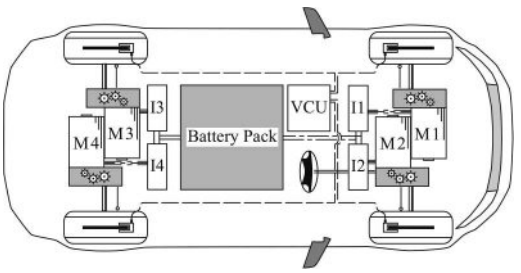


Figure 1. Schematic of the four-wheel-drive architecture of the vehicle demonstrator, where M1-M4 = switched reluctance motor; I1-I4 = inverter; and VCU = vehicle control unit.



Figure 2. Experimental testing of the vehicle demonstrator on the rolling road and at the Lommel proving ground (Belgium).

www.TechnicalBooksPDF.com

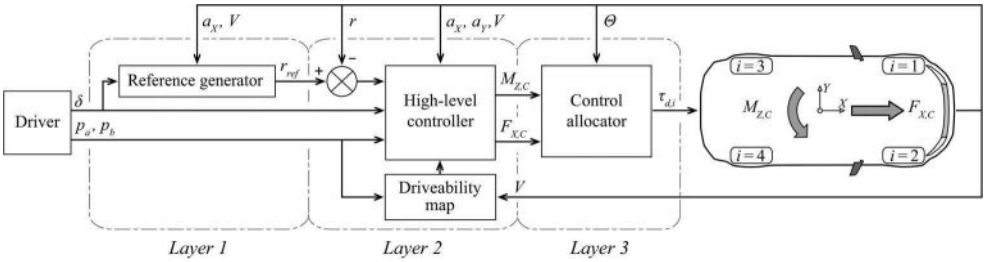


Figure 3. Modular structure of vehicle control system comprising three main layers.

2 TORQUE VECTORING CONTROL

2.1 *Control structure*

To allow easy implementation of the developed vehicle controllers, a modular control architecture has been adopted consisting of three main layers (Fig. 3):

1. In Layer 1, a reference generator defines the target values of the vehicle states (e.g., the reference yaw rate, r_{ref}) based on the driver inputs (steering wheel angle, δ, accelerator and brake pedal positions, p_a and p_b), and the measured/estimated states (e.g., vehicle speed, V, and longitudinal/lateral acceleration, $a_{X/Y}$).
2. A high-level controller is implemented in Layer 2 to determine the overall traction/braking force and yaw moment demands, $F_{X,C}$ and $M_{Z,C}$, to achieve the reference values of the vehicle states.
3. The reference torques, $\tau_{d,i}$, for the individual wheels corresponding to the values $F_{X,C}$ and $M_{Z,C}$ are computed in the Layer 3 by a low-level controller, i.e., the Control allocator. Θ is the vector of parameters (e.g., V) required for the calculation of the optimal wheel torque distribution.

For the experimental tests, the developed vehicle controllers were implemented on a dSPACE AutoBox system (VCU in Fig. 2) and the signals were transmitted through CAN.

2.2 *Vehicle dynamics enhancement*

Torque-vectoring allows enhancing the handling qualities of a vehicle well beyond the capabilities achievable with current conventional stability control systems (van Zanten et al., 1995) as the controller interventions can be seamlessly and continuously generated without variation of the net traction force (De Novellis et al., 2015a). In particular, the controlled distribution of the traction and braking torques among the wheels allows the design of the steady-state and transient cornering responses of the vehicle (De Novellis et al., 2012) and, thus, the creation of fundamentally different driving modes. For example, a model-based design procedure is used in De Novellis et al. (2015b) to define sets of vehicle understeer characteristics at different longitudinal accelerations and the corresponding reference yaw rates (implemented in Layer 1, section 2.1.) that

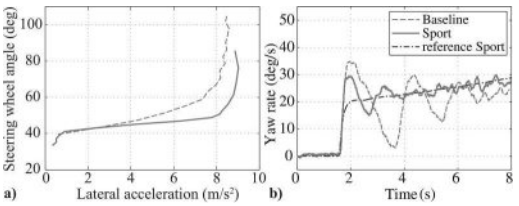


Figure 4. a) experimental understeer characteristics for the passive vehicle ("Baseline") and the active vehicle in "Sport" mode achieved during skid-pad tests. b) yaw rate response of the passive vehicle and the controlled vehicle (including reference yaw rate) during step steer tests with 100 deg of steering wheel angle amplitude at 100 km/h.

yield a sporty vehicle cornering behavior. That is, a Sport mode was designed to reduce the understeer gradient, extend the region of linear vehicle operation, and significantly increase the maximum lateral acceleration compared to the passive vehicle (Fig. 4a). The active safety benefits of the TV controller during highly-transient maneuvers are highlighted by the time history of the measured yaw rate during an extreme step steer test. Figure 4b shows that the controller allows a considerable reduction of the yaw rate oscillations and settling time. Hence, the vehicle behavior is more consistent and predictable so that driving in extreme conditions becomes easier.

In order to exploit the full benefits of TV control in a safe way in all possible driving conditions the road friction conditions need to be known or, at least, reasonably well estimated. Unfortunately, this is not a trivial task. As an alternative, the torque-vectoring algorithm can be coupled with sideslip control to create a more robust controller that shows consistent and safe performance nearly independent of the prevailing friction conditions (Lu et al., 2016). Also, the concurrent yaw rate and sideslip controller allows the vehicle to operate at specified sideslip angles to enhance active safety (Fig. 5). Conversely, the controller could be used to create a drift mode to improve the fun-to-drive aspect.

2.3 *Energy-efficiency improvement*

Owing to the actuation redundancy of EVs with multiple motors, TV control can be used to minimize the

www.TechnicalBooksPDF.com

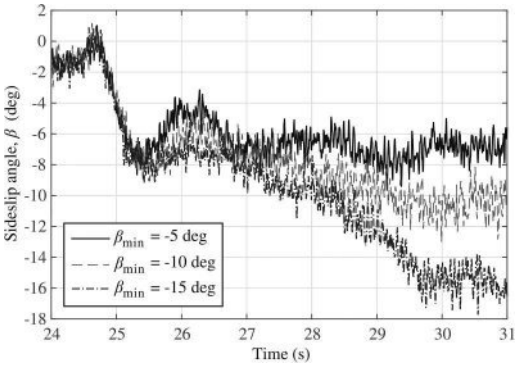


Figure 5. Vehicle sideslip angle during step steer tests with 100 deg of steering wheel angle amplitude at 90 km/h with three different predefined sideslip limits $\beta_{\min}$ (Lu et al., 2016).

overall energy consumption without compromising vehicle dynamics characteristics. In particular, power losses in the drivetrain and due to tire slips (which become significant at high acceleration levels) are major sources of energy consumption that can be influenced by the individual wheel torque control (Tjønnas et al., 2010, Chen & Wang, 2012, Pennycott et al., 2014). Considering the capabilities of the TV controller, the energy-efficiency can be improved in two ways:

– by distributing the traction/braking force and yaw moment demands of the high-level controller (section 2.1, Layer 2) among the wheels according to specific energy efficient control allocation (CA) strategies (section 2.1, Layer 3), see section 3.
– by defining reference understeer characteristics (section 2.1, Layer 1) that minimize energy losses, provided that vehicle handling behavior may be influenced, see section 4.

The combination of both ways is possible and should maximize the energy savings benefits of torque-vectoring control.

3 ENERGY EFFICIENT CONTROL ALLOCATION

The energy efficient CA strategy implemented on the case study EV was developed based on measurements of the drivetrain power losses obtained on a rolling road facility. The power losses were determined from the difference between the measured electrical power at the inverter and the measured mechanical power at the roller of the test bench so that the results include the losses in the electric motor drive, mechanical transmission, tire rolling resistance and tire slip on the roller. Figure 6 shows that the drivetrain power loss characteristics are strictly monotonically increasing functions of wheel torque with a single inflection point and vary with vehicle speed. Based on this observation,

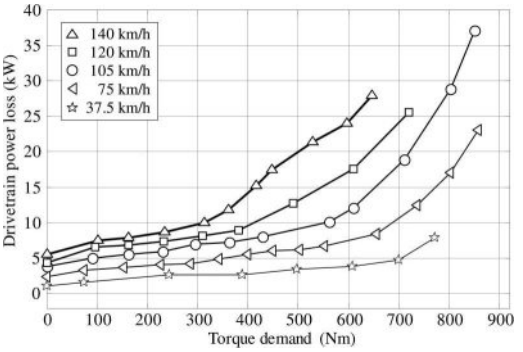


Figure 6. Measured power loss characteristics of a single electric drivetrain of the case study EV against torque demand at different vehicle speeds.

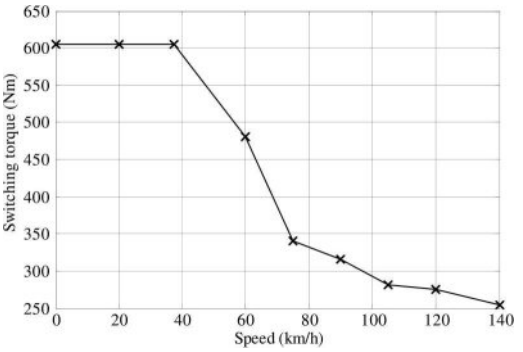


Figure 7. Switching torque for one vehicle side at different vehicle speeds.

a simple, computationally efficient torque distribution strategy for energy minimization is possible.

By assuming small steering angles and considering the basic vehicle geometry, the wheel torque distribution problem can be simplified by treating the two vehicle sides independently (Pennycott et al., 2014). That is, the torque demands corresponding to $F_{X,C}$ and $M_{Z,C}$ (section 2.1, Layer 2) for the left and right hand sides of the vehicle are given by:

$$\tau_{d,L/R} = \frac{1}{2}\left(F_X^C \mp \frac{M_Z^C}{d}\right)R \tag{1}$$

where d = half-track; and R = the wheel radius.

Using Equation (1), the developed energy efficient CA strategy (see details in Dizqah et al., 2016) employs a single drivetrain on each side of the vehicle when the respective torque demand on the left/right vehicle side ($\tau_{d,L/R}$) is lower than a specified switching value $\tau_{d,SW}$. Conversely, if the side torque demand is greater than $\tau_{d,SW}$ an even front-to-rear torque ratio on the particular side is used. To guard against drivability issues, the transition between the two torque distribution cases is smoothened with a sigmoid function.

The switching torque (Fig. 7) can be obtained offline by considering that the drivetrains of the case study

www.TechnicalBooksPDF.com

Table 1. Energy consumption along driving cycles.

	Energy consumption (kWh)			CA w.r.t. (%)	
Driving cycle	SA	ED	CA	SA	ED
NEDC	2.932	3.031	2.923	0.31	3.56
EUDC, 8% slope	5.838	5.739	5.716	2.09	0.40
SDDC	1.136	1.141	1.103	2.90	3.33

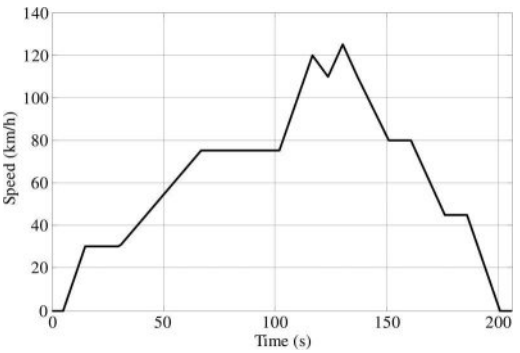


Figure 8. Speed profile of the SDDC.

EV have equal power losses P_{loss}. Then, $\tau_{d,SW}$ is found from the condition when the power loss of using only a single drivetrain is equal to the power loss of using an even distribution:

$$P_{loss}\,(\tau_{d,SW}, \boldsymbol{\Theta}) + P_{loss}\,(0, \boldsymbol{\Theta}) = 2P_{loss}\,(0.5\,\tau_{d,SW}, \boldsymbol{\Theta}) \quad (2)$$

The CA was experimentally tested on the vehicle demonstrator by completing different driving cycles on the rolling road and comparing the results with tests of the EV set up with either front-wheel-drive (Single Axle, SA) or four-wheel-drive (Even Distribution, ED) with constant 50:50 front-to-rear wheel torque distribution. The tested driving cycles included the New European Driving Cycle (NEDC) to simulate low to medium driving loads, and the Extra Urban Driving Cycle (EUDC) run with an emulated uphill constant road slope of 8% to replicate medium to high driving loads. For both driving cycles, the CA strategy yields the lowest energy consumption, see Table 1. In terms of the NEDC, the potential energy improvement of the CA is rather small (<1%) with respect to the SA mode, whereas substantial improvements (>2.9%) are achieved compared to the ED mode.

This behavior can primarily be ascribed to the relatively low drive torque required during the NEDC compared to the motor torque available on the case study EV, so that $\tau_{d,L/R} < \tau_{d,SW}$ is often true and the SA mode is close to being the most efficient torque distribution. This observation is confirmed by the greater energy savings achieved relative to the ED mode, and by the reversed trend for the EUDC with 8% slope, which requires a greater drive torque. In other words, an electric vehicle with less powerful drivetrains would show benefits more clearly in the two driving cycles. Thus, to emphasize the effect of the CA on energy consumption, a new driving cycle was created, it is called the Surrey Designed Driving Cycle (SDDC), see Figure 8. Over the SDDC, the CA algorithm is significantly better than the SA and ED modes, improving energy efficiency by 2.9% and 3.3%, respectively.

The concept of the simple, yet effective CA formulation is also valid during cornering and allows the car to operated with 2, 3 or 4 active motors. Tests of running the car at constant radius and velocity on a skid-pad showed energy consumption improvements of up to ~4% compared to the ED mode.

4 ENERGY EFFICIENT REFERENCE UNDERSTEER CHARACTERISTIC

To study the influence of understeer characteristics on energy consumption, experimental skidpad tests (60 m radius) were carried out with the EV at four lateral accelerations (a_Y: ~2, 4, 6 and 8 m/s^2) and different handling settings, while the overall drivetrain power P was calculated from the product of the voltage and current measured at the battery. The EV handling settings were achieved with an even front-to-rear torque distribution on each vehicle side and by changing the yaw moment demand of the TV controller. In this way, the EV was run with eleven different understeer characteristics – one of the passive vehicle (denoted as PV), five characteristics with progressively increasing understeer (denoted as U1 to U5) and five characteristics with progressively decreasing understeer (denoted as O1 to O5) with respect to the passive vehicle (Fig. 9a). The yaw moments corresponding to the different understeer characteristics are shown in Figure 9b. Positive yaw moments yield a destabilizing control action (reducing understeer) and negative yaw moments generate a stabilizing effect (increasing understeer).

For ease of comparison, the measured drivetrain power is expressed relative to the power required by the vehicle set up with the most energy efficient understeer characteristic, which is given by the steering wheel angle that minimizes P for a particular lateral acceleration.

As indicated by Figure 10a, the optimal handling characteristic is achieved by reducing understeer compared to the passive vehicle. In particular, the most energy efficient cornering behavior is close to neutral steering, which is typically associated with sports car characteristics and, thus, can be assumed to also enhance active safety and fun-to-drive aspects (see section 2.2). Over the measured lateral acceleration range, the optimal understeer characteristic allows energy savings of up to ~11% compared to the passive vehicle. This potential saving is considerably greater than the improvements achievable with the CA algorithm (see section 3). Also, it is expected that running the

www.TechnicalBooksPDF.com

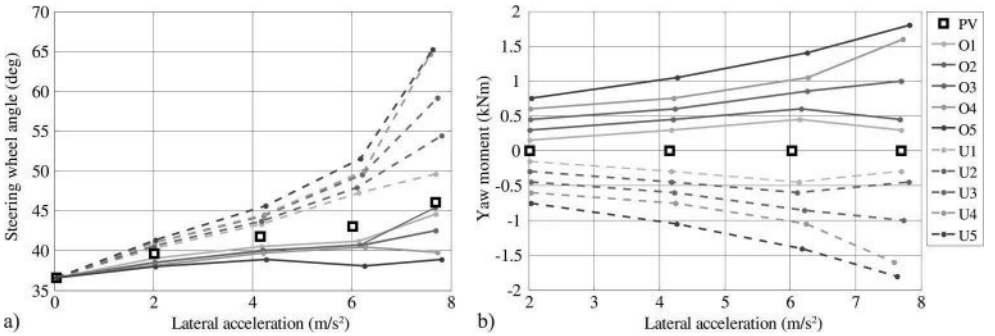


Figure 9. a) The experimentally measured understeer characteristics with different reference yaw moment settings. b) Reference yaw moment as a function of lateral acceleration for different understeer characteristics. The open black squares indicate the passive vehicle.

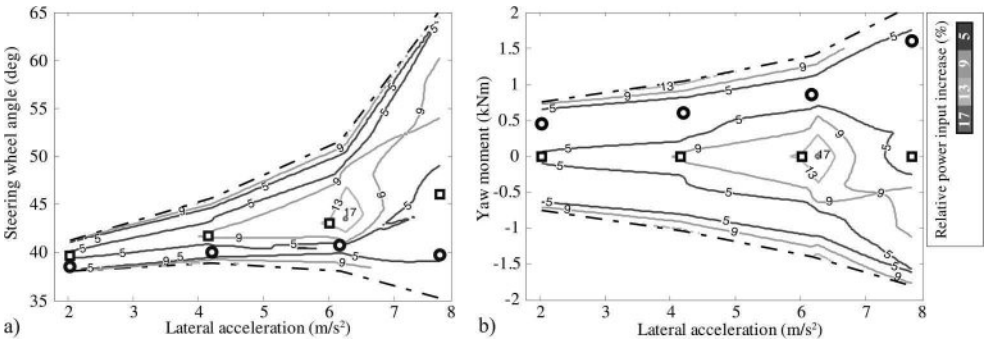


Figure 10. a) Map of understeer characteristics with iso-contour lines of relative drivetrain power increase with respect to the vehicle with the optimal understeer characteristic (indicated by black open circles). The passive vehicle understeer characteristic is shown by the black open squares and the boundaries of the measured region are indicated by the dash-dotted lines. b) Map of yaw moments with iso-contour lines of relative drivetrain power increase with respect to vehicle with optimal understeer characteristic. The optimum yaw moment is indicated by black open circles. The passive vehicle yaw moment is shown by the black open squares and the boundaries of the measured region are indicated by the dash-dotted lines.

vehicle with the CA algorithm and the optimal understeer gradient should yield further energy efficiency improvements.

Corresponding to Figure 10a, Figure 10b shows the relative power input increase contours as functions of yaw moment and lateral acceleration. As expected, to achieve the almost neutral steering behavior, the optimum yaw moment is always positive and monotonically increasing with a_Y. Interestingly, the relative power contours are nearly symmetric about the x-axis. Current work is concerned with this aspect.

5 CONCLUSIONS

The experimental work allows the following conclusions:

– Torque vectoring control is effective in improving energy efficiency by reducing power losses associated with the drivetrain and tires.
– The energy efficient CA algorithm allows energy savings typically between 2% and 3% along driving cycles and up to ∼4% during cornering conditions with respect to fixed torque distribution strategies.
– The optimal understeer characteristic in terms of energy efficiency is close to the condition of neutral steering for the specific electric vehicle.
– The energy efficient reference cornering response reduces measured input power by up to ∼11% for the case study vehicle demonstrator.

REFERENCES

Chen, Y., Wang, J. 2012. Fast and global optimal energy efficient control allocation with applications to overactuated electric ground vehicles. *IEEE Transactions Control Systems Technology* 20(5): 1202–1211.

Chen, Y., Wang, J., 2014. Adaptive energy-efficient control allocation for planar motion control of over-actuated electric ground vehicles. *IEEE Transactions Control Systems Technology* 22(4): 1362–1373.

De Novellis, L., Sorniotti, A., Gruber, P., Ivanov, V., Hoepping, K. 2012. Torque vectoring control for electric vehicles with individually controlled motors: state-of-the-art and future developments. In: *26th International Electric Vehicle Symposium (EVS26)*, *Los Angeles 6–9 May 2012*.

www.TechnicalBooksPDF.com

De Novellis, L., Sorniotti, A., Gruber, P. 2013. Optimal wheel torque distribution for a four-wheel-drive fully electric vehicle. *SAE International Journal of Passenger Cars* 6(1): 128–136.

De Novellis, L., Sorniotti, A., Gruber, P., Orus, J., Rodriguez Fortun, J.M., Theunissen, J., De Smet, J. 2015a. Direct yaw moment control actuated through electric drivetrains and friction brakes: theoretical design and experimental assessment. *Mechatronics* 26: 1–15.

De Novellis, L., Sorniotti, A., Gruber, P. 2015b. Driving modes for designing the cornering response of fully electric vehicles with multiple motors. *Mechanical Systems and Signal Processing*, 64–65: 1–15.

Dizqah, A. M., Lenzo, B., Sorniotti, A., Gruber, P., Fallah, S., De Smet, J. 2016. A Fast and Parametric Torque Distribution Strategy for Four-Wheel-Drive Energy Efficient Electric Vehicles. *IEEE Transactions on Industrial Electronics* 63: 4367–4376.

Fujimoto, H., Harada, S. 2015. Model-based range extension control system for electric vehicles with front and rear driving-braking force distributions. *IEEE Transactions on Industrial Electronics* 62(5): 3245–3254.

Jonasson, M., Andreasson, J., Solyom, S., Jacobson, B., Stensson Trigell, A. 2011. Utilization of actuators to improve vehicle stability at the limit: from hydraulic brakes toward electric propulsion. *Journal of Dynamic Systems, Measurement, and Control* 133(5): 051003.

Kang, J., Yoo, J., Yi, K. 2011. Driving control algorithm for maneuverability, lateral stability, and rollover prevention of 4WD electric vehicles with independently driven front and rear wheels. *IEEE Transactions on Vehicular Technology* 60(7): 2987–3001.

Lu, Q., Gentile, P., Tota, A., Sorniotti. A., Gruber, P., Costamagna, F., DeSmet, J. 2016. Enhancing vehicle cornering limit through sideslip and yaw rate control. *Mechanical Systems and Signal Processing* 75: 455–472.

Pennycott, A., De Novellis, L., Sabbatini, A., Gruber, P., Sorniotti A. 2014. Reducing the Motor Power Losses of a Four-Wheel Drive Fully Electric Vehicle via Wheel Torque Allocation. *Proceedings of the Institution of Mechanical Engineers, Part D: Journal of Automobile Engineering* 228(7): 830–839.

Tjønnas, J., Johansen, T.A. 2010. Stabilization of automotive vehicles using active steering and adaptive brake control allocation. *IEEE Transactions Control Systems Technology* 18(3): 545–558.

van Zanten, A., Erhardt, R., Pfaff, G. 1995. VDC, the Vehicle Dynamics Control System of Bosch. *SAE Technical paper* 950749.

Wang, R., Chen, Y., Feng, D., Huang, X., Wang, J. 2011. Development and performance characterization of an electric ground vehicle with independently actuated in-wheel motors, *Journal of Power Sources* 196: 3962–3971.

www.TechnicalBooksPDF.com

Advanced Vehicle Control – Edelmann, Plöchl & Pfeffer (Eds)
© 2017 Taylor & Francis Group, London, ISBN 978-1-138-02992-7

Steering redundancy for self-driving vehicles using differential braking

M. Jonasson
Volvo Cars, Active Safety and Vehicle Dynamics Functions, Gothenburg, Sweden
The Royal Institute of Technology (KTH), Vehicle Dynamics,
Department of Aeronautical and Vehicle Engineering, Stockholm, Sweden

M. Thor
Volvo Cars, Active Safety and Vehicle Dynamics Functions, Gothenburg, Sweden

ABSTRACT: This paper describes how differential braking can be used to turn a vehicle in the context of providing fail-operational control for self-driving vehicles. A vehicle model is developed with differential brake and steering inputs. The model is used to explain the bounds of curvature that differential braking provides and it is then validated with measurements in a test vehicle. Particular focus is paid on wheel suspension effects that significantly influence the obtained curvature. Finally, a model based controller is developed to control the curvature by differential braking. The controller is designed to compensate for the wheel angle disturbance that is introduced as a result of the control event.

1 INTRODUCTION

One of the goals of safety-critical systems is that a fault should not result in system failures. Since a self-driving vehicle isn't driven by a human driver, fail-operational ability must be inherent in the control design of the vehicle. Potential risks, addressed in this paper, are faults leading to failures with no steering capacity due to for example steering actuator faults, power blackout, communication shut down etc. Those risks could, if the design is not fail-operational, lead to a failure and a hazard threatening the passengers safety. During, and directly after, a fault occurs, the vehicle should be able to be controlled into a safe state which is often terminated by a full stop.

This work contains an analysis of the temporary use of differential braking to regain control of the vehicle in case of faults. Differential braking used for cornering is described in e.g. (Pilutti, Ulsoy, & Hrovat 1998, Moshchuk & et al. 2013). Few descriptions are however found in the literature of how wheel suspension geometry influences the curvature response during differential braking and analysis from experiments in real world vehicles are rare.

The outline is as follows; Section 2 describes the underlying problem that seeks a solution by differential braking and Section 3 describes the vehicle model that will be used throughout the paper. The model is validated by making comparisons of measurement data from a test vehicle. In Section 4 the vehicle model is used to calculate the maximum curvature that is possible to obtain during differential braking at steady-state. The differential braking generates longitudinal tyre forces, and together with the wheel suspension geometry, a steering alignment torque is induced. Section 5 discusses the scrub radius geometry and how it contributes the resulting curvature. Two different alignments of scrub-radius is experimentally tested by experiments and evaluated. In Section 6 a differential braking curvature controller is developed. The controller is developed to compensate for front wheel angle disturbance induced by the differential braking.

2 VEHICLE AND PROBLEM DESCRIPTION

The vehicle in this work is a conventional passenger car with front axle drive and steering. The mechanical steering system is provided with a steering actuator, mentioned to as Electric Power Assisted Steering (EPAS), which overlay an additive steering torque. Moreover, the vehicle has a friction brake system where brake torque can be applied at each wheel. See Table 1 for vehicle data.

One special case of a steering capacity failure is when the torque from the steering actuator completely disappears. At the same time, the driver is assumed to not take part in controlling the vehicle and is not applying any steering-wheel torque. To simulate the vehicle dynamic behavior after such a fault, an experiment has been done where the steering torque was forced to zero in a curve at 70 km/h. As illustrated in Figure 1, the vehicle will quickly leave the orbital motion and departure the road. The caster and pneumatic trail will generate a wheel alignment torque, which will turn the steering-wheel angle (SWA) to zero within approximately 0.8 s.

www.TechnicalBooksPDF.com

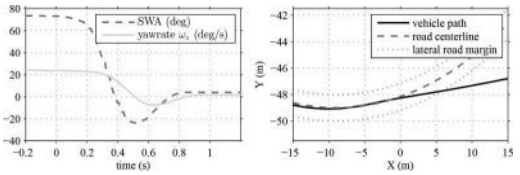


Figure 1. Fault insertion in the steering system.

To cope with the problem described above, i.e follow the desired path without lateral tracking error after a steering capacity failure, the work in this paper addresses the use of differential braking to control the path. The approach in this paper is to apply braking along one side of the vehicle to control the curvature. Since differential braking will influence the total longitudinal tractive force, they are coupled. It is for example not possible to maximize yaw torque and total brake force at the same time. The vehicle speed control is not part of the paper.

3 VEHICLE MODEL

3.1 *Vehicle model description*

The well-established bicycle model with front steering input and constant vehicle speed assumption is here complemented with longitudinal tyre forces. See for example (Rajamani 2012, Pilutti, Ulsoy, & Hrovat 1998) for a similar derivation. The longitudinal tyre forces are assumed to be small and limited to not influence lateral axle forces through combined slip. The model has lateral velocity v_y and yawrate ω_z as states and is described by the lateral force and yaw torque equilibrium equations;

$$m(\dot{v}_y+v_x\omega_z) = -(f_x^{FL}+f_x^{FR})\sin(\delta_f)+ (f_y^{FL}+f_y^{FR})\cos(\delta_f)+f_y^{RL}+f_y^{RR} \quad (1)$$

$$J_z\dot{\omega}_z = (f_y^{FL}-f_y^{FR})\sin(\delta_f)\frac{w}{2}+(f_y^{FL}+f_y^{FR})\cos(\delta_f)l_f - (f_y^{RL}+f_y^{RL})l_r-(f_x^{FL}+f_x^{FR})\sin(\delta_f)l_f+ (f_x^{FL}-f_x^{FR})\cos(\delta_f)\frac{w}{2}+(f_x^{RL}-f_x^{RR})\frac{w}{2} \quad (2)$$

where δ_f is the front wheel angle and v_x is the vehicle longitudinal speed. The vehicle has a mass m and yaw inertia J_z. The lateral distance from center of gravity (CoG) to front respectively rear axle are denoted l_f and l_r. Track width is denoted w. The lateral tyre forces f_y^i and longitudinal tyre forces f_x^i with $i=\{FL,FR,RL,RR\}$ are defined according to Figure 2.

The Equations 1 and 2 will now be re-formulated by assuming a small front steering angle by using $\sin(\delta_f)=0$ and $\cos(\delta_f)=1$, merging lateral tyre

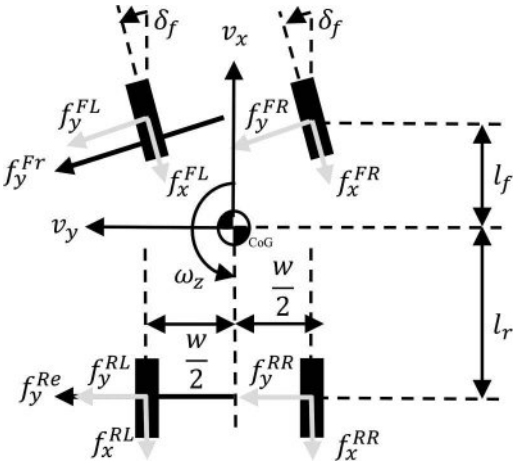


Figure 2. Vehicle model.

forces to lateral axle forces, f_y^{Fr} and f_y^{Re}, and by introducing a differential brake force F_b;

$$m(\dot{v}_y+v_x\omega_z) = f_y^{Fr}+f_y^{Re} \quad (3)$$

$$J_z\dot{\omega}_z = f_y^{Fr}l_f - f_y^{Re}l_r + F_b\frac{w}{2} \quad (4)$$

where the axle forces are defined

$$f_y^{Fr} = f_y^{FL}+f_y^{FR}, \quad f_y^{Re} = f_y^{RL}+f_y^{RR} \quad (5)$$

and where the virtual differential brake control signal F_b has been introduced such that

$$F_b = f_x^{FL}+f_x^{RL}-f_x^{FR}-f_x^{RR} \quad (6)$$

The tyre characteristics are assumed to be linear and tyre side-slip α_f and α_r to be small such that

$$f_y^{Fr} = -C_f\alpha_f = -C_f\left(\frac{v_y+l_f\omega_z}{v_x}-\delta_f\right) \quad (7)$$

$$f_y^{Re} = -C_r\alpha_r = -C_r\left(\frac{v_y-l_r\omega_z}{v_x}\right), \quad (8)$$

where the front and rear axle cornering stiffness C_f and C_r are parameters.

Further on, actuator dynamics, dead time and tyre relaxation are all lumped into first order systems with a time constant T_b for differential braking and T_s for steering.

$$\dot{F}_b = -\frac{1}{T_b}F_b+\frac{1}{T_b}F_b^{\text{req}}, \quad \dot{\delta}_f = -\frac{1}{T_s}\delta_f+\frac{1}{T_s}\delta_f^{\text{req}}, \quad (9)$$

where F_b^{req} and δ_f^{req} are actuator requests.

A vehicle's curvature is in general defined as

$$\rho = \frac{\omega_z+\dot{\beta}}{v_x}, \quad \beta = \arctan\left(\frac{v_y}{v_x}\right), \quad (10)$$

www.TechnicalBooksPDF.com

but for simplicity we will however here define the curvature with $\dot{\beta}$ neglected and for the calculation of curvature $\dot{\beta}$ is approximated to zero across the paper.

Selecting the state vector x and input vector u such that

$$x = \begin{bmatrix} v_y \\ \omega_z \\ \delta_f \\ F_b \end{bmatrix}, \quad u = \begin{bmatrix} \delta_f^{\text{req}} \\ F_b^{\text{req}} \end{bmatrix}, \quad y = \rho, \tag{11}$$

the complete vehicle model is then expressed in state-space form as

$$\dot{x} = Ax + Bu, \quad y = Cx \tag{12}$$

$$A = \begin{bmatrix} -\frac{C_f+C_r}{mv_x} & \left(-v_x - \frac{l_fC_f - l_rC_r}{mv_x}\right) & \frac{C_f}{m} & 0 \\ -\left(\frac{l_fC_f - l_rC_r}{J_zv_x}\right) & -\left(\frac{l_f^2C_f + l_r^2C_r}{J_zv_x}\right) & \frac{l_fC_f}{J_z} & \frac{w}{2J_z} \\ 0 & 0 & -\frac{1}{T_s} & 0 \\ 0 & 0 & 0 & -\frac{l}{T_b} \end{bmatrix} \tag{13}$$

$$B = \begin{bmatrix} 0 & 0 \\ 0 & 0 \\ \frac{1}{T_s} & 0 \\ 0 & \frac{1}{T_b} \end{bmatrix}, \quad C = \begin{bmatrix} 0 & \frac{1}{v_x} & 0 & 0 \end{bmatrix}. \tag{14}$$

The system in Equation 12 is also described in transfer function form;

$$y = G(s)u \tag{15}$$

$$G(s) = [G_s(s)\, G_p(s)] = C\,(sI - A)^{-1}\,B, \tag{16}$$

where the individual transfer functions from steering and differential braking are

$$\rho = G_s(s)\delta_f^{\text{req}}, \quad G_s(s) = \frac{b_2s^2 + b_1s + b_0}{a_4s^4 + a_3s^3 + \cdots + a_0} \tag{17}$$

$$\rho = G_p(s)F_b^{\text{req}}, \quad G_p(s) = \frac{c_2s^2 + c_1s + c_0}{a_4s^4 + a_3s^3 + \cdots + a_0}, \tag{18}$$

where the polynomial coefficients are vehicle speed dependent (coefficients are listed for 70 km/h in Table 1). At 70 km/h the poles of the systems are positioned in $\{-6.5 \pm 3.2i, -3.3, -10\}$.

3.2 *Vehicle model validation*

A validation test for the vehicle model described by Equation 12 with F_b^{req} as input and ω_z as state for validation has been done at two different vehicle velocities and is shown in Figure 3. The test was conducted by driving straight ahead at constant speed and high friction ($\mu \approx 1.0$) and then, at $t = 0$ s, requesting $F_b^{\text{req}} = \frac{mg}{2}$ N with steering-wheel angle fixed to zero. For the real vehicle test, the steering-wheel angle, vehicle velocity, angular velocities and accelerations were all measured through the CAN bus and filtered by a 30 Hz low pass filter. During the tests of the real vehicle, it was observed that the ABS was partly activated indicating that friction utilization was maximized along the braked side of the car. It is also clear from the lower subplot in Figure 3 that real world vehicle exhibited a linearly decreased speed of approximately 4.5 m/s^2. The yawrate response from the model is however based on constant speed, which explains the deviation of yawrate at the end of the manoeuvre. v_x is not a state in the model since we have here prioritized simplicity of a linear model. Expected model uncertainties are the axle cornering stiffnesses and the friction between brake pad and disc, and also, tyre and road. See Figure 2 for definition of physical entities and Table 1 for values of parameters.

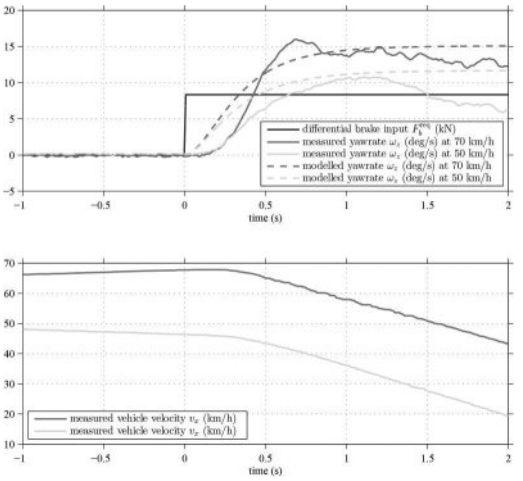


Figure 3. Step response validation test of yawrate with differential brake input at two different vehicle velocities.

4 STEADY-STATE CORNERING CURVATURE

This section is devoted to investigate and quantify the curvature that differential braking provides. By deriving the analytic expression of the filter coefficients $a0$, $b0$ and $c0$ in Equations 17, the steady-state cornering curvature is expressed as

$$\rho = G_s(0)\delta_f^{\text{req}} + G_p(0)F_b^{\text{req}} =$$

$$\frac{C_fC_rL}{C_fC_rL^2 + mv_x^2\,(l_rC_r - l_fC_f)}\delta_f^{\text{req}} +$$

$$\frac{w\,(C_f + C_r)}{2\,(C_fC_rL^2 + mv_x^2\,(l_rC_r - l_fC_f))}F_b^{\text{req}} \tag{19}$$

www.TechnicalBooksPDF.com

Table 1. Vehicle parameters.

Parameter	Value
vehicle mass (m)	1700 kg
vehicle yaw inertia (J_z)	2600 kgm^2
cornering stiffness front, rear (C_f, C_r)	97500,97500 N/rad
front,rear distance to CoG (l_f, l_r)	1.2,1.5 m
track width (w)	1.5 m
steering gear ratio (i)	15
time constant brakes, steering (T_b, T_s)	0.3,0.1 s
wheel radius (r_w)	0.32 m
pressure to torque front,rear (k^{Fr}, k^{Re})	24,12 Nm/bar
@70 km/h $a = (1, 26, 260, 1137, 1757)$	–
@70 km/h $b = (7.7, 128, 512)$	–
@70 km/h $c = (0.15, 1.37, 2.92)$e-3	–

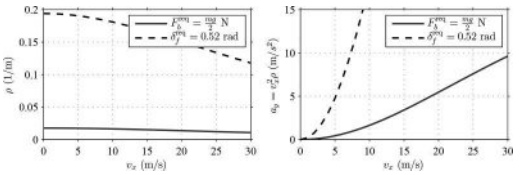


Figure 4. Linear model of steady-state curvature and lateral acceleration for either max. differential brake or steering input.

Figure 4 shows the upper bound of the linear model to what can be achieved of steady-state curvature and lateral acceleration for maximum differential brake input and steering. The maximum differential brake and steering input are assumed to be $F_b^{\text{req}} = \frac{mg}{2}$ N and $\delta_f^{\text{req}} = 0.52$ rad (=30°). The linear model doesn't consider friction, which for example implies that the magnitude of lateral acceleration from differential braking and steering exceeds g m/s^2 for $v_x > 30$ m/s and $v_x > 7$ m/s respectively. Since the vehicle is understeered ($l_r C_r \geq l_f C_f$), the largest curvature during zero steering angle is found

$$\rho_{\max} = \lim_{v_x \to 0} \rho = \frac{w\,(C_f + C_r)}{2\,(C_f C_r L^2)} F_b \leq \frac{w\,(C_f + C_r)\,\mu mg}{4\,(C_f C_r L^2)} \tag{20}$$

In Equation 20 it is assumed that the largest differential brake force is $F_b = \frac{\mu mg}{2}$, and hence it follows that the maximum curvature is limited and proportional to friction. For the vehicle in this study the upper bound of cornering curvature during high friction ($\mu = 1$) is 0.017 1/m which corresponds to a cornering radius of 59 m. Keeping the assumption of $\mu = 1$, Figure 4 gives us that the curvature for differential braking is bounded between 0.011 1/m and 0.017 1/m. The maximum curvature obtained by differential braking is smaller than for steering. For vehicle speeds below 14 m/s the lateral acceleration will not exceed 3 m/s^2 when using differential braking. The corresponding speed for steering is 4 m/s. If "normal driving" is considered as being able to reach lateral acceleration magnitudes of 3 m/s^2, differential braking cannot meet that under 14 m/s. The reduced cornering ability for differential braking will in turn increase the need for a careful path and speed planning.

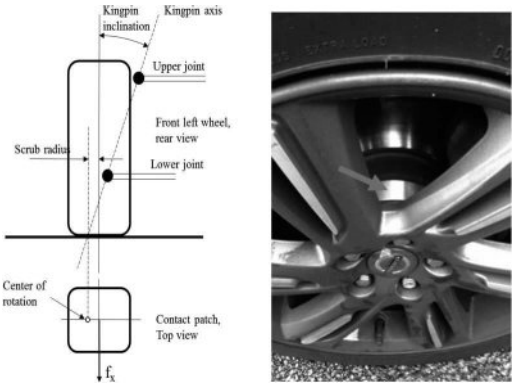


Figure 5. The scrub radius and here illustrated as negative (left). Spacers used to experimentally vary the scrub radius (right).

5 INFLUENCE OF SCRUB RADIUS

5.1 *Hands-on versus hands-off the steering wheel*

The curvature retrieved from differential braking in previous sections assumes zero steering angle. However, a brake force on a front wheel will, together with a moment arm mentioned to as *scrub radius*, induce an alignment wheel torque, which will influence steering and in turn the cornering curvature. This section seeks to experimentally quantify the scrub radius effects of the resulting curvature.

The scrub radius is a lateral displacement between the tyre's center of rotation, caused by the kingpin axis intersection with with the road plane, and the centerline of the tyre. When the center of rotation is outside of the centerline of the tyre, the scrub radius is defined as negative, otherwise it is positive. See Figure 5 for clarification. The differential brake test described in Section 3.2 was conducted with hands-on the steering-wheel, where the driver fixed the steering-wheel angle to zero. The test is here repeated but now with hands-off the steering-wheel i.e. no steering-wheel torque is applied during the test event. As shown in Figure 6, the steering-wheel angle is no longer zero caused by the (positive) scrub radius. At the end of the manoeuvre, when vehicle speed is lower, the steering angle is significantly increased up to 65°. This will in turn, contribute to even higher cornering curvature. The large steering-wheel angle corresponds to approximately 0.07 rad (=4°) wheel angle, which confirms that the small angle approximation made in Equations 1 and 2 is relevant. The experiment clearly demonstrate that the scrub radius effect substantially influences the physical limit of maximum cornering curvature. It should be mentioned that the scrub radius effect can be modeled and included in the vehicle

www.TechnicalBooksPDF.com

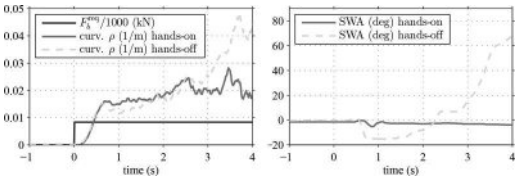


Figure 6. Step response test of curvature (left) and steering-wheel angle (right) for zero steering-wheel angle (hands-on) and zero steering-wheel torque (hands-off).

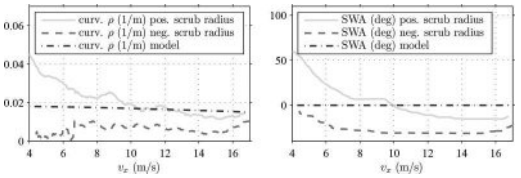


Figure 7. Influence of curvature and steering-wheel angle for positive versus negative scrub radius for $F_b^{\text{req}} = \frac{mg}{2}$ N.

model. This would be beneficial since such a model would predict the curvature better, but at the expense of a more complex model. The scrub radius is however uncertain since it for example varies for different wheel hubs, and consequently, the model becomes sensitive for the scrub radius parameter.

5.2 *Perturbation of the scrub radius*

The observation done in Section 5.1 showed that the scrub radius, when releasing the steering-wheel, increased the steering alignment torque and the cornering curvature significantly. The scrub radius was $+10$ mm. To further test the cornering ability for various scrub radius, it was changed to -15 mm. The modification of the vehicle has been made possible due to the use of so called spacers, which is a device mounted inside the rim which moves the contact patch outwards and hence creating the positive scrub radius. The hands-off differential brake test done in Section 5.1 was repeated with the two different scrub radii. As seen in Figure 7, the negative scrub radius will generate negative steering angles, which will counteract the cornering curvature from yaw torque, ending up in a smaller magnitude of total cornering curvature. The perturbation test demonstrates the high sensitivity of the cornering curvature with respect to different scrub radius. Figure 7 demonstrates that the scrub radius in particular influences the curvature for low vehicle speed.

6 CURVATURE CONTROLLER DESIGN

In order to tackle the steering fault described in the Introduction, we will here design an on-board curvature controller to be used after the occurrence of a fault when the vehicle is driven in autonomous mode. Note again that during the control event, the steering actuator nor the driver are assumed to steer the vehicle. When the fault is detected, the curvature controller starts to request differential brake force. The initial steering angle and its evolution, e.g. depending on the uncertain scrub radius, is here considered as a disturbance. By rearranging Equation 19, the differential brake request for static conditions is formulated as

$$F_b^{\text{req}} = \frac{1}{G_p(0)}\rho_{\text{req}} - \frac{G_s(0)}{G_p(0)}\delta_f, \tag{21}$$

where the first term in Equation 21 will be the feedforward compensator for the requested curvature ρ_{req} and the second term the feedforward compensator for rejecting the disturbance δ_f. The rejection of the steering disturbance is possible since δ_f is measured (through steering-wheel angle sensor) and that the influence of the curvature is modeled.

Due to model uncertainties and neglected dynamics for both $G_p(0)$ and $G_s(0)$, there will be a control error and disturbance will not be completely eliminated. Therefore a feedback loop is needed along with the two compensators. See (Brosilow & Joseph 2002) where the feedforward and feedback control design are separated. Equation 21 is now expressed

$$F_b^{\text{req}}(s) = \frac{2\left(C_f C_r L^2 + m v_x^2 \left(l_r C_r - l_f C_f\right)\right)}{w\left(C_f + C_r\right)}\rho_{\text{req}} - \frac{2C_f C_r L}{w\left(C_f + C_r\right)}\delta_f + C(s)e \tag{22}$$

$$C(s) = K_p\left(1 + \frac{1}{sT_i} + \frac{sT_d}{1 + sT_d/N}\right) \tag{23}$$

$$e = \rho_{\text{req}} - \rho. \tag{24}$$

To limit the high frequency gain of the derivative term, a low pass filter has been incorporated in the design of $C(s)$ which gives an upper bound of $K_p N$. Finally, the unfiltered curvature request is passed through a set-point rate-limiter filter, which protects for undesired derivative kicks during abrupt step changes in the curvature requests. See (Hägglund 2012) for PID filter design to avoid over shoots. The control structure in its entirety is illustrated in Figure 8. The control F_b is virtual and needs to be allocated to wheel individual brake pressures. The sign of F_b^{req} determines which side that should be actuated. There is a freedom in how F_b^{req} is distributed among the two tyres. The distribution is here done to preserve equal friction utilization and hence provide equal lateral force margins for good robustness. The lateral force component is here for simplicity neglected. Neglecting the wheel dynamics, the brake pressure request $p^{\text{req}} = [p^{FL,\text{req}}\, p^{FR,\text{req}}\, p^{RL,\text{req}}\, p^{RR,\text{req}}]^T$ to wheels are finally defined as

$$p^{\text{req}} = \begin{bmatrix} 0 & \frac{l_r r_w}{Lk^{Fr}} & 0 & \frac{l_f r_w}{Lk^{Re}} \end{bmatrix}^T F_b^{\text{req}} \quad \text{if } F_b^{\text{req}} \le 0 \tag{25}$$

www.TechnicalBooksPDF.com

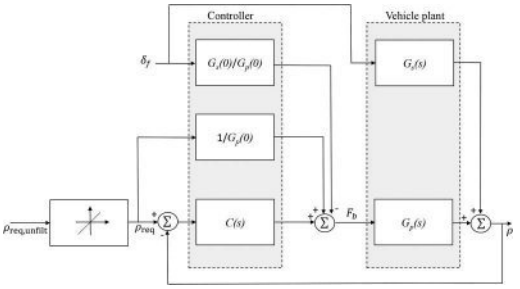


Figure 8. Curvature control structure consisting of two feedforward compensators, one feedback controller and a set-point filter.

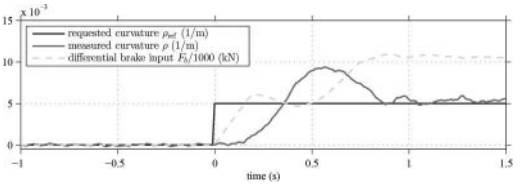


Figure 9. Close loop control of curvature.

$$p^{\text{req}} = \begin{bmatrix} \frac{l_r r_w}{Lk^{Fr}} & 0 & \frac{l_f r_w}{Lk^{Re}} & 0 \end{bmatrix}^T F_b^{\text{req}} \quad \text{if } F_b^{\text{req}} > 0, \quad (26)$$

where r_w is the wheel radius and k^{Fr} and k^{Re} are conversion factors from brake pressures to wheel torques depending on wheel geometry and hydraulic brake cylinders. The brake pressure request is send to a brake control unit, which is provided with a slip controller to prevent from wheel lock and limit longitudinal slip to approximately 10%.

The tuning of the PID controller was done with the Ziegler-Nichols method (Ziegler & Nichols 1942) where frequency information of the controlled system was used to determine the controller coefficients. The step response with the developed controller is shown in Figure 9. The time to reach 63% of the final curvature is by the closed loop controller reduced from approximately 0.4 to 0.3 s compared with the open loop response, but at the expense of an overshoot. The level of overshooting is a tuning issue, but here fast response has been prioritized to compensate for delays. The control error converges to zero and the remaining noise is caused by the wheel slip controller which work close to the slip limit.

Differential braking could lead to instability, which is not investigated in this paper. It is assumed that there exists a stability system monitoring and acting when margins to instability is below a threshold.

7 CONCLUSIONS

Analysis of a vehicle model and tests in real world vehicle has shown that differential braking could be used as an alternative to front axle steering. There are however physical lower limits on how large curvature that could be achieved compared with steering. This means that tyres will be saturated for smaller curvatures than for steering. A consequence is a strong dependence of vehicle parameters such as friction coefficient, which will limit the curvature and hence how fast curves can be entered. Compared with steering, differential braking could not provide as large lateral acceleration for lower speed. The scrub radius will influence the obtained curvature significantly for lower speeds, and hence the wheel suspension must be considered during the design of the vehicle. Since the scrub radius will change the steering angle during the differential braking, it is necessary to consider the effect of steering angle change during the control event. The developed controller, where the steering disturbance is rejected through a feedforward compensator, admits curvature to be controlled within physical limits.

REFERENCES

Brosilow, C. & B. Joseph (2002). *Techniques of ModelBased Control*. Prentice Hall PTR.

Häagglund, T. (2012). Signal filtering in pid control. *IFAC Conference on Advances in PID Control, Brescia, Italy*.

Moshchuk, N. K. & et al. (2013). Collision avoidance maneuver through differential braking. *Patent US 20130030651 A1*.

Pilutti, P., G. Ulsoy, & D. Hrovat (1998). Vehicle steering intervention through differential braking. *J. Dynamic Systems, Measurement, and Control 120(3)*, 314(8).

Rajamani, R. (2012). *Vehicle Dynamics and Control*. Springer US.

Ziegler, J. & N. Nichols (1942). Optimum settings for automatic controllers. *Transactions of the A.S.M.E 5(11)*, 759768.

www.TechnicalBooksPDF.com

ADAS

www.TechnicalBooksPDF.com

www.TechnicalBooksPDF.com

Advanced Vehicle Control – Edelmann, Plöchl & Pfeffer (Eds)
© 2017 Taylor & Francis Group, London, ISBN 978-1-138-02992-7

Risk predictive safe speed control for collision avoidance in right turn dynamic environment situation

Y. Fujinami, P. Raksincharoensak & Y. Akamatsu
Tokyo University of Agriculture and Technology, Koganei, Tokyo, Japan

D. Ulbricht & R. Adomat
Continental, Division Chassis & Safety, Lindau Bodensee, Bavaria, Germany

ABSTRACT: Collisions of vehicle-to-vehicle and vehicle-to-vulnerable road user during right turns at intersection account for a high number of other intersection accidents in Japan. Considering such situations, "intersection right turn collision avoidance system" is intensely required. We focus on right turn scenario that the ego vehicle needs to negotiate with oncoming objects such as automobiles, motorcycles, bicycles and pedestrians. This paper presents a risk predictive safe speed control algorithm that introduces speed control braking assistance for safe right turn combined with autonomous emergency braking to avoid collision with other participants during right turn at intersections. Our proposal uses on-board sensors such as radar and cameras to handle situations without depending on C2X/X2C communication and infrastructure. Full-vehicle simulation for a rapid system development is used to verify the effectiveness of the proposed ADAS.

1 INTRODUCTION

In spite of an annual decrease in road fatalities in Japan, the number of traffic accidents remains high (National Police Agency 2016). Accidents occurring at intersections account for about half of accidents overall (Cabinet Office 2016), indicating a need for intersection collision avoidance systems. For vehicle-to-vehicle and vehicle-to-vulnerable road user accidents at intersections, the collisions between vehicles making right turns and other vehicles or vulnerable road users going straight show the highest percentage in Japan which has a left-hand traffic system (ITARDA 2015).

As existing research works and commercialized products, there are vehicle-infrastructure cooperative collision prevention and collision avoidance systems using on-board sensors in addition to autonomous emergency braking (Nakamura et al. 2014). However, those complexities require infrastructural preparations (Harding et al. 2014).

We have developed a driver assistance system based on on-board sensors such as radars and cameras. Our main research objective is to further develop a safe speed control system to avoid collision during right turn. This system applies braking assistance not only to avoid collision with currently-visible objects but also to predict the potential collision with hidden objects which may dart out from blind spots by predicting trajectories of ego vehicle and other moving objects and anticipating darting-out objects from those blind spots. This research is a part of long collaboration between TUAT and Continental AG in the area of active safety systems. The paper describes the result of the last two-year project. The whole diagram of collision avoidance system is shown in Figure 1.

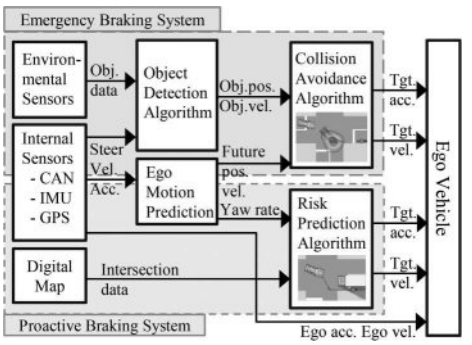


Figure 1. Overview of proposed Collision Avoidance System.

2 SYSTEM OVERVIEW

The proposed intersection right turn collision avoidance system consists of two systems: Emergency Braking System (EBS) and Proactive Braking System (PBS). EBS applies emergency brake to avoid collisions with visible dynamic hazards that appeared in front of ego vehicle during right turn. PBS is a system that applies comparative mild brake in advance with respect to potential risk of darting object from blind

www.TechnicalBooksPDF.com

spot where the object is occluded by a stop vehicle in an intersection.

3 ALGORITHM OF EMERGENCY BRAKING SYSTEM

Trajectories of vulnerable road users are difficult to predict because vulnerable road users have more degree-of-freedom in moving in traffic rather than automobiles which have constraints on driving lanes. In order to avoid collision with various types of road users, in the proposed EBS, the collision probability was used to predict their trajectories and calculate the target acceleration. Considering the collision probability, the system can take into account the variation of turning maneuver of ego vehicle and those of trajectories of avoidance objects. Therefore, the conflict area can be predicted. Moreover, considering collision probability enables the system to mitigate low collision risk beforehand by applying mild braking for lower collision probability.

3.1 *Motion prediction of ego vehicle*

Assuming that velocity and the acceleration of ego vehicle can be acquired, and the position and the velocity of surrounding objects can be acquired by environment perception sensors. Figure 2 shows diagram of ego vehicle trajectory. In order to simplify the idea, in this paper, sizes of objects are ignored.

Assuming that the ego vehicle makes circular turn in intersection, turning radius R_{turn} of ego vehicle to reach an arbitrary point (x_{pred}, y_{pred}) is defined as Equation 1:

$$R_{turn} = \frac{x_{pred}^2 + y_{pred}^2}{2y_{pred}} \tag{1}$$

From geometric relationship between the position of ego vehicle, the turning radius and the arbitrary point, turning angle of ego vehicle is defined in Equation 2:

$$\psi_{pred} = \arctan\left(\frac{x_{pred}}{R_{turn} - y_{pred}}\right) \tag{2}$$

By eliminating R_{turn} using Equation 1 and Equation 2, turning angle ψ_{pred} is calculated as shown in Equation 3:

$$\psi_{pred} = \arctan\left(\frac{2x_{pred}y_{pred}}{x_{pred}^2 - y_{pred}^2}\right) \tag{3}$$

From Equation 1 and Equation 3, circular-arc-distance from the current position of ego vehicle to the arbitrary point (x_{pred}, y_{pred}) is calculated as follows:

$$D = R_{turn}\psi_{pred} = \frac{x_{pred}^2 + y_{pred}^2}{2y_{pred}} \arctan\left(\frac{2x_{pred}y_{pred}}{x_{pred}^2 - y_{pred}^2}\right) \tag{4}$$

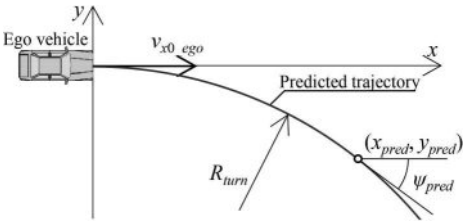


Figure 2. Relationships between ego vehicle and arbitrary point on ego vehicle trajectory.

The circular-arc-distance from the current position of ego vehicle to the arbitrary point is indicated as Equation 5:

$$D(t) = v_{0_ego}(t)t_{pred} + \frac{1}{2}a_{x_ego}t_{pred}^2 \tag{5}$$

where, $v_{0_ego}(t)$ = current longitudinal velocity of ego vehicle; a_{x_ego} = predicted longitudinal acceleration of ego vehicle; and t_{pred} = prediction time from current time.

By eliminating D using Equation 4 and 5, longitudinal acceleration to reach the point (x_{pred}, y_{pred}) at predicted time t_{pred} is expressed in Equation 6:

$$a_{x_ego}(t) = \frac{2R_{turn}\psi_{pred}}{t_{pred}^2} - \frac{2v_{0_ego}(t)}{t_{pred}} \tag{6}$$

Since ego vehicle is turning in a circle, lateral acceleration $a_{y_ego}(t)$ is calculated in Equation 7:

$$a_{y_ego}(t) = \frac{v_{0_ego}^2(t)}{R_{turn}} = \frac{2y_{pred}v_{0_ego}^2(t)}{x_{pred}^2 + y_{pred}^2} \tag{7}$$

In order to express the variance of ego vehicle acceleration in longitudinal and lateral directions to reach the arbitrary point at a certain predicted time horizon, we used Gaussian distribution as shown in Equation 8 and Equation 9 respectively.

$$h_{x_ego}(t) = \frac{1}{\sqrt{2\pi\sigma_{x_ego}^2}} \exp\left\{-\frac{\left(a_{x_ego}(t) - a_{x0_ego}(t)\right)^2}{2\sigma_{x_ego}^2}\right\} \tag{8}$$

$$h_{y_ego}(t) = \frac{1}{\sqrt{2\pi\sigma_{y_ego}^2}} \exp\left\{-\frac{\left(a_{y_ego}(t) - a_{y0_ego}(t)\right)^2}{2\sigma_{y_ego}^2}\right\} \tag{9}$$

where, σ_{x_ego} = standard deviation of ego vehicle longitudinal acceleration; σ_{y_ego} = standard deviation of ego vehicle lateral acceleration; a_{x0_ego} = current longitudinal acceleration of ego vehicle; and a_{y0_ego} = current lateral acceleration of ego vehicle.

By using these distributions, existence probabilities of ego vehicle at the point (x_{pred}, y_{pred}) on predicted time t_{pred} can be calculated.

www.TechnicalBooksPDF.com

3.2 *Motion prediction of avoidance object*

Figure 3 shows diagram of trajectory of avoidance object. Assuming that an avoidance object accelerates constantly, the longitudinal and the lateral acceleration to reach the point (x_{pred}, y_{pred}) at predicted time t_{pred} can be expressed in Equation 10 and Equation 11 respectively:

$$a_{x_obj}(t)=\frac{2}{t_{pred}^2}\left(x_{pred}-x_{0_obj}(t)-v_{x0}(t)t_{pred}\right) \quad (10)$$

$$a_{y_obj}(t)=\frac{2}{t_{pred}^2}\left(y_{pred}-y_{0_obj}(t)-v_{y0}(t)t_{pred}\right) \quad (11)$$

where, $x_{0_obj}(t)=$ current x-axis position of target object; $y_{0_obj}(t)=$ current y-axis position of target object; $v_{x0}(t)=v_{x0_obj}(t)+v_{x0_ego}(t)$; $v_{x0_obj}(t)=$ current x-axis velocity of target object; $v_{y0}(t)=v_{y0_obj}(t)+v_{y0_ego}(t)$; and $v_{y0_obj}(t)=$ current y-axis velocity of target object.

In order to express the uncertainty of target object acceleration to reach the arbitrary point at certain predicted time, we used Gaussian distribution as shown in Equation 12 and Equation 13:

$$h_{x_ego}(t)=\frac{1}{\sqrt{2\pi\sigma_{x_obj}^2}}\exp\left(-\frac{\left(a_{x_obj}(t)\right)^2}{2\sigma_{x_obj}^2}\right) \quad (12)$$

$$h_{y_obj}(t)=\frac{1}{\sqrt{2\pi\sigma_{y_obj}^2}}\exp\left(-\frac{\left(a_{y_obj}(t)\right)^2}{2\sigma_{y_obj}^2}\right) \quad (13)$$

where $\sigma_{x_obj}=$ standard deviation of x-axis acceleration of target object; and $\sigma_{y_obj}=$ standard deviation of y-axis acceleration of avoidance object;

By using these distributions, existence probabilities of target object at point (x_{pred}, y_{pred}) on predicted time t_{pred} can be calculated.

3.3 *Speed control algorithm*

Collision probability between the ego vehicle and the target object is defined by product of the probabilities of ego vehicle and avoidance object as shown in Equation 14 below:

$$h_{col}(t)=h_{x_ego}(t)\times h_{y_ego}(t)\times h_{x_obj}(t)\times h_{y_obj}(t) \quad (14)$$

In order to stop the ego vehicle before reach to the point (x_{pred}, y_{pred}), target deceleration is calculated from Equation 15:

$$a_{stop}(t)=\frac{\left(v_{0_ego}(t)\right)^2}{2D(t)} \quad (15)$$

Target deceleration of the EBS is calculated in three ways as shown in Equation 16:

$$a_{tar}(t)=\begin{cases}0 & \left(a_{tar}<a_{min}\right)\\ C\times h_{col}(t)\times a_{stop}(t) & \left(a_{min}\le a_{tar}\le a_{max}\right)\\ a_{max} & \left(a_{max}<a_{tar}\right)\end{cases} \quad (16)$$

where $a_{min}=$ minimum deceleration that EBS applies braking assistance; $a_{max}=$ maximum deceleration that EBS applies braking assistance; and $C=$ constant coefficient.

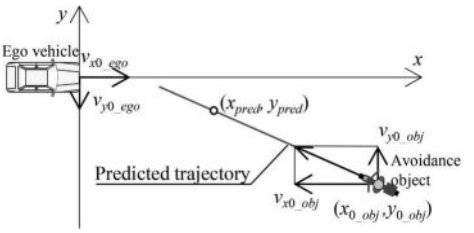


Figure 3. Relationships between avoidance object, ego vehicle and arbitrary point on avoidance object trajectory.

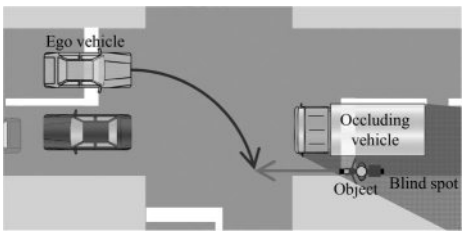


Figure 4. Risk predictive scene that a stop vehicle occluding an oncoming object in blind spot.

In this way, EBS can change the target deceleration depending on collision probability and EBS can apply mild brake in low collision probability region in advance accordance with the uncertainty of trajectory of the target object.

4 ALGORITHM OF PROACTIVE BRAKING SYSTEM

As shown in Figure 4, when an oncoming vehicle is occluding another oncoming object, the ego vehicle cannot recognize the occluded object in time. In this scenario, even if the ego vehicle is equipped with high performance EBS or other autonomous braking systems, the collision may be unavoidable if the velocity of ego vehicle is too high due to insufficient stopping distance. Accordingly, to avoid collision in those cases, the ego vehicle needs to decelerate in a defensive manner before recognizing the actual darting-out target object.

Our proposal PBS enables to reduce the velocity in advance to the value that the collision can be avoided with EBS capacity. The target velocity is calculated from the position of the occluding object by environment sensors and intersection topological information by digital map.

4.1 *Algorithm of darting-out prediction*

Considering that the turning radius r_{turn} at intersection and the topological information of the intersection can be predicted from the digital map and the environment sensors, the relative position of occluding vehicle to the ego vehicle can be acquired.

www.TechnicalBooksPDF.com

Figure 5 shows a diagram of scenario that PBS applies brake assistance.

In Figure 5, regarding θ is small enough and consider $\theta = 0$. Then, the displacement from front end of occluding vehicle to virtual conflict point is defined as Equation 17:

$$y_{0_PBS}(t) = \frac{X_{occ}(t) + x_{vir}\sin\psi(t)}{\cos\psi(t)} - r_{turn} \tag{17}$$

where, $X_{occ}(t)$ = longitudinal distance from the ego vehicle to right-front point of the occluding vehicle; x_{vir} = displacement from left side of the occluding vehicle to virtual object initial position; and $\psi(t)$ = current turning angle.

The arc length from the ego vehicle to virtual conflict point is indicated in Equation 18:

$$d(t) = r_{turn}\left(\frac{\pi}{2} - \psi(t)\right) \tag{18}$$

As shown in Figure 6, for the sake of simplicity in calculation, by converting the circular trajectory into the virtual straight trajectory. Then, the distance from the ego vehicle to a virtual conflict point can be expressed as Equation 19:

$$x_{0_PBS}(t) = d(t) \tag{19}$$

4.2 *Speed control algorithm*

Considering that a virtual target object darts out with velocity v_{vir}, the time to collision with the left-front bumper of the ego vehicle can be calculated as indicated in Equation 20:

$$t_2(t) = \frac{2y_{vir} + 2y_{0_PBS}(t) + w}{2v_{vir}} \tag{20}$$

where, y_{vir} = displacement from front of the occluding vehicle to virtual object initial position; and w = width of ego vehicle.

According to Equation 20, in order to avoid collision with virtual object successfully, the ego vehicle needs to stop with shorter time than the time $t_2(t)$ with maximum emergency brake. Therefore, the ego vehicle needs to decelerate to the velocity indicated in Equation 21:

$$v_{x1_PBS}(t) = a_{EBS}t_2(t) \tag{21}$$

where, a_{EBS} = maximum deceleration of EBS.

The stopping distance of the ego vehicle from the velocity $v_{x1_PBS}(t)$ can be expressed in Equation 22:

$$x_{1_PBS}(t) = -\frac{1}{2}a_{EBS}\left(t_2(t)\right)^2 + x_{safe} \tag{22}$$

where, x_{safe} = safety margin distance from the ego vehicle to the virtual conflict point.

Thus, in order to avoid collision with darting-out object from blind spot, the ego vehicle needs

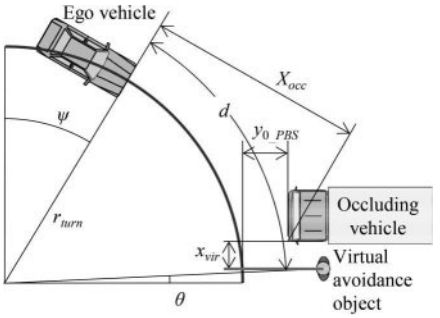


Figure 5. Relationships between ego vehicle, occluding object and virtual avoidance object at intersection right turning.

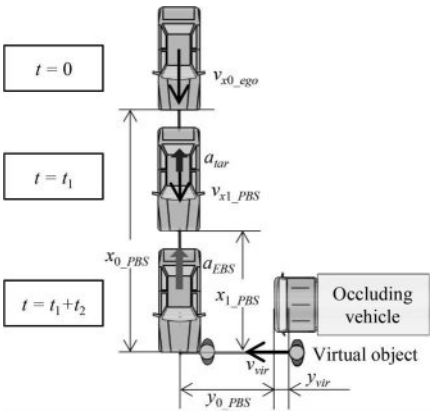


Figure 6. Transformed virtual straight trajectory and relationships between ego vehicle, occluding vehicle and virtual object.

to decelerate to $v_{1_PBS}(t)$ before reaching the position $x_{1_PBS}(t)$. Subsequently, the target deceleration for avoiding collision can be calculated as shown in Equation 23:

$$a_{tar}(t) = \frac{\left(v_{x0_ego}(t)\right)^2 - \left(v_{x1_PBS}(t)\right)^2}{2\left(x_{0_PBS}(t) - x_{1_PBS}(t)\right)} \tag{23}$$

5 SIMULATION

5.1 *Emergency braking system*

To evaluate right turn collision avoidance at an intersection with computer simulation, near crash incident scenario was constructed as shown in Figure 7. The initial position of the oncoming object was set to collide into the ego vehicle at the intersection if the ego vehicle keeps the velocity constant. The full-vehicle simulation was concluded by IPG Car Maker® software. Table 1 shows the simulation conditions and the simulation results are shown in Figure 8.

From the first and the second graphs of Figure 8 shows EBS applied brake assistance and decelerated

www.TechnicalBooksPDF.com



Figure 7. Experimental scenario using simulation when EBS applies emergency brake.

Table 1. Simulation conditions of EBS.

Definition	Symbol	Value	Unit
Maximum assistance deceleration	a_{max}	8.0	m/s^2
Minimum assistance deceleration	a_{min}	3.0	m/s^2
Standard deviation of ego vehicle	σ_{x_ego}	1.0	m/s^2
	σ_{y_ego}	1.0	m/s^2
Standard deviation of object	σ_{x_obj}	1.0	m/s^2
	σ_{y_obj}	1.0	m/s^2
Velocity of oncoming object	v_{obj}	10.0	m/s

the speed to avoid collision, and acceleration of ego vehicle was tracing the desired acceleration. From the fourth graph showing the trajectories, the ego vehicle could avoid collision with safety margin by EBS. From the third graph, ego vehicle avoided with mild brake which did not reach half of full capability. Since, when there was collision probability, even if it was small, EBS could intervene in early phase to suppress the risk of collision. In other words, once collision probability was decreased by EBS, after that EBS just applied mild brake for lower collision probability if trajectories were not changed drastically. Therefore, by considering collision probability, the ego vehicle could avoid collisions with anticipating the change of trajectories.

5.2 *Proactive braking system*

We constructed a scenario that an oncoming target object darted out from blind spot behind an occluding vehicle as shown in Figure 9, to evaluate and compare EBS with integrated system of EBS and PBS (EBS + PBS). The simulation conditions of EBS and PBS are shown in Table 1 and Table 2. Figure 10 shows the simulation result with only EBS. Figure 11 shows the simulation results with EBS + PBS. As can be noticed in Figure 10, EBS reacted to the darting-out object, but the ego vehicle could not avoid collision before it stopped. On the other hand, with EBS + PBS, as can be noticed in the fourth graph of Figure 11, the ego vehicle could avoid collision with the darting-out object. From the first and the second graphs of Figure 11, PBS applied mild brake and decelerated to target velocity before EBS applies stronger brake. From third graph, EBS + PBS selected the system which output higher brake amount and then activated proper brake assistance.

To verify the effectiveness of EBS + PBS, various conditions of the position of occluding vehicle, darting-out velocity and darting-out timing were used

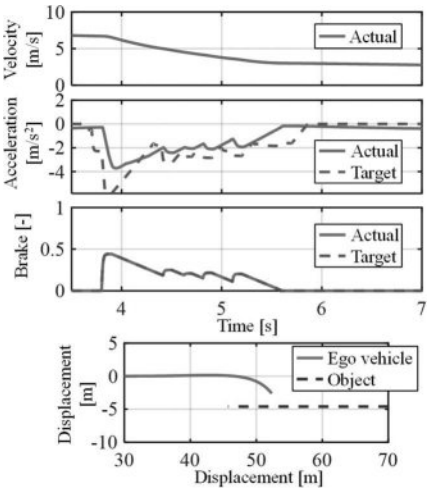


Figure 8. Simulation results of EBS at the intersection without occluding object.

Table 2. Simulation condition of PBS.

Definition	Symbol	Value	Unit
Predicted turning radius	r_{turn}	4.5	m
Darting-out position of virtual object	x_{vir}	0.5	m
	y_{vir}	0.5	m
Darting-out velocity of virtual object	v_{vir}	10.0	m/s
Width of ego vehicle	w	1.8	m
Maximum deceleration by EBS	a_{max}	8.0	m/s^2
Safety distance to avoid collision	x_{safe}	0.5	m

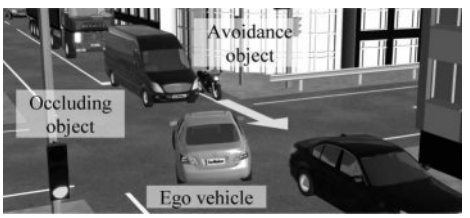


Figure 9. Experimental scenario that an avoidance object darts out from blind spot behind occluding vehicle using simulation.

to simulate in various darting-out situation. These three parameters were changed as shown in Table 3.

Figure 12 and Figure 13 show the collision avoidance failure rate when the darting-out timing of the target object is changed corresponding to the position of the occluding vehicle and the darting-out velocity of the target object. Comparing with Figure 12 and Figure 13, collision avoidance failure rates of EBS + PBS was effectively reduced in most cases compared to that of EBS. Especially, the number of possible cases with no collision increased from 27 cases to 48 cases. Furthermore, EBS + PBS could suppress the collision avoidance failure rates significantly when the position of occluding vehicle y_{0_PBS} was smaller ($y_{0_PBS} = 1.5$–2.3 [m]). Thus, EBS + PBS can enhance the avoidance

www.TechnicalBooksPDF.com

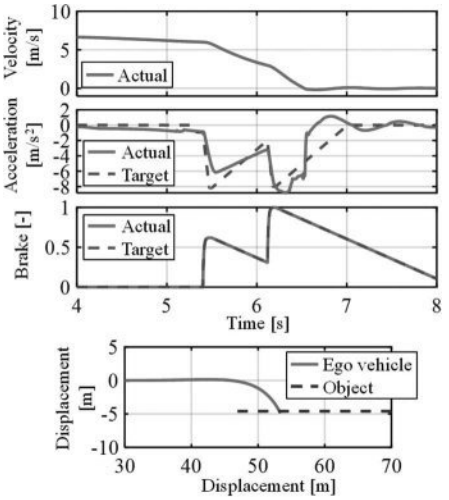


Figure 10. Simulation results of EBS at the intersection where a stop vehicle occluding oncoming object.

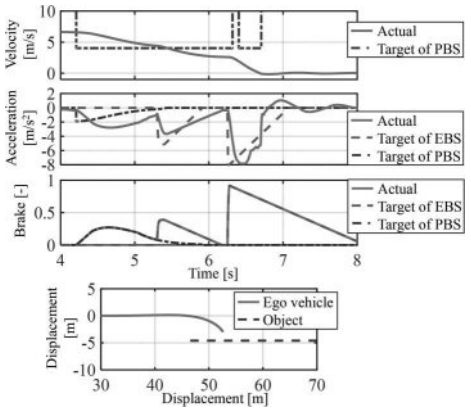


Figure 11. Simulation results of EBS + PBS at intersection where a stop vehicle occluding oncoming object.

performance in critical situation such as the case when the time-to-collision from when oncoming vehicle darts out is short and PBS effectively extended the safety performance of EBS.

6 CONCLUSION

Emergency Braking System and Proactive Braking System were proposed in the paper for safety intersection right turn in left-hand traffic. Emergency Braking System avoids collisions with visible dynamic hazards such as automobiles and vulnerable road users by considering collision probability. Proactive Braking System predicts the risk and decelerates the ego vehicle to a safe velocity in advance to avoid collision with darting object. From the simulation results, Emergency Braking System could avoid collision considering the possibility of trajectory change of the ego vehicle and

Table 3. Parameter arrays that changed for simulation.

Definition	Symbol	Value	Unit
Displacement from occluding vehicle	y_{0_PBS}	1.5, 1.9, 2.3, . . . , 5.1	m
Darting-out velocity	v_{obj}	2.0, 4.0, 6.0, . . . , 14.0	m/s
Darting-out timing	t_{out}	0.0, 0.2, 0.4, . . . , 1.8	s

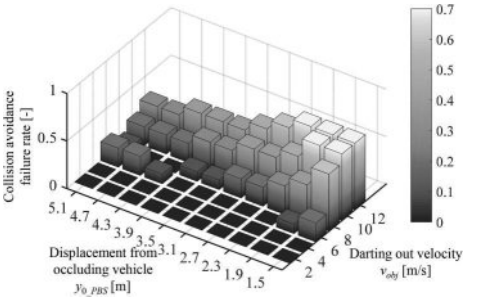


Figure 12. Collision avoidance failure rates of EBS.

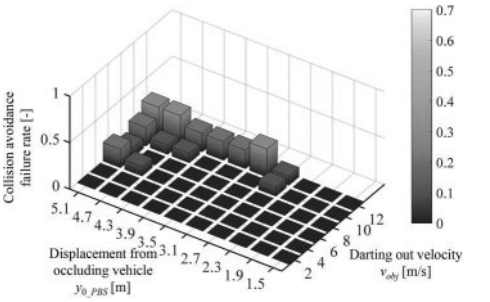


Figure 13. Collision avoidance failure rates of EBS + PBS.

the avoidance object by considering collision probability calculated from existence probabilities of the relevant objects. From the comparison of simulation results between EBS + PBS and Emergency Braking System, EBS + PBS was effective in avoiding more setting conditions in darting-out scenario during intersection right turns, and EBS + PBS was effective in collision avoidance performance in critical conditions, improving the safety in intersections.

REFERENCES

Cabinet Office, Government of Japan 2016. *Traffic safety white paper*: 34.

Harding, J. et al. 2014. *Vehicle-to-vehicle communications: readiness of V2V technology for application*: 105–112.

ITARDA, 2012. *Status of traffic accidents and analysis of human factor in signalized intersection*: 66–73, 101, 114.

Nakamura, S. et al. 2014. Effect evaluation of vehicle-infrastructure cooperative right-turn collision prevention system. *Proceedings of JSAE annual congress 49–14*: 23–28.

National Police Agency, Government of Japan, *Status of traffic accidents in 2015*: 1–2.

www.TechnicalBooksPDF.com

Advanced Vehicle Control – Edelmann, Plöchl & Pfeffer (Eds)
© 2017 Taylor & Francis Group, London, ISBN 978-1-138-02992-7

Speed control for reduced risk of collision with oncoming vehicles in obstacle avoidance scenarios

A. Arikere
TTC – Trollhättan Technical Center, AAM (American Axle & Manufacturing) Inc., Trollhättan, Sweden

M. Klomp
Vehicle Dynamics CAE, Volvo Car Corporation, Göteborg, Sweden

M. Lidberg
Department of Applied Mechanics, Chalmers University of Technology, Göteborg, Sweden

ABSTRACT: When a driver performs an evasive steering manoeuvre in order to avoid an obstacle, there is an increased risk of collisions with oncoming vehicles in the adjacent lane. A controller to reduce this risk of secondary collision by regulating the vehicle speed is designed and implemented. Simulations are preformed in IPG CarMaker with the new Volvo XC90 vehicle model and performance of the controller are compared with more conventional lateral stability controllers and unassisted manoeuvres. While lateral control can be of benefit in some cases, it can hurt in others. When combined with speed control however, consistent reductions in risk of secondary collisions are seen and in cases involving large velocity ratios or long obstacles, large reductions are observed.

1 INTRODUCTION

According to NHTSA, over 15 000 collisions with oncoming vehicles were reported in 2004 in the US alone and accounted for an economic cost of close to a billion USD (Yanagisawa et al. 2007). Such collisions are a distinct possibility when performing evasive steering manoeuvres to avoid obstacles as shown in figure 1.

Evasive steering manoeuvres are necessary in many cases for obstacle avoidance (Brännström et al. 2010). While several assist systems for the same are already being developed (Dang et al. 2012), they ultimately rely on the driver to ensure a clear adjacent lane. As a result, while they may help the driver avoid an obstacle, if the adjacent lane turns out not to be free, the driver may then face a greater threat of collision with an oncoming vehicle. This paper outlines an approach to reduce this risk of secondary collisions by controlling the vehicle speed in the manoeuvre so as to minimize a combination of the time spent and the distance traveled over the manoeuvre.

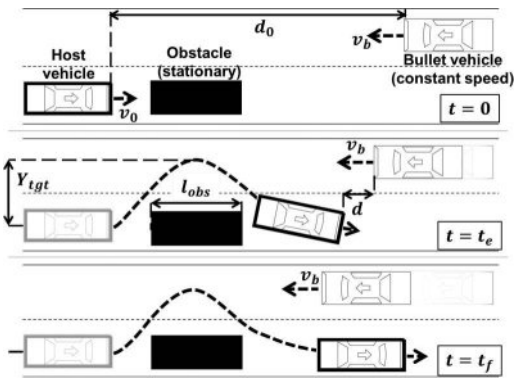


Figure 1. Obstacle avoidance with oncoming traffic.

The importance of controlling speed in this scenario can be illustrated by considering an extreme case wherein an aggressive lateral control intervention using differential braking during the manoeuvre can bring the host vehicle to a near halt in the wrong lane putting it squarely in the path of the oncoming vehicle (Arikere et al. 2015).

In the scenario considered in this paper, the driver initiates an evasive steering manoeuvre in order to avoid the obstacle. Awareness of the presence of an oncoming vehicle is not assumed for the driver. The vehicle is assumed to be able to detect the oncoming vehicle once the front edge of the longitudinal centre plane of the host vehicle clears the obstacle. This is in line with the industry practice of placing the radar and/or camera vision systems in the centre of the vehicle at the front. Due to the atypical and emergency nature of this manoeuvre, the driver steering intervention is expected to be inconsistent and unpredictable. The control system then attempts to reduce the risk of

www.TechnicalBooksPDF.com

Table 1. Manoeuvre parameters and their variations considered.

Parameters	Scenario A	Scenario B	Unit
Host initial velocity (v_0)	60	120	km/h
Bullet vehicle velocity (v_b)	120	60	km/h
Obstacle length (l_{obs})	15	3	m
Lateral displacement (Y_{tgt})	1.5	1.5	m

collision with said oncoming vehicle once the driver has started performing the steering manoeuvre. This task entails both lateral control to enhance vehicle response and stability and also speed control. The lateral control aspect is needed to ensure stability in the event of excessive or erratic steering interventions by a panicked driver. Additionally, it greatly increases the intensity of longitudinal interventions that can be performed without losing stability. The lateral control module used in this work is taken from Arikere et al. (2015). Note that this work considers only the vehicle dynamic control task in this manoeuvre and as such, other parts such as environmental perception and tactical decisions are working as required.

2 SCENARIO VARIATIONS AND ACTUATORS

As in Arikere et al. (2015), two variations of the scenario are considered (table 1) which represent the two extreme ends of the spectrum in terms of benefit of controlling the speed – one where it is expected to be of maximal benefit (Scenario A with large velocity ratio (v_b/v_0) and long obstacle (l_{obs})) and another where it is expected to have minimal benefit (Scenario B with small velocity ratio and short obstacle). The risk of collision with the oncoming vehicle in these scenarios is measured using the distance margin (d) which is the distance between the host vehicle and oncoming vehicle at the end of the manoeuvre. The end of the manoeuvre is defined as the instant when the host vehicle returns to the original lane after having passed the obstacle. Since steering interventions by a panicked driver in such an emergency situation tend to be inconsistent, different levels of steering severity are also considered for each scenario variation by changing the preview parameters of the driver model. The severity of the steering so achieved is measured using the steering effort metric (E_{str}). In this scenario, the steering is assumed to be controlled by the driver (represented by the driver model). (see Arikere et al. (2015), Klomp et al. (2014) for details about the driver model).

Two driveline setups are considered in this analysis: a traditional internal combustion (IC) engine and an electric drive based all-wheel drive driveline. The IC engine driveline is assumed to be too slow to be able to supply drive torques to the wheels reliably and is hence not used for speed control. Hence with an IC engine driveline, the brakes are used to perform both

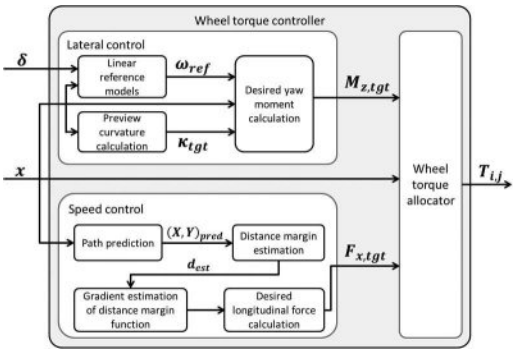


Figure 2. Wheel torque controller structure.

lateral and speed control. The electric driveline on the other hand, is assumed to be quick enough and when available, is used in conjuction with differential braking to perform torque vectoring and also used for speed control.

3 CONTROL DESIGN

The wheel torque controller is split into three major modules namely, lateral control, speed control and the wheel torque allocator. The overall structure of the controller is shown in figure 2.

3.1 *Lateral control*

The lateral control component consists of linear reference models to predict the yaw dynamics of the vehicle based on driver steering input, a preview curvature calculation part that determines the required curvature to avoid the obstacle or come back to the original lane and a desired yaw moment generator that outputs the yaw moment required for the vehicle to follow the target curvature. The lateral control component is taken from (Arikere, Lidberg, & Olsson 2015) and is hence not described further in this work.

3.2 *Speed control*

The speed controller consists of four modules, one each for path prediction, distance margin estimation, gradient estimation of the distance margin function with respect to host vehicle speed and finally, the desired longitudinal force generator that increases the distance margin.

First, the path prediction module generates a simple path constructed of circular arcs and straight lines that the host vehicle is expected to follow. A point mass vehicle and constant vehicle speed are assumed while generating the path. These assumptions are warranted in this case since the steering intervention has a dominant effect on the vehicle path and the distance margin, and since it is being performed by the

www.TechnicalBooksPDF.com

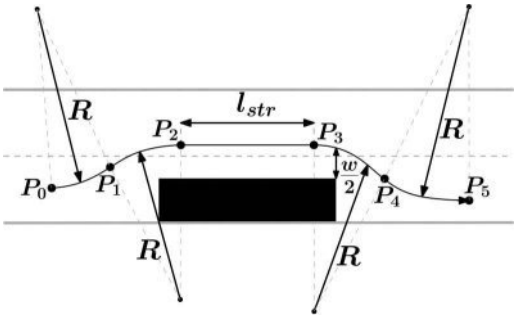


Figure 3. Predicted nominal path construction for speed control.

driver, is unknown to the controller. As such, simplyfing assumptions are necessary since more accurate predictions are not even possible.

As shown in figure 3, the path consists of six nodes that fully determine the path. The point $\boldsymbol{P_0}$ represents the current position of the host vehicle and the direction of the tangent at $\boldsymbol{P_0}$ represents its heading angle. Apart from the segement $\boldsymbol{P_2P_3}$, the remaining segments are made up of circular arcs with radius R given by the friction limit assuming an on-limit manoeuvre.

$$R = \frac{v_x^2}{\mu g} \tag{1}$$

where, v_x is the current vehicle speed and μ is the road friction which is assumed to be known.

The path is constructed assuming that the vehicle achieves the target lateral displacement as soon as possible and returns to original lane as soon as it clears the obstacle. Given these assumptions and a starting position $\boldsymbol{P_0}$ and a heading angle ψ_0, the points $\boldsymbol{P_1}$ and $\boldsymbol{P_2}$ are then determined. The point $\boldsymbol{P_1}$ is where the vehicle changes direction and starts turning right and $\boldsymbol{P_2}$ is when the vehicle has achieved the target lateral displacement and is travelling straight (zero heading angle).

$$\psi_1 = \arccos\left[\frac{1}{2R}(Y_0 - Y_{tgt} + R(1+\cos\psi_0))\right] \tag{2}$$

$$\psi_2 = 0 \tag{3}$$

$$\boldsymbol{P_1} = \boldsymbol{P_0} + R(\sin\psi_1 - \sin\psi_0, \cos\psi_0 - \cos\psi_1) \tag{4}$$

$$\boldsymbol{P_2} = \boldsymbol{P_1} + R(\sin\psi_1 - \sin\psi_2, \cos\psi_2 - \cos\psi_1) \tag{5}$$

Next, since the length l_{str} is unknown for the moment, the point $\boldsymbol{P_3}$ is temporarily set equal to $\boldsymbol{P_2}$ and the points $\boldsymbol{P_4}$ and $\boldsymbol{P_5}$ are provisionlly determined. Similar to points $\boldsymbol{P_1}$ and $\boldsymbol{P_2}$, $\boldsymbol{P_4}$ is when the vehicle changes direction again and starts turning left and $\boldsymbol{P_5}$ is when the vehicle is back at the starting Y position (=0) and is travelling straight again.

$$\psi_4 = -\arccos\left[\frac{1}{2R}(R(1+\cos\psi_3) - Y_3)\right] \tag{6}$$

$$\psi_5 = 0 \tag{7}$$

$$\boldsymbol{P_4} = \boldsymbol{P_3} + R(\sin\psi_3 - \sin\psi_4, \cos\psi_4 - \cos\psi_3) \tag{8}$$

$$\boldsymbol{P_5} = \boldsymbol{P_4} + R(\sin\psi_5 - \sin\psi_4, \cos\psi_4 - \cos\psi_5) \tag{9}$$

Now, the straight line segment is added between $\boldsymbol{P_2}$ and $\boldsymbol{P_3}$ such that at the leading edge of the obstacle, the path is a distance $w/2$ (half track width) away from the obstacle laterally. For this, first the point along the path where it just passes the obstacle has to be determined. This can happen either along $\boldsymbol{P_3P_4}$ or along $\boldsymbol{P_4P_5}$.

If $Y_4 < (w_{obs} + w/2)$, the path crosses the leading edge of the obstacle along $\boldsymbol{P_3P_4}$:

$$\psi_{obs} = -\arccos\left[\frac{1}{R}(w_{obs} + w/2 - Y_3 + R\cos\psi_3)\right] \tag{10}$$

$$X_{obs} = X_3 + R(\sin\psi_3 - \sin\psi_{obs}) \tag{11}$$

Else, the path crosses the leading edge of the obstacle along $\boldsymbol{P_4P_5}$:

$$\psi_{obs} = -\arccos\left[\frac{1}{R}(Y_4 - w_{obs} - w/2 + R\cos\psi_4)\right] \tag{12}$$

$$X_{obs} = X_4 + R(\sin\psi_{obs} - \sin\psi_4) \tag{13}$$

Given the X position of the leading edge of the obstacle as $X_{obs,fr}$, the length of the straight line segment to be added between $\boldsymbol{P_2}$ and $\boldsymbol{P_3}$ can be calculated as follows:

$$l_{str} = X_{obs,fr} - X_{obs} \tag{14}$$

With this, the point $\boldsymbol{P_3}$ can be fully determined and the points $\boldsymbol{P_4}$ and $\boldsymbol{P_5}$ are recalculated using the new $\boldsymbol{P_3}$ with equations (8) and (9).

$$\boldsymbol{P_3} = \boldsymbol{P_2} + (l_{str}, 0) \tag{15}$$

The path is continously reconstructed over the course of the manoeuvre in order to account for the deviations in the actual path that invariably occur due to the driver steering. Note that the equations given above are for the case when the vehicle is in the early stages of the manoeuvre. As such, many of the equations yield invalid values when the vehicle is further into the manoeuvre. For instance, when the vehicle is halfway into passing the obstacle, the estimate ψ_1 and ψ_2 will become invalid. The estimates are therefore checked every iteration and when they become invalid, it indicates that the vehicle is already past the point being determined. These estimates and points are then set equal to the current vehicle position and heading angle and the remaining points are estimated as usual. Shown in figure 4 is the evolution of the predicted vehicle path over the course of the manoeuvre and the actual vehicle path.

www.TechnicalBooksPDF.com

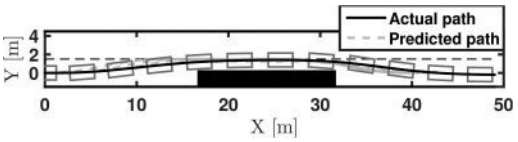


Figure 4. Predicted and actual vehicle path.

Once the path is fully determined, the distance margin is then estimated.

$$d = d_0 - \underbrace{\left(d_{h,x} + \frac{d_h}{v_x} v_b\right)}_{d_{tr}} \tag{16}$$

where, d_0 is the current distance between the host vehicle and the bullet vehicle, d_h is the length of the path (distance travelled by the host vehicle) and $d_{h,x}$ is the length of the predicted path along the $\boldsymbol{X}$ axis. The distance travelled by the two vehicles over the course of the manoeuvre is indicated as d_{tr}. Both the host and the bullet vehicle are assumed to travel at constant speeds in this estimation. The lengths d_h and $d_{h,x}$ are computed from the path parameters as follows:

$$d_h = l_{str} + \Sigma_{i=0}^{4}(-1)^i R(\psi_{i+1} - \psi_i) \tag{17}$$

$$d_{h,x} = l_{str} + \Sigma_{i=0}^{4}(-1)^i R(\sin\psi_{i+1} - \sin\psi_i) \tag{18}$$

The distance margin, d here is the objective that we intend to maximise by controlling the host vehicle speed. Hence the derivative of d with respect to the host vehicle speed, v_x should give an indication whether we need to increase or decrease vehicle speed to reduce the risk of collision with the oncoming vehicle. Since d_0 is a constant here, the expression for the derivative can be simplified as follows:

$$\frac{\mathrm{d}d}{\mathrm{d}v_x} = -\frac{\mathrm{d}d_{tr}(v_x)}{\mathrm{d}v_x} = J_{v_x} \tag{19}$$

The resulting slope of the objective (J_{v_x}) was then simply multiplied by a tunable gain factor to yeild a longitudinal force target ($F_{x,tgt}$). For safety, the resulting $F_{x,tgt}$ was also limited to a certain pre-determined bound to prevent saturating the tyres.

$$F_{x,tgt} = \min(\max(K_{long} J_{v_x}, -F_{x,max}), F_{x,max}) \tag{20}$$

Other more sophisticated methods such as running an optimisation within the controller or taking a *Newton Step*, etc to determine the optimal $F_{x,tgt}$ were tried out, however, due to non-smooth nature of the objective function, they resulted often in rapid and sudden interventions that sometimes made the situation worse. Furthermore, since the second derivative of the objective is discontinous, the *Newton Step* method could not be reliably applied. It was found that the simple method of multiplying the slope with a constant gain resulted in more robust behaviour, albeit in many cases, performed worse than the more sophisticated methods.



Figure 5. Simulation setup in CarMaker.

3.3 *Wheel torque allocator*

Finally, the control allocation block takes the longitudinal force target ($F_{x,tgt}$), the yaw moment target ($M_{z,tgt}$) and the vehicle states (x) and configuration as inputs and generates target wheel torques to be applied on the four wheels.

Once again, the wheel torque control module is largely taken from Arikere et al. (2015) with some minor changes to take into account the new input of $F_{x,tgt}$ as well. Mainly, the control allocator takes into account the capability of the actuator setup (whether it has electric propulsion and on which axle it has this capability), whether the vehicle is understeering or oversteering and the load distribution between the axles due to the vehicle centre of gravity and longitudinal acceleration, and tries to distribute the wheel torques accordingly to achieve the global force targets. The reader is directed to the section *Wheel force controller* in Arikere et al. (2015) for more details.

4 INCREASED DISTANCE MARGIN WITH SPEED CONTROL

Simulations are preformed with the controllers designed above in IPG CarMaker. A new Volvo XC90 vehicle model is used in the simulations (figure 5).

Figure 6 shows the performance of speed control when used with an IC engine driveline. As can be seen, using speed control provides consistently better performance. In scenario A, where maintaining speed is of benefit, it can be seen that differential braking alone can deteriotate performance in many cases. However, with speed control added, the system consistently performs better. In scenario B on the other hand where reducing speed is of benefit, differential braking works well on its own. As a result, adding speed control does not provide much benefit, but still manages to match the performance in the worst case and improve it slightly in some cases. Note also that the lighter shades of the plot for the “No control” case indicates that the vehicle fails to finish the manoeuvre in a stable fashion.

In figures 6(c) and 6(d), the steering profiles corresponding to the intercepts of the horizontal and vertical

www.TechnicalBooksPDF.com

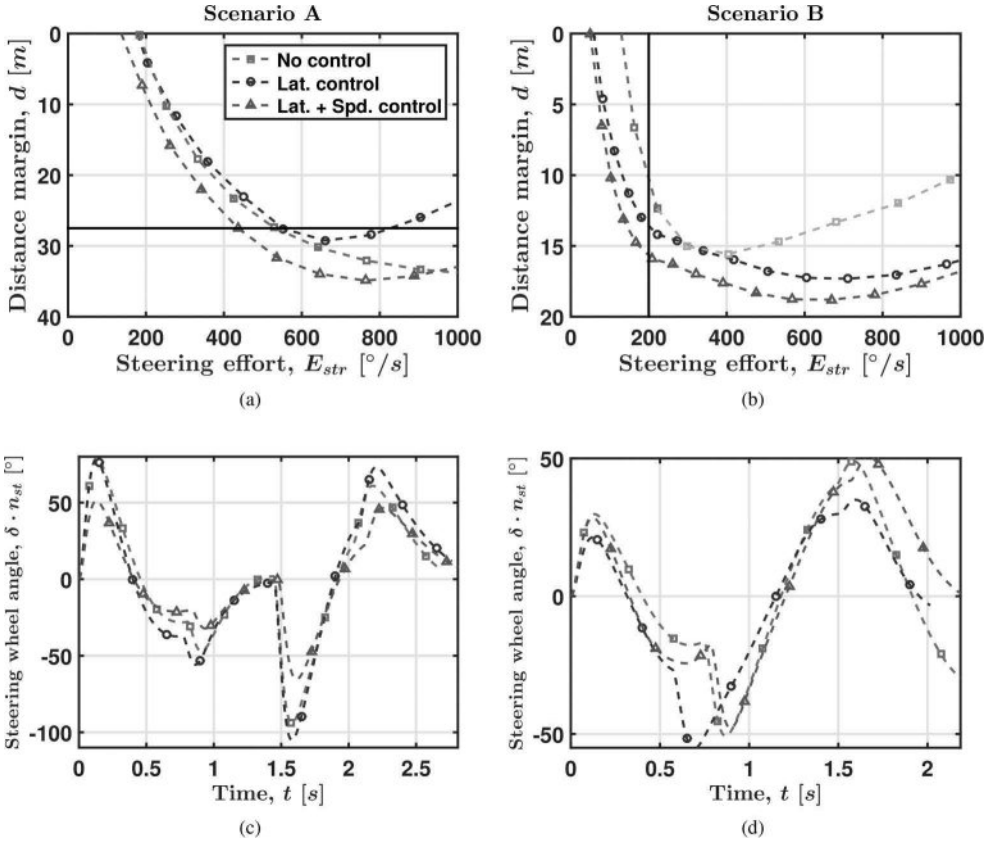


Figure 6. The pareto fronts for steering effort vs distance margin for scenario A and B using the speed controllers for an IC engine based driveline are shown in (a) and (b) respectively. Lateral control is performed using differential braking. Steering wheel angle profiles corresponding to the marked distance margin level (horizontal line) in (a) are shown in (c) and those corresponding to the marked steering effort level (vertical line) in (b) are shown in (d).

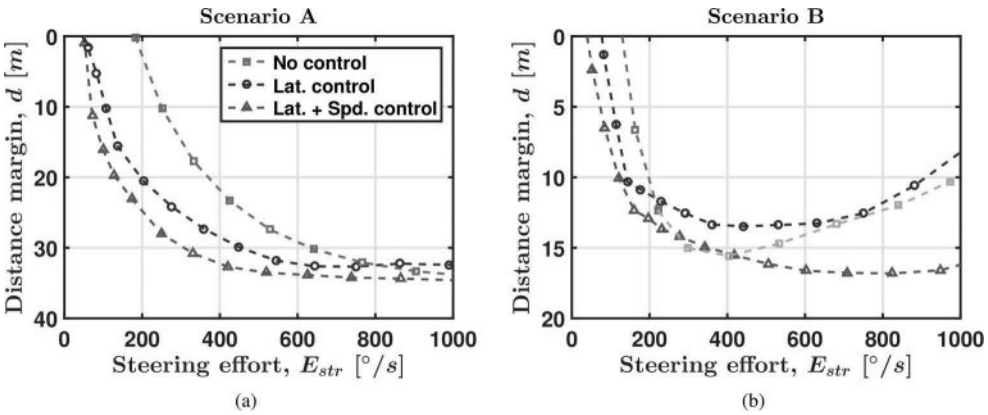


Figure 7. The pareto fronts for steering effort vs distance margin for scenario A and B using the speed controllers for an electrified driveline are shown in (a) and (b) respectively. Lateral control is performed using torque vectoring.

line in figures 6(a) and 6(b) are shown respectively. It can be seen that, in case of figure 6(c), although the steering profiles look similar, the peak steering rate and the steering amplitudes are significantly smaller for the case with speed control. On the other hand, in figure 6(d), it can be seen that even though the profiles look similar, the peak steering rates are nearly the same for all the cases. These observations match

www.TechnicalBooksPDF.com

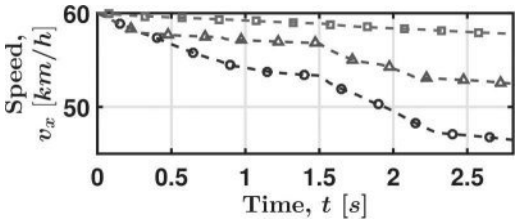


Figure 8. Speed profiles for the cases in figure 6(a) where $E_{str} \approx 400°/s$.

with what we expect from the steering profiles based on their steering effort values.

Shown in figure 7 is the performance of speed control when used with an electric driveline. Here, the electric driveline and the differential brakes are used together to achieve torque vectoring which is used for lateral control. Note that for safety, acceleration is not permitted and at best, the controller only maintains speed. In scenario A here, the use of torque vectoring benefits greatly as it performs lateral control without slowing the vehicle down. As a result, adding speed control here does not help much. In scenario B however, where reducing speed is of benefit, while torque vectoring alone is of help, adding speed control significantly increases the distance margin as it also slows the vehicle down. This is because when lateral control alone is performed with torque vectoring, the vehicle does not slow down which is detrimental for safety in this case. When speed control is added, the vehicle is slowed down in addition to performing lateral control which improves safety.

Figure 8 shows the speed profiles for the cases in figure 6(a) with steering effort (E_{str}) of 400°/s. As can be seen, when lateral control alone is performed, the vehicle is stabilised but at the cost of speed. Whereas when speed control is added, it manages to achieve a better tradeoff between lateral control and speed control which leads to a higher distance margin.

5 CONCLUSIONS

Simulations using the outlined strategy to control speed showed that large reductions in oncoming vehicle collision risk can be achieved in scenarios involving large velocity ratios and long obstacles. Smaller but consistent reductions in collision risk with oncoming vehicles can also be achieved in other scenarios.

Noticable increases in distance margin are achieved even when used with traditional IC engine drivetrains. However, for large and consistent improvements in distance margin over differential braking, an electrified drivetrain is needed. Large improvements are seen with electric drivelines even when only lateral control (torque vectoring) is performed. This benefit is amplified even further when speed control is added.

Since consistent improvements in distance margin are seen irrespective of the scenario or the type of drivetrain, speed control can therefore be seen as an effective option for mitigating the risk of collision with oncoming vehicles when evasive steering manoeuvres are performed for obstacle avoidance.

ACKNOWLEDGEMENTS

This project was partly funded by the Fordonsstrategisk Forskning och Innovation (FFI) program of VINNOVA and the vehicle models used in simulations were provided by Volvo Car Corporation. Their support is gratefully acknowledged.

The support of IPG in supplying an academic version of CarMaker for use in this research is also gratefully acknowledged.

REFERENCES

Arikere, A., M. Lidberg, & G. Olsson (2015, August). The tradeoff between distance margin and steering effort in obstacle avoidance manoeuvres with oncoming traffic. In *Proceedings of the 24th International Symposium on Dynamics of Vehicles on Roads and Tracks*, Graz, Austria.

Brännström, M., E. Coelingh, & J. Sjöberg (2010). Model-Based Threat Assessment for Avoiding Arbitrary Vehicle Collisions. *IEEE Transactions on Intelligent Transportation Systems 11*(3), 658–669.

Dang, D. T., D. J. Desens, D. U. Franke, P. D. D. Gavrila, L. Schäfers, & D. W. Ziegler (2012). Steering and Evasion Assist. In A. Eskandarian (Ed.), *Handbook of Intelligent Vehicles*, pp. 759–782. Springer London. DOI: 10.1007/978-0-85729-085-4_29.

Klomp, M., K. Olsson, & C. Sandberg (2014, January). Nonlinear steering control for limit handling conditions using preview path curvature. *International Journal of Vehicle Autonomous Systems 12*(3), 266–283.

Yanagisawa, M., J. D. Smith, & W. G. Najm (2007, April). Pre-Crash Scenario Typology for Crash Avoidance Research. Technical report DOT HS 810 767, NHTSA.

www.TechnicalBooksPDF.com

Advanced Vehicle Control – Edelmann, Plöchl & Pfeffer (Eds)
© 2017 Taylor & Francis Group, London, ISBN 978-1-138-02992-7

Torque-based steering assistance for collision avoidance during lane changes

Z. Ercan
Department of Mechanical Engineering, University of California, Berkeley, USA
Department of Control and Automation Engineering, Istanbul Technical University, Istanbul, Turkey

A. Carvalho, S. Lefèvre & F. Borrelli
Department of Mechanical Engineering, University of California, Berkeley, USA

H.E. Tseng
Ford Research Laboratories, Dearborn, MI, USA

M. Gokasan
Department of Control and Automation Engineering, Istanbul Technical University, Istanbul, Turkey

ABSTRACT: Lane changing is a cognitively demanding task that drivers perform frequently while driving on highways at high speed. This paper presents a predictive control framework which prevents collisions during lane change maneuvers. Approaches based on steering angle control are commonly used in the literature. These approaches may inadvertently take away the ultimate control authority of the driver. Also they involve a separate lower level steering control that requires subjective and complex steering feel calibration and steering torque constraints. The method proposed in this paper is based on a corrective torque formulation which incorporates the steering dynamics and driver response in the model. We tested the proposed controller in an experimental vehicle with a human driver. The results demonstrate that the proposed method avoids collision threats with minimum intervention.

1 INTRODUCTION

Studies show that 4 to 10 percent of road accidents occur during or around lane change maneuvers. In most cases, the drivers do not initiate an avoidance maneuver because they fail to notice the presence of other vehicles in the surroundings (Fitch et al. 2009).

There is an emerging research interest on driver steering assistance systems (DSAS) which use environment perception sensors and electronically controlled actuators to manipulate the steering of the vehicle in order to improve safety. Some of the systems could provide visual, haptic or auditory warnings to enhance the situational awareness of driver (Bartels et al. 2012). However, there are scenarios when an autonomous intervention could be necessary to prevent any means of collision. This paper focuses on the design and implementation of a DSAS which uses a column-type electric power steering (EPS) actuator to provide a torque intervention to the driver in order to prevent hazardous situations.

The works in Gray et al. (2013) and Anderson et al. (2010) focus on using steering angle as control input in design of semi-autonomous vehicle control. Although steering angle control provides robustness and simplicity, it does not consider the human-machine interactions arising from sharing the same physical interface and therefore the system does not let the driver intervene or take over smoothly. For example in the work of Gray et al. (2013), a lane departure avoidance system is proposed using a predictive controller to optimize a corrective steering angle. In order to realize the torque intervention in a vehicle equipped with EPS, the authors use a low-level controller to calculate corrective torque reference. This controller needs to be tuned so that the magnitude and rate of the corrective torque feels comfortable to the driver.

On the other hand, steering torque input is used to assist the driver in lane keeping applications in Minoiu-Enache et al. (2009) and Shimakage et al. (2002). The intervention is realized by a servo motor mounted in the steering column. However, these studies consider the driver torque as a disturbance and assume that driver does not apply any torque during the intervention.

From a practical point of view, another approach to realize such a safety intervention would be using the torque overlay function of the steering actuator (i.e. EPS). The torque overlay function enables the superimposition of a corrective torque to the assistive torque applied by the EPS. A lane keeping system using torque overlay function is proposed in the work of Kim et al. (2016). However, driver torque is considered as a disturbance in the control structure.

www.TechnicalBooksPDF.com

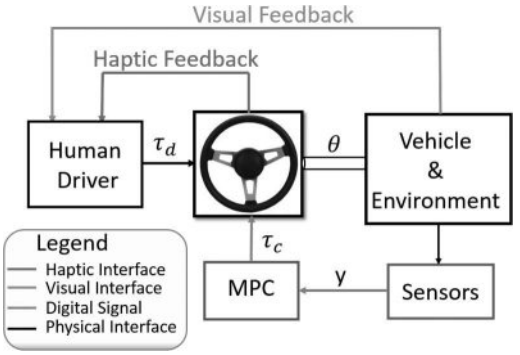


Figure 1. System architecture.

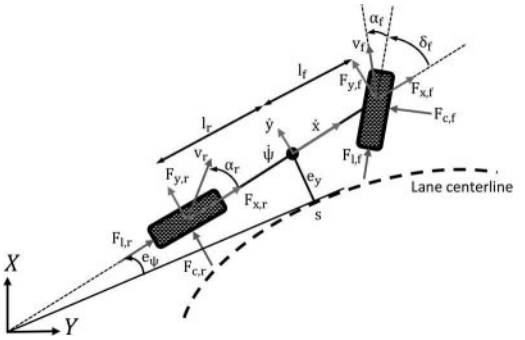


Figure 2. Notation used in the bicycle model.

The work presented in Zafeiropoulos and Cairano (2013) formulates the human-machine interactions as constraints on the driver's steering feel and the proposed controller improves the stability of the vehicle during aggressive maneuvers.

In this paper, we extend the work of Gray et al. (2013) to be directly implemented in a vehicle equipped with an EPS system. We propose a model predictive control (MPC) framework which optimizes a corrective torque as an input to the EPS actuator in order to prevent collisions during lane change maneuvers. We account for the human-machine interactions by modeling the steering dynamics of the driver-in-the-loop system. The corrective torque is optimized for smoothness and utilizes minimum effort. The resulting controller is always active but intervenes only if the safety constraints are violated.

2 SYSTEM DESCRIPTION

The system architecture is shown in Fig. 1. The human driver and the controller can both apply torque , respectively τ_d and τ_c, to the steering column. The steering wheel is the physical interface between the driver and the controller. The "Vehicle & Environment" block represents the ego vehicle (EV) (i.e. where the controller action is implemented) and the target vehicles (TVs) which are traveling in the vicinity of the EV. The "Sensors" block provides all the measurements related to the EV, road geometry, and relative positions and velocities of the TVs. The proposed controller is implemented in the "MPC" block which outputs a corrective torque input τ_c that is exerted on the steering column by the EPS actuator.

The main contributions of this paper are:

- An implementation of predictive, driver-in-the-loop control framework for safe, assisted driving. The control design uses a model of driver-in-the-loop steering dynamics.
- An approach for modeling driver-in-the-loop steering dynamics.
- Experimental validation of the proposed framework with a human driver in a commercial vehicle without any modification to the steering actuator.

3 MODELING

In this section, we introduce the mathematical models used in the controller to describe the motion of the EV and simulated TVs.

3.1 *Ego vehicle model*

We use a bicycle model to describe the dynamics of the EV as illustrated in Fig. 2. The following set of nonlinear differential equations describe the motion of the vehicle in a road-aligned coordinate frame (Rajamani 2011):

$$\ddot{x} = \dot{\psi}\dot{y} + a_x \tag{1a}$$

$$\ddot{y} = -\dot{\psi}\dot{x} + \frac{2}{m}\left(F_{y,f} + F_{y,r}\right) \tag{1b}$$

$$\ddot{\psi} = \frac{2}{I}\left(l_f F_{y,f} - l_r F_{y,r}\right) \tag{1c}$$

$$\dot{e}_\psi = \dot{\psi} - \kappa\dot{s} \tag{1d}$$

$$\dot{e}_y = \dot{x}\sin(e_\psi) + \dot{y}\cos(e_\psi) \tag{1e}$$

$$\dot{s} = \frac{1}{1-\kappa e_y}\left(\dot{x}\cos(e_\psi) - \dot{y}\sin(e_\psi)\right). \tag{1f}$$

The longitudinal and lateral velocity of the center of gravity (CoG) are denoted as $\dot{x}$ and $\dot{y}$, respectively, and $\dot{\psi}$ is the yaw rate. The longitudinal acceleration is denoted as a_x. e_y and e_ψ denote the lateral position of the vehicle with respect to the lane center line and the orientation of the vehicle with respect to the tangent at the road center line, respectively. The road curvature κ is assumed to be known at each time step. The longitudinal position of the vehicle along the lane center line is denoted as s. The parameters of the vehicle model are the mass m, moment of inertia I and distances from the CoG to front and rear axles, denoted as l_f and l_r, respectively.

www.TechnicalBooksPDF.com

Since we focus on the lateral control of the vehicle in this paper, we introduce the following assumption:

Assumption 1. *We assume zero longitudinal acceleration in the EV model that is used in predictive controller (i.e. $a_x = 0$ in (1a)).*

We consider a front steerable vehicle model where δ denotes the road steering angle of the front tires. Under normal driving conditions (i.e. small slip angles), the linear tire model provides a good approximation of the relationship between the lateral tire force and the tire slip angle. In the linear regime, the front (rear) lateral tire force $F_{c,f}$ ($F_{c,r}$) is proportional to the front (rear) tire slip angle α_f (α_r). That is,

$$F_{c,i} = -C_{\alpha_i}\alpha_i, \qquad i \in \{f, r\}, \tag{2}$$

where C_α denotes the cornering stiffness of the tire. The slip angles α_f and α_r are approximated as,

$$\alpha_f = \frac{\dot{y} + l_f\dot{\psi}}{\dot{x}} - \delta, \qquad \alpha_r = \frac{\dot{y} - l_r\dot{\psi}}{\dot{x}}. \tag{3}$$

The numerical values of the cornering stiffnesses of the front and rear tires are estimated experimentally. The lateral tire forces acting on the CoG in the vehicle body frame are represented by,

$$F_{y,f} = F_{c,f}\cos\delta, \qquad F_{y,r} = F_{c,r}. \tag{4}$$

The nonlinear bicycle model described in (1)–(4) is compactly written as,

$$\dot{\xi}(t) = f(\xi(t), u(t), \kappa(t)), \tag{5}$$

where the state vector is $\xi = [\dot{x}, \dot{y}, \dot{\psi}, e_\psi, e_y, s]^{\mathrm{T}}$, the control input is $u = \delta$ and κ is the curvature parameter.

3.2 *Driver-in-the-loop steering dynamics model*

We represent the equivalent rotational dynamics of the steering system of a vehicle as

$$J_s\ddot{\theta} + b_s\dot{\theta} = \tau_d + \tau_c - \tau_r, \tag{6}$$

where J_s and b_s represents the inertia and damping of the steering system respectively. τ_d represents the driver torque, τ_c is the corrective torque (i.e. input to the steering actuator) and τ_r is the equivalent alignment torque that is generated from road-tire interaction.

We consider a steering system where the driver and the steering actuator are mechanically coupled. During a safety intervention, the driver feels the corrective torque through the steering wheel and could respond to the intervention in different ways. The driver could either follow the corrective torque without resisting (i.e. compliant driver) or could oppose the intervention by generating a reaction torque (i.e. stiff driver).

The predictive controller requires a model that relates the actuator input τ_c to output θ in order to predict the future evolution of the steering dynamics. Using this model, we can relate the actuator input to the states of EV model presented in (1).

Hence, we propose the following assumptions to derive the "driver-in-the-loop steering model".

Assumption 2. *We define the driver torque as $\tau_d = \tau_{d,str} + \tau_{d,react}$ where $\tau_{d,str}$ and $\tau_{d,react}$ represent the steering and the reaction torque of driver respectively.*

Assumption 3. *Driver applies a steering torque that is equal to alignment torque (i.e. $\tau_{d,str} = \tau_r$) in the prediction horizon.*

Assumption 4. *The reaction torque of driver is defined as $\tau_{d,react} = J_{dr}\ddot{\theta} + b_{dr}\dot{\theta} + k_{dr}\theta$ where J_{dr}, b_{dr} and k_{dr} represent the dynamic properties of the driver's impedance which is coupled to the impedance of steering system (Pick and Cole 2007).*

Using the assumptions (2)–(4), we propose the "driver-in-the-loop steering model" from input τ_c to output θ as a second order single input-single output (SISO) system

$$\frac{d}{dt}\begin{bmatrix}\theta \\ \dot{\theta}\end{bmatrix} = \begin{bmatrix}0 & 1 \\ -\frac{k_{eq}}{J_{eq}} & -\frac{b_{eq}}{J_{eq}}\end{bmatrix}\begin{bmatrix}\theta \\ \dot{\theta}\end{bmatrix} + \begin{bmatrix}0 \\ \frac{1}{J_{eq}}\end{bmatrix}\tau_c, \tag{7}$$

where the parameters J_{eq}, b_{eq}, k_{eq} describe the equivalent inertia, damping and stiffness of the driver-in-the-loop steering system model.

Remark 1. *The parameters in (7) are used as tunable parameters to calibrate the torque intervention feel. These parameters change with respect to response of driver and should be identified online. However, in this paper we use constant values of the parameters which are tuned during experiments that are performed with a compliant driver.*

We augment the vehicle dynamics model (5) in section 3.1 with the steering model in (7). The augmented nonlinear vehicle model can be compactly written as $\dot{\zeta}(t) = f(\zeta(t), u(t), \kappa)$ where the state vector is $\zeta = [\dot{x}, \dot{y}, \dot{\psi}, e_\psi, e_y, s, \theta, \dot{\theta}]^{\mathrm{T}}$, the control input is $u = \tau_c$ and κ is the curvature parameter.

We discretize the differential equations using a forward Euler approach with fixed sample time T_s to obtain $\zeta_{k+1} = f^d(\zeta_k, u_k, \kappa)$ where k denotes the current discrete time step and $t = kT_s$.

3.3 *Simulated target vehicle model*

We use the Intelligent Driver Model (IDM) to simulate virtual TVs that are traveling around EV. This model represents the longitudinal dynamics of TVs

www.TechnicalBooksPDF.com

Table 1. IDM Parameters.

Parameter	Value	units
acceleration exponent μ	4	–
max. acceleration a	1.5	m/s^2
desired speed v_{des}	20	m/s
comf. deceleration b	1.15	m/s^2
min. gap to leading vehicle d_0	5.0	m
time gap to leading vehicle T	1.5	s

in a car following scenario (Treiber et al. 2000). The acceleration of the TV is calculated by

$$\dot{v} = a\left[1 - \left(\frac{v}{v_{des}}\right)^{\mu} - \left(\frac{d^*(v,\Delta v_p)}{d}\right)^2\right] \tag{8a}$$

$$d^*(v,\Delta v) = \begin{cases} d_0 + Tv + \frac{v\,\Delta v_p}{2\sqrt{ab}} & \text{if there is a PV} \\ 0 & \text{otherwise} \end{cases} \tag{8b}$$

The relative velocity is defined as $\Delta v_p \triangleq v_p - v$ where v_p is the velocity of preceding vehicle (PV). If there is a PV in front of simulated TV, the algorithm calculates the acceleration to track the desired distance d^*. If there is no PV (i.e. EV is not in front of TV), the algorithm calculates the acceleration to track the desired speed v_{des}. All the relevant parameters are given in the Table 1.

4 MODEL PREDICTIVE CONTROLLER DESIGN

In this section, we present the design of the predictive controller which employs the models presented in the previous section.

4.1 *Safety constraints*

We define a "safety box" around each TV to represent safe distance margins between the EV and the TVs, as illustrated in Fig 3. The front and rear safety distances are calculated by

$$d_{\text{front}} = d_0 + t_{\text{gap}} \max(0, \Delta v_t) \tag{9a}$$

$$d_{\text{rear}} = d_0 - t_{\text{gap}} \min(0, \Delta v_t), \tag{9b}$$

where d_0 is a constant safety distance, $\Delta v_t \triangleq v_t - v_e$ is the relative velocity and t_{gap} is the time headway which is a design parameter that relates the size of safety box to relative velocity.

Using the model in (8), we predict the position of TV and calculate safety boxes for each prediction in finite horizon. The collision avoidance constraints are formulated as upper and lower bounds on the lateral

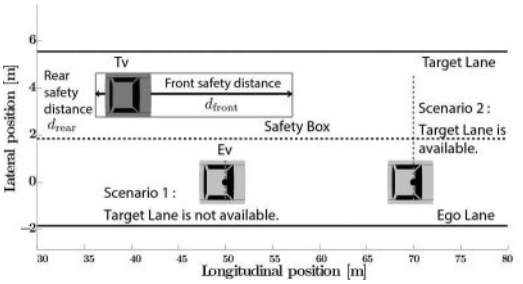


Figure 3. The safety box concept and calculation of safety constraints.

position e_y of the EV in the prediction horizon (i.e. for $i = 1 \ldots N+1$) using Eq. (10)

$$e_{y_{\min,i}} = 0.5(w_c - w_{lane}) \tag{10a}$$

$$e_{y_{\max,i}} = \begin{cases} 0.5(w_{lane} - w_c) & \text{if } s_{e,i} \in S_{t,i} \\ 1.5w_{lane} - 0.5w_c & \text{otherwise} \end{cases} \tag{10b}$$

where w_{lane} and w_c denote the width of lane and the EV. The subscript i denotes the prediction index, $s_{e,i}$ is the longitudinal position of EV at prediction index i and $S_{t,i} = [s_{t,i} - d_{rear}, s_{t,i} + d_{front}]$ denotes the size of safety box at prediction index i.

Finally, we can express the time-varying safety constraints in prediction horizon as,

$$e_{y_{\min,i}} \le e_{y,i} \le e_{y_{\max,i}} \quad \text{for} \quad i = 1 \ldots N+1. \tag{11}$$

Remark 2. *The size of the safety box is associated to the conservativeness of the intervention by the controller as the safety constraints are calculated based on safety box.*

4.2 *Input constraints*

We define magnitude and rate constraints on the actuator input (i.e. τ_c) in order to have a smooth and adequate level of torque intervention:

$$\tau_{\min} \le \tau_c \le \tau_{\max} \tag{12a}$$

$$\Delta\tau_{\min} \le \Delta\tau_c \le \Delta\tau_{\max}. \tag{12b}$$

4.3 *Optimal control problem*

We use the framework of nonlinear model predictive control (NMPC) for designing the DSAS controller. In NMPC, a constrained finite horizon optimal control (CFTOC) problem is solved at each time step. The first optimal input is applied to the vehicle and the process is repeated at the next time step using the new state measurement as the initial condition.

In the CFTOC problem (13), the optimization variables are the corrective torque input ($u = \tau_c$) and the

www.TechnicalBooksPDF.com

Table 2. Process model parameters.

Parameter	Value	Parameter	Value
m	1830 kg	l_f	1.1520 m
I	3477 kg m^2	l_r	1.6930 m
C_{α_f}	40703 N/rad	C_{α_r}	64495 N/rad
w_c	1.86 m	J_{eq}	0.5 kg m^2
b_{eq}	2.5 Nm s/rad	k_{eq}	6.25 Nm/rad

Table 3. MPC parameters.

Parameter	Value	Parameter	Value
T_s	0.1 s	T_{mpc}	0.2 s
$\tau_{\min}$	-5 Nm	$\Delta\tau_{\min}$	-5 Nm/s
$\tau_{\max}$	5 Nm	$\Delta\tau_{\max}$	5 Nm/s
$e_{y_{min}}$	-0.67 m	$e_{y_{max}}$	4.07 m
w_{lane}	3.4 m	Q, R	(10, 10)
M	10000	N	10

slack variable ϵ. The following numerical optimization problem is solved in real-time,

$$\min_{\mathbf{u}_k,\epsilon} \sum_{i=0}^{N-1} \left(||u_{i|k}||_Q^2 + ||\Delta u_{i|k}||_R^2 \right) + M\epsilon \tag{13a}$$

$$\text{s.t. } \zeta_{i+1|k} = f_d(\zeta_{i|k}, u_{i|k}, \kappa_{i|k}) \tag{13b}$$

$$\tau_{\min} \leq u_{i|k} \leq \tau_{\max} \tag{13c}$$

$$\Delta\tau_{\min} \leq \Delta u_{i|k} \leq \Delta\tau_{\max} \tag{13d}$$

$$e_{y_{\min,i+1}} - \epsilon \leq e_{y_{i+1}} \leq e_{y_{\max,i+1}} + \epsilon \tag{13e}$$

$$\epsilon \geq 0, \qquad i = 0 \ldots N-1$$

$$\zeta_{0|k} = \zeta_k \ , \quad u_{-1|k} = u_{k-1}, \tag{13f}$$

where N is the prediction horizon. $\zeta_{i|k}$ denotes the ith state prediction at time step k obtained by applying the optimal control input sequence $\mathbf{u}_k = \{u_{0|k}, u_{1|k}, \ldots, u_{N-1|k}\}$ to the discrete-time dynamics (13b) starting from the measured state at the current time step (13f). We impose the safety constraints as soft constraints (13e) by introducing the slack variable ϵ in order to keep the optimization problem feasible in case of constraint violations due to model mismatch. The actuator input constraints are formulated in (13c) and (13d).

5 EXPERIMENTAL RESULTS

The control design presented in Sections (3)–(4) has been validated experimentally on a test vehicle. The steering actuator is a production level EPS. The sensors, embedded computer and actuators communicate through a CAN bus. During the experiments, we used the parameters given in Table 2 and Table 3.

The objective of the test is to evaluate the system's ability to prevent high risk lane changes. We simulated a TV around the test vehicle (next called EV). At time $t = 2$ s, driver of the EV simulated an inattentive driver behavior by initiating a lane change maneuver while there is a fast TV in the target lane. The measured lateral position of the EV along with the open-loop (OL) predictions from the controller are illustrated in Fig. 4. The results show that the controller prevents the vehicle from departing the lane.

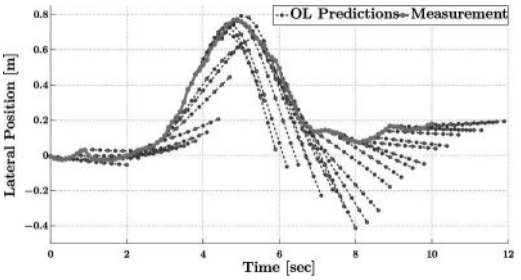


Figure 4. The lateral position and the open-loop predictions of the EV during the experiment.

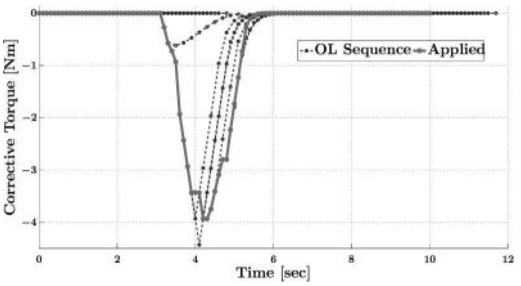


Figure 5. The corrective torque sequence during the experiment.

The predictive controller assessed the risk of collision by predicting the positions of the EV and TV and intervened only if it is safety critical. The corrective torque is illustrated in Fig. 5. The corrective torque is zero when the predicted driver actions result in a safe trajectory. However, if the predicted trajectory violates the safety constraints, an intervention is triggered to guide the driver back to the safe region of the road.

At time $t = 3.2$ s, the predictive controller started applying a clockwise (i.e. negative in magnitude) corrective torque to steer the vehicle to right. In Fig. 6, we illustrate a snapshot of the experiment at $t = 3.8$ s. It is observed that without intervention, the controller predicted the vehicle would leave the lane therefore violating the safety constraints. By applying the corrective torque, the controller updated its predictions to satisfy the safety constraints.

Starting from time $t = 3.8$ s, driver started to steer in clockwise direction as a result of corrective torque. The steering wheel angle measurements and the open-loop predictions are given in Fig. 7. The corrective torque

www.TechnicalBooksPDF.com

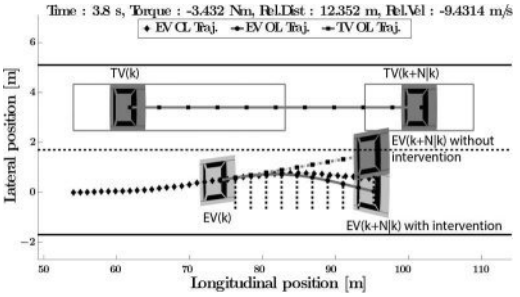


Figure 6. The snapshot at time $t = 3.8$ s. This figure shows the open-loop (OL) predictions of EV and TV along with the actual (closed-loop (CL)) trajectory of EV.

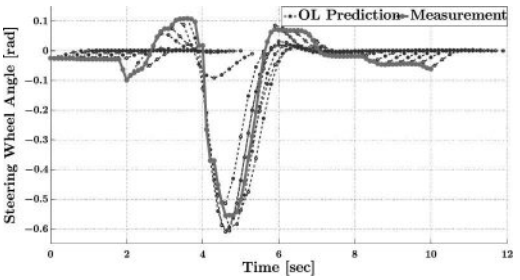


Figure 7. The steering wheel angle of EV during the experiment.

decayed to zero when driver steered back to safety portion of the road. Because of the rate constraints, the corrective torque is applied gradually which provides a smooth transition instead of rapid changes in corrective torque dynamics.

6 CONCLUSIONS

We propose a predictive, human-in-the-loop control framework for preventing collisions during lane change maneuvers. We focus on modeling the steering dynamics such that we could use the native input of the EPS actuator (i.e. torque) as a direct optimization variable in predictive controller. This has the following advantages:

- Compared to an optimal steering angle approach, a low-level controller is no longer needed to calculate the torque input from a desired corrective steering angle.
- The actuator limits can be systematically handled in the predictive controller.

As both the driver and controller act on the steering wheel, it is important to account for the reaction of the driver. Our approach enables this by modeling the driver-in-the-loop steering model which integrates the driver torque dynamics into steering system model.

We implement the presented control framework on a test vehicle and validate the performance with a human driver. The experimental results demonstrate the effectiveness of the proposed controller in preventing high risk lane change maneuvers.

As the next step of our research, we will work on experimental tests with more drivers, using different parameters in the driver-in-the-loop steering model to observe their affects on the steering feel of the drivers during intervention.

REFERENCES

Anderson, S. J., S. C. Peters, T. E. Pilutti, & K. Iagnemma (2010). An optimal-control-based framework for trajectory planning, threat assessment, and semi-autonomous control of passenger vehicles in hazard avoidance scenarios. *International Journal of Vehicle Autonomous Systems 8*(2–4), pp. 190–216.

Bartels, A., M.-M. Meinecke, & S. Steinmeyer (2012). *Lane Change Assistance*, pp. 729–757. Springer London.

Fitch, G. M., S. E. Lee, S. Klauer, J. Hankey, S. J., & T. Dingus (2009, June). Analysis of lane-change crashes and near-crashes. Technical report, National Highway Traffic Safety Administration.

Gray, A., M. Ali, Y. Gao, J. K. Hedrick, & F. Borrelli (2013). A unified approach to threat assessment and control for automotive active safety. *Intelligent Transportation Systems, IEEE Transactions on 14*(3), pp. 490–1499.

Kim, W., Y. S. Son, & C. C. Chung (2016, June). Torque-overlay-based robust steering wheel angle control of electrical power steering for a lane-keeping system of automated vehicles. *IEEE Transactions on Vehicular Technology 65*(6), pp. 4379–4392.

Minoiu-Enache, N., M. Netto, S. Mammar, & B. Lusetti (2009). Driver steering assistance for lane departure avoidance. *Control Engineering Practice 17*, pp. 642–651.

Pick, A. & D. J. Cole (2007). Dynamic properties of a driver's arms holding a steering wheel. *Proceedings of the Institution of Mechanical Engineers, Part D: Journal of Automobile Engineering 221*(12), pp. 1475–1486.

Rajamani, R. (2011). *Vehicle Dynamics and Control*. Mechanical Engineering Series. Springer.

Shimakage, M., S. Satoh, K. Uenuma, & H. Mouri (2002). Design of lane-keeping control with steering torque input. *JSAE Review 23*(3), pp. 317–323.

Treiber, M., A. Hennecke, & D. Helbing (2000). Congested traffic states in empirical observations and microscopic simulations. *Physical review E 62*(2), pp. 1805–1824.

Zafeiropoulos, S. & S. D. Cairano (2013, June). Vehicle yaw dynamics control by torque-based assist systems enforcing driver's steering feel constraints. In *2013 American Control Conference*, pp. 6746–6751.

www.TechnicalBooksPDF.com

Advanced Vehicle Control – Edelmann, Plöchl & Pfeffer (Eds)
© 2017 Taylor & Francis Group, London, ISBN 978-1-138-02992-7

Enhancing path tracking performance by using haptic shared steering control combined with DYC

S. Inoue & H. Inoue
Toyota Motor Corporation, Japan

T. Ozawa & P. Raksincharoensak
Tokyo University of Agriculture and Technology, Japan

M. Nagai
Japan Automobile Research Institute, Japan

ABSTRACT: This paper investigates a new shared control system which combines haptic steering guidance torque together with Direct Yaw-Moment Control (DYC) in order to enhance path tracking performance and achieve good human-machine cooperative characteristics. The experiment is conducted by using the driving simulator to verify the effectiveness of DYC on path tracking performance as well as the cooperative steering characteristics between human driver and steering assistance system. As the results, it is clarified that the proposed driver assistance system has positive shared control characteristics among the elderly drivers. Furthermore, the parameters of driver behavior model are identified using the experimental results. As a result, the haptic steering guidance torque can compensate the time delay in visual feedback of elderly drivers.

1 INTRODUCTION

The authors investigate an autonomous intelligent driving system to enhance safe and secured traffic society for elderly drivers (Nagai, M. & Inoue, H. 2014). One on the important issues for the intelligent driving system is how to develop the relationship between a human and the system. Since our goal is that a human driver is still in the loop, and a human driver performs to track a desired path, our study focus on steering shared control between a human driver and the intelligent driving system (Abbink, D.A. et al. 2012). Conventional steering assistance systems had a drawback in causing interference between the steering torque from a driver and steering assistance systems when setting the intensity of steering assistance level at large level (Yuhara, N. et al. 1997), (Iwano, K. et al. 2014), (Petermeijer, SM. et al. 2015). Therefore, reducing the degree of the interference together with maintaining good path-tracking performance is a challenging issue to realize good shared control characteristics between human and machine. From the above issues, this paper investigates a new shared control system which combines haptic steering guidance torque and Direct Yaw-Moment Control (DYC). The proposed system can potentially solve the interference problem, as DYC is used to control the lateral dynamics as an independent control input.

The experiment was conducted by using TUAT driving simulator to evaluate the proposed system. Furthermore, the parameters of driver model were identified using the above experimental results. The experiment results exhibit that DYC significantly reduces the interference as well as maintains good path tracking performance, and the steering assistance system potentially changes the driving characteristics of elderly drivers in the way that they tend to rely on the given steering guidance torque.

2 SHARED CONTROL SYSTEM DESIGN

Figure 1 shows the proposed system. The steering assistance system aims to induce the driving behavior of elderly drivers to be close to that of a reference driver model (equation 1).

$$\theta_{sw}^{*} = \frac{h_s}{1+\tau_{ns}s}\left\{Y_s - \left(Y_c + T_{ps}V\psi\right)\right\} \tag{1}$$

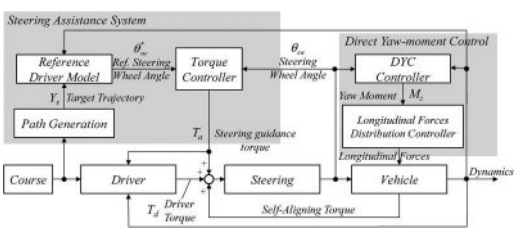


Figure 1. Human-machine shared control system.

www.TechnicalBooksPDF.com

where, θ^*_{sw} denotes the reference steering wheel angle, h_s denotes the reference driver gain, τ_{ns} denotes the reference time constant, Y_s denotes the reference lateral displacement at the preview point, Y_c denotes the lateral displacement of center of gravity, T_{ps} denotes the reference preview time, V denotes the vehicle speed, Ψ denotes the yaw angle. The haptic steering guidance torque control law is expressed as equation 2.

$$T_a = K_a\left(\theta^*_{sw} - \theta_{sw}\right) \tag{2}$$

where, T_a denotes the steering guidance torque, K_a denotes the steering guidance gain, θ_{sw} denotes the steering wheel angle. When steering wheel angle θ_{sw} does not correspond to the reference steering wheel angle θ^*_{sw}, the steering guidance torque T_a is provided to drivers as a haptic torque from steering wheel, to indicate the steering direction that he/she should apply to drive along the desired path.

The control law of DYC is expressed as equation 3.

$$M_Z = K_{mz} \times \frac{\theta_{sw}}{n} \tag{3}$$

where, M_z denotes the DYC input, K_{mz} denotes the DYC gain, n denotes the gear ratio. There are two aims in the design of DYC. The first effect is to reduce self-aligning torque. When self-aligning torque is decreased, driver torque and steering guidance torque are decreased consequently. The second effect is to improve the vehicle responsiveness with respect to the steering angle. According to these effects, the proposed system can reduce the degree of the interference between the driver torque and the steering guidance torque T_a.

3 SINGLE LANE CHANGE SIMULATION IN HUMAN-MACHINE CLOSED LOOP

3.1 *Driver model*

The simulation of a single lane change is conducted to evaluate the proposed shared control system. This section describes the driver model defined in this simulation. Equation 4 expresses the driver model with steering torque input (Yuhara, N. et al. 1997).

$$T_d = \frac{1}{1+\tau_v s}\left[H\left\{Y_d - \left(Y_c + T_p V\psi\right)\right\}\right] + \frac{1}{1+\tau_h s}\left(K_h T_a\right) \tag{4}$$

where, T_d denotes the driver torque, τ_v denotes the driver visual time constant, H denotes the driver compensatory gain based on the visual information, Y_d denotes the driver target lateral displacement, T_p denotes the driver preview time, τ_h denotes the driver haptic time constant, K_h denotes the driver compensatory gain based on the haptic information. The first term on the right side in the equation 4 indicates the torque with respect to the visual feedback information, whereas the second term indicates the torque with respect to the haptic steering information.

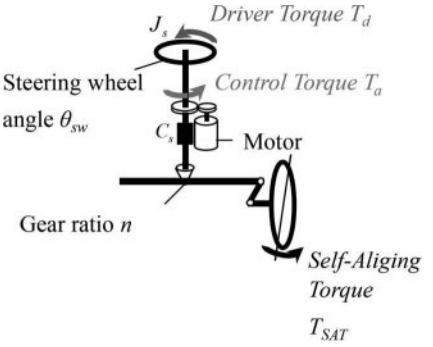


Figure 2. Steering model.

3.2 *Steering and vehicle model*

The steering model indicated in figure 2 is used in this simulation coupling with the above driver model with steering torque input. The steering equation of motion is expressed as equation 5.

$$\theta_{sw} = \frac{1}{J_s s^2 + C_s s}\left(T_d + T_m - \frac{T_{SAT}}{n}\right) \tag{5}$$

where, J_s denotes the moment of inertia of the steering wheel, C_s denotes the viscous damping coefficient of steering wheel side, T_m denotes the motor torque of the steering, T_{SAT} denotes the self-aligning torque. The motor torque of the steering T_m is expressed as equation 6.

$$T_m = K_{ps} \times \frac{T_{SAT}}{n} + T_a \tag{6}$$

where, K_{ps} denotes the coefficient of electric power steering. In this model, the complicated power steering mechanism and the torsional stiffness of the steering model are not considered. Moreover, the self-aligning torque T_{SAT} is transferred from the front tires to the steering shaft directly through the steering gear.

The linear equivalent two-wheel vehicle model is used in the simulation. The parameters of the vehicle model are defined assuming a mid-size vehicle.

3.3 *Simulation conditions*

The driving course which is a single lane change is shown in Figure 3. A vehicle is running at a constant speed of 16.6 m/s. The control conditions are shown in Table 1. These are "Without control", "Steering control", and "Steering + DYC control". Table 2 shows the parameters of the driver models. The driver target lateral displacement Y_d in the driver model is set with the center of the course at the preview point.

3.4 *Simulation results*

Figure 4 shows the simulation results. Where, 0 m of trajectory X refers to 0 s of time in the vertical axis. First of all, the effectiveness of the steering assistance

www.TechnicalBooksPDF.com

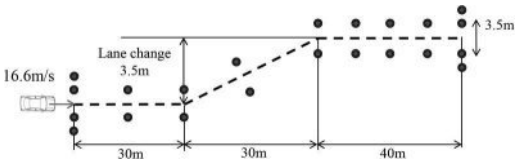


Figure 3. Driving course of single lane change.

Table 1. Simulation conditions.

Type	K_a [Nm]	K_{mz} [Nm]
Without control	0	0
Steering control	4	0
Steering + DYC control	4	4×10^4

Table 2. Driver parameters.

Parameters	Ref. Driver	Driver
Visual gain	0.4 rad/m	1.1N
Visual time constant	0.05 s	0.2 s
Haptic time constant	–	0.05 s
Preview point	1.3 s	1.2 s
Haptic gain	–	−0.5

system is focused on. In the case of "Without control", the starting point of changing is late (the first row). Moreover, the overshoot is confirmed from 70 m to 120 m. On the other hand, in the case of "Steering control" the more responsive and smoother vehicle trajectories are achieved. It is assumed that these results are caused by the relationship between parameters of the reference driver and the driver model. Since the reference time constant τ_n is smaller than the driver visual time constant τ_v, and the reference preview time T_{ps} is larger than the driver preview time T_p, the reference driver model is set to maneuver the steering wheel more adequately. The setting results in the changing of the driver torque (the forth row), and the induction of the driver's maneuver by the steering assistance occurred.

The effectiveness of DYC is verified by comparing "Steering control" with the case of "Steering+DYC control". In the case of "Steering+DYC", the reduction of the driver torque T_d is also observed in the fourth row. This result relates to the first effect of DYC. The responsiveness of the lateral acceleration at the start point is increased (the second row). This result relates to the second effect of DYC. Figure 5 shows the magnified figure of trajectory Y. The double-dashed line shows the trajectory of the reference driver Y_{ref}. It is confirmed that "Steering+DYC" effectively controlled the vehicle lateral motion making the vehicle closer to the reference trajectory Y_{ref}.

To evaluate the improvement of the shared characteristics in a quantitative way, the relationship between the path tracking performance and the torque interference is investigated by using the square integral

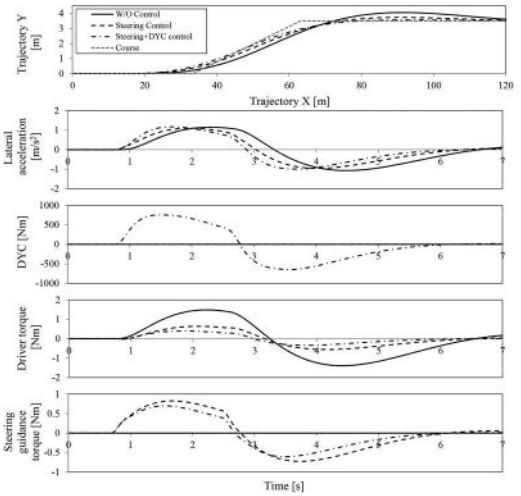


Figure 4. Simulation results of single lane change.

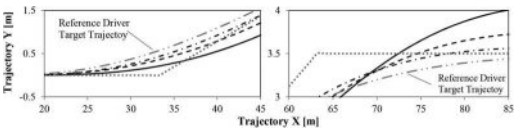


Figure 5. Magnified figure of trajectory Y (X = 20 ∼ 45 m, 60 ∼ 85 m).

values. Figure 6 shows the simulation results in which the X-axis indicates the square integral values of the difference between driver torque T_d and steering guidance torque T_a, the Y-axis indicates the square integral values of the trajectory of the vehicle Y_c deviation with respect to the target trajectory of the reference driver Y_{ref}. To investigate the influence of the steering guidance gain K_a, the several magnitudes ($K_a = 2$, 4, 6, 8 and 10) are simulated in a control condition. As can be noticed from the graph, the trade-off relationship between two evaluation indices in the case of "Steering control" (indicated with rhombus shape marks) is found. On the other hand, it is observed that the proposed system "Steering + DYC control" performs better path tracking performance with lower steering torque interference (squares). This tendency is emphasized with the higher DYC gain (triangles). From these results, the effectiveness of DYC is verified.

4 DRIVING SIMULATOR EXPERIMENT FOR SHARED CONTROL SYSTEM EVALUATION

4.1 *TUAT driving simulator*

Figure 7 shows TUAT driving simulator used in this experiment. TUAT driving simulator consists of a host computer, a visual system, an audio system, a steering system and a hexapod motion cueing controller. The driving simulator is equipped with the same driver

www.TechnicalBooksPDF.com

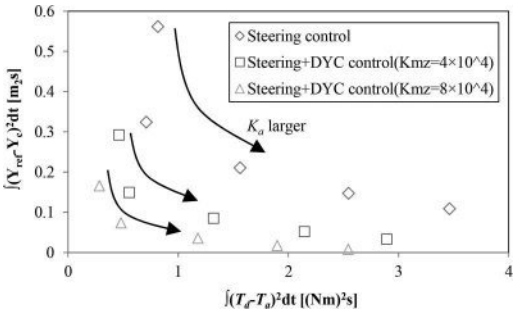


Figure 6. Relationship between torque interference and path tracking performance.

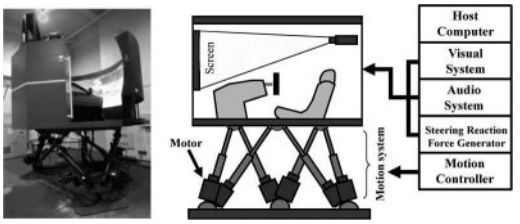


Figure 7. TUAT driving simulator.

operational interfaces as a real vehicle. The host computer calculates the vehicle behavior base on the input of driver operational interfaces and consequently generates the driving screen image. The hexapod motion cueing system is operated based on the calculated vehicle dynamics states.

4.2 *Experimental conditions*

The experiment was conducted by using TUAT driving simulator to evaluate the proposed shared control system (The ethical approval were obtained). Eight elderly drivers whose average age was 68 years old were employed to drive the simulator (4 females, 4 male. They usually drive their individual cars with daily scene.) The driving course which is a single lane change is shown in Figure 3. A vehicle is running at a constant speed of 16.6 m/s. The control conditions are shown in Table 1. There are "Without control", "Steering control", and "Steering+DYC control". The subjects were instructed to change a lane by using the steering guidance torque T_a. Meanwhile, since only steering guidance torque T_a cannot accomplish a single lane change, the subjects were instructed to conduct proactive maneuver of steering wheel. During the experiments, the subjects were not informed about the control conditions.

4.3 *Experimental results*

The effectiveness of DYC is confirmed in six drivers (A, C, E, F, G, and H) among eight drivers. Figure 8 shows the experimental results by Driver G.

In the graph, 0 m of trajectory X refers to 0 s of time in the horizontal axis. When "Steering control" is compared with the case "Without control", the trajectory Y (the first row) was improved as the overshoot is reduced in the region from 50 m to 70 m. Focusing on the steering torque (the fourth and fifth row), it is confirmed that the driver torque T_d was obviously improved to be smoother. This result indicates that the steering guidance torque T_a is effective to driver G.

The effectiveness of DYC is verified by experiments. As "Steering+DYC control" reduces the amount of driver torque T_d and steering guidance torque T_a, the reduction of the interference between the human and steering assist can be achieved (the sixth row). Figure 9 shows the experimental results by Driver G in which the upper figure indicates the square integral values of the difference between driver torque T_d and steering guidance torque T_a, the lower figure indicates the square integral values of the trajectory of the vehicle Y_c deviation with respect to the target trajectory of the expert driver Y_{ref}. Where, the integral time is from 0s to 7s. "Steering + DYC control" performs better path tracking performance with lower steering guidance level. Since similar control effectiveness of DYC is confirmed in the above six drivers, it is verified that the proposed haptic shared steering control system combined with DYC has positive shared control characteristics among the elderly drivers.

Figure 10 shows the square integral values by driver D. Comparing "Steering+ DYC control" with "Steering control", the torque interference is slightly reduced showing the same tendency in the case of driver G. On the other hand, the path tracking performance becomes worse compared with the steering control. Since the subjects were instructed to change a lane by using the steering guidance torque T_a before starting the experiments, it is considered that driver D also tried to change his maneuver by using the steering guidance torque T_a. From this viewpoint, driver D may not understand the assistance system intervention and then apply the steering guidance torque T_a inadequately. For these drivers, displaying the target path or improving the DYC law may be more effective. We will conduct more detailed study in the future works.

5 DISCUSSIONS

5.1 *Steering wheel angular velocity evaluation*

To evaluate the handling quality, steering wheel angular velocity is discussed. Figure 11 shows the time series data of steering wheel angular velocity by driver G and driver D. When "Steering control" is applied, the steering angular velocity of each driver was reduced compared to "Without control". Since this result indicates that the maneuver of a driver is improved to be smoother, the effectiveness of steering guidance torque T_a is confirmed. This tendency is enhanced when "Steering + DYC control" is applied. This tendency comes from the effects that

www.TechnicalBooksPDF.com

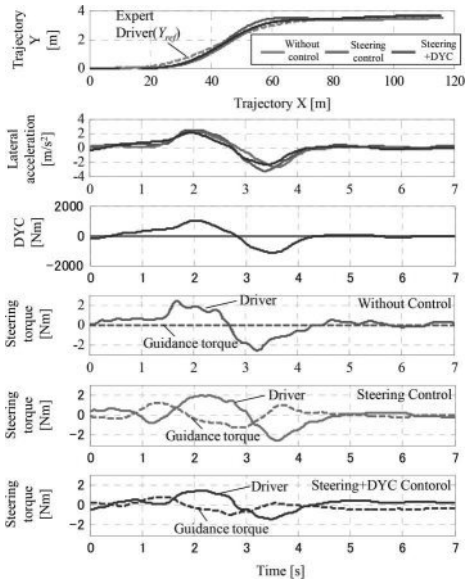


Figure 8. Experimental results of single lane change (Driver G).

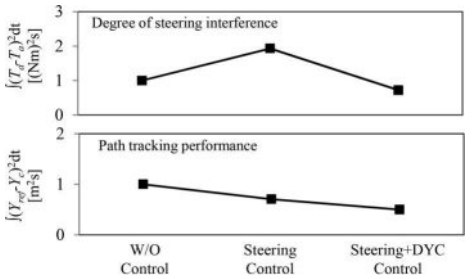


Figure 9. Square integral values of steering torque difference and deviation from desired path (Driver G, Normalized W/O control).

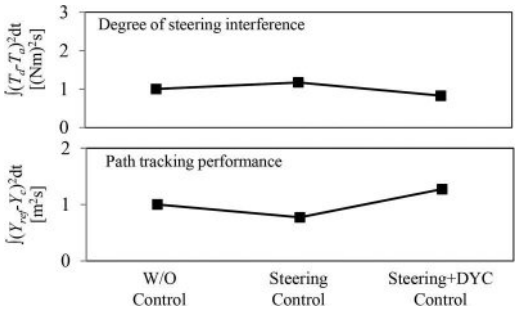


Figure 10. Square integral values of steering torque difference and deviation from desired path (Driver D, Normalized W/O control).

DYC improves the vehicle responsiveness with respect to the steering angle, and a driver can conduct path tracking in more relaxed manner. Figure 12 shows the square integral values of steering wheel angular

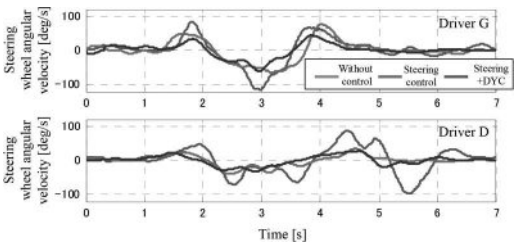


Figure 11. Time series data of steering wheel angular velocity.

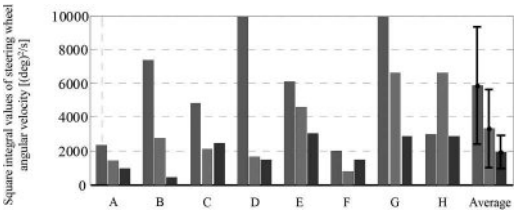


Figure 12. Square integral values of steering wheel angular velocity.

velocity among all drivers. Where, the integral time is from 0s to 7s. It is confirmed that except driver H, the square integral values of all drivers was reduced when steering guidance torque T_a was applied. It is also confirmed that the standard deviation was smaller when DYC was applied. These results indicate that drivers can conduct a single lane change with the proposed system in smooth manner.

5.2 *Driver model identification*

To analysis the change of driving behavior, the parameters of driver model are identified using the experimental results obtained in the previous section. The identified lateral driver model is equation 4. The identification chooses the parameters to minimize the error E which is defined with equation 7 by using equation 4 and the experimental results.

$$E = \int_{t1}^{t2} \left(\hat{T}_d - T_d\right)^2 dt \tag{7}$$

where, E denotes the error values regarding with square integral values of the driver torque, $\hat{T}_d$ denotes the estimated driver torque, t_1 denotes the start time of the integral region, t_2 denotes the end time of the integral region. In this study, $t_1 = 0$s and $t_2 = 7$s is selected. Figure 13 shows the relationship between the estimated driver torque $\hat{T}_d$ and the experimental driver torque T_d by driver G in the case of "Steering + DYC control". The estimated driver torque $\hat{T}_d$ is calculated by using the simulation model in the previous section with the identified parameters of the driver model. Since the estimated driver torque $\hat{T}_d$ fits with the measurement value, the estimated parameters are valid for discussions.

www.TechnicalBooksPDF.com

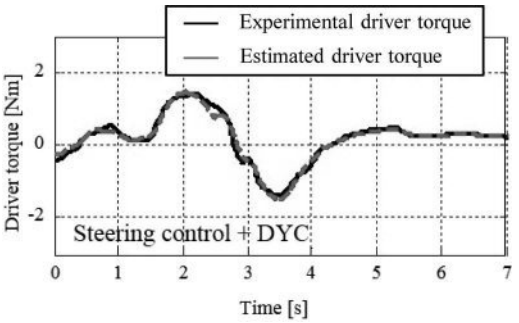


Figure 13. Relationship between estimated driver torque and that of experiment (Driver G).

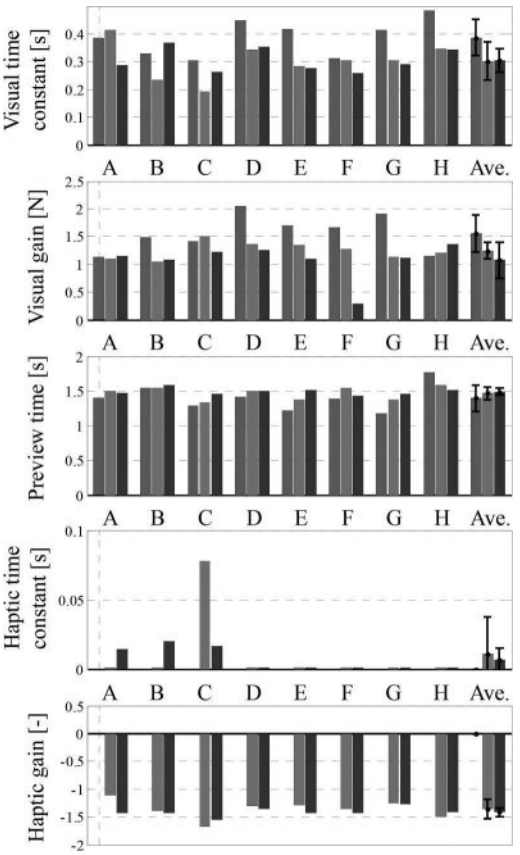


Figure 14. Identified parameters of all subjects.

Figure 14 shows the identified parameters among all drivers. It is particularly notable that the haptic time constant τ_h is very small, on the other hand, the visual time constant τ_v is large. Furthermore, it is found that steering guidance torque T_a can reduce the visual time delay compared to "without control". These results indicate that the steering guidance torque T_a can compensate the time delay in visual feedback. This characteristic is potential to be effective to elderly drivers in reducing the time delay in steering operation during path tracking.

The effectiveness of DYC is confirmed in the visual gain H and the haptic gain K_h. Comparing "Steering+DYC control" with "Steering control", drivers tend to reduce the visual gain H and emphasize the haptic gain K_h. This tendency implies that the drivers rely on the steering guidance torque T_a more strongly in the case of "Steering + DYC". Further analysis will be conducted in future works to evaluate the relationship between DYC and the change of the driver-vehicle closed loop control characteristics.

6 CONCLUSIONS

This paper has investigated a new shared control system which combines haptic steering guidance torque together with Direct Yaw-Moment Control (DYC) to obtain good path tracking performance and human-machine cooperative characteristics. It is verified that the proposed system performs better path tracking performance with lower steering guidance level by the experiment of the driving simulator. Furthermore, the parameters of driver model are identified using the above experimental results, and it is clarified that the steering guidance torque can compensate the time delay in visual feedback of elderly drivers.

ACKNOWLEDGMENT

This study has been conducted as a part of the research project "Autonomous Driving Intelligence System to Enhance Safe and Secured Traffic Society for Elderly Drivers" grated by Japan Science and Technology Agency (JST). The authors would like to thank the agency for providing financial support to conduct this research.

REFERENCES

Nagai, M. & Inoue, H. 2014. Research into ADAS with Autonomous Driving Intelligence for Future Innovation", Proceedings of Chassis Tech Plus 2014, Munich, Germany.

Abbink, D.A., Mulder, M. & Boer, E. 2012. Haptic Shared Control: smoothly shifting control authority. Cognitive Technology Work. Vol. 14: 19/28.

Yuhara, N., Horiuchi S., Iijima T., Shimizu K. & Asanuma N. 1997. An Advanced Steering System with Active Kinesthetic Feedback for Handling Qualities Improvement. Vehicle System Dynamics. Vol. 27. No. 5–6: 327–355.

Iwano, K., Raksincharoensak, P. & Nagai, M. 2014. Study on Shared Driving Characteristics between Driver and Collision Avoidance Steering Control Using Driving Simulator. 12th International Symposium on Advanced Vehicle Control.

Petermeijer SM, Abbink DA & de Winter JC. 2015. Should drivers be operating within an automation-free bandwidth? Evaluation haptic support systems with different levels of authority. Human Factor. Feb; 57: 5–20.

www.TechnicalBooksPDF.com

Advanced Vehicle Control – Edelmann, Plöchl & Pfeffer (Eds)
© 2017 Taylor & Francis Group, London, ISBN 978-1-138-02992-7

Evaluation of an evasive manoeuvre assistance system at imminent side collisions

D. Yang
Volvo Cars, Active Safety and Vehicle Dynamics Functions, Gothenburg, Sweden

M. Jonasson
Volvo Cars, Active Safety and Vehicle Dynamics Functions, Gothenburg, Sweden
The Royal Institute of Technology (KTH), Vehicle Dynamics, Department of Aeronautical and Vehicle Engineering, Stockholm, Sweden

T. Halleröd
Volvo Cars, Active Safety and Vehicle Dynamics Functions, Gothenburg, Sweden

R. Johansson
Volvo Cars, Safety Centre, Gothenburg, Sweden

ABSTRACT: In this paper, the performance of an Evasive Manoeuvre Assistance System is evaluated on the test track, where an imminent half-overlapping side collision scenario is reconstructed. The control function here aims to reduce the steering effort for an emergency swerve in front of obstacle and to ease the following recovery into the driver perceived safe zone. This is realized by combined differential braking and steering torque overlay, which improves the agreement between steering input and vehicle response. Preliminary test results have shown that the function has a great potential to reduce collision risk at the presence of suddenly appeared obstacle in front.

1 INTRODUCTION

Avoidance of obstacles that suddenly appears outside driver's comfort zone can be handled by reducing vehicle longitudinal speed, or to perform a yaw or sideward motion. Too quick appearance of the obstacle and limited deceleration efficiency without driver initiating and increasing braking may make it impossible to avoid the imminent collision by only reducing the vehicle speed. On the other hand, swerving around the obstacle by combined braking and steering can be more effective to avoid such collision. This type of swerving motion in crash-imminent situations is usually called an *evasive manoeuvre*.

However, this emergency evasive manoeuvre requires the driver to be very alert and skillful to execute brake and steer action rapidly, appropriately and simultaneously. It is more than common that normal human drivers tend to apply too little or too much steer in facing the forthcoming hazards, with noticeable delays to initiate braking as well (Malaterre, Ferrandez, Fleury, & Lechner 1988, McGehee, Mazzae, & Baldwin 1999). The conventional ESC system is designed to assist the driver to maintain vehicle stability assuming correct steering angle from driver. With insufficiently good steering input, ESC would not be the best choice to assist driver to perform a successfully evasive manoeuvre. In addition, conventional ESC does not use environmental sensors, such as camera, to detect threats.

Thereby, the control strategy, Evasive Manoeuvre Assistance System (EMAS) was introduced that aims to make the manoeuvre safer and more effective (Gurov, Sengupta, Jonasson, & Drugge 2014). The Fig. 1 below illustrates the working principle of EMAS in a rear-end collision avoidance scenario. In this paper, a generic EMAS functionality is developed in a fast-prototyping test vehicle and this implementation is achieved in order to study the potential benefit and risk of EMAS in real-world accident situation. EMAS here will not control the vehicle autonomously. The control must be initiated by the driver, who should be in the loop and be able to override EMAS all the time. This implies that driver takes the responsibility in the control of the vehicle motion.

Previous accident statistics have shown that most drivers do not steer in rear-end collisions although about 50% the collisions can be avoided by turning around object (Eckert, Hartmann, Sevenich, & Rieth 2011, Fausten 2010). Simulator studies have suggested that more than 50% of people chose to steer at imminent side collisions, e.g. with entering vehicle at

www.TechnicalBooksPDF.com

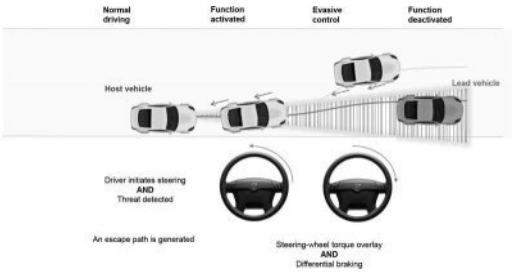


Figure 1. Evasive Manoeuvre Assistance System.



Figure 2. Photograph of test scenario with a suddenly tipped-over obstacle on a two-lane road.

intersections (Schittenhelm 2005). Reports of under-utilization of vehicle capabilities at crash-imminent manoeuvre were reviewed; drivers are more likely to brake than to steer, while the optimal maneuver is more frequently steering alone, or steering combined with braking, rather than braking alone (Adams 1994). In the present paper, an imminent side-collision scenario is reconstructed on the test track that most drivers would choose to steer. Fig. 2 photographs the test scenario, where a large-sized box is triggered and tipped over into the driving lane when the vehicle passes a certain reference point. The EMAS function was thereby evaluated under real-world collision avoidance circumstances.

2 FUNCTION DESIGN

The EMAS function is highly integrated with a class of Volvo's vehicle stability control functions on board, e.g. Active Yaw Control (AYC), Advanced Stability Control (ASC), Roll Stability Control (RSC) etc. At this stage, EMAS also shares certain control components such as friction estimator, vehicle states estimator, vehicle and tyre parameter estimator, vehicle model etc. with aforementioned functions. The coupling with other collision avoidance functions such as Autonomous Emergency Braking (AEB) is also within the scope of the function design.

The activation condition of EMAS function is an ongoing driver initiated side-motion, combined with the presence of a forthcoming collision and a feasible escape path. EMAS will thereby make use of environmental sensors like radars and cameras. The *priori* information that a single lane change is mostly likely to occur is given by:

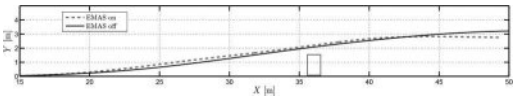


Figure 3. An example path with/without EMAS using a calibrated driver model in simulation. Red box: suddenly appearing obstacle.

- assessed threat in front *and*
- feasible escape path *and*
- driver initiated side-motion by steering

The control action exists as a *feed-forward* controller which requests brake pressures on the inner wheels and torque overlay on the steering wheel. The control inputs are proportional to the desired yaw moment calculated from the reference front axle side slip angle. In this case the controller strives to follow a driver preferred yaw motion. That is to say, EMAS predicts which heading direction the driver would like to control the vehicle towards. In the experiment, the steering wheel torque was applied by the standard Electric Power Assisted Steering (EPAS) system that allows maximum 2.5 Nm torque. The maximum brake pressure was limited by the desired wheel slips specified by the controller, together with the standard wheel slip regulator, e.g. Anti-lock Brake System (ABS). Thereafter, the function is promptly deactivated if:

- the threat becomes invalidated *or*
- the reference path is found to be infeasible due to e.g. limited space, too low road friction *or*
- the driver stopped side-motion by steering *or*
- the underlying vehicle instability is detected.

3 HYPOTHESIS

Before the experiment, a number of hypothesis were drawn from the experience of closed-loop simulations with a driver and vehicle model. Fig. 3 below shows an example of the simulated path swerving around the obstacle with/without EMAS ($v_x = 80$ km/h). The driver model was designed for a typical evasive manoeuvre; it was calibrated with vehicle test data and represents a skillful and attentive driver (Wang & Lokur 2016). It is, for instance, noticed that the driver gained more lateral displacement with the function active. The three hypothesis are:

- Hypothesis 1: System increases the probability for the driver to avoid the collision. This implies that the function helps the driver move the vehicle more laterally in front of the obstacle.
- Hypothesis 2: System does not increase risk for the driver to lose control on the vehicle motion. This implies that the driver easily controls the vehicle in the desired lane after avoiding the obstacle.
- Hypothesis 3: System will not intervene the driver too intrusively. This implies that the driver will not feel any disturbance from the function intervention.

www.TechnicalBooksPDF.com

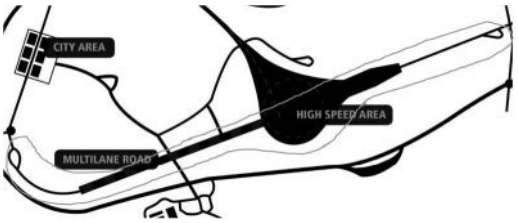


Figure 4. Overview of the used test track (blue circled area). Scale 1:8000.

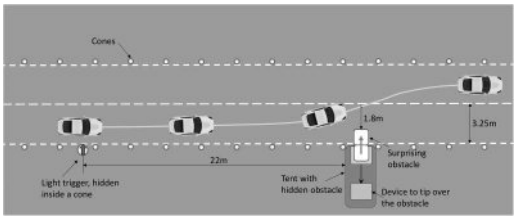


Figure 5. Test scenario of an imminent half-overlapping side collision with a suddenly tipped-over obstacle on a two-lane road.

The driver, vehicle and EMAS controller performs seamless interaction at the emergency situation.

4 METHOD

4.1 *Experimental set-up*

The experiment was carried out at the AstaZero (Active Safety Test Area and Zero) proving ground near Gothenburg in Sweden. The Multi Lane (ML) and High Speed Area (HSA) were closed exclusively for the experiment, see the blue circled area in Figure 4.

In total, 27 test subjects were recruited within the Volvo Cars Group, where 12 were women and 15 were men. The age is distributed such that approx. 20% were younger than 30 years old, 20% were older than 50 years old, while the rest are between 30 and 50 years old. All drivers have hold their Swedish driver license for at least 5 years with no less than 5000 km miles driven during the past year. No professional test drivers were involved. We have also excluded subjects who have had whiplash or neck or heart problems. Those who have participated in the development or tests of any collision avoidance systems e.g. EMAS, Lane Keeping Aid etc. were also filtered out.

The control algorithm was implemented in a Volvo S60 sedan test vehicle, which has Cruise Control system that can keep the entering speed identical between subjects. The vehicle was equipped with DEWESoft® measurement package, including IMU (Inertia Measurement Unit) and cameras. In DEWESoft®, a virtual lane was laid out in the middle of the actual driving lane on the test track. This could provide a measurement signal containing the heading angle relative to the lane. A virtual spot was also created at the position where the box fell down on the HSA; this gave two signals of the X and Y distance between the test vehicle and the fallen box.

4.2 *Test scenario*

The real-world scenario reconstructed here in the experiment is a typical pull-out event at the intersections or T-junctions of country roads. The challenge during our test scenario development was: due to safety reasons, enough open driving space should be allowed for this type of crash-imminent evasive manoeuvre; on the other hand, for best fidelity, road constraints should be laid out in a way that driver feels like driving on a real road. Since the scenario also requires a surprising pull-out obstacle, all equipments that trigger the obstacle need to be disguised and explained in a natural way.

The test scenario is illustrated in the Fig. 5 below. It is set up at the HSA track which has plenty of space in case of emergency. The straight lane marking was extended from the ML track to HSA so that a two-lane road was reconstructed there. The obstacle was designed as a plastic cubic skeleton box with white plastic cover on one side. A light trigger was positioned inside a cone which is about 22 m away from the up-coming obstacle; this gives approx. 1 s time-to-collision (TTC) as the obstacle will be tipped over onto the driving lane once the vehicle passes the trigger. All subjects drove with the Cruise Control function active at 80 km/h. The single lane width was 3.25 m, and the fallen obstacle makes the free space reduced to 1.8 m. Both sides of the road were painted with lane markings and constrained with tight-positioned cones. The scenario appears natural like a normal road repairs site and no test subjects suspected or questioned about this construction.

It is worth mentioning that a pilot testing were carried out before the final experiment, so as to determine the best parameters e.g. entering speed, TTC, overlapping distance etc. The criteria of being best is to make it necessary to steer in order to avoid the collision, and the steering activity should be in a sufficiently evasive manner that can trigger the EMAS function. Previous study has shown that upon imminent side collisions, drivers intend to *steer* around obstacles given a *shorter* TTC and *less* overlapping (Eckert, Hartmann, Sevenich, & Rieth 2011). The size of the obstacle was therefore determined such that it merely creates a half-overlapping scenario. The TTC was thereafter adapted to 1 s so that drivers would need to *steer* instead of braking alone. Furthermore, the fallen obstacle scenario here was considered superior to the common dummy-on-trail scenario that it could generate sufficient as well as identical overlapping over the test runs.

4.3 *Test procedures*

The experiment has a between-group design, which has 13 test subjects for each group with EMAS on

www.TechnicalBooksPDF.com

and off. The driving throughout the entire experiment was accompanied by a test leader on the passenger seat. Before executing the scenario elaborated above, the driver was offered to take a number of training runs within the blue circled area in Fig. 4. This is to ensure that driver gets relatively familiar with the test vehicle, as well as the road conditions etc. In the mean time, the spacious HSA track enables the driver to test various braking and steering manoeuvres there.

After getting into the car, the driver got a short introduction from the test leader about the secondary task that he/she was supposed to perform during the drive. The secondary task was to read numbers from a small screen placed above the passenger seat. It was five numbers (1-9) that lit up one by one with 0.5 s in between. The secondary task started by a recorded voice saying "Read the numbers now". The driver was then told that the purpose of the study was to investigate gaze and steering behaviours during secondary tasks. They were not told anything about the collision avoidance event. The secondary task was also designed in a way that the driver would feel naturalistic like in daily driving and be distracted to certain extent before the intrusion of surprising obstacle. At the end of the experiment, the driver filled out a questionnaire about the fidelity of the reconstructed driving session, evaluation of own driving experience and performance, as well as the interaction with the EMAS function (if active).

5 FUNCTION EVALUATION

The function performance is evaluated here according to the three hypothesis anticipated in Section 3.

5.1 *Collision risk*

Here two measures are used to indicate the risk of collision with/without the EMAS function. One is the vehicle lateral displacement (Y_{box}) measured when the vehicle front-right corner passing the obstacle rear-left corner, along the direction which is perpendicular to the current vehicle yaw angle. While the other one is to measure the maximum yaw angle (ψ_{max}) the vehicle reached until passing the obstacle, which indicates the enhancement of yaw capability with EMAS active. Table 1 has summarized the mean and standard deviation values of the these two measures. It can be seen that with EMAS, the Y_{box} was almost tripled with increased ψ_{max} even if the absolute value was not particularly large in this case. It is noticed that the standard deviations among the test subjects were relatively high, so it indicates a need of more subjects in order to reach higher statistic confidence.

Fig. 6 below shows the mean value of trajectories at the vehicle front-right corner. In total, five drivers without EMAS had collision with the obstacle, and one driver could avoid the collision by staying extreme near the left lane marking before steering around the obstacle; while one driver with EMAS had a slight side swipe with the obstacle. This result has clearly indicated the effectiveness of EMAS with respect to reduced collision risk. Considering the more severe consequence of small-overlapping accidents as compared to the full-overlapping ones, the benefit of reducing the collision risk here can not be underestimated. It is also interesting to find that after avoiding the obstacle, both groups were able to control the vehicle towards the same perceived safe zone, e.g. about 1 m beside the original lane. See Section 5.2 below with closer analysis of the vehicle stability throughout the entire event.

Table 1. Comparison of collision risk with/without EMAS function. Y_{box}: vehicle lateral displacement when passing obstacle; ψ_{max}: max yaw angle until passing obstacle.

	mean		standard deviation	
Measure	with	without	with	without
Y_{box} [m]	0.56	0.22	0.39	0.22
ψ_{max} [deg]	5.1	3.1	2.2	2.6

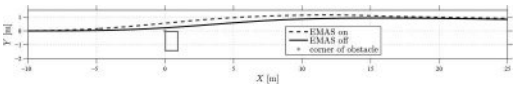


Figure 6. Trajectory (mean value) of all test subjects at the vehicle front-right corner, with/without EMAS function. Red box: suddenly appearing obstacle.

Table 2. Comparison of vehicle stability measures with/without EMAS function. β_{fmax}: max front side slip angle; β_{rmax}: max rear side slip angle; $\dot{\psi}_{max}$: max yaw rate; a_{ymax}: max lateral acceleration.

	mean		standard deviation	
Measure	with	without	with	without
β_{fmax} [deg]	1.44	0.79	0.43	0.54
β_{rmax} [deg]	1.99	0.82	0.74	0.63
$\dot{\psi}_{max}$ [deg/s]	18.14	9.61	4.19	6.60
a_{ymax} [m/s^2]	6.02	3.35	1.22	1.95

5.2 *Vehicle stability*

The EMAS function is designed to assist the driver to reduce the risk of imminent collisions, *without* introducing vehicle instability in any sense. Hence the maximum side slip angles at both front and rear axle, yaw rate and lateral acceleration were observed. Table 2 has summarized the mean and standard deviations of these four measures. It shows that under this scenario, EMAS could safely increase the yaw rate and lateral acceleration while still keeping the tyre side slip angles within the linear region.

www.TechnicalBooksPDF.com

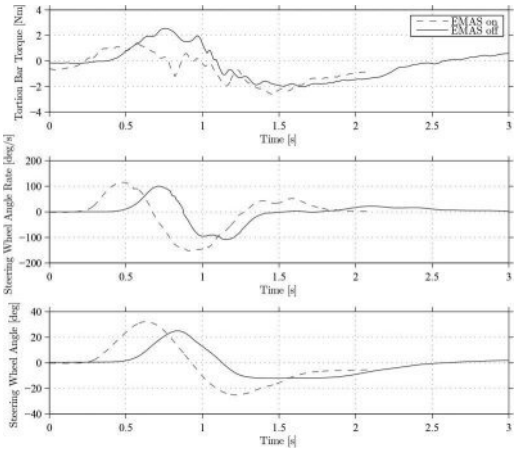


Figure 7. Steering activity (mean value) of all test subjects with/without EMAS function.

5.3 *Driver response and experience*

Under the circumstances of such emergent and surprising crash-imminent event, we aim to apply the assistance timely and appropriately without disturbing the driver's normal driving skill. The driver should feel intuitively with the function intervention. Therefore, both objective and subjective measures are used here to evaluate the function-driver interaction.

We define the state *start of steering* as the steering wheel angle becomes over 15 deg. It is found that with EMAS driver tends to reach the *start of steering* earlier, i.e. at 0.37 s compared to 0.57 s without EMAS. Fig. 7 below displays the objective measures of steering activity, with respect to torsion bar torque, steering wheel angle and angular velocity. The mean value of max torsion bar torque is shown to be lower with EMAS than without, which indicates the reduced steering effort from the driver. On the other hand, all of the three measures have a phase lead when EMAS was on; this again gives the function benefit in term of time winning and thus more agile during the emergent lateral motion.

Subjective evaluation was drawn from the answers in questionnaires. Generally, drivers have experienced no differences in terms of steering feeling, controllability of the vehicle and driving performance. Nevertheless, two drivers without EMAS expressed their suspicion afterwards that certain ABS and steering assistance system was active; while six drivers with EMAS has felt about steering and braking interventions from some type of stability control systems. The drivers did not note any unpleasantness with EMAS active during the manoeuvre.

6 SELECTED EXAMPLES

In this section, two representative examples of the test subjects with/without EMAS function are presented. The function was triggered at $t = 0.5$ s. Fig. 8

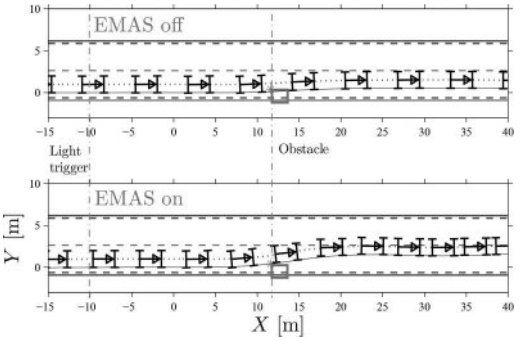


Figure 8. Trajectory of two exemplar test subjects with/without EMAS function. Blue curve: trajectory of the vehicle front-right corner. Red box: suddenly appearing obstacle.

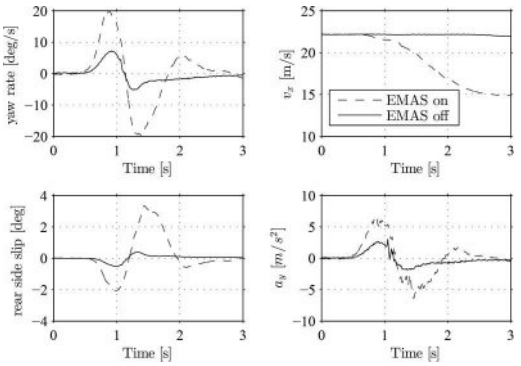


Figure 9. Vehicle states of two exemplar test subjects with/without EMAS function.

shows the full trajectory where a much stronger side-swerving motion is exhibited with EMAS. The driver without EMAS has collided with the obstacle while the one with EMAS could narrowly miss the collision. It should be noted that TTC = 1 s was so short that most drivers were at the risk boundary of collision. Fig. 9 shows the typical vehicle states during such evasive manoeuvre, which indicates that the EMAS function could enhance the lateral displacement in a safe and stable way. Fig. 10 shows the steering wheel angle as well as the EPAS torque request by the EMAS function. Fig. 11 displays the driver brake activities of these two examples that, the driver with EMAS started to brake down the vehicle by the end of the steering manoeuvre, while it took much more time for the driver without EMAS to start braking. This in some sense implies that EMAS could release the driver from the complex evasive manoeuvre earlier and thus ease the following recovery into the safe zone.

7 CONCLUSIONS

In this paper, an evasive manoeuvre assist system (EMAS) was evaluated at a crash-imminent scenario reconstructed at the test track. A half-overlapping

www.TechnicalBooksPDF.com

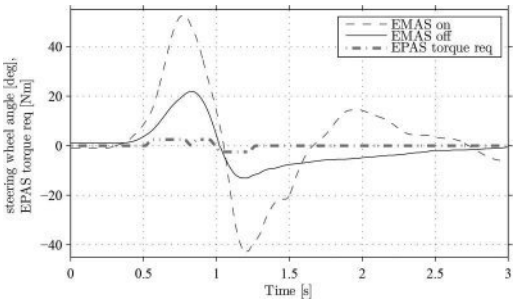


Figure 10. Steering wheel angle and EPAS torque request of two exemplar test subjects with/without EMAS function.

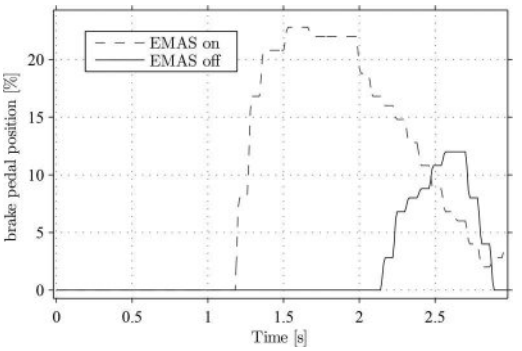


Figure 11. Brake pedal position of two exemplar test subjects with/without EMAS function.

side collision at the intersection of typical European country roads was reconstructed with real-world perspectives. The control function actively applies individual wheel braking and steering wheel torque overlay interventions so as to assist the driver to avoid the collision. Objective and subjective evaluation criteria were built according to three hypothesis drawn from previous results in the closed-loop simulations with a scenario-calibrated driver model.

It is found that the EMAS function could significantly reduce the collision risk under this type of half-overlapping accidents. This benefit is achieved by enhanced yaw and lateral motion capability, without damaging the bounded vehicle stability. EMAS is proven to have reduced the steering effort in swerving around the suddenly appearing obstacle in front. The function could appropriately and effectively assist a variation of drivers with different driving skills. The evaluation method developed here is considered novel that is applicable to a fleet of vehicle collision avoidance systems.

Future work remains to test the function at scenarios including different road users, e.g. oncoming vehicles and pedestrians from side. More test subjects could be involved in a larger scale experiment in order to increase the statistical confidence. The present EMAS function is expected to further adapt to the drivers who steer not too little but on the contrary too much, for instance, on the icy roads.

ACKNOWLEDGMENTS

This work was in part financed by the Swedish national competence centre ViP (Virtual Processing and Assessment by Simulation) driving simulation centre. The authors would like to extend appreciation to Mats Petersson for the research project management, and Anders Axelson for the expert insights during test method development.

REFERENCES

Adams, L. D. (1994). Review of the literature on obstacle avoidance maneuvers: braking versus steering. *University of Michigan Transportation Research Institute, Ann Arbor, USA. Report No. UMTRI-94-19*.

Eckert, A., B. Hartmann, M. Sevenich, & P. E. Rieth (2011). Emergency steer and brake assist – a systematic approach for system integration of two complementary driver assistance systems. *Proc. of the 22nd International Technical Conference on the Enhanced Safety of Vehicles (ESV), Washington DC, USA*.

Fausten, M. (2010). Accident avoidance by evasive manoeuvres – challenges and steps towards technical solutions. *http://www.ftm.mw.tum.de*.

Gurov, A., A. Sengupta, M. Jonasson, & L. Drugge (2014). Collision avoidance driver assistance system using combined active braking and steering. *Proc. of the 12th International Symposium on Advanced Vehicle Control (AVEC14), Tokyo, Japan*.

Malaterre, G., F. Ferrandez, D. Fleury, & D. Lechner (1988). Decision making in emergency situations. *Ergonomics 31(4)*, 643–655.

McGehee, D. V., E. N. Mazzae, & G. H. S. Baldwin (1999). Examination of drivers' collision avoidance behavior using conventional and antilock brake systems on the iowa driving simulator. *Human Factors & Vehicle Safety Research. NHTSA report No. 6-15-1999*.

Schittenhelm, H. (2005). Fahrverhalten und reaktionszeiten in kritischen situationen. *VDI-Bericht 1911. Düsseldorf, Germany*.

Wang, Y. & P. Lokur (2016). Effectiveness of evasive manoeuver assist function for different driver skills. *Chalmers University of Technology, Gothenborg, Sweden. Master thesis No. EX006/2016*.

www.TechnicalBooksPDF.com

Advanced Vehicle Control – Edelmann, Plöchl & Pfeffer (Eds)
© 2017 Taylor & Francis Group, London, ISBN 978-1-138-02992-7

Generalized predictive control based on vehicle path following strategy by using active steering system

Yang Cao & Fan Yu
School of Mechanical Engineering, Shanghai Jiao Tong University, Shanghai, P.R. China

ABSTRACT: In order to improve the path following capability of vehicles under disturbances, an active steering system based on Generalized Predictive Controller (GPC) is proposed, of which a Controlled Auto-Regressive Integrated Moving-Average (CARIMA) model is used as its inner model. Considering the complexity and uncertainty of vehicle parameters, a Recursive Least Square Method is applied to estimate the parameters in the CARIMA model. The controller uses the deviation between the vehicle actual and desired lateral positons as input and steering wheel angle as output. Based on input steering wheel angle from driver, the final corrected steering wheel angle is obtained. The controller performances are examined in Simulink-CarSim environment in some typical conditions, e.g. under strong lateral wind condition in standard double-lane-change, etc. Thus, the feasibility and effectiveness of the designed controller are proved theoretically.

1 INTRODUCTION

With the aim of improving the handling performance and lateral stability of vehicles, active steering system can be used, which can be independent of the driver steering wheel angle input to some extent.

In real driving scenario, the driver can usually maintain the deviation between vehicle actual trajectory and desired path within the allowable range through the steering wheel angle input (Rajamani R. 1999). However, due to driver uncertainty and external disturbances, e.g., lateral wind etc., the vehicle will deviate from the planned route in some cases. The present study is to investigate the related driver assistance systems which can intervene driver behavior under certain conditions to ensure the vehicle tracking capability.

In this paper, the acquiring and processing method of desired path is firstly presented. Then, a so called "CARIMA" model is proposed with its parameters which are identified by recursive least squares method with real vehicle test data and accordingly a steering controller based on generalized predictive controller is designed. The simulation results show that path-following performances of the designed controller can provides good performances, even under some cases with external strong disturbances.

2 DESIRED PATH

2.1 *Selection and pretreatment*

The purpose of the proposed active steering control is to assist the driver to follow the desired path, especially in situation of the vehicle under strong external disturbances, distracted drivers or other unforeseen circumstances which can cause vehicle deviates normally. Most active steering control normally include three steps, i.e., lane detection, desired path planning and steering angle correction. However, on-road lane detection (Li J. & Chen J. et al. 2014) and the planning of desired path is not the focus of this paper, and there have been a number of research works about lane detection, e.g., the existing lane detection approaches and their main technical difficulties, as well as a list of lane identification methods based on other special roads were comprehensively review by Yenikaya et al. (2013). Here, in order to facilitate the design of the controller, the centerline of the lane is selected as the desired path.

Because the desired path is often described in two-dimensional plane, it is inconvenience for controller to calculate the two axis value meanwhile. Hence, a method which can convert two-dimensional coordinate value to one-dimensional time value is applied in the present study. As shown in Fig. 1, in the scope of diver preview distance, the vehicle preparing position and the end of desired path is selected as the x-axis, and then Oxy coordinate system is obtained. After the x-axis is divided into n equal intervals parts, the path can be described by a set of y coordinate values, $y_1, y_2, \ldots, y_{n-1}$, corresponding x coordinate.

2.2 *Conversion of space to time description*

In Figure 2, x_t is current time coordinate, y_t is corresponding lateral displacement, and the coordinates x in time $t + T$ is obtained by the following equation,

$$x_{t+T} = vT\cos\alpha_t \tag{1}$$

www.TechnicalBooksPDF.com

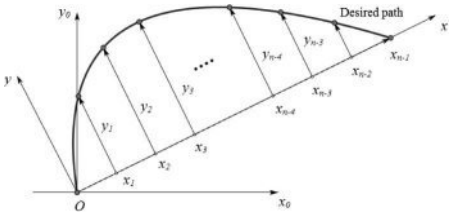


Figure 1. One dimensional code of desired path.

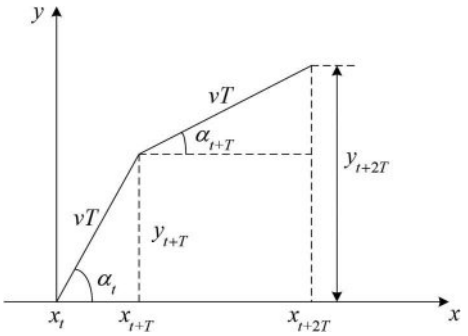


Figure 2. Path calculation in prediction horizon.

where, v is the vehicle speed, α_t is the direction angle of time t, equal to,

$$\alpha_t = \arctan\frac{y_{T+t} - y_t}{x_{T+t} - x_t} \tag{2}$$

in which x_{T+t} and y_{T+t} are the coordinate values of the next reference point respectively in x axis and y axis.

By substituting the longitudinal path coordinating value x_{t+T} derived by Equation (1) into the reference piont, the corresponding lateral displacement y_{t+T} can be obtained based on Equation (2).

3 VEHICLE MODEL AND IDENTIFICATION

3.1 *Vehicle model*

Different with other dynamic equations modelling method, we use an adaptive controlled auto-regressive and integrated moving average (CARIMA) model as vehicle model. The main difference of CARIMA model is that the model parameters are identified in an iterative approach, which does not need to have some prior knowledge of the physical structure of the system and also has good satisfaction in accord with vehicle test data, without being limited to the less DOF model.The CARIMA model, presented by Clarke (1987), is a predictive model based on generalized predictive control algorithm. Generally, it is effect for identification and with strong robustness to unmodeled dynamics meanwhile. A general CARIMA model is given by,

$$A(z^{-1})y(k) = B(z^{-1})z^{-d}u(k-1) + C(z^{-1})\xi(k)/\Delta \tag{3}$$

where,

$$A(z^{-1}) = 1 + a_1 z^{-1} + a_2 z^{-2} + \cdots + a_{n_a} z^{-n_a}$$
$$B(z^{-1}) = b_0 + b_1 z^{-1} + b_2 z^{-2} + \cdots + b_{n_b} z^{-n_b}$$
$$C(z^{-1}) = c_0 + c_1 z^{-1} + c_2 z^{-2} + \cdots + c_{n_c} z^{-n_c}$$
$$\Delta = 1 - z^{-1}$$

Here, $n_a = 4, n_b = 4, n_c = 0$, and $C(z^{-1}) = 1, \xi(k)$ is an uncorrelated zero mean random sequence with finite variance, and is the dead time, being selected as 1 in present study.

By applying some excitations to vehicle model of Carsim, the steering wheel angle $u(t)$ and vehicle lateral displacement $y(t)$ can be obtained for model parameters identification. It should be mentioned that the identified CARIMA model used herein is in the conditions with constant vehicle speed. However, due to combined online identification and self-correcting mechanism, the CARIMA model has strong robustness to variable conditions and parameters.

Therefore, the actual application can be made for a certain amount of switching mechanisms between a series of identification model of discrete vehicle speed to meet requirements of generalized predictive control usage under different continuous vehicle speeds.

In this paper, a C-Class car is taken as an example from Carsim, and a random steering wheel angle excitation is assumed as input to vehicle at speed of 50 km/h. According to measured vehicle lateral displacement data, recursive least squares method with forgetting factor, as shown in Equations (5) ~ (7), is used to obtain the corresponding CARIMA model parameters, i.e.,

$$\Delta y(t) = \varphi(t)\theta_0 + \xi(k) \tag{4}$$

where,

$$\varphi(t) = [-\Delta y(t-1), \ldots, -\Delta y(t-n_a), \Delta u(t-d-1), \ldots, \Delta u(t-n_b-d-1)]^T$$
$$\theta_0 = [a_1, \ldots, a_{na}, b_o, \ldots, b_{nb}]^T$$
$$\hat{\theta}(t) = \hat{w}(t-1) + K(t)[z(t) - \varphi^T(t)\hat{w}(t-1)] \tag{5}$$
$$K(t) = P(t-1)\varphi(t)[\varphi^T(t)P(t-1)\varphi(t) + \mu]^{-1} \tag{6}$$
$$P(t) = \frac{1}{\mu}[I - K(t)\varphi^T(t)]P(t-1) \tag{7}$$

in which, the forgetting factor μ is set as 0.972 in the present identification process, resulting in acceptable untill error less than 5% for model parameters.

In order to examine the identification precision of vehicle model, the same sinusoidal signal is input to the carsim model and corresponding identification model. The comparison of two model output results of lateral displacement shown in Figure 3, it is obvious to see that identification accuracy of CARIMA model is good enough and thus able to meet the requirements for controller design.

4 CONTROLLER DESIGN

The block diagram of the vehicle active steering GPC-based controller is illustrated in Figure 4, which

www.TechnicalBooksPDF.com

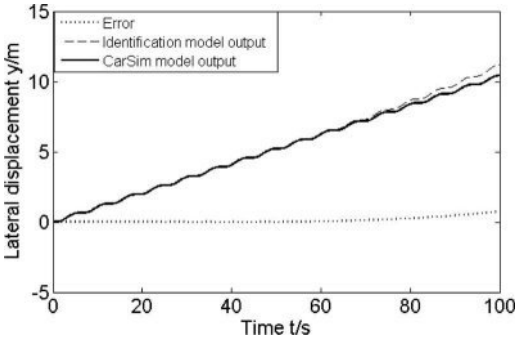


Figure 3. Result comparison between identification and Carsim model.

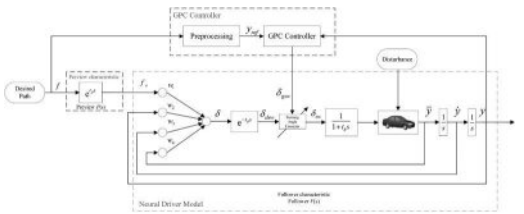


Figure 4. Scheme of active steering controller.

consists of a desired path, a driver preview module, a neural network driver model (Cao J. et al. 2013), a preprocessing module and the GPC controller. In the process of controller design, the neural network driver model is used to simulate the real driver, and a final vehicle steering wheel angle is obtained from the composited weighted GPC controller and the output of the neural network driver model.

Then, the parameters of the neural network driver model can be calculated accordingly by Cao (2013), as shown in Equation (8).

$$\begin{cases} w_1 = 1 \\ w_2 = -w_1 \\ w_3 = -t_p \\ w_4 = k_0 - \dfrac{t_p^2}{2} \\ K = \dfrac{t_p^3}{6} - k_0(T_{q1} + t_h + t_d) \\ k_0 = \dfrac{\dfrac{t_p^4}{24} - \dfrac{t_d t_p^3}{6}}{T_{q2} + t_h T_{q1} - t_d^2} \end{cases} \tag{8}$$

As a SISO system by using generalized predictive control method, its cost function is set as followed:

$$J = (Y - W)^T (Y - W) + \lambda \Delta U^T \Delta U \tag{9}$$

$$w(k+j) = \alpha^j y(k) + (1 - \alpha^j) y_r \tag{10}$$

where, $Y = [y(k+1)y(k+2), \ldots, y(k+n)]^T$ is the vehicle lateral displacement of future n steps.

$W = [w(k+1)w(k+2), \ldots, w(k+n)]^T$ is the lateral displacement of desired path in the future n steps, λ is the weighting parameter for controller with $(0 \le \alpha < 1)$ and y_r is the real set-point trajectory which can be obtained from the optimized desired trajectory.

In order to optimize the cost function described by Equation (9), the optimal prediction of Y need to be obtained.

Considering the following Diophantine equation [4],

$$1 = E_j(z^{-1})A(z^{-1})\Delta + z^{-1}F_j(z^{-1}) \tag{11}$$

where $E_j(z^{-1}) = 1 + e_{j1}z^{-1} + \cdots + e_{j,j-1}z^{-j+1}$

$F_j(z^{-1}) = f_{j0} + f_{j1}z^{-1} + \cdots + f_{jn}z^{-n}$,

If multipling $E_j(z^{-1})\ \Delta$ for Equation (10) in both sides and then combining Equation (11), the best prediction of $\hat{y}(k+i)$ can be therefore obtained as,

$$\hat{y}(k+j) = G_j(z^{-1})\Delta u(k+j-1) + F_j(z^{-1})y(k) \tag{12}$$

$$G_j(z^{-1}) = E_j(z^{-1})B(z^{-1}) = \frac{B(z^{-1})}{A(z^{-1})\Delta}[1 - z^{-j}F(z^{-1})] \tag{13}$$

It can be seen that Equation (12) contains known and unknown parts of time k, where the latter can be represented by,

$$f = H\Delta u(k) + Fy(k) \tag{14}$$

where

$$H = \begin{pmatrix} G_1 - g_0 \\ z(G_2 - z^{-1}g_1 - g_0) \\ \vdots \\ z^{n-1}(G_n - z^{-n+1}g_{n-1} - \cdots - z^{-1}g_1 - g_0) \end{pmatrix}$$

$$G = \begin{pmatrix} g_0 & & & 0 \\ g_1 & g_0 & & \\ \vdots & & \ddots & \\ g_{n-1} & g_{n-2} & \cdots & g_0 \end{pmatrix}$$

$$F = \begin{bmatrix} F_1 F_2 \cdots F_n \end{bmatrix}^T$$

Based on Equation (12), the optimal output prediction is obtained as,

$$\hat{Y} = G\Delta U + f \tag{15}$$

where

$$\hat{Y} = [\hat{y}(k+1)\hat{y}(k+2)\cdots\hat{y}(k+n)]^T$$

$$\Delta U = [\Delta u(k), \Delta u(k+1), \cdots \Delta u(k+n-1)]^T$$

Let $\partial J / \partial U = 0$, the control output $u(t)$ can be obtained as,

$$\Delta U = (G^T G + \lambda I)^{-1} G^T (W - f) \tag{16}$$

$$u(t) = u(t-1) + [1, 0, ..., 0]\Delta u \tag{17}$$

where Δu represents the first row of the optimal control output.

www.TechnicalBooksPDF.com

Table 1. Simulation parameters.

Variables	Value (Direction)	Unit
Road friction coefficients μ	0.85	–
Crosswind speed v_w	25	m/s
Wind direction	left side	–
Vehicle speed v	50	km/h
Vehicle mass M	1274	kg
Wheelbase L	2.578	m
Distance from front axle L_f	1.016	m
Front/ Rear track widths b	1.739	m
Yaw inertia I_z	1523	kgm^2

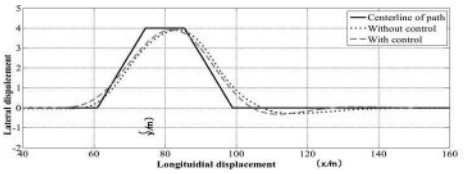
5 SIMULATION AND RESULTS

The present GPC control system (with $n = 15, m = 10, T = 0.08, \lambda = 6$) is evaluated through comprehensive simulations. In order to examine the performance of the proposed controller, the same car is selected in simulations. A standard double-lane change maneuver under the condition of strong crosswind is presented here along with corresponding variable dynamic model parameters.

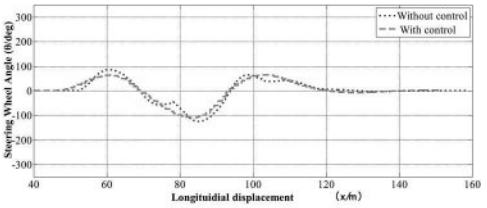
In the present paper, taking a strong crosswind disturbance as example, the steering wheel angle input and vehicle trajectory respecting with GPC controller and without any control is compared. Since the crosswind speed interval which has a major impact on safe driving is $v_w \in [10, 25]$ m/s (Abe M. 2015), so the crosswind speed of 25 m/s and vehicle speed of 50 km/h are selected as simulation parameters. Other simulation parameters are presented in Table 1.

The simulation results for the vehicle trajectory and steering angle of the path following control using a GPC method, are shown in Figure 5. Comparing the vehicle trajectory without controller, the GPC controller offers a more rapid and precise control performance. From Figure 5, it can be seen that, in the condition with strong crosswind, the active steering vehicle with GPC controller can follow the centerline of path more satisfactorily, and also has a quick response time and small overshoot in a double lane change manoeuvre. Meanwhile, the curve of vehicle steering angle is smoother and the peak value is lower, implying that the motion state of vehicle is more stable. Compared the results illustrated by Figure 5 and 6, it is can be seen that in the case of strong crosswind, the trajectory of vehicle with active steering controller is more stable, and also less affected by external disturbance than without GPC controller though the steering wheel angle becomes a bit fluctuation.

During the actual process of driving, vehicle parameters are often changes in a certain range. In order to examine the robustness and adaptability of GPC controller, the variation of vehicle dynamic model parameters (vehicle mass and speed) are added to simulations on the same crosswind. Figure 7 shows the vehicle trajectory under the condition of parameters

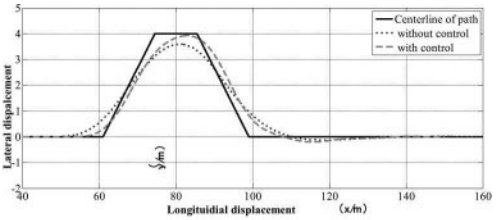


(a)Vehicle trajectory without crosswind

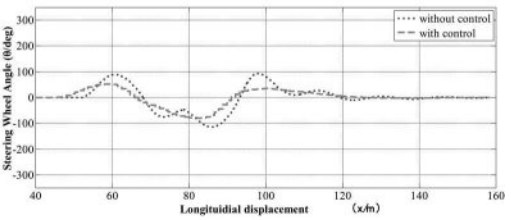


(b)Steering angle input without crosswind

Figure 5. Vehicle trajectory with strong crosswind.



(a)Vehicle trajectory with crosswind



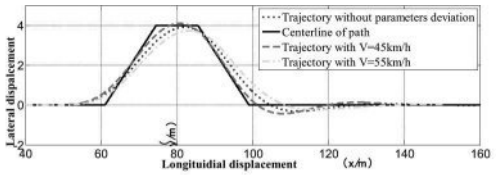
(b)Steering angle input with crosswind

Figure 6. Vehicle trajectory with strong crosswind.

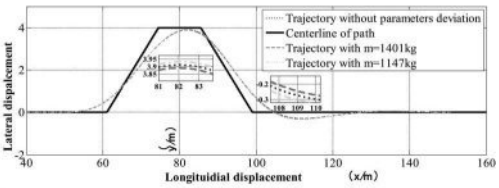
deviation. As is shown in the Figure, the controller still can assist driver to control in order to follow the centerline of path more satisfactorily, even if the vehicle speed has variation. Although, the tracking error with vehicle speed variation is larger than vehicle mass, which mainly because speed has more significant impact for vehicle system dynamics than mass, vehicle still can approximately tracking path centerline. Moreover, it is also conclued that vehicle with GPC controller have better path-following ability on the condition of low speed and small mass.

As can be seen from Figure 6, the GPC controller has relatively good robustness because the GPC controller has an online parameter identification and adaptive function. Hence, the vehicle can better track optimal trajectory to meet the needs of the active steering system even if the dynamic model parameters have a certain extent change.

www.TechnicalBooksPDF.com



(a)Vehicle trajectory with variable speed



(b)Vehicle trajectory with variable mass

Figure 7. Vehicle trajectory under parameters variation.

6 CONCLUSION

This paper proposed an active steering system based on Generalized Predictive Controller (GPC), of which a Controlled Auto-Regressive Integrated Moving-Average model (CARIMA) is used as the inner vehicle model. Firstly, considering the complexity and uncertainty of vehicle parameters, a Recursive Least Square Method with forgetting factor is applied to estimate the parameters in the CARIMA model using carsim data, which is also verified by vehicle test. Moreover, the scheme of path following controller including desired path preprocess is constructed, which uses the deviation between the vehicle actual and desired lateral positons as input and steering wheel angle as output. Based on input of steering wheel from driver, the final corrected steering wheel angle is obtained. Finally, the controller performances are examined in Simulink-CarSim environment in some typical conditions, such as under strong lateral wind condition and other disturbances in standard double-lane-change. Simulation results show that, the designed controller can effectively track desired path centerline to realize lane keeping even under strong side wind or other external disturbances. Meanwhile, the controller also exhibits a satisfactory robustness, for instance, which can still maintain good path following performance with the significant vehicle mass parameters variation in certain extent.

In future work, in order to reduce control deviation caused by the difference of speed between the vehicle and identification model and extend the availability of the GPC controller, a path following controller of different speeds and their switching mechanism will be investigated.

ACKNOWLEDGEMENT

This study is supported by the *National Natural Science Foundation of China (Grant No. 51375299)* and the *Research Program of State Key Laboratory of Mechanical System and Vibration (Grant No. MSV201505)*.

REFERENCES

Abe M. Vehicle handling dynamics: theory and application [M]. *Butterworth-Heinemann*, 2015.

Cao J, Lu H, Guo K, Zhang J. A driver modeling based on the preview-follower theory and the jerky dynamics [J]. *Mathematical Problems in Engineering*, 2013: Article ID 952106, 1–11.

Clarke D W, Mohtadi C, Tuffs P S. Generalized predictive control—Part I. The basic algorithm [J]. *Automatica*, 1987, 23(2): 137–148.

Li J, Chen J, Yi K, et al. Lane Tracking System Based on Adaptive Image Threshold under Different Illumination [J]. *Journal of Mechanical Engineering (in chinese)*, 2014, 2: 023.

Rajamani R. Vehicle dynamics and control. (2nd Edition) [M]. *USA: Springer*, 2012: 201–240.

Yenikaya S, Yenikaya G, Düven E. Keeping the vehicle on the road: A survey on on-road lane detection systems [J]. *ACM Computing Surveys (CSUR)*, 2013, 46(1): 2–2.

www.TechnicalBooksPDF.com

www.TechnicalBooksPDF.com

Advanced Vehicle Control – Edelmann, Plöchl & Pfeffer (Eds)
© 2017 Taylor & Francis Group, London, ISBN 978-1-138-02992-7

Target & control based lane keeping assistance system with center error correction algorithm

Eric Wang, Lih-Wei Jeng & Kang Li
Department of Mechanical Engineering, National Taiwan University, Taiwan

Chun Fan
Industrial Technology Research Institute (ITRI) R.O.C.

ABSTRACT: This paper aims to design a target point adjustment method to mitigate center error during vehicle lane keeping assistance control, this research is an advancement based on the Target & Control (T&C) driver steering model, which references characteristics exhibited by actual drivers. This paper will first introduce a lane keeping assistance control system that incorporates three essential models including vehicle dynamics model, electric power steering model and the T&C driver steering model, then by considering unavoidable system deviations such as positioning deviation and camera displacement etc., a supplementary control loop will be added to correct the center error without additional estimators or hardware sensors. Finally, the system stability and performance will be examined using root locus analysis, and the overall control strategy will be validated and verified using the CarSim simulation environment.

1 INTRODUCTION

Lane Keeping Assistance (LKA) control is an essential function of a well-designed autopilot vehicle system, the positioning deviation from the desired target path (center error) during system operation is often seen as the index that is used to judge controller performance. For instance, Tomizuka et al. in [1, 2] utilized H_∞ control to perform lane keeping assistance control for heavy duty vehicles at high speed with promising results in their earlier works; Cerone et al. in [3, 4] furthered the research with center of no more than 0.2 meters when cornering; Guldner et al. in [5, 6] achieved similar performance using guiding magnets with small center error. Apart from using camera or guiding magnets, Hernandez et al. in [7] used a fusion sensor of GPS with guiding magnets to create a smoother pathing in order to decrease lateral acceleration when cornering. Whichever method used, the collective goals are to minimize center error, which in turn will increase the performance of the lane keeping assistance controller.

Apart from the aforementioned lane keeping assistance control using different sensing methods, center error problem also exists for methods using different controller algorithms. For example, Perng et al. in [8] utilized fuzzy gain scheduling to perform lane keeping assistance control; or Guo et al. in [9] used the logics of genetic algorithm; or the Phase lead/lag controller designed by Taylor et al. in [10]; Lane keeping assistance controllers using H_∞, adaptive control, fuzzy logic and PID control by Chaib et al., all of which produced center error during lane keeping assistance control. The problem of lane following bias (producing center error) is not only a result of imprecise system models or vehicle dynamics model (difficult to produce due to nonlinear characteristics), but also stems from sensors and hardware installment/adjustment. For instance, Borrelli et al. in [11] designed two separate model predictive control models; one dealing with nonlinear characteristics, the other for linear time variant systems, the center error problem in this case stems mostly from sensor installment angle deviation.

To cope with these difficult to detect sensors and hardware installation problems, this research uses the Target & Control (T&C) driver steering model [12–15] as a basis to develop a method that aims to mitigate center error without additional hardware or sensors.

To cope with these difficult to detect sensors and hardware installation problems, this research uses the Target & Control (T&C) driver steering model [12–15] as a basis to develop a method that aims to mitigate center error without additional hardware or sensors.

This paper will first attempt to realize the lane keeping assistance control system based on the T&C driver steering model, with hardware in the loop experiments under high speed in order to recreate the phenomenon of lane following bias. By examining the cause of center error and analyzing simulation data, a hypothesis can be designed to enhance the original system in order to decrease center error produced, the proposed control system will then be subjected to simulation verification using CarSim simulation environment, and the results analyzed with root locus to examine the stability of the newly constructed system.

www.TechnicalBooksPDF.com

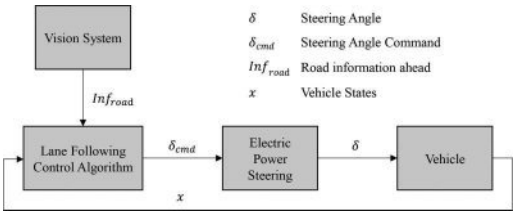


Figure 1. System architecture of the lane keeping assistance (LKA) system.

2 SYSTEM STRUCTURE AND MODELS

A brief introduction of the system structure will be given in this section, along with the vehicle dynamics model and electric power steering model used for theoretical analysis.

2.1 *System architecture*

Figure 1 shows system architecture of the lane keeping assistance control system, the road information acquired from vision system along with current vehicle states are sent to the lane keeping assistance control algorithm, the controller upon receiving the necessary information calculates a front axle steering angle command, the command is then sent to the EPS (Electric Power Steering) system to be converted into actual steering angle to achieve lane keeping assistance control.

2.2 *Vehicle dynamics model*

Lane keeping assistance control focuses heavily on the lateral dynamics and yaw dynamics of the target vehicle, therefore a sufficiently suitable vehicle model must be chosen for simulation accuracy, in this paper the steady state bicycle model is used [16–18] to analyze the stability of the control strategy under specific look ahead distance and vehicle velocity, the models are shown as below:

$$\frac{d}{dt}\begin{bmatrix}\dot{y}\\ \dot{\psi}\end{bmatrix}=\begin{bmatrix}A_{11} & A_{12}\\ A_{21} & A_{22}\end{bmatrix}\begin{bmatrix}\dot{y}\\ \dot{\psi}\end{bmatrix}+\begin{bmatrix}B_1\\ B_2\end{bmatrix}\delta \tag{1}$$

$$A_{11}=\frac{-2(C_f+C_r)}{mV_x} \quad A_{12}=-V_x+\frac{2(C_rL_r-C_fL_f)}{mV_x} \tag{2}$$

$$A_{21}=\frac{2(C_rL_r-C_fL_f)}{I_{zz}V_x} \quad A_{22}=\frac{-2(C_rL_r^2+C_fL_f^2)}{I_{zz}V_x} \tag{3}$$

$$B_1=\frac{2C_f}{m} \quad B_2=\frac{2L_fC_f}{I_{zz}} \tag{4}$$

The $\dot{y}$ and $\dot{\psi}$ represent lateral vehicle velocity and yaw rate respectively; δ is the front axle steering angle; C_f and C_r are front and rear wheel cornering stiffness; L_f and L_r are vehicle COG to front and rear wheel; m is the mass of the vehicle and I_{zz} is the inertial moment with respect to the z axis.

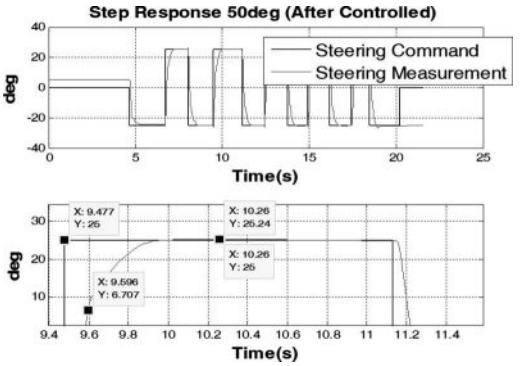


Figure 2. Step response.

2.3 *Electric power steering model*

The performance and stability of the lane keeping assistance control system relies heavily on the precision and accuracy of the electric power steering system model, therefore an accurately modeled system using a second order equation which fits the profile of the actual EPS performance is necessary, and is chosen to represent the EPS in this paper to strike a balance between accuracy and simplicity. The EPS model used in this paper has a bandwidth of 3 Hz with 0.8 damping ratio and is a standard second order response as shown in Eq. 5:

$$EPS(s)=\frac{355.31}{s^2+30.16s+355.31} \tag{5}$$

The model will be used to analyze the stability for the lane keeping assistance control system, in the later sections during CarSim verification the EPS model will also be used to investigate the effects of lane keeping assistance controller as well.

3 TARGET & CONTROL BASED LANE KEEPING ASSISTANCE CONTROL WITH HARDWARE IN THE LOOP SIMULATION

The lane keeping assistance function discussed in this paper utilizes the T&C driver steering model as the core control theory, therefore an understanding of T&C is required to better perceive the scope of this paper.

The T&C driver steering model functions by first deciding a desired target point for the vehicle to reach, then the system judges whether or not the vehicle will reach the target based on the current vehicle motion. If the current vehicle state does not allow the vehicle to reach the target point, then the driver steering model will attempt to steer the vehicle at a rate proportional to the angle difference between the future position projected based on current vehicle state and the desired target point, demonstrated in figure 3.

V_t, $V_{t+\Delta t}$ and T represent the current vehicle position, predicted vehicle position and desired target point

www.TechnicalBooksPDF.com

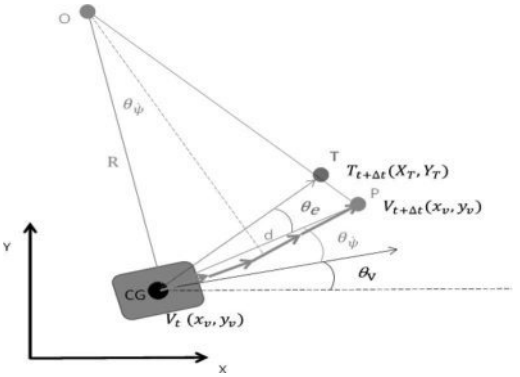


Figure 3. T&C driver steering model derivation.

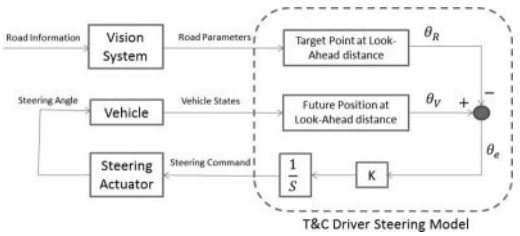


Figure 4. LKA system structure.

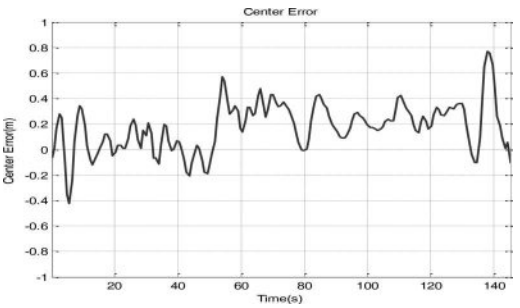


Figure 5. Center error (m) of the LKA system.

respectively, $\theta_{\dot{\psi}}$ is the angle that is formed with respect to the vehicle yaw rate, θ_V is the current vehicle heading and θ_e is the angle between target point T and predicted vehicle position.

The complete system structure of the lane keeping assistance system is as shown in figure 4.

The T&C driver steering model is the expanded version of the lane following control algorithm seen in figure 1. By implementing the control algorithm onto the experiment vehicle equipped with the same vision system, EPS and vehicle dynamics hardware in the loop simulation (HiLs) is conducted to verify the LKA system. The system is tested on a sedan driven at 33 m/s through the ARTC (Automotive Research & Testing Center R.O.C.) high speed vehicle testing ground. Details of the HiLs can be seen in figures 5 and 6.

When T&C driver steering model is implemented the desired target point is usually set at the center of

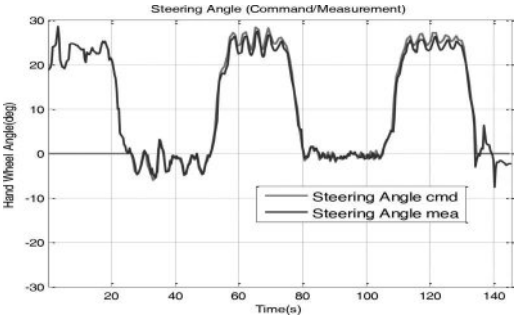


Figure 6. Steering angle (deg) of command and measured.

the roadway, and a center error will be produced during steady state cornering (when the steering wheel is fixed) dependent on the magnitude of the look ahead distance (seen in figure 5). Also, if the camera installed on the vehicle for lane marker recognition has angle deviation then center error will also be produced when cornering, which means that if the target point is not at the center of the road, larger center error will be produced during cornering. Therefore, a new control method will be proposed in this paper, under the assumption that the camera is installed on the vehicle with angle deviation. By using the current center error (minor-ly effected by camera angle deviation) to fix the steering angle command the future center error can be reduced, including the center error caused by steering normally and without camera angle deviation.

4 PHENOMENON OF LANE FOLLOWING BIAS

The vision system in the lane keeping assistance control system architecture requires a camera to be installed at the front of the vehicle to acquire road information, specifically the position of the lane markers and the vehicle position relative to it, if the camera was to be installed at a slightly deviated angle or position, then the acquired information would also produce measurement bias. In the T&C theory, the steering rate influences the angle between target point and future vehicle position, which in turn is influenced by command bias, producing center error during lane keeping assistance control.

The simulation is built under the Simulink and CarSim environment, if the camera had an angle deviation of 1 degree, with a velocity of 72 km/hr, and the look ahead distance is 1 times vehicle velocity then the LKA control gain is 1.32, which is the analytic result using root locus analysis as can be seen in figure 7.

The larger marker represents the closed loop poles of the LKA system under a gain of 1.32. The vehicle parameters used in simulation are as shown in table 1. The simulation route is as shown in figure 8, with a radius of curvature of 400 m for both corners of the lane change.

www.TechnicalBooksPDF.com

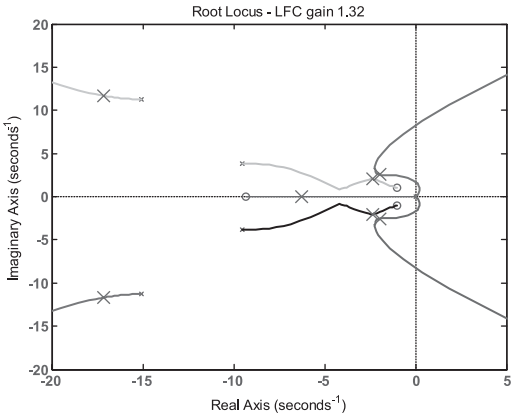


Figure 7. Root locus analysis of LKA system.

Table 1. Simulation Vehicle Parameters.

Vehicle body mass	1,989 kg
Vehicle body yaw moment of inertia	3,528 kgm^2
Vehicle body length	3.840 m
Vehicle body width	1.997 m
Front tire cornering stiffness	72000 N/rad
Rear tire cornering stiffness	93500 N/rad

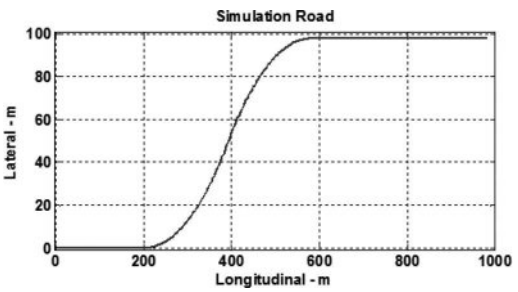


Figure 8. Simulation roadway.

Figure 9 shows the simulation results, when the vehicle is being driver at 72 km/hr with a look ahead distance of 1 times the vehicle velocity, a single degree of camera angle deviation can cause center error of 35 cm.

5 CONTROL STRUCTURE MODIFICATION AND ANALYSIS

To mitigate the center error caused by lane following bias, the control loop now has an additional feedback loop for center error with an extra integrator shown in figure 10.

In figure 10 an extra feedback loop can be observed, the y_r term now has feedback with K_I as its integrator gain. The new calculation method for angle error

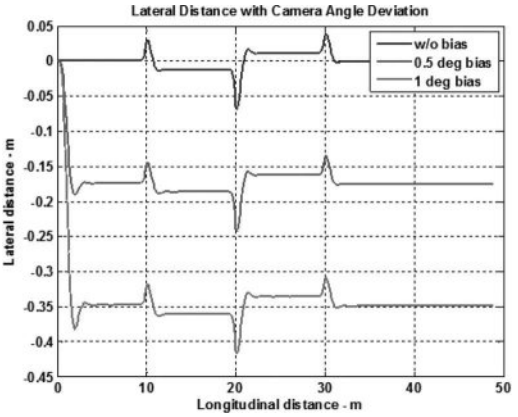


Figure 9. Center error under different camera angle deviation.

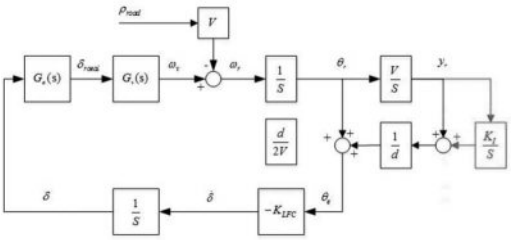


Figure 10. Proposed control system architecture.

is shown in figure 12. The new angle error equation is now:

$$\theta_e = \frac{d\rho}{2} - \left(\frac{\omega_v d}{2v} + \theta_r + \frac{y_r}{d} + \frac{y_r K_I}{ds}\right) \tag{6}$$

And steering angle equation:

$$\delta = \frac{-k}{s} * \frac{d^2 s^3 + 2vds^2 + 2v^2 s + 2K_I v^2}{2vds^3} \tag{7}$$

Since the stability of the control system will be affected by the gain of the additional integrator loop on the control system, the effects of this addition was analyzed using root locus for fixed gain LKA control, to determine the system stability due to the magnitude change of integrator gain K_I. From figure 12 it can be seen that as the gain increases the system becomes less stable.

6 SIMULATION RESULTS

The simulation conducted can be viewed in two main sections; the first one compares the new control structure with the original LKA system without camera angle deviation to test the performance of the new architecture; the second simulation compares the two control architectures with 1 degree of camera angle

www.TechnicalBooksPDF.com

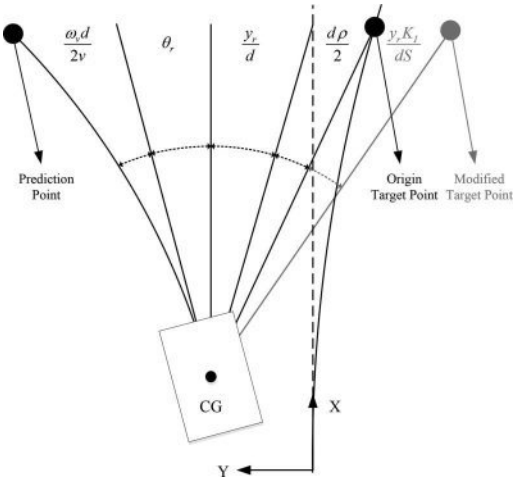


Figure 11. Angle error calculation method.

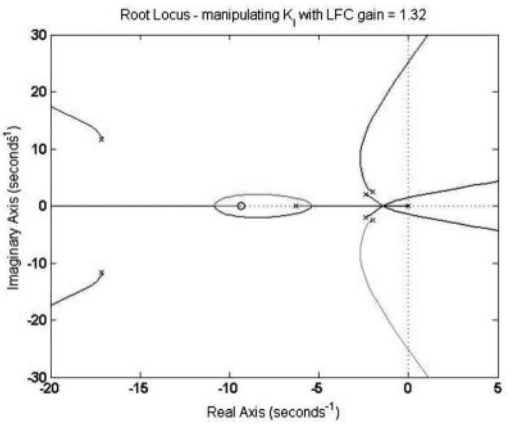


Figure 12. Root locus analysis of integrator gain under fixed LKA gain.

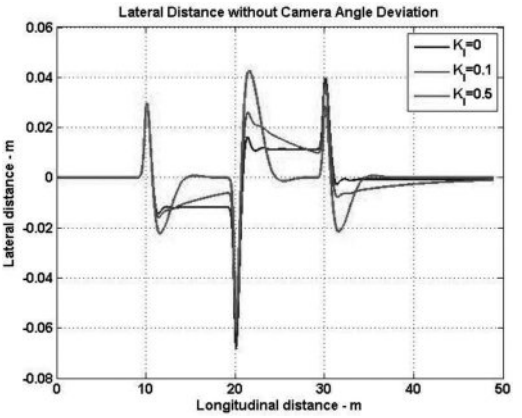


Figure 13. The effect of different integrator gain for LKA without camera angle deviation.

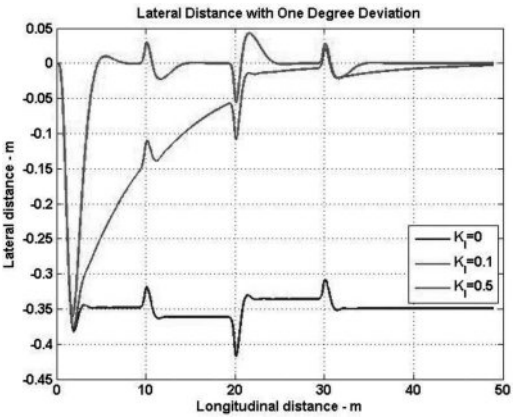


Figure 14. The effect of different integrator gain for LKA with 1 degree of camera angle deviation.

deviation, to test the performance of both and analyze the ability of the new structure to handle the problem. Both simulations are conducted under the same conditions to ensure comparability; the velocity of the vehicle is 72 km/hr with 1 times velocity of look ahead distance and a feedback gain of 1.32, the simulation vehicle and course remains the same as well.

Figure 13 demonstrates the results without camera angle deviation, it can be seen that the proposed new architecture successfully mitigates center error during cornering. As the integrator gain K_I increases, the decreasing effect of the center error also increases, however the instant during consecutive cornering produces a larger center error:

Figure 14 demonstrates the scenario with 1 degree of camera angle deviation, from the figure the effects of the new architecture can be seen, by increasing the integrator gain the center error can be mitigated faster, including lane following bias caused by steady state steering angle error and camera angle deviation. Conversely, the smaller the integrator gain the lower the effect.

7 CONCLUSION

This paper proposed a new control system based on the T&C (Target & Control) architecture by adding an additional integrator onto the center error term with an extra feedback loop to mitigate the lane following bias phenomenon, the new system attempted to affect the relationship of the angle error between target point of T&C driver steering model and the vehicle future position in order to decrease center error when cornering, and also to reduce the effect caused by camera angle deviation.

From system simulation and results analysis, under the same LKA gain, the larger in magnitude the integrator gain, the more effective the architecture

www.TechnicalBooksPDF.com

is at reducing center error, but with lowered system stability. Conversely the smaller the integrator gain, the architecture becomes less effective with a reduced reduction rate, but the overall system stability is increased. Further research on this topic is needed through systematic analysis in order to design an optimal match between vehicle velocity, look ahead distance, LKA gain and integrator gain, so the vehicle can be controlled more effectively and with better performance.

ACKNOWLEDGEMENT

This research is conducted with the research grant from the Ministry of Science and Technology R.O.C. (MOST), with the grant number MOST 104-2218-E-002-004, and also Industrial Technology Research Institute R.O.C. (ITRI) with grant number 05HT512013, the authors would like to acknowledge and thank MOST and ITRI for the funding which helps to make the research possible.

The authors would also like to thank Ding Yuan, T. Han-Shue Ph.D. and Hua-Chuang Automobile Information Technical Center Co., Ltd. (HAITEC), for idea contribution, support and providing resources for hardware simulation.

REFERENCES

[1] W. Jeng-yu and M. Tomizuka, "Robust H infinity lateral control of heavy-duty vehicles in automated highway system," in *American Control Conference, 1999. Proceedings of the 1999*, 1999, pp. 3671–3675, vol. 5.

[2] T. Meihua, "Experimental study of lateral control of heavy vehicles for automated highway systems (AHS)," in *American Control Conference, 2002. Proceedings of the 2002*, 2002, pp. 851–856 vol.2.

[3] V. Cerone, A. Chinu, and D. Regruto, "Experimental results in vision-based lane keeping for highway vehicles," in *American Control Conference, 2002. Proceedings of the 2002*, 2002, pp. 869–874, vol. 2.

[4] V. Cerone and D. Regruto, "Robust performance controller design for vehicle lane keeping," 2003.

[5] J. Guldner, W. Sienel, H.-S. Tan, J. Ackermann, S. Patwardhan, and T. Bunte, "Robust automatic steering control for look-down reference systems with front and rear sensors," *Control Systems Technology, IEEE Transactions on,* vol. 7, pp. 2–11, 1999.

[6] T. Han-Shue, J. Guldner, S. Patwardhan, C. Chieh, and B. Bougler, "Development of an automated steering vehicle based on roadway magnets-a case study of mechatronic system design," *Mechatronics, IEEE/ASME Transactions on,* vol. 4, pp. 258–272, 1999.

[7] J. I. Hernandez and K. Chen-Yuan, "Steering control of automated vehicles using absolute positioning GPS and magnetic markers," *Vehicular Technology, IEEE Transactions on,* vol. 52, pp. 150–161, 2003.

[8] W. Shinq-Jen, C. Hsin-Han, P. Jau-Woei, C. Chao-Jung, W. Bing-Fei, and L. Tsu-Tian, "The Heterogeneous Systems Integration Design and Implementation for Lane Keeping on a Vehicle," *Intelligent Transportation Systems, IEEE Transactions on,* vol. 9, pp. 246–263, 2008.

[9] J. Guo, P. Hu, L. Li, and R. Wang, "Design of automatic steering controller for trajectory tracking of unmanned vehicles using genetic algorithms," *Vehicular Technology, IEEE Transactions on,* vol. 61, pp. 2913–2924, 2012.

[10] C. J. Taylor, J. Košecká, R. Blasi, and J. Malik, "A comparative study of vision-based lateral control strategies for autonomous highway driving," *The International Journal of Robotics Research,* vol. 18, pp. 442–453, 1999.

[11] P. Falcone, F. Borrelli, J. Asgari, H. E. Tseng, and D. Hrovat, "Predictive Active Steering Control for Autonomous Vehicle Systems," *Control Systems Technology, IEEE Transactions on,* vol. 15, pp. 566–580, 2007.

[12] H. Jihua, T. Han-Shue, and B. Fanping, "Preliminary steps in understanding a target & control based driver steering model," in *American Control Conference (ACC), 2011*, 2011, pp. 5243–5248.

[13] T. Han-Shue, H. Jihua, B. Fanping, and B. Litkouhi, "Driver steering model based on a target & control scheme," in *American Control Conference (ACC), 2011*, 2011, pp. 4610–4615.

[14] "Development of the Lane Following Control System Based on the Driver Steering & Vehicle Dynamics Models," 2015.

[15] T. Han-Shue and H. Jihua, "Experimental Development of a New Target and Control Driver Steering Model Based on DLC Test Data," *Intelligent Transportation Systems, IEEE Transactions on,* vol. 13, pp. 375–384, 2012.

[16] T. D. Gillespie, *Fundamentals of vehicle dynamics* vol. 400: Society of Automotive Engineers Warrendale, PA, 1992.

[17] R. Rajamani, *Vehicle dynamics and control*: Springer Science & Business Media, 2011.

[18] J. Y. Wong, *Theory of ground vehicles*: John Wiley & Sons, 2001.

www.TechnicalBooksPDF.com

Advanced Vehicle Control – Edelmann, Plöchl & Pfeffer (Eds)
© 2017 Taylor & Francis Group, London, ISBN 978-1-138-02992-7

Adaptation of ADAS-functions by identifying driver fingerprint

G. Büyükyildiz, A. Hafner, R. Henze & F. Küçükay
Institute of Automotive Engineering, TU Braunschweig, Germany

M. Vollrath
Department of Engineering and Traffic Psychology, TU Braunschweig, Germany

ABSTRACT: Increased customer acceptance requires to focus on the driver in the vehicle development. An important issue is to determine the driver's ability to respond to situations appropriately in order to drive the vehicle safely. In this paper, a so-called driver fingerprint model has been developed which makes it possible to identify the specific driver characteristic. The fingerprint model is implemented on the vehicle as a real time application. For this purpose, relevant signals are extracted from the CAN-bus and used for modelling. Therefore longitudinal and lateral control behaviour of the driver will be analysed. Several examples of the process of determining the objective parameters are illustrated. The final fingerprint information of the driver will be used as input to adapt the thresholds of a Lane-Departure-Warning assistance system. Furthermore, based on a previous study, a comprehensive study of acceptance of the drivers for adaptive thresholds is in preparation.

1 INTRODUCTION

In order to reduce the number of traffic accidents, and increase the road safety the driver moves closer into the focus in the vehicle development and research. Several studies show that the human factor has the largest contribution to accidents (Vollrath 2010). The probability of an accident increases when the driving demands exceed the driver's performance capabilities (Fuller 2005). "Looked-but-failed-to-See" is also regarding accidents a frequent phenomenon (Brown 2005). Thus, the ability to perceive and process information and therefore the driver's control behaviour seem to be affected.

New advanced driver assistance systems must therefore include early in the application this linkage between the performance of the driver and the driving requirements in order to assist the driver in terms of comfort and safety optimally. This vehicle guidance, while supporting the driver, assists the driver in undesired driving situations depending on the system either by acoustic, optical or haptic feedback or intervention. The driver can usually change the system settings by pushing respective buttons, e.g. by selecting specific adjustment parameters (time gaps, warning thresholds etc.) for assistance systems. However, these systems work through algorithms which are based on the profile of average drivers. The ability of an adaptive adjustment to the driver in such safety and comfort functions makes the advanced driver assistance systems more interesting. An adaptation enables fulfilment of the needs and requests of the driver, so that a higher value and thus a higher acceptance can be achieved (Winkler & Vollrath 2016). A great effectiveness of the systems, also with regard to their acceptance, can be achieved if they are not only adjusted to the "average driver", but to the individual driver characteristics instead. "Although individual drivers have different driving styles and preferences, current systems do not distinguish among users" (Rosenfeld & Tsimhoni 2012). Similarly Yoshida (2003) also anticipates that adaptive automations will become more essential in the future and help to reduce traffic accidents; moreover with consideration of the aging of society.

A possible application of advanced driver assistance systems in terms of lateral dynamics could be adapting the threshold and warning points of the Lane-Departure Warning (LDW) with respect to the driver behaviour diversity for designing active safety functions. As a basis for such adaptation, a model of the driver-specific behaviour (primary via so-called "driving style identifier" of Institute of Automotive Engineering, Henze et al. 2011) is used. These kinds of models are often based on control system theory to describe the driver behaviour mathematically. To detect a change in the driver fingerprint, real driving data from test vehicle on similar traffic conditions are used for modelling. For this purpose, relevant vehicle, radar and track camera signals are extracted from the CAN bus and used for the driver modelling.

With help of the driver fingerprint, conclusions can be drawn on: the driving style, the driver's age/driver control behaviour and the driver performance (Fig. 1).

This study presents a method to identify a personal fingerprint of the driver with focus on the driving style.

www.TechnicalBooksPDF.com



Figure 1. Components of the driver fingerprint.

Therefore longitudinal and lateral control behaviour of the driver will be analysed. Several examples of the process of determining the objective parameters from longitudinal and lateral control behaviour are illustrated. The fingerprint model is briefly presented to show the advantages of this driver model. It is composed of three components. First sub-model aims to identify the driving style. To identify the driving style a "driving style identifier" will be used. The second sub-model serves to identify the control behaviour of the driver. The last and third sub-model identifies the driver performance with indirect measurement.

2 MODELLING AND RESULTS

2.1 *Driving style*

Murphey et al. (2009) defines driving style as a dynamic behaviour of a driver on the road. Basically, the driving style has to be interpreted as a natural, variable characteristic of the driver. During specific driving manoeuvres depending on the driving environment (e.g. sudden deceleration due to a vehicle cut in), the natural driving style can change suddenly. The driving environment could act as a potential inhibitor in that case. This requires a statistical long-term monitoring of the driving style which also recognizes the particular short-term effects. The concept of identifying specific driver characteristics according to driver style has been studied by many researches as follows.

2.1.1 *Related works*

Taubman-Ben-Ari & Gillath (2004) purposed a multidimensional measure of driving styles. They defined an eight-dimensional driving style inventory, each one representing a specific driving style-dissociative, anxious, risky, angry, high-velocity, distress reduction, patient and careful. Furthermore, associations between gender, age, driving history, personality, extraversion and driving style were analysed. On the other hand, Johnson & Trevedi (2004) categorises the driving style only to non-aggressive (typical) and aggressive. It concludes that the combination of rotation rates, accelerations and pitch are the most suitable signals to use their algorithm. The research Mijama & Itakura (2007) used the information from following distance and driving speed signals to categorise the different driver characteristics. It focuses additional on the gas and brake pedal pressures, also steering angle to classify the driver.

Compared to the related works in the literature, none of those combine the interaction between the driver and the driving environment for the final classification. Although Mijama & Itakura (2007) consider the following distance combined with velocity, the most identification methods in literature use the driver inputs such as gas and brake pressures, steering angles, which strongly depends on current vehicle characteristics. The classification under these circumstances could not be global. At this paper, the interaction between the driver and his car (motion states, vehicle independent parameters like acceleration, deceleration etc...) and with his environment during approach, follow-up and driving a curve (via radar, lane camera track signals) will be combined to generate the driving style. Consequently this leads to combination of the longitudinal and lateral behaviour of the driver to have maximum information about the driving style. This paper explores not only the methods to identify the driving style, but also how and why to use this information about the characteristics of the driver for better safety and comfort generally and give this information to use adaptive automation systems as a next step after true identification.

2.1.2 *Database and the driving style identifier*

In the context of this paper data, driving scenarios are addressed on well-developed national roads and motorways. To analyse the driver behaviour, the interaction between driver, driven vehicle and driving environment (3d, also known as DRV: driver-road-vehicle Henze et al. 2010) has to be considered and relevant range of drivers statistically recorded. For this purpose, real road traffic data were conducted to record driver behaviour and driving environment parameters (lane camera track signal and radar data) for integration into a database.

The first database from the driver performance road tests with limited conditions such as high speed limit of 180 kph, no usage of the assistance systems comprises 40 000 km and consist of 67 drivers, all of which driven on highway roads. Besides, the existing dataset is extended by consideration of environmental data (camera track signal and radar) in order to achieve a higher robustness for driving style classification. As the second database 11 800 km with 51 drivers on 61% extra urban and 20% highway roads, without any restrictions (free driving without any passengers) were merged into the database. Table 1 shows general information about the ages and genders of the participants of each database.

Figure 2 shows a schematic illustration of the driving style identifier with two function modules. The basis is the vehicle module (cf. function block 1), including longitudinal and lateral acceleration and driving speed for classification. The driving style,

www.TechnicalBooksPDF.com

Table 1. Participant information of the databases.

Feature	database 1 value	database 2 value
Mean Age (μ)	23.7	47.4
Std. Age (σ)	1.9	10.7
Gender Male	58	48
Gender Female	9	3

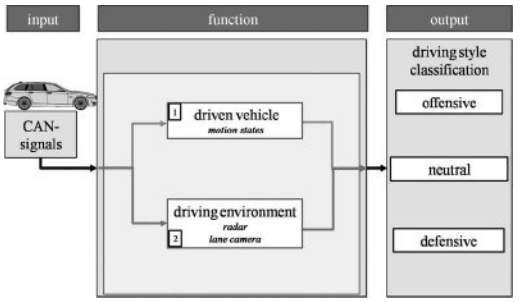


Figure 2. Schematic structure of the driving style identifier.

however, can be influenced as mentioned by the driving environment (e.g. in urban traffic) in certain precisely using the driving environment information (e.g. radar and/or lane camera track data) since a classification based on drive dynamics parameters alone is not sufficient in this case. Based up on this, the driving style identifier is extended by an additional analysis and decision unit (cf. function block 2). Though, it should be compatible with the existing model logic, which means that each function module is independent of the other modules and can be used according to the equipment level of the vehicle.

To identify the driving style from vehicle motion states, three criteria – independent of the vehicle – are used which allow an objective conclusion: the "safety limit of the standard (here in meaning of neutral) driver" (Schimmelpfennig & Nackenhorst 1985) usage of the friction circle and maximum use of the acceleration and deceleration potential.

The Figure 3 shows the exemplary characteristic and limit curves of the different classifications with respect to above mentioned criteria.

First curve above left is based on the statistics. (Schimmelpfennig & Nackenhorst 1985). It shows that the standard (neutral) driver e.g. sense certain lateral accelerations above dedicated driving velocities uncomfortable and therefore avoid them. The second curve above right represents the usage of the friction circle. This method does not depend on velocity. In the second curve above right, offensive drivers exhibit a significantly high use of the longitudinal and lateral acceleration potential of the vehicle at the same time, e.g. during braking and accelerating in a curve. However, defensive and neutral drivers drive the curves without significant longitudinal acceleration. Apart

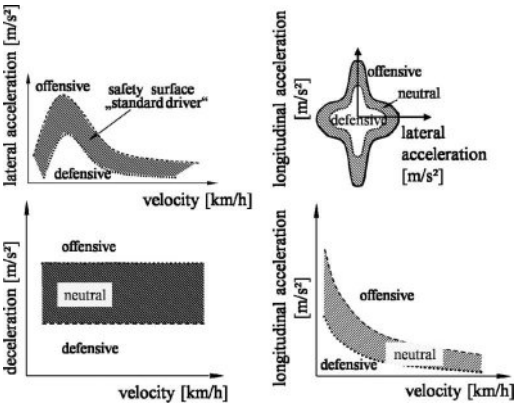


Figure 3. Characteristic limits to classification of the driver.

from these two lateral dynamics criteria, the driving style is derived from longitudinal dynamics criteria, with a differentiation between deceleration and acceleration behaviour. While the acceleration behaviour (bottom right) clearly depends on the weight-to-power ratio and the traction hyperbola – and therefore on the acceleration reserves –, the braking behaviour (bottom left) is nearly uninfluenced by them (Henze et al. 2011). With these methods, depending on the location of the driver inside the illustrated characteristic limits, the individual driving style information is derived for its classification. The precise calibration of all curves is based on the used database.

However, the driving style can be influenced by the driving environment (e.g. in urban traffic) in certain situations, which can be identified more precisely using the driving environment information (e.g. radar and/or track camera data). In that case, a classification based on only drive dynamics parameters is not sufficient. In addition to this, taking the driving environment information into account provides additional evaluable situations, so that the robustness of the detection is improved due to higher statistical relevance. Relevant driving situations such as approach, follow-up, driving in a curve are used to classify the characteristics of the driver in terms of driving style.

Figure 4 illustrates the driving situation approaching and following a vehicle as examples.

The time gap signal is used to identify the relevant driving segments. Time gap t_g represents the time required to reach the position of the rear of the leading vehicle (subject) with the front of the following vehicle (object). In the identified segments, characteristic parameters to describe the driver behaviour are developed and defined as objective parameters.

In Figure 5, objective parameter examples of the time gap t_g for the driving situation "follow up" after "approaching" a vehicle are shown. The gradient of the time gap signal during approach, the absolute minimum $t_{g,min}$ and the average value of the signal $t_{g,mean}$ during follow-up represent the characteristics of the driver behaviour.

www.TechnicalBooksPDF.com

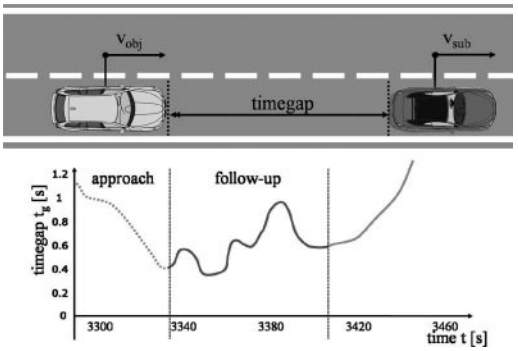


Figure 4. Characteristic limits to classification of the driver.

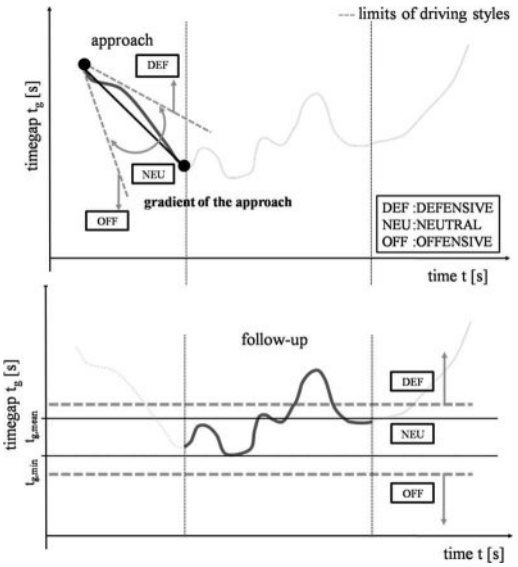


Figure 5. Objective parameter examples of the time gap signal as characteristic values.

In addition to the objective parameters related to the longitudinal behaviour mentioned above, objective parameters regarding lateral behaviour as lane keeping in curves are also generated and used for classification.

2.2 *Driver control behaviour*

In order to figure out the mathematical description of the driver and illustration of his control behaviour by different means, the system theory is used. Based on a closed-loop model a specific application model is developed as shown in Figure 6.

In order to describe the driver, longitudinal and lateral accelerations a_x and a_y, the steering wheel angle δ_L, yaw rate, the velocity (v) and the lateral position of the vehicle in the lane Y and curvature from the track camera are required. Based on the curvature signal of the track camera one ratio of the steering angle is determined in the anticipation block and corresponds

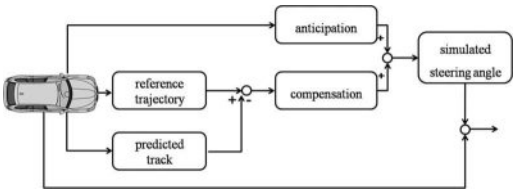


Figure 6. The structure of the driver model.

to the ideal driver, since no regulation is required. The reference trajectory describes the target trajectory. The current track is the prospective travelling trajectory, with an unchanged driver input, which is predicted through current vehicle states in case no further disturbances appear. Their difference is an input to the compensation block, which describes the feedback control of the steering angle. The sum of the anticipation and the compensation is the total steering angle which is returned as input into the vehicle. The non-modelled difference between the measured steering angle and simulated by the model driver steering angle could be caused due to the external disturbances such as lane grooves, side winds or road cambers.

To parameterise the compensation block, which mainly describes the human steering behaviour, genetic algorithm (GA) is used through response function in Laplace as follows:

$$H_C = V_C \frac{1}{1+Ts} e^{-s\tau_C}$$

In GA the biological evolution process is transferred as a principle to optimise the residual steering angle.

During the previous sensitivity analyses relevant characteristic control parameters are extracted. Some of them are the gain of the steering angle to lateral position V_c and the time constant T_c. T_c represents the delays caused by the motor nerves and inertia of the neuromuscular system of the human. Reaction time τ caused by the excitation of the sensory organ, which describes the transmission of information in the sensory nerves and information processing in the central nervous system. The prediction T_P considers, how foresighted the driver behaves, which is obtained from the prediction (Büyükyildiz, G. & Küçükay, F. 2015).

2.3 *Driver performance*

For more details to the sections 2.2 and 2.3 please refer to the documentations Büyükyildiz, G. & Küçükay, F. (2015) and Henze et al. (2011).

In order to demonstrate the potential of proposed fingerprint method, this paper focuses on the acceptance of the driver, when the thresholds and warning points are adapted to the fingerprint of the driver.

2.4 *Survey of customer acceptance*

In a previous study with two groups of participants (15 aged 20–50 y, 10 aged 50+ y) the favourite warning

www.TechnicalBooksPDF.com

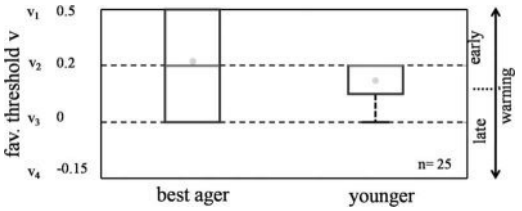


Figure 7. Boxplot of favourite threshold (LDW).

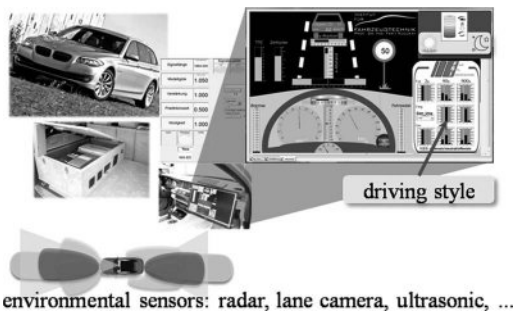


Figure 8. Test vehicle with measurement equipment and GUI of the fingerprint model for real time experience.

thresholds of lane-departure warning (LDW) systems among older (best ager) and younger drivers were analysed. An optical warning via LED strip as human-machine-interface (HMI) is chosen, which is installed on the dashboard. To trigger the thresholds the distance equation will be used as follows:

$$y = \frac{v(l_W - s_V) + s_V}{2}$$

whereby y is the lateral position (distance) from the lane centre to the lane markings, l_w is the lanewidth and s_v represents vehicle width. The maximum value of the variants "v" could be 1 and corresponds to the drive on the lane centre. Different four variants "v" of threshold were provided to the participants manually. Figure 7 presents boxplots of the favourite thresholds depending on lateral position.

The resulting preferences of participants will be used for the next customer acceptance adaptive survey, which is in preparation. Those favorite thresholds will be adapted to the fingerprint of the driver automatically instead of manually during test drives.

2.5 *Implemented fingerprint model*

Figure 8 shows the test vehicle (BMW F11 series 5) used for classification of the driving style for a real-time experience. In addition to the standard sensors (using CAN and FlexRay), the test vehicle is equipped with additional visualization equipment to record real road traffic data from the vehicle. It illustrates also the GUI for visualization of the final result of the fingerprint, which is provided as input to the lane departure warning assistance system to find out the desired variant of the driver.

3 SUMMARY AND OUTLOOK

In this paper, the database and method to generate the driver-specific fingerprint were presented. The knowledge of an objective classification is helpfull to design safety systems, but it has to be remarked that the involvement of the influence of traffic situations on classification would offer further improvement potential. The influence of the weather, for instance, cannot be captured completely and used for the classification at the moment. The integration and merging of environmental information like road conditions, coefficient of friction from different sources could increase the quality of the classification.

The adaptation to the driver (e.g. in case of dynamic driving) provides a higher potential for the further support and acceptance of the driver by means of road traffic safety. Improper warnings and interventions of the assistance systems could irritate the driver. A true adaptation can be reduced at the same time.

To further test the adaptive assistance functions and to cover wide range of whole driver, the next step includes comprehensive validation test drives and acceptance studies. The statistical robustness of the database can be improved with increased data volume. Corresponding test series and extensions are in preparation. The correlation of the subjective perception of safety to the driving style is also in preparation. The final driver classification depends mainly on the statistical distribution. In the future the current statistic data base could be linked through internet connection of other allowed cars by considering protection of data privacy that the classification becomes possible originating from the latest real road traffic data.

ACKNOWLEDGEMENTS

A part of this research was supported by the BMW Group, Munich.

REFERENCES

Bergholz, J. & Küçükay, F. 2008. Identifying the driver Performance, *World Automotive Congress*, 14–19 Sep, Munich.

Brown, I. D. 2005. Review of the 'Looked-but-Failed-to-See' Accident Causation Factor. *Road Safety Research Report* No. 60, Department for Transport, London.

Büyükyildiz, G. & Küçükay, F. 2015. Driver models based on lateral dynamics for adaptation of assistance systems, *3rd International Symposium on FASTzero*, 9–11. Sep.

Fuller, R. 2005. Towards a general theory of driver behaviour, *Accident Analysis & Prevention*, No. 37.

Henze, R. et al. 2010. The Driver as the Basis for Objectification of DRV characteristics, *FISITA World Automotive Congress*, 30 May–04 June, Budapest.

www.TechnicalBooksPDF.com

Henze, R. et al. 2011. Adaptation of ADAS-Functions by Monitoring Driver Characteristics. *Future Active Safety Technology, FASTzero'11*, 5.–9. September, Tokyo, Japan.

Johnson, D. A. & Trevedi, M. M. 2011. Driving style recognition using a smart phone as a sensor platform, *Intelligent Transportation Systems (ITSC)*, *14th International IEEE Conference on Washington*, DC, USA, Pages 1609–1615.

Miyajima, C. & Itakura, F. 2007. Driver Modeling Based on Driving Behavior and Its Evaluation in Driver Identification, *IEEE, Transactions on Intelligent Transportation Systems*, Vol. 95, Issue 2, Feb, Pages 427–437.

Murphey, Y. et al. 2009. Driver's Style Classification Using Jerk Analysis. Univ. of Michigan, Dearborn, MI, Member, *IEEE, Mar 30–Apr 2*, Pages 23–28.

Rosenfeld, A. & Tsimhoni, O. 2012. Towards Adapting Cars to Their Drivers, *AI Magazine*, Vol. 33, No. 4.

Rosenfeld, A. & Tsimhoni, O. 2012. Learning Driver's Behaviour to Improve the Acceptance of Adaptive Crusie Control, *Proceedings of the Twenty-Fourth Innovative Applications of Artifical Intelligence Conference*.

Schimmelpfennig, K.-H. & Nackenhorst, U. 1985. Bedeutung der Querbeschleunigung in der Verkehrsunfallrekonstruktion, Sicherheitsgrenze des Normalfahrers. *In: Verkehrsunfall und Fahrzeugtechnik*, Heft 4, Page 94ff.

Taubman-Ben-Ari, O. & Gillath, O. 2004. The multidimensional driving style inventory-scale construct and validation. *Journal of Accident & Prevention*, Volume 36, Issue 3, Pages 323–332.

Vollrath, M. 2010. Welche Fehler führen zu Unfällen? *Zeitschrift für Verkehrssicherheit*, 56(1), 31–36.

Winkler, S. & Vollrath, M. 2016. Timing of early warning stages in a multi stage collision warning system: Drivers' evaluation depending on situational influences, *Transportation Research Part F: Traffic Psychology and Behaviour*, Vol. 36, Jan, Pages 57–68.

Yoshida, T. et al. 2003. Adaptive Driver-assistance Systems, *Hitachi Review,* Vol. 53, No. 4.

Definitions/Abbreviations

DRV	driver-road-vehicle
GA	genetic algorithm
GUI	graphical user interface
HMI	human-machine-interface
LDW	lane departure warning

www.TechnicalBooksPDF.com

Advanced Vehicle Control – Edelmann, Plöchl & Pfeffer (Eds)
© 2017 Taylor & Francis Group, London, ISBN 978-1-138-02992-7

DrivingCube – A novel concept for validation of powertrain and steering systems with automated driving

C. Schyr
AVL Deutschland GmbH, Karlsruhe, Germany

A. Brissard
Ecole Nationale de l'Aviation Civile, Toulouse, France

ABSTRACT: The integration and validation of ADAS and self-driving functions requires new approaches in the vehicle development process. The concept of the AVL DrivingCube combines a highly-dynamic test bed for the powertrain, steering and brake system integrated in the complete vehicle with a detailed vehicle model operating in a virtual environment. Either physical sensors or behavioral sensor models connect the control units under test with the simulated environment. A mechanical decoupling of the wheel and steering actors at the driven and steered axle enable a virtual driving under all speed and load condition as encountered in real world situations. The presented test bed bridges the gap between conventional HiL systems and driving simulators and the real road test in order to enable efficient testing of the roadworthy vehicle in an controlled environment.

1 INTRODUCTION

1.1 *Motivation*

The validation of complex automated driving functions in all possible conditions and variations poses a new challenge in the automotive development. For example functions like Autonomous Emergency Braking, Adaptive Cruise Control and Steering Assist or even fully automated functions like chauffeur and parking systems require a huge amount of functional and non-functional validations within the integrated vehicle in a multitude of environmental situations and vehicle configurations.

The proven approach utilizing extensive vehicle testing on closed proving grounds and public roads fails when it comes to variation of those environmental conditions like driving maneuvers at the physical limits at different weather and lighting conditions. Also the injection of electric or electronic failures into the prototype vehicle cannot be performed in real road or track testing because of safety risks and potential damage to the vehicle and driver.

An established validation method is to connect the unit-under-test with an virtual environment to perform an extensive catalog of driving maneuvers. In the last years this method has been established for powertrain development (Pfister et al. 2009, Schyr et al. 2013), for steering system development (Specka et al. 2013), for integrated safety systems (Sattler et al. 2012) and for electric vehicles (Schyr 2013). For testing of ADAS and self-driving functions a multitude of HiL environments are available using physical or behavioral models for vehicle sensors (Ultrasonic, Camera, Lidar, Radar, GPS) and vehicle communication (Car2Car, Infrastructure2Car).

1.2 *Goals and ambition*

The paper presents a novel concept to bridge the gap between conventional HiL testing and real road testing for the efficient and reproducible validation of the fully integrated prototype vehicle as shown in figure 1. While in conventional HiL test environments the powertrain, steering and brake systems are simulated, the AVL DrivingCube includes those systems as complete units-under-test. This allows the operation of the vehicle in all driving situations under the same functional and energetic conditions as in the real road test (with respect to longitudinal and lateral dynamics).

In addition the DrivingCube creates an efficent cooperation platform for different domains and experts (Powertrain, Vehicle Dynamics, Sensors, HMI) to optimize and validate the integrated systems and functions in complex test scenarios. The evaluation of safety critical driving maneuvers under reproducible vehicle and environmental conditions including failure injection and human interaction is the main focus at those tests.

1.3 *Current technology*

End-of-Line benches for functional testing and calibration of sensors and their related software functions integrated into the complete assembled vehicle are

www.TechnicalBooksPDF.com

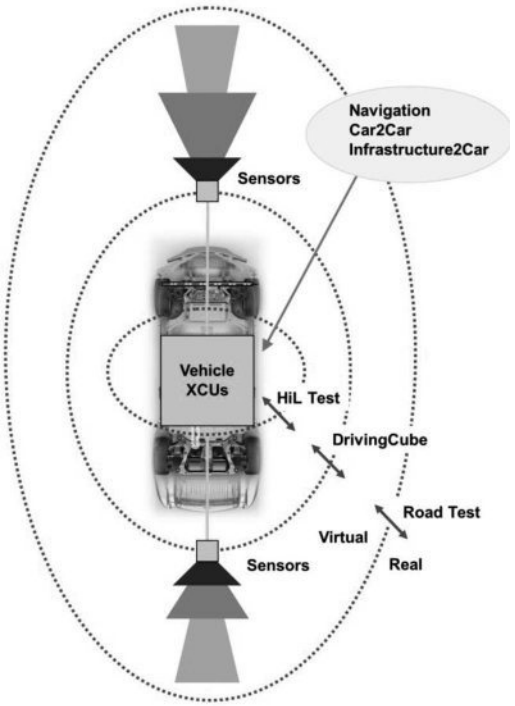


Figure 1. Bridging the gap between HiL and Road Test.



Figure 2. End-of-Line bench.

well know in mass production (Scheck 2007). The wheels are removed and the load dynos are connected with a turntable to the steered and driven axle as shown in figure 2. Due to articulated shafts and bevel gears the acceleration and brake dynamics is limited to slow maneuvers at low speed and load ranges.

The natural frequencies of the powertrain are shifted by the additional masses of shafts, bearings and bevel gears. In addition the actuation of precise steering counter forces based on high-fidelity tire simulation is difficult to achieve.

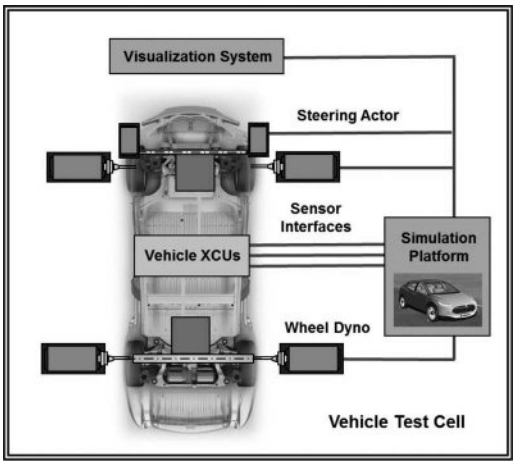


Figure 3. Layout of the test bed.



Figure 4. Highly dynamic powertrain test bed.

2 METHOD

2.1 *Mechanical modules*

The basic idea is to utilize a fast coupling system for mounting and dismounting of the roadworthy complete vehicle on a powertrain test bed as shown in figures 3 and 4. Low-inertia dynos with integrated wheel slip simulation ensure the same natural frequencies of the powertrain as encountered in driving tests on the real road (Brodbeck et al. 2001).

The steering rod is dismounted from the wheel carrier and mounted to steering force actors. This effectively decouples the rotational and translational dynamics of the actors at the driven and steered axle and allows the usage of proven highly dynamic electric motors to operate the powertrain, brake and steering systems in all driving situations up to the vehicle limits.

2.2 *Sensor modules*

The simulation of the vehicle motion is performed in a virtual enviroment with road and traffic models based

www.TechnicalBooksPDF.com

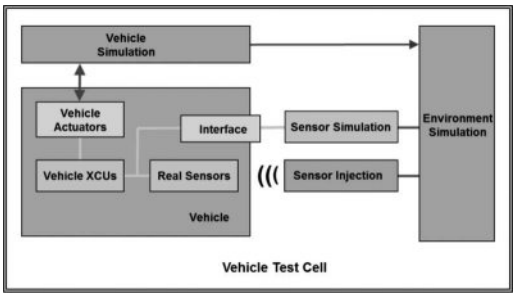


Figure 5. Integration of the vehicle with the virtual environment.

on standard OpenDRIVE (Dupuis 2010). A database provides the relevant enviromental models either as generic scenarios or as processed scenarios based on recordings from real driving tests.

The sensor interface between the virtual environment and the control units in the vehicle can be realized in two ways as shown in figure 5.

A sensor injection module interfaces to the virtual environment and transmits a generic physical signal extended with related attributes to the real sensor mounted in the vehicle. One example for this approach are radar target simulators with absorber box and receiver/transmitter (Heuel & McCarthy 2015). Another example is a multiple satellite signal generation including emulation of low signal levels, foliation and urban canyons, satellite drop out or the presence of interference and jamming signals (Geneder et al. 2014).

Otherwise generic sensor models extended with related attributes generate data streams, which are transmitted by cables and test interfaces to an injection point behind the real sensor in the vehicle. An example is the generation of a raw video data streams from the virtual environment and injected after the camera sensors (Haselhoff & Hakuli 2015).

2.3 *Thermal modules*

Driving at high speed and load conditions require a sufficient cooling of the vehicle. Typically a steady-state operation is possible well above 200 km/h. The blower is split into two parts to allow enough free space to integrate for example a radar multiple target simulator as shown in figure 6.

Optional a climatic chamber operates the complete vehicle and its sensors under extreme cold or hot environmental conditions. Actual chamber designs allow a temperature range from $-30°C$ to $+50°C$.

2.4 *Operational modules*

An automation system provides the capability for safe test operation also in failure situations and driving scenarios trespassing the physical limits of the actual tested vehicle and its sensor configuration.

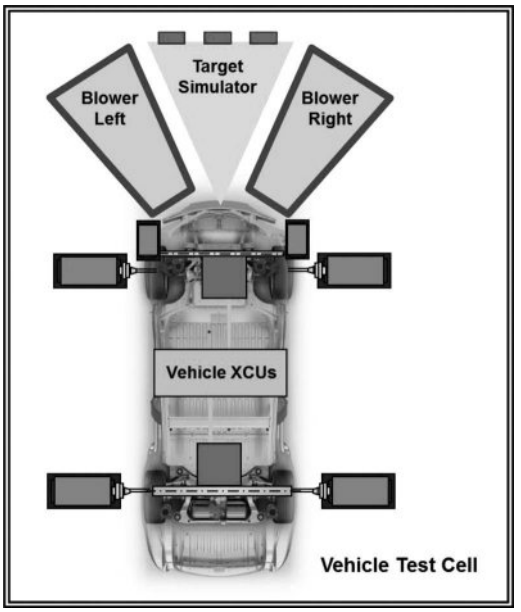


Figure 6. Radar target simulator with split blower.

A high-end visualization system connected to the simulation platform enables the validation of human related functions in the complete vehicle, similar to a conventional driving simulator. The main focus is here on the human-machine interface and take-over functions between fully autonomous, partly autonomous and manual driving in all possible scenarios.

For efficient test preparation and handling the vehicle can be mounted on a pallet system. In an adjacent preparation room the integration and function of the sensor interfaces is tested in advance, thus allowing a fully automatized 24/7 operation in the vehicle test cell.

3 APPLICATIONS

3.1 *Functional testing*

A main application of the DrivingCube is the validation of integrated functions like Emergency Brake Assist in a multitude of complex virtual environments like low-mu on a hill descent at bad visibility and heavy traffic. In figure 7 the comparison between an emergency braking maneuver with intervention from vehicle stability control on a test track and on the dynamic powertrain test bed can be seen. Parameters for this test run of a sportive compact car have been a dry and level road with standard friction and no wind as shown in figure 8.

3.2 *Non-functional testing*

The test bed can support the development process for ADAS and self-driving for functional integration

www.TechnicalBooksPDF.com

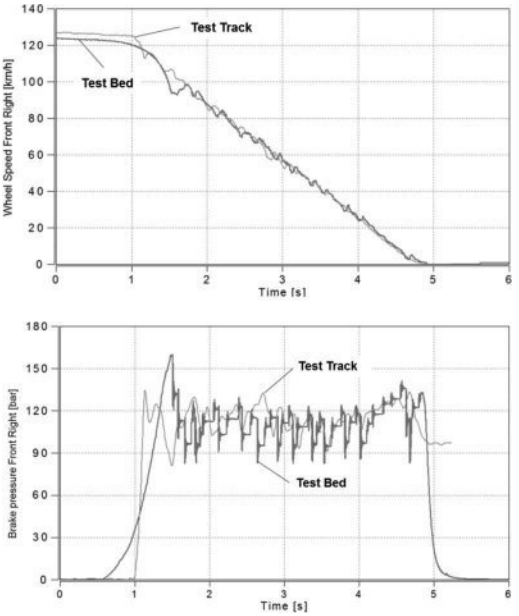


Figure 7. Emergency brake on real road vs. test bed.



Figure 8. Camera view of the emergency brake scenario in the virtual environment on the test bed.



Figure 9. Camera view of road crossing scenario at different weather conditions.

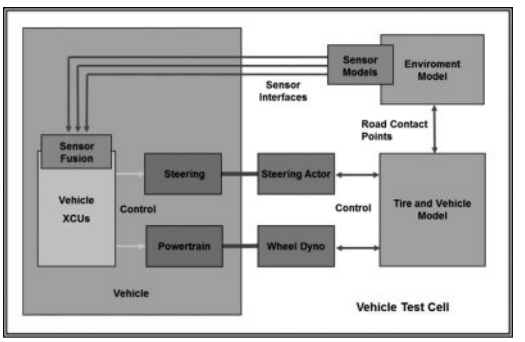


Figure 10. Closed-loop testing of robust sensor fusion.

and validation at a high Technology Readiness Level (TRL) as required by standards like ISO 26262.

As an example the validation of a new sensor platform is supported in a research project (RobustSENSE 2016). A fully autonomous demonstrator vehicle will be validated in a DrivingCube for secure and reliable operation in a multitude of harsh environmental conditions (like sun-flare, rain and snow) in different driving scenarios (like highway tunnel exit or urban road crossing).

The main advantage of the vehicle test bed is the immanent reactivity between ADAS and autonomous functions implemented in the vehicle control units, the longitudinal and lateral vehicle dynamics controlled by the actuated powertrain and steering systems and the dynamics and attributes of the sensors used for onboard fusion as shown in figure 10. Sensor attributs like degradation states can easily be modified within the augmented generic sensor models. Any modification or reparameterization of the onboard functions will be visible with the actual performed driving maneuver. The measured results for each test run based on comprehensive metrices are compared to the expected behaviour.

3.3 *Consumption, emission and range*

The validation of vehicle design and powertrain calibration for real driving emissions (RDE) will be an increasing challenge in the future. With further propagation of automated driving functions the need for precise measurement of fuel consumption and emission under all possible environmental conditions will arise. Using specific measuring systems like portable emission measurment (PEMS) as shown in figure 11, the DrivingCube supports the calibration of automated

www.TechnicalBooksPDF.com



Figure 11. Measurement of real emissions while automated driving.



Figure 12. Objective assessment of driveability while automated driving.

functions with respect to the given targets for fuel consumption and emission.

For battery electric vehicles a detailed analysis of power demand and expected range can be performed while automated driving on the test bed.

3.4 *Human perception*

The methodology pursued by the AVL Drive simulation tool to achieve an objective assessment of subjective impressions covers the objective assessment of longitudinal dynamics (operating and driving behaviour of engine and transmission), lateral dynamics (handling, steering, chassis suspension) and vertical dynamics (chassis suspension comfort). Based on measured variables supplied by sensors and control devices, a variety of operating modes are detected automatically, using fuzzy logic and behaviour patterns. These are physically evaluated in real time and assessed online by applying ratings in much the same way as driveability experts would do on the basis of their own subjective perception. For developing the rating modules for ADAS, this methodology was extended by adding an environment detection system (Holzinger et al. 2016).

This methodology can also be applied on the DrivingCube, where the required vehicle motion signals are generated from the detailed 3d vehicle model and the actual rating of the ADAS functions like adaptive crusie control or lane keeping are compared during a virtual test drive with a benchmark rating.

4 CONCLUSIONS AND OUTLOOK

The presented solution of a powertrain test bed extended with the capability to operate the powertrain, steering and brake systems under all possible speed and load conditions closes the gap between testing on real roads and testing in the HiL laboratory. The integration of sensors into the virtual environment can be either taken over from the HiL lab or specific sensor injection modules are used.

Current challenges are the optimal integration of this test environment into the vehicle development process, where an optimal data flow between the product data management and the local test automation and simulation system is established. The application and continuous extension of a road and scenario database generates a fully reactive knowledge platform, where critical test maneuvers for ADAS and autonomous functions be efficiently and safely reproduced and validated.

Another important key to successful usage is the necessary skill development at all different levels of engineers and managers involved to have a common understanding of the possibilites but also limitations of such a novel validation environment. Finally the DrivingCube will create an cooperative work platform for different domains and experts (Powertrain, Vehicle Dynamics, ADAS, HMI) to validate the integrated systems and functions in complex test scenarios.

REFERENCES

Brodbeck, P., Pfeiffer, M., Germann, S. & Schyr, C. 2001. Verbesserung der Simulationsgüte von Antriebsstrangprüfständen mittels Reifenschlupfsimulation. Getriebe in Fahrzeugen. VDI-Berichte 1610.

Dupuis, M., Strobl, M. & Grezlikowski, H. 2010. OpenDRIVE 2010 and Beyond – Status and Future of the de facto Standard for the Description of Road Networks. Driving Simulation Conference Europe.

Geneder, S., Pfister, F., Wilhelm, C. & Arnold, A. 2014. Development of Connected Powertrains at the Power Test Bed. Automobiltechnische Zeitschrift 116: 14–18.

Haselhoff, M. & Hakuli, S. 2015. ECUs für kamerabasierte Fahrerassistenzsysteme im Closed-Loop-Verfahren. Automobiltechnische Zeitschrift Extra: 30–33.

Heuel, S. & McCarthy, D. 2015. Real Time Radar Target Generation. Microwave Journal.

Holzinger, J., Schloemicher, T., Bogner, E. & Schoeggl, P. 2016. Objective Assessment of Comfort and Safety of Advanced Driver Assistance Systems. FISITA World Automotive Congress.

Pfister, F., Schyr, C. & LeRhun, F. 2009. Total Energy Efficiency Testing. The Chassis Dynamometer as a Mechatronic Development Platform. Automobiltechnische Zeitschrift 111: 847–852.

RobustSENSE. 2016. Robust and Reliable Environment Sensing and Situation Prediction, http://www.robustsense.eu.

www.TechnicalBooksPDF.com

Sattler, K., Raith, A., Brandmeier, T., Schyr, C. & Sadou, D. 2012. Maneuver-Based Testing of Integrated, Highly Interconnected Safety Systems. FISITA World Automotive Congress.

Scheck, J. 2007. Prüfplattform für mechatronische ausgestattete Fahrzeuge in Entwicklung und Produktion. Dissertation RWTH Aachen.

Schyr, C. 2013. Virtual Test Driving – Enabler for the Efficient Development of Electric Vehicle Technologies. Asia Smart Grid/Electromobility Conference.

Schyr, C., Hakuli, S. & Schick, B. 2013. Ganzheitliche Fahrzeugbewertung mittels X-in-the-Loop im Entwicklungsprozess am Beispiel Powertrain-in-the-Loop. MTZ-Fachtagung Virtual Powertrain.

Specka, F., Contini, A., Hakuli, S., Schick, B. & Pfeffer, P. 2013. Evaluation and optimization of steering behavior in overall vehicle context at the “Steering-in-the-Loop” test bench. VDI Tire-Chassis-Road Congress.

www.TechnicalBooksPDF.com

Advanced Vehicle Control – Edelmann, Plöchl & Pfeffer (Eds)
© 2017 Taylor & Francis Group, London, ISBN 978-1-138-02992-7

Close to reality surrounding model for virtual testing of autonomous driving and ADAS

F. Chucholowski, C. Gnandt & C. Hepperle
TESIS DYNAware GmbH

Sebastian Hafner

ABSTRACT: For the development of Advanced Driver Assistance Systems (ADAS) and Autonomous Driving, cost efficient virtual methods to understand the vehicle behavior within a complex environment are needed. These methods require an easily configurable virtual world as well as realistic illumination, reflection and weather conditions. Further the connectivity to existing ADAS development toolchains is significant for the success of these methods. To face these challenges, the paper presents an approach that uses technology of real-time computer graphics originally developed for computer games in combination with the execution of ADAS simulation systems. To highlight the value of this alternative approach, driving scenarios for snowy and rainy weather conditions are presented. Further simulation of ultrasonic sensors for testing parallel parking assist functions and the setup of a virtual development environment for a lane keeping assist are shown.

1 INTRODUCTION

The development of ADAS leading to autonomous vehicles is proceeding rapidly. By sensor fusion of vehicle data with vehicle surrounding data a complete and actual environmental model for the systems is provided to realize more and more functions intervening in the driving of vehicles, avoiding dangers and freeing drivers from tedious tasks. When in September 2013 a Mercedes-Benz S 500 INTELLIGENT DRIVE from the Daimler AG drove 100 km from Mannheim to Pforzheim fully automated, the control algorithms have to manage 3 major cities, 23 towns, 18 traffic circles and 155 traffic light crossings on the route. Among systems targeting highly automated driving (VDA 2015) there are also driver assistance systems, such as traffic sign recognition or lane keeping assist (Fu & Huang 2010, Gunia & Schüling 2011). Due to the complexity of the multitude of possible scenarios the requirements for development and test methods are vastly increasing.

Besides typical time and cost issues there are several other aspects that favor the usage of virtual development methods. Testing of system behavior in life-endangering situations, repeatability of maneuvers and what-if analysis are just some of the major advantages development methods based on simulating the real world in comparison with development purely based on measurement data derived from field tests.

Simulations of the environment in common ECU vehicle simulations e.g. in the field of vehicle dynamics and drivetrain are based on tire-road-contact, external forces and driver input. For interaction with the vehicle's full surrounding, a complex environmental model – a complete virtual world – is needed.

Most often the capabilities of established simulation approaches are exceeded. In modern vehicles, cameras and other sensors based on time-of-flight technology gather information of the surrounding environment. In this process, position and motion coordinates, color information of the road and infrastructure, obstacles and other traffic are measured and interpreted. The more accurate the measurement is, the closer the results of interpretation will be to the real world. For high simulation accuracy, elemental geometrical and optical details, as well as object visibility considering sensor physics and interferences are important. Thus idealization and simplification for virtual testing in real-time are not an adequate option anymore.

In this paper an approach that uses technology of real-time computer graphics originally developed for computer games is presented. The solution is evaluated for typical ADAS and autonomous vehicle development use-cases regarding feasibility and economic efficiency.

The most basic requirements are summarized in section 2. Details about the transition from pure computer graphics to technical simulation can be found in section 3. Section 4 describes the integration of the presented solution into vehicle simulation tool chains based on two typical use-cases and section 5 summarizes the results of the paper.

www.TechnicalBooksPDF.com

2 REQUIREMENTS

In this section typical but important and challenging requirements concerning environmental modeling in the field of ADAS development are described.

2.1 *Configurable virtual world*

Control algorithms in the field of ADAS and automated driving become more and more intelligent. Early applications were Adaptive Cruise Control with idealized radar sensors (Reif 2010), lane detection on a camera Hardware-in-the-Loop test bench (Gunia & Schüling 2011) or development of a park assistance system based on ultrasonic sensors (Jeong et al. 2010). The environmental model was rigid and characterized by technical objects. This was an acceptable accuracy for the systems being tested due to their relatively simple logic.

Contrary to this, a human driver uses a lot more information. He can e.g. predict the intention of a pedestrian by its viewing direction, facial expression and moving behavior. Control algorithms for autonomous vehicles are adopting these skills e.g. for interaction with unprotected traffic participants. This implies that a lot of details should be part of the surrounding model. Animation of traffic participants should be possible to fulfill this requirement with minimum effort in scenario generation.

2.2 *Realistic illumination, reflection and weather conditions*

As long as human drivers are steering vehicles, they rely on good sight and road illumination at night. The different sensors that are used also rely on information they gather from their surroundings. Therefore it is crucial that all inputs for sensors are as realistic as required. Light, reflection but also sight impairment caused by different weather conditions such as rain or snow have to be included in the environmental modeling approach. Also the brightness of variable message signs, which is dependent on the viewing angle, should be simulated to reduce their time span of visibility as they are passed.

2.3 *System connectivity and modularity*

Different development tools and approaches are available for virtual ADAS development. Each one of them contributes its specific features to the overall development toolchain. Similar to ADAS and functions that are connected in the vehicle these tools must also exchange data in a synchronized way. Therefore the environmental model should provide standardized interfaces and should be able to receive and send information from and to other systems.

Control algorithms are using sensor signals. Due to different development stages and scenarios at OEM and Tier-One companies the sensors can be part of the overall simulation approach or are integrated as HiL components. Thus the system architecture of an environmental model should support all different scenarios. Particularly regarding sensor and control algorithm information the design should be as modular as possible.

3 SURROUNDING MODEL TECHNOLOGY

Computer games process user inputs and draw images on screens in short intervals to allow interaction of the player with a virtual world. Instead of sending the images to a monitor, the data of a virtual vehicle camera in a traffic scene can be used as input for a control unit. Real-time computer graphics use numerous techniques, which have been optimized over decades, to achieve one goal: photo realistic rendering with high image rate. Therefore, only effects which have a direct impact on any visible pixel are considered for the rendering process. The sample space finally is a RGB-tuple for every pixel per time step. The more important elements are the background calculations which are essential for the image quality and level of correlation to reality. The intermediate rendering processes must be radically modified to emulate physical behavior which is different for every kind of sensor. Additionally they provide information which is directly used for technical simulations. The approach presented in this paper is based on the game development platform Unity (Unity Technologies 2016).

3.1 *Surface shading*

Visible images originate from propagation of light and spectral reflection on surfaces. The various kinds of reflections defined by material parameters are calculated by shaders. Shaders are programs that describe the characteristics of either a vertex or a pixel for a desired appearance. These rendering effects are calculated on the GPU providing high performance and a high degree of flexibility (Randima, & Kilgard 2003). Therefore it is possible to model several physical effects, which are disregarded in most computer games in favor of appealing graphics. According to the required model accuracy, objects and surfaces are defined by varied detail of meshes, surface mapping, or pre-rendered textures. To solve conflicting performance and accuracy demands, these methods are switched automatically during simulation based on view distance and other parameters (Unity Technologies 2016).

3.2 *Fluids*

A fluid can be simulated using shaders if it has a considerable size of surface like a wet spot on a road or water beside the road. Another important feature is precipitation, like rain fall or a cloud of leaves. These are thousands of small, nearly identical and randomly spread objects with similar movement pattern. Particle systems from game engines facilitate simulation of

www.TechnicalBooksPDF.com



Figure 1. Virtual test scene – driving through rainy weather conditions.



Figure 2. Virtual test scene - driving through snowy weather conditions.

these effects. The particles can be any size and shape, thus different kind of snowflakes, for example, can be configured and used in a winter scene. Existing configurations of weather elements from games are optimized for human perception including motion blur and other secondary effects.

Figures 1 and 2 show typical virtual test scenes where automated driving systems are challenged with different weather and ambient conditions. Since motion of particles affects all kinds of sensors and cameras differently, the particle systems must also be modified according for each of them. The particles fail to be realistic if they are too close to a virtual camera, especially after a collision with the windshield or the sensor. This is why noise emulation is used for modelling of the pollution.

3.3 *Complete toolchain*

Precipitation is one kind of animation, but there is a lot more motion in the vehicle's surrounding. Besides the obvious proper motion of the vehicle, there are traffic participants, infrastructure, branches of trees waving in the wind, and much more that might affect the algorithms interpreting the situation. This represents a particular advantage when using a game engine: Motion of ductile surfaces like clothing of pedestrians, branches and leaves are supported by default. Object oriented design allows to add any number of objects to one scene and to let them interact. Finally the visualization of instruments for driver assistance, characteristic values and simulation data is essential for interpretation of development results. Figure 3 shows a typical setup for validation of a parallel parking system.



Figure 3. Urban parallel parking scenario.

4 INTEGRATION IN VEHICLE SIMULATION TOOL CHAINS

Today's driver assistance systems are mostly integrated into the vehicle control systems via closed-loop. This is why simulation of these systems needs a complete vehicle model. Existing vehicle models are based on common simulation platforms like Simulink. Nevertheless the vehicle must interact with the surroundings simulated with computer graphics. Therefore the surrounding model is connected to existing simulation platforms in order to provide a complete virtual development environment. Vehicle and traffic simulation deliver precise results of vehicle motion. Secondary motion patterns, like spinning wheels and walk cycles of pedestrians, are calculated by the animation of the game engine.

Figure 4 illustrates a common system setup. UDP and TCP/IP network connections are used for connection and synchronization. Via its synchronized data exchange the animation can be connected to MiL, SiL or HiL systems for development and testing of control unit algorithms. The connection with other simulation systems such as DYNA4 (TESIS DYNAware 2016) is realized by common interfaces like Simulink s-functions, FMI or XML. When connected with DYNA4 scenario setup, open-drive road definitions and automatic terrain generation can be utilized. The overall system provides different possibilities for ADAS and autonomous vehicle virtual development and can be enhanced for future challenges as well.

4.1 *Application example: parallel parking assist*

Under specific conditions it has been possible to simulate a Time-of-Flight sensor on the GPU by using a special virtual camera together with an adapted shader (Hafner 2015). The approach allows the use of

www.TechnicalBooksPDF.com

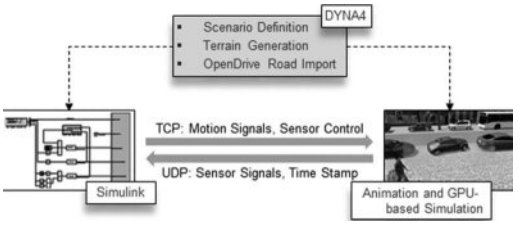


Figure 4. Overall system.

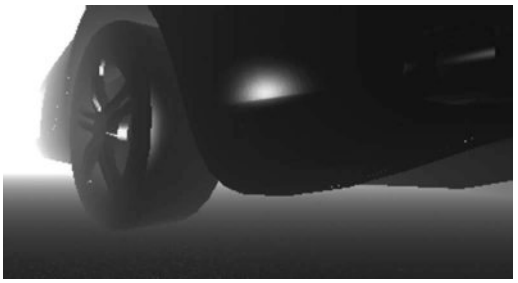


Figure 5. Rendered depth by GPU-supported shader for ultrasonic sensor.

common hardware without the loss of real-time capability. The animation is part of the complete modeling approach and synchronizes simulated sensor data with the rest of the overall model. The significant features and effects of ultrasonic sensors can successfully be reproduced in virtual tests and the new economic efficiency method fills the gap between common serially solved model equations and costly methods like raytracing (Hafner 2015). Figure 5 shows the rendered depth by the GPU-supported shader technology. Due to the promising results the approach will be transformed to other sensor physics like radar or laser scanners in the future.

4.2 *Application example: lane keeping assist*

A common approach to test optical control devices is a HiL test bench where virtual scenarios are displayed on a screen. The display is used as input for the optical ECU. This approach has some limitations e.g. for use-cases like driving in the night and blinding effect of headlights from oncoming vehicles.

Since the environmental simulation is also capable of sending information back to the overall simulation model, the virtual camera now provides visual information for a lane keeping assistant control algorithm developed in Matlab Simulink (Gerke & Roggero 2015). Raw data from the virtual camera mounted at the roof of the vehicle (figure 6) is used as input into the object detection algorithm. The animation is also used to visualize the overall results of the approach (figure 6, red surface). Different weather conditions – with and without rain – are simulated. The detected traffic lane objects are further processed by statistical methods and then grouped by rectangles (figure 7).

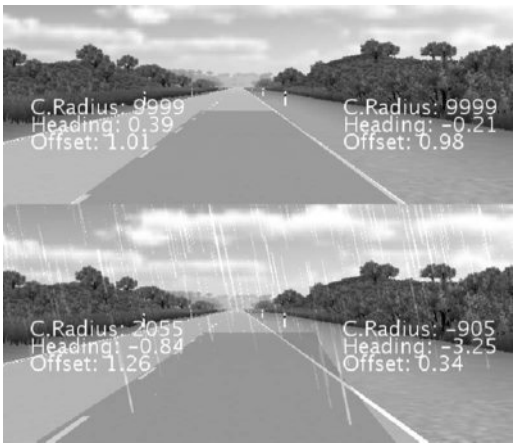


Figure 6. Visual input for lane keeping assist with different weather conditions.

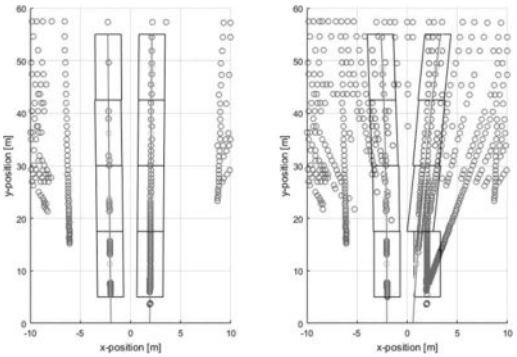


Figure 7. Processing of raw image data with (right side) and without rain (left side).

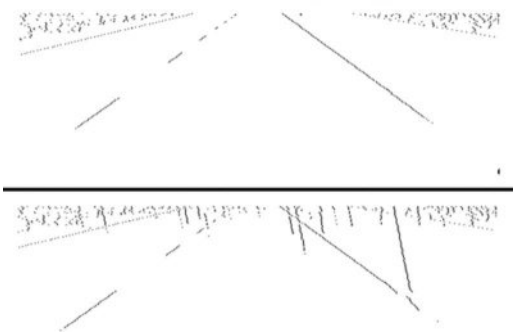


Figure 8. Final traffic lane information with (lower part) and without rain (upper part).

From this information the final traffic lane information is derived (figure 8).

The traffic lane information is then used as input into the lane keeping control algorithm. As can be seen the overall method provides reliable results with plausible correlation to the virtual world. Using the

www.TechnicalBooksPDF.com

environmental model without rain produces a quite smooth input for the control algorithm. The single lanes can clearly be recognized. Adding rain as an interfering element to the scene challenges the processing of the raw image (figure 7, ride side) but still produces reliable information for the control algorithm (figure 8, lower part).

5 CONCLUSIONS

The usage of a game engine for realizing an advanced environmental model is not a trivial endeavor, because most methods are made for human perception and not for technical simulation. By adapting them to physical laws and specific peculiarities of computer vision, a powerful and promising tool is available. The open system is extendable while having a user interface that is easy to operate and to configure at any time. Interfaces are designed according to established standards which allow integration into existing toolchains. It is possible to benefit from the latest technical innovations for computer games while having an economical efficient solution that runs on mid-priced PC systems with no additional hardware requirements. In consequence using the solution within the field of developing and testing ADAS and autonomous vehicles is a reasonable and valuable alternative to current test setups.

REFERENCES

Fu, M. Y. & Huang, Y. S. 2010. A survey of traffic sign recognition. *International Conference on Wavelet Analysis and Pattern Recognition:* 119–124.

Gerke, T. & Roggero, M. 2015. ADAS-Entwicklung mit Model-Based Design. *HANSER automotive (5–6):* 40–43.

Gunia, D. & Schüling, J. 2011. Model-Based Testing of Ford's Lane Keeping System. *ATZ 11/2011* (113): 28–31.

Hafner, S. 2015. Physical modeling of environment detection sensors, based on GPU-supported shader technology. *15. Internationales Stuttgarter Symposium:*1567–1586.

Hafner, S. 2015. Konzeptstudie zur echtzeitfähigen Simulation von Ultraschallsensoren mittels Computergrafik. *Master Thesis*.

Jeong, S. & Choi, C. & Oh, J. & Yoon, P. & Kim, B. & Kim, M. & Lee, K. 2010. Low cost design of parallel parking assist system based on an ultrasonic sensor. *International Journal of Automotive Technology* (11/3): 409–416.

Randima, F. & Kilgard M. 2003. *The Cg Tutorial: The Definitive Guide to Programmable Real-time Graphics*. Boston: Addison-Wesley.

Reif, K. 2010. Adaptive Cruise Control (ACC). *Fahrstabilisierungssysteme und Fahrerassistenzsysteme*: 158–175. Wiesbaden: Vieweg+Teubner

TESIS DYNAware 2016. *DYNA4 Driver Assistance. ADAS Development with Real-Time Simulation*. URL: http://www.tesis-dynaware.com/en/products/dyna4-driver-assistance. Call date: 10.01.2016

Unity Technologies 2016. *Unity. Game engine, tools and multiplatform*. URL: http://unity3d.com/unity. Call date 07.01.2016.

Verband der Automobilindustrie (VDA) 2015. Automatisierung: Von Fahrerassistenzsystemen zum automatisierten Fahren. *VDA Magazin*.

www.TechnicalBooksPDF.com

www.TechnicalBooksPDF.com

Vehicle following

www.TechnicalBooksPDF.com

www.TechnicalBooksPDF.com

Advanced Vehicle Control – Edelmann, Plöchl & Pfeffer (Eds)
© 2017 Taylor & Francis Group, London, ISBN 978-1-138-02992-7

Autonomous cruise control with cut-in target vehicle detection

Ashwin Carvalho, Alek Williams, Stéphanie Lefèvre & Francesco Borrelli
Department of Mechanical Engineering, University of California Berkeley, CA, USA

ABSTRACT: This paper presents a longitudinal control algorithm for autonomous vehicles on highways. The focus is on identifying target vehicles in the scene which are relevant from a control perspective. These not only include vehicles in the ego vehicle's lane, but also those in neighboring lanes that are likely to cut in. A learning-based framework is used to estimate the lane change probability of such vehicles and identify relevant targets. The ability of the proposed approach to detect target vehicle cut-ins early and yield smoother control actions is demonstrated using data collected from a passenger vehicle in real traffic on a highway.

1 INTRODUCTION

Autonomous or Adaptive Cruise Control (ACC) systems are present in many commercial vehicles today. By controlling the speed of the ego vehicle to match the speed limit and adapting the speed to that of the car in front, these systems help prevent rear-end collisions and relieve the driver of a tedious task. Moreover, they can easily be combined with autonomous lane-keeping systems to provide full autonomy on highways. Typically, ACC systems focus on one target vehicle at a time, namely the one currently in front of the ego vehicle. In this paper, we propose an improved algorithm which can handle other vehicles cutting in front of the ego vehicle.

2 PROBLEM DEFINITION

Commercial ACC systems use a combination of onboard radar and camera to identify a Primary Target (PT) – the car in front of the ego vehicle in its own lane. The relative distance and speed of the PT are then passed to the control algorithm, which determines an acceleration command for the ego vehicle such that a safe following distance is maintained. If a PT is not detected, the controller tracks a desired speed such as the road speed limit.

A challenging scenario for current ACC systems is to deal with target vehicles in neighboring lanes cutting in to the lane of the ego vehicle. The authors in Müller et al. (2011) recognize the vehicle cutting in as the PT when the Time to Lane-Crossing (TLC) of the target vehicle is within a threshold. In Moon et al. (2010), a fuzzy logic approach is used to compute the probability of a target vehicle entering into the ego vehicle's lane. These approaches are rule-based and not robust to noisy measurements. Moreover, they assume the existence of a single PT. In the case of multiple target vehicles, existing approaches choose the most relevant one based on some heuristics.

The contributions of this paper are as follows:

- Given the relative positions of surrounding vehicles from the sensor fusion system, and the road geometry from the camera, we propose a learning-based approach to estimate the probability of lane change for each vehicle in the scene. Target vehicles which are relevant for ACC (possibly more than one) are then identified in the ego vehicle's lane and adjacent lanes.
- We present a multi-target autonomous cruise controller. The reference acceleration is generated via a Learning-by-Demonstration (LbD) algorithm using the most relevant target vehicle (Lefèvre et al. 2016). The control strategy is based on robust Model Predictive Control (MPC), where the safety constraints are imposed for all relevant vehicles. This avoids the need for rules to decide the most safety-critical target vehicle.

The effectiveness of the proposed approach is demonstrated using data collected from our test vehicle. The sensor fusion and control algorithms are capable of running in real-time on embedded rapid control prototyping platforms.

A schematic of the system architecture is shown in Figure 1. The "Sensor Fusion" module combines the measurements from the sensors such as radar, camera, lidar and GPS/INS to provide estimates of the relative positions and velocities of target vehicles (TVs) in front of the ego vehicle (EV). The "Relevant Target Identification" module computes lane change probabilities of the detected TVs and identifies relevant TVs for ACC. These are denoted as *Relevant Targets* (RTs) as opposed to a single PT in the case of conventional ACC systems. Based on the above information, the "Controller" computes the desired acceleration command for the "Vehicle".

The remainder of the paper is organized as follows. Section 3 discusses the sensor fusion approach. The identification of RTs and the control algorithm are presented in Sections 4 and 5, respectively. Experimental

www.TechnicalBooksPDF.com

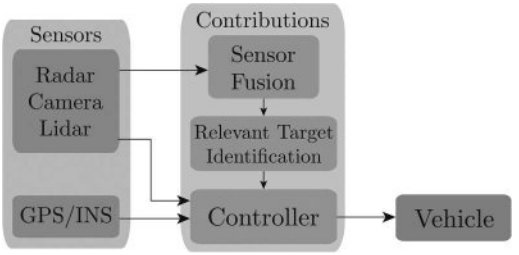


Figure 1. System architecture (described in Section 2). This paper focuses on the integration of the "Sensor Fusion", "Relevant Target Identification" and "Controller" modules for ACC.

results are discussed in Section 6 and concluding remarks are made in Section 7.

3 SENSOR FUSION AND TRACKING

The experimental vehicle used for this application is equipped with a radar, camera and lidar. Each sensor reports the relative positions and velocities of the TVs in front of the EV with respect to its body fixed coordinate frame. The main challenge of sensor fusion is data association, that is, deciding which measurements from the three sensors originate from the same TV. In our case, the individual sensors perform their own tracking, so we use a globally optimal probabilistic track-to-track association algorithm to determine which tracks pertain to the same real-world object.

Based on the work of Deb et al. (1997), we formulate the problem as a variation of the 3-dimensional assignment problem. Measurements from each of the three sensor tracks are grouped into triples to represent the hypothesis that those measurements have a common origin. The output of the algorithm is the optimal assignment which minimizes a chosen cost function. The cost of a triple is defined to be the negative log of the ratio of the probability that all three measurements in the triple pertain to the same object to the probability that all three measurements are spurious. The cost function is then the sum of the costs of all possible triples. The resulting optimization problem is a Mixed Integer Linear Program (MILP) which can be solved online. We use the open-source solver ECOS for solving the optimization problem (Domahidi et al. 2013).

A fused measurement of each associated TV's states is obtained by a convex combination of the measurements from each sensor. Additionally, a Kalman filter is used to estimate the relative positions and velocities of the TVs with respect to the EV.

4 IDENTIFICATION OF RELEVANT TARGETS

The main focus of this paper is to account for TVs cutting in to the path of the EV. This section presents a learning-based approach to infer the lane changing intent of vehicles in the neighboring lanes.

Based on the work of Lefèvre et al. (2014), we model the lane change decision making process for a given TV as a Hidden Markov Model (HMM). We define the following variables:

- $m_t \in \mathcal{M} = \{LK, LCL, LCR\}$ is the hidden mode or latent variable at time instant t (LK = lane keeping, LCL = lane change left, LCR = lane change right).
- z_t is the observed variable at time instant t. In our case, $z_t = e_{y_t}$, where e_y is the lateral position of the TV with respect to the centerline of the nearest lane. The variable e_y is estimated using a combination of the position of the TV relative to the EV obtained from the sensor fusion system and the road geometry information provided by the camera on the EV.

Remark 1. *Additional features such as the relative orientation of the TV with respect to its lane can be used to improve the performance of the lane change intention estimation.*

The joint probability distribution of the modes $m_{0:t} = \{m_0, \ldots, m_t\}$ and the observations $z_{1:t} = \{z_1, \ldots, z_t\}$ is given by

$$P(m_{0:t}, z_{1:t}) = P(m_0) \prod_{k=1}^{t} P(m_k|m_{k-1}) P(z_k|m_k), \tag{1}$$

where the *emission* probability density function $P(z_k|m_k)$ is modeled as a Gaussian distribution. The parameters which characterize the *prior* and *transition* probability mass functions $P(m_0)$ and $P(m_k|m_{k-1})$, respectively, and the means and covariances of the Gaussian emission density function are learned from data collected from our test vehicle using the Expectation-Maximization (EM) algorithm and the Bayesian Information Criterion (Lefèvre et al. 2014).

During online operation, at time t, inference on the HMM gives us a probability distribution over the hidden mode m_t for each TV conditioned on the history of observations $z_{1:t}$. That is, $P(m_t = i|z_{1:t})$ can be recursively computed as

$$P(m_t = i|z_{1:t}) \propto P(z_t|m_t = i) \sum_{j \in \mathcal{M}} P(m_{t-1} = j|z_{1:t-1}) P(m_t = i|m_{t-1} = j), \tag{2}$$

initialized with the prior distribution $P(m_0)$. The most likely mode m_t^{ML} at time t is defined as

$$m_t^{ML} = \arg\max_{i \in \mathcal{M}} P(m_t = i|z_{1:t}). \tag{3}$$

Among all TVs in front of the EV, we define the RTs as

- the TVs in the EV's lane,
- the TVs in the adjacent left lane whose most likely mode $m_t^{ML} = LCR$,

www.TechnicalBooksPDF.com

- the TVs in the adjacent right lane whose most likely mode $m_t^{ML} = LCL$.

The relative distances and velocities of the RTs are then passed to the controller described below. In the absence of a vehicle satisfying the above criteria, a *free-flow* mode is triggered wherein the controller tracks the road speed limit or a user-defined reference speed as in conventional cruise control systems.

5 CONTROLLER

The control strategy is based on combining LbD with MPC, previously presented in Lefèvre et al. (2016). The idea is to leverage the non-parametric nature of LbD and the safety guarantees provided by MPC. We extend our methodology to account for multiple RTs. A review of the control design is presented below. The details can be found in Lefèvre et al. (2016).

5.1 *Learning-by-Demonstration (LbD)*

The goal of LbD is to generate a reference acceleration for the MPC-based controller for the given driving situation. We use the frameworks of HMMs and Gaussian Mixture Regression (GMR) in this work. Similar to Section 4, the car-following behavior of the driver is modeled as a HMM. We define the following variables:

- $m_t \in \{1, \ldots, M\}$ is the hidden mode at time instant t, where M is the number of hidden modes.
- $z_t = [d_t^r, v_t^r, v_t]$ is the vector of observations at time t, where d^r and v^r are the relative distance and relative velocity of the *most relevant* TV, respectively, and v is the velocity of the EV. The determination of the most relevant target among the RTs is discussed later in Section 5.2.2.
- a_t is the acceleration of the EV at time instant t.

The joint distribution of the modes $m_{0:t} = \{m_0, \ldots, m_t\}$, observations $z_{1:t} = \{z_1, \ldots, z_t\}$ and accelerations $a_{1:t} = \{a_1, \ldots, a_t\}$ is given by

$$P(m_{0:t}, z_{1:t}, a_{1:t}) = P(m_0) \prod_{k=1}^{t} P(m_k|m_{k-1}) P(z_k, a_k|m_k). \quad (4)$$

where the emission density function $P(z_k, a_k|m_k = i)$ is modeled as a Gaussian $\mathcal{N}(\mu_i, \Sigma_i)$. The parameters that characterize the distributions in (4) are learned from data collected from a single driver. This allows us to personalize the driving behavior of the autonomous vehicle (Lefèvre et al. 2016).

During online operation, the reference acceleration a_t^{ref} at time t is computed using Gaussian Mixture Regression (GMR) as

$$a_t^{\text{ref}} = E[a_t|z_{1:t}] = \sum_{i=1}^{M} P(m_t = i|z_{1:t})[\mu_i^a + \Sigma_i^{az}(\Sigma_i^{zz})^{-1}(z_t - \mu_i^z)], \quad (5)$$

where $P(m_t = i|z_{1:t})$ is computed by the recursive algorithm in (2) and

$$\mu_i = \begin{bmatrix} \mu_i^z \\ \mu_i^a \end{bmatrix}, \qquad \Sigma_i = \begin{bmatrix} \Sigma_i^{zz} & \Sigma_i^{za} \\ \Sigma_i^{az} & \Sigma_i^{aa} \end{bmatrix}. \quad (6)$$

A sequence of reference accelerations $a_{t:t+N}^{\text{ref}}$ over a desired time horizon N can be obtained by iteratively simulating a^{ref} through the vehicle dynamics (described later in Section 5.2.3) and running (5) using the simulated features. In order to compute the predicted values of the features, the most relevant TV is assumed to move at a constant velocity over the horizon N.

5.2 *Model predictive control (MPC)*

The reference acceleration is tracked by a robust MPC-based controller where the future accelerations of the RTs are assumed to be bounded disturbances. The control inputs are chosen such that the collision avoidance constraints are satisfied for all possible values of this disturbance. The formulation of the robust safety constraints for the case of a single PT is introduced in Lefèvre et al. (2016) and summarized below. The approach is extended to handle all RTs present at the current time step.

5.2.1 *Robust safety constraints*

In order to ensure that the EV avoids rear-end collisions with the RTs for all possible future accelerations of the RTs, we take a worst-case approach. That is, the RTs are assumed to apply maximum braking starting from their current positions and velocities till they come to a halt. In Lefèvre et al. (2016), we show that the resulting safety constraints on the position and velocity of the EV over the prediction horizon for a given RT can be written as

$$\bar{d}_{t+k}^p - d_{t+k} \geq d_{\text{safe}} \qquad (k = 1, \ldots, N-1) \quad (7)$$

$$\bar{d}_{t+N}^p - d_{t+N} + \frac{v_{t+N}^2}{2a_{\min}} - \frac{(\bar{v}_{t+N}^p)^2}{a_{\min}^p} \geq d_{\text{safe}}, \quad (8)$$

where $\bar{d}_{t+1:t+N}^p$ and $\bar{v}_{t+1:t+N}^p$ are the predicted positions and velocities of the RT assuming a maximum braking of $a_{\min}^p$. The variable $a_{\min}$ is the maximum deceleration that be commanded by the controller on the EV and d_{safe} is the minimum relative safety distance. Note that the constraints (7) and (8) are imposed for all RTs present at time t.

5.2.2 *Safety margin*

Equation (8) introduces the notion of a safety margin. Intuitively, the LHS of (8) is the distance between the EV and the RT when they stop after applying maximum braking. For a given RT, we define the *normalized braking distance (NBD)* at time t as follows:

$$NBD_t = \frac{1}{d_{\text{safe}}} \left(d_t^p - d_t + \frac{v_t^2}{2a_{\min}} - \frac{(v_t^p)^2}{a_{\min}^p} \right). \quad (9)$$

www.TechnicalBooksPDF.com

We use this metric to determine the *most relevant* TV for the LbD approach presented in Section 5.1. That is, among the detected RTs, the vehicle with the smallest *NBD* is chosen as the most relevant TV. This metric is also used to compare the performance of our algorithm against existing approaches in the next section.

5.2.3 *Longitudinal dynamics model*

The following linear difference equations are used to describe the longitudinal motion of the EV for the MPC design:

$$\xi_{t+1} := \begin{bmatrix} d_{t+1} \\ v_{t+1} \end{bmatrix} = \begin{bmatrix} d_t + T_s v_t + \frac{1}{2} T_s^2 a_t \\ v_t + T_s a_t \end{bmatrix} =: f(\xi_t, a_t), \tag{10}$$

where ξ_t and a_t denote the EV state and control input at time t, respectively, and T_s is the sampling time.

5.2.4 *Online optimization problem*

In MPC, at each time step, a constrained finite horizon optimal control problem is solved. The first control input from the optimal input sequence is implemented, and the process is repeated at the next time step with the new measurements. At time t, the optimization problem to be solved online is given by

$$\min_{\mathbf{a}_t, \epsilon} \sum_{k=0}^{N-1} \left(\|v_{t+k+1} - v^{\text{ref}}\|_Q^2 + \|a_{t+k} - a_{t+k}^{\text{ref}}\|_R^2 + \|\Delta a_{t+k}\|_P^2 \right) + S\epsilon \tag{11a}$$

$$\text{s.t. } \xi_{t+k+1} = f(\xi_{t+k}, a_{t+k}) \tag{11b}$$

$$\bar{d}_{t+k+1}^{p_i} - d_{t+k+1} \geq d_{\text{safe}} - \epsilon \quad (i = 1, \ldots, N_{\text{RT}}) \tag{11c}$$

$$\Delta a_{t+k} = a_{t+k} - a_{t+k-1} \tag{11d}$$

$$a_{\min} \leq a_{t+k} \leq a_{\max} \tag{11e}$$

$$\Delta a_{\min} \leq \Delta a_{t+k} \leq \Delta a_{\max} \quad (k = 0, \ldots, N-1) \tag{11f}$$

$$\bar{d}_{t+N}^{p_i} - d_{t+N} + \frac{v_{t+N}^2}{2a_{\min}} - \frac{(\bar{v}_{t+N}^{p_i})^2}{a_{\min}^p} \geq d_{\text{safe}} - \epsilon \quad (i = 1, \ldots, N_{\text{RT}}) \tag{11g}$$

$$\xi_t = \xi(t), \quad a_{t-1} = a(t-1), \quad \epsilon \geq 0, \tag{11h}$$

where the expression $\|z\|_M^2 = z^T M z$ for a variable z and $\mathbf{a}_t$ denotes the control input sequence $\{a_t, \ldots, a_{t+N-1}\}$ to be optimized over. The reference speed is denoted by v^{ref} and the tracking error is penalized with a small value in Q. Actuator magnitude and slew rate limits are enforced in (11e) and (11f), respectively. The safety constraints (11c) and (11g) are imposed as soft constraints with a high penalty S on the slack variable ϵ. The subscript i in (11c) and (11g) denotes the ith vehicle out of the N_{RT} RTs present at time t. The optimization problem (11) is a standard nonlinear program which we solve using NPSOL (Gill et al. 1986).

6 EXPERIMENTS

The proposed ACC system was tested using sensory data collected from our experimental vehicle. Note that the system is capable of running in real-time on embedded rapid control prototyping platforms (see Lefèvre et al. (2016) for details). In this work, for a fair comparison of the proposed strategy with existing approaches, we simulate the effect of the control input on the motion of the EV but use real data to reconstruct the environment. It is assumed that the EV has no influence on TVs that cut-in to its path. The evaluation process is explained in more detail below.

6.1 *Data collection and scene reconstruction*

We collected manual driving data from our on-board vehicle sensors (radar, camera, lidar, GPS/INS) on highways. In order to accurately reconstruct the evolution of the environment, the inertial motion of the EV is estimated using the GPS/INS measurements. Combining this with the relative motion of the TVs perceived by the outward looking sensors allows us to estimate the inertial motion of the TVs. It is then straightforward to compute the apparent relative motion of the TVs with respect to the EV during a simulation involving the proposed controller. The TV data is passed to the sensor fusion and RT identification algorithms. The resulting RT data is used as an input to the MPC-based controller. Finally, the EV motion is simulated using (10), hence closing the loop.

We focus specifically on short segments of the datasets (around 10–15 s each) which involve a cut-in maneuver by a TV in the neighboring lane. The segment start time is chosen to be a few seconds before the TV initiates the lane change and the end time is when the TV completes the lane change.

6.2 *Evaluation methodology*

We compare the performance of the proposed ACC approach (denoted as *ACC*1) with the existing ACC system implemented on our experimental vehicle (denoted as *ACC*2). Note that the existing system uses a combination of radar and camera without any lane change intent estimation to identify a single PT. The PT identification is based on whether a candidate TV lies in a *virtual lane* constructed on the basis of the longitudinal velocity and yaw rate of the EV. The main difference between *ACC*1 and *ACC*2 lies in the identification of the RTs or the PT. For a fair evaluation, the same control strategy (presented in Section 5) is used for both approaches.

For each segment of the dataset involving a simulation of either *ACC*1 or *ACC*2, we compute the following metrics:

1. Absolute values of the mean and maximum deceleration, μ_a and p_a, respectively.
2. Absolute values of the mean and maximum negative jerk, μ_j and p_j, respectively.

www.TechnicalBooksPDF.com

Table 1. Means and standard deviations of the metrics defined in Section 6.2 for the proposed approach (*ACC*1) and the existing approach (*ACC*2) computed from 28 simulations.

Metric	Unit	*ACC*1	*ACC*2
μ_a	m/s^2	1.00 ± 0.46	1.91 ± 0.91
p_a	m/s^2	2.00 ± 1.12	3.01 ± 1.17
μ_j	m/s^3	2.04 ± 1.83	2.20 ± 1.68
p_j	m/s^3	8.69 ± 2.45	9.53 ± 1.29
NBD	–	9.57 ± 3.19	7.44 ± 3.43
TTCi	s^{-1}	0.20 ± 0.12	0.81 ± 1.24

3. Minimum normalized braking distance, *NBD*, as defined in (9), computed for the most relevant TV.
4. Maximum inverse time-to-collision, *TTCi*, defined as the ratio of the relative speed of the EV with respect to the most relevant RT and the relative distance.

Metrics (1) and (2) characterize the comfort of the system, where lower values correspond to a smoother behavior. Metrics (3) and (4) characterize the safety. A higher value of the *NBD* is desired while a lower value of *TTCi* implies lower collision risk.

6.3 *Results*

For a given approach (*ACC*1 or *ACC*2), the mean and standard deviation of the quantities described in Section 6.2 were computed for 28 segments from 4 datasets and are tabulated in Table 1. We see that *ACC*1 yields lower values of the mean and maximum deceleration as compared to *ACC*2 resulting in a more comfortable experience for the driver. The difference in the mean and peak negative jerk is less marked. This can be attributed to the fact that only aggressive cut-in maneuvers were selected for the analysis which required a sudden change in the acceleration commanded by the controller. The average values of the *NBD* and *TTCi* show that *ACC*1 yields a safer behavior than *ACC*2, validating the consideration of TVs' lane change intentions.

We further analyze an interesting and challenging situation recorded in one of the datasets where two TVs changed lanes in front of the EV within a short span of time. At time $t = 5.4$ s (from an arbitrary $t = 0$), the first TV (*TV*1) crosses the right boundary of the EV's lane, followed by the second TV (*TV*2) at time $t = 9.2$ s. The small relative distance and lower speeds of the TVs necessitates a braking maneuver by the EV. Figure 2 shows a comparison of the acceleration profiles for *ACC*1 and *ACC*2 when this scenario is reconstructed in simulation. It is seen that due to the lane change estimation of *TV*1, *ACC*1 starts braking at $t = 4.3$ s, 1.2 s before *ACC*2, resulting in a smoother acceleration profile. Later, when *TV*2 cuts in, *ACC*1 responds at $t = 8.1$ s, 1.8 s before *ACC*2. The deceleration command saturates in the case of *ACC*2 but not in the case of *ACC*1. A comparison of the metrics defined in Section 6.2 for both approaches is shown in Table 2.

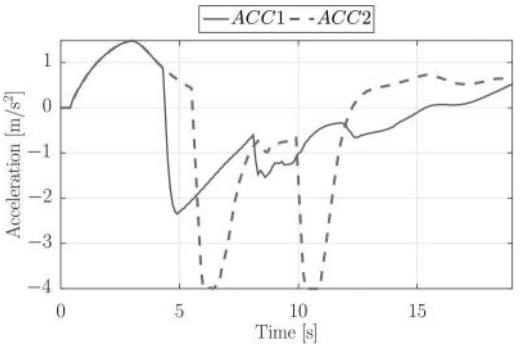


Figure 2. Comparison of the closed-loop acceleration profiles during a simulation of the scenario described in Section 6.3 of the proposed approach (*ACC*1, solid line) and the existing approach (*ACC*2, dashed line). *ACC*1 results in a smoother acceleration command that *ACC*2.

Table 2. Comparison of the metrics defined in Section 6.2 for *ACC*1 and *ACC*2 during a simulation of the scenario described in Section 6.3.

Metric	Unit	*ACC*1	*ACC*2
μ_a	m/s^2	0.95	2.05
p_a	m/s^2	2.35	4
μ_j	m/s^3	1.42	1.70
p_j	m/s^3	10	10
NBD	–	7.68	5.06
TTCi	s^{-1}	0.26	0.52

6.4 *Relevant target identification performance*

Finally, we compare the performance of the proposed RT identification methodology presented in Section 4 (*ACC*1) against the existing approach (*ACC*2). The metric used is the time difference between the two approaches recognizing a cutting-in TV as a RT or PT. It is observed that our method identifies a RT 1.28 ± 0.26 s before the existing approach.

The trajectory of a TV's lateral position e_y while it performs a cut-in maneuver from one of the datasets is shown in top plot of Figure 3. The middle plot shows the estimated most likely mode (defined in Section 4). We see that the estimator switches to the lane change right (*LCR*) mode 1.4 s before the estimated center of mass of the TV crosses the lane boundary. The bottom plot of Figure 3 depicts the binary variable indicating whether or not the TV has been identified as a RT for both methods *ACC*1 and *ACC*2. It is seen that *ACC*1 identifies the RT 1.85 s before *ACC*2 in this scenario.

7 CONCLUSIONS

This paper presents an approach for detecting target vehicle cut-ins for ACC systems. Data from multiple sensors (radar, camera and lidar) are fused to estimate

www.TechnicalBooksPDF.com

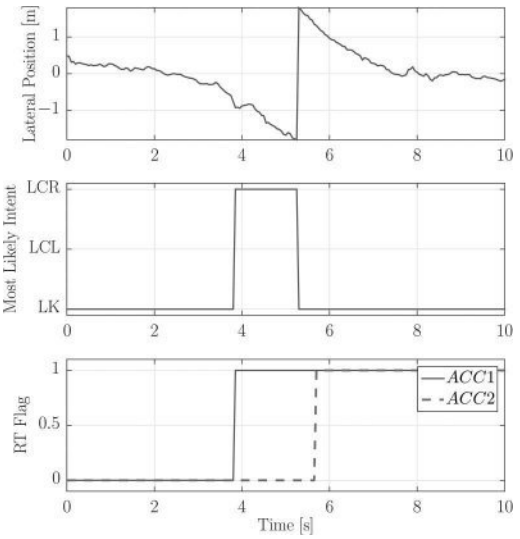


Figure 3. Results of the relevant target identification for a TV cut-in scenario from one of the datasets (described in Section 6.4). *ACC*1 identifies the RT 1.85 s before *ACC*2.

target vehicles' positions in their lanes. A learning-based lane change intention estimation algorithm identifies target vehicles which may change lanes into the path of the ego vehicle. A control strategy based on robust MPC is presented which considers safety with respect to all relevant target vehicles without the need for heuristics to select a single primary target. The proposed methodology is shown to improve the performance of the ACC system as compared to an existing approach, based on several metrics that consider comfort and safety.

ACKNOWLEDGMENTS

The authors would like to thank the Hyundai Motor Company for their support.

REFERENCES

Deb, S., M. Yeddanapudi, K. Pattipati, & Y. Bar-Shalom (1997). A generalized S-D assignment algorithm for multisensor-multitarget state estimation. *IEEE Transactions on Aerospace and Electronic Systems 33*(2), 523–538.

Domahidi, A., E. Chu, & S. Boyd (2013). ECOS: An SOCP solver for embedded systems. In *European Control Conference (ECC)*, pp. 3071–3076.

Gill, P. E., W. Murray, M. A. Saunders, & M. H. Wright (1986). User's guide for NPSOL (version 4.0): A Fortran package for nonlinear programming. No. SOL-86-2. Stanford University Systems Optimization Lab.

Lefèvre, S., A. Carvalho, & F. Borrelli (2016). A learningbased framework for velocity control in autonomous driving. *IEEE Transactions on Automation Science and Engineering.*

Lefèvre, S., Y. Gao, D. Vasquez, E. Tseng, R. Bajcsy, & F. Borrelli (2014). Lane keeping assistance with learning-based driver model and model predictive control. In *Proc. 12th International Symposium on Advanced Vehicle Control*.

Moon, S., H.-J. Kang, & K. Yi (2010). Multi-vehicle target selection for adaptive cruise control. *Vehicle System Dynamics 48*(11), 1325–1343.

Müller, D., J. Pauli, M. Meuter, L. Ghosh, & S. Müller-Schneiders (2011). A generic video and radar data fusion system for improved target selection. In *2011 IEEE Intelligent Vehicles Symposium (IV)*, pp. 679–684.

www.TechnicalBooksPDF.com

Advanced Vehicle Control – Edelmann, Plöchl & Pfeffer (Eds)
© 2017 Taylor & Francis Group, London, ISBN 978-1-138-02992-7

Padé approximation of delays in CACC-controlled string-stable platoons

H. Xing
Department of Mechanical Engineering, Dynamics and Control Group, Eindhoven University of Technology, Eindhoven, The Netherlands

J. Ploeg
Integrated Vehicle Safety Department, TNO, Helmond, The Netherlands

H. Nijmeijer
Department of Mechanical Engineering, Dynamics and Control Group, Eindhoven University of Technology, Eindhoven, The Netherlands

ABSTRACT: Cooperative Adaptive Cruise Control (CACC) improves road throughput by employing inter-vehicle wireless communications. The inherent communication time delay significantly limits the minimum inter-vehicle distance in view of string stability. Applying a Padé approximation leads to a model with a rational transfer function, which allows many control methods to compensate for this delay to a certain extent. Our objective is to find the lowest possible order of Padé approximations, which is sufficiently accurate in view of string stability. To this end, the minimum string-stable time gaps are chosen as the main criterion against which the quality of the Padé approximations is measured. The results indicate that it is feasible to apply a 2nd-order Padé approximation in the given CACC system.

1 INTRODUCTION

Advanced Driver Assistance systems have significantly developed in the last decades. Adaptive Cruise Control (ACC) systems equipped with radar or camera, which relieve the drivers' task by automatically keeping a desired inter-vehicle distance (Marsden, McDonald, & Brackstone 2001), are penetrating into the market. To realize a shorter inter-vehicle distance and, consequently, to improve highway capacity, Cooperative ACC (CACC) systems have been developed, which use wireless inter-vehicle communications (Naus et al. 2010, Shladover et al. 2012). String stability, which refers to the attenuation of the effects of disturbances in upstream direction of the string of vehicles, is a primary requirement for a vehicle platoon. CACC systems can significantly improve string stability, that prevent traffic jams while increasing highway throughput (Ploeg et al. 2011).

However, string stability can be affected by wireless communication impairments, such as time delays, sampling intervals, packet loss and communication constraints (Heemels & van de Wouw 2010). Thus, it is critical to take communication delays into account to design and analyze a CACC string (Liu et al. 2001, Naus et al. 2010, Ploeg et al. 2011, among others).

However, considering time delays leads to a non-rational transfer function, which poses a problem for many controller design methods. Consequently, many studies have paid attention to rational approximations of time delays. Padé approximation is widely used, since it often gives a better approximation of the delay system than other series of the same order (Golub & Van Loan 1989). However, the order of the Padé approximation, used in CACC systems (Kianfar et al. 2012, Öncü et al. 2014, Ploeg et al. 2014), was not explicitly motivated. Although a higher order Padé approximation leads to a more accurate representation, the resulting system is more complex. In addition, a too high-order Padé approximation may cause numerical problems.

This paper focusses on finding a suitable (low) order for the Padé approximation for the communication delay in view of string stability. To this end, the minimum string-stable time gap is chosen as the string stability property, in the sense that the minimum time gap for the approximated CACC system with selected order should be sufficiently close to the one of the original system. The selected order Padé approximation of a PD controller is quite possibly suitable to other linear controllers approximately realizing the same bandwidth as the PD controller, which suffices CACC (string) stability.

The outline of this paper is as follows. The next section introduces a model of a CACC-controlled vehicle string with wireless communication delay. Section 3 presents a frequency-domain method to pursue the appropriate order of the Padé approximation in view

www.TechnicalBooksPDF.com

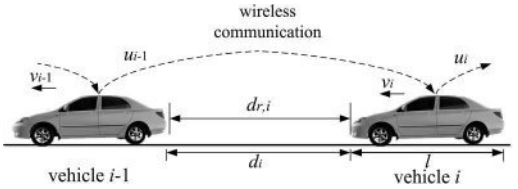


Figure 1. CACC-equipped string of vehicles.

of string stability, followed by time-domain analysis in Section 4. The last section summarizes the conclusions.

2 CACC-CONTROLLED PLATOON

2.1 *Platoon with communication delay*

A homogeneous CACC string is considered in this paper, as shown in Fig. 1, where l_i, v_i and u_i are the length, the velocity, and the desired acceleration of vehicle i, respectively; $d_{r,i}$ and d_i represent the desired distance and the actual distance between vehicle i and its preceding vehicle $i-1$, respectively.

In a CACC system, the wireless inter-vehicle link is employed for feedforward purposes. In our case the feedforward input is the desired acceleration u_{i-1} of the preceding vehicle. Although the wireless communication time delay has decreased largely with the recent developments of both software and hardware (Ploeg et al. 2014), it still has a significant effect on string stability of CACC. Thus, considering the wireless communication θ_c, the true feedforward input of vehicle i is

$$u_{i-1,c}(t) = u_{i-1}(t-\theta_c), \tag{1}$$

where θ_c consists of the total time delay due to queueing, contention, transmission, and propagation. Note that other network effects in wireless communication, such as packet loss and sampling effects, are not taken into account in this paper. The string is assumed to be homogeneous, which is why the communication delay θ_c is independent of the vehicle index i.

Considering non-linear dynamics of engine and drive train, and aerodynamic drag and rolling resistance, feedback linearization is often adopted to arrive at a suitable model for CACC design (Hedrick, Tomizuka, & Varaiya 1994). As a result, the acceleration a_i of vehicle i follows

$$\tau \dot{a}_i(t) + a_i = u_i(t), \tag{2}$$

where the vehicle actuator time constant τ represents the longitudinal vehicle response, which is set identical for both acceleration and brake situations, for the sake of simplicity. In addition, the transfer function $G(s)$ from the desired acceleration to the position reads,

$$G(s) = \frac{1}{s^2(\tau s+1)}, \tag{3}$$

where $s \in \mathbb{C}$ is the Laplace variable.

2.2 *CACC controller*

In a CACC string, each vehicle (except the lead vehicle) aims to keep a desired distance $d_{r,i}$ to its preceding vehicle. The constant time gap policy is utilized, which is the most common one to improve string stability, see Naus et al. (2010) and the references contained therein. Thus, the desired inter-vehicle distance involves a standstill distance and a velocity-dependent part:

$$d_{r,i}(t) = r + hv_i(t) \qquad i > 1, \tag{4}$$

where r represents the standstill distance, and h is a constant time gap. We pursue a small value of h to increase traffic throughput. However, inherent time delays in the wireless communication yield a lower bound for the time gap from a string-stability perspective (Naus et al. 2010, Ploeg et al. 2011).

To realize the vehicle-following objective, the inter-vehicle distance error e_i, defined as

$$e_i(t) = d_i(t) - d_{r,i}(t), \tag{5}$$

should asymptotically converge to zero. To this end, a variety of controllers have been proposed (Hedrick, Mcmahnon, & Swaroop 1993, Huang & Ren 1997, Stanger & del Re 2013, among others). However, a linear PD controller is most widely adopted, especially in experimental applications (Ploeg et al. 2011, Milanés et al. 2014). Adopting the controller structure in the work of Ploeg et al. (2011), a pre-compensator is used, introducing a new input ξ_i is as,

$$\xi_i(t) := h\dot{u}_i(t) + u_i(t). \tag{6}$$

Together with applying a standard PD controller, given by

$$K(s) = \omega_p + \omega_d s, \tag{7}$$

where ω_p and ω_d represent the proportional and derivative parameters, respectively, it leads to the controller of vehicle $i > 1$ to be,

$$\xi_i(t) = u_{i-1}(t-\theta_c) + \omega_p e_i(t) + \omega_d \dot{e}_i(t). \tag{8}$$

For analytic convenience,

$$\omega_p = \omega_d^2 \tag{9}$$

is chosen, which reduces an overflow of controller parameters in the sequel (Naus et al. 2010, Öncü et al. 2014). Consequently, the control structure with wireless communication delay θ_c can be depicted as in Fig. 2, where $H(s)$ and $D_c(s)$ are given by

$$H(s) = hs + 1 \qquad D_c(s) = e^{-\theta_c s}. \tag{10}$$

Thus, the transfer function $C(s)$ from the external input u_{i-1} to the inter-vehicle distance error e_i reads,

$$C(s) = \frac{G(s)(1-D_c(s))}{1+G(s)K(s)}. \tag{11}$$

www.TechnicalBooksPDF.com

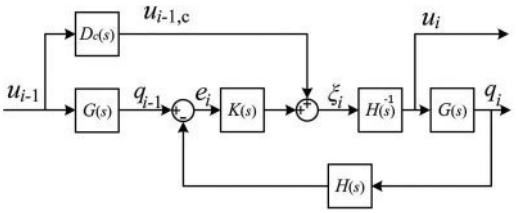


Figure 2. Block scheme of the CACC system.

Individual vehicle stability requires that all the roots of the denominator of (11) should have negative real parts, where the Routh-Hurwitz stability criterion can be applied, resulting in that the CACC string can be stabilized for $0 < \omega_d < \frac{1}{\tau}$. The PD controller (7) can provide the freedom to choose the bandwidth of (11) as the frequency at which $|G(j\omega)K(j\omega)|$ crosses 0 dB in the downwards sense.

Note that the communication delay θ_c occurring in the feedforward loop does not influence individual vehicle stability in the presented CACC structure.

3 STRING STABILITY BASED ON PADÉ APPROXIMATIONS

3.1 *Padé approximations of delays*

Padé approximation of a time delay yields a finite-dimensional state-space model with a rational transfer function:

$$e^{-\theta_c s} \cong \frac{\sum_{k=0}^{p} \beta_k (-\theta_c s)^k}{\sum_{k=0}^{p} \beta_k (\theta_c s)^k}, \tag{12}$$

where p represents the approximation order, and the coefficients β_k are given by

$$\beta_k = \frac{(2p-k)!p!}{(2p)!k!(p-k)!}. \tag{13}$$

Increasing the order can lead to a more accurate approximation, while the resulting model is more complex. The 1st-, 2nd-, and 3rd-order Padé approximations of a delay are represented as

$$P_1(s) = \frac{1 - \frac{1}{2}\theta_c s}{1 + \frac{1}{2}\theta_c s} \tag{14a}$$

$$P_2(s) = \frac{1 - \frac{1}{2}\theta_c s + \frac{1}{12}(\theta_c s)^2}{1 + \frac{1}{2}\theta_c s + \frac{1}{12}(\theta_c s)^2} \tag{14b}$$

$$P_3(s) = \frac{1 - \frac{1}{2}\theta_c s + \frac{1}{10}(\theta_c s)^2 - \frac{1}{120}(\theta_c s)^3}{1 + \frac{1}{2}\theta_c s + \frac{1}{10}(\theta_c s)^2 + \frac{1}{120}(\theta_c s)^3} \tag{14c}$$

To arrive at a suitable order of the Padé approximation, we apply a large range of system parameters, to find an order leading to similar string stability property as the aforementioned CACC system with pure delays.

3.2 *String stability*

Since the constant time gap policy (4) is introduced to achieve string stability, we choose the minimum string-stable time gap as the string stability property to arrive at the lowest possible Padé approximation order. In other words, the minimum string-stable time gaps for the CACC system with approximated delays and with pure delays should be sufficiently close. To this end, a range of values for the parameters of the vehicle actuator lag τ, the controller parameter ω_d, and the communication delay θ_c are considered.

In the frequently applied performance-oriented approach, string stability is characterized by the amplification in upstream direction of the signal of interest (Naus et al. 2010, Ploeg et al. 2011). Denote the string stability transfer function as $S(s)$, which describes the relation between a relevant (scalar) signal of vehicle i and the corresponding signal of its preceding vehicle $i-1$. In CACC systems, the signals of interest generally involve the inter-vehicle distance error, the acceleration, the velocity, and the distance. Then the system of interconnected vehicles is string stable if and only if

$$\sup_{\omega} |S(j\omega)| \leq 1, \tag{15}$$

with the frequency $\omega \in \mathbb{R}^+$. Note that $S(s)$ is independent of the vehicle index i due to the homogeneity assumption.

Let $E_i(s)$, $U_i(s)$, $V_i(s)$, and $Q_i(s)$ represent the Laplace transforms of the inter-vehicle distance error, the vehicle input (desired acceleration), the velocity, and the position of vehicle i, respectively. Under the assumption of homogeneous traffic, the string stability transfer function $S(s)$ does not depend on the choice of the signal, yielding,

$$\begin{aligned} S(s) &= \frac{E_i(s)}{E_{i-1}(s)} = \frac{U_i(s)}{U_{i-1}(s)} = \frac{V_i(s)}{V_{i-1}(s)} = \frac{Q_i(s)}{Q_{i-1}(s)} \\ &= \frac{1}{H(s)} \frac{D_c(s) + G(s)K(s)}{1 + G(s)K(s)} \end{aligned} \tag{16}$$

Substituting (3), (7), (10) and (16) in (15) yields

$$\sup_{\omega} \left(\left| \frac{1}{hj\omega + 1} \right| \cdot \left| \frac{e^{-\theta_c j\omega} + \frac{\omega_p + \omega_d j\omega}{(j\omega)^2(\tau j\omega + 1)}}{1 + \frac{\omega_p + \omega_d j\omega}{(j\omega)^2(\tau j\omega + 1)}} \right| \right) \leq 1 \tag{17}$$

to realize string stability.

In the case without communication delay, (17) reduces to

$$\sup_{\omega} \left| \frac{1}{hj\omega + 1} \right| \leq 1, \tag{18}$$

which is fulfilled for any non-negative time gap, i.e., $h \geq 0$ s. However, as previously stated, in reality a communication delay exists, which plays a significant role in designing the time gap for string stability.

www.TechnicalBooksPDF.com

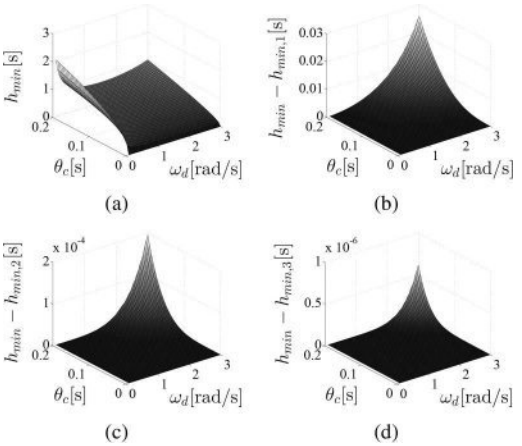


Figure 3. (a) The minimum string-stable time gap h_{min} for CACC with pure delays; differences $h_{min} - h_{min,p}$ of (b) the 1st-order, (c) the 2nd-order, and (d) the 3rd-order Padé approximations, with $\tau = 0.2$ s, $\theta_c \in [0, 0.2]$ s, and $\omega_d \in [0.1, 3]$ rad/s.

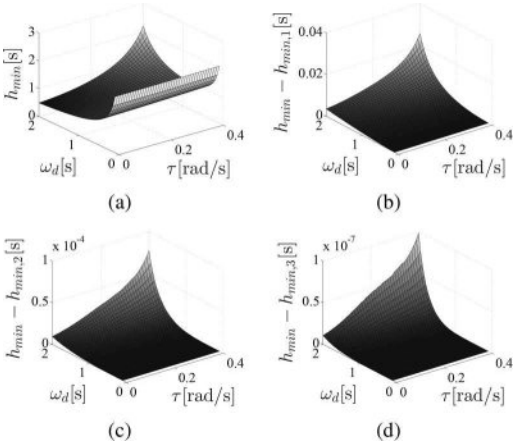


Figure 4. (a) The minimum string-stable time gap h_{min} for CACC with pure delays; differences $h_{min} - h_{min,p}$ of (b) the 1st-order, (c) the 2nd-order, and (d) the 3rd-order Padé approximations, with $\theta_c = 0.2$ s, $\tau \in (0, 0.4]$ s, and $\omega_d \in [0.1, 2]$ rad/s.

When $\theta_c > 0$ s, the magnitude of the string stability transfer function can be expressed as

$$|S(j\omega)| = \frac{1}{\sqrt{(h\omega)^2 + 1}} \left| \frac{M(j\omega)}{N(j\omega)} \right| \tag{19}$$

where

$$M(j\omega) = e^{-\theta_c j\omega} + \frac{\omega_p + \omega_d j\omega}{(j\omega)^2(\tau j\omega + 1)} \tag{20a}$$

$$N(j\omega) = 1 + \frac{\omega_p + \omega_d j\omega}{(j\omega)^2(\tau j\omega + 1)} \tag{20b}$$

from which it follows that string stability can be guaranteed for $h \geq h_{min}$, where

$$h_{min} = \sup_{\omega} \left(\frac{\sqrt{|\frac{M(j\omega)}{N(j\omega)}|^2 - 1}}{\omega} \right). \tag{21}$$

Substituting (14) and (20) in (21), results in an approximated minimum time gap $h_{min,p}$, where p represents the order of Padé approximation.

Thus, our objective is to find the lowest possible order p such that $h_{min,p}$ is sufficiently close to h_{min}. In practice, the time gap h is changed with increments of 0.1 s. Hence, a controller designed on the basis of Padé approximations should be significantly more accurate regarding string-stable time gap, which is why we assume a maximum error of 0.001 s, i.e.,

$$|h_{min} - h_{min,p}| < 0.001. \tag{22}$$

Note that $h_{min,p}$ is not guaranteed to be larger than h_{min}, i.e., string stability of the approximated system does not imply string stability of the system with pure delay.

Firstly, choose vehicle actuator lag $\tau = 0.2$ s, and controller parameter range $\omega_d \in [0.1, 3]$ rad/s, meeting the individual vehicle stability requirement $0 < \omega_d < \frac{1}{\tau}$. The time delay range $\theta_c \in [0, 0.2]$ s is considered, which covers possible communication delay of CACC systems, even when mild packet loss occurs. Fig. 3 shows the minimum time gap h_{min} and the differences $h_{min} - h_{min,p}$, with $p = 1, 2, 3$, as a function of θ_c and ω_d. Time gaps above the surface in Fig. 3(a) will guarantee string stability of the CACC string. Fig. 3(b) indicates that the differences $h_{min} - h_{min,1}$ are nearly 0.03 s for the 1st-order Padé approximation. In Fig. 3(c) and (d), for 2nd- and 3rd-order Padé approximations, $h_{min} - h_{min,p}$ are less than 2×10^{-4} s and 1.0×10^{-6} s, respectively, which meet the accuracy requirement (22). Hence, there is no necessity to consider a higher order Padé approximation.

Then, Fig. 4 shows the numerical results of the minimum time gap as a function of ω_d and τ, with a quite large value of $\theta_c = 0.2$ s, since the approximation of a large time delay yielding a sufficiently similar time gap h_{min}, is very likely to also suffice for smaller time delays. The value of the vehicle actuator lag is extended to a large range for passenger vehicles as $\tau \in (0, 0.4]$ s. A controller parameter in the range $\omega_d \in [0.1, 2]$ rad/s is adopted, where individual vehicle stability is guaranteed. Fig. 4(a) shows how the minimum time gap h_{min} depends on τ and ω_d with pure delays. In Fig. 4(b), (c) and (d), the differences of the minimum time gap between the model with pure delays and 1st-, 2nd- and 3rd-order Padé approximations are less than 3.0×10^{-2} s, 1.0×10^{-4} s and 1.0×10^{-7} s, respectively. Therefore, adopting 2nd- or 3rd-Padé approximations can obtain a sufficiently small value of the difference $h_{min} - h_{min,p}$. Note that the same process can be applied with independent proportional and derivative controller parameters, whereas the resulting differences $h_{min} - h_{min,p}$ have the close values for the

www.TechnicalBooksPDF.com

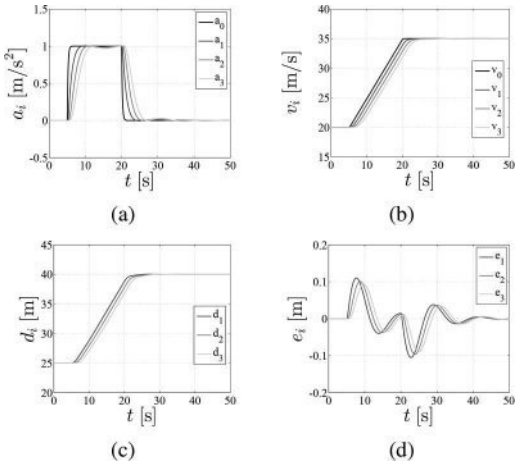


Figure 5. Time responses of (a) the acceleration a_i, (b) the velocity v_i, (c) the inter-vehicle distance d_i, (d) the distance error e_i of CACC with pure delays.

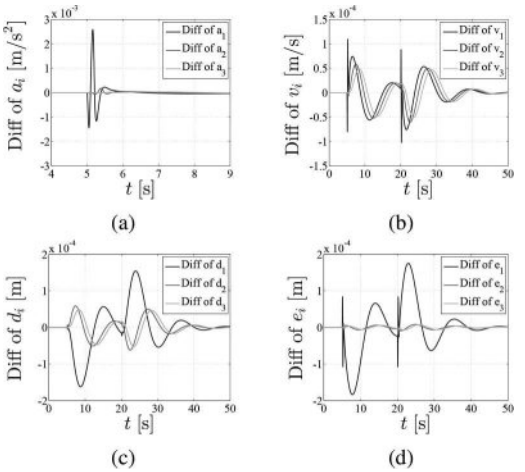


Figure 6. Differences of time responses of (a) the acceleration $a_i - a_{i,2}$, (b) the velocity $v_i - v_{i,2}$, (c) the inter-vehicle distance $d_i - d_{i,2}$, and (d) the distance error $e_i - e_{i,2}$, between the CACC models with pure delays and with 2nd-order Padé approximated delays.

corresponding orders of Padé approximations to these as shown in Fig. 3 and Fig. 4.

In summary, taking a 2nd-order Padé approximation for communication delays leads to similar minimum string-stable time gap for the original system with exact delays and for the system with the approximated delays.

4 SIMULATION IN TIME-DOMAIN

To validate the accuracy of the 2nd-order Padé approximation of the communication delays, time-domain simulations have been carried out for a CACC string with four vehicles with the standstill distance $r = 5$ m, the length of vehicle as $l = 3$ m, the vehicle actuator lag $\tau = 0.2$ s, and communication delay $\theta_c = 0.2$ s. According to Fig. 3(a), the controller gain is chosen as $\omega_d = 0.8$ rad/s and the time gap as $h = 1$ s to guarantee both string stability and individual vehicle stability.

The external input to the string is desired acceleration u_0 of the leading vehicle, and approximations of delays are most sensitive to a step response. Thus, the desired acceleration for the leading vehicle is set as follows,

$$u_0 = \begin{cases} 1 & 5\,\text{s} \leqslant t \leqslant 20\,\text{s} \\ 0 & \text{other} \end{cases}, \tag{23}$$

where the acceleration interval is chosen such that all follower vehicles can reach the desired acceleration. The initial velocity of all vehicles in this CACC string is $v_{initial} = 20$ m/s. All vehicles start with the desired distance 25 m.

Fig. 5 shows the time responses of the CACC string with pure delays. There is a slight overshoot in the acceleration responses in Fig. 5(a), fulfilling the frequency-domain string stability criterion (15) does not guarantee the absence of overshoot in time-domain (Ploeg et al. 2011, Ploeg et al. 2014). The velocity, inter-vehicle distance, and the distance error responses clearly show that this system is string stable from in Fig. 5(b), (c), and (d).

Applying the 2nd-order Padé approximation for communication delays, results in the approximated responses $a_{i,2}$, $v_{i,2}$, $d_{i,2}$ with the same input (22). The differences between the CACC string responses with pure delays and the ones with approximated delays are shown in Fig. 6, for vehicle 1, 2, and 3, which are CACC controlled. In Fig. 6, all differences of vehicle signals decrease with vehicle number i in the CACC string, i.e., the largest difference occurs in the responses of the first follower vehicle 1. We only zoom in around $t = 5$ s in Fig. 6(a), when the acceleration changes, to show the differences clearly. Similar results around $t = 20$ s are omitted here. The acceleration differences reach 3.0×10^{-3} m/s^2, which is much smaller than the step input of 1 m/s^2. Fig. 6(b) shows that the velocity differences due to the 2nd-order Padé approximation of delays are less than 1.5×10^{-4} m/s. The differences of inter-vehicle distances and the distance errors are less than 2.0×10^{-4} m as shown in Fig. 6(c) and (d), which are even less than the possible measurement noise of the inter-vehicle distance. Consequently, it is suitable to select a 2nd-order Padé approximation for communication delays in the string of CACC-equipped vehicles.

5 CONCLUSIONS

In CACC-controlled vehicle platoons, communication time delay inherently exists. Adopting a (low order) Padé approximation for the communication delay leads to a rational transfer function representation of the CACC string, which allows many controller

www.TechnicalBooksPDF.com

design methods. To arrive at a suitable Padé approximation order, the string stability properties of the system with pure delay and with approximated delay are compared. In particular, the minimum string-stable time gaps are selected as string stability property. With a PD controller, we obtain a satisfying behaviour in terms of bandwidth, as also shown in practice (Naus et al. 2010, Öncü et al. 2014). Hence, for linear controllers approximately realizing the same bandwidth, the results of the selection of Padé approximation orders are probable to hold as well. In this paper, the minimum string-stable time gap for the system with pure delay and for the system with approximated delay of various orders have been determined as a function of controller parameter ω_d, communication delay θ_c and vehicle actuator lag τ. With the frequency-domain analysis, a 2nd-order approximation appears to give satisfying results, providing a good balance between the (low) order and the accuracy in terms of minimum string-stable time gap. Time-domain simulations have been conducted to validate the results.

REFERENCES

Golub, G. H. & C. F. Van Loan (1989). *Matrix computations*. Baltimore, MD, USA: The Johns Hopkins Univ. Press.

Hedrick, J., M. Tomizuka, & P. Varaiya (1994). Control issues in automated highway systems. *IEEE Control Systems 14*(6), 21–32.

Hedrick, J. K., D. Mcmahnon, & D. Swaroop (1993). Vehicle modeling and control for automated highway systems. *PATH research report UCB-ITS-PRR-93-24*.

Heemels, W. & N. van de Wouw (2010). Stability and stabilization of networked control systems. In *Networked Control Systems*, pp. 203–253. Springer-Verlag.

Huang, S.-N. & W. Ren (1997). Design of vehicle following control systems with actuator delays. *International Journal of Systems Science 28*(2), 145–151.

Kianfar, R., B. Augusto, A. Ebadighajari, et al. (2012). Design and experimental validation of a cooperative driving system in the grand cooperative driving challenge. *IEEE Trans. Intell. Transp. Syst. 13*(3), 994–1007.

Liu, X., A. Goldsmith, S. Mahal, & J. Hedrick (2001). Effects of communication delay on string stability in vehicle platoons. In *Proc. IEEE Intell. Transp. Syst. Conf.*, pp. 625–630.

Marsden, G., M. McDonald, & M. Brackstone (2001). Towards an understanding of adaptive cruise control. *Transportation Research Part C: Emerging Technologies 9*(1), 33–51.

Milanés, V., S. E. Shladover, J. Spring, C. Nowakowski, H. Kawazoe, & M. Nakamura (2014). Cooperative adaptive cruise control in real traffic situations. *IEEE Trans. Intell. Transp. Syst. 15*(1), 296–305.

Naus, G. J. L., R. P. A. Vugts, J. Ploeg, M. Molengraft, & M. Steinbuch (2010). String-stable cacc design and experimental validation: A frequency-domain approach. *IEEE Trans. Veh. Technol. 59*(9), 4268–4279.

Öncü, S., J. Ploeg, N. van de Wouw, & H. Nijmeijer (2014). Cooperative adaptive cruise control: Network-aware analysis of string stability. *IEEE Trans. Intell. Transp. Syst. 15*(4), 1527–1537.

Ploeg, J., B. Scheepers, E. Van Nunen, N. Van de Wouw, & H. Nijmeijer (2011). Design and experimental evaluation of cooperative adaptive cruise control. In *Proc. IEEE Intell. Transp. Syst. Conf.*, pp. 260–265.

Ploeg, J., D. P. Shukla, N. van de Wouw, & H. Nijmeijer (2014). Controller synthesis for string stability of vehicle platoons. *IEEE Trans. Intell. Transp. Syst. 15*(2), 854–865.

Ploeg, J., N. Van De Wouw, & H. Nijmeijer (2014). Lp string stability of cascaded systems: Application to vehicle platooning. *IEEE Trans. Control Syst. Technol. 22*(2), 786–793.

Shladover, S. E., D. Su, & X.-Y. Lu (2012). Impacts of cooperative adaptive cruise control on freeway traffic flow. In *Proc. 91st TRB Annu. Meet*, pp. 1–17.

Stanger, T. & L. del Re (2013). A model predictive cooperative adaptive cruise control approach. In *Proc. American Control Conference (ACC)*, pp. 1374–1379.

www.TechnicalBooksPDF.com

Advanced Vehicle Control – Edelmann, Plöchl & Pfeffer (Eds)
© 2017 Taylor & Francis Group, London, ISBN 978-1-138-02992-7

A vehicle following controller for highly-actuated vehicles

R. de Castro, A. Schaub, C. Satzger & J. Brembeck
Department of Vehicle System Dynamics, German Aerospace Center (DLR), Institute of System Dynamics and Control, Germany

ABSTRACT: This work is concerned with the design of a vehicle following controller (VFC). The goal of the VFC is to determine appropriate control actions for a highly actuated electric vehicle such that the longitudinal and lateral motion of a target vehicle is followed. To achieve this goal, a combination of a non-linear guidance law, based on pure pursuit concepts, and a model-predictive method (for the longitudinal control) is explored. The proposed method is able to handle actuation dynamics, physical constraints, and preview information. It also promotes high-energy efficiency, by maximizing the use of regenerative braking. Simulation results demonstrate that the proposed approach can provide energy savings of up to 16% during transient maneuvers.

1 INTRODUCTION

Cooperative driving, where two or more vehicles perform cooperative sensing and maneuvering, is currently envisaged as a promising building block for addressing the growing challenges in transportation systems. For instance, the increase in traffic efficiency, safety and driving comfort offered by cooperative longitudinal control, such as cooperative adaptive cruise control (CACC), are well-known benefits of this technology (Naus et al. 2010). Within this context, the present article focuses on the development of a vehicle-following controller (VFC) for highly actuated electric vehicles (EVs). Our aim is to determine appropriate control actions such that the motion of a partner/target vehicle is followed.

For the longitudinal control, our attention lies in energy efficiency and intelligent braking management during vehicle-following scenarios. It is a well-known fact that, by decreasing the inter-vehicle separation reduction in aerodynamic drag can be achieved, particularly in heavy-duty vehicles (Besselink et al. 2016), which leads to energy savings. This work seeks further energy gains by focusing on the generation of energy-efficient acceleration profiles for EVs, particularly during braking phases. In EVs, the braking effort can be provided by two types of actuators: the electric motors and friction brakes. To split the braking torque among these actuators, several torque blending strategies have been proposed in the recent past, focusing on the maximization of the energy recuperation, fast transient response and safety aspects (Satzger et al. 2014, Ivanov et al. 2014). However, these torque blending works assume that the vehicle's acceleration demand is pre-determined, i.e. the torque blending component does not normally play an active role shaping the vehicle's acceleration. In this work, we go one step further and look at the generation of energy-efficient longitudinal acceleration profiles that promote the maximization of the energy recuperation. To achieve this goal, a Model Predictive Control (MPC) formulation is proposed. The MPC is particularly attractive because, besides its multi-objective nature, it allows embedding preview information to anticipate the motion changes in the target vehicle. This preview information can be generated based on the motion plans of the target vehicle (e.g. from the planned longitudinal acceleration of the target's CACC system) and then transmitted via car-to-car communications.

The lateral motion control of the vehicle is the second main topic of this work. In particular, we will revisit the pure-pursuit (PP) control approach (Paden et al. 2016, Park et al. 2007) in the context of vehicle following problems. It will be shown that by extending the original PP with additional damping, lateral string stability can be improved, which is particularly relevant when the VFC is employed in platooning.

2 ROMO AND THE VDC

The VFC was designed with an ego vehicle based on the ROboMObil (ROMO) in mind. The ROMO is an highly actuated drive-by-wire electric vehicle developed by the DLR (see (Bünte et al. 2014) for details). The wheels of this vehicle are equipped with the so-called Wheel Robots, each consisting of an in-wheel electric motor and steer-by-wire actuator, plus brake-by-wire units. In order to manage this high-degree of actuation, a hierarchical control framework was developed. As depicted in Figure 1, this framework contains the actuator control of the Wheel Robots on the lower level. The middle layer, called Vehicle Dynamics Controller (VDC), is responsible for the distribution of

www.TechnicalBooksPDF.com

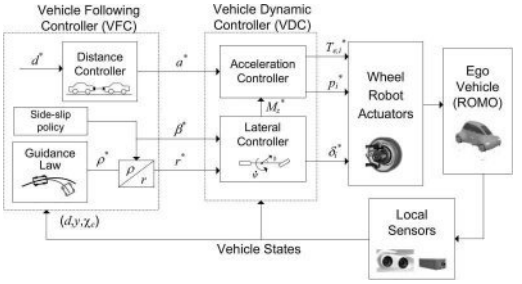


Figure 1. Block diagram of the vehicle following controller (VFC) and vehicle dynamics controller (VDC).

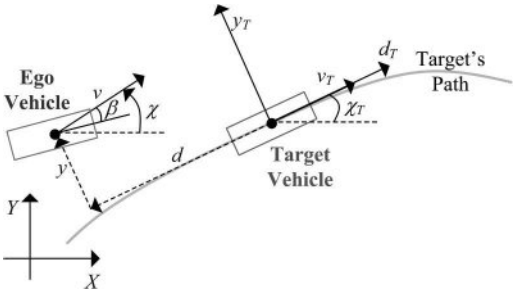


Figure 2. Geometric configuration of the vehicle following problem.

the control action among the Wheel Robots actuators, such that the kinematic demands (acceleration a^*, yaw-rate r^* and chassis side-slip angle β^*) are imposed. The VFC represents the upper most layer in this control framework, and operates as an external loop to the VDC. This Section provides details on the VDC's control-oriented model and on the kinematic model of the vehicle following problem.

2.1 *Kinematic model*

Let us consider the target vehicle (ego vehicle) with speed v_T (v), heading angle χ_T (χ) and path curvature ρ_T (ρ). In order to formulate the vehicle following problem, a reference frame, (d_T, y_T), attached to the center of mass of the target vehicle, is considered (see Figure 2). In this setting, the kinematic model of the pair ego/target vehicle can be compactly represented as (see (Soetanto et al. 2003) for details):

$$\dot{d} = v_T(1-\rho_T y) - v\cos(\chi_e) \quad (1)$$

$$\dot{y} = \rho_T v_T d + v\sin(\chi_e) \quad (2)$$

$$\dot{\chi}_e = \rho v - \rho_T v_T, \qquad \rho = (r+\dot{\beta})/v \quad (3)$$

where d is the inter-vehicle distance (projected along the d_T axis), y the lateral distance between the vehicles (i.e., ego vehicles position projected along the y_T axis), $\chi_e = \chi - \chi_T$ the difference in heading angles and β the side-slip angle of the ego vehicle. In what follows, it is assumed that the signals (d, y, χ_e) are measurable by the ego vehicle's perception sensors, such as onboard cameras.

2.2 *Modeling of the VDC*

The VDC is composed of an acceleration and lateral sub-controllers. The acceleration controller is responsible for manipulating two sets of actuators (the electric motors and friction brakes) such that the acceleration error $a - a^*$ is minimized. In order to describe a pragmatic model for this controller, let us introduce a_e, the acceleration provided by the electric motors and a_f, the acceleration generated by the friction brakes. The control-oriented model of these actuators is described by a first-order system, with time constant τ_j and delay t_j:

$$H_j(s) = \frac{a_j(s)}{a_j^*(s)} = \frac{1}{\tau_j s + 1} e^{-st_j}, \quad j \in \{e, f\} \quad (4)$$

where s is the Laplace operator. To distribute the braking effort among the actuators, the acceleration controller relies on a daisy-chain torque blending algorithm (see (Satzger et al. 2014) for details). The vehicle acceleration (a) is represented as:

$$sv = a = H_e a_e^* + H_f a_f^* - f_r/m \quad (5)$$

where f_r the resistive force, containing aerodynamic drag, rolling resistance and grade resistance.

The VDC's lateral controller provides independent yaw-rate (r) and side-slip angle (β) tracking capabilities. This latter feature is made possible due to the four-wheel steering configuration of the ego vehicle. The lateral controller relies on a combination of feedforward action, based on model inversion, and on a feedforward control based on disturbance-observer methods (see (de Castro et al. 2015) for details). Both inner loops were tuned to have a speed-dependent behavior with similar transient dynamics as the uncontrolled vehicle (de Castro et al. 2015). Their closed-loop response can be approximate by:

$$G_i(v) = \frac{i}{i^*} = \frac{1}{1 + 2\zeta_i(v)\tau_i(v)s + (\tau_i(v)s)^2}, \quad (6)$$

$$\tau_i(v) = \left(\frac{k_{i,1}}{v^2} + k_{i,2}\right)^{-1/2}, \zeta_i(v) = \frac{k_{i,3}}{v}\tau_i(v)$$

where $i \in \{r, \beta\}$, i^* is the reference value for i, k_{i1},k_{i2} and k_{i3} the parameters of the model.

3 VFC

The proposed VFC is decomposed into two main sub-components: *i*) a distance controller, and *ii*) a guidance law. This Section provides details on these two sub-components.

www.TechnicalBooksPDF.com

3.1 *Distance controller*

The primary aim of the distance controller consists in ensuring that the distance between the target and ego vehicles d follows the setpoint d^*. The secondary goal is concerned with energy, with particular focus on the generation of acceleration profiles that promote the maximization of the energy recuperation. In order to tackle these goals, let us revisit the longitudinal model between the ego and the target vehicles. Assuming small heading differences ($\cos(\chi_e) \approx 1$) and small lateral tracking errors ($|y| \ll 1/|\rho_T|$), (1) can be approximated as $\dot{d} \approx v_T - v$, $\ddot{d} \approx a_T - a$ where a_T represents the acceleration of the target vehicle. Defining the tracking error $e = d - d^*$, the auxiliary states $z_1 = e$ and $z_2 = \dot{e}$, and considering the control input $\mathbf{u} = [u_e \quad u_f]^T = [a_e^* \quad a_f^*]^T$, enable us to compactly write the error dynamics as:

$$\dot{z}_1 = z_2, \quad \dot{z}_2 = -z_3 - u_e + \varphi \tag{7a}$$

$$\tau_f \dot{z}_3 = z_3 + u_f(t - t_f) \tag{7b}$$

$$\varphi = (a_T - \ddot{d}^* + f_r/m) \tag{7c}$$

where φ is an exogenous input and z_3 captures the friction brakes' dynamics. The electric motor's dynamics, due to their fast response, were neglected. By discretizing the above model with a Zero-Order-Hold (ZOH) approximation and a sample time T_s, (7) can be represented as:

$$\mathbf{z}[k+1] = \mathbf{A}\mathbf{z}[k] + \mathbf{B}_u\mathbf{u}[k] + \mathbf{B}_\varphi\varphi[k] \tag{8}$$

$$\mathbf{e}[k] = \mathbf{C}\mathbf{z}[k] \tag{9}$$

where k is the time-step, $\mathbf{e} = [e \quad \dot{e}]^T$, and $(\mathbf{A}, \mathbf{B}_u, \mathbf{B}_\varphi, \mathbf{C})$ are matrices resulting from the ZOH discretization. Based on these considerations, the model-predictive control (MPC) problem can be posed as:

$$\mathbf{z}[k+1] = \mathbf{A}\mathbf{z}[k] + \mathbf{B}_u\mathbf{u}[k] + \mathbf{F}_g\hat{\varphi}[k], \tag{10}$$

$$\mathbf{e}[k] = \mathbf{C}\mathbf{z}[k], \quad \mathbf{z}[0] = \mathbf{z}_0 \tag{11}$$

$$\begin{bmatrix}\underline{a_e} & \underline{a_f}\end{bmatrix}^T \leq \mathbf{u}[k] \leq \begin{bmatrix}\overline{a_e} & \overline{a_f}\end{bmatrix}^T \tag{12}$$

$$T_s\underline{\Delta a} \leq \begin{bmatrix}1 & 1\end{bmatrix}(\mathbf{u}[k+1] - \mathbf{u}[k]) \leq T_s\overline{\Delta a} \tag{13}$$

$$\begin{bmatrix}\underline{e} & \underline{\dot{e}}\end{bmatrix}^T \leq \mathbf{e}[k] \leq \begin{bmatrix}\overline{e} & \overline{\dot{e}}\end{bmatrix}^T \tag{14}$$

In the above cost function, the first term, weighted with the matrix $\mathbf{Q} = \text{diag}([q_1 \quad q_2]) \geq 0$, penalizes the tracking and velocities errors, the second, weighted with $\mathbf{R} = \text{diag}([r_e \quad r_f]) > 0$, penalizes the control actions, and the third, weighted with $\mathbf{P}$, is the final state weight. The variable N represents the prediction window. Note that, by assigning $r_f \gg r_e$, we can directly promote the regenerative braking and penalize the deployment of the (energy) inefficient friction brakes.

With respect to the problem constraints, (10–11) contains the nominal model of the system, which is initialized with the current system state $\mathbf{z}_0$. In the implementation of this nominal model, it is assumed that a prediction $\hat{\varphi}$ for the exogenous variable φ is available. From the elements that compose φ, the acceleration of the target's vehicle, a_T, is the most difficult variable to predict. Hereto, it is assumed that the target vehicle regularly transmits predictions $a_{T,C2X}$, via car-to-car communications, which are then used as preview information in the construction of $\hat{\varphi}$, namely

$$\hat{a}_T[k] = \begin{cases} a_{T,C2X}[k] & \text{if } 0 \leq k \leq N_P - 1 \\ 0 & \text{otherwise} \end{cases} \tag{15}$$

where $N_P \leq N$ is the time-window of the preview information. The physical constraints of the actuators are enforced by (12). The comfort constraints (13) limit the vehicle's jerk (lower/upper bounded by $\underline{\Delta a}$, $\overline{\Delta a}$). Equation (14) imposes safety constraints on the tracking error (lower/upper bounded by $\underline{e}, \overline{e}$), and speed difference between vehicles (lower/upper bounded by $\underline{\dot{e}}$, $\overline{\dot{e}}$). These latter constraints are implemented as soft-constraints to avoid infeasible of the optimization problem.

A final note on longitudinal string stability is due. When the ego and the target vehicles are integrated into platoons of vehicles, ensuring longitudinal string stability (i.e., preventing the amplifications of longitudinal disturbances along the platoon) is an important requirement. As explained in (Kianfar et al. 2014), control-matching techniques can be employed to ensure this requirement.

3.2 *Guidance law*

The goal of the guidance law is to regulate the lateral tracking error, i.e., $y \to 0$. To achieve this goal, a non-linear control method, reliant on pure-pursuit (PP) concepts (Park et al. 2007), was designed. The main idea behind the method is to track the lateral motion of the target vehicle by planning a circular arc between the ego vehicle's and the target's position. The mathematical formulation is given by (see (Park et al. 2007) for details):

$$\rho^* = \frac{2}{L}\sin(\eta^* - \chi_e) + k_d\frac{2}{L}\sin(\eta^*) \tag{16}$$

where $L = \sqrt{d^2 + y^2}$, $\eta^* = \text{atan}(-y/d)$. It is worth pointing out that k_d is an additional tuning factor that provides the designer with additional flexibility to improve the controller performance.

Before proceeding to the analysis of the controller's properties, it is first necessary to define the mapping between the reference path curvature (ρ^*) and the VDC's motion demands (β^*, r^*). As explained in (3), these variables are related by the relation $\rho = (r + \dot{\beta})/v$. For simplicity, a zero side-slip policy ($\beta^* = 0$) is adopted, which leads to a yaw-rate reference $r^* = \rho^* v$. The curvature response

www.TechnicalBooksPDF.com

is given as $\rho \approx G_r(v)\rho^* + w/v^2$, where $G_r(v)$ is the response of the VDC's yaw-rate, w an acceleration disturbance, e.g., due to modelling approximations and non-modelled external forces acting on the vehicle.

A performance-oriented definition for the lateral string stability, analogous to the definitions employed in the longitudinal dynamics (Naus et al. 2010), is considered in this work:

$$\|\rho_i(j\omega)/\rho_{i-1}(j\omega)\|_\infty \leq 1, \quad i \in \{1,\ldots,N_{PL}\} \qquad (17)$$

where $N_{PL}+1$ is the number of vehicles in the platoon and ρ_i the curvature of the vehicle i. In the context of the VFC framework presented in Section 2, the above requirement can be translated to

$$|\rho(j\omega)/\rho_T(j\omega)| \leq 1, \qquad \forall\omega \qquad (18)$$

i.e., the curvature of the target vehicle is not amplified by the VFC. To facilitate the analysis of this requirement, it will be assumed that: *i*) all vehicles have the same speed ($v = v_T$); *ii*) small heading differences ($\sin(\chi_e) \approx 0$) and small lateral tracking errors. Under these approximations, (2), (3), (16) can be combined to produce the transfer function:

$$\frac{\rho}{\rho_T}(s) = \frac{2G_r(s)(1+k_d)\gamma^2 - 2G_r(s)\gamma k_d s}{s^2 + 2G_r(s)\gamma s + 2G_r(s)(1+k_d)\gamma^2} \qquad (19)$$

where $\gamma = v/d$. Next, let us consider, for a moment, that the dominant response of the yaw-rate controller, G_r, can be captured by a first-order model.

Proposition 1. *Consider* $G_r = 1/(\tau_r s + 1)$, *with* $\tau_r > 0$ *and the control law (16). The system is string stable-in the sense of (18)-, if i)* $d \geq 4\tau_r v$ *and ii)* $-1 \leq k_d \leq 0$.

Proof. Condition (18) can be written as $|\rho(j\omega)/\rho_T(j\omega)| = \sqrt{a/c} \leq 1$, where

$$a = (2\gamma^2)^2(1+k_d)^2 + (2\gamma k_d\omega)^2 \qquad (20)$$

$$c = (\omega^2 - 2\gamma^2(1+k_d))^2 + (2\gamma\omega - \tau_r\omega^3)^2$$

If $c \geq a$ the above conditions holds. This implies that the coefficients of the following polynomial are positive:

$$c \geq a \Leftrightarrow \tau_r\omega^6 + (1-4\tau_r\gamma)\omega^4 - 4\gamma^2(k_d^2+k_d)\omega^2 \geq 0$$

Consequently, lateral string stability requires: i) $\tau_r > 0$, *ii*) $(1-4\tau_r\gamma) \geq 0$, *iii*) $(k_d^2+k_d) \leq 0$, which renders the conditions listed in the proposition. □

For higher-order models of G_r the analytical analysis of (19) becomes cumbersome and it is difficult to gain insight into the problem. To overcome this hurdle, numerical analysis methods are used. In this analysis, besides the string stability, requirements for pole region assignment and disturbance attenuation are also included. In particular, we specify that the closed poles should be (up to) 10 times slower than the ones from the yaw-rate controller G_r, i.e., the real part of the poles of (19) should be lower than $-1/(10\tau_i(v))$. The disturbance rejection requirement is formulated as $\|G_{yw}(j\omega)W_d(jw)\|_\infty \leq 1$, where $G_{yw} = y/w$ is the transfer function between the lateral error and the disturbance w, and $W_d = (s/M_{d1} + \omega_d)/(s + \omega_d M_{d2})$ a weighting transfer function that specifies the level of disturbance attenuation, with parameters M_{d1}, M_{d2} and ω_d.

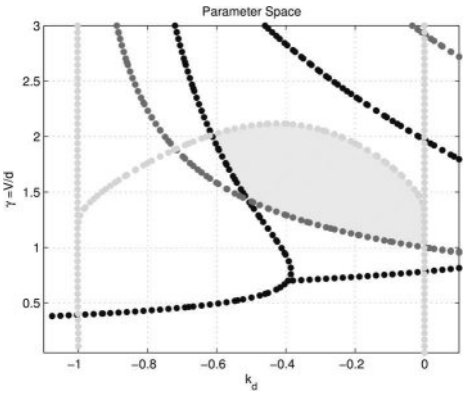


Figure 3. Set of parameters, depicted in gray, which comply with lateral string-stability requirements (green curves), disturbance rejection (red curves) and pole region assignment (blue curves).

The abovementioned requirements are mapped into the (k_d, γ) plane using the parameter space approach (Ackermann et al. 2002). The results for a velocity of 20m/s can be seen in Figure 3. It is interesting to note that, if the original PP control law is employed (with $k_d = 0$), then the maximum value of γ that renders string stability is $\bar{\gamma} = 1.4s^{-1}$. On the other hand, when the additional damping k_d factor is employed, higher values of γ are allowed. For instance, with $k_d = -0.4$ the controller tolerates a maximum $\overline{\gamma} = 2.1s^{-1}$, representing a 50% increase in comparison with the original PP law. It is worth highlighting that, since $\gamma \leq \overline{\gamma} \Leftrightarrow d \geq v/\overline{\gamma}$, higher values of $\overline{\gamma}$ enable the guidance law to operate with smaller inter-vehicle separation.

4 VALIDATION

The VFC was validated through several simulations carried out in a co-simulation environment between Matlab/Simulink and Dymola. The former is responsible for the implementation of the VFC, while the latter contains the vehicle dynamic model, the actuators and sensor models. These models are based on two Modelica libraries: the DLR's Powertrain, used to model the actuators and sensors, and the DLR's VehicleControls library, which contains a non-linear double track model for the vehicle dynamics. The MPC's numerical optimization problem was solved with the help

www.TechnicalBooksPDF.com

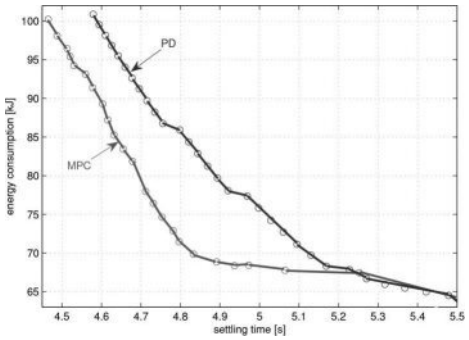


Figure 4. Transient and energy consumption performance of the MPC and PD controllers.

of the CVXgen solver (Mattingley and Boyd 2012). This controller was discretized with a sample time of $T_s = 50$ ms, and parameterized with a prediction window $N = 25$.

In order to illustrate the potential benefits of the VFC's distance controller, a comparison between the proposed MPC formulation and a proportional + derivative (PD) strategy was performed. The PD was selected for benchmarking, because it is one of the most common control strategies employed in the regulation of the vehicle's longitudinal dynamics (Naus et al. 2010). As reference maneuver for the comparison, the controllers are asked to bring the initial tracking error $e(0) = 15$ m to zero, with $d^* = 15$ m, $\dot{e}(0) = 0$ and $a_T = 0$ m/s^2. To assist in the search for the best parameterizations, the PD gains and the MPC's $\mathbf{Q}$ weights were varied in a discrete grid. The energy consumption and settling time t_s, determined as the time to reach the distance setpoint with an error bound of 2% and maximum overshoot of 0.5%, were considered as performance metrics for the comparison.

Inspecting the obtained results, depicted in Figure 4, one can find that for high settling times, e.g, $t_s > 5.2$ s, the MPC does not provide any energy benefits. In this operation range, the acceleration demands are relatively modest and the electric motor is able to handle all the actuation effort; thus, the less-efficient friction brakes are not deployed. On the other hand, when smaller settling times are requested, namely $t_s < 5.2$ s, energy savings are possible. In this situation, both braking actuators need to be deployed and the acceleration profile generated by the MPC is clearly more efficient. For example, for $t_s = 4.8$ s the MPC provides energy gains of up to 16% (in comparison with the PD) during the execution of the reference maneuver.

Figure 5 provides a time-domain comparison for the above mentioned control strategies, tuned for $t_s = 4.8$ s. Here, there are two main points worth highlighting. First, the MPC brakes slightly earlier than the PD and it also holds the regenerative for a longer period of time. This fact leads to a higher level of energy recuperation. Second, the MPC brakes less intensively then the PD. During this maneuver, the MPC produces a peak deceleration of -2.9 m/s^2, while the PD requires -4.2 m/s^2. This reduction in the peak deceleration,

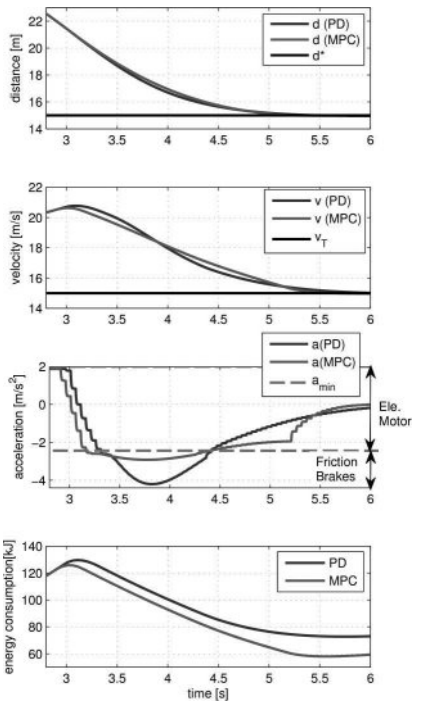


Figure 5. Time-domain comparison between the MPC and PD controllers.

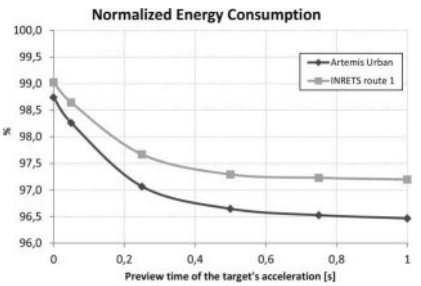
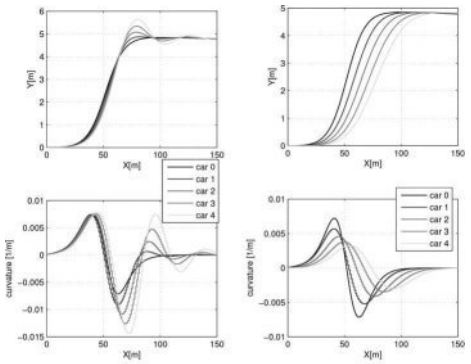


Figure 6. Normalized energy consumption (w.r.t PD controller) for different preview times for the target's acceleration ($\hat{a}_T$).

besides contributing to a reduction in the total energy consumption (less 16%), also has a positive effect in the driving comfort.

To investigate the effect of preview information (see (15)) in the MPC performance, as well as the potential for energy savings over a representative driving cycle, an additional simulation configuration was prepared. In this configuration, the speed profile of the target vehicle follows a pre-defined driving cycle (Artemis Urban or INRETS route 1), while the preview time window N_P is varied between 0 and 20 (equivalent to a maximum preview time of 1s). Figure 6 shows the obtained energy consumption results, normalized w.r.t. the PD controller. When no-preview information is used ($N_P = 0$), the MPC strategy provides 1 to 1.5% reduction in the total energy consumption.

www.TechnicalBooksPDF.com



(a) $k_d = 0$ (b) $k_d = -0.4$

Figure 7. Single lane change with a platoon of 5 vehicles ($v = 20\,\text{m/s}$, $\gamma = 2\,\text{s}^{-1}$).

Higher energy gains can be achieved, by exploring preview information. For instance, with a preview of 0.5s ($N_P = 10$), energy savings up to 3.4% are observed. Finally, by increasing the preview time to values higher than 0.5s appear to have a modest effect in the energy savings.

The second set of simulations focus on the validation of the VFC's guidance law, and its string stability properties. With this goal in mind, a platoon of 5 identical vehicles (1 leader + 4 followers) was simulated. During this simulation, a lane change maneuver at 20 m/s and $\gamma = v/d = 2\,\text{s}^{-1}$ was carried out. Two parameterizations for the guidance law were considered: *i*) original PP law, with $k_d = 0$; and *ii*) PP extended with extra damping ($k_d = -0.4$). Figure 7(a) illustrates the trajectory (in XY plane) and curvature results for the first parameterization. This data reveals that, as vehicles performs the lane change, the original PP amplifies the curvature throughout the platoon, leading to overshoot in the lateral position (almost 1 m for the last vehicle). On the other hand, the results obtained with the PP + extra damping, depicted in Figure 7(b), shows that the platoon is capable of satisfactorily execute the lane change without overshoot and without amplification of the curvature demands (although with a small performance penalization). This result confirms the string stability improvement of the proposed guidance law.

5 CONCLUSIONS

A vehicle following controller for highly actuated vehicles was developed. This controller was composed of a MPC-based distance controller for regulating the inter-vehicle separation. One of the main advantage of the proposed MPC formulation consisted in its capability to shape the vehicle's acceleration profile such that the regenerative braking is maximized. Simulation results demonstrated that, in comparison with state-of-the art solutions, this MPC formulation is able to provide energy savings up to 16% during transient maneuvers and up to 3.4% during longer driving cycles. Additionally, we also presented an extended version of the pure-pursuit guidance law suitable for tracking the lateral motion of the target vehicle. It was shown that the addition of damping factors in the pure-pursuit law is important to guarantee lateral string stability and to enable the controller's operation with shorter inter-vehicle separation. As future work, we plan to investigate robust MPC formulations for the distance controller and to perform experimental validation of the VFC in the ROMO.

REFERENCES

Ackermann, J., P. Blue, T. Bünte, L. Güvenc, D. Kaesbauer, M. Kordt, M. Muhler, & D. Odenthal (2002). *Robust control: the parameter space approach*. Springer-Verlag London.

Besselink, B., V. Turri, S. H. van de Hoef, K.-Y. Liang, A. Alam, J. Mårtensson, & K. H. Johansson (2016). Cyber-physical control of road freight transport. *Proceedings of the IEEE 104(5)*.

Bünte, T., L. M. Ho, C. Satzger, & J. Brembeck (2014). Central Vehicle Dynamics Control of the Robotic Research Platform. *ATZ Elektronik 9*, 58–64.

de Castro, R., T. Bünte, & J. Brembeck (2015). Design and Validation of the Second Generation of the Robomobil's Vehicle Dynamics Controller. In *International Symposium on Dynamics of Vehicles on Road and Tracks*.

Ivanov, V., D. Savitski, & B. Shyrokau (2014). A Survey of Traction Control and Anti-lock Braking Systems of Full Electric Vehicles with Individually-Controlled Electric Motors. *IEEE Transactions on Vehicular Technology*.

Kianfar, R., P. Falcone, & J. Fredriksson (2014). A Control Matching-based Predictive Approach to String Stable Vehicle Platooning. *19th World Congress of the International Federation of Automatic Control*, 10700–10705.

Mattingley, J. & S. Boyd (2012). CVXGEN: A code generator for embedded convex optimization. *Optimization and Engineering 13*(1), 1–27.

Naus, G., R. Vugts, J. Ploeg, M. Molengraft, & M. Steinbuch (2010). String-stable CACC design and experimental validation: a frequency-domain approach. *IEEE Transactions on Vehicular Technology 59*(9), 4268–4279.

Paden, B., M. Cap, S. Z. Yong, D. Yershov, & E. Frazzoli (2016). A Survey of Motion Planning and Control Techniques for Self-driving Urban Vehicles. *IEEE Transactions on Intelligent Vehicles (submitted)*.

Park, S., J. Deyst, & J. P. How (2007). Performance and Lyapunov Stability of a Nonlinear Path Following Guidance Method. *Journal of Guidance, Control, and Dynamics 30*(6), 1718–1728.

Satzger, C., R. de Castro, & T. Bünte (2014). A Model Predictive Control Allocation Approach to Hybrid Braking of Electric Vehicles. In *IEEE Intelligent Vehicles Symposium (IV14)*.

Soetanto, D., L. Lapierre, & A. Pascoal (2003). Adaptive, Non-Singular Path-Following Control of Dynamic Wheeled Robots. In *Proceedings of the 42nd IEEE Conference on Decision and Control*, pp. 1765–1770.

www.TechnicalBooksPDF.com

Advanced Vehicle Control – Edelmann, Plöchl & Pfeffer (Eds)
© 2017 Taylor & Francis Group, London, ISBN 978-1-138-02992-7

Distributed receding horizon control of a platoon of multiple CAVs with discontinuous-gear transmissions

Shengbo Eben Li
Department of Automotive Engineering, Tsinghua University, Beijing, China

Yang Zheng
Department of Engineering Science, University of Oxford, Oxford, UK

Yougang Bian & Keqiang Li
Department of Automotive Engineering, Tsinghua University, Beijing, China

ABSTRACT: The platooning of connected automated vehicles (CAVs) have the potential to significantly benefit the road transportation. This paper presents a distributed control algorithm for a platoon of vehicles with discontinuous gear transmissions using the receding horizon optimization. A directed graph is used to describe the underlying communication topology among different vehicles. Each vehicle is modeled as a three-state nonlinear system with mixed integer inputs. To achieve the coordination of multiple vehicles, each vehicle is assigned a local open-loop optimal control problem, of which the cost function is designed by penalizing on both tracking errors and fuel consumption. The equality terminal constraint is employed to guarantee the consensus of desired terminal state in the predictive horizon, which is critical for the asymptotical stability. Numerical simulations demonstrate that this algorithm has the potential to achieve the consensus of multi-vehicles in a platoon while improving fuel efficiency.

Keywords: Topics/Automated vehicles, heterogeneous platoon, distributed control, receding horizon optimization.

1 INTRODUCTION

The connection and automation of multi-vehicles has recently received considerable attentions due to its potential to significantly improve traffic capacity, safety and fuel efficiency [1]. The platooning of automated vehicles is one of its promising practices, which aims to ensure all the vehicles in a group move at the same speed and maintain a pre-specified distance.

The earliest study on platoon control could date back to the PATH program in last eighties. Since then, many issues on platoon control have been discussed, such as the spacing policies [2, 3], information exchange topologies [4, 5], powertrain dynamics [6] and communication delay [7]. Recently, many advanced control methods have been introduced into vehicular platoon automation to achieve systematic performance. For example, Stankovic *et al.* employed the inclusion principle to decompose an interconnected platoon into locally decoupled subsystems, and then deigned a decentralized overlapping controller [8]. Barooah *et al.* introduced a mistuning-based control method to improve the stability margin of platoons [9], and this method was extended to cover a realistic vehicle model in [10]. Dunbar and Derek (2012) proposed a distributed receding horizon controller and derived the sufficient condition to guarantee string stability [11]. Such method was recently extended to the case of unidirectional topologies in [12]. Ploeg *et al.* developed an $\mathcal{H}_\infty$ controller synthesis approach for linear platoons, in which string stability was explicitly satisfied by using linear inequality matrix (LMI) [13]. A recent review on platoon control can be found in [14].

Many existing studies are only applicable for homogeneous platoons, in which all nodes are assumed to have identical dynamic models for the convenience of theoretical completeness [1][14]. Besides, most of them do not account for input/state constraints and model nonlinearities. In practice, the constraints and nonlinearities do exist due to actuator saturation and salient nonlinearities involved in the powertrain system [15]. Additionally, with the rapid deployment of V2V techniques, various types of communication topologies are emerging (see Fig. 1). New challenges naturally arise for platoon control considering both the topological variety and dynamical nonlinearity. Based on the distributed receding horizon control (DRHC) framework, our paper proposes an innovative solution for the coordination of multiple vehicles with both nonlinear heterogeneous dynamics and topological variety. Note that the technique

www.TechnicalBooksPDF.com

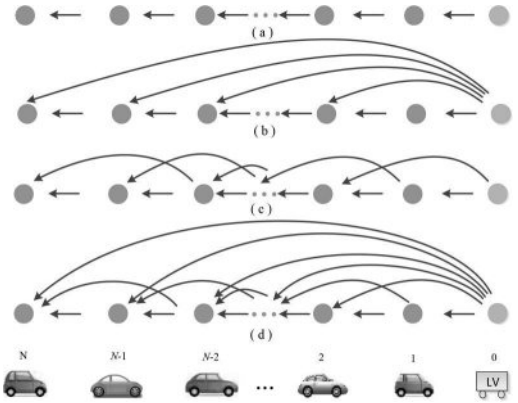


Figure 1. Examples of unidirectional topology [12]: (a) predecessor-following (PF), (b) predecessor-leader following (PLF), (c) two-predecessor following (TPF), (d) two-predecessor-leader following (TPLF).

of DRHC has been embraced by many industrial applications, *e.g.*, collision avoidance [15], thermal energy control [16], and vehicle stability [17]. A recent comprehensive review on DRHC can be found in [18].

In this study, a platoon is viewed as a group of connected automated vehicles (CAVs), which are dynamically decoupled but interact with each other by spatial geometry and communication topology. In a platoon, only the followers, which directly communicate with the leader, know the desired set point. Under the proposed DRHC, each follower is assigned a local open-loop optimal control problem only relying on the information of neighboring vehicles, in which the cost function is designed by penalizing on both tracking errors and fuel consumption. To theoretically guarantee the asymptotical stability, we use a neighboring average based terminal constraint, firstly proposed in [1][12]. Using this terminal constraint, asymptotical stability can be achieved through explicit parametric conditions on the weights of the cost functions for a special case [12]. The contributions of this paper are in two aspects: 1) the proposed DRHC algorithm is applicable for nonlinear and heterogeneous platoons with arbitrary communication topology, and the asymptotical stability can be proved in a special case [12]; 2) the fuel efficiency of a platoon is considered by optimizing the engine torque and gear position, which offers benefits comparing to conventional cooperative adaptive cruise control strategies. This work is an improvement of our previous result in [12] by considering fuel efficiency and discontinuous-gear transmission in a platoon.

The rest of this paper is organized as follows. In section 2, the dynamic model, fuel consumption, control objective and model of communication topology in a platoon are presented. Section 3 introduces the formulation of local optimal control problems and proposes a novel DRHC algorithm, followed by the simulation results in section 4. Section 5 concludes this paper.

2 PROBLEM STATEMENT

As shown in Fig. 1, this paper considers a heterogeneous platoon with a class of communication topologies running on a flat road with $N+1$ vehicles (or nodes), which includes a leading vehicle (LV, indexed by 0) and N following vehicles (FVs, indexed from 1 to N). The platoon is dynamically decoupled, but constrained by the spatial formation. Each vehicle has heteorgenous nonlinear dynamics with discontinuous-gear transmission. The control objective of DHRC is to achieve a global coordination in terms of movement and geometry, whicle improving the fuel efficiency of a platoon. This section presents the models of vehicle longitudinal dynamics, fuel consumption, control objective and communication topology.

2.1 *Vehicle model for platoon control*

This paper only considers the vehicle longitudinal dynamics, where several nonlinear components are involved, *e.g.*, engine, drive line, brake system, aerodynamic drag, tire friction, and rolling resistance. To strike a balance between accuracy and conciseness, the following discrete-time model for any following vehicle i is used [12][15].

$$\begin{cases} s_i(t+1) = s_i(t) + v_i(t)\Delta t \\ v_i(t+1) = v_i(t) \\ \quad + \dfrac{\Delta t}{\delta_i m_{\text{veh},i}}\left(\dfrac{i_{g,i}(t) i_{0,i}\eta_{T,i}}{R_i} T_i(t) - F_{\text{veh},i}\big(v_i(t)\big)\right) \\ T_i(t+1) = T_i(t) - \dfrac{1}{\tau_i} T_i(t)\Delta t + \dfrac{1}{\tau_i} u_i(t)\Delta t \end{cases}$$

$$\begin{aligned} &F_{\text{veh},i}\big(v_i(t)\big) = C_{\text{A},i} v_i^2(t) + m_{\text{veh},i} g f_i \\ &i_{g,i}(t) \in \mathbb{J}_i = \{i_{g1,i}, i_{g2,i}, i_{g3,i}, i_{g4,i}, i_{g5,i}\} \end{aligned} \tag{1}$$

where Δt is the discrete time interval; $s_i(t)$, $v_i(t)$ denote the position and velocity; δ_i is the rotational inertial coefficient; $m_{veh,i}$ is the vehicle mass; $i_{g,i}(t)$ and $i_{0,i}$ are the gear ratio of the transmission and final gear, $\mathbb{J}_i$ is the set of discontinuous gear ratio of the transmission; $C_{\text{A},i}$ is the coefficient of drag; g is the gravity constant; f_i is the coefficient of rolling resistance; $T_i(t)$ is the driving/braking torque; τ_i is the inertial lag; R_i is the tire radius; $\eta_{T,i}$ is the mechanical efficiency, and $u_i(t)$ is the desired driving/braking torque. The control input is subject to the box constraint:

$$u_i \in \mathcal{U}_i = \{u_{\min,i} \le u_i \le u_{\max,i}\}, \tag{2}$$

where $u_{min,i}, u_{max,i}$ are the bounds. For each node, the state is denoted as $x_i(t) = [s_i(t), v_i(t), T_i(t)]^T$, and the output is denoted as $y_i(t) = [s_i(t), v_i(t)]^T$. Further, (1) can be rewritten into:

$$\begin{aligned} x_i(t+1) &= \phi_i\left(x_i(t), i_{g,i}(t)\right) + \psi_i \cdot u_i(t), \\ y_i(t) &= C x_i(t) \end{aligned} \tag{3}$$

www.TechnicalBooksPDF.com

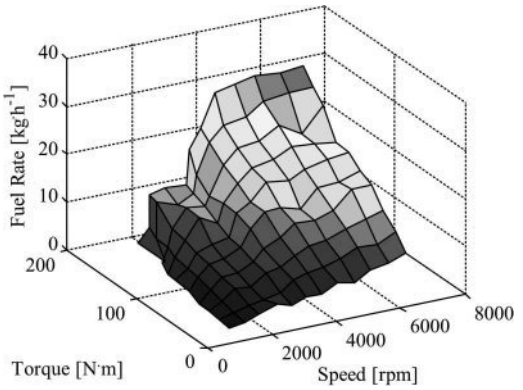


Figure 2. Steady-state engine map.

The model (1) for vehicle dynamics is inherently a third-order nonlinear system with mixed integer inputs, which can encapsulate a wide range of vehicles. Note that linear models are also widely used in platoon control for the sake of theoretical completeness, *e.g.*, [2]–[5][6][9] [10].

2.2 *Engine fuel consumption model*

To evaluate the fuel efficiency of a vehicle platoon, we use a steady-state engine map from a commercial vehicle as the fuel consumption model. The engine map is illustrated in Fig. 2. Besides, we assume that the engine can automatically cut off fuel supply during braking.

To simplify the fuel model for online optimization, the steady-state engine map is fitted by a 2-dimensional 4th-order polynomial [19]:

$$\begin{aligned} q_i(t) &= f\left(x_i(t), i_{g,i}(t)\right) \\ &= \sum_{j=0}^{4} \left(a_i T_i(t) + b_i n_i(t)\right)^j, \\ n_i(t) &= \frac{60 v_i(t)}{2\pi R_i} i_{g,i}(t) i_0, \end{aligned} \tag{4}$$

where a_i and b_i are fitting coefficients, T_i and n_i are the engine torque and speed.

2.3 *Objective of platoon control*

In this paper, the objective of platoon control can be divided into two parts:

1) The first part is to track the speed of the leader while maintaining a desired inter-vehicle space, *i.e.*,

$$\begin{cases} \lim\limits_{t\to\infty} \|v_i(t) - v_0(t)\| = 0 \\ \lim\limits_{t\to\infty} \left\|s_{i-1}(t) - s_i(t) - d_{i-1,i}\right\| = 0 \end{cases}, i \in \mathcal{N}, \tag{5}$$

where $d_{i-1,i}$ is the desired space between vehicle $i-1$ and i.

2) The second part is to minimize the fuel consumption $q_i(t)$ for each vehicle in the platoon.

2.4 Model of communication topology

The communication topology in a platoon can be modeled by a directed graph $\mathbb{G} = \{\mathbb{V}, \mathbb{E}\}$, where $\mathbb{V} = \{0, 1, 2, \ldots, N\}$isthe set of nodes and $\mathbb{E} \subseteq \mathbb{V} \times \mathbb{V}$ is the set of edges in connection [4][20]. The properties of graph $\mathbb{G}$ is further reduced into the formation of three matrices, *i.e.*, adjacency matrix $\mathcal{A}$, Laplacian matrix $\mathcal{L}$ and pinning matrix $\mathcal{P}$.

The adjacency matrix is used to describe the directional communication among the followers, which is defined as $\mathcal{A} = [a_{ij}] \in \mathbb{R}^{N\times N}$ with each entry expressed as

$$\begin{cases} a_{ij} = 1, & if\ \{j,i\} \in \mathbb{E} \\ a_{ij} = 0, & if\ \{j,i\} \notin \mathbb{E} \end{cases}, \quad i,j \in \mathcal{N}, \tag{6}$$

where $\{j,i\} \in \mathbb{E}$ means there is a directional edge from node j to node i. The Laplacian matrix $\mathcal{L} \in \mathbb{R}^{N\times N}$ is defined as $\mathcal{L} = \mathcal{D} - \mathcal{A}$, where $\mathcal{D} \in \mathbb{R}^{N\times N}$ is called the in-degree matrix, defined as

$$\mathcal{D} = diag\{deg_1, deg_2, \ldots, deg_N\}$$

where $deg_i = \sum_{j=1}^{N} a_{ij}$represents the in-degree of node i in $\mathbb{G}$. The pinning matrix $\mathcal{P} \in \mathbb{R}^{N\times N}$ is used to model how each follower connects to the leader, defined as

$$\mathcal{P} = diag\{p_1, p_2, \ldots, p_N\}$$

where $p_i = 1$ if edge $\{0,i\} \in \mathbb{E}$; otherwise $p_i = 0$. The neighbor set of node i is denoted by $\mathbb{N}_i = \{j | a_{ij} = 1, j \in \mathcal{N}\}$. A dual set is defined by $\mathbb{O}_i = \{j | a_{ji} = 1, j \in \mathcal{N}\}$. We further define the leader accessible set of node i as

$$\mathbb{P}_i = \begin{cases} \{0\}, & if\ p_i = 1 \\ \emptyset, & if\ p_i = 0 \end{cases}.$$

3 DESIGN OF THE DRHC ALGORITHM

This section introduces the formulation of DRHC for heterogeneous platoons. The desired set point of state and input of node i is

$$\begin{cases} x_{\mathrm{des},i}(t) = \left[s_{\mathrm{des},i}(t), v_{\mathrm{des},i}(t), T_{\mathrm{des},i}(t)\right]^T \\ u_{\mathrm{des},i}(t) = T_{\mathrm{des},i}(t), \end{cases}$$

where $s_{\mathrm{des},i}(t) = s_0(t) - i \cdot d_0$, $v_{des,i}(t) = v_0$ and $T_{des,i}(t) = h_i(v_0)$, which is used to counterbalance the external drag, defined as

$$h_i(v_0) = \frac{R_i}{i_{g,i}(t) i_{0,i} \eta_{T,i}} \left(C_{\mathrm{A},i} v_0^2 + m_{\mathrm{veh},i} g f_i\right).$$

www.TechnicalBooksPDF.com

In this section, we first propose a local open-loop optimal control problem only relying on the information of neighboring nodes, where the cost function is designed by penalizing on both tracking errors and fuel consumption. Then, the algorithm of DRHC is presented, with a remark on the asymptotical stability for a special case.

3.1 *Local open-loop optimal control problem*

For the sake of narrative convenience, the nodes in $\mathbb{N}_i$ are numbered as $i_1, i_2, \ldots, i_m$. Define

$$y_{-i}(t) = \left[y_{i_1}^T(t), y_{i_2}^T(t), \cdots, y_{i_m}^T(t)\right]^T,$$
$$u_{-i}(t) = \left[u_{i_1}(t), u_{i_2}(t), \cdots, u_{i_m}(t)\right]^T$$

as the vectors of outputs and inputs of nodes in $\mathbb{N}_i$, respectively. The same length of predictive horizon N_p is used in all local problems. Over the prediction horizon $[t, t+N_p]$, we define three types of trajectories:

$y_i^p(k|t)$: Predicted output trajectory,
$y_i^*(k|t)$: Optimal output trajectory,
$y_i^a(k|t)$: Assumed output trajectory,

where $k = 0, 1 \ldots, N_p$. The notation $y_i^p(k|t)$ represents the output trajectory that parameterizes the local optimal control problem. The notation $y_i^*(k|t)$ represents the optimal solution after numerically solving the local problem. The notation $y_i^a(k|t)$ is the assumed trajectory transmitted to the nodes in set $\mathbb{O}_i$, which is actually the shifted last-step optimal trajectories of node i.

Now, we define the local open-loop optimal control problem for each node i:

Problem $\mathcal{F}_i$: For $i \in \{1, 2, \ldots, N\}$ at time t

$$\min_{\substack{u_i^p(0|t),\cdots,u_i^p(N_p-1|t)\\ i_{g,i}{}^p(0|t),\cdots,i_{g,i}{}^p(N_p-1|t)}} J_i\left(y_i^p, q_i^p, u_i^p, y_i^a, y_{-i}^a\right)$$
$$= \sum_{k=0}^{N_p-1} l_i\left(y_i^p(k|t), u_i^p(k|t), y_i^a(k|t), y_{-i}^a(k|t), q_i^p(k|t)\right), \tag{7a}$$

subject to

$$x_i^p(k+1|t) = \phi_i\left(x_i^p(k|t), i_{g,i}{}^p(t)\right) + \psi_i \cdot u_i^p(k|t),$$
$$y_i^p(k|t) = C x_i^p(k|t), \tag{7b}$$
$$x_i^p(0|t) = x_i(t),$$
$$u_i^p(k|t) \in \mathcal{U}_i, \tag{7c}$$
$$q_i^p(k|t) = f\left(x_i^p(k|t), i_{g,i}{}^p(k|t)\right) \tag{7d}$$
$$y_i^p(N_p|t) = \frac{1}{|\mathbb{I}_i|}\sum_{j\in\mathbb{I}_i}\left(y_j^a(N_p|t) + \tilde{d}_{i,j}\right), \tag{7e}$$
$$T_i^p(N_p|t) = h_i\left(v_i^p(N_p|t)\right), \tag{7f}$$
$$i_{g,i}{}^p(0|t) = i_{g,i}{}^p(1|t) = \cdots = i_{g,i}{}^p(N_p-1|t) \tag{7g}$$

where $[u_i^p(0|t), \cdots, u_i^p(N_p-1|t)]$ and $i_{g,i}^p(0|t), \cdots, i_{g,i}^p(N_p-1|t)$ denote the unknown variables, $|\mathbb{I}_i|$ is the cardinality of $\mathbb{I}_i = \mathbb{N}_i \cup \mathbb{P}_i$, and $\tilde{d}_{i,j} = [d_{i,j}, 0]^T$ denotes the desired distance vector between i and j.

The function l_i in (7a) is the cost associated with node i:

$$l_i\left(y_i^p(k|t), u_i^p(k|t), y_i^a(k|t), y_{-i}^a(k|t), q_i^p(k|t)\right)$$
$$= l_{i,\text{track}}\left(y_i^p(k|t), u_i^p(k|t), y_i^a(k|t), y_{-i}^a(k|t)\right) \tag{8}$$
$$+\gamma\, l_{i,\text{fuel}}\left(q_i^q(k|t)\right),$$

There are two parts in the proposed cost function (8), and thus the proposed open-loop optimal control problem would have the ability to balance the tracking performance and fuel efficiency by adjusting the factor γ.

1) $l_{i,track}$ corresponds to tracking error, which is defined as

$$l_{i,\text{track}}\left(y_i^p(k|t), u_i^p(k|t), y_i^a(k|t), y_{-i}^a(k|t)\right)$$
$$= \left\|Q_i\left(y_i^p(k|t) - y_{\text{des},i}(k|t)\right)\right\|_2$$
$$+ \left\|R_i\left(u_i^p(k|t) - h_i\left(v_i^p(k|t)\right)\right)\right\|_2 \tag{9}$$
$$+ \left\|F_i\left(y_i^p(k|t) - y_i^a(k|t)\right)\right\|_2$$
$$+ \sum_{j\in\mathbb{N}_i}\left\|G_i\left(y_i^p(k|t) - y_j^a(k|t) - \tilde{d}_{i,j}\right)\right\|_2,$$

where $Q_i \geqslant 0$, $R_i \geqslant 0$, $F_i \geqslant 0$ and $G_i \geqslant 0$ are the weighting matrices. Note that Q_i also contains the information whether node i is pinned to the leader. If $p_i = 0$, node i is unable to know its desired set point, and therefore $Q_i = 0$ is always enforced. If $p_i = 1$, then $Q_i > 0$ in its penalization functions

2) $l_{i,fuel}$ corresponds to fuel consumption, which is defined as

$$l_{i,\text{fuel}}\left(q_i^q(k|t)\right) = q_i^p(k|t) \tag{10}$$

where $q_i^p(k|t)$ is 2-dimensional 4th-order polynomial defined in (4).

Remark 1: The gear position won't change so frequently, in order to simplify the problem, so we add (7g) in the optimal control problem. Besides, the formulation of problem $\mathcal{F}_i$ only needs the information from its neighbors, thus it is suitable for various communication topologies, including all of those shown in Fig. 1.

3.2 *Algorithm of DRHC*

The DRHC algorithm is shown as follows:

(I) Initialization:

At time $t = 0$, assume that all followers are moving at a constant speed.

(II) Iteration of DRHC:

At any time $t > 0$, for all node $i = 1, \ldots, N$,

1) Optimize Problem $\mathcal{F}_i$ to yield optimal control sequence $u_i^*(k|t), k = 0, 1, \cdots, N_p - 1$.

www.TechnicalBooksPDF.com

2) Compute the assumed control input for next step by disposing first term and adding one additional term, *i.e.,*

$$u_i^a(k|t+1)=\begin{cases}u_i^*(k+1|t), & k=0,1,\cdots,N_p-2\\ h_i\left(v_i^*(N_p|t)\right), & k=N_p-1\end{cases}. \quad (11)$$

The corresponding assumed output is also computed as

$$\begin{gathered}x_i^a(k+1|t+1)=\\ \phi_i\left(x_i^a(k|t+1),i_{g,i}^a(k|t+1)\right)+\psi_i u_i^a(k|t+1),\\ x_i^a(0|t+1)=x_i^*(1|t),\\ y_i^a(k|t+1)=Cx_i^a(k|t+1),\\ k=0,1,\cdots,N_p-1.\end{gathered} \quad (12)$$

3) Transmit $y_i^a(k|t+1)$ to the nodes in set $\mathbb{O}_i$, and then receive $y_{-i}^a(k|t+1)$ from the nodes in set $\mathbb{N}_i$; and compute $y_{\mathrm{des},i}(k|t+1)$ using the leader's information if $\mathbb{P}_i\neq\emptyset$.
4) Implement the control effort using the first element of optimal control sequence, *i.e.,* $u_i(t)=u_i^*(0|t)$,$i_{g,i}(t)=i_{g,i}^*(0|t)$.
5) Increment t and go to step (1).

Remark 2: The proposed algorithm of DRHC is essentially same with the techniques in [12]. One major difference is the introduction of fuel consumption penalization in the cost function (10). The benefit of this framework is that asymptotical stability can be achieved through explicit parametric conditions on the weights of the cost functions for a special case, which is stated in the following theorem.

Theorem [12]. Suppose that $\mathbb{G}$ is a unidirectional graph (see Fig. 1), there is no penalization on fuel consumption (*i.e.*, $\gamma=0$), and gear position is fixed. Then, a platoon under DRHC (4) is asymptotically stable if satisfying

$$F_i\geq\sum_{j\in\mathbb{O}_i}G_j,\ \ i\in\mathcal{N}. \quad (13)$$

The details of the proof have been reported in [12]. The key part is the use of an equality based terminal constraint (7e). Note that (13) is an explicit sufficient condition on the weights of the cost functions, which is easy to implement.

4 SIMULATION

To evaluate the proposed DRHC algorithm, a multi-vehicle platoon model is built in Matlab environment for numerical simulation. The platoon consists of five vehicles.

4.1 *Simulation setup*

The platoon tracks a virtual leading vehicle, where the leader's velocity profile is predefined as a combined city-highway driving profile, shown in Fig. 3.

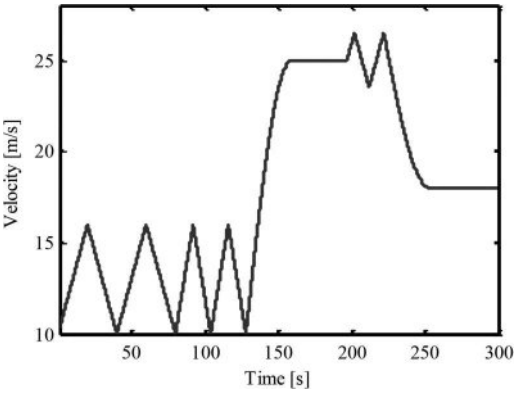


Figure 3. Combined city road-highway driving profile.

Table 1. Simulation setup.

Parameter	Notation	Value
Vehicle number	N	5
Time interval	Δt(s)	0.1 sec
Number of steps in predictive horizon	N_p	20
Weighting matrix	F_i	diag{10,10}
	G_i	diag{4,4}
	Q_i	diag{10,10}
	R_i	1
	γ	10

To evaluate the influence of the information topology, we implement the proposed method in the simulation under three types of information topology, *i.e.,* PF (predecessor-following), PLF (predecessor-leader following), and TPF (two-predecessor following); see Fig. 1 for illustrations. Besides, a baseline control method, which is actually used for cooperative adaptive cruise control system, is implemented in the simulation for fair comparisons. The baseline is actually an approximately linear quadratic controller to minimize ***Problem*** $\mathcal{F}_i$ without (7c)–(7g) and with γ, Q_i, F_i being zero. The fact that $\gamma=0$ means that there is no penalization on fuel consuption in the baseline control method. The simulation setup and vehicle parameters are listed in Table 1 and Table 2, respectively.

4.2 *Simulation results*

Fig. 4 shows the profiles of velocity and spacing errors when using the baseline control method. As shown in Fig. 5, simulation results show that the proposed method can achieve the consensus of multi-vehicles in a platoon according to the velocity and space error profiles. From Fig. 5, we find that, compared with the conventional method, the proposed method has better tracking performance in the sense of keep the desired space with respect to the leading vehicle. This benefits from the penalization on the difference between assumed input and real input, which reduces the prediction error and the tracking error between neighbor

www.TechnicalBooksPDF.com

Table 2. Vehicle parameters.

Coefficient rolling resistance f_i	0.028
Wheel radius R_i (m)	0.307
Mechanical efficiency $\eta_{T,i}$	0.9
Rotational inertial coefficient δ_i	1.0
Transmission gear ratio $i_{g,i}$	$\mathbb{J}_i = \{3.620, 1.925, 1.285, 0.933, 0.692\}$
Final gear ratio $i_{0,i}$	3.863
Gravity constant g(N/kg)	9.8
Desired distance $d_{i-1,i}$ (m)	20
Input limit $[u_{max,i}, u_{min,i}]$ (N.m)	$[-200,180]$

Vehicle Index	Vehicle mass $m_{veh,i}$ (kg)	Inertial lag τ_i (s)	Coefficient of air drag $C_{A,i}$ ($N \cdot s^2 \cdot m^{-2}$)
1	1920	0.62	0.516
2	1536	0.59	0.430
3	2112	0.65	0.473
4	1728	0.65	0.387
5	2496	0.68	0.344

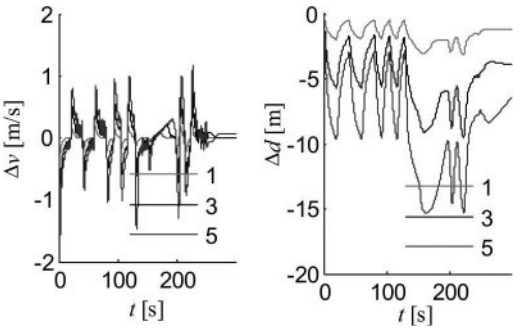


Figure 4. Velocity error and spacing error profiles for the baseline control method.

Table 3. Fuel consumption.

Method	Information flow topology	Average fuel consumption (L/100 km)	Average fuel saving (%)
Baseline	–	9.56	–
DRHC	PF	9.19	3.87%
	PFL	8.80	7.95%
	TPF	9.10	4.81%

vehicles. Please refer to [12] for the details discussions on the assumed and real inputs.

The fuel consumption results are tabulated in Table 3, which shows that the fuel efficiency can be improved under unidirectional information flow topologies.

From Table 3, it can be concluded that the proposed method can optimize the fuel efficiency which achieving stable tracking of leading velocity and position. The PLF has the best fuel benefit than two other topologies. This is understandable that the information from the leading vehicle help the followers to avoid or weaken unnecessary acceleration or deceleration caused by other followers. This benefit is at

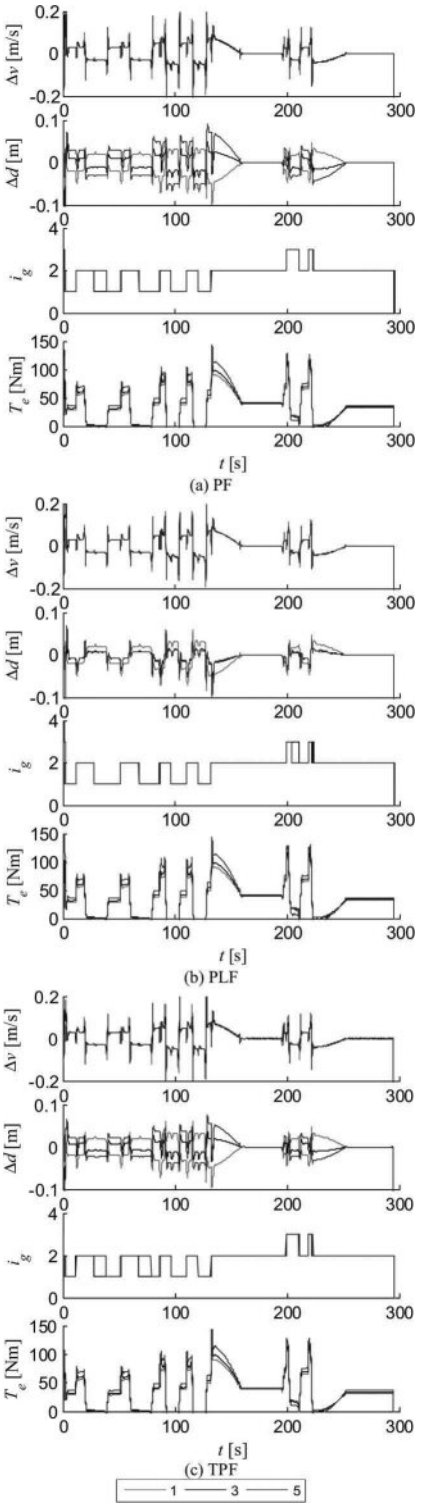


Figure 5. Profiles of velocity error, spacing error, gear position, and equivalent engine torque: (a) DRHC-PF (b) DRHC-PLF (c) DRHC-TPF.

www.TechnicalBooksPDF.com

the cost of more requirements on communication burden. The TPF topology is somewhat better than PF in fuel benefit because it has more communications with its predecessors, which also demonstrates the importance of communicating with more nodes when pursuing fuel economy in a platoon. In addition, the penalization on fuel consumption and tracking error is different with different communication topologies, which depends not only on the weighting matrices but also on the number of neighbor vehicles.

5 CONCLUSION

This paper proposes a distributed receding horizon control (DRHC) algorithm for heterogeneous platoons with nonlinear dynamics and discontinuous gear transmissions. To achieve the coordination of a platoon, each vehicle is assigned a local optimal control problem only relying on the information of neighboring nodes, in which the cost function is designed by penalizing on both tracking errors and fuel consumption. Numerical simulations demonstrate that the proposed method has the potential to achieve the consensus of multi-vehicles in a platoon. It is found that the fuel efficiency can be improved under this DRHC framework. Moreover, this approach is suitable for a broad class of communication topologies, which offers considerable benefit from the viewpoint of V2V communication. One future work is to address the complexity issue of local optimization problems, which is important for real implementations.

ACKNOWLEDGEMENT

This study is supported by NSF China with grant 51575293 and State-funded Sci&Tech program with grant 2016YFB0100906.

REFERENCES

[1] Y. Zheng, "Dynamic modeling and distributed control of vehicular platoon under the four-component framework," *Master's thesis*, Tsinghua University, 2015.

[2] G. J. L. Naus , R. P. A. Vugts , J. Ploeg , M. J. G. van de Molengraft and M. Steinbuch "String-stable CACC design and experimental validation: A frequency-domain approach", *IEEE Trans. Veh. Technol.,* vol. 59, no. 9, pp. 4268–4279, 2010.

[3] D. Swaroop, and J. Hedrick, "Constant spacing strategies for platooning in automated highway systems," *ASME Journal of Dynamic System Measure and Control*, vol. 121, no. 3, pp. 462–470, 1999.

[4] Y. Zheng, S. E. Li, J. Wang, D. Cao, and K. Li, "Stability and scalability of homogeneous vehicular platoon: Study on the influence of information flow topologies," *IEEE Trans. Intell. Transp. Syst.*, to be published. 2015.

[5] S. Yadlapalli , S. Darbha, and K. Rajagopal, "Information flow and its relation to stability of the motion of vehicles in a rigid formation," *IEEE Transaction on Automatic Control*, vol. 51, no. 8, pp. 1315–1319, 2006.

[6] L. Xiao, and F. Cao, "Practical string stability of platoon of adaptive cruise control vehicles," *IEEE Transaction on Intelligent Transportation System*, vol. 12, pp. 1184–1194, 2011.

[7] F. Gao, S. E. Li, Y. Zheng and D. Kum, "Robust Control of Heterogeneous Vehicular Platoon with Uncertain Dynamics and Communication Delay", *IET Intelligent Transport Systems*, 2016; accepted, online available.

[8] S. Stankovic, M. Stanojevic, and D. Siljak, "Decentralized overlapping control of a platoon of vehicles", *IEEE Trans. Contr. Syst. Technol*., 2000, vol. 8, pp. 816–831.

[9] P. Barooah, P. G. Mehta, J. P. Hespanha, "Mistuning-based control design to improve closed-loop stability margin of vehicular platoons", *IEEE Trans. Autom. Control*, 2009, vol. 54, no. 9, pp. 2100–2113.

[10] Y. Zheng, S. Li, et al. "Stability Margin Improvement of Vehicular Platoon Considering Undirected Topology and Asymmetric Control," *Control Systems Technology, IEEE Transaction on*, vol. 24, no. 4, pp. 1253–1265, 2016.

[11] W. Dunbar and D. Caveney, "Distributed receding horizon control of vehicle platoons: Stability and string stability," *IEEE Trans. Autom. Control*, vol. 57, no. 3, pp. 620–633, 2012.

[12] Y. Zheng, S. E. Li, K.Q. Li, Francesco Borrelli, and J. Karl Hedrick, "Distributed Model Predictive Control for Heterogeneous Platoon under Unidirectional Topologies", *IEEE Trans. Contr. Syst. Technol, accepted, to appear, 2016*.

[13] Ploeg J, Shukla D P, van de Wouw N, et al. "Controller Synthesis for String Stability of Vehicle Platoons." *IEEE Transactions on Intelligent Transportation Systems,* 2014.

[14] S. E. Li, Y. Zheng, K. Li, and J. Wang, "An overview of vehicular platoon control under the four-component framework," in *Proc. IEEE Intell. Vehicles Symp.*, Seoul, Korea, 2015, pp. 286–291.

[15] J.Q. Wang, S. E. Li, Y. Zheng, et al. "Longitudinal collision mitigation via coordinated braking of multiple vehicles using model predictive control," *Integrated Computer-Aided Engineering*, 2015, 22(2): 171–185.

[16] G. Mantovani, L. Ferrarini. "Temperature Control of a Commercial Building With Model Predictive Control Techniques". *Industrial Electronics, IEEE Transactions on*, vol. 62, no. 4, pp. 2651–2660, 2015.

[17] S. Di Cairano, H. Tseng, D. Bernardini and A. Bemporad "Vehicle yaw stability control by coordinated active front steering and differential braking in the tire sideslip angles domain", *IEEE Trans. Control Syst. Technol.*, vol. 21, no. 4, pp. 1236–1248, 2013

[18] R. R. Negenborn, J. M. Maestre. "Distributed model predictive control: An overview and roadmap of future research opportunities". Control Systems, IEEE, vol. 34, no. 4, pp. 87–97, 2014.

[19] S. E. Li, K. Deng, Y. Zheng, and H. Peng, "Effect of Pulse-and-Glide Strategy on Traffic Flow for a Platoon of Mixed Automated and Manually Driven Vehicles". *Computer-Aided Civil and Infrastructure Engineering*, vol. 30, no. 115, 2015.

[20] F. Lewis, H. Zhang, K. Hengster-Movric, A. Das, Cooperative Control of Multi-Agent Systems: Optimal and Adaptive Design Approaches. Springer-Verlag, London, 2014.

www.TechnicalBooksPDF.com

www.TechnicalBooksPDF.com

Advanced Vehicle Control – Edelmann, Plöchl & Pfeffer (Eds)
© 2017 Taylor & Francis Group, London, ISBN 978-1-138-02992-7

Obstacle avoidance control design: An experimental evaluation in vehicle platooning

M. Alirezaei, E. Semsar-Kazerooni & J. Ploeg
TNO, Department of Integrated Vehicle Safety, The Netherlands

ABSTRACT: In this paper, an obstacle avoidance controller (OA) based on the impedance control method is developed. The main goal of the OA controller is to guarantee robust gap making for a merging vehicle within a platoon of vehicles which are longitudinally automated. The proposed OA controller is developed in a simulation environment and later implemented and evaluated on test vehicles. Experimental results show the effectiveness of the proposed method for robust gap making and collision avoidance scenarios.

1 INTRODUCTION

Cooperative driving of highway vehicles has been identified as a promising strategy for autonomous or semi-autonomous vehicle control to enhance safety, improve traffic efficiency and increased fuel economy toward intelligent transportation systems (Semsar-Kazerooni 2015, Shladover 2013). Cooperative Adaptive Cruise Control (CACC) (Ploeg 2014, Milans 2014, Semsar-Kazerooni 2016) is an example of an automatic vehicle-following control system. CACC, using wireless communications for data exchange, allows a smaller inter-vehicle distance compared to adaptive cruise control (ACC). However, CACC in (Ploeg 2014) merely deals with safe inter-vehicle distance among the platoon member, in one lane. Extending cooperative driving to include maneuvering vehicles between the lanes is the next step towards automated driving (Alirezaei 2015). Therefore, an obstacle avoiding (OA) controller is necessary to see any object on the adjacent lanes as an obstacle and then to keep a safe distance to this obstacle. Different obstacle avoidance strategies are proposed in the literature. Many of these strategies are based on defining a potential function which becomes infinitely large, when the distance is too small. Therefore, the corresponding control action, i.e. the gradient of the potential function, would be infinitely large as the distance to obstacle decreases (Wolf 2008, Volpe 1990). This type of control action does not suit specific applications i.e. gap making for a merging vehicle. In this paper, an obstacle avoidance controller based on the impedance control strategy is proposed that aims at integrating existing CACC functionality with obstacle avoidance and gap making functionalities. The impedance control strategy, first proposed for robotic manipulator control, can be explained (Hogan 1985) by using a spring analogy to define virtual bumpers in 2D collision avoidance strategies. Using numerical simulations and experimental evaluation, we provide an assessment for the proposed OA controller. The paper is organized as follows: In Section 2 the platoon dynamics are presented. In Section 3 the OA controller design and proof of stability are shown. In Section 4 the simulation results are explained. In Section 5 and 6 the experimental results and conclusions are drawn.

2 PLATOON DYNAMICS

To investigate the behavior of the CACC and OA controllers on a platoon of vehicles, an appropriate model of a platoon is necessary. Consider the following dynamical model for vehicle i, $i = 1, \ldots, m$ in a platoon of m vehicles.

$$\begin{pmatrix} \dot{d}_{i-1|i} \\ \dot{v}_i \\ \dot{a}_i \end{pmatrix} = \begin{pmatrix} v_{i-1} - v_i \\ a_i \\ \frac{-1}{\tau} a_i + \frac{1}{\tau} u_i \end{pmatrix} \tag{1}$$

where $d_{i-1|i}$ is the distance between vehicle i and its preceding vehicle $i-1$, v_i the longitudinal velocity of vehicle i, a_i the longitudinal acceleration of vehicle i, u_i is the external input (desired acceleration), and τ is a time constant representing drive-line dynamics. Here a homogeneous string of vehicles is assumed which means τ is vehicle independent. The objective of each vehicle in a platoon is to follow the preceding vehicle at a desired distance $d_{r,i-1|i}$ according to

$$d_{r,i-1|i}(t) = r_{i-1|i} + h v_i(t) \tag{2}$$

where h is the so called time gap and $r_{i-1|i}$ is the stand-still distance between vehicle i and $i-1$. To regulate the inter-vehicle spaces to $d_{r,i-1|i}$, the spacing error e_i is then defined as

$$e_i(t) = d_{i-1|i}(t) - d_{r,i-1|i}(t) \tag{3}$$

www.TechnicalBooksPDF.com

The employed vehicle model in the control of the platoon is based on the vehicle model (1) and the spacing error e_i defined in (3). This model is represented as:

$$\begin{pmatrix} \dot{e}_i \\ \dot{v}_i \\ \dot{a}_i \end{pmatrix} = \begin{pmatrix} 0 & -1 & -h \\ 0 & 0 & 1 \\ 0 & 0 & \frac{-1}{\tau} \end{pmatrix} \begin{pmatrix} e_i \\ v_i \\ a_i \end{pmatrix} + \begin{pmatrix} 0 \\ 0 \\ \frac{1}{\tau} \end{pmatrix} u_i + \\ + \begin{pmatrix} 0 & 1 & 0 \\ 0 & 0 & 0 \\ 0 & 0 & 0 \end{pmatrix} \begin{pmatrix} e_{i-1} \\ v_{i-1} \\ a_{i-1} \end{pmatrix} \quad (4)$$

3 PLATOON CONTROL

In this section, design of a CACC controller which deals with safe inter-vehicle distance in one lane and an OA controller which includes maneuvering vehicles between the lanes are discussed.

3.1 *CACC*

The main objectives for the platoon control problem are zero steady state for the spacing error, i.e. $\lim_{t\to\infty} e_i(t) = 0$, and string stability. These objectives are achieved with the help of a cooperative adaptive cruise controller (CACC) designed in (Ploeg 2011). Considering a one-vehicle look-ahead CACC, the input ξ_{ic} is defined such that

$$h\dot{u}_i = -u_i + \xi_{ic} \quad (5)$$

where the control law for ξ_{ic} is chosen as

$$\xi_{ic} = u_{i-1} + k_{pi}e_i + k_{di}\dot{e}_i \quad (6)$$

where k_{pi} and k_{di} are the proportional and derivative action gains of vehicle i for CACC controller, respectively, and the feedforward term u_{i-1} is obtained through wireless communication. Using (4)–(6), the following closed-loop system is thus obtained:

$$\begin{pmatrix} \dot{e}_i \\ \dot{v}_i \\ \dot{a}_i \\ \dot{u}_i \end{pmatrix} = \begin{pmatrix} 0 & -1 & -h & 0 \\ 0 & 0 & 1 & 0 \\ 0 & 0 & \frac{-1}{\tau} & \frac{1}{\tau} \\ \frac{k_{pi}}{h} & \frac{-k_{di}}{h} & -k_{di} & \frac{-1}{h} \end{pmatrix} \begin{pmatrix} e_i \\ v_i \\ a_i \\ u_i \end{pmatrix} \\ + \begin{pmatrix} 0 & 1 & 0 & 0 \\ 0 & 0 & 0 & 0 \\ 0 & 0 & 0 & 0 \\ 0 & \frac{k_{di}}{h} & 0 & \frac{1}{h} \end{pmatrix} \begin{pmatrix} e_{i-1} \\ v_{i-1} \\ a_{i-1} \\ u_{i-1} \end{pmatrix}$$

or

$$\dot{z}_i = C_0 z_i + C_1 z_{i-1} \quad (7)$$

where $z_i = (e_i\ v_i\ a_i\ u_i)^T$ and the matrices C_0 and C_1 are defined, correspondingly. Ploeg (2011) has shown that for a bounded external input applied to the first vehicle and subject to some constraints on the controller gains, the above closed loop system will be exponentially stable. Figure 1 shows the block diagram

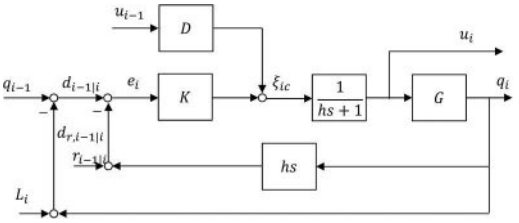


Figure 1. Block diagram of the controlled vehicles 2 and 4 of a platoon with CACC.

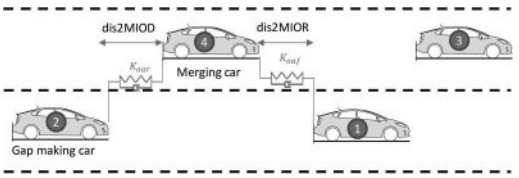


Figure 2. Vehicle topology in nominal merging scenario.

of the CACC controller. Where $G(s) = \frac{q_i(s)}{u_i(s)} = \frac{1}{s^2(\tau s+1)}$, $K(s) = k_{pi} + k_{di}s$, $D(s) = e^{-\theta s}$, θ is the communication delay and $q_i(s)$ is the Laplace transform of the vehicle i's position, $q_i(t)$. Here, u_i represents the entire external input implemented to vehicle i based on only the CACC control effort. In the next Section, the effect of the obstacle avoidance controller is explained.

3.2 *Obstacle avoidance controller*

The Obstacle Avoidance (OA) controller is based on the impedance control approach. In this controller, virtual springs and dampers are connected to the merging car, which apply desired acceleration to the forward and backward platoon vehicles to realize the safe gap. Figure 2 shows the schematic of the OA controller in the gap making and merging maneuver. In this maneuver, vehicle 2 makes a gap for vehicle 4 who wants to merge into the platoon in front of vehicle 2. In this case, car 4 is responsible for making the gap between 4 and 1 (car 1 is driving in cruise control), whereas both car 2 and 4 are responsible for making the gap dis2MIOD. The control block diagram for vehicles 2 and 4 can be expressed as in Figure 3. Then, the controller u_i can be defined such that

$$h\dot{u}_i = -u_i + \xi_{ic} + \xi_{ioa} \quad (8)$$

where the control effort correspond to CACC, ξ_{ic}, is already defined in (6) and the control laws for the obstacle avoidance controller ξ_{ioa} for vehicles 2 and 4 are chosen as

$$\xi_{2oa} = k_{poar}(d_{24} - d_{r,24}) + k_{doar}(\dot{d}_{24} - \dot{d}_{r,24}) \quad (9)$$

$$\xi_{4oa} = k_{poaf}(d_{14} - d_{r,14}) + k_{doaf}(\dot{d}_{14} - \dot{d}_{r,14}) - \xi_{2oa} \quad (10)$$

where k_{poaf}, k_{doaf}, k_{poar} and k_{doar} are the proportional and derivative actions of the impedance controller

www.TechnicalBooksPDF.com

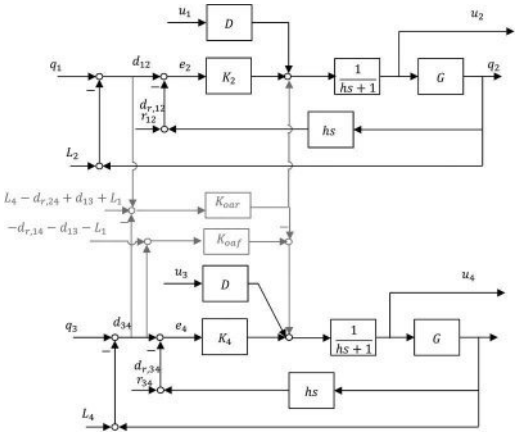


Figure 3. Block diagram of a controlled vehicle of a platoon with obstacle avoidance controller.

which are regulating obstacle avoidance in vehicles 4 and 2, respectively. d_{ij} and $d_{r,ij}$ are the real and desired projected distances between vehicle i and vehicle j, respectively.

The distances d_{14} and d_{24} can be expressed by the following equations:

$$d_{14} = d_{34} - d_{13} - L_1 \tag{11}$$

$$d_{24} = d_{12} + d_{13} - d_{34} - L_4 + L_1 \tag{12}$$

where L_1 and L_4 are the length of the vehicle 1 and 4 respectively. By substituting (6) and (9)–(12) into (8) the following inputs thus obtained:

$$h\dot{u}_2 = -u_2 + u_1 + k_{p2}e_2 + k_{d2}\dot{e}_2 + k_{poar}(d_{12} + d_{13} - d_{34} - L_4 + L_1 - d_{r,24}) + k_{doar}(\dot{d}_{12} + \dot{d}_{13} - \dot{d}_{34} - \dot{d}_{r,24}) \tag{13}$$

$$h\dot{u}_4 = -u_4 + u_3 + k_{p4}e_4 + k_{d4}\dot{e}_4 + k_{poaf}(d_{34} - d_{13} - L_1 - d_{r,14}) + k_{doaf}(\dot{d}_{34} - \dot{d}_{13} - \dot{d}_{r,14}) - k_{poar}(d_{12} + d_{13} - d_{34} - L_4 + L_1 - d_{r,24}) - k_{doar}(\dot{d}_{12} + \dot{d}_{13} - \dot{d}_{34} - \dot{d}_{r,24}) \tag{14}$$

In order to generate the state space equations for the system of CACC and OA, it is necessary to add and subtract extra terms to (13) and (14)

$$h\dot{u}_2 = -u_2 + u_1 + k_{p2}e_2 + k_{d2}\dot{e}_2 + k_{poar}(d_{12} + d_{13} - d_{34} - L_4 + L_1 - d_{r,24}) + k_{doar}(\dot{d}_{12} + \dot{d}_{13} - \dot{d}_{34} - \dot{d}_{r,24}) - k_{poar}(d_{r,34} - d_{r,12}) + k_{poar}(d_{r,34} - d_{r,12}) \tag{15}$$

$$h\dot{u}_4 = -u_4 + u_3 + k_{p4}e_4 + k_{d4}\dot{e}_4 + k_{poaf}(d_{34} - d_{13} - L_1 - d_{r,14}) + k_{doaf}(\dot{d}_{34} - \dot{d}_{13} - \dot{d}_{r,14}) - k_{poar}(d_{12} + d_{13} - d_{34} - L_4 + L_1 - d_{r,24}) - k_{doar}(\dot{d}_{12} + \dot{d}_{13} - \dot{d}_{34} - \dot{d}_{r,24}) - k_{poaf}d_{r,34} + k_{poaf}d_{r,34} - k_{poar}(d_{r,34} - d_{r,12}) + k_{poar}(d_{r,34} - d_{r,12}) \tag{16}$$

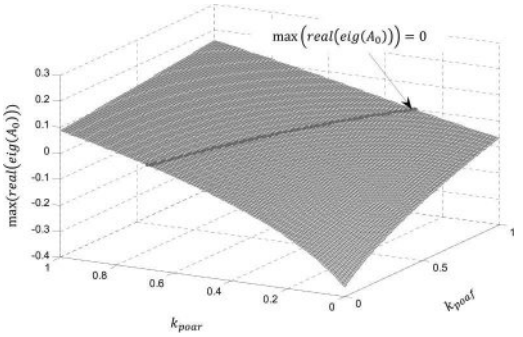


Figure 4. Eigen value of the system in the gain space (k_{poaf}, k_{poar}).

Using (15) and (16) and the model of platoon dynamics (7) the state space equation for the closed loop system in the presence of both CACC and OA controllers, is obtained as

$$\dot{x}_i = A_0 x_i + A_1 x_{i-1} + B \tag{17}$$

where $x = [e_2\ v_2\ a_2\ u_2\ e_4\ v_4\ a_4\ u_4]^T$ (see Appendix).

3.3 *Stability analysis*

In this section, the stability of the proposed closed loop system is investigated. In equation 17 the B matrix only affects the steady state behavior and equilibrium point. Let's assume that vehicles 1 and 3 (the preceding vehicles) are in CACC mode and following a virtual reference vehicle. Returning to the platoon closed loop model eq. 17, the stability of the system of 4 vehicle only depends on the eigenvalue of the A_0 matrix. Considering the system with OA, assuming that CACC parameters are fixed, the eigenvalues are affected by four parameters, being k_{poaf}, k_{poar}, k_{doaf}, k_{doar}. Figure 4 shows the gain space (k_{poaf}, k_{poar}) versus the closed loop largest eigenvalue of the system where $k_{doaf} = k_{doar} = 0$. The red line shows the stability border where the $max(real(eig(A_0))) = 0$. Figure 5 shows the stability region for different damping ratios. The area below the lines shows the stable region. As it can be seen, increasing the damping of the OA controller yields a larger stability region.

4 SIMULATION RESULTS

Several tests have been performed with the simulation environment to investigate the OA controller. However, here only the effect of initial conditions on the steady state behavior will be discussed. Figure 2 shows vehicle topology in the simulation where vehicles are driving with a speed of 80 km/h. We denote the distance from car 4 to the Most Important Object on the Right side and to the Most Important Object behind the host vehicle by *dis2MIOR* and *dis2MIOD*, respectively (see Figure 2). The desired value of 10 m is considered for *dis2MIOR* and *dis2MIOD*. Figure 6 shows the results

www.TechnicalBooksPDF.com

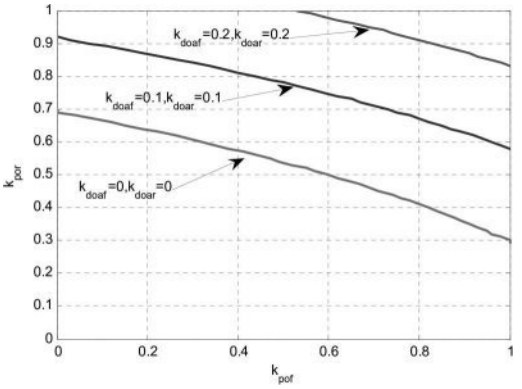


Figure 5. Stability region for different damping ratios, $k_{doaf} = k_{doar} = 0$ red line, $k_{doaf} = k_{doar} = 0.1$ green line, $k_{doaf} = k_{doar} = 0.2$ green line.

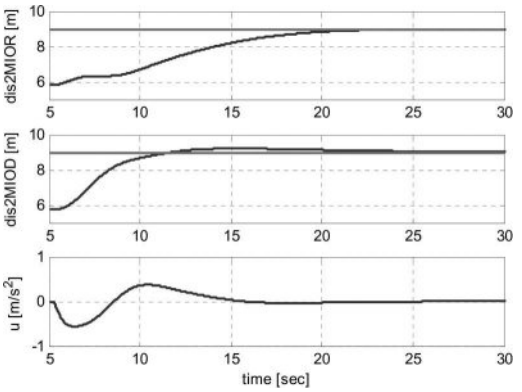


Figure 6. Simulation results for the merging car 4 with $d_{13} = 5.5$ m, distance to the Most Important Object on the Right side (dis2MIOR) (upper subplot), distance to the Most Important Object behind the host vehicle (dis2MIOD) (middle subplot) and the control input (lower subplot) and red lines shows desired distance.

for the first simulation where the initial distance of the car 4 with respect to car 1 is 5.5 m. As it can be seen, OA controller in car 4 applies smooth acceleration (lower subplot) and increases distance to car 1 (upper subplot). The controller on car 2 generates desired gap (middle subplot) for car 4 at the same time.

Figure 7 shows the result for the second simulation where the initial distance of car 4 with respect to car 1 is 11 m. As can be seen, the controller generates acceleration input (lower subplot) to adjust the distance between car 4 and car 1 (upper subplot).

5 EXPERIMENTAL RESULTS

The proposed control strategy is experimentally evaluated by implementing it on a real time computer, in driving car laboratories (CarLabs). The CarLabs are TOYOTA Prius (Fig. 8) which are equipped with

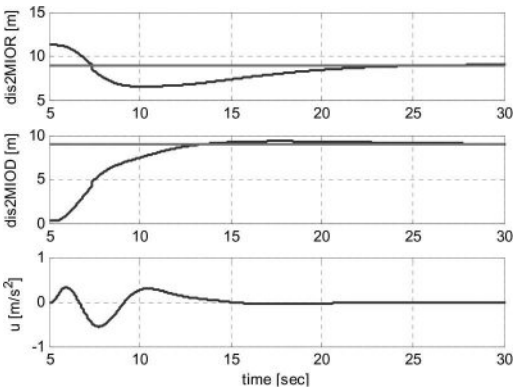


Figure 7. Simulation results for the merging car 4, distance to the Most Important Object on the Right side (dis2MIOR) (upper subplot), distance to the Most Important Object behind the host vehicle (dis2MIOD) (middle subplot) and the control input (lower subplot) and red lines shows desired distance.



Figure 8. Carlab.

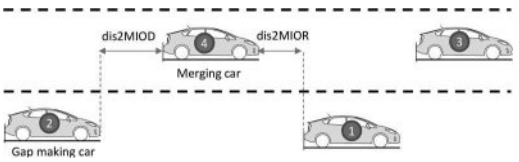


Figure 9. Vehicle topology in the first experiment.

a throttle and brake control system. Also the CarLabs are equipped with IEEE 802.11p-based wireless communication, allowing for communication of the desired vehicle acceleration at an update rate of 10 Hz. Furthermore, the CarLabs are equipped with environmental perception sensors like radar, camera and GPS. Using these sensors all CarLabs are able to measure dis2MIOR and dis2MIOD and their time derivatives. Several tests have been performed on a test track but for the sake of brevity only two sets of experiments will be shown. In both experiments all cars are driving at 45 km/h and the desired gap between cars is 10 m. Figure 9 shows the vehicle configuration in the first experiment. In this experiment, car 4 is going to merge between car 1 and car 2. So car 2 should make a safe gap for the merging car. Simultaneously, car 4 should make a safe distance to car 1.

Figure 10 shows that the OA controller provides smooth input (lower subplot) to the system and the dis2MIOR and dis2MIOD go to the desired value of 10m. The discontinuity in dis2MIOR around 32 sec

www.TechnicalBooksPDF.com

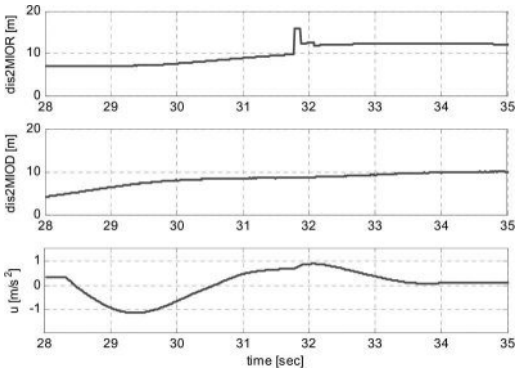


Figure 10. Experimental results for the merging car 4, distance to the Most Important Object on the Right side (dis2MIOR) (upper subplot), distance to the Most Important Object behind the host vehicle (dis2MIOD) (middle subplot) and the control input (lower subplot).

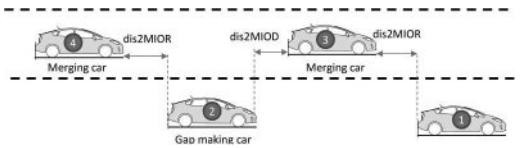


Figure 11. Vehicle topology in the second experiment.

is due to the environmental perception sensors which also has influence on the controller input.

Figure 11 shows the vehicle configuration in the second experiment. The goal of this experiment is to investigate some special conditions on the controller performance. In this experiment, car 3 is going to merge between car 1 and car 2. In this case there is no car in front of car 3. Furthermore, car 4 is going to merge behind car 2 so there is no car behind the merging car. So car 2 on one hand should make a safe gap for car 3 and at the same time, car 4 should make a safe distance to the gap making car.

Figure 12 shows the *dis2MIOR* and *dis2MIOD* and control input for car 3. As it can be seen, the controller applies smooth input to the system and realizes 10m gap in front and behind the host vehicle. Figure 13 shows the *dis2MIOR* and *dis2MIOD* and control input for car 4. As it can be seen first the distance between car4 and car2 (*dis2MIOR*) due to the gap making for the car 3 decreases and as soon as the controller in car4 is activated, the controller realizes the safe distance to car2.

6 CONCLUSION

The problem of designing an obstacle avoidance controller based on the impedance control method for cooperative driving has been presented. The proposed system has been evaluated in simulation and also tested in experiments under a variety of maneuvers. It has been proven that the proposed OA controller is capable

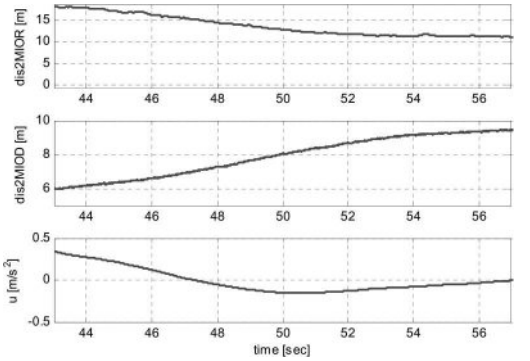


Figure 12. Experimental results for the merging car 3, distance to the Most Important Object on the Right side (dis2MIOR) (upper subplot), distance to the Most Important Object behind the host vehicle (dis2MIOD) (middle subplot) and the control input (lower subplot).

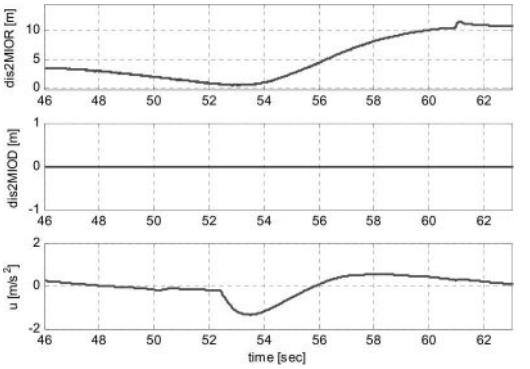


Figure 13. Experimental results for the merging car 4, distance to the Most Important Object on the Right side (dis2MIOR) (upper subplot), distance to the Most Important Object behind the host vehicle (dis2MIOD) (middle subplot) and the control input (lower subplot).

of generating a predefined gap between vehicles for a merging vehicle.

REFERENCES

Alirezaei, M. Jansen, S.T.H., Janssen, J.M., Experimental evaluation of collision avoidance system using state dependent Riccati equation technique. *24th International Symposium on Dynamics of Vehicles on Roads and Tracks*, Graz, Austria, 2015.

Hogan, N., Impedance control: an approach to manipulation. *ASME J. Dynamic Syst. Meas. Control*, 107:124, 1985.

Lidstrom, K., Sjoberg, K., Holmberg, U., Anderson J. and Bergh, F., A modular CACC system integration and design, *IEEE Trans. Intell. Transp. Syst.*, vol. 13, no. 3, pp. 1050–1061, Sep. 2012.

Milans, V., Shladover, S.E., Spring, J., Nowakowski, C., Kawazoe, H. and Nakamura, M., Cooperative adaptive cruise control in real traffic situations, *IEEE Trans. Intell. Transp. Syst.*, vol. 15, no. 1, pp. 296–305, Feb. 2014.

Ploeg, J., Scheepers, B.T.M., van Nunen, E., van de Wouw, N., and Nijmeijer, H., Design and Experimental Evaluation of

www.TechnicalBooksPDF.com

Cooperative Adaptive Cruise Control, *IEEE Conference on Intell. Transp. Syst.*, Washington, USA, October 5–7, 2011.

Ploeg, J., Shukla, D.P., van de Wouw, N. and Nijmeijer, H., Controller Synthesis for String Stability of Vehicle Platoons, *IEEE Transactions on Intelligent Transportation Systems*, vol. 15, no. 2, April 2014.

Ploeg, J., van der Wouw, N. and Nijmeijer, H., $\mathcal{L}_p$ String stability of Cascaded Systems: Application to Vehicle Platooning", *IEEE Transactions on Control Systems Technology*, vol. 22, no. 2 March 2014.

Semsar-Kazerooni, E., Ploeg, J., Interaction protocols for cooperative merging and lane reduction scenarios, *18th IEEE International Conference on Intell. Transp. Syst.*, Las Palmas, 2015.

Semsar-Kazerooni, E., Verhaegh, J., Ploeg, J., Alriezaei, M., Cooperative Adaptive Cruise Control: An Artificial Potential Field Approach, *IEEE Intelligent Vehicles Symposium*, Gothenburg, Sweden, 2016.

Shladover, S. E., Su, D. and Lu, X. Y., Impacts of cooperative adaptive cruise control on freeway traffic flow, *Transportation Research Record: Journal of the Transportation Research Board*, vol. 2324, 2013.

Volpe R. and Khosla, P., Manipulator control with superquadric artificial potential functions: Theory and experiments, *IEEE Trans. Syst., Man, Cybern.*, vol. 20, no. 6, 1990.

Wolf M. and Burdick, J., Artificial potential functions for highway driving with collision avoidance, *IEEE Int. conf. on robotics and automation (ICRA)*, May 2008.

APPENDIX

$$\mathbf{A}_0 = \begin{pmatrix} 0 & -1 & -h & 0 & 0 & 0 & 0 & 0 \\ 0 & 0 & 1 & 0 & 0 & 0 & 0 & 0 \\ 0 & 0 & -\frac{1}{\tau} & \frac{1}{\tau} & 0 & 0 & 0 & 0 \\ \frac{k_{p2}+k_{poar}}{h} & -\frac{k_{d2}+k_{doar}-h\,k_{poar}}{h} & -k_{d2} & -\frac{1}{h} & -\frac{k_{poar}}{h} & \frac{k_{doar}-h\,k_{poar}}{h} & 0 & 0 \\ 0 & 0 & 0 & 0 & 0 & -1 & -h & 0 \\ 0 & 0 & 0 & 0 & 0 & 0 & 1 & 0 \\ 0 & 0 & 0 & 0 & 0 & 0 & -\frac{1}{\tau} & \frac{1}{\tau} \\ -\frac{k_{poar}}{h} & \frac{k_{doar}-h\,k_{poar}}{h} & 0 & 0 & \frac{k_{p4}+k_{poaf}+k_{poar}}{h} & -\frac{k_{d4}+k_{doaf}+k_{doar}-h\,k_{poaf}-h\,k_{poar}}{h} & -k_{d4} & -\frac{1}{h} \end{pmatrix}$$

$$A_1 = \begin{pmatrix} 0 & 1 & 0 & 0 & 0 & 0 & 0 & 0 \\ 0 & 0 & 0 & 0 & 0 & 0 & 0 & 0 \\ 0 & 0 & 0 & 0 & 0 & 0 & 0 & 0 \\ 0 & \frac{k_{d2}+k_{doar}}{h} & 0 & \frac{1}{h} & 0 & -\frac{k_{doar}}{h} & 0 & 0 \\ 0 & 0 & 0 & 0 & 0 & 1 & 0 & 0 \\ 0 & 0 & 0 & 0 & 0 & 0 & 0 & 0 \\ 0 & 0 & 0 & 0 & 0 & 0 & 0 & 0 \\ 0 & -\frac{k_{doar}}{h} & 0 & 0 & 0 & \frac{k_{d4}+k_{doaf}+k_{doar}}{h} & 0 & \frac{1}{h} \end{pmatrix}$$

$$B = \begin{pmatrix} 0 \\ 0 \\ 0 \\ -\frac{-k_{poar}\,(r_{12}-r_{34})+k_{poar}\left(L_4+d_{r,24}-d_{13}-L_1\right)}{h} \\ 0 \\ 0 \\ 0 \\ -\frac{k_{poaf}\left(d_{r,14}+d_{13}+L_1\right)-k_{poaf}\,r_{34}+k_{poar}\,(r_{12}-r_{34})-k_{poar}\left(L_4+d_{r,24}-d_{13}-L_1\right)}{h} \end{pmatrix}$$

www.TechnicalBooksPDF.com

Automated driving

www.TechnicalBooksPDF.com

www.TechnicalBooksPDF.com

Advanced Vehicle Control – Edelmann, Plöchl & Pfeffer (Eds)
© 2017 Taylor & Francis Group, London, ISBN 978-1-138-02992-7

Collision avoidance system using state dependent Riccati equation technique: An experimental robustness evaluation

M. Alirezaei, S.T.H. Jansen, A.J.C. Schmeitz & A.K. Madhusudhanan
TNO, Department of Integrated Vehicle Safety, Automotive Campus, Helmond, The Netherlands

ABSTRACT: The capacity of a vehicle to avoid collisions is predominantly defined by the friction potential of the tyres. A robustness analysis of a Collision Avoidance System is executed by simulation and experiments for extreme changes in tyre friction. The collision avoidance controller which utilizes steering angle is based on the State Dependent Riccati Equation technique. This technique can consider nonlinearities and is fault tolerant by design. The controller has been extended with an estimation concept to obtain information of the road friction prior to execution of the steering action. The friction estimation concept is experimentally evaluated and the results show a reproducible reduction of the friction after entering a low friction road section. With a simulation study the control performance for varying conditions is elaborated, whereas experimental results are provided for extreme conditions of combined slip. The results demonstrate that the controller is capable to achieve collision avoidance for the variety of driving conditions with sufficient stability.

1 INTRODUCTION

The main cause of car collisions is human errors in judgement and decision making. Active safety systems for road vehicles, e.g. antilock braking system (ABS), vehicle dynamic control (VDC), active front steering (AFS) (Alirezaei 2010), have reduced the number of collisions during last years. However, the aforementioned systems do not take (a priori) environmental information into account, which limits the collision avoidance potential. Utilizing environmental perception sensors in active safety systems, such as autonomous emergency braking (AEB) and more advanced Collision Avoidance Systems (CAS), is improving current road safety standards by reducing the number of deaths and severe injuries (Alirezaei 2015, Kaempchen 2009).

CAS use steering and braking to avoid collisions. These systems typically operate close to the boundary of vehicle capability in order to avoid intervening when the driver may still be in control (Soudbakhsh 2011). The vehicle's limits of handling behaviour is governed by the tyre-road friction properties, and as a result is highly nonlinear. Hence, the controller for CAS should be able to cope with the nonlinearity of the system. Moreover, the CAS module is a safety system and has to be robust under a wide range of operating conditions (Guldner 1996).

The vehicle capability alters due to changes in properties of the system. Slowly time-varying system properties can be estimated and henceforth adapted i.e. mass and inertia, however environmental conditions that affect the tyre-road friction potential may alter abruptly. Hence, robustness of the CAS controller must be carefully evaluated for extreme changes in tyre behaviour.

The main subject of the present paper is the development of a CAS scheme using a standard electric power steering actuator in an optimal coordination towards regulating the vehicle dynamics and path following. The benefit of the proposed approach with State Dependent Riccati Equation (SDRE) control for collision avoidance maneuvers is that it can cope with the (speed dependent) vehicle lateral response nonlinearity and also is adaptive to change in the tyre-road friction potential.

In SDRE the nonlinear dynamics of the system is factorized into the state vector and the product of a matrix valued function that depends on the state itself. In doing so, the nonlinearities of the system are fully captured bringing the nonlinear system to a linear like structure having state-dependent coefficient (SDC) matrices. The nonlinear regulator is derived by minimizing an objective function which is formulated as a weighted integral of the system response and the actuator effort. The robustness of the proposed controller is assessed through simulation and experimental evaluation for collision avoidance maneuvers on high and low friction roads.

The paper is organized as follows: In Section 2 the system architecture is presented. In Section 3 the friction estimation concept is discussed. In Section 4, the nonlinear vehicle and path following model are described. In Section 5, the SDRE control law design for CAS is explained. Subsequently, in Section 6 worst case analysis is discussed. The simulation

www.TechnicalBooksPDF.com

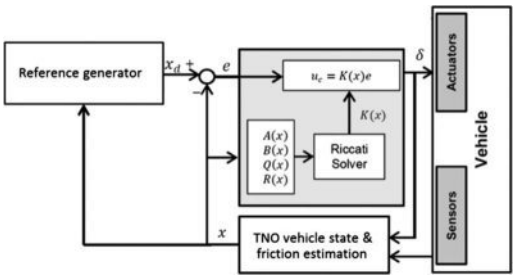


Figure 1. Schematic of the control system architecture.

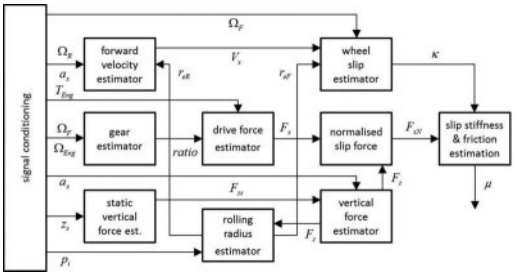


Figure 2. Block diagram of the friction estimation algorithm.

and experimental results are presented in Section 7 and 8 respectively. Finally in Section 9 conclusions are drawn.

2 SYSTEM ARCHITECTURE

Figure 1 shows the structure of the developed control system based on the SDRE technique. A reference path generator uses a vehicle model and sensor signals (i.e. distance to object and longitudinal velocity u) to provide the desired states x_d of the vehicle. A Vehicle State Estimator (VSE) estimates the current states x of the vehicle that are required for the vehicle model of the controller and to calculate the state error e_x between the desired and estimated states at the current operating point. Additionally, the VSE provides a friction estimate. The CAS control module includes: (i) a nonlinear scheme of the system's state space equations on the basis of the combined slip Pacejka tyre model; (ii) the objective of the control, which is to minimize the error in path following and fulfil stability requirements, in the form of a mathematical cost function and (iii) a numerical solver for the algebraic Riccati equation.

3 FRICTION ESTIMATION

In the experiments, the controller performance is evaluated for evasive maneuvers on dry asphalt and wet tiles (low friction surface). Friction changes during the maneuver are not considered, but friction estimation during straight line driving at cruise control speed prior to the maneuver is investigated.

For relatively large slip, the VSE module, which uses a vehicle model and the nonlinear Extended Kalman Filtering (EKF) technique, is able to give reliable friction estimates, see e.g. Leenen, R. & Maurice (2010). However, for the cruise control driving case, the tyre longitudinal slip is very small and the standard VSE will not detect the friction condition. Therefore, a separate friction estimation algorithm is investigated for this case. The friction obtained from this algorithm is used for reference generation in Figure 1, and at the same time feeds the EKF-based VSE with an initial estimate. Once the collision avoidance maneuver is initiated the EKF-based VSE will be able to update the friction estimate based on the lateral vehicle response.

The algorithm used for cruise control driving relies on the assessment of the longitudinal slip stiffness as proposed by e.g. Gustafsson (1997). The algorithm is shown schematically in Figure 2.

The (small) engine torque T_{Eng}, the engine speed Ω_{Eng} and the front wheel speeds Ω_F are used to estimate the longitudinal force F_x of the driven wheels. The static vertical loads F_{zs} of the vehicle are estimated using suspension stroke z_s sensors. Changes in vertical force during accelerating are calculated using the measured longitudinal acceleration a_x, resulting in vertical force F_z estimates that are used for normalizing the longitudinal force and obtaining the effective rolling radii r_e. The wheel speeds Ω are used to obtain the front wheel longitudinal slip κ. Since the vehicle is front wheel driven, it is assumed that the rear wheels are free rolling and their speed can be used to obtain the vehicle velocity required for the slip calculation of the front wheels. A Kalman filter is used to estimate the longitudinal vehicle velocity V_x, while simultaneously estimating the accelerometer bias. An empirical relation for the load dependent effective rolling radius characteristic of the tyre is used to account for the differences in rolling radii for the front and rear tyres. In this way, only one parameter, i.e. the normalized longitudinal slip stiffness, has to be estimated. A Recursive Least Squares (RLS) filter with forgetting factor is used for this. Finally, from the assumed relation between normalized slip stiffness and friction, the friction coefficient is estimated.

A linear relation between slip stiffness and friction coefficient is assumed that has been empirically identified from ABS braking tests. Experiments have been conducted on dry asphalt and wet tiles. The obtained Pacejka model scaling factors LKX and LMUX for the longitudinal slip stiffness and longitudinal peak friction respectively and the assumed linear relation, have been plotted in Figure 3, which is obtained from Schmeitz, A.J.C. and Alirezaei (2016). Note that the scaling is done with respect to the values for dry asphalt. It is observed that the obtained values (legend 'TNO vehicle') follow the same trend as those obtained from other studies, i.e. for low friction the slip stiffness decreases and the values for the wet tiles are near the values for ice. Finally, it is remarked that

www.TechnicalBooksPDF.com

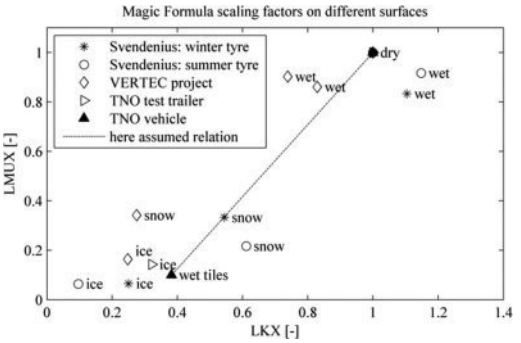


Figure 3. Relation between peak friction and slip stiffness scaling using Pacejka's Magic Formula scaling factors.

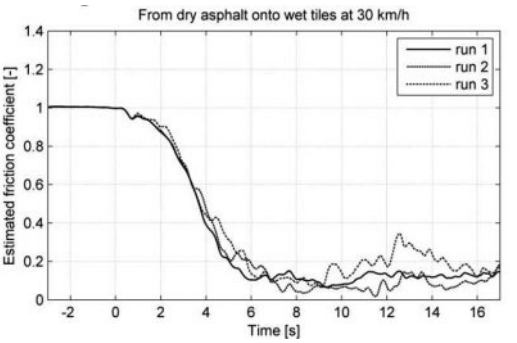


Figure 4. Friction estimation results when driving from dry asphalt onto wet tiles at 30 km/h; 3 repetitions are shown.

the used linear relation does not attempt to provide a general solution.

To demonstrate the operation of the estimator, the results of the friction estimation are plotted for 3 test runs in Figure 4, where the vehicle drives on cruise control with a speed of 30 km/h from the dry asphalt onto the wet tiles. The transition from asphalt to tiles is at about 0 s. When comparing the different runs, it is observed that the results are quite consistent regarding the detection of the low friction on the wet tiles. The observed variations in the estimated friction coefficient over time are considered caused by differences in water layer on the surface of the tiles and different vehicle driving path on the tiles.

The results show that even at very small slip, the slip stiffness method is able to identify changes in road friction. However, first it must be remarked that in this study two well-defined surfaces were considered, and therefore further studies will focus on applications for public roads (which will be less consistent). Secondly, the method has been found very sensitive to effective rolling radius variations. For this reason, the effective rolling radii were accurately identified. This is different compared to other implementations of the method, e.g. Gustafsson (1997), where the offset in the slip, caused by the effective rolling radii, is also estimated. Nevertheless for practical implementations, estimation of the effective rolling radii (or forward velocity) should be done, but preferably using a separate estimation concept, possibly making use of other sensors that can provide forward velocity information.

Finally, it is remarked that development of an all-encompassing friction estimator is still an active research topic. Not only must the performance of the estimator be assessed for different friction surfaces, also e.g. the braking case must be investigated, where the unavailability of a sufficiently accurate brake torque measurement at low slip is an issue.

4 VEHICLE AND PATH FOLLOWING MODEL

The proposed controller is based on a 4th order nonlinear vehicle and path following model. This model

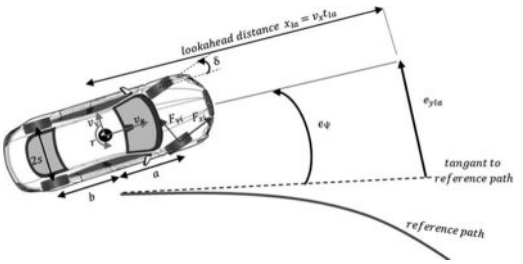


Figure 5. Vehicle and path following model.

is shown in Figure 5. Here, the vehicle dynamics as presented in (Alirezaei 2015) are briefly recalled:

$$\dot{v}_y = \frac{1}{M}\begin{Bmatrix}\left(F_{yfl}+F_{yfr}\right)\cos\delta+\left(F_{yrl}+F_{yrr}\right)\\+\left(F_{xfl}+F_{xfr}\right)\sin\delta\end{Bmatrix} - v_x r\,; \qquad (1)$$

$$\dot{r} = \frac{1}{I_z}\begin{Bmatrix}a\left[\left(F_{yfl}+F_{yfr}\right)\cos\delta+\left(F_{xfl}+F_{xfr}\right)\sin\delta\right]\\-b\left(F_{yrl}+F_{yrr}\right)+s\left(F_{xrr}-F_{xrl}\right)+\\s\left[\left(F_{xfr}-F_{xfl}\right)\cos\delta-\left(F_{yfr}-F_{yfl}\right)\sin\delta\right]\end{Bmatrix}; \qquad (2)$$

$$\dot{e}_{yla} = v_y + v_x t_{la} r + v_x e_\psi\,; \qquad (3)$$

$$\dot{e}_\psi = r - v_x / R\,, \qquad (4)$$

where lateral velocity v_y, yaw rate r of the vehicle, error in vehicle lateral position e_{yla} and heading angle error e_ψ with respect to the reference path are the states of the system. The input of the system is the front wheel steering angle δ. F_{xi} and F_{yi} represent the longitudinal and lateral forces for each wheel. The effect of roll dynamics is limited to the load transfer in the calculation of the tyre normal forces.

The Pacejka combined slip tyre model is used for describing the tyre force behavior (Pacejka 2002). The main reason to use such tyre model is that it improves the vehicle model accuracy at high slip maneuvers, and also considers the interaction of longitudinal and lateral tyre forces. Combined slip is included by the

www.TechnicalBooksPDF.com

weighting factors $G\,(G \le 1)$, which attenuate the so-called pure slip tyre forces:

$$F_{xi} = G_{xi}(\kappa_i, \alpha_i) F_{x0i}(\kappa_i, F_{zi})\,; \tag{5}$$

$$F_{yi} = G_{yi}(\kappa_i, \alpha_i) F_{y0i}(\alpha_i, F_{zi})\,, \tag{6}$$

where F_{x0i} and F_{y0i} are the pure slip tyre forces:

$$F_{x0i} = D_{xi} \sin(C_{xi} \tan^{-1}(B_{xi}\kappa_i))\,;$$

$$F_{y0i} = D_{yi} \sin(C_{yi} \tan^{-1}(B_{yi}\alpha_i))\,.$$

The tyre model parameters $(B_{xi}, C_{xi}, D_{xi}, B_{yi}, C_{yi}, D_{yi})$ have been derived by optimization using tyre measurement data. Finally, κ_i and α_i are the longitudinal and lateral tyre slip for the i-th wheel respectively.

5 SDRE CONTROL DESIGN

The SDRE method requires to transform the nonlinear dynamic equations (eq. 1–4) to a linear form called State Dependent Coefficient (SDC) formulation (Cimen 2008):

$$\dot{x} = A(x)x + B(x)u\,. \tag{7}$$

The SDRE method is a full state feedback control law that minimizes the performance index J,

$$J = \frac{1}{2}\int \{(x - x_d)^T Q(x)(x - x_d) + u^T R(x)u\}dt\,, \tag{8}$$

where Q and R are the state and input weighing matrices, which in general are state dependent. Here, the Q matrix is constant with more emphasize on the lateral error and the R matrix is speed dependent.

The state feedback law that optimizes the cost function (eq. 8) with respect to the constraints, which are the system equations (eq. 7), is: $u = -K(x)x$. Details regarding the calculation of the state feedback gain matrix $K(x)$, based on the solution of the Algebraic State Dependent Riccati Equation, can be found in Alirezaei, M. et al. 2015.

6 WORST CASE ANALYSIS

The robustness of the proposed CAS is investigated using the worst-case scenario, which assumes that the worst possible combination of structural (due to reduced order model) and non-structured uncertainties (parameters uncertainty) of a system may occur simultaneously (Parkinson et al., 1993, Alirezaei et al., 2011).

The worst case scenario is determined from the yaw rate response to the steering angle using a linear bicycle model:

$$\frac{r(s)}{\delta(s)} = \frac{a_1 s + a_0}{b_2 s^2 + b_1 s + b_0}\,, \tag{9}$$

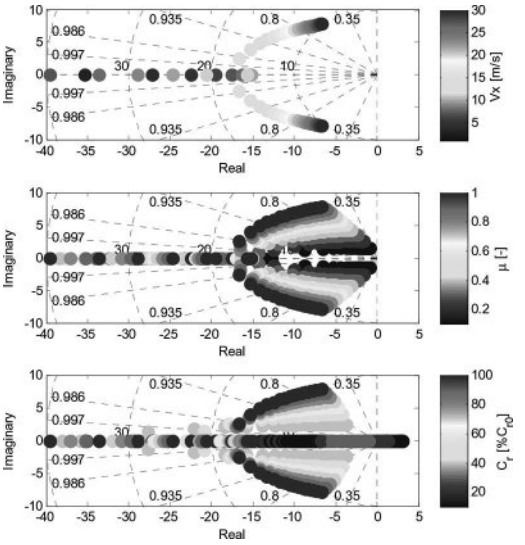


Figure 6. Poles of yaw rate transfer function for variation in speed (top subplot), friction and speed (middle subplot) and rear tyre cornering stiffness and speed (bottom subplot).

where:

$$a_0 = \frac{1}{v_x},\quad a_1 = \frac{m_r}{c_r},\quad b_0 = \frac{l}{v_x^2} + \frac{m_f}{c_f} - \frac{m_r}{c_r}$$

$$b_1 = \left(\frac{I_z(c_f + c_r)}{lc_f c_r} + \frac{am_r}{c_r} + \frac{bm_f}{c_f}\right)/v_x,\quad b_2 = \frac{mI_z}{lc_f c_r}\,,$$

and c_f, c_r are the effective axle cornering stiffness which are calculated as: $c_f = 2c_t c_c/(2c_t + c_c)$ and $c_r = 2c_t$, where c_t is the cornering stiffness of the tyre and c_c is the compliance of the steering system (Niessen et al. 2012). The longitudinal velocity, tyre-road friction coefficient and tyre cornering stiffness are used for the worst case scenario analysis. Following the assumptions of the friction estimation, a reduction of friction reduces cornering stiffness similar. Additionally, a reduction of the rear axle cornering stiffness is considered, as this causes oversteer, which is critical for vehicle stability.

The poles of the yaw rate transfer function indicate vehicle stability. The locations of the two poles of the yaw rate transfer function (eq. 9) are shown in Figure 6 for a speed range of $1\ \text{m/s} \le v_x \le 30\ \text{m/s}$, for different road friction $\mu = 0.1, 0.2, \ldots, 1$ and for different rear cornering stiffness $c_r = [0.1, 0.2, \ldots, 1]c_{r-n}$.

As can be seen in Figure 6, top subplot, when increasing the vehicle speed the poles displaces over circular arcs towards the imaginary axis, without ever crossing it (as the car is understeered). Increasing mu (Figure 6 middle subplot) magnifies the circular arcs for the poles, which corresponds to higher natural frequencies. Guldner 1996 has also shown the effect of friction on pole placement, but for the normal bicycle model without steering compliance. Considering compliance is more accurate concerning the effect of a friction change.

www.TechnicalBooksPDF.com

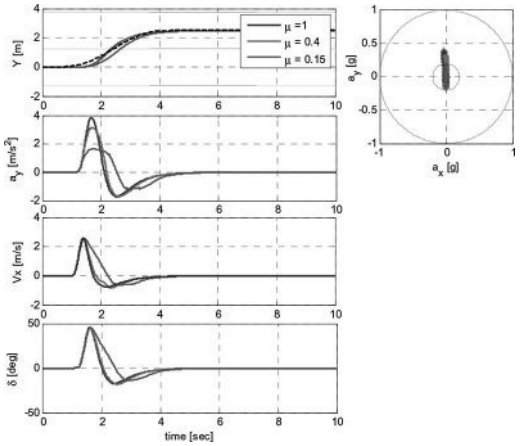


Figure 7. Vehicle response on different road friction: lateral vehicle position Y, lateral acceleration a_y, front wheel slip angle α_f, steering wheel angle δ and friction circle (top right).

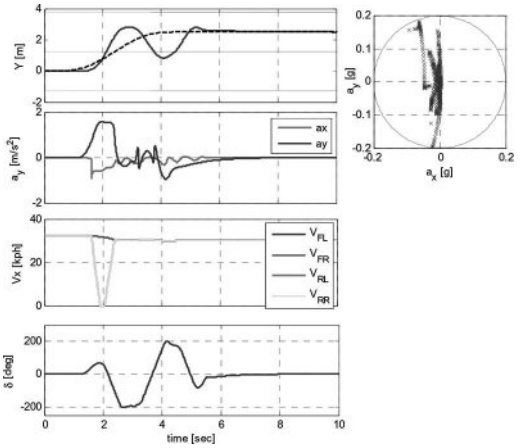


Figure 8. Vehicle response on low friction road surface and extreme oversteer condition: lateral vehicle position Y, lateral acceleration a_y, wheel speeds V, steering wheel angle δ and friction circle (top right).

Decreasing the rear axle cornering stiffness scales down the circular arcs of the poles and even poles cross the imaginary axis.

Based on the pole placement analysis, the worst case scenario occurs when simultaneously decreasing friction and rear tyre cornering stiffness. In this situation the vehicle is the least stable.

7 SIMULATION RESULTS

The proposed control strategy has been developed in simulation using a nonlinear vehicle model in Matlab/Simulink. The closed loop response of the vehicle with SDRE controller in an evasive manoeuvre for different road friction is shown in Figure 7. In this manoeuvre the lateral acceleration of the vehicle on the high friction surface is such that the vehicle operates in the linear region and the controller is able to control system. By decreasing the friction to 0.4, the vehicle gets into the nonlinear region and close to the limits of handling, and the controller is still able to control the vehicle and follow the path. Further decreasing friction means that the controller compromises path following with system stability.

The robustness of the controller is evaluated based on the worst case scenario, where the evasive manoeuvre is tested on low friction road. In this manoeuvre the vehicle speed is 32 km/h and after 1.5 s the hand brake is applied for 1 s. Figure 8 shows the lateral vehicle position, the lateral acceleration, the wheel speeds and the steering wheel angle. The friction circle is illustrated in the top right subplot. As can be observed, the vehicle lateral position oscillates after applying the hand brake. However, the controller is able to stabilize the vehicle and keeps the vehicle lateral position within road boundaries.

8 EXPERIMENTAL RESULTS

The controller performance is experimentally assessed using a CarLab, containing a rapid-control prototyping platform (Figure 9). The CarLab is a passenger car on which the standard steering system, ESC sensor set and ACC radar are addressed, only an additional camera is installed. Performance of the proposed controller has been examined for an extensive number of driving scenarios on a proving ground. It should be noted that the Electronic Stability Control (ESC) system of the CarLab is deactivated to prevent any intervention of the ESC system during the evasive maneuver. For the sake of brevity only two driving scenarios that highlight the robustness of the proposed method are discussed.

In the first scenario robustness and performance of the controller to a combined slip maneuver is evaluated. In this experiment the vehicle starts the evasive maneuver with a speed of 90 km/h and the driver applies full braking just before the controller applies the steering angle. Figure 10 illustrates the vehicle response. The controller provides proper steering angle and the vehicle follows the reference path. For comparison the non-combined slip response is plotted, where the brakes are applied only after steering. It is seen, that the controller is capable to maintain the same level of stability and manoeuvrability when braking is applied during cornering.

In the second driving manoeuvre, the robustness of the controller for the worst case scenario is investigated. The vehicle drives with a speed of 32 km/h on the low friction road and the driver applies the hand brake for about 1 s in the start of the maneuver.

Figure 11 shows the vehicle response. It can be seen that the vehicle lateral position deviates from the reference path after applying the hand brake at the time of about 2 s. However, the controller generates appropriate steering angle to stabilize lateral acceleration

www.TechnicalBooksPDF.com



Figure 9. TNO CarLab during an evasive maneuver.

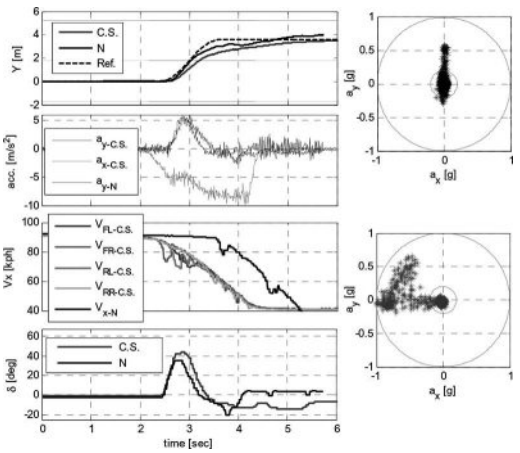


Figure 10. Vehicle response on high friction road surface and combined slip condition (ESC off): lateral vehicle position Y, lateral acceleration a_y, wheels speed V, steering wheel angle δ and friction circle (top right).

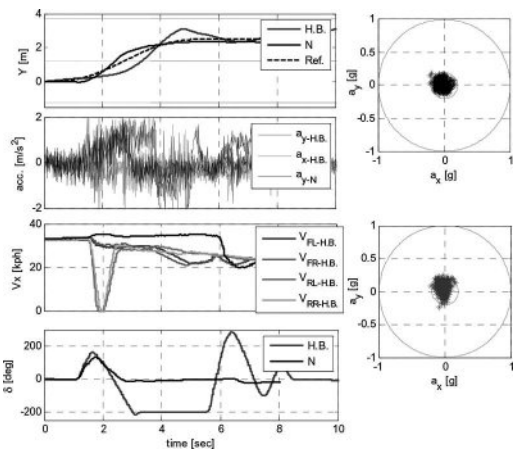


Figure 11. Vehicle response on low friction road surface and extreme oversteer condition (ESC off): lateral vehicle position Y, lateral acceleration a_y, wheels speed V, steering wheel angle δ and friction circle (top right).

of the vehicle and keeps the vehicle lateral position within road boundaries.

9 CONCLUSION

A robustness analysis of the Collision Avoidance System based on the SDRE method for extreme changes in tyre behaviour, as result of low friction and combined slip, has been presented. Friction estimation under very low drive forces has been demonstrated using a slip stiffness concept. When utilizing the identified friction the controller is capable to stabilize the vehicle under a variety of maneuvers while remaining within the lane boundaries. It is concluded that the proposed method shows sufficient robustness for the evasive maneuver on a low friction road and even in extreme oversteer conditions. Finally, with regard to collision avoidance on low friction roads, a reliable and robust all-encompassing friction estimator is a prerequisite, which will require further research.

REFERENCES

Alirezaie, M., Ghaffari, A., Kazemi, R., A SVFC approach to design a robust lane keeping assistance system, *Proc. Int. Symp.* AVEC, 2010.

Alirezaei, M., Corno, M., Ghaffari, A., Kazemi, R., Robust road departure avoidance based on driver decision estimation, *IFAC,* Volumes 44(1), 2011.

Alirezaei, M. et al. 2015. Experimental evaluation of collision avoidance system using state dependent Riccati equation technique. *Proc. of the 24th IAVSD Symposium*.

Cimen, T., State Dependent Riccati Equation (SDRE) Control: A survey, *IFAC*, 2008.

Guldner, J.,Tan, H. and Patwardhan, S., Analysis of automatic steering control for highway vehicles with look-down lateral reference systems, *Vehicle system dynamics*, Vol. 26, 1996.

Gustafsson, F. 1997. Slip-based tyre-road friction estimation. *Automatica* 33(6): 1087–1099.

Kaempchen, N., Schiele, B. and Dietmayer, K., Situation Assessment of an Autonomous Emergency Brake for Arbitrary Vehicle-to-Vehicle Collision Scenarios, *IEEE Transactions on Intelligent Transportation Systems*, Vol. 10, No. 4, 2009.

Leenen, R. and Maurice, J.P. 2010. State estimator for active vehicle control systems. *ATZ Elektron Worldw* (2010) 5: 16. doi:10.1007/BF03242294.

Niessen, B.C., Jansen, S.T.H., Besselink, I.J.M., Schmeitz, A.J.C. and Nijmeijer, H., An enhanced generic single track vehicle model and its parameter identification for 15 different passenger cars, *In Presentation at the 11th international symposium on advanced vehicle control (AVEC '12)*, Seoul, Korea, 2012.

Pacejka, H. B., Tyre and vehicle Dynamics, Butterworth-Heinemann, 2002.

Schmeitz, A.J.C. and Alirezaei, M. 2016. Analysis of wheel speed vibrations for road friction classification. *Vehicle System Dynamics* 54(4): 492–509.

Soudbakhsh, D. et al. 2011. An emergency evasive maneuver algorithm for vehicles. *IEEE Conference on Intelligent Transportation Systems*.

www.TechnicalBooksPDF.com

Advanced Vehicle Control – Edelmann, Plöchl & Pfeffer (Eds)
© 2017 Taylor & Francis Group, London, ISBN 978-1-138-02992-7

Autonomous drifting with onboard sensors

J. Gonzales
Department of Mechanical Engineering, University of California, Berkeley, USA

F. Zhang
Department of Mechanical Engineering, University of California, Berkeley, USA
Department of Automotive Engineering, Tsinghua University, Beijing, China

K. Li
Department of Automotive Engineering, Tsinghua University, Beijing, China

F. Borrelli
Department of Mechanical Engineering, University of California, Berkeley, USA

ABSTRACT: The authors present a controller that achieves autonomous drifting using *only* onboard inertial sensors. Related studies have achieved autonomous drift in passenger or RC cars using motion capture systems or a differential GPS. These systems provide very accurate measurements of position and velocity, but require infrastructure that constrains the location of the experiment.

The proposed design uses only IMU, encoders and camera for state estimation. A state feedback controller uses a single rigid body bicycle model to capture the vehicle dynamics, and the Pajecka tire model to capture the tire forces. We validate the control technique with an open source, low cost 1/10 scale RC vehicle developed at UC Berkeley.

1 INTRODUCTION

Drift, or high side slip cornering, occurs when a skilled driver intentionally maneuvers a vehicle to cause loss of traction in the wheels, but still maintains control of the vehicle. Drift causes a large side-slip angle β to emerge, which roughly speaking, indicates how much 'side-ways' the vehicle is traveling. This angle measures the gap between the lateral and longitudinal velocity vectors, as shown in Figure (1)

$$\beta = \tan^{-1} \frac{v_y}{v_x}. \tag{1}$$

In general, drift is characterized by rear tire saturation and high side slip angle from extreme maneuvers. By studying drift, we can design controllers that respond quickly and safely to unintentional drift conditions.

High side-slip maneuvers fall into one of two categories: sustained drift and transient drift. Sustained drift focuses on stabilizing the vehicle about an unstable equilibrium (e.g. steady state circular drift), while transient drift focuses on briefly maintaining a drift state (e.g. drift parking).

For sustained drift, researchers have validated various control techniques. Hindiyeh and coauthors developed a controller with a successive loop structure using a bicycle model and a tire brush model (Hindiyeh & Gerdes 2014). Velenis and coauthors designed a sliding model controller to maintain drift using a seven-state vehicle model with rear axes differentials (Velenis, Katzourakis, Frazzoli, Tsiotras, & Happee 2011). Cutler used reinforcement learning with a motion caption system to achieve sustained drift (Cutler 2015).

Work on transient drift has also emerged as a research topic for vehicle applications. Chakraborty and coauthors investigated methods for mitigation of unavoidable collisions using optimization, and found a drift maneuver to sometimes be optimal (Chakraborty, Tsiotras, & Diaz 2013). Kolter applied a mixed open-loop and close-loop control with a probabilistic framework to achieve a sliding park on a real vehicle (Kolter, Plagemann, Jackson, Ng, & Thrun 2010). Velenis and coauthors used optimization techniques to study high side-slip cornering in racing (Velenis & Tsiotras 2005).

To the authors' knowledge, all experimental validation for drift control algorithms have used a motion capture systems and/or a differential GPS system (Liniger, Domahidi, & Morari 2015) (Hindiyeh 2013). These systems provide very accurate measurements of position and velocity, but require infrastructure that constrains the location of the experiment.

This paper studies how to achieve drift using only onboard sensors. The remainder of this paper is organized as follows. The vehicle and tire models are

www.TechnicalBooksPDF.com

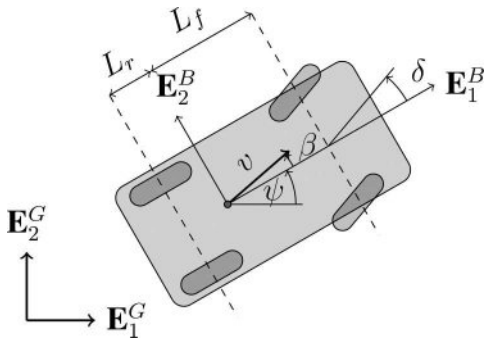


Figure 1. Vehicle model schematic.

discussed in Section 2. Then, drift equilibrium analysis and control algorithm are presented in Section 3 and Section 4, respectively. Model identification and state estimation are discussed in Section 5. The RC platform and experimental results are summarized in Section 6 and Section 7, respectively. Concluding remarks are given in Section 8.

2 VEHICLE MODEL

To capture the vehicle dynamics, we use a single rigid body model with lumped rear wheel and front wheels, called the dynamic bicycle model. The state vector consists of the slip angle β, longitudinal velocity v_x, and the yaw rate $r = \dot{\psi}$, and the input vector consists of the steering angle δ and the rear force F_{xR}, assuming a rear wheel drive system.

The equations of motion for the vehicle dynamics are obtained from the balance of linear and angular momentum, yielding

$$\dot{\beta} = \frac{1}{mv_x}(F_{yF} + F_{yR}) - r \tag{2a}$$

$$\dot{r} = \frac{1}{I_z}(L_f F_{yF} - L_r F_{yR}) \tag{2b}$$

$$\dot{v}_x = \frac{1}{m}(F_{xR} - F_{yF}\sin\delta) + v_x r\beta \tag{2c}$$

where F_{yR} is the lateral force at the lumped rear tire. The parameters m and I_z are the mass and moment of inertia about the z-axis, respectively, and L_f, L_r are geometric dimensions from the CoG to the axels, as shown in Figure (1). The dynamic equations in (2) will later form the basis of our stability analysis and controller design. For the tires, we use a Pajacka model to estimate the lateral force at high tire slip angles

$$F_y(\alpha) = \begin{cases} \mu F_z \sin(C\tan^{-1}(B\alpha)) & : |\alpha| \le \alpha_{cr} \\ -F_y^{\max}\mathbf{sign}(\alpha) & : |\alpha| > \alpha_{cr} \end{cases} \tag{3}$$

where the front and rear tire side slip angles are

$$\alpha_F = \tan^{-1}\left(\beta + \frac{L_f r}{v_x}\right) - \delta \tag{4}$$

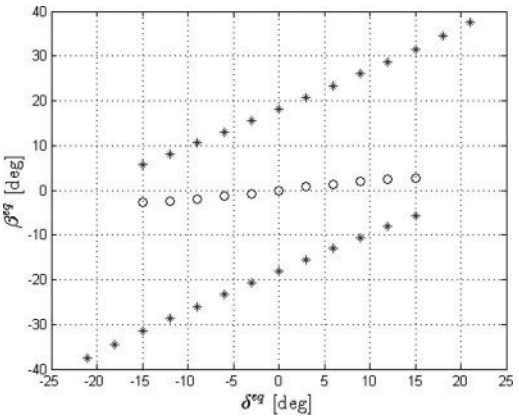


Figure 2. Equilibrium sideslip angle vs steering angle.

$$\alpha_R = \tan^{-1}\left(\beta - \frac{L_r r}{v_x}\right) \tag{5}$$

and $F_y^{\max}$ is the maximum lateral force as modeled by the 'friction circle', defined as follows

$$F_y^{\max} = \sqrt{(\mu F_z)^2 - F_x^2} \tag{6}$$

where μ is the coefficient of friction, F_z is the load force, B and C are fitting parameters, and α_{cr} is the critical slip angle, beyond which the tires cannot generate additional force

$$\alpha_{cr} = \tan\left(\sin^{-1}\left(\frac{\sqrt{F_z^2 - F_x^2}}{\mu F_z}\right)/C\right)/B. \tag{7}$$

3 DRIFT EQUILIBRIUM ANALYSIS

In general, countersteer, rear tire saturation, high side slip angles β, and high yaw rates r all characterize typical drift conditions. We first present an analysis on the behavior of the vehicle in *steady state* drift (i.e. continuous drift with constant state and input values). These equilibria states will help us build reference states in the controller formulation.

For any nonlinear system $\dot{\mathbf{z}} = f(\mathbf{z}, \mathbf{u})$, with $\mathbf{z}$ as the state vector and $\mathbf{u}$ as the input vector, the equilibrium of the system occur at values $\mathbf{z}^{eq}$ and $\mathbf{u}^{eq}$, such that $f(\mathbf{z}^{eq}, \mathbf{u}^{eq}) = \mathbf{0}$. That is, we solve for the equilibria state and input values by setting all of the system derivatives to zero. The analysis is discussed in depth in (Voser, Hindiyeh, & Gerdes 2010).

The equilibrium states of the three-state model are shown from Figure (2) to Figure (4). The vehicle parameters used here are summarized in Section 6, with the longitudinal speed set at $v_x = 1.2$ m/s. The plots illustrate two kinds of equilibrium: normal corning (circle) and drifting (asterisks). For normal cornering, the sideslip angle is small, and the yaw rate and steering angle hold the same sign. For drifting, the sideslip angle is large, and the yaw rate and steering angle have opposite signs.

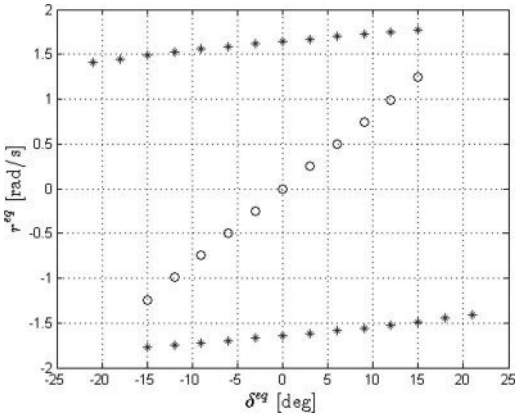


Figure 3. Equilibrium yaw rate vs steering angle.

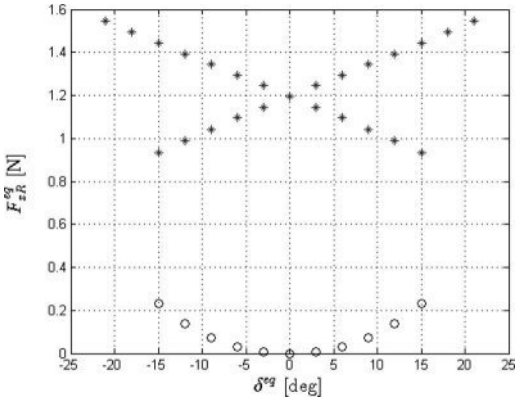


Figure 4. Equilibrium rear wheel force vs steering angle.

Table 1. Offline control design.

1 Define the equilibrium point
$\beta^{eq}, r^{eq}, v_x^{eq}, \delta^{eq}, F_{yF}^{eq}, F_{yR}^{eq}, F_{xR}^{eq}$
2 Linearize vehicle model about equilibrium point
3 Define the feedforward-feedback control policy
$\mathbf{u} = \mathbf{u}^{eq} + \Delta\mathbf{u}$
$\Delta\mathbf{u} = -K\Delta\mathbf{z}$
4 Compute the input limits $\mathbf{u}_{\min}, \mathbf{u}_{\max}$ using the friction circle
5 Find the region of attraction where LQR is stabilizing and does not violate input limits

4 CONTROL LAW

The objective of the controller is to stabilize the vehicle around the designed equilibrium drifting point. We construct an offline LQR controller with actuation limits according to Table 1, and apply an online scheme according to Table 2.

Table 2. Online control design.

1 Conduct open loop maneuver: drive the vehicle into the region of attraction (point 5 of Table 1)
2 Couduct close loop maneuver: compute synthetic inputs $F_{yF}^{des}, F_{xR}^{des}$ and map them to steering input, motor torque

We linearize the system around the equilibrium state and then transform the system to reflect the error dynamics, as below:

$$\Delta\dot{\mathbf{z}} = A\Delta\mathbf{z} + B\Delta\mathbf{u} \tag{8}$$

where $\Delta\mathbf{z} = [\Delta\beta, \Delta r, \Delta v_x]^T = (\mathbf{z} - \mathbf{z}^{eq})^\top$ is the state vector, and $\Delta\mathbf{u} = [\Delta F_{yF}, \Delta F_{xR}]^T = (\mathbf{u} - \mathbf{u}^{eq})^\top$ is the input vector. A and B are the Jacobian matrix of system states and control inputs.

The controller used here employs a feedforward-feedback structure, with F_{yF}^{des} and F_{xR}^{des} acting as synthetic inputs. These inputs are then mapped to motor (for F_{xR}) and servo (for δ) commands that control the vehicle. This is explained in detail in the next section.

The design of the LQR controller policy is based on the system in (8). We define a quadratic cost function

$$J = \int_{t=0}^{\infty} (\Delta\mathbf{z}^T Q \Delta\mathbf{z} + \Delta\mathbf{u}^T R \Delta\mathbf{u}) dt \tag{9}$$

where $Q = Q^T \geq 0$, $R = R^T \geq 0$. The control input u that minimizes the cost function is given by

$$\Delta\mathbf{u} = -R^{-1}B^T P\Delta\mathbf{z} = -K\Delta\mathbf{z} \tag{10}$$

where $P = P^T > 0$, which can be obtained by solving the Riccati Equation.

Since the LQR controller tries to maintain a state near the drift equilibrium point, the front wheels are often nearly or completely saturated. This means that the synthetic inputs F_{yF}, F_{xR} have a limited bandwidth to operate before saturating. To design for this, the control input should also satisfy the following constraint

$$\mathbf{u}_{\min} \leq \mathbf{u}^{eq} + \Delta\mathbf{u} \leq \mathbf{u}_{\max} \tag{11}$$

where $\mathbf{u}_{\min}$ and $\mathbf{u}_{\max}$ are set based on the fiction limit. The state space region where the LQR is stabilizing and does not violate the input limits is

$$\begin{aligned} &\max \quad \gamma \\ &\text{s.t.} \quad \Delta\mathbf{z}^T P \Delta\mathbf{z} \leq \gamma \\ &\qquad H\Delta\mathbf{z} \leq \mathbf{w} \end{aligned} \tag{12}$$

where $H = \begin{bmatrix} K \\ -K \end{bmatrix}, \mathbf{w} = \begin{bmatrix} \mathbf{u}_{\max} - \mathbf{u}^{eq} \\ \mathbf{u}_{\min} - \mathbf{u}^{eq} \end{bmatrix}$.

During online control, an open loop maneuver is conducted first to drive the vehicle into the attraction region. Once the system states are inside this

region, the closed loop maneuver is activated. The online control inputs are computed according the feedforward-feedback control policy. Further details, including the analytic expressions for the entries of A, B and computation of the region of attraction, are available in the technical report[1].

5 MODEL IDENTIFICATION AND STATE ESTIMATION

In this section, we discuss system parameters identification (namely pajecka model parameters) as well as the formulation of the state observer.

5.1 *Longitudinal dynamics*

We use a nonlinear observer to improve state estimation in the longitudinal dynamics. Based on equation (2), we define the following expression for the longitudinal rear force F_{xR}

$$F_{xR} = F_{\text{motor}} + F_f + F_{\text{drag}} \tag{13}$$

which consists of the input motor force F_{motor}, the friction force F_f, and the drag force $F_{\text{drag}} = C_D v_x^2$, where C_D is the aerodynamic drag coefficient. We add these terms in our observer to enhance model fidelity, and hence compute a more accurate estimate of the state. In the previous section on controller design, we intentionally ignore the friction and air drag force (i.e. assume $F_{xR} = F_{\text{motor}}$).

In order to solve for the constants F_f and C_D, we perform a nonlinear least squares optimization using the longitudinal model in (2) as follows,

$$\min_{F_f, C_D} \left|\left| \dot{v}_x - \frac{1}{m}(F_{xR} + F_f + C_D v_x^2) \right|\right|_2^2 \tag{14}$$
$$\text{s.t.} \quad F_f, C_D \geq 0$$

To generate experimental data, we run short step-input tests with a fixed steering angle, $\delta = 0$; each test has a different motor input F_{xR}.

5.2 *Tire model*

To identify the tire model, the RC is driven in circles, with fixed inputs to reach a steady state condition. After several tests from a range of steering angles δ and motor inputs F_{xR}, we solve the following optimization

$$\min_{B,C,\mu,\boldsymbol{\beta}} \left|\left| \begin{bmatrix} \dot{\beta} - \frac{1}{m v_x}(F_{yF} + F_{yR}) + r \\ \dot{r} - \frac{1}{I_z}(L_f F_{yF} - L_r F_{yR}) \end{bmatrix} \right|\right|_2^2$$
$$\text{s.t.} \qquad \forall i \in 1, 2, 3, \ldots n \tag{15}$$
$$\alpha_F, \alpha_R = \text{side slip in eq (5)}$$
$$F_{yF}, F_{yR} = \text{tire force in eq (3), (6)}$$

[1] Technical Report available here

Note that in the above optimization, the parameters $B, C, \mu \in \mathbb{R}$ are scalars, while $\beta \in \mathbb{R}^n$ is a vector.

5.3 *Optical flow*

We use an onboard camera to estimate longitudinal and lateral velocity using a technique called optical flow. Optical flow methods calculate the motion between two image frames by computing spatial and temporal gradients of the brightness, and then solving the following equation

$$I_x v_x + I_y v_y + I_t = 0 \tag{16}$$

where I_x, I_y, I_t are the two spatial derivatives and temporal derivative, respectively, and v_x is the optical flow along the x-direction, and v_y is the optical flow along the y-direction. The details of this computation are found in (Fleet & Weiss 2006).

For implementation, we capture images with an upward-facing two mega-pixel camera, and then apply the Lucas-Kanade optical flow algorithm using the Open Computer Vision (OpenCV) library.

5.4 *State estimation*

For state estimation, we apply an Extended Kalman Filter (EKF) that uses the vehicle model in (2), with the longitudinal dynamics in (13) and the tire model in (3). We model process noise $w[k]$ and measurement noise $v[k]$ at time step k as Gaussian with zero mean and covariance Q_k and R_k , respectively.

6 EXPERIMENTAL PLATFORM

The authors use a low-cost 1/10 scale RC vehicle platform, called Berkeley Autonomous Race Car (BARC)(UCB-MPC 2015), to validate the control design. The RC vehicle is shown in Figure (5). The BARC vehicle is a low-cost development platform for autonomous driving to achieve complex maneuvers such as drifting, lane changes, and obstacle avoidance. Another aspect emphasized in the software design is the cloud-services integration.

The RC vehicle is controlled through the use of a microcontroller and a suite of sensors. These electronics are enclosed in a custom-designed aluminum shell that is designed to hold the microcontroller and sensors and protect the on-board electronics. The sensor suite consists of an inertial measurement unit, a set of encoders (one for each wheel), and a two mega-pixel monocamera.

The BARC platform uses ROS, an open-source library and set of tools for programming robots. The architecture abstracts low level details, like timing, communication protocols, concurrency, and other processes by providing a simple programming paradigm with a well-written, easy-to-use set of application programming interfaces (APIs).

The parameters of RC-car and tires are summarized in Table 3.

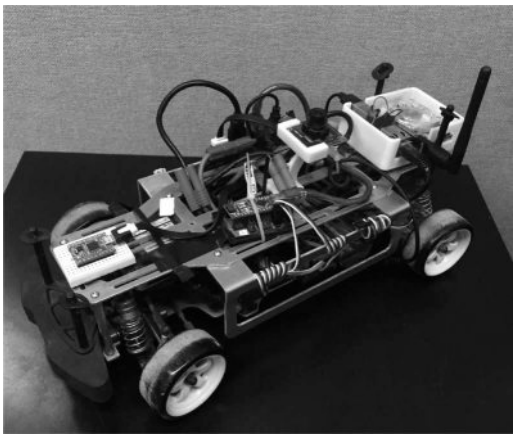


Figure 5. Berkeley Autonomous Race Car (BARC).

Table 3. RC-car parameters.

Parameter	Value	Parameter	Value
m [kg]	1.95	h [m]	0.05
I_z [kg · m^2]	0.24	B	7.4
L_f [m]	0.125	C	1.25
L_r [m]	0.125	μ	0.234

Table 4. CarSim vehicle parameters.

Parameter	Value	Parameter	Value
m [kg]	1830	h [m]	0.59
I_z [kg · m^2]	3287	B	12.6
L_f [m]	1.4	C	1.41
L_r [m]	1.65	μ	1.00

7 RESULTS

7.1 *Results from simulation*

We initially validated the controller design using Carsim, a high fidelity vehicle simulation software. We used an A-class vehicle as the plant since the software suite did not provide any models at the scale of an RC-car. The parameters of the vehicle and tires while stationary are summarized in Table 4. For simulation, we set the equilibrium drift point at $\beta = -0.32$ rad, $r = 0.36$ rad/s, and $v_x = 25$ m/s, with an initial state of of $\beta^{eq} = 0$ rad, $r^{eq} = 0$ rad/s, and $v_x^{eq} = 2\,5$m/s. We also designed a short open-loop maneuver to bring the vehicle in a region of the state space that would active the closed loop LQR controller. Once in the LQR region of attraction, the controller stabilizes the vehicle around that equilibrium state.

The vehicle states and control inputs during simulation are shown in Figure (6) and Figure (7). The blue lines in Figure (6) show the simulation measurements and the red lines show the control reference. For

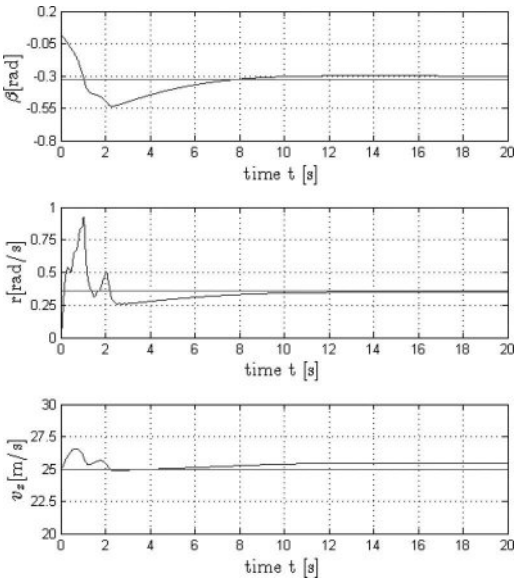


Figure 6. System states in CarSim simulation.

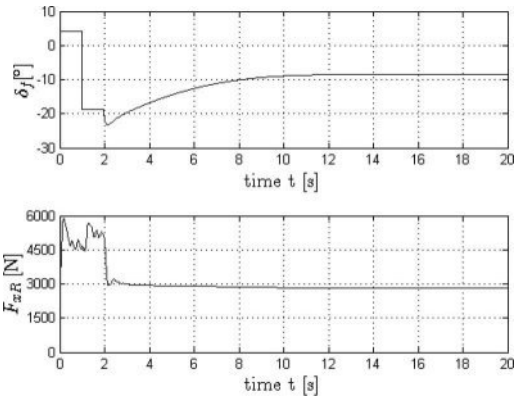


Figure 7. Control inputs in CarSim simulation.

$t < 2$ s, the open-loop maneuver is active, and at $t = 2$ s, the closed loop controller is activated. As Figure (6) shows, the state of the vehicle converges to a steady-state condition, and reaches an equilibrium of $x = \left[-0.48, 0.39, 26\right]^{\mathrm{T}}$ around $t = 10$ s. From the simulation results, we observe an interplay between the yaw rate and side slip angle dynamics, namely that in order for the magnitude of the side slip angle to increase, the magnitude of the yaw rate needs to decrease. Decreasing the rear lateral force decreases the yaw rate, but also decreases the longitudinal velocity. The LQR controller rapidly manipulates the steering angle and longitudinal force to satisfy these competing objective. We observe this from time $t = 3.5$ s onward.

Notice that, the final states do not exactly converge to the designed equilibrium state. This is due to model mismatch in the weight transfer and tire models.

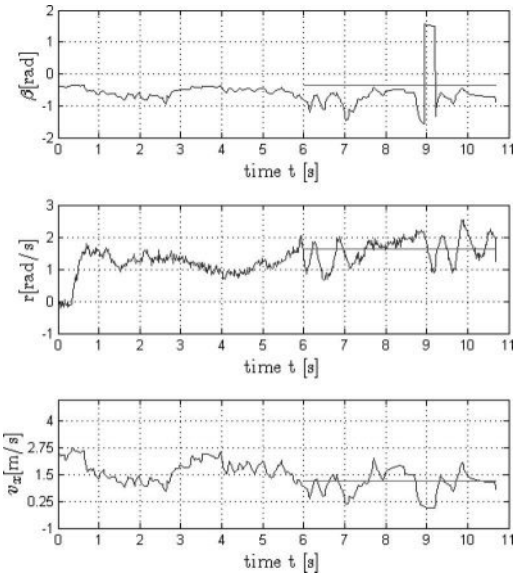


Figure 8. System states in an experiment with BARC car.

7.2 *Results from experimentation*

As with simulation, we apply an open loop and closed loop controller for the RC vehicle. The vehicle states and control inputs are shown in Figure (8) and Figure (9), with an initial vehicle state around $x = [0, 0, 2.7]^{\mathrm{T}}$, and the desired equilibrium state at $x = [-0.36, 1.62, 1.2]^{\mathrm{T}}$. Again, the blue lines denote the measured values and the red lines denote the control reference.

For the open loop maneuver, the RC-car accelerates to a certain the desired longitudinal speed and then turns to the left at a fixed degree. Shortly after turning, the LQR controller is activated, and the steering angle moves in the opposite direction (positive to negative), but the yaw rate still maintains a high positive value. At the same time, the rear wheel torque notably increases. Note that a distinct feature of drift comes from the difference in sign between the steering angle and yaw rate, so while the steering wheel is pointing one direction, the vehicle is actually rotating in the other direction. The peak value in side slip plot at 9 s is due to the sudden jump of lateral velocity measurement. A video of the experiment can be found here.

8 CONCLUSIONS

In this paper, we demonstrated an LQR control scheme capable of achieving autonomous drifting using *only* onboard inertial sensors, with a sensor suite consisting of an inertial measurement unit, encoders and camera. We provide validated our method through simulation, using CarSim, and through experimentation, using a 1/10 scale remote control vehicle.

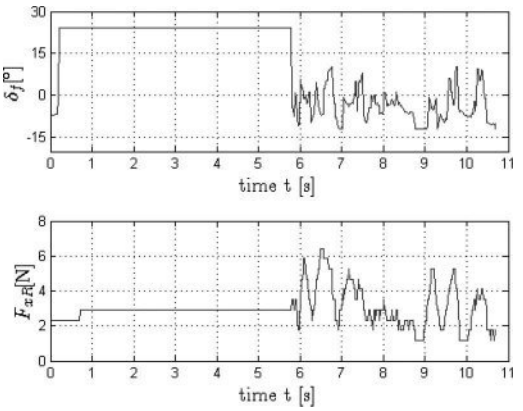


Figure 9. Control inputs in an experiment with BARC car.

Future work includes selecting better low cost sensors and enhancing filtering to get better measurements. The optical flow produces consistent measurements in an indoor setting, but can be challenging to tune and filter initially.

REFERENCES

Chakraborty, I., P. Tsiotras, & R. S. Diaz (2013). Time-optimal vehicle posture control to mitigate unavoidable collisions using conventional control inputs. In *2013 American Control Conference*, pp. 2165–2170. IEEE.

Cutler, M. J. (2015). *Reinforcement learning for robots through efficient simulator sampling*. Ph. D. thesis, Massachusetts Institute of Technology.

Fleet, D. J. & Y. Weiss (2006). *Handbook of Mathematical Models in Computer Vision*. Springer.

Hindiyeh, R. Y. (2013). *Dynamics and Control of Drifting in Automobiles*. Ph. D. thesis, Stanford University.

Hindiyeh, R. Y. & J. C. Gerdes (2014). A controller framework for autonomous drifting: Design, stability, and experimental validation. *Journal of Dynamic Systems, Measurement, and Control 136*(5), 051015.

Kolter, J. Z., C. Plagemann, D. T. Jackson, A. Y. Ng, & S. Thrun (2010). A probabilistic approach to mixed open-loop and closed-loop control, with application to extreme autonomous driving. In *Robotics and Automation (ICRA), 2010 IEEE International Conference on*, pp. 839–845. IEEE.

Liniger, A., A. Domahidi, & M. Morari (2015). Optimization-based autonomous racing of 1: 43 scale rc cars. *Optimal Control Applications and Methods 36*(5), 628–647.

UCB-MPC (2015). Berkeley autonomous race car project. http://www.barc-project.com/.

Velenis, E., D. Katzourakis, E. Frazzoli, P. Tsiotras, & R. Happee (2011). Steady-state drifting stabilization of rwd vehicles. *Control Engineering Practice 19*(11), 1363–1376.

Velenis, E. & P. Tsiotras (2005). Minimum time vs maximum exit velocity path optimization during cornering. In *2005 IEEE international symposium on industrial electronics*, pp. 355–360.

Voser, C., R. Y. Hindiyeh, & J. C. Gerdes (2010, dec). Analysis and control of high sideslip manoeuvres. *Vehicle System Dynamics 48*(sup1), 317–336.

Advanced Vehicle Control – Edelmann, Plöchl & Pfeffer (Eds)
© 2017 Taylor & Francis Group, London, ISBN 978-1-138-02992-7

A new nonlinear model predictive control algorithm for vehicle path tracking

Georg Schildbach
Elektronische Fahrwerksysteme GmbH

ABSTRACT: Model Predictive Control (MPC) is a powerful technique to control nonlinear, multi-input multi-output systems with input and state constraints. It has previously been considered for trajectory tracking control of automated vehicles in many projects. However, MPC faces several challenges in practice, mainly regarding computation time and difficulty of implementation. This paper presents a new MPC algorithm that addresses both challenges, specifically for the problem of trajectory tracking. The algorithm comes with a code generator for open-source, library-free C-code with static memory allocation. Thus it can directly be deployed to a wide range of embedded control units (ECUs). The algorithm consists of a single controller block, which only requires adjustment of specific vehicle and tuning parameters. Preliminary simulation results show the effectiveness of the code, with computation times in the range of a few milliseconds.

1 INTRODUCTION

Vehicle motion control. Motion control for the automation of vehicles typically comprise, at a minimum, one *planner* for trajectory generation and one *controller* for trajectory tracking (Campbell et al. 2010). The planner creates a reference trajectory (or path) that reflects decisions on where to avoid obstacles, when to change lanes, and how to achieve a given driving goal. The controller commands the steering and throttle/brake of the vehicle, with the objective of tracking a given reference trajectory.

For a good overall performance, the reference trajectory should be compatible with the vehicle dynamics and respect the actuation constraints, so that a good tracking performance can be achieved. If these requirements are not satisfied, the controller may be difficult to tune, produce large tracking errors, or even become unstable.

However, the planning of reference trajectories is a difficult problem that must be solved fast and with limited resources. Therefore, some requirements tend to be relaxed. Common approaches include decoupling of the lateral and longitudinal vehicle motion (i.e., computing paths instead of trajectories), neglecting dynamic feasibility (i.e., drivability of the path), ignoring actuator constraints, or sacrificing smoothness of the input signals (Dolgov et al. 2010). Other approaches choose a heuristic to find a coarse (sub-optimal) solution by limiting the search to a small subset of paths, e.g., defined by pre-selected basis functions or sampled at random (Werling et al. 2010).

Model Predictive Control (MPC). MPC is a holistic method to control nonlinear, multi-input multi-output systems with input and state constraints. As such, it is naturally suited for problems in vehicle control and has been used extensively in similar projects, e.g., Dolgov et al. 2010, Gao et al. 2010, Gutjahr and Werling 2015, Kong et al. 2015, Lima 2016, Ziegler et al. 2014. The novelty of this paper concerns a new solver and code generator, as discussed below.

The considered MPC formulation cannot make discrete choices, nor find a globally optimal path. Therefore it has to rely on a path planner for a reference trajectory (Dolgov et al. 2010). However, the MPC can significantly lower the requirements for the path planner and deliver an excellent control performance (Ziegler et al. 2014).

The MPC accepts a reference trajectory of no particular functional form (arc, clothoid, sigmoid, etc.), thus it can be applied in different situations (highway, parking, etc.). The input is a piecewise linear path with a desired velocity profile, both of which may be generated independently. The path does not have to be dynamically feasible or respect the vehicle's actor limits. The MPC automatically respects these limits, as well as safety constraints. Safety constraints specify driving areas that must be avoided at all cost, e.g., obstacles or lane boundaries. The controlled car follows a feasible and drivable trajectory close to the reference path, while using the actuation smoothly. Here 'close' and 'smooth' are defined by a tunable cost function.

New contributions. The key drawbacks of MPC implementations are its computational burden and integrating the controller on embedded control units (ECUs). This paper improves on both challenges by developing a new nonlinear active set (NAS) solver for the underlying nonlinear, multi-stage optimization program (NMOP) and generating corresponding C-code for a single controller block. The solver is easy to use, even for non-MPC-experts, and independent of other software packages. The open-source code

generator can be used to obtain library-free, static-memory C-code, which can simulated in Simulink or integrated on most ECUs:
`https://app.box.com/s/lmmkpakkx177362wz9b0t5ycs9opxe7h`

Existing solvers for NMOPs are mostly built on interior-point (IP) or sequential quadratic programming (SQP) methods (Diehl et al. 2009). IP methods are highly effective for medium-/large-scale linear and nonlinear programs. However, they have a limited capability for *warm-starting*, which can have a great impact on the computational burden of MPC (Axehill and Hansson 2008). SQP methods solve a sequence of local quadratic programs (QPs), e.g., by an active set method, which is very efficient for linear MPC problems. However, due to the highly nonlinear nature of vehicle motion control, convergence of the overall problem can be difficult or slow. The NAS instead performs a nonlinear line search, can be warm-started, and always preserves primal feasibility of the solution, while it monotonically improves the objective function value.

A variety of software already exists for solving NMOPs, including commercial packages such as PROPT (Rutquist and Edvall 2010) and FORCES (Domahidi 2013), or open-source projects such as IPOPT (Wächter and Biegler 2005) or ACADO (Houska et al. 2011). However, only some of them can generate stand-alone C code that can be integrated on ECUs, and none of them is specifically tailored for the vehicle path tracking problem.

2 PROBLEM DESCRIPTION

Model. In this paper, a kinematic bicycle model is used as the MPC model. It is illustrated in Figure 1 and its equations of motion read as

$$\frac{\mathrm{d}}{\mathrm{d}t}\begin{bmatrix}\xi\\ \eta\\ \varphi\\ v\\ \delta\end{bmatrix} = \begin{bmatrix} v\cos(\varphi+\beta)\\ v\sin(\varphi+\beta)\\ v\cos\beta/\left(l_f+l_r\right)\tan\delta\\ a\\ \dot{\delta}\end{bmatrix}, \qquad (1)$$

where

$$\beta = \tan^{-1}\left(\frac{l_r}{l_f+l_r}\tan(\delta)\right).$$

The model (1) has $n = 5$ states (global coordinates ξ, η, φ and augmented states v, δ) and $m = 2$ control inputs (a, $\dot{\delta}$). The two augmented states have been created as integrators of the two control inputs, in order to smooth the longitudinal and lateral dynamics. This allows for cost weights, and also rate limits, to be placed on the derivatives of v and δ, as detailed below.

The Center of Gravity (CoG) serves as the vehicle's coordinate reference point; see Figure 1. The vehicle model (1) has two parameters, the distance from the CoG to the rear axle (l_r) and to the front axle (l_f). Both parameters must be specified as `lf`, `lr` to generate code for the controller.

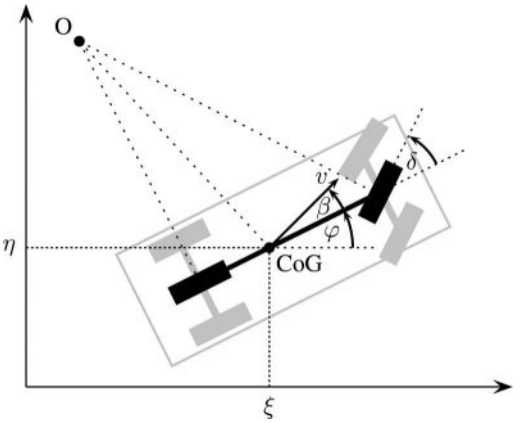


Figure 1. Kinematic bicycle model (black) of a four-wheel car (gray). CoG: center of gravity, O: instantaneous center of rotation.

The model (1) is formulated in continuous time; here $\frac{\mathrm{d}}{\mathrm{d}t}$ represents the derivative with respect to time t. It will be discretized according to a selected *sampling time* t_s (code parameter `dt`). The discrete prediction steps $t = it_\mathrm{s}$ are denoted by $i = 0, 1, 2, \ldots$. During each sample time period i, the control inputs (denoted $u_i \triangleq \left[a_i,\ \dot{\delta}_i\right]^\mathrm{T}$) are held constant. The differential equations (1) are integrated by a classical Runge-Kutta (RK4) scheme that yields the vehicle states (denoted $x_i \triangleq [\xi_i,\ \eta_i,\ \phi_i,\ v_i,\ \delta_i]^\mathrm{T}$) at the end of time step i. In short, the model is written as

$$x_{i+1} = f_{t_\mathrm{s}}\left(x_i, u_i\right), \quad \text{for } i = 0, 1, 2, \ldots. \qquad (2)$$

Reference. A desired *reference path* must be provided for the path tracker. There are few conditions on the path itself. In particular, it does not have to be drivable or of a specific functional form (arc, clothoid, sigmoid, etc.). It may even pass through obstacles, which are avoided explicitly by state constraints; see Figure 2 for an illustration.

The path is represented by a list of linear elements $j = 1, \ldots, N_\mathrm{path}$ with the following information: the coordinates of the starting point ξ_j η_j; the element's orientation φ_j; the reference speed v_j and steering angle δ_j; and the element's length l_j.

For the proper working of the path tracker, however, the path should be 'not too jerky' and the vehicle 'not too far' away from it. In other words, a simple projection of the CoG onto the piecewise linear path, to generate a local reference, should always be possible and meaningful. In this paper, the reference path will be static of a predefined size (parameter: `pathsize`). In practice, it may be generated or changed dynamically by a path planner.

Cost Function. Based on the projection of the CoG onto the reference path, a list of *reference states* ($x_{\mathrm{ref},i} \triangleq \left[\xi_{\mathrm{ref},i},\ \eta_{\mathrm{ref},i},\ \phi_{\mathrm{ref},i},\ v_{\mathrm{ref},i},\ \delta_{\mathrm{ref},i}\right]^\mathrm{T}$) is selected along the path. The objective is then to minimize the deviation of the model predicted vehicle

trajectory over a given number of time steps $i = 1, \ldots, N$, where N denotes the *prediction horizon*. The *cost function* is the sum of N quadratic stage cost terms $\ell_i : \mathbb{R}^m \times \mathbb{R}^n \to \mathbb{R}^+$:

$$\ell_i(u_{i-1}, x_i) = r_a(a_{i-1} - a_{\mathrm{ref},i-1})^2 + r_{\dot\delta}(\dot\delta_{i-1})^2 + q_\xi(\xi_i - \xi_{\mathrm{ref},i})^2 + q_\eta(\eta_i - \eta_{\mathrm{ref},i})^2 + q_\varphi(\varphi_i - \varphi_{\mathrm{ref},i})^2 + q_v(v_i - v_{\mathrm{ref},i})^2 + q_\delta(\delta_i - \delta_{\mathrm{ref},i})^2 \quad . \tag{3}$$

Here q_ξ, q_η, q_φ, q_v, q_δ denote (positive) *state weights* and r_a, $r_{\dot\delta}$ (positive) *input weights*. All weights are initially selected via parameters `Q` and `R`, and can be tuned online.

Input Constraints. The minimization of the cost function is subject to actuation limits. The code permits bounds on the control inputs ($i = 0, \ldots, N-1$)

$$a_{\min} \le a_i \le a_{\max} \quad , \tag{4a}$$

$$-\dot\delta_{\max} \le \dot\delta_i \le +\dot\delta_{\max} \quad , \tag{4b}$$

as well as rate constraints ($i = 0, \ldots, N-1$)

$$\dot a_{\min} \le (a_i - a_{i-1})/t_s \le \dot a_{\max} \quad , \tag{5a}$$

$$-\ddot\delta_{\max} \le (\dot\delta_i - \dot\delta_{i-1})/t_s \le \ddot\delta_{\max} \quad . \tag{5b}$$

All intervals must be non-empty and contain 0. The lower and upper limits of all constraints can be specified via parameters `amin`, `amax`, `dmax`, `d_amin`, `d_amax`, `d_dmax` in the MPC code:

$$u_{\min} \triangleq \left[a_{\min};\ -\dot\delta_{\max}\right] \quad , \tag{6a}$$

$$u_{\max} \triangleq \left[a_{\max};\ +\dot\delta_{\max}\right] \quad , \tag{6b}$$

$$\Delta u_{\min} \triangleq \left[\frac{\dot a_{\min}}{t_s};\ \frac{-\ddot\delta_{\max}}{t_s}\right] \quad , \tag{6c}$$

$$\Delta u_{\max} \triangleq \left[\frac{\dot a_{\max}}{t_s};\ \frac{+\ddot\delta_{\max}}{t_s}\right] \quad . \tag{6d}$$

Note that input constraints are formulated as hard constraints and their satisfaction will be guaranteed at all times by the MPC algorithm.

State Constraints. State constraints on the CoG coordinates ξ, η are used to model areas where it is undesirable or unsafe for the vehicle to drive. For example, the drivable area can be limited by road/lane boundaries, or occupied by other traffic participants.

State constraints are included in the optimization as soft constraints, to avoid infeasibility of the optimization program (Scokaert and Rawlings 1999). A reasonable safety margin should always be added to these constraints as a compensation for noise and model uncertainty. The slope (and shape) of the penalty function is manually adjustable. It should be selected such that state constraints are given priority over the cost function (3).

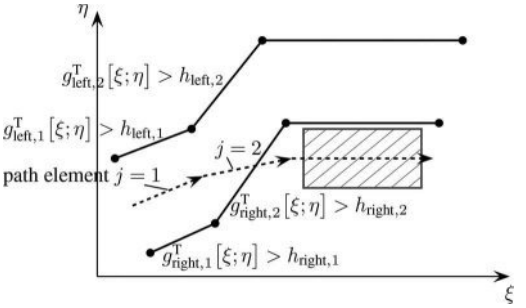


Figure 2. Example of reference path (dashed line) with state constraints (solid lines), around an obstacle (hatched gray rectangle).

To avoid discontinuities in the objective function, the kink in a linear penalty function is interpolated by a quadratic function. The interpolation is valid within a small neighborhood inside the infeasible region, as defined by a parameter $h_{\mathrm{tol}} > 0$ (`contolerance`). The constraints come in the form of two half-spaces, one to the left and one to the right of the controlled vehicle, as shown in Figure 2:

$$g^{\mathrm{T}}_{\mathrm{left},i}[\xi_i;\ \eta_i] \le h_{\mathrm{left},i} \quad , \tag{7a}$$

$$g^{\mathrm{T}}_{\mathrm{right},i}[\xi_i;\ \eta_i] \le h_{\mathrm{right},i} \quad . \tag{7b}$$

The time index $i = 1, ..., N$ indicates that there are two constraints at each prediction step. The constraints are associated with, and stored with, each linear element of the reference path. All state vectors in (7a) are normalized to

$$\left\|g_{\mathrm{left},i}\right\|_2 = 1 \quad , \qquad \left\|g_{\mathrm{right},i}\right\|_2 = 1 \quad . \tag{8}$$

The *penalty functions* $p_{\mathrm{left},i}(\cdot,\cdot)$ and $p_{\mathrm{right},i}(\cdot,\cdot)$ for all stages are added to the cost function, with a penalty parameter $p_{\mathrm{pen}} \ge 0$ (`conpenalty`):

$$p_{\diamond,i}(x_i) = p_{\mathrm{pen}} \cdot \begin{cases} \frac{1}{2h_{\mathrm{tol}}}\left(g^{\mathrm{T}}_{\diamond,i}[\xi_i;\ \eta_i] - h_{\diamond,i}\right)^2 \\ \qquad \text{if} \quad 0 < g^{\mathrm{T}}_{\diamond,i}[\xi_i;\ \eta_i] - h_{\diamond,i} \le h_{\mathrm{tol}} \\ g^{\mathrm{T}}_{\diamond,i}[\xi_i;\ \eta_i] - h_{\diamond,i} \\ \qquad \text{if} \quad h_{\mathrm{tol}} < g^{\mathrm{T}}_{\diamond,i}[\xi_i;\ \eta_i] - h_{\diamond,i} \end{cases} , \tag{9}$$

where $\diamond \in \{\mathrm{left}, \mathrm{right}\}$. Note that (9) and (3) are all continuously differentiable, and so is the overall objective function (Nocedal and Wright 2006).

Summary. The overall *nonlinear multi-stage optimization program* (NMOP) to be solved by the MPC at each time step reads as follows:

$$\min \quad \sum_{i=1}^{N} \ell_i(u_{i-1}, x_i) + p_{\text{left},i}(x_i) + p_{\text{right},i}(x_i) \tag{10a}$$

$$\text{s.t.} \quad x_{i+1} = f_{t_s}(x_i, u_i) \ , \tag{10b}$$

$$u_{\min} \le u_i \le u_{\max} \ , \tag{10c}$$

$$\Delta u_{\min} \le u_i - u_{i-1} \le \Delta u_{\max} \ , \tag{10d}$$

where $i = 0, \ldots, N-1$ in (10b–d).

The optimal control inputs over the prediction horizon, resulting from solving NMOP at time step k, are denoted $U_k^\star \triangleq [u_{0,k}^\star;\, u_{1,k}^\star;\, \ldots\, u_{N-1,k}^\star]^{\mathrm{T}}$. Here time index $k = 0, 1, 2, \ldots$ is used to represent the actual (i.e., closed-loop) time $t = kt_s$, as opposed to the prediction time steps $i = 1, \ldots, N$ inside the NMOP. The actual vehicle state (that is, $\xi_k, \eta_k, \phi_k, v_k, \delta_k$) is assumed to be measured in each time step k and then substituted for ξ_0, η_0, ϕ_0, v_0, δ_0 in (10b).

The reference path is piecewise linear (with N_{path} line segments), where each line segment $j = 1, ..., N_{\text{path}}$ includes the following information:

$$\left[\xi_j; \eta_j; \varphi_j; v_j; \delta_j; l_j; g_{\text{left},j}; h_{\text{left},j} g_{\text{right},j}; h_{\text{right},j}\right] \in \mathbb{R}^{12} \ .$$

3 NONLINEAR ACTIVE SET METHOD

Initialization. The iterations of the NAS method are counted with $j = 1, 2, \ldots$ (not to be confused with the numbering of path elements). $U_k^{(j)}$ denotes the computed input sequence at time step k after iteration j. The solver is initialized (warm started) with the shifted solution of the previous time step $k-1$:

$$U_k^{(0)} = \left[u_{1,k-1}^\star;\, u_{2,k-1}^\star;\, \ldots\, u_{N-1,k-1}^\star;\, u_{N-1,k-1}^\star\right] \ .$$

This sequence is canonically feasible with respect to the (input) constraints and generally yields a very good starting point in terms of the objective function.

Search Direction. At time k, the algorithm starts from $U_k^{(0)}$ and the corresponding initial set of active constraints $\mathcal{A}_k^{(0)}$. The *set of active constraints* at iteration j is a subset of the constraints (10c,d) in the NMOP,

$$\mathcal{A}_k^{(j)} \subset \{1, 2, \ldots, (4N-2)m\} \ . \tag{11}$$

There are $a = 1, 2, \ldots, (4N-2)m$ constraints in total, for which the following more general notation will be used:

$$g_l(u_{k,i}^{(j)}) \le 0 \ , \quad \text{where } g_l(u_{k,i}^{(j)}) = 0 \ \text{ if } \ l \in \mathcal{A}_k^{(j)} \ .$$

The first step in each iteration j is to find the *search direction* $\tilde{U}_k^{(j)} \in \mathbb{R}^{Nm}$,

$$\tilde{U}_k^{(j)} = \left[\tilde{u}_{0,k}^{(j)};\, \tilde{u}_{1,k}^{(j)};\, \ldots\, \tilde{u}_{N-1,k}^{(j)}\right] \ . \tag{12}$$

The search direction determines the next iterate via a *step size* $\alpha > 0$ from a line search procedure,

$$U_k^{(j+1)} = U_k^{(j)} + \alpha \cdot \tilde{U}_k^{(j)} \ . \tag{13}$$

The search direction is computed as the solution to the following *local QP*:

$$\min \quad \sum_{i=1}^{N} \tilde{u}_{i-1}^{\mathrm{T}} R \tilde{u}_{i-1} + \tilde{x}_i^{\mathrm{T}} Q \tilde{x}_i + e_{i-1}^{\mathrm{T}} \tilde{u}_{i-1} + f_i^{\mathrm{T}} \tilde{x}_i$$

$$\text{s.t.} \quad \tilde{x}_{i+1} = A_i \tilde{x}_i + B_i \tilde{u}_i \qquad \forall \ i = 0, \ldots, N-1 \ ,$$

$$g_l(\tilde{u}_{k,i}^{(j)}) = 0 \qquad \forall \ l \in \mathcal{A}_k^{(j)} \ .$$

Here $A_i \in \mathbb{R}^{n \times n}$ and $B_i \in \mathbb{R}^{n \times m}$ are the local linearization of the nonlinear model (2) around the current trajectory (corresponding to $U_k^{(j)}$). Here, the linearization is obtained analytically within the algorithm code. The linear cost vectors $e_{i-1} \in \mathbb{R}^m$ and $f_i \in \mathbb{R}^n$ are defined accordingly, by a linearization of the cost function (10a) around the current trajectory. The matrices $R \in \mathbb{R}^{m \times m}$ and $Q \in \mathbb{R}^{n \times n}$ carry the input and state weights on their respective diagonals.

Karush-Kuhn-Tucker (KKT) Conditions. The local QP for the search direction has only equality constraints and is strictly convex. It has a unique solution, which is characterized by its corresponding KKT optimality conditions (Boyd and Vandenberghe 2004, Sec. 5.5). The KKT conditions are solved as a sparse system of linear equations, similar to the approach in (Domahidi 2013).

First, define the vector of stage-wise decision variables $z \in \mathbb{R}^{N(m+n)}$ as

$$z \triangleq \left[\tilde{u}_0;\, \tilde{x}_1;\, \tilde{u}_1;\, \tilde{x}_2;\, \ldots;\, \tilde{u}_{N-1};\, \tilde{x}_N\right] \ . \tag{14}$$

The equality constraints on z imposed in the local QP can be expressed as

$$\underbrace{\begin{bmatrix} D_1 & & \cdots & 0 \\ C_1 & D_2 & & \vdots \\ \vdots & \ddots & \ddots & \\ 0 & \cdots & C_{N-1} & D_N \end{bmatrix}}_{=:G} z = \underbrace{\begin{bmatrix} 0 \\ 0 \\ \vdots \\ 0 \end{bmatrix}}_{=:h} \tag{15}$$

Let $O_{a_i \times n} \in \mathbb{R}^{a_i \times n}$ be the zero matrix and $I_{n \times n} \in \mathbb{R}^{n \times n}$ be the identity matrix, then

$$D_i \triangleq \underbrace{\begin{bmatrix} E_i & O_{a_i \times n} \\ B_i & -I_{n \times n} \end{bmatrix}}_{\in \mathbb{R}^{(a_i+n) \times (m+n)}} , \quad C_i \triangleq \underbrace{\begin{bmatrix} F_{i+1} & O_{a_{i+1} \times n} \\ O_{n \times m} & A_{i+1} \end{bmatrix}}_{\in \mathbb{R}^{(a_{i+1}+n) \times (m+n)}} ,$$

for appropriate matrices $E_i, F_i \in \mathbb{R}^{a_i \times m}$. Here a_i denotes the number of active constraints (bounds and rates) pertaining to the inputs of stage i. Thus $G \in \mathbb{R}^{(Nn+a) \times N(m+n)}$ and $h \in \mathbb{R}^{Nn+a}$, where $a \triangleq \sum_{i=1}^{N} a_i$.

Taking proper care with the setup of the active set, and avoiding redundancies, a_i becomes no larger than m, and G retains full row rank.

Using the above definitions, the KKT optimality conditions for the local QP can expressed as (Nocedal and Wright 2006, Ch. 16)

$$\begin{bmatrix} H & G^{\mathrm{T}} \\ G & O_{a\times a} \end{bmatrix} \begin{bmatrix} z \\ \lambda \end{bmatrix} = \begin{bmatrix} -f \\ 0 \end{bmatrix} \quad , \tag{16}$$

where $H \in \mathbb{R}^{N(m+n)\times N(m+n)}$ is the collective Hessian matrix and $f \in \mathbb{R}^{N(m+n)}$ is the collective linear term of the QP. Instead of solving (17) directly for z and the *Lagrangian multipliers* λ, the solution proceeds by block elimination (Boyd and Vandenberghe 2004, Sec. 5.5). As H is positive definite (because all cost weights are positive), substituting the first into the second line of (17) gives

$$z = -H^{-1}f - H^{-1}G^{\mathrm{T}}\lambda \tag{17a}$$

$$\Longrightarrow \qquad GH^{-1}G^{\mathrm{T}}\lambda = -GH^{-1}f \quad . \tag{17b}$$

In a first step, (17a) is solved for λ; in a second step, this λ is substituted into (17b) to obtain z.

The main effort is to factor the matrix $GH^{-1}G^{\mathrm{T}}$, which is positive definite (because H is positive definite and G has full row rank) and sparse. A generic Cholesky factorization (Demmel 1996, Sec. 2.7.1) yields a lower-triangular, non-singular, sparse factor L such that

$$GH^{-1}G^{\mathrm{T}} = LL^{\mathrm{T}} \quad . \tag{18}$$

With L given, λ can be computed very cheaply. The effort for the factorization itself, and for computing λ and z, increases only linearly with the prediction horizon N. An iterative refinement procedure (Demmel 1996, Sec. 2.5) is used to increase the numerical accuracy (parameter: `maxiterref`)

Backtracking Line Search. After computing the search direction $\tilde{U}_k^{(j)}$, the NAS algorithm performs a nonlinear line search. The desired *step size* α is computed by backtracking along $\tilde{U}_k^{(j)}$ (Nocedal and Wright 2006, Ch. 3). The line search starts from an upper bound $\alpha_{\max}$, whose generic value is 1. However, $\alpha_{\max} \in [0, 1]$ can actually be smaller if the line search is blocked by non-active constraints. So $\alpha_{\max}$ is selected as the highest value of α, capped at 1, which maintains feasibility of the iteration (13).

Since the line search is nonlinear, each evaluation of the cost function along the search direction requires a RK4 execution for integrating (2). This is computationally expensive, but guarantees exact evaluations and hence a strict monotonic improvement of the cost function. The line search procedure being thus expensive is the main rationale for computing a second-order search direction, rather than applying a first-order method (Richter et al. 2010).

Projected Newton Steps. If the line search hits a new active constraint, the search direction is projected onto this constraint. Then the projection is used to continue the line search, instead of computing a new search direction (Nocedal and Wright 2006, Sec. 16.7). This approach of Projected Newton methods is well known for optimization problems in control (Bertsekas 1982, Axehill and Hansson 2008).

The simplicity of the constraints in (10c,d), namely bounds and rates only, make the projection particularly easy. If the line search hits a bound, that particular element of the search direction can be set to zero. If the line search hits a rate constraint, only the corresponding two elements of the search direction have to be equated.

Termination. The NAS algorithm terminates if a local optimum is reached. Few active set iterations (about 2–8) usually suffice for convergence, except when the NMOP changes fundamentally from the previous time step (e.g., due the appearance of a new constraint). Generally, driving curvier paths at higher speeds, and especially the presence of obstacles, increases the required number of iterations.

The number of iterations can be limited (parameter `maxit`), and with it the total execution time of the algorithm. Hence the computational effort for hard problems may be distributed over multiple time steps. The advantage is that vehicle state measurements are updated more frequently than solving one hard problem to optimality, while the controller is running in open loop.

4 RESULTS

A simulation example is used to demonstrate the working of the code. The simulation is based on a high-fidelty model of an Audi Q7 on a winding road, which is the same as in Kong et al. 2015. The trajectory was previously recorded from GPS data.

The code generator also comes with a simulation model and two test tracks, the *winding road* and a *circle with four obstacles*. It can be initialized by running the Matlab script `codgen.m`, in which all parameters are specified. It requires a C-compiler to be installed, as it generates and compiles the controller C-code in the form of a Simulink S-function.

For the simulation, a sampling time of $t_s = 100$ ms is used with a variable horizon length of $N = 20, 30, 40$ steps. The number of nonlinear iterations (`maxit`) is limited to 2, with a maximum number of projected Newton steps (`maxiterproj`) of 10. The state constraints roughly correspond to the lane boundaries.

Path tracking. Figure 3 and Table 1 illustrate the distribution of the tracking error. A major cause is produced by tire slip. Thus the tracking error tends to be larger in (tight) curves and grows with the reference speed.

The tuning was chosen such that the input signals are smooth. The tracking error can be further reduced by changing the cost weights, but at the expense of more jerky inputs.

Computation times. Figure 4 and Table 2 show the distribution of computation times. Usually, the NAS

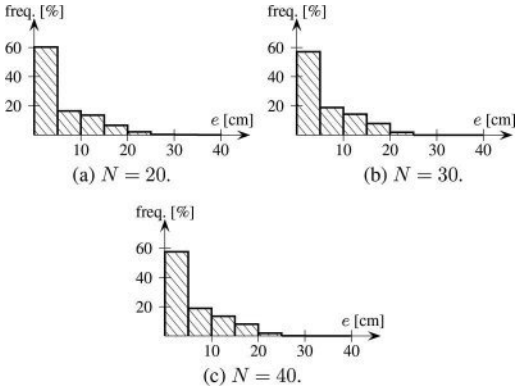


Figure 3. Distribution of tracking error.

Table 1. Tracking error, perpendicular to path.

horizon	$N = 20$	$N = 30$	$N = 40$
average [cm]	11.21	11.51	11.61
maximum [cm]	37.20	14.96	25.10

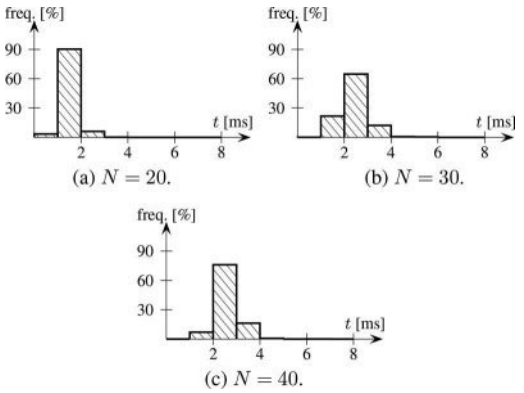


Figure 4. Distribution of computation times.

Table 2. Computation times, Intel Core i7, 2.80 GHz.

horizon	$N = 20$	$N = 30$	$N = 40$
average [ms]	1.03	1.93	2.11
maximum [ms]	<3.0	<5.0	<6.0

has not converged when the solver is aborted. Thus adding further iterations increases, in particular, the peak computation times, however this has almost no effect on the tracking error.

REFERENCES

Axehill, D. & A. Hansson (2008). A dual gradient projection quadratic programming algorithm tailored for model predictive control. In *47th IEEE Conference on Decision and Control*, Cancun, Mexico.

Bertsekas, D. P. (1982). Projected newton methods for optimization problems with simple constraints. *SIAM Journal on Control and Optimization 20*(2), 221–246.

Boyd, S. & L. Vandenberghe (2004). *Convex Optimization*. Cambridge: Cambridge University Press.

Campbell, M., M. Egerstedt, J. P. How, & R. M. Murray (2010). Autonomous driving in urban environments: Approaches, lessons and challenges. *Philosophical Transactions of the Royal Society A 368*(1928), 4649–4672.

Demmel, J. (1996). *Applied Numerical Linear Algebra*. Philadelphia (PA): SIAM.

Diehl, M., H. J. Ferreau, & N. Haverbeke (2009). Efficient numerical algorithms for nonlinear MPC and moving horizon estimation. In L. M. et al. (Ed.), *Nonlinear Model Predictive Control*, pp. 345–369. Berlin et al.: Springer.

Dolgov, D., S. Thrun, M. Montemerlo, & J. Diebel (2010). Path planning for autonomous vehicles in unknown semistructured environments. *The International Journal of Robotics Research 29*(5), 485–501.

Domahidi, A. (2013). *Methods and Tools for Embedded Optimization and Control*. Ph.D. dissertation, Eidgen¨ossische Technische Hochschule Z¨urich, Z¨urich, Switzerland.

Gao, Y., T. Lin, F. Borrelli, E. Tseng, & D. Hrovat (2010). Predictive control of autonomous ground vehicles with obstacle avoidance on slippery roads. In *ASME Dynamic Systems and Control Conference*, Cambridge (MA), United States, pp. 265–272.

Gutjahr, B. & M. Werling (2015). Optimale Fahrzeugquerf ührung mittels linearer, zeitvarianter MPC. In 10. *Uni-DAS Workshop Fahrerassistenz*, Walting, Germany.

Houska, B., H. J. Ferreau, & M. Diehl (2011). ACADO toolkit – an open-source framework for automatic control and dynamic optimization. *Optimal Control Application and Methods 32*, 298–312.

Kong, J., M. Pfeiffer, G. Schildbach, & F. Borrelli (2015). Kinematic and dynamic vehicle models for autonomous driving control design. In *IEEE Intelligent Vehicles Symposium*, Seoul, Korea, pp. 1094–1099.

Lima, P. F. (2016). *Predictive Control for Autonomous Driving with Experimental Evaluation on a Heavy-Duty Construction Truck*. Ph.D. dissertation, KTH Royal Insitute of Technology, Stockholm, Sweden.

Nocedal, J. & S. J. Wright (2006). *Numerical Optimization* (2nd ed.). New York: Springer.

Richter, S., C. N. Jones, & M. Morari (2010). Real-time MPC with input constraints using the fast gradient method. Technical report, Swiss Federal Institute of Technology, Zurich, Switzerland.

Rutquist, P. E. & M. M. Edvall (2010). PROPT – Matlab optimal control software. Technical report, Tomlab Optimization, Västarås, Sweden.

Scokaert, P. O. & J. B. Rawlings (1999). Feasibility issues in linear model predictive control. *AIChE Journal* 45, 1649–1659.

Wächter, A. & L. T. Biegler (2005). On the implementation of an interior point filter line search algorithm for large-scale nonlinear programming. *Mathematical Programming, Series A 106*(1), 25–57.

Werling, M., J. Ziegler, S. Kammel, & S. Thrun (2010). Optimal trajectory generation for dynamic street scenarios in a Fren´et frame. In *IEEE Conference on Robotics and Automation, Anchorage* (AK), United States.

Ziegler, J., P. Bender, T. Dang, & C. Stiller (2014). Trajectory planning for BERTHA – a local, continuous method. In *IEEE Intelligent Vehicles Symposium*, Dearborn (MI), United States, pp. 450–457.

Advanced Vehicle Control – Edelmann, Plöchl & Pfeffer (Eds)
© 2017 Taylor & Francis Group, London, ISBN 978-1-138-02992-7

Real-time optimal obstacle avoidance of MGV using modified Carathéodory-π solutions

S. Watanabe & M. Harada
Department of Mechanical Engineering, National Defense Academy of Japan, Kanagawa, Japan

ABSTRACT: This paper investigates the real-time optimal obstacle avoidance of a micro ground vehicle (MGV) using the modified Carathéodory-π solutions. The optimal control problem is sequentially solved by the pseudospectral optimal control theory as a minimum-time point-to-point maneuver. The MGV uses the generated optimal control law and optimal trajectory for its maneuver. When the vehicle approaches an obstacle, the cost function's value increases. The proposed approach is experimentally validated by controlling the real MGV in the indoor facility. Experimental results demonstrate the feasibility of commanding the MGV with the optimal solutions generated by this method.

1 INTRODUCTION

Technological advances in electronics miniaturization and manufacturing processes have facilitated the rapid development of numerous varieties of autonomous driving systems. An advanced vehicle control technology is necessary to include in a system that must respond rapidly to changes in the environment, such as a sudden appearance of obstacles during the autonomous operation. This obstacle avoidance control system is not only applicable to automatic operation of conventional manned vehicles, but also for the autonomous driving of unmanned ground vehicles. The real-time control technology based on optimal control theory is applicable for such a system.

In such systems, the model predictive control (MPC) (Maciejowski 2002) method has been widely used due to its high performance and adaptability (Ohtsuka 2015). In MPC, control variables are optimized online using a receding horizon with approximation of the optimal cost over the rest of the interval. Note that the MPC method requires a reference trajectory to follow, and its control implementation is by zero-order-hold inputs. Another approach, the "clock-based" real time optimal feedback control that generates the so-called Carathéodory-π trajectories is developed and experimentally verified by Ross et al (Ross & Sekhavat 2008). In this Carathéodory-π (C-π) controller, the optimal cost is calculated over the entire trajectory between the current position and the target position during each sampling time rather than in each sampling interval, and it generates time continuous control input. Although this method shows sufficient performance in real-time optimal control, it requires that the updates occur at frequencies that are faster than the Lipschitz frequency. This frequency is defined by the nonlinear system dynamics. In previous studies, we have modified the C-π controller by adding a tracking controller. This method is known as the modified Carathéodory-π (MC-π) controller for the system. The MC-π controller has been experimentally verified in the context of the control of unmanned systems (Watanabe & Harada 2014, Watanabe & Harada 2015). However, in that UGV system study, we have verified our approach only for the basic maneuver, the S-shape trajectory maneuver, and the K-turn trajectory maneuver, in an obstacle free environment.

In this study, we investigate real-time optimal obstacle avoidance maneuvers by the MGV using the MC-π controller. The obstacle appears suddenly in front of the MGV during the maneuver. The proposed approach is experimentally validated by controlling the actual MGV system in an indoor facility.

2 PROBLEM FORMULATION

2.1 *Vehicle dynamics*

Consider the configuration of the MGV shown in Fig. 1. Reduced order equations of motion are required to avoid a computational burden during the real-time control. Thus, in this paper, the kinematic equations of motion used, shown in Eq. (1), are the same as were used in our previous work cited above. Here, the nonlinear steering behavior of the actual MGV system is modeled by Eq. (2). The state vector is $\boldsymbol{X} = [x\, y\, \psi\, V\, \delta_f\, a_x]^T$, and the control vector is $\boldsymbol{U} = [V_c\, \delta_{fc}]^T$. The vehicle position (x, y) is placed taken to be the center of the rear axle. The other variables are the yaw

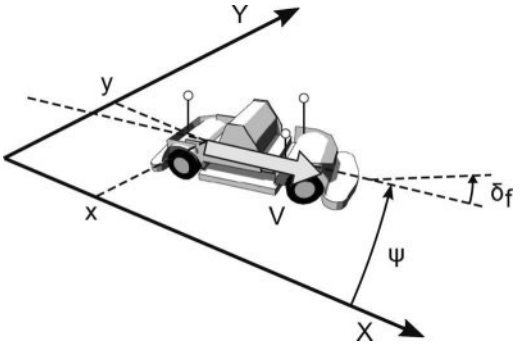


Figure 1. Coordinate System and Reference Frames of MGV.

angle ψ, the vehicle velocity V and its command input V_c, the front steering angle δ_f and its command input δ_{fc}, and the vehicle acceleration a_x.

$$\dot{\boldsymbol{X}} = \boldsymbol{f}(\boldsymbol{X},\boldsymbol{U}) = \begin{bmatrix} V\cos\psi \\ V\sin\psi \\ \dfrac{V}{L+\Lambda(\delta_f)}\tan\delta_f \\ \dfrac{1}{\tau_f}(\delta_{fc}-\delta_f) \\ -\omega_n^2 V - 2\zeta\omega_n a_x + k\omega_n^2 V_c \end{bmatrix} \quad (1)$$

$$\Lambda(\delta_f) = A\frac{1}{\sqrt{2\pi\sigma^2}}\exp(-\frac{1}{2\sigma^2}\delta_f^2) \quad (2)$$

2.2 *Control algorithms*

Fig. 2 shows the block diagram for the real-time optimal control system using the MC-π controller. The clock times are used to generate optimal analog signals $\boldsymbol{U}^*(t)$ and the optimal trajectory $\boldsymbol{X}^*(t)$. The C-π controller uses only the signal $\boldsymbol{U}^*(t)$ as the open-loop control, and the MC-π controller additionally uses the optimal trajectory $\boldsymbol{X}^*(t)$ as the reference command of the tracking controller. Thus, the control input $\boldsymbol{U}(t)$ into the system is the sum of both $\boldsymbol{U}^*(t)$ and $\boldsymbol{U_T}$(t) in the MC-π controller. The pair of solutions $\{\boldsymbol{U}^*(t),\boldsymbol{X}^*(t)\}$ is updated at each sampling time using the measured state $\boldsymbol{X}(t)$. The sequence of sampling, re-generating, and controlling continues until the mission task is satisfied.

Fig. 3 shows the typical time domain response of the C-π controller. The sampled state of the real system $\boldsymbol{X}(t_{i-1})$ at the sampling time t_{i-1} is used as the initial condition to generate the optimal trajectory $\{\boldsymbol{U}^*_{i-1}(t),\boldsymbol{X}^*_{i-1}(t)\}$ (blue line). However, due to the computational delay, the entire obtained solution cannot be applied to the system. Thus, the actual control signal extracted from the obtained solution $\boldsymbol{U}^*_{i-1}(t)$, is applied only to the system during the next computation interval from t_i to t_{i+1} (solid line). For this reason, data from the first interval, from t_{i-1} to t_i in the $\boldsymbol{U}^*_{i-1}(t)$, is rejected (dashed line).

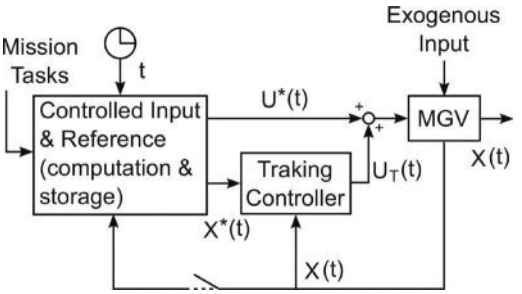


Figure 2. Clock-based feedback control using Modified Carathéodory-π solutions.

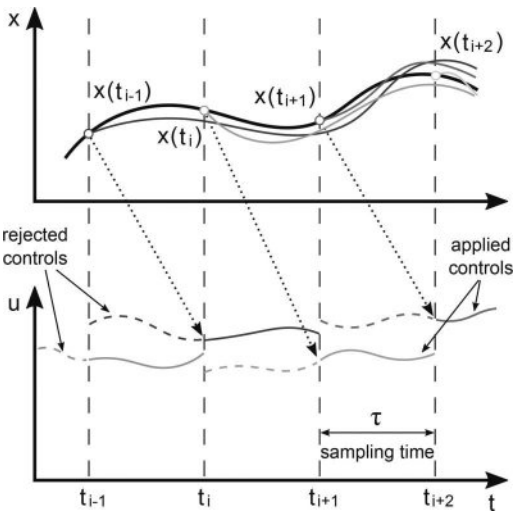


Figure 3. Practical implementation of control signals in clock-based feedback control.

The key to successful implementation of these feedback principles is sufficiently fast generation of open-loop controls. For a practical closed loop solution, the updates must happen at frequencies that are at, or faster than, the Lipschitz frequency. Although the precise computation of the Lipschitz frequency is not easy, it can be practically estimated by a numerical simulation. In practice, computation is still a constraint for the real-time control of this system. As a result, the experimental setup in this paper cannot satisfy this update limitation. Therefore, we implement the tracking controller using the preview driver model (Yoshimoto 1969) as an inner-loop feedback control to track the optimal trajectory, $\boldsymbol{X}^*(t)$, which is stored after previous computation. The predicted position (x_p, y_p) from the present position (x_0, y_0) is described by Eqs. (3) and (4) by introducing the prediction time T_p.

$$x_p = x_0 + \dot{x}_0 T_p + \frac{1}{2}\ddot{x}_0 T_p^2 \quad (3)$$

$$y_p = y_0 + \dot{y}_0 T_p + \frac{1}{2}\ddot{y}_0 T_p^2 \quad (4)$$

In the body axis, the longitudinal error ϵ_x and the lateral error ϵ_y is described by Eq. (5) using the current position (x_p, y_p) and the reference position (x_c, y_c). Then, standard proportional control is used to compensate for these errors, and it generates the feedback commands by Eqs. (6) and (7).

$$\begin{bmatrix} \epsilon_x \\ \epsilon_y \end{bmatrix} = \begin{bmatrix} \cos\psi & \sin\psi \\ -\sin\psi & \cos\psi \end{bmatrix} \begin{bmatrix} x_c - x_p \\ y_c - y_p \end{bmatrix} \tag{5}$$

$$V_c = K_{PV}\epsilon_x \tag{6}$$

$$\delta_{fc} = K_{P\delta}\epsilon_y \tag{7}$$

2.3 *Optimal control problem*

In the real-time optimal control, the optimal control problem is necessary to generate an optimal solution rapidly during the interval of the sampling. The nonlinear optimal control problem **B**, to minimize the cost function J while satisfying Eq. (1) at $t \in [t_i, t_f]$, can be stated as follows (Bryson & Ho 1975, Kato 1988).

$$(\mathbf{B}) \begin{cases} \text{Minimize} & J[\boldsymbol{X}(\cdot), \boldsymbol{U}(\cdot), t_f] = t_f - t_i \\ & \quad + \int_{t_i}^{t_f} F[\boldsymbol{X}(t), \boldsymbol{U}(t)]dt \\ \text{Subject to} & \dot{\boldsymbol{X}}(t) - \boldsymbol{f}[\boldsymbol{X}(t), \boldsymbol{U}(t)] = \boldsymbol{0} \\ & \boldsymbol{e}^L \le \boldsymbol{e}[\boldsymbol{X}(t_i), \boldsymbol{X}(t_f)] \le \boldsymbol{e}^U \\ & \boldsymbol{g}^L \le \boldsymbol{g}[\boldsymbol{X}(t), \boldsymbol{U}(t)] \le \boldsymbol{g}^U \end{cases}$$

Both boundary and path constraints are defined by the given maneuver conditions where the superscript L and U denote for each of the lower limit and the upper limit. The optimal solution is found by the pseudospectral (PS) method, which is capable of solving the problem in a fraction of a second, and the necessary conditions for optimality can be automatically verified (Fahroo & Ross 2001, Fahroo & Ross 2008).

2.4 *Generating obstacle*

Here we consider the minimum-time point-to-point maneuver task for the MGV. The complete cost function consists of the weighted sum of the two terms shown in Eq. (8). The first term on the right-hand side of Eq. (8) represents the maneuver time from t_i to t_f, and the second term represents the penalty cost which is defined by the distance between the MGV and the obstacle. The function h, in the second term, is given by Eq. (9), which uses the LP norm definition. Fig. 4 shows the value of the penalty function, where the location of the circle shaped obstacle ($p = 2$) is $(x_{obs}, y_{obs}) = (-0.05, 0.05)$.

$$J = t_f - t_i + \int_{t_i}^{t_f} W(e^{e^{-h(x(t),y(t))}})dt \tag{8}$$

$$h(x(t), y(t)) = (x - x_{obs})^p + (y - y_{obs})^p - r^p \tag{9}$$

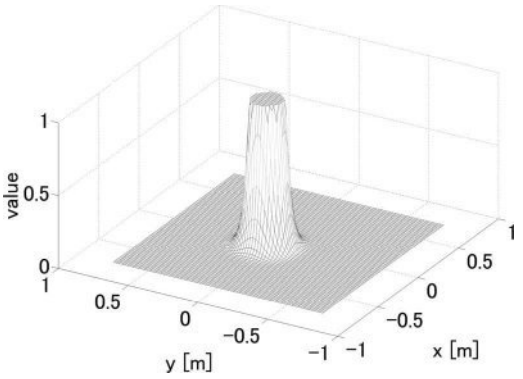


Figure 4. Value of the penalty function.

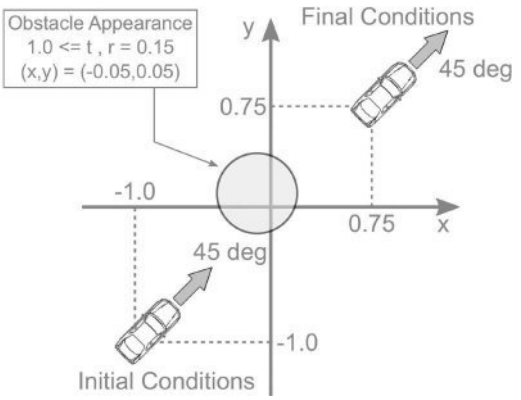


Figure 5. Numerical conditions.

3 NUMERICAL SIMULATIONS

3.1 *Simulation conditions*

Prior to the experiment, numerical simulations were conducted to compare the obstacle avoidance performance of the MC-π controller with the C-π controller. Fig. 5 shows the outline of the simulation scenario. The MGV moves from the initial position $[x_0, y_0] = [-1, -1]$ to the target position $[x_f, y_f] = [0.75, 0.75]$. Assume that the obstacle is unknown when the maneuver began, and it is detected forward and slightly to the left-hand side on the initial trajectory at time 1 second later. The real-time control method described in this paper will, in general, display a small difference between the optimal trajectory and the observed trajectory, as a result of sampling effects. Thus, we define the final position tolerance to be 0.15 m in radius and 10 deg in yaw angle. If the vehicle cannot satisfy this required tolerance in the prescribed time limit, the maneuver is aborted.

Table 1 lists the parameters used in the numerical simulations. Each control method considers the four sampling time sets and compares the results. In this numerical simulation, it is assumed that every optimal solution is obtained within the available sampling time.

Table 1. Numerical Parameters.

Sampling Time				
τ [s]				
0.5	1.0	1.5	2.0	
Obstacle				
x_{obs} [m]	y_{obs} [m]	r [m]	p [–]	W [–]
−0.05	0.05	0.15	2	3
MC-π				
K_{PV} [–]	$K_{P\delta}$ [–]	T_p [s]		
0.1	2.0	1.0		
Nodes				
Offline	Online			
41	18			

3.2 *Numerical results*

The simulation results are shown in Fig. 6. By increasing the sampling time, the avoidance of the obstacle is delayed. For both control methods, if the sampling time is $\tau \leq 1.0$ [s], the MGV reaches the goal without colliding the obstacle. In contrast, if the sampling time is $\tau \geq 2.0$ [s], all cases are a failure to avoid the obstacle. In the case of $\tau = 1.5$ [s], only the MC-π controller succeeds in executing the maneuver.

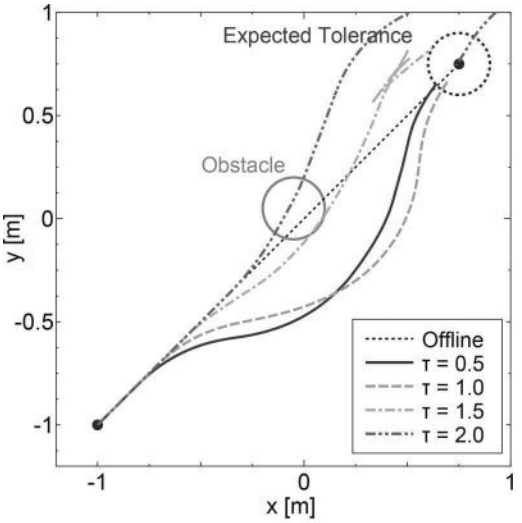
4 EXPERIMENTS

4.1 *Experimental setup*

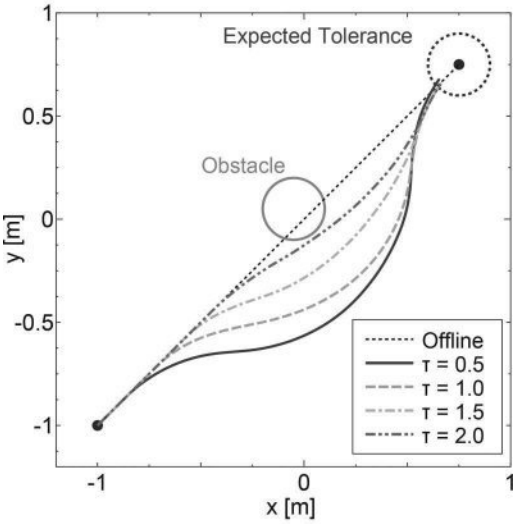
In contrast with the above simulations, this section explores the implementation of the MC-π real-time optimal controller in a real system. The vehicle's states are measured by the motion capture system with seven cameras to achieve redundant retro-reflective marker localization at 200 Hz with millimeter accuracy. The three-dimensional position of the reflective markers placed on the object can be recognized in the measurement space of 3 m (W) × 3 m (L) × 1.8 m (H). The system is run by a single program that manages the entire measurement and control process. Along with the main program, a separate optimization solver calculates the optimal control solution, using the vehicle state information, and transfers that solution back to the main program.

4.2 *Experimental results*

Fig. 7 shows the experimental results for each sampling time. The results are the same as the numerical computation, namely that the vehicle collides with the obstacle when the sampling time is $\tau >= 1.5$ [s] for C-π control and $\tau >= 2.0$ [s] for MC-π control. Otherwise, the MGV reaches the goal without colliding. In the following, we discuss the difference in the time



(a) Using C-π solutions controller



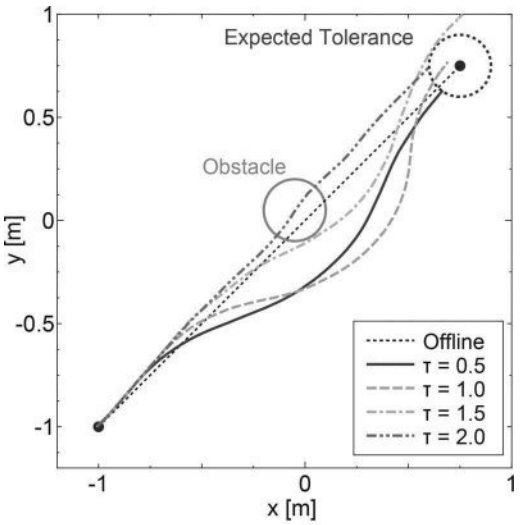
(b) Using MC-π solutions controller

Figure 6. Numerical results.

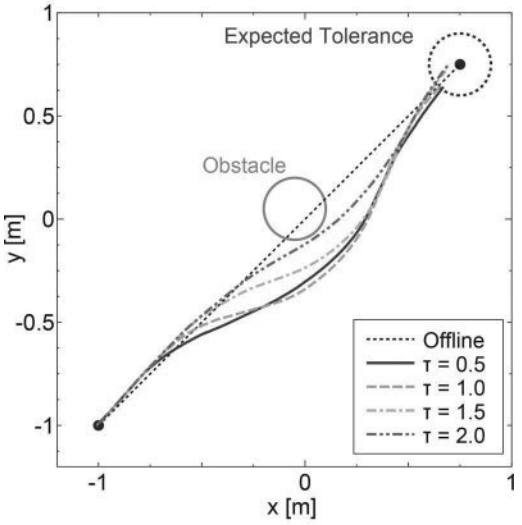
response between each controller for the $\tau = 1.5$ [s] case which, in this situation, results in the presence or absence of a collision.

The blue symbols on the trajectories indicate the sampling points. The short dash line indicates the obtained optimal trajectories from each sampling point, and the solid line is the actual trajectory observed. The first optimal trajectory generated is a straight line toward the target because the obstacle has not appeared yet at that time. The obstacle avoidance trajectories are generated starting after the second sampling however, due to the appearance of the obstacle.

The optimal trajectory is calculated in the interval between the sampling point and the next sampling



(a) Using C-π solutions controller



(b) Using MC-π solutions controller

Figure 7. Experimental results all.

point in real time. Thus, since the control signal during this interval is not available, we extract the corresponding time signal from the previous optimal control trajectory. For example, the actual control input δ_{fc} during the clock time $t = 3.0$–4.5 [s] is extracted from the optimal control trajectory which was obtained from the sampling period $t = 1.5$ [s]. Unfortunately, if the steering command for avoiding the obstacle is included before this extracted interval, the command is rejected. It is apparent that the right-turn command is not applied to the system during the clock time $t = 1.5$–3.0 [s]. Therefore, the C-π controller maneuver fails to avoid the obstacle, as a result of the sampling delay effect, for this particular sampling time value.

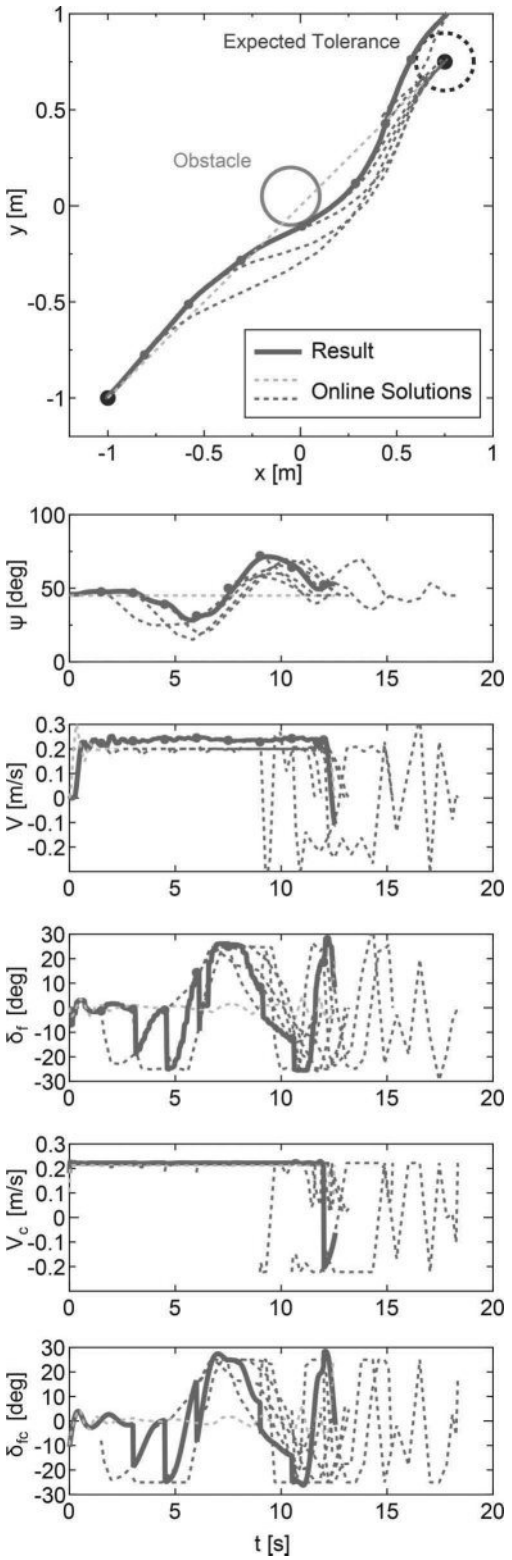


Figure 8. Experimental results using C-π controller ($\tau = 0.5$).

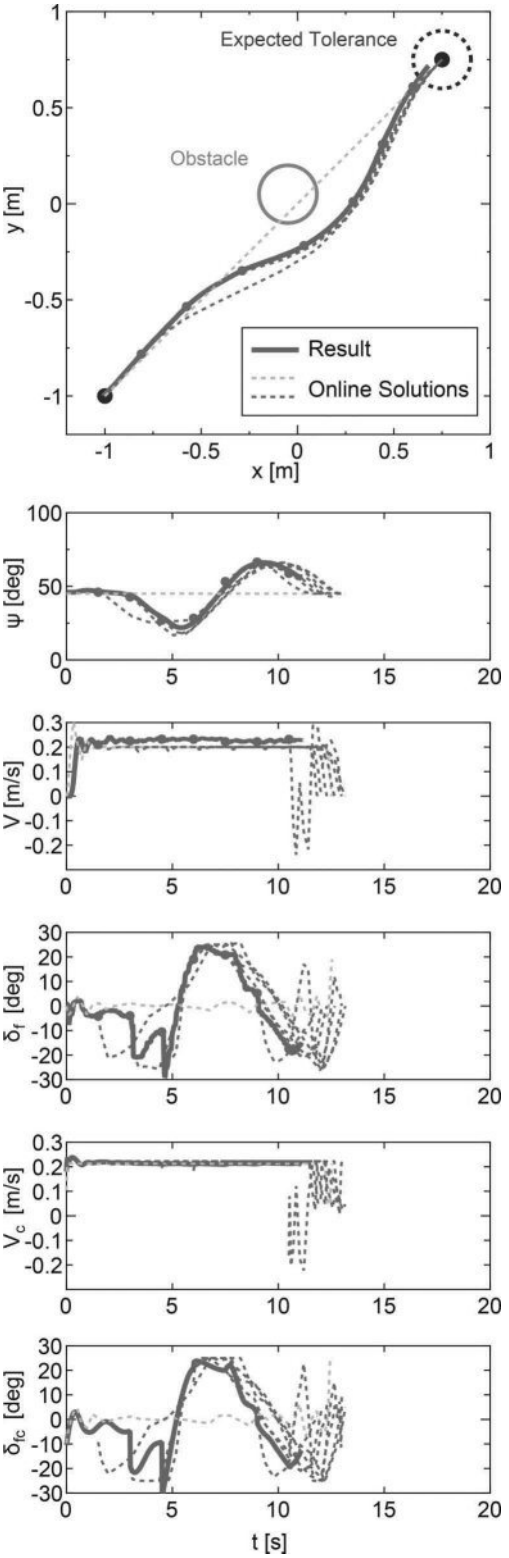


Figure 9. Experimental results using MC-π controller ($\tau = 0.5$).

Fig. 9 shows the results of the MC-π controller case. Just as in the C-π controller case, the obstacle avoidance trajectories are generated after the second sampling time. Since the actual MGV trajectory is on the left side of the reference trajectory at clock time $t = 3.0 \sim 4.5$ [s], the actual steering command is compensated to the right by the tracking controller, even if the calculated open-loop command is small. For this reason, the MGV can reach the goal without colliding with the obstacle. Consequently, the utility of the MC-π controller with the sudden appearance of an obstacle is experimentally verified.

5 CONCLUSIONS

The clock-based real-time optimal control, MC-π, was applied to the obstacle avoidance maneuver of an MGV, and its performance was evaluated by numerical simulation and by subsequent experiment with a physical MGV. The results show that the MGV successfully reaches the target, even with the sudden appearance of an obstacle, using the MC-π controller. This was found to be true even when the C-π control fails under the same conditions. In such cases, the additional tracking controller tracks the reference trajectory and keeps the MGV from collision with the obstacle.

REFERENCES

Bryson, A. E. & Y. C. Ho (1975). Applied optimal control. *Levittown, Taylor & Francis*, 481p.

Fahroo, F. & I. M. Ross (2001). Costate estimation by a legendre pseudospectral method. *Journal of Guidance, Control, and Dynamics 24 (2)*, 270–277.

Fahroo, F. & I. M. Ross (2008). Advanced in pseudospectral methods for optimal control. *AIAA Guidance, Navigation, and Control Conference AIAA 2008-7309*, 1–23.

Kato, K. (1988). Engineering optimal control. *University of Tokyo press*, 241p (in Japanese).

Maciejowski, J. M. (2002). *Predictive Control with Constraints (Adachi, S. and Kanno, M. (Trans.): Predictive Control with Constraints, Tokyo Denki University Press, 2005 (in Japanese))*. Pearson Education Limited.

Ohtsuka, T. (2015). *Practical Application of Control by Real-Time Optimization*. Corona Publishing (in Japanese).

Ross, I. M. & P. Sekhavat (2008). Optimal feedback control: Foundations, examples, and experimental results for a new approach. *Journal of Guidance, Control, and Dynamics 31 (2)*, 307–321.

Watanabe, S. & M. Harada (2014). Real-time optimal feedback control of ugvs using modified Carathéodory-π solutions. *Proc. of AVEC'14 TuA2-1*, 385–390.

Watanabe, S. & M. Harada (2015). Real-time optimal feedback control of mgvs in k-turn maneuver. *Proc. of 2015 JSAE Annual Congress (spring)*, 395–400 (in Japanese).

Yoshimoto, K. (1969). Simulation of man-automobile systems by the driver's steering model with predictability. *Bulletin of JSME 12 (51)*, 495–500.

Advanced Vehicle Control – Edelmann, Plöchl & Pfeffer (Eds)
© 2017 Taylor & Francis Group, London, ISBN 978-1-138-02992-7

Control target algorithm for direction control of autonomous vehicles in consideration of mutual accordance in mixed traffic conditions

Shohei Kitazawa & Tetsuya Kaneko
Osaka Sangyo University, Osaka, Japan

ABSTRACT: This paper describes the development and simulation verification of a direction control algorithm for autonomous vehicles in consideration of mutual accordance in mixed traffic conditions. This algorithm includes a driver model and a vehicle dynamics model. The driver model is composed of a risk potential driver model and a second-order prediction driver model with multiple preview points. We examined the capability of the algorithm to express human operation. In a traffic condition where there are multiple obstacles, we suggested an algorithm for real-time control target generation from the surrounding environment by using the risk potential and confirmed its effectiveness by simulation and experiment.

1 INTRODUCTION

Autonomous vehicle technology is expected to solve several road traffic issues, including reduction of road traffic accidents, relaxation of traffic jams, and movement support for elderly. Therefore, this technology has been receiving increased attention and several relevant experiments have been conducted [1, 2]. An autonomous vehicle algorithm, which is the focus of this study, simulates an expert driver's maneuvering in detail. In the future, when vehicles driven by human drivers are driven alongside autonomous vehicles, if an autonomous vehicle performs a maneuver peculiar to automatic control as to follow the traffic regulation strictly, as an example, the autonomous vehicles always run at the center of the traffic lane strictly, it is thought that the autonomous vehicle gives a sense of incongruity for other vehicles or walkers.

This paper describes the development and verification of target trajectory generation. In addition, direction control algorithm for autonomous vehicles is also verified by conducting field experiments and simulations that use a vehicle dynamics model with multiple degrees of freedom in consideration of mutual accordance in mixed traffic conditions.

2 CONTROL TARGET GENERATION ALGORITHM

In this study, we develop an algorithm that generates the trajectory of a control target for steering control application.

The control component in the autonomous vehicle is shown in Fig. 1. In particular, in this study, we have developed an algorithm that generates the trajectory of a control target for steering control application in real time. Our algorithm consists of a driver model and a vehicle dynamics model, which is shown in Fig. 2. It is explained below.

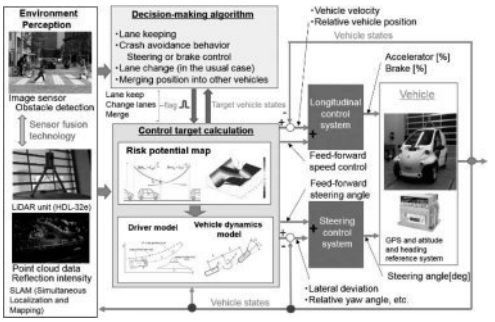


Figure 1. Control system for an autonomous vehicle.

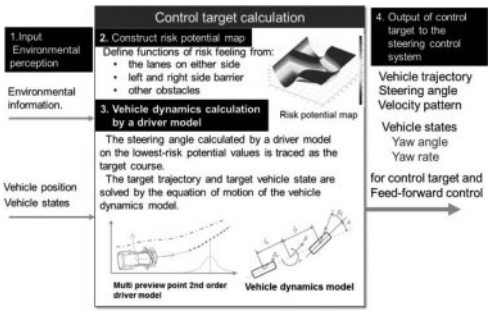


Figure 2. Flow of control target calculation algorithm.

2.1 *Risk potential driver model*

The driver model mimics the way in which a driver recognizes the environment around him/her. The model converts the information of obstacles and lane widths,

as obtained from the surrounding environment, as well as other information into function parameters that determine the risk potential.

When a human driver recognizes a large potential risk presented by an obstacle in his/her forward view, the driver makes every effort to avoid that obstacle. Simultaneously, the risks presented by the lanes on one side and the barrier on the other also lead to conscious driving actions that are typically related to collision avoidance. In other words, the driver estimates the risk being presented from all sides and aims to position his/her vehicle where the risk is the lowest.

By using the above concept, this model has been tested and proven through biomedical measurements, and also through subjective assessments of the relationship between the distance from an obstacle and the driver's heart rate [3, 4].

As a condition, the model contains map information that includes traffic lane information. Then, we define the risk level of objects in the front, rear, and lateral directions as an exponential function, as shown in Fig. 3. The risk potential values with the distance from the traffic obstacles, respectively, at preview time T_p are as follows:

$$R_{vfx} = C_{vf}\left(v_v, \dot{v}_v, \cdots\right) \cdot e^{-\frac{x_{vf}}{\tau_{vfx}\left(v_v, \dot{v}_v, \cdots\right)}} \tag{1}$$

$$R_{vrx} = C_{vr}\left(v_v, \dot{v}_v, \cdots\right) \cdot e^{-\frac{x_{vr}}{\tau_{vrx}\left(v_v, \dot{v}_v, \cdots\right)}} \tag{2}$$

$$R_{vy} = C_{vy}\left(v_v, \dot{v}_v, \cdots\right) \cdot e^{-\frac{y_v}{\tau_{vy}\left(v_v, \dot{v}_v, \cdots\right)}} \tag{3}$$

where x_{vf}, x_{vr}, y_v are the coordinates of the obstacle's front and rear reference points. C_{vf}, C_{vr}, C_{vy} are the gains of the risk potential function of the obstacles. τ_{vfx}, τ_{vrx}, τ_{vy} are the time constants of the exponential function indicating the increase in the risk potential as a function of the relative position. The relative velocity between the ego-vehicle and the recognition obstacle is calculated as follows:

$$\tau_{vfx} = C_{\tau fx} \times \left(V_1 - V_2\right) \tag{4}$$

$$\tau_{vrx} = C_{\tau rx} \times \left(V_1 - V_2\right) \tag{5}$$

$$\tau_{vy} = C_{\tau y0} + C_{\tau y} \times V_1 \tag{6}$$

where $C_{\tau fx}$, $C_{\tau rx}$, $C_{\tau y0}$ and $C_{\tau y}$ are the parameters of the time constant. V_1 and V_2 denote the velocity of the ego-vehicle and the recognition obstacle as shown in Fig. 4. We define the risk potential of the objects such as sidewall and traffic lane division. Then, we generate a risk potential map around the ego-vehicle by composing these potentials as shown in Fig. 5. We assume that the line of minimum points in the map is the virtual target course. Deviations from the risk potential ε are provided as feedback, which helps in determining the steering angle. Therefore, the steering gain with respect to the target deviation is obtained.

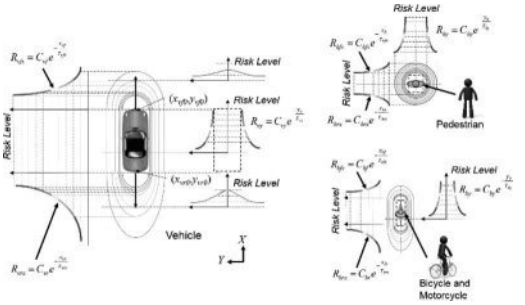


Figure 3. Schematic of risk potential from obstacles.

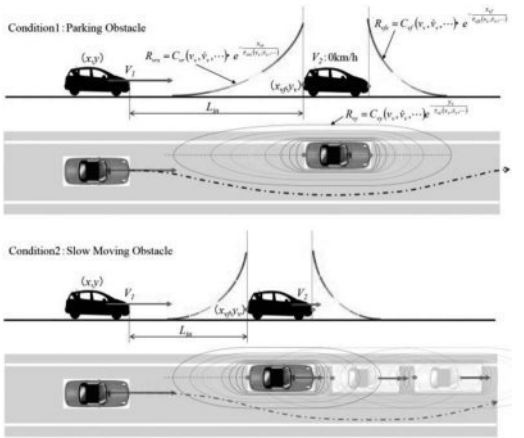


Figure 4. Schematic of risk potential from moving obstacle.

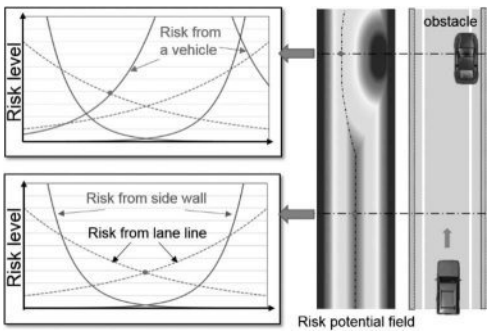


Figure 5. Concept of risk potential map for driver model.

2.2 *Multiple preview points driver model*

Considering the preview points of the driver model, the steering angle is normally determined based on the deviation from one preview point. Nevertheless, a human driver may change the look-ahead distance according to the operating conditions. In addition, a situation is not considered from a single viewpoint; the target path is also determined from the main preview point. Thus, with the proposed driver model, the preview point is assumed based on a multiple-preview-point driver model, and the steering angle for

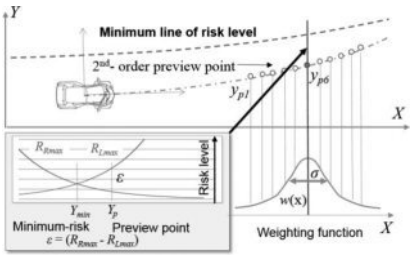


Figure 6. Driver model with multiple preview points.

the vehicle dynamics model is calculated by considering the weighted factor using standard deviation, as shown in Fig. 6 [5].

The second-order prediction driver model traces these lowest risk potentials as the target course, and the non-linear steering gain is calculated from the risk potentials at those points where the course deviates from the target on the map. A preview of the second-order prediction model of the vehicle in the lateral direction after T_p seconds is given by (7).

$$Y_{pi} = Y_0(\beta+\theta)\cdot T_{pi} + \frac{1}{2}(\dot{\beta}+\gamma)\cdot V\cdot T_{pi}^{\,2} \tag{7}$$

where Y_0 is the initial lateral position and V is the vehicle velocity. The preview point $y_{p1\sim11}$ is defined as the total for 11 points with intervals of 0.1 s both before and after a reference preview time $T_{p1\sim11}$.

As the weighting function, the normal distribution function of the standard deviation σ is specified for the preview distance $x_{p1\sim11}$ for each preview time, as given by (8).

$$w(x_i) = \frac{1}{\sqrt{2\pi}\sigma}\exp\left[-\frac{(x_{pi}-x_{p6})^2}{2\sigma^2}\right] \tag{8}$$

Furthermore, the mean value of the deviation of the risk feeling potential, ε_{ave}, which considers the weighting function, is given and the steering angle calculated by this multi-preview point model is given as follows:

$$\varepsilon_{ave} = \frac{1}{11}\sum_{i=1}^{11} w(x_i)\cdot\varepsilon_i \tag{9}$$

$$\delta = \int K_s\cdot\varepsilon_{ave}dt \tag{10}$$

where K_s is the steering gain of this driver model.

2.3 *Vehicle motion dynamics model*

We considered that an expert driver understands the motion of a vehicle and operates it appropriately. Therefore, we calculated the target trajectory and quantities of the vehicle state from the calculated steering angle by using a vehicle motion dynamics model. In this way, we calculated the control target for a vehicle.

The vehicle dynamics model is described using two degrees of freedom, namely, the sideslip and the yaw

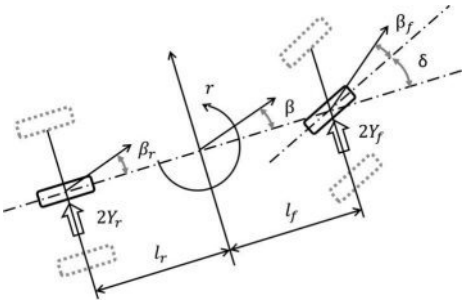


Figure 7. Vehicle dynamics model for control target calculation.

motion of the vehicle body, as shown in Fig. 7. The physical model with the minimum dimensions and the planar motion of the vehicle are given as follows.

$$mv(\dot{\beta}+r) = -2K_f\left(\beta+\frac{l_f}{v}r-\delta\right) - 2K_r\left(\beta-\frac{l_r}{v}r\right) \tag{11}$$

$$I\dot{r} = -2K_f l_f\left(\beta+\frac{l_f}{v}r-\delta\right) + 2K_r l_r\left(\beta-\frac{l_r}{v}r\right) \tag{12}$$

The steering angle calculated by the above mentioned driver model is substituted into the equation of motion, and the target trajectory and target vehicle state are calculated by solving the equation of motion. Furthermore, the vehicle trajectory, steering angle, and other variables related to the vehicle states calculated by the vehicle dynamics model are output to the steering controller of the control target [6].

3 EXPERIMENT VEHICLE SYSTEM

The constitution of the experiment vehicle used in this study is shown in Fig. 8. It is equipped with two computers for image processing and point cloud processing. In addition, it is equipped with Digital Signal Processing unit (DSP), which is used for control target calculation and vehicle control. Each processing computer shares information using User Datagram Protocol (UDP). The components of the experiment vehicle are described below.

3.1 *Environment recognition*

The surrounding environment of the ego-vehicle changes continuously. In this study, we used Light Detection and Ranging (LIDAR), which is a method used for environmental information acquisition. Ego-vehicle position estimation and obstacle detection were performed by Simultaneous Localization and Mapping (SLAM) using neighboring point group information. The output parameters of the ego-vehicle were the self-position and the yaw angle. The output parameters of the obstacles were the relative position and the relative velocity with respect to the ego-vehicle. The obstacles were detected in the range of

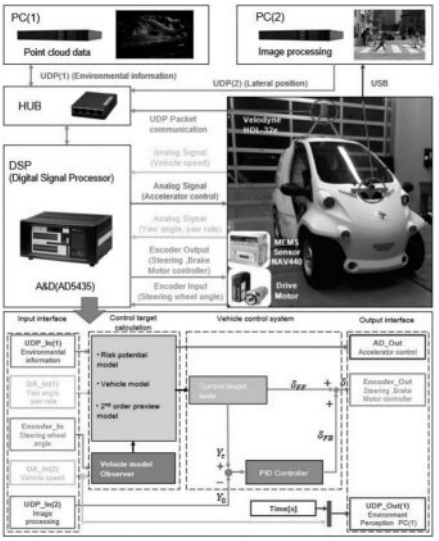


Figure 8. Sensors and hardware components for experiment vehicle.

a radius of 20 m by the ego-vehicle. The parameters were updated approximately at the interval of 0.1 s; this value is depend on the update rate of LIDAR. This information was given as an input to the control target algorithm. Using this information, the algorithm updated control target in real time.

3.2 *Steering control*

The feed forward steering angle and target trajectory of the ego-vehicle were calculated by control target calculation algorithm. On the other hand, the lateral position of the ego-vehicle was calculated by traffic lane detection using a Charge Coupled Device (CCD) camera. The lateral deviation between the target trajectory and ego-vehicle position was fed back to the control target. The steer motor was controlled by these values. In this way, we achieved the direction control of the experiment vehicle.

4 VERIFICATION OF ALGORITHM

This chapter describes the results of our field experiments in which an actual vehicle was maneuvered by a skilled driver. For the risk feeling potential of this algorithm, the parameter estimation results for the function were derived from the vehicle path patterns based on the measured data for obstacle avoidance under each condition.

4.1 *Experiment conditions*

The experiment was conducted in two scenarios.

Experiment scenario 1 assumed several conditions of the velocity of the ego- and the advancing obstacle vehicle around one traffic lane. The ego-vehicle overtook the advancing obstacle, as shown in Fig. 9.

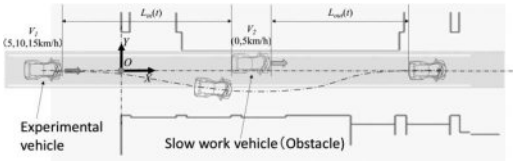


Figure 9. Experimental condition of overtaking (Scenario 1).

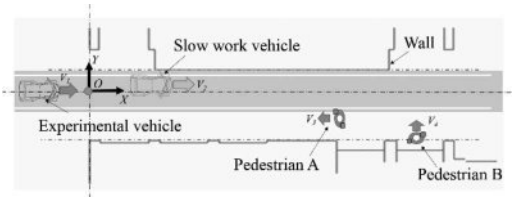


Figure 10. Experimental condition of complicated traffic situation (Scenario 2).

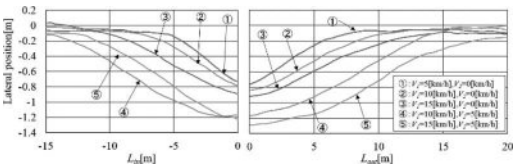


Figure 11. Comparison of trajectory for relative distance.

The ego-vehicle speed, V_1, was 5, 10, and 15 km/h, and the obstacle vehicle speed, V_2, was 0 and 5 km/h.

Experiment scenario 2 assumed several obstacles on the inside and outside of the targeted traffic lane, as shown in Fig. 10. The assumed obstacles were a slow work vehicle and two pedestrians. The ego-vehicle speed was maintained at about 10 km/h by the driver. The ego-vehicle avoided multiple obstacles smoothly.

The driver was skilled and drove the vehicle carefully ensuring safety. The ego-vehicle was steered freely while the driver felt the risk from obstacle(s). We estimated risk potential parameters from the trajectory of a skilled driver in this situation. Then, using these parameters, we expressed the driver's operation in this situation by our algorithm.

4.2 *Experimental results*

Fig. 11 shows the result of the trajectory of the overtaking situation (scenario 1). Every condition for speed had a different trajectory. Here, the relationship between the moving and maneuvered vehicles is described by an evaluation index approaching in the longitudinal direction in terms of the time-to-collision (TTC):

$$TTC_{in}(t) = \frac{L_{in}(t)}{V_2(t) - V_1(t)} \tag{13}$$

$$TTC_{out}(t) = \frac{L_{out}(t)}{V_2(t) - V_1(t)} \tag{14}$$

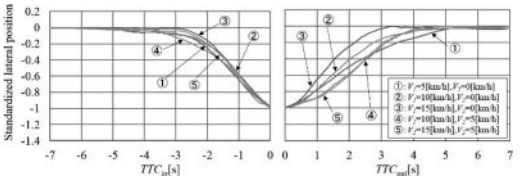


Figure 12. Standardized trajectory in experiment.

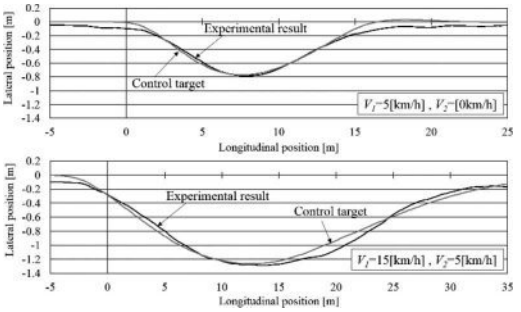


Figure 13. Comparison with vehicle motion (Human Motion) and control targets.

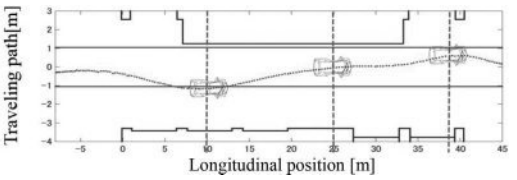


Figure 14. Travelling path of experiment scenario 2.

where $L_{in}(t)$ and $L_{out}(t)$ are the relative distances between the vehicles and $V_1(t)$ and $V_2(t)$ are the vehicle velocities. In addition, the differences in the lateral positions were standardized by the width of the lane change under each condition, as shown in Fig. 12. As a result, the difference in the vehicle velocity for the vehicular path specified by the TTC had a high degree of approximation. Therefore, the risk potential of longitudinal direction confirmed that it was a function of the relative velocity. The parameters of the risk potential model were adjusted based on the vehicular path specified by the abovementioned TTC. The parameters of the risk potential model were estimated from the vehicle velocity and the relative speed with respect to the other vehicle. We calculated a trajectory by control target calculation algorithm and compared it with the trajectory of the experiment, as shown in Fig. 13. It was confirmed that the calculated target trajectory could simulate the trajectory of the actual vehicle well.

Fig. 14 shows the result of the travelling path of a complicated traffic situation (scenario 2). The ego-vehicle avoided multiple obstacles and ran smoothly. Fig. 15 shows an example of the generated risk potential map based on this travelling path. The risk potential map was composed of the risk potential of surrounding environmental sidewalls, traffic lane, obstacle vehicle,

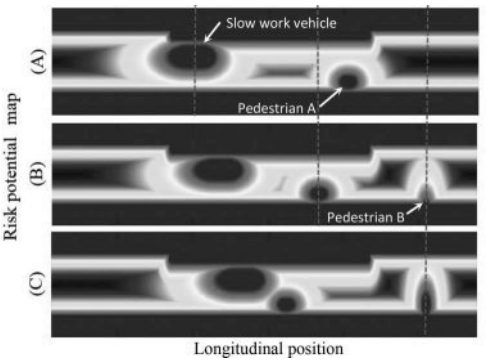


Figure 15. Example of the generated risk potential maps.

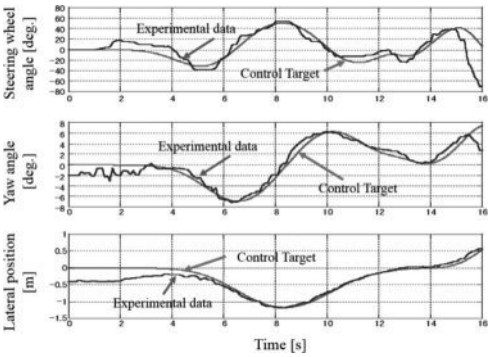


Figure 16. Calculation results of the control target and vehicle states.

and pedestrians; it was generated using the estimated parameters. The risk potential map shown in Fig. 15 indicates (A) overtaking the slow work vehicle, (B) passing pedestrian A, and (C) avoiding pedestrian B. The simulation results of the steering angle, yaw angle, and lateral position generated by the algorithm are shown in Fig. 16. The simulation results agree with the actual values.

From these results, we consider that a control target that is similar to that of a human driver can be generated by appropriately setting the risk potential parameter.

5 EXPERIMENT USING ACTUAL VEHICLE

By the acquisition of the environmental information and the calculation of the target trajectory in real time, the automatic steer control experiment by instruction control was performed to inspect this algorithm.

5.1 *Experimental conditions*

The experimental vehicle was a small electric vehicle as shown in Fig. 8. The experiment scenario was a complicated traffic situation, as shown in Fig. 10. The position and the movement of the obstacles were detected using LIDAR. In addition, we assumed that the attribute of the obstacle could be detected by

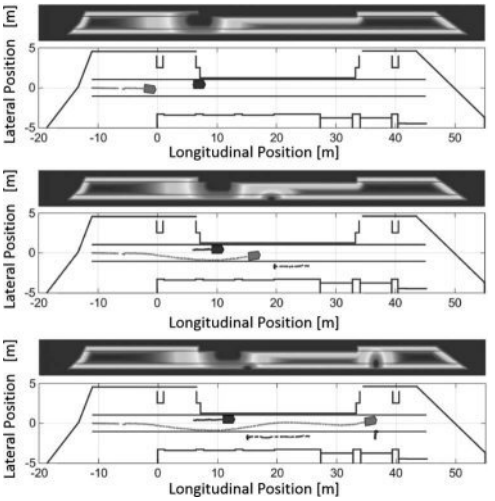


Figure 17. Detected position of obstacles and change of risk potential map.

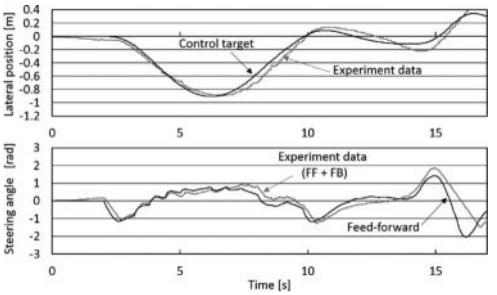


Figure 18. Lateral position and steering wheel angle of the experiment vehicle and control target.

a different method; we provided the information to the environmental recognition system in advance. The driver acquired the experimental vehicle for safety and adjusted the vehicle speed to about 10 km/h. The control target was updated at the interval of 0.6 s by control target calculation algorithm.

5.2 *Experimental results*

Fig. 17 shows the result of the detected position of the ego-vehicle and the obstacles, and the change in the risk potential map with time. When the ego-vehicle moved forward, obstacles were detected in turn. Risk potential was set for each obstacle and the minimum risk point was generated. Fig. 18 shows the result for the lateral position, and the steering wheel angle of the experimental vehicle and control target. Smooth control target was generated for multiple obstacles by the control target calculation algorithm. In addition, the travelling path of the experimental vehicle was controlled so as to follow the control target trajectory precisely using the feed forward steering wheel angle calculated by the algorithm and feedback control.

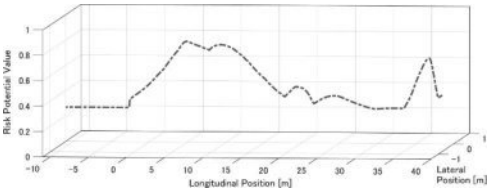


Figure 19. Transition of risk potential value.

In this result, we confirmed that this algorithm can generate appropriate control target under the environment with multiple moving objects. Fig. 19 is the transition of risk potential value. It was confirmed that the risk potential value was increased when ego-vehicle ran close to each obstacles. In this result, we confirmed that this algorithm can generate appropriate control target under the environment where there were multiple moving objects. In addition, calculating the risk potential value on the target trajectory, we think that this results can be utilized to the decision model.

6 CONCLUSION

In a traffic condition with multiple moving obstacles, we suggested a real time control target generation algorithm from the surrounding environment by using the risk potential and verified the effectiveness of the algorithm. The algorithm could simulate the steering operation of a human driver in detail by estimating the risk potential parameters.

In addition, the same algorithm was applied to the actual vehicle and tested. It is concluded that the mutual accordance between an autonomous vehicle and a human-driven vehicle can be achieved by using control target algorithm.

REFERENCES

[1] N. Suganuma, et al, “Public road experiment of autonomous vehicle at depopulated area” JSAE Annual Congress Proceedings, No. 14-15S, p. 390–394, 2015 (in Japanese).

[2] University of Michigan, Mobility Transformation Center: Mcity Test Facility, http://www.mtc.umich.edu/test-facility (2015).

[3] I. Kageyama, “On a Driver Model with Feeling of Risk in Forward View”, Trans. of JSAE, Vol. 24, No. 2, pp. 81–87, 1993. (in Japanese).

[4] T. Kaneko, “Calculation Algorithm for Motion Control Target for the Platooning of Autonomous Heavy Vehicles”, Proc. of 2014 UKACC 10th International Conference on Control, 2014.

[5] S. Rowell, A. A. Popov, J. P. Meijaard, “Parameter Study of Motorcycle Riding by Model Predictive Control”, Proc. of AVEC ’08, 2008.

[6] T. Kaneko, Y. Kuriyagawa, I. Kageyama, “Calculation Algorithm of Steering Control Target for Autonomous Heavy Vehicle under Mixed Traffic” Proc. ITS World Congress TOKYO, 2013.

Advanced Vehicle Control – Edelmann, Plöchl & Pfeffer (Eds)
© 2017 Taylor & Francis Group, London, ISBN 978-1-138-02992-7

Implementation of a modified Hamiltonian algorithm for control allocation

Y. Gao & T. Gordon
School of Engineering, University of Lincoln, UK

M. Lidberg
Department of Applied Mechanics, Chalmers University of Technology, Sweden

ABSTRACT: This paper is motivated by the problem of terminal understeer of a road vehicle. A relevant scenario is where a vehicle enters a curve at excessive speed and the control objective is to apply automatic chassis control to prevent the vehicle from drifting out of the lane. In a previous study, the optimization problem was formulated as the minimization of maximum path off-tracking; the optimal response approximates to that of a friction-limited particle model, leading to a parabolic path reference (PPR) with the target mass-centre acceleration vector fixed in the global frame. The present paper considers in greater detail how the acceleration target is realized on an experimental vehicle. The approach is based on a recently developed model-based control method – the Modified Hamiltonian Algorithm (MHA). Simulations with a full vehicle (CarMaker) model are carried out, and test-track experiments are conducted to test the controller and validate the simulations. Results show that transient effects such as actuator delays and rate limits can have a significant effect on performance. On the other hand, the controller appears robust to factors such as tyre wear and uncertainty in vehicle parameters, and closely approximates the particle reference once these transient effects are accounted for. Since the control architecture is adaptive to track a changing acceleration reference, these conclusions are likely to be valid across a wider range of scenarios.

1 INTRODUCTION

Vehicle motion control at the limits of friction has always been a challenging task (Kritayakirana & Gerdes 2012); under such conditions, the driver may easily lose control of the vehicle leading to possible accidents. One example is driving with excessive speed in curves which may lead to loss of directional control through yaw instability (oversteer) or front tyre force saturation (understeer), risking a run-off road crash in either case.

While conventional electronic stability control (ESC) is well suited to correcting oversteer, the understeer phenomenon is more strongly associated with path curvature; understeer mitigation is therefore directed towards increasing mean path curvature in response to increasing steering demands from the driver, and according to recent literature this relies on a progressive increase in lateral acceleration, coordinated with a reduction in vehicle speed.

These studies have shown that the optimal control for understeer mitigation targets the vehicle acceleration vector to follow a globally-fixed reference. Yaw motion control is important – for example to avoid excessive body sideslip – but tends to play a secondary role. The resulting motion for optimal understeer mitigation is therefore a parabola, giving rise to the 'parabolic path reference' (PPR) (Klomp, Lidberg, & Gordon 2014).

Directing the CG acceleration vector in global coordinates was also prioritised in two other scenarios: post-impact control and collision avoidance by lateral path deviation (collision avoidance by steering and/or differential braking). In the case of post-impact control, an initial light impact can lead to yaw instability and path deviations which are not easily controlled by the human driver. Research has shown that lateral deviation from the pre-impact path is correlated with the severity of any secondary collision, motivating a control which minimises deviation from the center of the initial direction of travel (Yang 2013). Hence, the priority is to maximize the mean CG acceleration in a direction normal to the lane centre. For collision avoidance, the target acceleration may also be prioritised normal to the initial path, but reversing direction after some time interval to recover vehicle motion parallel to the original path.

In (Yang, Gordon, Jacobson, & Jonasson 2012) the post-impact control problem was solved using Quasi-Linear Optimal Control (QLOC). In this formulation, the co-state equations were linearized and solved around a nominal predicted state trajectory. Combined with a terminal cost function (the velocity component in the direction of maximum crash risk, i.e. normal to the lane centre) the two-point boundary value problem can be solved by minimizing a Hamiltonian function, subject to friction limits at the individual tyres. It was shown that performance can

be very close to optimal (Yang, Gordon, Jacobson, & Jonasson 2012), motivating a further simplification in the form of the Modified Hamiltonian Algorithm (MHA) (Gordon & Gao 2014) – see below also. The core advantage of MHA, inherited from QLOC, is that a single costate ratio (denoted λ in the following) determines the balance between yaw moment and mass centre force control, and – the key innovation of MHA – this ratio can be estimated in real-time using a relatively simple adaptation strategy.

The resulting MHA architecture is then capable of flexible allocation of actuator controls based on the instantaneous direction of the target (friction-limited) acceleration vector of the vehicle mass-centre, as well as the adaptive λ ratio.

The core aim of the current paper is to test and evaluate the MHA controller in the context of a high fidelity vehicle model and also a test vehicle. The immediate context is to provide an effective lane departure prevention system and hence improve safety performance. We focus attention on the lower-level control elements relating to MHA and note that a successful evaluation of MHA opens up the possibility of a wide range of friction-limited applications in vehicle control for active safety.

2 CONTROL STRUCTURE

In the context of evaluating MHA performance in real-time, an inertially-fixed acceleration vector is convenient for testing, even though in other applications the direction may change over time, as with post-impact control on a curved road or in collision avoidance by lateral path deviation.

The general control structure is shown in the upper part of Figure 1. The acceleration target is obtained from road geometry in the form of a unit vector $\mathbf{p} = [p_x, p_y]^T$ in the direction of 'maximum crash risk', i.e. opposing the desired acceleration vector. The MHA operator is then tasked with delivering the required actuator commands.

2.1 *Reference generation*

In the specific case of PPR, a friction-limited particle model is used to generate the acceleration reference and, in the case of constant road curvature and constant friction, an analytical solution can be obtained. The mathematical relationship between the acceleration reference and road geometry is given by (Gao, Gordon, Lidberg, & Klomp 2016):

$$R = \frac{\upsilon_0^2}{\mu g \cos\theta} \tag{1}$$

where, θ defines the (constant) angle between acceleration reference direction and the global coordinate system – see Figure 2, μ is the friction coefficient, υ_0 is the initial speed, and R is the constant radius of the road segment.

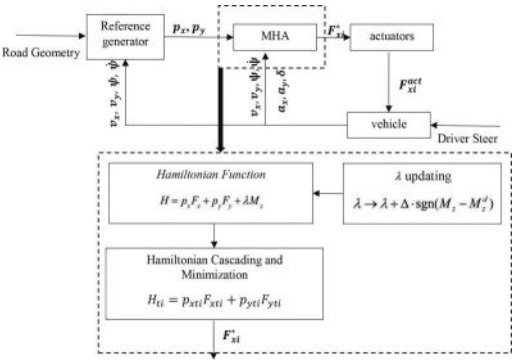


Figure 1. Control structure.

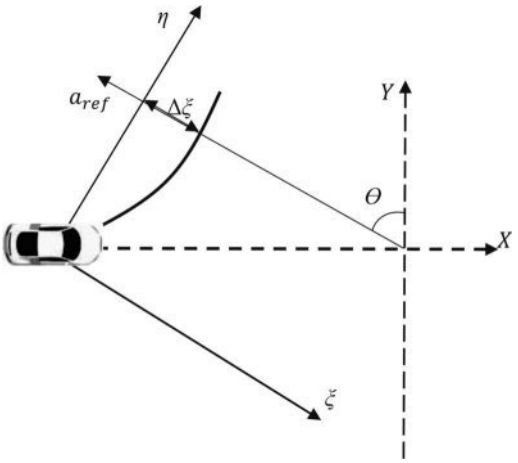


Figure 2. Schematic of the constant θ test strategy.

2.2 *Modified Hamiltonian algorithm*

The MHA block in the lower part of Figure 1 provides the required actuator control signals. While this can be achieved through nonlinear optimization methods, these are 'black-box' in nature and tend to be computationally expensive (Wang & Longoria 2009, Fredriksson, Andreasson, & Laine 2004). The MHA method, by contrast, takes a simpler and more transparent approach by directly minimising a linear combination of force and moment criteria as follows.

Let $a^d = [a_x^d, a_y^d]^T$ be the desired mass centre acceleration vector, which we assume to be on the limits of friction. The Hamiltonian function is linear in controls $H = p_x F_x + p_y F_y + \lambda M_z$, where $\mathbf{p}$ as a unit vector in the direction opposing the desired acceleration vector $\mathbf{p} = -\mathbf{a}^d / |\mathbf{a}^d|$. For yaw moment control, λ is adapted to track a desired yaw moment M_z^d

$$\lambda \rightarrow \lambda + \Delta \cdot sgn(M_z - M_z^d) \tag{2}$$

Here the update of λ follows a fixed increment per controller time step. And since the Hamiltonian function is linear in tire forces, the optimization can be

achieved through a local minimization at each individual tire. For more details, the readers should refer to (Gao, Gordon, Lidberg, & Klomp 2016). The next part of the paper is focused on the practical implementation of this method.

3 TESTING STRATEGY

Figure 2 illustrates 'constant θ' test strategy adopted in this paper, where θ is the angle between the acceleration vector and global Y coordinate. Several test-runs were performed, with different combinations of θ angles and initial velocities υ_0. As mentioned, the acceleration reference can be changing over time according to different control applications, while for testing an inertially-fixed acceleration reference was chosen for lower level control allocation, to simplify the testing procedure.

3.1 *Physical test conditions*

The physical experiments were performed on the *High Speed Test Area* at the AstaZero proving ground, Sweden. The test vehicle was a front-wheel-drive 2009 Saab 9-3 with a 250 hp V6 engine and a six-speed manual transmission. The vehicle was equipped with an additional set of four identical brake calipers controlled via an electro-hydraulic brake (EHB) system, enabling individual brake control. Real-time calculation of the controller was run on a MicroAutoBox, which is the dSPACE compact rapid prototyping unit; real-time control was performed through its software *ControlDesk* (Guide 2001) running on a separate host PC mounted in the vehicle.

Experimental data was captured via an RT3000 from Oxford Technical Solutions (Oxford-Technical-Solutions 2010), equipped with dual antenna model, which is an advanced precision Inertial and GPS Navigation system; it has a built-in signal filtering system and offers CAN messages as an output option. Data was recorded separately on two data acquisition systems: (i) real time control software ControlDesk (dSPACE) (ii) CANalyzer (Vector) software. Data from different sources was logged via multiple channels, specifically in our application, RT3000 and vehicle data was logged with 2 existing CAN channels and other internal variables of interests, such as braking pressure command, were logged via a further (private) CAN channel.

3.2 *Test procedure*

Several quasi-steady-state cornering tests were performed prior to the constant θ testing, to determine the road friction level. Results showed a limiting acceleration magnitude of around $9\,\mathrm{ms}^{-2}$. The steering manoeuvre for the MHA test was kept simple for this experiment; the driver was asked to perform a step steer, tuned according to equation 1 and according to a simple Ackerman steering condition:

$$\delta = \rho L/R \tag{3}$$

where ρ is the steering ratio. Here L is the wheelbase of the vehicle, and the steering ratio (ρ) for the tested vehicle was found to be 15.9.

The MHA test procedure comprises the following steps:

- drive along the local X direction at a given speed υ_0
- trigger the system braking and initiate step-steer at the same instant
- retain the steering angle till the end of the braking intervention

4 PERFORMANCE EVALUATION

As seen in equation 1, the road friction coefficient μ is needed for the calculation of the steering input. A number of steady state cornering (SSC) tests were performed on the test track to estimate the current road friction level. In the road model for CarMaker simulation (CarMaker 2014), road friction coefficient is tuned to match the speed and acceleration profile obtained from the SSC tests. The parameters in the vehicle model were also chosen to approximate the real test vehicle. In the ideal simulation environment, the commanded braking pressure can be achieved instantaneously, while in reality, physical limitations such as actuator delay (T_d) and limitation on braking pressure ramp-up rate (Λ) may lead to a degrading control performance. Prior to the MHA testing, a brake system check was performed to examine these factors. In simulation, these factors are modelled to approximate the real testing condition.

4.1 *Brake subsystem test*

Apart from checking that the EHB system is functioning properly, one objective of the subsystem test is to estimate parameters for any time delay in the system. From Figure 3, a time delay of $T_d = 70\,\mathrm{ms}$ is clearly observed in the system; also and there is a command signal rising rate $\Lambda \simeq 200$ Bar/sec. It can be also seen the actual braking pressure is following the commanded braking pressure closely; indicating that apart from the delay effect, the EHB system is suitable for a rapid control application.

4.2 *Vehicle simulation*

First we test whether the high fidelity simulation model can approximate the performance of the ideal particle, with constant maximum acceleration in the negative ξ direction. Simulation results are shown in Figures 4–6.

Figure 4 shows a good acceleration tracking performance in the direction of off-tracking (ξ) – with near constant acceleration and a parabolic shape for

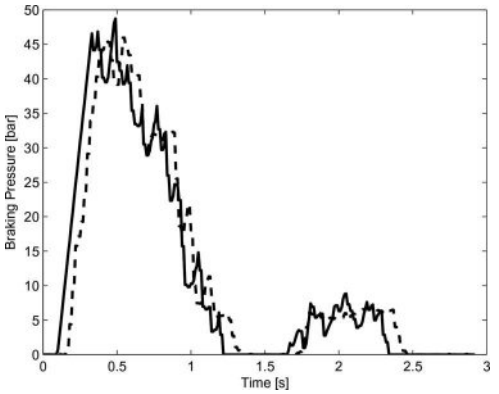


Figure 3. Commanded braking pressure and actual braking pressure profile for the braking system test.

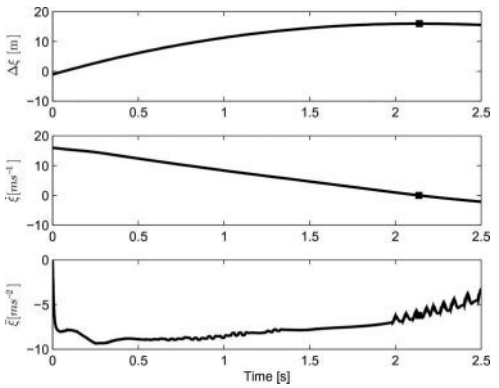


Figure 4. Displacement, velocity and acceleration component in the direction of off-tracking ξ, markers show point of maximum off-tracking.

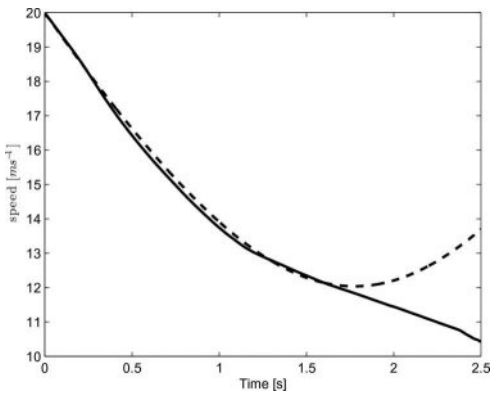


Figure 5. Speed profile from CarMaker simulation (dashed line: CarMaker vehicle model; solid line: particle model).

displacement. The point of maximum off-tracking occurs when $\dot{\xi} = 0$. Note that after the maximum off-tracking point, tracking the acceleration reference would involve distributing *traction* force on each

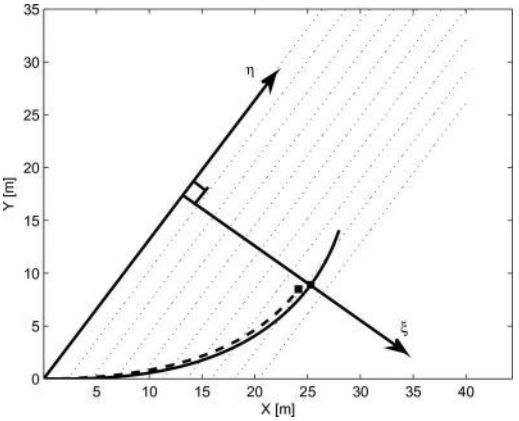


Figure 6. Vehicle path in Global coordinates (X,Y) and control reference coordinates (ξ,η). A series dotted lines represent constant ξ values.

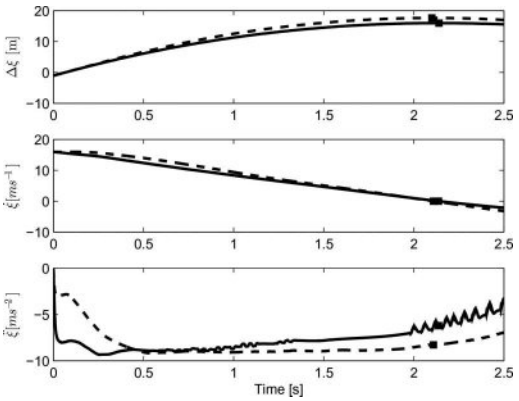


Figure 7. Simulation results of displacement, velocity and acceleration component in the direction of off-tracking ξ (solid line: T_d and Λ delays not included in the model; dashed line: $T_d = 70$, $\Lambda = 200$).

wheel but this is not applicable to the current EHB scenario. This explains a reduction of the acceleration in ξ after the maximum off-tracking point. Figure 5 shows that the vehicle speed profile is a close match to that of an ideal particle model up to the point of maximum off-tracking. Figure 6 shows more clearly the control objective; it is not to track a particular path reference but to minimize the off-tracking in the ξ direction, i.e. minimizing the number of lines of constant ξ that it passes. In real world application, the lines of constant ξ may quantify the risks of accidents and by minimizing the number of lines the vehicle passes, we can reduce the risk or severity of the accident in that direction.

Next, the actuator delay (T_d) and rate limit (Λ) are taken into account. In the Simulink model, these two factors are captured by introducing a transport delay block and rate limiter block. From Figure 7, actuator delay and rate limit are seen to have a significant influence on the overall control performance in the way of causing an initial transient effect. This can be explained

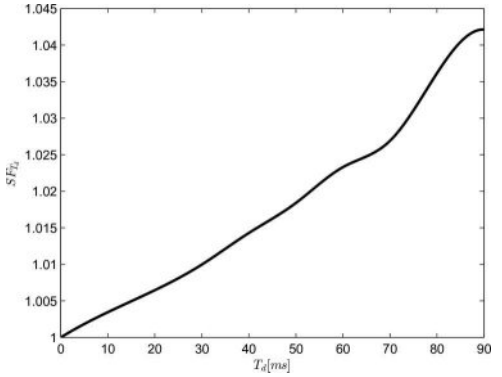


Figure 8. Normalized maximum off-tracking SF_{T_d} vs T_d – only actuator time delay is included.

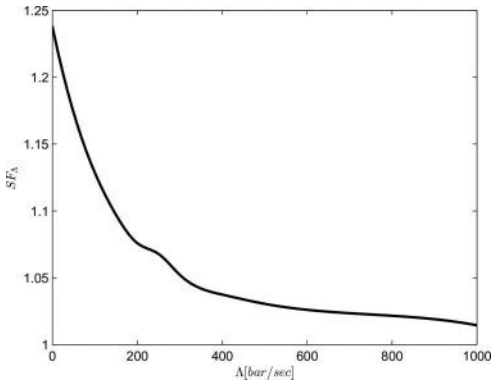


Figure 9. Normalized maximum off-tracking SF_Λ vs Λ – only actuator rate limit is included. SF_Λ tends asymptotically to approach 1 as $\Lambda \to \infty$.

as follows: at the start of the intervention, the speed reduction is more important than yaw moment control and MHA is commanding large braking pressure to slow the vehicle down but the actual braking pressure is restricted by the system hardware. Therefore, it takes longer for the acceleration vector to find the reference. However, the overall acceleration tracking performance is less oscillating owing to a smoother braking signal after the rate limiter block. A series of simulation test-runs were performed across a range of T_d and Λ values. A normalized value of the maximum off-tracking is chosen as the evaluation index $SF = \frac{\Delta\xi}{\Delta\xi_0}$ where $\Delta\xi_0$ is the off-tracking distance in the case without delay terms and subscripts Λ or T_d stand for the delay term included in the simulation. The trend is shown in Figure 8–9: a larger system delay and slower rate limit on braking pressure will lead to a larger maximum off-tracking.

4.3 *Test-track experiment*

The performance and robustness of the controller is evaluated through several test-runs with the experimental vehicle mentioned above. A number of

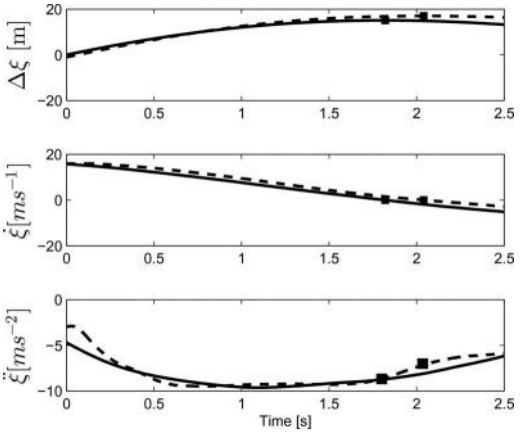


Figure 10. Displacement, velocity and acceleration component in the direction of off-tracking ξ, markers show the point of maximum off-tracking. (solid line: experiment; dashed line: simulation; markers: maximum off-tracking point).

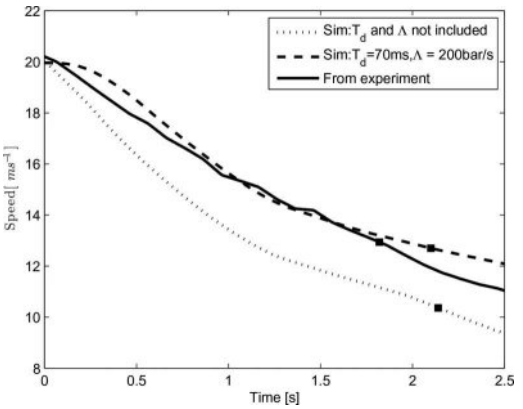


Figure 11. Speed profile comparison of systems with and without time delay.

different combinations of angles θ and initial velocities υ_0 were tested. It is found that the real-time control performance is consistently similar to the simulation results, confirming the viability of the control scheme. Due to the limited space, only one set of experimental results is presented in this paper – see Figures 10–12 ($\theta = 53°$ and $\upsilon_0 = 20$ m/s). Actuator delay and rate limit are considered in the simulation to make a fair comparison with the experimental results.

Figure 10 shows the time histories of the state variables resolved in the ξ direction, including comparison with simulation results. It can be concluded that MHA performs well in both simulation environment and in real time. Compared with previous simulation results in Figure 4, the experimental results verified that actuator delay and rate limit effect on control performance. It is also worth mentioning that, the outer edges of the tyres used for MHA testings were worn out to a certain extent during SSC testing; however they were capable of generating sufficient tire forces in a larger lateral

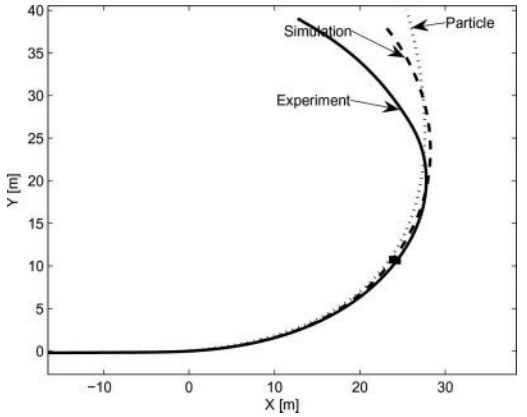


Figure 12. Vehicle trajectory comparison in global (X,Y) coordinates; solid line: from the experiment, dashed line: CarMaker simulation, dotted line: ideal particle.

slip angle range, this leading to larger body sideslip angles compared with simulation. The speed profile (see Figure 11) further confirm the conclusion that peak tyre forces were still achieved, in spite of the noted tyre wear.

Note that the driver was driving the vehicle sightly above the targeted speed, otherwise a better match to the simulation speed profile can be made. The trajectory from the experiment is shown in Figure 12, together with vehicle trajectory from simulation and ideal particle model and the results are aligned at local zero coordinates. Taken account of the actuator delay T_d and rate limit Λ, the trigger point for control performance evaluation (particle comparison) has been chosen at a delayed time instant (ΔT) after the start of braking command, where $\Delta T = T_d + 0.5\Lambda^{-1}P_{max}$. We can see that the path trajectories obtained using three separate ways match with one another very well.

5 CONCLUSIONS

In this paper, an efficient control allocation method (MHA) developed to operate at the limit of friction is studied. A simple constant θ test plan was designed to evaluate the controller, using a fixed direction of off-tracking (ξ). Controller performance was evaluated in terms of maximum distance travelled in the ξ direction, as well as via the acceleration performance relative to an ideal particle. Simulations with a full vehicle (CarMaker) model were carried out, and test-track experiments also conducted to test the controller and validate the simulations. Results show that transient effects such as actuator delays and rate limits can have a significant effect on performance. Taking account of such delays, the controller performs almost identically to a high fidelity simulation model. Also, since tyre and vehicle parameters were not closely matched to the test vehicle in the MHA algorithm, the controller appears robust to factors such as tyre wear and uncertainty in vehicle parameters.

Finally, since the control architecture is adaptive to track a changing acceleration reference, these conclusions are likely to be valid across a wider range of scenarios. Future work will seek to reduce the effects of transient delays and test the controller with non-constant acceleration references.

REFERENCES

CarMaker, I. (2014). Users guide version 4.5. 2. *IPG Automotive, Karlsruhe, Germany*.

Fredriksson, J., J. Andreasson, & L. Laine (2004). Wheel force distribution for improved handling in a hybrid electric vehicle using nonlinear control. In *Decision and Control, 2004. CDC. 43rd IEEE Conference on*, Volume 4, pp. 4081–4086. IEEE.

Gao, Y., T. Gordon, M. Lidberg, & M. Klomp (2016). An autonomous safety system for road departure prevention based on combined path and sideslip control. In *The Dynamics of Vehicles on Roads and Tracks: Proceedings of the 24th Symposium of the International Association for Vehicle System Dynamics (IAVSD 2015), Graz, Austria, 17–21 August 2015*, pp. 281. CRC Press.

Gordon, T. & Y. Gao (2014). A flexible hierarchical control method for optimal collision avoidance. In *Mechatronics-Mechatronika (ME), 2014 16th International Conference on*, pp. 318–324. IEEE.

Guide, C. E. (2001). dspace gmbh. *Paderborn, Germany*.

Klomp, M., M. Lidberg, & T. J. Gordon (2014). On optimal recovery from terminal understeer. *Proceedings of the Institution of Mechanical Engineers, Part D: Journal of Automobile Engineering*, 0954407013511796.

Kritayakirana, K. & J. C. Gerdes (2012). Autonomous vehicle control at the limits of handling. *International Journal of Vehicle Autonomous Systems 10*(4), 271–296.

Oxford-Technical-Solutions (2010). Inertial measurement system user manual.

Wang, J. & R. G. Longoria (2009). Coordinated and reconfigurable vehicle dynamics control. *IEEE Transactions on Control Systems Technology 17*(3), 723–732.

Yang, D. (2013). *Vehicle dynamics control after impacts in multiple-event accidents*. Chalmers University of Technology.

Yang, D., T. J. Gordon, B. Jacobson, & M. Jonasson (2012). Quasi-linear optimal path controller applied to post impact vehicle dynamics. *IEEE transactions on intelligent transportation systems 13*(4), 1586–1598.

Advanced Vehicle Control – Edelmann, Plöchl & Pfeffer (Eds)
© 2017 Taylor & Francis Group, London, ISBN 978-1-138-02992-7

Design of an automated steering controller with steering actuator dynamics and adaptive preview time

B.-C. Chen, C.-T. Tsai & Y.-M. Lin
National Taipei University of Technology, Taipei, Taiwan

K. Lee
Korea Polytechnic University, Siheung City, Korea

ABSTRACT: An automated steering controller is proposed to track the target path in this paper. Model predictive control (MPC) is employed to design the controller based on a 5-state road following bicycle model including the steering actuator dynamics. A path geometry change (PGC) index is designed to assess the severity of the path-following maneuver ahead of the vehicle. An adaption rule for adaptive preview time (APT) is designed as a linear function of PGC to adjust the prediction horizon of MPC. Simulation results show that the proposed algorithm can effectively reduce the path following error and the maximum lateral displacement while reducing the lateral acceleration and jerk for the lane following and lane change maneuvers.

1 INTRODUCTION

In order to reduce the human related factors for the traffic accidents, many research institutes have been investigating these issues to improve the vehicle safety. Advanced driver assistance system (ADAS) is one of the major solutions for traffic accidents caused by driver errors. Via the integration of sensing, communication, and control, a vehicle with the level 2 automation defined by National Highway Traffic Safety Administration (NHTSA) (Marshall 2013) can perform two partially decoupled tasks simultaneously. One task is the longitudinal speed control to maintain headway safety. The other task is the steering control to control the lateral motion of the vehicle to follow the desired path.

For automated steering control, it generates steering actions similar to the driver's behavior. Two types of approaches, model free and model based, are commonly used to designed the controller. The lateral displacement error and orientation error at the preview point are employed to calculate the steering angle command for the model free approaches (Broggi et al. 1999, Sotelo 2003, Cremean et al. 2006). As for model-based approaches (MacAdam 1981, Hwang et al. 2008, Kang et al. 2008, Kim et al. 2012, Chen et al. 2014), a 4-state road following bicycle model is often employed to design the controller. However, the steering action relies on the angle control of the electric power steering (EPS). The actuator dynamics should also be included for smooth control actions.

The preview horizons of the previous MPC approaches are set to be constant values. However, the driver actually adjusts the preview time according to the road geometry to avoid excessive lane departure. The preview time is reduced for driving from a straight road into a sharp curve. On the contrary, the preview time is increased for driving from a sharp curve into a straight road. MacAdam (2001) proposed an algorithm to adjust the preview time by checking the intersection of the predicted path (plus half the vehicle width) and either of the two road boundaries. The preview time is reduced by a certain amount if an intersection, i.e. lane departure, exists. If no intersection exists, the preview time is increased by a certain amount. In either case, the adjusted preview time is limited between minimum and maximum allowable values.

An automated steering controller is proposed to track the target path in this paper. MPC is employed to design the controller based on a 5-state road following bicycle model including the steering actuator dynamics. A path geometry change (PGC) index is designed to assess the severity of the path-following maneuver ahead of the vehicle. An adaption rule for adaptive preview time (APT) is designed as a linear function of PGC to adjust the prediction horizon of MPC.

The remainder of this paper is organized as follows: the 5-state bicycle model with the actuator dynamics is briefly introduced in Section 2. Followed by the design of APT using PGC in Section 3. Proposed control is presented in Section 4. Simulation results are presented in Section 5. Finally, conclusions are made in Section 6.

2 MODELLING

A 5-state road following bicycle model with a first-order actuator dynamics of the EPS as shown below is used to as the plant model for MPC.

$$\tau\dot{\theta}_o + \theta_o = \theta_c \tag{1}$$

where θ_o is the steering angle response of the EPS at the front wheel; θ_c is the steering angle command of MPC; τ is the time constant of the EPS.

The vehicle lateral displacement y and yaw angle error $\psi_e = \psi_e - \psi_d$ are included for path-following application. ψ is the yaw angle of the vehicle. ψ_d is the yaw angle of the tangent line of the road. The state-space representation can be expressed as follows.

$$\dot{\mathbf{x}}_m = \mathbf{A}_m\mathbf{x}_m + \mathbf{B}_m u \tag{2}$$

where $\mathbf{x}_m = [y v_y \ \ \psi_e r \ \ \theta_o]^T$ is the state vector; $u = \theta_c$ is the input; v_y is the lateral velocity; r is the yaw rate; θ_o is the steering angle response at the front wheel; $\mathbf{A}_m$ and $\mathbf{B}_m$ are system matrix and input matrix as shown below:

$$\mathbf{A}_m = \begin{bmatrix} 0 & 1 & v_x & 0 & 0 \\ 0 & \frac{-(C_{\alpha f}+C_{\alpha r})}{mv_x} & 0 & \frac{bC_{\alpha r}-aC_{\alpha f}}{mv_x} - v_x & \frac{C_{\alpha f}}{m} \\ 0 & 0 & 1 & 0 & 0 \\ 0 & \frac{bC_{\alpha r}-aC_{\alpha f}}{I_z v_x} & 0 & \frac{-(a^2C_{\alpha f}+b^2C_{\alpha r})}{I_z v_x} & \frac{aC_{\alpha f}}{I_z} \\ 0 & 0 & 0 & 0 & -\frac{1}{\tau} \end{bmatrix} \tag{3}$$

$$\mathbf{B}_m = \begin{bmatrix} 0 & 0 & 0 & 0 & \frac{1}{\tau} \end{bmatrix} \tag{4}$$

where v_x is the vehicle speed; m is the vehicle mass; a and b are the distances from the C.G. to the front and rear axles, respectively; I_z is the yaw-plane rotational inertia; $C_{\alpha f}$ and $C_{\alpha r}$ are the cornering stiffness of the front and rear axles, respectively.

F-Class Sedan in CarSim is selected as the target vehicle to obtain the parameter values of m, a, b, and I_z. Nominal values of $C_{\alpha f}$ and $C_{\alpha r}$ are obtained by minimizing the path errors between the trajectory responses of CarSim and the bicycle model.

The plant model used for MPC can then be expressed in the discrete domain as follows.

$$\mathbf{x}_{m,k+1} = \mathbf{\Phi}_m\mathbf{x}_{m,k} + \mathbf{\Gamma}_m u_k \tag{5}$$

$$y_k = \mathbf{H}_m\mathbf{x}_{m,k} \tag{6}$$

where k denotes for the kth samples. $\mathbf{\Phi}_m$, $\mathbf{\Gamma}_m$, and $\mathbf{H}_m$ can be expressed as follows.

$$\mathbf{\Phi}_m = \begin{bmatrix} 1 & T_s & v_xT_s & 0 & 0 \\ 0 & \frac{-(C_{\alpha f}+C_{\alpha r})T_s}{mv_x}+1 & 0 & \frac{(bC_{\alpha r}-aC_{\alpha f})T_s}{mv_x} - v_xT_s & \frac{C_{\alpha f}T_s}{m} \\ 0 & 0 & 1 & T & 0 \\ 0 & \frac{(bC_{\alpha r}-aC_{\alpha f})T_s}{I_z v_x} & 0 & \frac{-(a^2C_{\alpha f}+b^2C_{\alpha r})T_s}{I_z v_x}+1 & \frac{aC_{\alpha f}T_s}{I_z} \\ 0 & 0 & 0 & 0 & -\frac{1}{\tau}T_s+1 \end{bmatrix} \tag{7}$$

$$\mathbf{\Gamma}_m = \begin{bmatrix} 0 & 0 & 0 & 0 & \frac{T_s}{\tau} \end{bmatrix} \tag{8}$$

$$\mathbf{H}_m = [1 \quad 0 \quad 0 \quad 0 \quad 0] \tag{9}$$

where T_s is the sample time.

3 ADAPTIVE PREVIEW TIME

3.1 *Path geometry change index*

PGC is designed to assess the severity of the path-following maneuver ahead of the vehicle. The target path generated from the path planning module of the automated steering controller can be expressed as $y_r = f(x_r)$ in the body coordinate of the vehicle. We can select N_p sample points of preview distances as follows.

$$x_{r,j} = (j-1)\Delta x_r \tag{10}$$

where $\Delta x_r = v_s T_s$ is the increment of the preview distance during the sample time; j is an integer between 1 and $N_p + 1$; $T_s = 0.1$ sec is the sample time. For $j = 1, x_{r,1}$ is the origin which does not belong the set of N_p sample points.

The PGC index, which consists of the 1-norm of the first derivatives and the 1-norm of the second derivatives of the target path in the prediction horizon N_p, can be expressed as follows.

$$PGC = \frac{1}{N_p}\|f'(\mathbf{x}_r)\|_1 + \frac{1}{N_p-1}\|f''(\mathbf{x}_r)\|_1 \tag{11}$$

where $\mathbf{x}_r$ is the vector containing the origin and N_p sample points of preview distances as shown below.

$$\boldsymbol{x}_r = [x_{r,1} \quad x_{r,2} \quad \cdots \quad x_{r,N_p+1}]^T \tag{12}$$

The first and second derivatives at $x_{r,j+1}$ can be approximated as follows.

$$f'(x_{r,i+1}) = \frac{f(x_{r,i+1})-f(x_{r,i})}{\Delta x_r} \tag{13}$$

$$f''(x_{r,j+1}) = \frac{f'(x_{r,j+1})-f'(x_{r,j})}{\Delta x_r} \tag{14}$$

It takes $N_p + 1$ points of the target path to calculate $N_p - 1$ points of the second derivative for the preview distance. The first derivative can be employed to represent the orientation angle of the tangent line of the target path at the preview point. The second derivative can be employed to approximate the curvature of the target path at the preview point.

The PGC index is increased for driving from a straight road into a sharp curve. On the contrary, the PGC index is reduced for driving from a sharp curve into a straight road. The 1-norm in Equation 11 is used to prevent the cancellation of the positive and negative values of the first and second derivatives for the S-curve path.

3.2 *Adaptation rule*

An adaption rule for APT is designed as a linear function of PGC (Fig. 1) to adjust the prediction horizon N_p as shown below.

$$N_p = round(m_{PGC}PGC + 20) \tag{15}$$

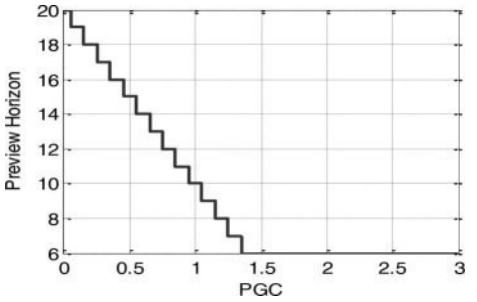


Figure 1. Adaption rule for APT.

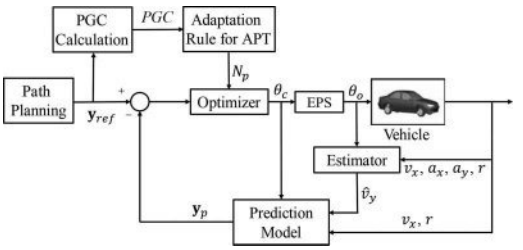


Figure 2. Proposed automated steering controller.

where m_{PGC} is used to specify the decay speed with respect to the PGC index. The minimum and maximum allowable values of N_p are set to be 6 and 20, respectively. The corresponding minimum and maximum preview time are 0.6 sec and 2 sec, respectively.

The larger the PGC index, the smaller the prediction horizon is. The preview horizon is reduced to a proper value to enhance the path tracking performance if the path geometry changes quickly in front of the vehicle. For a straight road ahead, the preview horizon is increased to a proper value to enhance the ride comfort with lower lateral acceleration and jerk.

4 CONTROLLER DESIGN

The proposed control is shown in Figure 2. The desired target path $\mathbf{y}_{ref}$ is obtained from the path planning module for lane following or lane change. The future trajectory $\mathbf{y}_p$ is predicted using the 5-state bicycle model. The optimizer is used to find the best set of the future control commands. Only the first element of the set is used as the steering angle command at the sample instant.

We can take difference operations on both sides of Equations 5 and 6 to obtain the following equations.

$$\Delta\mathbf{x}_{m,k+1} = \mathbf{\Phi}_m\Delta\mathbf{x}_{m,k} + \mathbf{\Gamma}_m\Delta u \tag{16}$$

$$y_{k+1} - y_k = \mathbf{H}_\mathrm{m}\mathbf{\Phi}_m\Delta\mathbf{x}_{m,k} + \mathbf{H}_\mathrm{m}\mathbf{\Gamma}_m\Delta u \tag{17}$$

where $\Delta\mathbf{x}_{m,k+1} = \mathbf{x}_{m,k+1} - \mathbf{x}_{m,k}$; $\Delta\mathbf{x}_{m,k} = \mathbf{x}_{m,k} - \mathbf{x}_{m,k-1}$; $\Delta u_{m,k} = u_k - u_{k-1}$. A new state vector can then be chosen as $\mathbf{x}_k = [\Delta\mathbf{x}_{m,k}\ \ y_k]^T$ to obtain the augmented model as follows.

$$\mathbf{x}_{k+1} = \mathbf{\Phi}\mathbf{x}_k + \mathbf{\Gamma}\Delta u_k \tag{18}$$

$$y_k = \mathbf{H}_m\mathbf{x}_{m,k} \tag{19}$$

where $\mathbf{\Phi}$ and $\mathbf{\Gamma}$ can be expressed as follows.

$$\mathbf{\Phi} = \begin{bmatrix} \mathbf{\Phi}_m & \mathbf{0} \\ \mathbf{H}_m\mathbf{\Phi}_m & 1 \end{bmatrix} \text{ and } \mathbf{\Gamma} = \begin{bmatrix} \mathbf{\Gamma}_m \\ \mathbf{H}_m\mathbf{\Gamma}_m \end{bmatrix} \tag{20}$$

The future control in the control horizon N_c can be described as

$$\Delta u_{k_i}, \Delta u_{k_i+1}, \cdots, \Delta u_{k_i+N_c-1}$$

where k_i is the sampling instant. The predicted state vector of the augmented model in the prediction horizon N_p can then be expressed as follows.

$$\begin{aligned}
\mathbf{x}_{k_i+1} &= \mathbf{\Phi}\mathbf{x}_{k_i} + \mathbf{\Gamma}\Delta u_{k_i} \\
\mathbf{x}_{k_i+2} &= \mathbf{\Phi}^2\mathbf{x}_{k_i} + \mathbf{\Phi}\mathbf{\Gamma}\Delta u_{k_i} + \mathbf{\Gamma}\Delta u_{k_i+1} \\
&\vdots \\
\mathbf{x}_{k_i+N_p} &= \mathbf{\Phi}^{N_p}\mathbf{x}_{k_i} + \mathbf{\Phi}^{N_p-1}\mathbf{\Gamma}\Delta u_{k_i} + \mathbf{\Phi}^{N_p-2}\mathbf{\Gamma}\Delta u_{k_i+1} \\
&\quad + \cdots + \mathbf{\Phi}^{N_p-N_c}\mathbf{\Gamma}\Delta u_{k_i+N_c-1}
\end{aligned}$$

The predicted output of the augmented model in the prediction horizon N_p can then be expressed as follows.

$$\begin{aligned}
y_{k_i+1} &= \mathbf{H}\mathbf{\Phi}\mathbf{x}_{k_i} + \mathbf{H}\mathbf{\Gamma}\Delta u_{k_i} \\
y_{k_i+2} &= \mathbf{H}\mathbf{\Phi}^2\mathbf{x}_{k_i} + \mathbf{H}\mathbf{\Phi}\mathbf{\Gamma}\Delta u_{k_i} + \mathbf{H}\mathbf{\Gamma}\Delta u_{k_i+1} \\
&\vdots \\
y_{k_i+N_p} &= \mathbf{H}\mathbf{\Phi}^{N_p}\mathbf{x}_{k_i} + \mathbf{H}\mathbf{\Phi}^{N_p-1}\mathbf{\Gamma}\Delta u_{k_i} + \\
&\quad \mathbf{H}\mathbf{\Phi}^{N_p-2}\mathbf{\Gamma}\Delta u_{k_i+1} + \cdots + \mathbf{H}\mathbf{\Phi}^{N_p-N_c}\mathbf{\Gamma}\Delta u_{k_i+N_c-1}
\end{aligned}$$

The prediction model can then be formulated as follows.

$$\mathbf{y}_p = \mathbf{F}\mathbf{x}_{k_i} + \mathbf{G}\Delta\mathbf{u}_p \tag{21}$$

where $\Delta\mathbf{u}_p$ is the input vector; $\mathbf{y}_p$ is the output vector; $\mathbf{F}$ and $\mathbf{G}$ are the system and input matrices, respectively. They are defined as follows.

$$\Delta\mathbf{u}_p = [\Delta u_{k_i} \quad \Delta u_{k_i+1} \quad \cdots \quad \Delta u_{k_i+N_c-1}]^T \tag{22}$$

$$\mathbf{y}_p = [y_{k_i+1} \quad y_{k_i+2} \quad \cdots \quad y_{k_i+N_p}]^T \tag{23}$$

$$\mathbf{F} = [\mathbf{H}\mathbf{\Phi} \quad \mathbf{H}\mathbf{\Phi}^2 \quad \cdots \quad \mathbf{H}\mathbf{\Phi}^{N_p}]^T \tag{24}$$

$$\mathbf{G} = \begin{bmatrix} \mathbf{H}\mathbf{\Gamma} & 0 & \cdots & 0 \\ \mathbf{H}\mathbf{\Phi}\mathbf{\Gamma} & \mathbf{H}\mathbf{\Gamma} & \cdots & 0 \\ \vdots & \vdots & \ddots & \vdots \\ \mathbf{H}\mathbf{\Phi}^{N_p-1}\mathbf{\Gamma} & \mathbf{H}\mathbf{\Phi}^{N_p-2}\mathbf{\Gamma} & \cdots & \mathbf{H}\mathbf{\Phi}^{N_p-N_c}\mathbf{\Gamma} \end{bmatrix} \tag{25}$$

The information signals required for obtaining the initial conditions the prediction model are y, v_y, ψ_e, r, and θ_o. y and ψ_e can be determined using the desired path generated from the path planning module. r and θ_o can be measured using the yaw rate sensor and steering angle sensor, respectively. v_y can be estimated using the extended Kalman filter (Chen & Hsieh 2008).

The optimal steering angle command is determined by minimizing the cost function as shown below, which

consists of the lateral displacement errors between the target path $\mathbf{y}_{ref}$ and the predicted path $\mathbf{y}_p$, and the steering angle command $\Delta\mathbf{u}_p$ within the prediction horizon.

$$J = \left(\mathbf{y}_{ref} - \mathbf{y}_p\right)^T \mathbf{Q}\left(\mathbf{y}_{ref} - \mathbf{y}_p\right) + \Delta\mathbf{u}_p^T \mathbf{R}\Delta\mathbf{u}_p \quad (26)$$

where **Q** and **R** are the adjustable weighting matrices. **R** is the weighting matrix related to the control effort. It is designed as a function of the prediction horizon N_p as shown below.

$$\mathbf{R} = \mathbf{R}_w \left(\frac{N_p}{20}\right)^2 \quad (27)$$

For a large preview horizon, the PGC index is small. It is easy to follow the desired path. Thus **R** should be increased to limit the steering control effort for better ride comfort. For a small preview horizon, the PGC index is large. It is less easy to follow the desired path. Thus **R** should be reduced to allow larger steering control effort for better path following. For the same target path, the excitations to the control are different for different vehicle speeds. $\mathbf{R}_w$ is designed as a diagonal matrix as shown below.

$$\mathbf{R}_w = (s_1 v_x + s_0)\mathbf{I} \quad (28)$$

where s_1 and s_2 are coefficients for adjusting the diagonal elements of $\mathbf{R}_w$ with respect to different v_x. The optimal control can then be obtained as follows.

$$\Delta\mathbf{u}_p = (\mathbf{G}^T\mathbf{Q}\mathbf{G} + \mathbf{R})^{-1}\mathbf{G}^T\mathbf{Q}\left(\mathbf{y}_{ref} - \mathbf{F}\mathbf{x}_{k_i}\right) \quad (29)$$

The optimal steering angle at the sampling instant is the summation of the steering angle at the previous sampling instant and the first element of $\Delta\mathbf{u}_p$ as shown below.

$$u_{k_i} = u_{k_i-1} + \Delta\mathbf{u}_p(1) \quad (30)$$

5 SIMULATION RESULTS

CarSim is used to evaluate the performance of the MPC with different fixed preview times (FPT) and the proposed MPC with APT. The preview times of $FPT_{0.6}$, FPT_1, $FPT_{1.5}$, and FPT_2 are set to be 0.6 sec, 1 sec, 1.5 sec, and 2 sec, respectively. The responses of FPT_1 are selected as the baseline for performance benchmark. The first scenario is a mild lane following maneuver of a curved road. The second scenario is a severe lane change maneuver with high lateral acceleration.

5.1 *Lane following*

A curved road is employed to evaluate the lane following performance of the proposed controller. With the entrance speed at 80 km/h, the radius of the curved road is set to be 230 m according to the regulation. The lane following responses are shown in Figure 3. Due

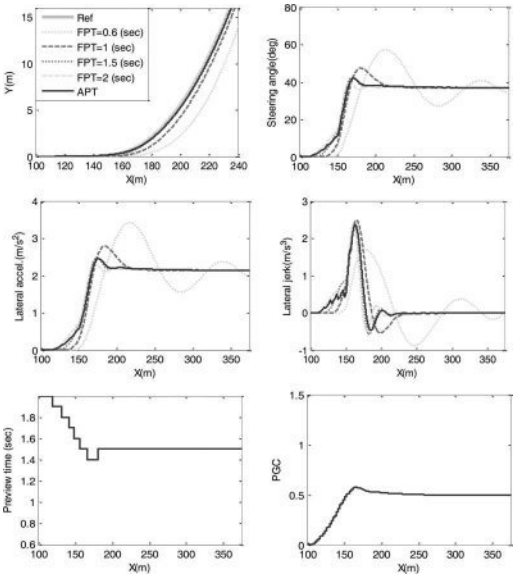


Figure 3. Lane following responses at 80 km/h.

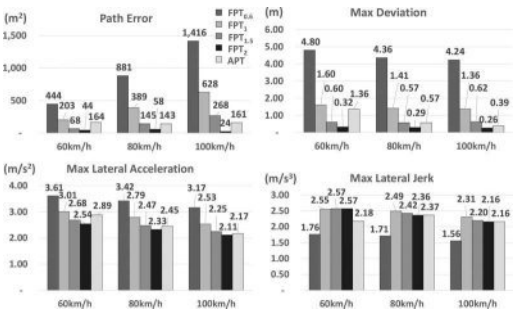


Figure 4. Lane following performances at different speeds.

to the short preview distance resulted from the short preview time, $FPT_{0.6}$ cannot see the curved road and steers the vehicle much later than the other controllers. It shows the most oscillatory steering responses and the largest path error. It also shows the largest maximum lateral displacement and maximum absolute acceleration. $FPT_{1.5}$, FPT_2, and APT have similar responses and are slightly better than FPT_1 due to longer preview distance. The PGC is slowly increased when the vehicle is approaching the curved road. The preview time is reduced accordingly for the proposed controller with APT, and is kept at 1.5 sec after entering the curved road.

Lane following performances at different speeds are summarized in Figure 4. The radiuses of the curved road are set to be 120 m and 390 m for the entrance speeds at 60 km/h and 100 km/h, respectively. In general, $FPT_{0.6}$ has the worst performance due to the short preview time. $FPT_{1.5}$, FPT_2, and APT are slightly better than FPT_1 due to longer preview distance. However, $FPT_{1.5}$ and FPT_2 are slightly worse than FPT_1 for the maximum absolute lateral jerk at 60 km/h.

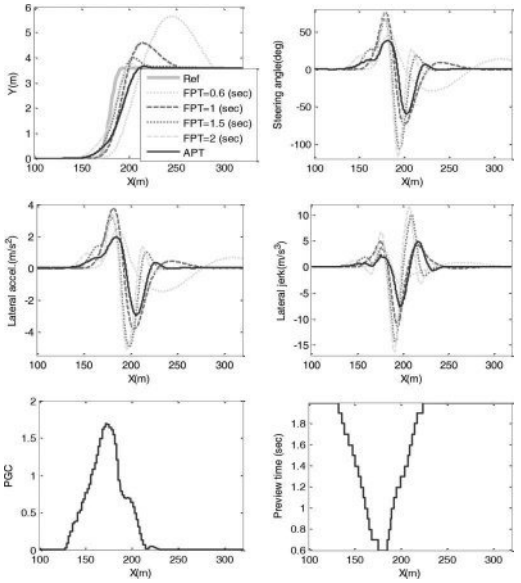


Figure 5. Lane change responses at 80 km/h.

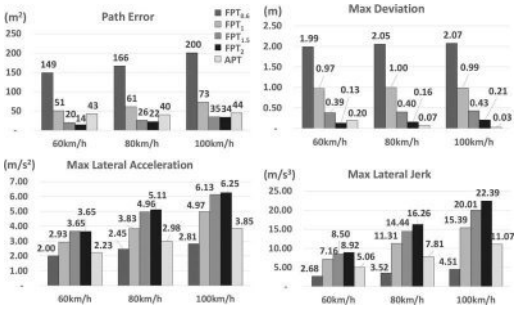


Figure 6. Lane change performances at different speeds.

5.2 *Lane change*

The first lane change of the ISO 3888-1 double lane change is employed as the test maneuver for a server lane change. The responses with the vehicle speed at 80 km/h are shown in Figure 5. The path errors and the maximum lateral deviations of $FPT_{1.5}$ and FPT_2 are smaller than those of FPT_1. However, the maximum absolute lateral accelerations and jerks of $FPT_{1.5}$ and FPT_2 are larger than those of FPT_1. Although $FPT_{0.6}$ has the smallest maximum absolute lateral accelerations and jerks, the path error due to the short preview time is too large for a successful lane change maneuver.

As for the proposed control with APT, it maintains the preview time at 2 sec before seeing the lane change path. After seeing the lane change path, the PGC index is increased and the preview time is reduced to 0.6 sec for tight path following. After the lane change path, the PGC is reduced for the straight path ahead and the preview time is increased to 2 sec for better ride comfort. The path error, the maximum lateral deviation, the maximum absolute lateral acceleration and jerk of APT are all smaller than those of FPT_1.

Lane change performances at different speeds are summarized in Figure 6. Similar results are also observed for vehicle speeds at 60 km/h and 100 km/h. Therefore, APT can perform a tighter path tracking and produce a more comfortable ride simultaneously for the test maneuver.

6 CONCLUSION

MPC is employed to design an automated steering controller based on a 5-state road following bicycle model including the actuator dynamics of EPS. The PGC index is designed to assess the severity of the path-following maneuver ahead of the vehicle. An adaption rule for APT is designed as a linear function of PGC to adjust the prediction horizon of MPC. For mild lane following maneuvers, the APT is slightly reduce after seeing the curved road to be followed. The proposed controller with APT has responses similar to the controllers with FPT of 1.5 sec and 2 sec. For severe lane change maneuvers, APT is reduced to 0.6 sec for tight path following when crossing the lane, and is increased to 2 sec for better ride comfort after the vehicle is in the adjacent lane. Simulation results show that the proposed controller with APT can effectively reduce the path following error while reducing the lateral acceleration and jerk for the test maneuvers.

ACKNOWLEDGEMENT

This research is supported by the Ministry of Science and Technology in Taiwan under the contract No. of MOST 103-2221-E-027-086-MY2 and 104-2622-E-027-016 -CC2.

REFERENCES

Broggi, A., Bertozzi, M., Fascioli, A., Guarino Lo Bianco, C., Piazzi, A. 1999. The ARGO Autonomous Vehicle's Vision and Control Systems. *International Journal of Intelligent Control and Systems* 3(4): 409–441.

Chen, B.C., Luan, B.C. & Lee, K. 2014. Design of Lane Keeping System Using Adaptive Model Predictive Control. *Proc. International Conf. on Automation Science and Engineering*, Taipei, Taiwan.

Chen, B.C. & Hsieh, F.-C. 2008. Sideslip angle estimation using extended Kalman filter. *Vehicle System Dynamics* 46(Suppl. 1): 353–364.

Cremean, L.B., Foote, T.B., Gillula, J.H., Hines, G.H., Kogan, D., Kriechbaum, K.L., Lamb, J.C., Leibs, J., Lindzey, L., Rasmussen, C.E., Stewart, A.D., Burdick, J.W. & Murray, R.M. 2006. Alice: An information-rich autonomous vehicle for high-speed desert navigation. *Journal of Field Robotics* 23(9): 777–810.

Hwang, J., Huh, K., Na, H. & Jung, H. 2008. Development of a Model Based Predictive Controller for Lane Keeping Assistance. *SAE Technical Paper* 2008-01-1454.

Kang, J., Hindiyeh, R.Y., Moon, S.-W., Gerdes, J.C. & Yi, K. 2008. Design and Testing of a Controller for Autonomous Vehicle Path Tracking Using GPS/INS Sensors. *Proc. 17th IFAC World Congress*, Seoul, Korea.

Kim, B.-A., Lee, S.-H., Lee, Y.O. & Chung, C.C. 2012. Comparative study of approximate, proximate, and fast model predictive control with applications to autonomous vehicles. *Proc. International Conf. on Control, Automation and Systems*, Jeju Island, Korea.

MacAdam, C.C. 1981. Application of an Optimal Preview Control for Simulation of Closed-Loop Automobile Driving. *IEEE Trans. Systems, Man and Cybernetics* 11(6): 393–399.

MacAdam, C. 2001. *Development of a Driver Model for Near/At-Limit Vehicle Handling*. GM Corp., Baxter Road, Ann Arbor, Michigan.

Marshall, J. W. 2013. NHTSA Role in The Future of Automated Vehicles. *2013 AAMVA regional conference*, Dover, DE.

Sotelo, M.A. 2003. Lateral control strategy for autonomous steering of Ackerman-like vehicles. *Robotics and Autonomous Systems* 45(3–4): 223–233.

Advanced Vehicle Control – Edelmann, Plöchl & Pfeffer (Eds)
© 2017 Taylor & Francis Group, London, ISBN 978-1-138-02992-7

Motion sickness in automated vehicles

T. Wada
Ritsumeikan University, Kusatsu, Shiga

ABSTRACT: In an automated vehicle, the driver is a passenger. It is said that the driver seldom gets motion sickness or carsickness compared to passengers. This suggests that motion sickness could be a problem in highly automated vehicles. Other changes such as seating posture or engaging in non-driving tasks can occur by introducing automated driving. In addition to such changes for drivers, changes in vehicle systems occur that are caused by the automated system taking control of the vehicle. This paper discusses motion sickness in automated driving by dividing the changes for drivers and those in vehicles. The countermeasures are also discussed from both viewpoints with emphasis on a vehicle control method that minimizes motion sickness based on a mathematical model of motion sickness.

1 INTRODUCTION

The technological aspects of automated vehicles or self-driving cars have been actively studied in recent years. The human factors in automated vehicles have also been studied. These research studies include a driver's response when the driving authority is being transferred back to the driver (Louw et al. 2015) (Blanco et al. 2015) and the driver's trust in automated driving (Abe et al. 2015).

In this study, the automated vehicle was assumed to be operated at level 3 or higher in SAE-J3016 levels of automated driving, in which the driver does not need to attend to the vehicle control or even monitor the traffic environment. In automated vehicles, the driver becomes a passenger. It is known that drivers seldom get carsickness compared to passengers. Thus, it is thought that the drivers of automated vehicles will tend to experience motion sickness more often.

Originally, automated vehicles began to be developed to increase the driver's comfort and productivity during transportation (Diels & Bos 2015). An increase in the occurrence of motion sickness during automated driving has a significantly negative impact on this original purpose. However, few studies have been performed on motion sickness in automated driving. Diels et al. discussed factors relating to motion sickness for automated driving in specific potential scenarios involving a change for drivers and proposed countermeasures for decreasing the occurrence of motion sickness (Diels & Bos 2015). Sivak et al. estimated the number of passengers who would experience carsickness during automated driving based on survey results about activities that people would like to do in an automated vehicle as well as some potential countermeasures (Sivak & Schoettle 2015). In addition to such changes for drivers, the vehicle system also undergoes certain changes that are caused by the automated system taking control of the vehicle.

Therefore, this paper discusses motion sickness in automated driving by dividing the changes for drivers and those in the vehicles. The countermeasures will be also discussed from both viewpoints. A vehicle control method that minimizes motion sickness will be introduced based on a mathematical model of motion sickness. An individual who is released from vehicle operation is referred to as an "occupant" in this paper even if he/she is expected to take over the driving operation from the vehicle automation when necessary.

2 QUANTIFICATION OF MOTION SICKNESS INCIDENCE IN AUTOMATED VEHICLES

When drivers are relieved of the driving operations in automated vehicles, the following two changes occur:

1) The individual who previously drove the car is transformed into a passenger;
2) The person who controls the vehicle is replaced by the automation.

The possibility of motion sickness in those riding in an automated vehicle is discussed based on these two points (Table 1).

2.1 *Changes for drivers: Transformed into passenger*

(a) Motion sickness susceptibility difference between driver and passenger

Rolnick & Lubow (1991) reviewed the factors contributing to motion sickness that differ between drivers and passengers, namely, controllability, perceived control, activity, visual information, and predictability.

Table 1. Potential effects of automated vehicle on motion sickness.

What is changed		Examples of changes	Possible risk factors of motion sickness
Changes for drivers caused byr being relieved of the driving operation	Difference by presence or absence of performing the driving operation	Difference between driver and passengers (control, activity, visual information, anticipation)	– Decrease of operation activity and anticipation
		Changes in posture and body movements (e.g., Seating in rear-facing position)	– Decrease in anticipation of road geometry ahead
	Increase of non-driving tasks	Addition of non-driving tasks (reading documents, tablet operation, etc.)	– Decrease in anticipation due to lack of visual information
		Gazing at an in-vehicle display or tablet	– Sensory conflict by inconsistency between the passengers body movement and what they see – Decrease of anticipation due to absence of visual information from the road environment
Changes in the vehicle system caused by the automation taking control of the vehicle	Changes in vehicle motion	Driving velocity pattern in curves	– Vehicle motion affects motion sickness
	Changes in in-vehicle equipment	Changes in the size of the front window	– Narrowing front visual image – Decrease in anticipation of the vehicle motion

The perceived control represents whether the driver feels he/she is in control of the vehicle; thus, it is thought to be identical to sense of agency (David et al. 2008). In a real-world automotive environment, the controllability and perceived control are identical. It is thought that increasing these factors reduces motion sickness (Reason 1978b). In the automated driving, the drivers are relieved of the control operation and become a passenger; thus, the susceptibility to motion sickness can be increased (Rolnick & Lubow 1991) (Reason 1978b). Activity is difficult to quantify. It has been reported that the effect of an activity on a person's motion sickness susceptibility depends on the type of activity being performed. A driving-related activity might reduce motion sickness, but a non-driving-related activity can increase it. The ability to predict future motion is thought to differ between the driver and passengers: a passenger's predictability might be reduced because they do not need to control the vehicle's motion. Regarding visual information, the visual field or other optical input to the eyes affects motion sickness. In addition, visual information is also strongly related to predictability. If the occupants could change their seating position or direction such as by facing toward the rear, this could affect their visual information and predictability. These points were discussed in Diels & Bos (2015) and Sivak & Schoettle (2015).

In addition, the driver is known to tilt his or her head toward the center of the curve when negotiating a curve, whereas a passenger's head moves in the opposite direction Wada et al. (2012). Wada et al. (2012) and Wada & Yoshida (2015) revealed that if a passenger tilts their head against the centrifugal force in slalom driving, in imitation of the driver's head movement, it significantly reduces the severity of motion sickness compared with tilting their head toward the centrifugal force. This indicated that head tilt affects the susceptibility to motion sickness.

(b) Increase of non-driving tasks

Being relieved of the driving operation increases an occupant's ability to use a tablet, watch a hand-held display, or engage in other non-driving activities. Because the occupant is not required to monitor the road in theory, he/she can look at the visual display for a long time. Inconsistency between a passenger's body movement and what they see can increase motion sickness (Reason 1978a). A decrease in anticipation of body movement as a result of looking at a display is also thought to be a risk factor.

2.2 *Changes in vehicle system: Driving operation replaced by automation*

No study could be found that investigated from the viewpoint of changes in vehicle system or driving operation being replaced by automation. It is possible to dramatically change the motion pattern or velocity profile of an automated vehicle. A human driver is thought to drive in a manner that prevents motion sickness even without passengers because a driver that does not want to get carsick functions as a type of motion sickness detector or predictor. On the other hand, to design the motion pattern for an automated

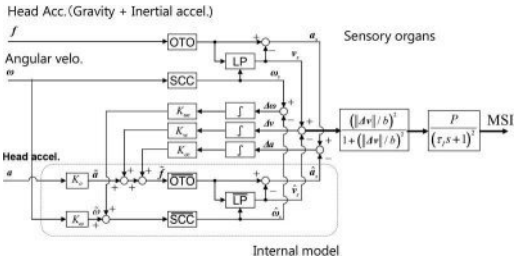


Figure 1. Mathematical model of motion sickness (Wada, Fujisawa, et al. 2010).

vehicle with a view to minimizing motion sickness, it is necessary to quantitatively evaluate the motion sickness severity for a given vehicle motion. Section 3 will introduce a mathematical model of motion sickness to estimate its incidence.

In addition, because no human controls the vehicle motion, the size and shape of the windows can be changed. Employing smaller windows may increase passengers' susceptibility to motion sickness because of reductions in the visual field and the ability to predict future movements (Griffin & Newman 2004). The effect could include the decrease in anticipation of body motion due to lack of visual information in front.

3 QUANTIFICATION OF MOTION SICKNESS INCIDENCE IN AUTOMATED VEHICLES

As a method to quantify severity of motion sickness, the motion sickness dose value (MSDV) is used, which is the integration of frequency-weighted acceleration (McCauley et al. 1976, Kato & Kitazaki 2006). On the other hand, Bles et al. (1998) proposed the subjective vertical conflict (SVC) theory, which postulates that motion sickness is caused by the accumulation of conflict between the vertical direction of the body sensed by the sensory organs and the predicted motion by an internal model that is thought to be established in the central nervous system. A mathematical model for the SVC theory was proposed, detailed for one degree-of-freedom (DOF) motion . (Bos & Bles 1998). We propose the 6DOF-SVC model (Fig. 1), which predicts motion sickness incidence (MSI) in 6 DOF motion in 3D space as an extension of the Bos & Bles (1998) model by introducing semi-circular canal and canal-otolith interaction.

Please refer to Wada, Fujisawa, et al. (2010) for the detail of the mathematical model.

4 COUNTERMEASURES

4.1 *Vehicle control*

4.1.1 *Design of vehicle motion minimizing motion sickness*

As mentioned before, it is necessary to consider motion sickness explicitly in designing vehicle motion of an automated vehicle. Given the mathematical model of motion sickness, the vehicle control that minimizes the MSI can be designed. In this section, a vehicle motion generation method that minimizes the predicted MSI by the 6DOF-SVC model is introduced (Wada et al. 2015).

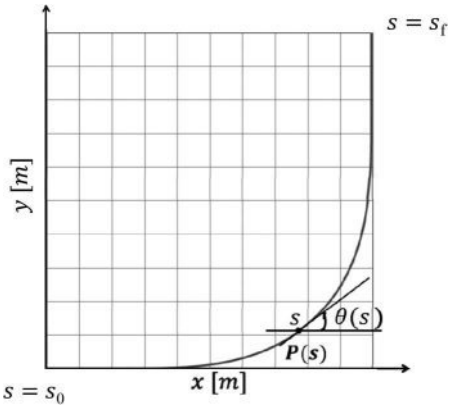


Figure 2. Description of road geometry (Wada et al. 2015).

(a) Road geometry

Consider single lane roads with curves where a driver should decelerate to an appropriate velocity before and/or during negotiating a curve, and then accelerate again when returning to a straight if necessary. Suppose that road geometry is given by a plane algebraic curve. For the sake of simplicity, assume that both ends of a curve with a constant curvature are connected to a straight via clothoid curves (Fig. 2). Let parameter s be an arc length at a point measured from a given origin; then, the road geometry can be described by specifying $\theta(s)$, which is the angle of tangent line at s measured from the x-axis of the road-fixed Cartesian coordinate system o-xy (Fig. 2).

(b) Vehicle control method

The deceleration control method that was derived from expert drivers' deceleration profile (Wada, Doi, et al. 2010) is expanded to acceleration/deceleration control here.

In a single block of road, including a curve defined as $s \in [s_0, s_f]$, as shown in Fig. 1, velocity patterns in which it is assumed that a vehicle drives at a constant velocity, decelerates to a certain velocity, drives at the constant velocity, accelerates to a given velocity, and drives at the velocity, are formulated as eq. (1).

$$v(s) := \begin{cases} f(v_0, v_0, s_0, s_1) & s_0 \le s < s_1 \\ f(v_0, v_a, s_1, s_2) & s_1 \le s < s_2 \\ f(v_a, v_a, s_2, s_3) & s_2 \le s < s_3 \\ f(v_a, v_f, s_3, s_4) & s_3 \le s < s_4 \\ f(v_f, v_1, s_4, s_f) & s_4 \le s \le s_f \end{cases} \quad (1)$$

$$f(v_i, v_j, s_k, s_l) := v_j - (v_j - v_i) d^3(s, s_k, s_l) \exp\{3(1-d(s, s_k, s_l))\}, \quad (2)$$

$$d(s,s_k,s_l) := \frac{s_l - s}{s_l - s_k}, \tag{3}$$

where v_o, v_f denote the velocity at $s = s_0$ and s_f, respectively, and v_a denotes the velocity at the constant velocity that is expected to appear in the curve. Scalars s_1 and s_2 are the start and end positions of the deceleration, and s_3 and s_4 are the start and end positions of the acceleration. Assuming that the occupant's head moves in accordance with the vehicle motion, the head acceleration and the angular velocity are determined by specifying the vehicle velocity on the road; thus, the predicted MSI is calculated using the 6DOF-SVC model. Therefore, the design of the velocity pattern can be formulated by following.

[Design of velocity profile]

Given: $v_0, v_f, \theta(s)$ $(s \in [s_0, s_f])$
Find $x := [s_1,\ s_2,\ s_3,\ s_4,\ v_a]$

which minimizes MSI calculated using 6DOF-SVC model.

s.t. $s_1 < s_2 < s_3 < s_4$

$$v_0 > 0,\ v_f > 0,\ v_a > 0$$

$$t_f - t_0 = T$$

where t_0 and t_f are the times when the vehicle is at $s = s_0$ and $s = s_f$, respectively.

This problem can be solved by employing appropriate nonlinear optimization method such as Neldar-Mead Simplex Method.

(c) Results

Fig. 3 shows the generated velocity profile for a road course designed to be driven at 20 km/h following the Road Construction Ordinance of the Ministry of Land, Infrastructure, Transport and Tourism in Japan, in which $v_0 = v_f = 10$ m/s was set. Driving time, T, was changed as 10 through 60 s. The velocity profiles in which the vehicle decelerated before entering the curve, drive at a constant speed, and accelerate again were successfully generated, and they confirmed our prediction.

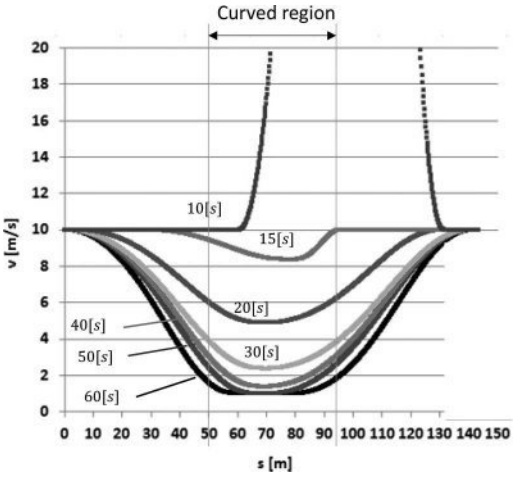


Figure 3. Generated velocity profile (Wada et al. 2015).

4.2 *Behaviors*

An occupant's behavior affects motion sickness. The seating posture can be modified to reduce motion sickness because it is known that sleeping and a supine posture reduce motion sickness (Diels & Bos 2015, Sivak & Schoettle 2015). Thus, the location and direction of the seats should be considered carefully.

In addition, from Wada et al. (2012) and Wada & Yoshida (2015), tilting the head angle toward the center of a curve reduces motion sickness. However, it should be noted that passive head movement might conversely increase motion sickness because motion sickness increases in a tilt train . (Persson 2008). Thus, a method to encourage such a head tilt naturally is needed to facilitate this. For this purpose, we proposed a postural control device using pneumatic balloon installed on the drivers' seat that encourages drivers' head tilt towards centripetal acceleration when negotiating a curve (Konno et al. 2011).

4.3 *User interfaces*

The chances that the occupants use a tablet or other devices can be increased while riding in automated vehicles. The display design of such devices plays a crucial role in decreasing motion sickness. In Diels & Bos (2015), a design guideline for such user interfaces is provided, but it is omitted here owing to lack of space.

There is a possibility to add visual information to provide road geometry ahead, etc., to increase the anticipation to reduce motion sickness. For this, effort in software to reduce motion sickness is possible. For example, Morimoto et al. (2008) successfully reduced motion sickness while watching a video in a passenger car by deforming a video image that was played on an in-vehicle monitor.

5 CONCLUSION

This paper discussed factors related to motion sickness in automated vehicles from the viewpoint of changes for drivers caused by being relieved from the driving operation and those in the vehicle system controlled by the automation. Considering the importance of quantifying motion sickness, a mathematical model of motion sickness was introduced with the goal of providing countermeasures. Finally, some countermeasures were proposed from the viewpoints of vehicle control, behavior, and a user interface, which put an emphasis on a vehicle control method to minimize MSI.

REFERENCES

Abe, G., Sato, K. & Itoh, M., 2015. Driver's Trust in Automted Driving when Passing Other Traffic Objects. In *2015 IEEE International Conference on Systems, Man, and Cybernetics*. IEEE, pp. 897–902.

Blanco, M. et al., 2015. Human Factors Evaluation of Level 2 and Level 3 Automated Driving Concepts. *Report No. DOT HS 812 182*.

Bles, W. et al., 1998. Motion Sickness: Only One Provocative Conflict? *Brain Research Bulletin*.

Bos, J.E. & Bles, W., 1998. Modeling Motion Sickness and Subjective Vertical Mismatch Detailed for Vertical Motions. *Brain Research Bulletin*, 47(5), pp. 537–542.

David, N., Newen, A. & Vogeley, K., 2008. The "sense of agency" and its underlying cognitive and neural mechanisms. *Consciousness and Cognition*, 17(2), pp.523–534.

Diels, C. & Bos, J.E., 2015. User Interface Considerations to Prevent Self-Driving Carsickness. In *7th International Conference on Automotive User Interface and Interactive Vehicular Applications*. pp. 14–19.

Griffin, M.J. & Newman, M.M., 2004. Visual Field Effects on Motion Sickness in Cars. *Aviation Space and Environmental Medicine*.

Kato, K. & Kitazaki, S., 2006. A Study for Understanding Carsickness Based on the Sensory Conflict Theory. In *SAE paper 2006-01-0096*.

Konno, H. et al., 2011. Analysis of Motion Sensation of Car Drivers and Its Application to Posture Control Device. In *SICE Annual Conference*. pp. 192–197.

Louw, T. et al., 2015. Driver Inattention During Vehicle Automation: How Does Driver Engagement Affect Resumption Of Control? In *4th International Driver Distraction and Inattention Conference*. Sydney.

McCauley, M.E. et al., 1976. Motion Sickness Incidence: Exploratory Studies of Habituation, Pitch and Roll, and the Refinement of a Mathematical Model. *Technical report 1733-2, Human Factors Research Inc., Santa Barbara Research Park, Goleta, California, USA.*

Morimoto, A. et al., 2008. Reduction of Car Sickness Caused by Watching Onboard Display for Rear-seat Entertainment. In *15th World Congress on Intelligent Transport Systems and ITS America's 2008 Annual Meeting*.

Persson, R., 2008. Motion sickness on tilting trains: Description and analysis of the present knowledge – Literature study.

Reason, J.T., 1978a. Motion sickness: Some theoretical and practical considerations. *Applied Ergonomics*, 9(3), pp. 163–167.

Reason, J.T., 1978b. Motion Sickness Adaptation: A Neural Mismatch Model. *Journal of the Royal Society of Medicine*, 71, pp. 819–829.

Rolnick, A. & Lubow, R.E., 1991. Why is the driver rarely motion sick? The role of controllability in motion sickness. *Ergonomics*, 34(7), pp. 867–79.

Sivak, M. & Schoettle, B., 2015. Motion Sickness in Self-driving Vehicles. *UMTRI Technical Report*, UMTRI-2015.

Wada, T. et al., 2012. Can Passenger's Active Head Tilt Decrease The Severity of Carsickness? *Human Factors*, 54(2), pp. 226–234.

Wada, T., Doi, S., et al., 2010. Characterization of expert drivers' last-second braking and its application to a collision avoidance system. *IEEE Transactions on Intelligent Transportation Systems*, 11(2), pp. 413–422.

Wada, T. et al., 2015. Design of Velocity Patterns of Automobiles Based on Subjective Vertical Conflict Theory (inJapanese). In *SICE SI2015*.

Wada, T., Fujisawa, S., et al., 2010. Effect of Driver's Head Tilt Strategy on Motion Sickness Incidence. In *The 11th IFAC/IFIP/IFORS/IEA Symposium on Analysis, Design, and Evaluation of Human-Machine System*.

Wada, T. & Yoshida, K., 2015. Effect of passengers' active head tilt and opening/closure of eyes on motion sickness in lateral acceleration environment of cars. *Ergonomics*, pp. 1–26.

Path planning

Advanced Vehicle Control – Edelmann, Plöchl & Pfeffer (Eds)
© 2017 Taylor & Francis Group, London, ISBN 978-1-138-02992-7

Study on update method of avoidance trajectory for the autonomous frontal obstacle avoidance system

S. Fujimori, H. Iwata & R. Hayashi
Tokyo University of Science, Katushika-ku, Tokyo, Japan

ABSTRACT: As one of automotive safety technologies, the authors have proposed the autonomous frontal obstacle avoidance system, which recognizes a frontal obstacle such as a pedestrian, predicts the location of collision based on the obstacle motion and avoids it by autonomous evasive steering. In addition, to respond to the change of the motion of the obstacle, an updating method of avoidance trajectory has been proposed. However, since the updating method does not take into account the road boundary, if the distance to the road boundary is not enough, the avoidance trajectory collides with the road boundary. In this paper, the authors solve this problem by deriving avoidance trajectory which accommodate to the road boundary and propose a method to choose the appropriate avoidance trajectory during avoidance action. Then, the newly proposed system is verified by numerical simulations. The results show that the newly proposed system is effective.

1 INTRODUCTION

Popularization of active safety technologies for automobile such as ABS and ESC have contributed to a remarkable decrease of the number of traffic accidents; however, over 4,000 traffic fatalities a year still occur in Japan. To realize society of zero traffic accidents, further technological innovations are needed. Automatic emergency braking (AEB) systems are now expected to reduce the number of accidents. In addition, since it has been reported that collision avoidance by steering is more effective at high speed (Horiuchi et al., 2006), collision avoidance technologies by evasive steering will also be effective to reducing the number of accidents.

Many researches about collision avoidance technologies by steering are being promoted from various viewpoint. For example, Glacer et al. (2010) have proposed a maneuver based trajectory planning in which the avoidance trajectory is expressed as a polynomial. Other researches include evasive motion control methods of the vehicle in which avoidance trajectories are not derived explicitly. Fujioka et al. (2008) proposed the optimal vehicle motion control method which minimizes the collision risk value and Ohmuro et al. (2010) proposed that which minimizes the resultant vehicle force. Shibata et al. (2014) utilizes potential field method, which is commonly used in robotics.

The authors have also proposed a collision avoidance technology using steering (Hayashi et al., 2011). The main feature is that it utilizes geometrically derived arc trajectories as avoidance trajectories. It enables to calculate avoidance trajectories with very low computational cost, and forecast availability of collision avoidance in advance of starting autonomous collision avoidance maneuver.

In addition, to respond to change of behavior of the obstacle during avoidance and compensate for the tracking error to the avoidance trajectory, an updating method of avoidance trajectory has been proposed (Nipun et al., 2011). However, the proposed avoidance trajectory does not take into account the road boundary. Therefore, when the distance to the road boundary is not enough, the avoidance trajectory collides with the road boundary.

Based on the aforementioned, in this paper, the authors solve this problem by revising avoidance trajectory during avoidance action, taking into account the road boundary. Then the autonomous frontal obstacle avoidance system is redesigned to incorporate trajectory updating function utilizing the revised avoidance trajectory. The redesigned system is examined by numerical simulations to evaluate the validity and effectiveness.

2 PREVIOUS AVOIDANCE SYSTEM

2.1 *Target scene and supposed vehicle*

The target situation of this study is emergency situations, such as a pedestrian jumping out from the roadside while the ego vehicle is driving along road boundaries such as walls as shown in Fig. 1. Assumed conditions are as follows:

(1) The road is straight with road boundaries on both sides in an urban area.
(2) Only a single obstacle appears from the roadside when the ego-vehicle is in motion.
(3) It is not available to avoid the obstacle by evading leftward.

(4) There is a space between the obstacle and the right-side road boundary for the vehicle to pass through.

The supposed vehicle is shown in Fig. 2. It is equipped with a laser range finder (LIDAR) to obtain the relative distances to objects over a wide range and vehicle motion sensors such as accelerometers, a speed sensor and a yaw rate sensor. In addition, a digital signal processor is installed on it to control the velocity and steering angle. The specifications of the vehicle is shown in Table 1.

2.2 *Outline of the previous system*

Fig. 3 shows the flow chart of the previous system. This system consists of four subsystem: surroundings recognition, obstacle position prediction, avoidance trajectory generation and desired steering angle profile generation. The following subsections describes them in detail.

2.2.1 *Surrounding recognition and obstacle position prediction*

It has been reported in the authors' previous study (Hayashi et al., 2012) that the obstacle and the road boundaries can be detected and the position of the frontal obstacle (x_{ob}, y_{ob}) and the road boundary l_{wr} can be measured by using LIDAR if they are in front of the vehicle.

To deal with moving obstacles like pedestrians, the previous studies also have proposed to utilize predicted position of the obstacle (x_{pr}, y_{pr}) instead of the current position of the obstacle.

Since the main purpose of this study is to verify the updating method of the avoidance trajectory, these subsystems are omitted and the predicted position of the obstacle (x_{pr}, y_{pr}) and the road boundary l_{wr} (see Fig. 1) are directly given to the system.

2.2.2 *Avoidance trajectory generation (and updating)*

In order to respond to the change of the obstacle's motion, the previous study has derived the avoidance trajectory starting with the angled vehicle posture to the road boundary as shown in Fig. 4. It is called trajectory A. In Fig. 4, O_v is current vehicle position, S is the steering switching point at which the vehicle should change turning direction from right to left, F is finishing position of avoidance. F is defined as the point at which the vehicle direction is in parallel to the road boundary. Turning radius R_A and central angle θ_A of the avoidance trajectory are determined by Eq. (1) and (2)

$$R_A = \frac{{x_{pr}}^2 + {y_{pr}}^2 - r^2}{2\left(r - x_{pr}\sin\theta_v - y_{pr}\cos\theta_v\right)} \tag{1}$$

$$\theta_A = \cos^{-1}\left(\frac{R_A\cos\theta_v + y_{pr}}{R_A + r}\right) \tag{2}$$

Table 1. Specifications of the supposed vehicle.

Definition	Symbol	Value	Unit
Weight	m	470	kg
Width	w	0.995	m
Wheelbase	l	1.71	m
Length from front axle to center of gravity	l_f	0.90	m
Length from rear axle to center of gravity	l_r	0.81	m
Minimum turning radius	R_{min}	3.3	m
Yaw moment of inertia	I_z	311	kgm^2
Stability factor	K	6.31×10^{-4}	–

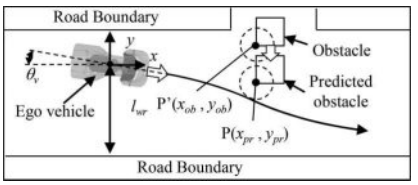


Figure 1. Target scene.

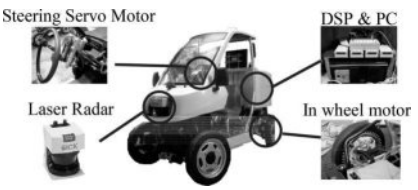


Figure 2. Supposed vehicle.

where, x_{pr} and y_{pr} are coordinates of the right edge of the obstacle, θ_v is the angle of the vehicle against the road boundary. r is the half width of the vehicle plus an extra margin of safety.

However, since the proposed avoidance trajectory neglects the road boundary, trajectory A is available only when F is more than r away from the road boundary as follows:

$$R_A\left(1 - 2\cos\theta_A + \cos\theta_v\right) \le l_{wr} - r \tag{3}$$

When the distance to the road boundary is not enough, i.e. Eq. (3) is not satisfied, the avoidance trajectory collides with the road boundary. This is the problem of the previous study.

2.2.3 *Generation of desired steering angle*

The desired steering angle δ_{sw}^* is calculated using the radius R^* as follows:

$$\delta_{sw}^* = \sigma\frac{1 + KV_0^2}{N}\frac{l}{R^*} \tag{4}$$

where V_0 is initial vehicle speed, K, N, l are the stability factor, steering gear ratio and wheelbase of the

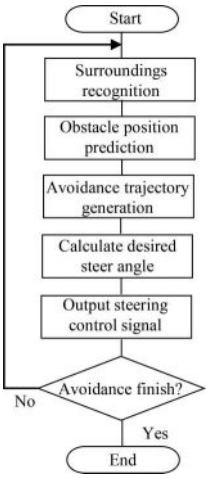


Figure 3. Flow chart of the frontal obstacle avoidance system.

vehicle, respectively. $\sigma = -1$ and it is replaced with 1 to switch turning direction from right to left after θ_v reaches θ^*. In addition to steering, the vehicle is decelerated with maximum deceleration ($-2\,\mathrm{m/s^2}$) to stop promptly.

3 THE THEORY OF AVOIDANCE TRAJECTORY

3.1 *The number of arcs needed to evade an obstacle and a road boundary*

This chapter describes the derivation of avoidance trajectories accommodating to the road boundary, which is the essential of this study. The derivation of avoidance trajectory differs depending on positional relationship among the vehicle, the obstacle and the road boundary and is divided roughly into two types.

3.2 *Avoidance trajectory by two arcs*

If the obstacle is on the vehicle's course, the vehicle should turn right to evade the obstacle first, and then turn left to evade the road boundary. Therefore, two turns are necessary to evade both of them at least. In this study, to minimize the maximum steering angle during avoidance, the avoidance trajectory is made by two arcs with the same radius and the radius should be as large as possible.

Avoidance trajectory by two arcs can be subdivided into two patterns: trajectory A and B.

Trajectory A is for cases that the road boundary is far enough from the vehicle (Fig. 4). In this case, the trajectory is calculated by using Eq. (1) and (2).

If Eq. (3) is not satisfied, trajectory A causes a collision with the road boundary. In such cases, trajectory B (Fig. 5) is able to avoid the obstacle without having a collision against the road boundary. It is formulated with the following geometrical conditions.

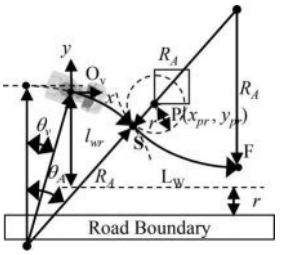


Figure 4. Trajectory A.

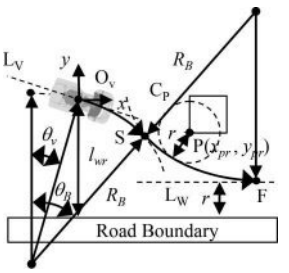


Figure 5. Trajectory B.

(B-i) The arc O_VS is circumscribed to the vehicle direction line L_V.
(B-ii) The arc O_VS pass through the current vehicle position.
(B-iii) Radius of the arc O_VS equals to that of the arc SF.
(B-iv) The arc O_VS is circumscribed to arc SF at the steering switching point S.
(B-v) The arc SF is circumscribed to the off-limit line L_W.
(B-vi) The off-limit circle C_P is inscribed in the arc SF. (C_P is a circle drawn centered on the right edge of the obstacle with radius r.)

From these conditions, the following fourth degree equation is obtained:

$$AR_B^4 + BR_B^3 + CR_B^2 + DR_B + E = 0 \tag{5}$$

where,

$$\left.\begin{aligned}
A &= a^2 - 4\left\{4 - (1+\cos\theta_v)^2\right\}\sin^2\theta_v \\
B &= 2ab - 8\left\{4 - (1+\cos\theta_v)^2\right\}x_{pr}\sin\theta_v \\
&\quad + 8(1+\cos\theta_v)(-l_{wr}+r)\sin^2\theta_v \\
C &= b^2 + 2ca - 4\left\{4 - (1+\cos\theta_v)^2\right\}x_{pr}^2 \\
&\quad + 16(1+\cos\theta_v)(-l_{wr}+r)x_{pr}\sin\theta_v \\
&\quad + 4(-l_{wr}+r)^2\sin^2\theta_v \\
D &= 2bc + 8(1+\cos\theta_v)(-l_{wr}+r)x_{pr}^2 \\
&\quad + 8(-l_{wr}+r)^2 x_{pr}\sin\theta_v \\
E &= 4(-l_{wr}+r)^2 x_{pr}^2 + c^2
\end{aligned}\right\} \tag{6}$$

where,

$$\left.\begin{aligned} a &= 4\left(1+\sin^2\theta_v\right)-\left(1+\cos\theta_v\right)^2 \\ b &= 2x_{pr}\sin\theta_v - 2\left(1+\cos\theta_v\right)\left(-l_{wr}+r\right) \\ &\quad + 2\left(y_{pr}-l_{wr}+r\right)+2r \\ c &= {x_{pr}}^2-\left(-l_{wr}+r\right)^2+\left(y_{pr}+l_{wr}-r\right)^2 \end{aligned}\right\} \quad (7)$$

The radius R_B is the largest real root among four roots of Eq. (5). It can be solved numerically with negligible computational cost. θ_B can be calculated by the following equation:

$$\theta_B = \cos^{-1}\left(\frac{R_B\left(1+\cos\theta_v\right)+r-l_{wr}}{2R_B}\right) \quad (8)$$

Trajectory B is available unless there is no space to pass between the obstacle and the road boundary.

3.3 *Avoidance trajectory by one arc*

If the obstacle is not on the vehicle's course as shown in Fig. 6, one left turn is enough to avoid both of the obstacle and road boundary. In this study, the following two trajectories are derived.

Trajectory C aims at restoring the yaw angle of the vehicle keeping the vehicle off the obstacle and is formulated with the following geometrical conditions.

(C-i) The arc $O_V F$ is circumscribed to the vehicle direction line L_V.
(C-ii) The arc $O_V F$ pass through the current vehicle position.
(C-iii) The off-limit circle C_P is inscribed in the arc $O_V F$.

From these conditions, the turning radius R_C and the central angle of the arc θ_C is solved as:

$$R_C = \frac{{x_{pr}}^2+{y_{pr}}^2-r^2}{2\left(r-x_{pr}\sin\theta_v-y_{pr}\cos\theta_v\right)}, \theta_C = \theta_v \quad (9)$$

Trajectory C is available when the finishing point F is more than r away from the road boundary. This is expressed as:

$$R_C\left(1-\cos\theta_v\right) \le l_{wr}-r \quad (10)$$

Trajectory D aims at restoring the yaw angle of the vehicle keeping the vehicle off the road boundary and is formulated with the following conditions.

(D-i) The arc $O_V F$ is circumscribed to the vehicle direction line L_V.
(D-ii) The arc $O_V F$ pass through the current vehicle position.
(D-iii) The arc $O_V F$ is circumscribed to the off-limit line L_W.

The radius R_D and the central angle θ_D are derived from these conditions as follows:

$$R_D = \frac{l_{wr}-r}{1-\cos\theta_v}, \theta_D = \theta_v \quad (11)$$

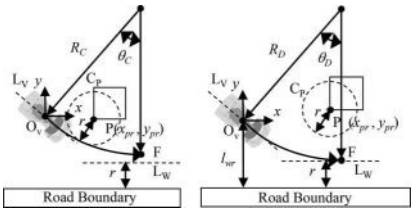


Figure 6. Trajectory C and Trajectory D.

4 AVOIDANCE TRAJECTORY GENERATION (AND UPDATING)

This study proposes to revise the avoidance trajectory generation subsystem of the previous study, replacing it with the subsystem described in this chapter. This subsystem updates the avoidance trajectory using the theory proposed in Chapter 3 to accommodate to change of behavior of the obstacle without colliding against the road boundary.

4.1 *Collision forecast*

The avoidance trajectory is to be revised only when necessary. Therefore, whether the current avoidance trajectory causes collision or not has to be forecast before revising the avoidance trajectory.

A collision is forecast to occur if the predicted obstacle position or the road boundary is on the vehicle's course. Since it is assumed to be impossible to avoid the obstacle by evading leftward, collision forecast with the obstacle is judged whether (x_{pr}, y_{pr}) is the right side of the chained line or not as shown in Fig. 7. In addition, the vehicle is forecast to collide with the road boundary if the broken line intersects with the road boundary.

If the current avoidance trajectory is forecast to cause a collision with them, the system updates the avoidance trajectory by the following method. Otherwise, the system continues to use the current trajectory.

4.2 *Avoidance trajectory selection*

If revision of avoidance trajectory is necessary, the system determines the number of arcs needed at first, utilizing trajectory D. Since trajectory D is the largest arc which does not cause collision with the road boundary, if trajectory D cause a collision with the obstacle, it means that one arc is not enough to avoid collision. Hence, the avoidance trajectory must be composed of two arcs then.

If the number of arcs necessary for collision avoidance is two, the system checks if trajectory A is available or not using Eq. (3). If trajectory A is available, the radius and central angle of avoidance trajectory arc are updated as $R^* = R_A$ and $\theta^* = \theta_A$. Otherwise, the system employs trajectory B, updating them as $R^* = R_B$ and $\theta^* = \theta_B$.

If the number of arcs is one, the system checks if trajectory C is available or not using Eq. (10). If

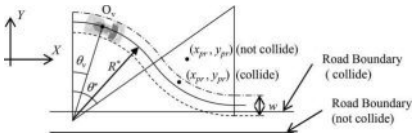


Figure 7. Forecast of collision.

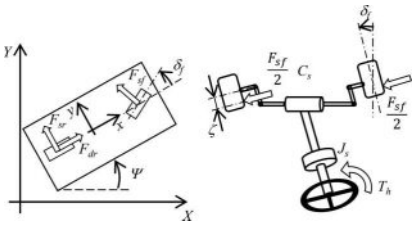


Figure 8. Vehicle model (bicycle model) and steering system model.

trajectory C is available, avoidance trajectory arc is updated as $R^* = R_C$ and $\theta^* = \theta_C$. Otherwise, the system employs trajectory D, updating it as $R^* = R_D$ and $\theta^* = \theta_D$.

5 VERIFICATION BY NUMERICAL SIMULATION

5.1 *Vehicle model and steering model*

Numerical simulation is executed to verify the validity and effectiveness of the revised system. The bicycle model is shown in Fig. 8. The equation of motion is expressed as:

$$\begin{cases} m(\dot{u} - v\gamma) = -F_{sf}\sin\delta_f + F_{dr} \\ m(\dot{v} + u\gamma) = F_{sf}\cos\delta_f + F_{sr} \\ I_z\dot{\gamma} = l_f F_{sf}\cos\delta_f - l_r F_{sr} \end{cases} \tag{12}$$

where u and v are longitudinal and lateral velocity, γ is yawrate, δ_f is steering angle of the front tire, F_{sf} and F_{sr} are the side forces of front and rear tire, and F_{dr} is the driving force of the rear tires. F_{sf}, F_{sr} and F_{dr} are expressed as:

$$F_{sf} = 2C_f\left(\delta_f - \tan^{-1}\frac{v + l_f\gamma}{u}\right) \tag{13}$$

$$F_{sr} = 2C_r\left(-\tan^{-1}\frac{v - l_r\gamma}{u}\right) \tag{14}$$

$$F_{dr} = ma_{vx} \tag{15}$$

where C_f and C_r are cornering stiffness of front and rear tires.

The steering system is simulated by the dynamics model shown in Fig. 8. The equation of motion in terms of steering wheel angle δ_{sw} is expressed as:

$$J_s\ddot{\delta}_{sw} = -C_s\dot{\delta}_{sw} + 2\xi C_f\left(\delta_{sw} - N\tan^{-1}\frac{v + l_f\gamma}{u}\right) + N^2T_h \tag{16}$$

Table 2. Condition of simulation.

	Predited obstacle position [m]	
Time [s]	x_{pr}	y_{pr}
0–0.5	10	−0.3
0.5	10	−0.8

where J_s is moment of inertia of the steering system, C_s is viscous damping coefficient of the steering system and ξ is pneumatic trail. Their values are $J_s = 13\ \mathrm{Nm}^2$, $C_s = 140$ Ns/rad, $\xi = 0.06$ m and $N = 18.7$. T_h is steering torque applied by a servo motor. The control law of the steering angle is as follows:

$$T_h = \begin{cases} 4.9\mathrm{N}\cdot\mathrm{m} & \left(\delta^*_{sw} - \delta_{sw} \geq 2\deg\right) \\ 0\mathrm{N}\cdot\mathrm{m} & \left(2\deg > \delta^*_{sw} - \delta_{sw} \geq -2\deg\right) \\ -4.9\mathrm{N}\cdot\mathrm{m} & \left(-2\deg > \delta^*_{sw} - \delta_{sw}\right) \end{cases} \tag{17}$$

The actual steering servo controller installed in the supposed vehicle seems to be a PID controller, whereas Eq. (19) is a kind of bang-bang control. However, it have been reported that the response of the steering system in the simulations with the bang-bang control law agrees well with that of actual experimental vehicle (Hayashi et al., 2011).

5.2 *Simulation conditions*

In this section, numerical simulations are executed. The condition of the position of the predicted obstacle is shown in table 2. l_{wr} is set at 4.5 m, r is set at 0.8 m, V_0 is set at 8 m/s and the avoidance system is activated at 0 second. Since the system avoids obstacle by autonomous evasive steering instead of the driver, the driver is supposed not to do any operation and this simulation ignores the impact of the driver. To verify the validity of the proposed system, it is compared with the previous system that does not perform the trajectory update (Hayashi et al., 2012) and the previous system that does not take into account the road boundary (Nipun et al., 2011). They are referred to as system 1 and 2, respectively.

5.3 *Simulation results*

Figures 9, 10 and 11 show the simulation result. Fig. 9 is the result of system 1, Fig. 10 is the result of system 2 and Fig. 11 is the result of the proposed system. In each figure, the upper figure shows the trajectories of the vehicle and the obstacle. The rectangles show the position and posture of the obstacle and the vehicle every 0.2 second, respectively. Each lower figure shows the time history data of avoidance trajectory and steering angle. In the graphs of avoidance trajectory, A to D mean that the avoidance trajectory is revised by each of the avoidance trajectory and H means that

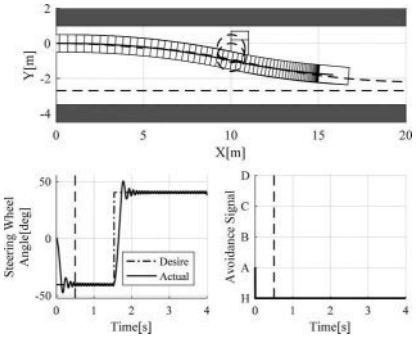


Figure 9. Simulation result (system 1).

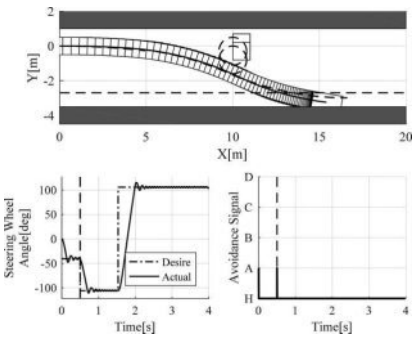


Figure 10. Simulation result (system 2).

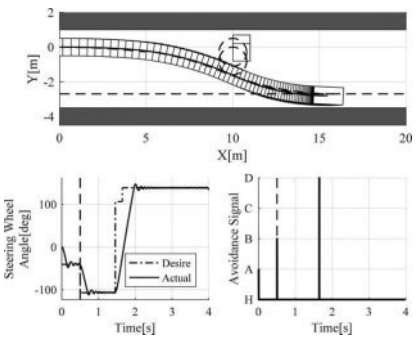


Figure 11. Simulation result (the proposed system).

the avoidance trajectory is not revised but the current trajectory is inherited.

Figure 9 indicates that system 1 causes a collision with the obstacle, because it cannot accommodate to change of the obstacle's motion. Although system 2 avoids the obstacle, it collides with the road boundary, because it does not take into account the road boundary. On the other hand, Fig. 11 indicates that the proposed system avoids the obstacle and road boundary without collision. The lower right figure of Fig. 11 indicates that the system revises avoidance trajectory to trajectory B when the obstacle changes its motion. After that, to compensate for the delay of the steering system, the system revises avoidance trajectory using trajectory D. For this reason, the steering wheel angle is increased. These results indicate that the proposed system is more effective than the previous systems.

6 CONCLUSION

This paper proposed a new updating method of avoidance trajectory for the autonomous frontal avoidance system, deriving the avoidance trajectory which starts with the angled vehicle posture to the road boundary, taking the road boundary into account. The new revised updating method is incorporated into the previously proposed system. The proposed system is examined by numerical simulations to evaluate the validity and effectiveness. The result indicates that the proposed trajectory updating method is valid and effective.

REFERENCES

Fujioka, T., Shibata, A., Tsukasaki, Y. & Sawada, S. 2008. Vehicle motion control for minimizing collision risk by use of optimal control theory. 2008 JSAE Spring Convention No. 8-08: pp. 21–26.

Glaser, S., Vanholme, B. & Mammar, S. 2010. Maneuver-Based Trajectory Planning for Highly Autonomous Vehicles on Real Road With Traffic and Driver Interaction. IEEE Transactions on Intelligent Transportation Systems Vol. 11 No. 3: pp. 589–604.

Hayashi, R., Isogai, J., Fujita, S., Raksincharoensak, P. & Nagai M. 2011. Development of autonomous forward obstacle avoidance system by using in-wheel-motor and steering control of micro electric vehicle. JSAE Transactions Vol. 42 No. 1: pp. 87–93.

Hayashi, R., Isogai, J., Raksincharoensak, P. & Nagai, M. 2012. Autonomous collision avoidance system by combined control of steering and braking using geometrically optimized vehicular trajectory. Vehicle System Dynamics: International Journal of Vehicle Mechanics and Mobility No. 50 Supp. 1: pp. 151–168.

Horiuchi, S., Hirao, R., Okada, K. & Nohtomi, S. 2006. Optimal steering and braking control in emergency obstacle avoidance. Transactions of the Japan Society of Mechanical Engineers Series C Vo. 72 No. 722: pp. 180–185.

Nipun, L., Hayashi, R & Nagai, M 2011. Study on trajectory modification method for the autonomous frontal obstacle avoidance system. TRANSLOG 2011 (20): pp. 233–236.

Ohmuro, A. & Hattori, Y. 2010. Optimum vehicle trajectory control for obstacle avoidance – a minimax problem of resultant vehicle force. Transactions of the Japan Society of Mechanical Engineers Series C Vol. 76 No. 772: pp. 3587–3594.

Shibata, N., Sugiyama, S. & Wada, T. 2014. Collision avoidance control with steering using velocity potential field. Proceedings of IEEE Intelligent Vehicles Symposium Proceedings pp. 438–443.

Advanced Vehicle Control – Edelmann, Plöchl & Pfeffer (Eds)
© 2017 Taylor & Francis Group, London, ISBN 978-1-138-02992-7

Development of collision probability based motion planning algorithm for automated driving vehicles

J. Suh, B. Kim & K. Yi
Aerospace and Mechanical Engineering Department, Seoul National University, Republic of Korea

ABSTRACT: This paper describes a lane change motion planning and control algorithm with collision probability for an automated driving in complex driving situations. An environment presentation model calculates tracking and prediction of other traffics' states. Using this information, collision probability is obtained by status of other vehicles. A hyperbolic tangent shaped lane change motion is defined to reduce acceleration jerk value for passenger's comfortability. In merging or split section of the road, the longitudinal acceleration, lane change timing and safe constraints are defined. The states of the subject vehicle are planned to change the lane safely. A lower-level controller is designed using a stochastic model predictive control (SMPC) with constraints to obtain desired control inputs.

1 INTRODUCTION

Lane change maneuver is a cause for various severe highway accidents due to the inaccurate estimation of surrounding traffic or illegal maneuver. An automated driving is regarded as a solution to reduce the human errors. Currently, automated driving has been widely considered as the mainstream of the automakers since it offers increased safety and comfortability. Many kinds of research have been attempted to integrate individual active safety systems for the improvement of an automated driving system to enhance safety and achieve zero fatalities (Bishop, 2000).

Previous researches for a lane change in automated driving systems shows cost function based approaches (Wei, 2010). L. Wan et al. analyzed a pattern of a lane change of human driver data to determine lane change timing (Wan, 2011). The learning based approach for lane change using a neural network for prediction the maneuver trajectory (Tomar, 2010).

Regarding general driving situations, lane change should be decided within a certain time frame to ensure the safe automated driving control. Since the lane change control requires the longitudinal and lateral control, it is hard to implement. Some studies exist about not the time necessary to change lanes but the distance and speed of the host vehicle, to be determined in advance (Vanholme, 2013).

Since lane change for automated driving system is required to predict not only other traffic but also the subject vehicle, an MPC approach has been implemented widely due to its capability to handle several constraints actively (Gray, 2013). The MPC method uses a dynamic model to predict future states of the system and calculates an optimal control sequence for every step under the constraints. In order to compensate for the effects of the control performance by uncertainties and disturbances, a robust MPC approach has been introduced and used to design an autonomous control algorithm (Mayne, 2005). However, robust MPC approaches that deal with worst-case disturbances may be too conservative and computationally expensive. The chance-constrained optimization in (Vitus, 2013) shows the tactical planning problem for automated driving vehicles in uncertain environments.

We focus on designing the automated control algorithm that manages potentially dangerous lane change situations while satisfying control performance on model parameter uncertainties and exogenous disturbances. The vehicle motion is defined in consideration of probabilistic prediction of future states of the surrounding environment to enhance safety on the potential behaviors of surrounding vehicles. In order to change lane in complex surrounding traffic situations, target state decision can manage lane change motion of automated driving. Then, an SMPC problem is formulated to determine the desired control input.

2 OVERALL ARCHITECTURE

The proposed automated driving system architecture is shown in Fig. 1. The proposed automated driving control algorithm consists of three layers. The Environment Representation block calculates probabilistic predictions of the states of surrounding vehicles and collision probability. All system modules make use of information from equipped various sensors. The probable behaviors of the surrounding vehicles are predicted over a finite prediction horizon with this

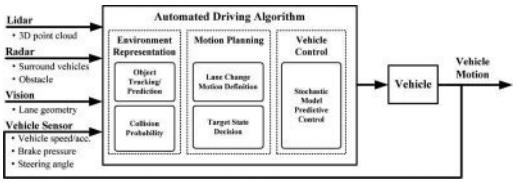


Figure 1. Overall architecture of the proposed algortihm.

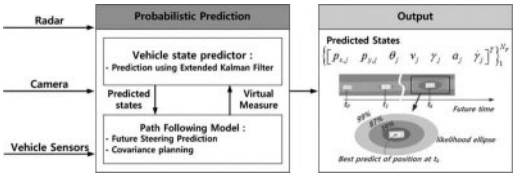


Figure 2. Overall architecture of the probabilistic prediction of surrounding vehicle's behavior.

information. The Motion Planning block uses the information of exterior sensors and human driver data along with the predicted information of the environment to determine the lane change or keeping motion of the subject vehicle. Target state decision is determined reference position and acceleration to change or keep lane for safety. The Vehicle Control block uses environment and planned vehicle motion information to formulate an SMPC to optimize the steering and longitudinal acceleration input to the vehicle. Due to the uncertainties of vehicle dynamics model, disturbance analysis, and uncertainty propagation are conducted.

3 ENVIRONMENT PRESENTATION MODEL

The environment representation has two main modules: object tracking/prediction and collision probability. The object tracking and prediction module compute the reachable sets for traffic participants. Markov chain is used to approximate the stochastic processes of each traffic participants. It is assumed that the driver may maintain the current vehicle behavior and keep the proper lane in the finite prediction horizon. A simple path following model and a vehicle state predictor interact with each other during one cycle of the prediction process.

3.1 *Object tracking and prediction*

One of a common approach to predict the future states of traffic situation surrounding the subject vehicles is a deterministic prediction which assumes that other vehicles surrounding the subject vehicle maintain its current movement during a finite time-horizon. However, since this approach ignores the probability of all possible movements of surrounding vehicles, it could not recognize unexpected driving situations properly. Therefore, the deterministic prediction causes incorrect interpretation of the current driving situation.

In order to compensate the shortcomings of the deterministic prediction of the behaviors of surrounding vehicles, the probability behaviors of surrounding vehicles are predicted, and the risk behaviors among the possible behaviors of other vehicles surrounding the subject vehicle are considered to determine the safe distance between subject and other vehicles.

For the prediction of the reasonable and realistic behaviors of surrounding vehicles, the interaction between vehicles and the restriction on surrounding vehicle's maneuver due to the road geometry should be considered. Therefore, in predicting the possible behaviors of surrounding vehicles, it is assumed that surrounding vehicles are driven with the consideration of the presence of other vehicles and interactive motions with other vehicles respectively. It means that the minimum safety distance between surrounding vehicles should be kept for collision avoidance.

Also, it is assumed that drivers of the surrounding vehicles maneuver the vehicles with the consideration of the road geometry. It means that the speed of the surrounding vehicle should be adapted to the road geometry and road condition.

In predicting reasonable ranges of the future states of surrounding vehicles, driving data is collected on the real road to analyze the probabilistic movement characteristics of the other vehicles. For the implementation of these assumptions, a path-following model is designed while interacting with a vehicle state predictor during one cycle of the prediction process. In the vehicle state predictor, the vehicle's probable position and its error covariance over a finite time horizon are predicted by Extended Kalman Filter using the desired yaw rate obtained by the path-following model as the virtual measurement.

Fig. 2 depicts the overall architecture of probabilistic prediction of surrounding vehicles. Using measurements from the various sensors, such as vehicle sensor, radar, and vision sensor, the range of the predicted states with corresponding uncertainty is determined. p_x is the longitudinal position of the vehicle, p_y is the lateral position of the vehicle, N_p denotes the length of the prediction horizon, and subscript 'j' means the j-th objects. In predicting the position of the surrounding vehicle, it is assumed that the size of the object is equivalent to the subject vehicle.

3.2 *Collision probability*

As the beginning of the collision probability estimation, we randomly generate a given number N state vectors based on the given initial probability density function from the prediction algorithm. The parameter N could be chosen by a designer as a trade-off between computational effort and collision probability approximation accuracy. The state vectors are called particles and denoted as:

$$\mathbf{x}_{n,p}^{i} = \begin{bmatrix} \hat{\mathbf{x}}_{host,p} \\ \hat{\mathbf{x}}_{n,p} \end{bmatrix} + \left(\sqrt{\begin{bmatrix} \hat{\mathbf{P}}_{host,p} & \\ & \hat{\mathbf{P}}_{n,p} \end{bmatrix}} \right) \cdot \tilde{\mathbf{r}}^{i} \quad (i = 1, \cdots, N) \quad (1)$$

where p is the predictive time step; $\hat{\mathbf{x}}_{host}$ is the predicted position and orientation state of the host vehicle; $\hat{\mathbf{x}}_n$ is

the predicted pose state of n-th traffic participant; $\hat{\mathbf{P}}$ denotes the appropriate size of the covariance matrix of each predicted state; $\tilde{\mathbf{r}}$ is a white noise random vector of the proper size.

For every possible pair of host and one of traffic participants, we investigate whether the vehicle bodies of the traffic participant can intersect the host vehicle at each predicted time step. A body-shaped diagram is introduced to determine the body intersection.

4 VEHICLE MODEL

A vehicle dynamics model should be derived to obtain the desired control inputs with SMPC approach. In this research, we design a linear parameter varying (LPV) model of the vehicle dynamics from nonlinear vehicle model.

The nonlinear differential equations are used to describe the motion of the vehicle in a Frenet coordinate frame

$$\dot{v}_x = v_y\gamma + a_x \tag{2a}$$

$$\dot{v}_y = -v_x\gamma + \frac{1}{m}\left(2F_{yf} + 2F_{yr}\right) \tag{2b}$$

$$\dot{\gamma} = \frac{1}{I_z}\left(2l_fF_{yf} - 2l_rF_{yr}\right) \tag{2c}$$

$$\dot{e}_\psi = \gamma - \kappa\dot{s} \tag{2d}$$

$$\dot{e}_y = v_x\sin\left(e_\psi\right) + v_y\cos\left(e_\psi\right) \tag{2e}$$

$$\dot{s} = \frac{1}{1-\kappa e_y}\left(v_x\cos\left(e_\psi\right) - v_y\sin\left(e_\psi\right)\right) \tag{2f}$$

where l_f and l_r denote the distance from the vehicle's center of gravity to the front and the rear axles, respectively; m and I_z denote the vehicle mass and yaw inertia, respectively; e_ψ is the orientation error of the vehicle with respect to the road; e_y denotes the lateral offset with respect to the center line of the lane; κ is curvature of the road from camera sensor; s denotes the longitudinal position of the vehicle along the road; F_{yf} and F_{yr} are lateral force of front and rear in the body frame, respectively.

5 MOTION PLANNING ALGORITHM

When driving on the road, an appropriate lane change is necessary for various reasons, such as preceding vehicle driving slower than the speed limit or the subject vehicle and plan to go out to the upcoming exit way. That is, the automated driving vehicle determines its lane keeping or change motion to adjust for following the traffic situations. As human drivers consider surrounding environments and predict the short period of future states of a subject and other vehicles, which is predicted by the object prediction information, in section 3, is used to plan the subject vehicle's motion. The reference acceleration calculation considers that the subject vehicle changes its lane safely in complex lane change situations. The *TTC*, which is calculated every predicted time steps, and *CP* are adopted for safe guarantee probabilistically.

5.1 *Lane change and keeping motion*

Vehicle behavior can be divided two parts mainly, lane keeping and lane change. Since the control strategy of lane keeping and change for automated driving vehicles is different, determining vehicle motion is critical to set the control strategy.

In order to obtain the lateral motion for lane change and longitudinal motion for lane keeping, when the subject vehicle changes or keeps the lane, lateral acceleration for lane change maneuver and longitudinal acceleration for following preceding vehicle had been standardized as a sinusoidal and trapezoidal shape in previous research (Wan, 2011). However, regarding ride quality, the sinusoidal shape has excessive acceleration jerk value. In this paper, a hyperbolic tangent path is suggested for low acceleration jerk.

We define the hyperbolic tangent path as follows:

$$e_y\left(t\right) = C_1\cdot\tanh\left(C_2\cdot t + C_3\right) + C_4 + v_{y,0}\cdot t + e_{y,0} + L_p \tag{3}$$

where C_* is a constant value from 1 to 4; subscript 0 denotes current information; L_p denotes preview distance; t denotes time parameter. There are two assumptions to derive hyperbolic tangent based lateral acceleration.

Assumption 1. Lateral velocity, $v_{y,0}$, is zero.
Assumption 2. The lateral motion does not rely on the longitudinal velocity.

When the host vehicle crosses from its originating lane to next lane, it travels the distance between current lateral position and center of next lane. Then the constant C_1 and C_4 can be derived intuitively as,

$$C_1 = \frac{\pm W_{road} - e_{y,0}}{2} \tag{4a}$$

$$C_4 = \frac{\pm W_{road} - e_{y,0}}{2} \tag{4b}$$

where W_{road} denotes road width.

Let differentiate (3), lateral acceleration can be obtained as (5).

$$a_y\left(t\right) = -2\cdot C_1\cdot C_2^2\tanh\left(C_2\cdot t + C_3\right)\cdot\mathrm{sech}^2\left(C_2\cdot t + C_3\right) \tag{5}$$

Using the lateral acceleration limit, $v_{y,0}$,

$$C_1\cdot C_2^2 = \frac{a_{y,\lim}}{a_{y,0}} \Leftrightarrow C_2 = \sqrt{\frac{\pm a_{y,\lim}}{a_{y,0}}\cdot\frac{1}{C_1}} \tag{6}$$

where $a_{y,0}$ is the original maximum value of lateral acceleration.

Since the hyperbolic tangent is origin symmetry, lane change starting time should have displacement to the right. Let define lane change process time, t_{LC}. The hyperbolic tangent based acceleration has to move

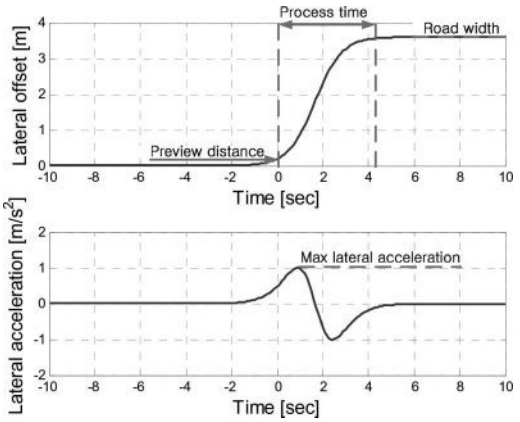


Figure 3. Hyperbolic tangent based lateral offset and lateral acceleration.

to the right up to half of lane change process time. The interaction formula between the parameter C_2 and C_3 can be expressed as,

$$\frac{C_3}{C_2} = -\frac{t_{LC}}{2} \tag{7}$$

Consider lateral offset after lane change process time which is center position of next lane. Then an equality constraint can be obtained as follows:

$$e_y\left(t_{LC}\right) = W_{road} \tag{8}$$

From (9) to (14), the lane change process time can be written as,

$$t_{LC} = \frac{2}{C_2}\tanh^{-1}\left\{\frac{W_{road} - C_4 - e_{y,0}}{C_1}\right\} \tag{9}$$

Fig. 3 shows the hyperbolic tangent based path and acceleration which reflects the parameters.

5.2 *Target state decision*

As mentioned above, when the lane change is necessary, the appropriate velocity and lateral motion are necessary. However, it may occur that the subject vehicle has to conduct lane change in some situations such as merge, split or intersection. Then the automated driving vehicle needs to adjust its longitudinal position and velocity to change the lane for matching the traffic flow to next lane.

In order to change lane smoothly, the desired lateral position is needed. According to ***Assumption 2***, the lateral lane change motion does not depend on vehicle acceleration or velocity. It means that general lateral motion for a lane change is similar in various situations.

For lane keeping, since the host vehicle needs to stay its originating lane regardless of preceding vehicle, the lateral position is determined the center of the

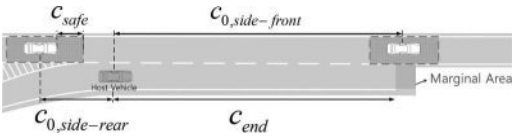


Figure 4. Lane change in limited situation.

originating lane. The longitudinal position and velocity are defined to follow the desired speed. However, if the preceding vehicle which is slower than the subject vehicle exists, the desired speed is set as the velocity of preceding vehicle.

For lane change, as far as safety is guaranteed, the velocity maintains the desired speed. However, the risk is predicted in near future, the longitudinal position and velocity of the host vehicle are determined to follow the traffic flow of the target lane, the destination of the host vehicle. In addition, we define the lateral position to change the lane like a human driver. It is assumed that the lateral acceleration is represented by a hyperbolic tangent shape when the host vehicle changes lanes and the initial lateral velocity is zero as in ***Assumption 1***. Recall the (3), the lateral position of reference trajectory can be rewritten as follows:

$$e_{y,ref,t+k|t} = \begin{cases} \left\{ C_1 \tanh\left(C_2 \cdot \left(t_{samp}k + t\right) + C_3\right) \right\} & \left|e_{y,t+k|t}\right| < W_{road} \\ +C_4 + e_{y,0} + L_p & e_{y,t+k|t} \geq W_{road} \\ W_{road} & e_{y,t+k|t} \leq -W_{road} \\ -W_{road} & \end{cases} \tag{10}$$

The lateral position has to change with time since the prediction horizon is not long enough to cover the entire lane change procedure. In addition, intuitively, the maximum reference lateral position of the lane change is the center point of the adjacent lane. Thus, the maximum reference lateral position is the road width.

When the host vehicle keeps its lane, it needs to maintain sufficient clearance between the host vehicle and the preceding vehicle. For this reason, the desired clearance should be defined. The desired clearance is regarded as boundary problem because if the clearance from the host vehicle to preceding vehicle is too far to consider, the host vehicle does not need to accelerate to adjust this clearance. However, if the clearance is too close to be a danger the host vehicle should slow down its speed to be safe. The desired clearance is defined as follows:

$$c_{des} = \tau_h \cdot v_x + c_{safe} \tag{11}$$

where τ_h is a headway time gap.

If there are constraints of time or distance such as the merging section or slow preceding vehicle, the host vehicle needs to change lane in limited time. Furthermore, if the adjacent vehicles exist in side-lane, safe area is defined as constraints. Fig. 4 shows an example for constrained situations.

c_0 denotes initial clearance; c_{end} denotes distance from the host vehicle to road end considering marginal area.

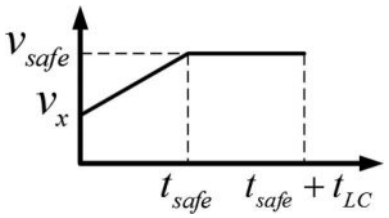


Figure 5. Velocity profile for constrained lane change.

For straightforward and fast planning for lane change, there is an assumption as follows:

Assumption 3. The vehicle accelerates with constant acceleration when the vehicle changes the lane.

From this assumption, the velocity profile is derived as shown in Fig. 5.

In order to solve this problem, three constraints are defined as follows:

$$\frac{v_x+v_{safe}}{2}t_{safe}-v_{side-rear}t_{safe}\geq c_{safe}+c_{0,side-rear} \tag{12a}$$

$$\frac{v_x+v_{safe}}{2}t_{safe}+v_{safe}t_{LC}\leq c_{end} \tag{12b}$$

$$\frac{v_x+v_{safe}}{2}t_{safe}+v_{safe}t_{LC}-v_{side-front}\left(t_{safe}+t_{LC}\right) \leq -c_{safe}+c_{0,side-front} \tag{12c}$$

where t_{safe} denotes acceleration completion time.

If there is no side-rear vehicle, (12a) is always satisfied. Not only end road situation like merging section but also slow preceding vehicle does not exist, (12b) is also satisfied. Similarly, (12c) does not need to consider when the side-front does not exist.

6 STOCHASTIC MPC BASED VEHICLE CONTROL

We present the background on the SMPC that is used to decide the desired control inputs for automated driving vehicle control performance. The receding horizon control problem with a chance-constraint is formulated using vehicle dynamics model and safe constraints (Suh, 2016). The SMPC is solved to determine a sequence of control inputs which are applied to the system. The solving process of the optimization problem repeated at each time step is formulated as follows:

$$\min \sum_{k=0}^{N_p-1}\mathbb{E}\left(\left\|x_{t+k+1|t}-x_{ref,k+1}\right\|_{\mathbf{Q}}^2+\left\|u_{t+k|t}\right\|_{\mathbf{R}}^2\right) \tag{13a}$$

$$s.t.\ \ x_{t+k+1|t}=\mathbf{A}_{l,k}x_{t+k|t}+\mathbf{B}_{l,k}u_{t+k|t}+\mathbf{D}_k w_k \tag{13b}$$

$$\Pr\left(g_{k+1}^T x_{k+1}\leq h_{k+1}\right)\geq 1-\varepsilon_k \tag{13c}$$

$$u_{t+k|t}\leq u_{\max} \tag{13d}$$

$$u_{t+k|t}\geq u_{\min} \tag{13e}$$

$$x_{t,t}=x(t) \tag{13f}$$

$$\left(k=0,\ldots,N_{p-1}\right)$$

where t denotes the current time instant; $\mathbf{Q}$ and $\mathbf{R}$ are weighting matrices; $x_{t+k|t}$ denotes the predicted subject vehicle state at time $t+k$ obtained by applying the control sequence u_t to the vehicle model (13b) with initial condition (13f); (13c) is a chance-constraint to be satisfied with a specified probability $0\leq\varepsilon\leq 0.5$; ε denotes the tunable risk parameter; (13d) and (13e) are maximum and minimum constraints, $u_{max}=[\delta_{f,lim}, a_{x,max}]^T$ and $u_{min}=[-\delta_{f,lim}, a_{x,min}]^T$ for control inputs, respectively. In this paper, $\delta_{f,lim}$ is 30 deg, $a_{x,min}$ is $-5\ \mathrm{m/s^2}$, and $a_{x,max}$ is $3\ \mathrm{m/s^2}$.

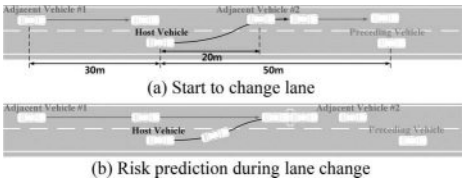


Figure 6. Simulation scenarios of unexpected traffic.

7 EVALUATION RESULTS

The proposed motion planning algorithm for lane change has been evaluated via computer simulations and real vehicle test. The computer simulation is conducted using MATLAB/Simulink and Carsim.

In order to show the effectiveness of the proposed control algorithm using probabilistic prediction, simulation results of control algorithm based on SMPC using deterministic prediction of surrounding vehicle are compared with those of the proposed algorithm. The primary features of the control algorithm based on SMPC using deterministic prediction can be represented as follows:

Remark 1. The environmental envelope defined using deterministic prediction is defined without respect to the possible behavior of the surrounding vehicle.

Remark 2. The target vehicle for the control of the longitudinal acceleration is generated by integrating the current states of the preceding vehicle in the originating lane and those of the vehicle in the adjacent lane.

Since an automated driving control algorithm should operate in a wide operating region, the performance of the proposed algorithm should be verified in the various driving situation. In this dissertation, comparison of probabilistic and deterministic is conducted via computer simulation.

In order to compare the decision performance, simulation scenario is set that the risk prediction is difficult. In other words, after the host vehicle judges present risk and determines to change lane, the other traffics change their motion suddenly. Simulation scenario is designed to reproduce the risky highway situation as shown in Fig. 6.

In this situation, initial velocities of adjacent vehicles are set to 80 kph, and those of host vehicle and preceding vehicle are configured to 60 kph. The host vehicle starts to accelerate until it judges lane change

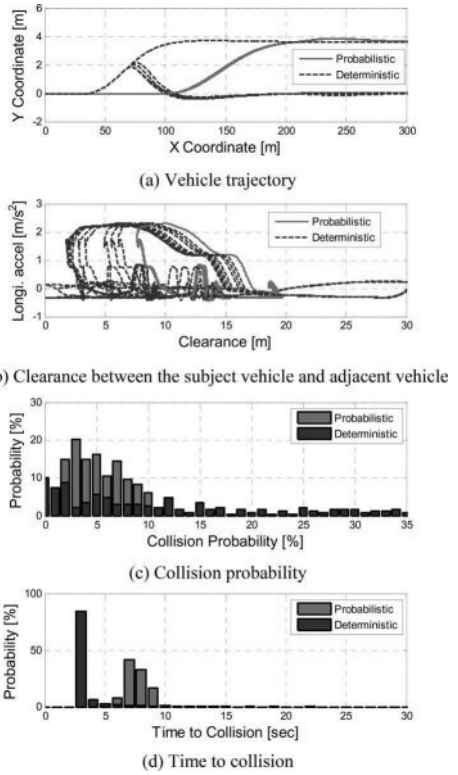


Figure 7. Comparison performance results between probabilistic and deterministic prediction.

safe. However, the adjacent vehicle #1 accelerates to prevent lane change of the host vehicle. The initial clearance between the host vehicle and the adjacent vehicle #1 is 30 meters, and between the host vehicle and the adjacent vehicle #2 is 20 meters. Also, the initial clearance between the host vehicle and the preceding vehicle is 50 meters.

Simulation studies have been repeated 11 times for comparing control algorithms which are a probabilistic and deterministic prediction. Each simulation has different acceleration magnitude of adjacent vehicle #1 0 to 2 m/s^2 with interval 0.2 m/s^2.

The simulation results are presented in Fig. 7. Fig. 7(a) shows the difference between vehicle trajectory using probability prediction and that using deterministic prediction. Depending on the acceleration of the subject vehicle #1, the automated driving algorithm using deterministic prediction cannot change lane successfully. Fig. 7(b) shows that clearance between the host vehicle and adjacent vehicle #1 is kept very similar. It means that the proposed algorithm has robust performance. In other words, an algorithm using deterministic prediction does not have reproducibility and robustness. To show the effectiveness of using probability prediction for the safe lane change, risk indices, collision probability and *TTC*, are plotted in Fig. 7(c) and (d). The average value of collision probability distribution using probabilistic prediction is smaller than that using deterministic prediction. Differently, the mean value of *TTC* data using probabilistic prediction is larger than that using deterministic prediction. It means that the probabilistic prediction is much safer than a deterministic prediction.

8 CONCLUSION

A collision probability based lane change motion planning for automated driving has been developed, and the performance of the proposed algorithm has been evaluated via computer simulation. To deal with the potential risk lane change situation, the current states and the possible risk behaviors of the surrounding environment during a finite time horizon are considered simultaneously to determine lane keeping and change motion. The control architecture based on an SMPC approach is used to calculate the desired steering angle and longitudinal acceleration with probabilistic constraints from uncertainties and disturbances.

Automated driving with the proposed algorithm shows smooth and safe driving behavior with safety in hazardous road traffic situations, such as lane keeping with preceding vehicle following, lane change in multi-vehicle environment and so on. Especially, a probabilistic prediction based automated driving control algorithm shows safer performance than a deterministic prediction.

REFERENCES

Bishop, R. 2000. A survey of intelligent vehicle applications worldwide. IEEE Intelligent Vehicle Symposium, 21–35.

Gray, A., Gao, Y., Hedrick, J., and Borrelli, F. 2013. Robust predictive control for semi-autonomous vehicles with an uncertain driver model. IEEE Intelligent Vehicles Symposium, 208–213.

Mayne, D., Seron, M., and Rakovic, S. 2005. Robust model predictive control of constrained linear systems with bounded disturbances. Automatica, 219–224.

Suh, J., Yi, K., Jung, K., Lee, H., Chong, H., and Ko, B. 2016. Design and evaluation of a model predictive vehicle control algorithm for automated driving using a vehicle traffic simulator. Control Engineering Practice, 92–107.

Tomar, R., Verma, S., and Tomar, G. 2010. Prediction of lane change trajectories through neural network, ITS Magazine.

Vanholme, B., Gruyer, D., and Lusetti, B. 2013. Highly automated driving on highways based on legal safety. Intelligent Transportation Systems, 333–347.

Vitus, M., and Tomlin, C. 2013. A probabilistic approach to planning and control in autonomous urban driving. Decision and Control (CDC).

Wei, J., Dolan, M., and Litkouhi, B. 2010. A prediction and cost function based algorithm for robust autonomous freeway driving, IEEE Intelligent Vehicle Symposium, 513–517.

Wan, L., Raksincharoensak, P., Maeda, K., and Nagai, M. 2011. Lane change behavior modeling for autonomous vehicles based on surroundings recognition, IJAT, 7–12.

Advanced Vehicle Control – Edelmann, Plöchl & Pfeffer (Eds)
© 2017 Taylor & Francis Group, London, ISBN 978-1-138-02992-7

Autonomous vehicle trajectory planning and control based on virtual disturbance compensation via simulation of feedback control systems

P. Raksincharoensak, T. Ehira, K. Shimono & Y. Tagawa
Department of Mechanical Systems Engineering, Tokyo University of Agriculture and Technology, Tokyo, Japan

ABSTRACT: This paper describes a new method for autonomous vehicle trajectory planning in obstacle avoidance maneuver. The concept of the controller design is based on the method called "inverse dynamics compensation via simulation of feedback control systems (IDCS)" which makes use of simulations in ideal environment to get high performance in control. Conventional trajectory planning method based on potential field mostly treats the vehicle dynamics as a particle, thus the vehicle path becomes unstable in high speed region which the vehicle dynamics cannot be neglected. The feedback simulation method is useful to embed the vehicle nonlinear characteristics for the trajectory planning algorithm. The repulsive force from potential field is treated as disturbance forces to the vehicle in the simulation model. The effectiveness of the control system is verified and compared with the conventional potential field algorithm.

1 INTRODUCTION

Research interest in the field of Advanced Driver Assistance Systems (ADAS) is currently increasing due to safety requirement. Nowadays, there are many variation of target driving scenario in preventing collision and the integration of ADAS functions by using a unified approach will be necessary in future to avoid the interference or conflict among various ADAS functions. Trajectory planning and control is one of important parts of autonomous vehicles as well as advanced driver assistance systems, especially when there is high collision risk in driving environment to get safe trajectory with satisfactory ride comfort. The famous trajectory planning technique in the field of mobile robots is called Potential Field (Khatib, 1986, Galceran et al. 2015, Wolf et al. 2008). The trajectory can be designed by changing the shape of potential field functions with respect to the distance to obstacles. Potential field basically is effective in the case of stationary obstacle avoidance maneuver. Conventional potential field theory reaches their limit when the vehicle is driving in high speed region and requires high acceleration, as it reaches the tire nonlinear region. Thus, the planned trajectory by the conventional potential field theory becomes unsuitable for the vehicle in highly dynamic maneuver. Moreover, the potential field parameters of each element in dynamic road environment are difficult to be identified in systematic way, especially in complex environments. For instance, the potential field parameters of the obstacle, road boundary and others must be tuned to obtain the appropriate desired vehicle trajectory. Therefore, when the vehicle speed is changed, the potential field parameters need to be changed to get the appropriate vehicle trajectory.

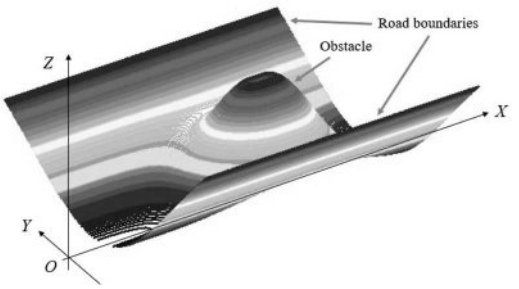


Figure 1. Obstacle avoidance on potential field.

The other approach is to use the optimal control theory. The optimal control can be used to determine the control input according to various control objectives which are determined by the performance index or the cost function. The authors combined the idea of risk potential field and optimal control theory in trajectory planning process (Raksincharoensak et al. 2016). Another representative method is to use the model predictive control theory (MPC) which is well known as a method that can achieve high performance and good robustness for many application by future prediction and its real-time solution update (Bauer et al. 2012, Balachandran et al. 2016, Falcone et al. 2007, Kim et al. 2012, Nishira et al. 2011).

This paper proposes a new trajectory planning method considering vehicle dynamics by using feedback simulation method. The driving situation is shown in Figure 1 together with an artificial potential field. The simulation of feedback control method is useful to include the vehicle nonlinear characteristics in trajectory planning. The repulsive force from

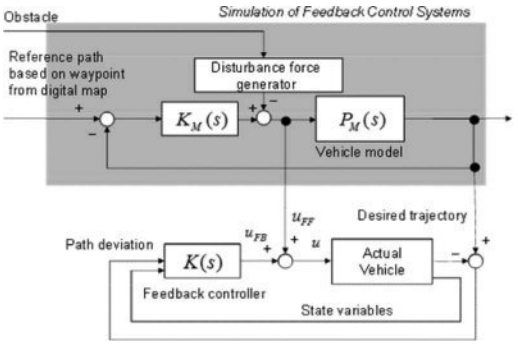


Figure 2. Block diagram of virtual disturbance compensation via simulation of feedback control systems.

potential field is treated as disturbance force to the vehicle in the simulation. The effectiveness of the control system is verified by computer simulation, and the comparison with the conventional trajectory planning by potential field algorithm is conducted.

2 CONTROL SYSTEM DESIGN

2.1 *Control system structure*

Figure 2 shows the schematic diagram of the proposed control system. Based on general autonomous vehicle configuration, the reference vehicle trajectory is assumed to be given by a series of waypoints from the digital map information. Separating the road boundaries based on the waypoints from road obstacles make us determine the potential field function parameters easier as we can handle only the repulsive force as the external virtual force acting on the vehicle. The repulsive from the obstacle is treated as a disturbance to the closed-loop control system with on-board nonlinear vehicle dynamics model. The feature of the proposed disturbance force feedback compensation simulation is that it can determine the desired avoidance trajectory and the desired feedforward control input, i.e. the front steering angle, simultaneously. The feedback control system is also added to compensate the deviation between the desired trajectory and the actual trajectory. Compared with the pure feedback control framework, this method provides superior stability of the controlled system. This control system design framework is based on the method called Inverse Dynamics Compensation via Simulation of Feedback Control Systems (Tagawa et al., 2011) which is a numerical method that obtains an approximate inverse dynamic solution via a feedback control simulation.

2.2 *IDCS controller*

This chapter describes the concept of the "inverse dynamics compensation via simulation of feedback control systems (IDCS)" which is a numerical method that obtains an approximate inverse dynamic solution via a feedback control simulation, using only the forward dynamic model of the linear or non-linear system (Tagawa et al. 2011). Simulations are ideal environments for feedback control, in the sense that they can be completely noise-free and precisely known, so that the feedback controller inside the IDCS framework can be tuned for the best possible performance. In reality, many control systems have undesirable features as unknown dynamics in the plant, model parameter errors, unexpected disturbances, signal noise and etc. These undesirable factors deteriorate the control performance, i.e. stability and good tracking performance. In contrast, the simulation environment can be made completely free from the above undesirable factors and the best control performance can be obtained.

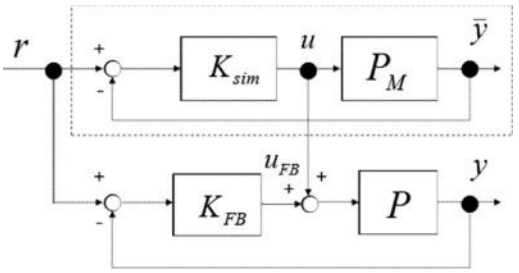


Figure 3. General expression of the block diagram of IDCS in parallel with a physical feedback closed-loop system.

Figure 3 shows the basic concept of IDCS, which merges the ideal control simulation performance with the real world, using the principle of inverse dynamics. The IDCS is not an analytical method for deriving an exact inverse dynamics of the system; instead, it is a numerical method for generating input/output signals that are close to those derivable from an analytical approach. Especially, in the IDCS framework, the system P can be a linear or a non-linear system. The method is useful for systems containing non-linearities that are difficult to obtain direct analytical solutions.

3 TRANSFER FUNCTION ANALYSIS

Based on the idea of IDCS method described in Chapter 2, the obstacle avoidance trajectory planning and control is designed. This chapter describes the analysis of avoidance trajectory planning and the control input generation by the feedback control simulation framework. Here to simplify the analysis, the linear two-wheel vehicle model is used. Considering the steering angle as the control input and the virtual repulsive force from obstacle as the disturbance to the vehicle, the equation of lateral and yaw motions can be expressed in the form of state space equation as follows:

$$\begin{bmatrix} \dot{\beta} \\ \dot{r} \end{bmatrix} = \begin{bmatrix} a_{11} & a_{12} \\ a_{21} & a_{22} \end{bmatrix} \begin{bmatrix} \beta \\ r \end{bmatrix} + \begin{bmatrix} b_{11} \\ b_{21} \end{bmatrix} \delta_{sw} + \begin{bmatrix} c_{11} \\ c_{12} \end{bmatrix} F_d \qquad (1)$$

where, β indicates the vehicle body side slip angle, r the yaw rate, δ_{sw} the steering wheel angle, F_d the repulsive force which is assumed to act at the center of gravity, the elements in matrices $a_{11}-a_{22}$, b_{11}, b_{21}, c_{11}, c_{21} are the coefficients which are determined from the equation of motions as follows:

$$a_{11}=-\frac{2(K_f+K_r)}{mV},\ a_{12}=-1-\frac{2(l_fK_f-l_rK_r)}{mV^2},$$
$$a_{21}=-\frac{2(l_fK_f-l_rK_r)}{I},\ a_{22}=-\frac{2(l_f^2K_f+l_r^2K_r)}{IV},$$
$$b_{11}=\frac{2K_f}{mVn},\ b_{21}=\frac{2l_fK_f}{In},\ c_{11}=\frac{1}{mV},\ c_{21}=0$$

where, m indicates the vehicle mass, I the yaw moment of inertia, $K_{f(r)}$ the front (rear) cornering stiffness, $l_{f(r)}$ the distance from the center of gravity to the front (rear) axle, and V the vehicle velocity.

From the closed-loop feedback control system shown in Figure 4, the relationship of the vehicle trajectory with respect to the reference trajectory (lateral displacement) and the force input can be expressed as the following equation.

$$Y(s)=\frac{C(s)G_v(s)}{s^2+C(s)G_v(s)}Y^*(s)+\frac{G_d(s)G_v(s)}{s^2+C(s)G_v(s)}F_d(s) \quad (2)$$

If the reference path is straight line and the initial Y coordinate of the road is fixed at the center of gravity of the vehicle, $Y^*(s)=0$ so the avoidance trajectory with respect to the disturbance force becomes as follows:

$$Y(s)=\frac{G_d(s)G_v(s)}{s^2+C(s)G_v(s)}F_d(s) \quad (3)$$

Here, considering that the feedback controller is PD controller, $C(s)$ is expressed as the following equation.

$$C(s)=K_p+K_ds \quad (4)$$

As the lateral acceleration can be expressed as the combination of side slip angle and yaw rate, $\ddot{y}=V(\dot{\beta}+r)$, the transfer function from the steering wheel angle and the disturbance force to the lateral acceleration are calculated as the following functions respectively.

$$G_v(s)=V\left(\frac{b_{11}s^2+(a_{12}b_{21}-a_{22}b_{11}+b_{21})s+(a_{21}b_{11}-a_{11}b_{21})}{s^2+(-a_{11}-a_{22})s+(a_{11}a_{22}-a_{12}a_{21})}\right) \quad (5)$$

$$G_d(s)=\frac{c_{11}s^2+(-a_{22}c_{11})s+a_{21}c_{11}}{b_{11}s^2+(a_{12}b_{21}-a_{22}b_{11}+b_{21})s+(a_{21}b_{11}-a_{11}b_{21})} \quad (6)$$

By substituting the relevant transfer functions indicated in Eq. (4), (5), (6) into Eq. (3), the transfer function of the lateral displacement can be obtained.

$$\frac{Y(s)}{F_d(s)}=\frac{G_d(s)G_v(s)}{s^2+(K_dG_v(s))s+(K_pG_v(s))} \quad (7)$$

$$\frac{Y(s)}{F_d(s)}=\frac{n_2s^2+n_1s+n_0}{s^4+d_3s^3+d_2s^2+d_1s+d_0} \quad (8)$$

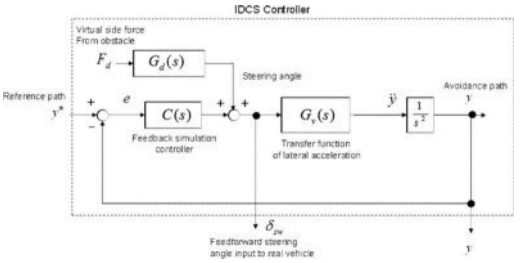


Figure 4. Analytical model for simulation of feedback control system.

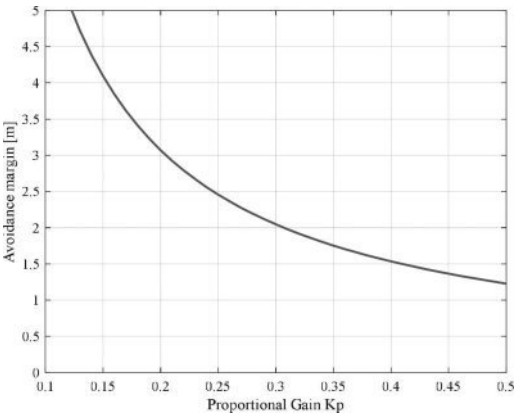


Figure 5. Change of avoidance margin with respect to the proportional gain.

where, each coefficient of the transfer function in Equation 8 can be expressed as follows:

$$n_2=\frac{1}{m},\ n_1=\frac{2(l_f^2K_f+l_r^2K_r)}{mIV},\ n_0=\frac{2(l_rK_r-l_fK_f)}{mI}$$
$$d_3=\frac{2(l_f^2K_f+l_r^2K_r)}{IV}+\frac{2(K_f+K_r)}{mV}+\frac{2K_f}{mn}K_d$$
$$d_2=\frac{2(l_rK_r-l_fK_f)}{I}+\frac{4K_fK_rl^2}{mIV^2}+\frac{4K_fK_rl_rl}{mIVn}K_d+\frac{2K_f}{mn}K_p$$
$$d_1=\frac{4K_fK_rl_rl}{mIVn}K_p+\frac{4K_fK_rl}{mIn}K_d,\ d_0=\frac{4K_fK_rl}{mIn}K_p$$

In Equation 8, let $s=0$, we will get the following relationship.

$$\frac{Y(0)}{F_d(0)}=\frac{n_0}{d_0}=\frac{l_rK_r-l_fK_f}{2K_fK_rnl}\frac{1}{K_p} \quad (9)$$

In Equation 9, it describes that the avoidance margin is dependent on the feedback simulation controller proportional gain K_p, and the margin is independent of vehicle speed. The relationship of the avoidance margin and the proportional gain is shown in Figure 5.

The dynamic characteristics of the avoidance path with respect to the virtual disturbance force can be analyzed from the transfer function in Equation 8. The poles are plotted as shown in Figure 6. The Bode

diagram of the lateral displacement with respect to the virtual force is shown in Figure 7.

The transfer function analysis gives us some basic understandings of how to determine the feedback controller gains in the simulation framework. However, in the actual feedback control simulation framework, the full vehicle which contains the nonlinear characteristics of tire is embedded in the simulation framework. In critical maneuver, there are some differences between the linear vehicle model and the actual full vehicle model, so the gains should be carefully set to avoid the unrealistic avoidance trajectory of the vehicle.

4 PHYSICAL FEEDBACK CONTROLLER

From the feedback controller simulation framework described in the previous chapter, the desired trajectory for obstacle avoidance and the feedforward steering wheel angle command can be obtained. However, there are some differences in the vehicle model used in the feedback controller simulation framework and the real vehicle. In this case, the physical feedback controller is needed to improve the path tracking performance. To make the vehicle trace the desired path, the feedback controller such as PD, LQ control theory, Model Predictive Control (MPC) theory can be used. As one example, this study employs the LQ control theory to design the physical feedback controller for the sake of simplicity in control input computation.

To design the path tracking controller, the equation of motion of the vehicle is expressed in the form of state space equation as follows:

$$\begin{bmatrix} \ddot{\psi} \\ \dot{\psi} \\ \ddot{y}_c \\ \dot{y}_c \end{bmatrix} = \begin{bmatrix} A_{11} & A_{12} & A_{13} & 0 \\ 1 & 0 & 0 & 0 \\ A_{31} & A_{32} & A_{33} & 0 \\ 0 & 0 & 1 & 0 \end{bmatrix} \begin{bmatrix} \dot{\psi} \\ \psi \\ \dot{y}_c \\ y_c \end{bmatrix} + \begin{bmatrix} B_{11} \\ 0 \\ B_{31} \\ 0 \end{bmatrix} \delta_{swFB} \qquad (10)$$

where, each element in the matrices is determined as follows:

$$A_{11} = -\frac{2(l_f^2 K_f + l_r^2 K_r)}{IV},\ A_{12} = \frac{2(l_f K_f - l_r K_r)}{I},\ A_{13} = -\frac{2(l_f K_f - l_r K_r)}{IV}$$

$$A_{31} = -\frac{2(l_f K_f - l_r K_r)}{mV},\ A_{32} = \frac{2(K_f + K_r)}{m},\ A_{33} = -\frac{2(K_f + K_r)}{mV},$$

$$B_{11} = \frac{2l_f K_f}{In},\ B_{31} = \frac{2K_f}{mn}$$

The steering wheel angle as the feedback control input is determined as the state feedback control law.

$$\delta_{swFB} = -K_{\dot{\psi}}\dot{\psi} - K_{\psi}\psi - K_{\dot{y}c}\dot{y}_c - K_{yc}y_c \qquad (11)$$

where, $K_{\dot{\psi}}$, K_{ψ}, $K_{\dot{y}c}$, K_{yc} are the feedback control gains which are determined by the LQ control theory. The performance index J is determined as shown in the following equation.

$$J = \int_0^{\infty} \left[q y_c^2 + r \delta_{swFB}^2 \right] dt \qquad (12)$$

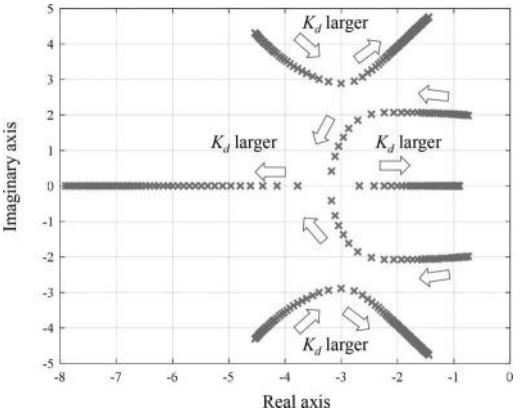


Figure 6. Poles of the transfer function from the virtual force to the lateral displacement.

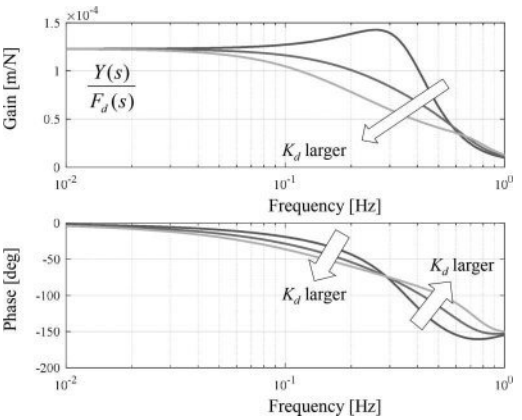


Figure 7. Bode plot of the lateral displacement with respect to the virtual force.

where, q and r are the weighting coefficients of the lateral deviation and the steering wheel angle input respectively.

5 SIMULATION

This chapter shows the effectiveness of the proposed trajectory planning method. The driving condition is set as obstacle avoidance maneuver as shown in Figure 8 at the velocity of 72 km/h (20 m/s). The obstacle is located at 100 m ahead of the vehicle. The repulsive potential field from the obstacle used in the simulation is as same as in the previous work of the authors (Raksincharoensak et al. 2016). Figure 9 shows the actual trajectory together with the desired trajectory from the simulation of feedback control system and Figure 10 shows the control input and the vehicle states during obstacle avoidance maneuver on dry road condition. The results exhibit that the proposed trajectory planning and control is valid.

Figure 11 shows the simulation result in dry road driving condition compared with the conventional

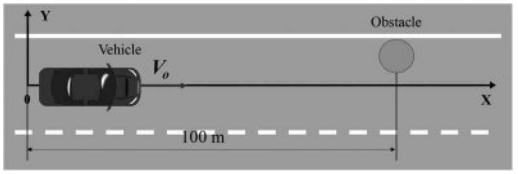


Figure 8. Target scenario for simulation.

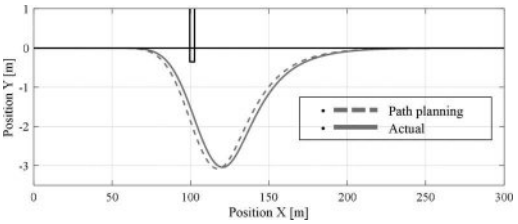


Figure 9. Result of obstacle avoidance maneuver on dry road by the proposed method.

potential field method which uses the gradient of the potential field as the force acting on the vehicle. In the case of conventional potential field, the same potential field function of the obstacle is used and the potential field function of the road boundary is also considered in order to generate the desired path. As the vehicle is treated as a point mass and the dynamics is not considered in the case of conventional potential field, the response of the lateral displacement with respect to the obstacle position is earlier than the case of the proposed control method. Both method shows good effectiveness in obstacle maneuver on dry road condition.

Next, the effectiveness of the proposed control method is verified on the wet road condition. Figure 12 and Figure 13 show the vehicle trajectory and the vehicle behavior during the obstacle maneuver respectively. Although the stability is deteriorated in the latter half of the maneuver, the proposed control method exhibits effective response in obstacle maneuver. Figure 14 shows the simulation result on the wet road driving condition compared with the conventional potential field method which uses the gradient of the potential field as the force acting on the vehicle. The result shows that the proposed trajectory planning by the proposed control method has superior performance compared with the conventional trajectory planning method. The proposed control method can make the vehicle avoid obstacle successfully on wet road condition whereas the trajectory planning based on the gradient of potential field makes the vehicle become unstable.

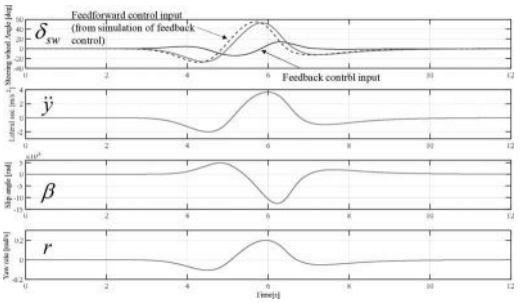


Figure 10. Control input and vehicle states in obstacle avoidance by the proposed method (dry road).

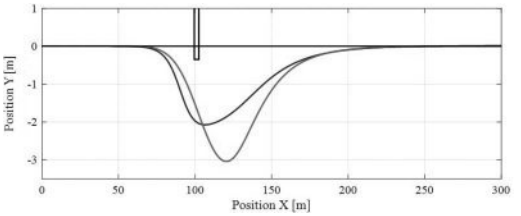


Figure 11. Comparison of vehicle trajectory between the proposed method (red line) and the conventional potential field method (blue line) on dry road.

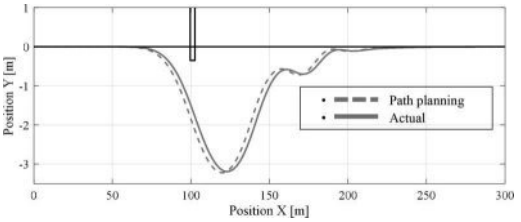


Figure 12. Result of obstacle avoidance maneuver on wet road by the proposed method.

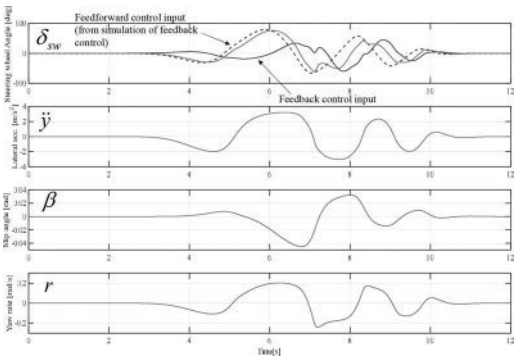


Figure 13. Control input and vehicle states in obstacle avoidance by the proposed method (wet road).

6 CONCLUSIONS

This paper described a new method for trajectory planning and control in obstacle maneuver using the concept of inverse dynamics compensation via simulation of feedback control systems. In the simulation of feedback control system, a virtual disturbance force generated from the obstacle is acted on the vehicle and the steering control is applied to correct the path. The steering control input in the simulation of feedback

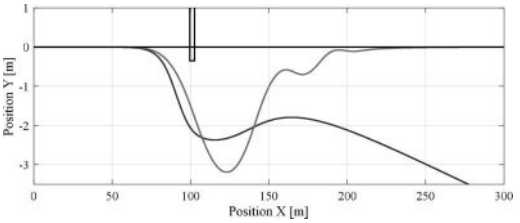


Figure 14. Comparison of vehicle trajectory between the proposed method (red line) and the conventional potential field method (blue line) on wet road.

control system is treated as the feedforward control input. Based on this idea, the characteristics of the desired path can be freely designed by using simple transfer function analysis. The nonlinear vehicle model can be used in the simulation of feedback control systems so that the vehicle model is close to the actual vehicle and thus the generated path becomes more realistic. The effectiveness of the proposed control system on the dry and the wet road conditions has been verified by the computer simulation.

This paper employs a simple PD controller in the simulation of feedback control system. However, the sophisticated controller design method, such as sliding mode control etc. can also be applied to enhance the performance of the control system.

REFERENCES

Balachandran, A., Brown, M., Erlien, S.M. and Gerdes, J.C. 2016. Predictive Haptic Feedback for Obstacle Avoidance Based on Model Predictive Control, IEEE Transactions on Automation Science and Engineering, Vol. 13, No. 1, January, pp. 26–31.

Bauer, E. et al. 2012. PRORETA3: An Integrated Approach to Collision Avoidance and Vehicle Automation, Automatisierungstechnik, Vol. 60, No. 12, pp. 755–765.

Falcone, P., Borelli, F., Asgari, J., Tseng, E. and Hrovat, D. 2007. A Model Predictive Control Approach for Combined Braking and Steering in Autonomous Vehicles, Proceedings of 15th Mediterranean Conference on Control and Automation, Athens, Greece.

Galceran, E., Eustice, R.M. and Olson, E. 2015. Toward Integrated Motion Planning and Control Using Potential Fields and Torque-Based Steering Actuation for Autonomous Driving, Proceedings of IEEE Intelligent Vehicle Symposium 2015, Seoul, Korea.

Khatib, O. 1986. Real-Time Obstacle Avoidance for Manipulators and Mobile Robots, International Journal of Robotics Research, Vol. 5, No. 1, pp. 90–98.

Kim, W., Kim, D., Yi, K. and Kim, H. J. 2012. Development of a path-tracking control system based on model predictive control using infrastructure sensors, Vehicle System Dynamics, Vol. 50, No. 6, pp. 1001–1023.

Nishira, H. et al. 2011. Application of Model Predictive Control to Cooperative Collision Avoidance Control System, Proceedings of the 1st International Symposium on Future Active Safety Technology toward Zero-Traffic Accidents (FAST-zero'11), Tokyo, Japan, No. 20117334, pp. 1–8.

Raksincharoensak, P., Hasegawa, T. and Nagai, M. 2016. Motion Planning and Control of Autonomous Driving Intelligence System Based on Risk Potential Optimization Framework, International Journal of Automotive Engineering, Vol. 7, pp. 53–60.

Tagawa, Y., Tu, J.Y. and Stoten, D.P. 2011. Inverse dynamics compensation via 'simulation of feedback control systems', Proc. of IMechE, Journal of Systems and Control Engineering, Vol. 225, No. 1, pp. 137–153.

Wolf, M. T. and Burdick, J. 2008. Artificial potential functions for highway driving with collision avoidance, Proc. IEEE Int. Conf. Robot. and Automation, pp. 3731–3736.

Advanced Vehicle Control – Edelmann, Plöchl & Pfeffer (Eds)
© 2017 Taylor & Francis Group, London, ISBN 978-1-138-02992-7

A hierarchical controller for path planning and path following based on model predictive control

Q. Wang & S. Müller
Technical University of Berlin, Berlin, Germany

ABSTRACT: In this research, a hierarchical controller based on model predictive control (MPC) for path planning and path following is developed. In the path planning level, obstacles' information is incorporated in the MPC framework. A new distance-direction based method is proposed for obstacle avoidance, which considers both the distance and moving direction of the obstacle. An alternative distance based method is analyzed for comparison. In the path following level, a bicycle model for MPC is utilized to improve the tracking of the reference from the higher level. Simulation results show that the distance-direction based method can better reflect the threat of the obstacle and generate more reasonable trajectories compared to the alternative distance based method.

1 INTRODUCTION

Recently, autonomous driving is one of the most popular topics among researchers and manufacturers, which can significantly enhance road safety, reduce traffic congestion, decrease fuel consumption and improve mobility (Katrakazas et al. 2015). Path planning and path following are the key steps to achieve autonomy. The main purpose of path planning and path following is to generate a feasible and collision-free trajectory from the start point to the end point for the vehicle to follow. At the same time constraints such as obstacles' information, road boundaries and vehicle dynamics should be taken into consideration.

Many researches on path planning use offline methods, where a trajectory is predefined through a given set of way points (Yoon et al. 2009). However, in case of unknown environment, it is difficult to get such a preplanned reference. In such situation, path planning for autonomous vehicles has to generate real-time trajectories. Model predictive control is an attractive method for real time path planning, due to its features of looking ahead and handling constraints on both control variables and state variables. Many researches have been carried out based on model predictive control method (Kim 2012, Yoon et al. 2008, Raksincharoensak 2015). In these works, distances to the nearest obstacles or parallax angles (an angle indicates the direction of the obstacle) are separately used to reflect the threat of obstacles (Park 2009). However, only using the distance or parallax angle cannot fully show the danger of obstacles, which sometimes results in generating not very reasonable avoidance trajectories. For example, it is meaningless to avoid one obstacle, which does not lie on the moving direction of the vehicle, even if it is the nearest one to the vehicle. Therefore, in this paper, distance-direction based MPC considering both distance and direction information of the obstacle is proposed, which can overcome the disadvantage mentioned above.

The remainder of the paper is structured as follows. At first, the control structure of the system is presented in section 2. The controller is divided into two levels: path planning and path following. The detailed formulation of the MPC controller is designed in section 3 and section 4. Section 5 discusses the simulation results, and conclusions are described in section 6.

2 CONTROL STRUCTURE

Figure 1 shows the block diagram of the controller. It consists of two layers: the path planning level and the path following level. In the path planning level, a point mass model is used in order to reduce computational load of the applied MPC algorithm. Obstacle's position, velocity and orientation are assumed to be already known in this level, and the outputs of this level are the desired vehicle position x_d and y_d in global coordinates and the velocity of the vehicle v. A bicycle model is adopted for MPC in the lower level, which is utilized to transfer the reference from the higher level to actual control signals for the vehicle.

The control inputs acquired from the path following level (steering angle δ_d and desired acceleration a_d) are sent to the TUBCarDynamics vehicle model. TUBCarDynamics is a simulation tool implemented in MATLAB/Simulink, which has been built for vehicle dynamic simulations.

3 PATH PLANNING LEVEL

In this section, two different path planning controllers based on model predictive control are designed. One

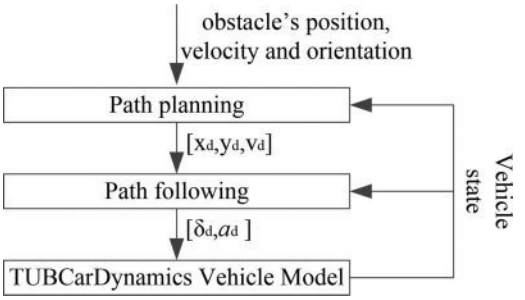


Figure 1. Overall structure of the controller.

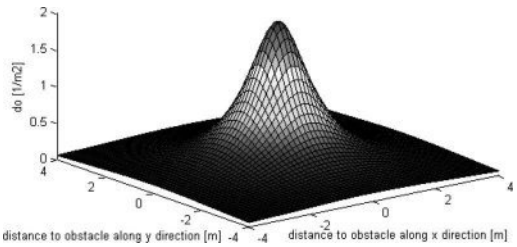


Figure 2. Potential function.

is a distance-based controller, which only takes the distance of the obstacle into account. The other is a distance-direction based controller, which considers both distance and direction information of the obstacle.

3.1 *Modeling*

In this level, a point mass model is used. One advantage of choosing a point mass model instead of e.g. a bicycle model is a reduced computational load. Another advantage is that no additional vehicle parameters are needed.

In order to avoid obstacles in real time, the following potential field function is utilized:

$$d_o = \frac{K}{(x-x_o)^2 + (y-y_o)^2 + \varepsilon} \tag{1}$$

where x and y, x_o and y_o are the coordinates of the vehicle and the obstacle, respectively; K is a constant potential gain, and ε is a slack variable for avoiding singularity. Here $K = 1$ and $\varepsilon = 1$.

From Figure 2 we can see that the value of the potential function d_o increases as the distance to the obstacle decreases and the value approaches zero as the distance to the obstacle becomes infinity. Therefore, the potential function can be used as an additional state for the system, which can keep the vehicle away from the obstacle.

In this paper, two example obstacles are modelled. The system equation of the point mass model consists of 10 state variables and 2 control inputs as shown in Figure 3 (Jain 2014): x, y and ϕ are the vehicle position and yaw angle in global coordinates; v is the

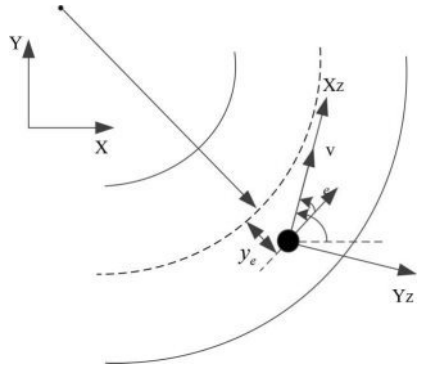


Figure 3. Point mass model.

velocity of the vehicle in vehicle coordinates; a_x and a_y are the longitudinal and lateral acceleration; a_{xd} and a_{yd} are the desired control inputs; τ_{ax} and τ_{ay} are time constants; y_e and ϕ_e are lateral error and heading error; ρ is the curvature of the road; x_{oi}, y_{oi}, v_{oi} and φ_{oi} ($i = 1,2$) represent the coordinates of the obstacle, the velocity and the heading direction of the obstacles. In this paper, the position, velocity and orientation of the obstacle and road information such as road curvature are assumed to be known.

$$\begin{aligned}
\dot{x} &= v\cos\varphi; \\
\dot{y} &= v\sin\varphi; \\
\dot{v} &= a_x; \\
\dot{\varphi} &= a_y / v; \\
\dot{a}_x &= -\tau_{ax} a_x + \tau_{ax} a_{xd}; \\
\dot{a}_y &= -\tau_{ay} a_y + \tau_{ay} a_{yd}; \\
\dot{y}_e &= v\sin\varphi_e; \\
\dot{\varphi}_e &= v\rho\cos\varphi_e - a_y / v; \\
\dot{d}_{o1} &= \frac{-2((v_{o1}\sin\varphi_{o1} - v\sin\varphi)(y_{o1} - y) + (v_{o1}\cos\varphi_{o1} - v\cos\varphi)(x_{o1} - x))}{((y_{o1} - y)^2 + (x_{o1} - x)^2 + 1)^2}; \\
\dot{d}_{o2} &= \frac{-2((v_{o2}\sin\varphi_{o2} - v\sin\varphi)(y_{o2} - y) + (v_{o2}\cos\varphi_{o2} - v\cos\varphi)(x_{o2} - x))}{((y_{o2} - y)^2 + (x_{o2} - x)^2 + 1)^2}.
\end{aligned} \tag{2}$$

3.2 *Collision cone*

For the evaluation of the threat of an obstacle, both the distance and the direction of the obstacle are important. In section 3.1, a potential function related to the obstacle's distance is described. In this section, we will discuss how to include information about the direction of the obstacle.

In (Belkhouche 2012) a collision cone is defined as shown in Figure 4. ξ is the visibility angle, which is the angle of upper and lower tangent lines between vehicle and obstacle and defines the collision cone width; v is the relative velocity between vehicle and obstacle; ψ is the angle between relative velocity and x axis; θ is the angle between the center line connecting obstacle and vehicle and the x axis.

It can be seen from Figure 4 that vehicle and obstacle will collide when

$$\psi \in \left[\theta - \frac{\xi}{2}, \theta + \frac{\xi}{2}\right] \tag{3}$$

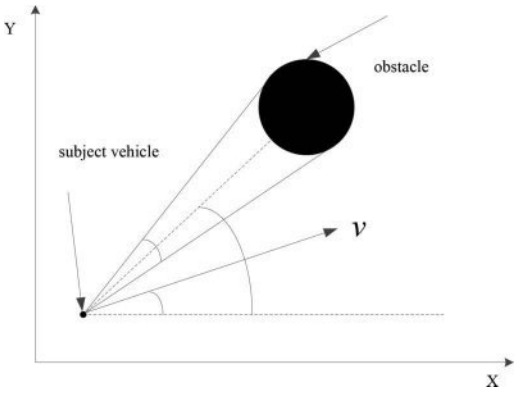


Figure 4. Collision cone.

Therefore, a collision coefficient B which indicates the threat of the obstacle is defined according to equation 4. $B=1$ means that the obstacle is dangerous and the vehicle has to take actions to avoid it; $B=0$ means that the obstacle will not influence the vehicle. B will be used as an additional weighting factor for the distance-direction method in section 3.3.2.

$$\begin{cases} if \quad \theta-\xi/2\le\psi\le\theta+\xi/2 \\ \qquad B=1 \\ \qquad else \\ \qquad B=0 \\ \qquad end \end{cases} \tag{4}$$

3.3 *Controller design*

Since a model predictive algorithm is solved in the discrete time domain, the system equations (2) are discretized as follows:

$$\begin{aligned} x_{k+1} &= f(x_k,u_k) \\ y_{k+1} &= h(y_k); \end{aligned} \tag{5}$$

where the state variables of the system are

$$x_k=[x \quad y \quad v \quad \varphi \quad a_x \quad a_y \quad y_e \quad \varphi_e \quad d_{o1} \quad d_{o2}]^T$$

and the control inputs of the system are $u_k=[a_{xd} \quad a_{yd}]^T$. The output vector is $y_k=[x \quad y \quad v]^T$.

3.3.1 *Distance based controller*

In order to solve the optimal problem, the following cost function is minimized to get optimal control inputs:

$$J=\sum_{k=1}^{H_p}(x_k-x_{ref,k})^2Q+(u_k-u_{ref,k})^2R \tag{6}$$

subject to

$$\begin{aligned} &x_{k+1}=f(x_k,u_k); \\ &\sqrt{{a_{xd}}^2+{a_{yd}}^2}\le\mu g. \end{aligned} \tag{7}$$

where k is the time step and H_p is the length of the prediction horizon; Q and R are diagonal weighting matrices as vectors described by equation 8; $x_{ref,k}$ and $u_{ref,k}$ are reference for the state variables and control inputs, respectively; μ is the tire-road friction coefficient; g is the gravity acceleration.

$$Q=\begin{bmatrix} Q_1 & 0 & 0 & \dots & 0 \\ 0 & Q_2 & 0 & \dots & 0 \\ 0 & 0 & Q_3 & \dots & 0 \\ 0 & 0 & 0 & \dots & Q_{10} \end{bmatrix}, R=\begin{bmatrix} R1 & 0 \\ 0 & R2 \end{bmatrix} \tag{8}$$

3.3.2 *Distance-direction based controller*

The system equations and constraints for the distance-direction based controller are the same as in section 3.3.1. But now the MPC cost function is altered. A coefficient B as mentioned in section 3.2 is added to the weighting factors Q_9 and Q_{10} as follows:

$$\begin{aligned} J=&\sum_{k=1}^{H_p}Q_1(x-x_{ref})^2+\dots+Q_9B_1(d_{o1}-d_{o1,ref})^2 \\ &+Q_{10}B_2(d_{o2}-d_{o2,ref})^2+R_1(a_{xd}-a_{xd,ref})^2+R_2(a_{yd}-a_{yd,ref})^2 \end{aligned} \tag{9}$$

From equation 9 we can see that if B_1 or B_2 equal zero, the corresponding terms in the cost function become zero. As a result, the controller takes no action towards the corresponding obstacle.

4 PATH FOLLOWING LEVEL

In the path planning level, a collision free trajectory is generated. In order to follow the path from the higher level, a lower level MPC is designed to transfer the reference trajectory to actual control inputs for the vehicle.

A bicycle model as shown in Figure 5 is used for MPC. The system equation is described by equation 9, where x and y are the coordinates of the vehicle in the global frame; ϕ is the heading angle and v is the velocity of the vehicle; l_f and l_r represent the distance from the center of gravity of the vehicle to the front and rear axles, respectively; β is the side slip angle of the vehicle; a is the acceleration of the vehicle and δ is the steering angle. Detailed information about this model can be found e.g. in (Kong 2015, Rajamani 2006).

$$\begin{aligned} \dot{x} &= v\cos(\phi+\beta); \\ \dot{y} &= v\sin(\phi+\beta); \\ \dot{\phi} &= \frac{v}{l_r}; \\ \dot{v} &= a; \\ \beta &= \tan^{-1}\left(\frac{l_r}{l_f+l_r}\tan\delta\right). \end{aligned} \tag{10}$$

The discretized state variables and control inputs of the system for MPC are $x_k=[x \quad y \quad \phi \quad v]^T$ and $u_k=[\delta \quad a]^T$, respectively.

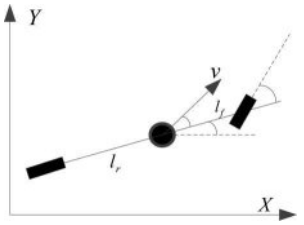


Figure 5. Bicycle model.

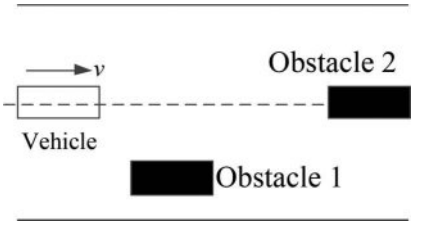


Figure 6. Static scenario.

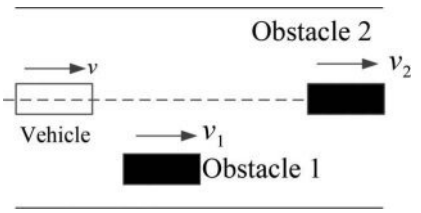


Figure 7. Dynamic scenario.

The cost function which should be minimized is

$$J = \sum_{k=1}^{N} (\eta_k - \eta_{ref,k})^2 W + u_k{}^2 S \tag{11}$$

subject to

$$\begin{aligned} |\delta| &\le \delta_{\max}; \\ |a| &\le \mu g. \end{aligned} \tag{12}$$

where W and S are weighting matrices; k is the time step and N is the prediction horizon; η_k is given as

$$\eta_k = \begin{bmatrix} 1 & 0 & 0 & 0 \\ 0 & 1 & 0 & 0 \\ 0 & 0 & 0 & 1 \end{bmatrix} x_k \tag{13}$$

5 SIMULATION

In order to validate the effectiveness of the new proposed distance-direction based MPC controller, numerical simulations have been carried out using TUBCarDynamics.

The MPC controller has been implemented as an S-function in Matlab/Simulink through the code generation functionality provided by ACADO Toolkit (Ariens et al. 2010).

In order to validate the proposed controller, simulations have been carried out first for a straight road. The reference for the vehicle is the road center line. Obstacles' information such as position, velocity and orientation are assumed to be already known. One static and one dynamic scenario are performed, as shown in Figure 6 and 7. In the simulation, the obstacles are assumed to be circular with a radius 1m and the vehicle is assumed as a point. The vehicle is assumed to move with a constant velocity 25m/s. In the simulation results, dashed lines represent the results generated by the distance-direction based method. In the following section this controller is named "New controller". Solid lines denote the results generated by the distance based controller and the controller is named "Old controller".

5.1 *Static scenario*

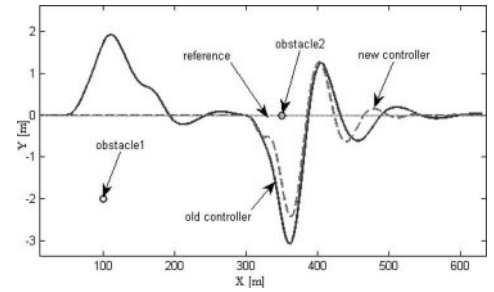
In this section, the two obstacles are supposed to stand still and are located at (100, −2) and (350, 0), respectively. From Figure 8(a)–(c), it can be seen that both controllers can generate collision free trajectories and keep a safe distance from the obstacles. However, the new controller only avoids obstacle 2 and ignores the undangerous obstacle 1. This makes the new controller more effective and more suitable for trajectory planning. Moreover, the new controller goes back to the reference more quickly than the old controller after avoiding the obstacle. Figure 8(d) and (e) denote the yaw rate and steering angle of the vehicle.

5.2 *Dynamic scenario*

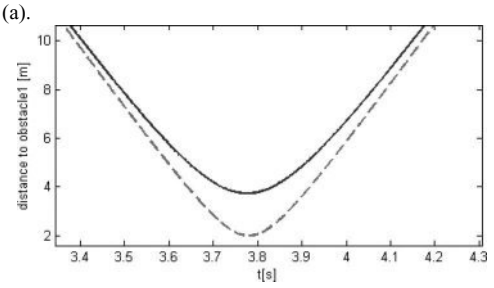
In this subsection, the two obstacles are located at (100, −2) and (350, 0), respectively, with a velocity of 10 m/s in the same direction as the vehicle. The advantage of the new controller is in this scenario even more notable. As shown in Figure 9(b) and (c), the minimum distance to obstacle 1 is longer than 2 m and the distance between the vehicle and obstacle 2 is longer than 1.5 m. These results indicate that the controllers also work successfully in dynamic scenario. The new controller generates more stable trajectory in comparison with the old controller by ignoring obstacle 1, which is not dangerous for the vehicle. From Figure 9(d) and (e), it can be seen that the yaw rate and steering angle generated by the old controller are more fluctuant than the new controller.

6 CONCLUSION AND OUTLOOK

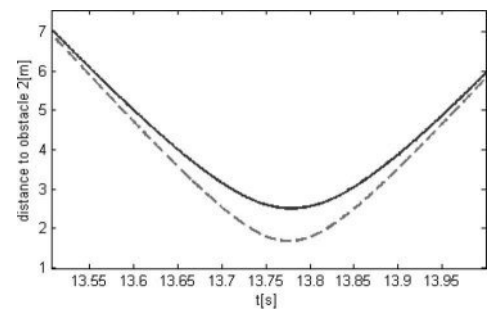
This paper presents a hierarchical controller for path planning and path following. Two kinds of path planning controller based on a point mass model are presented. One is a distance based MPC controller and the other is a distance-direction based MPC controller. A bicycle model is used for the path following level. Simulation results show that the distance-direction



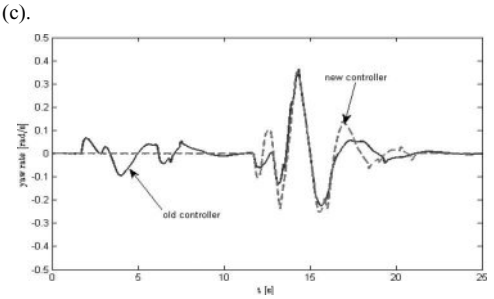
(a).



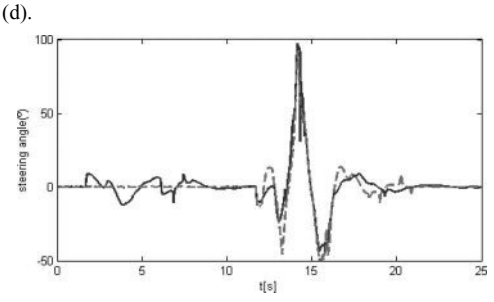
(b).



(c).

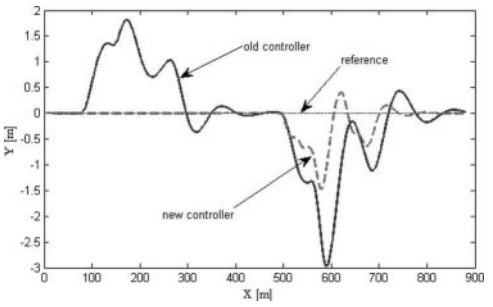


(d).

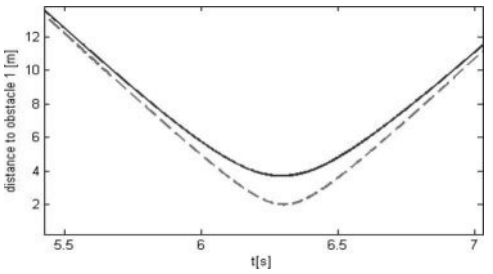


(e).

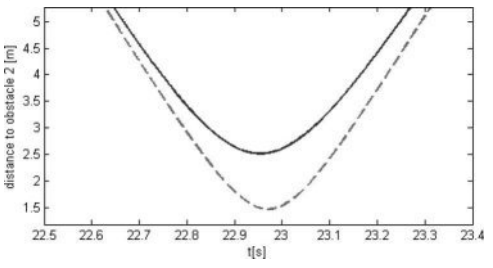
Figure 8. (a) trajectory, (b) distance between obstacle 1 and vehicle, (c) distance between obstacle 2 and vehicle, (d) yaw rate, (e) steering angle.



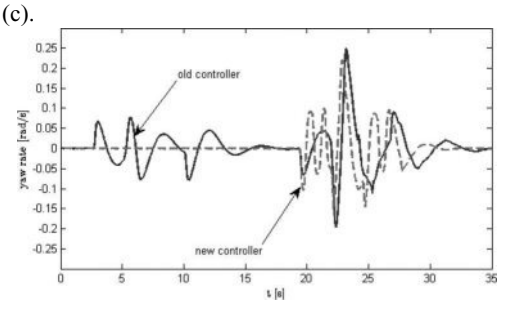
(a).



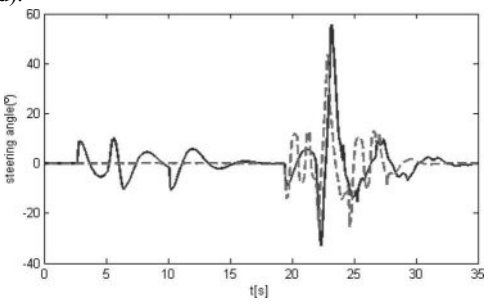
(b).



(c).



(d).



(e).

Figure 9. (a) trajectory, (b) distance between obstacle 1 and vehicle, (c) distance between obstacle 2 and vehicle, (d) yaw rate, (e) steering angle.

based method is more effective for generating collision free trajectories, showing great improvement over the distance based method. In the future, the distance-direction based controller will be extended to a more complex environment such as parking lots or intersections. Moreover, practical experiments with a scaled vehicle will be carried out.

REFERENCES

Ariens David et al. 2014. ACADO Toolkit User's Manual. http://www.acadotoolkit.org.

Belkhouche F. & Bendjilali B. 2012. Reactive path planning for 3-D autonomous vehicles. IEEE transactions on control systems technology (vol. 20, No. 1): 249–256.

Jain Varun. 2014. Autonomous driving system for road vehicles with model predictive path planner and global motion control. Master thesis. Kaiserslautern, Germany.

Katrakazas Christos et al. 2015. Real-time motion planning methods for autonomous on road driving: state of the art and future research directions. *Transportation research part C 60*: 416–442.

Kim Wongun et al. 2012. Development of a path tracking control system based on model predictive control using infrastructure sensors. *Vehicle system dynamics (vol. 50, No. 6)*: 1001–1023.

Kong Jason et al. 2015. Kinematic and dynamic vehicle models for autonomous driving control design. *IEEE Intelligent vehicles symposium*. Seoul, Korea.

Park J.M. 2009. Obstacle avoidance of autonomous vehicles based on model predictive control. *Proceedings of the institution of mechanical engineers, Part D: Journal of automobile engineering*: 1499–1516.

Rajamani Rajesh. 2006. *Vehicle dynamics and control*: 20–27.

Raksincharoensak P. et al. 2015. Vehicle motion planning and control for autonomous driving intelligence system based on risk potential optimization framework. *Proceeding of the 24th IAVSD Symposium*, Graz, Austria.

Yoon Yongsoon & Choe Tokson et al. 2008. Obstacle avoidance for wheeled robots in unknown environments using model predictive control. Proceeding of the 17th world congress, Seoul, Korea.

Yoon Yongsoon & Shin Jongho et al. 2009. Model predictive active steering and obstacle avoidance for autonomous ground vehicles. Control Engineering Practice 17.7: 741–750.

Roll-over prevention and risk assessment

Advanced Vehicle Control – Edelmann, Plöchl & Pfeffer (Eds)
© 2017 Taylor & Francis Group, London, ISBN 978-1-138-02992-7

A novel control mediation approach to active rollover prevention

Dong Zhang, Timothy Gordon & Yangyan Gao
School of Engineering, University of Lincoln, Lincoln, UK

Changfu Zong
State Key Laboratory of Automotive Simulation and Control, University of Jilin, Changchun, China

Mathias Lidberg
Chalmers University of Technology, Gothenburg, Sweden

ABSTRACT: This paper considers a novel approach to active rollover prevention, incorporating online estimation of the driver's intended path. The problem is formulated as one of minimizing lateral deviation from the intended path subject to friction and rollover limits. A recently published control allocation and moderation method is developed to be applicable to the rollover problem in such a way that speed is optimally reduced. Furthermore, a new Time-To-Rollover (TTR) metric, based on driving intention prediction, is incorporated into the system concept. Finally, mediation provides a general approach to designing a cooperative system, coordinating between the human driver and the onboard autonomous safety system to reduce the sensitivity of vehicle response to any sudden or emergency driver actions.

1 INTRODUCTION

Research focus on active chassis control for understeer mitigation has made remarkable progress in recent years. Klomp (2010) formulated the problem of combined speed and directional control to minimize off-tracking when the curve entry speed is too high, or equivalently the tire-road friction is too low. The presented parabolic path reference (PPR) strategy showed a fundamental result to solve this problem. Recently, a moderated particle reference (MPR) control method has been developed (Zhang, Gordon, Lidberg, & Zhang 2014). Demands from driver interpreter are fed into the moderator. However, so-called 'untripped' rollover accidents for high CoG vehicle, caused by high speeds and road curvature, have not been considered in PPR or MPR control so far.

Considerable research has focused on active anti-roll systems for high CoG vehicles. For example, Chen and Peng (2001) used a Time-to-Rollover (TTR) metric to design a warning and control system for SUVs; Schofield et al. (2006) presented a nonlinear control strategy which guarantees asymptotic tracking of a yaw rate reference, while bounding the roll angle for rollover prevention. Wielenga and Chace (2000) proposed a differential braking control method and Shim and Toomey (2004) proposed an active front steering (AFS) system for rollover prevention. A common theme for these methods of rollover prevention is a discrete, switched, intervention from the system, largely overriding the driver. Therefore there is a limitation in terms of keeping the driver in-the-loop.

In the present paper, driver inputs are fully taken into consideration and driver intent prediction is applied via a moderator (to limit driver demands) and mediator (to combine with the autonomous function). Derived from PPR, this control method considers rollover prevention as a constraint rather than the final control objective; rather, an intended path is inferred and the control objective is to minimize the lateral deviation from that path. As with PPR, speed is progressively and optimally reduced as part of the control strategy.

2 CONTROL STRUCTURE AND VEHICLE SYSTEM

2.1 *Control structure*

A control mediator is introduced to take account of both road (and potentially traffic) constraints, plus driver intentions. As shown in Figure 1, the mediator operates as a mapping in the vehicle G-G diagram. Inputs to the mediator are target accelerations obtained from the Rollover Prevention System a^{RPS} as well as from the driver interpreter a^{DI}. The output reference a^{ref} is for braking control allocation, providing a continuously updating safety margin. The whole control method is designed for maintaining drivability in the critical vehicle over-speed curving situation and in the meantime taking safety (via understeer mitigation and rollover prevention) into consideration.

The acceleration reference from the rollover prevention system a^{RPS} is taken as a constraint for control

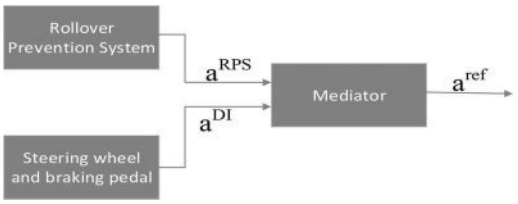


Figure 1. Mediator.

allocation in this paper, which can be calculated from the known vehicle parameters, road geometry and predicted driver steer input. The acceleration reference from driver a^{DI} can be calculated from the steering wheel angle and current vehicle velocity. The main theme of this paper is to develop a systematic control mediation method from the a^{RPS} and a^{DI} to control reference.

2.2 *Vehicle model*

In this part, we define a 4-DoF vehicle model as a rollover reference when considering the high CoG vehicle 'untripped' rollover situation. In this model, the main parameters should be matched with the real vehicle. In this we added a roll degree of freedom into the normal 3-DoF vehicle model shown in Figure 2 which is commonly used in vehicle yaw moment control. In this model, we need to make some simplifying assumptions in advance. First, we assume the vehicle is driving on a flat road; second, aerodynamic resistance is ignored, and third the pitching movement and pneumatic aligning moments are not considered.

$$m(\dot{U} - V\omega_r) = (F_{Lfl} + F_{Lfr})\cos\delta + F_{Lrl} + F_{Lrr} - (F_{Cfr} + F_{Cfl})\sin\delta \quad (1)$$

$$m(\dot{V} + U\omega_r) - m_s e\ddot{\phi} = (F_{Cfr} + F_{Cfl})cos\delta + F_{Crl} + F_{Crr} + (F_{Lfr} + F_{Lfl})\sin\delta \quad (2)$$

$$I_z\dot{\omega}_r = \frac{t}{2}(F_{Lrr} - F_{Lrl} + (F_{Lfr} - F_{Lfl})cos\delta + (F_{Cfl} - F_{Cfr})sin\delta) + a((F_{Cfl} + F_{Cfr})cos\delta + (F_{Lfr} + F_{Lfl})sin\delta) - b(F_{Crl} + F_{Crr}) \quad (3)$$

$$I_{xeq}\ddot{\phi} - m_s ges in\phi = m_s a_y e cos\phi - C_\phi\dot{\phi} - K_\phi\phi \quad (4)$$

In (4), the rotational inertia of sprung mass around X axis I_{xeq} is described as:

$$I_{xeq} = I_x + m_s h^2 \quad (5)$$

In Figure 2, U denotes V_x, and V denotes V_y. The lateral acceleration can be described as:

$$a_y = \dot{V}_y + V_x\omega_r \quad (6)$$

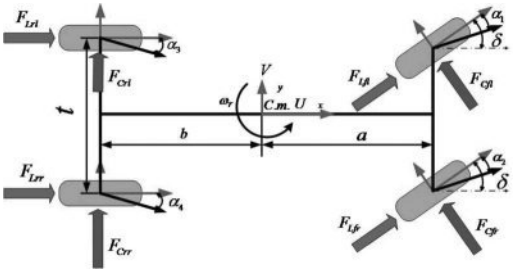


Figure 2. 3-DoF vehicle model.

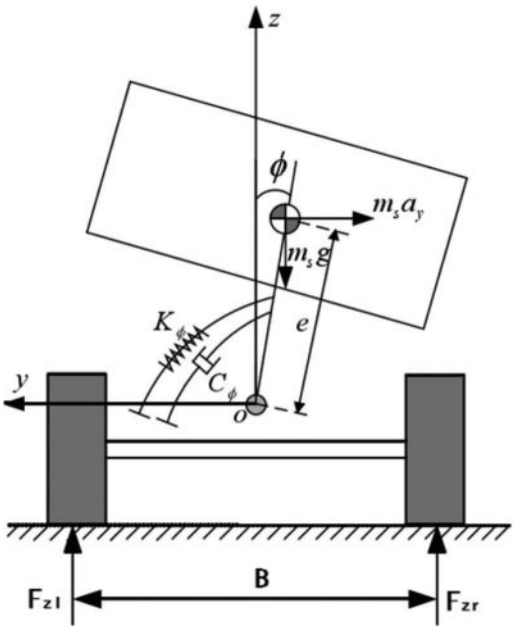


Figure 3. Vehicle rolling diagram in the vertical plane.

Based on the assumption of small tire slip angle and constant lateral speed,

$$\beta \approx \frac{V_y}{V_x} \quad (7)$$

$$\alpha_f \approx \delta_\omega - \beta - \frac{a}{V_x}\omega_r \quad (8)$$

$$\alpha_r \approx -\beta + \frac{b}{V_x}\omega_r \quad (9)$$

We assume a state-space equation expressed as:

$$\dot{x} = Ax + B\delta_\omega \quad (10)$$

In here, the state variable is:

$$x = \begin{bmatrix} \beta & r & \dot{\phi} & \phi \end{bmatrix}^T \quad (11)$$

Assuming that:

$$\sigma \approx C_f + C_r \quad (12)$$

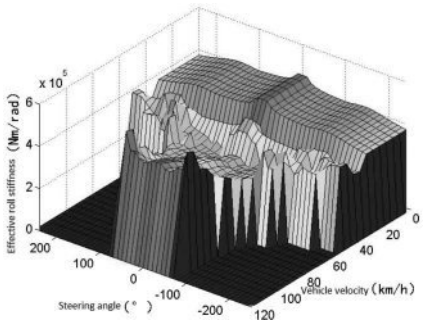


Figure 4. Parameter identification of roll stiffness (unloaded condition).

$$\rho \approx aC_r - bC_f \tag{13}$$

$$\kappa \approx a^2C_f + b^2C_r \tag{14}$$

then we can obtain:

$$A = \begin{bmatrix} -\frac{\sigma I_{xeq}}{m_s I_x V_x} & \frac{\rho I_{xeq}}{m_s I_x V_x^2} - 1 & -\frac{eC_\phi}{I_x V_x} & \frac{e(m_s ge - K\phi)}{I_x V_x} \\ \frac{\rho}{I_z} & -\frac{\kappa}{I_z V_x} & 0 & 0 \\ -\frac{\sigma e}{I_x} & \frac{\rho e}{I_x V_x} & -\frac{C_\phi}{I_x} & \frac{m_s ge - K\phi}{I_x} \\ 0 & 0 & 1 & 0 \end{bmatrix} \tag{15}$$

$$B = \begin{bmatrix} \frac{C_f I_{xeq}}{m_s I_x V_x} & \frac{C_f a}{I_z} & \frac{C_f e}{I_x} & 0 \end{bmatrix}^T \tag{16}$$

In addition, the classic Pacejka tire model is used for representing nonlinear tire behavior in this paper. Both the longitudinal and lateral forces of each tire under the combined slip are taken into consideration.

2.3 *Parameter identification of effective roll stiffness*

After extensive simulation, it was found that the parameter identification based on a fixed constant of effective roll stiffness K_ϕ is imprecise. This is most likely due to the nonlinear suspension properties. Thus a look-up table was used for roll stiffness as a function of steering angle and vehicle speed.

We considered the vehicle speed between 30 km/h–120 km/h, the steering wheel angle between ±240°, working in increments of 5 km/h and 10° respectively. With the TruckSim simulation results and vehicle state equation shown above, we can identify the vehicle parameter of effective roll stiffness in these simulation conditions. The results are shown in the Figure 4, 5.

2.4 *Validation of the vehicle model*

In order to verify the reliability of the 4-DoF vehicle model in Simulink, a step-steer response was evaluated with a comparison using TruckSim standard model. We consider the vehicle velocity as 55 km/h and the steering angle as 90° where the step-steer duration time is set to be about 1 second.

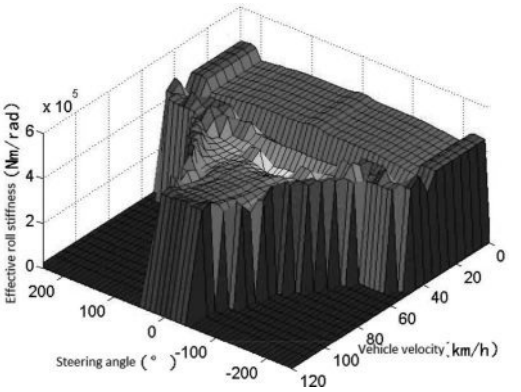


Figure 5. Parameter identification of roll stiffness (loaded condition).

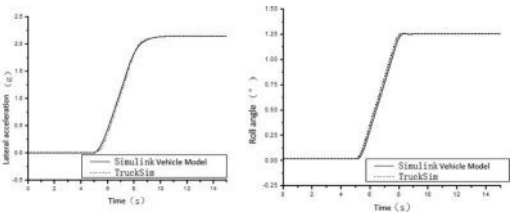


Figure 6. Comparison with the mathematical model (unloaded condition).

The comparison results in unloaded condition shown in Figure 6 demonstrated that the built 4-DoF vehicle model can correctly reflect the lateral acceleration and roll angle of the vehicle during experiments. And the comparison results in loaded condition are similar.

3 CONTROL DESIGN

The moderated particle reference (MPR) strategy is a simplification and generalization of PPR which is designed to minimize the maximum distance of off-tracking (Zhang, Gordon, Lidberg, & Zhang 2014). Different from a step-steer input (PPR), MPR is intended to operate across a wide range of driving conditions. In this section, we briefly introduce the PPR and MPR control theory, and based on these optimal braking control allocation algorithms, we take rollover prevention as a constraint for the control mediation.

3.1 *Optimal understeer mitigation control*

Based on Klomp, Lidberg, & Gordon (2014), it was assumed that the road geometry consists of a straight-line segment joined to a circular arc of constant curvature, and that a PPR intervention takes place at the curve entry point. The optimal control problem for minimizing the maximum off-tracking from the circular reference trajectory was thereby established. In the following, this type of control will be implemented

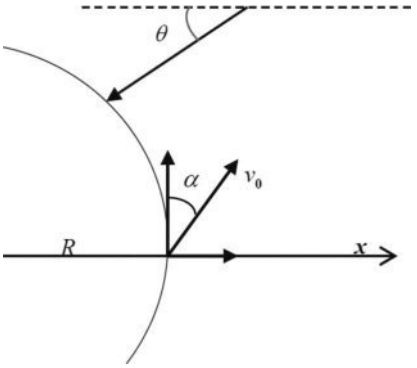


Figure 7. PPR calculation diagram.

via a new and efficient near-optimal control allocation approach for limit handling control, the Modified Hamiltonian Algorithm (MHA), previously presented by Gao, Lidberg, & Gordon (2015).

In this paper we assume $\alpha = 0$; based on the PPR theory, we can obtain:

$$cos\theta = \frac{\mu g R}{v_0^2} \tag{17}$$

In the PPR control method, we consider:

$$a_x^{ref} = a_x \tag{18}$$

$$a_y^{DI} = v^2 K_{ref} \tag{19}$$

where the reference path curvature K_{ref} denotes the drivers desired path curvature, which can be expressed as a function of road wheel angle δ of front wheels and the wheelbase L:

$$K_{ref} = \frac{\delta}{L} \tag{20}$$

So based on this analysis, we can see its very convenient to determine the magnitude and the direction of the desired synthetic acceleration vector when the reference lateral acceleration is beyond friction limits. Input variables are the current vehicle longitudinal acceleration demand and steering wheel angle, together with vehicle speed and a current estimate of tire/road friction. The basic idea is to compare the driver interpreter acceleration with the tire/road friction limits; when demands are within limits, desired vehicle states are directly applied; when the driver interpreter acceleration is beyond road/friction limits, demands are reduced in a systematic way. Extending this idea of MPR, considering rollover prevention, the reference acceleration is mapped to a new G-G diagram in a way that also respects the rollover prevention constraint.

3.2 *Lateral acceleration constraint for rollover prevention system*

Lateral-load Transfer Rate (LTR) is a parameter to describe the change of vertical tire load which is widely

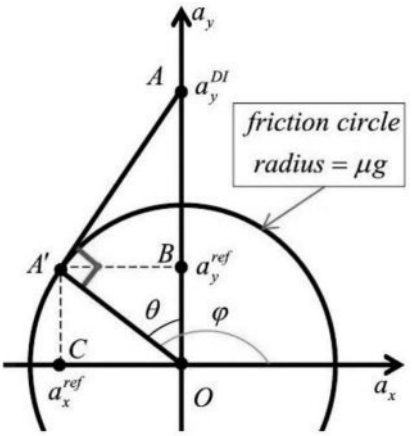


Figure 8. Friction circle interpretation of PPR.

used in the identification of vehicle rollover. LTR is defined as:

$$LTR = \frac{F_{zl} - F_{zr}}{F_{zl} - F_{zr}} \in [-1, 1] \tag{21}$$

where F_{zl} denotes the total left vertical tire forces and F_{zr} denotes the total right vertical tire forces. LTR ranges from -1 to 1, and when either right or left side of tires lifts off the ground, the LTR value can be -1 or 1. As the LTR of vehicle can not be determined directly from sensors, an equivalent transformation is needed:

$$\Sigma M = F_{zl}\frac{B}{2} + m_s a_y e cos\phi + m_s g e sin\phi - F_{zr}\frac{B}{2} = 0 \tag{22}$$

In this part, we ignore the unsprung mass, so $m_s = m$, and we assume the roll angle is very small, so $e\cos\phi = e(1-\phi)$ and $e\sin\phi = \phi$; then LTR can be described as:

$$LTR = \frac{2(\phi - 1)a_y e - 2g\phi e}{gB} \tag{23}$$

According to this simplified model, LTR is a simple function of lateral acceleration and roll angle, and we can find the lateral acceleration corresponding to $LTR = \pm 1$, i.e. at the onset of rollover. In this case lateral acceleration can be used as a trigger for roll control intervention, but in reality the above equation is too simple to give accurate rollover prediction.

Instead we perform TruckSim simulation experiments to determine the limiting steady-state acceleration a_y^* when the inner wheels lift, and code this as and equivalent LTR variable based on equation (23) (for simplicity in this paper $\phi = 0$ is assumed):

$$R_{threshold} = \frac{2ea_y^*}{Bg} \tag{24}$$

Based on the TruckSim simulation experiments for parameter identification of effective roll stiffness,

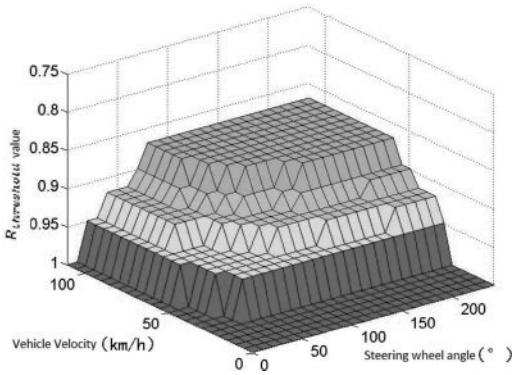


Figure 9. Unloaded condition of $R_{threshold}$.

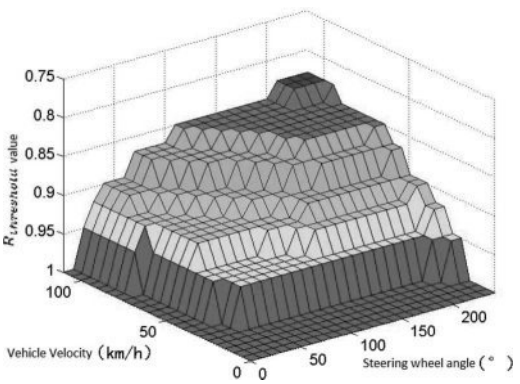


Figure 10. Loaded condition of $R_{threshold}$.

after extensive simulation experiments based on equation (21), we obtain the 3-D look-up table shown in Figure 9, 10 for $R_{threshold}$.

Hence, including this threshold in the control algorithm, we obtain a real-time lateral acceleration limitation for the control mediation:

$$a_y^{RPS} = \frac{R_{threshold} Bg}{2e} \tag{25}$$

3.3 *Mapping method for control mediation*

Based on the above lateral acceleration constraint, we can design the G-G diagram and mapping from driver interpreter to control reference as a control mediation approach.

In Figure 11, the red line shows the lateral acceleration constraint obtained from the rollover prevention system, the arrows showing the proposed mapping method from driver interpreter to control reference.

Based on the PPR control algorithm, the mapping from point A to A' is an optimal control allocation method which minimize the maximum off-tracking from the reference path (Zhang, Gordon, Lidberg, & Zhang 2014). It is known that the mapping line from

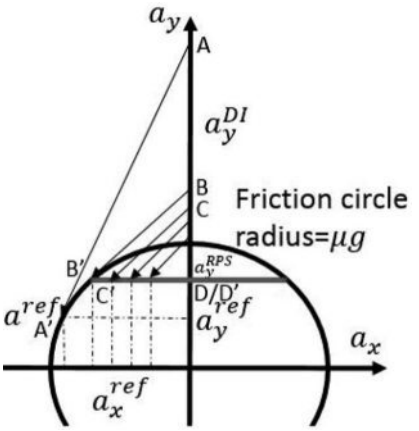


Figure 11. Mapping from driver interpreter reference acceleration to control reference acceleration.

A to A' is tangent to the friction circle and the θ can be calculated by equation (17). The mapping from point B to point B' in which the lateral acceleration is a_y^{RPS} is the threshold we still use the PPR tangent mapping method. At this point we can calculate that:

$$cos\theta = \frac{a_y^{RPS}}{\mu g} \tag{26}$$

If the driver demand of lateral acceleration is less than the point B, we propose to retain angle θ obtained from equation (26) for the mapping to the limitary friction circle. That is to say, the mapping lines are parallel to the mapping line from point B to B' if the lateral accelerations from driver interpreter are less than point B. Taking point C as an example, at this point the lateral acceleration demand is a_y^{DIc}. Then:

$$tan\theta = \frac{a_y^{DIc} - a_y^{RPS}}{a_x^{ref}} \tag{27}$$

Using θ from equation (26), we easily obtain the a_x^{ref} for longitudinal control reference.

On a macro level, this proposed control mediation method maintains the driver's drivability in this critical situation as well as take full use of road friction. In particular, the driver will experience increased braking in proportion to subsequent increases in steering wheel angle. Thus the proposed method emphasizes keeping the 'driver-in-the-loop' during the brake intervention, unlike more discrete methods which override the driver though full brake application for example.

3.4 *Time-To-Rollover validation*

To test and calibrate the lateral acceleration limitation a_y^{RPS}, a new Time-To-Rollover (TTR) metric based on driver intent prediction is presented as the real-time

rollover reference. TTR is defined as the time from the current instant to tire lift-off one side. Through the driver intent prediction, partially based on the known road geometry and vehicle speed, an improved TTR can be calculated.

In detail, we set the TTR threshold value as the action time of presented control method based on the known road geometry. In PPR control theory, the time period of T can be described as:

$$T = \frac{v_0 sin\theta}{\mu g} \tag{28}$$

This time value, T, represent the time to maximum off-tracking from initial PPR intervention on a road which is a uniform circular arc. Using the threshold given above, the following calibration check is designed to validate no rollover will occur up to that time, i.e. $TTR > T$.

Here, we take the point D shown in Figure 11 as the calibration point where the lateral acceleration is at the constraint and that there is no longitudinal braking imposed.

Based on the transfer function for roll dynamics (29), at the point D where the a_y was imposed as a_y^{RPS}, we can calculate the roll angle by integration after a time period of T to check whether the roll angle will exceed the threshold. With this method, the effectiveness of a_y^{RPS} as the rollover constraint can be verified.

$$\frac{\phi(s)}{a_y(s)} = \frac{me}{s^2 I_{xeq} + sC_\phi + K_\phi - mge} \tag{29}$$

After extensive simulations, is was found that the value of a_y^{RPS} obtained based on the dynamic LTR threshold above is a feasible constraint for rollover prevention, that is the TTR value always remains larger than the theoretical control action time. In other words, the vehicle will avoid rollover accidents during the time period of T. Hence, we can tentatively conclude that this proposed control mediator with the lateral acceleration constraint obtained above will effectively satisfy the requirement of rollover prevention during the known over-speed cornering situation. Further simulations, including with driver-in-the-loop will be required to fully test the method.

4 CONCLUSIONS

A novel control mediation approach to active rollover prevention is presented in this paper. This control method takes rollover prevention as a constraint and makes full use of road friction to minimize the maximum off-track from the reference path as well as maintain drivers drivability. After extensive simulations using TruckSim and a reduced-order model and based on the TTR validation, this new control mediation is found work effectively in different cornering conditions. In the future, this control method will be implemented in the University of Lincoln driving simulator in order to evaluate the effectiveness with respect to driver-vehicle interaction. The long-term goal will be to make the controller more adaptive to different types of driver, depending on their skills and depending on whether they are undertaking an emergency manoeuvre.

Table 1. Vehicle Parameters.

body mass	m_b	17500 kg
body roll moment of inertia	I_{roll}	9135.5 kgm^2
front wheel unsprung mass	m_f	667 kg
rear wheel unsprung mass	m_r	970 kg
vehicle height	h_v	3955 mm
steer ratio	r	25
height of CoG	h_c	810 mm
sprung mass	m_s	7550 kg

REFERENCES

Chen, B.-C. & H. Peng (2001). Differential-braking-based rollover prevention for sport utility vehicles with human-in-the-loop evaluations. *Vehicle System Dynamics 36*(4-5), 359–389.

Gao, Y., M. Lidberg, & T. Gordon (2015). Modified hamiltonian algorithm for optimal lane change with application to collision avoidance. *MM Science Journal* (MAR 2015), 576–584.

Klomp, M. (2010). *Longitudinal force distribution and road vehicle handling*. Chalmers University of Technology.

Klomp, M., M. Lidberg, & T. J. Gordon (2014). On optimal recovery from terminal understeer. *Proceedings of the Institution of Mechanical Engineers, Part D: Journal of Automobile Engineering*, 0954407013511796.

Schofield, B., T. Hagglund, & A. Rantzer (2006). Vehicle dynamics control and controller allocation for rollover prevention. In *2006 IEEE Conference on Computer Aided Control System Design, 2006 IEEE International Conference on Control Applications, 2006 IEEE International Symposium on Intelligent Control*, pp. 149–154. IEEE.

Shim, T. & D. Toomey (2004). Investigation of active steering/wheel torque control at the rollover limit maneuver. Technical report, SAE Technical Paper.

Wielenga, T. J. & M. A. Chace (2000). A study in rollover prevention using anti-rollover braking. Technical report, SAE Technical Paper.

Zhang, R., T. Gordon, M. Lidberg, & C. Zhang (2014). A moderated particle reference strategy for integrated chassis and driveline control.

Advanced Vehicle Control – Edelmann, Plöchl & Pfeffer (Eds)
© 2017 Taylor & Francis Group, London, ISBN 978-1-138-02992-7

The noise of acceleration signal as an indicator of the loss of control risk

C. Naude, T. Serre, M. Dubois-Lounis & J.-Y. Fournier
IFSTTAR Laboratory of Accident Mechanism Analysis, France

V. Ledoux
Cerema Technical Division for Territorial Development and Urban Planning, France

ABSTRACT: This study is based on various situations acquired by Event Data Recorders in a zone of interest, with a bend where several losses of control were reported in the past. The hypothesis is to consider that the noise of the lateral acceleration signal increases with the loss of control risk. This noise was quantified in the bend by two methods for 116 recordings, from normal driving passages to critical situations called incidents. In the most difficult part of the bend, the noise of incidents is superior to normal passages for both calculation methods, showing that the vehicles come closer to their grip limits. Moreover, the noise of lateral acceleration is then higher near the triggering than in the whole bend. Thus, this criterion is useful to evaluate the loss of control risk and the severity of incidents. This approach is complementary to other researches taking into account the vehicle dynamics.

1 INTRODUCTION

During the driving task, the most interesting and relevant situations are not only crashes but also hazardous situations considered as incidents, sometimes called near-crashes. These risky situations are critical because the vehicle reaches high dynamics demands in longitudinal, lateral or combined directions. Incident detection relies on the analysis of vehicle dynamic parameters and EDRs (Event Data Recorders) can be used to record these situations. Under slightly different circumstances these incidents could have resulted in injury or material damage crashes.

The objective of this study is to compare normal driving with incident situations on specific sites where accidents occurred. It is focused on lateral incidents linked to potential loss of control accidents.

Different approaches can be explored to estimate if a lateral incident could have turned into a loss of control. Lechner et al. (2008) focused on the lateral acceleration in a bend, linked to speed and radius of curvature. They developed a method based on real passages in bends, with simulations of the driving behavior at higher speeds until the loss of control. Bagdadi & Varheli (2013) estimated the severity of critical braking situations by using the consecutive peaks of jerk (derivative of acceleration). The method could be transferred to lateral jerk in steering, to characterize the brutality of solicitations. Doumiati et al. (2012) developed an observer of sideslip angle based on Kalman Filter, which could enable to estimate the closeness of a loss of control when the vehicle drifts without a high level of lateral acceleration (wet/icy road, worn tires…).

The friction forces play a significant role in driving safety. This paper deals with a new approach based on the noise of the acceleration signal recorded by EDR. It consists in quantifying this noise for lateral situations and evaluating its relevance to estimate the severity of an incident. The hypothesis is to consider that the noise of the acceleration signal increases with the loss of control risk, leading to think that the vehicle comes near its grip limits. The friction forces, which depend on the tires adhesion, the surface of the road and the load transfer of the vehicle, could then be evaluated thanks to the noise of the lateral acceleration. The study is based on various and numerous recordings in a sinuous zone of interest. This zone includes a bend where the vehicles often reach high levels of lateral acceleration. This bend was chosen because several accidents due to losses of control have been reported in the past. Thus the study aims for better understanding the loss of control accident mechanisms.

2 MATERIAL AND METHOD

2.1 *Experimental context*

The data are issued from the SVRAI project (Saving Lives through Road Incident Analysis Feedback) supported by the French government between 2010

and 2015. This project relies on the use of an Event Data Recorder called EMMA (Embedded data logger for accident mechanisms) specifically designed by IFSTTAR-LMA (Lechner et al. 2015) to record incidents. 51 EDR were implemented on public light vehicles fleets, in three regions of France. The data collection started in August 2012 and lasted one year (Ledoux et al. 2014).

EMMA acquires different signals from internal and external sensors:

- Longitudinal, lateral and vertical accelerations for usual vehicle behavior, at 100 Hz,
- Longitudinal and lateral acceleration in case of a crash (35 g accelerometers), at 100 Hz,
- GPS location and speed at 1 Hz,
- Eventually driver behavior data providing by the CAN bus of the car.

The data are analyzed, using real-time processing performed by embedded software. The EDR detects two kinds of situations.

The first driving situations detected concern "incidents" and are considered as risky, because the vehicle reaches high dynamics demands in longitudinal, lateral or combined directions. The processing is based on the following principles: when acceleration and jerk signals exceed simultaneously the thresholds, an event is triggered. From previous works (Bagdadi & Varheli. 2011, Nagaï et al. 2006, Lechner & Perrin 1993, Mongeot et al. 2006) the thresholds for triggering an incident in this experiment were set as follows:

- Speed < 80 km/h, and Acceleration norm > 0.6 g and Jerk > 2 g/s,
- Speed > 80 km/h and Acceleration norm > 0.5 g and Jerk > 2 g/s,
- Speed > 100 km/h and Acceleration norm > 0.4 g and Jerk > 2 g/s.

The acquired data concerned the 30 s before and the 15 s after the trigger and are stored in the device. The file containing the whole data set is automatically sent to a secured server using GSM network.

The second situations recorded are encountered when the vehicle is circulating on specific and predefined road sections, called zones of interest. These sections were chosen at the beginning of the experiment and correspond mostly to black spots where crashes were reported. When the equipped vehicle enters in such a zone defined by a GPS position and a length, the device stores the 30 s before, the driving through the zone, and the 15 s after its end.

Moreover, a preliminary analysis of the data recorded in the experiment stressed out the necessity to distinguish the different types of passages: normal driving without any dynamical triggering, slight events which are non-risky situations and real incidents, corresponding potentially to critical driving situations. Slight events are mostly characterized by very short durations of acceleration peaks beyond the threshold. Real incident criteria have higher durations of high accelerations, resulting from driver's actions, beyond a 3 Hz frequency. Examples of slight events and incidents are presented in Serre et al. (2013, 2014).

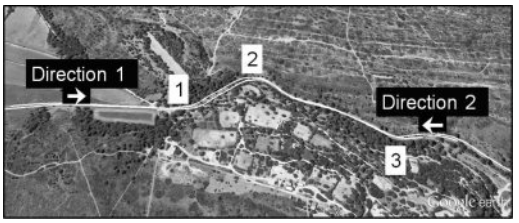


Figure 1. Presentation of the sinuous zone of interest with one passage in each direction.

2.2 *The sinuous zone of interest*

The study relies on the data collected over one zone of interest. This zone corresponds to a secondary road with a succession of left and right curves, and a speed limitation of 70 km/h. Figure 1 shows this zone with the trajectories of 2 specific recorded passages, one in each direction. The GPS location was implemented in the EMMA device in order to trigger in the most difficult bend (noted as n°2 on the figure). It is a bend of 86 m with a mean radius of curvature of 70 m and a minimum radius of 67 m.

This zone was chosen because:

- Several accidents occurred in this bend in the past. They were analyzed by the IFSTTAR teams devoted to in-depth study of accidents in the area of Salon de Provence (South of France). The methodology of these studies is detailed in Girard (1993) and Ferrandez et al. (1995).
- During the one year-experiment, this road section was circulated 249 times with different levels of lateral acceleration by 2 different equipped cars. The three different types of situations occurred in the same bend: passages with incidents, with slight events and without triggering (neither incident nor slight event).

The interest is to compare acceleration data recorded in the 3 different situations and to see if there is a hierarchy between them. For the recordings in one circulation direction (noted direction 1 on Figure 1), which is the direction of all the accidents in this bend, the levels of acceleration will be compared as well as the noise of the signal in the most difficult part of the bend.

2.3 *Noise of the lateral acceleration signal*

The noise of lateral acceleration was evaluated thanks to two different formulas: the order 2-moment (1) and the effective value of the noise (2):

$$M_1 = \overline{noise^2} \tag{1}$$

$$M_2 = \sqrt{\frac{1}{b-a}\int_a^b noise^2} \tag{2}$$

Table 1. Distribution of the various recordings according to the direction.

	Direction 1		Direction 2	
	Nb	%	Nb	%
Normal driving passages	61	53	109	79
Slight events	11	10	9	7
Incidents	44	38	15	11
Total	116	100	133	100

where *noise* = difference between raw acceleration and its moving average on one second.

Both methods were used first focused on one second around the triggering point; this means 0.5 s before the point and 0.5 s after. When there were several dynamical triggering points in the bend, the period taken into account was around all the points. The same calculations were also done 5 s around the GPS or triggering point(s). At a speed between 60 and 70 km/h, in one second the vehicle travels between 16 and 20 m, which correspond to the central part of the bend, whereas 5 s gives a distance between 83 and 98 m and correspond to the whole bend. These calculations allow the comparison of the noise just near the triggering and the noise in the bend. These periods of 1 s and 5 s were chosen to enable the discrimination of the noise between the triggering area and a larger area. The calculations were not extended to the 45 s of recordings because sometimes other triggering areas were recorded in other bends. It could have increase the global level of noise.

3 RESULTS

3.1 *Assessment of the recordings*

The data set in the zone of interest consists of 249 recordings in both directions: 59 incidents, 20 slight events and 170 passages without dynamical triggering. The difference between both directions, as it can be seen in Table 1, highlights the different levels of lateral acceleration in the most difficult bend. This bend is a right curve for direction 1, and a left curve for direction 2.

The higher dynamic demands are found in direction 1, for almost half of the passages, since events and incidents represent 48% of the whole passages against 18% in direction 2. Moreover, it has been noticed that for similar levels of speed the level of lateral acceleration in the same bend is higher in direction 1 than in direction 2. For this reason and because all the accidents reported were also in direction 1, the study is focused on this direction.

3.2 *Lateral acceleration and speed*

In direction 1, the mean levels of speed and accelerations of the 116 passages are shown in Figure 2.

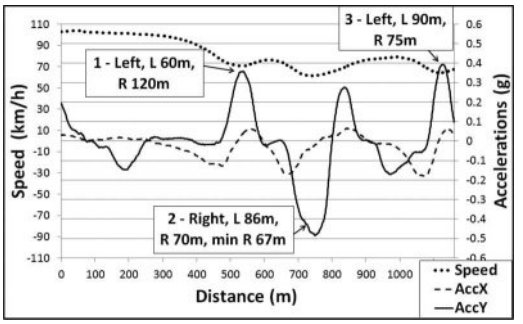


Figure 2. Average levels of speed (dotted line), longitudinal acceleration (dash line) and lateral acceleration (continuous line) in direction 1.

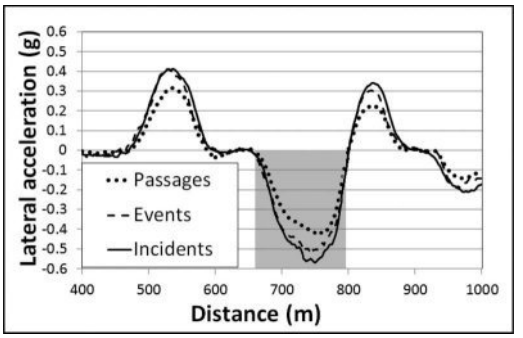


Figure 3. Average levels of lateral acceleration, the bend 2 corresponding to the shaded area.

The bend number 2 really appears as the bend where the highest level of lateral acceleration occurs.

Figure 3 shows the average lateral acceleration for the three types of passages. For the incidents the lateral acceleration reaches 0.56 g in the considered bend, while for the events it reaches 0.51 g and for the passages without dynamical triggering only 0.42 g.

The same hierarchy is observed on Figure 4 for the average speed of the three groups of recordings. However some events and some incidents trigger with a lower speed than other passages without triggering. It can be explained by the different trajectories of the vehicles in the bend which modify the radius of curvature.

3.3 *Noise of the acceleration signal*

An example of the different calculations of the noise is shown on Figure 5. There are one triggering point, thus the period of calculation extends from 0.5 s before the triggering until 0.5 s after, and lasts about one second. It can be noticed the higher level of noise in the short period around the triggering for both calculations.

Table 2 shows the values obtained with the average of calculations for both methods and for the different groups of recordings.

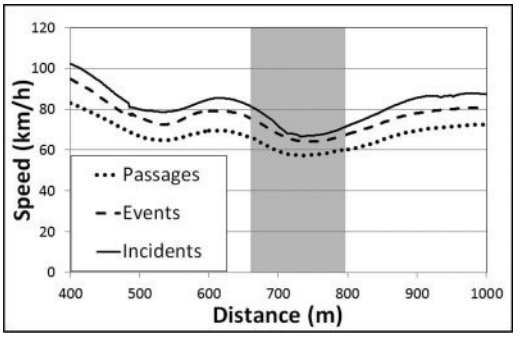


Figure 4. Average levels of speed: passages (dotted line), slight events (dash line) and incidents (continuous line).

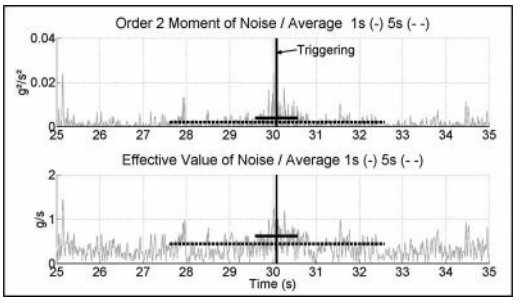


Figure 5. Example of calculation of the levels of noise of the acceleration 1 s (continuous dash) and 5 s (spaced dash) around the triggering points of an incident for both methods.

Table 2. Average noise for the 116 recordings in direction 1, for both methods and both intervals.

	Method (1)*		Method (2)**	
	1 s	5 s	1 s	5 s
Normal driving passages	0.065	0.068	0.024	0.025
Slight events	0.241	0.187	0.049	0.043
Incidents	0.388	0.282	0.062	0.053

* Order 2-Moment
** Effective Value

Figure 6 shows the hierarchy obtained for both methods, the values brought back to a similar scale in order to be compared ((1) values were multiplied by 15 and (2) values by 100). The standard deviations were added to see the extent of the results. It consequently enables to verify that the differences are significant.

For both methods, the hierarchy is consistent with what was expected: in the most difficult part of the bend, the noise of incidents is superior to the noise of events, which is superior to the noise of passages. The results calculated on 5 s respect the same hierarchy. Moreover, it can be noticed that the levels of noise on 5 s are significantly lower compared to 1 s, for the

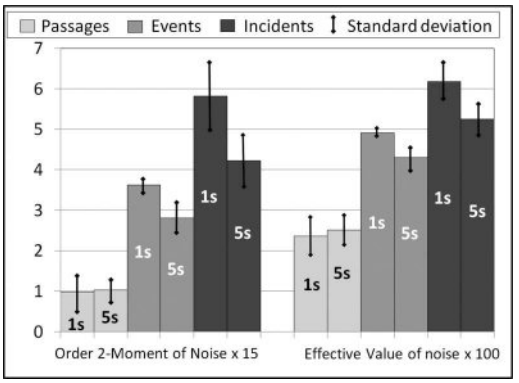


Figure 6. Average noise for both methods: passages (light grey), events (medium grey) and incidents (dark grey), 1 s and 5 s around GPS/triggering point(s), standard deviations (black dash).

slight events and the incidents, but not for the passages without triggering. This result is also consistent and proves that the noise is significant when the vehicle lateral acceleration increases and goes near the grip limits.

4 CONCLUSION AND DISCUSSION

In the bend considered, the hierarchy of lateral acceleration levels and the hierarchy of the noise of this acceleration are both distinct between passages without triggering, slight events with a short triggering, and incidents with a longer triggering. Both criteria classify the incidents more severe than events and events more severe than passages without triggering. It was almost obvious for the levels of acceleration because of the definition of the events and the incidents, but it was not for the noise of the acceleration. Moreover, the level of noise calculated very near the more difficult part of the bend is higher than the level of noise in a larger period, for the dynamical triggering situations. This comparison could be done in every bend whatever the radius of curvature, the surface of the road or the speed of the vehicle may be. The level of noise indicator brings something more than the level of the lateral acceleration, which depends on the radius of curvature of the road and the speed of the vehicle. The noise concerns the friction forces at the tire road interface, which play a significant role in the losses of control.

The results corroborate the observations done on numerous incidents. However the numbers taken into account are limited and the results should be confirmed by some studies of other zones of interest with a sufficient number of passages of different types.

The effective value method could be chosen in further studies because it better discriminates the different situations than the order 2-moment method. The calculation of the noise of lateral acceleration might be used to estimate the severity of an incident with lateral

triggering since it characterizes when a passage in a bend is critical.

This method could be extended to longitudinal triggering, since in braking the noise of the longitudinal acceleration may also be an indicator of the closeness of grip limits. Apart from the levels of longitudinal acceleration, lateral acceleration and speed around the triggering, and from the noise calculated according to this method, other criteria will be studied to estimate the severity of an incident:

- The risk of "loss of control" in a bend for lateral triggering incidents, with the calculation of the speed increment necessary for the lateral acceleration to exceed a loss of control threshold, taking into account the radius of curvature of the trajectory,
- The peaks of jerk (i.e. derivative of acceleration) which express the brutality of the solicitations endured by the vehicle,
- The consideration of the possible triggering of an active safety system such as the EBA (Emergency Brake Assistance), the ABS (Anti-lock Braking System) or the ESC (Electronic Stability Control).

The goal of these studies is to be able to highlight the most severe incidents in a further experiment with many vehicles equipped and many incidents recorded.

The study is also interesting because in this case there is clearly a link between accidents and incidents. Actually, 4 accidents were reported in the considered bend between 2002 and 2012 by the IFSTTAR teams devoted to in-depth study of accidents in the area of Salon de Provence, in the South of France. During the experiment, there was also an accumulation of incidents, especially in the same direction as the accidents (direction 1). The study of all passages gives elements for the understanding of the mechanisms of accidents. All the 4 accidents reported in the bend occurred with a dynamic loss of control, on wet road and by young drivers. These conditions, in addition to the difficulty of the bend, explain the occurrence of crashes.

Otherwise, all the losses of control reported and most of the critical incidents occurred in the right bend. This difference between right bend and left bend is confirmed by the statistical results of the project SVRAI on all the incidents, where it was noticed a large difference between the numbers of incidents in right/left curves (i.e. 41/14%), and higher levels of lateral acceleration in right turns than in left turns. This could be due to the fact that in France the vehicles circulate on the right side of the road. According to Lechner et al. (2015), this point has several consequences. First, on 2 way traffic roads, the drivers can feel more confident to reach high lateral accelerations in right curves, as the opposite lane of traffic on the left may act as a possible recovery area. Moreover, the right hand side driving offers more capabilities to increase the radius of curvature of left curves, by cutting the path using the opposite lane of traffic. Finally, considering a given curve, when a vehicle turns on the right, the radius of curvature is slightly lower than when the vehicle turns on the left; consequently the lateral acceleration (equal to V^2/R if one neglects the side slip and the road banking) is slightly higher.

Finally this research might also be useful to trigger a driver assistance system in order to prevent losses of control. To achieve this, the calculations should be performed in real time on the period preceding the triggering and not around the triggering as it was done in this study.

ACKNOWLEDGEMENTS

The authors thank the French Government (DSCR) for supporting the SVRAI project (Saving Lives through Road Incident Analysis Feedback). They thank other participants to the project, from IFSTTAR Laboratory of Accident Mechanism Analysis: S. Chauvet, O. Bellot, E. Michel, D. Lechner and M. Guilbot, for their contribution to the experiment.

REFERENCES

Bagdadi, O. & Várhelyi, A. 2011. Jerky driving – an indicator of accident proneness? *Accident Analysis and Prevention*, 43 (4), 1359–1363.

Bagdadi, O. &, Varhelyi, A. 2013. Development of a method for detecting jerks in safety critical events. *Accident Analysis and Prevention* 50: 83–91.

Doumiati, M. Charara, A., Victorino, A., Lechner, D. 2012. *Vehicle dynamics estimation using Kalman filtering: Experimental Validation.* Wiley-ISTE.

Ferrandez, F., Brenac, T., Girard, Y., Lechner, D., Jourdan, J-L., Michel, J-E., Nachtergaele, C. 1995. L'étude détaillée d'accidents orientée vers la sécurité primaire. *Presses de l'école nationale des Ponts et chaussées*, INRETS, Paris.

Girard, Y. 1993. In-depth investigation of accidents: the experience of INRETS at Salon de Provence. *ICTCT Congress, Salzburg.*

Lechner, D. & Perrin, C. 1993. The actual use of the dynamic performances of vehicles. *Journal of Automobile Engineering*, Proceedings Part D, Issue D4, IMechI. SAE Paper 18-207-D4-249.

Lechner, D., Thomas, D., Barletta, E., Menhour, L., Belon, S., Naude, C., Baque, L., Bellot, O. 2008. Recherche des Attributs pour le Diagnostic Avancé des Ruptures de la Route, Tâche 1.8.2 : Diagnostic de rupture d'un itinéraire, Rapport sur les différents points de développement de la méthode d'extrapolation. *209p. http://sari.ifsttar.fr/livrables/radarr/RADARR_1.8.2.pdf*

Lechner, D., Naude, C., Serre, T., Dubois-Lounis, M., Guilbot, M., Fournier, J-Y., Ledoux, V. 2015. Characterization of driving dynamics on road incidents collected by EDR, *Gothenburg, Sweden. FAST-zero'15. 9–11 September 2015.*

Ledoux, V., Subirats, P., Violette, E., Bonin, Y., Serre, T., Naude, C., Guilbot, M., Lechner, D. 2014. Using event data recorder to detect road infrastructure failures from a safety point of view. *AET/European Transport Conference. Francfort, Deutschland. 29 september–1st October 2014.*

Mongeot, H., Naude, C., Lechner, D., Marchi, M. 2006. Use of EDRs in French DOT cars: Initial Results of the Experiment. *ITS London. 8–12 October 2006.* N°1757.

Nagai, M., Michitsuji, Y., Kamata, M., Fujita, M., Shino, M., Maeda, K. 2006. Research on Incident Analysis using Drive Recorder. Part 2: Toward Active Safety Assessment, *FISITA.* Paper F2006V202, JSAE.

Serre, T., Naude, C., Chauvet, S., Fournier, J-Y., Lechner, D., Ledoux, V. 2013. Towards a classification of road incidents acquired from public fleets of vehicles. *FASTZERO'13. Nagoya, Japan. 22–26 September 2013.*

Serre, T., Naude, C., Chauvet S., Fournier, J-Y., Lechner, D., Ledoux, V. 2014. Causes of road incidents. *Transport Research Arena (TRA), Paris, France. 14–17 April 2014.*

Advanced Vehicle Control – Edelmann, Plöchl & Pfeffer (Eds)
© 2017 Taylor & Francis Group, London, ISBN 978-1-138-02992-7

Prediction based advanced emergency braking for vulnerable road users

T. Kim, K. Park & K. Yi
School of Mechanical and Aerospace Engineering, Seoul National University, Seoul, Korea

K. Min
Korea Transportation Safety Authority, Korea

ABSTRACT: This paper proposes an autonomous emergency braking (AEB) algorithm for vulnerable road users (VRU). In order to describe the behavior of pedestrian and cyclist using a single model, simple constant velocity model is used. The motion of vehicle is modeled using constant acceleration model to describe the evasive maneuver of driver. These predicted information is then used to judge whether a collision is inevitable or not. Proposed AEB is activated if a collision is inevitable based on the assumptions. The proposed risk assessment has been incorporated into an AEB system and simulation study has been conducted in real traffic scenarios

1 INTRODUCTION

Autonomous emergency braking (AEB) helps drivers to avoid or mitigate a collision based on the information about traffic situation. The USA Department of Transportation's National Highway Traffic Safety Administration (NHTSA) and the Insurance Institute for Highway Safety (IIHS) announced that 20 automakers have agreed to make AEB standard by September 1st, 2022. Therefore, AEB is predicted to be available to more consumers more quickly than would be possible through the regulatory process.

Recently, AEB for Vulnerable Road Users (VRU) has become one of the main issues for researchers and automakers. Although the number of collisions related with VRU is smaller than other car to car collisions, it is important to mitigate or avoid the car-to-VRU crashes due to their fatality.

Usually, VRU are defined as "non-motorized road users, such as pedestrians and cyclists as well as motor-cyclists". In this paper, we have focused on pedestrians and cyclists which are relatively slower and more vulnerable to vehicle collision than vehicle or motor-cycle. For the pedestrian protection system, many studies have been conducted to propose a pedestrian AEB. To describe the complex behavior of pedestrian, the motion of pedestrian has been modeled using various approaches such as a discrete choice pedestrian behavior model or markov model. (Abramson 2004, Antonini 2004, Wakim 2004) Using these kinds of pedestrian models, a collision between pedestrian and vehicle was predicted based on simple collision geometry. (Atev 2005, Ferrara 2004, Kumar 2005) Westhofen (2012) has proposed a movement area intersection based pedestrian protection system.

However, in the case of the cyclist protection system, relatively little work has been conducted compared to the pedestrian protection system. Although the motion of cyclist is similar with vehicle, the cyclist detection is closely related with the pedestrian detection. Since the body frame of cycle is thinner than the human body, it is difficult to distinguish the cyclist from the pedestrian. Therefore, AEB should be able to assess the risk of collision without VRU type identification. For this, Rosen (2013) has proposed an AEB for VRU which uses exactly a same decision algorithm for both types of VRU. The decision algorithm of Rosen activates the AEB only if VRU is in trigger area which represents the predicted path of the vehicle. As mentioned in Rosen's work, unwanted activations can be avoided with this approach. However, if the cyclist travels from the outside of the trigger area to the inside of it, AEB cannot be activated earlier enough to decelerate the vehicle to mitigate the collision.

This paper proposes an autonomous emergency braking algorithm for VRU which can deal with both types of VRU using the same decision algorithm. For this, simple constant velocity model is used to describe the motion of VRU. Also, the motion of host vehicle is described using constant acceleration model. In order to predict a collision between VRU and vehicle, current states of host vehicle and VRU are estimated based on the measured information from radar and camera sensors. And then, the future states of host vehicle and VRU are predicted to judge whether a collision is inevitable or not. Mode decision algorithm for AEB is proposed using two kinds of avoidance model: nominal avoidance maneuver and emergency avoidance maneuver. In order to evaluate the performance of the proposed autonomous emergency

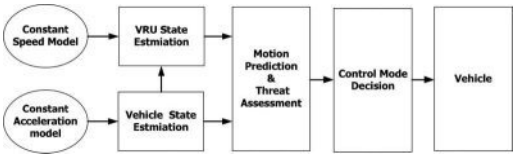


Figure 1. Schematic view of VRU AEB.

braking algorithm, computer simulation was conducted using vehicle simulation software, CARSIM and MATLAB/Simulink.

2 PREDICTION BASED AEB FOR VRU

In this paper, proposed AEB algorithm is activated if collision is inevitable with the consideration about predefined safety distance. Inevitable collision state means the situation when collision occurs with any feasible maneuver of driver or within the physical limits. (Savino 2016) In this situation, AEB should be activated to avoid or mitigate the imminent collision.

To predict the future collision, it is assumed that VRU doesn't react to avoid a collision. This assumption is reasonable for short time-to-collision scenarios. Therefore, it is assumed that VRU doesn't react about danger and cannot maneuver to prevent a collision. Using this assumption, the motion of VRU is modeled using constant velocity model. Although many researchers have proposed the advanced models which describe the behavior of pedestrian or cyclist, simple constant speed model is used to describe the characteristics of pedestrian and cyclist using same dynamic model. To predict the future position of VRU, relative position and velocity of VRU is estimated using the measured information.

The motion of host vehicle is modeled using constant acceleration model. The longitudinal acceleration and yaw acceleration are very important factors to predict the future states of the vehicles. To use the yaw acceleration information, vehicle state estimator is used based on the measurement information from vehicle chassis sensors. Also, in order to judge whether the driver can avoid a collision or not, proposed algorithm assumes that braking or steering is the only option for driver to avoid or mitigate the collision. Driver's evasive maneuver is modeled using desired acceleration tracking model. To describe the characteristics of driver's evasive maneuver, driving data of 100 peoples is used.

These predicted states of host vehicle and VRU are then used to judge if the driver needs additional braking to avoid or mitigate the collision. The pre-braking is applied autonomously if driver cannot avoid the collision with usual avoidance maneuver. The hard-braking is applied autonomously if driver cannot avoid the collision using the maximum acceleration within physical limits.

The schematic view of the propose AEB algorithm is shown in Figure 1. The detailed information about host vehicle state estimation and prediction are described in section 3. VRU state estimation and prediction is explained in section 4. Based on the predicted information, the threat of collision is then assessed in section 5. In section 6. The mode decision algorithm for VRU AEB is described. At last, the proposed AEB algorithm is evaluated via computer simulation using vehicle simulation software CARSIM, and MATLAB/Simulink.

3 HOST VEHICLE MOTION PREDICTION

In this section, future motion of host vehicle is predicted. For this, dynamic model of host vehicle is defined. The current state of host vehicle is estimated based on the chassis sensor measurement. The future motion of host vehicle is predicted using Taylor Method. Using a linear dynamic model, the future position of vehicle can be predicted for each time step of pre-defined prediction time horizon.

3.1 *Host vehicle state estimation*

As mentioned in section 2, the longitudinal acceleration and the yaw acceleration are important factors for the vehicle motion prediction. Therefore, motion of host vehicle is modeled as a constant acceleration model which assumes that the longitudinal acceleration and yaw acceleration are constant. For this, in estimation part, a linear kalman filter estimates the longitudinal velocity, yaw rate, longitudinal acceleration and yaw acceleration. State vector x_{host} and measurement vector z_{host} of estimator can be defined as follows:

$$x_{host} = \begin{bmatrix} v_x & \gamma & a_x & \dot{\gamma} \end{bmatrix}^T$$
$$z_{host} = \begin{bmatrix} v_x & \gamma & a_x \end{bmatrix} \quad (1)$$

where v_x: longitudinal velocity, γ: yaw rate, and a_x: longitudinal acceleration of vehicle.

The time derivatives of the longitudinal acceleration and yaw acceleration is assumed as a white noise. Detailed description about the host vehicle state estimation is explained in the research of Kim (2014).

3.2 *Host vehicle evasive maneuver prediction*

In order to judge whether the driver can avoid a collision or not, evasive maneuver of driver should be considered. In general cases, drivers can use steering, braking, accelerating or combination of them. However, proposed algorithm assumes that braking or steering is the only option for driver to avoid the collision. In city driving condition, it is difficult to avoid a collision using acceleration due to limited acceleration. Therefore, only braking and steering maneuvers are considered for the proposed AEB algorithm. If the driver tries to accelerate the vehicle, proposed AEB stops braking and gives the control authority to the driver to reduce the unnecessary braking.

To describe the future behavior of host vehicle using the constant acceleration model, prediction state vector $x_{host,p}$ can be defined as follows:

$$x_{host,p} = \begin{bmatrix} p_{x,p} & p_{y,p} & \theta_p & v_p & \gamma_p & a_p & \dot{\gamma}_p \end{bmatrix}^T \tag{2}$$

where subscript p: predicted, $p_{x,p}$: longitudinal position, $p_{y,p}$: lateral position, θ_p: heading angle, v_p: longitudinal velocity, γ_p: yaw rate, and a_p: longitudinal acceleration of vehicle. Predicted future position of host vehicle is expressed in the current host vehicle local frame.

The constant acceleration model of host vehicle can be expressed as follows:

$$\dot{x}_{host,p} = \begin{bmatrix} \dot{p}_{x,p} \\ \dot{p}_{y,p} \\ \dot{\theta}_p \\ \dot{v}_p \\ \dot{\gamma}_p \\ \dot{a}_p \\ \ddot{\gamma}_p \end{bmatrix} = \begin{bmatrix} v_p \cos\theta_p \\ v_p \sin\theta_p \\ \gamma_p \\ a_p \\ \dot{\gamma}_p \\ 0 \\ 0 \end{bmatrix} + \begin{bmatrix} 0 & 0 \\ 0 & 0 \\ 0 & 0 \\ 0 & 0 \\ 0 & 0 \\ 1 & 0 \\ 0 & 1 \end{bmatrix} w_p \tag{3}$$

where w_p: white noise with proper dimension. The derivatives of longitudinal acceleration and yaw acceleration are considered as a white noise.

Additionally, to judge whether the driver can avoid a collision or not, driver's evasive maneuver also should be predicted. As mentioned earlier, it is assumed that the drivers can avoid or mitigate a collision only using steering or braking. These steering or braking maneuver can be modeled using desired acceleration tracking model as follows:

$$\dot{x} = \begin{bmatrix} \dot{p}_{x,p} \\ \dot{p}_{y,p} \\ \dot{\theta}_p \\ \dot{v}_p \\ \dot{\gamma}_p \\ \dot{a}_p \\ \ddot{\gamma}_p \end{bmatrix} = \begin{bmatrix} v_p \cos\theta_p \\ v_p \sin\theta_p \\ \gamma_p \\ a_p \\ \dot{\gamma}_p \\ -k_a\left(a_p - a_{des}\right) \\ -k_\gamma \dot{\gamma}_p - k_\gamma\left(\gamma_p - \gamma_{des}\right) \end{bmatrix} + B w_p \tag{4}$$

where k_i: acceleration tracking gain, a_{des}: desired longitudinal acceleration, and γ_{des}: desired yaw rate. To describe the characteristics of steering and braking maneuver, each acceleration tracking gain is pretuned.

In this paper, two kinds of evasive maneuver models are defined: nominal avoidance model and emergency avoidance model. Nominal avoidance model describes the characteristics of driver's evasive maneuver and emergency avoidance model describes the possible avoidance maneuver within physical limits.

To describe the characteristics of driver's evasive maneuver, driving data of 100 peoples is used. Although vehicle can be decelerated with almost 0.8 g in dry road condition, drivers used the longitudinal acceleration less than the amount of 0.4 g even in the dangerous situation. In the case of steering avoidance, although the drivers can use the lateral acceleration larger than 0.8 g in steady state cornering situation, lateral acceleration is limited due to the short duration of the evasive maneuver and the physical limit of steering angular velocity. In nominal avoidance maneuver, drivers used the lateral acceleration under the amount of 0.2 g. However, 0.4 g of lateral acceleration can be used in physical manner.

Table 1. Maximum acceleration of evasive maneuver models.

Models	Maneuver	
	Braking	Steering
Nominal avoidance model	0.4 g	0.2 g
Emergency avoidance maneuver	0.8 g	0.4 g

Based on these information, the acceleration limitation of each model is shown in table 1.

In the case of steering maneuver, maximum yaw rate is calculated using maximum lateral acceleration as follows:

$$\gamma_{\max} = \max\left(|\gamma|\right) = \frac{a_{lat,\max}}{v_p} \tag{5}$$

where $\gamma_{\max}$: maximum yaw rate, and $a_{\text{lat,max}}$: maximum lateral acceleration.

In low speed driving condition, yaw rate is limited due to the maximum steering angle of the vehicle. The relation between steering wheel angle and yaw rate is as follows:

$$\delta_{\max} = \max\left(\delta\right) = GR \cdot \frac{L}{R_{\min}} = GR \cdot L \cdot \frac{\gamma_{\max}}{v_p} \tag{6}$$

where GR: steering gear ratio, L: vehicle length.

Using the equation (5) and (6), maximum yaw rate can be calculated as follows:

$$\gamma_{des} = \pm\gamma_{\max} = \pm\min\left(\frac{a_{lat,\max}}{v_p} \quad \frac{\delta_{\max} \cdot v_p}{GR \cdot L}\right) \tag{7}$$

4 TARGET VRU MOTION PREDICTION

In this section, the future motion of target VRU is predicted. To describe the motion of pedestrian and cyclist using a single model, a constant velocity model is used.

4.1 *Target VRU state estimation*

In this paper, the motion of VRU is modeled as a constant velocity model. In order to formulate the VRU state estimator easily, position and velocity of VRU related to the host vehicle are considered as a state variable.

In this paper, camera and radar are used to measure the relative position and velocity of target VRU.

Using these information, a kalman filter is used to estimate the relative position and velocity of VRU.

The dynamic equations of VRU can be expressed as follows:

$$\dot{\mathrm{x}} = \begin{bmatrix} \dot{p}_{x,rel} \\ \dot{p}_{y,rel} \\ \dot{v}_{x,rel} \\ \dot{v}_{y,rel} \end{bmatrix} = \begin{bmatrix} v_{x,rel} \\ v_{y,rel} \\ -a_{host} + v_{y,rel} \cdot \gamma_{host} + p_{y,rel} \cdot \dot{\gamma}_{host} \\ -v_{x,rel} \cdot \gamma_{host} - p_{x,rel} \cdot \dot{\gamma}_{host} \end{bmatrix} + \begin{bmatrix} 0 & 0 \\ 0 & 0 \\ 1 & 0 \\ 0 & 1 \end{bmatrix} \begin{bmatrix} \mathrm{w}_{a_x} \\ \mathrm{w}_{a_y} \end{bmatrix} \quad (8)$$

where $p_{i,rel}$: relative position of VRU, $v_{i,rel}$: relative velocity of VRU, subscript x/y: host vehicle local frame x/y axis, a_{host}: host vehicle longitudinal acceleration, γ_{host}: host vehicle yaw rate, w_a: white noise which represent the derivatives of relative velocities. This process model can be discretized by Taylor expansion. Using the measured position and velocity information, the current states of VRU can be estimated using linearized Kalman filter.

4.2 *Target VRU motion prediction*

Target VRU is modeled as a constant velocity model. Their future position and velocity can be described in current local frame of vehicle. The prediction state vector x_p of VRU is then expressed in fixed frame. The future states of VRU can be predicted using the simple dynamic equation:

$$\dot{\mathrm{x}}_p = \begin{bmatrix} \dot{p}_{x,p} \\ \dot{p}_{y,p} \\ \dot{v}_{x,\mathrm{p}} \\ \dot{v}_{y,p} \end{bmatrix} = \begin{bmatrix} v_{x,p} \\ v_{y,p} \\ 0 \\ 0 \end{bmatrix} + \begin{bmatrix} 0 & 0 \\ 0 & 0 \\ 1 & 0 \\ 0 & 1 \end{bmatrix} \begin{bmatrix} \mathrm{w}_{a_{x,p}} \\ \mathrm{w}_{a_{y,p}} \end{bmatrix} \quad (9)$$

where subscript p: predicted.

From the estimated current states of host vehicle and VRU, the initial state vector $x_{p,0}$ for motion prediction can be calculated as follows:

$$\mathrm{x}_{p,0} = = \begin{bmatrix} p_{x,\mathrm{p},0} \\ p_{y,p,0} \\ v_{x,\mathrm{p},0} \\ v_{y,\mathrm{p},0} \end{bmatrix} = \begin{bmatrix} p_{x,rel} \\ p_{y,rel} \\ v_{x,rel} + v_{host} - p_{y,rel} \cdot \gamma_{host} \\ v_{y,\mathrm{rel}} + p_{x,rel} \cdot \gamma_{host} \end{bmatrix} \quad (10)$$

where $p_{i,p,0}$: initial position of VRU, $v_{i,p,0}$: initial velocity of VRU, and subscript x/y: x/y axis of current local frame of the host vehicle.

5 THREAT ASSESSMENT

In this section, the potential threat between the host vehicle and target VRU is assessed. Based on the predicted information, it can be judged whether the host vehicle and target VRU will collide or not during the prediction time horizon. The schematic view of threat assessment is described in Figure 2.

In section 3&4, the following states were predicted:

$$\begin{aligned} \mathrm{x}_{host,j,p}[k] &= \begin{bmatrix} p_{x,p} & p_{y,p} & \theta_p \end{bmatrix}^T \\ \mathrm{x}_{tar,i,p}[k] &= \begin{bmatrix} p_{x,tar} & p_{y,tar} \end{bmatrix}^T \end{aligned} \quad (11)$$

where subscript i: target index, subscript j: host vehicle evasive maneuver model index, subscript p: predicted, k: predicted time step, p_x, p_y: predicted x, y position in current local frame of host vehicle.

Based on these states, relative future position of VRU with respect to the future position of host vehicle can be calculated as follows:

$$\mathrm{p}_{rel,i,j,p}[k] = \begin{bmatrix} p_{x,rel,i,j,p} \\ p_{y,rel,i,j,p} \end{bmatrix} = \begin{bmatrix} \cos\theta_p & \sin\theta_p \\ -\sin\theta_p & \cos\theta_p \end{bmatrix} \begin{bmatrix} p_{x,i,j,p} - p_{x,p} \\ p_{x,i,j,p} - p_{x,p} \end{bmatrix} \quad (12)$$

which is also expressed in Figure 2(b).

In order to activate the AEB before the collision became inevitable, safety area of host vehicle can be defined as follows:

$$D_{host}[k] = \left\{ (x,y) \;\middle|\; |x| < \left(\frac{L}{2} + C_{longi}\right) \,\&\, |y| < \left(\frac{t_w}{2} + C_{lat}\right) \right\} \quad (13)$$

where L: vehicle length, t_w: vehicle width, C_{longi}: longitudinal safety distance, C_{lat}: lateral safety distance, and x, y: host vehicle local frame at predicted time step k.

Also, to judge whether target VRU will collide with the host vehicle, two side edges of target VRU can be defined as shown in Figure 2(c) to represent the target VRU position. The position of the side edges of target VRU can be calculated as follows;

$$\begin{aligned} p_{rel,i,j,1}[k] &= \begin{bmatrix} p_{x,rel,i,j,p} \\ p_{y,rel,i,j,p} \end{bmatrix} + \begin{bmatrix} \cos\theta_p & \sin\theta_p \\ -\sin\theta_p & \cos\theta_p \end{bmatrix} \begin{bmatrix} 0 \\ +\frac{w_{target}}{2} \end{bmatrix} \\ p_{rel,i,j,2}[k] &= \begin{bmatrix} p_{x,rel,i,j,p} \\ p_{y,rel,i,j,p} \end{bmatrix} + \begin{bmatrix} \cos\theta_p & \sin\theta_p \\ -\sin\theta_p & \cos\theta_p \end{bmatrix} \begin{bmatrix} 0 \\ -\frac{w_{target}}{2} \end{bmatrix} \end{aligned} \quad (14)$$

where w_{target}: measured width of target VRU.

Using these information, it can be judged whether the *jth* evasive maneuver model of host vehicle will collide with the *ith* target at prediction time step k. In other words, if:

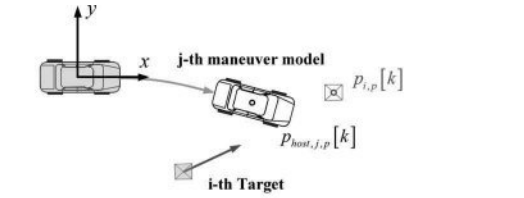
$$\mathrm{p}_{rel,i,j,3}[k] \in D_{host}[k] \; or \; p_{rel,i,j,2}[k] \in D_{host}[k] \quad (15)$$

then, the jth maneuver model of host vehicle is predicted to collide the ith target VRU at time step k.

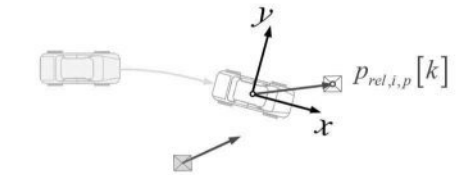
6 EMERGENCY BRAKING MODE DECISION

To avoid the unnecessary interruption of driver's control authority, driver's possible evasive maneuver should be considered for AEB system. In this paper, motions of host and target vehicles are assumed as follows:

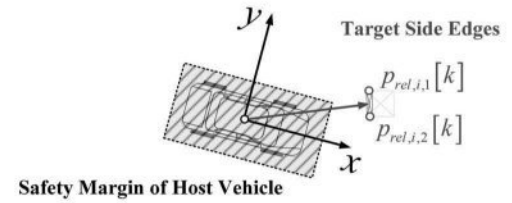
1) Host vehicle can avoid or mitigate a collision only using steering or braking



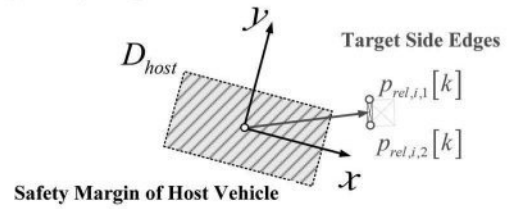
(a) Predicted information of host vehicle and target VRU



(b) Relative future position of VRU



(c) Safety margin of host vehicle



(d) Threat assessment

Figure 2. Threat assessment.

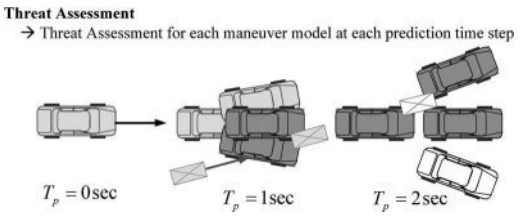


Figure 3. Mode decision.

2) Target vehicle maintain the current motion during prediction time horizon.

Based on these assumptions, driver's evasive maneuver models as well as the constant acceleration model can be predicted as Figure 3. As explained in section 5, the threat of collision can be assessed for each maneuver model at each prediction time step. If driver cannot avoid the collision with any kind of

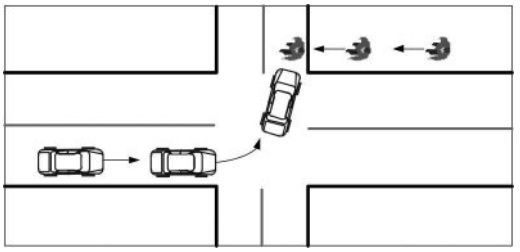


Figure 4. Simulation scenario.

models, AEB should be activated. In other words, if the collision became inevitable within the safety margin of host vehicle, AEB should be activated to avoid or mitigate the collision.

For control mode decision, two kinds of avoidance model of driver are defined: nominal avoidance maneuver and emergency avoidance maneuver. The nominal avoidance maneuver model describes driver's avoidance maneuver with steering or braking while the emergency avoidance maneuver model describes the possible steering or braking maneuver within the physical limitation on dry road. The pre-braking is applied autonomously if driver cannot avoid the collision using nominal avoidance maneuver. The hard-braking is applied autonomously if driver cannot avoid the collision using emergency avoidance maneuver.

7 SIMULATION RESULT

In order to evaluate the performance of the proposed AEB, simulation is conducted via vehicle simulation software Carsim and MATLAB/Simulink. To investigate the performance of the proposed algorithm, proposed prediction based AEB algorithm is compared with an AEB algorithm which is activated only if a target is in the pre-defined trigger area.

In this simulation, the test scenario was set as figure 4. The subject vehicle makes a left turn while the pedestrian is crossing the road from the far-side of the subject vehicle. The speed of subject vehicle and pedestrian were set as 20 km/h and 5 km/h each. It is assumed that the driver of subject vehicle and pedestrian didn't recognize a danger. Hence, AEB starts to decelerate when the collision became inevitable.

The simulation result is shown in Figure 5. As shown in Figure 5, both AEB algorithm stopped the vehicle before a collision occur. However, AEB based on trigger area was activated later than the proposed AEB. Hence, Trigger area based AEB used maximum braking to avoid the collision while the proposed AEB avoid the collision with smaller acceleration. This result shows that the proposed AEB shows better prediction performance.

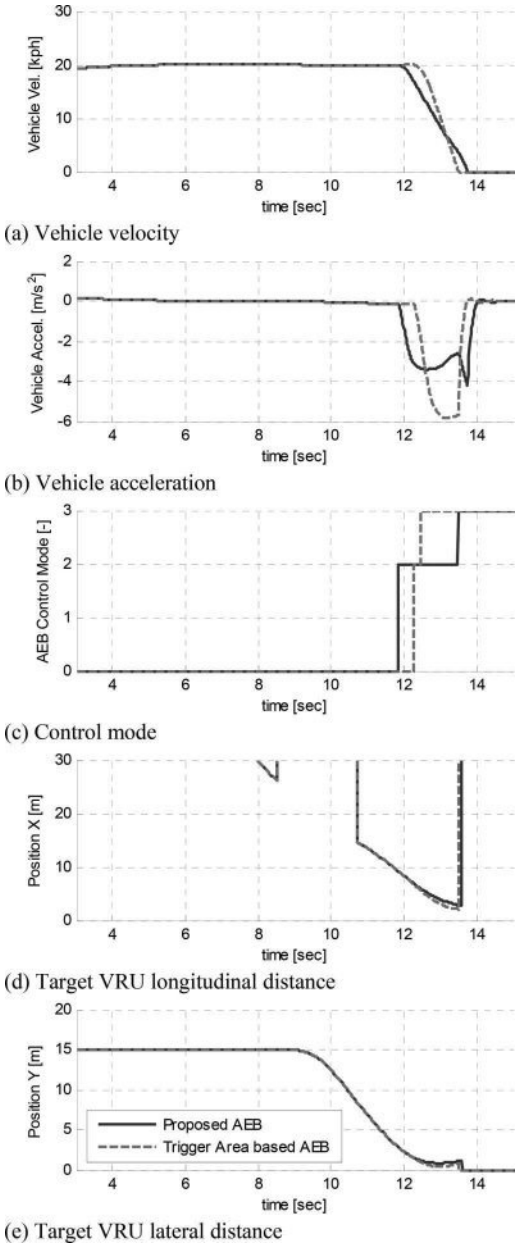


Figure 5. Simulation result.

8 CONCLUSION

In this paper, prediction based autonomous emergency braking (AEB) was proposed. In order to describe the behavior of pedestrian and cyclist using a single model, constant velocity model was used. To describe the evasive maneuver of the subject vehicle using longitudinal and yaw acceleration information, constant acceleration model was used. Using the estimated information, future behaviors of subject vehicle and target Vulnerable Road Users (VRU) were predicted. Predicted future position of vehicle and target VRU is then used to assess the risk of collision.

The performance of proposed AEB was verified via computer simulation using MATLAB/Simulink and Carsim. To evaluate the performance of the proposed AEB, the simulation result of proposed algorithm was compared with the result of trigger area based AEB algorithm in right turn collision with crossing pedestrian scenario. It was shown that the proposed AEB recognize a danger earlier than the trigger area based AEB.

REFERENCES

Abramson, Y. 2004. Hardware-friendly pedestrian detection and impact prediction. in Proc. IEEE Intell. Veh. Symp., Jun. 2004: pp. 590–595.

Antonini, G. & Venegas, S. 2004. A discrete choice pedestrian behavior model for pedestrian detection in visual tracking systems. in Proc. Adv. Concepts Intell. Vis. Syst., Brussels, Belgium, Sep. 2004.

Atev, S. et al. 2005. A collision prediction system for traffic intersections. in Proc. IEEE/RSJ Int. Conf. Intell. Robots Syst., Aug. 2005: 169–174.

Ferrara, A. 2004. Automatic pre-crash collision avoidance in cars. in Proc. IEEE Intell. Veh. Symp., Jun. 2004: 133–138.

Kim B. et al. 2014. An IMM/EKF Approach for Enhanced Multi-Target State Estimation for Application to Integrated Risk Management System. Vehicular Technology, IEEE Transactions on, Vol. 64, No. 3: 876–889.

Kumar, P. et al. 2005. Framework for real-time behavior interpretation from traffic video. IEEE Trans. Intell. Transp. Syst., vol. 6, no. 1, Mar. 2005: 43–53.

Rosen, Erik. 2013. Autonomous emergency braking for vulnerable road users. IRCOBI Conference Proceedings. No. IRC-13-71. 2013.

Savino, G. et al. 2016. Inevitable collision states for motorcycle-to-car collision scenarios.

Wakim, C. et al. 2004. A Markovian model of pedestrian behavior. in Proc. IEEE Int. Conf. Syst., Man, Cybern., Oct. 2004: 4028–4033.

Westhofen, D. et al. 2012. Transponder-and camera-based advanced driver assistance system. Intelligent Vehicles Symposium (IV), 2012 IEEE. IEEE, 2012: 293–298.

Lateral dynamics and optimization

Advanced Vehicle Control – Edelmann, Plöchl & Pfeffer (Eds)
© 2017 Taylor & Francis Group, London, ISBN 978-1-138-02992-7

Torsional moment representation in lateral load transfer equations

Devesh Srivastava
Honda R&D Co., Ltd.

ABSTRACT: One of the major factor in determining the understeer and oversteer characteristics of a vehicle dynamics is lateral load transfer. A new equation was proposed which included torsional moment in vehicle body considering both tire deformation and jacking force difference in front and rear. For race cars, the proposed equation enhanced the estimation accuracy of lateral load transfer value by ∼6%.

1 INTRODUCTION

Lateral load transfer (LLT) is the difference between inside and outside tire vertical load during cornering. The total LLT depends on the center of gravity (CG) height, track width and lateral acceleration, but individual LLT of front and rear is dependent on respective suspension's roll center (RC) heights and roll stiffness. LLT is an important factor in determining the understeer and oversteer (US/OS) characteristics of vehicle. Higher LLT in the front increases the understeer characteristics of vehicle. So it's important to have detailed understanding of LLT.

In order to calculate LLT accurately, detailed car specifications are needed. But in the early phase of vehicle performance development, many parameters are not determined. So, it's important to have some equation which quantitatively represents and fully explains the load transfer using few fundamental vehicle specifications.

Typical vehicle rolling model does not consider the effect of tire deformation due to jacking force. The tire deformation effects vehicle roll and the difference in front and rear roll causes torsional moments in vehicle body. However corresponding torsional moments are not represented in conventional equation.

2 CONVENTIONAL EQUATION

Vehicle roll model was used to solve LLT by Gillespie (1992). Similarly Abe (2009) gives the front and rear LLT as function of roll stiffness and RC height as shown in Equation 1 and 2.

$$\Delta W_F = \frac{\ddot{y} W_S}{t}\left(\frac{K_{\phi F} h_S}{K_{\phi F} + K_{\phi R} - W_S h_S} + \frac{l_R}{l} h_F\right) \tag{1}$$

$$\Delta W_R = \frac{\ddot{y} W_S}{t}\left(\frac{K_{\phi R} h_S}{K_{\phi F} + K_{\phi R} - W_S h_S} + \frac{l_F}{l} h_R\right) \tag{2}$$

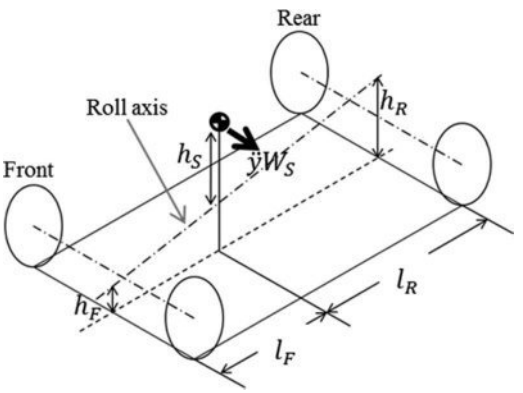


Figure 1. Vehicle roll axis model.

Here ΔW_F and ΔW_R denote the front and rear LLT respectively; ÿ denotes the lateral acceleration of the vehicle body; $K_{\varphi F}$ and $K_{\varphi R}$ are the roll stiffness of front and rear respectively; h_S is the vertical distance of sprung mass CG from roll axis; W_S is the weight of sprung mass; h_F and h_R are the heights of front and rear roll centers respectively; l_F and l_R are the distance of CG from the front and rear axle respectively; t is the track width of the vehicle and l is the wheelbase. From now, Equation 1, 2 will be referred to as 'Conv. Equation'. Following gives the derivation of Conv. Equation.

Consider the roll axis model of vehicle as shown in Figure 1.

Balancing the moment on sprung mass along the roll axis gives:

$$\left(K_{\phi F} + K_{\phi R}\right)\phi = \ddot{y} W_S h_S + W_S h_S \phi \tag{3}$$

Here, φ is the roll angle of vehicle. Balancing the moments for the unsprung mass around the roll center gives:

$$K_{\phi F}\phi = \Delta W_F d_F - \frac{\ddot{y} W_S l_R}{l} h_F \tag{4}$$

$$K_{\phi R}\phi = \Delta W_R d_R - \frac{\ddot{y} W_S l_F}{l} h_R \quad (5)$$

Solving the Equation 3, 4, 5 gives the Conv. Equation for LLT.

In Conv. Equation, jacking force at front and rear are represented by $l_F h_R / l, l_R h_F / l$ respectively. Mastinu (2014) explains that vehicle is subjected to jacking force due to lateral force during cornering. It uses similar equations for LLT and similar representation of jacking force.

In the case of race cars, it's important to consider the tire deformation because the stiffness of suspensions is comparable to tire stiffness. When roll axis is inclined, the front and rear have different jacking force which causes different amount of tire deformation resulting in torsional moment in sprung mass. Since, the above effects are not represented in Conv. Equations, the accuracy of LLT calculations is an issue to calculate race car vehicle dynamics.

3 PROPOSED METHOD

During cornering, lateral force acts at the contact patch of tire which causes rolling moment in vehicle. In steady state cornering, this rolling moment is equal to the moment due to LLT. The LLT has two components, one due to roll stiffness and the other due to Jacking force. The component of roll stiffness is explained in Conv. Equation but the component of Jacking force is not represented correctly. Following section will explain how the jacking force affects the LLT. For easier understanding, the effect of suspension roll is neglected in following section.

3.1 *Simple half car model*

Figure 1 represents a simple half car model to explain the proposed method. For simplicity, the unsprung mass as a whole is represented as tire. K_S and K_T represent the suspension and tire vertical stiffness respectively. Suspension kinematics determines the trajectory of contact patch of tire which is represented by the dotted line in Figure 2. The instantaneous center of this trajectory is called roll center (RC). In following analysis RC was considered fixed i.e. its height does not changes with suspension stroke, of the vehicle. During cornering, the vehicle is subjected to lateral force acting at the tire contact patch, which is represented by the lateral arrow at the contact patch of tire in Figure 2.

Due to the RC geometry, the lateral force causes a jacking force which acts at the RC and the reaction of jacking force acts in the tire contact patch, as shown in Figure 3. The Jacking force acting through the RC of vehicle doesn't contribute in vehicle roll. But the reaction of jacking force causes deformation in tire, thus creating a roll angle in sprung mass. Since this roll angle is caused due to reaction of jacking force,

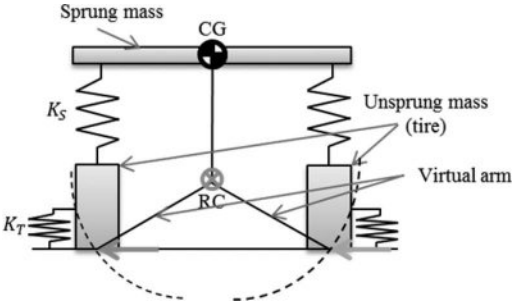


Figure 2. Half car model.

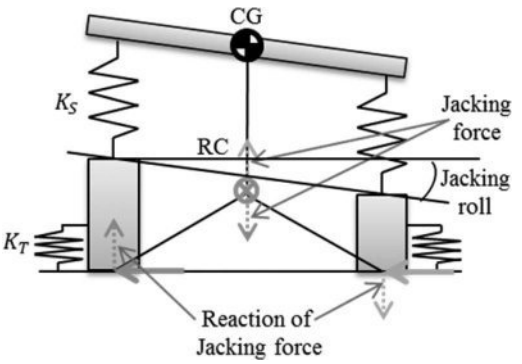


Figure 3. Jacking roll in half car model.

we will call this component of roll angle as 'Jacking roll'.

If RC is above ground, as in case of Figure 3, the reaction of jacking force would cause the stretch in inside tire and compression in outside tire, resulting in Jacking roll of sprung mass.

3.2 *Simple full car model*

Figure 4 shows the simple full car model. For simplicity of the explanation, front RC was fixed on the ground i.e. no jacking force. Only the rear RC was at some height. During cornering all the contact patches are subjected to some lateral force as shown in Figure 4. Full car model can be considered as connection of front and rear half car models. Because the RC of front half car is at ground, there is no jacking roll, while the rear RC is at some height, so there is some jacking roll similar to that in Figure 3.

The full car model with jacking roll in front and rear is shown in Figure 5. The front has no jacking roll while rear has some roll. It causes a torsional effect in vehicle body.

Since in the early phase of design, body torsional stiffness is unknown, it is considered as rigid. So a torsional moment, curved arrow around CG in Figure 6, is generated to make the sprung mass in non-twisted state.

Generated torsional moment depends on the roll stiffness of suspension. The higher the roll stiffness is,

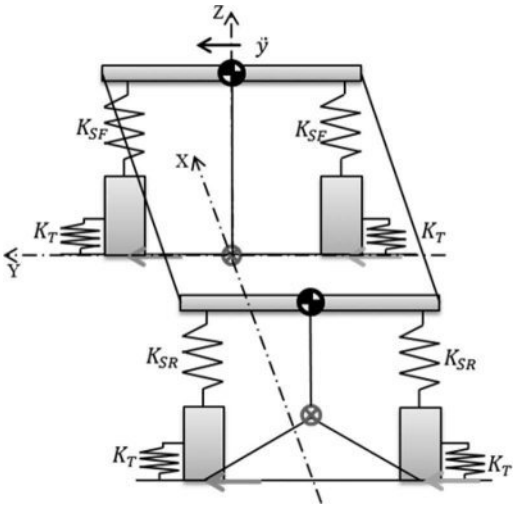


Figure 4. Simple full car model.

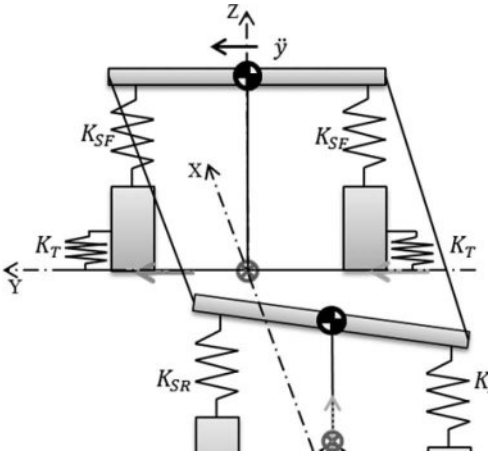


Figure 5. Simple full car model with jacking roll.

the higher the torsional moment is. In the case of Figure 6, torsional moment causes increase in front LLT and decrease in rear LLT, i.e. increasing understeer characteristics. Finally, the front and rear will have same roll angle and the body will be untwisted. This mechanism indicates how the torsional moment comes in LLT calculations.

4 EQUATION DERIVATION

The equations were derived by considering the vehicle as the arrangement of spring mass system as shown in Figure 7.

x denotes the change in vertical spring length due to lateral force. The subscript of spring deflection follows a common nomenclature. First letter denotes front (F) or rear (R), second letter denotes side, left (L) or right

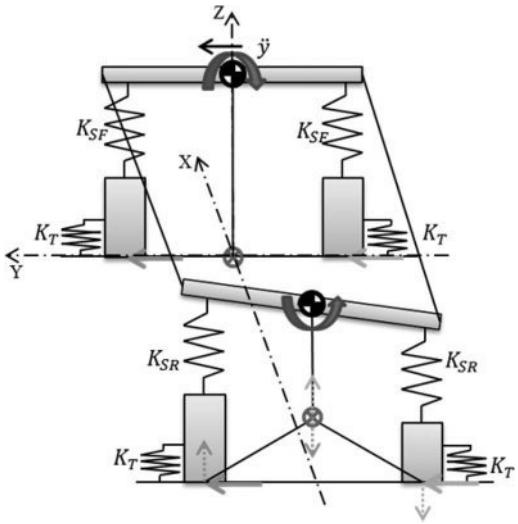


Figure 6. Torsional moment due to jacking roll.

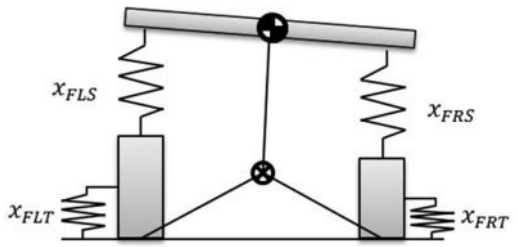


Figure 7. Half car model with spring deflections.

(R), and last letter denotes the spring compliance, suspension compliance (S) or tire compliance (T). Thus x_{FLT} denotes spring deflection in front left tire spring. K_T denotes the tire vertical stiffness while K_{SF} and K_{SR} denote stiffness of front and rear suspension respectively. The free body analysis of unsprung mass gave following:

$$F_F + K_T x_{FLT} = K_{SF} x_{FLS} \tag{6}$$

$$F_R + K_T x_{RLT} = K_{SR} x_{RLS} \tag{7}$$

F_F and F_R are the jacking forces in front and rear respectively and were given by:

$$F_F = \ddot{y}\frac{W_F h_F}{t}, \qquad F_R = \ddot{y}\frac{W_R h_R}{t}$$

W_F and W_R denotes the total weight on front and rear axle respectively. For equation derivation, lateral force effect was considered symmetrical along length of vehicle, i.e. $x_{FLS} = -x_{FRS}\, x_{FLT} = -x_{FRT}$. Now, since

the sprung mass or the chassis body is rigid, the front and rear roll angle should be equal, which gave:

$$\frac{x_{FLS}+x_{FLT}-x_{FRS}-x_{FRT}}{t} = \ldots \frac{x_{RLS}+x_{RLT}-x_{RRS}-x_{RRT}}{t} \quad (8)$$

The free body analysis of sprung mass gave following relation:

$$(K_{SF}x_{FLS}+K_{SR}x_{RLS})t = \ddot{y}Wh_S + W\left(h_S\frac{x_{FLS}+x_{RLS}}{t}+h_{CG}\frac{x_{FLT}+x_{RLT}}{t}\right) \quad (9)$$

where W denotes the total weight of the vehicle, h_S denotes the vertical distance of the CG of sprung mass from the roll axis, h_{CG} denotes the height of CG of the vehicle. There are 4 equations and 4 unknowns. Rearranging above Equations 6, 7, 8, 9 gives following LLT equation for front:

$$\Delta W_F = \frac{\ddot{y}WK_F}{t}*\ldots \frac{\left(h_{CGS}-\frac{Wh_S}{t^2}\left(\frac{l_Fh_F}{lK_{SR}}+\frac{l_Rh_F}{lK_{SF}}\right)+K_R\left(1-\frac{Wh_{CG}}{K_tt^2}-\frac{Wh_S}{K_{SR}t^2}\right)\left(\frac{l_Fh_R}{lK_{SR}}-\frac{l_Rh_F}{lK_{SF}}\right)\right)}{\left(\alpha(K_F+K_R)-\frac{Wh_S}{t^2}\left(\frac{K_RK_{SF}+K_FK_{SR}}{K_{SR}K_{SF}}\right)\right)} \quad (10)$$

where h_{CGS} denotes the height of the CG of sprung mass, K_F, K_R are the vertical stiffness of front and rear suspension:

$$\alpha = 1-\frac{Wh_{CG}}{K_tt^2}, \quad \frac{1}{K_F}=\frac{1}{K_{SF}}+\frac{1}{K_T}$$

Equation 10 gives the accurate representation of LLT. The equation for the rear can be obtained by replacing the front parameters to rear parameters. Since terms of Equation 10 are difficult to explain, further simplifications were made. The magnitude of stiffness of springs and tires are high compared to magnitude of weight of vehicle, so:

$$1 >> \frac{Wh_{CG}}{K_tt^2}+\frac{Wh_S}{K_{SR}t^2}, \quad \frac{Wh_S}{t^2}\left(\frac{l_Fh_F}{lK_{SR}}+\frac{l_Rh_F}{lK_{SF}}\right)\approx 0$$

Using the above approximations and after some rearrangement of Equation 10, following equations were derived:

$$\Delta W_F = \frac{\ddot{y}W}{t}*\ldots \frac{\left(K_Fh_S+(K_F+K_R)\frac{l_Rh_F}{l}+\frac{K_FK_R}{K_T}\left(\frac{l_Fh_R}{l}-\frac{l_Rh_F}{l}\right)\right)}{\left(\alpha(K_F+K_R)-\frac{Wh_S}{t^2}\left(\frac{K_RK_{SF}+K_FK_{SR}}{K_{SR}K_{SF}}\right)\right)} \quad (11)$$

The equation of the rear could be given by:

$$\Delta W_R = \frac{\ddot{y}W}{t}*\ldots \frac{\left(K_Rh_S+(K_F+K_R)\frac{l_Fh_R}{l}-\frac{K_FK_R}{K_T}\left(\frac{l_Fh_R}{l}-\frac{l_Rh_F}{l}\right)\right)}{\left(\alpha(K_F+K_R)-\frac{Wh_S}{t^2}\left(\frac{K_RK_{SF}+K_FK_{SR}}{K_{SR}K_{SF}}\right)\right)} \quad (12)$$

The meaning of the above equations are explained in the next chapter.

5 PROPOSED EQUATION ANALYSIS

Equation 11 and 12 shows the factors which contribute to weight transfer. The three terms in numerator represents three factors which contribute in LLT. The first part, i.e. h_S denotes the effect of load transfer due to rolling of vehicle about the roll axis. The second term, i.e. l_Fh_R/l denotes the load transfer due to the jacking force.

The last term denotes the load transfer due to difference in the jacking roll of front and rear of vehicle. This value had opposite sign in front (Equation 11) and rear (Equation 12) LLT. It proves that LLT due to jacking roll difference is torsional.

The last term of LLT depends on two factors, $l_Fh_R/l - l_Rh_F/l$ which could be considered as torsional moment arm and K_FK_R/K_T could be considered as torsion stiffness. For a given torsional moment arm, the magnitude of torsional effect is determined by the value of torsional stiffness i.e. K_FK_R/K_T. If the suspension spring stiffness value is close to the tire stiffness, the torsional stiffness will be high and eventually torsional moment due to difference in jacking roll will be high. Higher torsional moment increases the LLT, which affects the understeer characteristics of vehicle. So in case of passenger cars, where suspension spring stiffness is not high, the LLT due to jacking roll difference is not high. But in case of race cars, the suspension stiffness is quite high, so the LLT due to torsional stiffness will be high.

For the further analysis and calculations, Equation 10 will be used and it will be referred as 'Prop. Equation'. Some approximations were made while deriving equation 11 and 12 so it may not give exact results.

Table 1. Specifications of passenger and race car.

		Passenger car	Race car
Total weight (kg)	W	1325.6	664.3
Sprung weight (kg)	W_s	1223.7	637.1
Front to rear weight ratio (%)		50	5
CG height (mm)	h_{ca}	488.4	245
Front RC height (mm)	h_f	74.2	19
Rear RC height (mm)	h_r	159	78.5
Front spring stiffness (N/mm)	K_{sf}	30	200
Rear spring stiffness (N/mm)	K_{sr}	30	200
Tire vertical stiffness (N/mm)	K_t	250	270
Track width (mm)	t	1500	1420
Wheelbase (mm)	l	2600	3085

6 COMPARISON

A simulation software, CarSim, was used in order to compare Conv. Equation and Prop. Equation. During cornering, contact patch of the tires are subjected to lateral force. To simulate cornering behavior K&C test bed was used. Vehicle was placed on the K&C test bed and lateral force was applied. This procedure was used to eliminate other factors which might affect the LLT, such as steering mechanism and cornering drag.

As discussed in earlier chapter, the effect of torsional moment due to difference in jacking roll is small when the suspension spring is soft. So the comparison was done using two cases. The one was the case using passenger car specifications, and the other was using the race car specifications. Usually the suspension stiffness of race cars are comparable to their tire stiffness. Table 1 shows the model parameters of two cars:

Using data from Table 1, the value of torsional moment arm ($l_F h_R/l - l_R h_F/l$) of passenger car was 1.4 times larger than that of race cars from above specifications. However the value of torsional stiffness ($K_F K_R/K_T$) of race cars was 17 times higher than that of passenger cars. It is expected that the torsional moment due to jacking roll should be high in case of race cars due to its high torsional stiffness.

The analysis was done at the lateral acceleration of $0.5G$ ($1G = 9.8\,\mathrm{m/s^2}$). Since the front to rear weight distribution is equal, a force of $0.5/4 * W$ was applied to contact patch of each tire. The LLT values were calculated as the difference of left and right vertical tire load for front and rear.

7 RESULTS

Tables 2 and 3 shows the comparison of LLT between simulation to Prop. Equation and Conv. Equation respectively for passenger cars.

The values of both Conv. Equation and Prop. Equation were quite close to those from simulation and the percentage error was under 1%. It matches our understanding that Conv. Equation is comparable to Prop. Equation in case of passenger cars characteristics.

Table 2. Comparison of LLT between Simulation and Conv. equation for passenger car.

	Simulation LLT (N)	Conv. Equation LLT (N)	Difference %
Front	1072.6	1076.7	0.38
Rear	1251.0	1260.4	0.75

Table 3. Comparison of LLT between Simulation and Prop. equation for passenger car.

	Simulation LLT (N)	Conv. Equation LLT (N)	Difference %
Front	1072.6	1082.0	0.88
Rear	1251.0	1246.1	−0.39

Table 4. Comparison of LLT between Simulation and Conv. equation for race car.

	Simulation LLT (N)	Conv. Equation LLT (N)	% difference
Front	259.3	244.7	−5.65
Rear	298.7	312.7	4.75

Table 5. Comparison of LLT between Simulation and Conv. equation for race car with 3rd term Equation 11 and 12.

	Simulation LLT (N)	Conv. Equation LLT (N)	Difference (N)	3rd term of Eq. 11
Front	259.3	244.7	14.6	14.6
Rear	298.7	312.7	−14.0	−14.6

Table 4 shows comparison of LLT calculated by simulation to those calculated by Conv. Equation for race car. The Conv. Equation had 6% difference between simulation result and the error value had opposite sign in front and rear. Table 5 shows that the difference between LLT of simulation and Conv. equation is approximately equal to the 3rd term in Equations 11 and 12 which represents the torsional moment arising due to jacking roll. It proves that Conv. Equation does not have the Jacking roll effect.

Table 6 shows the comparison of LLT between simulation and Prop. Equation. Since the torsional moment due to jacking roll was considered for Prop. Equation, the percentage difference with simulation was quite small.

8 CONCLUSION

A new equation was proposed for the calculation of LLT in a vehicle using spring and mass model which

Table 6. Comparison of LLT bewtween Simulation and Prop. equation for race car.

	Simulation LLT (N)	Prop. Equation LLT (N)	% difference
Front	259.3N	259.4	0.04
Rear	298.7N	298.6	−0.02

showed that torsional moment arises due to difference in the jacking roll of front and rear. The torsional moment was negligible in case of passenger cars where the suspension stiffness is quite less than tire stiffness. But in case of race cars where suspension stiffness is comparable to tire stiffness, the torsional moment cannot be neglected. The LLT calculations from Conv. Equation and Prop. Equation were compared with a simulation tool, and it was found that the LLT from Prop. Equation was almost identical to Simulation. So the Prop. Equation can give accurate result using few fundamental vehicle specifications. So, for the calculation of LLT in early phase of vehicle performance development Prop. Equation should be used.

9 FUTURE WORK

For future work, study needs to be done on how the torsional moment varies with the other factors like the stiffness of the suspension springs or tires. The Prop. Equation may be expanded to include the effect of chassis torsional stiffness.

REFERENCES

Abe, M. & Manning W. 2009. Vehicle handling dynamics. Tokyo: Elsevier.

Gillespie, T. D. 1992. Fundamentals of Vehicle Dynamics. Warrandale: Society of automotive engineers.

Mastinu, G. & Ploechl, M. 2014. Road and off-road vehicle system dynamics handbook. London: CRC Press.

Advanced Vehicle Control – Edelmann, Plöchl & Pfeffer (Eds)
© 2017 Taylor & Francis Group, London, ISBN 978-1-138-02992-7

Optimizing suspension systems for feasibility, performance and cost

J. Wimmler, M. Wahle & M. Zimmermann
BMW Group, Munich, Germany

D. Schramm
University of Duisburg-Essen, Duisburg, Germany

ABSTRACT: Enhancing the efficiency in a vehicle development process requires reducing time-consuming tasks such as building prototypes or performing test drives by utilizing more efficient virtual approaches. A common one is numerical optimization. Often, optimization does not consider feasibility of the proposed design. The scope of this paper is a new method that simultaneously considers feasibility and therefore offers great potential for saving both, development time and cost. Based on performance targets of the overall vehicle: first, the requirements on properties of highly integrated subsystems are derived as permissible ranges, and second, suitable suspension architectures that fulfill those requirements are identified. As result, the decision making engineer is provided with objective criteria for choosing a suspension system that suits to his needs. Projections of solution box intervals to 2D design space diagrams are used to find the permissible ranges while the suspension architecture is evaluated by a multi-objective optimization. Two types of suspension architectures are compared in order to achieve their design goals.

1 INTRODUCTION

A vehicle suspension system, e.g., McPherson or double wishbone, is chosen in an early development phase with respect to many criteria, including performance, cost, and feasibility. For optimal performance, the suspension system has to be chosen in combination with other strongly interacting subsystems such as the steering system or tires, as shown in Figure 1 (Mäder 2012, Wimmler et al. 2015). At this point, however, little is known about the final design.

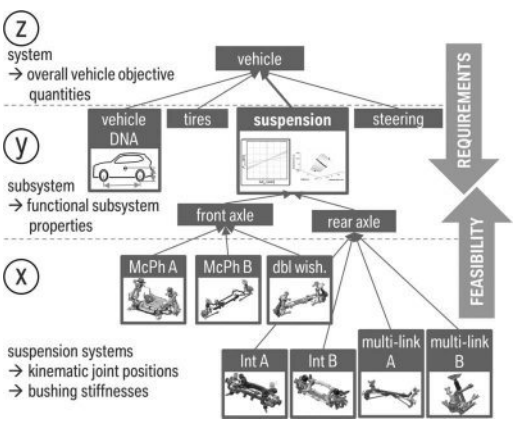


Figure 1. Overall System structure with the relevant performance measures on the system level (z), the subsystem level (y) and design variables on the component level (x).

2 METHODOLOGY

This paper presents a method for the integrated design of suspension systems based on requirement derivation with a particular focus on feasibility. Requirements on the subsystems are derived from the desired overall vehicle dynamics performance, e.g., self-steering-, transient-, and limit behavior. These requirements are independent of the final suspension type that will be chosen. In contrast to classical target cascading (Kim et al. 2003, Wei Chen et al. 2006) they are expressed as permissible ranges of subsystem properties, such as cornering stiffness or roll center height (Wimmler et al. 2015). In the following step the feasibility of those permissible ranges is checked by numerical optimization.

General problem statement. Find the biggest solution box that includes robust and feasible designs. A solution box is calculated by the product of intervals of the permissible ranges. Robustness is measured by the distance of the optimized suspension performance from the center of the solution box.

2.1 *Finding permissible intervals of subsystem properties*

To identify the permissible intervals for example the algorithms described in Eichstetter et al. (2012, 2015) and Zimmermann & von Hoessle (2012) can be used. They can also be found and readjusted manually by the use of projections of box intervals (see Figure 2).

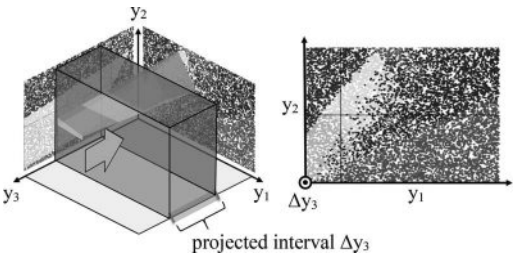


Figure 2. Projection of a solution space.

Table 1. Properties of the neural network set.

one layer feedforward network degrees of freedom:	67	number of objectives: max number of neurons:	50 24

Fast computing neural networks are used in order to reduce the numerical costs of time for the large number of simulations. Table 1 shows typical properties of a neural network set used in the later example.

All relevant suspension properties are considered to ensure the required vehicle performance.

2.2 *Securing the feasibility of the permissible intervals*

The feasibility space in this context contains all designs on the y-level, that may be realized by the design parameters on the x-level. When an overlap between the solution box and the feasibility space exist on the y-level, the requirements derived from the z-level are feasible. In order to ensure feasibility, all performance values of a particular design $y(x)$ have to lie within the former derived permissible ranges. The robustness of a design is measured through the average distance between the center of the permissible intervals and the performance values of a design. Feasibility of a design within the solution box is established in three steps (see Figure 3). First, the requirements are assessed using data of predecessor vehicles. If existing designs are included within the permissible ranges one of them may be chosen as final design. If modifications of an existing design are necessary in order to satisfy the requirements, then the design needs to be adapted in a second step by appropriate modification of design variables, such as kinematic joint positions or bushing stiffnesses. This can be accomplished by numerical optimization. If still no feasible solution can be identified, then in step 3, requirements on the subsystems (y-level) are rebalanced such that feasibility becomes possible, the whole procedure is shown in Figure 3.

Problem statement for feasibility optimization. For k design goals, the distance of the performance value y_i and the center of the permissible interval y_i^{target} should be minimized in relation to the associated permissible interval. In engineering design problems often it is important to find any feasible solution that satisfies all the requirements before optimizing the robustness.

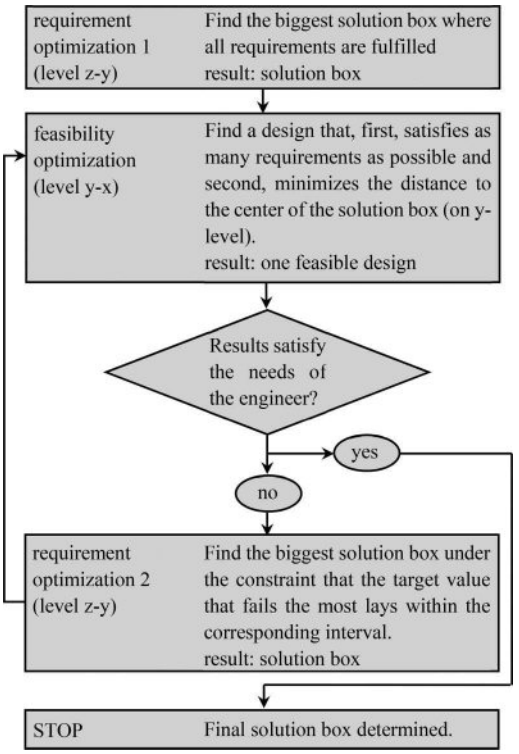


Figure 3. Algorithm to compute a solution box that takes feasibility into account.

Therefore, a penalty factor $p_v(y_i)$ is used in case a performance value does not meet the requirements. Consequently, if no design exists that satisfies the requirements the feasibility optimization will find the design with a minimum number of requirement violations. As a result, the number of requirements that have to be rebalanced is reduced.

$$\underset{y_1 \dots y_k}{\text{minimize}}\ z$$

$$\text{with} \qquad z = \sum_{i=1}^{k} w_i\, p_v(y_i) \left| \frac{y_i - y_i^{\text{target}}}{y_i^{\text{ub}} - y_i^{\text{lb}}} \right| \tag{1}$$

$$\text{and} \qquad p_v(y_i) = \begin{cases} 1 \ if\ y_i^{\text{lb}} \le y_i \le y_i^{\text{ub}} \\ k^2 \ else \end{cases}$$

If the desired robustness varies between the several requirements, a weighting factor w_i can be used. In Figure 4 a three-dimensional example is shown by two projections. Both upper diagrams show the design space interval of y_1 and y_2. The third parameter, y_3, is projected over its permissible range Δy_3. For the diagrams below Δy_2 is the projected interval while the design space interval is shown for y_1 and Δy_3. Variables which are projected are indexed by y_i^p while variables that are visible on the graph axes are indexed by y_i^y.

$$\Delta y_i := \{ y_i \in \mathbb{R} |\ y_i^{\text{lb}} \le y_i \le y_i^{\text{lb}} \} \tag{2}$$

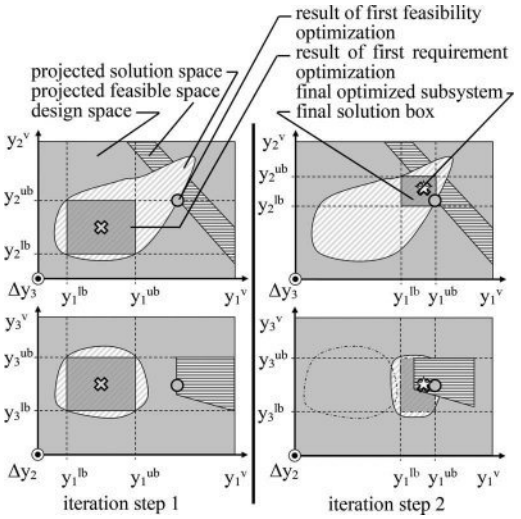


Figure 4. Projections of the solution space and feasible space for the functional suspension properties.

The diagonally hatched area represents the projected solution space wherein every design with a combination of the two y_i^y meets the requirements from the z-level for any $y^p \in \Delta y$. The horizontally hatched area represents the projected feasibility space. Contrary to the definition of the solution space, within this area at least one particular design of $y^p \in \Delta y$ may be realized on the x-level. On the left side of Figure 4 the first iteration step of the feasibility optimization is shown. Starting from the biggest solution box $\Omega_{g\ max}$ the optimization tries to find a set of x that satisfies the subsystem requirements such that all $y_i \in \Delta y_i$. Since no intersection between the solution box and feasibility space exists, the optimization delivers a design that fails one design target (in this case $y_1 \notin \Delta y_1$) and is as close as possible to the center of the solution box (grey dot). Based on the performance values $y(x)$ of the proposed design x, the requirements onto the subsystem are rebalanced such that, y_1^{ub} encloses $y_1(x)$ and the volume of the solution box is maximized (see Figure 4, right side).

Following this, the feasibility optimization is performed again and delivers a specific design that lays close to the center of the adapted solution box (star in Figure 4). For more complex tasks more than two iteration steps may be necessary.

3 APPLICATION

Vehicles are complex systems that have to satisfy a wide range of requirements regarding static and dynamic behavior. In addition, many different parameters from different subsystems influence the driving performance. Therefore it is crucial to take all relevant parameters into account and maintain consistency along the development process. In the following example, permissible intervals for functional properties of a suspension will be derived. Afterwards, a double wishbone and McPherson suspension system will be compared in terms of feasibility for the derived requirements. If one of the two suspension systems shows that it is not possible to reach those requirements, they will be rebalanced in order to enable the feasibility of the suspension system.

3.1 *Deriving requirements from overall vehicle targets on functional suspension properties*

Due to the large number of requirements involving the driving behavior of a vehicle, 54 objectives, z_i, ensure the desired performance. They act either as lower bound (e.g. maximum acceleration), upper bound (e.g. phase difference angle between yaw velocity and lateral acceleration at 1Hz) or as permissible interval between lower and upper bound (e.g. yaw velocity response). Based on those objectives, a set of permissible ranges for functional suspension properties, Δy, is derived. See Table 2 for an overview of the variables.

Fields with grey background color are only evaluated with an elastokinematic suspension model. The functional suspension properties may be expressed through multi-parameter plots, or, for better understanding, as ranges of characteristic curves (see Figure 5).

3.2 *Verification of feasibility considering kinematics*

After a set of permissible ranges for the functional suspension properties is found, the two suspension systems are evaluated by a feasibility optimization. For efficiency improvements, artificial neural networks (ANNs) are used here as well. Therefore, first a design of experiments (DOE) using Monte Carlo sampling is used. The ANNs in this chapter rely on a kinematic suspension model for fast calculation of the DOE. All relevant parameters such as kinematic point positions are varied within a range of $+-15$ mm. In the following step, a response surface is trained using the Neural Network Toolbox in Matlab® before the optimization is performed. Figure 6 compares the results of the optimization between both suspension systems. On the side of the double wishbone suspension system, we see that it satisfies the requirements in a robust manner since the performance lies close to the center of the permissible intervals.

The optimization result of the McPherson suspension system shows that it was not even possible to find any solution that satisfies the requirements. To enable the McPherson system, the requirements onto the suspension system have to be rebalanced in order to generate a feasible design on the x-level that satisfies the overall vehicle targets. Since each performance value in Figure 6 is shown in relation to the required performance interval, it can be estimated easily how much the individual requirements have to be adapted in order to ensure their feasibility. In this example the permissible intervals were adapted manually within four

Table 2. Overview of the functional suspension properties on the y-level.

Functional suspension properties	Value at construction level	Gradient wheel travel	Value at min. steering angle	Value at max. steering angle	Gradient vs. steering angle	Gradient vs. lateral force
toe (min)	A1	A2				A6
camber (min)	B1	B2	B3	B4		B6
scrub radius (mm)	C1	C2	C3	C4		
kinematic trail (mm)	D1	D2	D3	D4	D5	
steering linkage transmission ratio (mm/°)	E1	E2	E3	E4		
roll center height (mm)	F1	F2				
max. rack stroke (mm)	G1					
wheel load lever (mm)	H1	H2	H3	H4	H5	

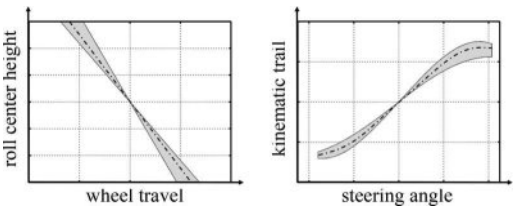


Figure 5. Permissible intervals of functional suspension properties (without variation of the construction level).

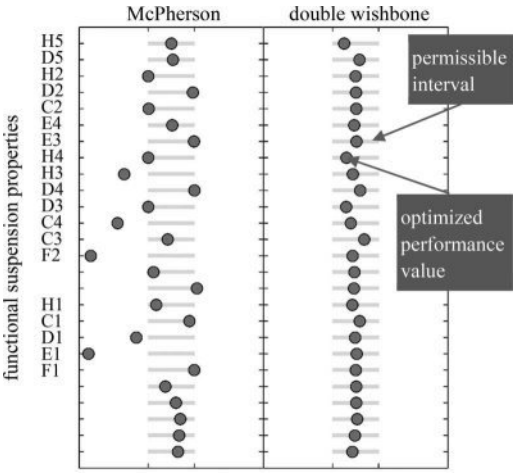


Figure 6. Results of the first iteration of the feasibility optimization.

iteration steps, using the projection method described in Chapter 2.2. Figure 7 shows relevant projections which were used in order to find a feasible design. An overview of the adapted permissible intervals is shown in Table 3.

Following this the McPherson suspension system is optimized again. Figure 8 compares the new result of the optimization with the old one and shows in which manner the kinematic joint positions have to be adapted. Now, since all the requirements are fulfilled the McPherson system can also be used. Nevertheless it has a lower robustness compared to the double

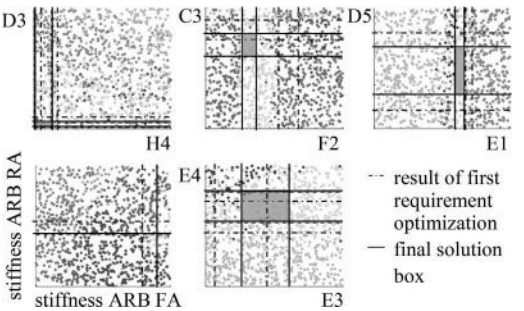


Figure 7. Projected view of the adapted permissible intervals on y-level.

wishbone suspension since the distance between the performance values of the design and boundaries of the permissible interval is smaller. As a result, the double wishbone suspension system would be the first choice. One reason for that could be the restricted maximum variation of the kinematic points seen in Figure 8.

3.3 *Verification of feasibility considering elastokinematics*

After ensuring the feasibility of the pure kinematic requirements, the elastokinematics have to be checked as well. Therefore ANNs are trained on the input/output data of elastokinematic simulations made in a multi-body simulation tool, in this case Adams®. The benefit in the use of this more complex model is that relevant additional objectives (see fields with grey background color in Table 2) and parameters of the subsystem may be considered now. Additional input parameters such as the bushing stiffness are parametrized with scaling factors in all three space directions, they can be varied between 0.5 and 1.5. To find a feasible solution for the elastokinematics, first, lower and upper bounds of the additional vehicle parameters y_i are adjusted such that the volume of the solution box is maximized. Second, the feasibility optimization is performed again, including the additional design measures y_i^{target} and design variables x_i. It is possible to acquire the position of the kinematic points from the former kinematic optimization

Table 3. Parameters that have to be changed in order to enable the McPherson suspension system.

Adapted intervals	F2	C3	D3	D5	H4	E1	E3	E4
Δ lower bound	−1.4	−13	−3	0.24	−0.9	−9	3.5	5
Δ upper bound	−1.6	−11	−3	−0.27	−0.9	6	3.0	5
Adapted parameters				Δ Value				
Δ pinion gear ratio (mm/revolution)				−0.7				
Δ ARB stiffness FA (N/mm)				+2.56				
Δ ARB stiffness RA (N/mm)				−1.53				

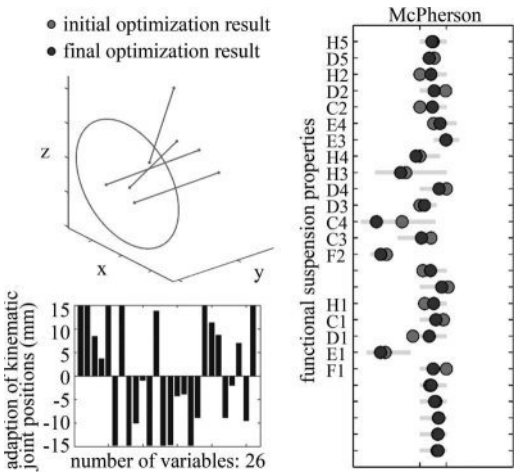


Figure 8. Results of the final kinematic feasibility optimization of the McPherson suspension.

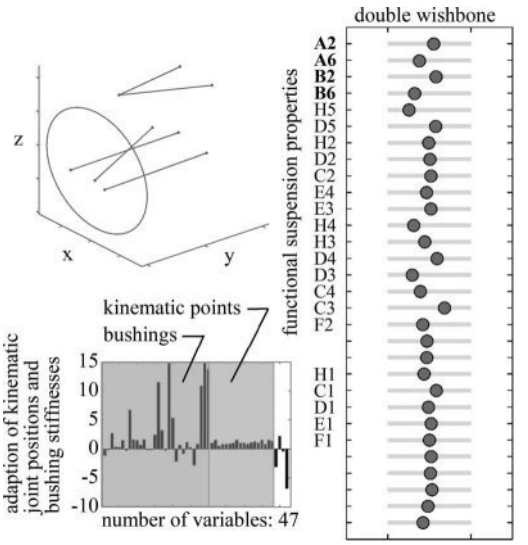


Figure 9. Result of the elastokinematic feasibility optimization of the double wishbone suspension.

or start from scratch. In this case the first approach will be used in order to reduce effort. An advantage of the second approach is that small variations of the performance values between the kinematic and elastokinematic model will be compensated. Figure 9 shows the results of the optimization.

4 FUTURE RESEARCH RELATED TO VEHICLE CONTROL

So far, the treated example just covers the mechanical suspension, since it is important to have a solid failsafe basis. Nevertheless, vehicle control systems play a key role in forming characteristic vehicle dynamics and increase of the spread between driving comfort and driving dynamics. In Figure 10, an example is shown where requirements on the suspension system are shifted by the use of torque vectoring. The torque vectoring is implemented as map-based, open-loop control system. Therefore, the torque difference between the left and right wheel is computed based on the vehicle velocity and the steering angle. The actuator is modeled with a first order time delay. Thanks to the possibility to shift solution spaces in specific directions, the need for design compromises within a vehicle platform possibly can be reduced while the differentiation of the vehicles character is increased.

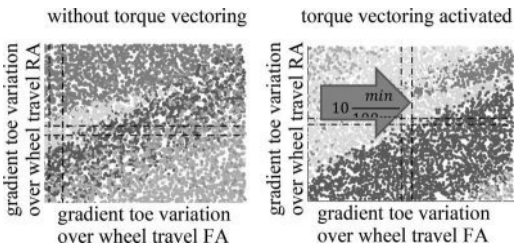


Figure 10. Link of the presented method to vehicle control.

5 CONCLUSION

Solution spaces for functional suspension properties were derived from overall vehicle targets. Based on the knowledge of a favorable design in terms of feasibility, the solution box was readjusted in order to find a set of requirements that is feasible. The final result combines the advantages of classical solution spaces and the all in one approach where kinematic points are optimized in order to find a result that satisfies overall vehicle targets. Thus, requirements on subsystems are decoupled, while the development engineer of the subsystem has several different options to choose his

design parameters, in order to satisfy the subsystem requirements. On subsystem-level the decision for a kinematic or elastokinematic model depends strongly on the time schedule and the messages that should be generated. The inclusion of control systems in this method offers great potential for the concurrent design in vehicle dynamics. Due to the simplified open-loop approach, the performance of the control system is not optimal. The method will show its full potential when the control systems are modeled in a more complete way, which will possibly increase the size of the solution space.

REFERENCES

Eichstetter, M., Redeker, C., Müller, S., Kvasnicka, P., Zimmermann, M. 2014. Solution spaces for damper design in vehicle dynamics. chassis. tech.

Eichstetter, M., Müller, S., Zimmermann, M. 2015. Product Family Design With Solution Spaces. Journal of Mechanical Design.

Fender, J., Graff, L., Harbrecht, H., Zimmermann, M. 2014. Identifying Key Parameters for Design Improvement in High-Dimensional Systems with Uncertainty. Journal of Mechanical Design.

Kim, H. M., Michelena, N. F., Papalambros, P. Y., Jiang, T. 2003. Target Cascading in Optimal System Design. Journal of Mechanical Design.

Mäder, D. 2012. Simulationsbasierte Grundauslegung der Fahrzeug-Querdynamik unter Berücksichtigung von Erfahrungswissen in der Fahrdynamikentwicklung. Dissertation.

Wei Chen, H. L., Kokkolaras, M., Papalambros, P. Y., Kim, H. M. 2006. Probabilistic Analytical Target Cascading: A Moment Matching Formulation for Multilevel Optimization Under Uncertainty. Journal of Mechanical Design.

Wimmler, J., Schramm, D., Wahle, M., Zimmermann, M. 2015. Concurrent Design of Vehicle Tires and Axles. chassis. tech.

Zimmermann, M. & von Hoessle, J. 2012. Computing solution spaces for robust design. International Journal for Numerical Methods in Engineering.

Advanced Vehicle Control – Edelmann, Plöchl & Pfeffer (Eds)
© 2017 Taylor & Francis Group, London, ISBN 978-1-138-02992-7

Multi-objective cooperative control of vehicle stability with electro hydraulic brake

Zhilin Jin, Chao Wang & Lei Zhang
Department of vehicle Engineering, Nanjing University of Aeronautics and Astronautics, Nanjing, China

Amir Khajepour
Department of Mechanical & Mechatronics Engineering, University of Waterloo, ON, Canada

ABSTRACT: In order to improve vehicle stability during critical situations at high speeds, a multi-objective cooperative control strategy is proposed with an Electro Hydraulic Brake (EHB). Taking the longitudinal, lateral, yaw, and roll motion into consideration, a four degree of freedom vehicle model is presented. As the actuator used to produce braking torque, the EHB is modeled and verified by experiments on a test bench. The yaw rate is used to design a yaw stability control strategy, and the Dynamic Rollover Index is presented to describe the vehicle rollover stability. Then, the LQR method is applied to design a multi-objective cooperative control strategy for vehicle yaw and roll stability. Also, the performance of the control strategies are analyzed by several typical case simulations, such as J-turn, fishhook and double lane change. The results show that the multi-objective cooperative control strategy for vehicle stability with the EHB can effectively reduce vehicle rollover risk and significantly improve the yaw stability of the vehicle.

1 INTRODUCTION

In recent years, vehicle rollover has been a hot topic in the field of active safety research. The National Highway Traffic Safety Administration annually reports accidents with increasing concerns regarding the rollover casualty rates and property damage of many types of vehicles. Statistics show that out of 5.687 million traffic accidents in United States in 2013, vehicle rollover accidents accounted only for 1.7%, but the number of casualties in vehicle rollover accidents accounted for 19.1% (NHTSA, 2015). There are two distinct types of vehicle rollover: tripped and un-tripped rollover. Tripped rollover is usually caused by the vehicle impacting something else; whereas, driver induced un-tripped rollover can occur during typical driving situations, such as excessive speed during cornering, obstacle avoidance and severe lane change maneuvers for a sport utility vehicle (SUV).

In order to reduce vehicle rollover accident, a lot of research about vehicle rollover dynamics and rollover prevention methods have been published in the past thirty years. Vehicle rollover dynamics includes stability analyses of vehicle rollover (Jin *et al*., 2014; Yao *et al*., 2014) and a prediction of the rollover propensity of vehicle (Jin *et al*., 2007; Czechowicz & Mavros, 2014). For example, a roll rate sensor together with the information from the conventional electronic stability control hardware was used to detect a vehicle's roll condition associated with a potential rollover (Xu & Tseng, 2007; Lu *et al*., 2007).

Rollover prevention, is also necessary to improve the stability of vehicle rollover. For example, active suspension or active anti-roll bar were used to improve roll stiffness and vehicle damping (Zhu & Ayalew, 2014; Muniandy *et al*., 2015). Active steering and differential braking were used to produce an anti-yaw moment to prevent vehicle rollover (Parida *et al*., 2014; Chiu *et al*., 2010). These measures of vehicle rollover prevention have their own characteristics. A large amount of space is required for the expensive active suspension and active anti-roll bar installation. Active steering changes the intention of manipulation of vehicle; while, braking forces should be produced instantly to meet the need of rollover prevention. In order to make full use of the advantages of these measures, the integrated chassis control strategy was presented in recent years (Seongjin, 2012). Fortunately, some advanced brake systems have been studied and applied to vehicle (Jin *et al*., 2012).

The contribution of this paper is to design a control strategy using differential braking based on the EHB system, which focuses on the rollover prevention for an SUV in critical driving maneuvers such as vehicle cornering and lane-change at high speeds. The dynamic equation of a nonlinear model of four degrees of freedom is established for vehicle rollover, including the dynamics of the EHB system. Then, a multi-objective coordinated vehicle stability control

*Supported by the Fundamental Research Funds for the Central Universities, NO. NS2016025.

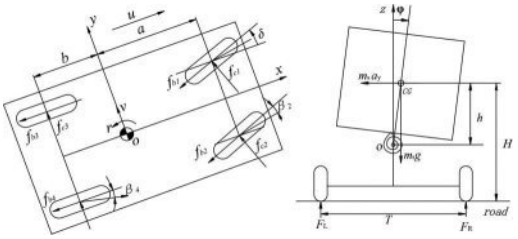


Figure 1. Four DOF model of vehicle.

strategy is proposed to obtain the yaw stability and roll stability of SUV. Furthermore, in this paper, some case studies are presented and concluding remarks are made.

2 VEHICLE MODEL

The effects of the unsprung mass and lateral wind are ignored in this research, whereas nonlinear characteristics caused by a large front wheel steering angle and the coupling relationship between longitudinal and lateral motions are taken into consideration. As shown in Fig. 1, a nonlinear model of four degrees of freedom is established for SUV rollover, including longitudinal, lateral, yaw, and roll motions.

From the above vehicle model, a frame of coordinates is fixed on the vehicle body. Then, the dynamic equations of longitudinal, lateral, yaw, and roll motions can be established from the principle of D'Alembert as follows.

Longitudinal motion:

$$m(\dot{u}-vr)=F_x \tag{1}$$

Lateral motion:

$$m(\dot{v}+ur)-m_s h\ddot{\varphi}=F_y \tag{2}$$

Yaw motion:

$$I_z\dot{r}=M \tag{3}$$

Roll motion:

$$I_x\ddot{\varphi}-m_s h(\dot{v}+ur)=m_s gh\varphi-c_\varphi\dot{\varphi}-k_\varphi\varphi \tag{4}$$

Then, the longitudinal force F_x, lateral force F_y and yaw moment M can be obtained as follows.

$$F_x=-(F_{b1}+F_{b2})\cos\delta-(F_{c1}+F_{c2})\sin\delta-F_{b3}-F_{b4} \tag{5}$$

$$F_y=-(F_{b1}+F_{b2})\sin\delta+(F_{c1}+F_{c2})\cos\delta+F_{c3}+F_{c4} \tag{6}$$

$$\begin{aligned}M=&-(F_{b1}+F_{b2})\sin\delta\cdot a+(F_{c1}+F_{c2})\cos\delta\cdot a\\&+\left[(F_{b1}-F_{b2})\cos\delta+(F_{c1}-F_{c2})\sin\delta\right]\cdot T/2\\&+(F_{b3}-F_{b4})\cdot T/2-(F_{c3}+F_{c4})\cdot b\end{aligned} \tag{7}$$

where m = total mass; m_s = sprung mass; u = longitudinal velocity; v = lateral velocity; r = yaw rate; ϕ = roll angle; a = distance from the center of gravity to front axle; b = distance from the center of gravity to rear axle; I_z = inertia of yaw moment; I_x = roll moment inertia; δ = front wheel steering angle; h = roll arm length; H = height of gravity center; k_ϕ = roll stiffness of suspension, c_ϕ = roll damping of suspension, T = track width; F_{bi} = longitudinal force of the tires; and F_{ci} = lateral force of the tires ($i = 1, 2, 3, 4$).

Considering the effects of roll steering and roll camber on the side characteristics of the tire, the slip angle of each wheel can be expressed as

$$\beta_1=\arctan\frac{v+ar}{u-rT/2}-\delta-c_f\varphi \tag{8}$$

$$\beta_2=\arctan\frac{v+ar}{u+rT/2}-\delta-c_f\varphi \tag{9}$$

$$\beta_3=\arctan\frac{v-br}{u-rT/2}-c_r\varphi \tag{10}$$

$$\beta_4=\arctan\frac{v-br}{u+rT/2}-c_r\varphi \tag{11}$$

Taking the nonlinear characteristics of the tire when cornering into consideration, the lateral forces can be calculated as:

$$F_{c1,2}=-k_f\beta_{1,2}+k_f\beta_{1,2}^3 \tag{12}$$

$$F_{c3,4}=-k_r\beta_{3,4}+k_r\beta_{3,4}^3 \tag{13}$$

where β_i = slip angle of tires ($i = 1, 2, 3, 4$); c_f = front wheels equivalent roll coefficient; c_r = rear wheels equivalent roll coefficient; k_f = cornering stiffness of front wheels; and k_r = cornering stiffness of rear wheels.

3 ELECTRO HYDRAULIC BRAKING

3.1 *Test bench of EHB*

To study the EHB system, the test platform is developed, as shown in Figure 2. As a brake-by-wire system, EHB has numerous advantages over a traditional brake system – its pressure gradients in a panic brake maneuver are greater than those obtainable with a conventional system since the accumulator can be set at a high pressure level, so it can determine a very fast pressure increase at the beginning of the maneuver. Also, EHB permits a different brake pressure to rise depending on the brake maneuver.

3.2 *Model of EHB*

From the working principle of the EHB system, there are three operation modes. (a) Pressure build-up. The wheel cylinder is connected to a high pressure accumulator fed by a pump. The brake fluid flows out of the high pressure accumulator into the wheel cylinder and the pressure of the wheel cylinder increases.

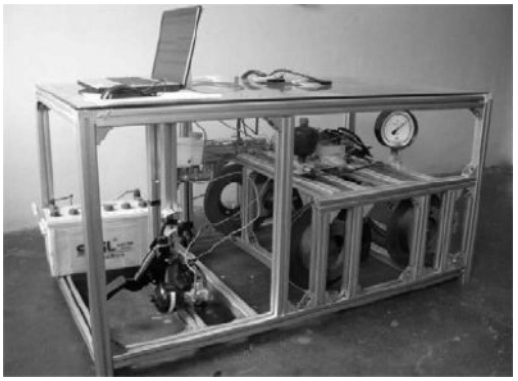


Figure 2. Test platform of EHB.

(b) Pressure holding. The connections from the wheel cylinder to the high pressure accumulator, to the master cylinder, and to the reservoir are interrupted, and the pressure of the wheel cylinder is kept constant. (c) Pressure reduction. The wheel cylinder is connected to the reservoir. The brake fluid flows out of the wheel cylinder into the reservoir and the pressure of the wheel cylinder drops.

The dynamic equations of the mode of pressure build-up and pressure reduction can be expressed as:

$$\frac{dp_w}{dt}=\frac{C_b A_b}{K_b V_b}\left[p_0\left(\frac{V_0}{V_0+qt}\right)^{\gamma}-p_w\right]^n \tag{14}$$

$$\frac{dp_w}{dt}=-\frac{C_b A_b}{K_b V_b}p_w^n \tag{15}$$

where C_b = flow coefficient of the solenoid valve; A_b = area of the orifice throttle; K_b = bulk modulus of the brake oil; V_b = volume of the wheel brake cylinder; n = index of the solenoid valve; p_w = pressure of the wheel cylinder; q = average flow rate; γ = adiabatic index; p_0 = initial pressure of the gas chamber of the accumulator; and V_0 = initial volume of the gas chamber of the accumulator.

3.3 *Model validation*

The parameters of the model have been determined by means of the regressive analytics (Jin *et al*., 2012).

As shown in Figure 3, both the experimental result and the simulation result can track the reference pressure signal within 100 ms. The wheel cylinder pressure builds up from 0 to 10 MPa and drops from 10 MPa to 0 within 100 ms. As much, the dynamic responsibility of the EHB system shows that it is fast and accurate. Also, the test result verifies that the model of EHB system is correct and reliable.

4 VEHICLE STABILITY CONTROL

From the principle of differential braking, the most effective anti-yaw moment can be obtained by applying a braking force at the front-outer wheel rather than

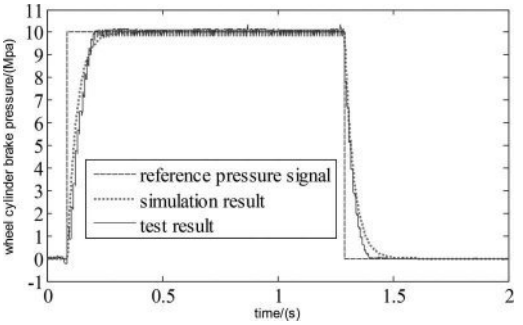


Figure 3. Dynamic performance of EHB system.

any other wheel when vehicle moves in a cornering (Chen & Peng, 2001). So, the controllable braking force by an EHB system is only applied to the front wheels. Although the actuator can provide enough brake torque, its magnitude at each wheel is still limited by other factors, such as the coefficient of road adhesion and the tire's vertical load. From the vehicle model, the brake force at each wheel is constrained by

$$F_{b1}\le\frac{\mu mg(1+DRI)b}{2(a+b)} \tag{16}$$

$$F_{b2}\le\frac{\mu mg(1-DRI)b}{2(a+b)} \tag{17}$$

where μ = coefficient of road adhesion.

The anti-yaw torque can be then expressed as follows.

$$M=\frac{T}{2}(F_{b1}-F_{b2}) \tag{18}$$

The desired anti-yaw moment will be calculated by the controller. Also, the braking pressure will only be applied at the front-outer wheel from the principle of differential braking. So, F_{b1} is zero and F_{b2} can be obtained from equation (18) when the desired anti-yaw torque is negative; F_{b2} is zero and F_{b1} can be obtained from equation (18) when the desired anti-yaw moment is positive.

4.1 *Yaw stability control*

When the vehicle is cornering, the desired yaw rate has a proportional relationship to the front wheel steering angle. To keep the vehicle stable, the desired yaw rate should be given as the vehicle turning at a constant value of the front wheel steering angle.

In this research, a two degrees of freedom linear model of vehicle is used to calculate the desired yaw rate. From the model, the desired yaw rate can be written as

$$r_d=\frac{u\cdot\delta}{L(1+Ku^2)} \tag{19}$$

where

$$K=\frac{m}{L^2}\left(\frac{b}{k_f}-\frac{a}{k_r}\right)$$

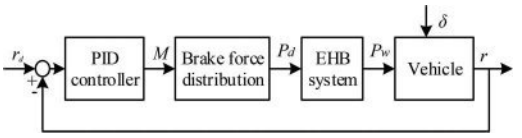


Figure 4. Block diagram of the yaw stability control.

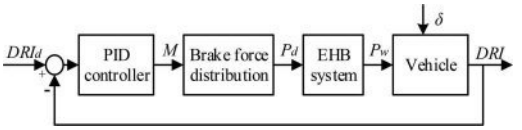


Figure 5. Block diagram of the roll stability control.

where L is the wheelbase of the vehicle.

As shown in Figure 4, a PID control algorithm is applied to calculate the anti-yaw moment. From the equation (18), the brake force can be distributed to the front-outer wheel. Then, the desired brake pressure of the front-outer wheel P_d can be obtained. Also, the EHB system will provide the real brake pressure of the front-outer wheel P_w to the vehicle.

4.2 *Roll stability control*

To improve roll stability of the vehicle, a roll stability control strategy should be designed. In the previous research (Jin *et al*., 2007), a dynamic stability factor (DSF) was defined to evaluate the dynamic rollover boundary of the vehicle. So, a dynamic rollover index (DRI) is proposed to detect the rollover propensity of the vehicle. From the *DSF*, the *DRI* can be expressed as follows.

$$DRI = \frac{Ha_y}{\frac{gT}{2} - \frac{m_s g h^2 \delta / L\left(k_\varphi - m_s g h\right)}{\left[\frac{1}{u^2} - \frac{m}{L^2}\left(\frac{a}{2k_r} - \frac{b}{2k_f}\right) - \frac{m_s h\left(c_f - c_r\right)}{L\left(k_\varphi - m_s g h\right)}\right]}} \tag{20}$$

Then, the block diagram of the roll stability control is shown in Figure 5. Also, a PID control algorithm is applied to calculate the anti-yaw moment, and the real brake pressure of the front-outer wheel to the vehicle can be provided by the EHB system.

4.3 *Multi-objective coordinated control*

As mentioned in the previous section, the yaw stability control strategy can improve yaw stability and the roll stability control strategy can improve roll stability of the vehicle efficiently. But the vehicle will roll over when only improving yaw stability, or it will over steer when only improving roll stability. So, a multi-objective stability should be taken into consideration when a control strategy is applied. As shown in Figure 6, a multi-objective cooperative control is designed for an SUV. Also a linear quadratic regulator (LQR) control method is used to obtain the anti-yaw moment.

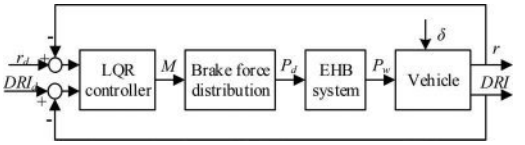


Figure 6. Block diagram of the multi-objective cooperative control for an SUV.

Table 1. Parameters of a sport utility vehicle.

Parameter	Value	Unit
H	1.0	m
T	1.52	m
I_x	753	kg.m^2
I_z	4510	kg.m^2
a	1.15	m
b	1.43	m
c_f	0.055	
c_r	0.07	
c_ϕ	3496	N.m.s/rad
g	9.81	m/s^2
h	0.7	m
k_f	37960	N/rad
k_r	39240	N/rad
k_ϕ	56957	N.m/rad
m	1988	kg
m_s	1663	kg
δ	5	degree

To design the LQR controller, a three degrees of freedom linear roll model of the vehicle is used. Then, the objective function of a multi-objective coordinated control strategy can be expressed as

$$J = \frac{1}{2}\int_0^\infty \left[y^T(t)Qy(t) + u_c^T(t)Ru_c(t)\right]dt \tag{21}$$

where

$x(t) = [v \quad r \quad \varphi \quad \dot{\varphi}]^T$, $y(t) = [DRI \quad r]^T$, $u_c(t) = M$,

$Q = \begin{bmatrix} q_{11} & 0 \\ 0 & q_{22} \end{bmatrix}$, and $R = 1$.

5 NUMERICAL CASES

In order to demonstrate the above control, this section presents three typical case studies for the stability of an SUV, including J-turn, fishhook and double-lane-change maneuvers. The vehicle's physical parameters in Table 1 are assumed. The initial longitudinal velocity is set to 100 km/h, the road adhesion coefficient is set to 0.8, and $q_{11} = q_{22} = 3 \times 10^5$.

Figure 7 shows the simulation results of vehicle stability in the J-turn maneuver.

As shown in Figure 7a, the desired yaw rate is 0.3 rad/s, the yaw rate of the vehicle can track the

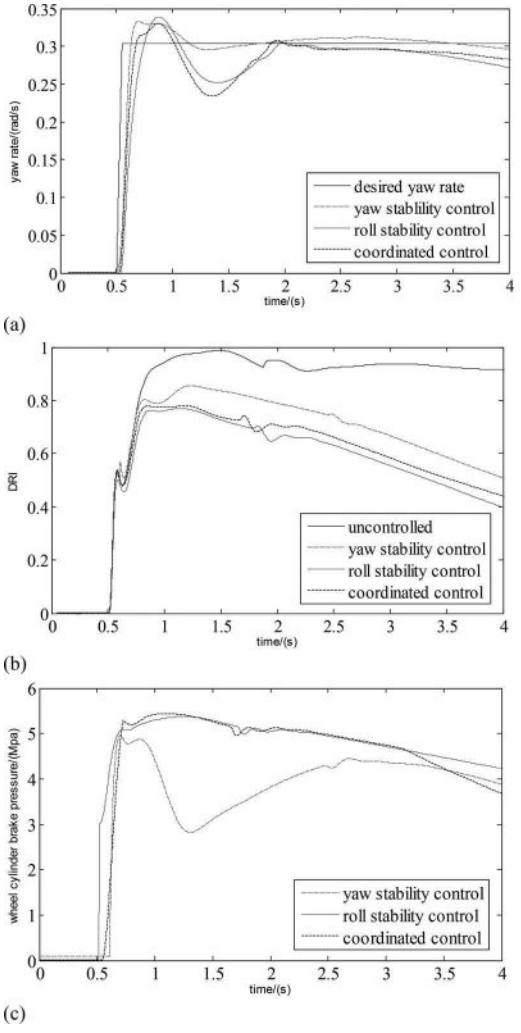


Figure 7. Results in the J-turn maneuver. (a) The yaw stability of the vehicle. (b) The roll stability of the vehicle. (c) The brake pressure of the front-outer wheel cylinder.

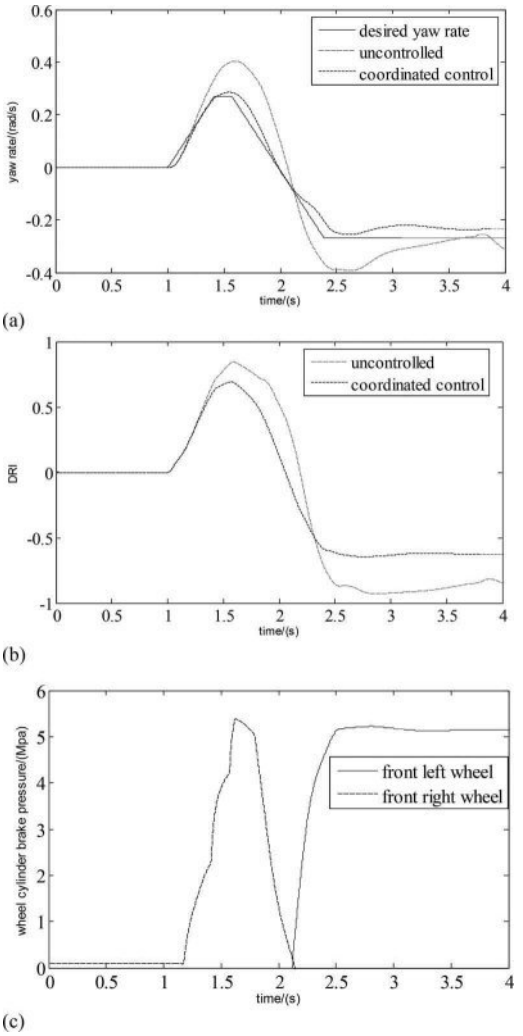


Figure 8. Results in the fishhook maneuver. (a) The yaw stability of the vehicle. (b) The roll stability of the vehicle. (c) The brake pressure of the front-outer wheel cylinder.

desired yaw rate very well with yaw stability control and the coordinated control strategy in the J-turn maneuver. In contrast, the yaw rate fluctuates with large overshoot when vehicle moves in J-turn maneuver using roll stability control strategy.

In Figure 7b, the maximum DRI can be decreased significantly with roll stability control and the coordinated control strategy in the J-turn maneuver. However, the maximum DRI is near a value signifying a lack of control when the vehicle moves in the J-turn maneuvers using yaw stability control strategy. Also, the EHB system can provide braking pressure in a timely manner, as shown in Figure 7c.

So, the multi-objective coordinated control strategy can guarantee vehicle rollover safety and significantly improve the yaw stability in the J-turn maneuver.

Figure 8 and Figure 9 show the dynamic stability of the vehicle in fishhook and double-lane-change maneuvers, respectively. It also shows that the coordinated control strategy can guarantee vehicle rollover safety and significantly improve the yaw stability in these maneuvers. So, the multi-objective coordinated control strategy is robust in different driving conditions.

6 CONCLUSIONS

(1) The EHB system can provide sufficient brake torque to prevent vehicle rollover in a timely manner.
(2) The multi-objective coordinated control strategy based on the EHB can guarantee vehicle rollover safety and significantly improve vehicle yaw stability.

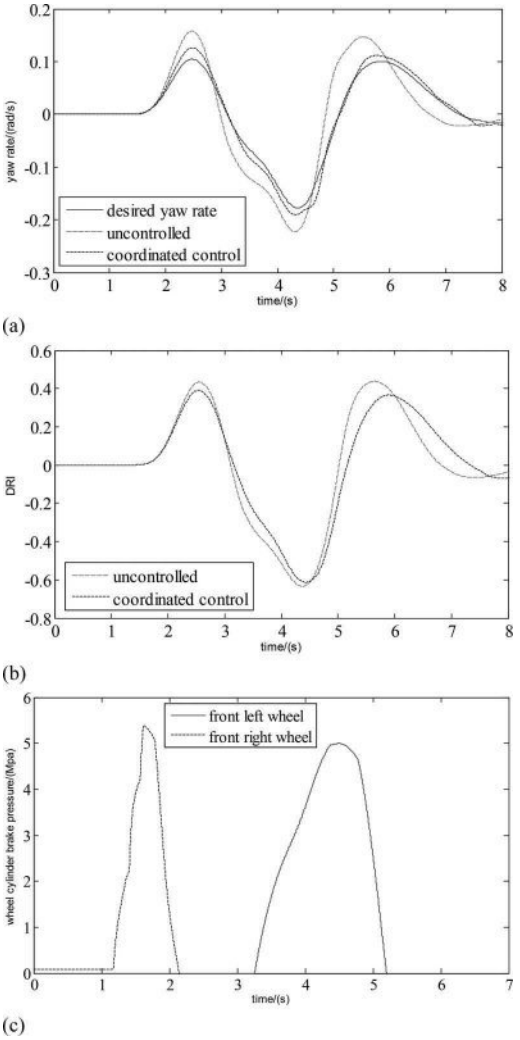


Figure 9. Results in the double-lane-change maneuver. (a) The yaw stability of the vehicle. (b) The roll stability of the vehicle. (c) The brake pressure of the front-outer wheel cylinder.

(3) The multi-objective coordinated control strategy is robust in different driving conditions.

REFERENCES

Chen, B. and Peng, H. (2001). Differential-braking-based rollover prevention for sport utility vehicles with human-in-the-loop evaluations. *Vehicle System Dynamics* 36(4–5): 359–389.

Chiu, J., Solmaz, S., Corless, M. and Shorten, R. (2010). A methodology for the design of robust rollover prevention controllers for automotive vehicles using differential braking. *International Journal of Vehicle Autonomous Systems* 8(2–4): 146–170.

Czechowicz, M., & Mavros, G. (2014). Analysis of vehicle rollover dynamics using a high-fidelity model. *Vehicle System Dynamics* 52(5): 608–636.

Jin, Z., Guo L., Shi, R., et al. (2012). Experimental Study on dynamic characteristics of electro hydraulic brake system for vehicle. *Journal of Mechanical Engineering* 48(12): 127–132.

Jin, Z., Weng, J., & Hu, H. (2007). Rollover stability of a vehicle during critical driving manoeuvres. *Proceedings of the Institution of Mechanical Engineers Part D: Journal of Automobile Engineering* 221(9): 1041–1049.

Jin, Z., Weng, J., Zhang, J., et al. (2014). Dynamic stability of a driver-vehicle rollover system with time delay. *Journal of Vibration Engineering and Technologies* 2(1): 59–71.

Lu, J., Messih, D., & Salib, A. (2007). Roll rate based stability control-the roll stability control system. *In Proceedings of the 20th Enhanced Safety of Vehicles Conference* (No. 07-0136).

Muniandy, V., Samin, P., & Jamaluddin, H. (2015). Application of a self-tuning fuzzy PI–PD controller in an active anti-roll bar system for a passenger car. *Vehicle System Dynamics* 53(11): 1641–1666.

NHTSA. (2015). A compilation of motor vehicle crash data from the fatality analysis reporting system and the general estimates system. Traffic safety facts 2013 report. US, Department of Transportation, Washington, DC, 77–85.

Parida, N., Raha, S., & Ramani, A. (2014). Rollover preventive force synthesis at active suspensions in a vehicle performing a severe maneuver with wheels lifted off. *IEEE Transactions on Intelligent Transportation Systems* 15(6): 2583–2594.

Seongjin, Y. (2012). Design of a robust controller for rollover prevention with active suspension and differential braking. *Journal of Mechanical Science and Technology* 26(1): 213–222.

Xu, L., & Tseng, H. E. (2007). Robust model-based fault detection for a roll stability control system. *IEEE Transactions on Control Systems Technology* 15(3): 519–528.

Yao, Z., Wang, G., Li, X., et al. (2014). Dynamic simulation for the rollover stability performances of articulated vehicles. *Proceedings of the Institution of Mechanical Engineers, Part D: Journal of Automobile Engineering* 228(7): 771–783.

Zhu, Q., & Ayalew, B. (2014). Predictive roll, handling and ride control of vehicles via active suspensions. *American Control Conference* 2102–2107.

Stability and modelling

Advanced Vehicle Control – Edelmann, Plöchl & Pfeffer (Eds)
© 2017 Taylor & Francis Group, London, ISBN 978-1-138-02992-7

Straight ahead running of a non linear car and driver model

F. Della Rossa, O. Sukharev & G. Mastinu
Politecnico di Milano, Milan, Italy

ABSTRACT: The paper deals with the bifurcation analysis of a validated simple model describing a vehicle+driver running straight ahead. The mechanical model of the car has two degrees of freedom and the related equations of motion contain the nonlinear tyre characteristics. The driver is described by a non linear model. Bifurcation analysis is adopted for characterizing straight ahead motion at different speeds for different drivers. A non linear sensitivity analysis is performed as function of driver's parameters. A wealth of unreferenced bifurcations is discovered both for the understeering and for the oversteering vehicle. For the understeering vehicle, a supercritical Hopf bifurcation may occur as forward speed is increased. Also tangent (fold) bifurcations occur as the speed (or disturbance) are further increased. For the oversteering vehicle a subcritical Hopf bifurcation occurs as the speed reaches a critical value. The prevision distance (a driver's control parameter) plays a fundamental role in straight ahead driving. Bot too short or too long prevision distances are negative for straight ahead running. Overtaking maneuvers, when the prevision distance is forced to be too short, may cause a stable limit cycle which is related with the driver stress during such manoeuvers.

1 INTRODUCTION

The non linear dynamic behaviour of a car running straight ahead is very rarely discussed in-depth in the literature, even if such running condition is the most frequent, and sometimes extremely dangerous. In most cases the interest is focused on the vehicle alone (i.e. without driver). However, the vehicle and the driver are two parts of a single system and their interaction can change the overall behaviour of the vehicle. In this paper, the combined dynamic behaviour of the vehicle and the driver is considered when the vehicle is running straight ahead. Many different driver models have been presented in the literature, with different applications and scopes [25]. In the following analysis, a preview tracking driver model is considered [2, 10, 11, 16, 18, 25]. This model is well suited to describe the lateral vehicle dynamics. The longitudinal dynamics are simply not considered here, since they are independent of the steering task of the driver [25]. A discussion about the influence of the driver and the steering system on the dynamic behaviour of a car can be found in [25, 8].

In this paper, the study of the nonlinear behaviour of a vehicle when running straight ahead is discussed in the framework of bifurcation analysis [13].

The paper is organized as follows. Firstly, the vehicle and driver models are introduced for simulating straight ahead motion. Two case studies are discussed, referring either to an understeering or to an oversteering vehicle. A bifurcation analysis is performed, referring to driver's parameters.

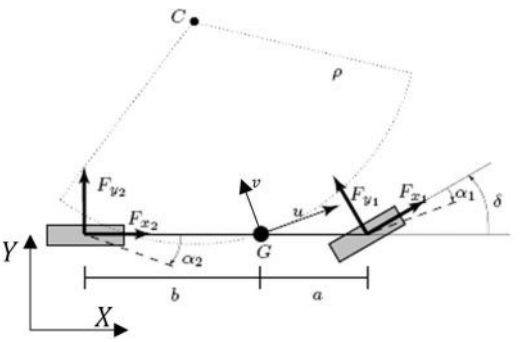


Figure 1. Representation of the single-track model.

2 SYSTEM MODEL

The mechanical model analysed in this paper is the well known 2 d.o.f. single-track model [5, 17, 18, 21, 23] shown in Fig. 1.

The main simplifying hypotheses are:

- the forward speed u = $\sqrt{(\dot{X}\hat{}2 + \dot{Y}\hat{}2)}$ is constant;
- the centre of gravity lies at the ground level;
- the vehicle body is modelled referring to its
- longitudinal axis;
- the resultant of the forces acting at the front and rear axles are applied at the centres of the axles;
- the slip angles α_i, i = 1, 2, and the steering angle δ (see Fig. 1) are small;
- no longitudinal forces are acting at the wheels.

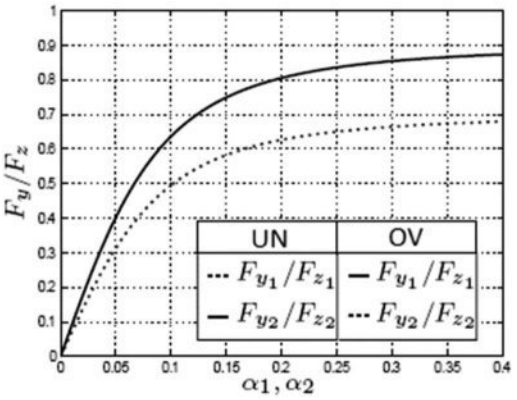


Figure 2. Tyre characteristics of the analyzed vehicle.

2.1 *Vehicle mathematical model*

Under the above hypotheses, the equations of motion with respect to the reference system on the vehicle read [23]

$$\begin{aligned} m(\dot{v} + ur) &= F_{y_1} + F_{y_2} \\ I_z\, \dot{r} &= F_{y_1}\, a - F_{y_2}\, b \end{aligned} \tag{1a}$$

where the dots stand for time-derivative, u and v are the longitudinal and lateral speeds respectively, r is the yaw rate, subscripts 1 and 2 refer, respectively, to the front and rear axle, F_{yi} is the lateral force on the ith (i = 1, 2) axle, m is the vehicle mass, a and b are the distances, respectively, of the front and the rear axle centre from the vehicle's centre of mass, I_z is the moment of inertia of the vehicle around the vertical axis at the centre of gravity. The front and rear slip angles can be obtained through the following equations:

$$\alpha_2 = (v - rb)/u,\ \ \delta - \alpha_1 = (v + ra)/u \tag{1b}$$

The lateral forces F_{yi} (α_i) $(i = 1, 2)$ can be expressed as functions of the slip angles α_i [23]. The functions F_{yi} (α_i), namely the tyre characteristics, can have very different shapes [5, 23]. In this paper, for the sake of space, we will analyze only two different tyre characteristics which cause the vehicle to be understeering (UN) or oversteering (OV). The functions used are reported in Fig. 2, where the two cases are shown. Notice that the two cases can be obtained one from each other just exchanging the front with the rear tyres.

In this work, we want to analyze straight ahead run asking the driver to follow a specific trajectory, i.e. we are not asking only to drive straight, i.e. asking that Y is proportional to X (case treated, e.g., in [5, 34]), thus we set $Y = mX$, with $m = \tan\theta$. We can always set, without loosing generality, $\theta = 0$. In this case, we can assume that $\dot{X} >> \dot{Y}$ (and therefore $u \sim \dot{X}$). Under this hypothesis, model (1) can be rewritten [35, 36] as

$$\begin{aligned} m\,\ddot{Y} &= F_{y_1} + F_{y_2} \\ I_z\,\ddot{\theta} &= F_{y_1} a - F_{y_2} b \end{aligned} \tag{2a}$$

where the double dots stand for second time-derivative of the vertical position and the trajectory angle, while the slip angles should be shifted taking into account the (non-stationary) trajectory's slope, i.e.,

$$\theta - \alpha_2 = \frac{\dot{Y} - b\dot{\theta}}{u},\quad \delta + \theta - \alpha_1 = \frac{\dot{Y} + a\,\dot{\theta}}{u} \tag{2b}$$

2.2 *Driver mathematical model*

A very simple driver model is proposed, inspired to what was proposed in [31, 32, 33, 34]. In particular, we assume that the driver inside the car is able to see a point $L(m)$ forward beyond the current position of the vehicle and is able to estimate the deviation of the lateral position of the vehicle (X, Y) with respect to a reference path (X_{ref}, Y_{ref})

$$\boldsymbol{e} = \begin{pmatrix} X \\ Y \end{pmatrix} + L \begin{pmatrix} \cos\theta \\ \sin\theta \end{pmatrix} - \begin{pmatrix} X_{ref} \\ Y_{ref} \end{pmatrix}$$

(note that in general, $\boldsymbol{e}$, is a two dimensional vector) and that the driver react with a gain h to this error with a delay τ_r (that we approximate with a Taylor expansion since the frequency at which a human can vary the steering angle does not exceed 3 *Hz*).

This is a quite simplified model that will be further improved by considering a more complex model with lead term. In any case this model is the simplest reasonable.

Since in this work we want to analyze only the straight ahead running, at steady state we can use a reference system in which X_{ref} can assume any value, while Y_{ref} has a precise constant value. So the final model of the driver simplifies to the differential equation:

$$\tau_r\, \dot{\delta} = -\delta + h\big(Y + L\, sin(\theta) - Y_{ref}\big) \tag{3}$$

2.3 *Vehicle + Driver mathematical model*

The complete model comprises Eq. (2) coupled with Eq. (3). We have a five-degree of freedom model, which reads

$$\begin{aligned} m\,\ddot{Y} &= F_{y_1} + F_{y_2} \\ I_z\,\ddot{\theta} &= F_{y_1} a - F_{y_2} b \\ \tau_r\, \dot{\delta} &= -\delta + h\big(y + L\sin(\theta) - Y_{ref}\big) \end{aligned} \tag{4}$$

Model equilibria are of the type $[Y, \dot{Y}, \theta, \dot{\theta}, \delta] = [Y_{ref}, 0, 0, 0, 0]$, and represents a vehicle that follows a precise straight trajectory with increasing abscissa (with velocity $\dot{X} = u$) and constant ordinate. The parameters of the model can be divided into three classes:

- the vehicle parameters (tyre characteristics, vehicle mass m, centre of gravity position a, b),
- the control parameters (the forward velocity u and the reference position Y_{ref}) and
- driver parameters (driver delay in control τ_r, reaction h, and ability of prevision L).

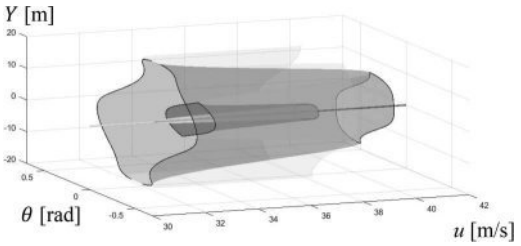


Figure 3. Asymptotic behaviour of model (3) in the UN case.

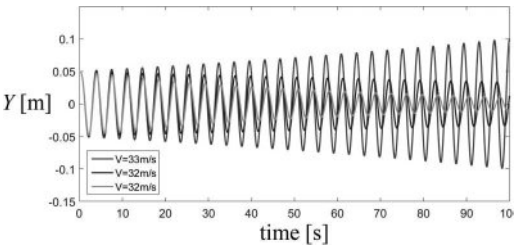


Figure 4. Transient from $Y(0) = 0.1$ m described by model (3) in the UN case.

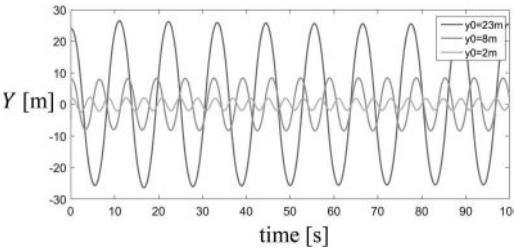


Figure 5. Different stable asymptotic behaviors predicted by model (3) in the UN case for $u = 36$ m/s.

3 ASYMPTOTIC REGIME ANALYSIS

Referring to the parameters reported in the following table, the asymptotic behaviour of the system model is studied for different forward velocity u and reference position $Y_{ref} = 0$.

Parameter	Value	Unit
Vehicle mass m	550	kg
Vehicle yaw moment of inertia I_z	750	kg m^2
Distance from front axle to c.g. a	1.64	m
Distance from rear axle to c.g. b	0.98	m
Delay in control τ_r	0.2	s
Reaction h	0.02	rad/s
Ability of prevision L	12	m

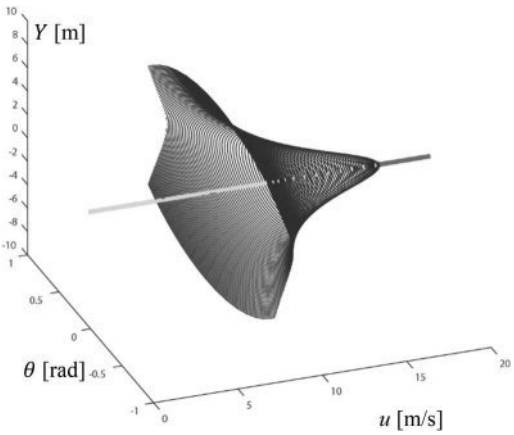


Figure 6. Asymptotic behaviours of model (3) in the OV case.

The analysis is performed by means of continuation algorithms [5, 6, 7, 34].

In the following plots the attactors are colored green and the saddles are colored red.

3.1 *Understeering vehicle*

Fig. 3 shows the behaviour of the understeering (UN) vehicle.

If $u < u^{\mathrm{UN}}_{LPC_0} = 30.8$ m/s the vehicle+driver is stable, i.e. whichever disturbance of whichever amplitude can be managed. If u $> u^{\mathrm{UN}}_{LPC_0} = 30.8$ m/s a stable limit cycle occurs. A Hopf bifurcation occurs. At higher speed a saddle limit cycle occurs. At $u = u^{\mathrm{UN}}_H = 32.37$ m/s, if the disturbance is relatively high the vehicle + driver may work on a relatively big stable limit cycle.

Fig.4 shows how transients may occur starting from speeds approaching $u^{\mathrm{UN}}_H = 32.37$ m/s.

Fig.5 shows how the vehicle + driver can work on different stable limit cycles.

3.2 *Oversteering vehicle*

Fig. 6 shows the behaviour of the oversteering (OV) vehicle.

The vehicle + driver is stable up to the speed $u^{\mathrm{OV}}_H = 17.06$ m/s. For higher speeds the straight ahead running is no more attainable (see Fig. 7). A subcritical Hopf bifurcation occurs. The results are consistent to the ones presented in [34].

We see that the UN and OV vehicle + driver have quite different behaviours referring to Hopf bifurcations. A supercritical Hopf bifurcation occurs for the UN vehicle+driver and a subcritical Hopf bifurcation occurs in the other case. This means that the OV vehicle is quite more dangerous than the UN one.

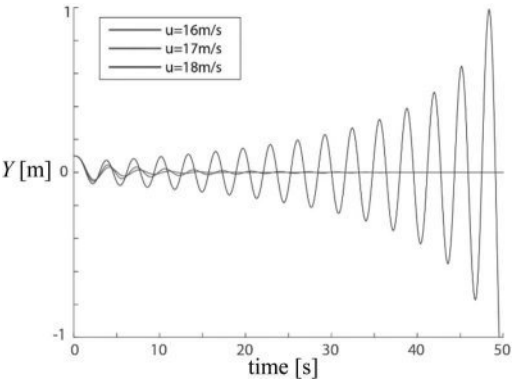


Figure 7. Transient from $Y(0) = 0.1$ m described by model (3) in the OV case.

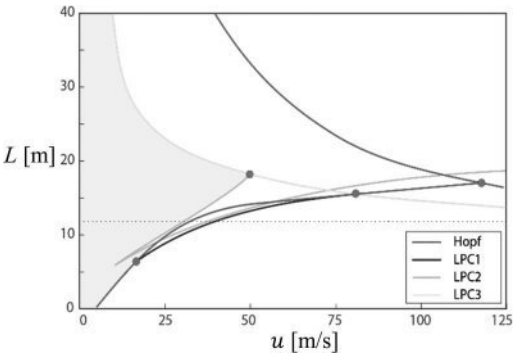


Figure 8. Bifurcation diagram of model (3) in the UN case.

4 PARAMETER SENSITIVITY ANALYSIS

Depending on the prevision distance L, two cases are to be considered for the UN and for the OV vehicle, respectively.

Fig. 8 shows the influence on stability of L and u for an UN vehicle + driver.

Shaded domain represent globally stable solutions. Green curves represent subcritical Hopf bifurcations. The other curves represent bifurcations in which a stable limit cycle collides with an unstable limit cycle and both disappear.

The dotted line is related to the plot in Fig.3. The first bifurcation that occurs is LPC2.

Stability loss occurs not only increasing u, but also increasing or decreasing L.

Fig. 9 shows the influence on stability of L and u for an OV vehicle + driver.

The green curve represents a Hopf bifurcation. The blu lines are node-saddle bifurcation. The shaded green domain refers to the combination of L and u parameters which guarantee a global stable behaviour. The dotted horizontal line refers to $L = 12$ m. We see that the global stable area is quite narrow.

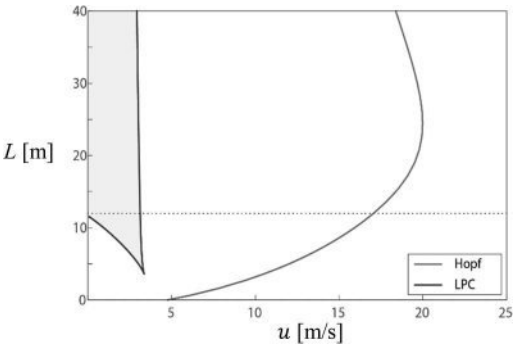


Figure 9. Bifurcation diagram of model (3) in the OV case.

5 CONCLUSION

When a vehicle + driver is running straight ahead, depending on parameters describing driver's control, the motion can be highly non linear.

For the understeering vehicle, supercritical bifurcations may occur that are related to stable limit cycles occurring after a critical speed is surpassed. Actually, at a certain speed (over the critical one), fold bifurcation may occur, i.e. three nested limit cycles may appear, namely a stable, an unstable and finally a high amplitude stable limit cycle are found.

For the oversteering vehicle a subcritical Hopf bifurcation typically occurs.

For the understeering vehicle, the straight ahead motion can be unstable if the prevision distance is too short or two long.

Driver stress during overtaking at high speed in a narrow lane is explained since the driver is forced to reduce the prevision distance and a stable limit cycle can be initiated by the driver.

REFERENCES

[1] R. Andrzejewski and J. Awrejcewicz, Nonlinear Dynamics of a Wheeled Vehicle, Springer, Berlin, 2005.
[2] A. Apel, and M. Mitschke, Adjusting vehicle characteristics by means of driver models, International Journal of Vehicle Design 18, 583–596, 1997.
[3] S. Bruni and G. Mastinu (eds.), Proceedings of the 19th IAVSD Symposium: Dynamics of Vehicles on Roads and Tracks, Milan, Italy, 2005.
[4] B. Catino, S. Santini, and M. Di Bernardo, MCS adaptive control of vehicle dynamics: An application of bifurcation techniques to control system design, Proceedings of the 42nd IEEE Conference on Decision and Control, Maui, Hawaii, pp. 2252–2257, 2003.
[5] F. Della Rossa, G. Mastinu, and C. Piccardi, Bifurcation analysis on an automobile model negotiating a curve, Vehicle System Dynamics 50, 1539–1562, 2012.
[6] A. Dhooge, W. Govaerts, and Yu. A. Kuznetsov, MATCONT: A MATLAB package for numerical bifurcation analysis of ODEs, ACM Trans. Math. Software, 29(2), 141–164, 2003.

[7] E. J. Doedel, A. R. Champneys, T. Fairgrieve, Yu. A. Kuznetsov, B. Oldeman, R. Paffenroth, B. Sandstede, X. Wang, and C. Zhang, AUTO-07P : continuation and bifurcation software for ordinary differential equations, 2007. url: www.dam.brown.edu/people/sandsted/auto/auto07p.pdf

[8] M. Gobbi, G. Mastinu, G. Previati, R. De Filippi, I. Lunetta, D. Moscatelli, Optimal design of an electric power steering system for sport cars, 23rd International Symposium on Dinamics of Vehicles on Roads and Tracks, 19–23 August, Qingdao, China, 2013.

[9] K. Hedrick (ed.), Proceedings of the 20th IAVSD Symposium: Dynamics of Vehicles on Roads and Tracks, Berkeley, CA, USA, 2007.

[10] Hoffmann, E.R., Human control of road vehicles, Vehicle System Dynamics 5, 105–126, 1975/76.

[11] H.Y. Hu and Z.Q. Wu, Stability and Hopf bifurcation of four-wheel-steering vehicles involving driver's delay, Nonlinear Dynamics 22, 361–374, 2000.

[12] Kondo, M., Ajimine, A., Driver's sight point and dynamics of the driver-vehicle-system related to it, Society of Automotive Engineers (SAE), 680104, 1968

[13] Yu. A. Kuznetsov, Elements of Applied Bifurcation Theory, 3rd ed., Springer, New York, 2004.

[14] D.-C. Liaw and W.-C. Chung, A feedback linearization design for the control of vehicle's lateral dynamics, Nonlinear Dynamics 52(4), 313–329, 2008.

[15] Z. Liu, G. Payre, and P. Bourassa, Nonlinear oscillations and chaotic motions in a road vehicle system with driver steering control, Nonlinear Dynamics 9, 281–304, 1996.

[16] MacAdam, C.C., Understanding and modeling the human driver, Vehicle System Dynamics 40(1–3), 101–134, 2003.

[17] G. Mastinu , F. Della Rossa, and C. Piccardi, Nonlinear Dynamics of a Road Vehicle Running into a Curve, Applications of Chaos and Nonlinear Dynamics in Science and Engineering-Vol. 2, Springer, 125–153, 2012.

[18] M. Mitschke, and H. Wallentowitz, Dynamik der Kraftfahrzeuge (4th ed. – in German), Springer, 2004.

[19] E. Ono, S. Hosoe, H.D. Tuan, and S. Doi, Bifurcation in vehicle dynamics and robust front wheel steering control, IEEE Transactions on Control System Technology 6(3), 412–420, 1998.

[20] G. Orosz, B. Krauskopf, and R.E. Wilson, Bifurcations and multiple traffic jams in a vehicle-following model with reaction-time delay, Physica D 21, 277–293, 2005.

[21] H. Pacejka, Simplified Analysis of Steady-state Turning, Vehicle System Dynamics 21, 269–296, 1973.

[22] H. Pacejka, Nonlinearities in road vehicle dynamics, Vehicle System Dynamics 15(5), 237–254, 1986.

[23] H. Pacejka, Tire and Vehicle Dynamics (2nd ed.), Elsevier, 2006.

[24] L. Palkovics and P.J.T. Venhovens, Investigation on stability and possible chaotic motions in the controlled wheel suspension system, Vehicle System Dynamics 21, 269–296, 1992.

[25] M. Plöchl, and J. Edelmann, Driver models in automobile dynamics application, Vehicle System Dynamics 45, 699–741, 2007.

[26] P.A. Shavrin, A chaotic dynamics of the vehicle on the plane, Proceedings of the International Conference on Physics and Control, St. Petersburg, pp. 474–478, 2005.

[27] Q. Zhu and M. Ishitobi, Chaos and bifurcations in a non linear vehicle model, Journal of Sound and Vibration 275, 1136–1146, 2004.

[28] Wallentowitz, H. "Integration of Chassis and Traction Control Systems", Proc. of AVEC '92, 1992, pp. 1–9.

[29] Guo, K. "A study on a Phase Plane Representation for Identifying Vehicle Behavior", Proc. of the 9th IAVSD Symposium, 1985, pp. 10–15.

[30] Hiramatsu, K. et al., "Driver Model for Lane Change Maneuver-Validity of Programmed Steering Model", Trans. of JSAE, No. 38, 1988, pp. 16–20. (in Japanese)

[31] J.R. Ragazzini, "Engineering Aspects of the Human Being as a Servo Mechanism", Meeting of the American Psychological Association, 1948.

[32] Angelo P. Verdi, George N. Ornestein, Richard P. Heydorn, "Effects of display Quickening on human transfer functions during a dual-axis compensatory tracking task", North American Aviation, Incorporated, 1966.

[33] Fumio Harashima, Satoshi Suzuki, "Human Adaptive Mechatronics-Interaction and Intelligence", 9th IEEE International Workshop on Advanced Motion Control, 2006.

[34] Fabio Della Rossa, Massimiliano Gobbi, Gianpiero Mastinu, Carlo Piccardia, Giorgio Previati, "Bifurcation analysis of a car and driver model", Vehicle System Dynamics, Vol. 52, 2014.

[35] Reza N.Jazar, "Vehicle Dynamics:Theory and Application", Springer, 2008.

[36] Masato Abe, "Vehicle Handling Dynamics", Elsevier, 2009.

Advanced Vehicle Control – Edelmann, Plöchl & Pfeffer (Eds)
© 2017 Taylor & Francis Group, London, ISBN 978-1-138-02992-7

Handling and stability control for an in-wheel-motor-driven electric vehicle

Yue Shi, Hui Lu & Fan Yu
School of Mechanical Engineering, Shanghai Jiao Tong University, Shanghai, P.R. China

ABSTRACT: This work is motivated to enhance the handling and stability performance of an in-wheel-motor-driven electric vehicle (EV). The EV prototype has been developed, and the vehicle parameters have been obtained through practical measurements and road tests. A corresponding multi-body dynamics model of the prototype has been built by using SolidWorks and Adams/Car. An Extended Kalman Filter (EKF) is utilized to estimate the vehicle motion states via a simplified full vehicle model with an empirical tire simulation model which has been verified with the experimental data obtained from CarSim Tire Tester. A fractional order PID (FO-PID) controller is designed for the handling and stability requirements of the EV. Simulations in some typical cases have been carried out, and the results show the effectiveness of the proposed control strategy.

1 INTRODUCTION

From 2010 to 2013, an average of 1.25 million people are killed by road traffic accidents every year, let alone much more injuries, which results in a growing interest in modification of vehicle structure and development of vehicle active safety technologies (WHO, 2015). Electric vehicle (EV) with their wheels independently driven by in-wheel motors is considered as one of the promising structures for future vehicles (Sakai, S. et al. 1999).

In this study, a handling stability control strategy is proposed, as shown in Figure 1. An EV prototype equipped with 4 in-wheel motors is developed by Shanghai Jiao Tong University. A multi-body dynamics model of the prototype is then built accordingly by using SolidWorks and Adams/Car, and serves as the control plant. An 8-DOF vehicle model with a nonlinear tire simulation model is established for calculating vehicle motions. An Extended Kalman Filter (EKF) is utilized to online estimate tire load distribution. A Fractional Order PID (FO-PID) controller is designed to trace the desired yaw motion based on a 2-DOF single-track vehicle model.

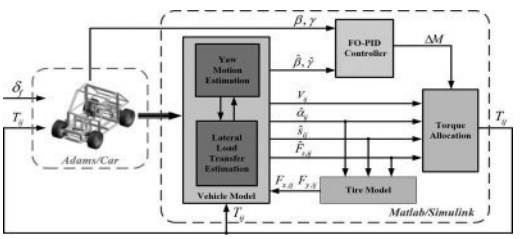


Figure 1. Overall scheme of control strategy.

2 EV PROTOTYPE AND VIRTUAL PROTOTYPING

2.1 *Development of EV prototype*

An EV prototype is developed by Institute of Automotive Engineering, Shanghai Jiao Tong University, as shown in Figure 2. A pair of Li-Ion battery packages, which are consisted of 64 cells, providing about 120V totally, are equipped to power the 4 in-wheel motors each of which can independently generate driving/braking toque to the corresponding wheel. The steering system is modified with an angular sensor mounted on the steering column to measure the steering wheel angle input by driver. The vehicle motion information is measured by an INS/GPS RT3002. The motor driving algorithm is implemented and running online with the utilization of AD5435, a real-time simulation machine. An uninterruptable power supply (UPS) is utilized to power the aforementioned devices.

In cooperation with Shanghai Motor Vehicle Inspection Center, the prototype undergoes a series of practical measurements and road tests, as shown in Figure 3. The obtained main vehicle parameters are presented in Table 1.



Figure 2. EV prototype and equipment.



(a) Test bench (b) Slalom test (c) DLC test

Figure 3. Scenarios of test bench measurement and road tests.

Table 1. Vehicle parameters.

Parameters	Values	Parameters	Values
Mass m (kg)	352.6	Yaw Inertia I_x (kg · m^2)	844.6
CG height h (mm)	370.0	Wheel base L (mm)	1916
Front track width B_f (mm)	1424	Rear track width B_r (mm)	1424
Wheel static load $F_{zs,fl}$ (N)	858.8	Wheel static load $F_{zs,fr}$ (N)	858.8
Wheel static load $F_{zs,rl}$ (N)	869.1	Wheel static load $F_{zs,rr}$ (N)	869.1

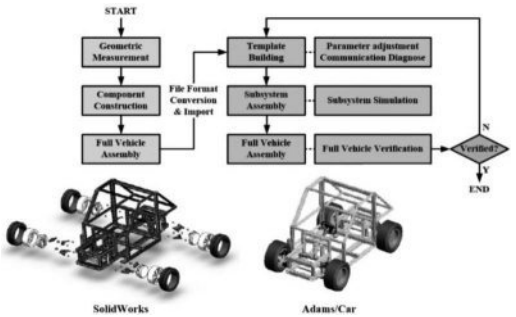
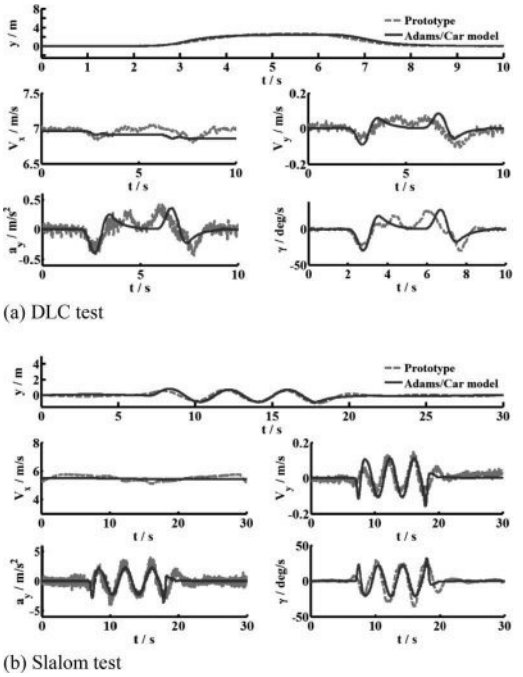


Figure 4. Flowchart of multi-body dynamics modelling.

2.2 *Multi-body dynamics modelling*

Adams is a commercially available virtual prototyping and motion simulation software which can automatically convert a graphically defined model to dynamic equations of motion, and is powerful in simulation and design. However, it is weaker in solid modelling compared to commercial CAD software (Li, Z. & Kota S. 2001). In the presenting study, a multi-body dynamics modelling method using Adams/Car collaborating with SolidWorks is utilized. The flowchart of the modelling procedure is presented in Figure 4.

Based on the geometric information of the EV parts, the physical attributes of the movable elements are respectively built and saved. These individual parts are then assembled by defining their relative position to each other, and the designed degree of freedoms of motion are checked. A symmetric diagnose is carried out to ensure the symmetry of the solid structure. The final version of the full vehicle assembly is locked up and got prepared for the modelling in Adams/Car.



(a) DLC test

(b) Slalom test

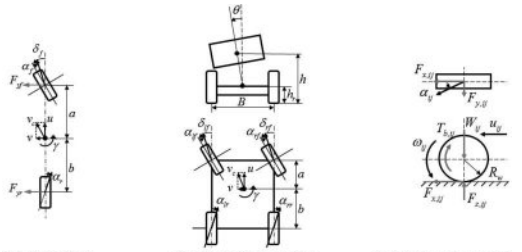
Figure 5. Comparison of simulation results with road test data.

Adams/Car provides an access to import a variety of file formats. In this case, Template Building mode is selected, and the SolidWorks files are converted to Parasolid format and imported into Adams/Car. The imported parts are fully created by defining hard points, attachments, feature parameters, mass properties, etc.. The templates are built corresponding to the categories of mechanical subsystems, namely the frame, the front and rear suspensions, the front and rear wheels, the steering system, and the braking system. Communicators are defined for exchanging information among the subsystems. A Joint Torque is built and applied to each in-wheel motor respectively, and defined as State Variable which can be controlled through the algorithms outside Adams/Car. Subsystems are then built based on the corresponding templates, and the multi-body model of the full vehicle is finally assembled.

2.3 *Multi-body dynamics model verification*

After setting the vehicle parameters and iteratively adjusting the characteristics for crucial force elements, the Adams/Car model is established. A series of simulation are carried out, and the results are compared with the experimental data of the road tests. Two typical examples, i.e. the Double Lane Change (DLC) test and the Slalom test, are presented in Figure 5.

In both cases, the virtual prototype is respectively required to trace the same trajectories as those do in the road tests. The driver model embedded in Adams/Car



(a) 2-DOF (b) 8-DOF model (c) Wheel model

Figure 6. Vehicle models for controller design.

is adopted. The comparison results of both cases identically indicate that the established Adams/Car model and the physical prototype fit well with each other in characteristics of dynamics responses, which in turn verifies the effectiveness of the established EV model in Adams/Car environment.

3 VEHICLE MODEL AND TIRE MODEL FOR CONTROLLER DESIGN

3.1 *Vehicle model*

To estimate the vehicle states with efficiency and accuracy, some simplified of vehicle models are established, as shown in Figure 6.

3.1.1 *Reference yaw motion*

The reference vehicle yaw motion is calculated by a 2-DOF single-track model, which is shown in Figure 6a, and can be expressed as:

$$\begin{cases} \dot{\beta}_{desired} = \dfrac{1}{mu}\left(F_{y,f} + F_{y,r}\right) - \gamma_{desired} \\ \dot{\gamma}_{desired} = \dfrac{1}{I_z}\left(aF_{y,f} - bF_{y,r}\right) + \Delta M, \end{cases} \tag{1}$$

3.1.2 *Lateral transfer load estimation*

During a harsh cornering, even for the prototype with relatively low CG height and rigid suspensions, the difference between the bilateral tire normal forces is significant, which in turn affects the limit of total tire force of each wheel. Therefore, an 8-DOF vehicle model, as shown in Figure 6b, describing linear and rotational motions about longitudinal and lateral direction, roll motion, and rotational motion of each wheel, is adopted. Considering the tire load distribution as the result of longitudinal and lateral accelerations coupling, the normal force of each wheel can be expressed as

$$\begin{cases} F_{z,fl} = \dfrac{1}{2}m\left(\dfrac{b}{L}g - \dfrac{h}{L}a_x\right) - m\left(\dfrac{b}{L}g - \dfrac{h}{L}a_x\right)\dfrac{h}{Bg}a_y \\ F_{z,fr} = \dfrac{1}{2}m\left(\dfrac{b}{L}g - \dfrac{h}{L}a_x\right) + m\left(\dfrac{b}{L}g - \dfrac{h}{L}a_x\right)\dfrac{h}{Bg}a_y \\ F_{z,rl} = \dfrac{1}{2}m\left(\dfrac{a}{L}g + \dfrac{h}{L}a_x\right) - m\left(\dfrac{a}{L}g + \dfrac{h}{L}a_x\right)\dfrac{h}{Bg}a_y \\ F_{z,rr} = \dfrac{1}{2}m\left(\dfrac{a}{L}g + \dfrac{h}{L}a_x\right) + m\left(\dfrac{a}{L}g + \dfrac{h}{L}a_x\right)\dfrac{h}{Bg}a_y. \end{cases} \tag{2}$$

The state-space representation of the system describe in Eq. (2) is given by

$$\begin{cases} \dot{X}(t) = f\left(X(t)\right) + b_w(t) \\ Z(t) = h\left(X(t)\right) + b_v(t), \end{cases} \tag{3}$$

where the vehicle state vector X is defined as:

$$X = \left[F_{z,fl}\ F_{z,fr}\ F_{z,rl}\ F_{z,rr}\ a_x\ \dot{a}_x\ a_y\ \dot{a}_y\right]^T, \tag{4}$$

and the measurement vector Z is defined as

$$Z = \left[a_x\ a_y\right]^T. \tag{5}$$

The state vector $X(t)$ can be estimated by using the EKF expressed by the following equations:

$$\begin{cases} \hat{X}_{k/k-1} = A_k \hat{X}_{k-1/k-1} \\ P_{k/k-1} = A_k P_{k-1/k-1} A_k^T + Q_k \\ K_k = P_{k/k-1} H_k^T \left(H_k P_{k/k-1} H_k^T + R_k\right)^{-1} \\ \hat{X}_{k/k} = \hat{X}_{k/k-1} + K_k\left(Z_k - H_k \hat{X}_{k/k-1}\right) \\ P_{k/k} = \left(I - K_k H_k\right) P_{k/k-1}, \end{cases} \tag{6}$$

where

$$\begin{cases} A_k = \partial f\left(\hat{X}_{k/k}\right)\big/\partial X \\ H_k = \partial f\left(\hat{X}_{k/k-1}\right)\big/\partial X. \end{cases} \tag{7}$$

3.1.3 *Wheel dynamics*

Considering the vehicle motions within the horizontal plane, the longitudinal and lateral velocities of each wheel are respectively given by

$$\begin{cases} u_{lf} = u - \dfrac{B}{2}\gamma \\ v_{lf} = v + a\gamma, \end{cases} \quad \begin{cases} u_{rf} = u + \dfrac{B}{2}\gamma \\ v_{rf} = v + a\gamma, \end{cases}$$
$$\begin{cases} u_{lr} = u - \dfrac{B}{2}\gamma \\ v_{lr} = v - a\gamma, \end{cases} \quad \begin{cases} u_{rr} = u + \dfrac{B}{2}\gamma \\ v_{rr} = v - a\gamma. \end{cases} \tag{8}$$

Consequently, the sideslip angles can be respectively written as:

$$\alpha_{lf} = \arctan\frac{v_{lf}}{u_{lf}} - \delta_f \quad \alpha_{rf} = \arctan\frac{v_{rf}}{u_{rf}} - \delta_f$$
$$\alpha_{lr} = \arctan\frac{v_{lr}}{u_{lr}} \qquad \alpha_{rr} = \arctan\frac{v_{rr}}{u_{rr}}. \tag{9}$$

The wheel slip ratio of each wheel can be expressed as

$$\begin{cases} s_{ij} = \dfrac{\omega_{ij}R_w - u_{ij}}{\omega_{ij}R_w}, \text{ when } \omega_{ij}R_w \geq u_{ij} \\ s_{ij} = \dfrac{u_{ij} - \omega_{ij}R_w}{u_{ij}}, \text{ when } \omega_{ij}R_w < u_{ij}, \end{cases} \tag{10}$$

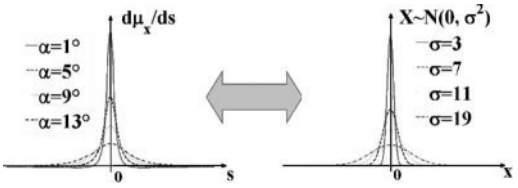


Figure 7. Analogy of curve feature: $d\mu_x/ds$ vs $X \sim N(0, \sigma^2)$.

where the wheel angular velocity ω_{ij} is directly measured by the in-wheel motor. The driving/braking torque is generated by the motor and applied to the wheel, i.e.

$$\begin{cases} J_w\dot{\omega}_{ij} = F_{x,ij}R_w - T_{b,ij}, \text{ when breaking} \\ J_w\dot{\omega}_{ij} = T_{d,ij} - F_{x,ij}R_w, \text{ when accelerating} \end{cases} \tag{11}$$

The estimated tire normal force, wheel slip ratio and sideslip angle will be used as the inputs of the proposed tire simulation model which is to be introduced in Section 3.2, and the lateral force calculated by the tire simulation model will be fed back to actuate the 2-DOF model.

3.2 *Tire model for simulation*

Although many tire models have been thoroughly studied, in this study, a tire simulation model more suitable for the proposed control strategy framework is proposed and described as below.

3.2.1 *Establishment of tire simulation model*

In this work, a tire similar to the ones equipped in the physical prototype is chosen from CarSim database. In order to obtain a suitable mathematical expression, a series of simulation experiments have been carried out to examine the effect of normal force and sideslip angle/wheel slip ratio on tire longitudinal/lateral force. By observing the differential features of the cluster of curves, interesting results shown in Figure 7 have been found out which are presented as below.

From the figure, it can be seen that under a certain normal force, the differential of F_x (or F_y) with respect to s (or α) possesses a similar shape as the normal distribution function (NDF) $X \sim N(0, \sigma^2)$. In addition, when considering combined slip situation, varying α for F_x for example, the curve deflects similarly as the NDF does with respect to different σ. Furthermore, the normal force F_z can be treated as constant around the operation point and eliminated, leaving the the tire-road friction coefficient μ_x (or μ_y) which shares the same shaped of curve as that of F_x (or F_y).

By modifying NDF, the fitting function of $d\mu_x/ds$ (or $d\mu_y/d\alpha$) with respect to s (or α) can be hereby expressed as

$$\begin{cases} \dot{y} = B\left[\dfrac{1}{\sqrt{2\pi}\sigma}\left(e^{-\frac{t^2}{2\sigma^2}} - e^{-\frac{p^2}{2\sigma^2}}\right) + C(t-p)\right] \\ \sigma = p/A, \end{cases} \tag{12}$$

where y represents μ_x (or μ_y), t represents s (or α), p represents s_{px} (or α_{py}) which is the slip ratio (or sideslip angle) corresponding to the maximum value of μ_x (or μ_y).

By integrating Eq. (12), the final format of the proposed tire mathematical expression model can be described as

$$\begin{cases} \mu_x = \int_0^s \dot{\mu}_x dt = A_x' \operatorname{erf}\left(\sqrt{2}\sigma_x s\right) + B_x' s^2 + C_x' s \\ \sigma_x = s_{px}/A_x \\ F_x = \mu_x F_z, \end{cases} \tag{13}$$

$$\begin{cases} \mu_y = \int_0^\alpha \dot{\mu}_y dt = A_y' \operatorname{erf}\left(\sqrt{2}\sigma_y \alpha\right) + B_y' \alpha^2 + C_y' \alpha \\ \sigma_y = \alpha_{py}/A_y \\ F_y = \mu_y F_z, \end{cases} \tag{14}$$

$$\mu_{com} = \sqrt{\mu_x^2 + \mu_y^2} \quad F = \mu_{com} F_z, \tag{15}$$

where

$$A' = \frac{B}{2},\ B' = \frac{BC}{2},\ C' = -\left(ABC\sigma + Be^{-\frac{A^2}{2}}\Big/\left(\sqrt{2\pi}\sigma\right)\right)$$
$$\operatorname{erf}(x) = \frac{2}{\sqrt{\pi}}\int_0^x e^{-t^2} dt. \tag{16}$$

3.2.2 *Tire model verification*

The proposed tire simulation model for the presented control frame work is then simulated in condition of sweeping F_z, s, and α, and the results are compared with the experimental data of CarSim Tire Tester.

As can be seen in Figure 8a and 8b, the proposed tire simulation model maintains good accuracy throughout the selected region, which in turn suggests that it is feasible to estimate the tire forces by given the information of the operation point (F_z, s, α).

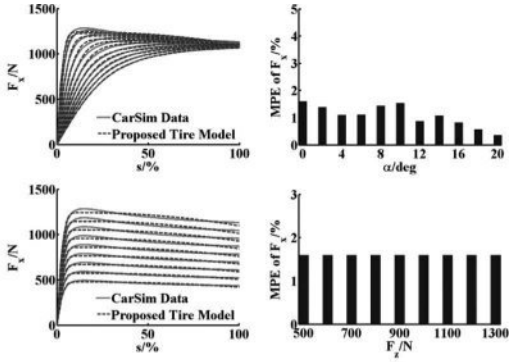
4 CONTROLLER DESIGN AND SIMULATION

4.1 *FO-PID controller design*

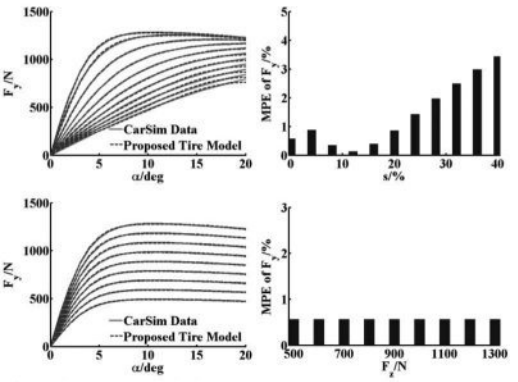
As the extension of conventional integer PID controllers, the FO-PID controller with 2 extra tuning parameters, λ and μ, is able to meet more design specifications, and consequently can be more robust to model uncertainty (Chen, Y.Q. et al. 2009). In this study, following the specific instruction by Monje C.A., et al. (2008), an FO-PID controller is designed to trace the desired yaw motion. The transfer function of the controller is defined as:

$$C(s) = PI(s)^{\lambda} \cdot PD(s)^{\mu} = \left(\frac{\lambda_1 s + 1}{s}\right)^{\lambda} \cdot k_c x^{\mu}\left(\frac{\lambda_2 s + 1}{x\lambda_2 s + 1}\right)^{\mu} \tag{17}$$

where $PI(s)^{\lambda}$ is to cancel the phase slope of the plant at desired crossover frequency ω_{cg}, and $PD(s)^{\mu}$ is to



(a) F_x with respect to different α and F_z



(b) F_y with respect to different s and F_z

Figure 8. Comparison of proposed tire simulation model with CarSim data.

fulfill the design specifications of ω_{cg} and ϕ_m. The design parameters, λ, λ_1, λ_2, μ and x are respectively given as follows.

For $PI(s)^{\lambda}$ controller,

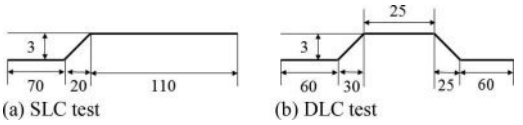
$$\begin{cases} \nu = \dfrac{\phi_u - \phi_{u-1}}{\omega_u - \omega_{u-1}} \dfrac{\text{rad}}{\text{rad/s}} \\ \psi' = \dfrac{\mathrm{d}\psi}{\mathrm{d}\omega}\Big|_{\omega=\omega_{cg}} = \lambda \dfrac{\lambda_1}{1+\left(\lambda_1\omega_{cg}\right)^2} = -\nu \\ \dfrac{\mathrm{d}\psi'}{\mathrm{d}\lambda_1} = \lambda\left[\left(\lambda_1\omega_{cg}\right)^2 - 1\right] \Big/ \left[1+\left(\lambda_1\omega_{cg}\right)^2\right]^2 = 0, \end{cases} \tag{18}$$

which gives

$$\lambda_1 = \frac{1}{\omega_{cg}} \qquad \lambda = -2\omega_{cg}\nu. \tag{19}$$

For $PD(s)^{\mu}$ controller,

$$\left[\frac{e^{j(-\pi+\varphi_m)}}{G\left(j\omega_{cg}\right)PI^{\lambda}\left(j\omega_{cg}\right)}\right]^{\frac{1}{\mu}} = a + jb$$
$$x = \frac{a-1}{a(a-1)+b^2} \qquad \lambda_2 = \frac{a(a-1)+b^2}{b\omega_{cg}}. \tag{20}$$



(a) SLC test (b) DLC test

Figure 9. Schematic diagram of simulation trajectory (Unit: m).

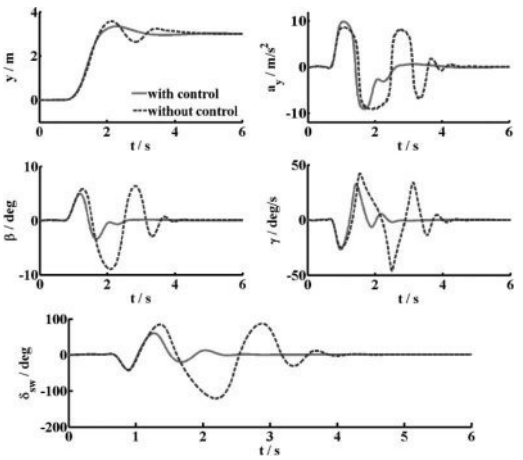


Figure 10. Comparison of performances with/without controller for SLC tests.

where $G(j\omega_{cg})$ represents the transfer function of the reference control plant model which in this case is chosen as a linear bicycle model.

It has been proved that the minimum positive x can ensure the maximum flatness of the phase curve of the compensator (Monje C.A., et al., 2008). Therefore, a very small initial value of μ, e.g. $\mu = 0.01$, is firstly selected, and a corresponding pair of (x, λ_2) can be obtained based on Eq. (20). By slightly increasing μ, the minimum positive x can be obtained and recorded, and the corresponding μ and λ_2 are also recorded as the desired design parameters.

4.2 *Simulation results*

The proposed handling and stability control strategy is implemented on a co-simulation platform established in Adams/Car and Matlab/Simulink. A series of simulations are carried out to examine the effectiveness of the control strategy. The settings of single lane change (SLC) and double lane change (DLC) tests are respectively shown in Figure 9a and 9b.

For the established Adams/Car model, the same driver model embedded in Adams/Car which traces the ideal trajectories via a PID controller is used in both cases with or without help of the proposed controller, respectively. The simulation results are presented below.

Figure 10 shows the motion responses of the virtual prototype and the driver's steering wheel angle input during a single lane change maneuverer. Though the

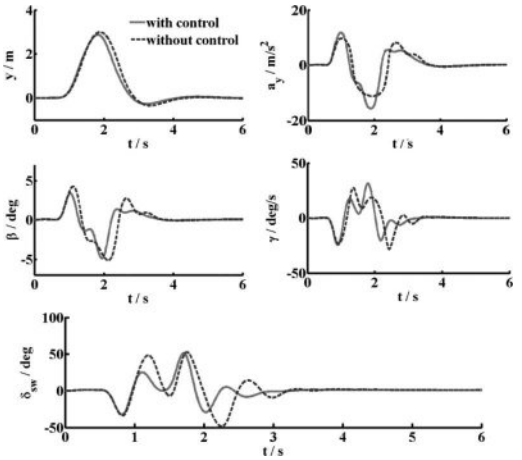


Figure 11. Comparison of performances with/without controller for DLC test.

vehicle is able to fulfill the lane change with or without the assistance of controller, the vehicle with the controller is able to better trace the desired trajectory in responding to driver's steering input. Specifically, the trajectory overshoot is reduced by about 40%, and the stabilization time is reduced by about 1.4 s. On the contrary, without the assistance of the controller, the driver has to roughly sweep the steering wheel in order to maintain the stability of the vehicle and trace the target trajectory. The SLC test shows that the proposed controller is capable of improving the vehicle's dynamics responses and reduce the driving load for the driver.

Similarly, the simulation results of DLC test, shown in Figure 11, also indicate that, with the help of the proposed control strategy, the vehicle handling performance is enhanced, and the driver is able to control the vehicle with less effort. As can be seen in the figure, at the end of each lane change maneuver, the maximum steering wheel angle is reduced from 50° to about 30°. In addition, the stabilization time is reduced by approximately 1 s.

5 CONCLUSIONS

Based on a physical EV prototype, a multi-body dynamics model is built using Adams/Car and SolidWorks, and is verified with road test data. A tire simulation model is designed in order to efficiently and accurately calculate tire forces within the proposed control strategy framework, for which the information of lateral transfer load and vehicle motion variables are estimated by an 8-DOF vehicle model. An FO-PID controller is adopted to improve the stability of the vehicle. Simulation results show that the proposed control strategy is effective to enhance the vehicle performance.

ACKNOWLEDGEMENT

This study is supported by the *National Natural Science Foundation of China* (Grant No. 51375299) and the *Research Program of State Key Laboratory of Mechanical System and Vibration* (Grant No. MSV201505).

REFERENCES

Chen, Y.Q., Petras, I. & Xue, D.Y. Fractional order control-a tutorial [C]. *2009 American control conference. IEEE*, 2009: 1397–1411.

Li Z., Kota S. Virtual prototyping and motion simulation with ADAMS [J]. *Journal of Computing and Information Science in Engineering*, 2001, 1(3): 276–279.

Monje C.A., Vinagre B.M., Feliu V., et al. Tuning and auto-tuning of fractional order controllers for industry applications [J]. *Control engineering practice*, 2008, 16(7): 798–812.

Sakai S., Sado H. & Hori Y. Motion control in an electric vehicle with four independently driven in-wheel motors [C]. *Mechatronics, IEEE/ASME Transactions on*, 1999, 4(1): 9–16.

World Health Organization. *Global status report on road safety 2015* [M]. World Health Organization, 2015.

Advanced Vehicle Control – Edelmann, Plöchl & Pfeffer (Eds)
© 2017 Taylor & Francis Group, London, ISBN 978-1-138-02992-7

Real-time simulation of elasto-kinematic multi-body vehicle models

Matthijs Klomp
Vehicle Dynamics, Volvo Car Group

Peter Sundström
Modelon AB

Albin Johnsson
Vehicle Dynamics, Volvo Car Group

ABSTRACT: This paper presents the development of a real-time capable high fidelity multi-body vehicle dynamics model based on differential algebraic equations (DAE) that is compiled into ordinary differential equations (ODE) form using index reduction, symbolic manipulation and equation sorting. This model is shown to closely match an offline high fidelity model based on high index solvers. The real-time model directly references the model parameters used by the offline model and can be distributed in executable form according to standard interfaces. The real-time performance is achieved by applying inlining of an implicit Euler solver into the model formulation to get stable execution with fixed time steps, and by parallelizing the execution over multiple processor cores. The presented approach gives a more accurate and configurable real-time model compared to the current, lookup-table based, solution.

1 INTRODUCTION

Development of virtual methods to improve the efficiency of the development by reducing cost and lead-time while at the same time improving quality and robustness is of strategic relevance and importance to the vehicle industry [1].

With the increase of mechatronic chassis systems, testing of these systems using hardware-in-the-loop requires real-time simulation models. Furthermore, the introduction of high-fidelity dynamic simulators has proven useful for testing and assessment of the human-machine interaction [2]. Nevertheless, with the increasing demands for virtual testing, currently used medium fidelity models are no longer sufficient to capture higher-order phenomena such as brake judder, wheel imbalance, choppiness, etc. In [3] the conclusion was that current real-time simulation models are valid to approximately 5 Hz, requiring higher order models for trustworthy evaluation of advanced driver support systems. Also component characteristics, such as suspension hard-point locations are usually not directly available in simplified vehicle models that use look-up table representations of the suspension.

This paper presents the development of a real-time high fidelity vehicle dynamics model developed with Dymola and the Vehicle Dynamics Library (VDL) that closely matches a model based on Adams/Car that is currently used for high-fidelity off-line simulations. The real-time model directly references the model parameters used for the off-line model and can be distributed as executable models using the functional-mockup interface (FMI) standard [4], [5].

2 BUILDING AND PARAMETERIZING MODELS

The modeling and parameterization scheme is based on the model topology being defined independent of the parameter data. In the off-line model, the topology with bodies and joints and/or bushings is stored in templates, and the data that parameterizes the model is stored in a parameter database. Thus, the equivalent topology is built for the real-time model which then reads data directly from off-line model data files.

2.1 *Topology definition*

The real-time model is based on Modelica, an object oriented language for developing models based on differential algebraic equations (DAEs) [6]. When the model is compiled to executable code, the models and the connections between them are transformed into one system of DAEs that goes through symbolic manipulation, index reduction and equation sorting to generate a formulation that can be simulated using ordinary differential equation (ODE) solvers.

The chassis used in this work has a double wishbone suspension at the front and an integral rear link suspension at the rear with a transverse leaf spring.

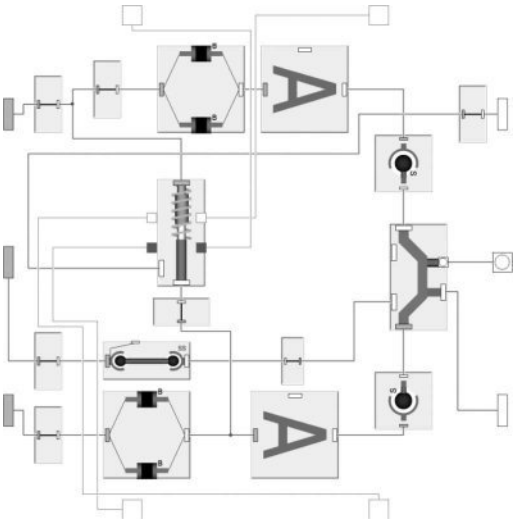


Figure 1. Front linkage layout.

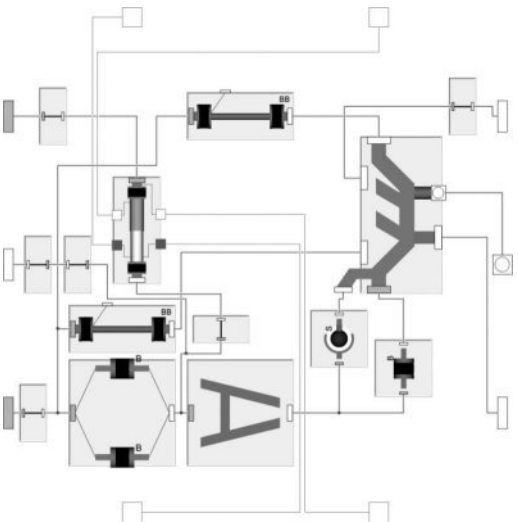


Figure 2. Rear linkage layout.

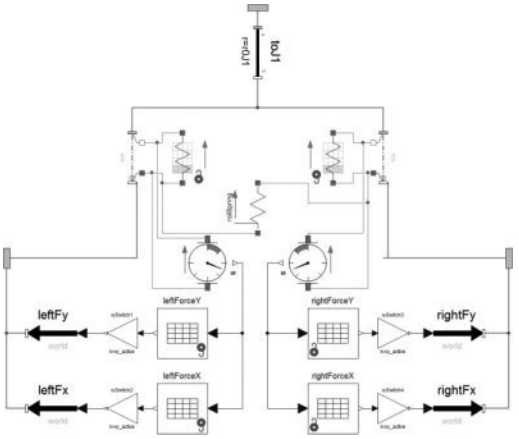


Figure 3. Transverse leaf spring model. Top attachment is to chassis, left and right are for the two linkage sides.

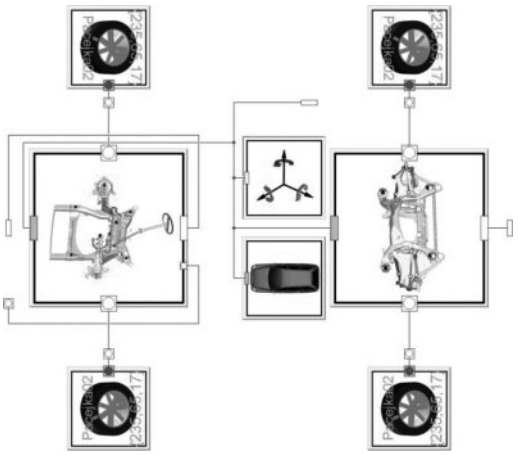


Figure 4. Model diagram of full chassis model.

Figure 1 shows the front linkage topology viewed in Dymola.

The front suspension is based on existing templates in VDL while the rear suspension is a custom topology, shown in Figure 2.

There's a lower H-arm connected with two bushings on the chassis side and a ball joint and a bushing on the upright side. Two additional link arms with two bushings each connect the upright to the chassis.

The transverse leaf spring in the rear suspension is modelled as a set of pure translational springs, shown in Figure 3. This is a simplification of a finite element (FE) based component in the offline model. The main reason for this simplification is to improve model performance as the model is meant to be used in real-time applications. There are three main spring components, one vertical stiffness between each side and the chassis as well as a roll stiffness directly attached between the two sides. In addition, there are lookup table based forces that can be defined as a function of wheel travel to incorporate the lateral and longitudinal force characteristics of the leaf spring. All these stiffnesses are tuned to the behavior of the offline model.

The front and rear suspensions are put together into a chassis model based on library templates, shown in Figure 4.

A 3D visualization of the full chassis is shown in Figure 5. The visualization includes 3d models of each individual linkage component based on CAD data.

The full chassis model has 252 continuous time states.

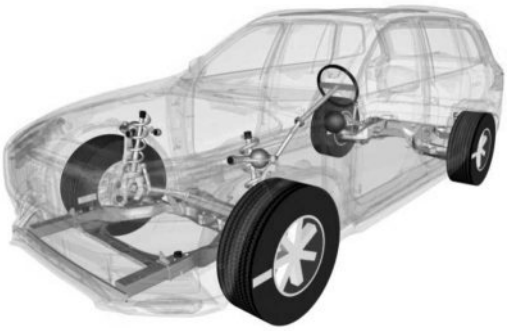


Figure 5. 3D visualization of the full chassis model.



Figure 6. Front suspension in test rig.

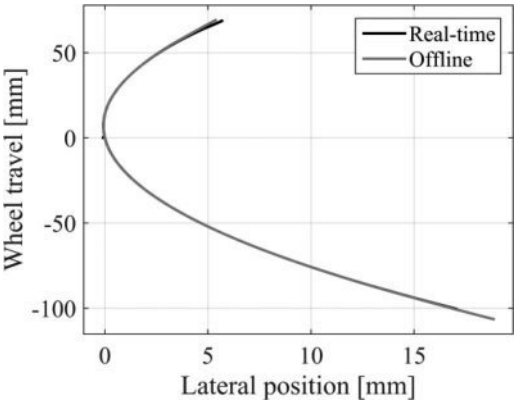


Figure 7. Front suspension in test rig.

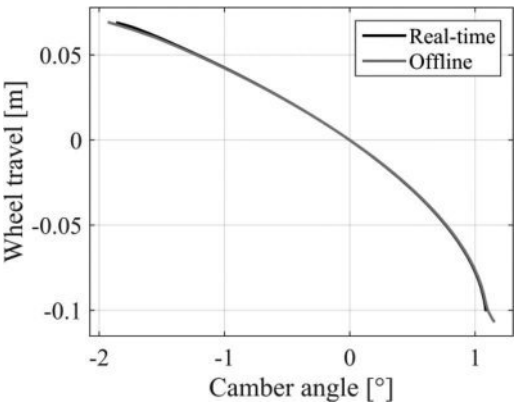


Figure 8. Front suspension in test rig.

2.2 *Parameterization*

In the real-time model, data is accessed using a general-purpose data handling method called DataAccess. Several file formats can be read with this method, including TeimOrbit which is the format used in the offline model.

In general, data-aware components are responsible for reading all the data that it requires from the data file. For example, a data-aware mass part only takes a data file path and a part name as parameters and then reads the associated mass and inertia data. Similarly, a bushing takes a bushing file path as input and then reads force and torque characteristics directly from the file.

Reading model data directly from the source data files eliminates the need to manually enter parameters in the real-time model and the associated risk of user error in doing so. Furthermore, the effort to parameterize the model with the data files can be done once and then the data files can be changed to update the model, assuming the topology stays the same.

3 MODEL CORRELATION

Initial validation of the real-time model has been carried out against its offline counterpart in order for it to be useful. For this purpose, test rig experiments were set up with the real-time model which excites the suspension in the same way as the existing test cases used with the offline model.

The test rig model keeps the chassis side of the suspension fixed relative to ground while moving wheel pads in the vertical direction to generate motion in the wheel centers. Additional force and torque can also be applied, either in the wheel center or in the contact patch. Figure 6 shows the front suspension when it is simulated in the test rig.

Figure 7 and Figure 8 shows examples of the correlation result for the front suspension in a parallel wheel travel test.

4 REAL-TIME ADAPTATIONS

Besides the symbolic manipulation of the model equations, which in itself gives very efficient simulation code, there are two main techniques used to improve real-time performance of the vehicle models. Inline integration and parallelization.

4.1 *Inline integration*

Inline integration [7] is a method to achieve real-time performance of stiff systems. With fixed step solvers, the discretization formulae of the solver are incorporated into the equations systems of the model before doing structural analysis and symbolic manipulation to allow further performance improvements.

In this case, an implicit Euler solver is used, which gives stability in each timestep even with larger timesteps, as opposed to an explicit solver which would need small enough timesteps with regard to system dynamics to achieve stability. The implicit solver is used successfully with timesteps up to 2 ms for the model in this paper. The drawback with is that this typically gives large non-linear equation systems requiring iterative solving.

4.2 *Parallelization*

When the above approach is applied to the chassis model it results in a single non-linear equation system of size {218}. The cost of solving non-linear equation systems increases exponentially with their size, meaning that large systems of equations needs to be avoided in order to achieve real-time performance. This can be done by introducing parallelization of the model equations. Methods for parallelizing model execution were introduced in [8].

By introducing decoupling elements between front and rear suspensions, left and right linkages and between linkages and wheels, the equation system can be divided into 13 smaller systems with sizes {30, 1, 1, 30, 1, 1, 21, 1, 1, 21, 1, 1, 21}. Two advantages are introduced by this decoupling. With the exponential increase in computational effort with equation system size, the reduction of the sizes of equation systems improve performance a great deal. Furthermore, the equation systems can now be solved in parallel, allowing the use of multi-core processors.

5 PERFORMANCE

The real-time model has been benchmarked with respect to performance on a regular desktop computer. This gives an indication of the turnaround times needed to execute the model. The performance is expected to improve even further when executed on a dedicated real-time platform. The accuracy of the model is also verified when using the real-time solver.

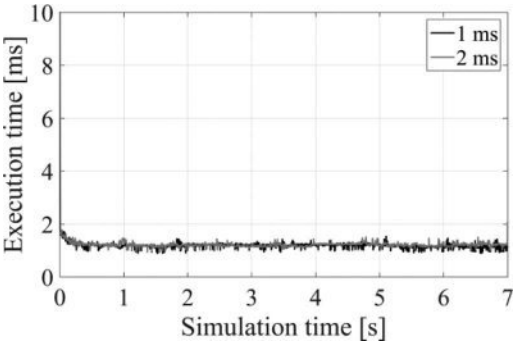


Figure 9. Real-time execution times per time step with 1 ms and 2 ms time steps. Each time step takes the same amount of time regardless of the length of the timestep.

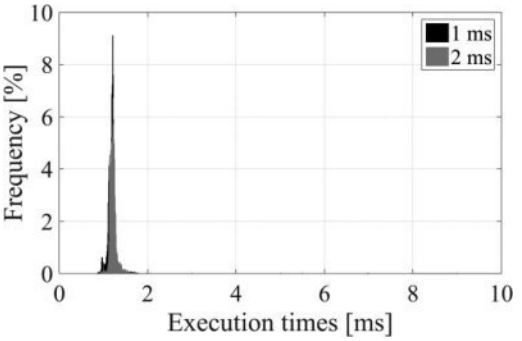


Figure 10. Real-time turnaround time per time step shown as histograms. Similar turnaround times are seen with both timesteps.

5.1 *Performance*

When running in Dymola on a regular Windows laptop (i7-3630QM CPU @ 2.40 GHz) the model simulates each time step at 1–1.5 ms turnaround time. Figure 9 shows the execution times for each time step during a double lane change maneuver. The model is stable with both 1 and 2 ms timesteps so even on a desktop computer the model can be simulated in real-time. With 2 ms timestep, each step apart from the initial ones are calculated within the duration of the timestep.

Figure 10 shows histograms for the execution times, showing that the time taken for each time step is stable at 1–1.5 ms.

5.2 *Accuracy*

The use of implicit solvers can have detrimental effects on model accuracy if important model dynamics are excluded by the larger timestep. Model accuracy with the real-time solver is verified by comparing with a variable step solver in Dymola. Figure 11 show lateral acceleration output with a frequency sweep as steering wheel angle input. The variable step solver Dassl,

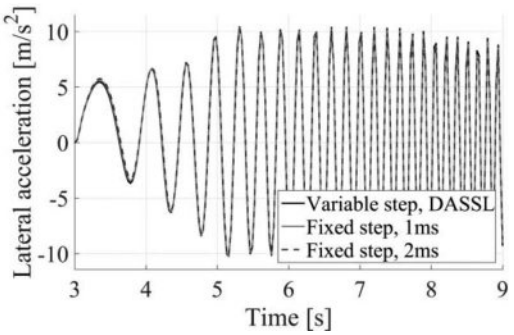


Figure 11. Solver comparison of lateral acceleration output with a frequency sweep as steering input.

is used as baseline and the real-time solver output is shown with 1 and 2 ms timesteps.

6 CONCLUSION

The DAE based model is shown to give real-time performance of high fidelity vehicle models on regular laptop computers. This is expected to improve when executed on a dedicated real-time platform.

The modeling and parameterization scheme which uses existing data files allows a shorter update cycle when adjusting model parameters on real-time platforms since lookup tables do not have to be regenerated.

The real-time model is useful for many different applications including driver-in-the-loop simulators and HIL system verification.

REFERENCES

J. Rauh, "Virtual development of ride and handling characteristics for advanced passenger cars," *Vehicle System Dynamics,* vol. 40, no. 1–3, pp. 135–155, 2003.

P. Goupil and G. Puyou, "A High Fidelity AIRBUS Benchmark for System Fault," in *Proceedings of the 4th European Conference for Aerospace Sciences (EUCASS)*, St. Petersburg, 2011.

W. C. Prescott, G. Heirman, M. Furman, J. De Cuyper, L. Dragon, A. Lippeck and H. Brauner, "Using High-Fidelity Multibody Vehicle Models in Real-Time Simulations," in *SAE World Congress & Exhibition – SAE 2012-01-0927*, Detroit, 2012.

J. Andreasson, N. Machida, M. Tsushima, J. Griffin and P. Sundström, "Deployment of high-fidelity vehicle models for accurate real-time simulation," in *Proceedings of the 1st Japanese Modelica Conference*, Tokyo, 2016.

J. Andreasson, H. Elmqvist, J. Griffin, D. Henriksson, S.-E. Mattson and H. Olsson, "Real-Time Simulation of Detailed Vehicle Models," in *Proceedings of the 12th International Symposium on Advanced Vehicle Control*, Tokyo, 2014.

"Modelica," 2016. [Online]. Available: www.modelica.org.

H. Elmqvist, M. Otter and F. E. Cellier, "Inline Integration: A new mixed symbolic/numeric approach for solving differential-algebraic equation systems," in *Proceedings of the European Simulation Multiconference*, Prague, 1995.

H. Elmqvist, S. Mattson and H. Olsson, "Parallel Model Execution on Many Cores," in *Proceedings of the 10th International Modelica Conference*, Lund, 2014.

Advanced Vehicle Control – Edelmann, Plöchl & Pfeffer (Eds)
© 2017 Taylor & Francis Group, London, ISBN 978-1-138-02992-7

Control of a variable-geometry suspension as independent wheel steering

B. Németh, D. Fényes & P. Gáspár
Institute for Computer Science and Control, Hungarian Academy of Sciences, Hungary

ABSTRACT: The paper presents the modeling and control design of a variable-geometry suspension system, which is applied as independent wheel steering for in-wheel electric vehicles. The variable-geometry suspension modifies the tilting of the wheel, which has an effect on the steering of the wheels through the variation of the scrub radius. In the paper the model of the suspension-steering system and the relationship between the steering and the suspension geometry are formulated using nonlinear dynamical equations. The model is validated through a high-fidelity multi-body suspension model SimMechanics. In the paper the robust combined feedforward-feedback control design of the independent steering system is presented. Finally, the proposed control system is used in different vehicle scenarios.

1 INTRODUCTION AND MOTIVATION

The variable-geometry suspension is a novel intelligent actuator in road vehicle control. The purpose of the actuator is to modify the geometry of the vehicle suspension, by which the lateral and vertical dynamics of the vehicle are improved. Familiar applications of the variable-geometry suspension system are the rear-wheel steering with the modification of the toe-angles (Lee, Lee, Ha, & Han 1999, Goodarzia, Oloomia, & Esmailzadehb 2010), the improvement of vehicle handling (Lee & Han 2001) and trajectory tracking through wheel tilting (Németh & Gáspár 2013). The system is also used for the control of narrow tilting vehicles (Piyabongkarn, Keviczky, & Rajamani 2004). The advantages of the variable-geometry suspension are the simple structure, low energy consumption and low cost compared to other mechanical solutions such as an active front wheel steering, see (Evers, van der Knaap, Besselink, & Nijmeijer 2008, Lee, Sung, & Lee 2005).

The in-wheel electric drive offers new possibilities in the steering of the vehicle, such as independent steering. The goal of the independent steering concept is to improve the lateral dynamics of the vehicle using individually controlled wheels. The independent steering control for the rear wheels to modify the toe angle is presented by (Lee, Lee, Ha, & Han 1999). The analysis of the independent wheel-steering system for heavy vehicles is found in (Ronci, Artuso, & Bocci 2011). (Wang, Wang, Jin, & Song 2011) proposes an indirect power steering measure called differential drive torque assisted steering, and validates its feasibility. (Hu, Jing, Wang, Yan, & Chen 2015) presents a fault-tolerant control approach for a four-wheel independently actuated electric vehicle in order to realize normal driving requirements when the active steering system is in complete failure. In this paper the variable-geometry suspension control is applied for independent steering control purposes. The advantage of this solution is that the controls of the variable-geometry suspensions are independent from each other. Thus, the steering of the left and right wheels can also be achieved independently. The contributions of the paper are the modeling and validation of the suspension system and the robust control design of the trajectory tracking control.

The paper is organized as follows. The modeling of the independent steering incorporating the variable-geometry suspension model in Section 2. Then the modeling of the lateral dynamics is presented is in Section 3. The robust control design of the system in a hierarchical structure is found in Section 4. Section 5 demonstrates the efficiency of the control system. Finally, Section 6 summarizes the contribution of the paper.

2 MODELING OF THE VARIABLE-GEOMETRY SUSPENSION

In this section the modeling of independent steering is proposed. The variable-geometry suspension performs the modification of the wheel position and orientation. Thus, the wheel camber angle and the scrub radius of the suspension vary. In the following, the formulation of the lateral vehicle model with the consideration of the camber angle and scrub radius is presented.

The purpose of the variable-geometry suspension is to perform the wheel camber angle and the scrub radius modification. The camber angle results in a lateral force on the tyre-ground contact. Since the longitudinal force has a rotatory effect on the wheel, the scrub radius of the wheel influences the steering dynamics of the wheel. Therefore, a lateral force from the wheel steering through the scrub radius modification results.

Since the variable-geometry suspension has one actuator in each wheel, it is necessary to find a suspension construction with which the lateral force generation of the camber and the scrub radius is in coordination. Thus, the forces from the wheel tilting and the steering from the scrub radius have the same effect on the vehicle dynamics. In the paper the McPherson construction is used to perform the motion of the wheel. The actuator is incorporated in the suspension between the wheel hub and the wheel. It is able to generate an active torque M_{act} around B to tilt the wheel. However, it also has a countereffect $-M_{act}$ on the hub. In the McPherson construction the suspension is able to rotate around the connection point A of the chassis. Moreover, the arm connects the hub D and the chassis C with joints, which are able to guarantee the rotation and the motion of the suspension.

The scheme of the variable-geometry suspension is shown in Figure 1. Several forces influence the motion of the suspension and the wheel. The force of the suspension compression and damping F_{susp} is formulated as

$$F_{susp} = s_{susp}\left(\frac{z_w + z_{w,0}}{\sin\epsilon_1}\right) + d_{susp}\frac{\dot{z}_w}{\sin\epsilon_1} \tag{1}$$

where s_{susp} and d_{susp} are the stiffness and damping coefficients, $z_{w,0}$ is the joint position, resulting from the static suspension compression.

The lateral force on the tyre is F_y. It is derived from the Magic Formula, see (Pacejka 2004). F_{tyre} is the force from the tyre compression, which has a direction to the wheel:

$$F_{tyre} = \frac{(r_w\cos\gamma - l_{tyre}\sin\gamma - r_w - z_w) + z_{tyre,0}}{\cos\gamma\ /s_{tyre}} \tag{2}$$

where s_{tyre} is the tyre stiffness, r_w is the wheel radius and $z_{tyre,0}$ is the static compression of the tyre.

The motion of the suspension is described by three dynamic equations. First, the vertical motion of the wheel hub z_w is formulated (3). Second, the torque on the suspension is described to derive the rotation of the wheel hub ϵ_3, see (4). Third, the tilting of the wheel γ is formulated (5).

$$m_{susp}\ddot{z}_w = -F_{susp}\sin\epsilon_1 + F_{tyre}\cos\gamma + \\ + F_{arm}\sin\epsilon_2 \tag{3}$$

$$J_{susp}\ddot{\epsilon}_3 = F_{susp}l_{susp} + F_{arm}l_{arm} - M_{act} \tag{4}$$

$$J_w\ddot{\gamma} = M_{act} - F_{tyre}l_{tyre} - F_y l_y \tag{5}$$

The arm of the lateral tyre force is

$$l_y = r_w\cos\gamma - l_{tyre}\sin\gamma. \tag{6}$$

where r_w and l_{tyre} are construction parameters.

Since the inertia and the stiffness of the suspension through F_{susp} and F_{arm} are high, the effect of M_{act} on the suspension motion is relatively small. Thus, in practice the angle ϵ_3 is constant, thus $\ddot{\epsilon}_3 = 0$. Therefore, F_{arm} is computed as:

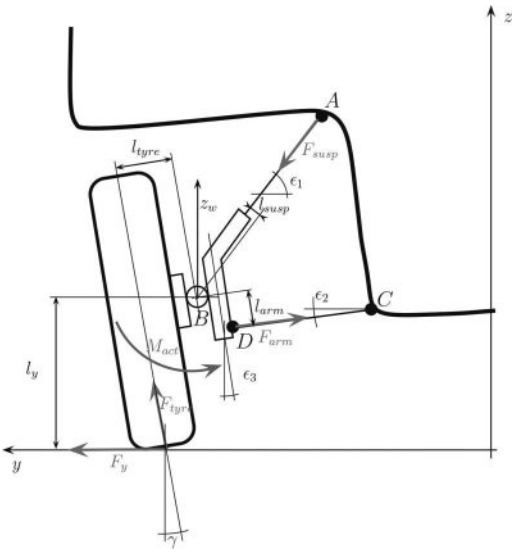


Figure 1. Scheme of the suspension construction.

$$F_{arm} = \frac{M_{act} - F_{susp}l_{susp}}{l_{arm}} \tag{7}$$

Thus, it is assumed that ϵ_1, ϵ_2 and l_{arm}, l_{susp} can be handled as constant suspension parameters.

The nonlinear variable-geometry suspension model is validated through the complex mechanical multibody simulation system Matlab/SimMechanics. In SimMechanics the construction of the suspension has been built, and the modification of the wheel camber angle has been analyzed, see Figure 2. In the multibody simulator the wheel and the arms are defined as body elements, whose mass and inertia values are calculated using a computer-aided design software. In the mechanical model several physical constraints using joint elements are involved, by which the connection points of the bodies are constructed. The tyre-ground contact is modeled as an elastic connection, which is able to guarantee the compression of the tyre. Furthermore, the lateral and longitudinal motions of the tyre are allowed using planar joint constraints.

Since the presented model formulates the motion of the suspension and the wheel, it can be used for control design purposes. Therefore, the nonlinear suspension model (3)–(5) is transformed into a linear control-oriented form. During the linearizing the following assumptions are made.

- In the formulation small wheel tilting angles are considered. As a result $\cos\gamma = 1$ and $\sin\gamma = \gamma$ approximations are placed into (3). . .(5).
- Since γ values are small, the lateral tyre force F_y is approximated in a linear form: $F_y = C\alpha$, where α is

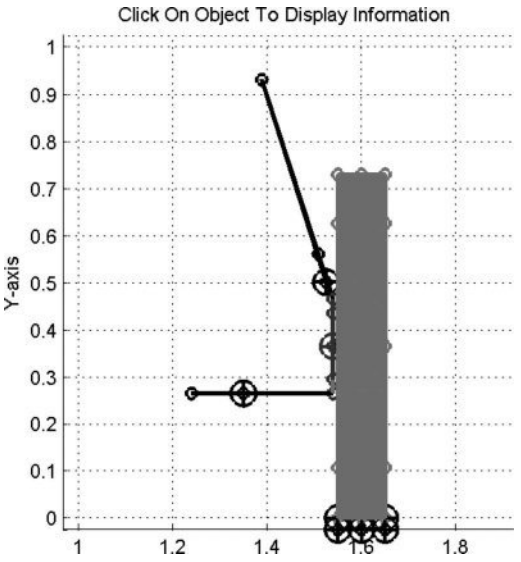


Figure 2. SimMechanics model of the suspension.

the side-slip angle of the tyre. During the wheel tilting motion $\alpha = \tan\left(\frac{r_w\dot{\gamma}}{v}\right) \approx \frac{r_w\dot{\gamma}}{v}$ yields the lateral side-slip angle, which is the angle between the longitudinal and the lateral component of the velocity vector. Thus, the resulting lateral tyre force is

$$F_y = C\frac{r_w\dot{\gamma}}{v} \tag{8}$$

- The static compressions of the suspension and the tyre are neglected, see (1) and (2).

The approximations yield the following transformed model of equations (3)...(5)

$$m_{susp}\ddot{z}_w = \left(1 + \frac{l_{susp}}{l_{arm}}\frac{\sin\epsilon_2}{\sin\epsilon_1}\right)(-s_{susp}z_w - \\ -d_{susp}\dot{z}_w) + s_{tyre}(-l_{tyre}\gamma - z_w) + \frac{\sin\epsilon_2}{l_{arm}}M_{act} \tag{9}$$

$$J_w\ddot{\gamma} = M_{act} - s_{tyre}l_{tyre}(-\gamma l_{tyre} - z_w) - \\ - C\frac{r_w\dot{\gamma}}{v}(r_w - l_{tyre}\gamma) \tag{10}$$

It can be seen that in (10) a nonlinear term $C\frac{r_w\dot{\gamma}}{v}\cdot l_{tyre}\gamma$ is found. Since in the approximation the small wheel camber angles are considered, the $\gamma \approx 0$ is used to avoid the nonlinearities. Thus, the following state-space representation of the variable-geometry suspension model is yielded

$$\dot{x}_{susp} = A_{susp}x_{susp} + B_{susp}u_{susp} \tag{11}$$

where the state vector is $x = \begin{bmatrix}\dot{z}_w & z_w & \dot{\gamma} & \gamma\end{bmatrix}^T$ and $u = M_{act}$.

3 MODELING OF THE LATERAL DYNAMICS

The lateral motion of the vehicle is influenced by the modification of the camber angle. Moreover, the camber angle influences the scrub radius of the wheel, which results in wheel steering. The lateral dynamics of the vehicle is influenced in two ways: the wheel camber angle and the steering angle have lateral force effects. Therefore, in the lateral dynamics both effects are considered.

The lateral motion is described by the following equations, see (Rajamani 2005)

$$J\ddot{\psi} = C_1 l_1\left(\delta - \beta - \frac{\dot{\psi}l_1}{v}\right) - C_2 l_2\left(-\beta + \frac{\dot{\psi}l_2}{v}\right) \tag{12}$$

$$mv(\dot{\psi} + \dot{\beta}) = C_1\left(\delta - \beta - \frac{\dot{\psi}l_1}{v}\right) + C_2\left(-\beta + \frac{\dot{\psi}l_2}{v}\right) \tag{13}$$

where m is the vehicle mass, J is the yaw-inertia of the vehicle, l_1 and l_2 are geometric parameters, C_1 and C_2 are cornering stiffness values, ψ is the yaw angle of the vehicle and β is the side-slip angle.

The steering rotation of the wheel is formulated using a dynamical equation, such as

$$\ddot{\delta}_i = \frac{r_{\delta,i}F_{l,i}}{J_{\delta,i}} \tag{14}$$

where i represents the left $i = l$ or the right $i = r$ wheel. $r_{\delta,i}$ is the scrub radius, $F_{l,i}$ is the longitudinal traction/braking force on the wheel and $J_{\delta,i}$ is the inertia of the steering system for one wheel.

In the actuation of the variable-geometry suspension the scrub radius $r_{\delta,i}$ through the camber angle γ is modified. The relationship between γ and $r_{\delta,i}$ is determined by the suspension geometry and the positions of the suspension arms. Thus, in the formulation of the relationship between γ and $r_{\delta,i}$ the chassis roll angle is considered. The relation of γ and $r_{\delta,i}$ is examined using SimMechanics simulations of the suspension construction, the results are shown in Figure 3.

The analysis presents that the relationship between γ and $r_{\delta,i}$ can be approximated by a linear function, and the roll angle can be handled as a nonlinear offset in the formulation. Thus, the following model is formed:

$$r_{\delta,i} = \varepsilon_1\gamma_i + \varepsilon_2\varphi^2 + \varepsilon_3\varphi + \varepsilon_4 \tag{15}$$

where $\varepsilon_{1...4}$ are construction parameters and φ is the chassis roll angle. Thus, (14) is transformed as

$$\ddot{\delta}_i = \frac{\varepsilon_1 F_{l,i}}{J_{\delta,i}}\gamma_i + \frac{(\varepsilon_2\varphi^2 + \varepsilon_3\varphi + \varepsilon_4)F_{l,i}}{J_{\delta,i}}. \tag{16}$$

In case of a single-track model (12) δ represents a common steering wheel, computed as the average of the left and right steering wheel angles:

$$\delta = \frac{\delta_l + \delta_r}{2} \tag{17}$$

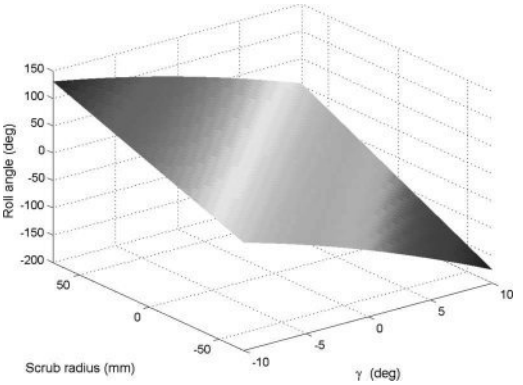


Figure 3. Relation between the scrub radius and the camber angle.

The lateral dynamics of the vehicle is formed using (12), (16) and (17). The states of the model are defined as $x_{lat} = \left[\dot{\psi}\ \beta\ \dot{\delta}_l\ \delta_l\ \dot{\delta}_r\ \delta_r\right]^T$. The chassis roll angle is handled as a disturbance of the system, such as $w_{lat} = [\varepsilon_2\varphi^2 + \varepsilon_3\varphi + \varepsilon_4]$. The state-space representation is

$$\dot{x}_{lat} = A_{lat}x_{lat} + B_{lat,1}w_{lat} + B_{lat,2}u_{lat} \tag{18}$$

where the control input vector is $u_{lat} = \left[\gamma_l\ \gamma_r\right]^T$.

4 CONTROL DESIGN OF THE SUSPENSION SYSTEM

In the followings the control design of the independent steering system is presented. The goal of the control is to guarantee the trajectory tracking of the vehicle through the modification of the front wheel steering angle. The control strategy covers two layers:

- the high-level control computes the required steering angle δ_{ref}, with which the predefined trajectory is computed,
- the torque actuation is calculated by the low-level control, which realizes the steering angle command of the high-level layer. It means that the low-lever control must guarantee the tracking of δ_{ref}. For the design of the control the model (11) is used, see (Németh, Fényes, & Gáspár 2016).

In the rest of the paper the design of the high-level control using a combined robust feedback-feedforward strategy is presented. The control is based on the control-oriented lateral vehicle model (18). It contains a disturbance, which is the roll angle of the chassis. Since the chassis roll angle is considered to be measured, w_{lat} is a measured disturbance of the system. In the control strategy the input u_{lat} contains two elements, such as

$$u_{lat} = \begin{bmatrix}\gamma_{l,ff} + \gamma_{l,fb} \\ \gamma_{r,ff} + \gamma_{r,fb}\end{bmatrix} \tag{19}$$

where the index $_{ff}$ is related to the feedforward compensation of the disturbance, while $_{fb}$ is denoted to the feedback control input.

The feedforward compensation of the disturbance is computed as follows. (16) is rewritten using the sum $u_{lat,ff} + u_{lat,fb}$, such as

$$\ddot{\delta}_i = \frac{\varepsilon_1 F_{l,i}}{J_{\delta,i}}\gamma_{i,ff} + \frac{\varepsilon_1 F_{l,i}}{J_{\delta,i}}\gamma_{i,fb} + \frac{(\varepsilon_2\varphi^2 + \varepsilon_3\varphi + \varepsilon_4)F_{l,i}}{J_{\delta,i}} \tag{20}$$

The role of $\gamma_{i,ff}$ is to compensate the measured disturbance φ. Thus, the feedforward control input is derived from the equation

$$\frac{\varepsilon_1 F_{l,i}}{J_{\delta,i}}\gamma_{i,ff} + \frac{(\varepsilon_2\varphi^2 + \varepsilon_3\varphi + \varepsilon_4)F_{l,i}}{J_{\delta,i}} = 0 \tag{21}$$

which results that

$$\gamma_{i,ff} = -\frac{\varepsilon_2\varphi^2 + \varepsilon_3\varphi + \varepsilon_4}{\varepsilon_1}. \tag{22}$$

However, in practice the measurement of φ is imprecise. It means that the compensation of the measured disturbance incorporates an error φ_e. The state-space representation of the compensated system is

$$\dot{x}_{lat} = A_{lat}x_{lat} + B_{lat,1}\varphi_e + B_{lat,2}u_{lat,fb} \tag{23}$$

The value of the disturbance, which is resulted by φ_e, is in the range of the sensor noise. Thus, the feedforward compensation reduces the disturbance significantly. The rest of the disturbance is compensated through the robust feedback controller.

The feedback is designed based on the robust $\mathcal{H}_\infty$ control method. The role of the feedback is to guarantee the trajectory tracking of the vehicle. It means that the vehicle must follow a reference yaw-rate signal $\dot{\psi}_{ref}$. The performance is defined as

$$z_{lat,1} = \dot{\psi}_{ref} - \dot{\psi} \qquad |z_{lat,1}| \to min \tag{24}$$

where $\dot{\psi}_{ref}$ is computed using the velocity and the steering wheel angle of the driver, see (Rajamani 2005). Moreover, the performance $z_{lat,1}$ must be reached using minimum control input $u_{lat} = \left[\gamma_l\ \gamma_r\right]^T$:

$$z_{lat,2} = u_{lat,fb} \qquad |z_{lat,2}| \to min \tag{25}$$

The performances are compressed in a vector $z_{lat} = \left[z_{lat,1}\ z_{lat,2}\right]^T$. The state-space representation of the system for the control design which incorporates the performances and the measurement is the following:

$$\dot{x}_{lat} = A_{lat}x_{lat} + B_{lat,1}\varphi_e + B_{lat,2}u_{lat,fb} \tag{26a}$$

$$z_{lat} = C_{lat,1}x_{lat} + D_{lat}u_{lat,fb} \tag{26b}$$

$$y_{lat} = C_{lat,2}x_{lat} \tag{26c}$$

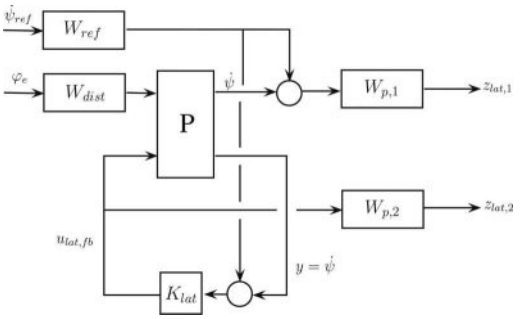


Figure 4. Closed-loop interconnection structure.

where the measured signal is $y = \dot{\psi}$. The augmented plant for the $\mathcal{H}_\infty$ design is illustrated in Figure 4. In the robust control design weighting functions are considered, which are formed as transfer functions, e.g. $W_{p,1}$, $W_{p,2}$ are the weights on the performance signals and W_{ref} scales the reference signal. In the robust control design the disturbance of the system is also handled through the block W_{dist}. This transfer function represents the amplitude and frequency range of the chassis roll measurement error.

The objective of $\mathcal{H}_\infty$ control is to minimize the $\mathcal{H}_\infty$-norm of the cosensitivity function $T_{z_\infty w}$. More precisely, the problem can be stated as follows (Scherer & Weiland 2000, Boyd, Ghaoui, Feron, & Balakrishnan 1997). The LMI problem of $\mathcal{H}_\infty$ performance is formulated as follows: the closed-loop RMS gain from w to z_∞ does not exceed Γ if and only if there exists a symmetric and definite positive matrix X_∞ such that

$$\begin{bmatrix} A_{cl}X_\infty + X_\infty A_{cl}^T & X_\infty B_{cl} & C_{cl}^T \\ B_{cl}^T X_\infty & -\Gamma I & D_{cl}^T \\ C_{cl} & D_{cl} & -\Gamma I \end{bmatrix} < 0 \qquad (27)$$

with $\Gamma > 0$. It means that it is necessary to find an admissible control K_{lat} for the open-loop plan P, which satisfies the following design criteria:

- the closed-loop system must be asymptotically stable,
- the closed-loop transfer function from w to z_∞ satisfies the constraint:

$$\|T_{z_\infty w}\|_\infty < \Gamma, \qquad (28)$$

for a given real positive value Γ,

where the index $_{cl}$ is related to the matrices of the closed-loop system. The resulted robust control design guarantees the trajectory tracking of the vehicle through the computation of the appropriate $\gamma_{l,fb}$, $\gamma_{r,fb}$.

Finally, the control inputs of the high-level layer are computed as

$$\gamma_i = \gamma_{i,ff} + \gamma_{i,fb} \qquad (29)$$

The resulted γ_l, γ_r signals are used as the reference of the low-level layer, see (Németh, Fényes, & Gáspár 2016).

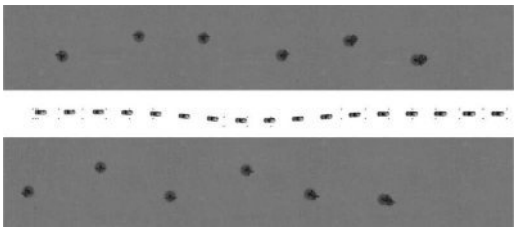
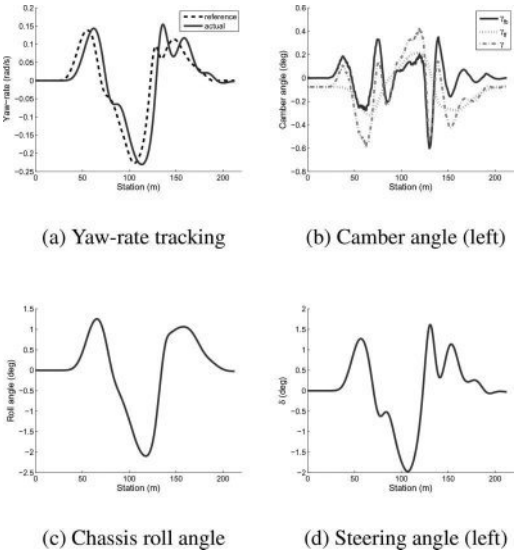


Figure 5. Vehicle trajectory.



(a) Yaw-rate tracking (b) Camber angle (left)

(c) Chassis roll angle (d) Steering angle (left)

Figure 6. Simulation results.

5 SIMULATION EXAMPLE

Finally, a simulation example is presented, in which the efficiency and the operation of the suspension system is demonstrated. In the simulation the vehicle must perform a double-lane change maneuver, which is formulated as a trajectory tracking control task. The selected vehicle is a full-size passenger car, whose mass is 1690 kg, the front suspensions are McPherson types. The simulation scenario is performed in CarSim, the control algorithm is implemented in Matlab/Simulink.

The course and the trajectory of the vehicle are illustrated in Figure 5. Since the vehicle avoids lane departure during the maneuvers, the designed control is successful, the steering of the front wheels is adequately actuated. In this simulation the velocity of the vehicle is 130 km/h. The details of the simulation are shown in Figure 6.

The yaw-rate tracking performance is shown in Figure 6(a). It can be seen that the tracking of the vehicle is performed with only a small error. This is the reason why lane departure is avoided. The camber angle control input of the front left wheel is presented in Figure 6(b). The feedforward input γ_{ff} compensates for the effect of the chassis roll, see Figure 6(c). Moreover, the feedback signal γ_{fb} guarantees the yaw-rate tracking.

The total camber angle, which is the sum of γ_{ff} and γ_{fb} yields the steering angle, see Figure 6(d).

As a consequence, the resulted control strategy is able to guarantee the trajectory tracking of the vehicle through the modification of the camber and the steering angles.

6 CONCLUSIONS

In the paper the modeling and control of independent steering based on the variable-geometry suspension have been proposed. In the presented solution the variation of the camber angle and the scrub radius of the wheels are actuated. The nonlinear formulation and the control-oriented linearizing of the suspension system, together with the modeling of the lateral dynamics have been presented. The multi-body analysis of the suspension system showed that the chassis roll angle has an important role in the positioning of the wheels. In the paper a robust combined feedforward-feedback control strategy is proposed, which is able to guarantee the trajectory tracking of the vehicle and to compensate for the disturbance effect of the chassis roll.

ACKNOWLEDGEMENT

The research was supported by the National Research, Development and Innovation Fund through the project "SEPPAC: Safety and Economic Platform for Partially Automated Commercial vehicles" (VKSZ 14-1-2015-0125).

This paper was partially supported by the János Bolyai Research Scholarship of the Hungarian Academy of Sciences.

REFERENCES

Boyd, S., L. E. Ghaoui, E. Feron, & V. Balakrishnan (1997). *Linear Matrix Inequalities in System and Control Theory*. Philadelphia: Society for Industrial and Applied Mathematics.

Evers, W., A. van der Knaap, I. Besselink, & H. Nijmeijer (2008). Analysis of a variable geometry active suspension. *International Symposium on Advanced Vehicle Control, Kobe, Japan*.

Goodarzia, A., E. Oloomia, & E. Esmailzadehb (2010). Design and analysis of an intelligent controller for active geometry suspension systems. *Vehicle System Dynamics 49*(1), 333–359.

Hu, C., H. Jing, R. Wang, F. Yan, & N. Chen (2015). Fault-tolerant control of FWIA electric ground vehicles with differential drive assisted steering. *9th IFAC Symposium on Fault Detection, Supervision and Safety for Technical Processes, Paris, France 48*(21), 1180–1185.

Lee, H., U. Lee, S. Ha, & C. Han (1999). Four-wheel independent steering (4wis) system for vehicle handling improvement by active rear toe control. *JSME International Journal Series C 42*(4), 947–956.

Lee, S., H. Sung, & U. Lee (2005). A study to the enhancement of vehicle stability by active geometry control suspension (AGCS) system. *13th International Pacific Conference on Automotive Engineering, Gyeongju, Korea*, 1–6.

Lee, U. K. & C. S. Han (2001). A suspension system with a variable roll centre for the improvement of vehicle handling characteristics. *Proceedings of the IMechE, Part D: Journal of Automobile Engineering 215*(6), 677–696.

Németh, B., D. Fényes, & P. Gáspár (2016). Independent wheel steering control design based on variable-geometry suspension. *8th IFAC Advances in Automotive Control, Kolmarden, Sweden*.

Németh, B. & P. Gáspár (2013). Control design of variable-geometry suspension considering the construction system. *IEEE Transactions on Vehicular Technology 62*(8), 4104–4109.

Pacejka, H. B. (2004). *Tyre and vehicle dynamics*. Oxford: Elsevier Butterworth-Heinemann.

Piyabongkarn, D., T. Keviczky, & R. Rajamani (2004). Active direct tilt control for stability enhancement of a narrow commuter vehicle. *Int. J. Automotive Technology 5*(2), 77–88.

Rajamani, R. (2005). Vehicle dynamics and control. *Springer*.

Ronci, M., P. Artuso, & E. Bocci (2011). Four independent wheels steering system analysis. *SAE Technical Paper*.

Scherer, C. & S. Weiland (2000). *Lecture Notes DISC Course on Linear Matrix Inequalities in Control*. Delft, Netherlands: Delft University of Technology.

Wang, J., Q. Wang, L. Jin, & C. Song (2011). Independent wheel torque control of 4WD electric vehicle for differential drive assisted steering. *Mechatronics 21*, 63–76.

Simulator and test-rig

Advanced Vehicle Control – Edelmann, Plöchl & Pfeffer (Eds)
© 2017 Taylor & Francis Group, London, ISBN 978-1-138-02992-7

Model-based steering ECU application using offline simulation (software in the loop)

M. Niegl & P.E. Pfeffer
Competence Center Vehicle Dynamics, Munich University of Applied Sciences, Munich, Germany

A. Contini
Institute of Mechanics and Mechatronics, TU Wien, Vienna, Austria

ABSTRACT: New methods for the application of the Electronic Control Unit (ECU) of Electric Power Steering (EPS) are required to reduce work load. Yet the application is done on proving grounds and is based on subjective evaluation of steering feel performed by an experienced engineer [1]. This paper shows the Software in the Loop (SiL) procedure to parametrize the ECU by vehicle and steering model simulation. First, with the topology, consisting of the Design of Experiment (DoE) Tool AVL CAMEO, IPG CarMaker, a model of a Steering ECU and the post processing tool MXevaluation, a comparison to the Model-Based Steering ECU application on a steering test bench is done. The simulation data is used to make a (statistic) behavior model of the whole system. The loop of the automated simulation and database generation is started by AVL CAMEO which varies the ECU parameters. Afterwards CarMaker runs a simulation and MXevaluation calculates Objective Parameters. Then, with a generated behavior model and the Objective Parameters of a benchmark vehicle, the ECU parameters can be optimized. Consequently the effort on proving grounds will decrease significantly and it will be easier to implement a growing number of new functions in the ECU.

1 INTRODUCTION

With increasing vehicle types and a growing number of different ECU applications for “Comfort”, “Sport” or “Sport +”, the effort to adapt steering (ECU) parameters in modern vehicles is growing disproportional. The steering feel is an important customer criterion for handling, safety and comfort. The tuning of the steering behavior on a steering system Hardware in the Loop (HiL) test bench was the first step to reduce man hour and costs due to better repeatability and constant test conditions in comparison to tests on proving grounds [2]. However, it was still necessary to change ECU parameters for damping and the boost curve step by step towards the subjective or objective target behavior. This procedure was enhanced by Contini et al. with an automated model based tuning procedure [3]. Instead of modifying the ECU parameters according to the own experience by hand, the engineer is using a DoE-Tool like AVL CAMEO to get a behavior model of the whole vehicle system due to ECU parameter variation. Every maneuver, like a Weave Test, which is automatically simulated with IPG CarMaker, is post processed. The post processing calculates, for example, several steering wheel torque levels at certain lateral acceleration points. These values characterize the shape of the hysteresis in a torque vs. lateral acceleration plot. Then AVL CAMEO optimizes the behavior, specifically the ECU parameters, to a certain target behavior. A similar procedure is used for the ECU application (also called calibration) of direct gasoline injection engines to reduce fuel consumption and optimize engine characteristics in a multidimensional room [4]. Of course a high quality vehicle model including a validation on the test bench is a requirement for good tuning results. This procedure still needs the steering system as hardware and a steering test bench for the optimization of the steering behavior. In contrast, this paper will show the possibilities to tune the ECU model-based using offline simulation without any vehicle or steering hardware.

2 MODEL-BASED ECU APPLICATION (SIL)

2.1 *The topology of the method*

The method described above was Hardware in the Loop. One step further is using the methods Model or Software in the Loop. Consequently, neither the steering system nor the test bench is needed for the tuning itself. Figure 1 shows how the topology is modified once again to reduce workload.

AVL CAMEO is the tool used for the Design of the Experiment, the database of the Objective Parameters and changed ECU parameters. Also, in AVL CAMEO, the modelling of the behavior of the system is done, as

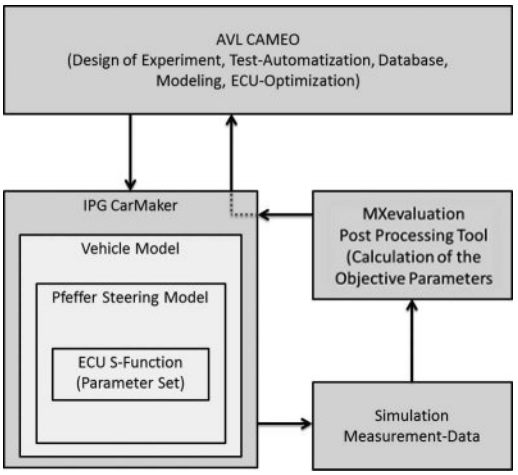


Figure 1. Topology model-based ECU application.

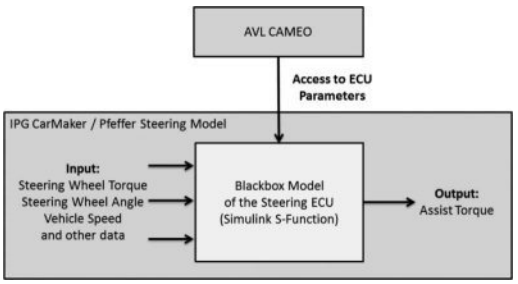


Figure 2. Interface for the ECU S-function.

well as the following optimization of the ECU parameters in regard to the Objective Parameters, which describe steering behavior. The steering system on the HiL test bench is substituted by the Pfeffer MXsteering model with an integrated ECU-S-function [5]. The whole system runs on a workstation PC without a real-time operating system. Thus the steering model is in the loop (MiL), not the hardware, in addition, the ECU software is in the loop (SiL).

2.2 *Interface of the ECU S-function*

The steering model is to be parametrized on a steering test bench first. The ECU blackbox model must be provided by a steering system supplier, e.g. as an S-function in Mathworks Simulink. The steering model is integrated in an IPG CarMaker vehicle model. The Interface in between the steering model is shown in Figure 2.

The input data of the ECU S-Function is the steering wheel torque, steering wheel angle, steering wheel angular velocity and the vehicle speed for example. The output data is the calculated assist torque on the column or rack of the steering system. The data for input and output is provided by CarMaker through direct variable access.

IPG CarMaker Name	Description
MX.WT.SWTvsSWA.k_at_10pc_maxSWA	average gradient over range ± x °, where x = 10 % of peak steering angle
MX.WT.SWTvsSWA.k_at_0SWA	gradient evaluated at zero steering angle
MX.WT.SWTvsSWA.k	Torque amplitude / angle amplitude
MX.WT.YawVelvsSWT.Resp_Deadband	abscissa deadband
MX.WT.AYvsSWA.Angle_Deadband	abscissa deadband
MX.WT.AYvsSWA.Steering_Hystersis	area bounded by hysteresis loop and ordinate values ± 1 m/s^{2}", divided by 2 m/s^{2} (equivalent to average angle deadband).
MX.WT.SWTvsAY.SWT_at_1AY_pos	± torque levels at ± 1 m/s^{2}" while steering away from centre
MX.WT.SWTvsAY.SWT_at_1AY_neg	
MX.WT.SWTvsAY.AY_at_0SWT_pos	± lateral acceleration levels at 0 N m
MX.WT.SWTvsAY.AY_Hysteresis	abscissa deadband

Figure 3. Objective parameters for weave test charaterization.

2.3 *Objective parameters for optimization*

A post processing tool, called MXevaluation is used to calculate Objective Parameters out of the simulation data. It was developed by MdynamiX AG which is an affiliated institute of Munich University of Applied Sciences. This tool can, for instance, calculate over 40 Objective Parameters for a Weave test maneuver out of simulation or measurement data. These parameters are based on ISO-Standards and scientific work like Harrer [6], which correlates the subjective steering feel with the Objective Parameters for on-center maneuver. Figure 3 shows the top ten Objective Parameters, chosen for the model-based optimization regarding Harrer's correlation of subjective ratings and Objective Parameters [6].

MXevaluation was originally written in Matlab code. For the usage in CarMaker all scripts were compiled and stored in an executable file. This file is linked to CarMaker with a Tcl script, which is executed automatically after every simulation. All of the parameters have their own CarMaker variables, so AVL CAMEO can simply access and store them in its database. The naming of the variable is systematically: "MX" is short for MdynamiX, "WT" means Weave Test. The next abbreviation describes the axes of the diagram, in which the parameter could be visualized. "SWT" is Steering Wheel Torque, "SWA" is Steering Wheel Angle, "AY" is lateral Acceleration and "YawVel" is Yaw Velocity. The meaning of the parameters in detail is shown in Figure 3. The tool can also be used for post processing maneuvers like Step-Input, Transition-Test, Frequency response and many more.

2.4 *ECU optimization using weave tests*

To evaluate steering feel, Objective Parameters calculated from Weave Tests are suited [6]. AVL CAMEO is used for test preparation, test execution and the optimization. During the preparation, the maneuver, the ECU parameters, as well as their limits and the Objective Parameters are defined. CAMEO generates a database of systematically varied ECU parameters with the method of Design of Experiments (DoE). A typical test for a steering system would contain five ECU parameters for one maneuver at a certain vehicle velocity. In this paper the lower variation limit was

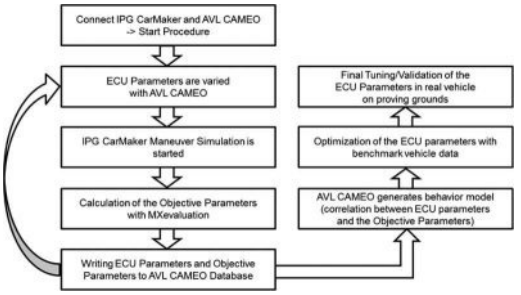


Figure 4. Model-based steering ECU application using offline simulation.

always zero. The upper limit was increased with ECU parameter "1" to ECU Parameter "5". This was necessary because of an internal rule. For an adequate quality behavior model that would be more than 300 sets of parameters, specifically over 300 maneuver simulations. In the described case the system and the useful limit for every ECU parameter were already known. 160 maneuvers were enough to achieve a good model quality. These maneuvers are automatically started in CarMaker with CAMEO and took about one hour. The speed of the simulation and post processing could be decreased simply in the future. Every maneuver has some pretests which could be excluded. After the last maneuver, a behavior model is generated out of the database, where the ECU parameters and the Objective Parameters are stored. Typical target behavior could be a Weave Test of a predecessor model, specifically the Objective Parameters of that test. The optimization runs in CAMEO, as a result there is often more than one ECU parameter set, which fits the target behavior best. Next there are different possibilities to validate the chosen parameter set. The best way is to run a CarMaker simulation with this set first. If the steering system works like expected, the next step would be a validation on a HiL test bench or with a real vehicle on proving grounds. The whole process of "Model-Based Steering ECU Application Using Offline Simulation" is shown in Figure 4.

After the offline optimization it is also possible to continue with tests on a HiL test bench. This would be useful, if there are small differences/updates between the actual hardware of the steering system or the ECU software and their models. The final tuning on proving grounds is still necessary to cover situations of daily traffic. In addition, the feedback optimization of higher frequencies, especially from 5 to 15 Hertz, is important for the customer but not characterized with simulated maneuvers and Objective Parameters [7].

3 RESULTS

3.1 *Model-quality and steering behavior*

The result of the described modelling of the steering system, vehicle model, the ECU parameters and the responding Objective Parameters is shown in Fig. 5.

Response Name	Model Type	Positive Only	Model Quality
MX.WT.AYvsSWA.Angle_Deadband	Automatic (iNN II)		
MX.WT.AYvsSWA.Steering_Hystersis	Automatic (iNN II)		
MX.WT.SWTvsAY.AY_at_0SWT_pos	Automatic (iNN II)		
MX.WT.SWTvsAY.AY_Hysteresis	Automatic (iNN II)		
MX.WT.SWTvsAY.SWT_at_1AY_neg	Automatic (iNN II)		
MX.WT.SWTvsAY.SWT_at_1AY_pos	Automatic (iNN II)		
MX.WT.SWTvsSWA.k	Automatic (iNN II)		
MX.WT.SWTvsSWA.k_at_0SWA	Automatic (iNN II)		
MX.WT.SWTvsSWA.k_at_10pc_maxSWA	Automatic (iNN II)		
MX.WT.YawVelvsSWT.Resp_Deadband	Automatic (iNN II)		

Figure 5. Quality of the behavior model.

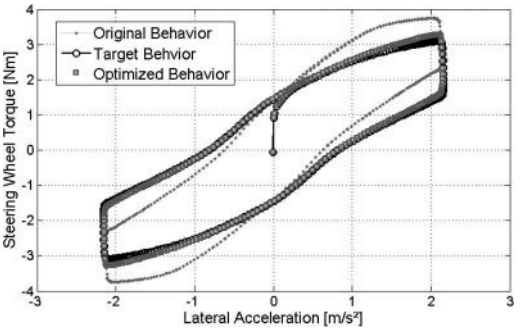


Figure 6. Weave test result steering wheel torque vs. lateral acceleration.

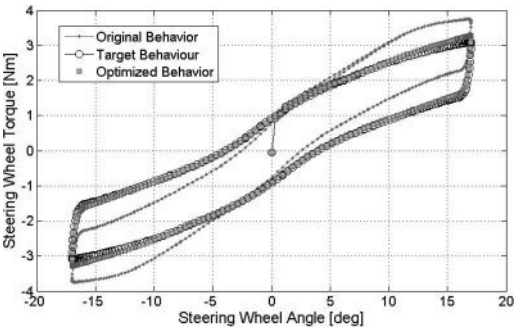


Figure 7. Weave test result steering wheel torque vs. steering wheel angle.

AVL CAMEO evaluates four Objective Parameters with the green (grey) arrow as high model quality and six with the yellow (white) one as good quality. Like expected, the repetition points of the simulations were congruent.

The maneuver was a Weave Test with an amplitude of 17.5 degree, 80 kph and a frequency of 0.2 Hz. Figure 6 and 7. show the original (thin, grey dotted line), the target (thick, black dotted line) and the optimized (thick, grey dotted line) behavior. The figures have different x-axis, first it is the lateral acceleration and second it is the steering wheel angle. The y-axis is the steering wheel torque.

It is shown that the Model-Based Steering ECU application is useful to tune the steering behavior effectively at the on-center. Before the optimization, the

	ECU P 1	ECU P 2	ECU P 3	ECU P 4	ECU P 5
Original Behavior	58,67%	38,69%	41,11%	35,54%	119,14%
Target Behavior	100,00%	100,00%	100,00%	100,00%	100,00%
Optimized Behavior	65,29%	108,73%	105,13%	93,40%	107,89%

Figure 8. Comparison of the ECU parameters.

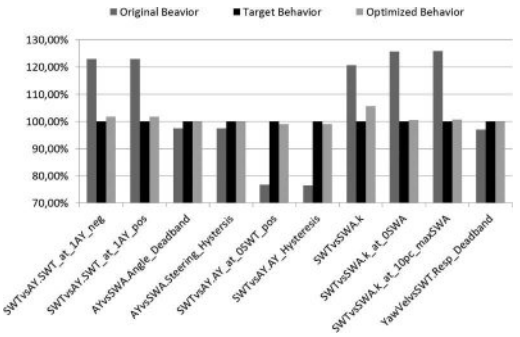


Figure 9. Comparison of the objective parameters.

steering wheel torque does not fit to the target behavior. On the contrary, the hysteresis are nearly congruent to the target hysteresis once the optimization of the ECU parameters for the assist torque level is done. The steering wheel torque over 2 m/s^2 or 15 degree is not fitting exactly. This region is not optimized anymore with the chosen Objective Parameters. The areas of the three hysteresis are about the same size. Usually the area must be tuned with ECU parameters for damping using the same method. In this example the damping parameters are the same for all the parameter sets to show the optimization for one ECU function.

3.2 *Comparison of the different ECU parameter sets*

Figure 8 shows the values of ECU parameters (ECU P) in percentage of the target behavior. The original tuning differs partly more than 60 percent in comparison to the target. It is noticeable, that after the optimization, the differences are in between 10 percent, although the ECU parameters have not been directly optimized. Only the first ECU parameter differs still heavily.

This is not an insufficient optimization by CAMEO. In the modelling process of the tool it is visible, that the effect of "ECU P 1" to the Objective Parameters is nearly zero in comparison to the others. "ECU P 1" is only for tuning the zero torque region, which has nearly no influence on this test scenario.

The analysis of the Objective Parameters in Figure 9 shows a similar result: Before the optimization some Objective Parameters differ up to 26 percent of the target. After the model-based tuning most of them are in between 2 percentile. Only the stiffness "MX.WT.SWTvsSWA.k" differs 6 percent, which is still very close to the target. Some parameters, for example "AYvsSWA.Angle_Deadband" or "AYvsSWA.Steering_Hysteresis" and "YawVelvsSWT.

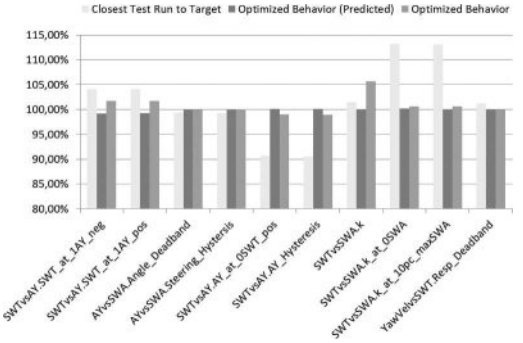


Figure 10. Qualitiy of the behavior prediction.

Resp_Deadband" have nearly the same values for Original, Target and Optimized Behavior. These parameters are strongly influenced by the extended sense of the steering feel [8]. Also, they could be optimized with variation of the steering gear ratio.

Another result is the good quality of the modeling and the precise prediction of the steering behavior with AVL CAMEO. This can be shown with the Objective Parameters in Figure 10. The ECU parameter set "Closest Test Run to Target" is one set out of the 160 tests where the target behavior is reached best. However, there are differences up to 13.2 percent. In contrast, the predicted behavior of CAMEO is always closer to the optimized behavior, respectively the target. The differences are less than 2 percent. Only the stiffness parameter "SWTvsSWA.k" was not predicted as good as the others.

Subsequently it is not sufficient to make just enough tests without the modelling afterwards and it should be considered to simulate a few more maneuvers than 160.

4 VALIDATION OF THE RESULTS

A further validation of the tuned ECU parameters with a vehicle on proving grounds is not essential. This validation was already done implicitly. The vehicle model is validated with real vehicle measurements. The steering model was parametrized with the steering in the loop (HiL) test bench of Munich University of Applied Sciences. Part of the parametrization procedure is also a validation with open and closed loop maneuvers. The ECU algorithm (S-function) was provided and validated by a supplier. The ECU parameter sets of the target and the original tuning were both tested on proving grounds and with the steering in the loop test bench. The ECU parameters and the simulation result of the model-based tuning using offline simulation match the ECU parameters and the result of the target behavior. Based on these conditions the whole process is validated. In future projects the validation respectively the whole model based process will be done directly.

5 CONCLUSION AND OUTLOOK

Fully automated tuning of the steering behavior with a SiL optimization toolchain can be very efficient. However, a smart test design has to be done and the parametrization of the steering system and the tuning on proving grounds are still necessary. The considerable advantages are that a huge amount of maneuvers can be simulated during the night without a test engineer. The simulation runs much quicker than real time and the repeatability is ensured. After the behavior model is finished, many different ECU applications can be generated easily with their own target values. The modelling is also useful to find ECU parameters with a strong or weak impact on the steering feel. For automobile manufacturers it is considerably simpler to generate a remarkable steering feel or behavior, using the described methods and Objective Parameters. The steering feel can change marginal over the model range, but customers are more satisfied, if the they can feel the brands unique steering application. In future, the quality and performance of the toolchain can be improved with faster post processing, more maneuvers, or more precise target values. Especially the off-center region between 2 m/s^2 and 10 m/s^2 is not tuned by the shown Weave Test maneuver. The optimization should be done with every vehicle velocity used in the ECU algorithm. The damping parameters also have a high impact on the steering feel and should be tuned. Still all of these tasks can be done with the shown topology. Another possible field of study would be an optimization of the hardware parameters like the stiffness of the column with the shown method.

REFERENCES

[1] P.E. Pfeffer, M. Harrer (ed.) “Lenkungshandbuch”, Wiesbaden, Vieweg+Teubner, 2011

[2] F. Specka, A. Contini, S. Hakuli, B. Schick, P.E. Pfeffer “Bewertung und Optimierung des Lenkverhaltens im Gesamtfahrzeug am “Steering-in-the-Loop” Prüfstand”, Reifen Fahrwerk Fahrbahn, 2013

[3] A. Contini, et al. “Model Based Boost Curve Application for different Vehicle Speeds on a Steering-in-the-Loop Test Bench”, VDI Berichte Nr. 2241, 15. Internationale VDI-Tagung, 2015, pp. 293–305.

[4] H.-M. Koegler “DGI-Engine Calibration, Using New Methodology with CAMEO”, SAE_NA Technical Paper Series, 01-012, 2001

[5] P.E. Pfeffer “Interaction of Vehicle and Steering System Regarding On-Center Handling”, PhD Dissertation, University of Bath, 2006

[6] M. Harrer, “Characterisation of Steering Feel”, PhD Dissertation, University of Bath, 2007

[7] R. Schimpf “Charakterisierung von Lenksystemen mit Hilfe eines Lenksystemprüfstands”, PhD Dissertation, TU Wien, 2016

[8] H. J. Wolf “Ergonomische Untersuchung des Lenkgefühls an Personenkraftwagen”, PhD Dissertation, TU München, 2009

Advanced Vehicle Control – Edelmann, Plöchl & Pfeffer (Eds)
© 2017 Taylor & Francis Group, London, ISBN 978-1-138-02992-7

Control system of a wheel-based "auto.mobile-driving simulator"

T. Tüschen, S. Ernst, D. Beitelschmidt & G. Prokop
Technische Universität Dresden – Chair of Automobile Engineering, Dresden, Germany

W. Tischer
AMST Systemtechnik GmbH, Ranshofen, Austria

ABSTRACT: Driving Simulators have always been a valuable development tool in the automobile industry. Till today they are the only evaluation tool to assess human machine/vehicle interactions. But recent trends in the automobile development process, like autonomous driving functions, show that common driving simulators concepts are not able to meet today's development requirements.

The "auto.mobile-driving simulator", a wheel based driving simulator approach, addresses this problem by using a completely new motion concept. The fact that the simulator is based on wheels allows it on one hand to be used independently from local restrictions and on the other hand the simulation of high frequent accelerations.

For the correct simulation of the vehicle motion and driver perception, an advanced control concept is necessary. Due to the use of wheels as a non-linear force transmission element, contrary to common driving simulator, a quasi-inverted vehicle model is required for the control system.

1 INTRODUCTION

1.1 *Driving simulators*

The automotive sector is currently in an unprecedented technological change. Apart from the utilization of new drive concepts, the essential and primary important change is the broad launch of advanced driver assistance systems (ADAS) and autonomous driving functions in automobiles. Starting from already established driver assistance systems, for instance the adaptive cruise control (AAC), over more recent assistance systems, such as semi-automated driving, to highly automated driving, the driving task is getting into the focus of the automobile developement. On one hand, the driving task will be taken over by the vehicle to a higher degree, but on the other hand, critical situations of handover scenarios, while fully automated driving is not available or desired, are considered to gain huge importance. Although it might sound contradictory when talking about automated functions, this in turn signifies that the development process has to be focused more on the driver and the human-machine-interface (HMI). Studies have shown that even simple ADAS, for instance ACC, are already leading to increasing response time in critical handover scenarios (Larsson et al. 2014, Merat et al. 2014). In addition, (Carsten et al. 2012) have shown that the drivers' visual attentiveness to the road decreases with the increasing level of automation. This in turn can lead to and not preventing a higher danger potential. Unfortunately, simulated driver models are not capable to assess the quality of the HMI or the danger potential of the handover scenario, respectively. In consequence, testing and validating of ADAS and automated driving by a real driver under repeatable and even more important safe environment conditions have already become important and will in the future be the key pillar to reliably evaluate the effectiveness of such systems.

In addition, the development phases in vehicle engineering are continuously getting shorter and more cost-effective. Simultaneously, more vehicle derivates are entering the market. To accomplish these efficiency enhancements, as much as possible of the engineering process has to be virtualized. Accordingly, the automobile industry reduces the amount of prototype testing by using sophisticated simulation methods. But as soon as requirements related to subjective evaluations of vehicle characteristics have to be considered, real prototypes or driver-in-the-loop simulations are becoming crucial. To investigate the functionality and the interaction of HMI also in early phases in the vehicle development, driving simulators which are capable to depict even complex maneuvers with high immersion are therefore strongly required.

1.2 *Limitations*

The majority of current state-of-the-art driving simulators in the automobile industry are sharing a very similar design. A parallel kinematic mechanism – usually in form of a hexapod (Stewart platform), is used in nearly every dynamic simulator as the main part of the motion system. The hexapod allows limited motion in all six translational and rotational directions of motion.

These simulators have a disadvantage determined by their motion system: they are very limited in their motion space. Even hexapods with long cylinders have a plane motion space of only up to 1–2 meter. To compensate this limited motion space, a technique called Tilt-Coordination is used in driving simulators. By tilting the driver, a transformation of the gravity vector leads to a horizontal perceived motion (Fischer 2009). Unfortunately, the Tilt-Coordination is very limited by the humans' perception which often leads to a misperception in the simulator up to simulator sickness (Tueschen et al. 2016). Since the vehicle motion simulation by using only a hexapod does not comply with the recent requirements, the dynamic driving simulators are often upgraded with a single or double slide system (Zeeb 2010, Murano et al. 2009). Depending on the concept, it is thereby possible to present an additional longitudinal/lateral motion. But even these systems are still very limited in their motion space and simulation quality (Tueschen et al. 2016).

2 AUTO.MOBILE-DRIVING SIMULATOR

2.1 *Concept idea*

The main idea of a wheel based driving simulator (WBDS) is to be unbound and independent from any external source. Hence, it is possible to use the WBDS on any sufficient level surface. Thus, contrary to a sled system, the motion space of the system is theoretically unlimited.

The concept of the auto.mobile-driving simulator (Fig. 1) consists of three main parts: a simulation dome, a tripod with a ring bearing, and a wheel-based motion platform.

The design and the function of the simulation dome are very similar to current driving simulators. It contains a cockpit mockup, the visualization and the acoustic environment. Altogether, it simulates the drivers' environment and generates the visual and auditory stimuli.

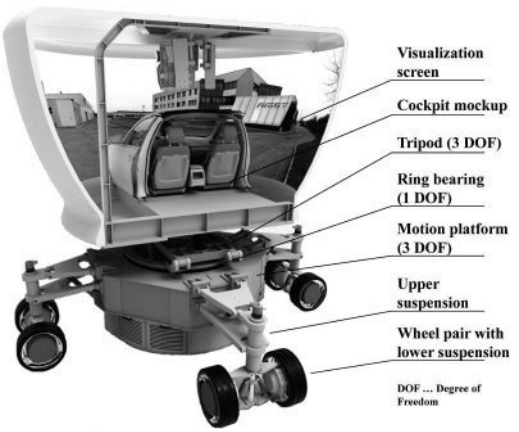


Figure 1. auto.mobile-driving simulator.

Underneath the simulation dome, a tripod and ring bearing are installed as one of the two independent motion systems. The tripod provides 3 degrees of freedom (3 DOF). The ring bearing (1 DOF) decouples the yaw motion of the simulation dome from the motion platform. Hence, the simulator is able to yaw the simulation dome independently from the motion platform which is crucial for the motion concept of the simulator.

The lower wheel-based motion platform is the key difference to common driving simulator concepts. It is a self-moving system with four wheel pairs which can travel freely in the horizontal plane (3 DOF). Each wheel pair consists of two separately driven wheels, which are both connected to a steering axis via a suspension kinematic. Additionally, the steering axis is connected with the platform with a further independent suspension kinematics and allows an unlimited steering of the wheel pair (Tueschen et al. 2016). The motion platform allows the simulator to accelerate with up to 10 m/s^2. The accumulator for the electrical wheel-hub motors, the steering, and the auxiliary devices are also installed in the motion platform, which makes the simulator independent from any external system.

2.2 *Motion concept*

Contrary to cylinder or sled actuated systems; a wheel-based simulator needs to deal with the tire as a non-linear and non-holonomic force transmission element. Due to the fact, that the tire has a dynamic, rolling-speed-based response time (relaxation length) (Bakker et al. 1987) (Fig. 2) the simulation quality is highly dependent on the rolling speed of the tire. Additionally, the motion velocity of the simulator differs from the simulated car. For instance, while the simulated car is driving at a constant speed, the simulator is in stand-by and resting at a defined position. To be able to still react to a sudden driver input (e.g. lane change) it is crucial to avoid the delay in the response time. To address the issue of the situation dependent dynamic phase delay induced by the relaxation length, it is necessary that the rolling-speed remains above a minimum level. In the auto.mobile-driving simulator concept, this is enabled by the redundant yaw DOF. By rotating the motion platform and simultaneously counter-rotating the simulation dome, the driver

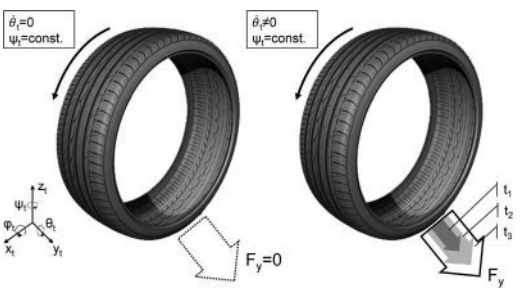


Figure 2. Non-holonomic constraint, relaxation length.

remains in the same orientation while the wheels still have a defined speed. It is also possible to have a yaw motion and a horizontal motion in superposition. In this way it is possible to adjust the wheel rotation to a defined speed, independently from the horizontal motion of the simulator. Hence, the dynamic phase delay can be reduced to a nearly static delay.

3 CONTROL SYSTEM

3.1 *Overview*

As mentioned above, the significant difference to state-of-the-art simulators is the wheel-based motion platform. Hence, a new control algorithm needs to be developed.

In short, all conventional driving simulators are operated by a nearly identical control system. The input of the driving simulation feeds a Motion Filter, which is responsible to manipulate the feed-in signals by taking the given motion space as well as the human perception thresholds into account. Thereby, it is mandatory that the driver will not perceive a difference between the simulated and the expected forces. Based on the fact that the human perception thresholds are inaccurate, it is possible to manipulate the acting forces or even substitute complete motion sequences without distorting the perceived forces in the simulator. Unfortunately, this concept does not work very well in most of the simulators due to their very limited motion space.

The manipulated motion cues are then processed by the Motion Control into a defined cylinder length (velocity, acceleration) or depending on the system into traverse path of the sledge system.

Due to the fact, that cylinders and sledge systems are linear systems, the control task is not very sophisticated and successfully implemented in driving simulators.

Since the tire is a non-holonomic constraint and has a non-linear force transmission behaviour, the main challenge of the "auto.mobile-driving simulator" is the control system (Fig. 3).

The following explanations in particular shed light on the motion platform concept, while the tripod and ring bearing motion are not explained in detail.

3.2 *Motion filter*

The first main part of the Control System is the Motion Filter (MF). The task of the WBDS MF is to calculate the motion of the simulators centre of gravity (CoG) according to the simulated vehicle input, by taking the simulators actuators and the size of the motion space into account. Contrary, to common MF (e.g. Classical Washout (Fischer et al. 2011)) the newly designed MF will take advantage of the wide motion space by avoiding the active use of the Tilt-Coordination technique. This in turns signifies that the simulation quality will increase.

Further, the MF calculates the optimum rotational speed of the motion platform and its counter rotation of the simulation dome. It is for this reason that MF increases its input from 6 degrees of freedom (DoF) up to 7 DoF.

3.3 *Motion control*

3.3.1 *Structure*

The second main part of the Control System, the Motion Control (MC), receives its input from the MF

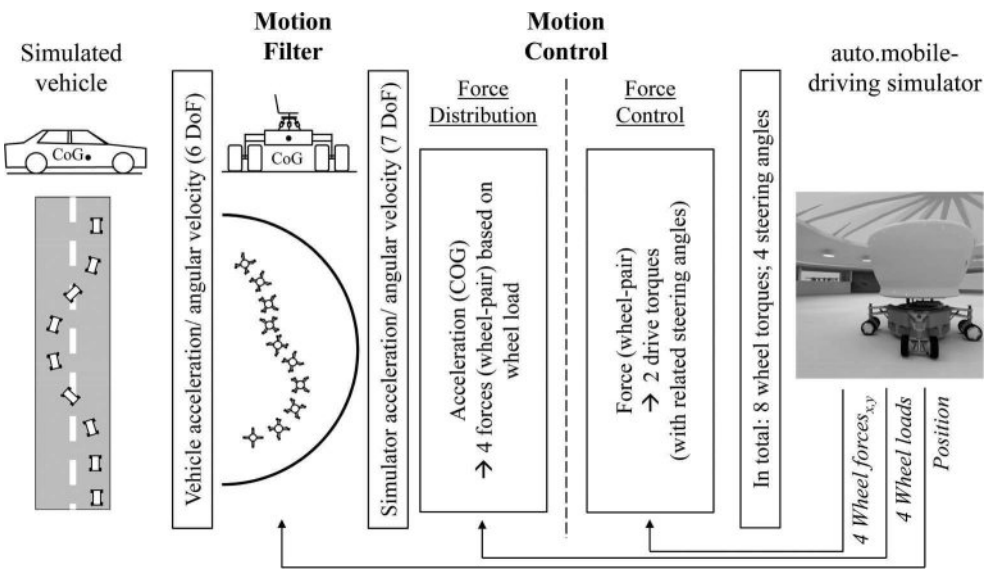


Figure 3. Control system.

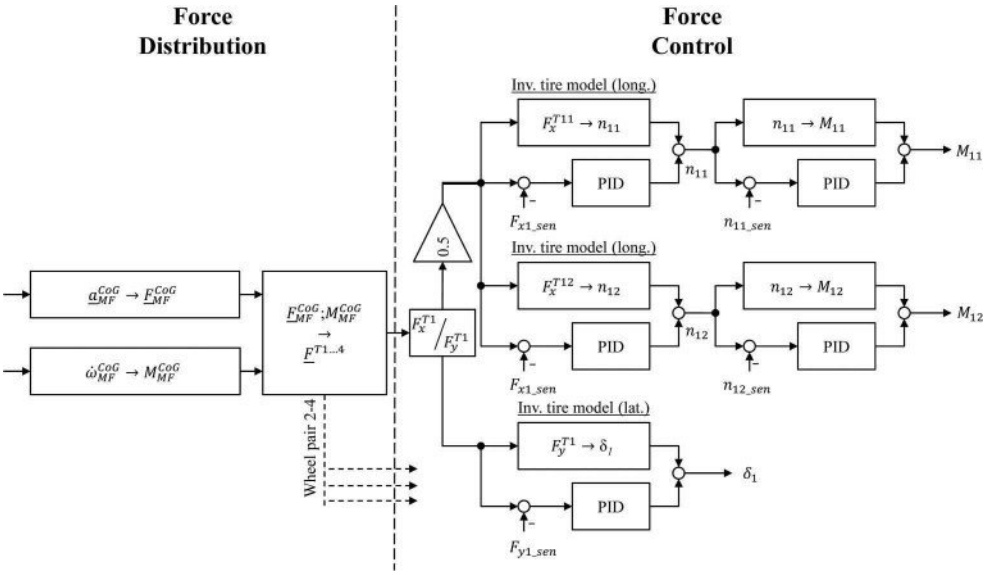


Figure 4. Motion control.

with the information of the desired acting forces of the simulators CoG and its rotational speed. The task of the MC is to convert this input into eight drive torques for the electrical motors and the steering angle for each wheel pair. This algorithm is again separated into two control algorithms (Fig. 4): the Force Distribution and the Force Control.

3.3.2 *Force Distribution*

The Force Distribution algorithm can be understood as an inverted vehicle simulation. In common vehicle control systems the input is the desired torque (throttle) and steering angle, which the vehicle converts into a motion. This can be described as "multiple input-single output" process which needs to be inverted for the Force Distribution into a "single input-multiple output" process. It is important to keep in mind that the WBDS, with its four wheel-pairs, is an overdetermined system. This in turns means that there is no unique solution for the output signals.

The given input of the Force Distribution is a force and torque in the CoG for which it is necessary to find the suitable outputs of the wheel torques and steering angles.

At first the Force Distribution algorithm calculates the necessary force ($\underline{F}_{tot}$) and torque (M_{tot}) to realize the desired MF motion input in the CoG (see Equation 1 & 2 below) taking the rolling resistance; air resistance and derived MF Force ($\underline{F}_{MF}$) as well as MF torque (M_{MF}) into account. (Fig. 5)

$$\underline{F}_{tot}^{CoG} = \underline{F}_{roll}^{CoG} + \underline{F}_{air}^{CoG} + \underline{F}_{MF}^{CoG} \tag{1}$$

$$M_{tot}^{CoG} = M_{roll}^{CoG} + M_{MF}^{CoG} \tag{2}$$

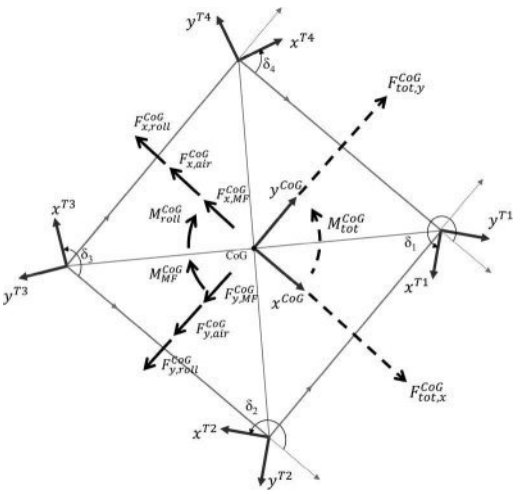


Figure 5. Force distribution.

This total force and torque demand in the CoG needs to the distributed to the tire according their force potential with regard to their dynamic wheel load.

By calculating the tire contact force via an extended and inverted double-track model, it is possible to calculate the potential lateral and longitudinal force transmission of the wheel pairs. Then, $\underline{F}_{tot}$ in the CoG is distributed to the four wheel-pairs ($\underline{F}_F$; *wheel-pair i = 1-4*) depending on their transferable force potential. To realize M_{tot}, a compensation force ($\underline{F}_M$; *wheel-pair i = 1-4*) is added to $\underline{F}_F$ (Equation 3). (Fig. 6)

$$\underline{F}^{Ti} = \underline{F}_F^{Ti} + \underline{F}_M^{Ti} \tag{3}$$

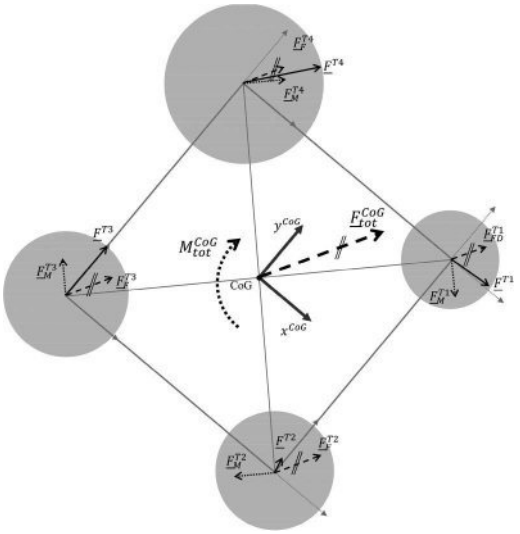


Figure 6. Force potential.

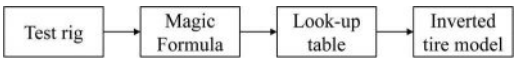


Figure 7. Design of the inverted tire model.

3.3.3 *Force control*

The more sophisticated task is to transform the distributed forces into two drive torques of each wheel-pair, as well as the steering angle.

By measuring a particular tire on a test rig, an existing Pacejka "Magic Formula" tire model was parameterized (Bakker et al. 1987). With the help of this tire model, look-up tables (LUT) for the longitudinal and lateral direction are generated and used as input values for the inverted tire models (Fig. 7).

The creation of the LUT and the functionality of the inverse tire models are described using the example of the longitudinal direction. To determine the longitudinal force, wheel load, camber, as well as slip angle and slip are needed for the "Magic Formula" tire model (Fig. 8). Slip and longitudinal force are stored in a LUT (the last two columns in Figure 8). To determine a value for the slip from the LUT with a given longitudinal force, the actual values of camber, wheel load, and slip angle must be provided. Camber and wheel load can be measured directly for each wheel on the driving simulator. The actual value of the slip angle can be measured on the driving simulator or the most recent calculated value of the inverse lateral tire model can be used. A rounding procedure is used to determine an interpolation range depending on the input values. The selection process is shown in Figure 8. (input values: $\gamma = -3°, Fz = 10\,kN,\ \alpha = -5°$) It can be seen that always the value with the smallest deviation is selected. Accordingly, a higher resolution of the input values improves the accuracy of the model.

As result of the process, the slip characteristic of the tire is received in each operating condition (Fig. 9). It is

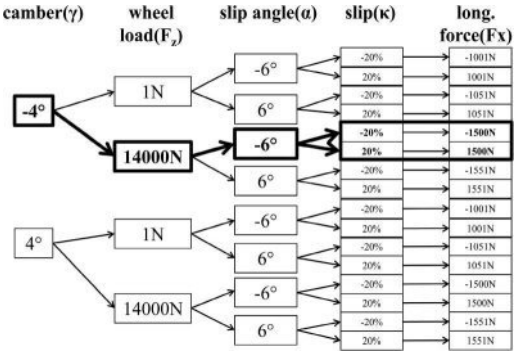


Figure 8. Look-up-table.

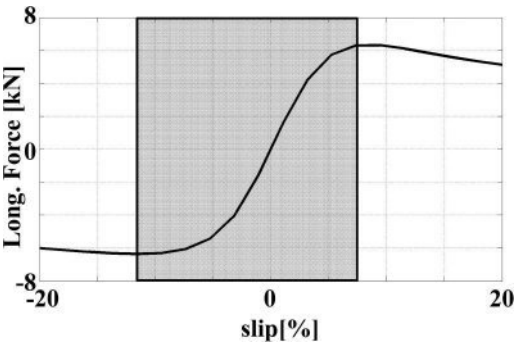


Figure 9. Inverted slip.

obvious, that for an inversion of values above the maximum force, the system is no longer explicit. In this range, for one force value at least two slip values exist. To ensure an explicit inversion, only the range between maximum and minimum of the longitudinal force is used for the interpolation (marked grey in Figure 9).

The slip (κ) is linearly interpolated, after inverting the signals. With this value, the rotational speed (n) of the tire can be determined by the following Equation 4.

$$n = \frac{v_x \cdot (\kappa + 1)}{r_{dyn}} \tag{4}$$

$v_x = longitudinal\ speed$;
$r_{dyn} = dynamic\ radius\ of\ the\ tire$

With the rotational speed, the motors can be controlled via drive torque. The inverse tire model for controlling the lateral dynamics is analogous to that of the longitudinal dynamics. Instead of slip and longitudinal force, the slip angle and the lateral force are stored in the LUT. The steering angle of the wheels can be calculated by the slip angle

The inverted tire models in turn are used as open-loop control. A parallel closed-loop with a simple PID controller is installed to primarily gain a lower derivation in the range of quasi static force demand.

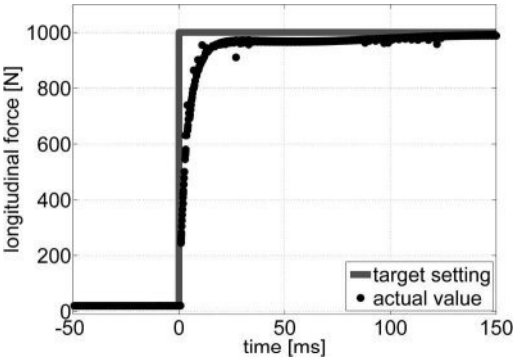


Figure 10. Longitudinal force step response.

4 RESULTS AND CONCLUSION

In the experiment below, an exemplary plausibility check for the functionality of the inverse tire model is shown. Investigations are calculated using a multibody model of the driving simulator. Longitudinal and lateral dynamics are considered independently in the plausibility test. For this, fixed steering angles are given in investigating the longitudinal dynamics. For each wheel pair of the driving simulator, a longitudinal force is given. For the longitudinal dynamic study, the force vectors are commutated and have the same amount. In Figure 10 a force step specification for the longitudinal force and the system response is shown for one wheel pair of the driving simulator.

REFERENCES

Bakker, Egbert, Lars Nyborg, and Hans B. Pacejka. "Tyre Modelling for Use in Vehicle Dynamics Studies." *SAE Technical Paper Series* (1987): n. pag.

Carsten, O., F. C. H. Lai, Y. Barnard, A. H. Jamson, and N. Merat. "Control Task Substitution in Semiautomated Driving: Does It Matter What Aspects Are Automated?" *Human Factors: The Journal of the Human Factors and Ergonomics Society* 54.5 (2012): 747–61.

Fischer, Martin, Håkan Sehammar, and Göran Palmkvist. "Applied Motion Cueing Strategies for Three Different Types of Motion Systems." *Journal of Computing and Information Science in Engineering J. Comput. Inf. Sci. Eng.* 11.4 (2011): 041008.

Fischer, Martin. *Motion-Cueing-Algorithmen Für Eine Realitätsnahe Bewegungssimulation*. Braunschweig: DLR, 2009. Print.

Larsson, Annika F.l., Katja Kircher, and Jonas Andersson Hultgren. "Learning from Experience: Familiarity with ACC and Responding to a Cut-in Situation in Automated Driving." *Transportation Research Part F: Traffic Psychology and Behaviour* 27 (2014): 229–37.

Merat, Natasha, A. Hamish Jamson, Frank C.h. Lai, Michael Daly, and Oliver M.j. Carsten. "Transition to Manual: Driver Behaviour When Resuming Control from a Highly Automated Vehicle." *Transportation Research Part F: Traffic Psychology and Behaviour* 27 (2014): 274–82.

Murano, Takahiko, Takashi Yonekawa, Masami Aga, and Sueharu Nagiri. "Development of High-Performance Driving Simulator." *SAE International Journal of Passenger Cars – Mechanical Systems SAE Int. J. Passeng. Cars – Mech. Syst.* 2.1 (2009): 661–69.

Zeeb, Eberhard. "Daimler's new full-scale, high-dynamic driving simulator–a technical overview". *Actes INRETS* (2010): 157–165.

Tueschen, Tüschen, Felix Kocksch, Denise Beitelschmidt, Günther Prokop. "'auto.mobile-driving simulator' – suspension design of a wheel-based driving simulator". *Proceedings of Chassis Tech Plus* (2016): 411–434.

Advanced Vehicle Control – Edelmann, Plöchl & Pfeffer (Eds)
© 2017 Taylor & Francis Group, London, ISBN 978-1-138-02992-7

Tire-suspension hardware-in-the-loop simulation system compensating delay of testing machine

T. Hosono, Y. Udagawa, S. Kawaguchi & T. Shiiba
Department of Mechanical Engineering, Meiji University, Kanagawa, Japan

ABSTRACT: This paper aims to reduce the influence of the delay in a tire-suspension hardware-in-the-loop simulation (HILS) system to improve the accuracy of the analysis. The HILS system was developed to evaluate the vehicle dynamics characteristics including the non-linear properties of the tire and the suspension components. A hybrid method was used for the reduction of the influence of the delay in the HILS system. The influence of the delay was compensated by using the lateral force measured in the actual tire and the lateral force calculated from the tire model. A vehicle dynamics analysis with the HILS system was conducted to assess the influence of the delay in the HILS system.

1 INTRODUCTION

An accurate description of the tire characteristics is important for the vehicle dynamics analysis. However, the characteristics of the tire are complex (Pacejka 2002), and the actual usage of the tire is affected by the suspension properties (Dixon 1996). The nonlinear properties of the tire and the suspension components, a tire-suspension hardware-in-the-loop simulation (HILS) system was developed by authors (Shiiba et al. 2011). When the vehicle dynamics analysis is executed, a phase delay is arisen by a low-pass filter on a measured data. In addition, the movement of the 6-DOF motion platform is delayed. These delays affect the accuracy of the analysis because a real-time vehicle dynamics analysis is executed with measured tire forces in this system.

The purpose of this study is to reduce the influence of the delay in the HILS system. The hybrid method was conducted in the HILS system by using the lateral force from the model to compensate the measured lateral force for the reduction of the delay. The vehicle dynamics analysis with the HILS system was carried out. The results show that the influence of the delay was suppressed in the HILS system.

2 TIRE SUSPENSION HILS SYSTEM

2.1 *System overview*

The tire-suspension HILS system is shown in Figure 1. This system consists of a tire, a suspension system, a 6-DOF motion platform, a flat belt rolling device, a brushless DC motor for a rack gear to give a steering angle, and a tire force transducer. In this system, the DC servo motor for the rack gear can give the steering angle to the tire. The tire force are measured with the transducer attached to the knuckle. The flat belt is rotated by the AC motor. The motion platform can give various conditions of a road input. In this system, the left front tire and the suspension of the experimental vehicle are used which was developed in our laboratory as shown in Figure 2. The specifications of the vehicle is displayed in Table 1.

Table 1. Specifications of experimental vehicle.

Overall length [mm]	2205
Overall height [mm]	1100
Wheel base [mm]	1865
Tread [mm]	1165
Total weight [kg]	240
Weight distribution [–]	41.7:58.3
Yaw moment of inertia [kgm^2]	123.6

The procedure of the measurement and the simulation in HILS system is shown in Figure 3. The real-time vehicle dynamics analysis is executed with measured tire forces in this system. The state variables of the vehicle such as the yaw rate and the slip angle are calculated in the vehicle dynamics analysis. The motion platform of this system is controlled in real-time based on the results of the vehicle dynamics analysis. The change of wheel alignments caused by the suspension components affects the tire conditions. Thus, this system realizes various contact conditions between the tire and the road with the real-time vehicle dynamics analysis. The movement of the motion platform, the rotational speed of the flat belt, and the steering angle are controlled by a digital signal processor board

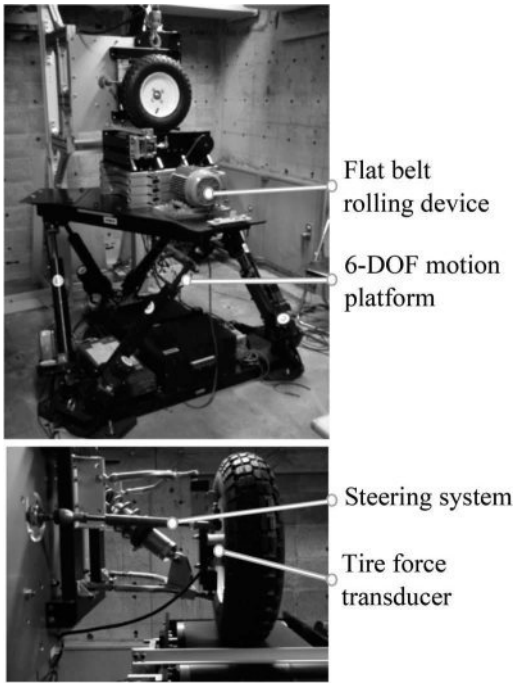


Figure 1. Tire-suspension testing machine.



Figure 2. Experimental vehicle.

(DSP board). The vehicle behavior is calculated with the measured values in this DSP board.

The advantage of the developed system is described as follows: Because the HILS system is equipped with a tire-suspension system of an actual vehicle, this system can evaluate the performance of the actual parts such as the spring and the damper. The merit of this system compared with an ordinary component test is that the system can carry out evaluation tests of such components with the actual running conditions of the vehicle. Also, the merit of this system compared with the actual running test is that accurate measurements are realized by this system. For example, the precise measurement of the change of the wheel alignment is

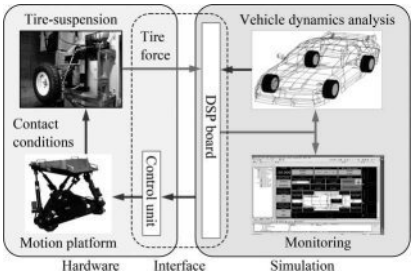


Figure 3. Overview of HILS system.

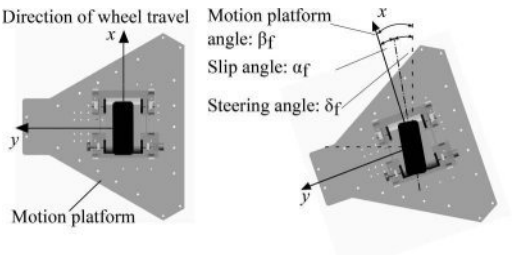


Figure 4. Control method of 6-DOF motion platform for realization of slip angle.

possible in the developed system, whereas it is very difficult in running tests. In addition, the system realizes various test conditions with high repeatability.

2.2 *Vehicle model*

In this study, a two-wheel vehicle model was used. The equation of the vehicle planar motion are written as follows:

$$mV(\dot{\beta}+r) = 2(F_{yf}+F_{yr}) \tag{1}$$

$$I\dot{r} = 2(l_f F_{yf} - l_r F_{yr}) \tag{2}$$

where m is the vehicle mass, I is the yaw moment of inertia, β is the vehicle slip angle, r is the yaw rate, F_{yf} and F_{yr} are the lateral force acting on the front tire and the rear tire, l_f and l_r the distances from the center of gravity to the front and the rear wheel axes. In this study, a linear tire model was used to calculate the lateral tire force.

2.3 *Control of 6-DOF motion platform*

In order to realize the contact condition of the tire in cornering, an appropriate slip angle is given to the tire by controlling the 6-DOF motion platform and the DC servo motor for the rack gear. The motion platform gives the slip angle at the position of the front wheel based on the analysis results, and the steering angle is given by the DC servo motor as shown in Figure 4. As a result, the lateral force and the self aligning torque arise depending on the slip angle.

Furthermore, in order to achieve the vehicle behavior accurately in the HILS system, the 6-DOF motion

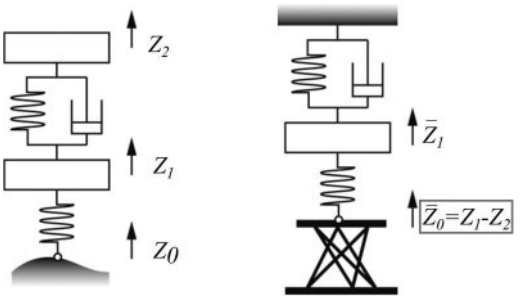


Figure 5. Control method of 6-DOF motion platform in vertical direction.

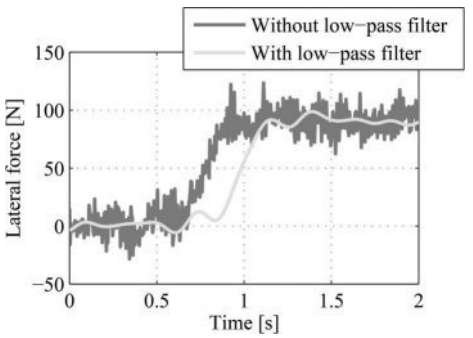


Figure 6. Noise of transducer.

platform is controlled based on the relative motion between the vehicle body and the road surface in the result of the vehicle dynamics analysis. In the vertical direction, the relative displacement between the vehicle and the road surface is used to determine the height of the motion platform as displayed in Figure 5.

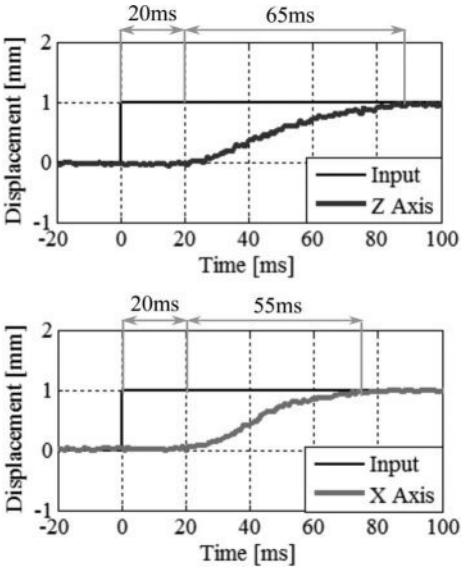


Figure 7. Results of step response test.

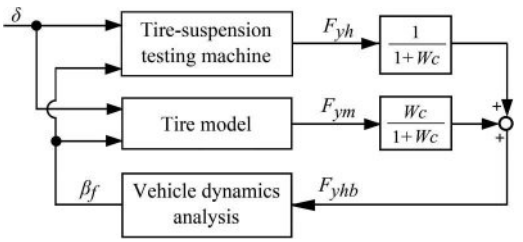


Figure 8. Block diagram of HILS system with hybrid method.

3 COMPENSATION OF HILS SYSTEM

3.1 *Causes of delay in HILS system*

There are two principal causes of the delay in the tire-suspension HILS system. The first cause is a phase delay due to a low-pass filter. Because the tire forces measured with the transducer are noisy, a low-pass filter has to be used to eliminate the noise as shown in Figure 6.

The second cause is the delay of the 6-DOF motion platform. The step response tests in the vertical direction and the longitudinal direction were conducted to evaluate the delay of the motion platform by using the laser displacement sensor. Figure 7 indicates that dead times of 20 ms and the dynamic delay of 60 ms are arisen. These delays affect the accuracy of the analysis.

3.2 *Compensation with hybrid method*

The delay in the HILS system affect the analysis result because the real-time vehicle dynamics analysis is executed by using the measured tire force directly in the system. On the other hand, although the delay is not arisen, the analysis result only with the tire model could be influenced by a modeling error. The hybrid method which is proposed by authors is conducted by using the measured lateral force and the lateral force from the model. The lateral force from the model and the measured lateral force are used to suppress the influence of the delay in the HILS system and the modeling error on the analysis result.

The block diagram of the HILS system with the hybrid method is shown in Figure 8. In this figure, δ is the steer angle, F_{yh} is the lateral force which is measured in the hardware, F_{ym} is the lateral force which is calculated from the tire model, F_{yhb} is the hybrid lateral force which is the mixture of F_{yh} and F_{ym}, β_f is the motion platform angle. In this HILS system, the lateral force is calculated in the tire model simultaneously with the measurement of the lateral force. Afterward, F_{yh} and F_{ym} which are multiplied by $1/(1+W_c)$ and $W_c/(1+W_c)$ respectively are added together. The hybrid lateral force is reflected in the vehicle dynamics analysis.

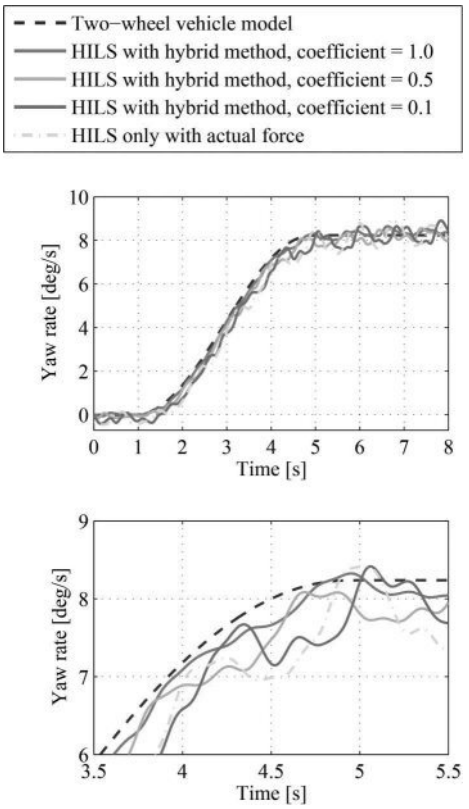


Figure 9. Influence of delay on analysis result.

3.3 *Evaluation of HILS system with the hybrid method*

Virtual running tests were carried out to assess the HILS system with the hybrid method under the conditions that the vehicle velocity was 30 km/h. The weight coefficient for the hybrid method was 0.1, 0.5 and 1.0. For comparison, the simulation with the tire model under the same condition was also conducted.

The results of the tests are shown in Figure 9. From the results, according as the weight coefficient was increased, the delay of the yaw rate was reduced. It is shown that the influence of the delay in the HILS system on the analysis result was suppressed by using the hybrid method.

In addition, virtual running tests were also conducted to examine the influence of the modeling error on the analysis result in the HILS system with the hybrid method. In this test, the modeling error of 35% in the tire model was considered. The steering input, the vehicle velocity and the weight coefficient for the hybrid method were the same as before.

The test results are depicted in Figure 10. From the results of these tests, according as the weight coefficient was decreased, the difference in the yaw rate between the HILS system with the hybrid method and the HILS only with actual force was small. It is indicated that the influence of the modeling error on

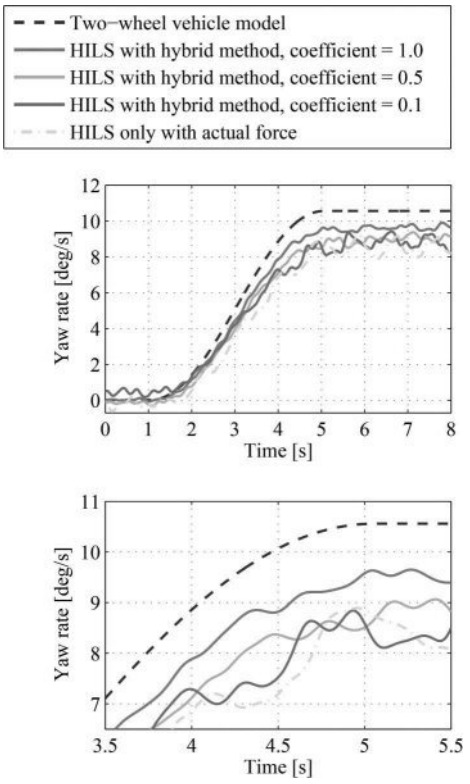


Figure 10. Influence of modeling error on analysis result.

the analysis results was reduced by using the hybrid method.

4 CONCLUSIONS

In this study, the hybrid method was used for the reduction of the influence of the delay in the tire-suspension HILS system and the influence of the modeling error. The influence of the delay and the modeling error were compensated by using the lateral force measured with the actual tire and the lateral force calculated with the tire model. The HILS system with the hybrid method was evaluated by conducting the vehicle dynamics analysis with the HILS system. From the results, it is shown that the influence of the delay in the HILS system with the hybrid method and the influence of the modeling error were suppressed.

REFERENCES

Dixon, J. C. (1996). *Tires, Suspension and Handling*. Society of Automotive. Enginees, Inc.

Pacejka, H. B. (2002). *Tyre and Vehicle Dynamics*. Elsevier's Science and Technology Rights Department in Oxford, Elsevier Ltd.

Shiiba, T. et al. (2011). Performance evaluation of electoromagnetic damper with tire-suspension hils system. In *Multi Body Dynamics 2011, ECCOMAS Thematic Conference*.

Advanced Vehicle Control – Edelmann, Plöchl & Pfeffer (Eds)
© 2017 Taylor & Francis Group, London, ISBN 978-1-138-02992-7

Evaluation of coupled suspension system using four electromagnetic dampers by motor HILS system

Y. Imai, Y. Fukumori & R. Hayashi
Tokyo University of Science, Katsushika-ku, Tokyo, Japan

K. Nakano & Y. Suda
The University of Tokyo, Meguro-ku, Tokyo, Japan

ABSTRACT: The electromagnetic damper (EMD) is an oil-less shock absorber which absorbs vibration by converting vibration energy to electric energy by an electric motor. In the previous study, the authors proposed a coupling method of four EMDs with an electric circuit which enables the damping characteristics of bouncing, rolling, and pitching motion of a vehicle to be tuned independently. In this study, the authors focus on hardware-in-the-loop simulation (HILS) to verify the effectiveness and validity of the coupled EMD. The experimental setup which is composed of coupled motors is built for the hardware of HILS system and vehicle dynamics simulations with four motors are carried out. The results show that the proposed coupling method is valid and effective.

1 INTRODUCTION

Ride comfort and drivability of automobiles depends on suspension systems. In order to improve these performances, various methods for motion control with hydraulic shock absorbers have been developed, such as passive suspension with a non-linear damping force characteristic by structural contrivance and active suspension system (Buma et al., 1991) using actuator forces based on state quantity.

In recent years, with the aim of de-oiling, energy saving and high performance, active suspension systems using an electric motor have been proposed (Simon et al., 2008) (Yoshioka et al., 2010). And then, as a new component of next-generation suspension system, the authors proposed an electromagnetic damper (Suda et al., 2000) utilizing interconversion to kinetic energy and electric energy by electric motor.

The electromagnetic damper has two remarkable features. One is that the electromagnetic damper has various functions such as a passive damper, an actuator, an energy regenerator, a sensor, and a spring, depending on the electric circuit connected to its electric motor. By designing the electric circuit, the electromagnetic damper can realize non-linear damping characteristics which a practical oil damper has (Hio et al., 2004), and realize the energy saving active suspension by the function of an actuator and a generator (Kawamoto et al., 2006).

The other is that coupling of multiple electromagnetic dampers can be constructed more easily than that of hydraulic dampers because electric motors can be connected with conductive wires, which can be installed in the vehicle more easily than hydraulic pipelines.

Focusing attention on this feature, the authors have proposed a coupling method of four EMDs (Fukumori et al., 2016). The method enables the damping characteristics of bouncing, rolling, and pitching motion of a vehicle to be tuned independently. However, the effectiveness and validity have not been verified by an experimental setup representing an automobile.

This study focus on hardware-in-the-loop simulation (HILS) to verify the effectiveness of the coupled EMD. In this study, the authors build an HILS system which is composed of four motors and an electric circuit as the hardware in the HILS. A full vehicle dynamics model is used as the simulation model in the HILS. The effectiveness of the proposed coupling method is examined by the hardware-in-the-loop simulations.

2 PRINCIPLE AND MODEL OF THE EMD

2.1 *Principle of electromagnetic damper*

Figure 1 shows the basic concept of the electromagnetic damper for automobiles, which is a representative example of the electromagnetic devices. Its basic structure is shown in figure 2. The electromagnetic damper is composed of an electric motor, a ball screw, and a nut. The stroke of the electromagnetic damper rotates the ball screw and the motor, and the electromagnetic force of the motor produced by the self-induced voltage generates the damping force in the direction of the damper stroke.



Figure 1. Electromagnetic damper (2nd prototype).

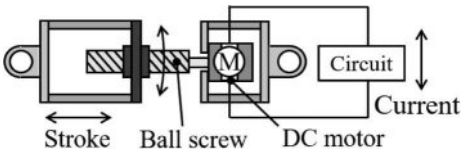


Figure 2. Basic structure of electromagnetic damper.

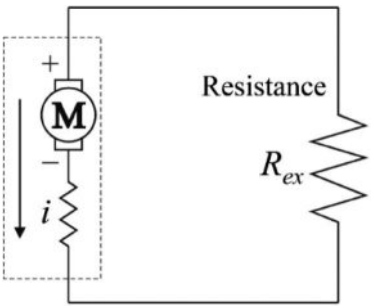


Figure 3. A motor connected to a resistance.

2.2 *Model of electromagnetic damper*

In this paper, the authors utilize a DC motor for the electromagnetic damper. The induced voltage e of the motor and the output force of the motor f is expressed as follows:

$$e = -G\dot{z} \tag{1}$$

$$f = -Gi \tag{2}$$

where z is stroke of the electromagnetic damper, and i is current of the motor. G is a specific constant of the electromagnetic damper, which is an equivalent of the torque constant of the motor converted from rotational to translational motion. When the motor is connected to a resistance R_{ex} as shown in figure 3, the output force f is expressed as follows:

$$f = -\frac{G^2}{r + R_{ex}}\dot{z} \tag{3}$$

where r is the internal resistance of the motor.

In addition to this, the electromagnetic damper generates inertia force (Hayashi et al., 2006), which originates in the inertia moment of the rotor of the motor, and friction forces at mechanical contact points. However, this study neglects these forces and assumes that electromagnetic dampers generate only electromagnetic force since these forces are not significant in this study.

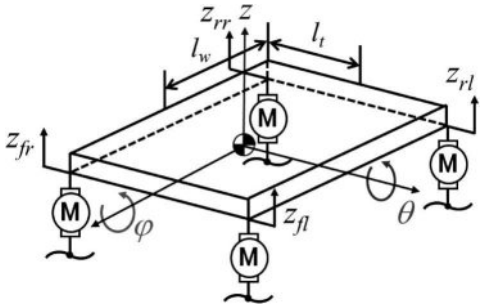


Figure 4. 3DOF model.

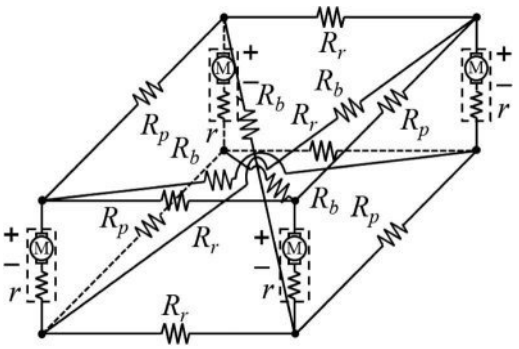


Figure 5. Circuit of proposed system.

3 COUPLING OF EMDS

In this chapter, the authors describe the theory of the proposed coupled damper in the 3 DOF system; bounce, roll and pitch as shown in figure 4. z_{fr}, z_{fl}, z_{rr}, and z_{rl} indicate the stroke of each electromagnetic damper, l_t and l_w indicate halves of the tread and wheelbase of an automobile, z indicates the bounce displacement, and ϕ or θ indicate roll or pitch angle.

Stroke of each dampers z_{fr}, z_{fl}, z_{rr}, and z_{rl} are expressed as follows:

$$z_{fr} = z - l_t\phi - l_w\theta \tag{4}$$

$$z_{fl} = z + l_t\phi - l_w\theta \tag{5}$$

$$z_{rr} = z - l_t\phi + l_w\theta \tag{6}$$

$$z_{rl} = z + l_t\phi + l_w\theta \tag{7}$$

The authors have proposed an electric circuit which enables to tune the damping characteristics of bouncing, rolling, and pitching motion independently. The circuit is shown in Figure 5.

In Figure 5, R_t, R_r, and R_p indicate resistances to tune damping characteristics of bouncing, rolling and pitching motion, respectively. When the four electromagnetic dampers are coupled by this circuit, the

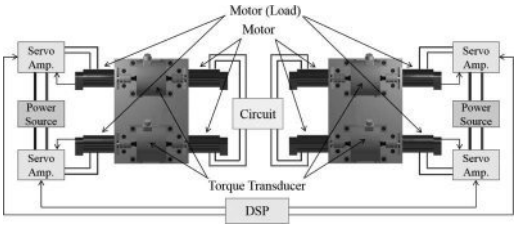


Figure 6. Conceptual diagram of experimental Setup.

currents of the motors i_{fr}, i_{fl}, i_{rr} and i_{rl} are expressed as follows by Kirchhoff's law:

$$i_{fr} = -\frac{G}{r+R_b}\dot{z} + \frac{Gl_t}{r+R_r}\dot{\phi} + \frac{Gl_w}{r+R_p}\dot{\theta} \tag{8}$$

$$i_{fl} = -\frac{G}{r+R_b}\dot{z} - \frac{Gl_t}{r+R_r}\dot{\phi} + \frac{Gl_w}{r+R_p}\dot{\theta} \tag{9}$$

$$i_{rr} = -\frac{G}{r+R_b}\dot{z} + \frac{Gl_t}{r+R_r}\dot{\phi} - \frac{Gl_w}{r+R_p}\dot{\theta} \tag{10}$$

$$i_{rl} = -\frac{G}{r+R_b}\dot{z} - \frac{Gl_t}{r+R_r}\dot{\phi} - \frac{Gl_w}{r+R_p}\dot{\theta} \tag{11}$$

From Eqs. (8)–(11), the bounce damping force F_b, roll damping moment M_r, and pitch damping moment M_p are expressed as follows:

$$F_b = -4\frac{G^2}{r+R_b}\dot{z} \tag{12}$$

$$M_r = -4\frac{G^2 l_t^{\,2}}{r+R_r}\dot{\phi} \tag{13}$$

$$M_p = -4\frac{G^2 l_w^{\,2}}{r+R_p}\dot{\theta} \tag{14}$$

These equations indicate that R_b, R_r, and R_p determine the damping characteristics with relation to bounce, roll and pitch independently.

4 EXPERIMENT

4.1 *Experimental setup*

As basic experiments of independent damping tuning of the 3 DOF, torque characteristics test was carried out using four pairs of motors and an electric circuit. The experimental setup is shown in figure 6, figure 7, and figure 8. The tested motors are loaded by the other electric motors, and the output torques of the motors are measured. The tested motors are DC motors whose rating output, torque constant and internal resistance are 150 W, 60 mN · m/A, and 1.3 Ω.

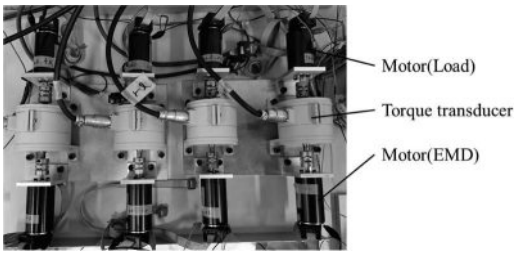


Figure 7. Picture of motors (Load), torque transducers and motors (EMD).

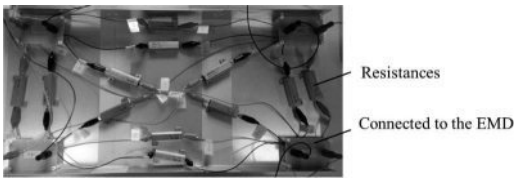


Figure 8. Picture of the circuit.

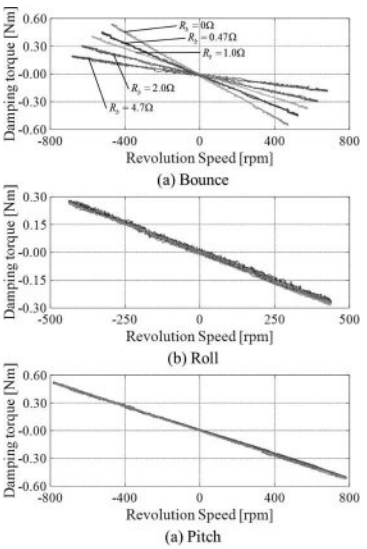


Figure 9. Damping torque (Bouncing independently).

4.2 *Independent damping tuning experiment*

The damping torque of each motor was measured under the situation where the four motors were coupled electrically by the proposed circuit, and the revolution speed of the each motor is controlled so that the body in figure 4 makes bouncing, rolling, and pitching motion in the form of sine wave. The condition of resistances in proposed circuit is that resistance R_p and R_r are kept at 1.0 Ω, and the resistance R_b is varied as 0 (shorted), 0.47, 1.0, 2.0, and 4.7 Ω.

The bounce, roll, and pitch damping torque characteristics against bounce, roll and pitch revolution speed of the motor are shown in figure 9. The revolution speed is equivalent to suspension stroke. Figure 9

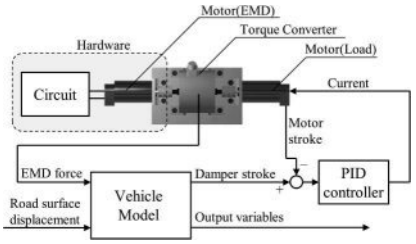


Figure 10. HILS system.

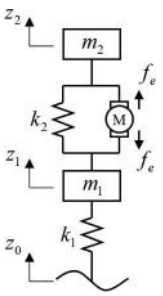


Figure 11. Quarter vehicle model.

indicates that the change of resistance R_b varies only the bounce damping characteristic without any effect on pitch and roll damping characteristics. In a similar way, the other experimental results show that the resistance R_r, and R_p changes the damping characteristics of bouncing and rolling independently.

5 HILS TO BE USED IN THIS STUDY

5.1 *HILS system*

Figure 10 shows the HILS system used in this study. The HILS system consists of hardware and a simulation model, and the behavior of the hardware is taken into account in the simulation loop. In this study, the hardware is motors of EMDs and the circuit, and the vehicle excluding dampers are simulated by a computational model. Ball screws and planetary gears of EMDs are also simulated. The vehicle model has two inputs and two outputs. The inputs are the damping force generated by EMDs and road displacements. The outputs are the stroke of the EMDs and output variables. The motor for load controls the rotation angle of the motor of the EMD using PID control so that it coincide with the calculated stroke of the vehicle model. And then, the force of EMD induced by the stroke is measured and fed back to the calculation model. The output variables include vertical acceleration, pitch angle, roll angle of the body, which should be evaluated as experimental results.

5.2 *Validation of the HILS system*

This section describes the validity of the HILS system by using the quarter vehicle model shown in Figure 11. The specifications are shown in Table 1.

Table 1. Specifications of the quarter vehicle model.

Description	Symbol	Value
Tire stiffness	k_1	240000 [N/m]
Spring stiffness	k_2	18000 [N/m]
Unsprung mass	m_1	50 [kg]
Sprung mass	m_2	400 [kg]

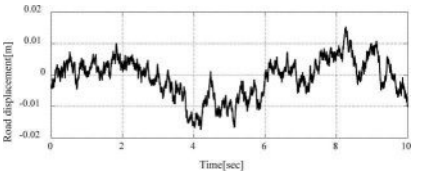


Figure 12. Road displacement.

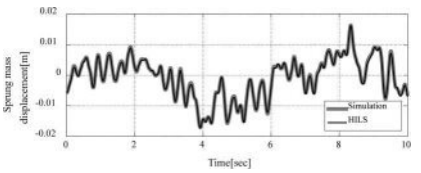


Figure 13. Time history of sprung mass displacement.

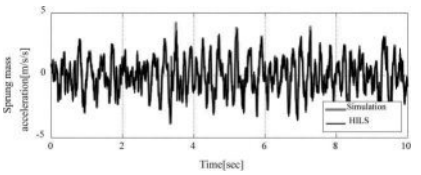


Figure 14. Time history of sprung mass acceleration.

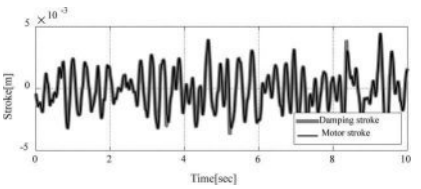


Figure 15. Time history of damper stroke and motor stroke.

The EMD motor is connected to a resistance of 0.0 Ω so that the EMD works as a viscous damper whose damping coefficient is 15560 N/(m/s). Then the road displacement shown in Figure 12 is input to the vehicle model. The road displacement is equivalent to ISO class A road when the vehicle is running at 60 km/h.

Figure 13 and 14 shows the time history of sprung mass displacement and acceleration, and Figure 15 and 16 shows the time history of EMD stroke and damping force, as the experimental results. In those figures, simulation results, in which a calculation model of the EMD are used instead of using hardware, are also shown. The behaviors of the sprung mass and damper

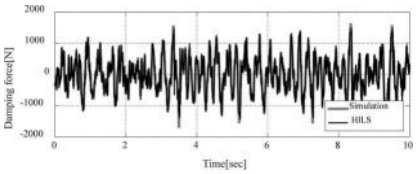


Figure 16. Time history of damping torque.

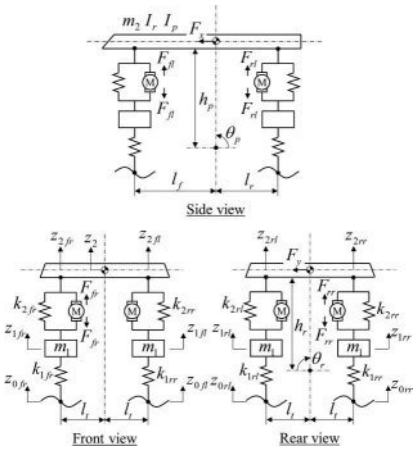


Figure 17. Full vehicle model.

stroke by HIL simulation agree well with those by the simulation without hardware. This indicates that the HILS system is valid and capable of testing EMD motors connected to a circuit.

6 EXPERIMENT USING HILS

6.1 *Full vehicle model and the specifications*

In this chapter, the performance of the coupled EMD is examined using the HILS system. The vehicle model is a full vehicle model shown in Figure 17, in which bouncing, rolling and pitching are considered as the motion of the vehicle body. The vehicle is assumed as a commonly used ordinary vehicle. The specifications the vehicle are shown in Table 2. The normal shock absorber is replaced with electromagnetic dampers. The same motors as in section 4.1 are used as the hardware. Considering the gear ratio, they work as EMDs whose specifications are in Table 3.

6.2 *Anti-rolling and anti-pitching suspension system with the proposed coupling method*

The behavior of the vehicle is tested by HILS with vertical disturbances to the wheels from the road displacement, lateral force acting on the car body generated by steering and longitudinal force generated by accelerating and braking. The time history of road disturbances input to the wheels are shown in figure 18.

In the case where longitudinal and lateral forces act on the car body by acceleration, deceleration and

Table 2. Values of the parameters.

Description	Symbol	Value
Unsprung mass	m_1	50 [kg]
Sprung mass	m_2	1600 [kg]
Roll moment of inertia	I_r	1000 [kgm^2]
Pitch moment of inertia	I_p	2400 [kgm^2]
Tire stiffness	k_1	240000 [N/m]
Front spring stiffness	k_{2f}	18000 [N/m]
Rear spring stiffness	k_{2r}	22500 [N/m]
Distance between gravity center of spung mass and front suspension	l_f	1.2 [m]
Distance between gravity center of sprung mass and rear suspension	l_r	1.5 [m]
Tread	$2l_t$	1.5 [m]

Table 3. Specifications of the electromagnetic damper.

Description	Symbol	Value
Motor constant	G	132.6 [V/(m/s)]
Internal resistance	R	1.13 [Ω]

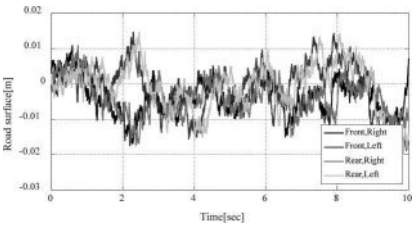


Figure 18. Road disturbances.

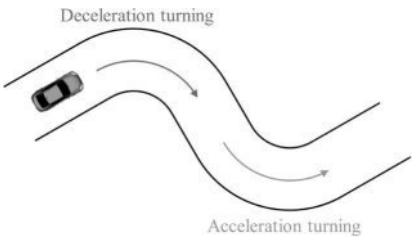


Figure 19. Driving scene.

steering, it is effective to use the proposed circuit and temporarily harden the damping against pitching and rolling motion. In this paper, it is assumed that a vehicle is driving a winding road as shown in figure 19. The time history of the lateral and longitudinal accelerations are shown in figure 20.

In order to obtain the same performance as normal shock absorbers in terms of bouncing motion, the resistance R_b is kept at 4.7 Ω. Resistances R_r and R_p are changed from 4.7 to 0 Ω while lateral and longitudinal forces act. The time history of resistance values are shown in Figure 21. For the HIL simulation of

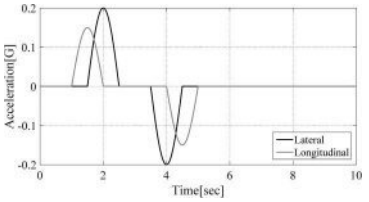


Figure 20. Lateral and longitudinal acceleration.

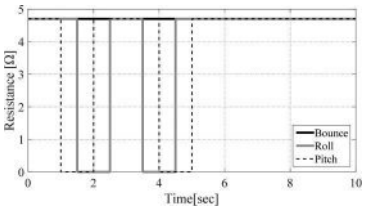


Figure 21. Time history of the Resistances.

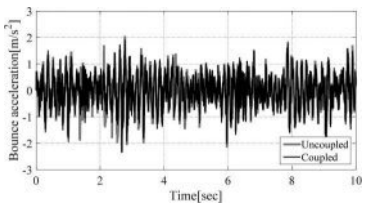


Figure 22. Bounce acceleration.

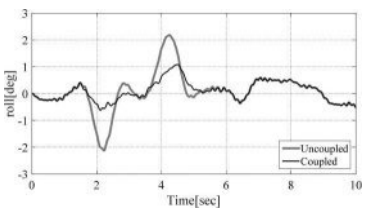


Figure 23. Roll angle.

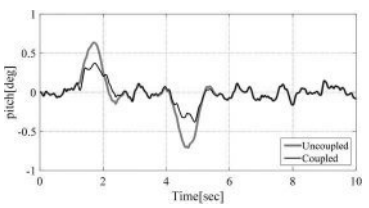


Figure 24. Pitch angle.

normal dampers, each EMD motor is independently connected to resistances of 4.7 Ω and unvaried during the simulation.

As the results of the HIL simulations, time histories of bouncing acceleration, roll angle and pitch angle of the vehicle body are shown in Figure 22, 23 and 24. For comparison, those by uncoupled normal dampers are also shown.

As can be noticed from these results, the coupled electromagnetic damper reduces the rolling and pitching motion more than uncoupled electromagnetic damper without leaving an effect on the bouncing motion. Therefore, these results indicate that the proposed method potentially improves the stability of the vehicle without sacrificing ride comfort.

7 CONCLUSION

In this paper, the authors build a HILS system for the electromagnetic dampers and examined the coupling method of four electromagnetic dampers proposed by the previous study, which enables the damping characteristics of bouncing, rolling and pitching motion of a vehicle to be tuned independently. As a result of the HIL simulation, the validity of the proposed coupling method and the effectiveness of the coupled electromagnetic damper is indicated.

The switching law of the resistance used in this study is just to show clearly the validity of the proposed coupling method by HIL simulation. More realistic and effective control law is desirable for a practical vehicle control. Our future work is to study a new vehicle control method utilizing the coupled electromagnetic damper, aiming at improving ride comfort and vehicle stability.

REFERENCES

Buma, S., Satou, H., Yonekawa, T., Ohnuma, T., Hattori, K. and Sugihara, M., 1991. Synthesis and Development of Active Control Suspension, Transaction of the Japan Society of Mechanical Engineers, Series C, Vol. 57, No. 534, pp. 257–263.

Fukumori, Y., Hayashi, R., Okano, H., Suda, Y. and Nakano, K., 2015. Study on coupled shock absorber system using four electromagnetic dampers, Proc. of the MOVIC2016, 2510.

Hayashi, R. and Suda, Y., 2006 Study on Control of Acceleration Characteristic of Electro-magnetic Device, CD-ROM Proceedings of JSME Dynamics and Design Conference 2006, 519. (In Japanese).

Hio, K., Shiima, T., Kondo, T. and Yamagata, H., 2004. A Study on Nonlinear Damping Force Characteristics of Electromagnetic Damper for Automobiles, JSAE Transaction, vol. 35, no. 1, pp. 167–172.

Kawamoto, Y., Suda, Y., Inoue, H. and Kondo, T., 2006. Velocity Feedback Control of Electromagnetic Suspension Considering Energy Consumption, Proceedings of JSME Mechanical Engineering Congress 2006, Vol. 7, No. 06-1, pp. 111–112.

Simon, T., Matthew, C.B. and Jiabin, W., 2008. Design and Control of a Linear Electromagnetic Actuator System for Active Vehicle Suspension, Proceedings of the International Symposium on Advanced Vehicle Control 2008, pp. 373–378.

Suda, Y., Suematsu, K., Nakano, K., and Shiiba, T., 2000. Study on Electromagnetic Suspension for Automobiles – Simulation and Experiments of Performance, Proc. of the 5th AVEC, pp. 699–704.

Yoshioka, K., Buma, S., Cho, J.S., Kanda, R. and Yahagi, T. 2010. Study of Preview Control for Electric Active Suspension, Transaction of the Japan Society of Mechanical Engineers, Series C, Vol. 76, No. 770, pp. 2372–2379.

Driver

Advanced Vehicle Control – Edelmann, Plöchl & Pfeffer (Eds)
© 2017 Taylor & Francis Group, London, ISBN 978-1-138-02992-7

Investigation on the lane tracking steering control with two preview points to make preview time shorter

K. Nishizaki, H. Mouri, H. Furusho & P. Raksincharoensak
Department of Mechanical Systems Engineering, Tokyo University of Agriculture and Technology, Tokyo, Japan

ABSTRACT: Lane marker detection is indispensable for a lane-keeping-control algorithm. However, it is impossible to detect lane markers when the curvature of the lane the vehicle is travelling on is large or when there is another car in front of the vehicle with short distance. For lane marker detection, it is desirable to set a preview point close to the vehicle. Therefore, by analyzing the block diagram of driver-vehicle system, we propose a method to reduce preview distance without lane tracking performance deterioration by increasing preview points from the conventional one point to two points. Furthermore, it is revealed that it is possible to set arbitrary dynamics of lane tracking performance that could not be realized before.

1 INTRODUCTION

As the driver's steering model used for the control of autonomous vehicle, a control method has been proposed to enable the vehicle to generate the target value of vehicle state (e.g., yaw rate, lateral acceleration) required for achieving future target lateral displacement, which is determined by lateral deviation at the preview point (Boer, 1996; Kuwabara *et al*., 1998; Mouri *et al*., 2004; Ono *et al*., 2011; Asai *et al*., 2012). In this control method, the target yaw rate required for arriving at the front target point after a certain time is determined, and the vehicle is steered to achieve it. As a result, the vehicle tranvels along the course. Kuwabara *et al.* summarized basic findings about its tracking performance and stability. However, Ono *et al.* proposed a third prediction model that enables tracking a target course where curvature changes in proportion to time. Asai *et al.* pointed out that a limit is imposed on the damping performance of transient tracking characteristics. As a countermeasure, they proposed a method in which steering angle is controlled by using lateral displacement at a point near the vehicle.

But, if the preview point is too close to the vehicle, the tracking performance becomes too sensitive especially in high speed driving. Therefore, the preview point should not be set too close to the vehicle. However, if the target course has too large curvature or there is another car ahead of the vehicle with short distance, the lane marker to detect disappears, and it becomes impossible to observe the preview point. If the preview point is positioned too far from the vehicle, the resolution of the camera, which is used to detect lane markers, is not sufficient, and observation errors of the target lateral displacement increase. Therefore, it is desirable to position the preview point as close to the vehicle as possible.

In this study, at first we examine a vehicle that performs course tracking by generating the target yaw rate and explain that the preview point should not be set close to the vehicle.

After that, it is revealed that the problems mentioned above can be resolved by using dual preview points, and at the same time it becomes possible to realize the required damping performance of tracking characteristics.

2 EXPLANATION OF BASIC CONTROL RULES

This section will introduce control algorithms that have been proposed and summarize their properties.

2.1 *Calculation of the target yaw rate*

Figure 1 presents a schematic diagram of the target yaw rate calculation method. When the vehicle displaces by Δy_c in the lateral direction while travelling at a speed of V for T_p seconds, the average yaw rate γ^* is given by equation (1) if the side slip angle of the vehicle is ignored.

$$\gamma^* = \frac{2}{T_p^2 V}\Delta y_c \tag{1}$$

When target displacement at the preview point is e_y, the target yaw rate γ^* can be expressed by equation (1). However, the distance after T_p seconds is expressed by $l_p = VT_p$. Reference (4) indicated that if curvature changes in proportion to time, γ^* in equation (1) is not the current target yaw rate but the future target yaw rate after a dead time of $T_p/3$ seconds. However, here we focus on the case where curvature does not

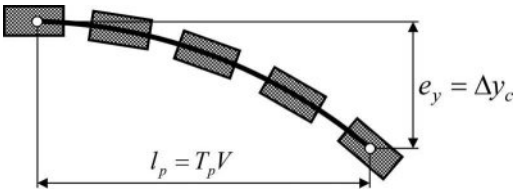


Figure 1. Schematic diagram of target yaw rate calculation.

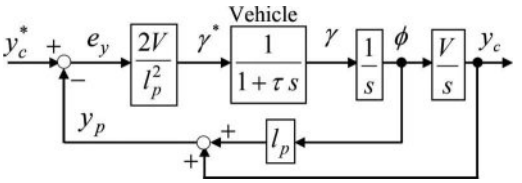


Figure 2. Block diagram of course tracking based on the preview model.

change in proportion to time, and such dead time is not considered.

$$\gamma^* = \frac{2V}{l_p^2} e_y = \frac{2}{T_p^2 V} e_y \qquad (1)'$$

Because the steady yaw rate during travelling on a course with a constant curvature of ρ is ρV, front relative displacement e_y from equation (1)' is given by equation (2).

$$e_y = \frac{l_p^2}{2} \rho \qquad (2)$$

Vehicle characteristics were assumed as first order delay characteristic, as expressed by equation (3), where γ is yaw rate that is generated actually.

Vehicle characteristics were assumed as first order delay characteristic, as expressed by equation (3), where γ is yawrate that is generated actually.

$$\gamma = \frac{1}{1+\tau s} \gamma^* \qquad (3)$$

2.2 *Dynamic characteristics of course tracking*

Figure 2 represents a block diagram of the system. Here, ϕ is the yaw angle. The transfer function of vehicle lateral displacement y_c from the target lateral displacement y_c^* is expressed by equation (4).

$$\frac{y_c}{y_c^*} = \frac{\frac{2V^2}{l_p^2}}{\tau s^3 + s^2 + \frac{2V}{l_p} s + \frac{2V^2}{l_p^2}} \qquad (4)$$

Equation (4) is approximated by the second order vibration system on the assumption that τ is close to zero. Natural frequency ω_n and damping ratio ζ can be obtained by the following equations:

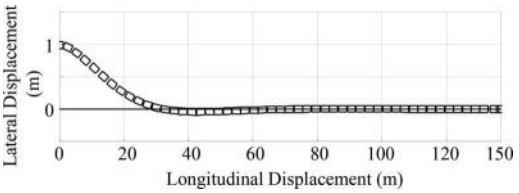


Figure 3. Vehicle trace corresponding to initial value response (100 km/h, preview time = 0.5 sec).

$$\omega_n = \frac{\sqrt{2}}{l_p} V \qquad (5)$$

$$\zeta = \frac{1}{\sqrt{2}}. \qquad (6)$$

Natural frequency ω_n of course tracking is determined by equation (5); thus, in order to keep the same tracking response, it is necessary to increase preview distance l_p in accordance with the increase of vehicle speed. Although the algorithm of equation (2) is intuitive and simple, it represents the same damping characteristics as obtained using the optimal regulator described in Reference (2). Damping coefficient ζ is determined uniquely by equation (6) and cannot be changed by any control parameter such as preview distance l_p.

Although the value obtained in equation (6) is satisfactory for common control performance in many cases, it is not satisfactory for lane keeping. For example, vehicle trace during automatic driving using this algorithm is depicted in figure 3.

When automatic driving starts from a point outside the target course, the vehicle trace converges after once crossing and going beyond the target course. When leaving driving to a machine, such behavior leads to driver anxiety. Therefore, the dynamic characteristics of course tracking should be designed arbitrarily. Moreover, the calculation here assumes that time constant τ of the vehicle is zero, and the damping characteristics become worse when the time constant increases.

3 THE NEW ALGORITHM WITH TWO DUAL PREVIEW POINTS

To solve this problem, we consider a method that uses dual preview points. A block diagram of this method is presented in figure 4. Preview distances are denoted as l_{p1} and l_{p2}, lateral displacements at preview points are denoted as y_{p1} and y_{p2}, and target lateral displacements at preview points are denoted as e_{y1} and e_{y2}. Vehicle dynamic characteristics are omitted in the following description to explore essential performance. By setting the time constant τ of the vehicle to zero,

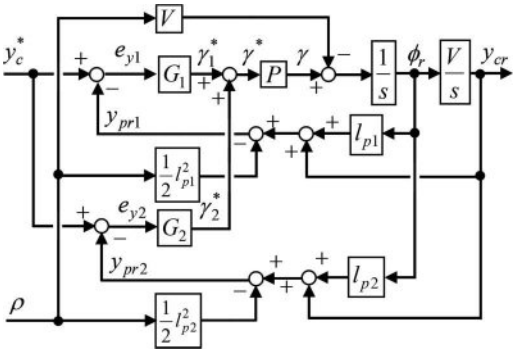


Figure 4. Block diagram of the dual preview point model.

we assume that target yaw rate γ^* is equal to vehicle yaw rate γ. In other words, the transfer function of vehicle characteristics is set to $P = 1$.

When target course y_c^* and curvature ρ are input, the transfer functions of lateral displacement y_{cr} are as expressed by equations (7) and (8), respectively. Suffix r indicates that it is a value relative to the target course.

$$\frac{y_c}{y_c^*} = \frac{V(G_1+G_2)}{s^2 + (l_{p1}G_1 + l_{p2}G_2)s + V(G_1+G_2)} \tag{7}$$

$$\frac{y_{cr}}{\rho} = \frac{V}{2} \cdot \frac{l_{p1}^2 G_1 + l_{p2}^2 G_2 - 2V}{s^2 + (l_{p1}G_1 + l_{p2}G_2)s + V(G_1+G_2)} \tag{8}$$

Based on equations (7) and (8), natural frequency ω_n and damping ratio ζ can be expressed by equations (9) and (10).

$$\begin{cases} \omega_n = \sqrt{V(G_1+G_2)} \\ 2\zeta\omega_n = l_{p1}G_1 + l_{p2}G_2 \end{cases} \tag{9}$$

$$\zeta = \frac{l_{p1}G_1 + l_{p2}G_2}{2\sqrt{V(G_1+G_2)}} \tag{10}$$

Furthermore, the condition for not generating steady deviation during a steady curve travelling is calculated by equation (11), assuming the steady state gain in equation (13) is zero.

$$l_{p1}^2 G_1 + l_{p2}^2 G_2 - 2V = 0 \tag{11}$$

For example, when ζ, ω_n, and l_{p1} are determined, l_{p2}, G_1, and G_2 can be obtained as follows:

$$l_{p2} = \frac{2V(V - \zeta\omega_n l_{p1})}{\omega_n(-\omega_n l_{p1} + 2\zeta V)} \tag{12}$$

$$G_1 = \frac{2\omega_n^2 V(2\zeta^2 - 1)}{-\omega_n^2 l_{p1}^2 + 4\zeta\omega_n l_{p1} V - 2V^2} \tag{13}$$

$$G_2 = \frac{\omega_n^2(2\zeta V - l_{p1}\omega_n)^2}{(-\omega_n^2 l_{p1}^2 + 4\zeta\omega_n l_{p1} V - 2V^2)V}. \tag{14}$$

Furthermore, when l_{p1}, l_{p2}, and ω_n are determined as another case, ζ, G_1, and G_2 can be obtained as follows:

$$\zeta = \frac{2V^2 + \omega_n^2 l_{p1} l_{p2}}{2\omega_n(l_{p1} + l_{p2})V} \tag{15}$$

$$G_1 = \frac{2V^2 - \omega_n^2 l_{p2}^2}{(l_{p1} - l_{p2})(l_{p1} + l_{p2})V} \tag{16}$$

$$G_2 = \frac{-2V^2 + \omega_n^2 l_{p1}^2}{(l_{p1} - l_{p2})(l_{p1} + l_{p2})V} \tag{17}$$

Combinations of natural frequency ω_n and damping ratio ζ with l_{p1}, l_{p2}, G_1, and G_2 to satisfy equations (9), (10), and (11) can be obtained according to the performance specifications that we want to achieve. Using these solutions, dynamic characteristics of target course tracking can be set arbitrarily, and a steady curve travelling without steady-state deviation can be achieved at the same time.

4 STUDY OF BASIC CONTROL RULES

4.1 *Range of feasible performance*

Here, we investigate the coverage of tracking performance that can be achieved by setting dual preview points. We arrange equations by defining the ratio of l_{p1} and l_{p2} as k. The relationship between l_{p1} and l_{p2} is expressed by equation (18).

$$l_{p2} = k l_{p1} \tag{18}$$

When equation (18) is substituted for equations (9), (10), and (11), the quadratic equation expressed by equation (19) can be obtained.

$$k\omega_n^2 l_{p1}^2 - 2\zeta\omega_n(1+k)V l_{p1} + 2V^2 = 0 \tag{19}$$

From this equation, the following can be calculated:

$$\begin{aligned} l_{p1} &= \frac{\zeta(1+k) \pm \sqrt{\zeta^2(1+k)^2 - 2k}}{k\omega_n} V \\ l_{p2} &= \frac{\zeta(1+k) \pm \sqrt{\zeta^2(1+k)^2 - 2k}}{\omega_n} V \end{aligned} \tag{20}$$

$$\begin{aligned} G_1 &= \frac{k\omega_n^2 \left\{\zeta^2(1+k) - k \mp \zeta\sqrt{\zeta^2(1+k)^2 - 2k}\right\}}{V(1-k)} \\ G_2 &= \frac{\omega_n^2 \left\{1 - \zeta^2(1+k) \pm \sqrt{\zeta^2(1+k)^2 - 2k}\right\}}{V(1-k)} \end{aligned} \tag{21}$$

From equation (20), the condition to make l_{p1} and l_{p2} real number solutions is given as follows.

$$\zeta^2 \geq \frac{2k}{(1+k)^2} \tag{22}$$

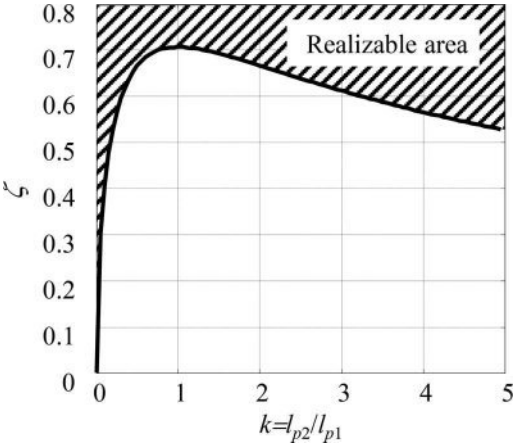


Figure 5. Realizable area of damping ratio ζ.

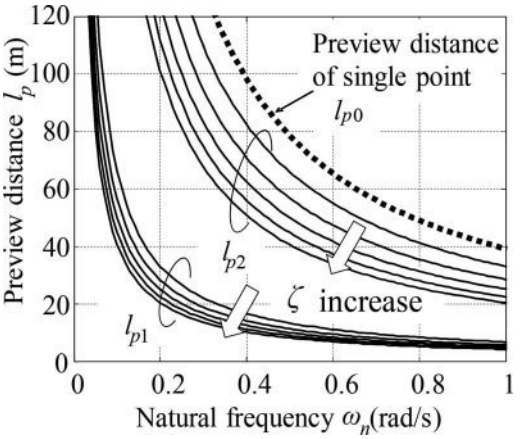


Figure 6. Changes in preview distance for the natural frequency of the system ($\zeta = 0.8$ to 1.2, by 0.1 increments).

Figure 5 plots the relationship between k and ζ obtained from equation (22). The hatched portion represents the feasible range. Because $k < 1$ can be achieved by exchanging l_{p1} and l_{p2} with each other, it is sufficient to consider only the realm of $k > 1$ in practice. As expressed by equation (20), both l_{p1} and l_{p2} have two solutions corresponding to the double sign of $\pm$. In other words, there are two combinations of these solutions. However, the solution of equation (19) on the plus side means a considerably distant preview point; therefore, we use mainly solutions on the minus side of equation (19).

4.2 *Preview distance*

We investigate relationships with the preview time for dual preview points and for a single preview point. Figure 6 shows the preview times obtained while varying damping ratio ζ at $k = l_{p2}/l_{p1} = 5$ for $\zeta > 1/\sqrt{2}$. Preview times for dual preview points are denoted by l_{p1} and l_{p2}, and that for a single preview point is denoted by l_{p0}.

When $\zeta = 1/\sqrt{2}$, l_{p2} and l_{p0} are equal. When ζ is larger than $1/\sqrt{2}$, both l_{p1} and l_{p2} are smaller than l_{p0}. To raise the value of damping ratio ζ by selecting dual preview points, it is not necessary to select far dual points; instead, it is better to select dual points that are closer than the single point.

To investigate the relationship with preview points to achieve the same natural frequency, we calculate the ratio between l_{p0} and l_{p1} by defining it as r, as expressed by equation (23). The quadratic equation expressed by equation (19) is used for calculation.

$$r = l_{p1}/l_{p0} \tag{23}$$

$$k\omega_n^2 l_{p1}^2 - 2\zeta\omega_n(1+k)Vl_{p1} + 2V^2 = 0 \qquad \text{Repeated (19)}$$

With a single preview point, since the natural frequency is $\omega_n = \sqrt{2}l_p/V$ this relationship is substituted for equation (19).

$$2k\frac{l_{p1}^2}{l_{p0}^2} - 2\sqrt{2}\zeta(1+k)V^2\frac{l_{p1}}{l_{p0}} + 2V^2 = 0$$

$$\rightarrow \qquad kr^2 - \sqrt{2}\zeta(1+k)V^2 r + V^2 = 0 \tag{24}$$

The solution of the quadratic equation is given by equation (25).

$$r = \frac{l_{p1}}{l_{p0}} = \frac{\sqrt{2}\zeta(1+k) \pm \sqrt{2\zeta^2(1+k)^2 - 4k/V^2}}{2k}V^2 \tag{25}$$

Figure 7 shows Comparison of preview distances between the single preview point and dual preview point models. Under the condition that keeps the damping ratio constant, if the value of k is increased (i.e., l_{p2} is relatively increased in comparison with l_{p1}), l_{p1} decreases. In other words, the preview point that is closer to the vehicle can be positioned just in the vicinity of the vehicle. Even in that case, the longer preview distance l_{p2} does not exceed the preview distance for a single preview point $l_p 0$.

4.3 *Dynamic characteristics of tracking can be set arbitrarily*

Figure 8 plots the behavior of course tracking when the target course changes stepwise. The results of a single preview point and dual preview points are shown in the same figure. The top figure depicts the responses of lateral displacement in order of time series. With a single preview point, the damping ratio is fixed to $\zeta = 1/\sqrt{2}$. In contrast, with dual preview points, it can be designed arbitrarily. Here, the damping ratio is set to $\zeta = 1.0$.

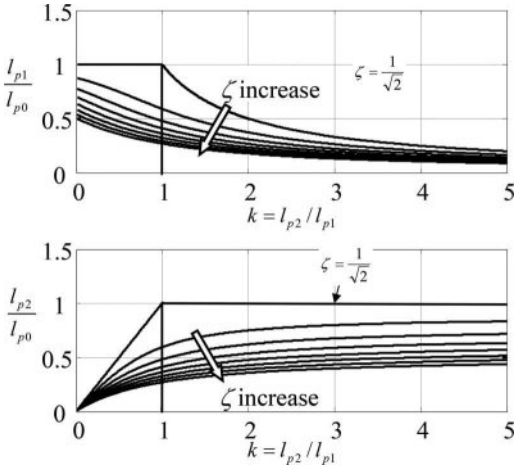


Figure 7. Comparison of preview distances between the single preview point and dual preview point models ($\zeta = 0.707$ to 1.507, in 0.1 increments).

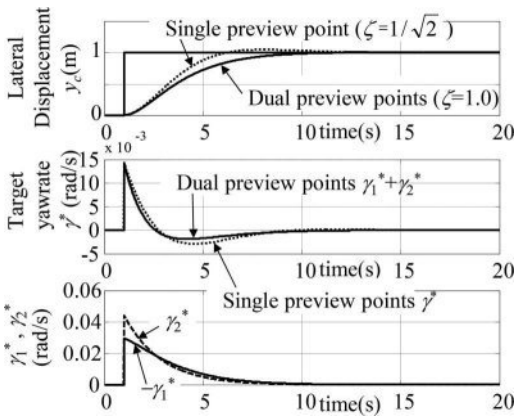


Figure 8. Step responses of single and dual preview point models.

The middle figure of figure 8 depicts the responses of the target yaw rate. With dual preview points, the yaw rate converges sooner than with a single preview point. Because the target yaw rate is generated in proportion to the forward target lateral displacement e_y with a single preview point, its dynamic characteristic is the dynamic characteristics of e_y. In contrast, with dual preview points, the target yaw rate is generated as $G_1 e_{y1} + G_2 e_{y2}$ and does not agree with the dynamic characteristic of e_{y1} or e_{y2}.

This state is depicted in the bottom figure of figure 8. For comparison, the sign γ_1^* is reversed to $-\gamma_1^*$. Although γ_1^* and γ_2^* in the figure are proportional to e_{y1} and e_{y2}, the sum of γ_1^* and γ_2^* becomes target yaw rate γ^*; therefore, the target yaw rate γ^* for dual preview points is generated as a signal that has a dynamic characteristic that differs from either γ_1^* or γ_2^*. When target yaw rate γ^* is set by deducting $-\gamma_1^*$, which is delayed in phase from γ_2^*, γ^* advances more than γ_2^*. Simply put, γ^* is a signal produced by applying a high-pass filter to γ_2^*, and differential effect is made based on it.

Table 1. The experiment condition.

Setting	Single preview point	Dual preview points
Vehicle speed	100 km/h	100 km/h
Natural frequency	2.4 rad/s	2.4 rad/s
Damping ratio	$1/\sqrt{2}$	1
Preview distance	27.8 m	12.8, 10.2 m

5 EXPERIMENT

In this theory, time constant τ and dead time of data communication or operation is considered as zero. In order to investigate the effect of the τ and dead time with dual preview model and single preview model, we conducted the lane tracking experiment with the both systems by driving simulator.

The experiment condition is shown in Table 1. In the experiment, the equivalent two-wheel vehicle model is used as the vehicle model in driving simulator, and the model is controlled to fit the reference first order system.

In addition to the condition, we conducted the experiment that time constant τ is changed to $1/4\pi$, $1/2\pi$ and $1/\pi$ and the dead time (100 ms) was added to the both systems.

Figure 9, 10 shows the vehicle trajectory with single preview point and dual preview points respectively. In the case of the system with single preview point, it was found that the more the time constant increased or dead time was added, the larger the overshoot became. In constrast, in the case of the system with dual preview points, it was found that the vehicle trajectory was almost the same and didn't generate the overshoot regardless of the time constant and dead time change. As a result, the system with dual preview points realized the target lane tracking performance without being affected by the time constant and the dead time.

6 CONCLUSION

As a result of studying the lane-keeping characteristics of a vehicle that generates a yaw rate so that it follows the relative target point, the following findings were obtained.

1. By increasing the number of preview points from one to two, the coexistence of a steady curve travelling without deviation and arbitrary design of tracking dynamic characteristics becomes possible. Since two preview distances and their gains were added as control parameters, the degree of

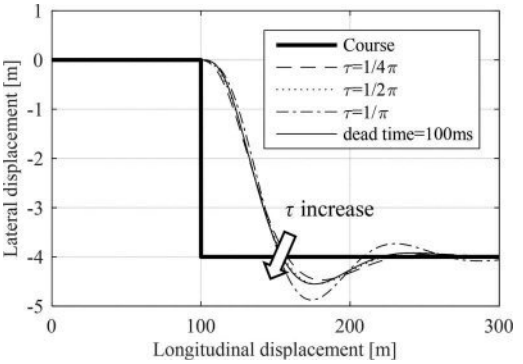


Figure 9. Vehicle trajectory of single preview point model when time constant τ is changed and the dead time was added to the system.

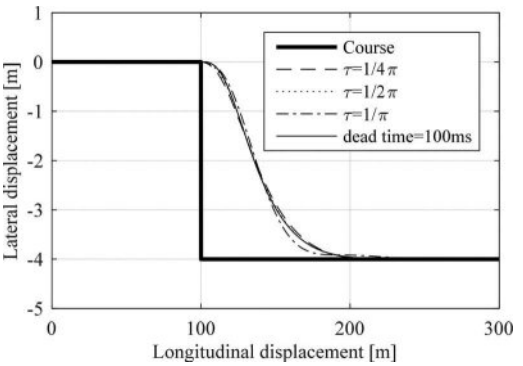


Figure 10. Vehicle trajectory of dual preview points model when time constant τ is changed and the dead time was added to the system.

freedom to design feed-forward and feedback independently increased; as a result, this performance was achieved.

2. By setting preview points at two positions in the vicinity of the vehicle that are nearer than the single preview point, the characteristics of $\zeta > 1/\sqrt{2}$, can be achieved while keeping the same natural frequency.
3. As result of the experiment, the system with dual preview points realized the target lane tracking performance without being affected by the time constant and the dead time of the vehicle.

REFERENCES

Asai, S., Amano, M., Hattori, Y. and Ono, E. (2012). Improvement and Experimental Validation of Lane-keeping Control Based on a Bat's Flight Model. *The JSAE Transactions* **43**, **1**, 33–38.

Boer, E. R. (1996). Tangent Point Oriented Curve Negotiation. *The IEEE Proceedings of the Intelligent Vehicle Symposium 1996* **5501565**, 7–12.

Fujioka, T. (2007). Theoretical Research on the Stability of the Closed System Composed of Look-ahead Driver and a Planer Vehicle. *Proceedings of the JSAE Spring Convention* **11-07**, **20075092**, 29–34.

Huang, J. and Konaka, E. (2012). Multiple Look-Ahead Distance Scheam for Lateral Control of Vision-Based Vehicles. Proceedings of the 19th World Congress on Intelligent Transport Systems **AP-00106**.

Kondo, M. (1967). *Basic car engineering*. The latter period volume. Yokendo. Tokyo.

Kuwabara, K., Narikiyo, T. and Fuwa, K. (1998). Basic Study on Lateral Control for Automated Vehicle System: A Design Method of Trajectory Control System with Preview Function. *Trans. of the Japan Society of Mechanical Engineers* **C64**, **622**, 2140–2147.

Mouri, H. and Furusho, H. (1999). Investigation of Automatic Path Tracking–Control method for a curved path. *Trans. of the Society of Automotive Engineers of Japan* **30**, **2**, 105–111.

Mouri, H., Shirato, R. and Nagai, M. (2004). A Study of a Vehicle Control for Tracking a Target Point. *The 7th International Symposium on Advanced Vehicle Control AVEC'04* **20044829**, 59–64.

Notomi, S. and Horiuchi, S. (1998). A Path Tracking Control System Using Generalized Predictive Control Theory. *Proceedings of the JSAE Autumn Convention* **62–98**, **9837814**, 9–12.

Ono, E., Amano, M., Hosoe, S., Hiryu, S. and Riquimaroux, H. (2011). Similarities between Bat Flight and Driver-operated Vehicle Trajectories and Their Unified Model. *The JSAE Transactions* **42**, **6**, 1275–1280.

Yoshimoto, K. (1969). Simulation of Man-Automobile Systems by the Driver's Steering Model with Predictability. *The Bulletin of JSME* **12**, **51**, 495–500.

Advanced Vehicle Control – Edelmann, Plöchl & Pfeffer (Eds)
© 2017 Taylor & Francis Group, London, ISBN 978-1-138-02992-7

Bayesian network-based identification of driver lane-changing intents using eye tracking and vehicle-based data

X.H. Li & M. Rötting
Chair of Human Machine Systems, Technische Universität Berlin, Germany

W.S. Wang
Department of Mechanical Engineering, Beijing Institute of Technology, Beijing, China
Department of Mechanical Engineering, University of California Berkeley, CA, USA

ABSTRACT: A Bayesian network decision-making method is proposed by combining driver's eye-tracking data and vehicle-based data together to identify driver lane-changing intents. First, experiments are conducted in a driving simulator with eye-tracker device to obtain the data when a subject driver makes lane-changing maneuvers. Second, collected data are analyzed in machine learning method using Bayesian decision-making approach to predict driver's lane-changing intents. Last, to show the benefits of our proposed method, comparison experiments are made between the data fusion way and only using eye tracking data or vehicle-based data. The results show that the Bayesian network with data fusion method performs better than using single information to recognize driver's lane-changing intents. At the same time, thresholds of Lane-changing probability and vehicle-based data as restricting condition choosing work is discussed in order to select the best identification parameter.

1 INTRODUCTION

More than 90% of traffic accidents are related to human error (Vorndran 2007). Under such background, various advanced driver assistance systems (ADAS), like adaptive cruise control systems, blind spot assist systems etc., have been developed to help increase driving safety or release the workload of drivers. However, research is still needed to make those driver assistance systems better acceptable by drivers. Thus, it is crucial to understand or recognize driver behavior (Plöchl & Edelmann 2007). Among the various driver behaviors, lane-changing (LC) or lane-keeping (LK) maneuver is one of the most frequently used but hard to be identified in advance. LC maneuvers, if handed improperly, it has high possibility to cause a traffic accident (Mokhiamar & Abe 2002). Statistical study shows that 89% of LC accidents are fully because of driver at fault (Luoma, Sivak, & Flannagan 1995). Due to this reason, recognizing driver's LC intents is important to improve driving safety especially for the scenario that drivers overtake cars.

Many efforts for recognizing driver's LC intents have been made using two main kinds of methods: *video or camera-based* and *driving data-based*. For video or camera-based method, it is proposed by (McCall & Trivedi 2006) that an steerable filters method to track lanes to recognize LC intents. The gaze data collected by an eye-tracker were believed as credible information to release human-machine-interaction (Ji, Zhu, & Lan 2004), especially in driving conditions. Driver's gaze data could largely reflect what he/she is looking at and thus can be used to recognize driver intents. In (Zhang, Avery, & Wang 2007), an uncalibrated method to detect the lane is developed using video camera. However, the video- or camera-based detecting methods would be easily affected by environment disturbances. For driving data-based method (Wang, Xi, & Chen 2014), driver operating data (e.g., steering wheel, throttle opening) is utilized. Similarly, the driver's handing data also give us hints about what he/she is going to do next. When overtaking car is necessary (blocked by the slow driving front car), behavior like looking at the side mirrors is an important hint that he/she will make LC maneuver. However, it is not safe to say that looking at the side mirrors frequently means the driver will indeed make a LC maneuver because of the surrounding cars state (the speed of the side or rear cars). Thus, by combining both eye gaze data and driving operating data (steering wheel angle and throttle opening), better prediction rate of making LC behavior could be achieved. To overcome the drawbacks of only using camera or only driving data, an information fusion method is developed by combining eye-tracking data and vehicle-based data together to identify driver's LC intents.

The experimental work presented in this paper aims at identifying driver left LC intents. The proposed

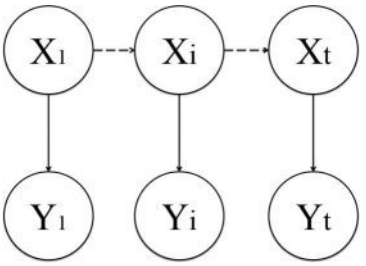


Figure 1. Bayesian Network.

Bayesian network method, experimental design, data collection and prediction results analysis as well as the selection work of Lane-changing probability and restricting thresholds is illustrated in the following sections.

2 METHODS

A Bayesian Network is a directed acyclic graph (DAG) net work, which is shown in figure 1, where Y node means observation variable and X node means its parent. Specially, for continuous node (represent as square) with discrete parent (represented as circle) in figure 2. Here we assumed that the continuous node follows conditional Gaussian distribution, so the probability of observation given its parent can be written as:

$$P(Y = y|X = k_i) \sim N(y; \mu_i, \Sigma_i), i \in \{1...n\}, \quad (1)$$

where k_i is the each value of discrete variable and μ_i and Σ_i are the mean and covariance of respective discrete variable.

In this work, a two-layer Bayesian network has been made with the decision-making layer (Lane-changing or Lane-keeping) and the observation layer (vehicle yaw state and driver's interest area), shown as figure 3. In this LC network, LC-node is discrete node while yaw-node and driver eye's area of interest node (AoI-node) are continuous nodes; at the same time, node that marked in shadow means it is evidence node which can be observed, as we can see the yaw-node and AoI-node, and accordingly LC-node is the node to be inferred.

Here, junction-tree algorithm is used to infer the LC probability given the evidence we observe $P(LC = 1|evidence)$ (Murphy 1999).

3 FEATURE PARAMETER SELECTION

3.1 *Eye-tracking data*

Gaze data monitored by eye-tracker have been widely used to show the subject's AoI and gaze behavior is

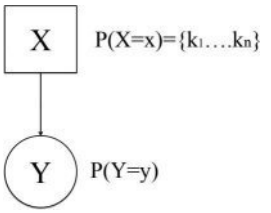


Figure 2. Bayesian continuous node with discrete parent.

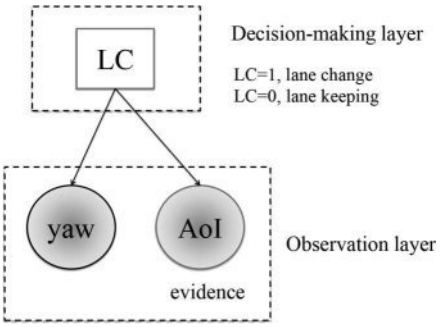


Figure 3. Lane-changing Bayesian network.

a good way to be an indicator of information gathering, therefore it could be used to derive information about the drivers next planned objective in order to identify intended maneuvers. Based on the paper from (Tijerina, Garrott, Stoltzfus, & Parmer 2005), during left LC procedure, the chance of looking at the left mirror are 65%–85% and the duration on average is 1.1 s.

In our work, the time-proportion (between 0 and 1) of looking at the left mirror has been used as one evidence to identify left LC intents. So at certain moment, the left-looking ratio can be calculated by:

$$R_{left} = \frac{T_{left}}{T_{tw}} \quad (2)$$

where R_{left} is the ratio of looking at left mirror, T_{left} is the duration of looking at the left mirror and T_{tw} is certain time-window selected.

Although gaze data could show driver intents much more seconds in advance (Henning, Georgeon, Wynn, & Krems 2008), there are also more false predictions. Owing to this, using vehicle-based data can be a complementary part of video or camera-based approach to reduce false prediction rate.

3.2 *Vehicle-based data*

Vehicle-based data, like steering wheel angle, yaw angle, throttle or brake pedal signal, have long been used as parameters in driver behavior identification (Angkititrakul, Terashima, & Wakita 2011). In our work, yaw data are selected as vehicle-based data, since yaw angle gives explicit information about



Figure 4. LC experiment scenario.



Figure 5. Driving simulator and SMI eye-tracking glasses.

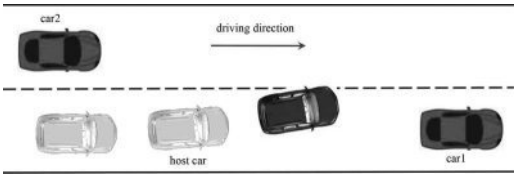


Figure 6. Definition of LC timing.

whether the car is heading to the left or right thus could be used as a parameter to recognize LC intents.

However, on one hand, it is normally too late to recognize LC intents, compared with eye-tracking data or other human factor data; on the other hand, it is hard to realize synchronization between eye-tracking data and vehicle-based data.

Therefore, yaw data are not selected as one evidence in the LC Bayesian network as AoI (marked as red circle in figure 3) to calculate the probability $P(LC = 1|evidence)$, but rather used as a threshold evidence (marked as black circle in figure 3) to achieve less false positive rate. Further discussion about the advantage in this way will be shown in the following section.

4 EXPERIMENTS AND DATA PROCESSING

4.1 *Driving task*

The driving experiments were conducted in a driving simulator with a total of 10 subjects (6 male and 4 female) for a minimal of 22 years old (M = 25.9). All of the participants had normal vision, had held driver licenses for a minimal of 4 years (M = 7.15).

The driving task took place in a two-lane motorway with a length of 10 km, which can be seen in figure 4. In the driving scenario, simulated traffic like front cars and side cars could interact with the driver-controlled car by accelerating, decelerating or lane-changing just like in real traffic situation.

During the experiment, participates were instructed to wear an eye-tracker, and after gaze calibration they were guided to drive in a warming up scenario in order to be familiar with the simulator. In the experimental task, participants were told to drive on the right-most lane throughout the experiment and to only use the left-most lane for the purpose of overtaking slow-moving cars. The whole driving tasks were repeated 10 times and lasted approximately an hour and all the subjects were not paid by their participation.

4.2 *Equipment*

The driving simulator, on which the experiments conducted, is a seat-box based driving simulator.

The eye-tracking device that was used to monitor driver's gaze feature are SMI eye-tracking glasses, which allows driver to move their heads, making it a non-intrusive way to monitor driver's eye movement behavior. This non-intrusive property also stops driver from being affected, so compared with other eye tracking devices, the gaze data collected is more accurate. Meanwhile, this eye-tracking glasses could also record video as first person view, which is beneficial for gaze data extraction. Both of the equipments are shown in figure 5.

4.3 *Data processing*

To synchronize vehicle-based data and eye-tracking data, 30 Hz sampling rate was set in the simulator and eye-tracking device. The whole data was separated into two groups, one used for training and another used for testing.

4.3.1 *Definition of LC timing*

As all the data we collected are time series data, it is necessary to mark the LC maneuver timing for further data processing and analysis. The moment that the host car just hits the central line, which can be seen in figure 6, was labeled as the beginning of LC. The red cars are computer-controlled cars while the blue car is driver-controlled car, whose position (approaching the central line) had been marked as the LC start.

4.3.2 *Gaze data*

Gaze data were collected by the SMI eye-tracking glasses. The AoI for the left mirror was specified in the SMI BeGaze software, so time series gaze data could be easily classified from other eye movement behaviors.

Having AoI time series data, R_{left} can be calculated. According to the paper (Lethaus, Baumann, Köster, & Lemmer 2011), 5 s window is enough to predict LC intents, so here $T_{tw} = 5$ s window is preferably chosen in equation 2.

For each group of R_{left} data, we manually labeled them as LC class and LK class. 5 s time series data before the beginning of each left LC timing (see figure 6) were marked as LC class and the normal driving data without any LC maneuver were marked as LK class. Both LC class and LK class data were used for learning LC Bayesian network.

4.3.3 *Yaw data*

Vehicle yaw data were extracted in the driving simulator. Here we normalize the yaw angle to $[-1, 1]$, in which positive means that the vehicle is heading to left and negative means heading to right.

5 PREDICTING LANE-CHANGING INTENTS

With all the data has been well-processed, the probability of LC maneuver taken, namely $P(LC = 1|evidence)$, could be calculated using the proposed LC Bayesian network.

However, to predict whether driver has intent to make LC maneuver or not, a probability threshold should be given. Thus, $T_{LC} = \{0.6, 0.7, 0.8, 0.9\}$ were set respectively as a threshold to predict LC intents. For example, if the T_{LC} is set to 0.9, it means LC intents only be identified when $P(LC = 1|evidence) \geq 0.9$.

As is mentioned in section 3.2, yaw threshold was chosen as a restricting condition to improve the performance of LC prediction. Based on our raw data, in normal driving (without any intent of making LC), yaw value fluctuated between interval $(-0.002, 0.002)$ and the maximal yaw value before a clear LC maneuver was approximately 0.005, thus $T_{yaw} = \{0.002, 0.003, 0.004, 0.005\}$ was selected. For example, if T_{yaw} is set to 0.002, it means that $yaw < 0.002$ will be directly identified as LK.

The LC predicting logic can be represented as follow:

if $P(LC = 1|evidence) \leq T_{LC}$
  if $yaw \leq \mathrm{T}_{yaw}$
    lane-changing
  else lane-keeping
else lane-keeping
end

The performance of each threshold value would be discussed in the following section.

6 EXPERIMENT RESULTS AND ANALYSIS

In this section, the results of LC predicting are presented and the procedure of choosing appropriate threshold is discussed.

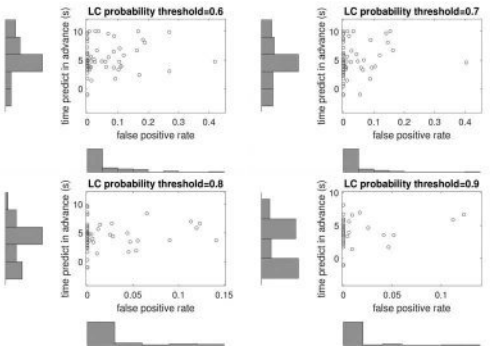


Figure 7. Only using eye-tracking data to predict LC intents.

Table 1. Mean of t_{ad}, FPR and MPR by only using eye-tracking data to predict.

Theshold	t_{ad} (s)	FPR	MPR
$T_{LC} = 0.6$	5.215	0.053	0.063
$T_{LC} = 0.7$	4.533	0.032	0.125
$T_{LC} = 0.8$	3.532	0.016	0.203
$T_{LC} = 0.9$	2.204	0.007	0.406

To evaluate performance of the proposed method, two parameters have been chosen: predicting false positive rate (FPR) and predicting time in advance (t_{ad}). FPR indicates the number of LK data sample which is incorrectly identified as LC data sample, while t_{ad} is the value that how long ahead of time one LC intents can be predicted. Driver LC intents can be a few seconds earlier than executing an actual LC maneuver, even though the driver may cancel his intent because of certain traffic reason. But in this work, t_{ad} longer than 10s' LC intents are identified as false prediction. Also, if there is no prediction before a real LC maneuver taken, one miss-prediction will be marked, and finally, miss-prediction rate (MPR) is calculated.

The overall distribution results and the detail performance of only using eye-tracking data to predict LC intents are shown in figure 7 and table 1, respectively. From the table we can see, as the increase of T_{LC}, mean of t_{ad} and FPR decreases from 5.215 s to 2.2 s and 0.053 to 0.007, respectively, while the MPR increases from 0.063 to 0.406. That is to say, lower threshold can get earlier prediction and lower miss-prediction but also lead to higher false positive rate. The situation of higher threshold has the opposite result.

Figure 8 and table 2 show the prediction results of predicting LC intents by only using yaw data. Compared with the results of only using eye-tracking data, the trends of t_{ad} and FPR by only using yaw data are the same, but it is much later (0.5–2.2 s) to recognize LC intents using yaw data than eye-tracking data. However, what is worth mentioning that yaw data can achieve almost 0 miss-prediction rate.

The analysis above shows the performance of both using yaw data and eye-tracking data to recognize LC

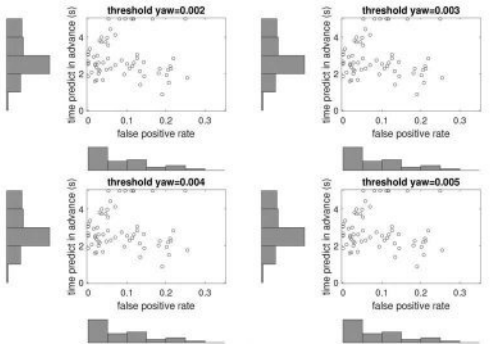


Figure 8. Only using vehicle data to predict LC intents.

Table 2. Mean of t_{ad}, FPR and MPR by only using vehicle data to predict.

Theshold	t_{ad} (s)	FPR	MPR
$T_{yaw} = 0.002$	2.893	0.085	0
$T_{yaw} = 0.003$	2.237	0.031	0
$T_{yaw} = 0.004$	1.887	0.013	0
$T_{yaw} = 0.005$	1.705	0.005	0

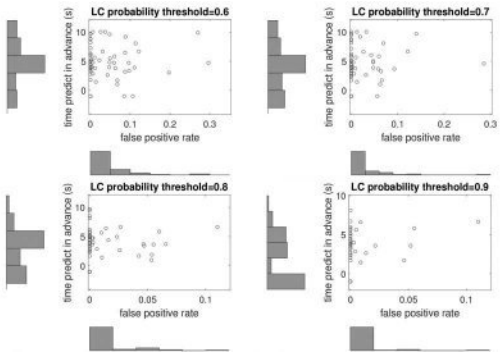


Figure 9. Fusing vehicle data and eye-tracking data to predict LC intents under $T_{yaw} = 0.002$.

intents. And clear drawbacks can be seen from figure 7, 8 and table 1, 2. This is the reason why the way of using data fusion has been implemented in order to get better predicting performance.

Figure 9–12 present the results of fusing both yaw data and eye-tracking data to predict LC intents under different thresholds, and more detail performance can be seen in table 3. The trend of t_{ad}, FPR and MPR is the same as what it discussed above when only considering single threshold. Using data fusion method, compared with only using eye-tracking data, the prediction time is as late as only using yaw data, but it can achieve significant low false positive rate.

Here we need to emphasize the importance of low FPR. Although recognizing LC prediction is essentially a classification work with only LC and LK class that need to be identified, a higher FPR prediction

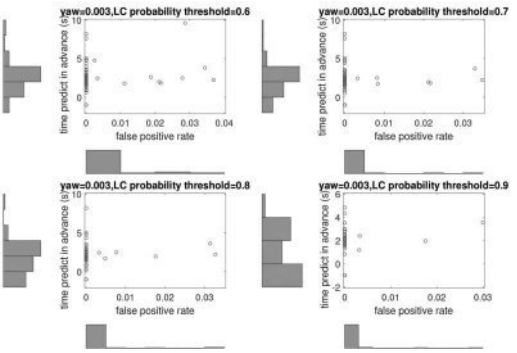


Figure 10. Fusing vehicle data and eye-tracking data to predict LC intents under $T_{yaw} = 0.003$.

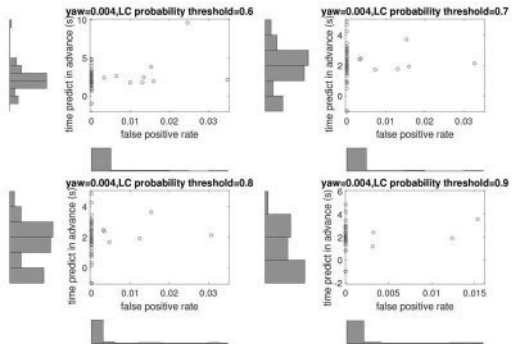


Figure 11. Fusing vehicle data and eye-tracking data to predict LC intents under $T_{yaw} = 0.004$.

has more negative influence on actual driving task. Because LC maneuver is naturally low infrequence driving behavior in normal driving, if false prediction is high, the predicting system would be completely rejected by the driver.

Owing to the above reasons, lower FPR, MPR and higher t_{ad} should be considered in selecting thresholds. From the prediction performance (see in table 3) we can see that the thresholds group of $\{T_{yaw} = 0.003, T_{LC} = 0.6\}$, $\{T_{yaw} = 0.004, T_{LC} = 0.6\}$ and $\{T_{yaw} = 0.005, T_{LC} = 0.6\}$ are better candidates. The MPR of the three groups are the same. Although FPR of the first group is 0.001 higher than the other groups, considering the performance of T_{td} in the first group, the thresholds group $\{T_{yaw} = 0.003, T_{LC} = 0.6\}$ has been chosen as thresholds in the LC predicting network and implemented in testing group data. The performance is shown in figure 13. By calculating, the mean of t_{ad} and FPR are 2.845 s and 0.007 respectively, which is similar to the expectation of the selected thresholds.

7 CONCLUSION

This study has shown that Bayesian network can provide a reliable predictive model in identifying

Table 3. Mean of t_{ad}, FPR and MPR by fusing vehicle data and eye-tracking data to predict.

	$T_{yaw} = 0.002$			$T_{yaw} = 0.003$			$T_{yaw} = 0.004$			$T_{yaw} = 0.005$		
Thrshold	t_{ad} (s)	FPR	MPR	t_{ad} (s)	FPR	MPR	t_{ad} (s)	FPR	MPR	t_{ad} (s)	FPR	MPR
$T_{LC} = 0.6$	2.722	0.004	0.063	2.510	0.003	0.078	2.197	0.002	0.078	2.114	0.002	0.078
$T_{LC} = 0.7$	2.251	0.003	0.141	2.098	0.002	0.141	1.800	0.001	0.141	1.720	0.001	0.141
$T_{LC} = 0.8$	1.751	0.002	0.234	1.592	0.002	0.234	1.405	0.001	0.234	1.328	0.001	0.234
$T_{LC} = 0.9$	0.989	0.001	0.438	0.855	0.001	0.438	0.821	0.001	0.438	0.707	0.001	0.453

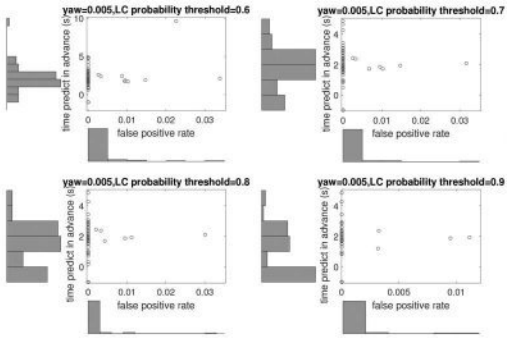


Figure 12. Fusing vehicle data and eye-tracking data to predict LC intents under $T_{yaw} = 0.005$.

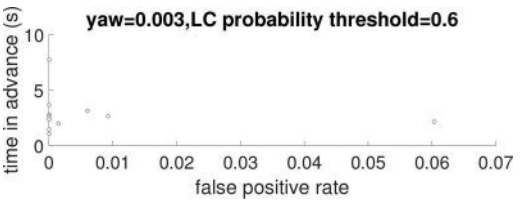


Figure 13. Using selected thresholds to predict LC intents.

lane-changing intents. Only using yaw data and eye-tracking data method to predict lane-changing intents has been implemented. The results demonstrated that gaze pattern gives earlier hints before a lane-changing maneuver but gets more false positive rate and miss-prediction rate. Thus, yaw data, shown to be a later but less miss-predictive feature to identify lane-changing behavior, can be a supplementary parameter combined with using eye-tracking data.

Multi-thresholds selection work has been discussed in combining eye-tracking and yaw data method. That is, the larger the thresholds are, the more accurate the predictive model is, but the later that it predicts and the more possibility that it makes miss-prediction. The above strategy provides a method of choosing the well-behaved thresholds, especially when using lane-changing predictive decision as the input of ADAS.

Future studies would implement the proposed Bayesian network predictive method to comprehensive lane-change maneuvers as well as the implementation of on-line predicting.

REFERENCES

Angkititrakul, P., R. Terashima, & T. Wakita (2011). On the use of stochastic driver behavior model in lane departure warning. *IEEE Transactions on intelligent transportation systems 12*(1), 174–183.

Henning, M. J., O. Georgeon, T. Wynn, & J. F. Krems (2008). Modelling driver behaviour in order to infer the intention to change lanes. In *Proceedings of European Conference on Human Centred Design for Intelligent Transport Systems*, Volume 113.

Ji, Q., Z. Zhu, & P. Lan (2004). Real-time nonintrusive monitoring and prediction of driver fatigue. *Vehicular Technology, IEEE Transactions on 53*(4), 1052–1068.

Lethaus, F., M. R. Baumann, F. Köster, & K. Lemmer (2011). Using pattern recognition to predict driver intent. In *International Conference on Adaptive and Natural Computing Algorithms*, pp. 140–149. Springer.

Luoma, J., M. Sivak, & M. J. Flannagan (1995). Rapid communication effects of driver-side mirror type on lane-change accidents. *Ergonomics 38*(10), 1973–1978.

McCall, J. C. & M. M. Trivedi (2006). Video-based lane estimation and tracking for driver assistance: survey, system, and evaluation. *Intelligent Transportation Systems, IEEE Transactions on 7*(1), 20–37.

Mokhiamar, O. & M. Abe (2002). Active wheel steering and yaw moment control combination to maximize stability as well as vehicle responsiveness during quick lane change for active vehicle handling safety. *Proceedings of the Institution of Mechanical Engineers, Part D: Journal of Automobile Engineering 216*(2), 115–124.

Murphy, K. P. (1999). A variational approximation for bayesian networks with discrete and continuous latent variables. In *Proceedings of the Fifteenth conference on Uncertainty in artificial intelligence*, pp. 457–466. Morgan Kaufmann Publishers Inc.

Plöchl, M. & J. Edelmann (2007). Driver models in automobile dynamics application. *Vehicle System Dynamics 45*(7–8), 699–741.

Tijerina, L., W. Garrott, D. Stoltzfus, & E. Parmer (2005). Eye glance behavior of van and passenger car drivers during lane change decision phase. *Transportation Research Record: Journal of the Transportation Research Board* (1937), 37–43.

Vorndran, I. (2007). Unfallgeschehen im straenverkehr 2006 (roadtraffic accident). In *Statistisches Bundesamt*.

Wang, W., J. Xi, & H. Chen (2014). Modeling and recognizing driver behavior based on driving data: a survey. *Mathematical Problems in Engineering 2014*.

Zhang, G., R. Avery, & Y. Wang (2007). Video-based vehicle detection and classification system for real-time traffic data collection using uncalibrated video cameras. *Transportation Research Record: Journal of the Transportation Research Board* (1993), 138–147.

Advanced Vehicle Control – Edelmann, Plöchl & Pfeffer (Eds)
© 2017 Taylor & Francis Group, London, ISBN 978-1-138-02992-7

Influence of different ground truth hypotheses on the quality of Bayesian networks for maneuver detection and prediction of driving behavior

T. Rehder & L. Louis
Department of Research and Technology, BMW Group, Munich, Germany

W. Muenst
Department of Research, Objective Software GmbH, Munich, Germany

D. Schramm
Chair of Mechatronics, University of Duisburg-Essen, Duisburg, Germany

ABSTRACT: Semi or fully automated driving requires anticipating the driving behavior of traffic participants to increase safety, comfort and a cooperative driving experience. For the task of prediction machine learning techniques are often applied to learn driving behavior from measured data. Due to the very subjective nature of predicting driving maneuvers, in this paper, the significance of the effort and time spent in the right kind of labeling for time series data and its direct relevance to the performance of the trained models is shown.

1 INTRODUCTION

One of the main trends of future mobility is to increase the level of assistance and automation, which increases both safety and comfort while driving. But to assure a safe, comfortable and especially a cooperative driving experience, anticipation of the driving behavior of traffic participants is needed.

Figure 1 shows a typical highway scenario. The semi or fully automated vehicle (in the remainder called *ego vehicle* in short) on the left lane approaches a vehicle in front on the right lane (object 1) with $8\,\mathrm{m\,s^{-1}}$ relative velocity. Object 1 is going to merge into the ego vehicle's lane at t_0 because of a slower truck in front (object 2). The lane change maneuver starts at t_{change}, when object 1 begins to move in lateral direction. But the motivation of object 1 to change the lane starts even earlier at t_{motiv}, because the slower object 2 in front is getting too close. To allow for a cooperative interaction between the traffic participants, the ego vehicle should anticipate the lane change motivation of object 1 as early as t_{motiv}.

To predict the driving behavior of the surrounding traffic participants, a model is needed that represents their future driving actions based on the current traffic situation. Often probabilistic models that can be learned from data [4, 6] are used to infer the most likely driving behavior of a traffic participant. In general, supervised classification methods like Bayesian Networks (BN) need class labels in a data set that the algorithm learns the model parameters from. Often these labels are defined by a human expert, but the task of labeling is not standardized in any way and every expert defines the labels slightly differently.

Depending on the class that needs to be labeled, labels can either be of subjective or of objective type. In case of the traffic scenario shown in Figure 1, the label of the lane change of object 1 at t_0 can be defined objectively as there can be set up a clear definition of when a vehicle is matched to a specific lane and when the matched lane changes. Even the start of the lane change at t_{change} can be determined in an objective manner by taking into account the lateral movement over the entire duration of the lane change, although it is hard for any algorithm to label this point in time reliably because of sensor noise. For the label of t_{motiv}, there exists no distinct definition as the motivation to change the lane depends on a driver's individual awareness of the situation and on the personally accepted minimal time distances to surrounding vehicles. Therefor the label of t_{motiv} is a subjective label.

In this paper the significance of the effort spent in labeling time series data and the performance of learning the parameters used for maneuver prediction are shown. For both, the labels for the objective start of the lane change maneuver and the subjective start of the lane change motivation, different labeling strategies are compared in terms of applicability to different labeling tasks, classification quality, time spent in the labeling process and scalability on the size of data sets.

The remainder of this paper is organized as follows: In section 2 the most commonly used methods for generating ground truth hypotheses via labeling

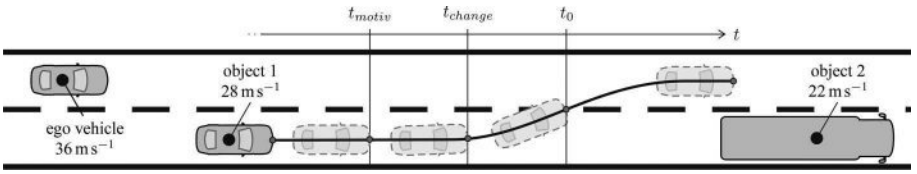


Figure 1. Lane change motivation of object 1 due to slower object 2 in front.

time series data are explained. In section 3 the driving data is depicted that is used to train the algorithms for both maneuver detection and intention recognition of lane changes, which in turn are described in section 4. The results of comparing the different labeling strategies are shown in section 5. Finally, section 6 gives a conclusion and an outlook to future work.

2 LABELING METHODS

For labeling driving maneuvers, like lane changes, several methods exist to label time series data to supervise a classification algorithm like a Bayesian Network. In the following an overview of the most frequently used labeling methods is given.

2.1 *Manual offline labeling*

Labeling data for supervised learning is often done offline as a post-processing step by a human expert who has a deep understanding of the domain the data is taken from. One way of reviewing and labeling the driving data manually is to process the data first to show all relevant sensor measurements in a highly compressed form. The expert can then zoom in on relevant sequences and define the labels precisely (see Figure 3 for an example).

However, if a deep awareness of the recorded driving situation is needed (e.g. when defining subjective labels), the data has to be played back in real-time so the expert is able to see things from the driver's perspective and define the labels as close to the original driver's intentions as possible. The quality of the labels depends on the grade of immersion into the driving situation, which itself again depends on the the quality of the recorded data and on the representation of the data.

One main advantage of manual labeling is that measurement errors (like self-localization errors or false detections of traffic objects) can be recognized by a human expert quickly and can be marked as invalid, so they will not be used for training. Moreover, an expert is able to detect relevant characteristics in the data even if the measurements are noisy. The disadvantage of the manual labeling process is obviously the time it takes to review all data and define all labels by hand. Therefore manual labeling does not scale with the amount of driving data for the training and evaluation of the learning algorithms.

2.2 *Automatic offline labeling*

Characteristics in sensor measurements can be used to find the start and/or the end of a lane change in data sequences automatically. An expert manually sets up a definition of the maneuver once and based on that definition more maneuvers can be found automatically. For example, the end of a lane change can be defined as the point in time when the center of the vehicle's front crosses the lane marking (see t_0 in Figure 1). Assumptions about the process of the lane change, e.g. a constant average duration T_{motiv} of the lane change motivation and a constant average duration T_{change} of the actual changing of the lane, can then be used to compute the start time of the motivation or the actual lane change with

$$t_{motiv} = t_0 - T_{motiv} \quad \text{and} \quad t_{change} = t_0 - T_{change}. \tag{1}$$

The lane change duration can either be defined by an expert (see [9, 5, 1]) or be computed, for example by defining a maximum entropy for the separation of the two classes $C = \{lane\ change, keep\ lane\}$ and then computing the mean lane change duration with the help of mutual information like in [7].

For the latter, let D be the set of all values of the lateral position d_{lat} relative to the lane the vehicle is driving on at time t_k where $t_k < t_0$. Presumed every value of N measurement instances of d_{lat} at time t_k is unique, there exist $N-1$ possible cut-points $s \in S$ to split D in two portions D_1 with $D < s_n$ and D_2 with $D > s_n$. According to [3], every cut-point s_n now induces a class information entropy

$$H_I(D,s) = \frac{|D_1|}{|D|} H_C(D_1) + \frac{|D_2|}{|D|} H_C(D_2), \tag{2}$$

where $H_C(D)$ is the class entropy defined as

$$H_C(D) = -\sum_i P(C_i,D) log_2 P(C_i,D). \tag{3}$$

The cut-point s_n minimizing the class information entropy H_I is the entropy-optimal cut-point $s*$ with $H_{I,min} = H_I(D,s*)$. $H_{I,min}$ can be seen as a quality indicator of the class split, so as long as $H_{I,min}$ is lower than a defined threshold $\delta_{H,max}$, D can be split well enough into the two classes of C, which means that the average lane change started even before t_k. Computing $H_{I,min}$ is iteratively repeated for a decreasing t until $H_I(D,s*) >= \delta_{H,max}$, which marks the average

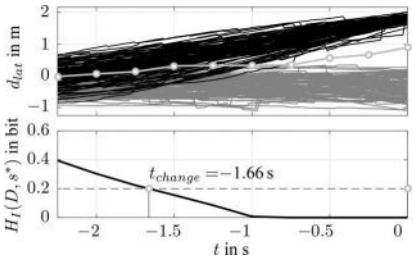


Figure 2. Top: Lateral position of all recorded *lane change* sequences in black and *keep lane* sequences in gray. Bottom: Optimal split class information entropy plotted in black solid, entropy threshold $\delta_{H,max} = 0.2$ in black dashed.

start time t_{change} of a lane change relative to t_0 (see Figure 2).

The main advantage of the automatic labeling process is that it is fast and scales with a growing amount of data that needs to be labeled. Compared to defining the lane change duration for the automatic labeling by hand, the estimation of T_{change} with help of class information entropy, the labeling relies more on the true characteristics of the data. The disadvantage of the automatic labeling methods presented here is that all maneuvers are labeled with the same maneuver duration, regardless of the characteristic of the individual maneuver, e.g. a slow and a fast lane change are both labeled with the same T_{change}. Another downside is that there are parameters (the entropy threshold $\delta_{H,max}$ or the label duration T_{change} itself) that need to be tuned manually. Moreover estimating the class information entropy has high computational costs (especially for high dimensional feature spaces).

2.3 *Semi-automatic offline labeling*

Obviously, it can be helpful to improve and speed up the manual labeling process by combining manual and automatic labeling. For example, the end time t_0 of a lane change maneuver can be found automatically in the data relatively easy, but the duration T_{change} of an individual lane change is hard to determine algorithmically. A human supervisor can then be employed to adjust the maneuver start time for each automatically found label instance manually.

At this point it also has to be mentioned that there exist research fields called *semi-supervised learning* (with the distinction of *inductive* and *transductive* techniques) and *active learning* (which is sometimes also called *query learning*), but in this paper we do not investigate the applicability of these techniques, as they focus more on the learning algorithms and less on the process of labeling. For an in-depth view on semi-supervised learning see [2], for a literature review on active learning see [10].

2.4 *Manual online labeling*

Sometimes even for an expert it is hard to label data in a post-processing step by just seeing recorded videos or analyzing sensor measurements, because driving scenarios can be very complex. To overcome this, labels can also be acquired directly while driving and while recording data. The driver or a co-driver can either define labels by recording audio comments or by manipulating buttons. Where audio comments need to be processed manually offline in order to generate class values for the classifier's training, push-buttons can be evaluated programmatically, which makes the post-processing a lot easier.

The advantage of labeling while driving is, that the expert has a good situation awareness and can define the label in the same way as he acts in the traffic environment. A negative impact of labeling while driving is that it may distract the driver from the driving task, which on one hand is safety-critical and on the other hand affects the quality of the labels. Depending on the number of different labels that need to be defined and on the complexity of the current traffic situation, the driver can be overexerted with labeling while driving. However, based on the problem statement (such as only evaluating satisfaction or comfort of longitudinal distances) a co-driver can be employed to do the labeling. The labeling of the co-driver does not affect the safety while driving and he can concentrate fully on the labeling process. But it remains an open question, whether the traffic situation can be assessed from the perspective of the co-driver's seat as good as from the driver's point of view, especially because the co-driver is not in responsibility of the vehicle control.

3 DRIVING DATA

Because the focus of this paper lies on the evaluation of different labeling strategies, the objective of the maneuver prediction has been limited to the lane change prediction of the ego vehicle. Even more, the focus has been limited to lane changes to the faster lane (which is on the left on German highways), because the criticality and therefore the need for an anticipation of this maneuver is potentially the highest. The assumption is that, given measurements of extrinsic features, a general model of the lane change behavior can be derived that is also valid to infer other traffic participant's driving behavior, provided that additional sensor noise from the environmental sensors is taken into account.

To compare the different labeling strategies described in section 2, overall 158 min and 294 km of real world driving data on a German highway have been recorded with a prototype vehicle. The test vehicle was equipped with a 360-degree environment surround view consisting of six LIDAR sensors to track other traffic objects. A highly precise digital map was available that delivered information about lanes.

The driving data was taken during a driver study, in which 13 different co-drivers (3 women and 10 men) were employed to do a manual online labeling of their intentions to change lane, as described in subsection 2.4. During the study, the driver took over

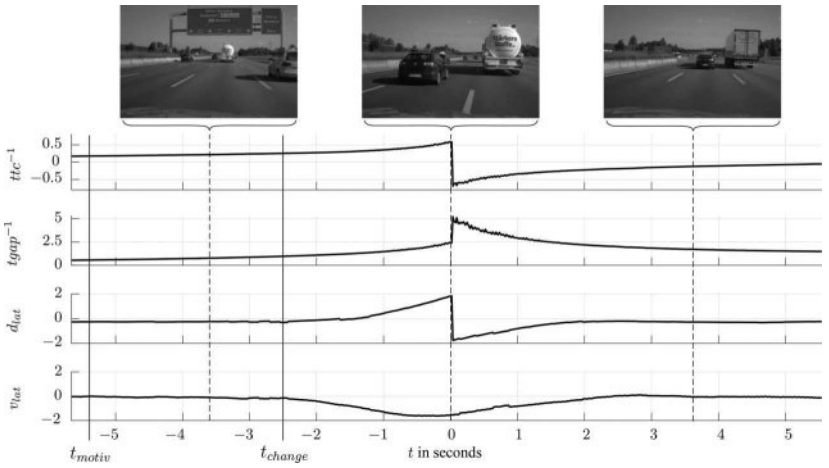


Figure 3. Example of a lane change scenario with manual online label for t_{motiv} and semi-automatic offline label for t_{change} (solid vertical lines). The lane change takes place at $t_0 = 0$, the dashed vertical lines mark the time reference for the camera images shown at the top.

the role of a chauffeur, keeping the current lane and driving at speeds of the (advisory) speed limit. The co-driver was ordered to take over the responsibility to decide when to change the lane and to indicate lane change intentions via special function buttons, whose exertions were shown to the driver in the head-up display of the vehicle. The driver was ordered to execute the lane change wish as soon as it was possible and safe. Because the wing mirrors of the vehicle were of course still adjusted to the driver, the co-driver himself could not check if his lane change wish was realizable. This study setup was intended to deliver clean labels of the start of subjective lane change intentions of the study participants at t_{motiv}, not mixed up with the influence from knowing if a lane change was realizable at all.

Overall 77 manual labels for intentions to change lane to the left could be gathered during the study. To compare the effectiveness of the different labeling strategies described in section 2, these lane changes have been re-labeled several times according to the different labeling strategy to be tested. As features for the detection of already started maneuvers we use lane relational features, in particular the lateral distance d_{lat} and lateral velocity v_{lat} relative to the lane the vehicle is currently driving on. For the anticipation of lane change motivations we use inter-vehicle relational features, namely the well known time to collision $ttc = \Delta d_{pre}/\Delta v_{pre}$ and the time gap $tgap = \Delta d_{pre}/v_{ego}$ relative to the preceding vehicle on each lane. For a better scaling of the features' values the inverse of both the *ttc* and *tgap* is used. Figure 3 shows an exemplary recording of a lane change to the left in a situation similar to the scenario shown in Figure 1, but here in the perspective of object 1 (in this case the test vehicle).

To train and test the maneuver prediction described in the next section based on the different labeling strategies, the recorded time series data has at first been cut into smaller sequences of a maximum of 5 minutes driving time each and afterward been split into a training and a test set in the ratio of 0.6 to 0.4. With an average sample time of 20 ms, the ratio of data points for the label *lane change* compared to the label *keep lane* is approximately 0.97 to 0.03 for the training data of the maneuver detection (depending on the labeling strategy, in this case t_{change} labeled manually offline). The ratio for the training data of the maneuver intention is with 0.89 to 0.11 a little less skewed, which is because of $t_{motiv} \leq t_{change}$ relative to t_0 for the manual online labeling. But in general, training data with an unbalanced ratio of the class distribution causes most predictors to underestimate the likelihood of the class that is less represented in the data. Therefore, in this paper the data has been undersampled to synthesize equally distributed data, which is a common practice.

4 MANEUVER PREDICTION

In this paper we distinguish between the prediction of a lane change maneuver that already started (LC) and the anticipation of a driver's lane change intention (LCI). For both the prediction of LC and LCI we propose a Bayesian Network (BN), whose parameters are being trained based on the labels defined by the different labeling strategies described in section 2 and based on the data depicted in section 3. The two separate net structures for inferring the probabilities for LC and LCI are depicted in Figure 4. While the structure for inferring LC is straightforward, to compute the probability for LCI, for every drivable lane ttc^{-1} and $tgap^{-1}$ to the next vehicle in front on that lane are being used to compute the driver's contentedness C_i on an individual lane i. The probability for the LCI is then

computed depending on the driver's contentedness on all of the available lanes. For a detailed description of this particular prediction framework, see [8].

5 RESULTS

The labeling methods described in section 2 are compared for the tasks of predicting the start of a lane change motivation and the prediction of the start of the lane change maneuver independently.

Labeling the start of the lane change maneuver at t_{change} has been done automatically with different values of T_{change} defined manually (1 s and 3 s) and with $T_{change} = 1.66$ s, which was found by defining a maximum class information entropy of $\delta_{H,max} = 0.2$ on the data (see subsection 2.1). Moreover, every lane change has been labeled semi-automatically offline, so t_0 has been found in the data automatically and an expert defined the corresponding t_{change} for every label manually (as described in subsection 2.3). This resulted in an average labeled lane change duration of $T_{change} = 3.05$ s with a standard deviation of $\sigma = 0.80$. The semi-automatic labeling process took about 2 hours for the nearly 3 hours of driving data.

Because the labels for the maneuver intention at t_{motiv} are of subjective type, the labeling strategies being compared are manual online labeling (see subsection 2.4 and section 3) and automatic offline labeling with different values of T_{motiv} defined manually (1 s, 5 s and 10 s). The labels of the manual online labeling process show an average lane change motivation duration of $T_{motiv} = 5.45$ s with a standard deviation of $\sigma = 2.42$.

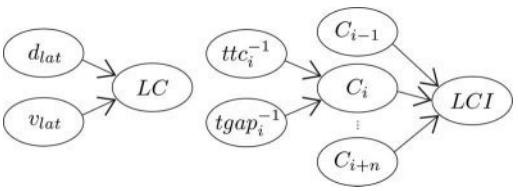


Figure 4. Overview of the structures of the two BN used for inferring a lane change detection probability LC and a probability LCI of a single driver's lane change intention.

Figure 5 shows the Receiver Operating Characteristic curves (ROC) of the resulting BN performance for the different labeling strategies, where TPR is the true positive rate and FPR is the false positive rate of the maneuver classifications. On the top, the results for the prediction of the start of the lane change maneuver (LC) are shown, the curves at the bottom show the results for the lane change intention recognition (LCI). To pick the optimal classification threshold from the ROC, [11] proposed (among other metrics) the minimum distance to the optimal ROC point at [0, 1], which can be found by computing

$$d_{opt} = \sqrt{(1 - TPR)^2 + FPR^2}. \tag{4}$$

6 DISCUSSION AND CONCLUSION

In this paper, different strategies for labeling time series data for the use as training data for a supervised classification problem have been pointed out. The application was the prediction of lane changes during highway driving, for which a Bayesian Network was defined to demonstrate the differences in the prediction results for the differently labeled training sets.

For labeling the start of a lane change to answer the purpose of predicting a lane change maneuver as soon as it starts, it could be shown that the automatic labeling, which is sparsely time consuming, is favorable over semi-automatic labeling, in which a lot of

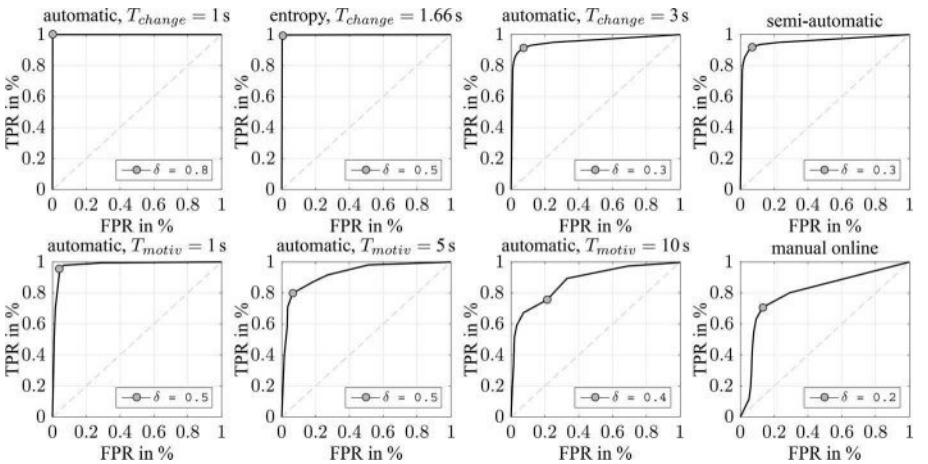


Figure 5. Receiver Operating Characteristics (ROC) curves compared for different labeling strategies. The optimal threshold according to (4) is marked with a circle. First row: Results of predicting LC. Second row: Results of predicting LCI.

work needs to be done manually. The main challenge in labeling the start of the maneuver is to choose an adequate constant maneuver duration that trades off a long prediction time against a high prediction accuracy according to the problem statement. Choosing the labeling duration based on class information entropy can be helpful, because it leaves the expert with only one parameter that needs to be tuned manually that gives a direct hint to the classification quality to expect from the prediction algorithm.

An interesting part in the investigation was the manual online labeling process that was performed in a driver study. We wanted to know if a manual labeling process is needed to gather labels that are normally hidden and subjective in nature, like the lane change intention of a driver. We found out that manual labeling is not necessarily needed, yet maybe not even recommended, because the labels can only be acquired in a tedious process and the prediction performance does not seem to profit from the manually defined labels at all. But the reason for the relatively poor results of the manual online labeling could also be located in differing individual driving behavior of the study participants or a poor situational awareness of the traffic situation from the co-driver's perspective. These open questions need to be investigated in further research.

REFERENCES

[1] Sarah Bonnin et al. General Behavior Prediction by a Combination of Scenario-Specific Models. *IEEE Transactions on Intelligent Transportation Systems*, 15(4), 2014.

[2] Oliver Chapelle et al. *Semi-Supervised Learning*. The MIT Press, 2006.

[3] Usama M. Fayyad and Keki B. Irani. Multi-Interval Discretization of Continuous-Valued Attributes for Classification Learning. 2013.

[4] Daphne Koller and Nir Friedman. *Probabilistic Graphical Models: Principles and Techniques*. The MIT Press, 2009.

[5] P. Kumar et al. Learning-based approach for online lane change intention prediction. *IEEE Intelligent Vehicles Symposium*, 2013.

[6] Kevin Murphy. *Machine Learning – A Probabilistic Perspective*. The MIT Press, 2012.

[7] Tobias Rehder et al. (German) Effektive Nutzung von hochdimensionalen kontinuierlichen Umfelddaten zur Prädiktion von Fahrverhalten mit Bayesschen Netzen. *Automatisierungssysteme, Assistenzsysteme und eingebettete Systeme für Transportmittel*, 2015.

[8] Tobias Rehder et al. Learning Lane Change Intentions through Lane Contentedness Estimation from Demonstrated Driving. *IEEE 19th International Conference on Intelligent Transportation Systems*, 2016.

[9] Julian Schlechtriemen et al. When will it change the lane? A probabilistic regression approach for rarely occurring events. *IEEE Intelligent Vehicle Symposium*, 2015.

[10] Bur Settles. Active Learning Literature Survey. Technical report, University of Wisconsin-Madison, 2009.

[11] Bowen Song et al. ROC operating point selection for classification of imbalanced data with application to computer-aided polyp detection in CT colonography. *International Journal of Computer Assisted Radiology and Surgery*, 9, January 2014.

Advanced Vehicle Control – Edelmann, Plöchl & Pfeffer (Eds)
© 2017 Taylor & Francis Group, London, ISBN 978-1-138-02992-7

Driving behavior modeling for avoidance of road rushing out pedestrians in non-intersection areas

H. Imanaga, R. Iwaki, I. Yamaguchi & N. Uchida
Japan Automobile Research Institute (JARI), Tsukuba, Japan

ABSTRACT: This study aims at modeling avoidance maneuvers for rushing out pedestrians in non-intersection areas. Avoidance maneuvers are foot moving speed from the gas pedal to the brake pedal, considering time to collision when releasing the gas pedal, deceleration waveform considering time to collision and driving speed at starting braking. Modeling data are measured by experiments reconstructing a typical pedestrian rushing out scene from behind a parked vehicle, using the JARI-ARV which can superimpose computer graphic pedestrians or vehicles to the landscape displayed in front of the real vehicle. The subjects of the experiments are 109 drivers. The input of the model is gas pedal releasing timing (substitution of pedestrian perception). On the other hand, the output is remaining distance to the collision point of the pedestrian. The model we developed can be used as an evaluation tool for checking driver performance for avoidance maneuvers by braking.

1 INTRODUCTION

The number of traffic accident fatalities dropped below 5,000 in 2010 in Japan. However, the rate of decrease is slowing. The number of fatalities in 2015 was 4,117 which was 3 more fatalities than in 2014. Focusing on fatal accidents, car to pedestrian cases are still a major pattern in Japan. According to a Japanese police report in 2014, these accidents comprise 36.4% of all of fatal accidents. Especially, cases of pedestrian rush out account for 24.6% of fatalities. In more than 80% of cases, the maneuver of the car is 'go straight'.

Preventing the occurrence of human errors is important to reduce these accidents. According to Treat et al., 1979, more than 90% of accidents occurred because of human errors. For accident mechanism analysis of active safety, it is important to elucidate driver's behaviors in accident situations, continuously. In other words, it is important to find driver behavior parameters dominating the occurrence of accidents and to use modeling for driver behavior.

The objective of this study is to make a driver behavior model in the situation of encountering a rush out pedestrian in non-intersection areas. As a first step, modeling behavior area confines deceleration maneuvers to braking from perceiving the rush out pedestrian to stopping by braking.

2 MODELING BEHAVIOR OF AVOIDANCE MANEUVERS FOR RUSHING OUT PEDESTRIANS

The avoidance maneuvers for rushing out pedestrians are simplified and shown in Figure 1. The event starts when a pedestrian rushes out. The driver perceives the pedestrian, and starts avoidance maneuvers. The first action is gas pedal release. Next, the driver tries to start braking. Finally, the vehicle stops.

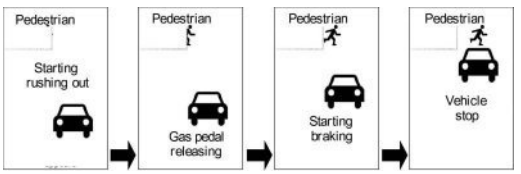


Figure 1. Depiction of braking avoidance behavior for a rush out pedestrian.

In this study, driver behavior when a driver encounters a rushing out pedestrian is split into four phases as shown in Table 1. The 'pedestrian perception' phase is from the pedestrian starting rushing out to the driver perceiving the pedestrian. However, as it is difficult to observe the timing of perception, gas pedal release timing is used as a substitution of perception timing. Next is the 'foot moving' phase. This is from the release of the gas pedal to starting braking. Third is the 'start braking' phase, which is from starting braking to reaching peak deceleration. Finally, the 'keep braking' phase, which is from peak deceleration to the vehicle stopping. In the modeling, the four phases are numerically expressed, respectively.

3 SCENE RECONSTRUCTION APPARATUS

The data for modeling are measured by subjects driving a pedestrian rushing out scene as reconstructed in the experiments. The reconstruction apparatus is

Table 1. Avoidance maneuvers phases for rushing out pedestrians.

Phase	Term of each phases
Pedestrian perception	From the pedestrian starting rushing out to the driver perceiving the pedestrian
Foot moving	From the driver releasing the gas pedal to pressing the brake pedal
Start deceleration	From starting braking to reaching maximum deceleration
Keep deceleration	After reaching maximum deceleration until vehicle stopping



Figure 2. JARI-ARV for scene reconstruction apparatus.



Figure 3. Superimposed CG objects on the real-time frontal viewing screen.

the JARI-ARV, shown in Figure 2. The base of the JARI-ARV is a station wagon type vehicle (the total engine displacement is 2.45[L]). There are three displays and cameras in front of the front screen for capturing the front view in real-time. Additionally, traffic participants such as pedestrians, bicycles, or cars are superimposed to the front displays' landscape as computer graphics using augmented reality technology shown in Figure 3.

This apparatus takes advantage of the merits of both a driving simulator and real vehicle in one experiment. It allows reconstruction of risky traffic situations safely, and controls various parameters such as rush out timing in the experiments as can be done with a driving simulator. On the other hand, a driver feels almost the same sense as when driving a real vehicle.

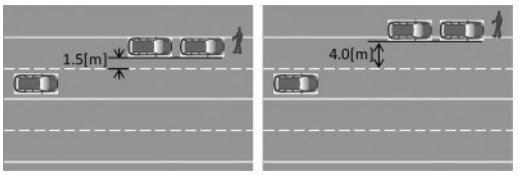


Figure 4. Reconstructing the pedestrian rushing out scene.

4 EXPERIMENT

4.1 *Reconstructing a scene of a pedestrian rushing out*

In the reconstructed scene, a pedestrian rushes out from behind a parked vehicle on the left side in a non-intersection area, shown in Figure 4. This is a typical scene of encountering a rushing out pedestrian, chosen by drive video recorder analysis in Japan (Kawakoshi et al., 2012). In this study, about 50% of rush out pedestrians come from behind a visual obstruction. Furthermore, about 70% of visual obstructions are traffic participants such as a parked vehicle.

The experimental control conditions are lateral distance, enlightened driving speed, and starting rushing out timing.

- Lateral distance to the parked vehicle is 1.5 or 4.0 [m]
- Enlightened driving speed for the subjects as drivers is 30, 40 or 50 [km/h]
- The pedestrian starting rushing out timing is 2.0, 3.5 or 5.0 [sec]

The rushing out timing is expected time to reach the pedestrian. It is equal to Time to Collision (TTC). Actual timing of starting rushing out is defined by the distance to the pedestrian calculated by TTC per enlightened speed (e.g. In the case the enlightened speed is 40[km/h] and TTC is 2.0 [sec], the pedestrian starts when the driver reaches 22.2 [m](=40 [km/h]*2.0 [sec]) from the pedestrian). The pedestrian's walking speed is calculated by lateral distance and this TTC.

4.2 *Driving course in the experiment*

The experiments were performed in the JARI test course (urban area type), shown in Figure 5. Each subject driver circled around the course seven times (Table 2). The subjects were split into 12 groups. These groups had each experimental condition (TTC: 2.0 or 3.5 [sec], enlightened driving speed: 30, 40 or 50 [km/h], lateral distance: 1.5 or 4.0 [m]).

The first circle is a warm-up period for settling into driving the JARI-ARV. The second to fourth circles are a cover story in which subjects do not experience a critical event. Each subject was ordered to drive 30, 40 and 50 [km/h] when beside the parked vehicle shown in Figure 4. In these circles, there was no rushing out pedestrian. In Circle Five, each subject drove their group's enlightened driving speed and encountered a

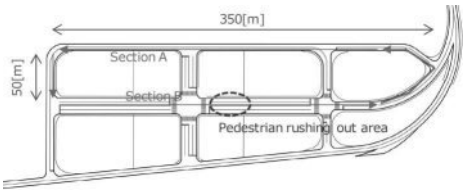


Figure 5. Driving course in the experiment.

Table 2. Contents of each circle.

Circle No.	Running content
1	Training (No CG participants)
2	Keep velocity of 30[km/h] (cover story)
3	Keep velocity of 40[km/h] (cover story)
4	Keep velocity of 50[km/h] (cover story)
5	Pedestrian rushing out (TTC: short)
6	Pedestrian rushing out (TTC: long)

rushing out pedestrian with their encountering timing (TTC: 2.0 or 3.5 [sec]). Circle Six is the same conditions as Circle Five except the encountering timing, which is 5.0 [sec] of TTC.

The subject drivers learned the enlightened driving speed by following a leading vehicle in Section A before driving in Section B. In the experiment, as a cover story, the objective of the experiment was observing if the subjects kept the enlightened driving speed without a leading vehicle in the Section B area.

4.3 *Subjects of the experiment*

The subjects were selected considering sex (male or female) and age group (20–29, 30–39, 40–49 or 50–59). They were not pro-drivers, but do usually drive. The total number of drivers was 109 persons. Each experiment group (different experimental conditions) had eight to ten subjects with different sex and age group combinations.

5 THE RESULTS OF THE EXPERIMENT

5.1 *Rate of crashing into the rushing out pedestrian*

The rates of crashing into the rushing out pedestrian are shown in Table 3. Total data is 199 cases (each subject drives TTC 2.0 or 3.5 [sec] and 5.0 [sec]). 87.9% of the cases (175 cases) successfully avoid a crash. According to rushing out timing, the rates of 2.0, 3.5 or 5.0 [sec] are 50.0, 94.1, and 100.0 percent, respectively.

5.2 *Behavioral characteristics of avoidance maneuvers*

5.2.1 *Timing of gas pedal release*

Figure 6 shows the time length from starting rushing out to gas pedal release by experiment conditions (enlightened driving speed and rushing out timing). Rushing out timing affects release timing. In the case rushing out timing is 2.0 [sec], drivers take avoidance maneuvers quickly compared to other conditions. If a driver did not feel enough avoidance time, they would rapidly take avoidance action after pedestrian perception. There was not a clear trend for the lateral distance condition.

Table 3. Result of deceleration avoidance.

Conditions		No. of subjects: Total	No. of subjects: Successful avoidance	Successful avoidance rate
All		199	175	87.9%
Lateral distance [m]	1.5	94	81	86.2%
	4.0	105	94	89.5%
Enlightened velocity [km/h]	30	59	55	93.2%
	40	72	61	84.7%
	50	68	59	86.8%
Rushing out timing [sec]	2.0	42	21	50.0%
	3.5	51	48	94.1%
	5.0	106	106	100.0%

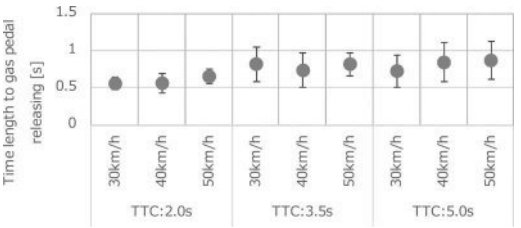


Figure 6. Time length to gas pedal releasing.

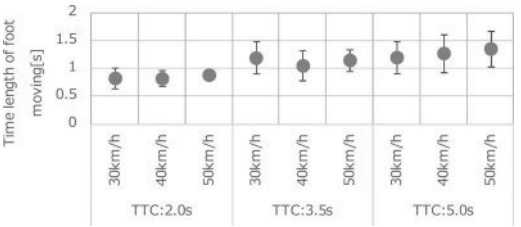


Figure 7. Time length of foot moving.

5.2.2 *Time length of foot moving*

Figure 7 shows foot moving time length from gas pedal to brake pedal. The same trends as in the case of timing of gas pedal release can be seen in this phase.

5.2.3 *Strength of braking*

Figure 8 shows maximum deceleration by braking. These are strongly affected by rushing out timing and enlightened driving speed. In cases of less time for avoidance (it is related to rushing out timing), a driver had to brake strongly. On the other hand, enlightened driving speed also affects the degree of deceleration. If a vehicle will stop in the unit distance, the degree of deceleration is proportional to the driving speed.

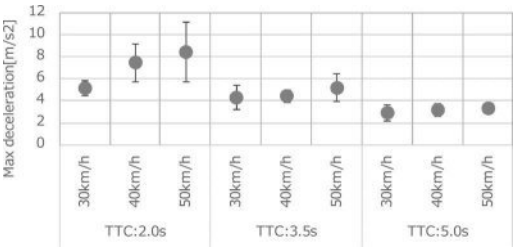


Figure 8. Maximum deceleration.

Enlightened driving speed is proportional to the actual driving speed. Thus, these trends are quite reasonable.

5.3 *Trend of avoidance maneuvers*

There are two major trends identified in this analysis. Firstly, the degree of time length tightness to starting braking maneuver expressed as TTC when perceiving a rushing out pedestrian affects the speed of gas pedal release or starting braking.

Secondly, the degree of braking deceleration is affected by the TTC and the driving speed at starting braking.

6 AVOIDANCE MANEUVER MODELING

6.1 *Model structure*

As shown in Chapter Five, drivers take avoidance maneuvers considering their driving situation such as their driving speed or encountering timing of a rushing out pedestrian. Here, we develop a model of typical avoidance maneuvers with braking.

The model structure is shown in Figure 9. The input of the model is Time to collision (TTC) and the driving speed when the driver releases the gas pedal. This is a substitution of the TTC of perception timing when a pedestrian starts rushing out (this is difficult to observe). On the other hand, the output is remaining distance to the pedestrian when the vehicle stops because of an avoidance maneuver.

Firstly, start braking timing expressed by TTC is estimated from the gas pedal release timing, in the model. Next, the deceleration waveform from start braking to vehicle stopping is estimated by the TTC of starting braking and the driving speed at this timing. Then the remaining distance to the rushing out pedestrian is estimated.

6.2 *Data for modeling*

Before modeling, data of each subject is split into three groups, 'fail to avoid', 'successful avoidance using steering maneuver', 'successful avoidance using braking maneuver', respectively. The data of 'fail to avoid' and 'successful avoidance' using steering maneuver data are not used for modeling, because the aim of the model is modeling braking avoidance maneuvers

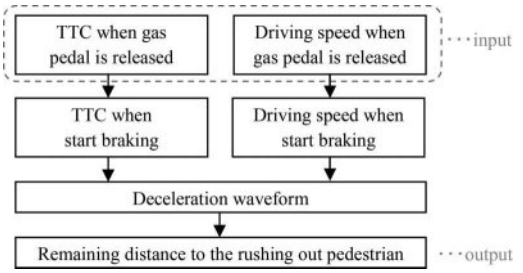


Figure 9. Model structure.

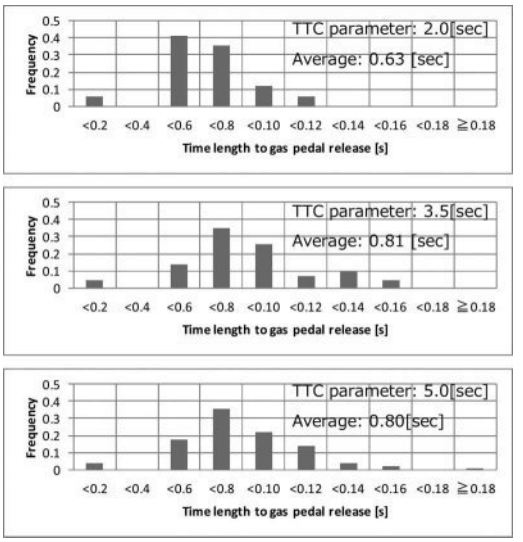


Figure 10. Time length distribution for releasing the gas pedal.

that allow avoiding a collision with a rushing out pedestrian.

6.3 *Modeling of each phase*

6.3.1 *Timing of the gas pedal release*

In the model, timing of the gas pedal release is used as the input parameter as the TTC of gas pedal release calculated by the driving speed and remaining distance at this time.

Figure 10 shows the distribution time length from the pedestrian starting rushing out to the driver releasing the gas pedal. In the case the experimental condition of rushing out timing was 2.0 [sec], most of the subjects needed 0.4 to 0.6 [sec] to release the gas pedal. On the other hand, when timing conditions were 3.5 or 5.0 [sec], most of them needed 0.6 to 0.8 [sec] to release. In these cases, the subjects had much more leeway for taking avoidance maneuvers.

6.3.2 *Time length of foot moving*

Figure 11 shows the relationship between TTC at gas pedal release and time length from gas pedal release to start braking. A linear relationship can be seen between

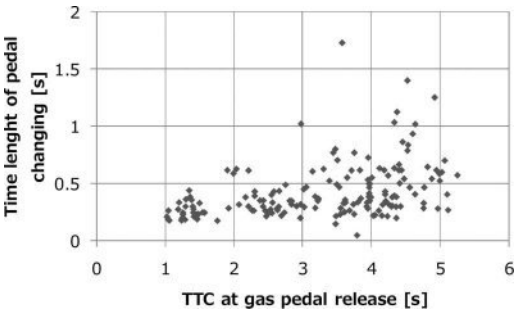


Figure 11. Relationship between gas pedal release and start braking.

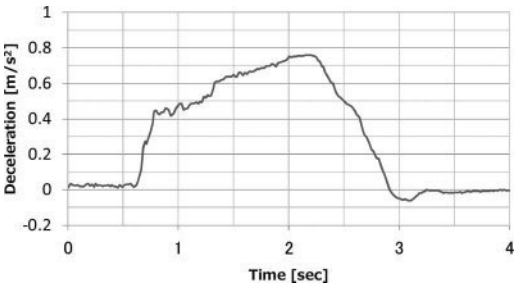


Figure 12. Typical deceleration waveform.

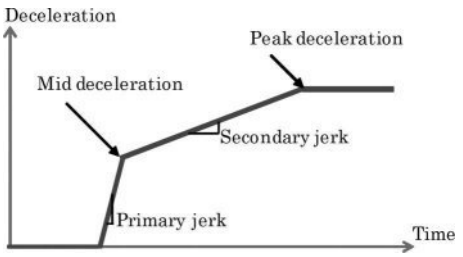


Figure 13. Assumed deceleration waveform.

the two variables. Model function is estimated using regression analysis as equation (1).

$$T_{cng} = 0.124 \cdot TTC_{gOFF} \quad (R^2 = 0.78) \quad (1)$$
$$(24.1)$$

where, T_{cng} denotes time length from gas pedal release to starting braking [sec], and TTC_{gOFF} denotes TTC at starting braking [sec]. The number in a bracket under the parameter of regression function denotes the t-value of each parameter.

6.3.3 *Deceleration waveform*

Figure 12 shows a typical deceleration waveform of braking using the JARI-ARV. In the modeling of deceleration waveform, the shape shown in Figure 13 is assumed.

In this assumed waveform, the value of mid and peak deceleration and time length from starting braking to mid and peak deceleration have to be estimated.

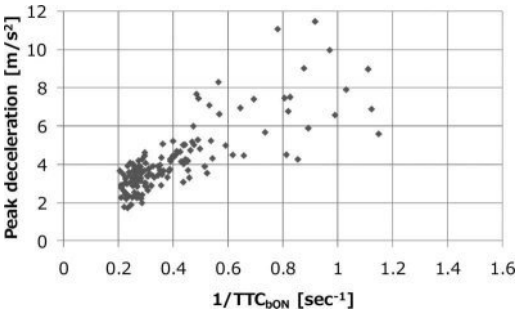


Figure 14. Relationship between TTC at starting braking and peak deceleration.

Fig. 14 shows the relationship between TTC at starting braking and peak deceleration. In the figure, the TTC are expressed as an inverse number. The figure shows a linear relationship between the two variables. Equation (2) is a estimated function.

$$D_{max} = 6.82 \cdot TTC_{bON}^{-1} + 0.288 \cdot V_{ped} - 2.11 \quad (R^2 = 0.78) \quad (2)$$
$$(17.2) \qquad (5.61) \qquad (-3.30)$$

where, D_{max} denotes peak deceleration [m/s^2], TTC_{bON} denotes TTC at starting braking [sec], and V_{ped} denotes actual driving speed at starting braking [m/s]. Other variables of identifying the shape of deceleration waveform are estimated as equation (3), (4), and (5).

$$J_s = 0.314 \cdot D_{max} \quad (R^2 = 0.83) \quad (3)$$
$$(22.4)$$

$$D_{mid} = 0.565 \cdot D_{max} \quad (R^2 = 0.93) \quad (4)$$
$$(38.0)$$

$$J_p = 6.42 \cdot D_{mid} - 4.63 \quad (R^2 = 0.765) \quad (5)$$
$$(18.4) \qquad (-4.98)$$

where, D_{mid} denotes mid deceleration [m/s^2], J_p denotes primary jerk [m/s^3], J_s denotes secondary jerk [m/s^3].

In the model, it is assumed that the maximum deceleration is kept after reaching maximum deceleration.

6.4 *Validation of the whole model*

Figure 15 shows a validation of this model. The vertical axis denotes actual remaining distance in the experiment. The horizontal axis denotes estimated remaining distance calculated by the model. There are data in which the subjects did not stop. In these cases the subjects had enough time for the pedestrian to pass the collision zone.

In the case of severe situations that have not so much remaining distance (shown in the lower left side of the figure), the model estimate is much more severe than the actual distance. Thus, this model prevents misjudgment of bad results (the model says a maneuver can avoid a crash, however the maneuver actually cannot avoid it).

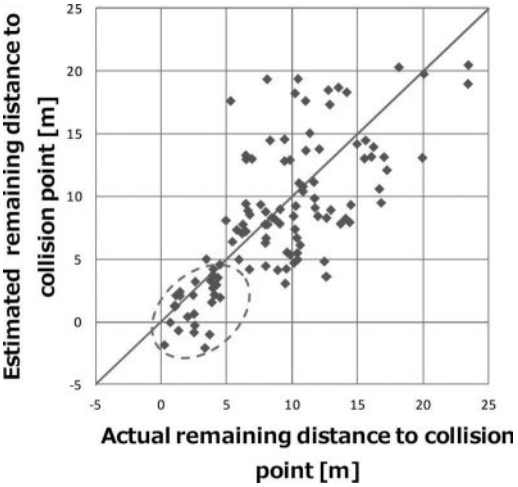


Figure 15. Model validation.

*The numbers are the remaining distance to the rushing out pedestrian when the vehicle stops, considering pedal release timing and driving speed

Remaining time when driver releases gas pedal [sec]	Driving speed when staring braking[km/s]						
	30	35	40	45	50	55	60
1.9	2.6	2.5	2.2	1.9	1.5	1.1	0.7
1.85	2.5	2.3	2.0	1.6	1.2	0.8	0.3
1.8	2.4	2.1	1.8	1.4	0.9	0.5	-0.0
1.75	2.2	1.9	1.6	1.1	0.7	0.2	-0.4
1.7	2.1	1.7	1.4	0.9	0.4	-0.2	-0.8
1.65	1.9	1.6	1.2	0.7	0.1	-0.5	-1.1
1.6	1.8	1.4	1.0	0.4	-0.2	-0.8	-1.4
1.55	1.7	1.3	0.8	0.2	-0.4	-1.1	-1.8
1.5	1.5	1.1	0.6	-0.0	-0.7	-1.4	-2.1
1.45	1.4	0.9	0.4	-0.2	-0.9	-1.6	-2.4
1.4	1.2	0.8	0.2	-0.4	-1.1	-1.9	-2.7
1.35	1.1	0.6	0.0	-0.6	-1.4	-2.2	-3.0
1.3	1.0	0.5	-0.1	-0.8	-1.6	-2.4	-3.3
1.25	0.9	0.3	-0.3	-1.0	-1.8	-2.6	-3.5
1.2	0.7	0.2	-0.5	-1.2	-2.0	-2.9	-3.8
1.15	0.6	0.1	-0.6	-1	Crashing condition		0
1.1	0.5	-0.1	-0.8	-1.5	-2.4	-3.3	-4.2
1.05	0.4	-0.2	-0.9	-1.7	-2.5	-3.5	-4.5
1	0.3	-0.3	-1.0	-1.8	-2.7	-3.6	-4.6

Figure 16. Model application examples for prediction of remaining distance of vehicle stopping.

6.5 *Model application*

Figure 16 shows estimated remaining distance to the rushing out pedestrian when the vehicle stops. In this simulation, the pedestrian starts rushing out at the timing of TTC 2.0 [sec]. The remaining distance is estimated in the various conditions of driving speed and pedestrian perception timing (gas pedal releasing). This model expresses driver performance of avoidance maneuver by braking. This model can be used in various fundamental discussions about active safety device, for example, "What is the threshold to braking that a device can have instead of a driver?"

7 CONCLUSION

This paper provides an avoidance maneuver model in the case of encountering a rushing out pedestrian, from behind a parked vehicle as visual obstruction, in a non-intersection area. It considers maneuvers in four phases: pedestrian perception, foot moving, start braking, and keep braking. One possible application for using the model as an active safety device developing tool, considering the threshold that a driver cannot avoid the crash, is introduced.

In future, we must continue to improve the model. The first task is modeling of pedestrian perception timing. The present model inputs the pedestrian perception timing (actually, gas pedal releasing timing). However, it is better to estimate this from driving behavior such as gaze allocation or braking preparation, which can be observed before a pedestrian starts rushing out. The second task is model translation to other vehicles. Each vehicle has their own characteristics of braking. Thus, conditions may be different from the JARI-ARV's braking.

ACKNOWLEDGEMENTS

This research was supported by the developing and demonstrating project of the Enhanced driving assistance system at next generation sponsored by Ministry of Economy, Trade and Industry, Japan.

REFERENCES

Iwaki, R., Wakasugi, T., Morales Teraoka, E.Y., Tanaka, S., & Uchida, N. 2013 Analysis of Driver Response to Road Crossing pedestrian, JSAE proceedings, No. 146-13, 1–7

Iwaki, R., Sato, K., Wakasugi. T., & Uchida, N. 2015 Analysis and Modeling of Driver behavior on Pedestrian Crossing Road Situation (1st report: Modeling of driver's response), 3rd International Symposium on Future Active Safety Technology Toward zero traffic accidents (FAST-zero' 15)

Iwaki, R., Imanaga, H., Yamaguchi, I. & Uchida, N. 2015 Driving Behavior for Avoiding Road Crossing Pedestrian at Non-Intersection Area (First report), JSAE proceedings, No. 35-15A, 822–827

Imanaga, H., Iwaki, R., Yamaguchi, I. & Uchida, N. 2015 Driving Behavior for Avoiding Road Crossing Pedestrian at Non-Intersection Area (Second report), JSAE proceedings, No. 35-15A, 828–833

Kawakoshi, M, Uchida, N., Mochida, T., & Bargman, J. 2012 Analysis of contributing factors in car-pedestrian accidents using incident video recording data JSAE proceedings, No. 57-12, 1–4

Treat, J. R., Tumbas, N. S., McDonald, S. T., Shinar, D., Hume, R. D., Mayer, R. E., Stansifer, R. L., & Castellan, N. J. 1979. Tri-level study of the causes of traffic accidents: final report Volume1: Causal Factor Tabulations and Assessments, Report No. DOT-HS-805085

Advanced Vehicle Control – Edelmann, Plöchl & Pfeffer (Eds)
© 2017 Taylor & Francis Group, London, ISBN 978-1-138-02992-7

Modelling the effect of sensory dynamics on a driver's control of a nonlinear vehicle

C.J. Nash & D. Cole
Department of Engineering, University of Cambridge, UK

ABSTRACT: In previous work a linear model of driver steering control was developed which takes account of human sensory dynamics and limitations. In this paper various approaches to modelling a driver's control of a nonlinear vehicle are compared. In contrast to research focussed on modelling the optimal driver, the aim of this work is to develop a realistic model of driver steering behaviour. Simulations were run to compare various nonlinear state estimators and controllers. In general a trade-off was found between simulation time, which could also represent mental load, and controller performance. Experiments are planned to compare the results of these simulations against measured steering behaviour from human drivers.

1 INTRODUCTION

With the growing popularity of active vehicle control systems it is increasingly important to understand how a driver controls a vehicle. Various different approaches have been taken to modelling this control task, with many recent studies following a receding-horizon optimal control scheme (Cole et al. 2006). However, there is a lack of research into how the dynamics and limitations of drivers' sensory systems affect perception and control during driving. A review of the literature showed that control tasks carried out by humans are affected by characteristics of sensory systems such as delays, thresholds and frequency responses (Nash et al. 2016).

In our previous work a new model of driver steering control was developed incorporating models of human sensory dynamics, based on receding-horizon optimal control and assuming optimal integration of multiple noisy sensory measurements. The model was validated using published results from a control task carried out by pilots in a flight simulator (Zaal et al. 2009), and was found to fit these results well (Nash and Cole 2016a). Similar experiments involving a vehicle steering task were designed and carried out by drivers, and an identification procedure was used to find parameter values for the model to fit the results (Nash and Cole 2016b). The model was found to fit the results well, and parameter values were found to be realistic when compared with sensory measurements reported in the literature (Nash et al. 2016).

The new driver model was derived for a linear vehicle, however in more extreme manoeuvres the vehicle may operate near the friction limit of the tyres and the operating point of the vehicle may vary rapidly. It is therefore necessary to develop a model which can describe a driver's control of nonlinear vehicle dynamics. Previous research in this area has generally focussed on modelling the optimal driver, with full state feedback and no sensory dynamics, delays or noise (Ungoren and Peng 2005, Thommyppillai et al. 2009, Keen and Cole 2011). The aim of this work is to find suitable controllers and state estimators for a more realistic nonlinear driver model that takes account of the limitations of a human driver.

2 DRIVER MODEL STRUCTURE

The structure of the new driver model is shown in Figure 1 (Nash and Cole 2016b). Currently it is assumed that the vehicle is travelling at constant speed; longitudinal control will be considered in future work. The driver controls a plant which combines the vehicle dynamics with the driver's sensory and neuromuscular dynamics, in order to follow a target path while compensating for disturbances on the vehicle. A state estimator is used to calculate an estimate of the plant states based on the driver's noisy sensory measurements.

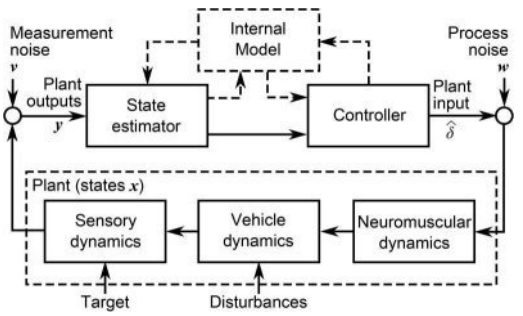


Figure 1. Structure of new driver model.

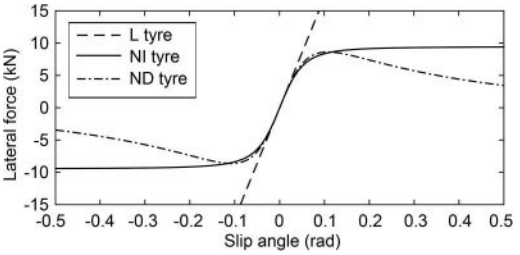


Figure 2. Nonlinear tyre characteristics. Vertical force is 9.5 kN.

A controller calculates an optimal plant input $\hat{\delta}$ to minimise a cost function J, weighting the plant input against path-following error e:

$$J = \sum_{k=1}^{\infty} \left(e(k)^2 + q_\delta \hat{\delta}(k)^2 \right) \tag{1}$$

Both the controller and the state estimator make use of an internal model of the plant to predict future trajectories of the plant states. The internal model may not fully match the true system dynamics, with its accuracy likely to be dependent on driver experience (Keen and Cole 2011).

2.1 *Sensory and neuromuscular dynamics*

Previous studies have investigated drivers' neuromuscular dynamics in detail (Pick and Cole 2007), however for simplicity a second-order transfer function is used in this model. Models of the driver's sensory dynamics were chosen based on results from the literature (Nash et al. 2016). The driver's visual system is represented as a measurement of the lateral path-following error plus a 'preview' of the upcoming road path. Models of the driver's vestibular system are also included, using transfer functions to represent the otoliths, which measure acceleration, and semi-circular canals, which measure angular velocity. Each of the sensory systems also contains a time delay and sensory noise, arising from the physical properties of the human neurosensory system.

3 NONLINEAR VEHICLE SIMULATIONS

Simulations were run using the driver model to control a nonlinear vehicle. The basic equations of motion for the vehicle were based on the single-track model described in (Nash and Cole 2016b), travelling at a constant speed of 40 m/s. Two different vehicles were simulated, one with understeering characteristics and one with oversteering characteristics. This was achieved by varying the balance of the vertical loads between the front and rear tyres. The loads on the front (F_{zf}) and rear (F_{zr}) tyres were 9.5 kN and 15 kN for the understeering vehicle, and 12kN and 13kN for the oversteering vehicle. Nonlinear tyres were included with lateral characteristics described by the 'magic formula' (Pacejka and Bakker 1992). Three different tyres were simulated: a linear tyre (L), a nonlinear tyre with force monotonically increasing as a function of slip angle (NI), and a nonlinear tyre with force decreasing past the friction limit (ND). The force-slip characteristics of these three tyres are shown in Figure 2, and the nonlinear tyre parameters are given in Table 1. All three tyres have the same cornering stiffness at zero slip angle ($C_f/F_{zf} = C_r/F_{zr} = 18$ rad^{-1}).

Table 1. Nonlinear tyre parameters.

Tyre	B	C	D	E
Nonlinear increasing (NI)	12	1.5	1	1
Nonlinear decreasing (ND)	9	2.2	0.909	0.5

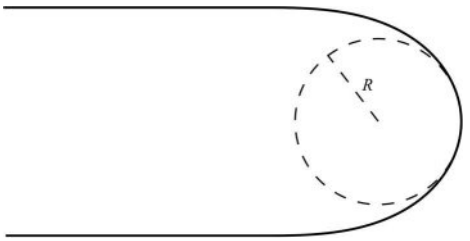


Figure 3. Target path used in simulations.

The target used for the simulations was a 180° clothoid corner as shown in Figure 3, with the minimum radius R varied to change the operating point of the tyres and the difficulty of the path-following task. Simulations were run with and without measurement and process noise, and also with and without an impulse disturbance added in mid-corner to model a wind gust or bump in the road. Experiments are planned using a driving simulator to test human drivers under similar conditions to these simulations.

4 CONTROLLERS AND STATE ESTIMATORS

Various controllers and state estimators were implemented, varying in their complexity to represent different assumptions about the driver's internal model. Optimal control of a nonlinear plant is a difficult task, which can be simplified through linearisation or transformation of the system dynamics. It is hypothesised that drivers may carry out similar simplifications to reduce their mental load.

The nonlinear plant equations can be written in discrete time state-space form:

$$\begin{aligned} \boldsymbol{x}(k+1) &= f(\boldsymbol{x}(k)) + \mathbf{B}\hat{\delta}(k) + \mathbf{G}\boldsymbol{w}(k) \\ \boldsymbol{y}(k) &= \mathbf{C}\boldsymbol{x}(k) + \boldsymbol{v}(k) \end{aligned} \tag{2}$$

where $\boldsymbol{x}$ is the plant states, $\boldsymbol{y}$ is the plant outputs, $\hat{\delta}$ is the plant input, $\boldsymbol{w}$ is the process noise (including white

noise representations of the target and disturbances) and $\boldsymbol{v}$ is the measurement noise. The equations can be linearised about states $\boldsymbol{x}_{\mathrm{L}}$ with the approximation:

$$f(\boldsymbol{x}(k)) \approx \mathbf{A}_{\mathrm{L}}\boldsymbol{x}(k) = \left.\frac{\mathrm{d}f}{\mathrm{d}\boldsymbol{x}}\right|_{\boldsymbol{x}=\boldsymbol{x}_{\mathrm{L}}} \boldsymbol{x}(k) \tag{3}$$

Five different model predictive controllers were implemented, with varying levels of approximation to the nonlinear plant dynamics. These were:

- L0: Linearisation about zero slip angle, $\boldsymbol{x}_{\mathrm{L}} = \mathbf{0}$. A time-invariant controller is derived as for the linear driver model (Nash and Cole 2016b).
- LP0: Linearisation about the initial state $\boldsymbol{x}_0$ of the prediction interval. A new control sequence is calculated at each time step using the MPC derivation presented by Cole et al. (2006), with a constant $\mathbf{A}_{\mathrm{L}}$ linearised about $\boldsymbol{x}_{\mathrm{L}} = \boldsymbol{x}_0$.
- LPF: Linearisation about each state of the prediction interval. The solution starts from a nominal state trajectory $\mathbf{X}_0 = \boldsymbol{x}_0, \ldots, \boldsymbol{x}_{N_p}$, which is the previous optimal sequence shifted by one time step. The linearised matrix $\mathbf{A}_{\mathrm{L}}$ is calculated about each nominal state $\boldsymbol{x}_{\mathrm{L}} = \boldsymbol{x}_n$, and used in an adapted form of the linear MPC derivation in a similar way to Keen and Cole (2011).
- LPF*: LPF constrained to stop the slip angles exceeding 0.107 rad, with a cost on the change in control sequence from the nominal trajectory.
- FNO: Full nonlinear optimisation. The full nonlinear equations are used to predict the plant trajectory over the prediction interval. The Matlab optimisation function *fminunc* is used to find an optimal control sequence at each time step.

Four variations on a Kalman filter were implemented as state estimators and compared with full state feedback. The implementations were all provided by the EKF/UKF Matlab toolbox (Hartikainen et al. 2011), and are based around different approximations to the true nonlinear plant dynamics:

- FSF: Full state feedback: The state estimate is exactly the same as the real states. This removes the effects of sensory dynamics.
- LKF: Linear Kalman filter: A time-invariant Kalman filter is found by linearising the plant states about zero slip angle.
- EKF1: First order extended Kalman filter. A linearised approximation to the plant states is found at each time step.
- EKF2: Second order extended Kalman filter. A quadratic approximation to the plant states is found at each time step.
- UKF: Unscented Kalman filter. The nonlinear plant equations are approximated at each time step using an unscented transform.

5 RESULTS

Two main outcomes of the simulations were analysed: the time taken to run each simulation and the extent to which each combination of controller and state estimator was able to minimise the cost function.

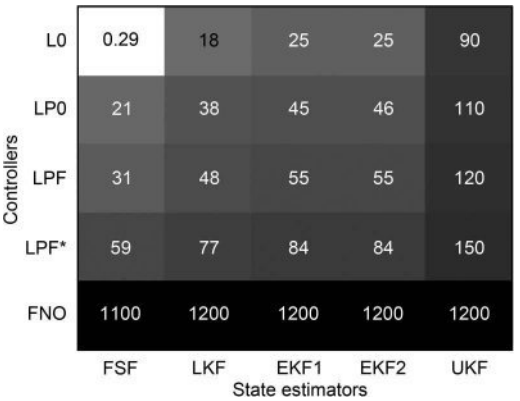


Figure 4. Average time taken (s) for simulation to run using each combination of controller and state estimator.

5.1 *Simulation time*

The computational efficiency of each model may be considered as a measure of the mental load on the driver, assuming they are making similar computations. It also affects the practicality of the model for use in engineering applications. The average time taken for simulating each combination of controller and state estimator is shown in Figure 4. There are significant differences between the simulation times, with the times increasing with the accuracy of the approximation to the nonlinear plant. This could reflect the trade-off the driver must make between accuracy and mental load.

5.2 *Controller performance*

The performance of each combination of state estimator and controller can be evaluated by finding the total value of the controller cost function over each simulation. The best performance does not necessarily imply the most realistic, as drivers may carry out sub-optimal control. However this comparison allows the different methods to be compared as a precursor to finding the best fit to experimental results.

The controllers all performed similarly for the linear tyre. A comparison of the different controllers for the nonlinear tyres (with no disturbance or noise) is shown in Figure 5. The cost has been normalised by the cost using the FNO controller. The FNO controller therefore always has a normalised cost of 1, so it can be seen from Figure 5 that FNO was the best performing controller in all cases. For the understeering vehicle with NI tyres the controller performance generally increased with the accuracy of the approximation to the nonlinear dynamics, although LP0 performed better than LPF. However, the modifications carried out for LPF* resulted in a performance as good as FNO. The results for the oversteering NI vehicle are similar,

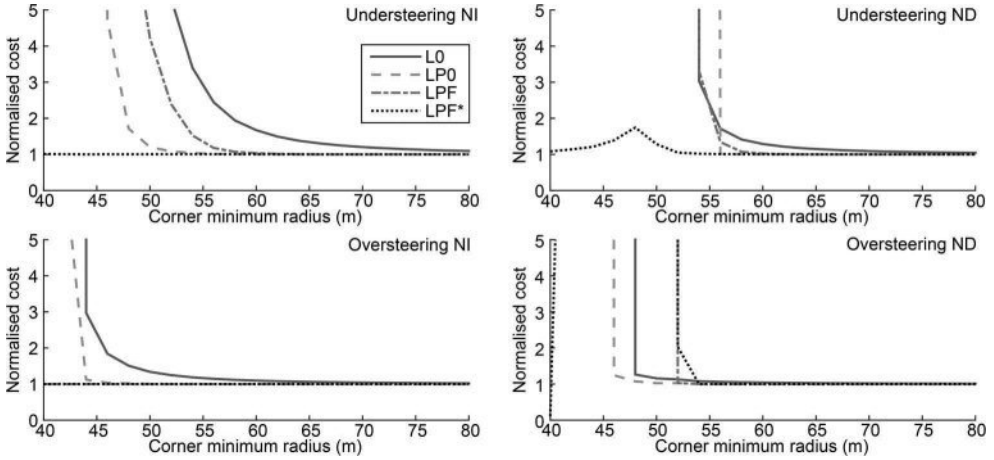


Figure 5. Comparison of the performance of each controller for simulations without added disturbances or noise and with FSF. The total value of the cost function over each simulation has been normalised by the value found for the FNO controller.

however controller LPF performed as well as LPF* and FNO. This may be because the oversteering vehicle becomes unstable before the tyre force saturates, so the constraints on slip angle are not necessary.

For the ND tyre, the linearised controllers were unable to control the vehicle once the tyre operating point moved beyond the force peak. Adding constraints to prevent this (LPF*) was successful for the understeering vehicle, however LPF* still did not perform as well as FNO for some of the corners. It may be possible to improve the performance of LPF* by tuning the additional cost. For the oversteering vehicle with ND tyres, even controller LPF* was unable to control the vehicle at lower radii, except for the corner with radius 40 m where LPF* outperformed FNO.

The performance of the different controllers with an added disturbance but no noise was qualitatively very similar to the results shown in Figure 5, although with larger overall costs. In some cases controllers LP0 and LPF* performed slightly better than FNO. For a linear plant with white noise disturbances an MPC controller will give an optimal performance, however this is not guaranteed with a nonlinear plant or transient disturbances. Therefore FNO is not guaranteed to be the best controller with disturbances.

5.3 *State estimator performance*

The performance of the state estimators across the different simulations was also compared. In general there was less variation in performance than for the controllers. With no disturbance or noise and with linear tyres, all state estimators performed similarly. For the nonlinear tyres, LKF was not able to give an accurate state estimate, resulting in a higher total cost. However, for the understeering vehicle all the nonlinear state estimators were found to perform similarly, and as well as FSF. The same was seen for the oversteering vehicle with NI tyres, however the performance

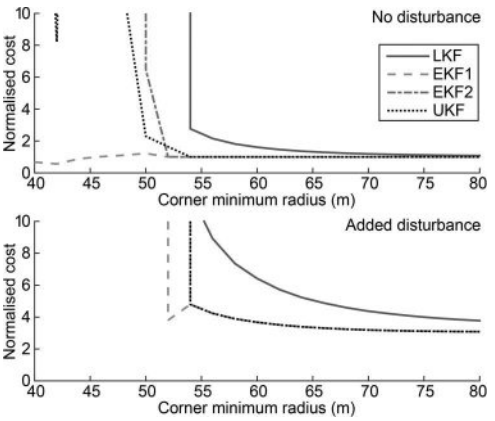


Figure 6. Comparison of the performance of each state estimator for simulations using the oversteering vehicle with ND tyres, no noise and FNO. The total value of the cost function over each simulation has been normalised by the value found with FSF.

of the nonlinear state estimators did differ for the oversteering vehicle with ND tyres.

With an added disturbance, the state estimators all performed worse than FSF. This is due to the driver's sensory delays, as the driver is not aware of the disturbance until around 0.2 s after it has occured. In contrast, with FSF the driver has access to all the delay states so is aware of the disturbance straight away, and can react quicker in order to achieve a lower cost. While the state estimators all performed worse than FSF, their performance relative to each other was the same as for the target-only simulations, with the nonlinear state estimators all performing similarly except for the oversteering vehicle with ND tyres.

The performance of the different state estimators for the oversteering vehicle with ND tyres is compared in Figure 6, with and without disturbances. In both

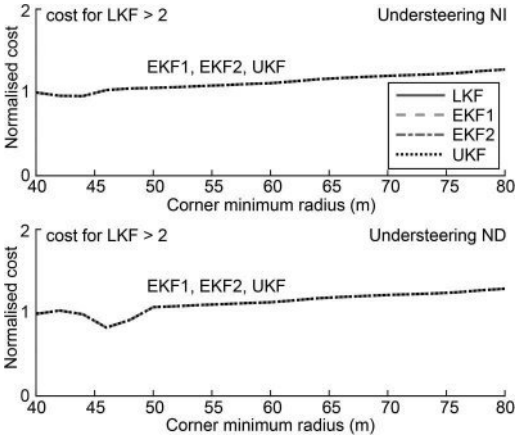


Figure 7. Comparison of the performance of each state estimator for simulations with added noise, using FNO. The total value of the cost function over each simulation has been normalised by the value found with FSF.

cases the state estimators performed as expected for corners with minimum radii greater than around 55 m, where the vehicle starts to become unstable. Below this the state estimates from EKF2 and UKF do not allow the controller to control the vehicle. When there is no disturbance the system can always control the vehicle with EKF1, which even performs better than FSF in some cases. With an added disturbance the system also stops being able to control the vehicle with EKF1, but at a lower radius than EKF2 and UKF.

5.4 *Process and measurement noise*

With added process and measurement noise the performance of the controllers was very similar to the results shown in Figure 5. Similarly to the simulations with a disturbance, for the oversteering vehicle with ND tyres some of the linearised controllers performed better than FNO for some corners. This is because an MPC controller perturbed by white noise isn't guaranteed to perform optimally for a nonlinear plant.

As in the simulations with a disturbance, all linearised Kalman filters performed similarly except for the oversteering vehicle with ND tyres. In general LKF performed worse than these and FSF performed better. However, as shown in Figure 7, in some cases with the understeering vehicle the linearised Kalman filters were better than FSF (with normalised costs less than 1). This may be because the linear Kalman filters effectively smooth the estimated states, reducing potentially suboptimal controller responses to process noise in the nonlinear region of the tyre.

6 DISCUSSION

The results of the simulations can be used to investigate the effect of a driver's sensory dynamics on the control of a nonlinear vehicle. They can also be used to evaluate the controllers and state estimators for use in a driver model, both in terms of how well they model a realistic driver and the practicality of using them in engineering applications. It is also possible to suggest improvements to the controllers which may allow them to run faster or more accurately.

6.1 *Effect of sensory dynamics*

The effect of a driver's sensory dynamics on the control of a nonlinear vehicle can be investigated by comparing the performance of the best state estimator (EKF1) with the results using FSF. Without disturbances or noise the results were the same, showing that for pure target-following the driver's control strategy is not significantly affected by sensory dynamics. However, in real driving there will be disturbances from sources such as wind gusts and road bumps, and driver noise from uncertainties in the driver's sensorimotor system and internal model of the vehicle. With disturbances and/or noise, the cost using EKF1 was generally much higher than with FSF, showing that limitations resulting from the driver's sensory dynamics make it more difficult for the driver to respond to disturbances and noise.

6.2 *Controllers and state estimators*

The results of the simulations showed a large variation in controller performance, and also in time taken to run each controller. In general the performance increased with the time taken, highlighting a trade-off between optimality and complexity. It is possible that the driver makes a similar trade-off in order to reduce their mental load, so the best performing controller may not necessarily be the most realistic. However the driver may use simplifying methods or learned responses to achieve a performance close to optimality without a large 'online' mental load. Experiments are planned using a driving simulator to test how the performance of a real driver compares to the simulations.

LKF was found to perform worse than the other state estimators for nonlinear tyres, as expected. FSF was generally found to perform best with disturbances or noise, however this isn't a good representation of a real driver who is affected by sensory dynamics and delays. In most cases all the nonlinear Kalman filters performed similarly, so it is sensible to choose EKF1 which takes the least time to simulate. For the oversteering vehicle with ND tyres differences were seen between the nonlinear Kalman filters, however EKF1 was found to perform best. Further work is required to understand this driving condition, however it is still possible to get a reasonable overview of driver behaviour while avoiding this specific case.

6.3 *Improvements to controllers*

Various methods can be used to improve the optimality and efficiency of the controllers. It has already been shown that the performance of controller LPF can be improved by adding constraints to limit slip angles, and costs to keep the solution close to the linearised

operating point (LPF*). Similar constraints and costs were tested for LP0, however they were found not to be effective. An advantage of FNO over LPF* is that it is able to operate beyond the limit of tyre friction, however it may be possible to develop a combined controller that uses LPF* for smaller slip angles and FNO for larger slip angles.

The practicality of some of the more complex controllers is somewhat limited by the computation time, with each simulation using FNO taking around 10 minutes to complete. There are various approximations which can be made to try and reduce this time, and if done carefully they may not significantly impact the performance of the controller. The simulations were run at a sample frequency of 100 Hz, however driver steering control is unlikely to act over such a high bandwidth. It may therefore be possible to reduce the sample frequency, or maintain a high sampling rate for simulating the plant dynamics while running the controller less frequently. Recent research has investigated intermittent control, where the driver updates their control sequence less frequently and relies on their previous computation in the interval between calculations (Johns and Cole 2015). It may also be possible to calculate some portion of the control strategy offline to reduce the online computational load, which could model drivers' learned behaviours from previous driving experience. Further speed increases may be achieved by writing the algorithms in a compiled language such as C++.

7 CONCLUSION

Simulations have been run to compare various controllers and state estimators for modelling a driver's control of a nonlinear vehicle. In choosing the controller there is generally a trade-off between computation time (mental load) and controller performance. The different nonlinear Kalman filters performed similarly except for an oversteering vehicle with 'nonlinear decreasing' tyres, where a first order extended Kalman filter was found to perform best. Further work is necessary to understand this driving condition. Nonlinear Kalman filters performed as well as full state feedback for pure target-following, showing that the driver's sensory dynamics do not have a significant effect. However with added disturbances or noise the driver's delays and noisy sensory systems resulted in a worse control performance. Experiments are planned to compare the simulations to measured behaviour from human drivers.

ACKNOWLEDGEMENTS AND DATA

This work was supported by the UK Engineering and Physical Sciences Research Council (EP/P505445/1, studentship for Nash). Supporting data is available at http://dx.doi.org/10.17863/CAM.595.

REFERENCES

Cole, D. J., A. J. Pick, & A. M. C. Odhams (2006). Predictive and linear quadratic methods for potential application to modelling driver steering control. *Vehicle System Dynamics 44*(3), 259–284.

Hartikainen, J., A. Solin, & S. Särkkä (2011). Optimal Filtering with Kalman Filters and Smoothers – a Manual for the Matlab toolbox EKF/UKF.

Johns, T. A. & D. J. Cole (2015). Measurement and mathematical model of a driver's intermittent compensatory steering control. *Vehicle System Dynamics 53*(12), 1811–1829.

Keen, S. D. & D. J. Cole (2011). Application of time-variant predictive control to modelling driver steering skill. *Vehicle System Dynamics 49*(4), 527–559.

Nash, C. & D. Cole (2016a). Development of a novel model of driver-vehicle steering control incorporating sensory dynamics. In M. Rosenberger, M. Plöchl, K. Six, and J. Edelmann (Eds.), *The Dynamics of Vehicles on Roads and Tracks*, pp. 57–66. Graz, Austria: CRC Press.

Nash, C. J. & D. J. Cole (2016b). Identification of a novel model of driver steering control incorporating human sensory dynamics. *Manuscript submitted for publication*.

Nash, C. J., D. J. Cole, & R. S. Bigler (2016). A review of human sensory dynamics for application to models of driver steering and speed control. *Biological Cybernetics* 110(2–3), 91–116.

Pacejka, H. B. & E. Bakker (1992). The magic formula tyre model. *Vehicle System Dynamics 21*(S1), 1–18.

Pick, A. J. & D. J. Cole (2007). Dynamic properties of a driver's arms holding a steering wheel. *Proceedings of the Institution of Mechanical Engineers, Part D: Journal of Automobile Engineering 221*(12), 1475–1486.

Thommyppillai, M., S. Evangelou, & R. S. Sharp (2009). Car driving at the limit by adaptive linear optimal preview control. *Vehicle System Dynamics 47*(12), 1535–1550.

Ungoren, A. & H. Peng (2005). An adaptive lateral preview driver model. *Vehicle System Dynamics 43*(4), 245–259.

Zaal, P. M. T., D. M. Pool, M. Mulder, & M. M. van Paassen (2009). Multimodal Pilot Control Behavior in Combined Target-Following Disturbance-Rejection Tasks. *Journal of Guidance, Control, and Dynamics 32*(5), 1418–1428.

Advanced Vehicle Control – Edelmann, Plöchl & Pfeffer (Eds)
© 2017 Taylor & Francis Group, London, ISBN 978-1-138-02992-7

Fundamental study on driver model for lateral and longitudinal control to advanced driver assistance systems

Ichiro Kageyama, Yukiyo Kuriyagawa & Yiyun Wang
Nihon University, College of Industrial Technology, Izumicho, Chiba, Japan

ABSTRACT: This paper deals with construction of driver model for evaluation of Advanced Driver Assistance Systems using driver's control action. This driver model has constructed by two blocks, one is longitudinal control and the other is lateral control. And, this model separate into two parts, one is feed forward control informed by road curvature and the other is feed back control using 3rd order prediction. At first stage of this research, we mainly describe the feed forward control parts using road curvature on forward view. And, we discuss about the gain of the feed forward control and also about change of the preview time. Finally, we show the possibility of evaluation for driver control action by using of these parameters.

Keywords: Driver modeling, Lateral control, Longitudinal control, Steering, Braking

1 INTRODUCTION

Normally, in the field of automotive engineering, research on drivers has been done for two categories, one is control algorithm on driver model, and the other is from a viewpoint of human factors. As for the research from the viewpoint of the control, a driver model have been constructed to clarify the relationship between vehicle behavior and driver's characteristic at the first stage of development for several new system such as ADAS. On the other hand, research on human factor has been done for design of human-machine interface, evaluation for driver's ability, influence of driver's condition, and so on. For such purpose, various evaluation methods have been proposed by using of vital reactions, subjective rating, interview to panels, and so on.

On the other hand, recently, research on autonomous vehicles has been carried out in many countries. At the first stage of the development, these vehicles run on mixed traffic conditions with ordinary drivers. Therefore, it is important to evaluate admissibility of the vehicle by drivers around the vehicles, and so on. From such purpose, it is important to construct a new driver model for such system evaluation. The driver's control algorithm, however, is still at the research stages, and is not yet established, especially for evaluation method for driver behavior. In this research, we try to understand and to evaluate the driver characteristics by using of control algorithm in the field of control engineering.

This study is approved by Ethical Review Board of Nihon University on human experiments (S2015-005).

Table 1. Specification of experimental vehicle.

Wheel base	2.8 m
Length between CG and front axle	1.35 m
Length between CG and rear axle	1.45 m
Vehicle mass	1948 kg
Moment of inertia	1600 kgm^2
Cornering stiffness for front tire	87 kN/rad
Cornering stiffness for rear tire	157 kN/rad

2 DRIVER MODEL

Normally, driver's steer action is classified into 3 parts as follows:

(1) The steering control for vehicle positioning along the road.
(2) Appropriate speed control according to the road shape and environment condition.
(3) The steer noise from driver or road called remnant.

Usually, the most important task of a driver for vehicle control is positioning on road described by (1) and (2).

Therefore, it is necessary to examine the driver model including these elements. In this paper, we used an experimental vehicle (shown in Fig. 1 and Table 1) which we can measure not only vehicle responses and position but also front view and eye mark of the driver.

2.1 *Outline of the experiment*

At the first stage of this research, we need to examine the possibility to construct a new driver model



Figure 1. Experimental vehicle.

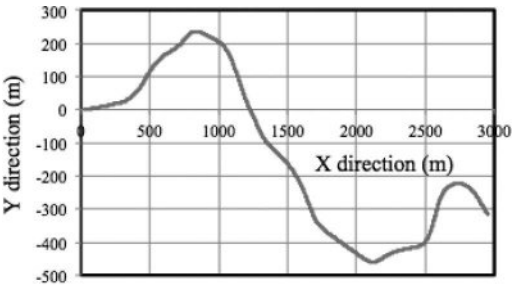


Figure 2. Course shape for experiment.

using analysis in relationship between a driver's input and output not only for longitudinal direction but also lateral direction. The data of the vehicle behavior controlled by 4 subjects had been measured with the vehicle on ordinary road. We told them to run freely carefully safely by the favorite driving speed within the speed limit. The road shape using experiment is shown in Fig. 2 measured by RTK-GPS, and, an example of vehicle response is shown in Fig. 3.

2.2 *Steer for positioning on road*

As for examination of main information for positioning, the correlation between the steer angle and various input to the driver were calculated using the experimental data on the course. As the result, the road curvature at forward view (0.98 s) has the highest correlation to the steer angle as shown in Fig. 4. In this case, the correlation coefficient is about 0.962. For the other driver results, the values are almost over 0.9. From these results, it seems that the main information to the driver for positioning control is road curvature as feed forward information. The time, which indicates the highest correlation, therefore, is defined as the equivalent preview time. Using the data, it is shown the relation between the steer angle and the steer angle calculated with road curvature as shown in Fig. 5. The forward road curvature, therefore, is adopted as feed forward information for steer control.

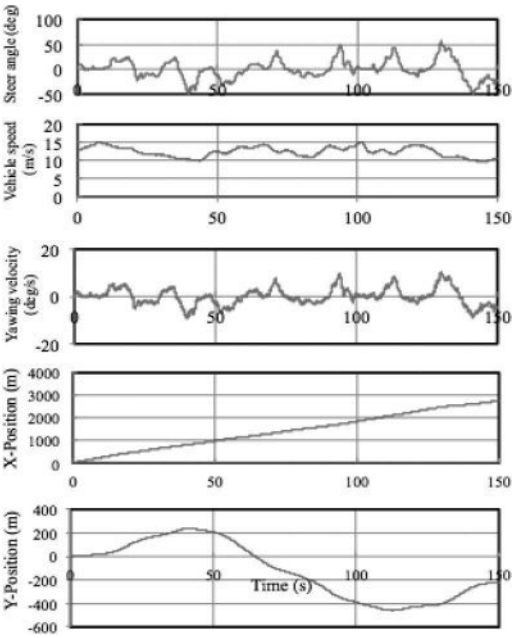


Figure 3. Example of the experimental data.

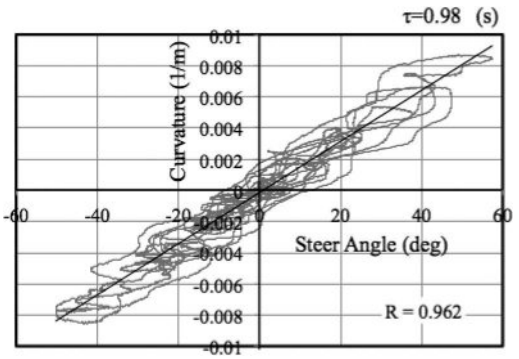


Figure 4. Relation between steer angle and road curvature.

2.3 *Feedback steer for tracking*

As mentioned above, it was found that the main information for positioning was feed forward using road curvature. However, it is impossible to realize the stable control using only this feed forward value, because of noise or turbulence from inside and outside of the vehicle. In other words, the feedback for the tracking to the desired course is needed. The feedback steer can be calculated by subtracting the element of feed forward steer from experimental data.

The purpose of this research is to analyze the change of driver's characteristics during driving. Therefore, we need to decide what kind of algorithm to describe the feedback model. Here, because the feed forward steering possesses the preview time as it is clear from Fig. 5, the preview control model is also used in the model for feedback steer. Fig. 6 indicates a general

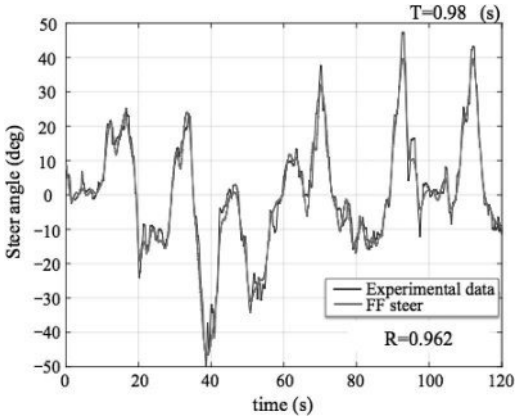


Figure 5. Comparison between experimental steer and analytical feed-forward steer.

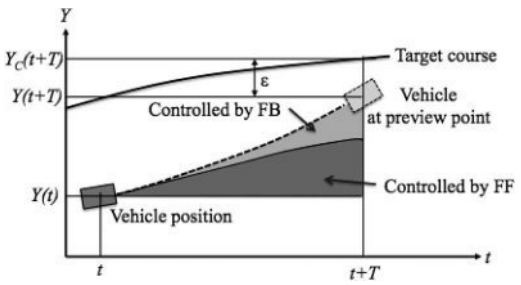


Figure 6. Preview/prediction model with feed forward control.

idea of preview + feed forward model. And, lateral position at preview point is described as follows,

$$Y(t+T) = Y(t) + \dot{Y}(t)T + \frac{1}{2}\ddot{Y}(t)T^2 + \frac{1}{3!}\dddot{Y}(t)T^3 + \cdots + \frac{1}{n!}Y(t)^{(n)}T^n + \cdots \quad (1)$$

In recent years, a literature indicated that jerk is one of the important information to decide control timing between longitudinal and lateral motion[1]. In this paper, therefore, the scalability of this model is considered and the 3rd order prediction model is adopted for feed back model. Feedback steer was calculated by deduction of feed-forward steer from the steer angle of the experimental result controlled by drivers in this model construction. In this analytical model, however, feedback steer includes so much noise, because the feed forward steering is dominant in this analysis. Therefore it wasn't possible to get the high correlation coefficient, an example of results is shown in Fig. 7. From this figure, it is found that that feedback steering is shown qualitatively.

2.4 *Lateral control model*

From the results above, it is shown that the total driver model for lateral control to analyze driver behavior

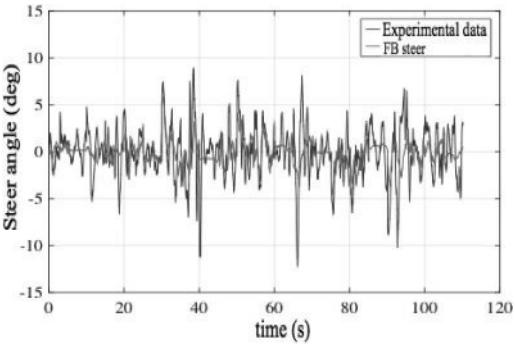


Figure 7. FB model using 3rd order prediction.

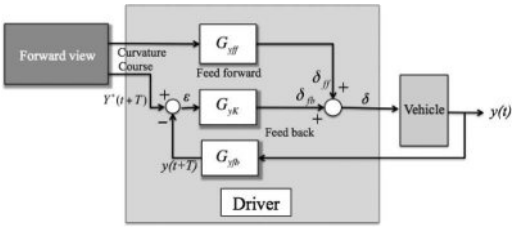


Figure 8. Total driver model.

is constructed by combine model using the feed forward and the feedback. Comparison between the result of this model and experimental result is shown in Fig. 8. The model output has good description for ordinary drivers behavior. The information flow chart for the driver control is constructed such as Fig. 8. As the driver characteristic of the driver is identified using this model, an example of analytical results between driver control action for steering and model output is described as shown in Fig. 9. As a result, the driver model for lateral direction in the feed forward steering is able to express by the steering gain and the length of forward view point, and it is expressed using the equivalent front view length and the gain for feedback model.

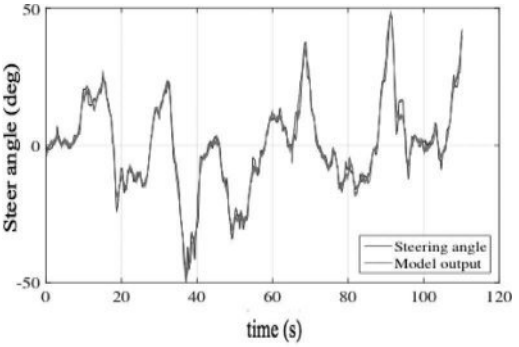
3 LONGITUDINAL DRIVER MODEL

In order to construct an overall driver model for evaluation of driver behavior, it is important to construct a longitudinal direction control model as well as a lateral directional control model. The vehicle responses controlled by several drivers had been measured on ordinary road using experimental vehicle.

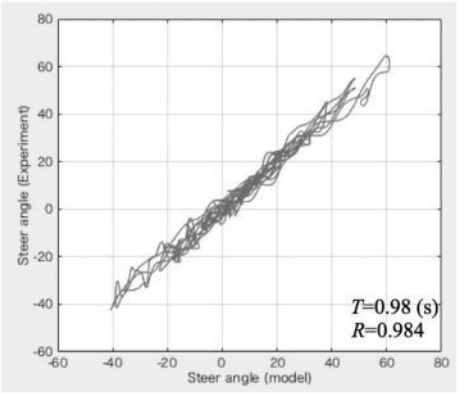
Speed control on ordinary road at our experiment, however, isn't performed so strictly such as Fig. 10. It seems that this result came from ordinary driving condition by subject.

3.1 *Longitudinal control model*

In this paper, this model is constructed by the relationship between the longitudinal acceleration and road



(a) Time history of the model output and experiment



(b) Relation between mole output and experiment

Figure 9. The result of lateral control model.

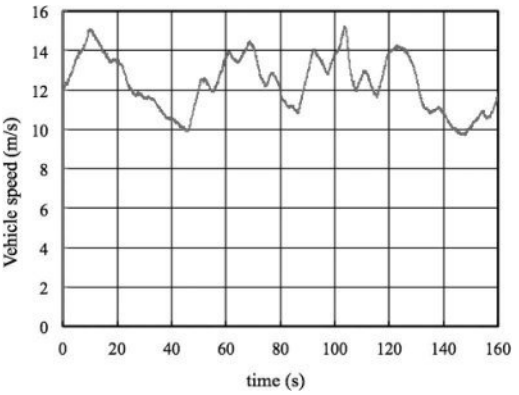


Figure 10. Vehicle speed during experiment.

curvature using preview time. The longitudinal acceleration is related to movement of the gas pedal and the brake pedal, so it seems that a driver controls vehicle speed using road curvature as one of main information for longitudinal control. In this case, therefore, the relation between longitudinal control action and road curvature is just feed forward control by driver, and the correlation coefficient between the two is almost

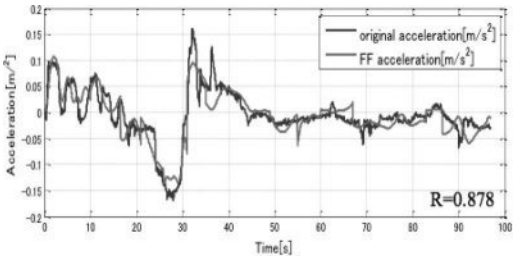


Figure 11. Relation between experimental data and model using road curvature.

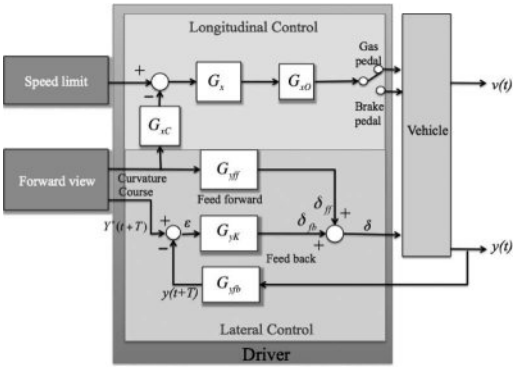


Figure 12. Total model.

0.878 as shown in Fig. 11. We, therefore, decide to adopt an assumption not to use a feedback control for the speed control. The model output for longitudinal characteristics has good description for ordinary drivers behavior.

3.2 *Total driver mode*

In the chapter 2.4 and 3.1, we have constructed the two models, one was longitudinal model and the other is lateral model. Therefore, We need to combine two models into total driver model. The input of the two models is the curvature of the forward road. And, speed limit is also one of the inputs of the longitudinal model.

In the algorithm of the longitudinal control model being above-mentioned in this research, it's made only feed forward as shown in Fig. 12.

Drivers usually get environment information especially road shape from their front view. This information is related to feed forward control and feedback control. The position information of a preview, therefore, has been analyzed using a correlation analysis during 5 seconds for each in the analysis above. The preview point of the driver was measured using eye mark recorder during an experiment to inspect these possibilities in this research. An example of preview point during the experiment is shown in Fig. 13. In this figure, a circular mark indicates the eye point. The positions of the viewpoints are calibrated into preview time using vehicle speed as shown in Fig. 14. From this figure, it is found that the average of preview time is



Figure 13. Preview point using eye-mark recorder.

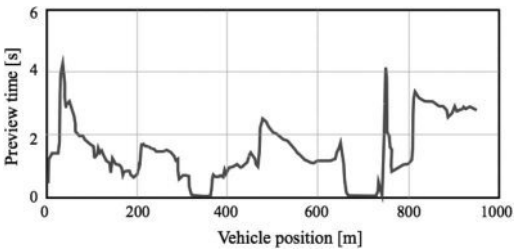


Figure 14. Preview time measured by eye-mark recorder.

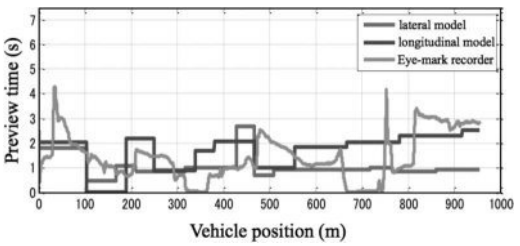


Figure 15. Change of preview times of driver.

around 1–2 seconds, and it's always fluctuating. However, the preview time isn't always identical with the preview time to control on the preview model, because a driver is also using the peripheral vision effectively. However, the preview time isn't always identical with the preview point to control on the model, because a driver is also using the peripheral vision effectively.

Therefore, preview time is analyzed using a correlation method as a parameter, and the highest coefficient of correlation is assumed as the information acquisition location. The preview times for longitudinal, lateral direction, and the result of Eye-mark recorder are shown in Fig. 15. As a result of the Eye-mark recorder, there is slightly difference to the analytical results of the model, but it is shown well qualitatively.

4 CONCLUSION

The driver model for control action analysis using not only lateral control but also longitudinal control was constructed by using feed-forward control and preview and prediction control. The feed-forward control in the steering action is the dominant term in ordinary driver's control. The driver model can be described by several parameters "actual preview time", "steering gain", "ratio between feedback and feed-forward steer". For the next stage, we need to realize a driver evaluation method using several parameters connected to this driver model.

As the next stage, it's necessary to consider the changes in the drivers. And, it's necessary to construct the method to evaluate drivers who use ADAS.

REFERENCES

[1] Yamakado et al.: Study of Motion Evaluation and Control Systems using Jerk Information: 1st Report, A Jerk Sensor and its application to Vehicle Motion Control Systems Transaction of JSME(C), Vol. 64(619), pp. 873–879, 1998.

[2] I. Kageyama et al.: Study on construction of driver model for advanced driver assist system, Proc. of JSAE, 2015 (CD).

[3] I. Kageyama et al.: On construction of driver model for analysing driver characteristics, Proc. of FAST-zero 2015 (CD).

Advanced Vehicle Control – Edelmann, Plöchl & Pfeffer (Eds)
© 2017 Taylor & Francis Group, London, ISBN 978-1-138-02992-7

Model predictive control to represent interaction of driver and active accelerator pedal

C.W. Rosier & D. Cole
University of Cambridge, Cambridge, UK

ABSTRACT: Accelerator pedals with force feedback, also known as active accelerator pedals, are increasingly available in the car industry. The pedals can be used to assist the driver in observing speed limits, maintaining a safe distance to the car in front, and minimising energy consumption. A review of the published literature reveals that the action of these pedals is sometimes disliked by the driver, but there is limited theoretical understanding of the interaction between driver and active pedal. This paper proposes a mathematical game theoretical model of the interaction using model predictive control theory (MPC). Two control strategies are introduced: decentralised control and cooperative control. A brief parameter study demonstrates the influence of the adjustable parameters of the controllers. The work is directed towards the heavy goods vehicle application, where the potential of active accelerator pedals to reduce energy consumption is not yet fully explored.

1 INTRODUCTION

This paper describes part of a larger programme of work to reduce the energy consumption of heavy goods vehicles (HGVs) using an active accelerator pedal to provide force feedback to the driver.

Previous research on pedal force feedback has focused on three main applications: speed limiting (Varhelyi (2004)), maintaining safe following distances (Mulder (2011)), and reducing energy consumption (Azzi (2011)). The previous research has identified several advantages and disadvantages of pedal force feedback. It assists the driver in a continuous manner and does this without distracting the driver's vision. It can also maintain its effects in the long term. However, active accelerator pedals have to be built into the vehicle at time of manufacture; it is not straightforward to fit them to an existing vehicle. More significantly, the force feedback is often disliked because it is regarded as interfering; it is judged as 'effective' but not always 'attractive'.

Abbink (2011) investigated the interaction between a driver's foot and a pedal with force feedback during a vehicle following task. Admittance functions (displacement/force) of the foot were identified and compared to admittances measured for three classical tasks: the driver relaxes the foot; the driver maintains the pedal postion in the presence of force disturbances; or the driver maintains a constant force on the pedal in the presence of disturbances. It was found that the admittance of the driver's foot during the vehicle following task was similar to the relatively high value seen during the constant force task. The measured admittances of the classical tasks showed significant influence at frequencies up to about 1 Hz, which is probably attributable to cognitive action. Above 10 Hz responses were thought to be dominated by inertial properties of the foot. At intermediate frequencies the admittances were thought to be affected mainly by reflex action and muscle co-contraction.

The aim of the work described in the present paper is to develop a mathematical model of the driver's cognitive control of a vehicle with active pedal force, for the frequency range up to about 1 Hz. The model will be the basis of further work to devise improved active pedal force strategies that are both effective and attractive. In section 2 the mathematical models of the vehicle and driver are described. The interaction between driver and active pedal is represented in section 3 using mathematical game theory, building upon recent work by Na & Cole (2013). Two control strategies are developed: decentralised control and cooperative control. In section 4 a brief parameter study is presented. The paper ends with a conclusion.

2 VEHICLE AND DRIVER MODELS

A block diagram of the vehicle and driver models is given in figure 1. The driver is required to control the vehicle to follow a target speed profile $\mathbf{T}_1$, which the driver can preview. This is a more general representation of a vehicle following task, for which the driver can be considered to formulate a target speed profile on the basis of the speed and distance of the vehicle ahead.

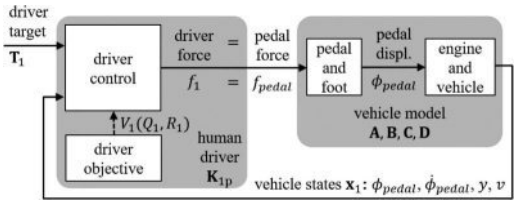


Figure 1. Driver model block diagram.

2.1 *Vehicle model*

The vehicle is modelled as a mass ($m = 36.6$ Mg) driven by a traction force (equal to $T_{max} \times \phi_{pedal\%}$ where $T_{max} = 1400$ Nm and $\phi_{pedal\%} = \phi_{pedal}/\phi_{pedalmax}$) that opposes inertia force, rolling resistance ($C_r = 6.62 \times 10^{-3}$), gradient (an upwards incline of angle $\theta = 3°$) and linearized aerodynamic drag $\frac{1}{2}\rho v U C_d A$ where v is vehicle speed, $\rho = 1.225\,\mathrm{kg\,m^{-3}}$, $U = 22.5\,\mathrm{m\,s^{-1}}$ and $C_dA = 6.62\,\mathrm{m^2}$. The vehicle parameter values are from Hunt et al. (2011). The pedal and foot dynamics are modelled as a rotational inertia ($I_{pedal} = 0.256\,\mathrm{kg\,m^2}$), connected to ground by a torsional spring ($\kappa_{pedal} = 0.088\,\mathrm{N\,m\,rad^{-1}}$) and parallel torsional damper ($C_{pedal} = 0.01\,\mathrm{N\,m\,s\,rad^{-1}}$), all with respect to rotation about the pedal axis. The length of the pedal arm is 0.16 m.

The discrete-time state-space equations of the vehicle model are:

$$\mathbf{x_1}(k+1) = \mathbf{A}\mathbf{x_1}(k) + \mathbf{B}f_{pedal}(k) \tag{1}$$

$$\mathbf{z_1}(k) = \mathbf{C}\mathbf{x_1}(k) \tag{2}$$

The states $\mathbf{x}_1(k)$ are pedal displacement (ϕ_{pedal}) and velocity ($\dot{\phi}_{pedal}$) and vehicle longitudinal displacement (y) and velocity (v). The outputs $\mathbf{z}_1(k)$ are the pedal displacement and vehicle velocity. In the drive-cycle following task the reference $\mathbf{T}_1$ is an array of target speeds at N_p discrete time steps in the future. In the case of a passive pedal, the control input to the vehicle f_{pedal} is equal to the force output of the driver f_1, as shown in Figure 1.

The vehicle model specified here is used as the driver's 'internal' model for the control calculation described in the section 2.2, and for the calculation of the vehicle response to the driver's control action.

2.2 *Driver model*

The driver controls the vehicle with force f_1 applied to the accelerator pedal, as illustrated in figure 1. Subscript 1 denotes the driver.

The 'internal' vehicle model is used to predict the response to the driver's future control action, up to a prediction horizon that is N_p discrete time steps ahead. Following Maciejowski (2002):

$$\mathbf{Z_1}(k) = \mathbf{\Psi}\mathbf{x_1}(k) + \mathbf{\Theta}\mathbf{U_1}(k) \tag{3}$$

where

$$\mathbf{Z_1}(k) = \begin{Bmatrix} \mathbf{z_1}(k+1) \\ \mathbf{z_1}(k+2) \\ \vdots \\ \mathbf{z_1}(k+N_p) \end{Bmatrix},$$

$$\mathbf{U_1}(k) = \begin{Bmatrix} f_1(k) \\ f_1(k+1) \\ \vdots \\ f_1(k+N_p-1) \end{Bmatrix},$$

$$\mathbf{\Psi} = \begin{bmatrix} \mathbf{CA} \\ \mathbf{CA}^2 \\ \vdots \\ \mathbf{CA}^{N_p} \end{bmatrix} \text{ and}$$

$$\mathbf{\Theta} = \begin{bmatrix} \mathbf{CB} & 0 & \cdot & \cdot & \cdot & 0 \\ \mathbf{CAB} & \mathbf{CB} & 0 & \cdot & \cdot & \cdot \\ \mathbf{CA^2B} & \mathbf{CAB} & \mathbf{CB} & 0 & \cdot & \cdot \\ \cdot & \cdot & \cdot & \cdot & \cdot & \cdot \\ \cdot & \cdot & \cdot & \cdot & \cdot & \cdot \\ \mathbf{CA^{N_p-1}B} & \cdot & \cdot & \cdot & \mathbf{CAB} & \mathbf{CB} \end{bmatrix}$$

A cost function consisting of speed error (compared to target speed r_v), pedal displacement (a placeholder for a more detailed energy use model) and driver pedal force is defined:

$$V_1(k) = \sum_{i=1}^{N_p} q_{1v}\left(v(k+i) - r_v(k+i)\right)^2 + \sum_{i=1}^{N_p} q_{1\phi}\,\phi^2(k+i) + \sum_{i=0}^{N_p-1} r_{1f}\,{f_1}^2(k+i) \tag{4}$$

$$V_1(k) = \sum_{i=1}^{N_p} \|\mathbf{z}_1((k+i) - \mathbf{r_1}(k+i)\|^2_{\mathbf{Q}_1} + \sum_{i=0}^{N_p-1} \|f_1(k+i)\|^2_{\mathcal{R}_1}. \tag{5}$$

Define:

$$\mathcal{Q}_1 = \begin{bmatrix} \mathbf{Q_1}\,(1) & & \\ & \ddots & \\ & & \mathbf{Q_1}(N_p) \end{bmatrix},$$

$$\mathcal{R}_1 = \begin{bmatrix} \mathbf{R_1}(0) & & \\ & \ddots & \\ & & \mathbf{R_1}(N_p-1) \end{bmatrix}, \text{ and}$$

$$\mathbf{T_1}(k) = \begin{Bmatrix} \mathbf{r}(k) \\ \mathbf{r}(k+1) \\ \vdots \\ \mathbf{r}(k+N_p-1) \end{Bmatrix}$$

where $\mathbf{Q}_1$ is a diagonal matrix of weightings on the outputs at time steps 1 to N_p of the prediction. The pedal displacement weighting is given the symbol $q_{1\phi}$, and vehicle velocity, q_{1v}. The driver pedal force weighting, $\mathbf{R}_1 = r_{1f}$. The vector $\mathbf{r}(k)$ is reference values at time step k. For all outputs apart from speed, this is

zero. The cost function is now rewritten without the summation and in terms of the predicted speed errors:

$$V_1(k) = \|\boldsymbol{\Theta}\mathbf{U}_1(k) - \boldsymbol{\varepsilon}_1(k)\|^2_{\mathcal{Q}_1} + \|\mathbf{U}_1(k)\|^2_{\mathcal{R}_1} \quad (6)$$

where the predicted speed errors, $\boldsymbol{\varepsilon}_1(k)$, are defined as $\boldsymbol{\varepsilon}_1(k) = \mathbf{T}_1(k) - \boldsymbol{\Psi}x_1(k)$. Rewriting once more:

$$V_1(k) = \left\| \begin{bmatrix} \boldsymbol{S}_{\mathcal{Q}_1}\{\boldsymbol{\Theta}\boldsymbol{U}_1(k) - \boldsymbol{\varepsilon}_1(k)\} \\ \boldsymbol{S}_{\mathcal{R}_1}\boldsymbol{U}_1(k) \end{bmatrix} \right\|^2 \quad (7)$$

where $\mathbf{S}^{\mathrm{T}}_{\mathcal{Q}}\mathbf{S}_{\mathcal{Q}} = \mathcal{Q}$ and $\mathbf{S}^{\mathrm{T}}_{\mathcal{R}}\mathbf{S}_{\mathcal{R}} = \mathcal{R}$.

In order to minimise the cost function, the least squares solution is sought and can be found using QR decomposition:

$$\boldsymbol{U}_{1opt}(k) = \boldsymbol{K}_{1full}\boldsymbol{\varepsilon}(k) \quad (8)$$

where

$$\boldsymbol{K}_{1full} = \begin{bmatrix} \boldsymbol{S}_{\mathcal{Q}_1}\boldsymbol{\Theta} \\ \boldsymbol{S}_{\mathcal{R}_1} \end{bmatrix} \backslash \begin{bmatrix} \boldsymbol{S}_{\mathcal{Q}_1} \\ 0 \end{bmatrix}.$$

Applying the receding horizon method, the optimal pedal force at time step k is

$$f_1(k) = \boldsymbol{K}_{1w}\boldsymbol{\varepsilon}_1(k) \quad (9)$$

where $\mathbf{K}_{1\mathrm{w}}$ is the first row (corresponding to first control action) of $\mathbf{K}_{1\mathrm{full}}$.

Using equation (9), and the substitution $\mathbf{K}_{1p} = [-\mathbf{K}_{1\mathrm{w}}\boldsymbol{\Psi} \;\; \mathbf{K}_{1\mathrm{w}}]$, the control law can be written as:

$$f_1(k) = \boldsymbol{K}_{1p}\begin{Bmatrix} \boldsymbol{x}_1(k) \\ \boldsymbol{T}_1(k) \end{Bmatrix} \quad (10)$$

3 ACTIVE PEDAL FORCE

The active pedal force is generated by a controller that acts alongside the human driver, as shown in figure 2. The active pedal force, denoted f_2, and the force generated by the driver f_1, combine to give the total force f_{pedal} applied to the pedal.

3.1 *Decentralised control*

In decentralised control (figure 2) the driver and active pedal act with no knowledge of each other's objective or action. The active pedal controller is derived in the same manner as described in section 2.2 for the driver, but with different target $\mathbf{T}_2$ and cost function weights $\mathcal{Q}_2$ and $\mathcal{R}_2$. However the controller acts on the same states such that $\mathbf{x}_2 = \mathbf{x}_1$. The active pedal force is given by:

$$f_2(k) = \mathbf{K}_{2p}\begin{Bmatrix} \mathbf{x_2}(k) \\ \mathbf{T_2}(k) \end{Bmatrix} \quad (11)$$

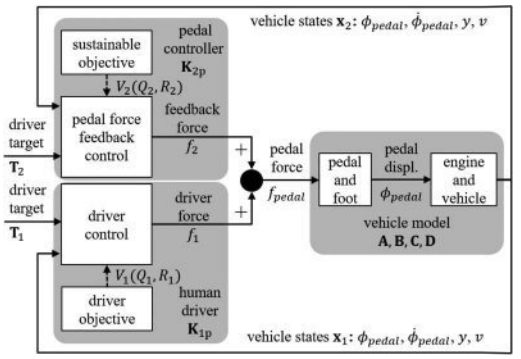


Figure 2. Decentralised feedback block diagram.

3.2 *Cooperative control*

In cooperative control the driver and active pedal take each other's objective and action into account by defining a global cost function, see Rawlings & Mayne (2009) and Na & Cole (2013). The block diagram for cooperative control is very similar to the decentralised control shown in figure 2, but the two controllers are aware of each other's objective and action.

To derive the cooperative controllers, begin with a pair of prediction equations (one for each controller):

$$\boldsymbol{Z}_a(k) = \boldsymbol{\Psi}_a\boldsymbol{x}(k) + \boldsymbol{\Theta}_a\boldsymbol{U}_a(k) + \boldsymbol{\Omega}_a\boldsymbol{U}_b(k) \quad (12)$$

where $a = 1, 2$ and $b = 3 - a$. A value of 1 indicates the human driver, and value of 2 the active pedal. In comparison to equation (3) it can be seen that the response is now assumed to depend on both controls.

The objective is defined as a weighted sum of the individual controllers' cost functions. Parameters ρ_1 and ρ_2 (where $\rho_1 + \rho_2 = 1$) define the weighting:

$$\begin{aligned} V_a^{\mathrm{coop}}(k) = \frac{1}{2}\sum_{j=0}^{N_p} \Big[& \big(\mathbf{z}(k+j) - \mathbf{r}_1(k+j)\big)^{\mathrm{T}} \\ & \cdot \rho_1 \boldsymbol{\mathcal{Q}}_1 \big(\mathbf{z}(k+j) - \mathbf{r}_1(k+j)\big) \\ & + \big(\mathbf{z}(k+j) - \mathbf{r}_2(k+j)\big)^{\mathrm{T}} \\ & \cdot \rho_2 \boldsymbol{\mathcal{Q}}_2 \big(\mathbf{z}(k+j) - \mathbf{r}_2(k+j)\big) \Big] \\ & + \frac{1}{2}\rho_{\mathrm{a}} \sum_{j=0}^{N_u-1} [f_{\mathrm{a}}(k+j)^{\mathrm{T}} \boldsymbol{\mathcal{R}}_{\mathrm{a}} f_a(k+j)] \end{aligned} \quad (13)$$

This can be rewritten in matrix form and in terms of the tracking errors:

$$\begin{aligned} V_a^{coop}(k) = & \left\| \boldsymbol{\Theta}^{coop}\boldsymbol{U}_a(k) - \boldsymbol{\varepsilon}_a^{coop}(k) \right\|^2_{\mathcal{Q}^{coop}} + \\ & \|\boldsymbol{U}_a(k)\|^2_{\mathcal{R}_a^{coop}} \end{aligned} \quad (14)$$

where

$$\mathbf{Z}^{\text{coop}}(k) = \begin{bmatrix}\mathbf{Z}_1(k)\\ \mathbf{Z}_2(k)\end{bmatrix},$$

$$\mathbf{T}^{\text{coop}}(k) = \begin{bmatrix}\mathbf{T}_1(k)\\ \mathbf{T}_2(k)\end{bmatrix},$$

$$\boldsymbol{\mathcal{Q}}_{\text{i}}^{\text{coop}} = \rho_i \begin{bmatrix}\mathbf{Q}_i & 0 & \cdots & 0\\ 0 & \mathbf{Q}_i & \cdots & 0\\ \vdots & \vdots & \ddots & \vdots\\ 0 & 0 & \cdots & \mathbf{Q}_i\end{bmatrix},$$

$$\boldsymbol{\mathcal{R}}_i^{coop} = \rho_i \begin{bmatrix}\mathbf{R}_i & 0 & \cdots & 0\\ 0 & \mathbf{R}_i & \cdots & 0\\ \vdots & \vdots & \ddots & \vdots\\ 0 & 0 & \cdots & \mathbf{R}_i\end{bmatrix} \text{ and}$$

$$\boldsymbol{\varepsilon}_a^{\text{coop}}(k) = \mathbf{T}^{\text{coop}}(k) - \boldsymbol{\Psi}^{\text{coop}}(k)\mathbf{x}(k) - \boldsymbol{\Omega}^{\text{coop}}\mathbf{U}_{\text{b}}(k). \tag{15}$$

Rewriting one final time:

$$V_a^{coop}(k) = \left\| \begin{matrix} \boldsymbol{S}_{\mathcal{Q}^{coop}}\{\boldsymbol{\Theta}^{coop}\boldsymbol{U}_a(k) - \boldsymbol{\varepsilon}_a^{coop}(k)\} \\ \boldsymbol{S}_{\mathcal{R}_a^{coop}}\boldsymbol{U}_a(k) \end{matrix} \right\|^2 \tag{16}$$

which leads to the optimal controllers:

$$\boldsymbol{U}_a(k) = \boldsymbol{K}_{a\,full}^{coop}\boldsymbol{\varepsilon}_a^{coop}(k) \tag{17}$$

where

$$\mathbf{K}_{\text{afull}}^{\text{coop}} = \begin{bmatrix}\mathbf{S}_{\mathcal{Q}^{\text{coop}}}\boldsymbol{\Theta}^{\text{coop}}\\ \mathbf{S}_{\boldsymbol{\mathcal{R}}_{\text{a}}^{\text{coop}}}\end{bmatrix} \setminus \begin{bmatrix}\mathbf{S}_{\mathcal{Q}^{\text{coop}}}\\ 0\end{bmatrix}.$$

Substituting both equations ($a = 1$ and $a = 2$) back into the error definitions (15) gives:

$$\mathbf{U}_a(k) = \left[-\mathbf{K}_{\text{a full}}^{\text{coop}}\boldsymbol{\Psi}^{\text{coop}} \;\; \mathbf{K}_{\text{a full}}^{\text{coop}}\right]\begin{bmatrix}\mathbf{x}(k)\\ \mathbf{T}^{\text{coop}}(k)\end{bmatrix} - \mathbf{K}_{\text{a full}}^{\text{coop}}\boldsymbol{\Omega}^{\text{coop}}\mathbf{U}_{\text{b}}(k) \tag{18}$$

and then into each other:

$$\boldsymbol{U}_a(k) = \left[\boldsymbol{\Lambda}_a^{coop} \;\; \boldsymbol{\Gamma}_a^{coop}\right]\begin{Bmatrix}\boldsymbol{x}(k)\\ \boldsymbol{T}^{coop}(k)\end{Bmatrix} \tag{19}$$

where

$$\boldsymbol{\Lambda}_{\text{a}}^{\text{coop}} = \left[\mathbf{I} - \mathbf{K}_{\text{a full}}^{\text{coop}}\boldsymbol{\Omega}^{\text{coop}}\mathbf{K}_{\text{b full}}^{\text{coop}}\boldsymbol{\Theta}^{\text{coop}}\right]^{-1} \cdot \left[-\mathbf{K}_{\text{a full}}^{\text{coop}}\boldsymbol{\Psi}^{\text{coop}} + \mathbf{K}_{\text{a full}}^{\text{coop}}\boldsymbol{\Omega}^{\text{coop}}\mathbf{K}_{\text{b full}}^{\text{coop}}\boldsymbol{\Psi}^{\text{coop}}\right]$$

$$\boldsymbol{\Gamma}_{\text{a}}^{\text{coop}} = \left[\mathbf{I} - \mathbf{K}_{\text{a full}}^{\text{coop}}\boldsymbol{\Omega}^{\text{coop}}\mathbf{K}_{\text{b full}}^{\text{coop}}\boldsymbol{\Theta}^{\text{coop}}\right]^{-1} \cdot \left[\mathbf{K}_{\text{a full}}^{\text{coop}} - \mathbf{K}_{\text{b full}}^{\text{coop}}\boldsymbol{\Omega}^{\text{coop}}\mathbf{K}_{\text{b full}}^{\text{coop}}\right]$$

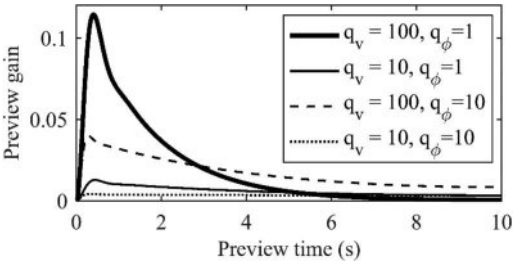


Figure 3. Gains on predicted speed errors for two different driver styles with a prediction horizon of 10s.

Now, by applying the receding horizon approach, the two cooperative controllers, $\mathbf{K}_{\text{a}}^{\text{coop}}$ are derived:

$$f_a(k) = \mathbf{K}_{\text{a}}^{\text{coop}}\begin{Bmatrix}\mathbf{x}(k)\\ \mathbf{T}^{\text{coop}}(k)\end{Bmatrix} \tag{20}$$

where

$$\boldsymbol{K}_a^{coop} = \left[\boldsymbol{\Lambda}_a^{coop}(1,:) \;\; \boldsymbol{\Gamma}_a^{coop}(1,:)\right]$$

where $\boldsymbol{\Lambda}_a^{\text{coop}}(1,:)$ means the first row of $\boldsymbol{\Lambda}_a^{\text{coop}}$ and so on.

4 RESULTS

In this parameter study the weightings on pedal force (r_f) are set to 1 throughout. The effect of the cost function on the behaviour of the driver or active pedal acting alone is examined in figure 3. The weighting on pedal displacement (q_ϕ) is initially set to 1. It can be seen that by increasing the weighting on speed error (q_v from 10 to 100), the gains on predicted speed errors increase, particularly in the first few seconds. Increasing the weight on pedal displacement (q_ϕ from 1 to 10), reduces the gains, although the peak occurs earlier in time.

In figures 4 and 5 the target speed is an unexpected step from 10 m s^{-1} to 15 m s^{-1}. Thus the controllers do not see the speed change until it occurs. This might occur for example if a slow vehicle ahead suddenly changes lane and allows the prevailing speed limit of the road to be reached. Figure 4 illustrates the speed change behaviour of two drivers with different cost function weightings. The driver with higher weighting on speed error q_v can be seen to accelerate faster, as expected. The other driver is content with larger speed errors because it means that pedal forces and displacements are reduced. If the controller with higher q_v is the human driver, and the other is the active pedal, and they operate in a decentralised manner, the illustrated outcome is achieved. The vehicle speed remains close to the unassisted human driver, since their weighting on speed error is the most significant weighting in either cost function.

Alternatively, the driver and active pedal may have different targets. Figure 5 demonstrates the effect of

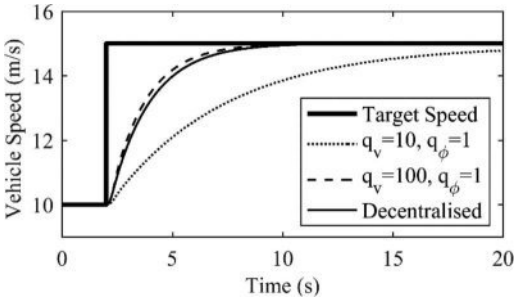


Figure 4. Speed change for driver ($q_v = 100, q_\phi = 1$) and sustainable controller ($q_v = 10, q_\phi = 1$) independently and when working in parallel as decentralised control.

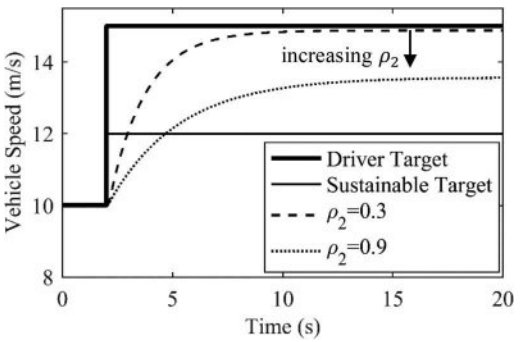


Figure 5. Speed change for cooperative control case with different driver and sustainable target speeds. The drive and sustainable controller have identical weightings to Figure 4.

having different target speeds in a cooperative arrangement, but using the same driver and pedal cost function weightings as before. The driver's target is 15 m s^{-1} whereas the active pedal's target is a more environmentally sustainable 12 m s^{-1}. The value of ρ_2 is either 0.9, meaning the active pedal's objective is more important, or 0.3 where the driver's objective is more important. The resulting speed is a compromise between the two targets, depending on the relative weighting on the two controllers' objectives, as well as the controllers' individual weightings on speed error, applied force, and pedal displacement.

The trade-off between speed error, applied force and pedal displacement are investigated further by calculating response to a modified version of the Millbrook Heavy Duty Suburban drive cycle (Barlow (2009)). Root mean square values of these quantities are shown in figure 6 for the human driver alone (w/o feedback, solid circles). The q_v values of the driver vary from 2 to 100,000 and $q_\phi = 1$. The graph shows the expected trade-off: smaller speed errors require larger pedal displacements (shown as a percentage of full travel) and pedal forces. The graph also shows the results for the driver with an active pedal (w/feedback, open diamonds) using $q_v = 10$, $q_\phi = 1$ and a decentralised control strategy. The trade

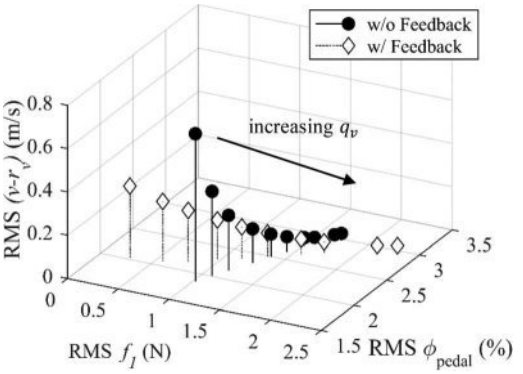


Figure 6. Trade off diagram for the decentralised control strategy.

off is similar although at low values of driver q_v, the active pedal allows the driver to maintain small speed errors with less applied pedal force. At high values of driver q_v, the active pedal results in the driver applying larger force than without the active pedal, because the decentralised strategy is not optimal.

Future work involves: adding more detail to the driver and vehicle models in order to calculate vehicle energy consumption; identifying and validating the driver model with data from driving simulator experiments; and devising active pedal control strategies that are both effective and attractive.

5 CONCLUSION

Mathematical game theory has been proposed to provide insight to the interaction between driver and active accelerator pedal in a drive cycle task. Model predictive control theory has been used to implement two different control strategies: decentralised and cooperative. A brief parameter study reveals that a range of responses can be derived by varying target speeds, cost function weights and balance of cooperation. Future work will aim to identify the control strategies from driving simulator experiments, and to devise active pedal control strategies.

ACKNOWLEDGEMENTS

This work is funded by the Centre for Sustainable Road Freight (www.csrf.ac.uk) and the Engineering and Physical Sciences Research Council (Grant EP/K00915X/1).

REFERENCES

Abbink, D., Mulder, M., van der Helm, F., Mulder, M., Boer, E., 2011. Measuring neuromuscular control dynamics during car following with continuous haptic feedback, IEEE Transactions on Systems Man and Cybernetics Part B-Cybernetics, 41(5), p. 1239–1249.

Azzi, S., Reymond, G., Merienne, F., Kemeny, A., 2011. Eco-driving performance assessment with in-car visual and haptic feedback assistance, Journal of Computing and Information Science in Engineering, 11(4), p. 181–190.

Barlow, T., Latham, S., McCrae, I., Boulter, P., 2009. A reference book of driving cycles for use in the measurement of road vehicle emissions. HIS, Bracknell, UK.

Hunt, S., Odhams, A., Roebuck, R., Cebon, D., 2011. Parameter measurement for heavy-vehicle fuel consumption modelling, Proceedings of the Institution of Mechanical Engineers Part D-Journal of Automobile Engineering, 225, p. 567–589.

Maciejowski, J., 2002. Predictive Control: With Constraints, Prentice-Hall, London.

Mulder, M., Abbink, D., van Paassen, M., Mulder, M., 2011. Design of a haptic gas pedal for active car-following support, IEEE Transactions on Intelligent Transportation Systems, 12(1), p. 268–279.

Na X. and Cole D.J., 2013. Linear quadratic game and non-cooperative predictive methods for potential application to modelling driver–AFS interactive steering control, Vehicle System Dynamics, 51(2), p. 165–198.

Rawlings, J. and Mayne, D., 2009, Model predictive control: theory and design, Nob Hill Pub, Madison, Wis.

Varhelyi, A., Hjalmdahl, M., Hyden, C., Draskoczy, M., 2004. Effects of an active accelerator pedal on driver behaviour and traffic safety after long-term use in urban areas, Accident Analysis and Prevention, 36 (5), p. 729–737.

Advanced Vehicle Control – Edelmann, Plöchl & Pfeffer (Eds)
© 2017 Taylor & Francis Group, London, ISBN 978-1-138-02992-7

Inferring driver's deceleration intent in vehicle platoon system by using feedback estimators

H. Suzuki
Nippon Institute of Technology, Saitama, Japan

T. Ishikura
Graduate School of Nippon Institute of Technology, Saitama, Japan

T. Nakatsuji
Hokkaido University, Sapporo, Japan

ABSTRACT: This research proposed a particle filter and unscented Kalman filter to estimate the velocity and headway of three platooned vehicles and to predict the deceleration intent of the last vehicle expected to occur a few seconds later. In the state equations of the PF and the UKF, the trend and the GHR model were both tested as the updated algorithms of the vehicle velocity. Numerical analyses using the field test data showed that both PF an UKF successfully estimated the velocity and headway of platooned vehicles and also predicted the trend and intensity of the driver's deceleration intent that occurred 1.5 s later. However, the prediction contains some uncertainty, because the acceleration and deceleration behaviors include the randomness of the human driver. Relaying the forecasted uncertain intent to the following car driver is the key issue, although the inferred intention was not completely accurate and appropriate interface is needed.

1 INTRODUCTION

Rear-end collisions in longitudinal car-following situations occasionally cause severe multiple-collision accidents, especially in high-density and high-speed traffic. Use of the autonomous collision avoidance system (ACAS), which is one of the active safety measures of the Advanced Driver Assistance System (ADAS), may provide a solution to this problem. Instead of the direct vehicle control provided by an ACAS, an estimation or prediction of driver intentions can also provide a useful solution to accident avoidance. For example, if a driver's intended braking and lane-changing actions can be inferred in advance, appropriate measures may be applied to prevent ensuing accidents.

To date, numerous studies have investigated ways to infer a driver's intent in terms of active safety. The most popular research has used mathematical approaches to infer the lane-changing intent. These approaches include sparse Bayesian learning (SBL), support vector machines (SVM), and particle filters (PFs) (McCall et al. 2007, Doshi and Trivedi 2008, 2009a, 2009b, Salvucci 2004, Gunnarson et al. 2006). The intention inference has been extended to the problem of judging stop-or-go decision making at signalized intersections by using machine learning techniques, for example, SVM-Bayesian filter (SVM-BF), hidden Markov model (HMM), Bayesian network (BN), and linear regression analyses (LRA) (Aoude et al. 2012, Kumagai et al. 2006, Mabuchi & Yamada, 2013). Other interesting research has investigated the inference of turning behavior at intersections (Liebner et al. 2013, Lidstorm & Larsson 2008). By measuring the vehicle velocity and position, the driver's intention was predicted regardless of turning signal activation.

With the exception of studies by Saito et al. (2012a, 2012b), significantly less attention has been given to the estimation and prediction of a driver's longitudinal behavior, even though it has considerable applicability to the rear-end collision avoidance problem. However, the driver's longitudinal behavior has been a focus in the research on enhanced brake lighting systems (Sivak & Flannagan 1993, Neurauter et al. 2009, Schaudt et al. 2013). These studies investigated systems that detect when a driver places his/her foot on the brake pedal (cover BP) and reports this action to the driver of the following car by illuminating an amber light indicator placed near the high-mount stop lamp. Because the following driver is able to recognize the braking intent of the preceding car at an earlier time and thus react more quickly when the brake light actually appears, the risk of a rear-end collision can be decreased. However, the algorithm in the above studies is quite primitive, because the system measures only the cover BP. Additionally, according to the results of a field test using a test car, only 80% of cover BP actions lead to actual brake pedal operation.

The current study proposes an alternative algorithm for predicting a driver's deceleration intent based on the unscented Kalman filter (UKF) and a particle filter (PF) integrated with the conventional car-following model. The proposed approach estimates the headway and velocity of multiple cars in a platoon and then predicts the driver's deceleration intent that is expected to occur a few seconds later. The precision levels of the proposed algorithms are evaluated by using the data collected on a field test carried out on a test track.

2 THEORETICAL BACKGROUND

2.1 *State-space model*

The following state and measurement equations are defined as the state-space model, which is required for the feedback estimation:

$$\mathbf{x}_k = \mathbf{f}\left(\mathbf{x}_{k-1}\right) + \mathbf{v}_{k-1} \quad \text{and} \quad \mathbf{y}_k = \mathbf{g}\left(\mathbf{x}_k\right) + \mathbf{n}_k . \tag{1}$$

Here, $\mathbf{x}_k$ and $\mathbf{y}_k$ are state and measurement variables, respectively, at time k, $\mathbf{v}_k$ and $\mathbf{n}_k$ are system and measurement errors, respectively, and $\mathbf{f}$ and $\mathbf{g}$ are possibly nonlinear functions. Let $\mathbf{y}_{1:k}$ and $\mathbf{x}_{1:k}$ denote the sets of all available measurement and state variables up to time k as follows:

$$\mathbf{y}_{1:k} \equiv \left\{\mathbf{y}_1, \mathbf{y}_2, \ldots, \mathbf{y}_k\right\} \quad \text{and} \quad \mathbf{x}_{1:k} \equiv \left\{\mathbf{x}_1, \mathbf{x}_2, \ldots, \mathbf{x}_k\right\}. \tag{2}$$

Then, the estimation problem is to calculate the posterior probability $p(\mathbf{x}_k|\mathbf{y}_{1:k})$ when given a set of all measurements $\mathbf{y}_{1:k}$. If measurement $\mathbf{y}_k$ is available, the posterior is updated through Bayes' rule:

$$p\left(\mathbf{x}_k|\mathbf{y}_{1,k}\right) = \frac{p\left(\mathbf{x}_k|\mathbf{y}_{1,k-1}\right) \cdot p\left(\mathbf{y}_k|\mathbf{x}_k\right)}{p\left(\mathbf{y}_k|\mathbf{y}_{1,k-1}\right)}. \tag{3}$$

Here, $p(\mathbf{y}_k|\mathbf{x}_k)$ is a likelihood function that describes the likelihood of $\mathbf{x}_k$ given measurement $\mathbf{y}_k$. The prior probability of $\mathbf{x}_k$, which is $p(\mathbf{x}_k|\mathbf{y}_{1:k-1})$, is given by

$$p\left(\mathbf{x}_k|\mathbf{y}_{1,k-1}\right) = \int p\left(\mathbf{x}_k|\mathbf{x}_{k-1}\right) \cdot p\left(\mathbf{x}_{k-1}|\mathbf{y}_{1,k-1}\right) d\mathbf{x}_{k-1}. \tag{4}$$

Additionally, $p(\mathbf{y}_k|\mathbf{y}_{1:k})$ is defined as

$$p\left(\mathbf{y}_k|\mathbf{y}_{1,k-1}\right) = \int p\left(\mathbf{y}_k|\mathbf{x}_k\right) \cdot p\left(\mathbf{x}_k|\mathbf{y}_{1,k-1}\right) d\mathbf{x}_k . \tag{5}$$

2.2 *Particle filter (PF)*

The PF is a feedback estimator that theoretically places random particles in a probability field in order to yield an accurate posterior probability density function (PDF) based on Bayes' theorem (Arulampalam et al. 2002). The key idea of the PF is to represent the required posterior PDF by a set of random samples with associated weights and to compute the estimates based on these samples and weights (Doucet & Johansen 2011). The estimates obtained through the filtering process are suboptimal. The estimation process of the PF is as follows:

1. Initial sampling: Generate initial particles $\hat{\mathbf{x}}_0^{(i)}$ $(i = 1, 2, \ldots, M)$ at $k = 0$ from the initial probability density function $p(\hat{\mathbf{x}}_0)$.
2. Importance sampling: Generate a one-step prediction of samples $\tilde{\mathbf{x}}_k^{(i)}$ and $\tilde{\mathbf{y}}_k^{(i)}$ based on the state and measurement equations:

$$\tilde{\mathbf{x}}_k^{(i)} = \mathbf{f}\left(\hat{\mathbf{x}}_{k-1}^{(i)}\right) + \mathbf{v}_{k-1}^{(i)} \quad \text{and} \quad \tilde{\mathbf{y}}_k^{(i)} = \mathbf{g}\left(\tilde{\mathbf{x}}_i^{(i)}\right) + \mathbf{n}_k . \tag{6}$$

3. Importance weight: Calculate the importance weight $\tilde{w}_k^{(i)}$ for each sample with the following equation:

$$\tilde{w}_k^{(i)} = w_k^{(i)} \frac{p\left(\tilde{\mathbf{x}}_k^{(i)}|\mathbf{x}_{k-1}^{(i)}\right) p\left(\mathbf{y}_k|\tilde{\mathbf{x}}_k^{(i)}\right)}{q\left(\tilde{\mathbf{x}}_k^{(i)}|\mathbf{x}_{k-1}^{(i)}, \mathbf{y}_{1,k}\right)} \left(i = 1, 2, \ldots, M\right). \tag{7}$$

   Larger weight is given to particles that have prediction $\tilde{\mathbf{y}}_k^{(i)}$ closer to the actual measurement $\mathbf{y}_k$.
4. Resampling: The particle $\tilde{\mathbf{x}}_k^{(i)}$ is updated to $\hat{\mathbf{x}}_k^{(i)}$ in proportion to the importance weight $\hat{w}_k^{(i)}$.
5. Normalize weight: Normalize the importance weight to $\hat{w}_k^{(i)}$ by

$$\hat{w}_k^{(i)} = \frac{\tilde{w}_k^{(i)}}{\sum_{j=1}^{M} \tilde{w}_k^{(j)}} . \tag{8}$$

6. Estimation: From the updated particles $\hat{\mathbf{x}}_0^{(i)}$, compute the estimate by

$$\hat{\mathbf{x}}_k \approx \frac{1}{M} \sum_{i=1}^{M} \hat{\mathbf{x}}_k^{(i)} \left(= \sum_{i=1}^{M} \hat{w}_k^{(i)} \tilde{\mathbf{x}}_k^{(i)} \right). \tag{9}$$

2.3 *Unscented Kalman filter (UKF)*

The UKF is one of the *derivative-free* Kalman filters, which require no partial derivative calculations of the state and measurement equations (Haykin 2011). The conventional extended Kalman filter (EKF) provides a first-order approximation of the optimal estimates, whereas the unscented Kalman filter captures the posterior mean and covariance accurately by second-order Taylor expansions using a minimal set of carefully chosen sample points called sigma points (Haykin 2011). The first step to use the UKF is to generate sigma point $\mathbf{\Phi}_k$ by Equations 10 to 12:

$$\boldsymbol{\sigma}_{i,P} = \left(\sqrt{\left(N + \lambda\right)\mathbf{P}_k}\right)_i , \tag{10}$$

$$\begin{cases} \hat{\Phi}_{0,k-1} = \hat{\mathbf{x}}_0 \\ \hat{\Phi}_{i,k-1} = \hat{\mathbf{x}}_{k-1} + \boldsymbol{\sigma}_{i,P} \quad \left(i = 1, \ldots, N\right) \\ \hat{\Phi}_{i,k-1} = \hat{\mathbf{x}}_{k-1} - \boldsymbol{\sigma}_{i-N,P} \quad \left(i = N+1, \ldots, 2N\right) \end{cases}, \tag{11}$$

$$\tilde{\mathbf{\Phi}}_k = \mathbf{f}\left(\hat{\mathbf{\Phi}}_{k-1}\right), \tag{12}$$

where $\boldsymbol{\sigma}_i$ is the i-th column vector of the lower triangle matrix when applying Cholesky decomposition to $\mathbf{P}_k$, N is the number of state variables, and λ is a scaling parameter. One-step prediction of the state variables $\tilde{\mathbf{x}}_k$ and the error covariance $\mathbf{M}_k^{xx}$ are then given by

$$\tilde{\mathbf{x}}_k = \sum_{i=0}^{2N} h_i \tilde{\Phi}_{i,k}, \tag{13}$$

$$\mathbf{M}_k^{xx} = \sum_{i=0}^{2N} h_i \left[\tilde{\Phi}_{i,k} - \tilde{\mathbf{x}}_k\right]\left[\tilde{\Phi}_{i,k} - \tilde{\mathbf{x}}_k\right]^T + \mathbf{V}_{k-1}. \tag{14}$$

Here, h_i is the weight defined as $h_i = 1/(2(N+\lambda))$. The same procedure is applied to compute the one-step prediction of measurement variables $\tilde{\mathbf{y}}_k$.

$$\boldsymbol{\sigma}_{i,M} = \left(\sqrt{(N+\lambda)\mathbf{M}_k}\right)_i, \tag{15}$$

$$\begin{cases} \tilde{\Omega}_{0,k-1} = \tilde{\mathbf{x}}_0 \\ \tilde{\Omega}_{i,k} = \tilde{\mathbf{x}}_k + \boldsymbol{\sigma}_{i,M} \quad (i = 1,\ldots,N) \\ \tilde{\Omega}_{i,k} = \tilde{\mathbf{x}}_k - \boldsymbol{\sigma}_{i,M} \quad (i = N+1,\ldots,2N) \end{cases}, \tag{16}$$

$$\tilde{\Psi}_k = \mathbf{g}\left(\tilde{\Omega}_k\right), \tag{17}$$

$$\tilde{\mathbf{y}}_k = \sum_{i=0}^{2N} h_i \tilde{\Psi}_k. \tag{18}$$

Then, the covariance $\mathbf{M}_k^{yy}$ and $\mathbf{M}_k^{xy}$ are defined as follows:

$$\mathbf{M}_k^{yy} = \sum_{i=0}^{2N} h_i \left[\tilde{\Psi}_{i,k} - \tilde{\mathbf{y}}_k\right]\left[\tilde{\Psi}_{i,k} - \tilde{\mathbf{y}}_k\right]^T + \mathbf{W}_{k-1}, \tag{19}$$

$$\mathbf{M}_k^{xy} = \sum_{i=0}^{2N} h_i \left[\tilde{\Phi}_{i,k} - \tilde{\mathbf{x}}_k\right]\left[\tilde{\Psi}_{i,k} - \tilde{\mathbf{y}}_k\right]^T. \tag{20}$$

The Kalman gain $\mathbf{K}_k$ is computed by Equation 21 from the error covariance $\mathbf{M}_k^{yy}$ and $\mathbf{M}_k^{xy}$. In addition, the optimal estimates $\hat{\mathbf{x}}_k$ and $\mathbf{P}_k$ are updated by Equations 22 and 23. In Equations 14 and 19, $\mathbf{V}_k$ and $\mathbf{W}_k$ are the covariance of the system and the measurement noises.

$$\mathbf{K}_k = \mathbf{M}_k^{xy}\left(\mathbf{M}_k^{yy}\right)^{-1}, \tag{21}$$

$$\hat{\mathbf{x}}_k = \tilde{\mathbf{x}}_k + \mathbf{K}_k\left(\mathbf{y}_k - \tilde{\mathbf{y}}_k\right), \tag{22}$$

$$\mathbf{P}_k = \mathbf{M}_k^{xx} - \mathbf{K}_k \mathbf{M}_k^{xx} \mathbf{K}_k^T. \tag{23}$$

3 MODEL FORMULATION

3.1 *Vehicle platoon*

Consider multiple vehicles traveling along a corridor, as shown in Figure 1. Let v_i and d_i denote the velocity and headway of the i-th vehicle, respectively. Assuming that the 2nd vehicle is equipped with sensors to measure d_2, d_3, and v_2, what the PF and UKF do is to calculate the velocity and headway, v_1, v_2, v_3, d_2, and d_3, of all three cars preceding the host vehicle. If all these variables are identified in real time, the acceleration rate of the 3rd vehicle, a_3, which is expected to occur a few seconds later, can be predicted in advance by the Gazis-Herman-Rothery (GHR) model, which is a well-known car-following model.

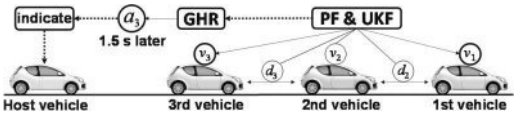


Figure 1. Four-vehicle platoon.

If the predicted a_3 is reported to the following 4th (host) vehicle earlier than the 3rd-car brake pedal operation is reported, the following driver thus reacts much faster when a brake light actually appears, and the risk of a rear-end collision can be decreased. As the number of vehicles in the platoon increases, the collision risk is reduced and amplified along the platoon, and so the traffic becomes safer and more stable.

3.2 *Model to update velocity and headway*

The conventional model to update the velocity is defined as a simple trend model, and the headway is computed by a conservation equation as follows:

$$v_i(k) = v_i(k-1) \quad (i = 1,2,3), \tag{24}$$

$$d_i(k) = d_i(k-1) + \left[v_{i-1} - v_i\right]_{(k-1)} \Delta t \quad (i = 2,3). \tag{25}$$

As can be seen in Equation 24, the trend model does not guarantee accuracy, because the velocity is assumed to be equal between two consecutive time steps $k-1$ and k. To improve the estimation accuracy, we introduce the GHR car-following model for describing the velocity and rewrite Equation 24 into 26:

$$v_i(k) = \begin{cases} v_i(k-1) & (i=1) \\ v_i(k-1) + \left[\alpha \dfrac{v_i^n}{d_i^m}\left(v_{i-1} - v_i\right)\right]_{(k-T)} \Delta t & (i=2,3) \end{cases}. \tag{26}$$

Here, Δt is the discrete time step and α, m, and n are the parameters for the GHR model. T is the reaction time of a vehicle ($T > 0$). The trend model should be still used for v_1 because no vehicle is ahead of the 1st car.

3.3 *Estimation of velocity and headway*

A problem of the estimation is calculating the state variables $\mathbf{x}_k = [v_2, d_2, v_3, d_3, v_1]_{(k)}^T$ from the measurements $\mathbf{y}_k = [v_2, d_2, d_3]_{(k)}^T$. Then, the state and measurement equations can be written in vector-matrix form as follows:

$$\begin{cases} \mathbf{x}_k = \mathbf{F}\left[\mathbf{x}_{k-1}, \mathbf{u}_{k-1}\right] + \mathbf{v}_{k-1} \\ \mathbf{y}_k = \mathbf{G}\left[\mathbf{x}_k, \mathbf{u}_k\right] + \mathbf{n}_k \end{cases}. \tag{27}$$

In Equation 27, $\mathbf{u}_k$ is a known exogeneous input. The function **F** could be a trend model or the GHR model for the velocity update and the conservation equation for the headway calculation. **G** is defined as a simple coefficient:

$$\mathbf{G} = \begin{pmatrix} 1 & 0 & 0 & 0 & 0 \\ 0 & 1 & 0 & 0 & 0 \\ 0 & 0 & 0 & 1 & 0 \end{pmatrix}. \quad (28)$$

3.4 *Prediction of deceleration intent*

The driver's deceleration intent could be a reflection of the acceleration rate of a vehicle. After state variables $\mathbf{x}_k$ are estimated through the feedback process of the PF and the UKF, the prediction of the acceleration rate $a_i(k+T)$ that is expected to occur T seconds later is given by the GHR model as follows:

$$a_i(k+T) = \alpha w \frac{v_i^n}{d_i^m}(v_{i-1} - v_i) + \alpha(1-w)\frac{v_i^n}{d_{i-1}^m + d_i^m}(v_{i-2} - v_{i-1}) \quad (i=3) \quad (29)$$

Equation 29 considers not only the preceding vehicle immediately ahead but also the vehicle in front of the preceding vehicle (i.e., pre-preceding vehicle) for computing the acceleration rate. Here, w $(0 < w < 1)$ is the balancing factor for deciding which preceding car has more influence on the acceleration rate of the following vehicle.

4 NUMERICAL EXPERIMENT

4.1 *Field data collection*

A car-following experiment using ten test vehicles was carried out on a test track at Tomakomai in Hokkaido, Japan in 2001. The participants were requested to travel at a steady speed around 60 km/h and were advised to keep a constant headway. When the 1st vehicle accelerated and decelerated in various patterns, the drivers were to react with the preceding and/or pre-preceding vehicles as they normally would.

In this research, we selected the data from the first three cars of the ten-vehicle platoon and prepared five car-following scenarios for the evaluation.

4.2 *Conditions*

The parameters of the GHR model are set as $\alpha = 1.2$, $m = n = 1$, and $\Delta t = 0.1$ s. The reaction time of driver T is assumed to be 1.5 s based on the car-following data. The balancing factor w of 0.5 means that we treat the influence of preceding and pre-preceding cars equally for calculating the acceleration rate. The variance of noises $\mathbf{v}(k)$ and $\mathbf{n}(k)$ are 0.1 and 0.2–0.3, respectively. The number of particles in the PF is set to 1000 and the scaling parameter λ in the UKF is 5.

Because v_1 and v_3 are not observed but are the keys to predict the deceleration intent, the performances of the PF and UKF are evaluated by comparing v_1 and v_3 with the true values and the estimates by the trend and GHR models for the state equation. The predicted acceleration a_3 is then assessed by computing the root mean square errors (RMSE) defined as follows:

$$RMSE = \sqrt{\sum_{i=1}^{N}(\hat{x} - x)^2 \Big/ N}. \quad (30)$$

where $\hat{x}$ is the estimate, x is the true value, and N is the total number of data.

4.3 *Estimation of velocity and headway*

4.3.1 *Velocity estimation*

Figure 2 illustrates the v_3 estimates by the PF and the UKF for a car-following scenario. By using the trend model defined by Equation 24, a small delay occurs for the whole time period, whereas by using the GHR model in Equation 26, the delay was eliminated to yield a more accurate estimate. Much less difference was seen in the estimation accuracy between the PF and the UKF.

As expected in the model development stage, v_1 (Fig. 3) was not as accurate as v_3 because the GHR model cannot be integrated with the state equation for modeling v_1. The delay remains in the estimation

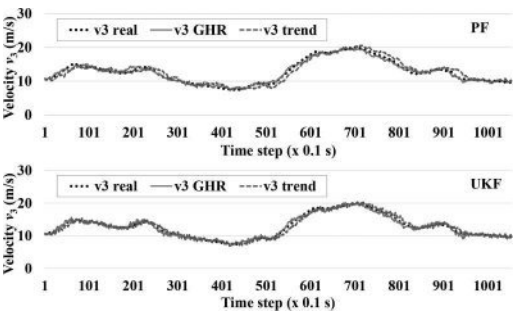


Figure 2. Estimation of v_3 (upper: PF, lower: UKF).

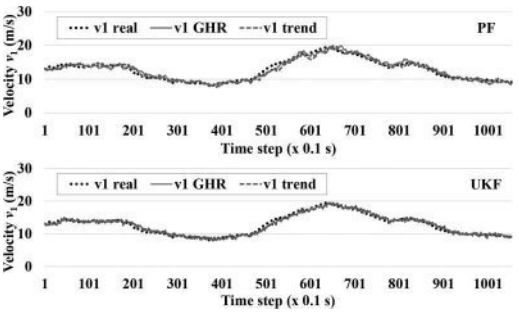


Figure 3. Estimation of v_1 (upper: PF, lower: UKF).

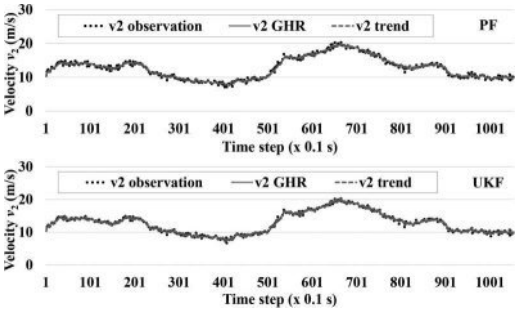


Figure 4. Estimation of v_2 (upper: PF, lower: UKF).

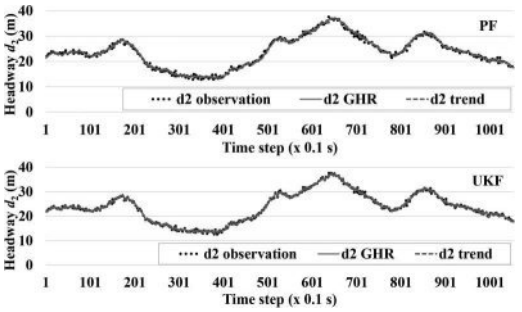


Figure 5. Estimation of d_2 (upper: PF, lower UKF).

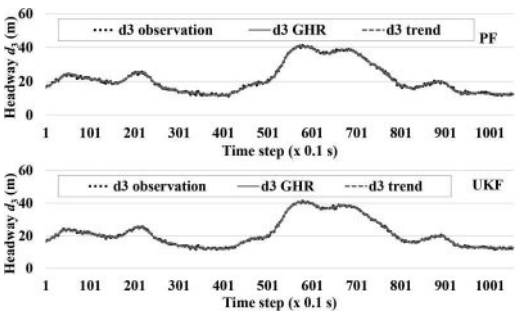


Figure 6. Estimation of d_3 (upper: PF, lower: UKF).

for both PF and UKF (Fig. 3). For the v_2 estimation, depicted in Figure 4, it was found that the PF and UKF could eliminate the measurement noise to make the observed v_2 more reliable.

4.3.2 *Headway estimation*

The estimates of d_2 and d_3 by the PF and the UKF are given in Figures 5 and 6, respectively. Because d_2 and d_3 are measured at the 2nd vehicle, the two estimators removed the measurement noise. Little or no difference was seen between the trend and the GHR models as well as between the PF and the UKF. The means and standard deviations of RMSEs are summarized in Figure 7. As shown in the figure, the estimation accuracy was satisfactory for all state variables as the RMSE are almost less than 1 m/s or 1 m.

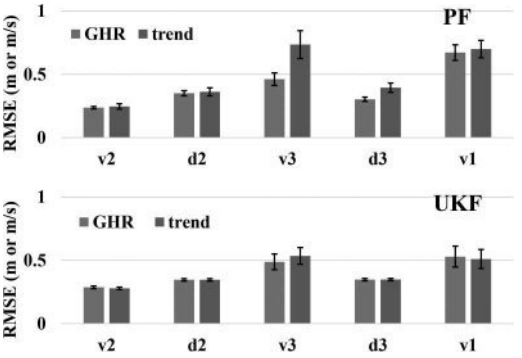


Figure 7. RMSEs for all state variables (upper: PF, lower: UKF).

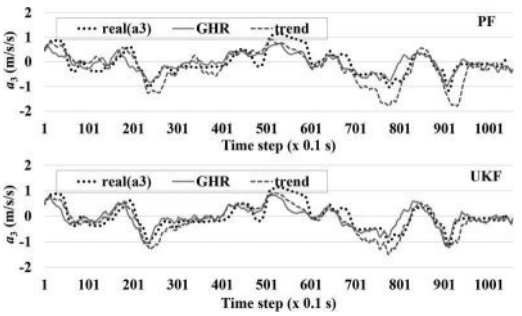


Figure 8. Prediction of a_3 (upper: PF, lower; UKF).

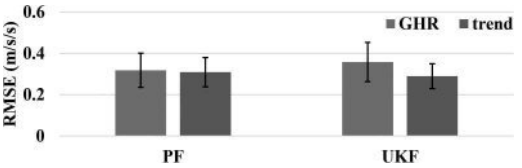


Figure 9. RMSE of predicted a_3 for PF and UKF.

4.4 *Prediction of deceleration intent*

Figure 8 depicts an example of the a_3 prediction that is expected to occur 1.5 s later, The prediction and the actual observation were compared. Here, the prediction was given as the moving average for ten steps (i.e., 1 s).

It seems that the algorithm using the GHR model shows better goodness-of-fit than that by the trend model both in the PF and the UKF. Especially, for the maximum deceleration rate, the trend model overestimates the deceleration rate, whereas the prediction by the GHR model fits the observation. The RMSE of the a_3 prediction is given in Figure 9. Little or no or difference is found in the precision between the PF and the UKF estimators.

4.5 *Discussion*

It is confirmed that our proposed algorithm tends to capture the trend and intensity of the driver's

deceleration intent and is able to predict the intent with precision. Obviously, however, the computed intent never completely fits the real observations, because the driver's intent contains a high level of behavior uncertainty (Fig. 8).

The key issue is to report the forecasted deceleration intent to the following car driver by taking into account its uncertainty. This issue is beyond this research, but an appropriate human machine interface (HMI) could be designed in further research to encourage the driver to prepare much earlier for the deceleration of the preceding car.

5 CONCLUDING REMARKS

This research proposed a particle filter and unscented Kalman filter to estimate the velocity and head-way of three platooned vehicles and to predict the deceleration intent of the last vehicle expected to occur 1.5 s later. In the state equations of the PF and the UKF, the trend and the GHR model were both tested as the updated algorithms of the vehicle velocity. A numerical analysis using the field test data showed the following.

- In the velocity estimation, the algorithm that used the GHR model yielded better goodness-of-fit than that using the trend model for both the PF and the UKF.
- The accuracy of the headway estimates were satisfactory, because the measurement noise was eliminated due to the filtering process by the PF and the UKF.
- Little or no difference between the PF and the UKF was found in the accuracy of the velocity and headway estimations.
- The proposed algorithm successfully predicted the trend and intensity of the driver's deceleration intent that occurred 1.5 s later. However, the prediction contains some uncertainty, because the acceleration and deceleration behaviors include the randomness of the human driver.

Additional studies should be conducted on how to report the predicted intent to the following car driver. Designing an appropriate HMI is also a key issue to encourage a driver to prepare for the deceleration of the preceding vehicle.

This work was supported by JSPS KAKENHI Grant Number 15K01230.

REFERENCES

Aoude, G. S., Desaraju, V. R., Stephens L. H. & How, J. P. 2012. Driver Behavior classification at intersections and validation on large naturalistic data set, *IEEE Trans. on Intelligent Transport Systems* 13(2): 724–736.

Arulampalam, M. S., Maskell, S., Gor-don N. & Clapp, T. 2002. A tutorial on particle filters for online nonlinear/non-Gaussian Bayesian tracking, I*EEE Transactions on Signal Processing* 50(2): 174–188.

Doshi, A. & Trivedi, M. 2008. A comparative exploration of eye gaze and head motion cues for lane change intent prediction, *2008 IEEE Intelligent Vehicles Symposium*: 49–54.

Doshi, A. & Trivedi, M. 2009. On the roles of eye gaze and head dynamics in predicting driver's intent to change lanes, *IEEE transactions on Intelligent Transportation Systems* 10(3): 453–462.

Doshi, A. & Trivedi, M. 2009. Investigating the relationships between gaze pattern, dynamic vehicle surround analysis and driver intentions, *Intelligent Vehicles Symposium*: 887–892.

Doucet, A. & Johansen, A. M. 2011. A tutorial on particle filtering and smoothing: fifteen years later, Oxford Handbook of Nonlinear Filtering.

Gunnarsson, J., Svensson, L., Bengtsson, E. & Danielsson, L. 2006. Joint driver intention classification and tracking of vehicles, *Nonlinear Statistical Signal Processing Workshop 2006 IEEE*: 95–98.

Haykin, S. 2001. Kalman filtering and neural networks, John Wiley & Sons.

Kumagai, T. & Akamatsu, T. 2006. Prediction of human driving behavior using dynamic Bayesian network, *IEICE Trans. of Inf. & Syst.*, E89-D(2): 857–860.

Lidstrom, K. & Larsson, T. 2008. Model-based estimation of driver intentions using particle filtering, *11th International IEEE Conference on Intelligent Transportation Systems*: 1177–1182.

Liebner, M., Baumann, M., Klanner, F. & Stiller, C. 2013. Velocity-based driver intent inference at urban intersections in the presence of preceding vehicles, *Intelligent Transportation Systems Magazine Summer 2013*: 10–21.

Mabuchi, R. & Yamada, K. 2013. Prediction of driver's stop or go at yellow traffic signal from vehicle behavior, *2013 IEEE Intelligent Vehicles Symposium (IV)*: 1161–1166.

McCall, J. C., Wipf, D. P., Trivedi, M. M. & Rao B. D. 2007. Lane change intent analysis using robust operators and sparse Bayesian learning, *IEEE Trans. on Intelligent Transportation Systems* 8(3): 431–440.

Rothery, R.W. 1998. Car following models, in "Revised Monograph on Traffic Flow Theory". In: Gartner, N. Messer, C. J., Rathi, A. K. (Ed.). FHWA.

Neurauter, M. L., Llaneras, R. E. & Wierwille, W. W. 2009. The design and assessment of attention-getting rear brake light signals, *Proc. of the Fifth International Driving-Symposium on Human Factors in Driver Assessment, Training and Vehicle Design*: 529–535.

Saito, Y., Hashimoto, N., Tsugawa, S. & Kato, S. 2012. Development of deceleration intention indicating system of forward vehicle: effect of the system, *15th International IEEE Conference on Intelligent Transportation Systems*: 852–857.

Saito, Y., Hashimoto, N., Tsugawa, S. & Kato, S. 2012. Development on indicating system of information of deceleration intention to following vehicle – suggestion and fundamental experiment-, *2012 IEEE International Conference on Vehicular Electronics and Safety*: 157–162.

Salvucci, D. D. 2004. Inferring driver intent: a case study in lane-change detection, *Proceedings of the Human Factors Ergonomics Society 48th Annual Meeting*.

Schaudt, W. A., Bowman, D. S., Baker, S., Hanowski, R. J. & Flanigan, C. 2013. Field evaluation of an enhanced rear signalling system for heavy trucks, *IET Intelligent Transport Systems* 7(3): 345–350.

Sivak, M. & Flannagan, M. J. 1993. Fast-rise lamp as a collision-prevention device, Report No. UMTRI-93-5.

Advanced Vehicle Control – Edelmann, Plöchl & Pfeffer (Eds)
© 2017 Taylor & Francis Group, London, ISBN 978-1-138-02992-7

Driver's steering torque modeling based on lateral deviation and reaction torque

Hidehisa Yoshida, Junya Yamakawa & Toyoyuki Honjo
National Defense Academy, Yokosuka, Japan

ABSTRACT: During high-speed driving, it can be experientially understood that it is a steering work during steering operation not by the steering angle but by the torque added to the steering wheel. This research uses the driver's steering torque for the driver model construction. The proposed basic driver model considers both lateral deviation, as viewed in front of the vehicle, and reaction torque of steering axis for the model input. The driver's steering torque during the lane change steering and a crosswind disturbance response by DS experiments are examined. Identified driver parameters by the proposed model are shown.

1 INTRODUCTION

The need of steering avoidance technology exists for situations such as high-speed driving or low road surface friction. Future research and development are expected. In a corporative steering assistance system, if an assistance system which cooperates driver's steering operation are different from driver's recognition, the danger of an accident rises in the actual driving conditions.

It is known that the driving characteristic is modified by the assistance effect (McRuer, D. T. and Jex, H. R., 1967). In order to design an effective driving assistance system, it is necessary to take various driving characteristics and how they affect steering into consideration.

During high-speed driving, lane-changing steering is possible to operate by a small steering angle, and it can be experientially understood that it is not a steering work by the steering angle but a steering work by the torque added to the steering wheel. In the case of steering assist, steering operation is intervened by an assistance system and a driver (Nagai, M. et al. 2006).

In this research, for the construction of necessary driver model for design, effect evaluation and verification of the steering assistance system under high-speed driving, it is the goal of this research that the steering torque model of the driver over a series of the steering action is modeling to understand the physical meaning. In this research, the driver's steering torque during the lane change steering and a crosswind disturbance response by driving simulator (DS) experiments are examined. Identified driver parameters by the proposed model are shown.

2 TORQUE MODEL OF DRIVER STEERING

Proposed modeling of the driver steering model is examined by steering torque in the lane-changing which steers on the basis of front field of view and reaction torque of steering wheel. This modeling subject is to reproduce a steering torque response by the driver who controls actively as usual by his car in high-speed running.

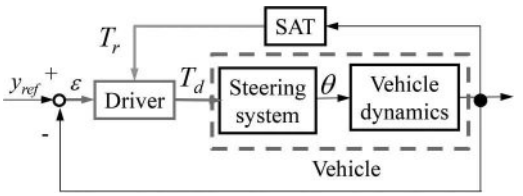


Figure 1. Block diagram of driver steering control to the vehicle behavior. The inputs of a driver's steering are lateral deviation ε and steering reaction torque on a steering wheel T_r. The output of a driver's steering is steering torque T_d.

In this research, modeling of the driver's steering torque is based on the transfer function expression by Equation (1). Figure 1 shows block diagram of this driver model. This research examines both a model identification and a modeling of steering torque in which the driver inputs to the steering wheel in the DS experiment.

$$T_{dm}(s) = G_1(s)\,\varepsilon(s) + G_2(s)\,T_r(s) \tag{1}$$

The DS used in this research shown in Figure 2 reproduces a front field of view on the monitor, the noise of the vehicle and the steering reaction torque on the steering wheel.

2.1 *Driver model inputs*

Most studies of a driver model using steering angle input are based on the driver's steering to maintain a desired course and the lateral position input from the front viewpoint (Kondo, M., 1958). The steering model



Figure 2. Driving simulator (DS) for this research reproduces a front field of view on the monitor, the noise of the vehicle, and the steering reaction torque on the steering wheel.

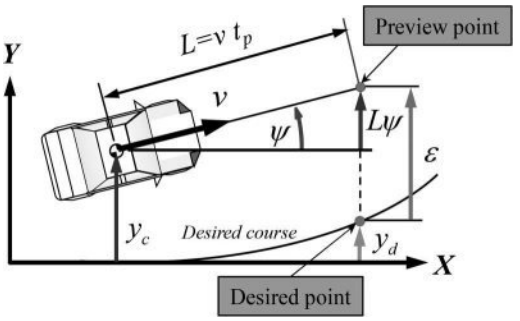


Figure 3. Driver's steering input ε based on the lateral deviation to the desired course in the front view point.

in this research is also based on this. Figure 3 shows the driver's steering input based on the lateral deviation to the desired course in the front viewpoint. This lateral deviation ε in the Equation (2) is determined by the experimental data on both the lane change steering and a crosswind disturbance response.

$$\varepsilon(t) = y_c + L\psi - y_{ref} \tag{2}$$

On the steering shaft of DS steering wheel, the reaction torque based on self-aligning torque shown by multiplying the caster trail ξ and front tire lateral force F_{yfl}, F_{yfr} of left and right is reproduced.

$$T_{SAT} = -\xi\left(\boldsymbol{F}_{yfl} + \boldsymbol{F}_{yfr}\right) \tag{3}$$

2.2 *Transfer of steering operation modes*

It is possible to interpret lane changing in a high-speed driving scenario by dividing it into two segments. One segment is when the lane-changing starts (course changing operation) and the other is when the driving course is corrected in order to keep driving in the new lane (lane keeping operation). In the initial course change operation, a comparatively large steering operation is carried out, and the vehicle body attitude angle increases. After the course change operation, a steering

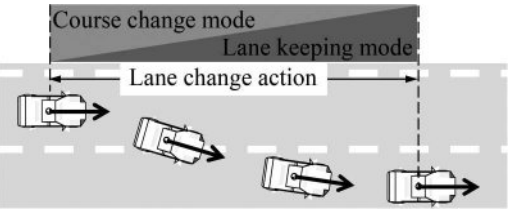


Figure 4. Outline of steering torque model transition in the lane change from course change mode to lane keeping mode.

correction is conducted for the purpose of keeping the lane so that the vehicle will not deviate from the desired course.

So in this driver model, it is proposed that the two steering operation mode transfer is considered as a concept. This concept of steering operation mode transition in high-speed running is shown in Figure 4.

Our proposed driver model of the driver's steering torque which includes course change operation mode T_{dmc}, lane keeping operation mode T_{dmk}, and the effect of reaction torque T_{dmr} is considered in Equation (4).

The transition weight function α (Equation (5)) in Equation (4) is proposed for the steering action change continuously from course change mode to lane keeping mode based on lateral deviation ε in the front view point which is the visual information of the driver. This transition weight function α is made dimensionless.

$$\begin{aligned} T_{dm}(s) &= T_{dmc} + T_{dmk} + T_{dmr} \\ &= (1-\alpha)\left\{G_h \frac{1}{(\tau_2 s+1)(\tau_3 s+1)} e^{-\tau_{L1} s}\right\}\varepsilon(s) \\ &\quad + \alpha\left\{G_h \frac{\tau_1 s+1}{(\tau_2 s+1)(\tau_3 s+1)} e^{-\tau_{L1} s}\right\}\varepsilon(s) \\ &\quad + \left\{-G_r\, e^{-\tau_{L2} s}\right\} T_r(s) \\ &= G_h \frac{\alpha\tau_1 s+1}{(\tau_2 s+1)(\tau_3 s+1)} e^{-\tau_{L1} s}\varepsilon(s) - G_r e^{-\tau_{L2} s} T_r(s) \end{aligned} \tag{4}$$

$$\alpha = \frac{y_{ref}(t) + \varepsilon(t)}{y_d} \tag{5}$$

2.3 *Crosswind disturbance response of steering operation*

On the lane change operation, transition weight function α changes by the lateral deviation ε. During crosswind disturbance, the lateral force by a crosswind force is impressed upon the vehicle compulsorily on straight line driving at high-speed. After that a driver steers a vehicle only to maintain a lane passively by lane keeping operation. So, lane keeping operation ($\alpha = 1$) applies to steering during crosswind disturbance in this driver model.

3 DRIVER PARAMETERS

3.1 *Driving simulator experiment*

During the DS experiment, the driver is asked to change to the adjacent lane (single lane change) or to keep to his own lane by the steering wheel operation equal to a highway situation in which the examinee normally uses.

The examinees drive on a 2 lane highway. The drive line is straight, and the width of a lane is 3.6 m. It is also asked of the driver to keep a constant speed of 100 km/h by their own pedal operation.

In the experiment of crosswind disturbance shown in Figure 5, strong crosswind velocity $w = 15$ m/s constant (which needs to cancel to run on the highway) is impressed from the lateral direction of the body which goes for 3 seconds on the vehicle run in 100 km/h, and the experiment which makes the body deviate from a lane compulsorily is made.

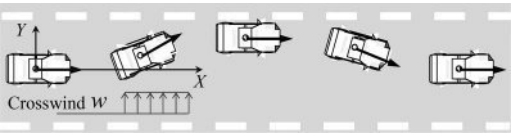


Figure 5. Outline of crosswind disturbance experiment. Driver controls the vehicle velocity keeping 100 km/h and to keep the own lane during a crosswind blowing.

3.2 *Driver steering response*

The model identification on the steering torque operation during crosswind disturbance was carried out. Figure 6 shows the DS experimental result. (a) shows the lateral position, desired course and lateral deviation in the front viewpoint. (b) shows the reaction torque on the steering shaft. (c) shows the result of calculating Equation (4) using examples of experimental result.

The blue line at Figure 6(c) is steering torque T_d, obtained by a DS experiment. The red dashed line shows steering torque T_{dmk} for the lane keeping operation mode. The redspot line has shown steering torque T_{dmr} in proportion to the reaction torque. The red continuous line has shown steering torque T_{dm} which the mode of these two are totaled.

The steering torque T_{dmk} of the lane keeping mode at the beginning doesn't generate the driver's steering torque by a sudden crosswind input but controls to keep the lane near $t = 5$ [s]. The steering torque T_{dmr} of reaction torque mainly generates the driver's steering torque at the beginning.

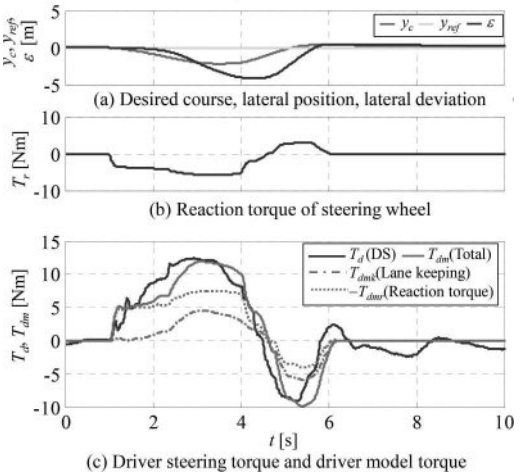


Figure 6. Output of driver steering torque based on DS experiment result by calculation from the driver model with components of lane keeping mode and reaction torque mode.

Table 1. Subjects for DS experiment of crosswind disturbance.

	Gender	Age	Driving experience [Years]	Driving frequency [per month]
a	Male	45	25	4
b	Male	33	16	8
c	Male	30	8	8
d	Male	22	3	1

3.3 *Driver parameter of crosswind disturbance*

The model identification on the steering torque during crosswind disturbance experiments by the four examinees that they showed in Table 1 was carried out. Driver parameter of lead time τ_1 and the proportional gain G_r for the steering reaction torque are examined. The preview time as $t_p = 1.5$ [s] (constant) lag time as $\tau_{L1} = 0.2$ [s] (constant) in the front view point and proportional gain $G_h = 0.3$ (constant) for the lateral deviation ε in the front view point are set. In order to ensure properness of the transfer characteristic, $\tau_2 = 0.05$ [s], $\tau_3 = 0.01$ [s] are constant.

3.4 *Driver parameters*

The driver parameters identified by the steering response experiment during crosswind disturbance is examined. Figure 6 shows the lead time τ_1 and reaction torque gain G_r. Mean value and standard deviation of each examinee of the driver parameter are shown. They are not observed in the examinee by the 5% significant using Bonferroni-correction.

When the driver steers during a lane-change steering, the steering response is active steering intended by the driver and it tends to be the looseness of the driver parameter by every driver. On the other hand, steering response by crosswind disturbance is passive steering for a driver, and there is no difference on the looseness of the driver parameter. It is supposed that the ability of steering by a sudden disturbance causes few differences by every driver.

The lane-changing experiment by the five subjects was carried out (Yoshida and Yamaguchi, 2015).

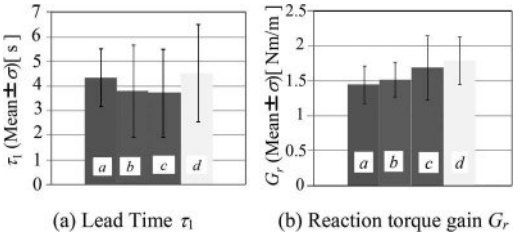


Figure 7. Mean value and standard deviation of every subject difference at driver parameters on proposed driver model during crosswind disturbance experiment.

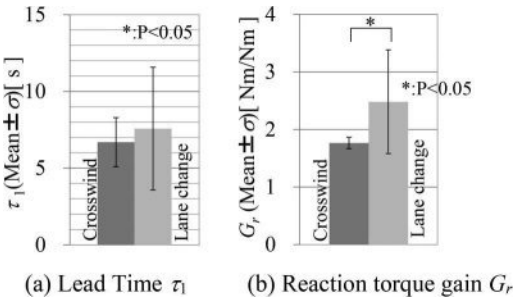


Figure 8. Mean value and standard deviation of driver parameter τ_1 and G_r compared with results by crosswind disturbance and lane-changing.

Figure 8 shows the characteristic parameters identified by experimental results by crosswind disturbance and lane-changing as same as Figure 7. It is confirmed that the mean and the standard deviation on the lead time τ_1 and reaction torque gain G_r are small together, compared with the intended steering in lane changing.

4 CONCLUSION

This research uses the driver's steering torque for the driver model construction. The proposed basic driver model considers both lateral deviation, as viewed in front of the vehicle, and reaction torque of steering axis, for the model input. The driver's steering torque during a crosswind disturbance response by DS experiments are examined. Parameters of proposed model are shown.

From the results of the significance test of driver parameter of model identification from the lane change steering and crosswind response, it is proven that the proportional gain for the reaction torque may be unique to every subject.

This work was supported by Grant-in-Aid for Scientific Research (C), (25350491) from the Ministry of Education, Culture, Sports, Science and Technology of Japan.

REFERENCES

Iguchi. M., 1970, Man-Machine Systems, *Kyoritsu Shuppan Co., Ltd.*, 14–45. (in Japanese)

Kondo, M., 1958, Basic Relation which Exists between Steering of Car and Dynamics, *Trans. of JSAE*, No. 5, 40–43. (in Japanese)

McRuer, D. T. and Jex, H. R., 1967, A Review of Quasi-Linear Pilot Models, *IEEE Trans.*, HFE-8-3, 231–249.

Nagai, M., Shitamitsu, K., Yoshida, H. and Mouri, H., 2006, Over-Ride Characteristics of Lane-Keeping Control System using Steering Torque Input: A Study on Lateral Wind Response with a Driving Simulator, *Review of Automotive Engineering, JSAE*, 27(2), 273–248.

Yoshida, H. and Yamaguchi, H., 2015, Primitive Modelling of Driver's Steering Torque using Field of Front View and Reaction Torque, *Proc. of FAST-zero'15*, *Gothenburg, Sweden*, 606–911.

Advanced Vehicle Control – Edelmann, Plöchl & Pfeffer (Eds)
© 2017 Taylor & Francis Group, London, ISBN 978-1-138-02992-7

Modelling human steering behaviour at the limit of adhesion using robust nonlinear model predictive control

G. Braghieri & D. Cole
Department of Engineering, University of Cambridge, Cambridge, UK

ABSTRACT: The aim of the work is to measure, understand and model the steering behaviour of a human driver at the limit of adhesion. A robust nonlinear model predictive control strategy is implemented. The behaviour of the controller is investigated for nonlinear vehicles travelling at constant speed on circular paths at or near the limit of adhesion. The controller successfully maintains the vehicle as close to the path as the tyre friction allows. A parameter study shows that weighting values in the cost function, the driver's refractory period, and parameters of the driver's neuromuscular system have significant influence on the control action. Comparison to data from a driving simulator experiment indicates that the simulated control action bears some similarity to that of the human driver, although there are some discrepancies that require further investigation.

1 INTRODUCTION

The aim of the work is to measure, understand and model the steering behaviour of a human driver at the limit of a car's adhesion. With such a model it should be possible to obtain a better understanding of vehicle handling quality. This understanding might then enable desirable qualities to be designed into the vehicle during the early stages of the development process. Timings and Cole (Timings & Cole 2014) considered the vehicle steering task as a robust control problem. They assumed that the driver uses feedforward, open-loop control to generate nominal control actions (steering, throttle, brake). In the absence of disturbances and uncertainties these control actions would result in the vehicle trajectory matching that expected by the driver. However the presence of disturbances and uncertainties means that the driver must also perform feedback, closed-loop control to ensure that the vehicle trajectory follows the expected trajectory within acceptable limits. Timings and Cole used a Linear Quadratic Regulator (LQR) to represent the driver's feedback control action, but this has shortcomings when the vehicle is operating in the very nonlinear regime at the limit of adhesion. Johns and Cole (Johns & Cole 2015) extended the work of Timings and Cole by replacing the LQR feedback controller with a model predictive controller (MPC), to give better performance near the limit of adhesion, and to account for the intermittent nature of human cognitive behaviour. Although the intermittent MPC matched measured behaviour quite well, it had shortcomings when the tyres had a negative slope beyond the saturation point.

The objectives of the present work are to extend the work in (Timings & Cole 2014) and (Johns & Cole 2015) by employing a fully nonlinear optimisation in the MPC and by validating the model against data collected from a moving-base driving simulator. In this paper the vehicle and driver model are described, representative simulation responses are shown, and preliminary results from validation against a moving-base driving simulator experiment are presented.

2 VEHICLE MODEL

The vehicle model used for this study is a single-track 'bicycle' model with a random lateral force acting at the centre of mass and a random yaw moment to provide external disturbances. Figure 1 shows the vehicle model with the associated physical quantities. The equations of motion read:

$$M_t(\dot{v} + u\dot{\psi}) = F_{yf} + F_{yr} + F_{dist} \tag{1}$$

$$I_z\ddot{\psi} = aF_{yf} - bF_{yr} + M_{dist} \tag{2}$$

where M_t is the vehicle mass, I_z its rotational inertia, v the vehicle lateral velocity, u the forward velocity, ψ the absolute yaw angle, $\dot{\psi}$ the yaw rate, a the distance of the centre of mass (CoM) from the front axle and, b the distance of the centre of mass from the rear axle. F and M are forces and moments acting on the vehicle, where subscript $_y$ indicates the lateral direction, $_r$ and $_f$ rear and front respectively and $_{dist}$ disturbance. Tyres are nonlinear and modelled using a simplified version of the Pacejka magic formula (Pacejka 2002):

$$F_y = F_z\mu_{max}\sin(Q_y \arctan(\frac{\alpha\pi}{2\arctan(Q_y)})) \tag{3}$$

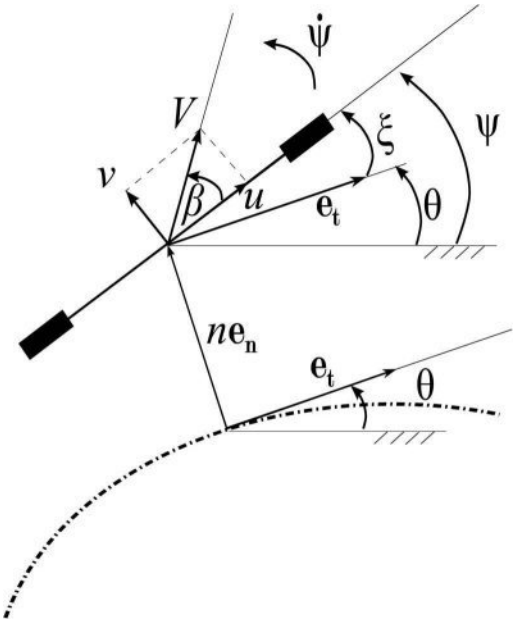


Figure 1. Vehicle model and coordinate description.

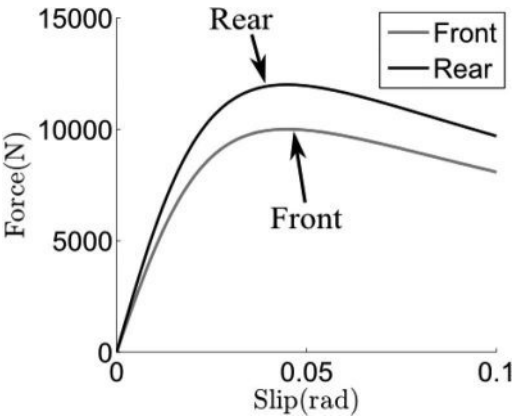


Figure 2. Front and rear tyre characteristics, lateral force as a function of slip angle.

where F_z is the vertical force, μ_{max} the maximum friction, Q_y is a shape factor and α the lateral slip. Figure 2 shows an example of front and rear tyre characteristics; while the slope is initially constant, it flattens out at saturation and becomes negative as slip increases further.

A second-order low pass filter placed in series with the steering angle input to the vehicle to account for the dynamics of the driver's neuromuscular system and the vehicle's steering mechanism:

$$\ddot{\delta}_{sw} + 2\zeta_n\omega_n\dot{\delta}_{sw} + \omega_n^2\delta_{sw} = \omega_n^2\delta_{com} \tag{4}$$

where δ_{com} is the hand wheel angle command signal from the driver, δ_{sw} is the resulting hand wheel angle, ω_n is the neuromuscular and steering system natural frequency and ζ_n the damping ratio.

3 DRIVER MODEL

In the field of robust control, Mayne et al (Mayne, Kerrigan, van Wyk, & Falugi 2011) developed a tube-based robust nonlinear MPC strategy. The strategy involved the use of two model predictive controllers: one for determining the optimal nominal trajectory which is performed offline using artificially contracted boundary conditions to account for the possible effect of disturbances; and one for following the nominal trajectory in the presence of disturbances which is performed online. In the vehicle control task the online controller minimises the difference between the nominal trajectory $\mathbf{x}(t)^*_{nom}$ and the trajectory $\mathbf{x}(t)_{tot}$ of the disturbed vehicle, which can be expressed as

$$\dot{\mathbf{x}}_{tot}(t) = \mathbf{f}(t, \mathbf{x}_{tot}(t), \mathbf{u}_{tot}(t)) + \mathbf{w}(t) \tag{5}$$

where $\mathbf{w}(t)$ is a random disturbance vector, $\mathbf{x}_{tot}(t)$ the system state, $\mathbf{u}_{tot}(t)$ the control input vector and $\mathbf{f}(t, \mathbf{x}_{tot}(t), \mathbf{u}_{tot}(t))$ the nonlinear function describing the system dynamics.

The nominal trajectory is defined by the distance along the centreline, s, and the track orientation angle, θ. The approach proposed by Perantoni in (Perantoni & Limebeer 2014) allows to describe the position of the vehicle in terms of the perpendicular offset from the nominal trajectory, n and the angle between the vehicle centreline and the tangent to the nominal trajectory, ξ, as shown in Figure 1. This formulation is convenient as the lateral path error (LPE) is n and enters the cost function as a state.

The online MPC problem can now be defined. The nominal states and controls and the nominal trajectory are assumed to be known. The nonlinear driver model takes in the nominal states $\mathbf{x}^*_{nom}(t)$ and solves an optimal control problem to keep the states $\mathbf{x}_{tot}(t)$ close to the nominal values under the action of disturbances. A control sequence, which consists of a sequence of commanded steering inputs $\boldsymbol{\delta}_{com}(t)$ for this specific problem, is then calculated and applied to the disturbed nonlinear vehicle. A sufficiently general problem formulation in continuous time is

$$\begin{aligned} \min_{(\mathbf{x}_{tot}, \delta_{com})} \quad & \int_{t_0}^{t_f} V(t, \mathbf{x}_{tot}(t), \delta_{com}(t)) \\ \text{subject to} \quad & \dot{\mathbf{x}}_{\boldsymbol{tot}} = \mathbf{f}(t, \mathbf{x}_{tot}(t), \delta_{com}(t)) \\ & 0 = \mathbf{g}(t, \mathbf{x}_{tot}(t), \delta_{com}(t)) \\ & 0 \geq \mathbf{h}(t, \mathbf{x}_{tot}(t), \delta_{com}(t)) \end{aligned} \tag{6}$$

where $V(t, \mathbf{x}_{tot}(t), \delta_{com}(t))$ is a general stage cost, $\mathbf{f}$ the vehicle dynamics, $\mathbf{g}$ the equality constraints and $\mathbf{h}$ the inequality constraints.

The cost function is required to minimise the lateral path error n and course angle error $\xi + \beta$ from the nominal trajectory. In addition the cost function must penalize the 'commanded' hand wheel angle velocity. Transcribed the problem into a standard NLP using a direct collocation method based on the trapezoidal rule, the quadratic cost function can be expressed as:

$$V_{opt} = \mathbf{n}Q_1\mathbf{n}^T + (\boldsymbol{\xi} + \boldsymbol{\beta})Q_2(\boldsymbol{\xi} + \boldsymbol{\beta})^T + \dot{\boldsymbol{\delta}}_{com}Q_3\dot{\boldsymbol{\delta}}_{com}^T \tag{7}$$

where Q_i are the square diagonal cost function matrices with q_i on the leading diagonal and V_{opt} the optimal control stage cost. The vehicle-driver dynamics enter the system as equality constraints $\mathbf{f}(t, \mathbf{x}(t), \boldsymbol{\delta}_{com}(t))$. The states of the vehicle are the vehicle equations 1 and 2, together with the equations describing the geometry of the track and the vehicle position, hence n, ξ and ψ. Physically infeasible values of tyre slip are prevented by constraint **h**. The problem is solved using IPOPT, a state of the art nonlinear solver which is particularly efficient and robust because it makes use of logarithmic barrier functions to eliminate equality constraints (Falugi, Kerrigan, & VanWyk 2010). Each barrier problem is then solved using a filter line-search.

The online control is implemented in a receding horizon mode in order to account for the random disturbances. Normally this would involve applying the first element of the calculated optimal control sequence to the disturbed vehicle, then recalculating the optimal control sequence at the next time step. Johns (Johns & Cole 2015) instead implemented intermittent control to better represent the human cognitive process, in which there is a time delay (refractory period) between recalculation of the optimal control sequence. During the refractory period the optimal control sequence is played out in a 'serial ballistic' fashion.

4 RESULTS

The behaviour of the controller is investigated using a circular nominal trajectory. The vehicle speed is set to a constant value and the radius of the nominal trajectory is set to achieve the desired operating point on the tyre characteristic. The parameter values used in the simulation are shown in Table 1. The vehicle parameters represent a small high peformance passenger car. The parameter values of the controller are from (Timings & Cole 2014) and disturbance levels from (Lin, Ulsoy, & LeBlanc 2000).

Two different vehicle configurations are used. The baseline configuration is a vehicle that has an understeering (US) characteristic and is stable. A vehicle with an oversteering (OS) characteristic is obtained by moving the centre of mass rearwards, such that $a = 1.38$ m and $b = 0.92$ m.

The radius of the nominal trajectory is chosen to put the tyres close to saturation. The cost function weights represent typical human driver behavior. The weight on the lateral path (q_1) error is set to 1. The weight on slip angle (q_2) is set to a very small value since the driver's primary objective is regarded to be minimising lateral path error. The weight on commanded hand wheel angle velocity (q_3) is set to give realistic levels of handwheel angle and velocity.

Table 1. Simulation parameters.

Parameters	Symbol	Value
Mass	M_t	1050 kg
Moment of inertia	I_z	1500 kg m^2
Front axle to CoG distance	a	0.92 m
Rear axle to CoG distance	b	1.38 m
NMS natural frequency	ω_n	18.85 rad/s
NMS damping factor	ζ_n	0.707
Vehicle forward speed	u	40 m/s
Steering gain	G_{sw}	17
Controller sampling rate	T_d	0.02 s
Refractory period	T_r	0.5 s
Lateral disturbance force standard deviation	F_{dist}	730 N
Moment disturbance standard deviation	M_{dist}	360 Nm
LPE cost function weight	q_1	1
Heading angle cost function weight	q_2	1E-6
HWA rate cost function weight	q_3	1E-3
Maximum tyre friction	μ_{max}	1.2734
Tyre shape factor	Q_y	1.5978

The controller is successful at allowing both vehicles to follow the nominal trajectory, despite the disturbances causing the tyres to enter their negative slope region.This was not possible using the comepnsatory controllers used in (Timings & Cole 2014) and (Johns & Cole 2015). Figure 3 shows that for the understeering vehicle both front and rear tyre slips vary around a mean value, as expected for the vehicle navigating a circular path. The front tyre saturates first and the controller is successful at keeping the slip angle at the saturation point. Figure 4 shows that the oversteer vehicle exhibits a similar behaviour but with the rear tyres successfully held close to their saturation point.

The controller is also evaluated in a more demanding scenario by setting a nominal path radius which is smaller than the minimum radius that the understeering vehicle's tyres can physically achieve. The weight on the heading angle error is increased to 1 as it is now more important for the driver to maintain the correct direction rather than stay close to the nominal path. The lateral path error increases until the vehicle finds the radius where the vehicle is at the limit of adhesion. Figure 5 shows that the path error settles to a near constant value. The tyre slip responses are not shown but are similar in nature to those in Figure 3.

A parameter study was performed to investigate the effect of changing the values of the controller's parameters. The baseline configuration is as described in Table 4; a run in the baseline configuration is included in all the studies. The hand wheel angle response is

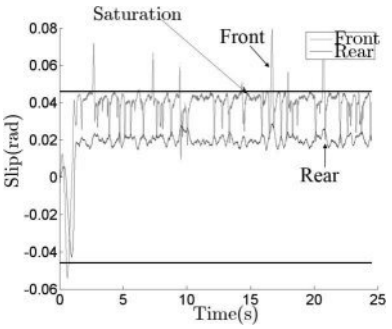


Figure 3. US vehicle slip.

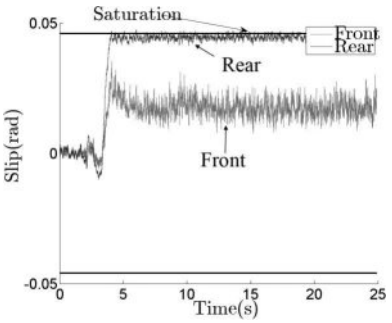


Figure 4. OS vehicle front and rear slips.

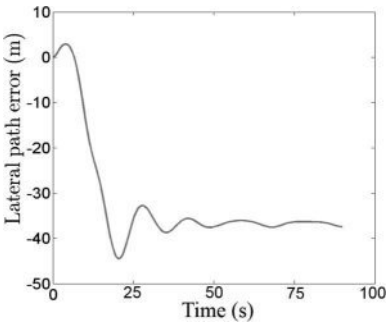


Figure 5. Lateral path error for a nominal radius much smaller than physically achievable.

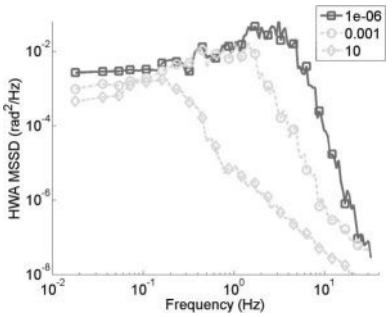


Figure 6. HWA MSSD for changing HWA speed weight.

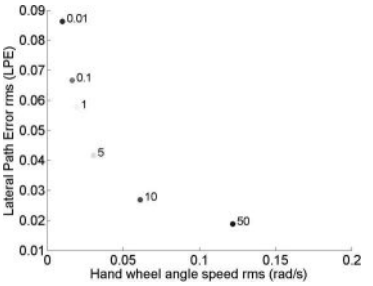


Figure 7. Trade off between hwa speed and lateral path error for changing HWA speed cost function weight.

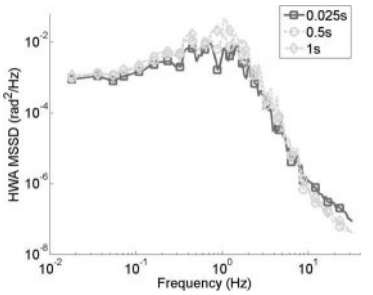


Figure 8. HWA MSSD for increasing refractory period.

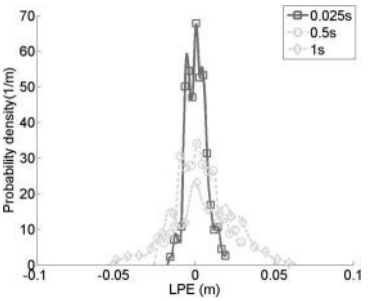


Figure 9. LPE pdf for increasing refractory period.

assessed using probability density function (pdf), root mean square (rms) and the mean square spectral density (MSSD). The mean value of HWA is subtracted from the signal before calculating the MSSD to reduce spectral leakage.

Figure 6 shows that increasing the weight q_3 on the HWA rate decreases the frequency content of the signal and reduces the roll off frequency as well as the decay slope. Decreasing the weight has the opposite effect. Figure 7 shows the trade off between rms path error and rms HWA rate.

Figure 8 shows that increasing the refractory period tends to increase the steering activity at frequencies in the region of 1 Hz. The lateral path error also increases with update time as shown in Figure 9. This is the expected behaviour: a longer time interval between control updates causes larger path errors, which in turn require larger control activity.

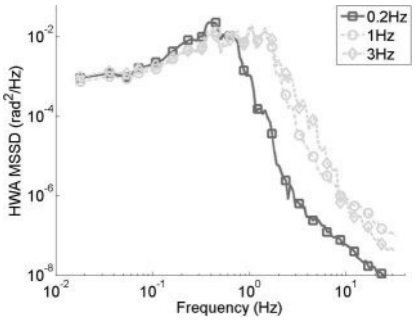


Figure 10. HWA MSSD for increase NMS natural frequencies.

Table 2. Driving simulator vehicle parameters.

Parameters	Symbol	Value
Mass	M	735 kg
Inertia	I_z	1100 kg m^2
CoG to front axle distance	a	1.61 m
CoG to rear axle distance	b	1.89 m
Steering gain	G_{sw}	11
Lateral force disturbance standard deviation	F_{dist}	640 N
Moment disturbance standard deviation	M_{dist}	270 Nm

Figure 10 shows that increasing the natural frequency of the NMS increases the bandwidth and magnitude of the steering activity, although the increase is not very significant when the NMS frequency is increased above 1 Hz.

5 VALIDATION

In this section the controller is compared to the steering responses of a professional racing driver steering a single-seat racing car on a circular path in a moving-base driving simulator. Vehicle data is given in Table 2. The driver steered the vehicle at constant speed under the action of lateral and yaw disturbances. Time histories from the driving simulator experiments were used to identify parameter values of the driver model and the tyre model (full details of the vehicle model used in the driving simulator were not available for confidentiality reasons). Careful examination of the measured HWA time histories, Figure 11, revealed steering bevaviour that exhibited zero-order hold (ZOH) behaviour (on average 0.24 s) after a short duration (on average 0.22 s) of serial ballistic control. This is in contrast to the assumption of purely serial ballistic control made in Section 3, where the control only settles to a constant value after typically 3 s. The driver model was changed to include this behaviour by assuming that the first part of the refractory period is serial ballistic for 0.22 s and ZOH for the following 0.24 s, giving a

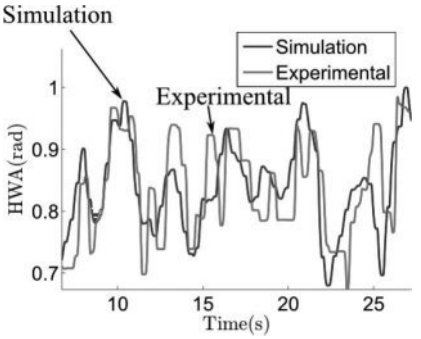


Figure 11. Measured and simulated hand wheel angle time history.

Table 3. Identified driver model parameter values.

Parameters	Symbol	Value
NMS natural frequency	ω_n	16.2 rad/s
NMS damping factor	ζ_n	0.69
Refractory period	T_r	0.36 s
Path error weight	q_1	1
Course error weight	q_2	1E-6
HWA rate weight	q_3	0.47

total refractory period of 0.46 s. Since the data only pertains to one driver and one type of manoeuvre it is not known at this stage whether this steering control behaviour is characteristic of other drivers and other manoeuvres.

Other driver model parameters identified from the experiments were: NMS natural frequency ω_n; NMS damping factor ζ_n; weight on lateral path error q_1; weight on course error q_2; and weight q_3 on hand wheel rate $\dot{\delta}$. The refractory period, fitted assuming SBH only, was included as well to compare its value to the measured one; the value reported in Table 2 is for reference only as it has not been used in the validation. To avoid the risk of over-fitting, the course angle weight was set to 1E-6, the lateral path error weight is set to 1. The remaining parameter values were identified by minimising the difference between the MSSDs of the measured and simulated HWA:

$$V_{val} = \sum_{i=1}^{i=m} (\mathrm{MSSD}_{exp,i} - \mathrm{MSSD}_{sim,i})$$

where V_{val} is the validation stage cost and m the number of data points. Since the lateral path error weight is set to 1, the only weight to be optimised is the HWA rate q_3. The initial parameters are chosen carefully to reduce running time. Results are shown in Table 2. The NMS parameter values are within the expected range (Timings & Cole 2014).

Figure 12 compares the experimental and simulated HWA MSSDs (note that the mean values of HWA have been removed). The simulation generally underpredicts the experiment. This is likely to be because the

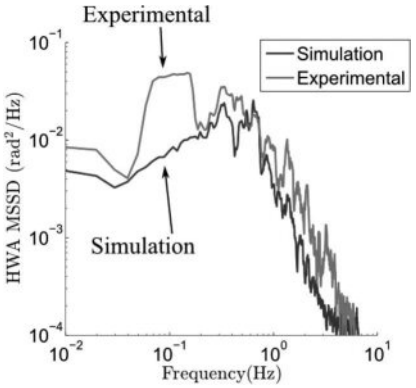


Figure 12. Comparison between the experimental and simulated HWA MSSD.

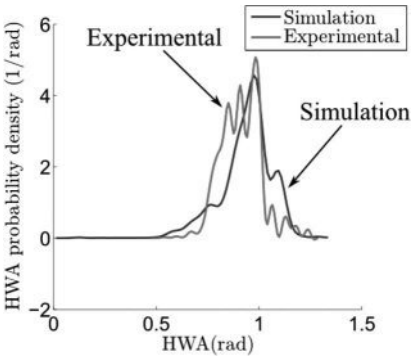


Figure 13. Comparison between the experimental and simulated HWA pdf.

simulation does not include a random component of driver response arising from sensorimotor noise. However there is a particular discrepancy between 0.05 Hz and 0.2 Hz which requires further investigation. Figure 13 shows a good agreement in terms of mean and standard deviation for the HWA pdfs. The agreement for the LPE pdf in Figure 14 is satisfactory.

Further work is underway to extend the driver model to include combined steering and longitudinal control, and to identify and validate the driver model over a wider range of human test subjects and manoeuvres.

6 CONCLUSION

Robust nonlinear model predictive control has been applied to the human steering control task. Simulation results show that the controller is able to maintain stable control of a nonlinear vehicle at the limit of adhesion on a circular path in the presence of disturbances. In particular the controller is successful at controlling a vehicle with tyres that have a negative slope force-slip characteristic beyond the saturation

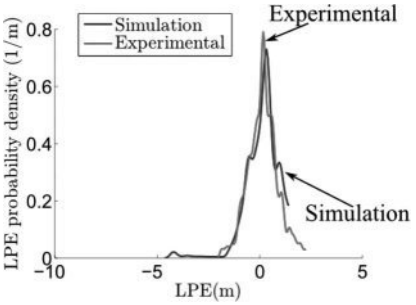


Figure 14. Comparison between the experimental and simulated LPE pdf.

point. A parameter study shows that a trade off exists between rms hand wheel angle rate and rms lateral path error. Increasing the natural frequency of the driver's neuromuscular system increases the hand wheel angle activity. Increasing the refractory period increases the lateral path error and the steering activity. The controller was identified and validated using experimental data obtained from a moving-base driving simulator. The identified values of cost function weights and neuromuscular parameters fell within plausible ranges. Comparison of measured and simulated HWA was satisfactory, although there is scope for further work to improve the agreement.

ACKNOWLEDGEMENTS

This work was supported by the Engineering and Physical Sciences Research Council (EP/P505445/1, studentship for Braghieri) and Renault Sport F1 Team (RG72244).

REFERENCES

Falugi, P., E. Kerrigan, & E. VanWyk (2010). Imperial college london optimal control software user guide. Technical report, Imperial College London, England, UK.

Johns, A. & D. Cole (2015). Measurement and mathematical model of a driver's intermittent compensatory steering control. *Vehicle System Dynamics 53*(12), 1811–1829.

Lin, F., A. Ulsoy, & D. J. LeBlanc (2000). Vehicle dynamics and external disturbance estimation for vehicle path prediction. *IEEE Transactions on Control Systems Technology 8*(3).

Mayne, D., E. Kerrigan, E. van Wyk, & P. Falugi (2011, July). Tube-based robust nonlinear model predictive control. *International Journal of Robust and Nonlinear Control 21*(11), 1341–1353.

Pacejka, H. (2002). *Tyre and vehicle dynamics*. Butterworth Heinemann.

Perantoni, G. & D. Limebeer (2014). Optimal control for a formula one car with variable parameters. *Vehicle System Dynamics 52*(5), 653–678.

Timings, J. & D. Cole (2014). Robust lap time simulation. *Proc. IMechE, Part D: J. Automobile Engineering 228*, 1200–1216.

Advanced Vehicle Control – Edelmann, Plöchl & Pfeffer (Eds)
© 2017 Taylor & Francis Group, London, ISBN 978-1-138-02992-7

A skill learning process model for driving a car

Kazuhide Togai & Asako Ohno
Osaka Sangyo University, Osaka, Japan

Takuya Matsumoto & Hisashi Tamaki
Kobe University, Kobe, Hyogo, Japan

ABSTRACT: For driver assistance system design and model based vehicle development, what kind of concept and property are required for a driver model have been studied from published literatures. A driver model requires driving skill level parameters because human drivers have various skill levels. The skill level can be raised with proficiency and sometimes changes with environment change. A model framework and a concept to represent skill level are proposed. A mechanism that ensures systematic learning is introduced and learning process is illustrated with a driving agent model. Finally, an extended human body concept is introduced to explain unconscious operation as skill being acquired.

1 INTRODUCTION

For driver assistance system design and model based vehicle development, what kind of concept and property are required for a driver model have been studied from published literatures. A driver model requires driving skill level parameters because human drivers have various skill levels.

The skill level can be raised with proficiency and sometimes changes with environment change. A model framework and a concept to represent skill level are proposed. A mechanism that ensures systematic learning is introduced and learning process is illustrated with a driving agent model. An extended human body concept is introduced to explain unconscious operation as skill being acquired.

Finally, relationship between operation frequency and task level is to be discussed for skillfulness.

2 PHYSICAL LIMITATION OF A HUMAN DRIVER

2.1 *Driver's property described in published papers*

The car was put into practical use in the 1880s. It is about 130 years ago. Information processing, i.e. electronic control, was introduced into some vehicles in 1973, it is only 40 years ago. Apollo spacecraft landed on the moon in 1968 and that is earlier than the introduction of electronic control systems into cars. Driver models have been studied from that time. However, those have not been developed separately from automotive industry. Needs for application and available technology (concepts & tools) have been assumed as a background for model studies.

Attempt to quantify the response of human operation has been made since the 1930s in the field of medicine and physiology. There is delay time from visual information recognition to operation by a driver. Simple reaction-time experiments (the time from a stimulus to response with perception) show that visual response times under near ideal conditions are about 0.2 s (Macadam, 2003). It was reported that the delay time is 0.3–0.5 seconds and may not be reduced by learning or training (Kageyama, 2005). Feedback control performance, e.g. stability, in human driving is mainly governed by response of a driver. Ornstein proposed a second order system with dead time transfer function of a model of a human operator for pursuit-type manual tracking tasks in early 1960s (Ornstein, 1963). Transfer function models have been developed after works related feedback control theory by Black, Nyquist and Bode in 1940s.

Macadem and Kageyama who have studied driver models for the steering over the years, published neural network models in the 1980s. Then, their Research subject has changed to explicit parameters models.

Human machine interface (HMI) also involves in this area, HMI approach has not deal with dynamic models in many cases so far, even if the approach is qualitative and quantitative. Sano has proposed dynamic model for tactile.

2.2 *Prediction dependent operation*

A machine system control (PID for example) may be used as a driver model for the purpose of target path tracking control or target speed tracking control. Feedback is the main operation in those controls. Feedback control is easier to be applied because it requires

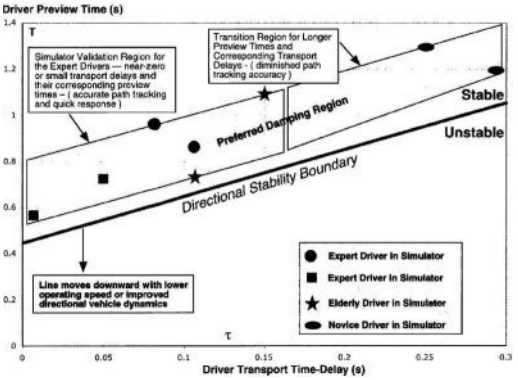


Figure 1. Relationship between preview and stability.

fewer controller parameters and knowledge for control targets. And future information is not also required.

A driver looks forward and can predict immediate future. Kageyama and Macadem, previously mentioned, proposed a driving operation model consisted of feedback and feed forward. There is no such clear division in human operation consisting of feedback and feed forward with prediction. Machine control concept has been applied to the model construction. Whether the operation after looking the result is valid depends on the response of the driver. Macadem (2003) discussed the matter in relation to driver prediction as shown in Figure 1.

2.3 *Driving skill model for driver assistance*

SRK (Skill, Rule and knowledge) models were proposed for human behavior analysis, and have been used to describe error behaviors (Cacciabue, 2007). It can be used as a driver model qualitatively. Human behavior may change (interaction) looking at the response of the target. It is necessary to extend the model to represent dynamic behavior and individual characteristics of a driver (Miyajima, 2007).

Generally a human drives a vehicle. Vehicle performance is determined by the driver included in a system (Controlled System) (Ito, 2009). The model is considered to be applicable widely from evaluation of behavior of a vehicle with driver assistance for this reason. So that learning process and driving skill representation is particularly needed. In other words, requirements are if un-skilled driving behavior can be represented and if accustoming process to vehicle property can be described with the model.

3 DRIVERS PROPERTY RELATED TO SKILL LEVEL

3.1 *General framework of driver models*

Process from environment information including the target speed to driving apparatus operation is constructed with functionalities of recognition, judgment

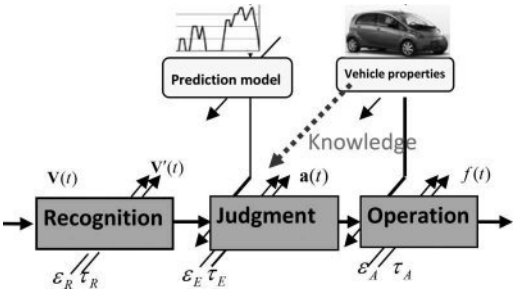


Figure 2. Information transfer in a driver mode.

and operation. The recognition system takes information required for driving from the environment and transfers processed information to the judgment system. The judgment system sets targets required for operation based on the received information. The operation system manipulates driving apparatus. Feedback functionality is contained in the judgment system. A Target modification module is added. Functionality of the module is to read the target profile in advance and modify the profile for response delay compensation and smoother operation. Further, a vehicle property module for judgment is added. Gain from operation amplitude to vehicle acceleration is to be learned as a vehicle property and stored in the module. Driver model structure and information transfer process with delays and errors are shown in Figure 2.

Typical driving behaviors of a beginner and an expert can be described a driver model based on the driver model framework (Tamaki, 2012). Information errors and response delays are taken as skill parameters in the model.

3.2 *Feed forward operation is essential*

Accuracy of information to be transferred and response delay in above mentioned driver model are closely related to skill level of a driver. Those factors deteriorate control performance including stability. Response delay, i.e. mainly dead time, is not be reduced largely by training or learning because of the nerve system property including processing in the brain.

Influence of response delay on driving was analyzed by authors. For speed tracking driving, system response is approximated with a first order delay transfer function (Togai, 2013).

$$G_{vc}(s) = \frac{K}{1+Ts} e^{-Ls} \tag{1}$$

where, K: total gain (plant and controller), L: total dead time, T: time constant of the target plant.

Stable condition of the closed loop system is that the open loop gain must be smaller than 1.0 when the phase lag exceeds −180 degrees. From the stable condition, it is derived that allowed stable gain is reverse proportional to the dead time L.

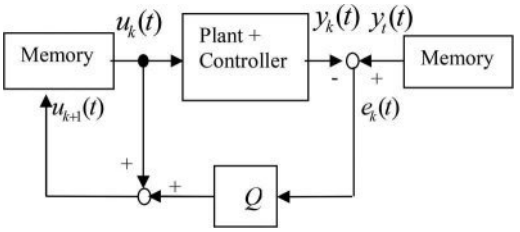


Figure 3. Iterative learning control law.

Response delay of a human driver in a vehicle control system is significantly larger, e.g. ten times, than that of an electronic controller, so that sufficient feedback gain to track a target speed is not feasible in a human driver included system. That means feedback error compensation is not a major control mean for a human driver.

Target and result are physical quantity (e.g. voltage) in an electronic control system, so that those values can be directly calculated. That is different from driving operation of a human at all. External state (curvature of the road, the vehicle speed, for example) recognition is a major task for a driver. Proficiency is also a major factor.

As described, dead time in a control system deteriorates the system stability significantly. Sufficiently large feedback gain is not feasible.

As described above, feed forward control is essential of human driving behavior. For the feed forward control, time profile of operation is required.

3.3 *Accurate operation acquirement through learning*

Beginners may not well understand vehicle response property at first. But, they may have knowledge, such that, acceleration or deceleration is proportional to accelerator or brake position and can recognize target tracking error. It is well known that target error feedback to next time input makes the output converging to an input profile that drives the car with smaller tracking error. The control scheme was introduced in Robotics at the first time (Arimoto, 1984). The control strategy is shown in a block diagram on Figure 3. The strategy does not require knowledge of the target plant construction and parameters. Operation input is replaced by previous time operation and error.

$$u_{k+1} = u_k + Q(y_t - y_k) \tag{2}$$

where u_k: kth input data profile, y_k: kth output, y_t: target profile, Q: feedback gain (Matrix).

The strategy is applied to the target speed tracking. A constant accelerator position for target acceleration and a constant brake position for target deceleration regardless of the target speed are set at the beginning as shown in Figure 4. After ten time driving and learning iterations, resulted speed approaches to the

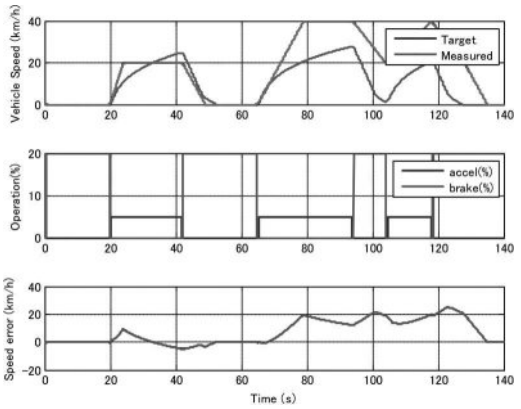


Figure 4. Driving behavior with initial values.

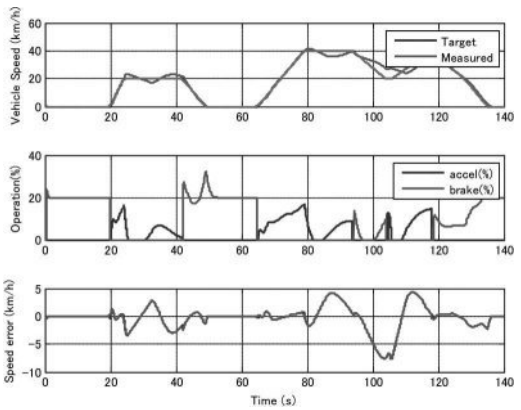


Figure 5. Driving behavior after 10 times of irrelative learning.

target as shown in Figure 5. Further learning up to 100 times reduced the tracking error. However, that does not mean the optimal learning to be feasible. It is required to memorize operation input and error every a certain interval. The number is huge and a human modify the task not to use huge energy.

Furthermore, as the input operation profile is depending on the target vehicle property, once the vehicle would be changed, then the same learning would be required again. Even if all the input profile could be memorized, structure of the target plant would not be obtained with this strategy only and the learning result would not be applied to different vehicles.

Relationship between driver operation and response comes out gradually as resulted output becoming close to the target. Some features of the target plant may be found, for example, accelerator position increasing as speed increasing, and those can be hint to next stage learning that includes rule making.

If the driver would know vehicle response to driving operation, the person could learn parameters that represent character of the vehicle. Then, learning can

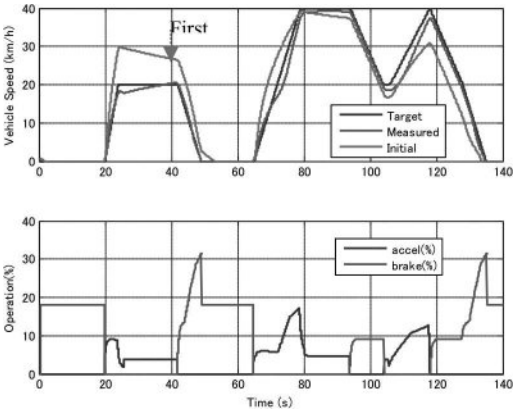


Figure 6. Driving behavior after road load gain learning.

be done systematically and be completed within fewer times. That is said to be a pattern matching between a specific vehicle speed target profile and a specified operation profile for a vehicle. After some target speed tracking driving of a car equipped with an Internal Combustion engine and a transmission, a driver would find empirically that vehicle acceleration is accelerator position dependent, the required position is increasing as vehicle speed increasing, accelerator position at constant speed depends on vehicle speed and further braking force is required just before the vehicle stop.

Those early learned knowledge was used to select features of vehicle speed response to driving operation and to construct a driver model which updates model learning parameter using target speed, resulted speed and speed error. Operation output profile is generated with characteristic parameters. For example, three parameters for start from stand still, acceleration and constant speed cruising. The model parameters can be learned as the following three steps.

At first, initial accelerator position setting is arbitral with no speed increase correction for acceleration. Acceleration dependent initial accelerator position is learned to adjust vehicle speed to the target at certain acceleration. The initial accelerator position coefficient is modified by the speed error just after the launch, e.g. one second.

In the second step, speed dependent increment of the accelerator position is learned to meet speed-increasing rate to that of the target. Speed errors at two time instances during acceleration are used to correct coefficients instead of comparing observed acceleration with the target.

Finally, accelerator position during constant speed cruising, in which driving force is equivalent to running resistance, was learned from speed error and speed gradient. Resulted target speed tracking and operation is shown in Figure 6.

It may be taken time to obtain vehicle acceleration and deceleration property corresponding to pedals operation force. The driver may not operate those pedals unconsciously during property learning.

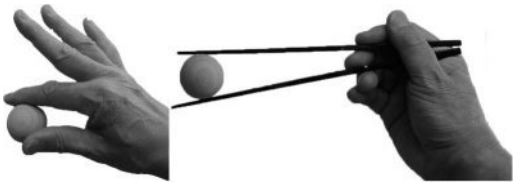


Figure 7. Extended fingers – Chopsticks.

4 UNCONSCIOUS OPERATION AND VEHICLE AS A EXTENDED BODY PART

4.1 *Extended human body – tools are extended arms and legs*

Operations in human driving behavior become under unconscious after gaining a certain skill level. Immediate driving target profile is determined from driving purpose and environment. The target can be described in two dimensional path and speed profile. The steering, the brake or the accelerator is operated unconsciously according to the target profile pattern. Human behavior can be classified being based on rule, knowledge and skill by proficiency level according to the SKR model. If the driver is not a very beginner, his/her driving operation is directly derived from the target driving purpose without considering the target.

The consequence may be called direct mapping from a target to an operation profile comparing with an electronic control process in which the operation profile is calculated from the target and measured result step by step. That is resembled to pick up operation with a pair of chopsticks shown in Figure 7. At first, operation force and gap of the chopsticks may be considered. The chopsticks become to be operated without thinking the additional length to fingers as if that is a part of fingers or extended fingers.

Driving behavior to reach a destination is said to be a travel with extended legs that are adjusting speed and direction of the car as walk or run on own legs. Images through eyeglasses are actually different from those of eyes, however those are regarded as the same in our conscious.

4.2 *Extended human body behavior at out of experienced environment*

At the beginning of typewriting learning, persons look keys pressed by fingers, they look only a display or paper after some blind touch skill obtained. But, when the index fingers do not rest on the base keys, spelled words are totally different from intended. And the wrong positioning may not be noticed instantly because of perceived notion. An accelerator, a brake pedal, a steering wheel and a gearshift lever are operated on blind touch based. Sometimes the shift position may be set at L instead of D, which is expected by a driver. That may be acceptable for safety. But, an extreme case is wrongly being depressed accelerator when the driver intends to stop the vehicle with the

brake pedal. The person believes to press the brake. That means the vehicle is controlled with positive feedback.

Once vehicle response goes beyond expected range that is based on experience or learning, it is hardly to operate unconsciously corresponding to a target pattern. When tires are locked on slippery road surface, braking force is not proportional to the operating force, but largely reduced regardless to the applied force. Unstable vehicle behavior is easily imagined in that case where the braking system turns to be in positive feedback. Steering operation on lower friction road may lead to similar situation, i.e. intended vehicle behavior is not resulted by usual unconscious operation.

As far as vehicle environment where drivers can easily adapt themselves lays at extendable rage from their experience or learning, drivers run a vehicle with comfort. Once the environment goes beyond the range, drivers may feel unrest or even fear which sometimes turn to be danger condition. The range is closely related driver's experience and skill. A driver with standard skill level can steer a vehicle without difficulty within slip limit of tires, while a racing driver control vehicle steer using the tire slip actively to pass thorough tight curves at high speed.

4.3 *Is autonomous driving system technology applicable directly to driver assistance system?*

As mentioned before, vehicle control by a human driving should be considered as an extended human body based on experience and learning. Existing autonomous driving systems are self-contained. It is not correct to say that a driver assistance system could be realized based on an autonomous driving system without difficulty.

If any driver could not learn skills based on experiences, a driver assistance system could be designed from an autonomous driving system extension. A driver can decide which operation is preferable. A system which has multiple supervisors who insist own reason is not consistent or danger.

The autonomous driving system does not precede the driver assistance system, and vice versa.

5 SKILLFULLNESS – HIGH FREQUENCY & REPEATED ACCURACY REQUIRED

5.1 *Higher speed path tracking task*

If the steering angle is fixed at theta, distance in orthogonal direction to the initial direction of movement from the initial point during dt time is described the following equation.

$$x_o = \theta v dt \tag{3}$$

where x_o: distance from the initial point, v: vehicle speed, θ: steering angle at a tire, dt: elapsed time.

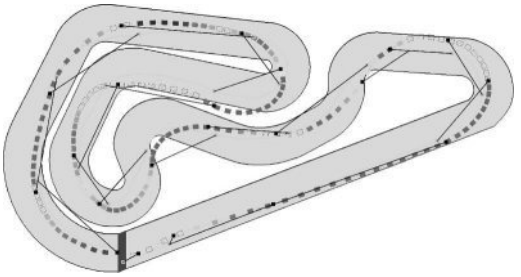


Figure 8. Path tracking with higher speed.

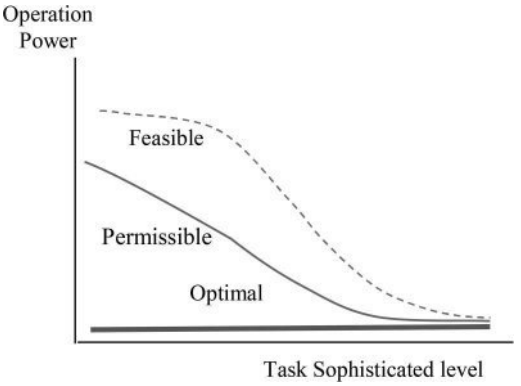


Figure 9. Feasible operation profile and task level.

Width of a path becomes more narrow comparing to length of traveling as vehicle speed increasing.

Quick and accurate steering operation is required to maintain a vehicle with in the path width when a vehicle is driven along a curve with higher speed. That is typical driving in a motor racing circuit as shown in Figure 8.

5.2 *Sophisticated task and skill level*

Frequency of steering target is proportional to vehicle speed when driving task is a Sinusoidal shape path tracking. If the frequency is sufficient lower, there may be some correction of operation can be taken. That means space of available operation profile is large during low speed, while feasible operation is limited at higher vehicle speed.

Skillful operation needs appropriate operation at required timing with repeatable accuracy. Accelerator 50% to WOT and accelerator 50% PWM with appropriate frequency may be resulted approximately the same output power of an engine. However, the latter need higher power than the former. A human takes less power consuming operation during repeated operation. That is one of natures of skillfulness shown in Figure 9.

5.3 *Rope jumping and HMI*

A human driver operates a vehicle based on prediction and feed forward as described. When vehicle control

hands over to a human driver, sufficient time for prediction and feedforward is required for safety. That is like participating into rope jumping.

6 CONCLUSIONS

Even if resulted trajectory of a vehicle might be the same between an autonomous driving system and a human driver, processes to determine operational profile are different. Human driver is not good at target tracking with feedback because of slower response comparing with an electronic controller. A driver cannot trace the target speed of an emission test cycle only with feedback control as shown with the transfer function analysis. Feed forward control is required for the tracking purpose instead of feedback. Operation profile for the feed forward can be obtained through iterative learning.

Once operational profile has been obtained by learning, an operation to a target is conduced unconsciously as skill level being raised. Sometimes tools, e.g. chopsticks, are used an extension of fingers or hands without notice the difference. Once sitting in the cockpit of a car, a driver may feel making a run to a destination as if on own foot.

A driver makes final decision as the supervisory controller in a vehicle control system. The driver feels running and observing a vehicle directly although vehicle is driven through a power train or a brake system and instruments, e.g. a speed meter, bring information. And individual vehicle property is compensated in driver's extended body.

During task sophisticated level low, there may be wide range of operation profile. PWM type of operation is one of those. However, when the task level being raised, few permissible operation profile is remaining and feedback operation may not be allowed. That is one aspect of skillfulness. A driver operates a vehicle with own target profile corresponding to the environment. That is like participating into rope jumping.

REFERENCES

Arimoto, S., Kawamura, S. 1984. Bettering operation of robot*ics, Journal of Robotic system, Vol. 1–2, pp. 123–140*.

Cacciabue, P. C. (Editor), 2007, Modelling Driver Behaviour in Automotive Environments: Critical Issues in Driver Interactions with Intelligent Transport Systems, *Springer*.

Ito, M. 2009. Control Mechanisms that we learn from the brain, *Journal of Society of Automotive Engineers of Japan, vol. 63, no. 5*.

Kageyama, I. 2005. Study on Evaluation of Driver's Behaviour at Running on Narrow Road, *JSAE20055849*.

Kageyama, I. 2007. Construction of driver model for analyzing driver behaviour, *JSAE20075284*.

Macadam, C.C. 2003. Understanding and Modeling the Human Driver, Vehicle System Dynamics, C.C. Macadam, *Taylor & Francis*.

Miyajima, C., Nishiwaki, Y., Ozawa, K. et al. 2007. Driver Modeling Based on Driving Behaviour and Its Evaluation in Driver Identification, *Proceedings of the IEEE, Vol. 95 (1), 427–437*.

Ornstein, G.N. 1963. The Automatic Analog Determination of Human Transfer Function Coefficients. *Med. Electron. Bio. Eng. 1 (2)*.

Tamaki, H. Togai, K. 2012. Driving Agent Model for Driver Assistance and MBD Part 1 – Concept Design of Skill Learning Process, *AVEC' 12*.

Togai, K. Tama 2008. Emission test cycle driving agent and expertise in driving behaviour, *Review of automotive Engineering JSAE, pp. 387–391, Vol. 29, No. 3*.

Togai, K. Tamaki, H. 2013. Model Structure and Learning Process for a Driver Model Capable to Improve Driving Behaviour, *JCET, Vol. 3, Iss. 2 May, pp. 41–49*.

Steering

Advanced Vehicle Control – Edelmann, Plöchl & Pfeffer (Eds)
© 2017 Taylor & Francis Group, London, ISBN 978-1-138-02992-7

In vehicle truck steering-system modeling and validation

Jan Loof, Igo Besselink & Henk Nijmeijer
Department of Mechanical Engineering, Dynamics and Control Group, Eindhoven University of Technology, Eindhoven, The Netherlands

ABSTRACT: In this paper a multi-body 44-DOF tractor semi-trailer model is coupled to a 4-DOF steering-system which includes friction and hydraulic power-steering. An extended wheel hub geometry is used to provide the correct feedback torque from the wheels. A tie-rod with stiffness has been included to connect left and right. An instrumented tractor semi-trailer is used to verify the steering-system model predictions during driving. The focus lies on the prediction of the steering-wheel torque and the vehicle velocity and steering-wheel angle are prescribed as an input for the simulation. Two tests are discussed in this paper, a J-turn at 80 km/h and sinusoidal steering-wheel input with a frequency of 0.4 Hz at 65 km/h. The comparison of the measured signals and the predicted values shows that the steering-system model is accurate. The non-linearities caused by friction and hydraulic assistance system can clearly be seen in both the measurement and the simulation.

1 INTRODUCTION

In 2016 a total 35 million heavy-duty trucks are registered. The amount of trucks is expected to grow in the future. By 2030 a growth of 17% is expected in Europe while in Asia and the Middle East this growth is expected to be more in the direction of 150% to 200% [7]. Statistics show that trucks and in particular tractor semi-trailers are over-represented in accidents in comparison to cars. Research show that causes for this lie in poor rear and side visibility leading to blind spot crashes [10, 12]. Since truck drivers are often exposed to long working hours with a low concentration level this can result in fatigue and high-way hypnosis which can lead to loss-of-control accidents and road departures [11]. Furthermore the size of trucks is growing as well, this includes extra articulation points which result in complexer dynamics [2]. To support the driver under these difficult circumstances, a number of support systems are currently available on high-end trucks or are being developed. These systems include and are not limited to: anti-lock braking system, electronic stability control, adaptive cruise-control, intelligent speed adaption, forward collision warning, automatic emergency braking, blind spot information, lane departure warning and curve-speed warning.

Lateral control by manipulation of the steering angle of the front wheels is a novel feature and not commonly available on the truck market. As a part of a Dutch STW project 'Truck Merging Support', a merging and lane changing/keeping assistant is being developed to improve safety. To investigate the possibilities for supported truck driving the current steering-system is first modeled and analyzed. Literature in passenger cars reveals that the modeling of the hydraulic power-steering system is necessary [3, 9] and that friction cannot be neglected [8] especially around the center position. Previous work [5, 6] describes the modeling and model verification of a steering-system of a commercial vehicle by means of test-bench measurements outside the vehicle. The aim in these papers is to predict input and output angles, input and output torques and pressures in the steering-system. This has resulted in the steering-system model shown in Figure 4.

In this paper the steering-system model is implemented in a multi-body truck model. A number of tests have performed with a real instrumented vehicle on a proving ground. The model predictions are compared with the measured signals to verify the model's validity. This paper is organized as follows: In section 2 the vehicle model and steering-system model will be discussed, section 3 describes the instrumentation of the test vehicle, section 4 discusses the tests performed and the model predictions and section 5 contains the conclusions.

2 VEHICLE AND STEERING-SYSTEM MODEL

In previous research on active cabin suspension a 44 degree of freedom (DOF) multi-body truck model has been developed and validated [4]. As shown in Figure 1, this model contains five axles, the chassis of the tractor and trailer contain torsional flexibility and cabin and engine suspension are included. This model is constructed by making use of MATLAB

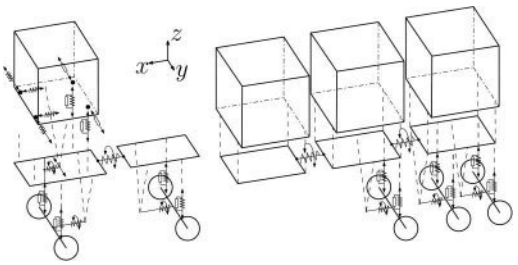


Figure 1. 44 DOF multi-body truck model as in [4].

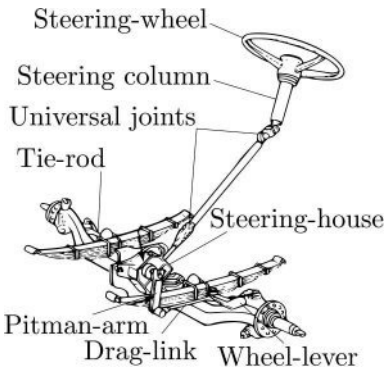


Figure 2. Components in a typical truck steering-system [1].

SimMechanics. The tyre-road interface is taken care of by usage of the TNO-Delft tyre.

The steering-system of a truck generally contains components as in Figure 2. The driver controls the steering-wheel which is connected to the steering-house via the steering-column and two universal joints. These universal joints are necessary to facilitate the height adjustment and for the cabin motion. The steering-house contains a hydraulic power-steering system which amplifies the input torque given by the driver. The output of the steering-house is connected to the pitman-arm which moves the drag-link. This drag-link movement is converted into a steering motion of the left wheel by means of the wheel lever. The left wheel is connected via a tie-rod to the right wheel.

The steering-system model (Figure 4a) is based on [5, 6]. The steering-wheel is modeled by an inertia, J_{sw}, with friction, $T_{fric,sw}$, due to the bearings. The torque felt by the driver is refered to as T_{sw} and the steering-wheel angle as δ_{sw}. The steering-wheel is connected to the input of the steering-house via two universal joints. The stiffness between the steering-wheel and the steering-house is combined in one equivalent spring k_{sc}. The input to the steering-house has an angle $\delta_{sh,in}$ and inertia $J_{sh,in}$. Due to the bearing-friction, $T_{fric,hua}$, is assumed here as well. The input of the steering-house is connected to the output via two springs in series which represent the torsion-bar and the spindle, the stiffness equals k_{tb} and k_{sp} respectively. A small damper d_{hua} is added to include material damping. A fixed gear ratio i_{sh} results from the spindle lead and sector shaft radius.

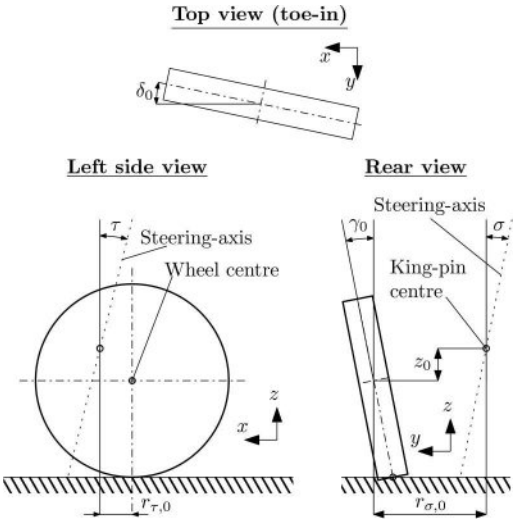
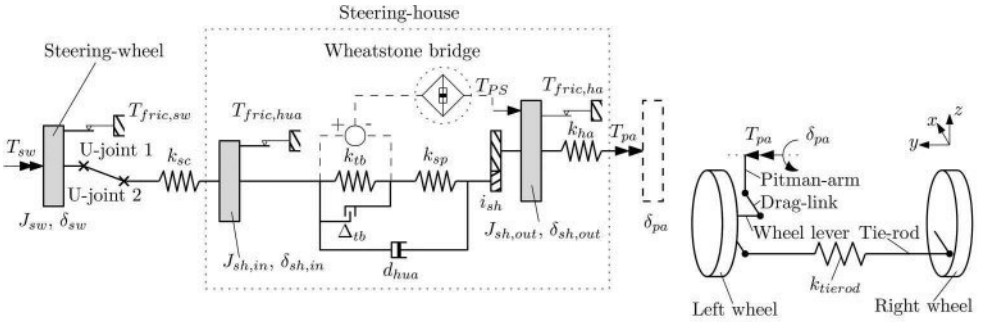


Figure 3. Left wheel hub geometry with caster angle τ, king-pin inclination angle σ, static camber angle γ_0, static toe angle δ_0, static caster offset $r_{\tau,0}$, static wheel center offset $r_{\sigma,0}$ and static vertical hub offset z_0.

The inertia of the components after the spindle until the pitman-arm are lumped into one equivalent parameter $J_{sh,out}$. The output of the steering-house rotates with angle $\delta_{sh,out}$. Friction $T_{fric,ha}$ is present on the output as well due to the seals of the hydraulic piston. The power-steering system is modeled as a symmetric Wheatstone bridge where the deflection of the torsion-bar controls the valve openings which results in a pressure difference across the piston. The stiffness in between the steering-house and the left wheel is captured in one parameter k_{ha}. The pitman-arm, drag-link and uprights are modeled in MATLAB SimMechanics. The inertaction happens at the pitman-arm rotation point where a torque is applied on the SimMechanics model and the angle is fed back to the Simulink model. To generate the correct feedback torque from the wheels to the steering-system the wheel hub geometry contains the caster angle, king-pin inclination angle, camber angle, toe angle, caster offset, wheel center offset and a vertical hub offset as shown in Figure 3 for the left wheel. Both wheels are connected via the tierod with stiffness k_{tierod} and include Ackermann steering. Friction on the king-pin is accounted for by dry friction.

3 TEST VEHICLE

An instrumented tractor semi-trailer is used to verify the steering-system model in combination with the multi-body truck model. The vehicle is equipped with various sensors as in Figure 5. The cabin is equipped with a 3-axis accelerometer (a_{xC}, a_{yC}, a_{zC}) and a 3-axis gyroscope (r_{xC}, r_{yC}, r_{zC}) at the driver position. The front and rear part of the chassis are equipped



(a) Steering-system model used in the simulations, this model is based on [5, 6]. This part is modeled in MATLAB Simulink.

(b) MATLAB SimMechanics part of the front axle and steering-system

Figure 4. Steering-system and front-axle model. The steering-system model is modeled in MATLAB Simulink and the front-axle is modeled in MATLAB SimMechanics. The interaction takes place at the pitman-arm where a torque, calculated by the Simulink model is applied to the pitman-arm in SimMechanics and the angle from SimMechanics is used in Simulink again.

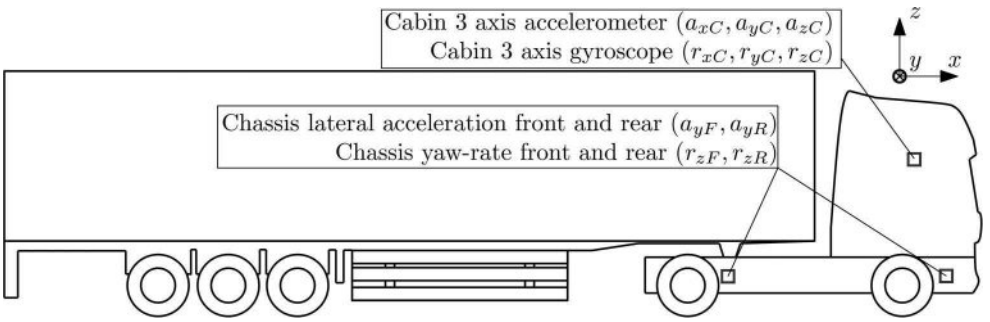


Figure 5. Side view of the motion sensors in the truck, here the following nomenclature is used: C = cabin, F = front, L = left, R = rear, a = accelerometer and r = gyroscope.

with an accelerometer which only measures in the lateral direction (a_{yF} and a_{yR}) and a gyroscope which measures the yaw-rate (r_{zF} and r_{zR}).

The steering-system is instrumented with a measurement steering-wheel to measure the steering-wheel torque and steering-wheel angle (T_{sw} and δ_{sw}). The pitman-arm angle, δ_{pa}, is measured as well as the left and right king-pin angles ($\delta_{kp,L}$ and $\delta_{kp,R}$). To measure the force transferred between the wheels and the steering-house, the drag-link force, F_{dl} is measured.

4 VALIDATION OF THE MODEL

A number of tests are executed with the instrumented vehicle on a proving ground. The following tests have been done:

- Steady-state cornering from standstill to 65 km/h.
- J-turns at 80 km/h.
- A sinusoidal steering input at 65 km/h, frequency content between 0.1 and 2.7 Hz.

All the tests have been performed by a driver and not with a steering-robot. Therefore there can be some difference between similar tests and sinusoidal inputs may not always be a 100 % symmetric. The steady-state cornering tests have been used to tune the cornering and self aligning stiffness of the tyres. The J-turns are used to evaluate the model response to a step input and the sinusoidal input tests can be used to assess the model accuracy for specific frequencies. Due to the limited space only two experiments will be discussed; a J-turn since it contains information about on-center driving, a dynamic response and the steady-state behavior. Also a sinusoidal input with a frequency of 0.4 Hz will be discussed since this is a frequency which occurs a lot during high-way driving. For confidentiality reasons all graphs in this paper have been scaled and made unit-less.

In order to mimic the experiments it is important that the vehicle model has the same forward velocity as the real vehicle. To do so a cruise-controller is implemented in the model. The measured forward velocity is used as an input for the model. Furthermore the measured steering-wheel angle is used as an input to the model. As a road input for the model a flat road is assumed. In reality the road is never exactly flat and some inclination is always present. The assumption is made however that the road roughness can be neglected as well as the inclination.

Figure 6 shows the measured and predicted signals of the steering-system during a J-turn. A left-hand turn

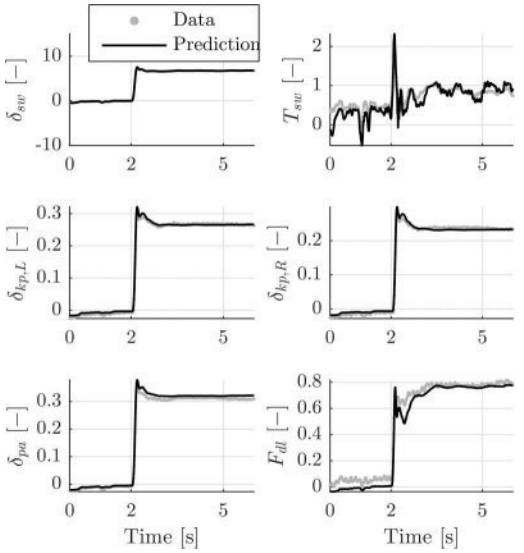


Figure 6. Steering-system signals during a J-turn.

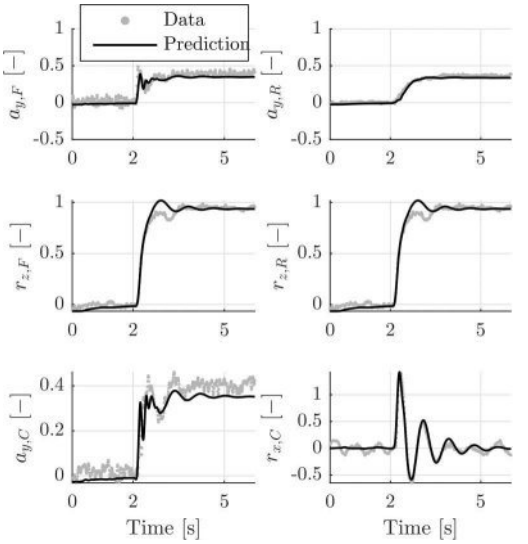


Figure 7. Chassis and cabin signals during a J-turn.

is made by applying a step-steer input after 2 seconds. The vehicle speed during this experiment is kept constant by means of the cruise control system. The final steering-wheel position is held until the end of the test. The angles are predicted accurately by the model, both the left and right king-pin angle are predicted accurately due to inclusion of the tie-rod stiffness. The pitman-arm angle seems slightly under-predicted. The drag-link force is predicted accurately as well, during straight-line driving a small difference is seen, probably due to the road inclination which is not present in the model. The step-response and end value appear to be predicted well. The steering-wheel torque already shows a lot of vibrations even when driving straight. Since there is friction present in the system, small movements of the steering-wheel will results in torque felt by the driver. It is important to predict this behavior as well since in contributes to the on-center feeling. The peak value at 2 seconds is caused by the sudden change and is largely friction related. The steady-state value is mainly caused by the tyre feed-back and the power-steering system. Figure 7 shows the accelerometers and gyroscopes. Interesting to see here is that the front and rear accelerometer signal differ quite a lot when the step input is applied. The model predicts similar behavior as well. The yaw-rates front and rear appear to be quite similar. The lateral acceleration in the cabin and the roll-rate in the cabin are analyzed to evaluate what the driver experiences . Both are predicted accurately as well. Interesting to see here is that the lateral acceleration in the cabin differs from both chassis measured lateral accelerations again when the step is applied.

Secondly, a sinusoidal input with a frequency of 0.4 Hz at a vehicle speed of 65 km/h is analyzed. During this experiment the vehicle speed is kept constant by the cruise-control system. Figure 8 shows

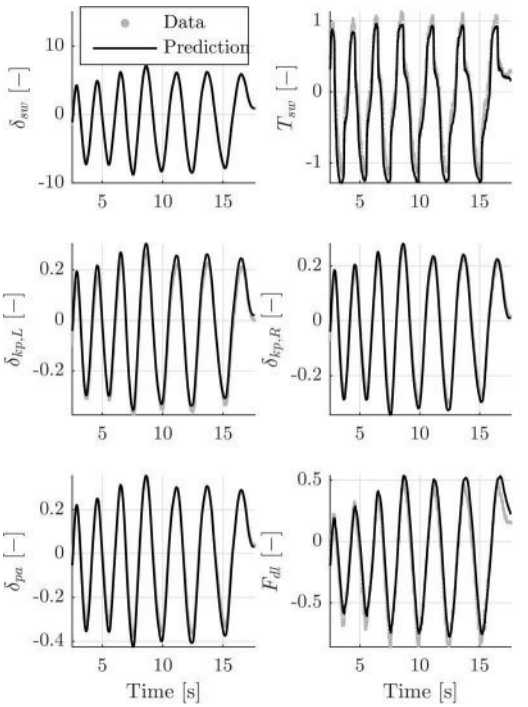


Figure 8. Steering-system signals during a sinusoidal input.

the steering-system signals. Again the angles in the steering-system are predicted with a good accuracy. The drag-link force shows some mismatches around the peaks for negative values. The steering-wheel torque prediction appears to be accurate, the peak values are predicted accurately for negative values and diverge a little bit for positive values. An important thing to notice here is the sudden jump when

the steering-wheel motion changes direction. Both the measurement and the simulation show this jump in steering-wheel torque, this is something that the driver definitely notices and is caused by the friction on the input side of the steering-house. Figure 9 shows the accelerometers and gyroscopes during this experiment. Minor differences between the data and prediction exist and the measured signal of the front accelerometer seems to contain a more noise. The roll-rate prediction shows the same general trend but some differences exist.

Figure 10 shows the steering-wheel torque as a function of steering-wheel angle for this test. From this figure it becomes clear that there is friction present in the system since change of steering-wheel angle direction results in a jump in torque. Also the non-linearity of the hydraulic system can be seen in the curved shape of this plot. The top-right graph shows the lateral acceleration as a function of steering-wheel angle. From this graph it can be concluded that the phase of the signal is also correctly predicted.

Since the steering-wheel torque is important for the drivers perception , the bottom four graphs in Figure 10 show the lateral acceleration and yaw-rate as a function of steering-wheel torque. Again the non-linearity of the hydraulic power-steering system is observed since the lines are curved. Friction is visible in these graphs as well since the signal jumps horizontally upon changing direction in lateral acceleration. The bottom two figures show the yaw-rate front and rear as a function of steering-wheel torque. Again here a curved shape is seen and the horizontal jumps show the friction present in the system.

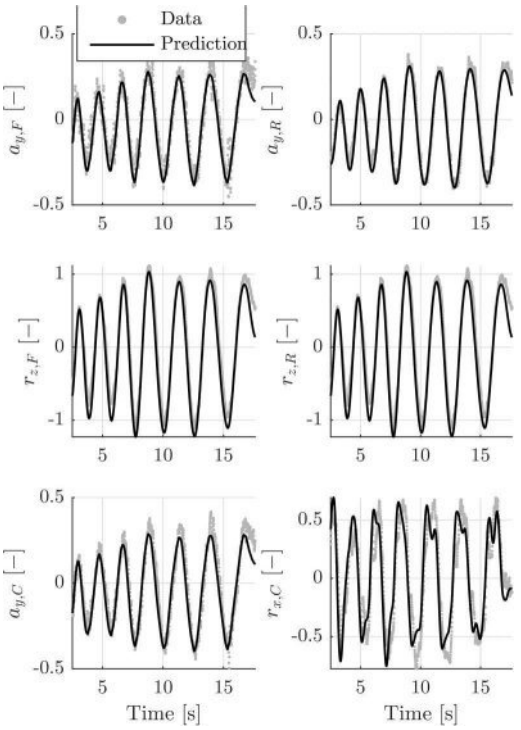


Figure 9. Chassis and cabin signals during a sinusoidal input.

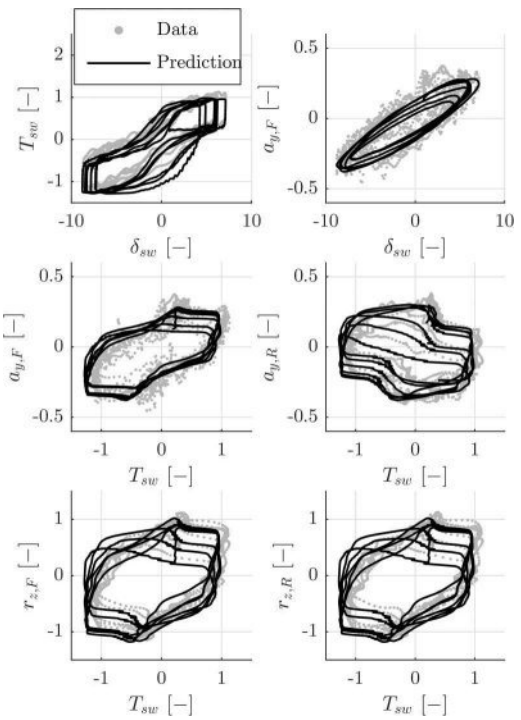


Figure 10. Steering-wheel torque as a function of steering-wheel angle and accelerations and yaw-rates as a function of steering-wheel angle or torque during a sinusoidal input.

5 CONCLUSIONS

A truck steering-system model has been coupled to a multi-body tractor semi-trailer model. A steady-state cornering test with an instrumented vehicle has been done to estimate the self-aligning stiffness and the cornering stiffness of the tyres. This instrumented vehicle is also used to perform a J-turn and a 0.4 Hz sinusoidal input to verify the steering-system model predictions.

Overall the conclusion is drawn that this steering-system model in combination with the multi-body truck model and the hub geometry is able to predict all measured signals in a satisfactory manner. The angles, accelerations and yaw-rates can be predicted with a high accuracy while the steering-wheel torque, roll-rate of the cabin and the drag-link force appear to be harder to predict.

6 FUTURE WORK

Future work will consist of verification with tests using a different input frequency. When the model is completely verified it will be used to investigate the possibilities of making the steering-system active by means of an extra actuator. This active steering-system

can be used to analyze different support systems such as a merging support and a lane keeping/changing assistant.

ACKNOWLEDGMENTS

This research was supported by the Stichting voor de Technische Wetenschappen (Dutch Technology Foundation) STW.

REFERENCES

[1] S. Bennett. *Heavy duty truck systems*. Cengage Learning, 2015.

[2] I. Besselink, J. Pauwelussen, and B. Kraaijenhagen. Greening and safety assurances of future modular road vehicles. In *VDI Commercial vehicles 13th International Conference*, 2015.

[3] A. DellAmico. Pressure control in hydraulic power steering systems. 2013.

[4] W.-J. Evers, I. Besselink, A. van der Knaap, and H. Nijmeijer. Development and validation of a modular simulation model for commercial vehicles. *International Journal of Heavy Vehicle Systems*, 16, 2009.

[5] J. Loof, I. Besselink, and H. Nijmeijer. Component based modeling and validation of a steering system for a commercial vehicle. In *24th IAVSD - Dynamics of Vehicles on Roads and Tracks*, 2015.

[6] J. Loof, I. Besselink, W. Post, and H. Nijmeijer. Development of a truck steering system model including hydraulics to predict the steering wheel torque. In *9th Graz Symposium Virtual Vehicle*, 2016.

[7] P. Mock. European vehicle market statistics, 2013.

[8] P. E. Pfeffer, M. Harrer, and D. Johnston. Interaction of vehicle and steering system regarding on-centre handling. *Vehicle System Dynamics*, 46(5):413–428, 2008.

[9] M. Rösth. Hydraulic power steering system design in road vehicles: Analysis, testing and enhanced functionality. 2007.

[10] C. Schoon, M. Doumen, and D. de Bruin. The circumstances of blind spot crashes and short- and long-term measures, 2008.

[11] H. Summala and T. Mikkola. Fatal accidents among car and truck drivers: effects of fatigue, age, and alcohol consumption. *Human Factors: The Journal of the Human Factors and Ergonomics Society*, 36(2):315–326, 1994.

[12] SWOV. Swov fact sheet. blind spot crashes, 2015.

Advanced Vehicle Control – Edelmann, Plöchl & Pfeffer (Eds)
© 2017 Taylor & Francis Group, London, ISBN 978-1-138-02992-7

A design of the lead-steer in active front steering system using lead-lag compensator

Janghyun Jung, Raewook Chung, Jinhyuck Heo, Junwook Oh & Jooho Lee
Hyundai Motor Company, Hwaseong, The Republic of Korea

ABSTRACT: Active Front Steering (AFS) system controls steering 'gear ratio' of vehicle, which is defined as a ratio of ground wheel steer to steering wheel angle, in order to improve vehicle agility in low speed and directional stability in high speed; AFS raises the gear ratio in low speed, and lowers the gear ratio in high speed. However, a low gear ratio in high speed could compromise yaw rate responsiveness of AFS vehicle, especially in obstacle-avoiding maneuver. Lead Steer Control has been introduced to compensate the yaw rate responsiveness of AFS vehicle in high speed. In this paper, a Lead Steer Control logic is developed based on the lead-lag compensator. Performance and stability of the control logic are designed based on the 'vehicle–control logic' model in closed-loop manner, and verified by real vehicle tests. The verification result shows a significant improvement in responsiveness and directional stability of AFS vehicle in high speed driving.

1 INTRODUCTION

Active Front Steering(AFS) system has been implemented in several mass production vehicles in order to improve vehicle dynamics performance and steering convenience, and therefore customer satisfaction.

AFS system can vary 'gear ratio', which can be defined as a ratio of ground steer angle to steering wheel angle, by implementing a mechanism such as strain wave gear, or planetary gear in the steering system. Figure 1, shows general construction of AFS system.

The agility and directional stability of vehicle are always compromising goals in conventional vehicle development. However, the new level freedom based on AFS gives automakers opportunities to improve agility and stability of vehicles in the same time.

AFS can be controlled to raise the gear ratio in low speed driving condition to improve steering agility, and reduce steering effort during parking condition. In the meantime, AFS can be controlled to lower the gear ratio in high speed driving condition to improve directional stability (Figure 2).

However, in spite of improvement of directional stability at high speed, yaw rate responsiveness of vehicle can be compromised due to low gear ratio; Yaw rate time delay of vehicle can be enlarged, thus drivers might feel awkwardness and looseness.

Most of all, obstacle-avoiding performance might be significantly compromised by the reduced yaw rate responsiveness of vehicle in high speed driving.

In this paper, Lead Steer Control logic is developed based on lead-lag compensator, in order to improve the

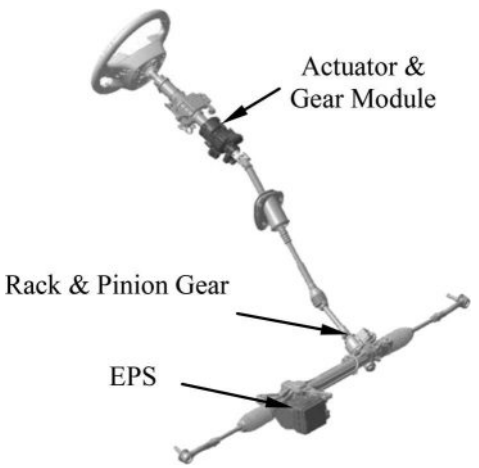


Figure 1. General components of AFS system.

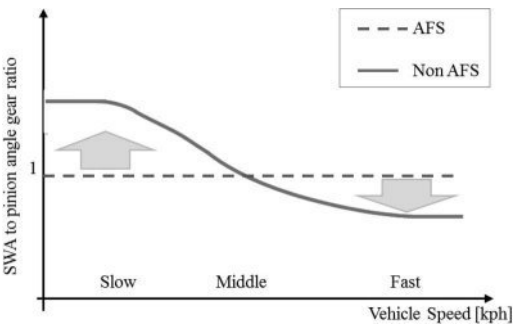


Figure 2. Typical gear ratio setup of AFS.

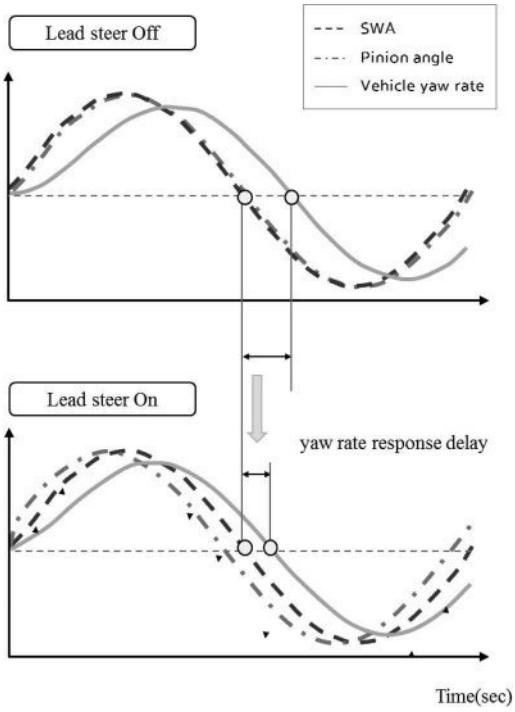


Figure 3. Concept of Lead Steer control to reduce yaw rate response delay (phase lead effect).

yaw rate responsiveness of AFS vehicle in high speed driving, while directional stability is maintained.

2 LEAD STEER CONTROL CONCEPT

As shown in Figure 2, the gear ratio of AFS is lower than 1.0 at high speed driving condition. The low gear ratio can improve directional stability of vehicle, but it can also compromise vehicle yaw rate response during high speed steering input such as obstacle avoiding maneuver.

The concept of Lead Steer Control is to compensate the low AFS gear ratio at high-speed driving by applying additional ground steer angle, especially for the high speed steering input such as obstacle avoiding maneuver.

As shown in Figure 3(a), The yaw rate response of vehicle will be delayed due to tire dynamics and steering compliance, etc.

If an additional ground steer angle (pinion angle) is applied according to driver's steering input, the yaw rate delay can be reduced significantly (Figure 3(b)).

The additional ground steer angle shall be proportional to the driver's steering wheel angle and steering wheel angle speed, in order to reflect driver's steering intention.

Figure 4 and 5 show schematic diagram of conventional map-based Lead Steer Control.

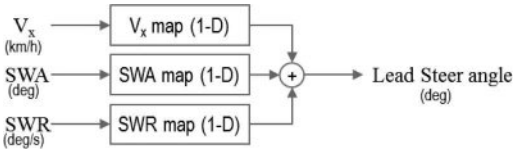


Figure 4. Conventional map-based Lead Steer control.

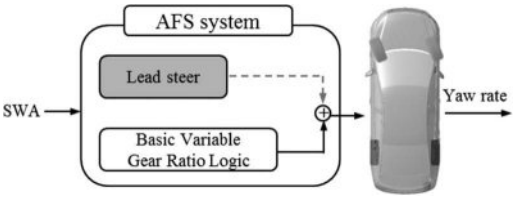


Figure 5. Schematic architecture of Lead Steer control.

The amount of lead steer angle has been determined based on heuristic trial-and-error test, which is inefficient to develop an optimal performance.

3 DEVELOPMENT OF LEAD STEER CONTROL BASED ON LEAD LAG COMPENSATOR

3.1 *Overview*

This paper presents the development of Lead Steer control logic based on lead-lag compensator. In this way, Lead Steer control can be designed considering system dynamics characteristics, and the mathematical approach enables to eliminate heuristic factors in control logic development, thus improve the development efficiency.

The control logic is developed in following steps.

1) Development of vehicle dynamics model and System identification for vehicle characteristic parameters
2) Design led-lag compensator
3) Closed-loop analysis for system stability
4) Verification of design based on vehicle test

3.2 *Vehicle model and system identification*

Bicycle model of 2-degree of freedom is introduced for vehicle dynamics model. As shown in Eq. (1), vehicle dynamics model can be defined as second-order differential equation. (Tetsushi Mimuro, Masayoshi Ohsaki. Hiromichi Yasungga, Kohji Satoh, (1990))

$$\begin{bmatrix} mV + \dfrac{2(l_f K_f - l_r K_r)}{V} & mV \cdot s + 2(K_f - K_r) \\ I_z \cdot s + \dfrac{2(l_f{}^2 K_f + l_r{}^2 K_r)}{V} & 2(l_f K_f - l_r K_r) \end{bmatrix} \begin{bmatrix} \dot{\psi} \\ \beta \end{bmatrix} = \frac{2}{i_s} \begin{bmatrix} K_f \\ l_f K_f \end{bmatrix} \cdot \delta_h \quad (1)$$

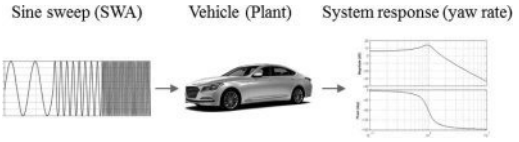


Figure 6. System identification process.

where,

s	the Laplace transform operator
Ψ	yaw velocity (yaw rate)
β	side-slip angle
δ_h	Steering wheel angle
V	Vehicle forward speed
m	Vehicle mass
I_z	Yawing moment of inertia
l_f	Distance from front axle to C.G
l_r	Distance from rear axle to C.G
K_f	Equivalent front cornering power
K_r	Equivalent rear cornering power
i_s	Overall steering gear ratio

Then the vehicle dynamics model can be approximated as second-order transfer function of yaw rate with respect to steering wheel input.

$$TF_{vehicle} = \frac{\dot{\psi}}{\delta_h} = \frac{1 + T_f \cdot s}{1 + 2\zeta \frac{s}{w_n} + \frac{s^2}{w_n^2}} \tag{2}$$

where,

w_n	Natural frequency
ζ	Damping ratio
T_f	Lead time constant of yaw rate

If system characteristic parameters such as natural frequency, damping ratio, and time constant are identified, system dynamic characteristics can be analyzed.

In this paper, system identification technique (System ID) is introduced to identify system characteristics parameters.

System identification is a typical technique to identify dynamic system characteristics when the target plant is black box, or the plant is highly complicated for mathematical modeling.

In System ID, sine sweep input is applied to plant, and dynamic response of the plant is measured in frequency domain. Characteristic parameters of transfer function of plant model can be estimated by comparing the responses of transfer function and real plant; least square curve fitting method is one of the general techniques to compute the parameters.

In this paper, steering wheel input of sine sweep between 0.1 Hz and 2.0 Hz at 120 kph is applied to vehicle in order to measure characteristic parameters.

Figure 7 shows estimation result of characteristic parameters of transfer function (2). And matching precision is 98.3%.

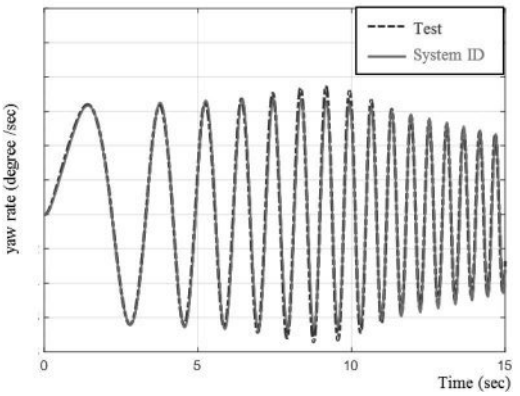


Figure 7. System ID result.

3.3 *Development of Lead Steer controller*

In this paper, a Lead Steer controller is developed based on lead-lag compensator.

Generally, obstacle-avoiding maneuver occurs within steering wheel speed of 1–2 Hz range. Therefore, the objective of Lead Steer control is to amplify AFS output pinion angle in this range, according to driver's steering wheel input.

The transfer function of Lead Steer controller can be defined as Eq. (3)

$$TF_{lead-steer} = k \times \frac{s+a}{s+b} \times \frac{s+c}{s+d} \tag{3}$$

where,

$$k = \frac{b \times d}{a \times c}$$

a	Zero of Lead compensator
b	Pole of Lead compensator
c	Zero of Lag compensator
d	Pole of Lag compensator

Gain k is introduced to eliminate steady state offset of lead-lag compensator as below.

$$TF_{lead-stear@steady-state} = \frac{b \times d}{a \times c} \times \frac{0+a}{0+b} \times \frac{0+c}{0+d} = 1 \tag{4}$$

Therefore, transfer function of vehicle-controller can be defined as Eq. (5)

$$TF_{total} = TF_{lead-steer} \times TF_{vehicle} \tag{5}$$

Figure 8, 9 show phase and magnitude plot of Lead-Steer compensator. Phase of AFS output pinion angle around steering wheel speed 1 Hz is significantly leaded and magnitude is amplified as well. Although the magnitude over 4 Hz is amplified, it is of no significance because driver's steering wheel input shall be physically restrained under 4 Hz.

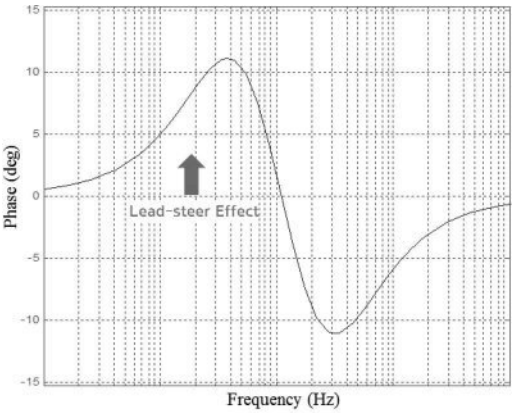


Figure 8. Phase plot of Lead Steer controller.

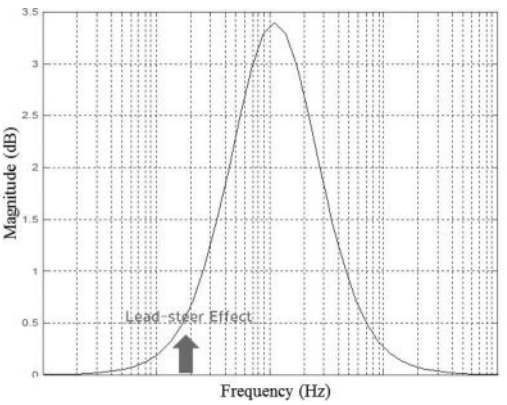


Figure 9. Magnitude plot of Lead Steer controller.

In order to verify the stability of Lead Steer controller, a closed loop frequency analysis is carried out. Figure 11 shows bode plot for the closed loop system of vehicle and Lead Steer controller.

As shown in Figure 10, gain margin and phase margin of closed loop system are infinite, thus the control system is stable.

4 VALIDATION OF LEAD STEER CONTROL

The lead control design is validated by real vehicle test. A D-segment sedan is used for the test. A number of test cases are carried out with steering input of 0.5 Hz, 1 Hz, 1.5 Hz, and 2 Hz at vehicle speed of 120 kph.

Vehicle lateral acceleration is maintained at 0.4 g.

In order to guarantee the consistency of the tests, a steering robot is applied for the steering input and real time data acquisition system is equipped in the vehicle, while vehicle speed is maintained by cruise control system (Figure 11).

Performance of Lead Steer control can be validated by comparing yaw rate response of vehicle with Lead Steer control to vehicle without Lead Steer control.

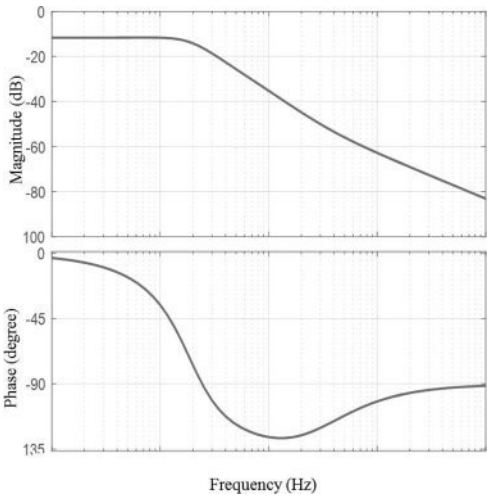


Figure 10. Bode plot for closed loop system of vehicle and Lead Steer controller.



Figure 11. Steering robot and real time data acquisition system.

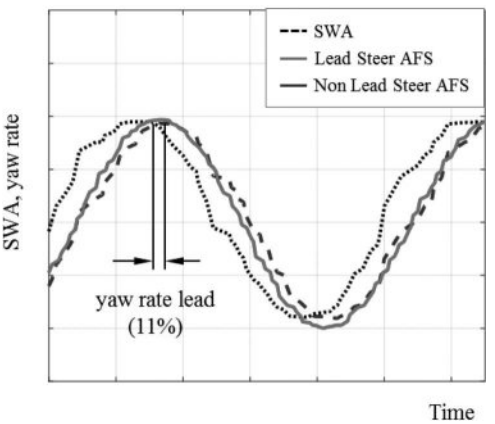


Figure 12. Lead steer performance at 1 Hz sine weave on 120 kph vehicle speed.

The test result of percent of yaw rate lead time change is shown in Figure 12 and Figure 13.

The result shows that lead steer controller improve yaw rate time as much as 11% at 1 Hz sine weave test on 120 kph vehicle speed and 12.8% at 1.5 Hz sine weave test on 120 kph vehicle speed.

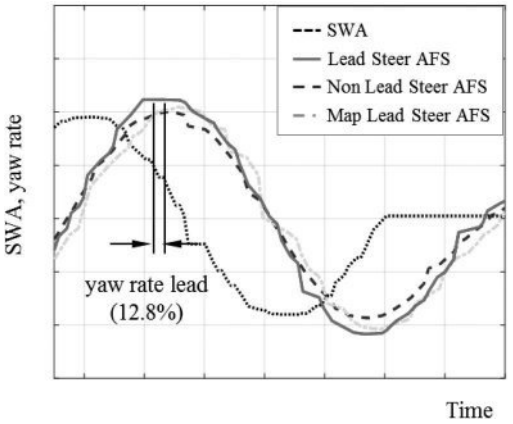


Figure 13. Lead steer performance at 1.5 Hz sine weave test on 120 kph vehicle speed.

5 CONCLUSION

Active Front Steering (AFS) system controls steering 'gear ratio' of vehicle in order to improve vehicle agility in low speed and directional stability in high speed. However, a low gear ratio in high speed could compromise yaw rate responsiveness of AFS vehicle, especially in obstacle-avoiding maneuver.

A heuristic map based Lead Steer control has been applied to AFS in order to compensate vehicle yaw rate responsiveness, which is not efficient to develop optimal performance.

In this paper, a Lead Steer control logic is developed based on the lead-lag compensator.

A vehicle dynamics model is approximated second-order transfer function, and system characteristics parameters are measured by system identification method.

Performance and stability of the control logic are pre-designed and validated based on the 'vehicle–control logic' system model.

The performance of Lead Steer control logic is validated by real vehicle test. The verification result shows a significant improvement in yaw rate responsiveness and directional stability of AFS vehicle in high speed driving.

Based on the verification result, it can be concluded that Lead Steer control using mathematical lead-lag compensator is much more efficient to develop the performance compared to conventional map based Lead Steer control; the performance and stability can be pre-designed by mathematical simulation, thus it can significantly reduce the trial-and-error in development.

REFERENCE

Tetsushi Mimuro. Masayoshi Ohsaki. Hiromichi Yasungga, Kohji Satoh, 1990, Four Parameter Evaluation Method of Lateral Transient Response, *SAE*, 901734, 52

Advanced Vehicle Control – Edelmann, Plöchl & Pfeffer (Eds)
© 2017 Taylor & Francis Group, London, ISBN 978-1-138-02992-7

The influence of time delay on stability of the steering simulator

Yuyao Jiang, Weiwen Deng, Jian Wu & Sumin Zhang
State Key Laboratory of Automotive Simulation and Control, Jilin University, Changchun, China

Keke Zhang
SAIC Motor Technical Center, Shanghai, China

ABSTRACT: Steering simulator is a device used to replicate or design the steering response of a vehicle while offering the steering feedback torque for the driver. Time delay of the steering simulator is inevitable and has significant influence on the performance and stability of the system. In this paper, from the point of view of the system design, a stability criterion considering the time delay of the system is derived based on an energy-based approach. The time delay effects on the steering simulator are also quantitatively analyzed in this paper. The criterion derived in this paper can be used as a guideline on the design of steering torque feedback systems, including the maximum allowed time delay of the system, dynamic response of the servo motor, and the computational efficiency of the processor. The proposed method and the derived stability criterion are verified by both simulation and experiment.

1 INTRODUCTION

Steering simulator is a device used to replicate or design the steering response of a vehicle while offering the steering feedback torque for the driver (David 2010). It is an important part of a driving simulator or a vehicle equipped with a steer-by-wire system, since the steering feedback torque renders the vehicle-road interaction and is considered very important for driving a vehicle. (Katzourakis et al 2011, Jarlmark 2005).

The most common approach for a steering simulator used either in a driving simulator or a steer-by-wire system is that the servo motor is directly connected to the steering wheel (Fankem 2014, Oh et al. 2004). Due to data communication, algorithm computation and other nonlinear factors of the system, time delay is inevitable from steering wheel angle input to steering torque feedback. Unlike steering feel under traditional vehicle that driver feels the steering feedback torque simultaneously when the steering is applied, time delay in steering simulator usually has significant adverse effect on the performance and stability of the steering simulator, such as the steering feedback torque range in which the steering feel can be simulated stably. If the time delay is large enough, the steering feel may not be acceptable and the system may even become unstable. Especially for small-sized and low-cost driving simulators, which are usually equipped with low-cost processor and servo motor, the influence of time delay on the stability and performance of the system is more evident.

A great deal of research has been conducted from literature review on time delay effect on the performance and stability of the system. Gualino et al. (2006) proved that the time delay of the system is one of the most critical factors on steering feel, and large delay may destabilize the system by hardware-in-loop experiments. Zhang (2009) also concluded that the system time delay should not be too large to influence the return-to-center performance of the system. Amberkar et al. (2004) pointed out that the time delay can lead to poor steering feel and have a destabilizing effect on the system. Besides, to improve the stability and return-to-center performance affected by the time delay of the steering simulator, a return torque compensation algorithm is usually applied in the system. For example, Fahami et al. (2015) added the compensation torque for a realistic feedback torque consisting of the inertia torque and damping torque potential to reduce the vibration and stabilize the system. Amberkar et al. (2004) also researched the influence of damping used to improve the system stability and reduce free control oscillations. Although various time delay effects have been investigated and some algorithms have been proposed to mitigate the adverse effects, most research on the time delay effects on the steering simulator has been conducted with its focus mainly on system analysis. The analysis results are usually on qualitative level, which cannot be directly used as guideline on the design of the system. In fact, time delay is also one of the important parameters that must be considered in the design process of a steering simulator. Therefore, from the point of view of system design, analyzing

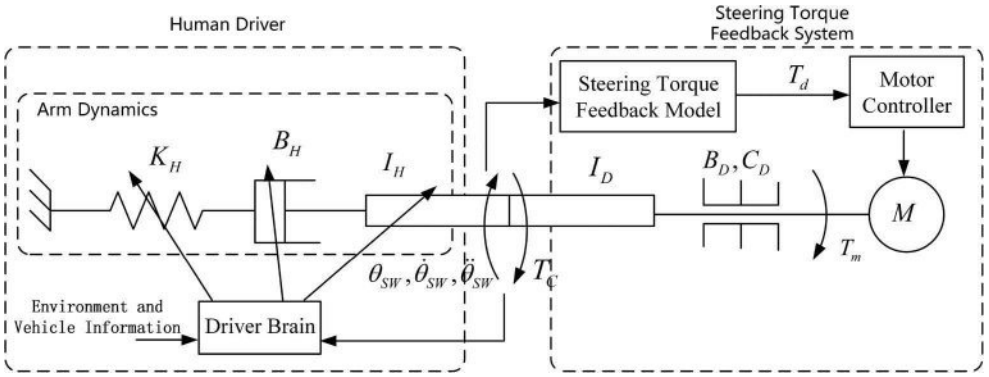


Figure 1. System block diagram of steering simulator.

the time delay effects on the stability of the steering simulator quantitatively is critically important on the performance of the steering feel to ensure true replication of steering feel for a driver simulator or desired steering feel for a steer-by-wire system.

To provide a guideline for the design of a steering simulator, a stability criterion considering the whole time delay of the system is derived based on an energy-based approach in this paper, which can be used as a guideline on the design of the steering simulator, including the response of the servo motor, the computational efficiency of the processor and the communication rate of the system. According to the criterion, the maximum allowed time delay of the steering simulator can be calculated based on the system requirement of the steering feedback torque range that system should simulate stably. The steering feel range simulated stably by the steering simulator can also be identified base on the time delay and other characteristics of the system according to the criterion derived in this paper.

This paper is organized as follows. In Section 2, the system is described and modelled. In Section 3, the stability criterion considering the time delay of the system is derived based on an energy-based approach. The time delay effects on the stability of the steering simulator are also analyzed in this section. In Section 4, the derived stability criterion and the analysis results of time delay are verified by both simulation and experiment.

2 SYSTEM DESCRIPTION

2.1 *System description and modeling*

The architecture and mechanism of the steering simulator is shown in Figure 1. As shown in Figure 1, according to the environment information and vehicle states, a desired steering wheel angle is decided in the driver brain, and then the driver turns the steering wheel. The steering wheel angle θ_{SW}, steering wheel angular velocity $\dot{\theta}_{SW}$ and steering wheel angular acceleration $\ddot{\theta}_{SW}$ are acquired by sensors and send to steering torque feedback model to calculate the desired steering feedback torque T_d that is realized by the servo motor controlled by the motor controller. Finally, the driver feels the feedback torque through the steering column and the mechanical inertia of the motor, which is defined as the mechanical part of the steering simulator.

2.2 *System modeling*

The inertia, damping and friction of the mechanical part of the steering simulator are all considered in modeling. Because the mechanical stiffness of the system is usually not big, the influence of the stiffness is neglected in the modeling. The model of the mechanical part is shown in Equation (1),

$$I_D\ddot{\theta}_{SW} + B_D\dot{\theta}_{SW} + C_D\,\mathrm{sgn}(\dot{\theta}_{SW}) = T_h - T_m \tag{1}$$

where I_D is the inertia of mechanical part; B_D is the damping coefficient of the mechanical part; C_D is the coulomb friction; T_m is the motor output torque; T_h is the driver input torque, as shown in Equation (2),

$$T_h = I_H\ddot{\theta}_{SW} + B_H\dot{\theta}_{SW} + K_H\theta_{SW} \tag{2}$$

where I_H, B_H and K_H are the inertia, damping and stiffness of the driver's arm respectively. They are all adaptive variables.

The main influencing factors of steering feedback torque are vehicle speed and steering wheel angle. Other factors, such as tire feedback torque and power assistance, are all related to the two factors. Therefore, the steering torque feedback model is established as an equivalent stiffness-damping-friction system according to the basic characteristics of the steering system, as shown in Equation (3).

$$T_d = K_V(v)\cdot\theta_{SW} + B_V(v)\cdot\dot{\theta}_{SW} + C_V(v)\cdot\mathrm{sgn}(\dot{\theta}_{SW}) \tag{3}$$

where K_V, B_V and C_V are the equivalent stiffness, damping and friction of the steering feel respectively, and they are all variables related to vehicle speed v.

Table 1. Dimensionless parameters.

Parameters	Symbol	Dimensionless
Sample Interval	T_s	
Steering feel stiffness	K_V	
Time	t	$\tau = t/T_s$
Time delay	t_d	$\tau_d = \frac{t_d}{T_s}$
Steering wheel angle	θ_{SW}	$\zeta(\tau) = \theta_{SW}(t)$
Steering wheel velocity	$\dot{\theta}_{SW}$	$\dot{\zeta}(\tau) = \dot{\theta}_{SW}(t) \cdot T_s$
Steering wheel acceleration	$\ddot{\theta}_{SW}(t)$	$\ddot{\zeta}(\tau) = \ddot{\theta}_{SW}(t) \cdot T_s^2$
Torque	T	$\varphi = \frac{T}{K_V}$
System inertia	I_D	$i_D = \frac{I_D}{K_V T_s^2}$
System damping	B_D	$\beta_D = B_D/(K_V T_S)$
System coulomb friction	C_D	$\sigma_D = C_D/K_V$
Steering feel damping	B_V	$\beta_V = B_V/(K_V T_s)$
Steering feel coulomb friction	C_V	$\sigma_V = C_V/K_V$

The servo motor system is assumed to be an ideal torque tracking system just with a time delay, as shown in Equation (4). It can track the desired steering feedback torque effectively. The time delay t_d in this part is equivalent to the system's all time delays derived from communication, calculation and other nonlinear factors.

$$T_m(t) = T_d(t - t_d) \tag{4}$$

According to the analysis above, the model of the steering simulator is shown in Equation (5).

$$\begin{cases} I_H \ddot{\theta}_{SW} + B_H \dot{\theta}_{SW} + K_H \theta_{SW} = T_h \\ I_D \ddot{\theta}_{SW} + B_D \dot{\theta}_{SW} + C_D \operatorname{sgn}(\dot{\theta}_{SW}) = T_h - T_m \\ T_d = K_V \cdot \theta_{SW} + B_V \dot{\theta}_{SW} + C_V \operatorname{sgn}(\dot{\theta}_{SW}) \\ T_m(t) = T_d(t - t_d) \end{cases} \tag{5}$$

2.3 *Dimensionless analysis*

In order to reduce the number of analysis parameters, dimensional analysis is operated in this part. The sample time and the equivalent stiffness of steering feel is selected as basic parameters that other parameters are related to. The dimensionless analysis results are shown in Table 1.

Then the Equation (5) can be written as Equation (6).

$$\begin{cases} i_D \ddot{\zeta}(\tau) + \beta_D \dot{\zeta}(\tau) + \sigma_D \operatorname{sgn}(\dot{\zeta}) = \varphi_h(\tau) - \varphi_m(\tau) \\ \varphi_d(\tau) = \zeta(\tau) + \beta_V \dot{\zeta}(\tau) + \sigma_V \operatorname{sgn}(\dot{\zeta}) \\ \varphi_m(\tau) = \varphi_d(\tau - \tau_d) \end{cases} \tag{6}$$

According to Equation (6), the driver torque input $\phi_h(\tau)$ can be written as Equation (7).

$$\begin{aligned} \varphi_h(\tau) = {} & i_D \ddot{\zeta}(\tau) + \beta_D \dot{\zeta}(\tau) + \sigma_D \operatorname{sgn}(\dot{\zeta}) + \varphi_m(\tau) \\ & - \varphi_d(\tau) + \varphi_d(\tau) \end{aligned} \tag{7}$$

3 STABILITY ANALYSIS OF THE SYSTEM

3.1 *Passive analysis*

Both the mechanical part of the steering simulator and the steering system simulated by the steering simulator are typical nonlinear and passive systems. Therefore, an energy-based approach is proposed in this section to analyze the stability of the system. A stable steering simulator is obviously a passive system, which does not produce energy, and can dissipate the energy loaded by the driver. In this paper, the driver torque input T_h is as the energy source. Then, according to Equation (7), the generalized work done by the driver in a general time interval $[\tau_0, \tau_1]$ can be written as Equation (8),

$$\begin{aligned} \int_{\tau_0}^{\tau_1} \varphi_h(\tau)\dot{\zeta}(\tau)d\tau = {} & V(\tau_1) - V(\tau_0) \\ & + E_d(\tau_0, \tau_1) - E_g(\tau_0, \tau_1) \end{aligned} \tag{8}$$

where,

$$\begin{aligned} V(\tau_1) - V(\tau_0) &= \int_{\tau_0}^{\tau_1} \left[i_D \ddot{\zeta}(\tau) + \zeta(\tau) \right] \dot{\zeta}(\tau) d\tau \\ &= \frac{1}{2} i_D \left[\ddot{\zeta}(\tau) \right]^2 + \frac{1}{2} \left[\zeta(\tau) \right]^2 \geq 0 \end{aligned} \tag{9}$$

$$E_d(\tau_0, \tau_1) = \int_{\tau_0}^{\tau_1} \left[\left(\beta_D + \beta_V \right) \dot{\zeta}(\tau) + \left(\sigma_D + \sigma_V \right) \operatorname{sgn}(\dot{\zeta}) \right] \dot{\zeta}(\tau) d\tau \tag{10}$$

$$E_g(\tau_0, \tau_1) = \int_{\tau_0}^{\tau_1} \left[\varphi_d(\tau) - \varphi_m(\tau) \right] \dot{\zeta}(\tau) d\tau \tag{11}$$

$V(\tau_1) - V(\tau_0)$ is a positive define function and the sum of rotational kinetic energy and elastic potential energy. Therefore, it can be the energy storage function and the lyapunov function of the system; $E_d(\tau_0, \tau_1)$ is the dissipative energy of the system; $E_g(\tau_0, \tau_1)$ is the generated energy derived from the time delay. To guarantee the passivity of the system, the system needs to satisfy the inequality shown as Equation (12).

$$V(\tau_1) - V(\tau_0) \leq \int_{\tau_0}^{\tau_1} \varphi_h(\tau)\dot{\zeta}(\tau) d\tau \tag{12}$$

This can be further derived as Equation (13).

$$E_d(\tau_0, \tau_1) \geq E_g(\tau_0, \tau_1) \qquad \forall \tau_1 > \tau_0 \tag{13}$$

This means the energy generated by the time delay can be dissipated by the damping and friction of the system itself and the system simulated. To guarantee the establishment of the Equation (13), the lower bound of $E_d(\tau_0, \tau_1)$ and the upper bound of $E_g(\tau_0, \tau_1)$ are shown in Equation (14) and (15) respectively.

$$E_d(\tau_0, \tau_1) \geq \left[\left(\beta_D + \beta_V \right) \dot{\zeta}(\tau) + \left(\sigma_D + \sigma_V \right) \right] \left| \zeta(\tau_1) - \zeta(\tau_0) \right| \tag{14}$$

$$E_g(\tau_0, \tau_1) \leq \left(\left| \ddot{\zeta} \right|_{\max} + \beta_V \left| \ddot{\zeta} \right|_{\max} \right) \tau_d \left| \zeta(\tau_1) - \zeta(\tau_0) \right| \tag{15}$$

where $\tau \in (\tau_0, \tau_1)$. Then the stability criterion of the system is shown in Equation (16).

$$\left(\left| \ddot{\zeta} \right|_{\max} - \tau_d \left| \ddot{\zeta} \right|_{\max} \right) \beta_V + \sigma_V + \left(\beta_D - \tau_d \right) \left| \dot{\zeta} \right|_{\max} + \sigma_D \geq 0 \tag{16}$$

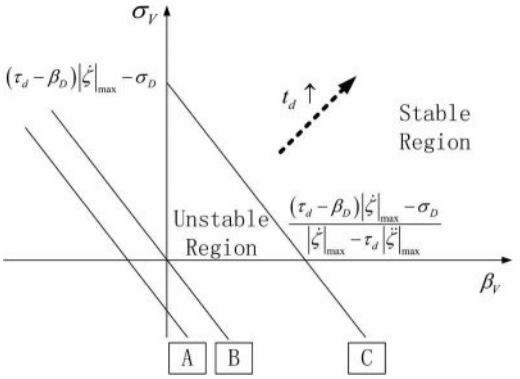


Figure 2. The stability criterion of the steering simulator in $\beta_V-\sigma_V$ coordinates, in which, A is the criterion line when $\tau_d=0$; B is the criterion line when $\tau_d=\beta_D+\sigma_D/|\dot{\zeta}|_{\max}$; C is the criterion line when $\tau_d>\beta_D+\sigma_D/|\dot{\zeta}|_{\max}$.

3.2 *The analysis of the system criterion*

The stability criterion of the system shown in Equation (16) is described in Figure 2. When $\tau_d \le \beta_D+\sigma_D/|\dot{\zeta}|_{\max}$, the system is always stable regardless of the steering feel simulated. That is because both the steering simulator and the steering system simulated are passive system. The whole system composed by two passive systems without any time delay is also a passive system. That means, the system will be always stable when the time delay of the system is small enough. However, the time delay in this condition is usually too small that almost no system can satisfy this condition. When $\tau_d > \beta_D+\sigma_D/|\dot{\zeta}|_{\max}$, the $\beta_V-\sigma_V$ region is divided into two parts, the stable region and the unstable region. The unstable region of the system increased as the time delay of the system increases.

4 SIMULATION AND EXPERIMENTS

To verify the derived stability criterion and the analysis results of time delay above, both simulation and experiments have been conducted in this paper. To avoid the disturbance of human factors, the free response condition is chosen in both simulation and experiment tests. This condition refers to the response of the steering wheel after an initial steering wheel angle given by the driver, and the subsequent response would be free of driver inputs. This condition well represents the stability performance of the system.

Assume that the elastic potential energy simulated by the system is totally translated into the rotational kinetic energy of the system after the initial moment. Then, the maximum steering wheel angular velocity $\dot{\theta}_{SW_\max}$ and the maximum steering wheel angular acceleration $\ddot{\theta}_{SW_\max}$ can be calculated by Equation (17) and Equation (18).

$$\frac{1}{2}K_V\theta_{SW_\max}^2=\frac{1}{2}J_D\dot{\theta}_{SW_\max}^2 \tag{17}$$

Table 2. Parameters used in simulation.

Parameter	Symbol	Unit	Value
Inertia (steering simulator)	J_D	$kg\cdot m^2$	0.06
Damping (steering simulator)	B_D	$N\cdot m\cdot s$	0.005
Coulomb friction (steering simulator)	C_D	$N\cdot m$	0.01
Stiffness (steering feel)	K_V	$N\cdot m$	1
Initial steering wheel angle (driver input)	$\theta_{SW_\max}$	rad	1.59
Sample time	T_s	ms	1

Table 3. Simulation conditions.

Condition	1	2	3
t_d [ms]	3	50	80

$$J_D\ddot{\theta}_{SW_\max}=K_V\theta_{SW_\max} \tag{18}$$

4.1 *Verification by simulation*

To conduct the simulation tests, the steering simulator is modeled in Matlab/Simulink®. The parameters used in simulation are shown in Table 2.

The simulation conditions are shown in Table 3. Three conditions are chosen for simulation tests, in which the time delay t_d of the system are 3 ms, 50 ms and 80 ms respectively. In every condition, 100 points in $\beta_V-\sigma_V$ coordinates are chosen to be conducted in simulation. Whether the system is stable at each point will be decided by the simulation results at each point. In condition 1, the time delay is very small and the inequality $\tau_d \le \beta_D+\sigma_D/|\dot{\zeta}|_{\max}$ is established. In condition 2 and 3, inequality $\tau_d > \beta_D+\sigma_D/|\dot{\zeta}|_{\max}$ is established, and the time delay in condition 3 is bigger than that in condition 2.

The simulation results of condition 1, 2 and 3 are shown in Figure 3, Figure 4 and Figure 5 respectively. Within the white-colored region, the system is stable, while in the gray-colored region, the system is unstable. The color of each grid is decided by the simulation results of the point at the bottom left corner of this grid. A stability criterion curve calculated by theory results derived above (Eq. (16)) is represented with straight lines as shown in the left side of these figures (Figs 4–5). Some detailed simulation results of specific points are shown in the right side of these figures (Figs 3–5).

As shown in Figure 3, the whole region is a stable region, which matches well with the analytical results from the criterion in the condition of $\tau_d \le \beta_D+\sigma_D/|\dot{\zeta}|_{\max}$.

Figure 4 and 5 show the results when $\tau_d > \beta_D+\sigma_D/|\dot{\zeta}|_{\max}$. Both unstable and stable regions are clearly separated by the criterion line, which can also verify the derived stability criterion. Because a conservative

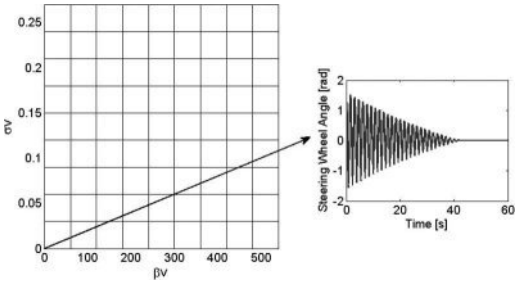


Figure 3. Simulation results of Condition 1 in which the time delay is 3 ms.

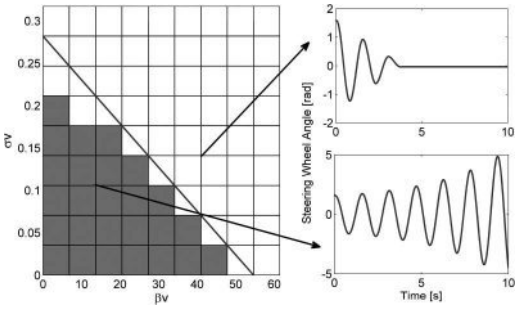


Figure 4. Simulation results of Condition 2 in which the time delay is 50 ms.

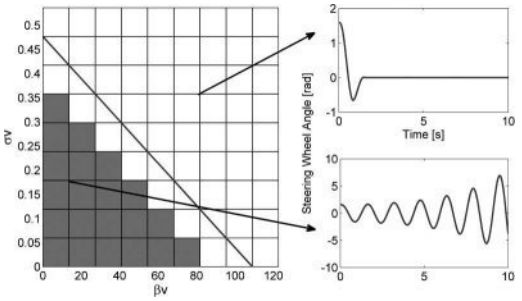


Figure 5. Simulation results of Condition 3 in which the time delay is 80 ms.

method is used in theory analysis part, the simulation results are conservative too. Besides, compared the criterion curve and the unstable region both in Figure 4 and 5, we can see that the unstable region increases with the increase of time delay, and the criterion curve is also moved up with the increase of the time delay. That also well verifies the theory analysis results of time delay above.

4.2 *Verification under HIL platform*

The steering simulator used in this section is in direct-connected form in which the steering wheel and the servo motor are connected directly. Therefore, the damping and friction of the system itself is small enough to neglect. The inertia of the system is identified as 0.07 kg.m^2 by the least square approach. The parameters of the HIL platform are shown in Table 4.

Table 4. Parameters used in experimental tests.

Parameter	Symbol	Unit	Value
Inertia (steering simulator)	J_D	kg · m^2	0.07
Stiffness (steering feel)	K_V	N · m	0.5
Damping (steering feel)	B_V	N · m · s	0.03
Coulomb friction (steering feel)	C_V	N · m	0.03
Initial steering wheel angle (driver input)	θ_{SW_max}	rad	1.59
Sample time	T_s	ms	1

Table 5. Experimental tests.

Test	t_d ms	B_V N · m · s	C_V N · m
1	129	0.1	0.03
2	129	0.03	0.03
3	58	0.03	0.03

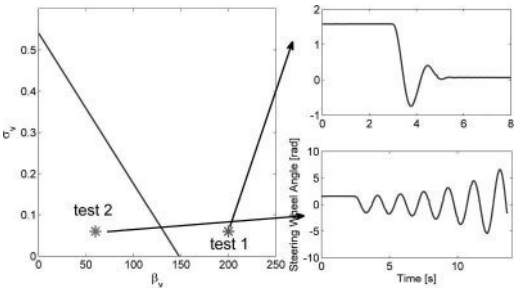


Figure 6. Experimental results of Test 1 and 2.

The experimental tests are shown in Table 5. Comparing Test 1 to Test 2, different points in the same $\beta_V - \sigma_V$ coordinates, representing different characteristics of the steering feel, are simulated with same time delay. Comparing Test 2 to Test 3, the characteristics of steering feel simulated in the two tests are the same, while the time delay of the system is different.

The experimental results of Test 1 and 2 are shown in Figure 6. The line in the left side of Figure 6 represents the criterion curve calculated by Equation (16). The $\beta_V - \sigma_V$ points in Test 1 and 2 are located in stable region and unstable region respectively, and the experimental results of these two points are also stable and unstable respectively, which agree well with the theoretical analysis results above.

When the time delay decreases to 58 ms (Test 3), the stable region of the system is increased, and the

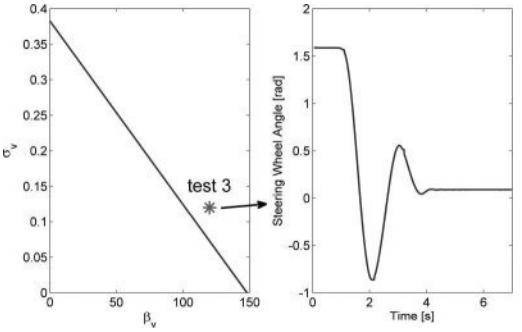


Figure 7. Experimental results of Test 3.

steering feel point of Test 2 becomes stable, as shown in Figure 7. Thus, the derived criterion is further verified to be valid via the experiments.

5 CONCLUSIONS

The time delay of the steering simulator is inevitable from steering wheel angle input to steering torque feedback, and has significant influence on the performance and stability of the system. It is also an important factor must be considered in the design process of a steering simulator. In this paper, a stability criterion considering the time delay of the system is derived based on an energy-based approach, and the time delay effects on the stability of the steering simulator are also quantitatively analyzed in this paper. The stability criterion can be used as a design guideline for steering simulator with time delay to ensure system stability. According to the criterion, the allowable time delay of the steering simulator can be calculated based on the requirements of the steering feel range that the system should simulate stably. Besides, to a finished steering simulator, the steering feel range that the system could simulate stably can also be identified according to the criterion base on time delay and other characteristics of the system.

ACKNOWLEDGEMENT

This research is supported by China National Natural Science Foundation (U1564211) and National Key Research and Development Program (2016YFB0 100904).

REFERENCES

Amberkar, S., Bolourchi, F., Demerly, J., & Millsap, S. 2004. A control system methodology for steer by wire systems. *Steering & Suspension Technology Symposium*.

David, J. 2010. Vehicle steering systems—hardware-in-the-loop simulator, driving preferences, and vehicle intervention. *Dissertations & Theses – Gradworks*.

Fankem, S. 2014. A new model to compute the desired steering torque for steer-by-wire vehicles and driving simulators. *Vehicle System Dynamics,* 52(sup1), 251–271.

Fahami, S. M. H., Zamzuri, H., & Mazlan, S. A. 2015. Development of estimation force feedback torque control algorithm for driver steering feel in vehicle steer by wire system: hardware in the loop. *International Journal of Vehicular Technology*, 2015, 1–17.

Gualino, D., & Adounkpe, I. J. 2006. Force-Feedback System Design for the Steer-By-Wire: Optimization and Performance Evaluation. *Intelligent Transportation Systems Conference, 2006. ITSC '06*. IEEE (pp. 181–187). IEEE.

Jarlmark, J. 2005. Modelling and validation of steering system response to road and driver induced forces. *The Dynamics of Vehicles on Roads and on Tracks*, 41, 371–380.

Katzourakis, D., Abbink, D., Happee, R., & Holweg, E. (2011). Steering force feedback for human–machine-interface automotive experiments. *IEEE Transactions on Instrumentation & Measurement*, 60(1), 32–43.

Oh, S. W., Chae, H. C., Yun, S. C., & Han, C. S. 2004. The design of a controller for the steer-by-wire system. *Jsme International Journal,* 47(3), 896–907.

Zhang Yi. 2009. Research and Development of Steering Wheel Return Simulation System. *Doctoral dissertation, Wuhan University of Technology*.

Advanced Vehicle Control – Edelmann, Plöchl & Pfeffer (Eds)
© 2017 Taylor & Francis Group, London, ISBN 978-1-138-02992-7

Study on reactive steering torque control for bar type steering in high speed range

S. Tamakawa, H. Tanabe, K. Sato, H. Mouri & P. Raksincharoensak
Department of Mechanical Systems Engineering, Tokyo University of Agriculture and Technology, Tokyo, Japan

ABSTRACT: A previous study confirmed that changing a driver's grip position impairs drivers' maintenance of an appropriate steering angle. Therefore, we developed the bar-type steering system with a low steering gear ratio. Adjusting the steering reaction of bar-type steering reduced the difficulty of steering with a low steering gear ratio at high speed. We designed a reactive torque control system to improve maneuverability and verified its performance using a driving simulator. Here, we report the maneuverability of bar-type steering at high speeds.

1 INTRODUCTION

A driver is required to perform some complex operations simultaneously and it makes driving difficult. Therefore, a beginner is required to learn driving at a driver's school for safely. Furthermore, an experienced driver must continue driving to maintain their driving skill for executing such complex operations without awareness. Among driving skills, passing the steering wheel from one hand to another, which occurs while driving at a low speed, is said to be a particularly difficult skill (Kitahara et al. 2013).

In the initial stage of developing the steering wheel, the steering torque during low-speed driving was reduced by a large steering gear ratio. Therefore, the driver was required to operate the steering wheel at large angles at low speeds. Today, however, the steering torque can be set arbitrarily using electric power steering or steer-by-wire technology. Therefore, the steering gear ratio also can be set freely. A steering system with a low gear ratio is desirable to eliminate the need for passing the steering wheel from one hand to another. However, it is reported that if a low gear ratio is set while using a steering wheel, the driver cannot drive well, and, as a result, the vehicle meanders (Kitahara et al, 2013). For such reasons, we have proposed a bar-type steering system to enable safe driving at a low gear ratio (Tamakawa et al. 2015a). By using this steering system, even a driver with little driving experience is able to steer intuitively and therefore drive the vehicle just as he or she wants.

In high-speed running, the range of steering angles used is smaller than in low-speed running. Even at an ordinary steering gear ratio, the driver is required perform fine steering to drive within a small range of steering angles. In a steering system with a low gear ratio, in particular, the vehicle response to the steering angle becomes larger than in an ordinary steering gear ratio. Therefore, further fine steering is required. In this case, the driver must perform the abovementioned fine steering exactly. Human operation resolving ability is insufficient for such operation, so it is expected that high-speed driving at a low gear ratio will become difficult.

Motorcycles enable high-speed running even at a low gear ratio. In motorcycles, a sufficiently large torque occurs during high-speed running. Referring to this, we sought to develop a steering system that enables safe high-speed operation at a low gear ratio from the viewpoint of vehicle behavior including both steering angle and steering torque.

2 DISCUSSION OF STEERING TORQUE

As shown in Table 1 and Figure 1, the steering torque was set while changing the elastic coefficient for the steering angle. Figure 2 shows the experiment course. The lateral position of the vehicle running on the target course was moved instantly on the screen. The driver's maneuver to return to the target course was then observed. In this case, the timing of moving the lateral position was varied randomly. The vehicle speed is kept constant at 180 km/h without the driver's maneuver. The subjects consisted of three males in their twenties and each subject steered only. Figure 3 illustrates the configuration of the simulator used for

Table 1. Steering system specifications.

		Bar-type steering system
Steering gear ratio		1
Elastic coefficient [N · m/deg]	k_0	0
	k_1	1.2
	k_2	2.4
	k_3	3.6
	k_4	4.8
Viscosity coefficient [N · m · s/deg]		0.12
Friction coefficient [N · m]		0.16

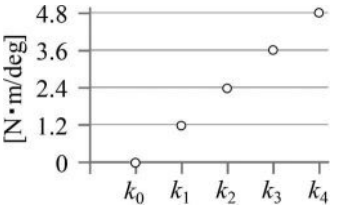


Figure 1. Setting elastic coefficients.

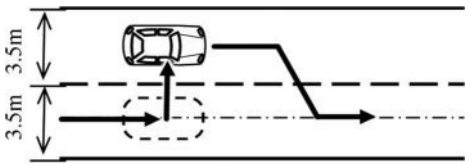


Figure 2. Experiment course.

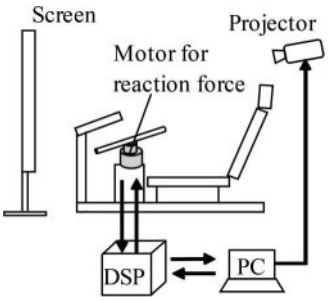


Figure 3. Configuration of the driving simulator.

the experiment. A system controller (AD5435 made by A&D Co.) was used for signal processing and vehicle behavior controlling, and a CarSim (made by Virtual Mechanics Co.) was employed for drawing the experiment course.

The experiment in this study was implemented in accordance with the rules of the Study Ethical Review Board of Tokyo University of Agriculture and Technology and after obtaining the informed consent of each subject.

3 EXPERIMENT RESULTS

The experiment result for Subject A1 is shown below as an example. The steering angle is depicted in Figure 4 and the yaw angle, in Figure 5.

As depicted in Figure 4, correction steering increased at smaller elastic coefficients. However, when the elastic coefficient increased, the steering angle converged faster. Also from Figure 5, it can be seen that meandering decreases when the elastic coefficient increases.

Information of steering torque cannot be obtained with a small elastic coefficient, so the driver drives by inputting the angle. At high speed, the required steering angle is small and the driver is urged to perform driving within a minute range of steering angle as

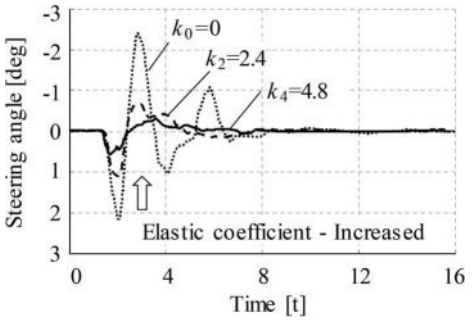


Figure 4. Time-series data of steering angle.

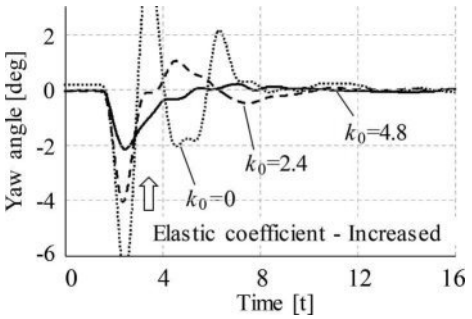


Figure 5. Time-series data of yaw angle.

described in Section 1, particularly at a low gear ratio. In this case, exact steering is difficult with the limited angle-resolving ability of the driver. When the elastic coefficient is increased, the required steering torque increases, and the driver becomes able to drive by inputting both the angle and the torque. Furthermore, as the elastic coefficient is increased, the torque that the driver should input increases. In this case, the resolving ability improved substantially because it becomes possible to adjust the torque over a wider range. Based on this result, high-speed running using a bar-type steering system has become possible.

4 EXPERIMENT OF VARYING DAMPING OSCILLATION PROPERTIES

The previous section discussed the result of lowering the steady state gain of vehicle behavior for the steering torque. This section examines the dynamic characteristics from the steering torque to the vehicle. Therefore, we changed the dynamic characteristics of yaw rate of the vehicle when inputting the steering torque with the steady state gain decreased as described in the previous section and observed the changes in steering wheel operation when changing lanes.

The driving simulator calculated vehicle behavior from the vehicle models expressed by equations (1) and (2) using steering angle as input.

$$G(s) = \frac{\gamma}{\theta} = \frac{k_g \omega_{ng}^{\ 2}}{s^2 + 2\zeta_g \omega_{ng} + \omega_{ng}^{\ 2}} \quad (1)$$

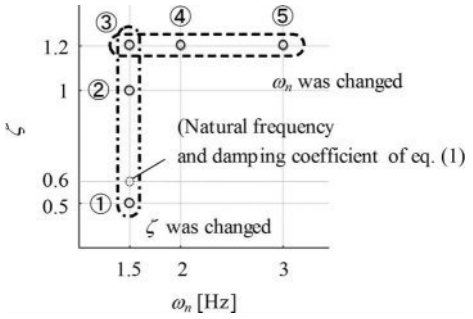


Figure 6. Specification of natural frequency and damping coefficient using in experiment.

$$B(s)=\frac{\beta}{\theta}=\frac{k_b\omega_{nb}^{\ 2}}{s^2+2\zeta_b\omega_{nb}+\omega_{nb}^{\ 2}} \tag{2}$$

$$\text{where,}\begin{cases} k_g=4.09 \\ k_b=-1.46 \\ \omega_{ng}=\omega_{nb}=1.5\,[\text{Hz}] \\ \zeta_g=\zeta_b=0.6 \end{cases}$$

Transfer function $F(s)$ from the steering torque to the yaw rate of the vehicle was defined as a second order delay system expressed by equation (3). To realize this, transfer function $H(s)$ from the steering angle to steering torque was defined by equation (4).

$$F(s)=\frac{\gamma}{T}=\frac{k\omega_n^{\ 2}}{s^2+2\zeta\omega_n+\omega_n^{\ 2}} \tag{3}$$

$$H(s)=\frac{T}{\theta}=\frac{G(s)}{F(s)} \tag{4}$$

Experiments were conducted by setting steady state gain to k = 1.36 deg/s/Nm in equation (3) and by varying natural frequency ω_n and damping coefficient ζ. Various specifications (① to ⑤) are shown in Figure 6. Experiments were conducted while changing the damping coefficient (specifications ①, ② and ③) and while changing natural frequency ω_n (specifications ③, ④, and ⑤). Figures 7 to 9 depict the respective frequency characteristics. Eight males in their twenties participated as subjects, and each experiment was conducted four times.

As the experiment course, a lane change course as depicted in Figure 10 was used. Each subject performed only steering while vehicle speed was adjusted to constant 180 km/h by the simulator.

5 EXPERIMENT RESULTS

The averaged result of four experiments on Subject A2 is shown as an example. Figure 11 depicts time-series data of yaw rate to the steering torque while changing damping coefficient ζ, and Figure 12, the same data obtained while changing natural frequency ω_n.

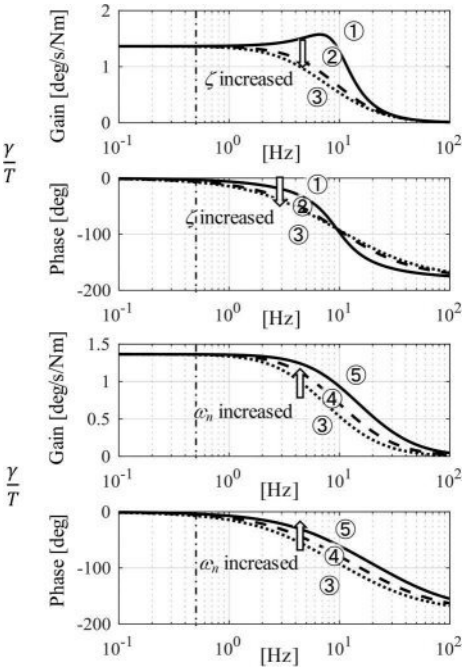


Figure 7. Frequency characteristics of transfer function $\frac{\gamma}{T}$.

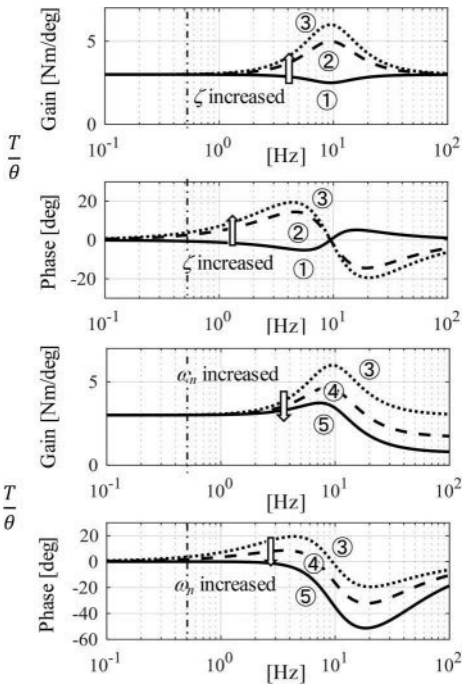


Figure 8. Frequency characteristics of transfer function $\frac{\gamma}{\theta}$.

Under these experiment conditions the second peak (☆ in Fig. 11) becomes larger and the overshoot of correction steering after the lane change (★ in Fig. 11) also increased when damping coefficient ζ is increased

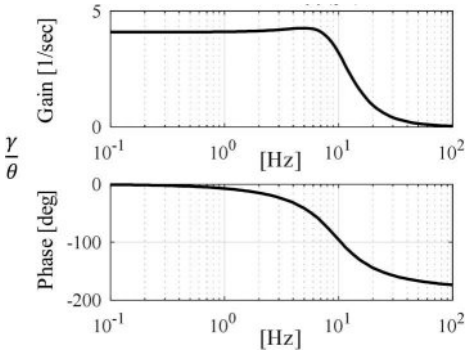


Figure 9. Frequency characteristics of transfer function $\frac{\gamma}{\theta}$.

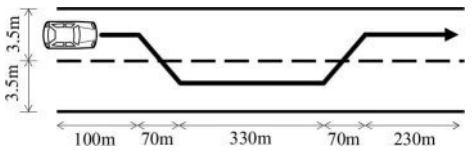


Figure 10. Experiment course.

(①→②→③). From Figure 11, it can be seen that the main frequency component of steering is about 0.5 Hz. Extra steering wheel operation increased because the phase delay became larger in the low-frequency area around 0.5 Hz (one-dot broken line in Figs. 7 and 8) when damping coefficient ζ was increased. Also from the subjective evaluation, delay becomes remarkable and driving becomes more difficult when damping coefficient ζ was increased and the subject felt fatigue when extra steering wheel operation increased. Other subjects exhibited roughly the same trend.

The second peak (in Fig. 11) and the overshoot of correction steering after the lane change (in Fig. 11) decreased when natural frequency ω_n was increased (③→④→⑤). Also subjective evaluation, indicated that response is good and the subject can perform steering just as he wanted when natural frequency ω_n was increased. Other subjects showed roughly the same trend.

6 DRIVING METHOD AND PHASE DELAY

The vehicle characteristic γ/θ is constant, so a relationship exists between phase delay of γ/T and the phase delay of steering torque characteristic T/θ such that if one increases, the other decreases (Fig. 13). The experiment result shows that a smaller phase delay of γ/T makes driving easier. At this time, the phase delay of T/θ has become large.

As described in Section 3, this experiment was conducted while the steady state gain of the yaw rate to steering torque was lowered. In other words, a small steering angle occurs if a large steering torque is input. As a result, the driver mainly used steering torque T as the manipulated variable rather than steering angle θ. Therefore, the driver uses the responsiveness of yaw

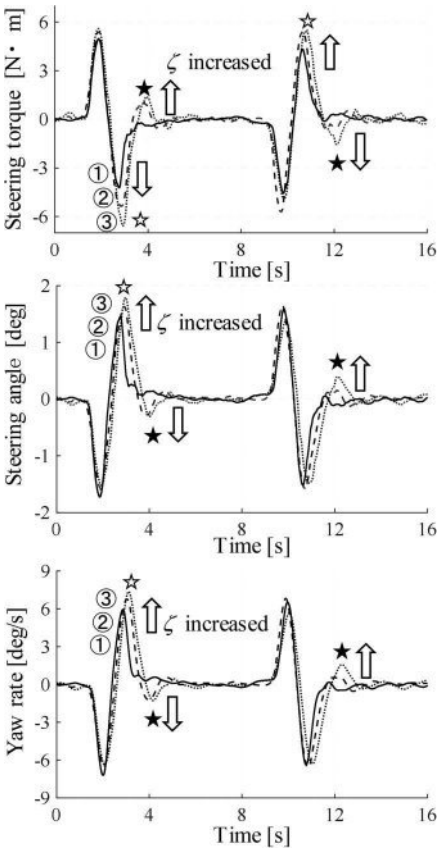


Figure 11. Time-series data while ζ is changed.

rate γ from steering torque T and feels driving is easier if the phase delay of steering torque from steering angle θ is large.

We conducted experiments by preparing two specifications in which the steady state gain of the steering torque to the steering angle differs from each other. In one specification, reducing the steering gear ratio increased steady state gain. In this specification, a large steering torque is required for lane changing. In the other specification, the gear ratio was increased so that lane changing can be made with a small steering torque. In the abovementioned two specifications, we investigated the relationship between the phase delay of yaw rate to the steering torque and the ease of driving. We call the specification where a large steering torque is required "torque-input driving" because the driver drives mainly based on the steering torque. We call the other specification "angle-input driving" because the driver drives based on the steering angle.

7 EXPERIMENT METHOD

Table 2 lists the specifications of the steering system of each driving method. In torque-input driving, a low gear ratio was adopted to increase the steering torque.

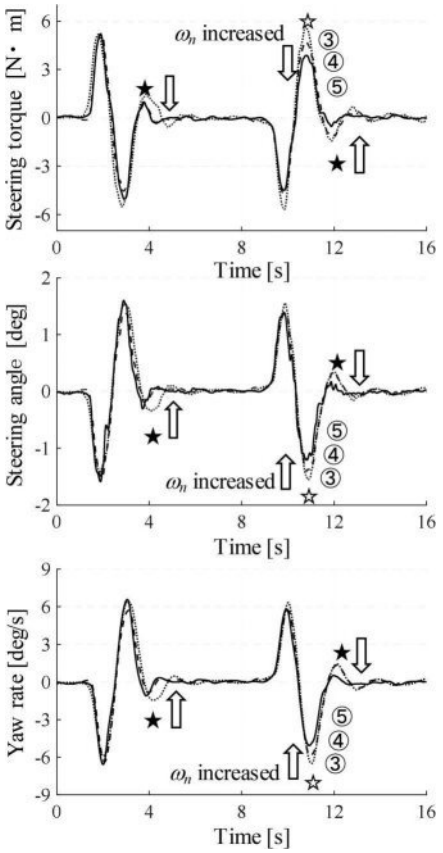


Figure 12. Time-series data while ω_n is changed.

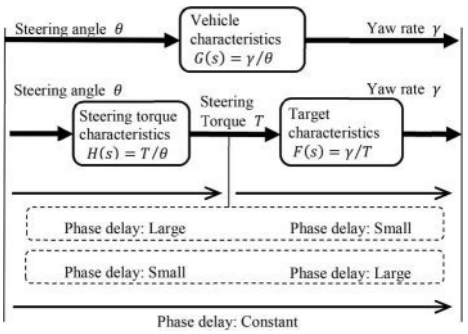


Figure 13. Phase delay of each characteristic.

Table 2. Steering system specifications.

Driving method	Steering gear ratio	Steady gain (Steering torque/ Front wheel steering angle)
Torque-input Driving	1	3 [Nm/deg]
Angle-input driving	25	1 [Nm/deg]

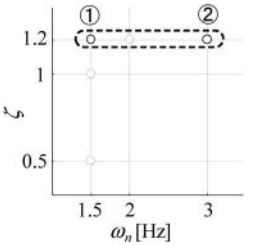


Figure 14. Natural frequency of yaw rate to the steering torque.

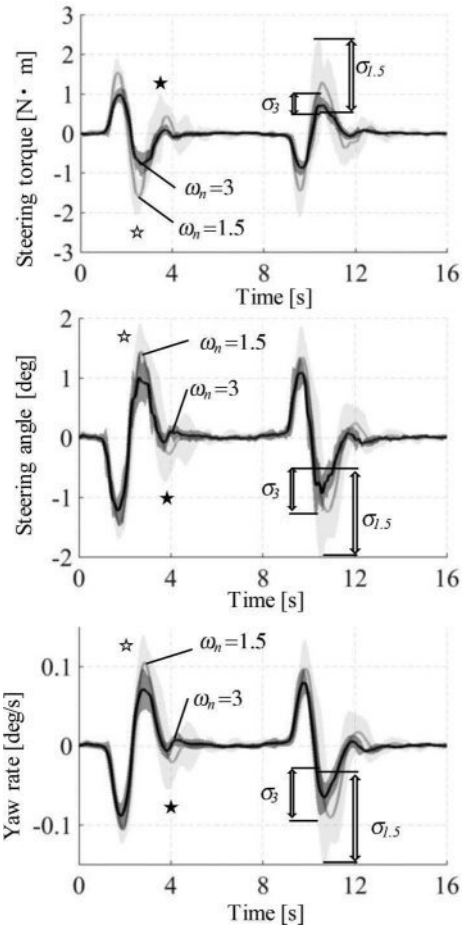


Figure 15. Time-series data of torque-input driving.

In angle-input driving, on the other hand, a high gear ratio was adopted to reduce the steering torque. As in the case of the previously conducted experiment, the vehicle changed lanes while running on the course shown in Figure 13 at a speed of 180 km/h.

We conducted experiments while changing the natural frequency ω_n of yaw rate to the steering torque. Each specification (①, ②) is shown in Figure 14. The subjects were five males in their twenties, and each experiment was conducted 10 times.

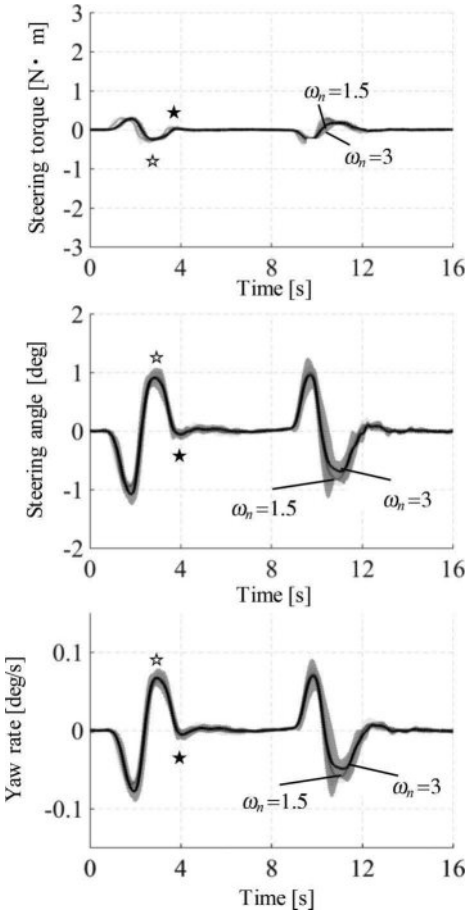


Figure 16. Time-series data of angle-input driving.

8 EXPERIMENT RESULT

The experiment result for Subject A3 is shown as an example. The solid line represents the average, and the widths above and below the painted portion represent the standard deviation of 10 trials. Figure 15 plots the time-series data in torque-input driving, and Figure 16 plots time-series data in angle-input driving.

In torque-input driving, the second peak (☆ in Fig. 15) and the overshoot of correction steering (★ in Fig. 15) decreased as the natural frequency of yaw rate to the torque increased. Furthermore, standard deviations (standard deviation $\sigma_{1.5}$, σ_3 in Fig. 15) also decreased, so the course traceability improved.

In angle-input driving, on the other hand, no change occurs in time-series data if the natural frequency of yaw rate to the steering torque changed (☆ and ★ in Fig. 16). Furthermore, the differences in standard deviation also are very small. Other subjects exhibited roughly the same trend.

From the above, in torque-input driving, driving becomes easier when the delay in yaw rate from steering torque is reduced. In angle-input driving, on the other hand, confirmed that the influence of the delay in yaw rate on the ease of driving is small.

In other words, the same result as predicted in Section 5 was obtained.

9 CONCLUSION

We investigated the ease of driving with a bar-type steering system while running at a high speed and obtained the following findings.

- When the steering torque is increased, convergence becomes faster resulting in less meandering.
- In the area of low natural frequency ω_n of yaw rate to the steering torque, extra steering decreases when damping coefficient ζ is small, resulting in easier driving. When ω_n is large, damping coefficient ζ has little influence on the ease of driving.
- When the natural frequency ω_n of yaw rate to the steering torque is large, extra steering wheel decreases, resulting in easier driving.
- Where a large steering torque is required, the driver drives using steering-torque information. Therefore, the ease of driving does not change if the phase of steering torque is delayed from the steering angle. On the other hand, the experiment confirmed that driving becomes difficult if the yaw rate is delayed from the steering torque that the driver relies on.
- Where little steering torque occurs during driving, the driver drives using the steering angle as input. Therefore, the experiment has confirmed that the steering torque it has little influence on the ease of driving if it is delayed from the steering angle.

REFERENCES

Horiguchi, N. et al. 2006. Investigation on Relationship between Steering Effort and Performance of Driver – Vehicle Closed Loop System Forcus on the Dumping Feature (2nd report). *Proc. of JSAE*. No. 4-06: 27–30.

Kitahara, K. et al. 2013. Proposal of New Steering System Considering the Direction of Upper Limb Motion. *Trans. of JSME Series C*: 38–46.

Kubota, M. et al. 2015. An investigation on the effect of transient assistant torque input on steering effort. *Proc. of JSAE* No. 75-05: 9–14. 2011.

Kushiro, I. et al. 2006. Vehicle Steering Behavior by Low Frequency Sinusoidal Torque Input. *Proc. of JSAE* No. 12-06: 13–18.

Tajima, T. et al. 2011. Study of the Next-generation Steering System – Study of the Twin Lever Steering System –. *Proc. of JSAE* No. 75-11: 7–12.

Tamakawa, S. et al. 2015a. Proposal new steering system to improve maneuverability under the low speed drive. *Proc. of annual convention of JSME* No. 15-1.

Tamakawa, S. et al. 2015b. Study on maneuverability of bar type steering in high speed range. *Proc. of Kanto branch 22nd convention of JSME* No. 160-1.

Yamazaki, I. et al. 2000. A Study of Driving with Control Stick – Report 2: Considering the Lateral and the Longitudinal Motion Control Simultaneously –. *Trans. of JSAE* Vol. 31, No. 1: 75–81.

Electric power steering

Advanced Vehicle Control – Edelmann, Plöchl & Pfeffer (Eds)
© 2017 Taylor & Francis Group, London, ISBN 978-1-138-02992-7

H_∞ filtering design for driver torque estimation in electric power steering system

Kazusa Yamamoto
JTEKT Europe, Irigny, France
Department of Control Systems, University Grenoble Alpes, GIPSA-lab, Grenoble, France

Pascal Moulaire
JTEKT Europe, Irigny, France

Damien Koenig & Olivier Sename
Department of Control Systems, University Grenoble Alpes, GIPSA-lab, Grenoble, France

ABSTRACT: This paper describes a method to estimate the driver torque in an Electric Power Steering (EPS) system without taking into account the torque sensor signal. First, a pinion-type EPS model is expressed by Newton's law of motion considering the effort transmitted from the road as an unknown input. Then, the design of a H_∞ filter is proposed to estimate the driver torque. The formulation aims at minimizing the estimation error in the presence of the external force induced by the road sollicitations and sensor noises. The efficiency of this H_∞ filter is assessed through simulation results using input data gathered from experimental tests on a real car. Furthermore these results are compared with torque measurements obtained on the experimental car for validation purpose only.

1 INTRODUCTION

Nowadays, modern vehicles are equipped with more and more electronic systems which help the driving process. Among them, steering systems help the driver to turn the vehicle in the desired direction, improving both safety and comfort. Currently, most of car manufacturers are using Electric Power Steering (EPS) systems. Indeed, compared to Hydraulic Power Steering (HPS), they improve fuel efficiency, and are easy to integrate into vehicle, etc.

In EPS systems, an electric motor provides an assistance torque to reduce the amount of effort required from the driver to turn the wheels. An Electronic Control Unit (ECU) computes the supplied torque according to a motor torque control strategy. It mainly consists of an assistance map depending on the vehicle speed and on the measured torque sensor signal [1].

Hence, EPS assistance strategies are based on the applied steering torque depicted by torque sensor measurements. However, a failure of this sensor may lead in a loss of assistance, which must be prevented. Indeed, developing a controller based on an estimation of the driver torque would cover such a case and improve global performance since torque sensor measurements and actual driver torque differs [2], [3]. Moreover, this strategy reduces the production costs and can improve the driver feeling. Both topics represent major challenges for EPS system suppliers.

Several works have already been carried out on driver torque estimation in EPS systems. Some of them [3], [4] have developed an estimator considering as a measured input the torque sensor signal. In that case, it is straightforward to reconstruct the driver torque as it is equivalent to the measurement during static steering. Nevertheless, Marouf et al. proposed in [2] a Sliding Mode Observer (SMO) to estimate the driver torque, in which measurements are the steering wheel angle and the absolute angular position of the assist motor. Moreover, in [5], the authors have designed a Proportional Integral Observer (PIO) with the same assumptions on measurements availability.

This paper follows the same idea in order to avoid the need of torque sensor signal and the design of a H_∞ filter that estimates the driver torque is presented. Likewise, the steering wheel angle and the assist motor angle are required inputs measurements. However, no assumption is made on the driver torque dynamics is made, since it is considered as the fault to estimate. The chosen design objective is to minimize the effects of road disturbances and sensor noises on the driver torque estimation error, in an H_∞ framework.

The paper is organized as follows. In section 2, a linear EPS mechanical model is introduced. Next section presents a method to estimate driver torque through the design of a H_∞ filter. Then, section 4 is dedicated to simulation results and validation is done on experimental results obtained on a real test car.

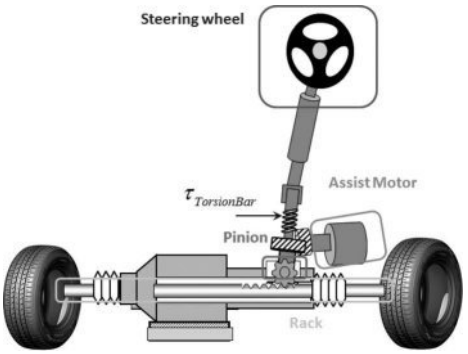


Figure 1. P-EPS simplified mechanical model.

2 EPS SYSTEM MODEL

The studied system is referred to as a pinion-type EPS (P-EPS) mainly composed by the assist motor, the pinion and the rack part. Moreover, the driver action is transmitted through the steering wheel to the torsion bar. Hence, it brings to distinguish four main parts. An illustration of a simplified mechanical model is shown in Figure 1.

The model is obtained by applying Newton's laws of motion and neglecting dry friction. The P-EPS model is governed by the following equations (for further details see [5]):

$$J_c\ddot{\theta}_c = \tau_d - \left(D_{tb}(\dot{\theta}_c - \dot{\theta}_p) + K_{tb}(\theta_c - \theta_p)\right) - B_c\dot{\theta}_c \quad (1)$$

$$J_m\ddot{\theta}_m = \tau_m - \left(D_g(\dot{\theta}_m - G\dot{\theta}_p) + K_g(\theta_m - G\theta_p)\right) - B_m\dot{\theta}_m \quad (2)$$

$$\begin{aligned} J_p\ddot{\theta}_p &= \left(D_{tb}(\dot{\theta}_c - \dot{\theta}_p) + K_{tb}(\theta_c - \theta_p)\right) \\ &- R_p\left(D_{pr}(R_p\dot{\theta}_p - \dot{X}_r) + K_{pr}(R_p\theta_p - X_r)\right) \\ &+ G\left(D_g(\dot{\theta}_m - G\dot{\theta}_p) + K_g(\theta_m - G\theta_p)\right) \end{aligned} \quad (3)$$

$$\begin{aligned} J_r\ddot{X}_r &= \tau_{road} - \left(D_r\dot{X}_r + K_rX_r\right) - B_r\dot{X}_r \\ &+ D_{pr}(R_p\dot{\theta}_p - \dot{X}_r) + K_{pr}(R_p\theta_p - X_r) \end{aligned} \quad (4)$$

where the variables are θ_c the steering wheel angle (rad), θ_m the assist motor angle (rad), θ_p the pinion angle (rad), X_r the rack position (m). The mechanical parameters are described in Table 1.

Hence a state-space representation of the P-EPS system (denoted *Plant*) is the following:

$$\begin{cases} \dot{x} = Ax + Bu + Ed + Ww \\ y = Cx + Nn \end{cases} \quad (5)$$

with $x = (\dot{\theta}_c\ \dot{\theta}_m\ \dot{\theta}_p\ \dot{X}_r\ \theta_c\ \theta_m\ \theta_p\ X_r)^T \in \mathbb{R}^8$ are the internal states, $d \in \mathbb{R}$ is the driver torque to be estimated, $w \in \mathbb{R}$ the road reaction torque is the unknown input, and $u \in \mathbb{R}$ the assist motor torque is the control signal. The available measurements are $y = (\theta_c\ \theta_m)^T \in \mathbb{R}^2$ which are affected by white gaussian noise $n \in \mathbb{R}^2$. Moreover N is the weighting matrix associated to n in the form $N = \beta I$ with $\beta \in \mathbb{R}^+$.

Table 1. EPS system mechanical parameters.

Notation	Description	Unit
J_c	Steering column inertia	kg.m^2
B_c	Steering column viscous friction	N.m/(rad/s)
K_{tb}	Torsion bar stiffness	N.m/rad
D_{tb}	Torsion bar damping	N.m/(rad/s)
J_p	Pinion/gear inertia	kg.m^2
K_{pr}	Pinion/rack stiffness	N/m
D_{pr}	Pinion/rack damping	N/(m/s)
R_p	Pinion/rack reducer	m/rad
J_r	Rack and tie rods mass	kg
B_r	Rack viscous friction	N/(m/s)
K_r	Rack stiffness	N/m
D_r	Rack damping	N/(m/s)
G	Worm/gear reduction ratio	–
J_m	Motor inertia	kg.m^2
B_m	Motor viscous friction	N.m/(rad/s)
K_g	Worm/gear stiffness	N.m/rad
D_g	Worm/gear damping	N.m/(rad/s)

3 H_∞ FILTERING APPROACH

The main objective is to estimate the unmeasured input d subject to the road disturbance w and sensor noises n affecting the system (5), using a H_∞ filter design. In the following, the known input u is not considered, but can be easily included in the filter equations.

3.1 *Synthesis of H_∞ filter*

In this part, the method followed to design the H_∞ filter is presented. As usual in the H_∞ approach, it is based on weighting functions that represent the specificaitons of the input/output signals of interest. It is worth noticing that such a scheme, as shown in Figure 2 with the extended representation with weighting functions and the H_∞ filter $F(s)$, is used for synthesis only and that the implementation only considers $F(s)$ with as inputs the measurements y.

Besides, the estimation is designed on a filtered driver torque obtained using $T(s)$. Then, a weighting function on the driver torque is introduced such that $d_f = T(s)d$. This allows to specify the frequency range on which estimation performance is expected. In practice, the driver torque average range is up to 2 Hz and does not exceed 5 Hz even in emergency case. Hence, in this paper the H_∞ filter problem is not designed as in the form of a state estimation like in [6], [7] to avoid assumption on driver torque dynamic.

$$\begin{cases} \dot{x}_t = A_tx_t + B_td \\ d_f = C_tx_t + D_td \end{cases} \quad (6)$$

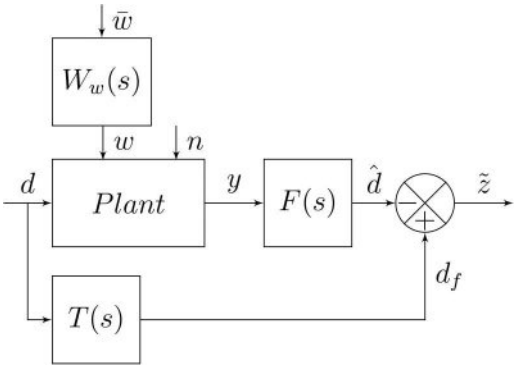


Figure 2. Block diagram of H_∞ filter synthesis.

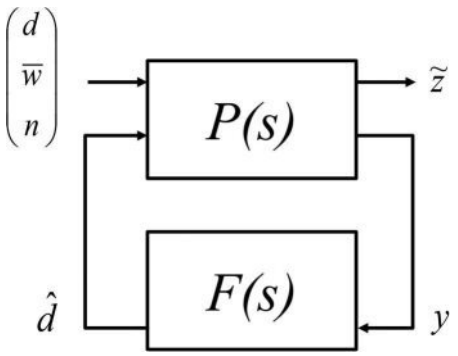


Figure 3. H_∞ general control configuration.

Moreover a weighting function is introduced on the road disturbance such that $w = W_f(s)\bar{w}$ in order to specify the frequency range and amplitude of disturbance attenuation.

$$\begin{cases} \dot{x}_w = A_w x_w + B_w \bar{w} \\ w = C_w x_w + D_w \bar{w} \end{cases} \tag{7}$$

In this application framework, both additional weighting functions are considered of first order i.e $n_t = 1$ and $n_w = 1$ which represent the number of state in (6) and (7). Hence the augmented state space representation:

$$\begin{cases} \dot{x}_a = A_a x_a + B_w w_a + 0.\hat{d} \\ \tilde{z} = C_z x_a + D_{zw} w_a - \hat{d} \\ y = C_y x_a + D_{yw} w_a + 0.\hat{d} \end{cases} \tag{8}$$

where $x_a = (x^T \; x_t^T \; x_w^T)^T \in \mathbb{R}^{10}$ is the extended state vector, $w_a = (d^T \; \bar{w}^T \; n^T)^T \in \mathbb{R}^4$ the external inputs and $\tilde{z} = d_f - \hat{d}$ is the estimation error to be minimized.

The synthesis of H_∞ filter is done, according to general control configuration shown in Figure 3.

Then, $P(s)$ including the extended state is described below:

$$P = \begin{pmatrix} A_a & B_w & B_u \\ C_z & D_{zw} & D_{zu} \\ C_y & D_{yw} & D_{yu} \end{pmatrix} \tag{9}$$

where:

$$A_a = \begin{pmatrix} A & 0 & WC_w \\ 0 & A_t & 0 \\ 0 & 0 & A_w \end{pmatrix}, \; B_w = \begin{pmatrix} E & WD_w & 0 \\ B_t & 0 & 0 \\ 0 & B_w & 0 \end{pmatrix},$$

$B_u = (0\,0\,0)^T$, $C_z = (0\; C_t\; 0)$, $D_{zw} = (D_t\; 0\; 0)$, $D_{zu} = -1$, $C_y = (C\; 0\; 0)$, $D_{yw} = (0\; 0\; N)$, $D_{yu} = 0$.

Denoting the H_∞ filter $F(s)$ as:

$$\begin{cases} \dot{x}_f = A_f x_f + B_f y \\ \hat{d} = C_f x_f + D_f y \end{cases} \tag{10}$$

Now the problem is to design the standard H_∞ filter $F(s)$ that minimizes the L_2 gain of the overall system from w_a to $\tilde{z}$. The system is given by:

$$\begin{cases} \dot{x}_{ag} = A_{ag} x_{ag} + (E_{ag} \quad W_{ag} \quad N_{ag})\, w_a \\ \tilde{z} = C_{ag} x_{ag} + D_{ag} w_a \end{cases} \tag{11}$$

where:

$$A_{ag} = \begin{pmatrix} A & 0 & WC_w & 0 \\ 0 & A_t & 0 & 0 \\ 0 & 0 & A_w & 0 \\ B_f C & 0 & 0 & A_f \end{pmatrix}, \; E_{ag} = \begin{pmatrix} E \\ B_t \\ 0 \\ 0 \end{pmatrix},$$

$$W_{ag} = \begin{pmatrix} WD_w \\ 0 \\ B_w \\ 0 \end{pmatrix}, \quad N_{ag} = \begin{pmatrix} 0 \\ 0 \\ 0 \\ B_f N \end{pmatrix}, \quad C_{ag} = (-D_f C \quad C_t \quad 0 \quad -C_f), \quad D_{ag} = (D_t \quad 0 \quad -D_f N),$$

$x_{ag} = \left(x^T \quad x_t^T \quad x_w^T \quad x_f^T\right)^T \in \mathbb{R}^{18}$, $\tilde{z} = d_f - \hat{d}$.

The H_∞ filter synthesis problem is as follows: given the system (11), find matrices A_f, B_f, C_f and D_f such as $||T_{\tilde{z}w_a}||_\infty \leq \gamma_\infty$. This is solved by using a Linear Matrix Inequality (LMI) approach following [8]. If there exist symmetric matrices R, S satisfying the following LMI system:

$$\begin{pmatrix} N_R & 0 \\ 0 & I_{n_{w_a}} \end{pmatrix}^T \begin{pmatrix} AR + RA^T & RC_z^T & B_w \\ * & -\gamma I_{n_z} & D_{zw} \\ * & * & -\gamma I_{n_{w_a}} \end{pmatrix} \begin{pmatrix} N_R & 0 \\ 0 & I_{n_{w_a}} \end{pmatrix} < 0 \tag{12}$$

$$\begin{pmatrix} N_S & 0 \\ 0 & I_{n_z} \end{pmatrix}^T \begin{pmatrix} A^T S + SA & SB_w & C_{\tilde{z}}^T \\ * & -\gamma I_{n_{w_a}} & D_{zw}^T \\ * & * & -\gamma I_{n_z} \end{pmatrix} \begin{pmatrix} N_S & 0 \\ 0 & I_{n_z} \end{pmatrix} < 0 \tag{13}$$

Table 2. Influence of weighting function $T(s)$ on the H_∞ filter synthesis.

$T(s)$ 1st order w_n	5 Hz	10 Hz	25 Hz
γ_∞	0.15	0.27	0.51
steady state gain	0.91	0.75	0.49
$T(s)$ 2nd order $\zeta = 0.7$ and w_n	5 Hz	10 Hz	25 Hz
γ_∞	0.12	0.12	0.34
steady state gain	0.98	0.98	0.69

$$\begin{pmatrix} R & I_n \\ I_n & S \end{pmatrix} \geq 0 \tag{14}$$

with $N_R = Ker \begin{pmatrix} B_u^T \\ D_{zw}^T \end{pmatrix}$, $N_S = Ker \begin{pmatrix} C_y \\ D_{yw} \end{pmatrix}$. Then, a positive definite matrix X is obtained as:

$$\begin{pmatrix} S & I_n \\ N^T & 0 \end{pmatrix} = X \begin{pmatrix} I_n & R \\ 0 & M^T \end{pmatrix}, \quad MN^T = I_n - RS \tag{15}$$

Hence, (16) is a LMI in $\begin{pmatrix} A_f & B_f \\ C_f & D_f \end{pmatrix}$, the solution gives the parameter of the H_∞ filter.

$$\begin{pmatrix} A_{ag}^T X + X A_{ag} & X(E_{ag} & W_{ag} & N_{ag}) & C_{ag}^T \\ * & & -\gamma_\infty I & & D_{ag}^T \\ * & & * & & -\gamma_\infty I \end{pmatrix} < 0 \tag{16}$$

3.2 *Analysis of H_∞ filter synthesis*

A compromise between estimation performance and disturbance rejection shall be found through the design parameter of the H_∞ filter. Indeed, the ideal case is to get $T(s) = 1$ which means to estimate the driver torque regardless of his frequency content. Hence, Table 2 shows the influence of the weighting function $T(s)$ on H_∞ filter synthesis. Variations of the cut-off frequency and order of $T(s)$ have been performed. Then, the estimation performance has been assessed through the steady state gain $T_{\tilde{d}d}(\omega = 0)$ (that should be close to 1) and the maximal disturbance rejection $||T_{\tilde{z}w_a}||_\infty \leq \gamma_\infty$ (*i.e.* value of γ_∞ is expected to be as small as possible).

In view of Table 2, increasing the bandwidth of $T(s)$ leads to a degradation of estimation, (as γ_∞ gets close to 1). The previous overview shows that a second order filter $T(s)$ is convenient. From (11), the transfer matrix $T_{\tilde{z}w_a} = [T_{\tilde{z}\tilde{d}};\ T_{\tilde{z}\tilde{w}};\ T_{\tilde{z}n}]$ of the sensitivity functions is as follows:

$$T_{\tilde{z}\tilde{d}}(s) = C_{ag}(sI - A_{ag})^{-1}E_{ag} + D_t \tag{17}$$

$$T_{\tilde{z}\tilde{w}}(s) = C_{ag}(sI - A_{ag})^{-1}W_{ag} \tag{18}$$

$$T_{\tilde{z}n}(s) = C_{ag}(sI - A_{ag})^{-1}N_{ag} + D_k N \tag{19}$$

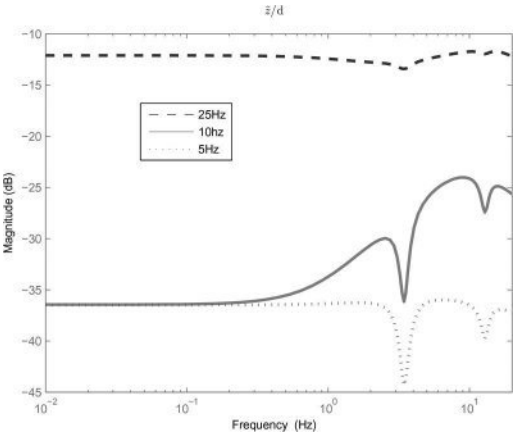


Figure 4. Influence of various $T(s)$ design on $T_{\tilde{z}\tilde{d}}(s)$.

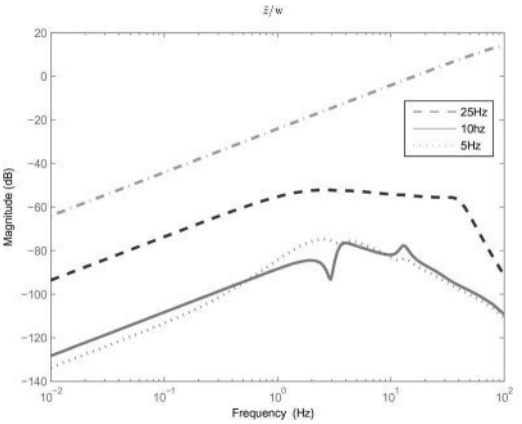


Figure 5. Influence of various $T(s)$ design on $T_{\tilde{z}w}(s)$.

Figures 4, 5 and 6 illustrates the sensitivity function deduced from (17)–(19) with different tuning for $T(s)$. It is again noticed that a cut-off frequency at 25 Hz gives less efficient results than with 5 Hz or 10 Hz. Indeed, the optimization problem is harder to be solved when considering a greater frequency range. As both remaining synthesis show similar performance, the one designed with 10 Hz is preferable.

For simulation part, the driver torque is estimated following a H_∞ filter $F(s)$ design method where $T(s)$ is a 2nd order filter with cut off frequency at 10 Hz.

4 SIMULATION RESULTS

In this section, simulation results are presented using the H_∞ filter designed in the previous section. The Figure 7 illustrates the experimental implementation scheme. It is worth noting that, to evaluate the estimation error, a sensor is available on the experimental

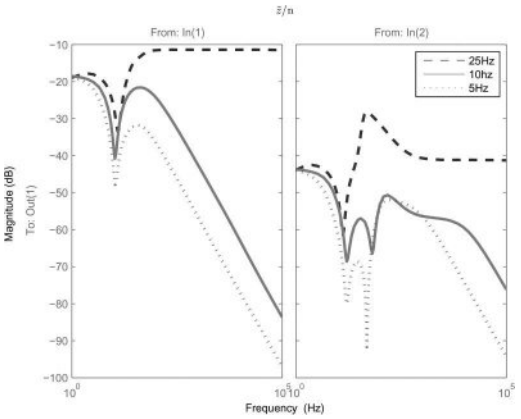


Figure 6. Influence of various $T(s)$ design on $T_{\tilde{z}n}(s)$.

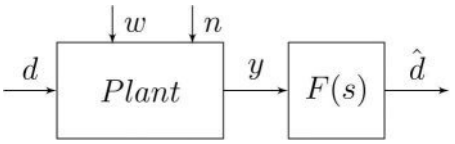


Figure 7. Block diagram of H_∞ filter implementation.

test car for driver torque measurement, referred to as $d_{measured}$.

4.1 *Simulation case 1*

According to the representation in Figure 7, the following simulation scenario has been considered. A sinusoidal driver torque of $d = 5$ Nm at 0.5 Hz is applied as input. The disturbance affecting the plant is represented by the road effort. At the beginning, it is a constant of $w = 1$ kN and changed to $w = 5$ kN at 2.5 s. Also sensor noises of amplitude $N = 1e^{-2}$ is added to the measured output.

Figure 8 shows the measured driver torque $d_{measured}$, the estimated driver torque $\hat{d}$, the filtered driver torque d_f (synthesized signal) and the resulting estimation error $\tilde{z} = d_f - \hat{d}$ and $z = d_{measured} - \hat{d}$.

The root mean squared error (RMSE) is calculated as:

$$RMSE(z) = \sqrt{\frac{\sum_{i=1}^{m} z(i)^2}{m}} \tag{20}$$

where $z = d_{measured} - \hat{d}$ *i.e.* difference between the real data and the estimated value, m is the number of data points. The normalized RMSE (NRMSE) on the whole range is computed by:

$$NRMSE(z) = \frac{RMSE}{d_{measured}^{max} - d_{measured}^{min}} \tag{21}$$

The obtained errors are: RMSE(z) = 0.27 Nm (resp. NRMSE(z) = 2.67%) and RMSE($\tilde{z}$) = 0.076 Nm (resp.

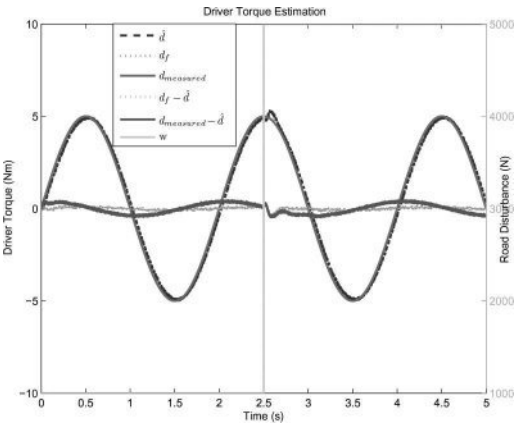


Figure 8. Driver torque estimation – Sinusoidal driving case 1.

NRMSE($\tilde{z}$) = 0.74%). The H_∞ filter estimates accurately the applied driver torque $d_{measured}$, since the computed error is small enough. Thus, the H_∞ filter have an acceptable performance level. It is worth noticing that the H_∞ filter has been designed introducing the weighting function $T(s)$ and that the optimization problem has been solved for $\tilde{z}$, which explains this slightly better estimation result.

4.2 *Simulation from experimental input data*

In this case, the simulation environment takes only the H_∞ filter $F(s)$ part from Figure 7, to validate the performance of the estimation using as inputs real measurements i.e. $y = (\theta_c \ \theta_m)^T$. Data acquisition has been done on a development car equipped with a P-EPS system and several specific sensors (motor resolver, torque sensor, steering sensor and driver torque sensor).

The first test case comes from a particular driving condition where the driver follows an '8' shaped pattern on the track at a constant speed of 20 kph. This involves to get a sinusoidal driver torque. Figure 4 shows the comparison between the measured driver torque and the estimated torque.

Another test measurements come from parking maneuver. The driver turns slowly the steering wheel with a small steering angle amplitude. As it is in parking, the effort required from the driver is high. The comparison between the measured driver torque and the estimated torque shown in Figure 10 emphasizes the efficiency of the estimation.

The resulting errors are: for experimental data 1 is RMSE(z) = 3.18 Nm, NRMSE(z) = 6.63% and for experimental data 2 is RMSE(z) = 1.1 Nm, NRMSE(z) = 4.94%. Since experimental data are gathered from real system where non-linearity (mainly friction) are influent, whereas in the H_∞ filter design this element has been neglected, the estimation results differ from the two types of simulation. Moreover, road disturbance condition differs from parking to rolling,

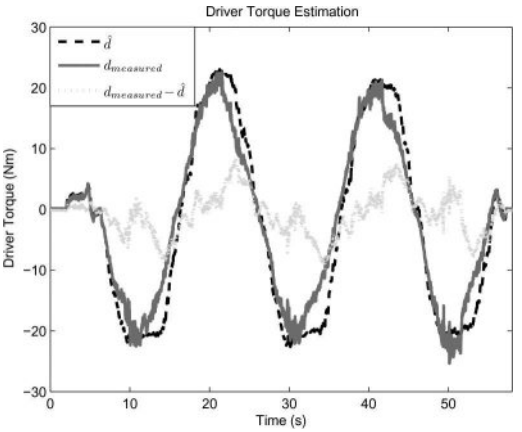


Figure 9. Driver torque estimation using experimental data – Sinusoidal driving.

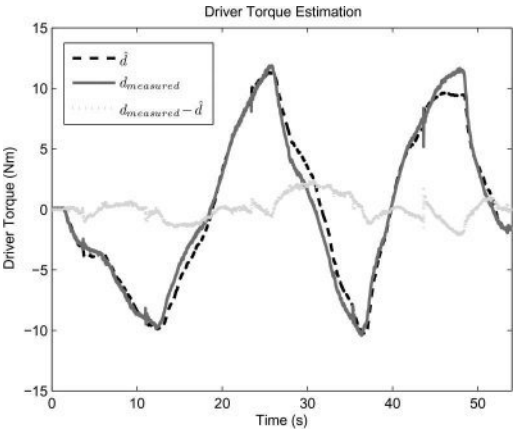


Figure 10. Driver torque estimation using experimental data – Parking maneuver.

this explains the variation in performance level. However, according to the above simulation results, good performance of the driver torque estimation by H_∞ filter strategy is obtained using experimental data as inputs.

5 CONCLUSION

In this paper, an H_∞ filter has been designed subject to minimization objective on road disturbance and sensor noises. Then, performance has been evaluated by simulation using experimental measurements.

The estimation of driver torque presented in this paper is application-oriented and aims to be a back-up calculation to cover failure of torque sensor signal. As this is a software strategy, it could be easily implemented in the ECU. Moreover, it only requires measurements from sensors existing on board of most of mass produced vehicle equipped with an EPS system.

Even though driver torque estimation might be affected by friction on EPS system in practice (due to its non-linearity), the design of a robust controller could result in reducing the unwanted effect to the driver. Hence, future works will concentrate on the whole design of an observer-controller system to provide assistance torque without using torque sensor.

ACKNOWLEDGMENT

This study has been supported by JTEKT corporation in Japan: Miyama Shinpukujicho Okazaki-shi, Aichi-ken, 444-2106 Japan.

REFERENCES

[1] V.N. Sulakhe, M.A. Ghodeswar, M.D. Gite, Electric Power Assisted Steering, Journal of Engineering Research and Applications, vol. 3, pp. 661–666, 2013

[2] A. Marouf, M. Djemaï, C. Sentouh and P. Pudlo, A new Control Strategy of an Electric Power Assisted Steering system, IEEE Trans. Veh. Technol., vol. 61, pp. 3574–3589, 2012

[3] R.C. Chabaan, Torque Estimation in Electrical Power Steering Systems, IEEE Veh. Power Propuls. Conf., Dearborn (USA), pp. 790–797, 2009

[4] J. Tordesillas Illán, V. Ciarla and C. Canudas de Wit, Oscillation annealing and driver/tire load torque estimation in Electric Power Steering systems, IEEE Int. Conf. Control Appl., Denver (USA), pp. 1100–1105, 2011

[5] K. Yamamoto, D. Koenig, O. Sename and P. Moulaire, Driver torque estimation in Electric Power Steering system using an H_∞/H_2 Proportional Integral Observer, CDC, pp. 843–848, 2015

[6] H. Li and M. Fu, A Linear Matrix Inequality Approach to Robust H_∞ Filtering, IEEE Trans. Signal Processing, vol. 45, pp. 2338–2350, 1997

[7] I. Yaesh and U. Shaked, A Transfer Function Approach to the Problems of Discrete-Time Systems H_∞ Optimal Linear Control and Filtering, IEEE Trans. Automatic Control, vol. 36n pp. 1264–1271, 1991

[8] P. Gahinet and P. Apkarian, A Linear Matrix Inequality Approach to H_∞ Control, Int. J. Robust Nonlinear Contr., vol. 4, pp. 421–448, 1994

Advanced Vehicle Control – Edelmann, Plöchl & Pfeffer (Eds)
© 2017 Taylor & Francis Group, London, ISBN 978-1-138-02992-7

Design of equivalent friction using a motor control for Electric Power Steering (EPS)

Satoshi Ohno & Atsuhiko Yoneda
Honda R&D Co., Ltd.

ABSTRACT: To enhance the on-center steering feel, a design method of equivalent friction control was proposed for electric power steering (EPS). In this method, friction torque was generated artificially by motor control for a low speed steering maneuver because it was easier to generate friction torque than mechanical elements. The proposed method was used to design the steering torque characteristics and it was found that the friction torque had the appropriate torque range. When the steering torque characteristics was designed with considering the appropriate range of friction, the on-center steering feel was enhanced. Finally the proposed method was validated in actual vehicle tests.

1 INTRODUCTION

Electric Power Steering (EPS) reduces steering effort by motor to assist the driver's steering maneuver as shown in Figure 1 (Shimizu et al. 1991). Additionally, EPS control system is important to enhance steering feel (Shimizu 2003, Ohniwa et al. 2007, Wilhelm et al. 2014).

In previous research, power function is proposed to express an appropriate steering torque characteristic (Misaji et al. 2002, Kushiro et al. 2009). Power function is convenient to get better linear steering feel. When manual steering torque is larger than a target steering torque characteristic using power function (hereafter, target), EPS can enhance the steering feel by reducing of the manual steering torque with the power assist torque. However, as shown the shaded area in Figure 2a, when a manual steering torque in a small steering angle area is smaller than the target, the target is not easy to be achieved. It is because the conventional EPS control cannot generate negative motor torque in the small steering angle area.

In this research, a design method of the equivalent friction using motor control (equivalent friction control) was proposed to achieve the target in the small steering angle area. The idea of the proposed method is shown in Figure 2b. If appropriate friction is generated in that area, a total of the manual steering torque and friction becomes larger than the target. Therefore, it is considered that the target can be achieved by using the power assist torque. In the steering system, mechanical friction exists and can be used to design the steering torque (Ono et al. 2015). However it is difficult to provide friction stably due to an individual difference and an aged deterioration. Therefore, authors thought that friction reproduced by using the motor torque control was effective in this research, because equivalent friction control (Ohno et al. 2015) can be applied to achieve the target based on the idea of Figure 2b.

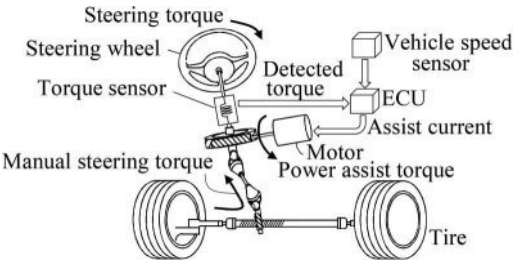


Figure 1. EPS structure.

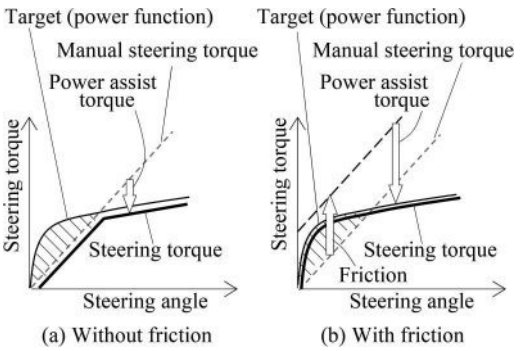


Figure 2. Steering torque characteristic with friction.

2 DESIGN OF APPROPRIATE FRICTION

To enhance the on-center feel, friction characteristic was investigated with conventional damping control to balance the stability and the response.

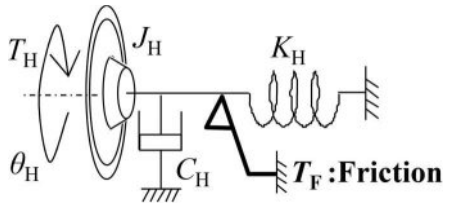


Figure 3. Simple steering model.

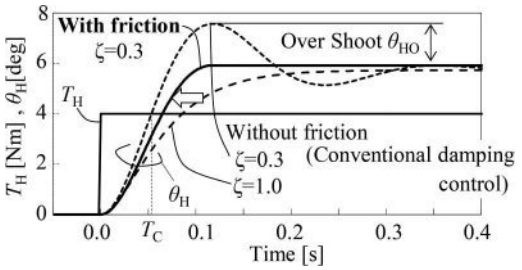


Figure 4. Effect of friction in step response of steering.

2.1 *Modeling*

Effect of friction in the steering system is considered using model as shown in Figure 3.

In case of the conventional damping control (without friction), a relationship between a steering torque T_H and a steering angle θ_H is shown as following Equations 1 and 2.

$$(1+G_A)T_H = J_H\ddot{\theta}_H + C_H\dot{\theta}_H + K_H\theta_H \quad (1)$$

$$J_H = J_{SW} + n_M^2 J_M \quad (2)$$

A damping coefficient C_H is a control gain of the conventional damping control. K_H means an entire stiffness that includes a tire, a suspension, a steering gearbox, a steering column shaft and a steering torque sensor. G_A is an assist gain of EPS. Parameters were set as envisioned in the use of a compact vehicle (Table 1 in Appendix).

A step response of the conventional damping control is shown in Figure 4. A damping ratio ζ is changed by the damping coefficient C_H of the damping control. When $\zeta = 1.0$, the steering response is decreased, and when $\zeta = 0.3$, the steering stability is decreased. It is difficult to balance the steering response and the steering stability by using C_H only.

In case of the model with friction T_F, the relationship between T_H and θ_H is shown as following Equations 3 and 4.

$$T_H = J_H\ddot{\theta}_H + C_H\dot{\theta}_H + K_H\theta_H + T_F \quad (3)$$

$$T_F = \begin{cases} -T_E & if\left(\dot{\theta}_H = 0 \wedge |T_E| \le T_{FS}\right) \\ -\mathrm{sgn}\left(\dot{\theta}_H\right)\cdot T_{FS} & if\left(\dot{\theta}_H \ne 0 \vee |T_E| > T_{FS}\right) \end{cases}, \quad (4)$$
$$\left[T_E \equiv T_H - J_H\ddot{\theta}_H - C_H\dot{\theta}_H - K_H\theta_H\right]$$

The Coulomb friction T_F that was used in this research is defined in Equation 4.

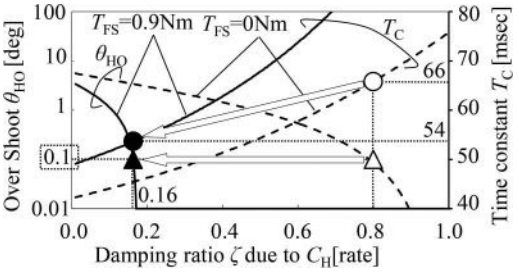


Figure 5. Analysis of step response with friction.

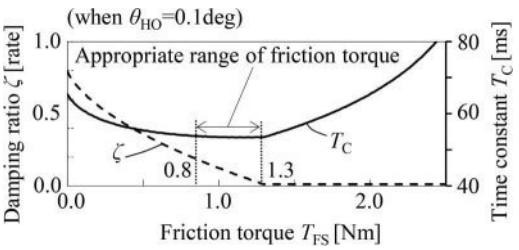


Figure 6. Effect of friction torque T_{FS} ($\theta_{HO} = 0.1$ deg).

Step response with friction T_F is also plotted in Figure 4. It is known that when appropriate friction is applied, the steering response is enhanced with keeping the same level of stability even the damping coefficient C_H is reduced (Ohno et al. 2015).

How to get an appropriate range of friction torque is described in the next section.

2.2 *Appropriate range of friction torque*

To evaluate the effect of friction, an overshoot of steering angle θ_{HO} was defined as an index of the stability and a time constant T_C was defined as index of a response. They are explained in Figure 4. Authors defined that the stability was sufficient when the overshoot angle θ_{HO} was smaller than 0.1 deg.

θ_{HO} and T_C are observed in Figure 5 with variation of ζ and T_{FS}. If friction torque 0.9 Nm was applied, ζ could be reduced from 0.8 to 0.16. And T_C could be also reduced from 66 to 54 msec.

Figure 6 shows the effect of friction T_F change. It could be observed that the response of the steering system could be enhanced at the appropriate range of friction torque ($T_{FS} = 0.8 - 1.3$ Nm).

However, as shown in Figure 7, the upper and the lower value of the appropriate range of friction torque was changed depending on the assist gain G_A in the left term of Equation 1.

2.3 *Design method of appropriate friction*

In this section, in order to achieve the target (Figure 2), a design method of friction is proposed. The target T_H* is shown in Equation 5.

$$T_H{}^* = A\,\theta_H{}^N + B \quad (5)$$

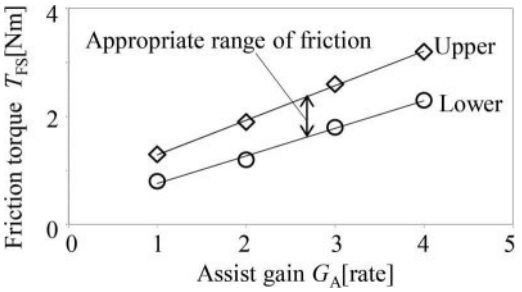


Figure 7. Appropriate range of friction torque.

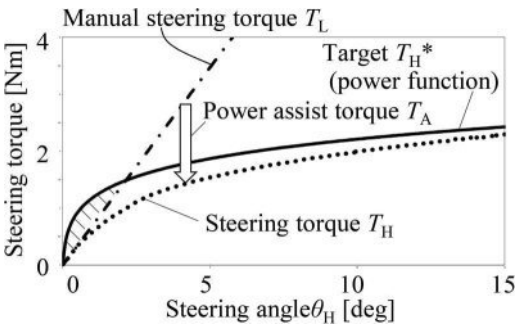


Figure 8. Steering torque characteristic without friction.

Here, the Figure 2a was expanded. The parameter set of power function (A, N, B) was defined to achieve the good steering feel of actual vehicle. The calculation result of the target T_H* using Equation 5 is shown in Figure 8.

The steering torque T_H is derived by subtracting the manual steering torque by the power assist torque as shown in Equation 6.

$$T_H = T_L(\theta_H) - T_A(T_H) \tag{6}$$

$T_L(\theta_H)$ is the manual steering torque and it can be derived K_H and θ_H as shown Equation 7.

$$T_L(\theta_H) = K_H \theta_H \tag{7}$$

$T_A(T_H)$ is the power assist torque. The power assist torque $T_A(T_H)$ in Figure 8 is shown in Figure 9.

Then, when friction is applied, the relationship between T_H and θ_H is shown in Equation 8.

$$T_H = T_L(\theta_H) + T_F(\theta_H) - T_A(T_H) \tag{8}$$

Required friction torque $T_F(\theta_H)$ can be calculated as Equation 9 to achieve the target T_H*.

$$T_F(\theta_H) = T_H^* - T_L(\theta_H) + T_A(T_H) \tag{9}$$

Required friction torque $T_F(\theta_H)$ is shown in Figure 10.

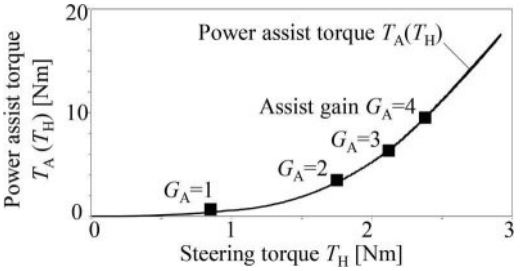


Figure 9. Power assist torque $T_A(T_H)$.

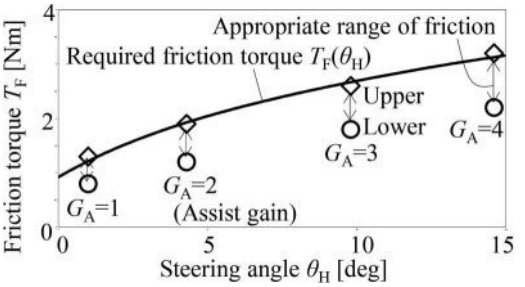


Figure 10. Required friction torque $T_F(\theta_H)$.

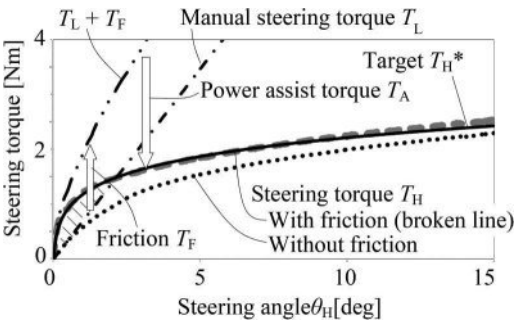


Figure 11. Steering torque characteristic with friction.

Required friction torque $T_F(\theta_H)$ is within the appropriate range of friction torque shown in Figure 7.

In Figure 11, calculation result using Equations 8 is plotted as broken line. This means that the result reproduces the target T_H* sufficiently.

To realize the required friction torque $T_F(\theta_H)$, motor control is convenient rather than mechanical components. It is because mechanical components have uncertainty, such as an individual difference and an aged deterioration.

Additionally, to correspond to the uncertainty of mechanical components, the $T_F(\theta_H)$ should be located close to the upper limit of the appropriate range of friction torque.

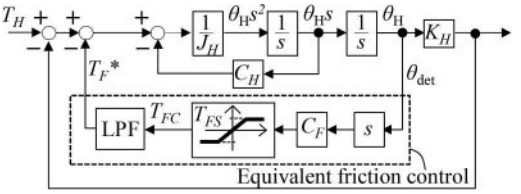


Figure 12. Block diagram of the linear approximation for friction.

3 DESIGN OF CONTROL METHOD USING EQUIVALENT FRICTION

To apply the proposed idea to an actual vehicle, the following items were required.

(1) A linear approximation method for friction
(2) A hardware structure
(3) Friction adjustment for control method

3.1 *The linear approximation method for friction*

In order to generate control friction T_F* by using motor torque control, the linear approximation method for friction was proposed as shown in Figure 12.

The control friction T_F* is given as following Equations 10 and 11.

$$T_{FC}=\begin{cases} -T_{FS} & if\left(C_F\theta_{det}s<-T_{FS}\right) \\ C_F\theta_{det}s & if\left(-T_{FS}\le C_F\theta_{det}s<T_{FS}\right) \\ T_{FS} & if\left(T_{FS}\le C_F\theta_{det}s\right) \end{cases} \quad (10)$$

$$T_F^*=\frac{\omega_C}{s+\omega_C}T_{FC} \quad (11)$$

θ_{det} is a detected angle of steering angle sensor. C_F is an linear approximation coefficient of the control friction. C_F should be large as possible to generate the Coulomb friction torque stably. In order to eliminate a differential noise of a steering angle sensor, L.P.F. is used that is given by Equation 11 and its cut off frequency of 20 Hz.

To verify the linear approximation method, the Coulomb friction T_F was calculated by Equation 4 and the control friction T_F* was calculated by Equations 10 and 11. Then they were compared.

Firstly, a result in a static condition is shown in Figure 13. Input frequency of the steering torque T_H was set 0.2 Hz. A characteristic with the Coulomb friction T_F (dotted line) and a characteristic with the control friction T_F* (solid line) was equivalent. The reason of this result was that the linear approximation coefficient C_F was sufficiently high.

Secondly, a transfer function $G_F(s)$ was calculated to clarify an effective frequency range of the control friction T_F* as following Equation 12.

$$G_F(s)=\frac{\theta_H}{(1+G_A)T_H}=\frac{1}{J_H s^2+C_H s+K_H}\left(1-\frac{T_F}{(1+G_A)T_H}\right) \quad (12)$$

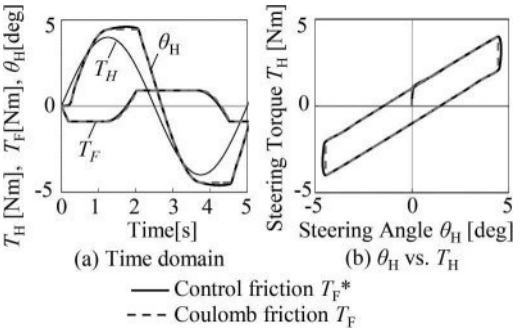


Figure 13. Comparison between the Coulomb friction T_F and the control friction T_F*.

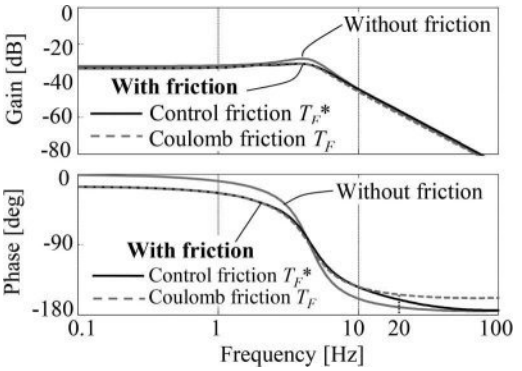


Figure 14. Frequency characteristics of G_F (θ_H/T_H).

A result of frequency characteristics is shown in Figure 14. Input frequency of the steering torque T_H was set from 0.1 to 100 Hz. A characteristic with the Coulomb friction T_F (dotted line) and a characteristic with the control friction T_F* (solid line) is equivalent from 0.1 to 20 Hz. It was thought that a difference from 20 to 100 Hz was sufficiently small because the gain at 20 Hz was smaller than a steady-state gain by 25 dB.

3.2 *Hardware structure*

In order to apply the proposed idea to an actual vehicle, a steering angle sensor needed to be installed to detect θ_H into steering system hardware structure.

Three types of hardware structure to install the steering angle sensor are introduced in Figure 15.

The steering angle sensor was equipped just after the steering wheel (Figure 15a). The steering angle sensor was equipped between the steering torque sensor and the motor (Figure 15b).

Relationship of the steering torque T_H, a gearbox angle θ_G and the steering angle θ_H are shown as following Equations 13, 14, and 15.

$$T_H=K_{TS}\left(\theta_H-\theta_G\right) \quad (13)$$

$$n_M T_M=K_{TS}\left(\theta_G-\theta_H\right)+K_H\theta_G \quad (14)$$

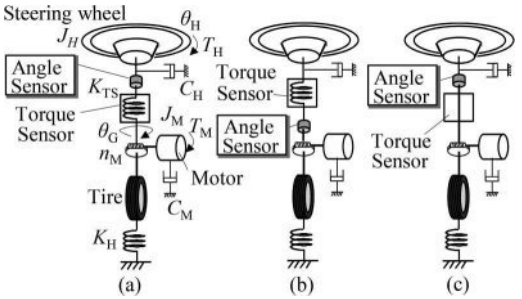


Figure 15. Hardware structures for installing the steering angle sensor.

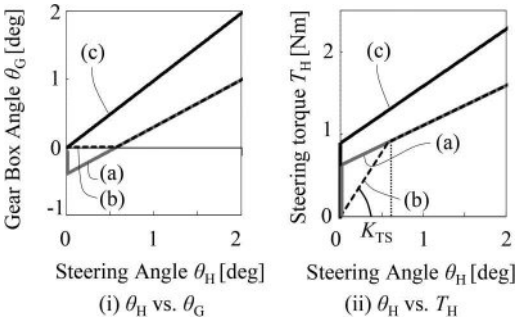


Figure 16. Comparison of three structures with friction control.

$$n_M T_M = -T_F^* \tag{15}$$

θ_H vs. θ_G and θ_H vs. T_H are plotted in Figure 16 for the structure (a), (b), and (c).

In case of the structure (a), the gearbox angle θ_G was been negative value as shown in Figure 16(i). It occurred because the steering torque sensor was twisted in an opposite direction by the control friction T_F*. However, the negative angle value does not occur when the mechanical friction is used. Therefore the structure (a) was thought unsuitable for the control friction.

In case of the structure (b), the steering torque characteristic cannot be controlled because the steering torque has a gradient due to the torsional rigidity of the steering torque sensor K_{TS} when the steering angle is close to 0 deg and the steering torque is less than the control friction T_F*.

Therefore, to achieve the sufficient torsional rigidity of the steering torque sensor, we applied a magnetostrictive torque sensor that has same rigidity with steering rod as shown in the structure (c).

3.3 *Friction adjustment for control method*

In order to generate the control friction T_F* according to the steering angle θ_H as shown in Figure 10, an adjustment map was made and added into the block diagram as shown in Figure 17.

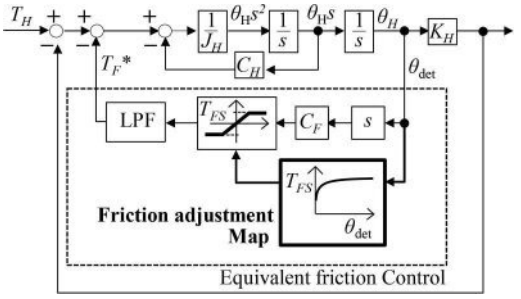


Figure 17. Block diagram with a friction adjustment map.

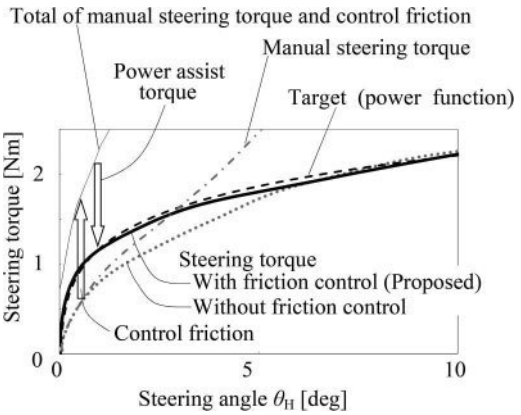


Figure 18. The measurement result of the steering torque characteristic in an actual vehicle test Vehicle Speed: 100 km/h.

4 VALIDATION

The proposed method was validated by using an actual vehicle (compact vehicle). The measurement result is shown as Figure 18.

When proposed method was not applied (without friction control), the manual steering torque was smaller than the target (power function) on the small steering angle area. Therefore it was impossible to achieve the target using the power assist.

When the proposed method was applied (with friction control), the target could be reproduced. Finally the proposed method was validated.

5 CONCLUSION

In this paper, the design method of the equivalent friction using the motor torque control for EPS was proposed to enhance the on-center steering feel. The conclusions were obtained as below:

(1) It was found that the friction torque had the appropriate range to enhance the on-center steering feel. And the range was changed depending on the assist gain of EPS.

(2) The design method of friction was proposed to achieve the target steering torque by means of the appropriate range of friction torque.
(3) The linear approximation method for friction, the steering system hardware structure, and the control method (block diagram) were proposed to achieve the motor control which realized the appropriate friction.
(4) The magnetostrictive torque sensor was applied to the proposed method to achieve the sufficient torsional rigidity that was necessary to generate friction torque.
(5) The proposed method was validated in the actual vehicle tests.

REFERENCES

Kushiro, I., et al., 2009. Steering System for the On-center Handling, *Transactions of Society of Automotive Engineers of Japan*, Vol. 40, No. 2: 233–238.

Misaji, K., et al., 2002. Vehicle Dynamics Evaluation by Analytical Method of Equivalent Linear System using the Restoring Force Model of Power Function Type, *Proceedings of AVEC'02*: 843–848.

Ohniwa, Y., et al., 2007. Stabilization on a Control for Moment of Inertia of EPS, *Transactions of Society of Automotive Engineers of Japan*, Vol. 38, No. 2: 207–212.

Ohno, S., et al., 2015. Proposal of equivalent friction control on Electric Power Steering (EPS), *Transactions of the Japan Society of Mechanical Engineers*, Vol. 81, No. 830.

Ono, K., et al., 2015. Development of Steering Feel Process, *Proceedings of 2015 the Japan Society of Automotive Engineers Annual Congress (Autumn)*, No. S027: 128–131.

Shimizu, Y., et al., 1991. Development of Electric Power Steering, *Transactions of the Society of Automotive Engineers*, No. 910014.

Shimizu, Y., 2003. Applications of Control Method in the Advance Steering System – Steering Reaction Torque and Variable Gear Ratio – , *JSAE SYMPOSIUM New Technologies in Active Safety*, No. 04-03: 37-60.

Wilhelm F., et al., 2014. Control for the Linearization of Electric Power Steering, *Proceedings of AVEC'14*:16–21.

APPENDIX

Table 1. Nomenclature.

Symbol	Meaning	Value	Unit
T_H	Steering torque	–	Nm
T_F	Friction torque	–	Nm
T_{FS}	Maximum friction torque	–	Nm
T_F*	Control friction torque	–	Nm
T_A	Power assist torque	–	Nm
T_M	Motor torque	–	Nm
T_H*	Target steering torque characteristic using power function	–	Nm
T_L	Manual steering torque	–	Nm
θ_H, θ_{HO}	Steering wheel angle, its overshoot	–	rad
θ_G	Gearbox angle	–	rad
θ_{det}	Detected angle of steering angle sensor	–	rad
K_H	Stiffness of manual steering torque	40	Nm/rad
K_{TS}	Stiffness of torque sensor		
	(1) Conventional Figure 15a,15b	90	Nm/rad
	(2) Magnetostrictive Figure 15c	3900	Nm/rad
J_H	Inertia of steering system	–	kgm^2
J_{SW}	Inertia of steering wheel	0.023	kgm^2
J_M	Inertia of motor	0.079×10^{-3}	kgm^2
C_H	Viscosity of steering	–	Nms/rad
C_F	Linear approximation coefficient of friction	100	Nms/rad
ω_C	Cut-off parameter of L.P.F.	125.7	rad/s
ζ	Damping ratio due to C_H	–	rate
n_M	Gear ratio (Worm wheel)	18.5	rate
G_A	Assist gain of EPS	–	rate
A, B, N	Power function parameters	3.27, −2.1, 0.12	–

Advanced Vehicle Control – Edelmann, Plöchl & Pfeffer (Eds)
© 2017 Taylor & Francis Group, London, ISBN 978-1-138-02992-7

The relationship between the resonance frequency of a steering system and the tire-road friction coefficient

L. Chen, Y. Luo, M. Bian, Z. Qin & K. Li
State Key Laboratory of Automotive Safety and Energy, Tsinghua University, Beijing, China

ABSTRACT: Some researchers found the relationship between the resonance frequency of an in-wheel motor (IWM) drive system and the tire-road friction coefficient (TRFC), and used it to estimate TRFC. This paper tries to establish a similar relation between the road condition and the electric power steering system (EPS) frequency response, by analysing the dynamic characteristics. System modelling is conducted by coupling a lateral-relaxation-length based dynamic tire model and a simplified motor model. Then detailed analysis of the system dynamics in the frequency domain is provided by a deduced frequency response function, considering different system parameters, such as longitudinal velocity and the gear ratio. As a result of analysis, a function of the system resonance frequency (RF) which is related to TRFC is presented. Comparison of the RF is made between EPS and IWM to propose a TRFC estimation idea based on frequency domain data fusion. The correctness of the RF equation is demonstrated using a simulation model.

1 INTRODUCTION

Since the forces between the tires and road interface primarily determine the states of vehicle motion, the knowledge of tire-road friction coefficient (TRFC) can be extremely useful for many vehicle active safety control systems, including electric power steering (EPS), direct yaw torque control system (DYC), adaptive cruise control system (ACC) and unified chassis control, to get a better performance. Particularly, reliable estimation of friction coefficients at each wheel will enable both traction and stability control systems, reduce wheel skid and enhance driving stability. Many researches on vehicle stability control have also proposed the explicit use of tire-road friction information in determination of the desired yaw rate and other control system variable (Rajamani, R. 2005, Yanada, M. et al. 2005).

Abundant literatures illustrated the state of art of the estimation of tire-road friction coefficient, and several different approaches have been proposed, which can be classified into two categories: cause-based and effect-based.

Some researchers of cause-based method try to detect factors that affect the friction coefficient, using optical camera, ultrasonic sensor or other sensors to detect road coverings (such as ice, snow, etc.) so as to estimate the friction coefficient (Yanada, M. et al. 2005).

Effect-based methods directly focus on the vehicle motion effects generated by the determinate control input under certain tire-road friction condition. The effects were shown in the tire as acoustic characteristic, tire-tread deformation and wheel slip. Hong, S. et al. 2013 introduced a certain sensor that was fixed to the inner surface of the tire to observe tire deformation. However this method needed a specially equipped sensor and a signal transmitting apparatus. Gustafsson, F. 1997, and Lee, C. 2004 deemed that the slope between the slip ratio and friction coefficient curve could give the information. But as the longitudinal tire force can't be accurately estimated by using engine torque or braking pressure. Meanwhile, when driving the vehicle in a static situation, the slip ratio is small and sensitive to the noise of wheel speed signal. In a word, there are some limitations about the slope-based method just using time-domain information. Ono, E. et al. 2003 tried to estimate road condition using the frequency characteristic of wheel speed signals during braking (Umeno, T. et al. 2002). Bartram, M. et al. 2010 found the influence of the tyre/road contact interface on driveline vibrations.

While vehicle is traveling, the angular velocity of the wheel can be considered as two parts, namely the high-frequency and low-frequency signals. Slope-based estimation accuracy depends on the tire force and slip ratio, and each parameter can be influenced by the high-frequency signal and static deviation of the lower one. For high-frequency signal, unlike the difficulty to accurately obtain the output torque of engine or braking pressure, in-wheel drive systems can control and capture the wheel driving torque in high frequency (Mutoh, N. 2012), which may bring a chance to estimate the friction coefficient using high frequency information of wheel speed. So unlike the normal traditional method using lower frequency

information, Chen, L. et al. 2016 proposed to detect the difference of road condition based on a deduced relation between TRFC and the high motor-wheel resonance frequency. If this theory is also suitable for the lateral situation, a similar frequency relation should exist in the electric power steering system, and can be used to estimate TRFC.

In this paper, the dynamic characteristics of a steering system are focused on to estimate the tire-road friction coefficient. With a brief review of the traditional concept of lateral relaxation length and static tire model, a dynamic tire model for normal driving is introduced. After a PMSM mathematical model is studied, a transfer function from control signal of the motor to the steering column dynamics can be obtained. Then an insight into the steering system dynamics in the frequency domains is provided, through checking the impact of different parameters. As a result of these analysis, the paper obtains the equation of the system resonance frequency which is related to the tire-road friction. Comparison of the RF is given between EPS and IWM to propose a TRFC estimation idea based on frequency domain data fusion. A simulation model is applied to effectively reproduce the resonance phenomenon, and shows the correctness of this RF function.

The paper is organized as follows. In Section 2, a dynamic tire model and a mathematical model of the steering motor are established. Section 3 illustrates the deduction process of the frequency response function. The resonance phenomenon and the distinctive frequency are found in Section 4, observed in Section 5. Conclusions are given in the end.

2 SYSTEM MODELLING

2.1 *Electric power steering system*

Electric power steering system in this article is a column-assist-type, whose steering motor through the worm gear structure is connected to the steering column, steers front wheels by rotation of the steering column.

Considering the torque balance of the the steering column, the system can be modelled as:

$$T_h + T_m G_m - \frac{T_a}{G_s} = B_d \dot{\theta}_d + J_d \ddot{\theta}_d \tag{1}$$

where, T_h is the torque input of the driver, T_m is the motor torque, G_m is the worm gear ratio, T_α is the aligning torque of the front axle, G_s is the gear ratio of the steering system form the steering wheel angle to the steering angle of the front wheel. θ_d is the steering angle of the column, B_d is damping coefficient, J_d is the equivalent moment of inertia.

2.2 *Tire model*

For the sake of simplicity, only lateral motion will be considered in this paper. The dynamics of suspension dynamics, road slope and so on are also neglected.

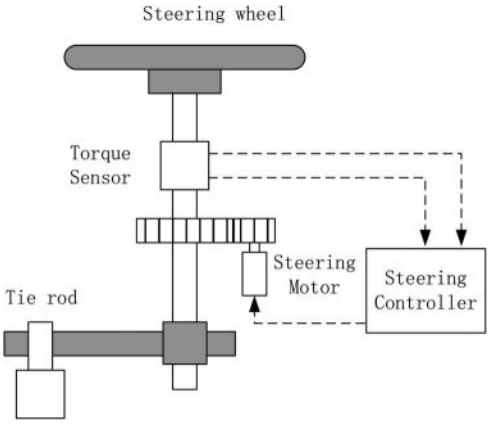


Figure 1. Schematic diagram of EPS (Ji-Hoon, K. et al. 2002).

The tire system is then described as the following form.

$$\begin{aligned} T_\alpha^S &= k_\alpha \alpha \\ \alpha &= -\frac{\theta_d}{G_s} + \frac{v_y + l_f \omega_r}{v_x} \\ k_\alpha &= b\mu_{\max} + c \end{aligned} \tag{2}$$

where T_α^S is the steady aligning torque, k_α and α are the aligning stiffness and the sideslip angle of the front axle, respectively. v_x and v_y is the longitudinal and lateral velocity of the vehicle at the point of the centre of gravity (CoG), ω_r is the yaw rate of the vehicle around the vertical axis. l_f is the distance from the front axle to CoG. $\mu_{\max}$ is the TRFC. b and c are two constants.

Some researchers show that the dynamic reaction of the tire force to disturbances can be approximated well using the first order systems. The non-linear relaxation length-based model is used to describe the dynamic aligning torque T_α^D derived from the steady aligning torque force T_α^S (Pacejka, H.B. 2002).

$$\tau \dot{T}_\alpha^D + T_\alpha^D = T_\alpha^S \tag{3}$$

The time constant τ can be derived from the relaxation length r_y as follows:

$$\tau = \frac{r_y}{v_x} \tag{4}$$

In this study, to minimize the complexity of the calculation process, the non-linear characteristics of r_y is ignored, and r_y is set as a constant.

2.3 *I-PMSM model*

The following assumptions are made before establishing the mathematical model of I-PMSM:

1) Neglect the saturation of the electric motor ferrite core.

2) Neglect turbulent flow and hysteresis loss in the electric motor.
3) The currents in the electric motor are symmetrical three-phase sinusoidal currents.
4) d-axis inductance equals to q-axis inductance.

Hence, in this study, the motor model can be simplified as Equation (5) (Song, Z. et al. 2013):

$$T_m = Ki \tag{5}$$

where K is a constant coefficient, i is the current of the motor.

3 TRANSFER FUNCTION DEDUCTION

Assume that the motor torque includes two kinds of information, low frequency and high frequency, shown as follows.

$$T_m = T_0 + T_1 \sin(2\pi f \cdot t) \tag{6}$$

where T_0 is a constant value, standing for the low frequency information, while $T_1 \sin(2\pi f \cdot t)$ is the high frequency information, T_1 is the amplitude, f means the frequency.

After substituting Equation (6) into Equation (1), the steering dynamic function can be described as Equation (7).

$$T_h + G_m\left(T_0 + T_1 \sin(2\pi f \cdot t)\right) - \frac{T_\alpha^D}{G_s} = B_d\dot{\theta}_d + J_d\ddot{\theta}_d \tag{7}$$

With the derivative on both sides of Equation (7), Equation (8) will be obtained as

$$G_m(2\pi f)T_1 \cos(2\pi f \cdot t) - \frac{\dot{T}_\alpha^D}{G_s} = B_d\ddot{\theta}_d + J_d\dddot{\theta}_d \tag{8}$$

Then combine Equation (7) with (8) through multiplying Equation (8) by τ and adding up to Equation (7):

$$T_h + G_m T_0 + G_m T_1\left[(2\pi f\tau)\cos(2\pi f \cdot t) + \sin(2\pi f \cdot t)\right] - \tau\frac{\dot{T}_\alpha^D}{G_s} - \frac{T_\alpha^D}{G_s} = B_d\dot{\theta}_d + (\tau B_d + J_d)\ddot{\theta}_d + \tau J_d\dddot{\theta}_d \tag{9}$$

Considering the dynamic and static tire model (Equation (2) and (3)), the equation above can be simplified as

$$T_h + G_m T_0 + aG_m T_1 \sin(2\pi f \cdot t + \phi) - \frac{k_\alpha\alpha}{G_s} = B_d\dot{\theta}_d + (\tau B_d + J_d)\ddot{\theta}_d + \tau J_d\dddot{\theta}_d$$
$$a = \sqrt{1 + (2\pi f\tau)^2},\ \phi = \arctan(2\pi f\tau) \tag{10}$$

Differentiating Equation (10) with respect to time, it can be expressed as:

$$2\pi f a G_m T_1 \cos(2\pi f \cdot t + \phi) - \frac{k_\alpha\dot{\alpha}}{G_s} = B_d\ddot{\theta}_d + (\tau B_d + J_d)\dddot{\theta}_d + \tau J_d\ddddot{\theta}_d$$
$$\dot{\alpha} = -\frac{\dot{\theta}_d}{G} + \frac{\dot{v}_y + l_f\dot{\omega}_r}{v_x} \tag{11}$$

In this paper, only the straight and moderate driving case is studied, which means that the longitudinal vehicle speed is approximately equal to the wheel rotation speed multiplied by effective rolling radius, and the steering angle of steering wheel is nearly zero. As the moment inertia of vehicle rather larger than the one of steering system, so the derivative of the rotation speed ω_r and the lateral velocity v_y can be treated as zero, compared to the one of the steering angle. $\dot{v}_y + l_f\dot{\omega}_r \approx 0$. Under these assumption, Equation (11) can be rewritten as:

$$2\pi f a G_m T_1 \cos(2\pi f \cdot t + \phi) = \frac{k_\alpha\dot{\theta}_d}{G_s^2} + B_d\ddot{\theta}_d + (\tau B_d + J_d)\dddot{\theta}_d + \tau J_d\ddddot{\theta}_d \tag{12}$$

Assume:

$$T_2 = T_1 \cos(2\pi f \cdot t + \phi) \tag{13}$$

Equation (12) can be rearranged as:

$$2\pi f a G_m T_2 = \frac{k_\alpha\dot{\theta}_d}{G_s^2} + B_d\ddot{\theta}_d + (\tau B_d + J_d)\dddot{\theta}_d + \tau J_d\ddddot{\theta}_d \tag{14}$$

Assume $\omega_d = \dot{\theta}_d$. With Laplace transform on both sides of Equation (14), it can be written as:

$$2\pi f a G_m T_2(\lambda) = \left[\frac{k_\alpha}{G_s^2} + B_d\lambda + (\tau B_d + J_d)\lambda^2 + \tau J_d\lambda^3\right]\omega_d(\lambda) \tag{15}$$

where, λ is the Laplacian operator.

Then, ignoring the highest-order term $\tau J_d\lambda^3$ the transfer function from control signal of the motor to the steering column dynamics can be shown as:

$$\frac{T_2(\lambda)}{\omega_d(\lambda)} = \frac{\frac{k_\alpha}{G_s^2} + B_d\lambda + (\tau B_d + J_d)\lambda^2}{2\pi f a G_m} \tag{16}$$

But, in practical application, the current of the motor can be measured directly instead of the motor torque. So Equation (16) should be rearranged with Equation (5) as:

$$\frac{i(\lambda)}{\omega_d(\lambda)} = \frac{\frac{k_\alpha}{G_s^2} + B_d\lambda + (\tau B_d + J_d)\lambda^2}{2\pi f\sqrt{1 + (2\pi f\tau)^2}KG_m} \tag{17}$$

So the amplitude ratio between the current and the rotation speed is shown as:

$$\frac{A(i)}{A(\omega_d)} = \left|\frac{i(j2\pi f)}{\omega_d(j2\pi f)}\right| = \frac{\left|\frac{k_\alpha}{G_s^2} - (\tau B_d + J_d)(2\pi f)^2 + jB_d(2\pi f)\right|}{2\pi f\sqrt{1 + (2\pi f\tau)^2}KG_m} = \frac{\left|\frac{k_\alpha}{G_s^2} - \left(\frac{B_d r_y}{v_x} + J_d\right)(2\pi f)^2 + jB_d(2\pi f)\right|}{2\pi f\sqrt{1 + \left(\frac{2\pi f r_y}{v_x}\right)^2}KG_m} \tag{18}$$

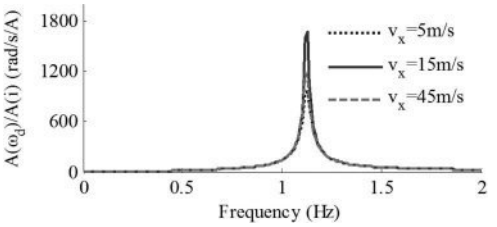


Figure 2. Amplitude ratio under different velocities*.
*Parameters: $k_\alpha = 2000$ Nm/rad; $r_y = 0.05$ m; $G_s = 20$; $G_m = 4$; $K = 6$ Nm/A; $B_d = 0.03$ Nm-s/rad; $J_d = 0.1$ kg-m^2.

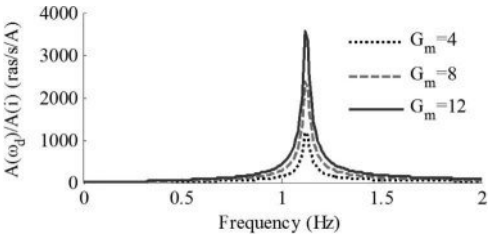


Figure 3. Amplitude ratio under different worm gear ratios*.
*Parameters: $k_\alpha = 2000$ Nm/rad; $r_y = 0.05$ m; $G_s = 20$; $v_x = 5$ m/s; $K = 6$ Nm/A; $B_d = 0.03$ Nm-s/rad; $J_d = 0.1$ kg-m^2.

4 RESONANCE FREQUENCY

With Equation (18), different impacts of system parameters on the steering column can be analysed.

4.1 *Effect of longitudinal velocity*

Figure 2 shows three amplitude ratio-frequency curves under different longitudinal velocities.

This figure implies that, for most frequency range, the amplitude ratios are similar under different velocities, which means that longitudinal velocity shows little effect on the curve shape. When the frequency locates in the range 1.1–1.2 Hz, the curves reach separated peak points. Meanwhile, the peak value at 15 m/s is the highest among the three curve. It reflects that the velocity impact on the peak value is not linear, which should be considered in the control algorithm of EPS. The frequency of the peak point is called as steering system resonance frequency in this paper.

4.2 *Effect of gear ratio*

Figure 3 shows three amplitude ratio-frequency curves under different worm gear ratios.

This figure implies that, steering system resonance frequency is not influenced by worm gear ratios. And the velocity impact on the curve shape is linear, which can easily be understood through Equation (18).

Figure 4 shows three amplitude ratio-frequency curves under different steering ratios.

The steering ratio is an important parameter in the system design in order to reach a balanced

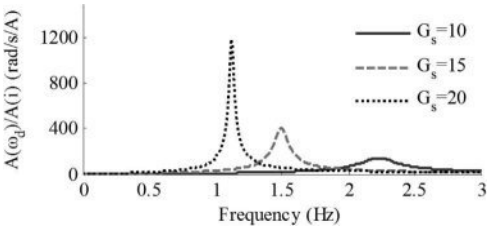


Figure 4. Amplitude ratio under different steering ratios*.
*Parameters: $k_\alpha = 2000$ Nm/rad; $r_y = 0.05$ m; $G_m = 4$; $v_x = 5$ m/s; $K = 6$ Nm/A; $B_d = 0.03$ Nm-s/rad; $J_d = 0.1$ kg-m^2.

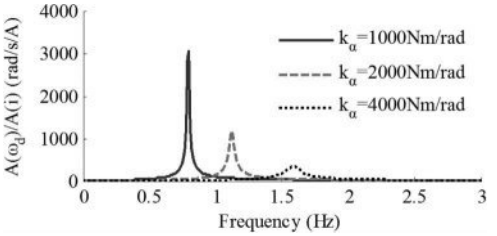


Figure 5. Amplitude ratio under different aligning stiffness*.
*Parameters: $G_m = 4$; $r_y = 0.05$ m; $G_s = 20$; $v_x = 5$ m/s; $K = 6$ Nm/A; $B_d = 0.03$ Nm-s/rad; $J_d = 0.1$ kg-m^2.

optimization between manoeuvre ability and comfort. This figure clearly implies that, the smaller steering ratio is given, the low peak value and the higher system resonance frequency can be reached.

4.3 *Effect of aligning stiffness*

Figure 5 shows three amplitude ratio-frequency curves under different aligning stiffness.

The aligning stiffness's impact shows the opposite trend to the one of the steering ratio. As this parameter can be influenced strongly by the vertical tire force and tire-road friction coefficient, its real-time estimation should be included in the EPS control algorithm.

4.4 *Steering system resonance frequency*

The resonance frequency cannot be obtained directly from Equation (17). From Figure 2–5, it shows that the empirical value of resonance frequency is smaller than 3 Hz.

With this empirical value, approximate conversion can be made on Equation (18).

$$\min\left[\frac{A(i)}{A(\omega_d)}\right] \approx \min\left[\frac{\left|\frac{k_\alpha}{G_s^2} - J_d(2\pi f)^2 + jB_d(2\pi f)\right|}{2\pi f K G_m}\right] = \min\left[\left|\frac{jB_d}{G_m} + \frac{\frac{k_\alpha}{G_s^2} - J_a(2\pi f)^2}{2\pi f K G_m}\right|\right] \tag{19}$$

After some mathematical deduction, the resonance frequency can be expressed as:

$$f_0 \approx \frac{1}{2\pi G_s}\sqrt{\frac{k_\alpha}{J_d}} = \frac{1}{2\pi G_s}\sqrt{\frac{b\mu_{\max} + c}{J_d}} \tag{20}$$

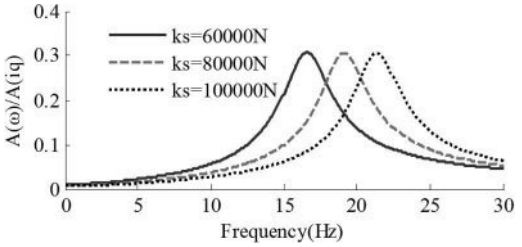


Figure 6. Resonance frequency of IWM* (Chen, et al. 2016).
*k_s is the longitudinal stiffness, ω is the wheel speed, i_q is the in-wheel motor current.

Apparently, Equation (20) explains the regular patterns discussed above and shown in Figure 2–5. As mentioned in the Introduction, Equation 20 shows the relationship between TRFC and the resonance frequency, which is similar to the motor-wheel resonance frequency function proposed in the reference (Chen, et al. 2016). Meanwhile, Using Equation 20, a TRFC estimation method which utilizes the high-frequency information of the motor current and steering column rotation speed can be investigated.

4.5 *RF Comparison between IWM and EPS*

As shown in Figure 5, the empirical value of the steering system resonance frequency is 1–3 Hz. Comparatively, the empirical value of the in-wheel motor drive system is 10 times of the former one, about 10–30 Hz, shown as Figure 6.

If the estimated TRFCs for each direction can be regarded as two measurements for the same signal subjected to different disturbances, they are significantly distinct from the viewpoint of frequency response and the model error. The estimated longitudinal TRFC can quickly response to the changing of road conditions, but the accuracy can be easily influenced by the model (the relation function between the IWM resonance frequency and the longitudinal TRFC) error and the "sensing error". In the research, "sensing error" refers to the error in the frequency domain, which actually means the noise or unstable and instantaneous vibration of the signal in the time domain. So, comparatively, even though the estimated lateral TRFC cannot quickly response to the changing of road conditions, it is relatively robust against the sensing instantaneous vibration and model errors.

5 SIMULATION OF RESONANCE FREQUENCY

A bicycle vehicle model which integrates the EPS and IWM is built to test the correctness of the resonance phenomenon. The main parameters of the vehicle model are listed in Table 1.

In this simulation, the setting of the road surface is shown as Figure 7. With the given values of G_s, J_d, b, c, the steering system resonance frequency (RF) can be calculated using Equation 18. During 0–9 s, the RF is 2 Hz, and during 9–18 s, the RF is 1 Hz. The steering and driving motor torque demand is a kind of band-limited white noise around zero in order to keep a constant longitudinal velocity and go straight, shown as Figure 8.

It can be seen clearly in Figure 9 that the oscillation cycle is respectively 0.5 s and 1 s before and after the time point of 9 s. This result coincides with the RF calculated in the last paragraph, and illustrates that the TRFC have a strong impact on the steering system dynamic response and Equation 18 is reasonable.

The true value of wheel speed without noise was shown as Figure 10. It can be seen clearly that the signal before 9 s was more compressed than the one after 9 s. The oscillation cycle of the in-wheel motor system in Fig 10 was rather shorter than the one of the

Table 1. The main parameters of the vehicle model.

Parameter	Values
Vehicle mass (kg)	1274
Wheel base (mm)	2578
Front and rear axle load ratio	7:13
Yaw inertia (kg-m^2)	1523
r_y (m)	0.05
v_x (m/s)	15
G_s (−)	15.9
G_m (−)	4
K (Nm/A)	4
b (Nm/rad)	5000
c (−)	0
J_d (kg-m^2)	0.1
B_d (Nm-s/deg)	0.03

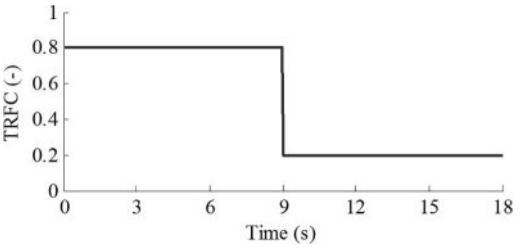


Figure 7. Setting of the TRFC.

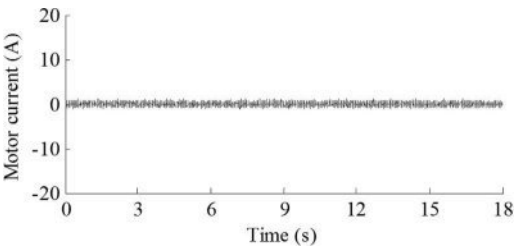


Figure 8. Current control input.

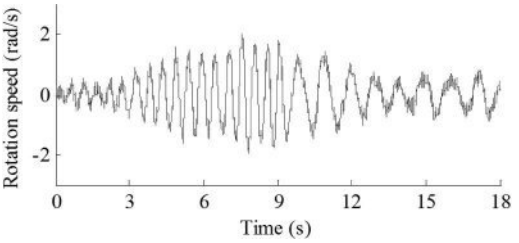


Figure 9. The steering wheel rotation speed.

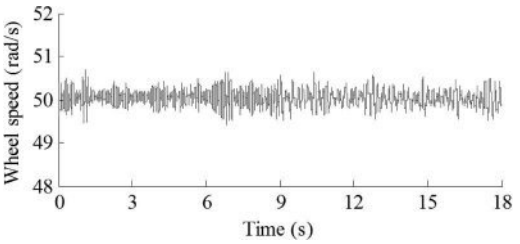


Figure 10. Wheel rotation speed without noise.

EPS in Figure 9, which verified the discussion in 'RF Comparison between IWM and EPS'.

So, in order to accurately capture the dynamic changing of road conditions, the higher-frequency information of the longitudinal TRFC estimation should be extracted. At low frequencies, the value from the lateral TRFC estimation is mainly used against model errors. To implement this idea, first order filters (Piyabongkarn, D. et al. 2009) are found to be adequate for the combination of the two directions' TRFC. The combination format is proposed as Equation (21).

$$\hat{\mu}_{\max} = \frac{1}{\tau_0 s + 1}\mu_{\max - y} + \frac{\tau_0 s}{\tau_0 s + 1}\mu_{\max - x} \tag{21}$$

where τ_0 is a time constant, $\mu_{\max -y}$ is the estimated TRFC based on the steering RF, $\mu_{\max -x}$ is the one based on the IWM RF.

6 CONCLUSION

In this paper, a relationship between RF of a steering system and TRFC is observed by studying the dynamic characteristics. The insight into the system dynamics in the frequency domains is provided through a deduced system transfer function. The transfer function is be obtained by combining dynamic tire model with PMSM mathematical model. The relationship is verified by a simulation model.

Contributions of this paper:

- By introducing the notion of the lateral relaxation length, a transfer function of the dynamic steering system is obtained to explains the parameters impact in frequency domain;
- An equation of steering system resonance frequency is deduced, which is related to TRFC. As a future research direction, it can be used to propose an estimation method of the road condition without the information of the sideslip angle and aligning torque.
- Using frequency domain data fusion, the estimated combined TRFC can achieve quick response to the changing of road conditions in high frequency domain and stability to the signal noise in lower frequency domain.

ACKNOWLEDGMENTS

The authors are grateful for the sponsorship from the the National Natural Science Foundation of China (Grant No. 51575295 and Grant No. U1564208) and the National Key Research and Development Program of China (2016YFB0100905).

REFERENCES

Bartram, M. et al. 2010. A study on the effect of road friction on driveline vibrations. *Proceedings of the Institution of Mechanical Engineers, Part K: Journal of Multi-body Dynamics*, 224: 321–340.

Chen, L. et al. 2016. Tire–road friction coefficient estimation based on the resonance frequency of in-wheel motor drive system. *Vehicle System Dynamics*, 54(1):1–19.

Gustaffson, F. 1997. Slip-based tire-road friction estimation. *Automatica*, 33(6): 1087–1099.

Hong, S. et al. 2013. Tyre–road friction coefficient estimation based on tyre sensors and lateral tyre deflection: modeling, simulations and experiments. *Vehicle System Dynamics*, 51(5): 627–647.

Ji-Hoon, K. et al. 2002. Control logic for an electric power steering system using assist motor. *Mechatronics*, 12(3): 447–459.

Lee, C. et al. 2004. Real-time slip-based estimation of maximum tire-road friction coefficient. *IEEE/ASME Transactions on Mechatronics*, 9(2): 454–458.

Mutoh, N. 2012. Front-and-rear-wheel-independent-drive type electric vehicle (FRID EV) with the outstanding driving performance suitable for next-generation electric vehicles. *2012 IEEE International Electric Vehicle Conference.*

Ono, E. et al. 2003. Estimation of automotive tire force characteristics using wheel velocity. *Control Engineering Practice*, 11: 1361–1370.

Pacejka, H.B. 2002. *Tyre and vehicle dynamics*. Oxford: Butterworth-Heinemann.

Piyabongkarn D, Rajamani R, Grogg J A, et al. 2009. Development and experimental evaluation of a slip angle estimator for vehicle stability control. *IEEE Transactions on Control Systems Technology*, 17(1): 78–88.

Rajamani, R. 2005. *Vehicle Dynamics and Control*, New York.

Song, Z. et al. 2013. Rule-based fault diagnosis of hall sensors and fault-tolerant control of PMSM. *Chinese Journal of Mechanical Engineering*, 26(4): 813–822.

Umeno, T. et al. 2002. Estimation of tire-road friction using tire vibration model. *SAE Technical Papers*, 2002-01-1183.

Yanada, M. et al. 2005. Road surface condition detection technique based on image taken by camera attached to vehicle rearview mirror. *Review of Automotive Engineering*, 22: 163–168.

Steer-by-wire/ADAS

Advanced Vehicle Control – Edelmann, Plöchl & Pfeffer (Eds)
© 2017 Taylor & Francis Group, London, ISBN 978-1-138-02992-7

Upperbounds on the closed loop sensitivity for the control of a steer-by-wire vehicle

Tom van der Sande, Peter Zegelaar, Igo Besselink & Henk Nijmeijer
Dynamics & Control, Department of Mechanical Engineering, Eindhoven University of Technology, The Netherlands

ABSTRACT: This paper proposes guidelines for controller design for steer-by-wire vehicles with the inclusion of non-linear tire behavior. For the nominal vehicle model, the velocity dependency of the yaw dynamics is removed. By using an H_∞ approach, bounds on the closed loop sensitivity are presented. From these bounds guidelines for the controller design are derived. Using a validated multi-body vehicle model, it is shown that the yaw dynamics are stabilized for an extreme manoeuvre.

1 INTRODUCTION

The task of driving a car is something that most people take for granted. However, when the vehicle exhibits unexpected behavior, the average driver fails to maintain the vehicle in a stable and controlled state [12]. Car manufacturers have already been working on preventing this problem for many years by incorporating active safety systems in cars. This has mostly been done by extending the braking system with additional functionality, such as ABS [5] and ESC.

A more recent development that receives a lot of interest is steer-by-wire. With a steer-by wire system, there is no physical connection between the steering wheel and front wheels anymore, allowing for greater flexibility compared to existing systems. On the one hand the steering wheel torque can be chosen freely, this is discussed extensively in [3]. Besides this, the vehicles yaw dynamics can be influenced easily with steer-by-wire, not only in limit handling situations, but also for normal driving. For instance [15] uses a steer-by-wire system to change the vehicles front cornering stiffness as observed from the steering wheel. A full state feedback controller is introduced to modify the handling dynamics. With a modified Chevrolet Corvette it is shown that the observed cornering stiffness can be reduced in practice.

A clear distinction in the literature for steer-by-wire design is that either a linear controller [1], [2] is used in what is in essence a highly non-linear system, or non-linear controller [14], [4] is used, which requires detailed knowledge of the vehicle dynamics. With both approaches, favorable results are achieved in the region for which the controllers are designed. Other operating conditions, beyond the design region of the controller, however, are often not discussed.

In this paper the focus will be on the design of a controller for the yaw dynamics of a vehicle equipped with steer-by-wire. The objective is to provide guidelines on how to design the controller such that, given a certain operating range of the tire, yaw stability of the controlled vehicle is guaranteed. Besides this, the yaw and lateral dynamics are dependent on the forward velocity. This dependency will also be accounted for in the design of the controller.

The outline of this paper is as follows. In section 2 the vehicle model is discussed. The control objective and controller design are handled in section 3. Simulation results obtained with a multi-body vehicle model are shown in section 4. Finally, conclusions are drawn in section 5

2 VEHICLE MODEL

For design of the controller, the single-track vehicle model is used [8]. This model only considers the planar dynamics, i.e. the lateral velocity, v_y and yaw-rate, r_z. The left and right tires are lumped together into one equivalent tire on the vehicle centerline. The forward velocity, v_x, is assumed to vary slowly with respect to the other dynamics. Therefore the longitudinal dynamics are neglected. The equations of motion are

$$m\left(\dot{v}_y + v_x r_z\right) = F_{y1} + F_{y2} \tag{1}$$

$$I_{zz}\dot{r}_z = aF_{y1} - aF_{y2}. \tag{2}$$

In this model the vehicle mass is represented by m and its yaw inertia by I_{zz}. The parameters a and b represent the distance between the front and rear axle to the center of gravity respectively. Although simple, the single track vehicle model, does represent the relevant dynamics of the vehicle. By including non-linear tire behavior, a good representation of the lateral and yaw dynamics of the vehicle is achieved. A model with more degrees of freedom would overcomplicate the following analysis and would obfuscate

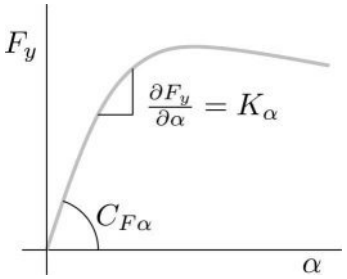


Figure 1. Lateral force, F_y versus side slip angle α with the cornering stiffness indicated by $C_{F\alpha}$ and the local gradient of the lateral force K_α.

the mathematical insight that is still present with the presented two degrees-of-freedom model.

To account for the non-linear tire behavior as shown in Fig. 1, the local gradient of the lateral force, K_α, is introduced in the model. This variable can be interpreted as a linear approximation of the lateral force versus slip angle when linearizing around a tire side slip angle operating point. When linearizing around $\alpha = 0$ it is equal to the cornering stiffness, $C_{F\alpha}$. Obviously, K_α changes as a function of the tire side slip angle, α. This can be captured in an approach where it is assumed that the local gradient of the lateral force varies within a pre defined range. The vehicle dynamics then become

$$\dot{x}_p = \begin{bmatrix} \dot{v}_y \\ \dot{r}_z \end{bmatrix} = A_p x_p + B_p \delta_{rack}, \tag{3}$$

$$y_p = r_z = C_p x_p, \tag{4}$$

$$A_p = -\begin{bmatrix} \frac{K_{\alpha1}+K_{\alpha2}}{mv_x} & \frac{aK_{\alpha1}-bK_{\alpha2}}{mv_x} + v_x \\ \frac{aK_{\alpha1}-bK_{\alpha2}}{I_{zz}v_x} & \frac{a^2K_{\alpha1}+b^2K_{\alpha2}}{I_{zz}v_x} \end{bmatrix}, \tag{5}$$

$$B_p = \begin{bmatrix} \frac{K_{\alpha1}}{m} \\ \frac{aK_{\alpha1}}{I_{zz}} \end{bmatrix}, \quad C_p = \begin{bmatrix} 0 & 1 \end{bmatrix}. \tag{6}$$

with x_p the perturbed state vector, y_p the perturbed output state and A_p, B_p and C_p the perturbed state space matrices. The local gradient of the lateral force is assumed to be within the range

$$K_{\alpha1} \in [K_{\alpha1}^-, K_{\alpha1}^+] \text{ with } K_{\alpha1n} = \frac{K_{\alpha1}^- + K_{\alpha1}^+}{2} \tag{7}$$

$$K_{\alpha2} \in [K_{\alpha2}^-, K_{\alpha2}^+] \text{ with } K_{\alpha2n} = \frac{K_{\alpha2}^- + K_{\alpha2}^+}{2}. \tag{8}$$

The nominal local gradient of the lateral force, $K_{\alpha1n}$ and $K_{\alpha2n}$, are chosen as the average between the minimum value, $K_{\alpha1}^-$ and $K_{\alpha2}^-$, and the maximum value, $K_{\alpha1}^+$ and $K_{\alpha2}^+$ respectively. If $K_{\alpha1}^-$ goes to zero, steering cannot influence the vehicle dynamics anymore. It is assumed that the mass, inertia and distances to the center of gravity are constant and that the tires do not saturate fully. The transfer function between the steering angle input and yaw-rate output is expressed as

$$G_p(s) = C_p (sI - A_p)^{-1} B_p, \tag{9}$$

with $s = j\omega$ the Laplace variable. A summary of the vehicle model parameters is given in Table 1.

Table 1. Single track model vehicle parameters, based on a BMW 318i.

Parameter	Value	Unit
m	1734	kg
a	1.422	m
b	1.303	m
I_{zz}	1900	kgm^2
$K_{\alpha1}^-$	52000	N/rad
$K_{\alpha1}^+$	148000	N/rad
$K_{\alpha2}^-$	64000	N/rad
$K_{\alpha2}^+$	189000	N/rad

2.1 *Yaw-rate response*

The vehicle yaw-rate response to a steering wheel angle changes as a function of the local gradient of the lateral force as is shown in Fig. 2. This figure shows that for different combinations of the front and rear gradient of the lateral force, $K_{\alpha i}$, the vehicle exhibits different yaw behavior. This is also expressed in the steady state yaw-rate response, which is also known as the steady state yaw velocity gain

$$k_{\delta \to r_z} = \frac{(a+b)K_{\alpha1}K_{\alpha2}v_x}{(a+b)^2K_{\alpha1}K_{\alpha2} + (bK_{\alpha2} - aK_{\alpha1})mv_x^2}, \tag{10}$$

which is significantly influenced by both local gradients. Besides this tire parameter dependency, (10) also shows that the steady state yaw-rate response is dependent on the forward velocity v_x. This dependency is also found in the eigenfrequency and dimensionless damping, which are expressed as

$$f_e = \frac{1}{2\pi}\sqrt{\frac{(a+b)^2K_{\alpha1}K_{\alpha2} + (bK_{\alpha2} - aK_{\alpha1})mv_x^2}{I_{zz}mv_x^2}} \tag{11}$$

$$\beta_e = \frac{K_{\alpha1}(I_{zz} + a^2m) + K_{\alpha2}(I_{zz} + b^2m)}{2\sqrt{I_{zz}m\left((a+b)^2K_{\alpha1}K_{\alpha2} + (bK_{\alpha2} - aK_{\alpha1})mv_x^2\right)}} \tag{12}$$

respectively. At higher frequencies only the front local gradient of the lateral force influences the vehicle yaw-rate, since

$$G_p(j\omega)\,|_{\omega\to\infty} = \frac{K_{\alpha1}a}{I_{zz}\omega}. \tag{13}$$

One combination of parameters deserves special attention, as its behavior is significantly different

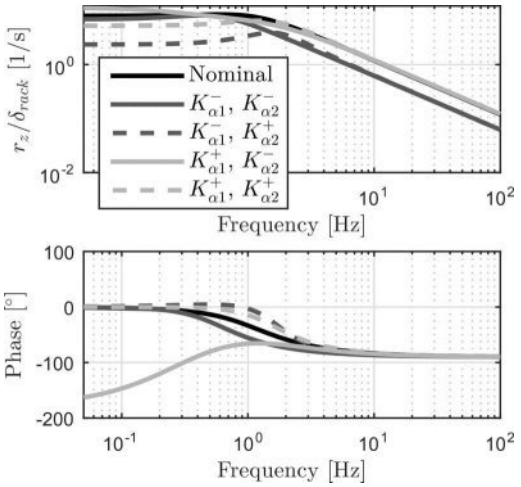


Figure 2. Yaw-rate response as a function of steering input for a range of values of the local gradient of the lateral force for $v_x = 30$ m/s.

from the other combinations of local gradient of the lateral force, as shown in Fig. 2. In this particular case the front gradient of the lateral force is high ($K_{\alpha 1}^+ = 148000$ N/rad) and the rear one is low ($K_{\alpha 2}^- = 64000$ N/rad), the vehicle is significantly oversteered and has a critical velocity of only 17.9 m/s. This results in a right half plane pole and thus an unstable vehicle.

3 CONTROLLER DESIGN

The yaw-stability of a vehicle is of utmost importance. Besides this, the vehicle body side slip angle is often seen as a limiting factor in vehicle handling [13], [7]. However, since this state is impossible to measure with affordable sensors, only the yaw-rate of the vehicle will be considered as input for the controller. A standard negative feedback control loop is chosen, where a reference yaw-rate is prescribed, depending on the driver inputs. Note that this reference model can be designed as any physically feasible model. Its design, however, is beyond the scope of this paper. The control error is defined as the difference between the reference yaw-rate and measured yaw-rate.

3.1 *Control objective*

The control objectives are defined as follows

1. A small yaw-rate error $e = r_{zref} - r_z$ overshoot.
2. Stability, all closed loop poles should thus have a negative real part.
3. Fast convergence of the error dynamics. Ideally the poles are placed such that the response of the closed loop is beyond human capabilities, i.e. a bandwidth beyond approximately 4 Hz [11], so performing better than the best driver.
4. Nominal closed loop dynamics that are independent of forward velocity, v_x.

Note that all these objectives refer to the closed loop behavior, i.e. from r_{zref} to r_z. This does not imply that the vehicle behavior as experienced by the driver, which includes the reference model, has to fulfill all these criteria.

The range of parameter variation of the local gradient of the lateral force as presented in (7), (8) requires a control topology that is robust for a variation in these parameters. A suitable method is H_∞-control. This control method takes a nominal model, $G_n(s)$, and accounts for an uncertainty by using

$$G_p(s) = G_n(s)\left(1 + w_{iI}(s)\Delta_{iI}\right)^{-1}, \tag{14}$$

where $w_{iI}(s)$ is the weighting filter designed such that $|\Delta_{iI}(j\omega)| \leq 1$ for all ω.

3.2 *Disturbance model*

As (14) shows, the disturbance model chosen is of the inverse multiplicative type. The magnitude of the uncertainty as a result of the varying local gradient of the lateral force is expressed as [9]

$$l_{iI}(\omega) = \max_{G_p \in \Pi} \left| \frac{G_n(j\omega) - G_p(j\omega)}{G_p(j\omega)} \right| \tag{15}$$

where it is assumed that the uncertainty makes a disc shaped region around the nominal plant with radius $l_{iI}(\omega)$. All possible plants as a result of the parameter variation are indicated by Π. The objective is now to design the weighting filter $w_{iI}(s)$ such that

$$|w_{iI}(j\omega)| \geq l_{iI}(\omega), \forall\omega. \tag{16}$$

This radius of the disc shaped region, $l_{iI}(\omega)$, can be calculated using standard MATLAB tools such as wcgain. For the parameters as listed in Table 1 this is shown in Fig. 3. This figure shows that with increasing forward velocity, the uncertainty at low frequencies increases. At high frequencies the uncertainty becomes independent of the forward velocity. Both these observations will be proven in section 3.3.

The Nyquist criterion states that robust stability for the controlled system can be guaranteed if

$$\left|1 + L(s)\left(1 + w_{iI}(s)\Delta_{iI}\right)^{-1}\right| > 0, \quad \forall\omega \tag{17}$$

which can be rewritten as

$$|1 + L(s)| - |w_{iI}(s)| > 0, \quad \forall\omega \tag{18}$$

$$\left| \frac{w_{iI}(s)}{1 + L(s)} \right| < 1, \quad \forall\omega. \tag{19}$$

The distance to the point -1 in the Nyquist plot is given by $|1 + L(s)|$ with $L(s) = C(s)G_n(s)$ and $C(s)$ a stabilizing controller. The uncertainty weighting filter

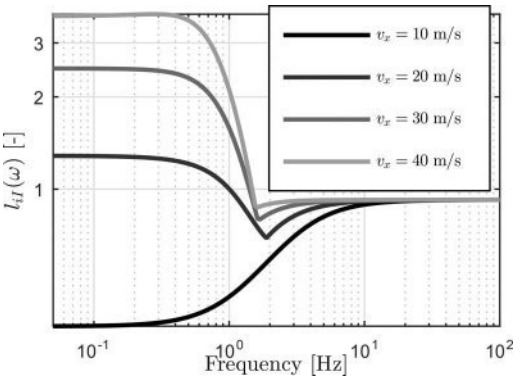


Figure 3. Uncertainty radius, $l_{iI}(s)$ as a function of frequency for various forward velocities.

$w_{iI}(s)$ defines the distance to the point -1. This can be rewritten to the stability condition

$$|S(s)| < \frac{1}{|w_{iI}(s)|}, \quad \forall\omega \tag{20}$$

with $S(s)$ the sensitivity function which is defined as

$$S(s) = \frac{1}{1+L(s)} = \frac{1}{1+C(s)G_n(s)}. \tag{21}$$

3.3 *Uncertainty bounds*

Fig. 2 and Fig. 3 show that the yaw-rate response and uncertainty radius depend on the forward velocity, v_x. In this section the uncertainty weighting $w_{iI}(s)$ will be derived analytically to capture this phenomena.

The steady-state yaw-rate gain $k_{r\to\delta}$ is expressed in (10), given this expression, the uncertainty radius at $\omega = 0$ can be derived as

$$l_{iI0} = l_{iI}(\omega)|_{\omega\to 0} = \max_{G_p\in\Pi}\left|\frac{k_{n,\delta\to r_z} - k_{\delta\to r_z}}{k_{n,\delta\to r_z}}\right| = \tag{22}$$

$$\frac{mv_x^2\left(aK_{\alpha 1n}K_{\alpha 1}^-\left(K_{\alpha 2}^+ - K_{\alpha 2n}\right) + bK_{\alpha 2n}K_{\alpha 2}^+\left(K_{\alpha 1n} - K_{\alpha 1n}^-\right)\right)}{K_{\alpha 1}^-K_{\alpha 2}^+\left(mv_x^2(bK_{\alpha 2n} - aK_{\alpha 1n}) + K_{\alpha 1n}K_{\alpha 2n}(a+b)^2\right)}.$$

At high frequencies (14) reduces to

$$G_p(j\omega)|_{j\omega\to\infty} = \frac{aK_{\alpha 1}mv_x^2 j\omega}{I_{zz}mv_x^2(j\omega)^2} = \frac{aK_{\alpha 1}}{I_{zz}\omega} \tag{23}$$

which gives

$$l_{iI\infty} = l_{iI}(\omega)|_{\omega\to\infty} = \frac{K_{\alpha 1n}}{K_{\alpha 1}^-} - 1, \tag{24}$$

which is independent of the forward velocity, v_x, as Fig. 3 already showed. Referring back to the stability limit formulated in (20) and the fact that $S(\omega = \infty) = 1$ by definition the ratio between the nominal and minimum local gradient of the lateral force is defined as

$$\frac{K_{\alpha 1n}}{K_{\alpha 1}^-} < 2. \tag{25}$$

Obviously, this constraint has been accounted for in the selection of the parameters as presented in Table 1.

The uncertainty has now been analytically determined for low and high frequencies. Furthermore, the dynamics of the single-track model are of second order. This also holds for the uncertainty radius as Fig. 3 shows. It is therefore proposed to model the uncertainty radius $w_{iI}(s)$ as

$$w_I(s) = l_{iI0}\frac{\frac{1}{(2\pi f_{w1})^2}s^2 + \frac{\beta_{w1}}{\pi f_{w1}}s + 1}{\frac{1}{(2\pi f_{w2})^2}s^2 + \frac{\beta_{w2}}{\pi f_{w2}}s + 1} \tag{26}$$

with f_{w1} and f_{w2} crossover frequencies and β_{w1}, β_{w2} damping terms. For this second order filter it holds that

$$\left(\frac{f_{w2}}{f_{w1}}\right)^2 = \frac{l_{iI\infty}}{l_{iI0}}. \tag{27}$$

Using this, together with (22) and (24), the magnitude of f_{w1} and f_{w2} can be derived as

$$f_{w1} = f_w + f_{w\Delta} = f_w + \frac{1-\sqrt{\frac{l_{iI\infty}}{l_{iI0}}}}{1+\sqrt{\frac{l_{iI\infty}}{l_{iI0}}}}f_w \tag{28}$$

$$f_{w2} = f_w - f_{w\Delta} = f_w - \frac{1-\sqrt{\frac{l_{iI\infty}}{l_{iI0}}}}{1+\sqrt{\frac{l_{iI\infty}}{l_{iI0}}}}f_w. \tag{29}$$

The parameters f_w, β_{w1} and β_{w2} are chosen such that up to $v_x = 40$ m/s the weighting filter, $w_{iI}(s)$, is an upper-bound for the disturbance radius $l_{iI}(\omega)$, the parameters are listed in Table 2.

Table 2. Disturbance weighting filter $w_{iI}(j\omega)$ parameters.

Parameter	Value	Unit
f_w	0.9	Hz
β_{w1}	1	–
β_{w2}	0.5	–

3.4 *Velocity canceling controller*

One of the control objectives is to make the nominal closed loop behavior independent of the forward velocity. Under the assumption that the nominal vehicle model is known, a controller can be designed that cancels these nominal dynamics. Recall that the steady state gain, eigenfrequency, dimensionless damping

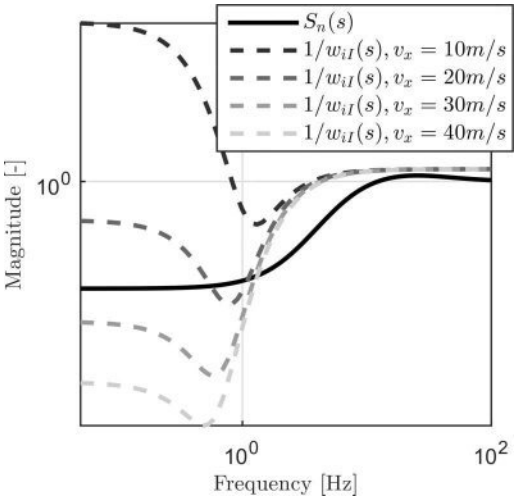


Figure 4. Sensitivity of the nominal plant with the v_x canceling controller, $S_n(s) = 1/(1 + L_1(s))$ and the uncertainty bounds, $w_{iI}(s)$ as a function of forward velocity. Here, $f_c = 10$ Hz and $\beta_c = 2$.

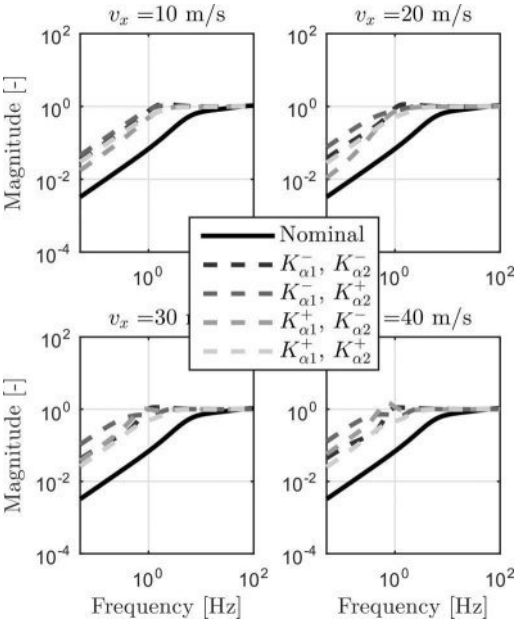


Figure 5. Sensitivity of the controlled plant $S_2(s) = 1/(1 + L_1(s))$ including all bounds of the disturbance.

were provided in (10), (11) and (12) respectively. With the zero defined as

$$s = -\frac{(a+b)\,K_{\alpha 2}}{amv_x} \tag{30}$$

the controller is defined by

$$C_1(s) = \frac{1}{k_{n,\frac{r_z}{\delta}}} \frac{1}{\frac{amv_x}{(a+b)K_{\alpha 2nom}}s+1} \frac{\frac{1}{(2\pi f_c)^2}s^2 + \frac{\beta_c}{\pi f_c}s+1}{\frac{1}{(2\pi f_c)^2}s^2 + \frac{\beta_c}{\pi f_c}s+1}. \tag{31}$$

Note the addition of the second order dynamics. These are included to achieve high frequency roll-off. The open loop transfer function from $r_{zref} - r_z$ to r_z becomes

$$L_1(s) = C_1(s)G_n(s) = \frac{1}{\frac{1}{(2\pi f_c)^2}s^2 + \frac{\beta_c}{\pi f_c}s + 1}, \tag{32}$$

where the eigen frequency f_c and dimensionless damping β_c can be chosen freely to achieve the desired open loop transfer function and closed loop sensitivity. The sensitivity function of the nominal controlled plant $S_n(s)$ is shown in Fig. 4. Here, f_c and β_c have been chosen as 10 Hz and 2 respectively, such that the peak in the sensitivity is smaller than $1/w_{iI}(s)$.

3.5 *Performance controller*

Fig. 4 shows that for high frequencies the sensitivity is smaller than the inverse of the uncertainty bound. However, for low frequencies, it surpasses these bounds. This shows the need for a controller that stabilizes the plant for all uncertainties and thus suffices (20). To achieve stability an integral action has be included in the controller such that $S(\omega \to 0) \to 0$. Furthermore, to improve stability at the bandwidth frequency a lead filter is included. Finally, to achieve a 5 Hz bandwidth a gain is included. Due to space considerations, the exact design is omitted here.

4 SIMULATION RESULTS

The performance of the controller is shown using a validated multi-body model of a BMW 318i [10]. The multi-body model contains a full description of all suspension links and also non-linear tire behavior, which implies that the local gradient of the lateral force decreases with larger tire side slip angles. As a reference model, a neutral steered single track vehicle model is chosen. The maneuver shown will be a sine with dwell [6], which is an open loop maneuver. This avoids having to model the driver.

In Fig. 6 the results of the controlled vehicle are compared with that of the vehicle without control. The constant line in the yaw-rate and lateral acceleration plot for the uncontrolled vehicle indicates that it exhibits unstable behavior and has spun. The controlled vehicle does manage to track the reference yaw-rate by reducing the steering wheel angle, δ_{rack}, thereby effectively damping the potential yaw-rate overshoot. Furthermore, when the reference yaw-rate returns to zero, the controller applies a steering action in the opposite direction. This is again done to stabilize the yaw dynamics.

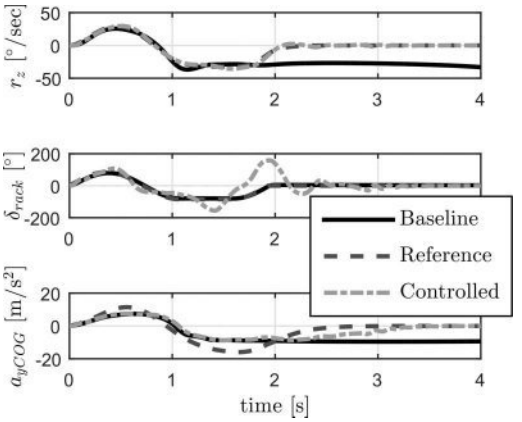


Figure 6. Simulated sine with dwell manoeuvre with yaw-rate, steering angle and lateral acceleration for the vehicle with and without control with a forward velocity of $v_x = 30$ m/s.

5 CONCLUSIONS

The objective of this paper is to provide guidelines on how to design the controller for a steer-by-wire vehicle such that given a certain operating range, the yaw stability of the vehicle is guaranteed. Using inverse modeling of the vehicle's yaw dynamics, the forward velocity dependency is canceled in the controller.

The guidelines are determined using H_∞ analysis with an inverse multiplicative uncertainty. It is shown that at high frequencies, the stability bound is only determined by the ratio between the minimum and nominal gradient of the lateral force. At low frequencies this bound is determined by a multitude of factors, including the forward velocity. To meet the bound at all frequencies, a controller is developed, which requires an integrating action to fulfil the stability requirements at low frequencies.

The performance of the controller with respect to the uncontrolled vehicle is shown using a validated multi-body model of a BMW. An open loop sine with dwell manoeuvre is performed which clearly destabilizes the uncontrolled vehicle. The controlled vehicle tracks the proposed yaw-rate by applying corrective steering.

REFERENCES

J. Ackermann. Robust car steering by yaw rate control. In *Proceedings of the IEEE Conference on Decision and Control*, volume 4, pages 2033–2034, 1990.

J. Ackermann and W. Sienel. Robust yaw damping of cars with front and rear wheel steering. *IEEE Transactions on Control Systems Technology*, 1(1):15–20, 1993.

S. Anand. *Personalizing steering experience using steer-by-wire systems*. PhD thesis, Eindhoven University of Technology, 2014.

C. Beal and J. Gerdes. Model predictive control for vehicle stabilization at the limits of handling. *IEEE Transactions on Control Systems Technology*, 21(4):1258–1269, 2013.

M. Gerard. *Global Chassis Control and Braking Control using Tyre Forces Measurement*. PhD thesis, Technische Universiteit Delft, 2011.

ISO. ISO19365 passenger cars – vehicle dynamic simulation and validation – sine with dwell stability control testing – in development, 2016.

S. Mammar and D. Koenig. Vehicle handling improvement by active steering. *Vehicle System Dynamics*, 38:211–242, 2002.

H. Pacejka. *Tire and Vehicle dynamics (Third Edition)*. Butterworth-Heinemann, 3rd edition, 2012.

S. Skogestad and I. Postlethwaite. *Multivariable Feedback Control: Analysis and Design*. John Wiley & Sons, 2005.

T. Van der Sande. *Control of semi-active active suspension and steer-by-wire for comfort and handling*. PhD thesis, Eindhoven University of Technology, 2015.

T. Van der Sande, I. Besselink, and H. Nijmeijer. Steer-by-wire: A study into the bandwidth and force requirements. In *Proceedings of AVEC12, Seoul, Korea*, 2012.

A. van Zanten. Evolution of electronic control systems for improving vehicle dynamic behavior. In *Proceedings of AVEC 2002*, 2002.

C. Voser, R. Hindiyeh, and J. Gerdes. Analysis and control of high side slip manoeuvers. *Vehicle System Dynamics*, 48:317–336, 2010.

T. Weiskircher and S. Müller. Control performance of a road vehicle with four independent single-wheel electric motors and steer-by-wire system. *Vehicle System Dynamics*, 50:sup1:53–69, 2012.

P. Yih and J. Gerdes. Modification of vehicle handling characteristics via steer-by-wire. *IEEE Transactions on controls sytems technology*, 13(6):965–976, 11 2005.

Advanced Vehicle Control – Edelmann, Plöchl & Pfeffer (Eds)
© 2017 Taylor & Francis Group, London, ISBN 978-1-138-02992-7

Evaluation of handling performance in steer-by-wire vehicle

F. Takagi, T. Shiiba, R. Ishizaki, K. Tamura & H. Hata
Department of Mechanical Engineering, Meiji University, Kanagawa, Japan

ABSTRACT: The purpose of this study is to investigate the steering control method of the Steer-by-Wire system in order to realize a desirable vehicle performance for drivers. A control law for the steering angle and torque that is effective in a high speed lane change is proposed in this paper. Because of the close relationship between the driver and the control system, it is necessary to consider the effect of the control system on drivers to evaluate the validity of the control. In order to evaluate the proposed control method for the Steer-by-Wire system, evaluation tests using a driving simulator were conducted. The relationship between the driver and the control system were evaluated from a view point of the steering angle in the steering correction process and the convergency of the yaw rate. From these test results, it is shown that the proposed control method were effective for the handling performance.

1 INTRODUCTION

A driver controls a car in complex ways according to vehicle speed. It is said that the driver input is mainly steering angle when vehicle speed is slow, and the driver input is mainly steering torque when vehicle speed becomes higher (Mouri et al. 2007). It is necessary to grasp and improve the response of vehicles for each input in order to realize desirable vehicles for drivers. Steer-by-Wire (SbW) systems are currently under development by automotive industries, which offer interesting new approaches in designing driver-steering wheel interactions (Amberkar et al. 2004, Igarashi et al. 2014). SbW systems control steering angle and steering torque independently of the operation of a driver. For that reason, the system is considered effective to improve the handling performance for each input.

In this paper, a steering control method of the SbW system which controls steering angle and steering torque independently was proposed. Evaluation tests using a driving simulator were conducted.

2 CONTROL SYSTEM OF STEER-BY-WIRE

2.1 *Equation of motion including steering system*

In this study, a two wheel vehicle model was used in order to focus on the basic nature of a vehicle motion. The equation of motion of the two wheel vehicle model is represented as follows:

$$mV(r+\dot{\beta}) = 2F_{yf} + 2F_{yr} \tag{1}$$

$$I_z\dot{r} = 2l_fF_{yf} - 2l_rF_{yr} \tag{2}$$

where m is the vehicle mass, V is the vehicle speed, r is the yaw rate, β is the vehicle body slip angle, F_{yf} and F_{yr} are the front and rear lateral force, I_z is the yaw moment of inertia, and l_f and l_r are the length between the center of gravity and front and rear wheel axis.

In addition, a model of the steering system was used in order to consider the properties of the steering system. The equation of motion of the steering system is represented as follows:

$$I_h\ddot{\theta} + C_h\dot{\theta} + \frac{\xi}{N}F_{yf} = T_h \tag{3}$$

where θ is the steering angle, I_h is the moment of inertia of steering system, C_h is the damping coefficient of the steering system, ξ is the trail, N is the steering gear ratio, and T_h is the steering torque.

Equations (1)–(3) are rewritten in the form of the state equations as (4) and (5). The input is the steering angle and the output is the steering torque.

$$\begin{bmatrix} \dot{\beta} \\ \dot{r} \end{bmatrix} = \begin{bmatrix} a_{11} & a_{12} \\ a_{21} & a_{22} \end{bmatrix} \begin{bmatrix} \beta \\ r \end{bmatrix} + \begin{bmatrix} b_{11} & 0 & 0 \\ b_{21} & 0 & 0 \end{bmatrix} \begin{bmatrix} \theta \\ \dot{\theta} \\ \ddot{\theta} \end{bmatrix} \tag{4}$$

$$\begin{bmatrix} T_h \end{bmatrix} = \begin{bmatrix} c_{11} & c_{12} \end{bmatrix} \begin{bmatrix} \beta \\ r \end{bmatrix} + \begin{bmatrix} d_{11} & d_{12} & d_{13} \end{bmatrix} \begin{bmatrix} \theta \\ \dot{\theta} \\ \ddot{\theta} \end{bmatrix} \tag{5}$$

where a_{11}–d_{13} are represented as follows.

$$a_{11} = \frac{-2(C_f + C_r)}{mV} \tag{6}$$

$$a_{12} = -1 - \frac{2(l_fC_f - l_rC_r)}{mV^2} \tag{7}$$

Table 1. Vehicle dimensions.

Vehicle mass m	1200 [kg]
Front cornering power C_f	40000 [N/deg]
Rear cornering power C_r	38000 [N/deg]
Length between mass center and front wheel axis l_f	1040 [mm]
Length between mass center and rear wheel axis l_r	1560 [mm]
Trail ξ	10 [mm]
Yaw moment of inertia I_z	1500 [kgm^2]
Moment of inertia of steering system I_h	0.01 [kgm^2]
Attenuation coefficient of steering system C_h	0.4 [Nms/deg]
Steering gear ratio N	10

$$a_{21} = \frac{-2(l_f C_f - l_r C_r)}{I_z} \tag{8}$$

$$a_{22} = \frac{-2(l_f^2 C_f - l_r^2 C_r)}{I_z V} \tag{9}$$

$$b_{11} = \frac{2C_f}{mVN} \tag{10}$$

$$b_{21} = \frac{2l_f C_f}{I_z N} \tag{11}$$

$$c_{11} = -\frac{\xi C_f}{N} \tag{12}$$

$$c_{12} = -\frac{\xi C_f l_f}{NV} \tag{13}$$

$$d_{11} = \frac{\xi C_f}{N^2} \tag{14}$$

$$d_{12} = C_h \tag{15}$$

$$d_{13} = I_h \tag{16}$$

Furthermore, the dimensions of the vehicle considered in this study are shown in Table 1.

2.2 *Control law of steering angle*

The series of the process of the turning motion of a vehicle causes a delay of the response of the lateral acceleration. Especially, a delay of the lateral acceleration is increased as vehicle speed becomes higher. It is considered that decreasing the phase delay of the lateral acceleration leads to the improvement in response of the vehicle, which yields better handling performance (Sano et al. 1980, Doi et al. 1991).

In this study, the phase delay of the lateral acceleration was reduced by using a feedforward controller which advances the phase of the steer angle to the operation of the driver. This is depicted schematically in Figure 1. $H(s)$ is the transfer function from the steering angle to the yaw rate and $G(s)$ is the controller. $G(s)$ is represented as (17).

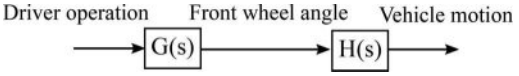


Figure 1. Control of steering angle.

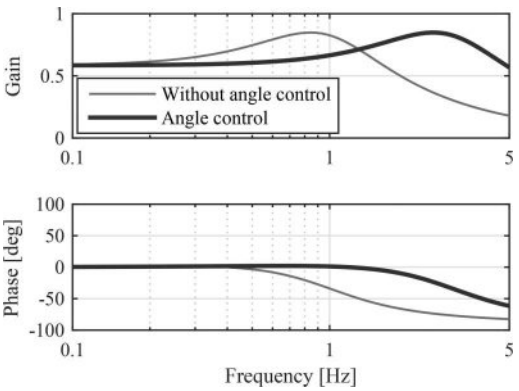


Figure 2. Frequency response of yaw rate to steering angle.

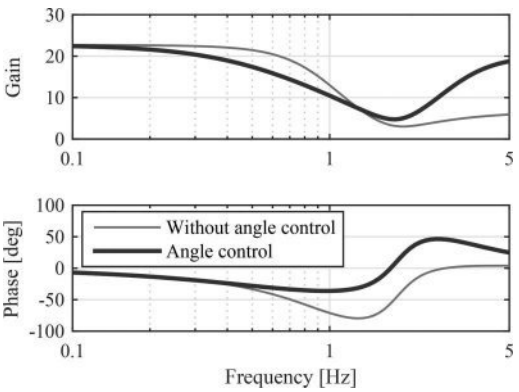


Figure 3. Frequency response of lateral acceleration to steering angle.

$$G(s) = \frac{H(s * \frac{1}{\alpha_a})}{H(s)} \tag{17}$$

The resonance frequency of the yaw rate was multiplied by α_a. Figure 2 shows the frequency response of the yaw rate to the steering angle. α_a was set to 3.0. The vehicle speed was 140 km/h. Figure 3 shows the frequency response of the lateral acceleration to the angle of the steering wheel. As can be seen from Figure 3, the phase delay of the lateral acceleration is reduced. Figure 4 shows the relationship between the operation of a driver and the steer angle. As can be seen from Figure 4, the steer angle is quicker than the operation of the driver.

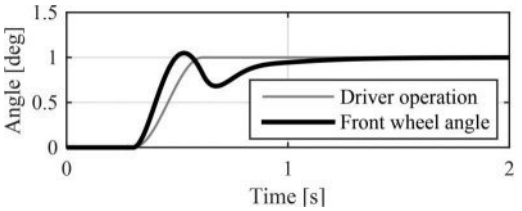


Figure 4. Relationship betweeen driver operation and steer angle.

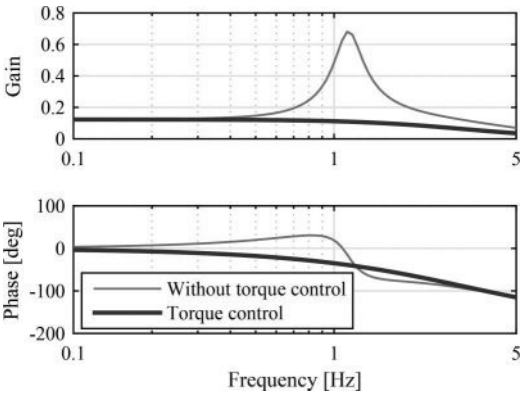


Figure 5. Frequency response of steering angle to steering torque.

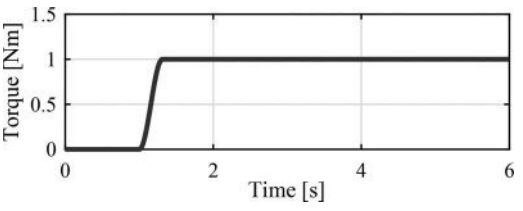


Figure 6. Input torque.

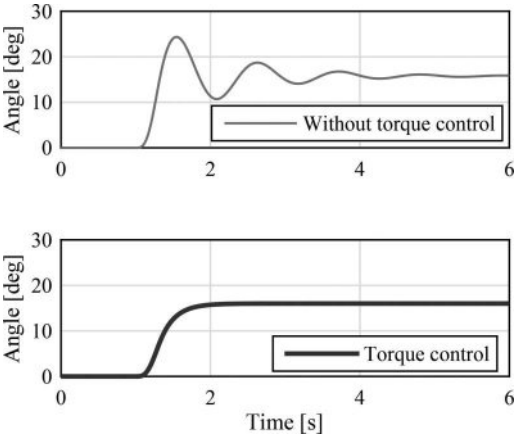


Figure 7. Stability of steering angle.

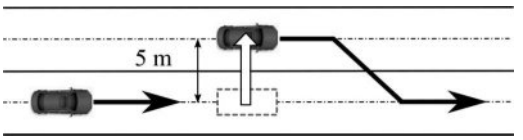


Figure 8. Lane change test.

2.3 *Control law of steering torque*

The damping of the vehicle decreases as vehicle speed becomes higher, which causes the instability of the vehicle. The loss of the damping is caused by the coupling term between the vehicle system and the steering system. Therefore, eliminating the relationship between the vehicle system and the steering system leads to an increase in the damping of the vehicle.

The factor c_{11} and c_{12} in (5) were the coupling terms between the vehicle system and the steering system. Regarding the control law of the steering torque, the steering torque represented as (18) was considered for the SbW system.

$$T_h = d_{13}\ddot{\theta} + d_{12}\dot{\theta} + d_{11} \tag{18}$$

Figure 5 shows the frequency response of the steering angle to the steering torque. The vehicle speed was 140 km/h. As can be seen from Figure 5, the damping of the vehicle was improved by the proposed control method.

In order to evaluate the stability of the vehicle with the steering torque control, the steering torque was input as shown in Figure 6. The vehicle speed was 140 km/h. As can be seen from Figure 7, the steering torque control improved the damping of the vehicle.

3 LANE CHANGE TEST

3.1 *Configuration of lane change test*

An evaluation test was conducted with a driving simulator. The effect of the proposed control method was examined with four kinds of vehicle model: a vehicle without any control, a vehicle with the steering angle control, a vehicle with the steering torque control, and a vehicle with both control. The setting of the test course is shown in Figure 8. In this course, a driver was told to maintain the right side traffic lane. In order to evaluate the behavior of the driver and the vehicle according to a disturbance, the lateral position of the vehicle was suddenly changed to the left side traffic lane, and the driver operated the vehicle to return to the right side traffic lane. The vehicle velocity was set to 140 km/h. The number of the test subjects was three.

3.2 *Result of lane change test and evaluation*

Figure 9 shows an example of the test result by driver A. In this study, two indices were used for the evaluation. The first index was the peak value in the steering

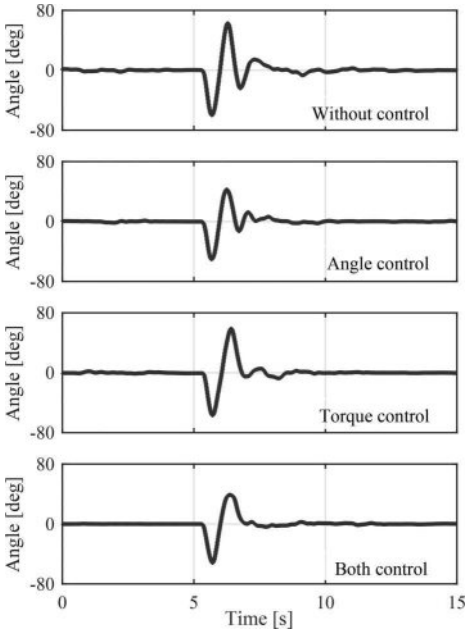


Figure 9. Results of lane change test.

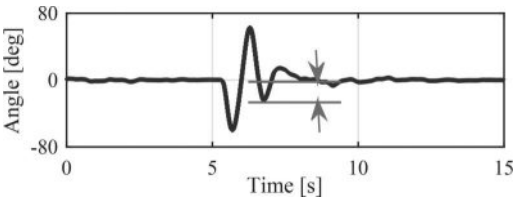


Figure 10. Peak value in steering correction process.

correction process as shown in Figure 10. The second index was an integrated value of the yaw angular acceleration which was calculated from the measured yaw rate between 6 and 10 seconds as shown in Figure 11. This index was applied to evaluate the convergency of the yaw rate.

Figure 12 and Figure 13 show the average value of the two indices for five-time trials. As can be seen from Figure 12, the vehicle with the steering angle control tended to make the peak value in the steering correction process smaller than the steering torque control. As indicated in Figure 13, the vehicle with the both control tend to make the performance index of convergency small. From these results, the combination of the steering angle control and the steering torque control were effective for the improvement of the handling performance in this situation.

4 CROSS WIND TEST

4.1 *Configuration of cross wind test*

In this test, the behavior of the vehicle which is affected by cross wind was evaluated, in order to grasp the

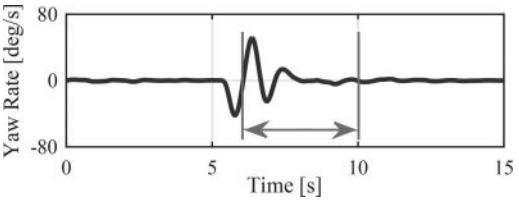


Figure 11. Convergency of yaw rate.

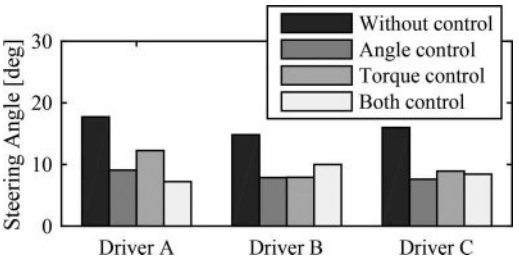


Figure 12. Average of peak value.

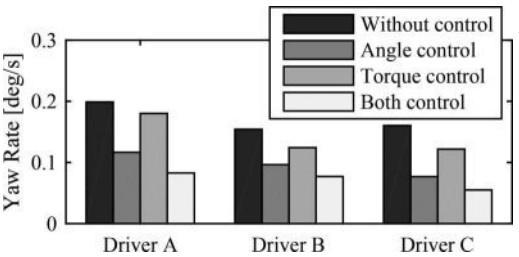


Figure 13. Convergency of yaw rate.

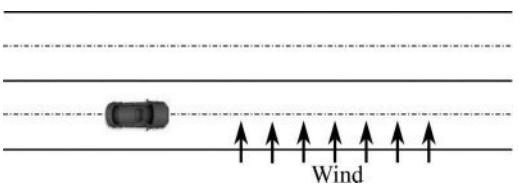


Figure 14. Cross wind test.

relationship between a driver and a vehicle behavior (Takeda et al. 2014). Figure 14 shows the setting of the test course. The vehicle was subjected to a gust of wind from the right side at 5 seconds. The wind speed was 15 m/s. The kinds of vehicle model and test subjects were same as the lane change test.

4.2 *Result of cross wind test and evaluation*

Figure 15 shows an example of the test result by driver A. In this test, the index for the evaluation was the first peak of the steering angle after cross wind was given as shown in Figure 16. Figure 17 shows the average value of the index for five-time trials. It can be seen that the first peak became large in the vehicle with the torque control. It is because the driver in the vehicle

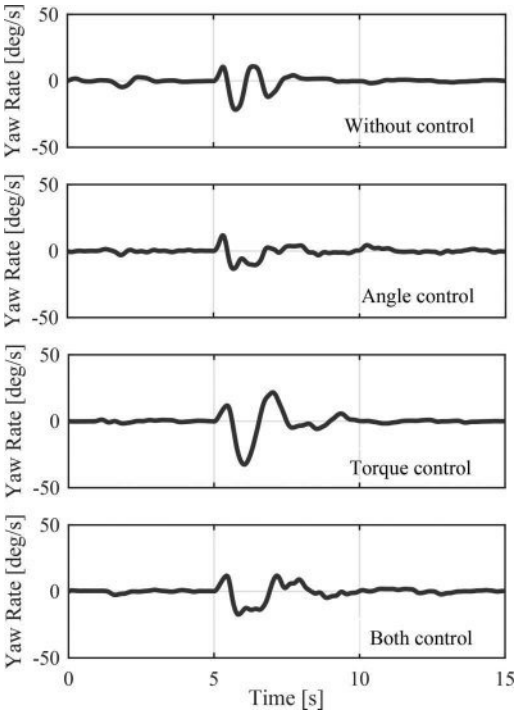


Figure 15. Results of cross wind test.

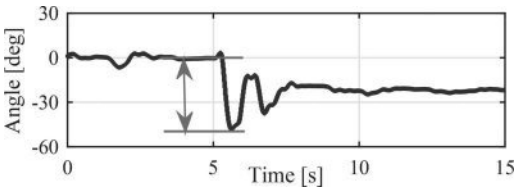


Figure 16. Index for evaluation of cross wind test.

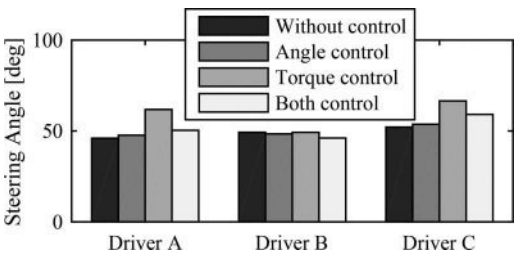


Figure 17. Average of first peak value.

with the torque control cannot recognize the effect of the cross wind by steering torque information as shown in Figure 18. As a result, the steering maneuver was delayed.

In order to inform a driver of disturbances by steering torque, the modified steering torque control was investigated, in which the steering torque is

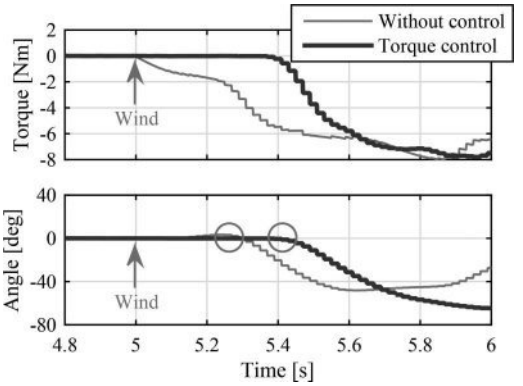


Figure 18. Comparison between vehicle without control and vehicle with torque control.

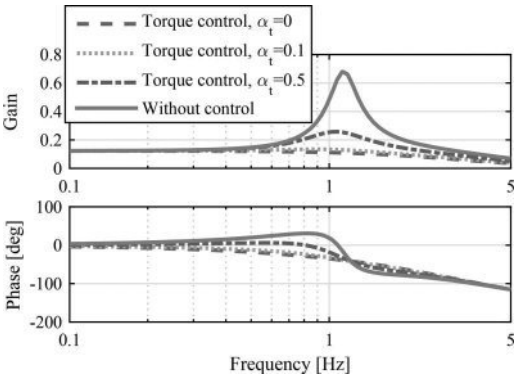


Figure 19. Difference due to strength of coupling.

represented as (19). The strength of the coupling was changed by α_t which was set to 0, 0.1 and 0.5.

$$[\ T_h\ ] = \alpha_t [\ c_{11}\ \ c_{12}\ ][\ \beta\ \ r\ ]^T + [\ d_{11}\ \ d_{12}\ \ d_{13}\ ]\left[\ \theta\ \ \dot{\theta}\ \ \ddot{\theta}\ \right]^T \quad (19)$$

Figure 19 shows the frequency response of the steering angle to the steering torque. Even in the case that α_t is 0.5, the damping of the vehicle is improved.

The evaluation test was conducted with the modified control method of the steering torque. The setting of the test course was same as Chapter 4.1. Figure 20 shows the average value of the index for five-time trials. As can be seen from this figure, in the case that α_t was 0.5, the peak value was minimized.

The lane change test was conducted again in order to investigate the validity of the modified control method of the steering torque. The setting of the test course and the index for the evaluation were same as Chapter 3.1. The effect of the proposed control method was examined with four kinds of vehicle model: a vehicle without any control, a vehicle with the steering angle control, a vehicle with the steering torque control, and a vehicle with both control. In this test, α_t was set to 0.5.

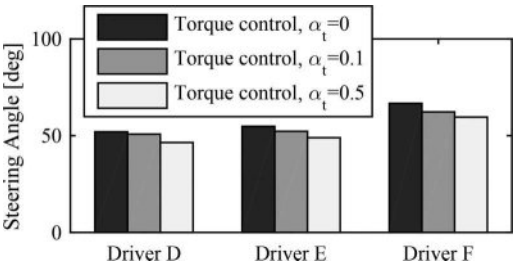


Figure 20. Average of first peak value.

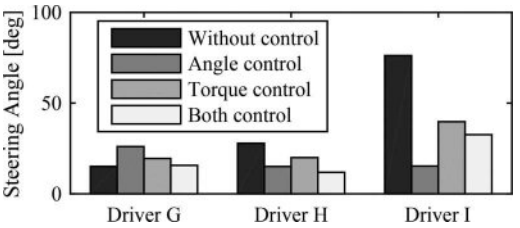


Figure 21. Peak value in steering correction process.

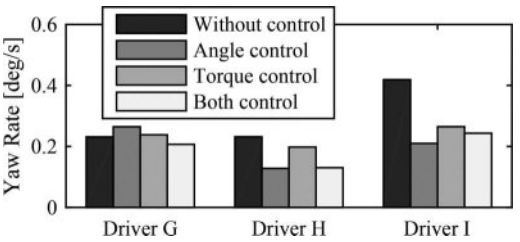


Figure 22. Convergency of yaw rate.

Figure 21 and Figure 22 show the average value of the two indices for five-time trials. The results in Figure 21 and Figure 22 indicate that the steering torque control make the value of the two indices small. It was shown that the combination of the steering angle control and the steering torque control were effective for the improvement of the handling performance.

5 CONCLUSION

In this study, the control laws of the steering angle and the steering torque for the Steer-by-Wire system were investigated. A control law for the steering angle and torque that is effective in a high speed lane change is proposed. Regarding the control law of the steering angle, the phase delay of the lateral acceleration was reduced by using a feedforward controller which advances the phase of the steer angle to the operation of the driver. Regarding the control law of the steering torque, the damping of the vehicle was improved by eliminating the relationship between the vehicle system and the steering system. In order to evaluate the effect of the proposed control method, evaluation tests with the driving simulator was conducted.

The result of the cross wind test revealed that the driver cannot recognize the effect of the cross wind by steering torque information. In order to solve this problem, the strength of the coupling between the vehicle system and the steering system was changed. From the test result, the modified control law of the steering torque in the case that α_t was set to 0.5 was effective for the improvement of the driver operation. In order to evaluate this proposed control method, the lane change test was conducted. From the test results, it was shown that the modified method was effective for the improvement of the handling performance.

REFERENCES

Amberkar, S. et al. (2004, 8). A control system methodology for steer by wire systems. In *2004 SAE World Congress*, Detroit, Michigan, pp. 39–64.

Doi, S. et al. (1991, 2). Vibration and motion control of vehicle by active suspension and steering systems. In *Transactions of the japan society of mechanical engineers series c*, Japan, pp. 606–613.

Igarashi, K. et al. (2014, 5). Development of control algorithm for a steering system capable of controlling tire angles and steering force independently. In *JSAE Annual Congress (Spring)*, Number 36–14, Japan, pp. 15–18.

Mouri, H. et al. (2007). A study on effects of transient steering efforts characteristics on driver's steering behavior. In *SAE Paper, Society od Automotive Engineers*, Number 2007-01-0823, America.

Sano, S. et al. (1980). Influence of vehicle response parameters on drivers control performance. In *FISITA 18th International Congress*, Hamburg.

Takeda, Y. et al. (2014). Independent control of steering force and wheel angles to improve straight line stability. In *JSAE Annual Congress (Spring)*, Number 36–14, Japan, pp. 19–22.

Advanced Vehicle Control – Edelmann, Plöchl & Pfeffer (Eds)
© 2017 Taylor & Francis Group, London, ISBN 978-1-138-02992-7

Fault detection scheme for a road vehicle with four independent single-wheel electric motors and steer-by-wire system

Bruno dos Santos, António Lopes & Rui Esteves Araújo
INESC TEC, Faculty of Engineering, University of Porto, Portugal

ABSTRACT: Unknown input observers (UIO) can be used in the model-based fault diagnosis (FD) system to reduce or eliminate the effect of unknown disturbances present on the process and used to create a set of residuals that are decoupled and sensitive to faults. In this work, a new FD scheme of the In-Wheel motors electric vehicle (IWM-EV) with active front steering was carried out, as well as the design of the fault isolation banks of UIOs. These banks are used to generate residuals that are robust againts to noise and are sensitive to only one fault. This way the faults in the steering or in-wheel actuator are detected and isolated with a higher rate of accuracy. The proposed FD scheme is verified by Carsim® and Matlab/Simulink® cosimulation.

1 INTRODUCTION

The road map on road transport published by ERTRAC, EPOSS and SMARTGRIDS in 2010 had the expectation that the adaptation of conventional vehicles to electric power train was the first milestone (Ertrac, EPoSS, & SmartGrids 2012). At the present stage, most compact electric vehicle (EV) are based on today's drive train platforms with one central electric motor. However the potential of novel power drive concepts is not completely achieved with these first generation vehicles. Multiple electric motors mounted close to the wheels or even in the wheel opens the development of new compact vehicle drive train architectures.

System redundancy could be explored in order to achieve high safety and robustness requirements. The redundancy available in multi-motor electric vehicles should be exploited, in the event of an actuator failure, to redistribute the control effort among the remaining working actuators such that stability is retained and recover to a safe state. Also (Zhang, Cocquempot, Jiang, & Yang 2013) and (Rongrong & Junmin 2011) points the importance of using fault detection and identification (FDI) scheme with fault tolerant control (FTC) systems in order to actively reconfigure the system in order to mitigate the faults effects. Several works have been presented related to the detection of fault in electric vehicles. In (Ho & Ossmann 2014) it is used structured residuals in order to detect and isolate fault in sensors and actuators. In this work the linear track-model with side slip state is extended to the new type of powertrain is used.

In this work, we are concerned with the fault diagnosis system for an IWM-EV with active front steering. The selected powertrain is equipped with four independent electric drives, which can individually generate traction and braking forces at the tires. The steering system is assumed to be a steer-by-wire (SBW) system which is able to control the front wheel steering angle independently of the drivers input with the steering wheel. Due to the high complexity associated with this new class of powertrains, the probability of malfunctions in components (sensors, actuators) is increasing. In this context, it is crucial to develop new algorithms for FD of vehicle components and increasing vehicle safety using fault diagnosis systems.

The main objective of this work is to present a new FD for the vehicle motion controller. To this aim, we propose a structure based on three processing blocks (see figure 1). The first processing block is related to wheel fault detection: a wheel force observer was employed to estimate the difference between the expected forces and the ones applied in the vehicle. In the second block, we employ the inverse model of the yaw rate in order to reconstruct the steering input. For that we use an observer to estimate the lateral velocity of the vehicle. The last block is composed by a set of bank of observers based on the vehicle dynamics in the yaw rate and longitudinal velocity.

The paper is organized as follows. In section 2 the vehicle model is presented. The fault detection scheme and some details are presented in section 3. In section 4 the supervision algorithm, that isolates the fault based on the residual is explained. The FD simulation is presented in section 5 with some discussion about the results. In the final section some conclusions and insights for the future work are discussed.

2 VEHICLE MODEL

In this section the vehicle model used in order to design the FDI scheme is explained bellow. The rotational

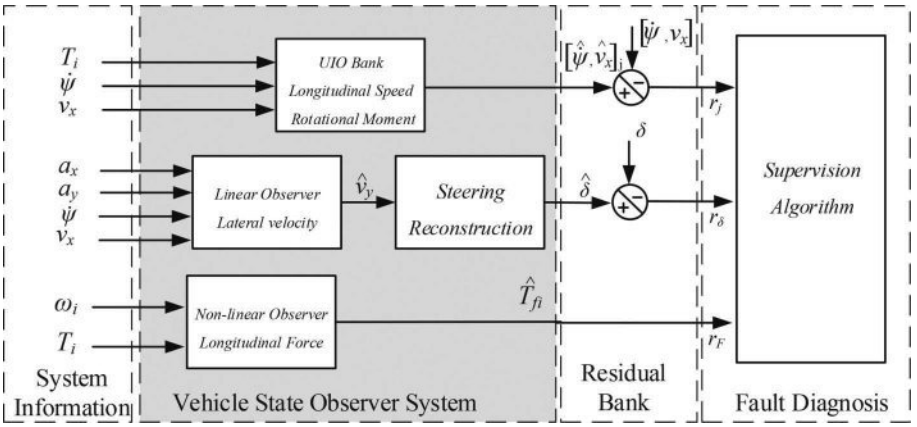


Figure 1. Diagram of the fault diagnosis algorithm developed.

dynamic of the wheel is presented as (Savaresi & Tanelli 2010):

$$I_w\dot{\omega}_i = -R\cdot(F_{xi}+F_{ri})+T_i \qquad (1)$$
$$i\in\{FL,FR,RL,RR\}$$

where T_i are the torque inputs applied in each individual wheel and I_w is the wheel moment of inertia and R is the wheel radius. The F_{ri} is the wheel rolling forces. Finally, the forces F_{xi} arise from the tire/road interaction. The linear force is represented by the following model:

$$F_{xi} = N_i\left(\frac{R\omega_i - v_{\omega i}}{v_{\omega i}}\right) \qquad (2)$$

where N_i is the longitudinal stiffness coefficient, v_{ω_i} and ω_i are the linear and angular wheel speed, for $i\in\{FL,FR,RL,RR\}$.

The total lateral force F_y of the system is expressed by (3) and it is assumed that there is no difference between the lateral forces applied in the left and right tires.

$$F_y = 2F_{yf}+2F_{yr} \qquad (3)$$

where F_{yf} and F_{yr} represents the lateral force present in the front and rear wheels respectively. In the present formulation it will be considered that the lateral forces are defined as a linear model expressed by:

$$F_{yf} = C_f\left(\delta - \frac{v_y + l_r\dot{\psi}}{v_x}\right),\quad F_{yr} = C_r\left(\frac{l_f\dot{\psi}-v_y}{v_x}\right) \qquad (4)$$

The vehicle motion can be expressed by the Newton–Euler equations which describes the lateral and longitudinal dynamics of the CoG of a rigid body (Jazar 2008). The presented planar model is based on the rotational, and translational motion of the vehicle, neglecting the vertical dynamic of the suspension system. The proposed model is based on the two-track vehicle model and is defined as:

$$\begin{cases} \dot{v}_x &= v_y\dot{\psi}+\frac{1}{m}\left(\sum(F_{xi}+F_{ri})+F_{wind}\right)\\ \dot{v}_y &= -v_x\dot{\psi}+\frac{F_{yf}+F_{yr}}{m}\\ I_z\ddot{\psi} &= l_fF_{yf}-l_rF_{yr}\\ &\quad +0.5\cdot l_s\left(F_{xFL}+F_{xRL}-F_{xFR}-F_{xRR}\right)\end{cases} \qquad (5)$$

The constant of l_f, l_r and l_s express the distance of the front and rear axis to the center of gravity of the system and the distance between the wheels of the vehicle. The vehicle mass is symbolized by m and the rotational moment of inertia of the vehicle is defined as I_z. The state variables of the system are the longitudinal and lateral velocity of the vehicle, v_x and v_y respectively, and the yaw rate $\dot{\psi}$. The force F_{wind} is the aero-drag force. Also the longitudinal wheel force F_{xi} is the one defined in (2).

The nonlinear system is linearised around the equilibrium point $\mathbf{x}_0 = [V\ 0\ 0]^T$. Also the wheel angular acceleration is $\dot{\omega}_i = 0$ and the rolling forces are omitted. In this conditions the fault free linear system is obtained:

$$\begin{cases}\dot{\mathbf{x}} = A\,\mathbf{x}+B\,\mathbf{u}\\ \mathbf{y} = C\,\mathbf{x}\end{cases} \qquad (6)$$

where:

$$\mathbf{x}=\begin{bmatrix}v_x\\ v_y\\ \dot{\psi}\end{bmatrix},\quad \mathbf{y}=\begin{bmatrix}v_x\\ \dot{\psi}\end{bmatrix},\quad \mathbf{u}=\begin{bmatrix}F_{xl}\\ F_{xr}\\ \delta\end{bmatrix},$$

$$A=\begin{bmatrix}-2K_wV & 0 & 0\\ 0 & \frac{-2(C_f+C_r)}{mV} & \frac{-2(l_fC_f-l_rC_r)-mV^2}{mV}\\ 0 & \frac{-2(l_fC_f-l_rC_r)}{I_zV} & \frac{-2(l_f^2C_f+l_r^2C_r)}{I_zV}\end{bmatrix},$$

$$B=\begin{bmatrix}\frac{1}{m} & \frac{1}{m} & 0\\ 0 & 0 & \frac{2C_f}{m}\\ \frac{l_s}{2I_z} & \frac{-l_s}{2I_z} & \frac{2(l_f+l_r)C_f}{I_z}\end{bmatrix},\ C=\begin{bmatrix}1 & 0 & 0\\ 0 & 0 & 1\end{bmatrix}.$$

2.1 *Fault model*

Actuators faults can be represented as additive faults (Isermann 2006). When a fault occurs, the control input variable presents a faulty component which is modelled by the equation (7). In this situation, the fault free model control input $\mathbf{u}$ is now defined by $\mathbf{u}_f$ which is the new control variable when the faults are considered. In this conditions, it is considered the fault presents in each individual wheel actuator (f_{FL}, f_{FR}, f_{RL}, f_{RR}) and in the steering wheel (f_δ) in the fault vector $\mathbf{f}$. The steering fault is exclusive to the front axes. Faults on the left and right wheel cannot be isolated using only the linear model. The isolation between front and rear wheel is made by the wheel force observer.

$$\mathbf{u}_f = \mathbf{u}\left(I_3 - \begin{bmatrix} 1 & 0 & 1 & 0 & 0 \\ 0 & 1 & 0 & 1 & 0 \\ 0 & 0 & 0 & 0 & 1 \end{bmatrix}\mathbf{f}\right) \tag{7}$$

$$\mathbf{f} = \begin{bmatrix} f_{FL} & f_{FR} & f_{RL} & f_{RR} & f_\delta \end{bmatrix}^T$$

3 FAULT DIAGNOSIS STRUCTURE

The proposed fault detection and diagnosis scheme is presented in figure 1. This solution is composed by three main elements: the system observers, defined by multiple unknown input observers that estimate the fault free state, the residual bank, where the observed variables are compared with the actual system information, and the fault diagnosis algorithm. The system information is obtained by means of sensor measurements provided by Inertial Measurement Unit (IMU) sensors as well as the expected actuator inputs provided by the control system.

3.1 *Wheel force observer*

In order to reconstruct the longitudinal force in each individual wheel, it is proposed a wheel force observer based on sliding mode techniques. The following observer is defined for each wheel $i \in \{FL, FR, RL, RR\}$ and is based on the rotational dynamic presented in (1):

$$\dot{\hat{\omega}}_i = b_i\, T_i - \frac{R\hat{F}_{xi}}{I_\omega} + l_i\, e_i + v_i, \tag{8}$$

where $b_i = 1/I_w$, l_i is the linear observer gain, $\hat{F}_{xi}$ is the linear force estimation using equation (2) and v_i is the following discontinuous term:

$$v_i = (\rho_i + \rho_{0i})\ sign(e_i) \tag{9}$$

Let's assume a quadratic Lyapunov function, $V_i = e_i^2/2$, where $e_i = \omega_i - \hat{\omega}_i$. The derivative of the proposed function would be defined as:

$$\dot{V} = -l_i\, e_i^2 + e_i\left(\frac{-R\,F_{xi} + T_{fi}}{I_w} + \frac{R\hat{F}_{xi}}{I_\omega} - v_i\right) \tag{10}$$

Considering v_i as (9) and assuming $|\rho_{0i}| > R\,|F_{xi} - \hat{F}_{xi}|^{max} + T_{fi}/I_w$, where T_{fi} is the faulty component of $\mathbf{T_i}$. The result (10) is reduced to:

$$\dot{V} \leq -l_i e_i^2 - \rho_i ||e_i|| < 0 \tag{11}$$

Ensuring asymptotic stability for the proposed observer.

In order to estimate the wheel fault, it is first assumed that both the error and his derivative are zero. With these assumptions the error expression (with $\rho_i \gg l_i$ and $F_{xi} - \hat{F}_{xi} \approx 0$) is:

$$\dot{e}_i = 0 \Leftrightarrow \frac{R\,F_{xi} - T_{fi}}{I_w} = \frac{R\,\hat{F}_{xi}}{I_w} - l_i e_i - v_i \Leftrightarrow$$

$$\hat{T}_{fi} \approx I_\omega v_i.$$

3.2 *Steering reconstruction*

The proposed steering reconstruction is based on the yaw rate model defined previously in (5) where the lateral forces are modelled by (4).

Almost all the variable are available. In order to simplify the calculation the yaw-rate derivative is set to be close zero $\dot{\psi} \approx 0$. Nonetheless, it is assumed that the information of the lateral velocity is not available for measurement, which hinders the estimation of the steering variable. In order to overcome this difficulty, a linear observer is designed in order to closely track the lateral velocity of the system.

The state space system of the longitudinal/lateral motion is used from the system of equation (6), the observer can be defined as:

$$\begin{cases} \begin{bmatrix} \dot{\hat{v}}_x \\ \dot{\hat{v}}_y \end{bmatrix} = \begin{bmatrix} 0 & \dot{\psi} \\ -\dot{\psi} & 0 \end{bmatrix}\begin{bmatrix} \hat{v}_x \\ \hat{v}_y \end{bmatrix} + \begin{bmatrix} a_x \\ a_y \end{bmatrix} + L\mathbf{e}_y \\ \hat{\mathbf{y}} = \begin{bmatrix} 1 & 0 \end{bmatrix}\begin{bmatrix} \hat{v}_x \\ \hat{v}_y \end{bmatrix} \end{cases} \tag{12}$$

where the longitudinal/lateral wheel forces are replaced by the acceleration measured by the sensors. The observer gain matrix is represented by L which is defined so that the resulting observer error $\mathbf{e}_y = (\hat{\mathbf{y}} - \mathbf{y}) \to 0$ when $t \to \infty$. The observation stability is obtained by defining the following gain matrix (for more information refer to (Ungoren, Peng, & Tseng 2002)):

$$L = \begin{bmatrix} 2a|\dot{\psi}| & (a^2 - 1)\,\dot{\psi} \end{bmatrix}^T \tag{13}$$

where a is a positive scalar. However, the system observability presented in (12) is lost when the yaw rate variable becomes zero, in order to overcame this shortage, the fault detection is only valid for $\dot{\psi} \neq 0$.

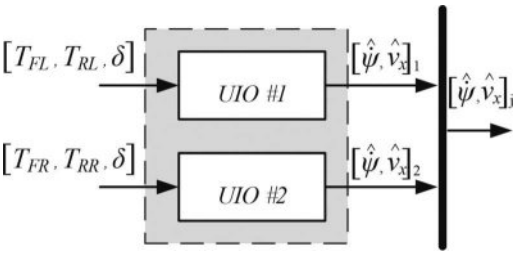


Figure 2. UIO bank observer.

3.3 *UIO bank with fault isolation*

The structure of the UIO bank is presented in the figure 2. As already mentioned, the measurements obtained from the sensors are fault free and the fault detection scheme is defined for actuators faults only. The UIO bank consists of two different observers (figure 2) that aim to decouple actuators faults obtaining a clear estimation that will dissociate the system faults (Chen & Patton 1999). The model for each UIO is based on the linear model defined in equation (6). The control input is replaced by the fault model presented in equation (7). The resulting system is described by:

$$\begin{cases} \dot{\mathbf{x}}_j = A\mathbf{x}_j + B_j\mathbf{u}_j + D_j\mathbf{d}_j + B_{fj}\mathbf{f}_j \\ \mathbf{y}_j = C\mathbf{x}_j \end{cases} \tag{14}$$

where $B_j \in \Re^{n\times(m-1)}$ is the system input matrix B, without the column regarding the unknown input j; $b_j \in \Re^{n\times 1}$ refers to the column of the matrix B that was isolated from B_j; $D_j = [b_j]$ is the new perturbation distribution matrix. The fault distribution $B_{fj} \in \Re^{n\times(m-1)}$ is equal to B_j.

The UIO observer based on residual generation that detect and isolate faults has a structure as described in the following system of expressions:

$$\begin{cases} \dot{\mathbf{z}}_j = & F_j\mathbf{z}_j + T_jB_j\mathbf{u}_j + K_j\mathbf{y} \\ \hat{\mathbf{x}}_j = & \mathbf{z}_j + H_j\mathbf{y} \\ \hat{\mathbf{y}}_j = & C\hat{\mathbf{x}}_j \\ \mathbf{r}_j = & V_j(\mathbf{y} - \hat{\mathbf{y}}_j) \end{cases}, \quad \text{for } j \in \{1,2\} \tag{15}$$

where $\hat{\mathbf{x}}_j \in \Re^n$ corresponds to the estimated state vectors and $\mathbf{z}_j \in \Re^n$ corresponds to the observer state and $F_j \in \Re^{n\times n}$, $T_j \in \Re^{n\times n}$, $K_j \in \Re^{n\times p}$, $H_j, \in \Re^{n\times p}$ are the matrix needed to build the observer with unknown input decoupling. The matrix V_j is a gain factor in order to obtain the residual.

The residual for the group of actuator j has only one side of the longitudinal traction as presented in figure 2. If a fault occurs in the group j, The detection logic is as following:

$$\begin{cases} \|r_j\| < & Th_j \\ \|r_b\| > & Th_j \end{cases}, \quad \text{for } b \in \{1,2\}\setminus j \tag{16}$$

where Th_j is the threshold value for each actuator.

UIO design

The state estimation error is defined by: $(\mathbf{e}_j = \mathbf{x}_j - \hat{\mathbf{x}}_j)$, it follows that $\mathbf{e}_j = T_j\mathbf{x}_j - \mathbf{z}_j$, where $T_j = I - H_jC$. Using the equations (15) and (14), the time derivative of the error is given by (For the sake of simplicity, the index j is omitted):

$$\begin{aligned} \dot{\mathbf{e}} \;=\; & F\mathbf{e} + (TB - G)\,\mathbf{u} + (TD)\,\mathbf{d} + \\ & + (TB_f)\mathbf{f} + (TA - KC + FHC - F)\,\mathbf{x} \end{aligned} \tag{17}$$

In order to design the UIO, is necessary to met the following conditions:

$$\text{(C1) } G = TB \text{ (cancel } \mathbf{u}\text{)}; \quad \text{(C2) } TD = 0 \text{ (cancel } \mathbf{d}\text{)}$$

$$\text{(C3) } F = TA - LC \text{ } (F \text{ is "Hurwitz"}); \quad \text{(C4) } K = L - FH$$

$$\text{(C5) } rank(TB_f) = rank(B_f) \quad \text{(C6) } T = I - HC$$

If the conditions are respected the state estimation error becomes $(\dot{\mathbf{e}} = F\mathbf{e} + TB_f\mathbf{f})$ and the residual corresponds to $\mathbf{r} = VC\mathbf{e}$.

In order to cancel the perturbation it is necessary to first check if $rank(CD) = rank(D)$ in order to guarantee a solution for the system $HCD = D$ (from the condition (C2) and (C6)). One generalized solution for H can be expressed by (Darouach, Zasadzinski, & Xu 1994):

$$H = D(CD)^{+} + H_0(I - (CD)(CD)^{+}) \tag{18}$$

where $(X)^{+}$ is the generalized inverse matrix given by $(X)^{+} = ((X)^T(X)^{-1})(X)^T$, since X is full rank. H_0 is an arbitrary matrix of appropriate dimensions. This matrix give some freedom on the design. The eigenvalues of F can be arbitrary located by choosing a suitable matrix L, only if the pair (TA, C) is observable. If this condition can not be applied it is possible to found a K_1 that the observer is asymptotically stable if and only if (TA, C) are detectable.

4 SUPERVISION ALGORITHM

Based on the residuals created, it is possible to isolate and identify faults in the actuators (steering and wheel actuators) using a residual table. The table identifies a possible fault using the several residual signatures.

The response to fault situation in residual r_1 and r_2 can be obtained by using the error expression from equation (15). Taking in account the observation error $\dot{\mathbf{e}} = F\mathbf{e} + TB_f\mathbf{f}$ and the residual $\mathbf{r} = VC\mathbf{e}$ it is possible to predict the residual behaviour for additive fault. The wheel observer gives the fault signature for each individual wheel and the steering reconstruction provides the information of steering alteration.

The detection is obtained by comparing the residuals with appropriate threshold and its sign is also used. The table 1 shows the possible patterns for the residuals.

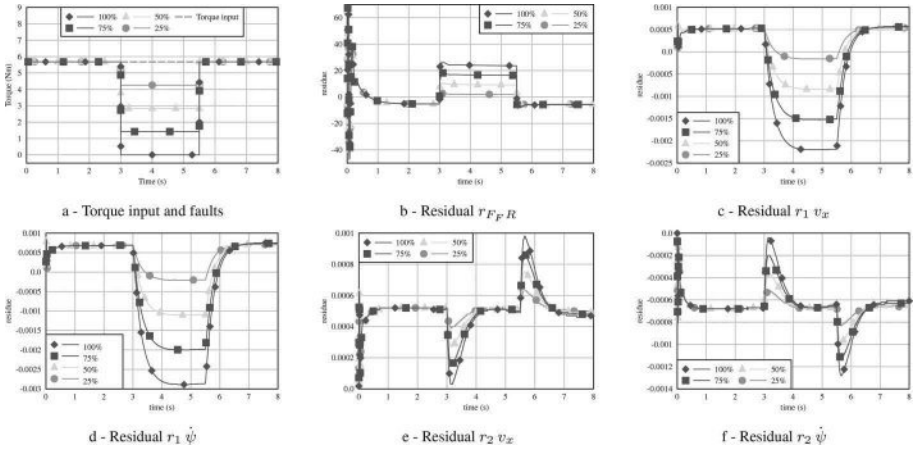


Figure 3. Simulation results for the motor fault test.

Table 1. Residual from the several actuator faults; 0 – residual is insensitive against the respective threshold, + residual is sensitive and positive, – residual is sensitive and negative.

			Faults in actuators				
			f_δ	f_{FL}	f_{FR}	f_{RL}	f_{RR}
Residual Signature	r_1	v_x	–	0	–	0	–
		$\dot{\psi}$	–	0	–	0	+
	r_2	v_x	+	–	0	–	0
		$\dot{\psi}$	–	–	0	+	0
	r_δ		+	0	0	0	0
	r_{F_i}	FL	0	+	0	0	0
		FR	0	0	+	0	0
		RL	0	0	0	+	0
		RR	0	0	0	0	+

Table 2. Vehicle Parameter used in the simulations.

Variable	Symbol	Value
Vehicle mass	m	1100 kg
Yaw inertia	I_z	996 kg m^2
Distance from front axle and COG	l_f	1.2 m
Distance from rear axle and COG	l_r	1.3 m
Track width	l_s	1.5 m
Aerodynamic drag constant	K_w	0.3401
Wheel radius	R	0.3 m
Wheel inertia	I_w	1.1kg m^2
Cornering stiffness front tire	C_f	24500 N/rad
Cornering stiffness rear tire	C_r	26900 N/rad
Longitudinal velocity	V	10 m/s

5 SIMULATION RESULTS

To illustrate the fault detection algorithm scheme performance a computer simulation was carried out. The vehicle model was emulated through the tool Carsim® in co-simulation with Matlab/Simulink® software where the proposed solution was implemented. In order to demonstrate the capacity to detect faults in actuators two fault scenarios are defined: Firstly without steering input ($\delta = 0$) and constant acceleration the fault is injected in the front right wheel actuator. Secondly, a J-turn maneuver with steer fault is considered. In both case the torque in each wheel is constant and set to 5.6 Nm. The vehicle parameters are presented in table 2. In the simulation gaussian white noise ($\sigma^2 = 10^{-5}$) was added to all measured signals. The signals are filtered by a low pass filter.

In the first simulation, an abrupt fault is injected in the front right wheel. The result is presented in figure 3. At $t = 3$ s the torque goes from the initial value to the faulty value. After 2.5 s the wheel torque goes back to the initial value. In this test several fault amplitude have been tested (figure 3.a). The results present a good detection for faults above $f_{FR} = 0.25$. Both residual r_1 and r_2 have an offset in the fault free operation. This phenomenon is due to the observer structure (H_1 matrix) and by the unavoidable modelling errors. In other words, the fault diagnosis algorithm uses models which do not fully agree with the real vehicle due to model uncertainties. The residuals react as specified by their respective signatures. The residual r_1 (figure 3.c and figure 3.d) respond has expected on table 1. The residual r_2 (figure 3.e and figure 3.f) is the one that isolates the left torque faults and is insensitive to the right wheel. However, at the fault instant, a perturbation occurs, due to the abrupt change on the input, which will be ignored by the fault evaluation mechanism as the value goes to zero. From the wheel actuator fault it is possible to see that the residual have the same behaviour has the set in signature table.

In the second scenario, a step fault is injected in the front steering axis. The result are presented in figure 4. At $t = 3$ s the steering goes from the initial value to the faulty value. In this test several fault amplitude have been tested (figure 4.a). The residual can detect, even for small fault values the steering faults. Both residual

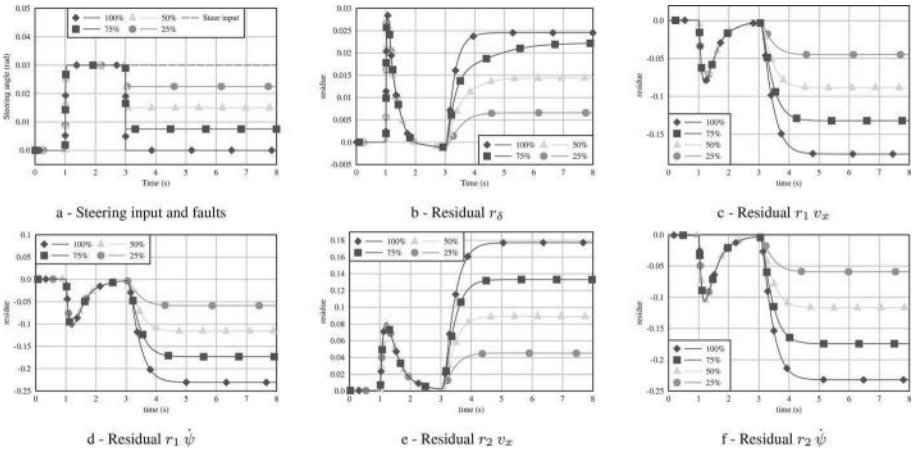


Figure 4. Simulation results for the steer fault test.

r_1 and r_2 (figure 4.(c–f)) have a response in the steering change in the fault free operation. This is due to the yaw rate dynamics of the model. Although, after some time, the false fault signal goes to zero. The residuals react as specified in the table 4 by their respective signatures in the presence of fault. As expected, the residuals response for r_1 and r_2, associated with the steering fault is more significant than the wheel actuator case.

6 CONCLUSION AND FUTURE WORK

In this paper, a scheme for detection and isolation of actuator faults in an over-actuated EV was presented. The proposed approach is based on using UIO for calculating a set of residuals. The algorithm was combined with a vehicle state observer consisting of a nonlinear wheel force observer, a linear observer for lateral velocity estimation with steering reconstruction and a set of UIO for longitudinal speed and yaw rate estimations. The observer designs for linearised system have been considered regarding its application to fault diagnosis algorithm. Existence and convergence conditions for the observers have been established. The proposed technical solution allows to decoupling residuals from unknown inputs while keeping sensitivity to faults. The results obtained are promising and motivates further research on improving the proposed approach. The first step could be conducted to reduce sensitivity to the steering input. The fault detection extension in order to detect fault in sensors is the second step. Also, the use of fault detection scheme in order to reconfigure the control system in case of fault is scheduled as future work.

ACKNOWLEDGEMENT

This work is financed by the ERDF European Regional Development Fund through the Operational Programme for Competitiveness and Internationalisation – COMPETE 2020 Programme within project POCI-01-0145-FEDER-006961, and by National Funds through the Portuguese funding agency, FCT – Fundação para a Ciência e a Tecnologia as part of project UID/EEA/50014/2013 through the scholarship SFRH/BD/90418/2012.

REFERENCES

Chen, J. & R. J. Patton (1999). *Robust model-based fault diagnosis for dynamic systems*. Springer.

Darouach, M., M. Zasadzinski, & S. Xu (1994). Full-order observers for linear systems with unknown inputs. *IEEE Transactions on Automatic Control 39*(3), 606–609.

Ertrac, EPoSS, & SmartGrids (2012). European Roadmap Electrification of Road Transport 2 Edition. Technical Report June, European Road Transport Research Advisory Council.

Ho, L. M. & D. Ossmann (2014). Fault Detection and Isolation of Vehicle Dynamics Sensors and Actuators for an Overactuated X-by-Wire Vehicle. pp. 6560–6566.

Isermann, R. (2006). *Fault-diagnosis systems: An introduction from fault detection to fault tolerance*. Springer.

Jazar, R. N. (2008). *Vehicle Dynamics: Theory and Application*. Springer.

Rongrong, W. & W. Junmin (2011). Fault-tolerant control with active fault diagnosis for four-wheel independently-driven electric ground vehicles. In *American Control Conference (ACC), 2011*, pp. 3954–3959.

Savaresi, S. M. & M. Tanelli (2010). *Active Braking Control Systems Design for Vehicles*. Advances in Industrial Control. Springer London.

Ungoren, a. Y., H. Peng, & H. E. Tseng (2002). Experimental verification of lateral speed estimation methods. *Proceedings of the Advanced Vehicle Control* (2), 361–366.

Zhang, X., V. Cocquempot, B. Jiang, & H. Yang (2013). Active fault diagnosis based on fault-tolerant control with control constraints for an electric 4WD vehicle. *10th IEEE International Conference on Control and Automation*, 1724–1729.

Advanced Vehicle Control – Edelmann, Plöchl & Pfeffer (Eds)
© 2017 Taylor & Francis Group, London, ISBN 978-1-138-02992-7

Study on active safety for aquaplaning assistance

T. Raste
Continental, Frankfurt (Main), Germany

D. Frerichs
Institute of Automatic Control and Mechatronics, Technical University of Darmstadt, Germany

ABSTRACT: Accidents in severe weather arise mainly due to a drastic loss of friction between the tires and the road surface. Aquaplaning situations are extremely dangerous and present a problem for even the most skilled drivers. This paper describes a simulation environment for developing and evaluation of an active safety system for aquaplaning assistance. A simplified, empirically adapted tire model is used to study the principle effects of a vehicle aquaplaning. A control system is designed and used for closed-loop simulations to evaluate the assistance strategy. A number of test cases demonstrate the suitability of the assistance concept and also yield possible starting points for further development.

1 INTRODUCTION

Adverse weather conditions involving reduced traction as a consequence of wet, snowy and icy surfaces have been major contributory factors to traffic accidents in Europe. Extreme weather conditions are responsible for 39% of all accidents in Germany, Ditze et al. (2010).

One of the most dangerous situations is aquaplaning, which is difficult to predict and manage for the driver. The aquaplaning situation depends on both vehicle and tire condition as well as on environmental influences such as water film thickness on the road surface. During aquaplaning steering generally is not possible, because tire adhesion is lost such that both front wheels cannot transfer lateral forces any more.

Today's measures to avoid the risks of aquaplaning are almost exclusively infrastructure-based such as roadway draining and speed limits. The aim of this work is to analyze vehicle dynamics and controllability in aquaplaning situations and sketch an active safety system to assist the driver safely through this dangerous situation.

2 VEHICLE MODEL

2.1 *Nonlinear two-track model*

A two-track planar vehicle model (1.2) described in von Vietinghoff (2008) is used as a basis for the analysis of effects when the vehicle is aquaplaning. For simulation purposes of the overall closed-loop system, the commercial tool IPG CarMaker is used.

$$\sum_k \boldsymbol{F}_k = \sum_k \begin{bmatrix} F_{x,k} \\ F_{y,k} \end{bmatrix} = m\boldsymbol{a} \quad , \tag{1}$$

$$\sum_k \boldsymbol{r}_k \times \boldsymbol{F}_k = J_z \ddot{\psi} \quad . \tag{2}$$

Since the forces from all wheels are modeled separately, the effect of loss of friction on the lateral and yaw motion is directly considered in the model. The chosen approach for the horizontal tire forces is discussed in the next chapter. The vertical forces are approximated from static equilibrium, cf. Orend (2005), leading to functions depending on the longitudinal and lateral vehicle acceleration.

2.2 *Linear single-track model*

For control design, a linear single-track bicycle model is deduced from the two-track model. Due to the aquaplaning behavior the front tire forces are neglected. The left and right lateral tire forces of the rear axle are combined to a single force with linear dependency on the wheel slip angle. The vehicle is controlled by a longitudinal force difference ΔF_x on the rear axle. This control action can be provided by wheel individual braking or torque vectoring. The linear vehicle model is given in state space form by

$$\begin{aligned} \dot{\boldsymbol{x}} &= \boldsymbol{A}\boldsymbol{x} + \boldsymbol{B}\boldsymbol{u} + \boldsymbol{E}\boldsymbol{s} \\ \boldsymbol{y} &= \boldsymbol{C}\boldsymbol{x} + \boldsymbol{D}\boldsymbol{u} + \boldsymbol{G}\boldsymbol{s} \\ \boldsymbol{z} &= \boldsymbol{C}_z\boldsymbol{x} + \boldsymbol{D}_z\boldsymbol{u} + \boldsymbol{G}_z\boldsymbol{s} \end{aligned} \quad , \tag{3}$$

$$\boldsymbol{x} = \begin{bmatrix} \dot{\psi} \\ \beta \end{bmatrix}, \boldsymbol{u} = \Delta F_x, \boldsymbol{y} = \boldsymbol{z} = \dot{\psi}, \boldsymbol{s} = M_z \quad . \tag{4}$$

The state vector **x** contains yaw rate and side slip angle as state variables. Control input **u** is the rear axle longitudinal force difference and system output **y** is the yaw rate. The vector **z** contains the interesting variables

to be controlled, here the yaw rate. The disturbance input **s** is an unknown yaw torque M_z. The system matrices are given by

$$\boldsymbol{A} = \begin{bmatrix} -\frac{l_f^2 C_r}{J_z v} - 1 & \frac{l_r C_r}{J_z} \\ \frac{l_r C_r}{m v^2} & \frac{C_r}{m v} \end{bmatrix}, \boldsymbol{B} = \begin{bmatrix} \frac{b_r}{J_z} \\ 0 \end{bmatrix}, \boldsymbol{C} = [1 \quad 0], \tag{5}$$

$$\boldsymbol{E} = \begin{bmatrix} \frac{1}{J_z} \\ 0 \end{bmatrix}, \boldsymbol{C}_z = [1 \quad 0], \boldsymbol{D} = \boldsymbol{G} = \boldsymbol{D}_z = \boldsymbol{G}_z = 0, \tag{6}$$

with vehicle mass $m = 1564$ kg, moment of inertia $J_z = 2230$ kgm^2, distance from center of gravity to rear axle $l_r = 1.575$ m, rear track width $b_r = 1.582$ m and rear tire cornering stiffness $C_r = 119332$ N/rad. The vehicle speed v is considered to be a slowly varying parameter. Disturbances are modeled as the output of a homogeneous linear system with the disturbance state $\mathbf{x}_s$

$\mathbf{x}_s$

$$\begin{aligned} \dot{\boldsymbol{x}}_s &= \boldsymbol{A}_s \boldsymbol{x}_s \\ \boldsymbol{s} &\approx \boldsymbol{C}_s \boldsymbol{x}_s \end{aligned} . \tag{7}$$

Approximation of the disturbance by a piecewise constant function leads to a simple integrator model with

$$\boldsymbol{A}_s = 0, \boldsymbol{C}_s = 1 \ . \tag{8}$$

3 EXTENDED TIRE MODEL

3.1 *Tire force*

The tires are modeled by two different force magnitude models with isotropic tire properties, meaning that the friction and stiffness are equal in all directions. The first model is used for phase plane analysis purposes based on vehicle model (1.2) and calculates the lateral forces considering the longitudinal force as input directly controlled e.g. by a brake system, Klomp (2010). The parameters are the tire-road friction μ, the vertical force F_z, the wheel slip angle α and a stiffness parameter C_y,

$$F_y = \sqrt{(\mu F_z)^2 - F_x^2} \tanh\left(\frac{C_y}{\mu}\alpha\right) . \tag{9}$$

The second model is used for vehicle simulations with the commercial tool IPG CarMaker and replaces the contained tire model at the front axle. The model considers the combined slip $\boldsymbol{\sigma}$, constituted by the longitudinal slip λ and wheel slip angle α,

$$\boldsymbol{\sigma} = \begin{bmatrix} \sigma_x \\ \sigma_y \end{bmatrix} = \frac{1}{1+\lambda} \begin{bmatrix} \lambda \\ \tan\alpha \end{bmatrix} \ , \tag{10}$$

to calculate both longitudinal and lateral forces,

$$\boldsymbol{F} = \begin{bmatrix} F_x \\ F_y \end{bmatrix} = \mu F_z \sin\left(C \arctan\left(B \frac{\|\sigma\|}{\mu}\right)\right) \frac{1}{\|\sigma\|} \boldsymbol{\sigma} . \tag{11}$$

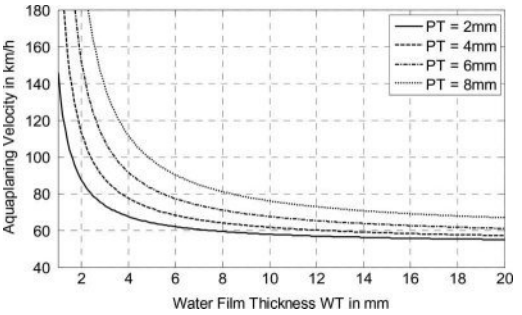


Figure 1. Aquaplaning velocity vs. water film thickness WT for different tread depths PT and a tire width B = 195 mm.

Table 1. Parameter of the aquaplaning velocity model.

$a_{10} = 0.0031875$	$a_{11} = 0.0025$
$a_{20} = -0.011875$	$a_{21} = 0.23$
$a_{30} = -0.0025$	$a_{31} = 0.0075$
$a_{40} = 4.4535$	$a_{41} = -0.9042$

The parameters are chosen as $B = 12.54$ and $C = 1.08$. The inverse of the model (11) will be used for wheel slip control purposes such that a desired slip λ_d based on the longitudinal force control input ΔF_x can be calculated. The model (12) is used to derive the tire slip from predetermined forces, Orend (2005),

$$\boldsymbol{\sigma} = \frac{\mu}{B} \tan\left(\frac{1}{C} \arcsin \frac{\|\boldsymbol{F}\|}{\mu F_z}\right) \frac{1}{\|\boldsymbol{F}\|} \boldsymbol{F} . \tag{12}$$

3.2 *Tire-road friction*

The tire-road friction coefficient μ is not given as an external parameter such as in typical vehicle dynamics and handling simulations. Instead the friction is modeled as a function of the aquaplaning velocity shown in Figure 1.

The aquaplaning velocity is the vehicle speed at which the front tire is lifted from the road due to water pressure. The mathematical model is a nonlinear function of the water film thickness WT, cf. Herrmann (2008),

$$v_{aq} = e^{\left(a_0 + \frac{a_1}{WT}\right)} \ , \tag{13}$$

with the parameter a_0 and a_1 depending on the tread depth PT and tire width B,

$$\begin{aligned} a_0 &= a_{10} PT^2 + a_{20} PT + a_{30} B + a_{40} \\ a_1 &= a_{11} PT^2 + a_{21} PT + a_{31} B + a_{41} \end{aligned} . \tag{14}$$

It is worth to note that in this paper WT, PT and B are assumed as given in mm in the formulas. All other quantities are expected to be in SI units.

The friction value μ is modeled as a nonlinear decreasing function of the vehicle speed v up to a minimum value when the aquaplaning velocity is reached,

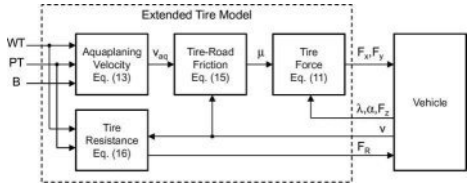


Figure 2. Extended tire model for aquaplaning simulation.

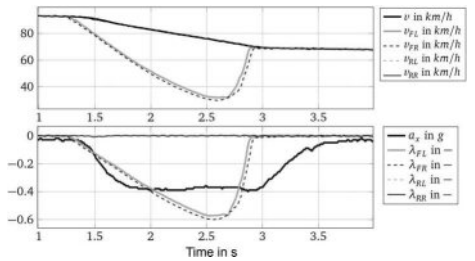


Figure 3. Vehicle test results from a straight drive through a basin with water film thickness WT = 40 mm and neutral gear. Shown are from top to bottom vehicle speed, wheel speed, longitudinal acceleration and wheel slip.

Görich (1993). We consider in the following $\mu_0 = 0.8$ and $\mu_{\min} = 0$.

$$\mu = \begin{cases} -\frac{\mu_{min}+\mu_0}{v_{aq}^2} v^2 + \mu_0, & v < v_{aq} \\ \mu_{min}, & v \geq v_{aq} \end{cases} . \qquad (15)$$

3.3 *Tire resistance*

The water displacement causes a "spin down" tire resistance force F_R, which is higher than typical rolling resistances. The water displacement resistance model is linearly increasing with the water film thickness WT and depends on vehicle speed v and tread depth PT with the parameters $k_1 = 0.79$, $k_2 = -0.1$ and $k_3 = 4.1$, Gengenbach (1967),

$$F_R = (k_1 v + k_2 PT + k_3) WT \quad . \qquad (16)$$

3.4 *Model validation*

Figure 2 shows the structure of the extended tire model used for aquaplaning simulations.

The extended tire model is validated with measurement data from vehicle tests. These tests were conducted with a front driven vehicle in a water basin with 40 mm water film thickness. The validation shows a high conformity between simulation and measurement, Frerichs (2015), see figure 3 and 4.

4 ACTIVE SAFETY ASSISTANCE

In an aquaplaning situation the driver needs assistance in two distinct ways: firstly, to stabilize the vehicle in case of disturbances and secondly, to guide the vehicle safely along the course of the road.

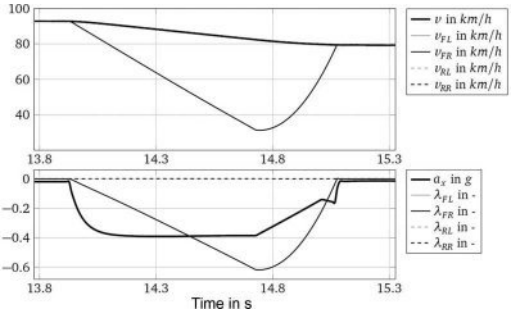


Figure 4. Simulation results of a straight drive through a basin with water film thickness WT = 40 mm and neutral gear. Shown are from top to bottom vehicle speed, wheel speed, longitudinal acceleration and wheel slip.

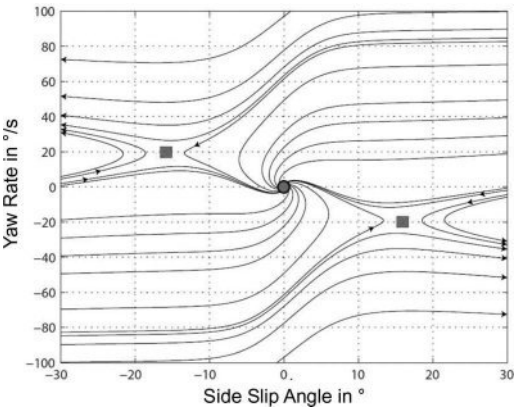


Figure 5. Dry road vehicle trajectories in phase plane for vehicle speed 100 km/h, zero steer angle and homogeneous friction $\mu = 1$ at front and rear axle. Note that beyond the saddle points (squares) the vehicle is unstable without active safety assistance.

4.1 *Phase plane analysis*

On the basis of the nonlinear two-track vehicle model a numerical stability analysis in the phase plane shows significant differences between homogeneous friction, figure 5, and aquaplaning, figure 6. In the case of homogeneous friction beyond the saddle points the stability gets compromised without active safety assistance. This is a typical use case for Electronic Stability Control, which guides the vehicle back into the stable region, van Zanten & Kost (2016). In the case of aquaplaning the system is globally stable, but performes very weakly damped oscillations without active safety assistance.

4.2 *Steering-by-braking control strategy*

The assistance strategy in aquaplaning situations is direct yaw control with rear individual braking. A

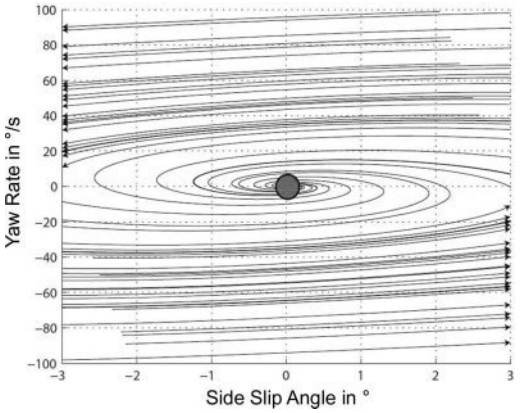


Figure 6. Aquaplaning vehicle trajectories in phase plane for vehicle speed 100 km/h, zero steer angle, friction $\mu = 0$ at front axle and friction $\mu = 0.8$ at rear axle. Note that the vehicle is globally stable, but performes very weakly damped oscillations without active safety assistance.

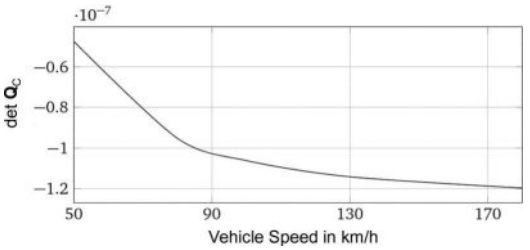


Figure 7. Determinant of the controllability matrix calculated for different vehicle speeds.

numerical calculation of the determinant of the controllability matrix

$$\boldsymbol{Q_C} = [\boldsymbol{B} \quad \boldsymbol{AB}] \tag{17}$$

of the linear bicycle model (3) shows a relatively weak, but nevertheless present controllability, see figure 7. Here, it is considered that the rear wheels run in the track of the front wheels, thus ensuring high friction with only minimal rolling resistance.

Consequently, the objective of the active safety system is to control the vehicle by means of differential braking at the rear axle. The assistance is triggered by evaluating slip and other signals provided by a standard Electronic Stability Control system.

The controller is designed as a linear-quadratic regulator with gain-scheduling in combination with feedforward control and disturbance rejection. The control law is given by

$$\boldsymbol{u} = -\boldsymbol{K_x x} - \boldsymbol{K_s \hat{x}_s} + \boldsymbol{K_w w}. \tag{18}$$

Reference signal $\boldsymbol{w}$ is the desired yaw rate derived from a stationary vehicle model with steer angle as input and wheel base $l = 2.888$ m, understeer gradient $EG = 0.000295$ and vehicle speed v as parameter,

$$\boldsymbol{w} \equiv \dot{\psi}_d = \frac{v}{l + EGv^2}\delta \ . \tag{19}$$

The feedforward control gain $\boldsymbol{K}_\mathrm{w}$ is given by

$$\boldsymbol{K_w} = -\left[\boldsymbol{C}(\boldsymbol{A} - \boldsymbol{BK}_x)^{-1}\boldsymbol{B}\right]^{-1} \ . \tag{20}$$

External yaw disturbances acting on the vehicle are estimated and compensated applying the method provided by Müller & Lückel (1977). The approach is based on the assumption that stationary, for non-vanishing disturbances and no feedforward control, the interesting control variables $\boldsymbol{z}$ are controlled to zero. The system state is then in general a linear combination of the disturbance state, i.e.

$$\left.\begin{matrix} \boldsymbol{x}(t) & = & \boldsymbol{S_s x_s}(t) \\ \boldsymbol{z}(t) & \rightarrow & 0 \end{matrix}\right\} \ for\ t \rightarrow \infty \ . \tag{21}$$

The disturbance observer (22) provides an estimation of the disturbance state,

$$\begin{bmatrix} \dot{\hat{\boldsymbol{x}}} \\ \dot{\hat{\boldsymbol{x}}}_s \end{bmatrix} = \begin{bmatrix} \boldsymbol{A} & \boldsymbol{EC}_s \\ \boldsymbol{0} & \boldsymbol{A}_s \end{bmatrix} \begin{bmatrix} \hat{\boldsymbol{x}} \\ \hat{\boldsymbol{x}}_s \end{bmatrix} + \begin{bmatrix} \boldsymbol{B} \\ \boldsymbol{0} \end{bmatrix} u + \begin{bmatrix} \boldsymbol{L}_x \\ \boldsymbol{L}_s \end{bmatrix} (\boldsymbol{y} - \hat{\boldsymbol{y}}). \tag{22}$$

With the system description (3.7) the control law (18), the assumption (8) and assuming stationary conditions, the gain $\boldsymbol{K}_\mathrm{s}$ for disturbance rejection can be calculated from the linear matrix equation (23). Note that in general the disturbance rejection gain $\boldsymbol{K}_\mathrm{s}$ depends on the state feedback $\boldsymbol{K}_\mathrm{x}$.

$$\begin{bmatrix} \boldsymbol{S}_s \\ \boldsymbol{K}_s \end{bmatrix} = \begin{bmatrix} \boldsymbol{A} - \boldsymbol{BK}_x & -\boldsymbol{B} \\ \boldsymbol{C}_z - \boldsymbol{D}_z\boldsymbol{K}_x & -\boldsymbol{D}_z \end{bmatrix}^{-1} \begin{bmatrix} -\boldsymbol{E} \\ -\boldsymbol{G}_z \end{bmatrix} \ . \tag{23}$$

The control structure is further extended by an inner-loop longitudinal slip control described in Semmler (2002) to access the full control potential whilst ensuring that the rear axle will not be destabilized during the intervention. The sign of the control variable $\boldsymbol{u}$ determines which rear wheel is in slip control mode. The overall control structure of the aquaplaning active safety assistance is shown in figure 8.

5 SIMULATION RESULTS

The active safety assistance is validated by simulation with a number of test cases. In order to be able to realistically evaluate the active safety system it is assumed that the water film thickness is 7 mm and the tire tread depth is 8 mm. The maximum friction at the rear axle is limited to $\mu = 0.8$.

The test cases are designed to analyze the influence of the vehicle speed, the gradient and magnitude of driver steering excitation and disturbances on the control performance. Figure 9 shows the effect of slip

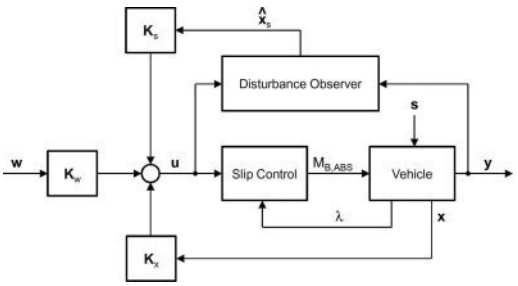


Figure 8. Control structure of the aquaplaning active safety assistance system with inner-loop slip control and outer-loop yaw rate control.

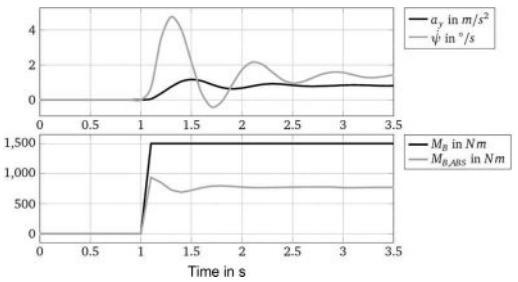


Figure 9. Simulation of inner-loop slip control response during aquaplaning with vehicle speed 130 km/h. Excitation with ΔF_x step ramp. Slip control causes a saturation effect which limits the maximum possible lateral acceleration and yaw rate.

control on the aquaplaning assistance potential. The required wheel brake torque M_B, derived from the input ΔF_x, is limited to the feasible torque $M_{B,ABS}$. The maximum lateral acceleration a_y of 0,8 m/s^2 is due to the limited friction at the rear axle. Note that the outer-loop yaw rate control is switched off, such that the damping behavior is very poor.

Figure 10 illustrates the performance of the overall control system. The system is excited by a steering wheel angle δ_H step, first order filtered with the filter constant $\tau = 0.3$ s. The desired yaw rate is followed with sufficient damping behavior. Figure 11 shows the case with a much higher steering input, leading to saturation of the control action and therefore a not satisfactory performance.

The disturbance rejection performance is shown in figure 12. Although the disturbance is compensated the transient and stationary behavior could further be improved.

The test cases show that the magnitude of the driver steering has a significant influence, because there is a risk that the braking actuator saturates and the control loop is not closed any more. A limitation of the steering angle should be considered in that case. This measure may also be beneficial to avoid heavy yaw excitation when leaving the aquaplaning area.

Further simulation results show significant differences when the steering gradient is varied. Slow

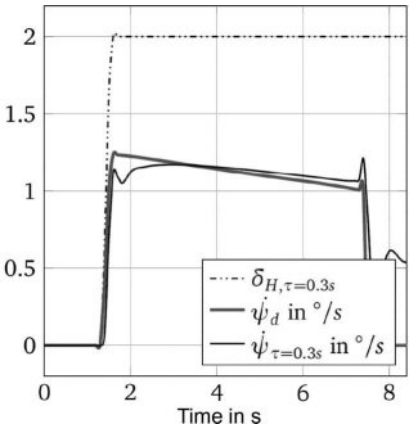


Figure 10. Simulation of aquaplaning with vehicle speed 100 km/h. Excitation by low steering wheel angle δ_H step, first order filtered. Damping and yaw rate following behavior is sufficient.

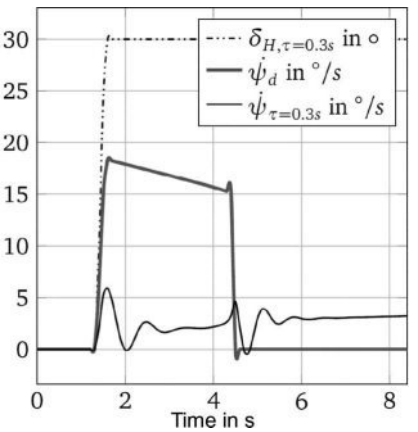


Figure 11. Simulation of aquaplaning with vehicle speed 100 km/h. Excitation by high steering wheel angle δ_H step, first order filtered. Damping and yaw rate following behavior is not sufficient due to actuator saturation.

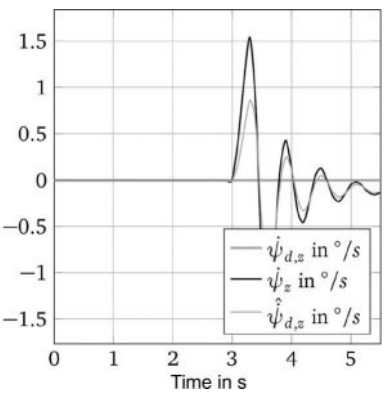


Figure 12. Simulation of aquaplaning with vehicle speed 130 km/h. Excitation at $t = 3$ s by side wind step disturbance with lateral wind speed of 70 km/h.

steering allows a good assistance with sufficient tracking behavior. Fast steering leads to significant overshoot of the vehicle yaw rate and should be avoided. The influence of the vehicle speed when entering the aquaplaning situation is less significant, assumed that the friction at the rear wheels is not affected.

6 CONCLUSIONS

A simulation environment has been designed to study an active safety system with the purpose to assist the driver when the vehicle aquaplanes. An extended tire model reproduces the effect of the surface water leading to a complete loss of grip at the front wheels. The proposed assistance strategy based on state feedback and feedforward control is actuating the rear brakes and enables an adequate amount of yaw damping as well as a minimum guidance capability. From the selected test cases some possible starting points for further development can be identified.

The long-term strategy is "Vision Zero" leading to zero traffic-related fatalities, injuries and road accidents. Continental and other automotive suppliers support the worldwide Global NCAP "Stop the Crash" campaign to raise awareness of live-saving technologies.

REFERENCES

Ditze, M.; Golatowski, F.; Laum, N.; Varhelyi, A.; Gustafsson, S.; Geramani, K. (2010). A Survey on Intelligent Vehicle Safety Systems for Adverse Weather Conditions. In, *Proc. of FISITA World Automotive Congress*, Budapest.

Frerichs, D. (2015). Design and Simulation of Vehicle Dynamics Control to Improve Stability during Aquaplaning. *Master Thesis, Technical University,* Darmstadt (in German).

Gengenbach, W. (1967). The Behavior of Passenger Car Tires on Dry and Wet Roads. *PhD Thesis, Technical University,* Karlsruhe (in German).

Görich, H.-J. (1993). System That Detects the Current Friction Potential of a Passenger Car During Driving. *PhD Thesis*, VDI-Verlag, Düsseldorf (in German).

Herrmann, S.R. (2008). Simulation Model of Water Drainage and Aquaplaning on Road Surfaces. *PhD Thesis,* Stuttgart (in German).

Klomp, M. (2010). Longitudinal Force Distribution and Road Vehicle Handling. *PhD Thesis, Chalmers University of Technology*, Gothenburg.

Müller, P.C. & Lückel, J. (1977). Disturbance Rejection Control in Linear Multivariable Systems. In *Regelungstechnik,* Heft 2, pp. 54–59 (in German).

Orend, R. (2005). Modelling and Control of a Vehicle with Single-Wheel Chassis Actuators. In *Proc. of IFAC World Congress*, Prague.

Semmler, S., Isermann, R.; Schwarz, R.; Rieth, P. (2002). Wheel Slip Control for Antilock Braking Systems Using Brake-By-Wire Actuators. In *Proc. of SAE World Congress*, Detroit.

von Vietinghoff, A. (2008). Nonlinear vehicle control in critical lateral driving situations. *PhD Thesis, Technical University*, Karlsruhe (in German).

van Zanten, A. & Kost, F. (2016). Brake-Based Assistance Functions. In *Winner, H.; Hakuli, S.; Lotz, F.; Singer, C. (eds.) Handbook of Driver Assistance Systems.* Springer, Switzerland.

Subjective evaluation and handling

Advanced Vehicle Control – Edelmann, Plöchl & Pfeffer (Eds)
© 2017 Taylor & Francis Group, London, ISBN 978-1-138-02992-7

Validation of a moving base driving simulator for subjective assessments of steering feel and handling

G.L. Gil Gómez, C. Andersson Eurenius, J. Donnay Cortiñas & E. Bakker
Volvo Car Group, Vehicle Dynamics Centre, Gothenburg, Sweden

M. Nybacka & L. Drugge
KTH Royal Institute of Technology, School of Engineering Sciences, Department of Aeronautical and Vehicle Engineering, Division of Vehicle Dynamics, Stockholm, Sweden

B. Jacobson
Vehicle Dynamics, Applied Mechanics, Chalmers University of Technology, Gothenburg, Sweden

ABSTRACT: Moving Base Driving Simulators (MBDS) have a large potential to increase effectiveness in vehicle dynamics development. MBDS can reduce dependency on vehicle-prototypes by allowing subjective assessments (SA) of models. Little is, however, known about the relation of SA in MBDS and in physical vehicles. This paper aims to increase this knowledge, and proposes and implements a methodology to validate MBDS for SA of steering feel and handling. Firstly, vehicle models were generated from Kinematics & Compliance measurements of real vehicles. These models were validated versus objective tests, with steering robots, of the physical vehicles. These vehicles and their MBDS-models were assessed by expert drivers, using a scanned-test track in the MBDS. Comparison of the SA in both environments enabled the MBDS validation. Promising results, with higher SA accuracy for handling than for steering feel, indicates that the major improvement effort should focus on the steering model and its simulation in the MBDS.

1 INTRODUCTION

Moving base driving simulators (MBDS) are a key step towards a more effective vehicle dynamics development, reducing time and cost, and allowing engineers to focus, in a reliable way, on specific parameters by eliminating parasitic effects and external factors. (Mohajer *et al.* 2015 & Hjort *et al.* 2014)

Mohajer explains that reliable results require a high level of fidelity and accuracy, which is attained by means of motion, visual, sound and haptic cues (corresponding to vestibular, visual, auditory, and kinaesthetic sensory information). Depending on their fidelity, usability, complexity and costs, MBDS can be classified as high-, mid- or low-level. High-level simulators offer all kind of cues and normally include a wide field-of-view and a full cockpit. This cabin is often mounted on a hexapod coupled to a moving platform that increases the workspace on the horizontal plane. This configuration offers more than 6-DOF, as it is the case of the MBDS in Figure 1.

Murano *et al.* (2009) claims that to be felt as realistic and to avoid motion sickness, these horizontal platforms require to travel approximately the same distance as the simulated real vehicle. For example, to properly reproduce normal driving (0.3 g longitudinal and lateral accelerations) in an intersection, a movement capability of 35×20 m is demanded. For more advanced driving, the limitations in displacements and power of the actuator cannot normally reproduce full vehicle dynamics, therefore not matching the visual cueing. This reduced *physical validity* negatively affects *perceptual validity* (driver's perception of self-motion), which has to be increased by motion cueing, that is, a coherent coordination of all the available cues (Reymond & Kemeny, 2000). Unlike Murano, Berthoz *et al.* (2013) claim that drivers prefer the motion cue scaled down to 40–70%. However, no motion feedback severely degrades driver's performance in fast manoeuvres, because artificial environments disturb driver behaviour.

Behavioural validity is therefore conditioned to physical and perceptual validity; it means that drivers behave similarly in MBDS as in real traffic. This validity has been the main focus of previous research, as MBDS allows to study drivers' behaviour and interactions with active safety systems under stressful, dangerous, or non-legal situations (Blana, 1996; Burenger-Koch, 2005; Murano *et al.* 2009).

However, according to Mohajer (2015), and to the best of the authors' knowledge, there is little research about subjective assessments (SA) of vehicle dynamics in MBDS. A pair of examples are: Cossalter *et al.* (2010), on a motorcycle simulator, and Hjort *et al.* (2014), who introduce a methodology for subjective and objective validation of MBDS for on-the-limit

handling. Hjort maintains that MBDS seldom perform well in these situations; therefore, validated reliable models are required. However, as Hjort states, their method was not fully developed.

This paper proposes and implements a further developed validation methodology for MBDS regarding steering feel (controllability) and handling (stability), giving special focus to the relation of SA in real vehicles and in their respective MBDS-models.

2 MATERIAL AND METHODS

Figure 1 shows the Driver-in-Motion simulator, which has 9-DOF with three horizontal cylinders that move a hexapod (VI-Grade, 2015). This is the simulator validated in this study.

The proposed validation methodology follows the workflow shown in Figure 2. This workflow is divided in two parallel branches: a virtual and a physical branch. The former includes the models and the MBDS. The latter comprises the tests on the real vehicle, which were used to gather data for parameterizing the models and as the reference for the posterior validation of these models and of the MBDS. The steps in this methodology are presented below in order of appearance, from left to right, in Figure 2.



Figure 1. Driver-in-Motion simulator at Volvo Car Group.

2.1 *Test vehicle configurations*

Three vehicle configurations were driven in both the MBDS and in reality. This amount was considered appropriate for a first case study, as it allows to compare, real-SA and MBDS-SA, per configuration; and to evaluate, in addition, how these SA evolve between different configurations in these two test environments.

These three set-ups were a Volvo V40 in: (i) its standard configuration, (ii) without the front antiroll bar (ARB), and (iii) without the rear ARB. These extremely simple modifications greatly influence characteristics such as roll control or understeering coefficient, and therefore steering feel and handling.

Moreover, ARB tuning is an integral part of vehicle dynamics development. Although removing an ARB is not within the realistic tuning range, the authors consider this approach appropriate, because going from large to smaller changes allows to easily identify the limitations of the MBDS.

An extra model was generated from MSC Adams. This process represents the real development workflow, in which real vehicles are not available in early stages and therefore, the MBDS models are obtained from more complex multibody dynamics models.

2.2 *Generation of the vehicle models*

MBDS require real-time capable models. In this project, VI-CarRealTime was used. This software performs at real-time by being based on look-up tables, which can be obtained from Kinematics and Compliance (K&C) tests. These tests accurately describe the kinematics characteristics of the vehicle suspension and steering geometries, the compliance characteristics of their components, and the centre of gravity and

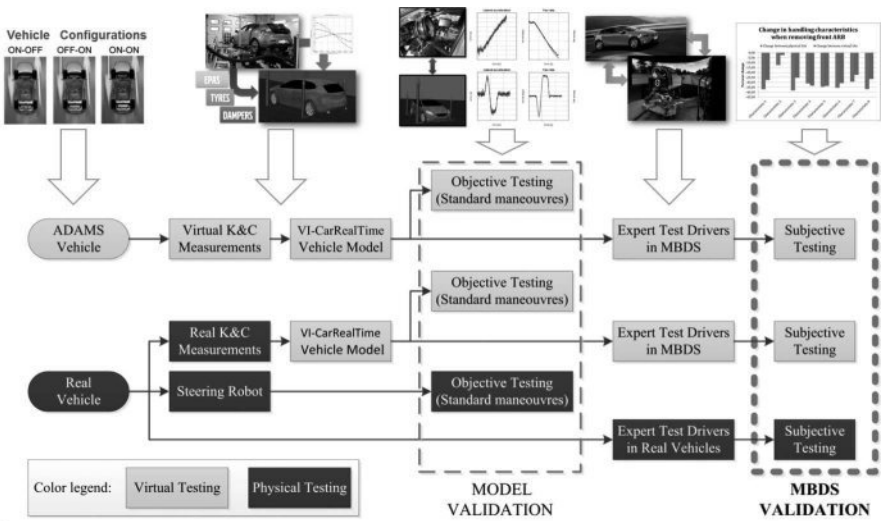


Figure 2. Workflow of the methodology proposed and implemented to validate the MBDS.

moments of inertia of the vehicle. Virtual and real K&C tests were performed in this study:

- The virtual K&C tests were run in MSC Adams, to represent model-based development.
- The real K&C tests were done in an Anthony Best Dynamics' SPMM 4000 machine, to ensure the best possible parameterization of VI-CarRealTime.

To model the non-linearity of the system, these tests included: single-event tests; asymmetric left-right bounce-level tests; and measurements at three bounce levels. The intermediate level corresponded to curb weight plus a driver and a passenger, which corresponds to the weight, on the passenger seat, of the required equipment in later objective testing.

The steering characteristics were measured with the help of a steering robot, which implemented a limit-to-limit sweep of the steering rack. A braking robot was also mounted, and applied when required.

These quasi-static tests were complemented with the curves of the characteristics of the dampers and of the power steering system; as well as with the tire model, for which the magic formula was used, parameterized by the tire manufacturer.

2.3 *Validation of the models*

After their generation, the models were verified (for executability, stability and robustness) and validated by comparison and adaptation at different loads, operating ranges and time scales, i.e., steady state, slow and fast transients (Klemmer et al. 2011). This was done by back-to-back objective tests, executed in the real vehicles and in VI-CarRealTime. Different operating cases were achieved by using different standard manoeuvres: on-centre handling (ISO 13674), swept steer (SAE J266), frequency response and step input (ISO 7401), constant radius (ISO 4138), and sine with dwell (Forkenbrock, 2007).

These open-loop manoeuvres were programmed on a steering robot to test the real vehicle configurations. This method eliminates driver's influence and increases test repeatability (Harrer et al. 2006, Pfeffer et al. 2008). The selected steering robot, from Anthony Best, was equipped with angle and torque sensors; with a throttle actuator; and with a differential GPS and an OTS Inertial platform, RT3002, to measure the current states of the vehicle.

In the virtual-environment case, the manoeuvres were initially programmed in CarRealTime. However, as it is practically impossible to reproduce the same manoeuvres in the physical and virtual environments (Cossalter et al. 2010), time-vectors recorded in the physical tests were used as model inputs. This ensured that the models were exactly exposed to the same stimulus as in the physical testing. These inputs were the steering wheel angle (SWA) and the longitudinal velocity.

The validation was done comparing: (i) time series data of relevant steering and handling measurements: lateral acceleration, yaw rate, sideslip angle, roll angle, and steering wheel torque (SWT) (Mohajer et al. 2015); and (ii) key metrics as the described in the standards. According to Klemmer, the comparison was done for the highest and lowest tested inputs, to ensure the validity of the models for a wide operating range. Note that non-linear effects lead to simulation results being generally only valid within a limited input window (Garrott et al. 1997).

Table 1. Detailed test drivers' information.

Driver	Gender	Age	Experience (years)
A	Male	54	30
B	Male	35	7
C	Male	29	0.5

Table 2. A subset of the SA questions*.

Level 2	Level 3	Level 4	Level 5
		Response Roll Control	Window
Steering Feel	Straight-ahead Controllability	Torque Feedback	Deadband Build-up Friction Damping

*Further detail can be found in Gil Gómez et al. (2015).

2.4 *MBDS validation*

To validate the MBDS, drivers' SA obtained first in the real vehicle were compared to those obtained later in the MBDS. This test order was followed by Hjort et al. (2014) and recommended by Molino et al. (2005): "If simulation is an abstraction of reality, it is better to let nature to be first instructor"

Three expert drivers participated in this study (see Table 1). More drivers were planned, but around ¾ of the physical test had to be cancelled, or rescheduled, due to poor weather conditions. Furthermore, Driver A could unfortunately not complete the tests in the MBDS due to motion sickness.

To ensure that the drivers were exposed to similar experiences in both environments, great effort was invested on keeping the tests alike: For instance, in the real-vehicle tests, tire pressure was checked to reflect the model. The vehicle weight was kept at curb plus two (as the objective tests emulates this configuration), by having a test leader as passenger in each real drive. This test leader drove the cars to the test track, where test drives were limited to three laps, and he also gave support with the SA questionnaire, which is presented in Table 2. The MBDS-tests used a V40 cockpit and the same test track, which had been laser scanned, and to avoid motion sickness, again only three laps were allowed.

To avoid including a bias, the real-vehicle tests were always executed in the same order: 1st) configuration *ii*, 2nd) configuration *iii,* and 3rd) configuration *i*. To analyse SA repeatability (an issue identified by Gil Gómez et al. 2015), the test series in the real vehicle

were blind and repeated twice. That is, configurations *ii – iii – i* were tested followed by a pause and configurations *ii – iii – i* again. The second time, the SA was done using a tablet version of the questionnaire (Gil Gómez et al. 2016).

In the MBDS the test-sequence was similar, but with no model repetition. Instead, as it is difficult beforehand to identify the best model (Hjort et al. 2014), different parameterizing technics were studied: First, the models obtained by real-K&C measurements of configurations *ii, iii* and *i*. Second, configurations *ii* and *iii* obtained by virtually removing ARB in the model *i* obtained from real-K&C. Last, model *i* derived from virtual-K&C in MSC Adams.

The SA in the MBDS was answered in the tablet (to reduce transcription time), and complemented by an interview about general driving feel and improvements suggestions in the vehicle configuration.

The comparison of the SA (MBDS vs. real vehicles), and the outcome of the interview, were used to validate the performance of the MBDS. The results were firstly studied car by car. However, it was observed that a relative analysis led to better results. That is, analysing how SA changed (for each driver) between different vehicle configurations.

3 RESULTS AND DISCUSSION

3.1 *Objective validation (model validation)*

Figure 3 shows that the initial model was already realistic. However, this model, directly obtained from the K&C tests, was not considered good enough. The responses of the model were normally too low for the lowest SWA inputs, whereas too high for the highest. Moreover, some mechanical properties of the steering system, such as stiffness and inertia of the components of the steering column, were missing, as they are not measured by the K&C test. Furthermore, as shown in Figure 4 (left), activating the power steering model led to unstable results.

Therefore, a fine-tuning iteration of the model was performed:

- For the tires, the lateral and longitudinal peak friction coefficients were increased to 1.0 (they were initially set to 0.8), to allow for larger lateral accelerations. The relaxation length was modified to decrease tire oscillations (Luty, W. 2001), and therefore reduce stability issues, although this strategy alone did not lead to large improvements.
- For the ARB, theoretical parameters were used, as the values obtained by K&C seemed to be non-symmetrical, too stiff, and vehicle-roll was too low.
- For the steering system, the mechanical properties of its components were included; and a simpler Simulink-model was used for the power steering. It calculated SWT as function of SWA, steering rack force, longitudinal velocity and lateral acceleration. Figure 4 (right) shows that this simpler solution led to a significantly higher numerical stability.

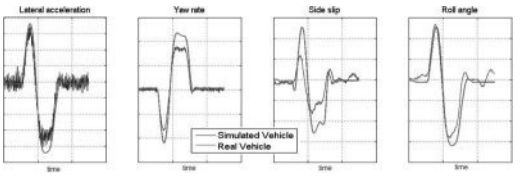


Figure 3. Example of the initial model validation. Comparison of real and simulated sine with dwell tests of configuration *i*.

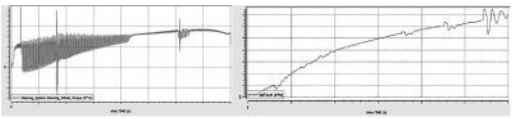


Figure 4. SWT during constant radius test. Numerical instability of the initial model vs. the stable simpler Simulink model.

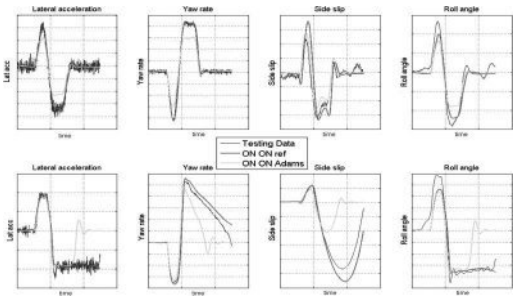


Figure 5. Final validation. Comparison of configuration *i* (ON-ON): modified real-K&C model (ref) vs virtual-K&C model during a sine with dwell. Top: low SWA. Bottom: high SWA.

Figure 5 shows that these modifications clearly improved the simulation results. In general, the modified model represents the physical testing more accurately than the initial model. The figure also illustrates that the K&C-based models are better than the non-modified model obtained from Adams. This trend is repeated for all manoeuvres.

Figure 6 presents results for the two models of configuration *ii*. The one obtained by removing, virtually, the rear ARB from the standard configuration model; and the one obtained from real K&C measurements of the vehicle without the rear ARB. The former does not perform so well as the latter for the sine with dwell. However, the two models show smaller differences for the rest of the manoeuvres. Additionally, the differences between these two models are slightly larger than for the two non-front-ARB models, because this latter modification affected less the K&C results.

To complete the validation, the objective metrics (OM) were also compared. Comparing absolute values did not result in an effective method; however, the comparison of the OM between all vehicle configurations allowed to identify that 83% of the selected handling OM (62% for steering) changed in the same

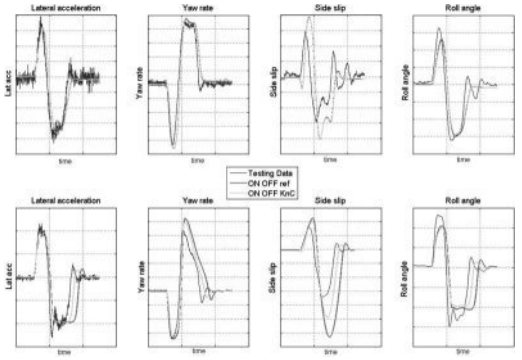


Figure 6. Results of the "ON-OFF ref" and "ON-OFF KnC" models. The former is derived from the model in Figure 5 removing, virtually, the rear ARB. The latter is the model derived from measuring the real vehicle without rear ARB in the real K&C rig. They are compared with the data gathered from the physical testing during two sine with dwell manoeuvres.

direction in the model as in reality, with an average deviation of 15.9% (6.3% for steering). This relative evaluation is considered important because the MBDS is intended to properly represent the direction of the changes in vehicle response.

3.2 *Subjective validation (MBDS validation)*

Regarding the SA in the MBDS, bad weather conditions led to a low number of drivers completing the tests. This affects the statistical significance of the results. However, it is nevertheless a good example of a motivation for validated MBDS, where tests are non-dependent of weather conditions.

Furthermore, a first result is that one driver could not complete the tests in the MBDS due to motion sickness, which is caused by lack of physical validity and/or by poor model/motion-cueing harmonisation. This reduces drivers' performance and motivation, and is therefore an issue that needs to be taken into consideration. Some methods to help avoiding it are presented in literature, e.g.: ReliefBand (a medical device), which seems to offer some simulator sickness relief against increased MBDS exposure; independent visual background (IVB) (Mollenhauer et al. 2004) and the better performing "natural" IVB, which uses "meaningful" objects, such as clouds, as fixed background (Lin et al. 2002).

On the other hand, another driver did seem completely unaffected by motion sickness, thus completing the six tests without a break. However, testing so many cars (even only for three laps) during a single test day was identified as a high demanding task, thus complicating for the drivers to keep high level of concentration. This agrees with Blana (1996), who claims that simulator testing is more physically/effort demanding and more frustrating than driving on a similar real driving condition.

Regarding the interviews, the results were promising. All drivers assessed the standard configuration as

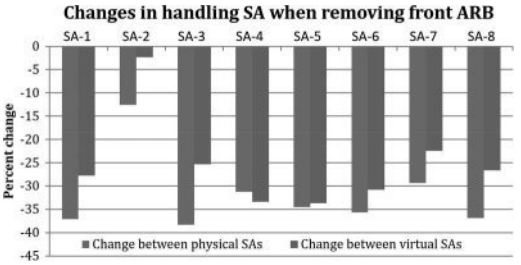


Figure 7. Example of the relative change in SA for test in the real vehicles and in the MBDS, in this case between the standard configuration and the configuration without the front ARB.

being the best, not identifying any obvious improvement to be implemented in the vehicle. In contrast, for the other configurations, the main concerns were detected, and increasing ARB stiffness in the axle where it had been removed was normally suggested. Improvements on steering feel were also desired. This agrees with the results of the SA study.

The comparison of the SA ratings between all vehicle configurations allowed to identify if the drivers felt that the vehicle behaviour changed in a similar way in the real car and in the MBDS. Figure 7 shows that for handling 94% of the SA (78% for steering) changed in the same direction, with an average deviation of 6.3% (18.7% for steering). This outcome reflects the results previously obtained for the OM, where handling metrics offered better results too. This is probably due to the steering model, which had to be simplified because of numerical instabilities; and for which some parameters could not be directly obtained from the K&C measurements.

4 CONCLUSIONS

In summary, the following conclusions can be listed:

- The model derived from real K&C gave results closer to the real objective tests than the model derived from virtual K&C (MSC Adams). Furthermore, measuring all configurations in the real K&C was generally better than simply removing, virtually, the ARB from the standard configuration model.
- In virtual objective testing, in the model, using recorded inputs from real testing improved the validation, as the model is consequently excited with exactly the same inputs as the reference real test.
- The comparison of OM did not give as good results as the comparison of time signals. This might have been caused by the OM adding more complexity because of the post-processing tools.
- The longer the drivers tested in the simulator the more comfortable they felt doing virtual evaluations. There might be an effect of adaptation to the MBDS, indicating that training sessions in the MBDS can be beneficial for vehicle dynamics development.

– Despite of blind testing, the expert drivers normally suggested to increase the stiffness in the axle without ARB. Whereas, for the production vehicle, no clear suggestions were identified. This is a promising result towards development in the MBDS.
– The validation of the SA in the MBDS also led to very positive results, specially for handling. Further work in the development of the MBDS should therefore focus on the development of the steering model in VI-CarRealTime, and of the method to gather steering parameters from the real vehicle.
– As future work it is left, therefore, the study of how to improve the models of the steering feel and the steering assistance; as well as, how to properly modify ARBs in the model without real K&C.

Finally, as MBDS are continuously upgraded with new features, to identify if these upgrades improved the simulator, validations have to be performed periodically against field-testing in natural environments (Molino et al. 2005; Blana 1996). The method proposed here allows to keep the models and the real-SA as calibration references for motion cueing validations. That is, for a second validation only a new SA session in the MBDS is required. Thus, increasing the effectiveness of the validation.

ACKNOWLEDGEMENT

The authors would like to acknowledge gratefully the financial support from FFI – Strategic Vehicle Research and Innovation [2012-04609].

The authors would also like to extend their thanks to the vehicle dynamics, CAE and vehicle and rig testing teams at Volvo Car Group for their participation and all their support and help in this project.

REFERENCES

Andersson Eurenius, C. & Cortiñas, J. 2015. Validation of a Moving Base Driving Simulator for Subjective Assessments of Steering and Handling. Göteborg: Chalmers University of Technology (*Diploma work* – nr: 2015:69).

Berthoz, A., Bles, W., Bülthoff, H.H., Grácio, B.J. et al. 2013. Motion scaling for high-performance driving simulators. *IEEE Transactions on Human-Machine Systems,* 43(3): 265–276.

Blana, E. 1996. Driving simulator validation studies: A literature review. *Working paper 480. Institute of Transport Studies, University of Leeds, Leeds, UK.*

Bruenger-Koch, M. 2005. Motion parameter tuning and evaluation for the DLR automotive simulator. *Proc. Driving simulation conference, North America 2005.*

Cossalter, V., Lot, R. & Rota, S. 2010. Objective and subjective evaluation of an advanced motorcycle riding simulator. *European Transport Research Review* 2(4): 223–233.

Forkenbrock, G.J. & Boyd, P.L. 2007. Light vehicle ESC performance test development, *In proceedings of the 20th International Technical Conference on the Enhanced Safety of Vehicles*, Paper Number 07-0456, Lyon, France.

Garrott, W.R., Grygier, P.A., Christos, J.P., Heydinger, G.J., Salaani, K., Howe, J.G. & Guenther, D.A. 1997. Methodology for validating the National Advanced Driving Simulator's Vehicle Dynamics (NADSdyna), *SAE Tech. Paper* 970562.

Gil Gómez, G.L., Nybacka, M., Bakker, E. & Drugge, L. 2015. Findings from subjective evaluations and driver ratings of vehicle dynamics: steering and handling. *Vehicle System Dynamics: International Journal of Vehicle Mechanics and Mobility*, 53(10):1416–1438.

Gil Gómez, G., Vestlund, J., Bakker, E., Berger, C. et al. 2016. Improving subjective assessment of vehicle dynamics evaluations by means of computer-tablets as digital aid, *SAE Technical Paper 2016-01-1629.*

Harrer, M., Pfeffer, P. E. & Johnston, D. N. 2006. Steering feel: objective assessment of passenger cars analysis of steering feel and vehicle handling. *FISITA World Automotive Conference*. Yokohama, Japan, 22–27 October 2006.

Hjort, M., Kharrazi, S., Eriksson, O. & Hjälmdahl, M. 2014. Validating on the-limit properties of a driving simulator. *Proc. New development in driving simulation design and experiments: Driving simulation conference Europe 2014*

ISO 4138, 2012. Passenger cars – Steady-state circular driving behaviour – Open-loop test methods (ISO 4138:2012, IDT), *International Organization for Standards*.

ISO 7401, 2011. Road vehicles – Lateral transient response test methods – Openloop-test methods (ISO 7401:2011, IDT), *International Organization for Standards*.

Klemmer, J., Lauer, J., Formanski, V. et al. 2011. Definition and application of a standard verification and validation process for dynamic vehicle simulation models. *SAE Int. J. Mater. Manuf.* 4(1):743–758.

Lin, J.J.-W., Abi-Rached, H., Kima, D.-H. et al. 2002. A natural independent visual background reduced simulator sickness. *Human Factors and Ergonomics Society Annual Meeting Proceedings* 46(26):2124–2128.

Luty, W. 2011. An Analysis of Tire Relaxation in Conditions of the Wheel Side Cornering Angle Oscillations, *Journal of KONES Powertrain and Transport*, 18(1):325–332.

Mohajer, N., Abdi, H., Nelson, K. & Nahavandi, S. 2015. Vehicle simulators, a key step towards road vehicle dynamics improvement, *Vehicle System Dynamics,* 53(8):1204–1226.

Moline, J.A., Katx, B.J., Opiela, K.S. & Moyer, M.J. 2005. Validate first; simulate later: A new approach used at the FHWA higway driving simulator. *Proc. Driving simulation conference, North America 2005.*

Mollenhauer, M.A. & Romano, R.A. 2004. The evaluation of a motion base driving simulator in a cave at tacom. *Proc. 24th Army Science Conference.*

Murano, T., Yonekawa, T., Aga, M. & Nagiri, S. 2009. Development of high-performance driving simulator. *SAE Int. J. Passeng. Cars – Mech. Syst.* 2(1):661–669.

Pfeffer, P. E., Harrer, M. & Johnston, D. N. 2008. Vehicle dynamics measurements. *Proc. of the Institution of Mechanical Engineers, Part D: Journal of Automobile Engineering*. 222(5):801–813.

Reymond, G. & Kemeny, A. 2000. Motion cueing in the Renault driving simulator. *Vehicle System Dynamics,* 34(4): 249–259.

SAE J266, 1996. Steady-state directional control test procedures for passenger cars and light trucks. Surface vehicle recommended practice. *SAE International.*

VI-Grade. 2015. DiM – Driver-in-motion brochure. 2 April 2015 [ONLINE] Available at: http://www.vi-grade.com/index.php? pagid=download_det&did=1224. [Accessed 26 May 2016].

Advanced Vehicle Control – Edelmann, Plöchl & Pfeffer (Eds)
© 2017 Taylor & Francis Group, London, ISBN 978-1-138-02992-7

Tire handling subjective evaluation related to model parameters of three driver models

Saskia Monsma
HAN Automotive Research, HAN University of Applied Sciences, Arnhem, The Netherlands

Martijn van Oort
Sogeti Netherlands B.V., Vianen, The Netherlands

Paul Bremmer
Apollo Tyres Global R&D, Enschede, The Netherlands

ABSTRACT: For subjective evaluation of tire handling, test drivers perform certain maneuvers and rate the handling of a tire. To know more about how these driver opinions are formed, this paper presents a method for modelling the adapting behavior of a driver. This method is based on field experiments were two professional tire test drivers and eight nonprofessional, but highly skilled drivers performed several double lane changes with different tires and different values for the vehicle speed. Three different preview driver models were implemented. The results show that the amount of driver workload is reflected in driver parameter changes and that these can be related to tire handling differences. For differences due to different tires the professional test drivers group in combination with a discrete preview driver model with four driver parameters showed the best results for the parameter lead term constant.

1 INTRODUCTION

Vehicle handling performance is difficult to measure. It is to a large extend determined by the vehicle, its dimensions, suspension, loading, tires, etc. However, handling is not only determined by the vehicle; it also depends on drivers perception. Drivers have different opinions on what is 'good' vehicle handling, depending on their experience, skills and preferences. Therefore, handling is considered as a property of the total closed-loop driver-vehicle system.

Tires have a significant influence on vehicle handling, this influence referred to as 'tire handling'. Good handling tires can improve vehicle handling, but the opposite is even more true: vehicle handling can deteriorate or even can become unsafe with inappropriate tires (Von Glasner & Ahlgrimm 2011). Assessing tire handling can be done with objective, measurement-based tests, done with tire testing equipment in the laboratory, outdoors with special test equipment or by using simulations. These objective tests can give a good indication of the tire handling performance, but is not representing the real life closed-loop system, including the driver. Therefore, current practice for the assessment of tire handling is subjective: a vehicle driven on a track by a skilled and experienced test driver (Figure 1). The test driver performs several handling maneuvers and based on these tests, rates the tire handling behavior. This is repeated for different tires while keeping all other conditions (vehicle, driver, environment, road, and maneuver) as constant as possible, to relate the handling differences directly to tire differences. This tire handling subjective assessment method provides the valuable test driver's opinion about the realistic tire handling performance to tire manufacturers or car magazines, but gives little insight in how this opinion is formed.



Figure 1. Test vehicle used for this research.

Insight in how this driver opinion is formed can often not be derived from overall handling performance measures, because this is influenced by the inherent compensating nature of a driver. That a human controller adapts its behavior to the dynamics of the controlled system was already recognized by McRuer and his fellow researchers in the early sixties of the previous century (McRuer et al. 1965; McRuer & Krendel

1959a; McRuer & Krendel 1959b) where pilot behavior was modelled based on linear control theory. This is in accordance with general human control behavior later found by several researchers and summarized by Jagacinski & Flach (Jagacinski & Flach 2003). This adapting effect is also found in vehicle handling, for example in a study of Vos et al. (Vos, de et al. 1999) where vehicle handling conditions were manipulated by varying lane width and rear tire pressure, resulting in different vehicle understeer behavior. Despite these varying handling conditions, drivers were able to maintain a constant performance level by adapting their control behavior, in this case steering effort. Subjective assessment revealed higher ratings for lower steering effort, which indicates a negative correlation between the amount of adaptation or driver effort required to keep the performance up and the subjective rating. This compensating driver behavior was also found by De Waard (Waard, de 1996), who described task performance and drivers workload as functions of task demand. Especially the identified 'task related effort region' is of interest here: to keep the task performance high for increasing task demand (for example, driving a handling maneuver at the same speed with a less good handling vehicle), the driver has to put in more effort, increasing his or her workload, to keep the performance on the same high level (driving the maneuver at the same speed as the better handling vehicle).

To get more information on how the driver's opinion is formed, the driver's steering is modelled with three different driver models with parameters reflecting driver effort and workload, which can be related to subjective evaluation (Abe et al. 2009). The parameters values are analyzed to see if they can explain the adaptive behavior of the driver. This method, together with the performed field experiment, is explained in the next section. The results are described in section 3 and discussed, followed the conclusions in section 4.

2 METHOD

This paper analyses a method derived in previous research (Monsma 2015) to provide information on how drivers perceive tire handling by modeling and simulating the driver in closed-loop handling assessments based on field experiments and analyzing the fitted driver model parameters. The assumption is made, that the driver adapts to changing task demands due to driving a handling maneuver with different tires and speeds, and that this adaptation is reflected in changing driver model parameters. In addition, a negative correlation is assumed: the more driver adaptation required, the more workload, the lower the tire handling is rated.

For this method, a field experiment was performed, consisting of two groups of test drivers: one group of two professional tire test drivers of a tire manufacturer and one group of eight non-professional, but highly skilled drivers, representing car magazine test drivers. The handling maneuver driven was a double lane change conform ISO (ISO 1999), but with a larger offset between the lanes to increase the difficulty. This maneuver was driven several times by each driver with 3 different tires (referred to as tire 2, 5 and 6, with increasing mean rated value of the overall handling performance) and at two different defined speeds, to impose different task demands on the driver. The speeds were chosen per driver group in such a way that the drivers acted in the task related effort region, meaning that the drivers could keep the task performance on a high level (hitting no cones), but the mental workload (indicated by each driver for each maneuver) for the two different speeds was respectively low and high. This resulted in a total of 360 double lane changes used for this research.

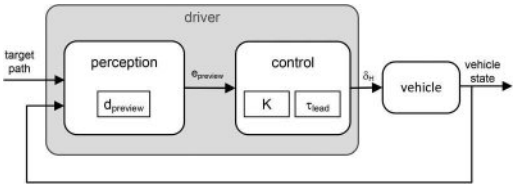


Figure 2. Driver model A with three adaptable driver parameters.

The mental workload or perceived effort of the driver was self-assessed by each driver after driving the double lane changes for one tire on one speed by indicating this on the rating scale mental effort (Zijlstra & Doorn 1985). This validated the assumption that the mental workload was negatively correlated with the tire handling rating: in general, the highest perceived mental workload corresponded with the lowest tire handling rating and vice versa.

For simulating the driver, three different driver models were implemented, referred to as A, B and C.

2.1 *Driver model A*

Figure 2 shows driver model A with two parts, a perception part and a control part with a total of three adaptable driver model parameters.

The target path is a continuous path the driver wants to follow, which is taken as the average of all driven double lane changes of that driver. The middle line of the first lane is taken as the global X-axis. Based on this target path and the actual vehicle position and orientation the preview error $e_{preview}$, is derived as shown in Figure 3. The only parameter of this perception part is the driver's preview distance $d_{preview}$.

The driver control part is the quasi-linear model (McRuer & Krendel 1959a; McRuer & Krendel 1959b), which is often used as driver model (Plöchl & Edelmann 2007) and which is described in the Laplace domain as:

$$H(s) = \left(\frac{e^{-\tau s}}{\tau_N s + 1}\right) \cdot \left(\frac{K(\tau_{lead} s + 1)}{\tau_{lag} s + 1}\right) \quad (1)$$

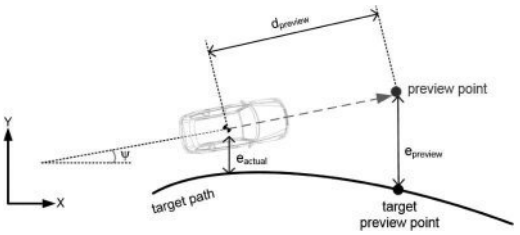


Figure 3. Continuous target path with one parameter $d_{preview}$.

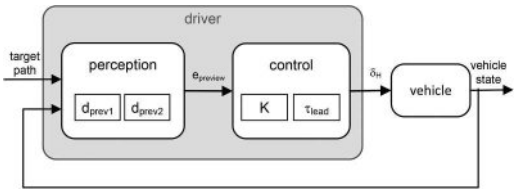


Figure 4. Driver model B with four adaptable driver parameters.

The term in the first parenthesis represents inherent human limitations, a reaction time delay τ and neuromuscular lag time constant τ_N. Both values are set to the average value between limits found in literature, giving 0.15 s for τ and 0.06 s for τ_N. The term in the second parenthesis represents human adaptive behavior, consisting of a gain K, a lag time constant τ_{lag} and a lead time constant τ_{lead}. As τ_{lag} has limited influence for the steering task modeled here, this value is set to 0.08 s. The adaptable parameters of this control part are therefore K and τ_{lead}.

2.2 *Driver model B*

Driver model B (Figure 4) differs from driver model A in the perception part.

Driver model B has a target path, which is defined as the middle position between the cones of every lane. This results in a discrete path with only two Y-positions: the middle of the first and last lane and the middle of the second lane. The point where the driver focuses on the next lane target path, before actually reaching it, is implemented in two driver model parameters: d_{prev1} and d_{prev2} as shown in Figure 5. The preview error $e_{preview}$ is derived similar to the continuous target path of driver model A.

2.3 *Driver model C*

Driver model C is based on driver model B, but it has additional driver experience modeled, see Figure 6.

The driver experience is implemented as a feedforward part that models the basic steering control necessary for performing a double lane change with two consecutive and opposite sine waves starting when the driver shifts focus to the other lane. The adaptable parameters for this part are the sine period T_{sine} and

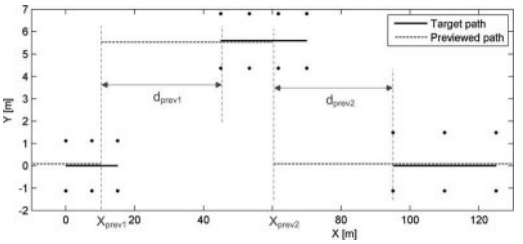


Figure 5. Perception part with discrete target path with two parameters d_{prev1} and d_{prev2}.

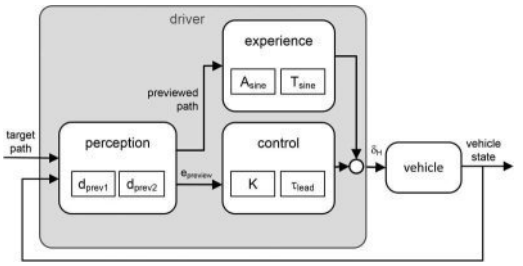


Figure 6. Driver model C with six adaptable driver parameters.

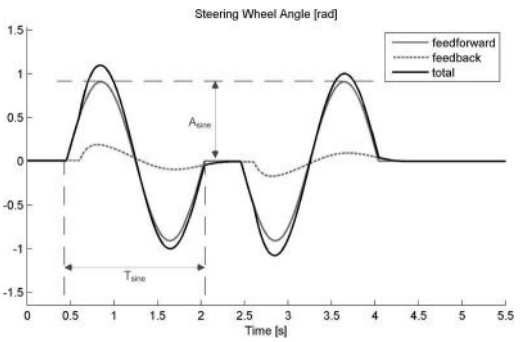


Figure 7. Steering wheel angle output as sum of feedforward and feedback steering wheel angle.

amplitude A_{sine}. The output steering wheel angle is the sum of the feedforward and the feedback part, see Figure 7.

2.4 *Parameter estimation*

The driver model parameters were estimated by performing closed loop simulations with a validated vehicle model including the different Magic Formula tire models of the different tires used. For each maneuver, the adaptable parameters of each driver model A, B and C are estimated by taking the optimal values for these parameters so that the model outputs, i.e. the steering wheel angle δ_H and the driven path Y of the vehicle, fits the measured output best in the least squares sense. Because the driver parameters are not independent, the set of optimized parameters is

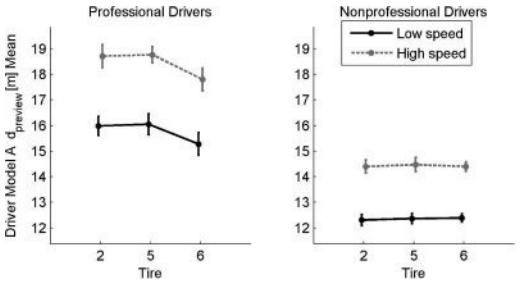


Figure 8. Mean values of the preview distance $d_{preview}$ of driver model A, grouped by drivers group, tire and speed.

not unique. By fitting these two signals at the same time to the measured signals, the variation in the set of optimized driver parameters is reduced to values representing more realistic behavior. This estimation resulted in 360 × 3 sets of optimal model parameters, one for each double lane change, for each driver model A, B and C.

3 RESULTS AND DISCUSSION

For analyzing the results, the mean values of all driver model parameters were analyzed grouped by the three independent variables: drivers group, speed and tire. The mean values were plotted with an error bar representing the standard error of the mean, which indicates how accurate the estimation of the mean is likely to be. The variables speed and tire are manipulated to influence the driver's task demand and therefore the driver's mental workload or adaptation. Because this is done in the task related effort region, the driver will increase his workload, puts in more effort to keep the performance at the high level.

For the analysis, a driver model parameter is considered speed dependent, if the mean values for low speed are all higher or lower than the mean values for high speed. High speed corresponding with high driver's workload or adaptation and low speed with low workload or adaptation. A driver model parameter is considered tire dependent, if the mean values monotonically increase or decrease for respectively tire 2, 5 and 6, for both speed demands, corresponding to decreasing workload for the tires. An example is given in Figure 8, where the mean value of the driver parameter preview distance $e_{preview}$ of driver model A is shown, grouped by drivers group, speed and tire.

The figure shows that for both drivers groups the preview distance of driver model A is speed dependent: a higher speed gives a larger preview distance. This parameter is not tire dependent, as it is almost constant between tires, with the exception of tire 6 for the professional drivers group. The small error bars indicate a high accuracy of the estimation of the mean.

A complete presentation and analysis of all driver parameter results would not fit in this paper, therefore a summary of the most important results is given. This analysis also included another driver parameter, the preview time, which is the preview distance multiplied with the driven speed. For all driver models, this showed to be a strong speed dependent parameter having all values higher (model A) or lower (model B and C) for higher speed and no overlap in error bars. This indicates in both cases (for continuous target path of model A and discrete target path of model B and C) that the drivers 'look ahead' more than only compensating the higher speed. This anticipation is also modelled by the lead term time constant τ_{lead}. This driver parameter shows speed dependency for all driver models for the nonprofessional drivers group, but only for model B for the professional drivers group. Analyzing these two mutual dependent driver model parameters revealed indeed this compensating behavior for the professional drivers group: a relative high preview time was accompanied by a relative low lead term constant. This could indicate that an increased look ahead distance has the same function as anticipating. Mutual dependency is also seen for gain and preview distance and for driver model C parameters gain and A_{sine} Speed dependence is also seen for the gain and preview distance of driver model A and the period T_{sine} of driver model C, which is as expected, as for higher speed the steering should be faster.

Tire dependency of the driver model parameters is less than for the speed dependency, as is as expected, because the differences in task demand between different speeds is much higher than between different tires. Overall tire dependencies of the parameters are seen more for the professional drivers than for the nonprofessional drivers. Where the preview times all showed strong speed dependency, this is not seen for tire dependency, only for driver model A the preview time shows some tire dependency. The lead term time constant of driver model B is having tire dependency for all drivers. The period T_{sine} shows tire dependency for the professional drivers.

This research confirmed previous research (Monsma & Oort, van 2010; Jagacinski & Flach 2003) that the lead term time constant is a good candidate for representing driver's workload or adaptation related to the tire handling subjective evaluation. As stated, the driver model parameters were chosen to represent relevant, realistic driver behavior, to be able to explain the adaptation of the driver. This also implied that the driver model parameters were not mutually independent, which can cause parameter values compensating each other as Pauwelussen showed in his research (Pauwelussen 2012) for driver parameters preview distance and steering gain. As this also represents real driver behavior, this can give more insight, but can give unambiguous results. Care should be taken for such mutually dependent parameters, like the preview time and the lead term time constant as they could compensate each other. On the other hand, this could very well be also the case in real driver behavior, where different drivers could use different mechanisms for adaptation. By analyzing them in combination, this problem can be dealt with. Another option could be to make one parameter constant, so that all adaptation is done within the other parameter. For modeling the driver adaptation to tires, driver model B seems to be

a good compromise: having a simple, realistic perception part using a discrete preview path, but also having less driver model parameters than model C.

4 CONCLUSION

This research showed that driver adaptation is related to perceived tire handling behavior reflected in subjective assessments. This driver adaptation was modelled with three driver models to give more insight in how this driver opinion is formed. For the relative large driver adaptation to speed all three models for both driver groups reflected the driver adaptation. For the relative small driver adaptation for different tires, model B reflected the driver adaptation well for both driver groups in the driver parameter lead term constant τ_{lead}. Dependency of model parameters can make parameters compensate each other, making the results less clear. Analyzing the parameters in combination could clarify this and could give an indication of how the driver's perception works.

REFERENCES

Abe, M., Kano, Y. & Shibahata, Y., 2009. Driver model based vehicle handling quality evaluation. *IAVSD*.

Von Glasner, E.G. & Ahlgrimm, J., 2011. The influence of tyre characteristics on the dynamic performance of vehicles. In *13th European Automotive Congress, EAEC*. Valencia, Spain.

ISO, 1999. ISO 3888-1:1999(E) passenger cars – Test track for a severe lane-change manoeuvre – Part 1: Double lane change.

Jagacinski, R.J. & Flach, J., 2003. *Control theory for humans: Quantitative approaches to modeling performance*, CRC.

McRuer & Krendel, 1959a. The human operator as a servo system element Part I.

McRuer & Krendel, 1959b. The human operator as a servo system element Part II.

McRuer, D.T. et al., 1965. Human pilot dynamics in compensatory systems.

Monsma, S., 2015. Feel the Tire – Tire Influence on Driver's Handling Assessment.

Monsma, S. & Oort, van, M.J.M., 2010. Subjective evaluation of handling behaviour related to tyre dependent driver parameters. In *AVEC*. Loughborough, UK, pp. 574–597.

Pauwelussen, J.P., 2012. Dependencies of driver steering control parameters. *Vehicle System Dynamics*, 50(6), pp. 939–959.

Plöchl, M. & Edelmann, J., 2007. Driver models in automobile dynamics application. *Vehicle System Dynamics*, 45(7), pp. 699–741.

Vos, de, A.P., Godthelp, J. & Käppler, W.D., 1999. Subjective and objective assessment of manual, supported, and automated vehicle control. *Vehicle Performance: Understanding Human Monitoring and Assessment*, pp. 97–120.

Waard, de, D., 1996. *The measurement of drivers' mental workload*. University of Groningen.

Zijlstra, F. & Doorn, L. Van, 1985. *The construction of a scale to measure perceived effort*.

Special vehicles

Advanced Vehicle Control – Edelmann, Plöchl & Pfeffer (Eds)
© 2017 Taylor & Francis Group, London, ISBN 978-1-138-02992-7

Intelligent based terrain preview controller for a 3-axle vehicle

J.T. Economou, D.J. Purdy, D. Galvão Wall, D. Diskett & D. Simner
Centre for Defence Engineering, Cranfield University, Defence Academy of the United Kingdom, Shrivenham, Swindon, UK

ABSTRACT: ABSTRACT: The paper presents a six-wheel half longitudinal model and the design of a dual level control architecture. The first (top) level is designed using a Sugeno fuzzy inference feedforward architecture with and without preview. The second level of controllers are locally managing each wheel for each axle. As the vehicle is moving forward the front wheels and suspension units will have less time to respond when compared to the middle and rear units, hence a preview sensor is used to compensate. The paper shows that the local active suspensions together with the Sugeno Fuzzy, (locally optimised using subtractive clustering), Feedforward control strategy is more effective and this architecture has resulted in reducing the sprung mass vertical acceleration and pitch accelerations.

1 INTRODUCTION

The design of conventional, passive, suspension systems is reaching a limit for high speed off-road conditions. One of the main users of fast off-road vehicles is the military, where it has shown (Sher et al. 1988) that one of the main contributors to survival is vehicle speed. A possible way of increasing the vehicle speed while reducing the vibration exposure of the crew is the use of an active suspension system combined with terrain preview. In a review of the literature (Sharp et al. 1995) it was noted that the use of terrain preview (Purdy et al. 2010, Kiyotsugu 2003) together with an active suspension system would need to be used on "special test surfaces" for example; very rough (off-road) to be of any benefit. In this work a three axle military vehicle, Figure 1, is used to investigate the possible benefits of a Sugeno (Feng 2006, Tagaki et al. 1985) based Fuzzy controller (using subtractive clustering) (Economou et al. 2006) to improve its performance at isolating the crew from the terrain. This work extends that done by (Mehrishi 2007, Berrouila 2008, Bo 2010, Purdy et al. 2010) and (Purdy et al. 1997). Fuzzy Logic is a universal approximator, which enables modelling of complex process by input-output maps via a rule-base approach. In (Feng 2006) the historical ambiguity of fuzzy systems, although very successful in a wide range of industrial applications, is restored showing a state of the art survey of results offering not only guaranteed stability but also good performance. In (Economou et al. 2006), the use of optimization is explored in relation to fuzzy consequent variants and the derivation of the membership functions in relation to input–output data demonstrating that the fuzzy rules can be obtained in the presence of data. Hence the proposed fuzzy rule base (membership functions for example) are optimsed using fuzzy clustering methods as used in (Economou et al. 2006). The use of fuzzy logic in this paper is based on the Sugeno singleton fuzzy inference framework (Tagaki et al. 1985) providing bump-stop prediction based on look ahead terrain sensing Figure 1. This approach enables the use of a look ahead distance and thus time for a given vehicle velocity while acting at a pre-selected time depending on the suspension dynamics. This although in first instance appears similar to observer based solutions it differs because it prepares the vehicle to respond as well as possible for given known terrain profiles. The proposed control architecture results in the reduction of the sprung mass vertical accelerations (vertical, pitch) which consequently results in reducing the risk to injury to the vehicle passengers (Barnaby et al. 2009).

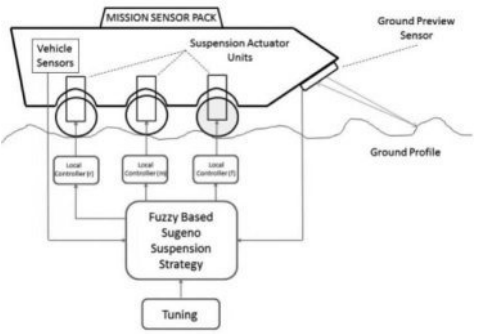


Figure 1. Overview of the dual level control architecture.

It is shown in this paper that the use of fuzzy Sugeno (using subtractive clustering) feedfoward control architecture with preview data together with the active suspension system results in reducing the vertical and pitch sprung mass accelerations. Furthermore

the analysis demonstrates the effect of the preview distance in relation to the controller performance.

2 THEE AXLE VEHICLE MODELLING

The active suspension for a single actuator system is shown in Figure 2, while the vehicle suspension for the tree axle vehicle system schematic is shown in Figure 3 respectively.

The vehicle model is based on the single wheel station model given in (Purdy et al. 1997) and used by (Mehrishi 2007, Berrouila 2008, Bo 2010, Purdy et al. 2010). The vehicle model is restricted to eight degrees of freedom, these being pitch and bounce of the vehicle body, vertical motion of each axle and one for each actuator, and is in effect a half vehicle model. The model is developed so that the simulation can be run with any combination of the suspension actuators being passive or active.

The suspension actuator is shown diagrammatically in Figure 2. In this diagram the motion of the top of the actuator is z_1 and the bottom z_2, the mechanical stiffness k_d, flow restriction through the damper valve R and the floating and piston areas a_d and a_p respectively. The oil in the device is assumed to be incompressible.

Letting the motion across the actuator be:

$$z_w = z_1 - z_2 \tag{1}$$

The force generated by the actuator is:

$$f_a = a_p P_2 \tag{2}$$

where P_2 is the pressure above the piston.

The flow into the actuator:

$$q = \dot{\eta} a_d + \left(P_1 - P_2\right)/R \tag{3}$$

Where $\dot{\eta}$ is the motion of the floating piston and P_1 is the pressure between the damper valve and the floating piston, which is given by:

$$P_1 = \eta k_d / a_d \tag{4}$$

The flow through the damper value is given by;

$$\dot{z}_w a_p = \left(P_1 - P_2\right)/R \tag{5}$$

These equations are manipulated to give the equations of motion for the actuator with the addition of bump and rebound stops to limit the suspension travel.

The validation of the actuator model and data for the active suspension system, as a single wheel station, has been taken from (Mehrishi 2007).

The individual actuator model has been used in a half vehicle model with three axles as shown in Figure 3. The wheel stations have been numbered with the front one being number 1. The bump stops are shown and the tyres are modelled with by a linear spring k_t, which is capable of leaving the ground and the unsprung, axle, mass is given by m_u. The list of symbols is shown in Table 1.

Table 1. Nomenclature, list of symbols.

Symbol	Explanation
m_s	Vehicle sprung mass
m_{u_i}	Vehicle unsprung mass for i-th axle
q_i	Servo flow for i-th damper
z_s	Sprung mass vertical displacement
z_{u_i}	Axle vertical displacement for i-th axle
$z_{z_{t_i}}$	Tyre verical displacement for i-th wheel
z_{s_i}	Spring displacement for i-th wheel
z_{g_i}	Vertical ground displacement
v	Vehicle forward velocity
x_p	Preview distance
i	Wheel/axle/suspension index {1, 2, 3}
k_t	Tyre stiffness
k_d	Spring stiffness
k_b	Bump-stop stiffness
R	Damper valve restriction
a_p	Lower piston area
a_d	Top piston area
z_{s_i}	i-th spring vertical displacement
$z_{sus_{max}}$	Suspension maximum displacement
x_i	Axle distance from C.G.
I_s	Sprung mass inertia
$\Lambda(z_{gi})$	Tyre force
P_i^2	Pressure at top section for i-th suspension
P_i^1	Pressure at lower section for i-th suspension

For the vehicle sprung mass the following equation applies (body bouncing motion):

$$m_s \ddot{z}_s = -\left(F_{s_1} x_1 + F_{s_2} x_2 + F_{s_3} x_3\right) + m_s g \tag{6}$$

For the vehicle sprung mass the following equation applies (body pitch motion):

$$I_s \ddot{\theta} = F_{s_1} x_1 + F_{s_2} x_2 + F_{s_3} x_3 \tag{7}$$

For the vehicle unsprung mass the following equation applies:

$$m_{u_i} \ddot{z}_{u_i} = F_{s_i} + \left(\frac{m_u}{i}\right) g - k_t \Lambda(z_{g_i}) \tag{8}$$

The suspension motion displacements, velocities and accelerations are given from for each wheel station $i = \{1, 2, 3\}$ from the following equations:

$$\begin{cases} z_{s_i} = z_s - x_i \theta \\ z_{w_i} = z_{s_i} - z_{u_i} \end{cases} \tag{9}$$

$$\begin{cases} \dot{z}_{s_i} = \dot{z}_s - x_i \dot{\theta} \\ \dot{z}_{w_i} = \dot{z}_{s_i} - \dot{z}_{u_i} \end{cases} \tag{10}$$

$$\begin{cases} \ddot{z}_{s_i} = \ddot{z}_s - x_i \ddot{\theta} \\ \ddot{z}_{w_i} = \ddot{z}_{s_i} - \ddot{z}_{u_i} \end{cases} \tag{11}$$

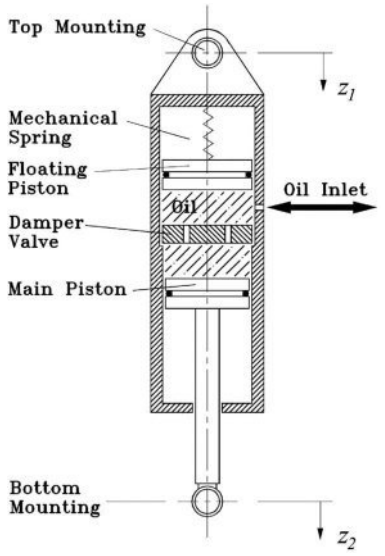


Figure 2. Active suspension actuator.

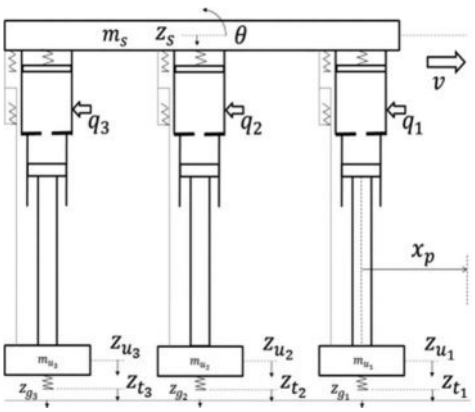


Figure 3. Axle forces for a dual bump road surface.

Based on the flow continuities the following expressions are valid for each actuator:

$$q_i R = \dot{z}_{s_i} a_d R + (P_1^i - P_2^i) \tag{12}$$

$$P_1^i = \frac{z_{s_i} k_d}{a_d} \tag{13}$$

3 VEHICLE MODELLING SIMULATION

Firstly, the vehicle is simulated for the same input profile with a passive suspension for all three axles. Thereafter the vehicle is run for the same road displacement (disturbance) with a proportional gain controller with the ride height set to zero for all three axles and lastly with the addition of a sprung mass acceleration feedback for all three axles.

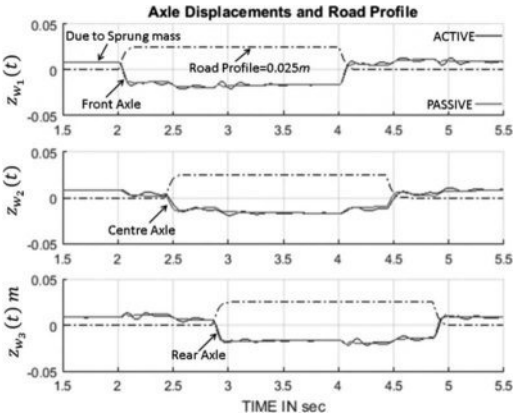


Figure 4. Without preview: axle displacements and road profile for axles 1, 2, 3 respectively (passive and active suspension).

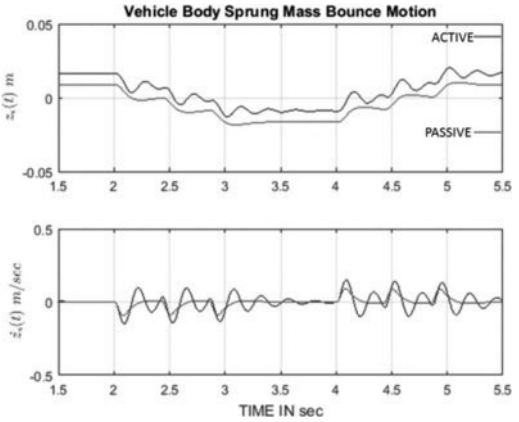


Figure 5. Without preview: vehicle sprung mass characteristics (passive and active suspension).

The axle controllers are local to the axle and fixed to the three different settings for three vehicle simulation runs. The block diagram in Figure 7, represents the local controllers together with the feedforward Fuzzy Sugeno control architecture (with/without terrain preview).

The results for running the vehicle for the same road input for three different suspension conditions (i.e. passive suspension, and active suspension) are summarised in Figures 4, 5 and 6. Note that the road input $z_{g_i} < 0$ for bumps and positive for portholes as indicated in Figure 4.

The body sprung mass is much more effective when appropriately tuned with the ride height local controller K_{p_i} and the sprung mass acceleration at point 1 gain K_{q_i}. For the results shown in Figures 5, 6 and 7 the local controllers for each axle are identical.

Clearly the active suspension for all three axles results in a reduced pitch acceleration with an improved settling time as shown in Figure 6.

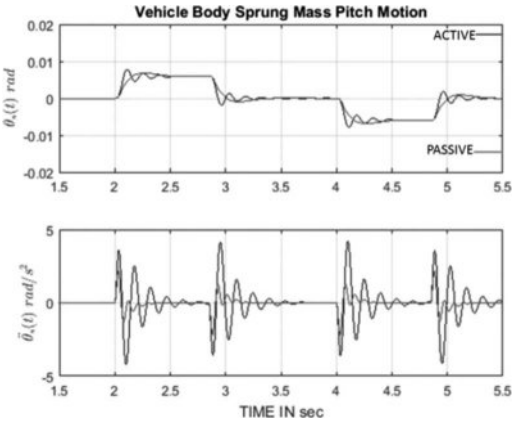


Figure 6. Without preview: vehicle sprung mass pitch motion (passive and active suspension).

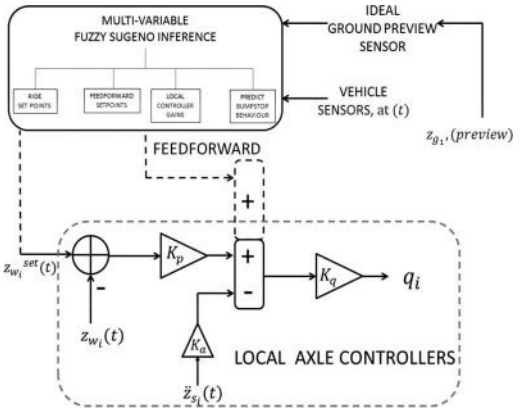


Figure 7. Fuzzy Sugeno Architecture with Local Controllers.

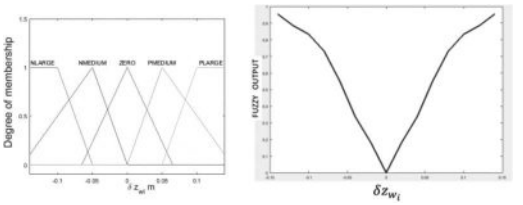


Figure 8. Fuzzy Sugeno Bumpstop Membership Functions and Output.

4 SUGENO FUZZY LOGIC STRATEGY

The Sugeno fuzzy inference design framework was utilised for two separate cases: Firstly, it was used to predict bumpstops using the look ahead sensor while running a vehicle model in advance of the real vehicle reaching the bumps. Secondly, it was used for the design of the feedforward fuzzy Sugeno controller with and without a preview sensor.

For both cases the local conventional control units are active. For the second case the fuzzy Sugeno feedfoward based control strategy wass implemented with the option of the preview being on or off for a range of parametric preview distance settings. In (Kiyotsugu 2003) the authors preduced a servo-motor preview controller for a servo-mechanism. The control method was based on an H^{∞} with preview for different preview times. For all inputs the system will settle within 60 steps while the preview was ranged between one to 10 steps.

The method in (Kiyotsugu 2003) indicated that as the preview was increased the system response was improved, however the input was a step and was lacking the complexity of the multi-axles responses affecting each other. To address this specific challenge the feedforward fuzzy Sugeno controllers used in this paper have a similarity with the control law shown in (Kiyotsugu 2003), whereby (T) is the time corresponding to the preview time in relation to the running time (t):

$$u_i^{ff}(t) = w_i^1 . F_s^z\left(z_{g_i}^f(T)\right) + w_i^2 . F_s^\theta\left(z_{g_i}^f(T)\right) \qquad (14)$$

w_i^1, w_i^2: are the control weights for the fuzzy Sugeno vertical acceleration and body pitch acceleration controllers: $F_s^z(z_{g_i}^f(T))$, $F_s^\theta(z_{g_i}^f(T))$ respectively. The local sensors per suspension unit (feedback, active suspension) is tuned without considering the preview data.

Hence the overall control law for each axle (i) is given from:

$$\widetilde{u_i}(t) = u_{fb}(t) + u_i^{ff}(t) =$$

$$\widetilde{u_i}(t) = \ddot{z}_{s_i}(t).K_a + \left(z_{w_i}^{ref}(t) - z_{w_i}(t)\right).K_p \quad + \left\{w_i^1 . F_s^z\left(z_{g_i}^f(T)\right) + w_i^2 . F_s^\theta\left(z_{g_i}^f(T)\right)\right\} \qquad (15)$$

It is expected that as the vehicle speed increases the preview controller will offer a better vehicle rynamic response.

The Sugeno fuzzy inference was also the basis for predicting bumps by using the look-ahead sensor. This was mainly utilised by running a model of the vehicle ahead of time (in relation to the preview sensor). This provides useful information in relation to what would happen to the vehicle accelerations ahead of time. Figure 8 shows the membership functions and input/output characteristic of the bumbstop. Instead of simple logic the advantage for using the fuzzy logic method is smoother results as the suspension enters the bumpstop region.

Regarding the fuzzy controllers: $F_s^z(z_{g_i}^f(T))$ and $F_s^\theta(z_{g_i}^f(T))$ model data were used to identify the number of necessary membership functions using the subtractive clustering method as also applied in (Economou et al. 2006). Therefore the fuzzy Sugeno based control system takes into account both the sprung mass acceleration in relation to the bumps as

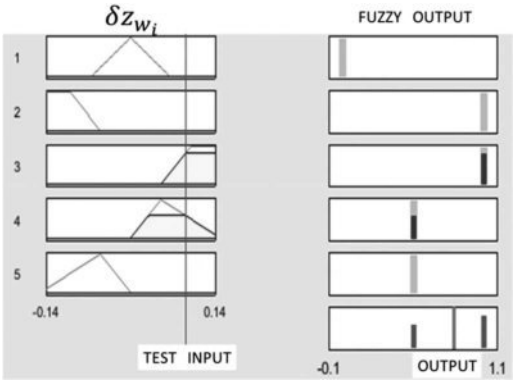


Figure 9. Fuzzy Sugeno Bumpstop Membership Functions and Singleton Outputs.

seen from the preview sensor. For a generic input variable vector: $z = [z_r^i, z_m^i, z_f^i]$, whereby z_r^i represents the rear i-th sensor.

The Sugeno paremetrisation in the form of a rule base can be shown using the following expression (valid for $i = 1$):

$$Rule\ i\text{: } IF\ z_r^1(t) is\ \mu_{i1}(z_r^1) AND\ z_m^1(t)\ is\ \mu_{i1}(z_m^1) AND.. \\ ..z_r^1\ is\ \mu_{i1}(z_r^1) \quad THEN \quad y_i = b_i \tag{16}$$

Therefore each Sugeno decision, (16), depends on both vertical sprung vehicle mass acceleration and sprung mass pitch angular acceleration. The membership functions: $\mu_{i1}(z_r^1), \ldots, \mu_{i1}(z_m^1)$ are optimised using the subtractive clustering method.

Lastly, in order to capture the fusion of multiple rules being fired at the same time (but potentially at a a different degree) we would need to utilize the defuzzification process described in equation (17):

$$y^*(t) = \frac{\sum_{i=1}^{max} \beta_i . y_i(t)}{\sum_{i=1}^{max} \beta_i} \tag{17}$$

However, expression (17) can be rewritten in terms of the membership functions instead of the firing strengths, equation (18):

$$y^*(t) = \frac{\sum_{i=1}^{max} \{\mu_{i1}(z_r^1) \wedge \mu_{i2}(z_m^1) \wedge \mu_{i3}(z_r^1)\} . y_i(t)}{\sum_{i=1}^{max} \{\mu_{i1}(z_r^1) \wedge \mu_{i2}(z_m^1) \wedge \mu_{i3}(z_r^1)\}} \tag{18}$$

The advantage of the expression in equation (18) is the instant response whereby combined with the feedforward and sensor look-ahead strategy offers a better overall response. Hence:

$$y^*(t) = \left\{ F_s^z \left(z_{g_i}^f(T) \right),\ F_s^\theta \left(z_{g_i}^f(T) \right) \right\} \tag{19}$$

Figures 10(a),10(b), show the vertical and pitch sprung mass accelerations respectively in relation to the road filtered disturbance. A second order filter was used to smooth the disturbance profile and therefore remove

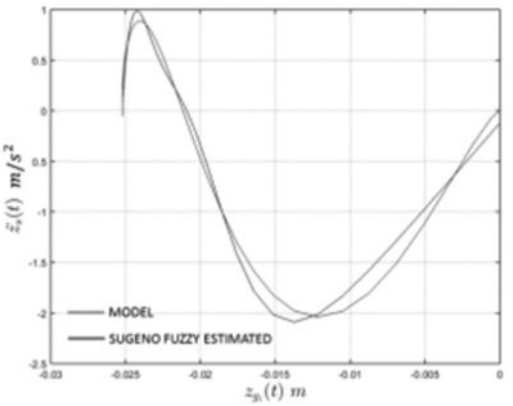


Figure 10(a). Vehicle Sugeno Fuzzy Estimated and Reference Model Comparisons (Vertical Sprung Mass Acceleration and Road Disturbance).

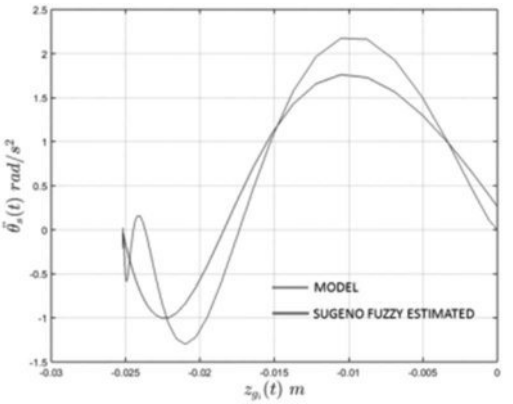


Figure 10(b). Vehicle Sugeno Fuzzy Estimated and Reference Model Comparisons (Pitch Angular Sprung Mass Acceleration and Road Disturbance).

and rapid transitions, equation 17 (where γ is the dc correction gain).

$$\frac{z_{g_i}^f(s)}{z_{g_i}(s)} = \frac{\gamma . \omega_n^2}{s^2 + 2\zeta\omega_n . s + \omega_n^2} \tag{20}$$

The model, fuzzy estimated phase portrait is shown in Figure 10(c).

5 SIMULATION RESULTS

The vehicle look-ahead sensor system prepares the tuned active suspension system in advance of the ground disturbances. Figure 11 shows a range of simulation results. The blue line shows the reference/nominal accelerations as a benchmark. The remaining three (green, red, magenta), show the vehicle's response with the Sugeno fuzzy feedforward controllers for increasing preview distance. The Sugeno

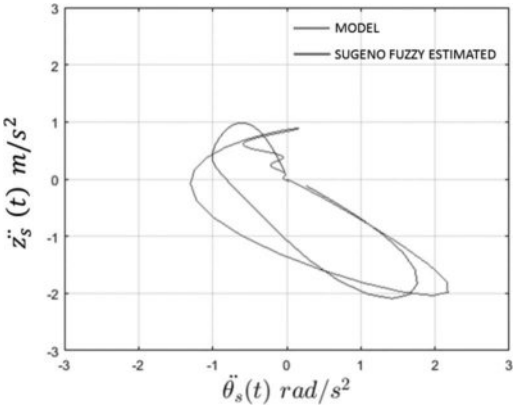


Figure 10(c). Phase Portrait – Vehicle Sugeno Fuzzy Estimated and Reference Model Comparisons (Vertical, Pitch Sprung Mass Accelerations).

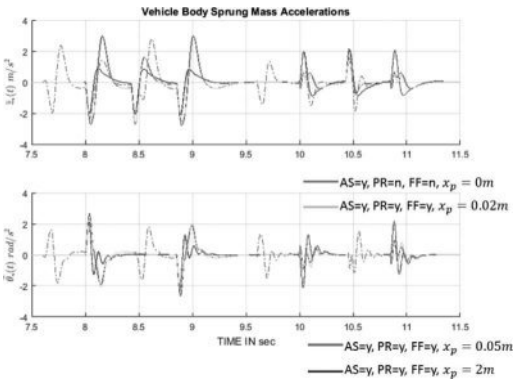


Figure 11. Vehicle Sprung Mass Accelerations with Variable Preview Distance x_p.

fuzzy controllers are locally optimised using the subtractive clustering algorithm (Economou et al. 2006).

Clearly, the active suspension system performs well. The control strategy with the 2 m preview (fuzzy Sugeno feedforward) for the given distance overreacts thus creating controller based oscillations after 9.5 s.

As per (Donohew et al. 2009) these need reducing in order to retain passenger comfort. The preview controller's response for a reduced preview distance has resulted in a much better range of accelerations especially for $x_p = 0.02$ m.

6 CONCLUSIONS

A two-level intelligent based controller architecture is developed for a non-linear 3-axle single line vehicle model travelling on a rough terrain. The simulation results show the passive suspension, active suspension without and with a feedforward preview controller incorporating a prediction of bump stops ahead of the vehicle. The subtractive clustering optimisation algorithm was utilised to obtain the Sugeno fuzzy feedforward gains in relation to the road disturbances. The results showed that the look ahead distance is a critical parameter which affected the results.

For short look ahead distance the feedforward Sugeno fuzzy controllers could prepare the suspension and therefore the sprung mass vertical acceleration and pitch angular acceleration was improved. However, as the model was run for much larger preview distances for the given vehicle velocity the preview feedforward Sugeno fuzzy controller was over-compensating thus resulting in adverse accelerations effects.

REFERENCES

Berrouila, L., 2008. Experimental and Theoretical Investigations of Active Suspension with Preview Control, *MSc Thesis*, Cranfield University, CDS Shrivenham.

Bo, F., 2010. Implementation of a fuzzy logic terrain preview controller on the active suspension rig, *MSc Thesis*, Cranfield University, SoE.

Donohew, B.E. & Griffin, M.J. 2009. Motion Sickness with Fully Roll-Compensated Lateral Oscillation: Effect of Oscillation Frequency. *Aviation, Space, and Environmental Medicine*, 80 (2).

Economou, J.T. & Colyer, R.E., 2006. Fuzzy-hybrid modelling of an Ackerman steered electric vehicle. *Elsevier International Journal of Approximate Reasoning*, 41 (3): 343–368.

Feng, G. 2006. A survey on analysis and design of Model-Based Fuzzy Control Systems. *IEEE Transactions on Fuzzy Systems* 14 (5): 676–697.

Kiyotsugu Takaba, 2003. A tutorial on preview control systems. *SICE Annual Conference in Fukui*, Fukui University, Japan.

Mehrishi, S., 2007. Active Suspension system with preview for off road military wheeled vehicles. *MSc Thesis*, Cranfield University, CDS Shrivenham.

Purdy, D. J. & Bulman, D. N., 1997. An Experimental and Theoretical Investigation into the Design of an Active Suspension System for a Racing Car. I.Mech.E., *Journal of Automobile Engineering (Part D)*, 211: 161–173.

Purdy, D, Mehrishi, S & Berrouila, L., 2010. Design and Implementation of an active Suspension system with terrain Preview. *Proc. of FISITA*, F2010C126.

Purdy, D. J., Mehrishi, S. & Berrouila, L., 2010. Design and implementation of an active suspension system with terrain preview, *FISITA World Automotive Conference*, Budapest.

Sharp, R. S., 1995. In J. P. Pauwellussen and H. B. Pacejka (eds), *Preview control of active suspensions. In Smart Vehicles.* Swets and Zeitlinger, 166–182.

Sher, E., Refael, S & Luria, D., 1988. Agility and manoeuvrability as passive defence for armoured vehicles. *Proc. Inst. of Mech. Eng. part D, Journal of Automobile Engineering*, 202 (D1):65–70.

Takagi, T. & Sugeno, M., 1985. Fuzzy identification of systems and its applications to modeling and control. *IEEE transactions on systems, man, and cybernetics*, (1): 116–132.

Advanced Vehicle Control – Edelmann, Plöchl & Pfeffer (Eds)
© 2017 Taylor & Francis Group, London, ISBN 978-1-138-02992-7

Optimal control of lateral stability for articulated heavy vehicles based on adaptive dynamic programming approach

Bin Li & Subhash Rakheja
Department of Mechanical & Industrial Engineering, Concordia University, Montreal, Quebec, Canada

Zhijun Fu
College of Mechanical Engineering, Zhejiang University of Technology, Xiacheng, Hangzhou, Zhejiang, China

ABSTRACT: In this paper, a novel nonlinear optimal controller based on adaptive dynamic programming (ADP) is proposed to enhance lateral stability of articulated heavy vehicles. The proposed ADP based optimal controller uses a single neural network (NN) called critic to approximate a value function, and permits online updating of the control law with varying vehicle dynamic characteristics. The proposed controller is designed such that the actual vehicle states are forced to track the desired values via active braking considering model uncertainties. A braking torque distribution algorithm is subsequently used to generate the desired corrective yaw moment established from the ADP based controller. The effectiveness of the proposed controller is demonstrated through simulation results obtained under lane change maneuver in a co-simulation environment involving Matlab/Simulink and TruckSim. The simulation results show that the proposed controller is very effective in terms of improving lateral stability of articulate heavy vehicles in limiting driving conditions.

1 INTRODUCTION

Articulated heavy vehicles are the dominant mode of freight transportation via roads in North America and Europe [1]. Owing to their large sizes and inertia, and high mass center, articulated heavy vehicles exhibit relatively lower roll and yaw stability limits compared to other road vehicles, and thereby pose greater road safety risks. Most heavy vehicles experience three types of maneuver-induced instabilities: rollover, loss of control (LOC), and trailer yaw oscillations. While rollover is generally considered as the major safety concern for heavy vehicles, LOC is also a significant safety concern [2]. Loss of control is referred to the loss of lateral/yaw stability, jackknife or plow. Due to the unreasonably high fatal crashes and economic costs, there is an increasing need for improving the stability and safety of articulated heavy vehicles in academia and industry.

In the development of vehicle control systems for improving handling and stability performance, how to handle model uncertainties and nonlinearities is a challenging task. Like passenger cars, many active control methods have been used to improve the lateral stability of articulated heavy vehicles such as linear quadratic regulator (LQR) [3], sliding mode control [4] and adaptive control [5], while LQR control is the most implemented control algorithm. The main disadvantage of conventional optimal control lies in that the system model has to be known for solving Hamilton-Jacobi-Bellman (HJB) equation in an offline manner to find the optimal control law. And the control gains cannot be adaptive to uncertain vehicle parameters and external disturbances once they are determined. Vehicle dynamic control is known to be a nonlinear problem in nature because of the tire nonlinearity at limit driving conditions and the variations in vehicle parameters such as payload. Thus, an efficient control approach is needed to cope with uncertain vehicle dynamics with tire nonlinearity and parameter variations.

Recent research has shown that adaptive dynamic programming (ADP) based control, a novel approximate optimal control scheme, can overcome the requirement for an exact model and meanwhile achieve the optimal control, and a survey of these research can been found in [6]. Werbos [7] firstly introduced the general actor-critic (AC) framework for ADP-based optimal control design. The critic NN approximates the performance function, and the actor NN approximates an optimal control law and generates the actions or control signals. An online optimal control algorithm [8] with the ACI (actor-critic-identifier) architecture is proposed to solve the model uncertain continuous-time infinite horizon optimal control problem without the knowledge of system drift dynamics, but the knowledge of the input dynamics is required. Further, a simplified ACI structure are proposed in [9], where just one critic NN instead of the action-critic

dual network is used to approximate the solution of the HJB equation and calculate the optimal control action, which greatly simplifies the algorithm architecture. It should be noticed that most ADP based optimal control is studied for regulation problem rather than tracking problem. Very recent studies in [10] developed an optimal tracking control for model uncertain system in continue-time domain based on the complex action-critic dual network architecture. As far as we know, there is very limited ADP based optimal tracking control research for model uncertain system. Meanwhile, to the best of the authors' knowledge, ADP based controller design for vehicle stability control has rarely been touched, few recent studies can be found for the Anti-lock Brake Systems (ABS) controller design with ADP in [11].

In this paper, we proposed a novel optimal tracking control algorithm based on a single NN critic framework for solving the online optimal tracking problem of heavy vehicles, which simplifies the structure of the computation model and reduces the computational cost. The proposed controller forces the actual vehicle states are forced to track the desired values via active braking considering model uncertainties. A braking torque distribution algorithm is subsequently designed to generate the desired corrective yaw moment established from the ADP based controller.

The rest of the paper is organized as follows. Section 2 presents the vehicle model for controller design and simulations. In Section 3, the proposed ADP based optimal tracking control is given in detail. Simulation results are presented in Section 4. Finally, conclusions are made in Section 5.

2 VEHICLE DYNAMICS MODEL

In this section, two vehicle models are presented: TruckSim software platform for simulations and yaw-plane vehicle model for controller design.

2.1 *TruckSim software platform*

TruckSim is a parametric vehicle dynamics software used widely for simulating and analyzing the dynamic characteristics of medium to heavy trucks. The vehicles are characterized in datasets of mass properties, kinematic and compliance data, tire force and moment characteristics and powertrain, etc. It can simulate the vehicle performance with the designed controller in customer-specified driving scenarios. In this study, TruckSim is used to develop tractor semitrailer model, perform the validation of developed optimal controller in Simulink and provide the vehicle dynamic response.

2.2 *Yaw-plane vehicle model*

To study the dynamics in yaw plane of tractor semitrailer combination, a single track 4DOF vehicle model [12, 13], as shown in Figure 1, is used to generate the desired vehicle states for the control system design.

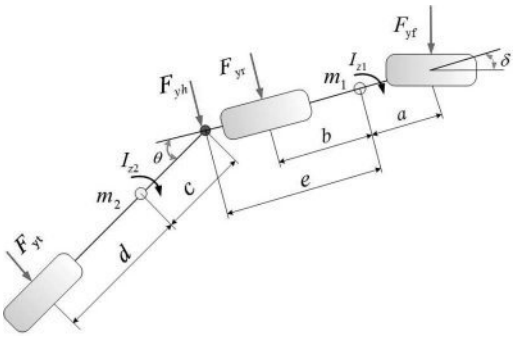


Figure 1. Simplified vehicle model in yaw plane.

In the model, the tires on each axle are lumped into a single tire at the center of each axle. It is assumed that the front steering angle δ, the articulation angle θ, and the tire slip angles are small. Furthermore, the aerodynamics' effect on the vehicle combination and roll motion are ignored. The equations of motion for the tractor and semitrailer are expressed as below.

$$m_1\left(\dot{v}_{y1} + v_{x1}\gamma_1\right) = F_{yf} + F_{yr} - F_{yh} \tag{1}$$

$$I_{z1}\dot{\gamma}_1 = aF_{yf} - bF_{yr} + eF_{yh} + \Delta M_t \tag{2}$$

$$m_2 a_{y2} = F_{yt} + F_{yh} \tag{3}$$

$$I_{z2}\dot{\gamma}_2 = cF_{yh} - dF_{yt} + \Delta M_s \tag{4}$$

where m_1 and m_2 are the mass of the tractor and semitrailer, respectively. v_{x1} and v_{y1} are the longitudinal and lateral velocity of the tractor. γ_1 and γ_2 are the yaw rate of the tractor and semitrailer, respectively. a, b, c, d and e are the vehicle characteristic lengths. a_{y2} is the lateral acceleration at the center of mass of semitrailer. ΔM_t and ΔM_s are the corrective yaw moment obtained from active braking control for tractor and semitrailer, respectively. q is the articulation rate. I_{z1} and I_{z2} are the yaw moment of inertia of tractor and semitrailer, respectively. F_{yf}, F_{yr} and F_{yt} are cornering forces developed by tractor front and rear, and trailer axle tires, respectively.

In this model, the following constraints are considered:

$$\gamma_2 = \gamma_1 + q \tag{5}$$

$$a_{y2} = \dot{v}_{y1} + v_{x1}\gamma_1 - e\dot{\gamma}_1 - c(\dot{\gamma}_1 + q) \tag{6}$$

The lateral forces developed at the tractor front and rear axle, and semitrailer axle wheels are assumed to be proportional to the tire slip angle. The details of tire lateral forces can be found in [13]. Combined Equation 1 through 6, the motion equation can be written in a matrix form:

$$M\dot{x} = Kx + B_1\delta + B_2 u \tag{7}$$

where M, K, B_1 and B_2 are the mass matrix, stiffness matrix and input matrices, respectively. δ is the front

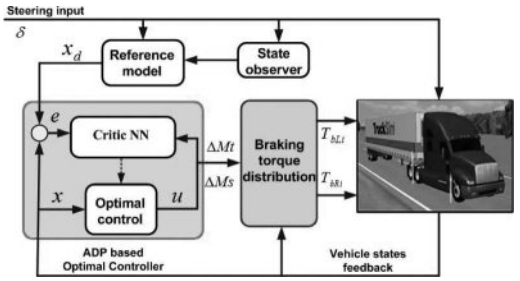


Figure 2. Schematic diagram of ADP based optimal control.

steering angle commanded by the driver. u is the control inputs, i.e, corrective yaw moments for tractor and semitrailer. x is the system state variables as below,

$$x = [v_{y1} \quad \gamma_1 \quad q \quad \theta]^T$$

To observe the dynamics of the model, the equation above can be converted into state space format, shown as

$$\dot{x} = Ax + E\delta + Bu \tag{8}$$

where $A = M^{-1}K$, $E = M^{-1}B1$, $B = M^{-1}B2$. The details of matrices A, E and B can be found in [13].

Note that the system (8) is actually a nonlinear system due to the time varying longitudinal speed included in the denominators of matrix components. Moreover, the uncertainties of tire cornering stiffness pose a challenge for the controller design.

3 ADP OPTIMAL CONTROLLER DESIGN

In this paper, an ADP approach based optimal controller is developed, aiming to improve the lateral stability of articulated heavy vehicles in limit driving situations. The proposed controller is designed in a manner that the actual vehicle responses are forced to track the desired responses obtained from linear vehicle model. The overall structure of the proposed control system is presented in Figure 2. The desired responses for articulated heavy vehicle is obtained on the basis of the reference vehicle model. The corrective yaw moments required to track the reference model are computed using an ADP based optimal controller. The brake torque distribution scheme is subsequently designed to produce the required corrective yaw moments. Once the corrective yaw moments are obtained, a braking torque distribution scheme is designed to optimally distribute the braking torque among different wheels. T_{bRi} and T_{bLi} refer to the braking torques applied to right-and left-track wheels.

3.1 *Reference vehicle model*

The main purpose of control system in this paper is to make the actual vehicle states follow the desired states response. In this section, a reference model is presented to produce the desired vehicle state. Based on the Section 2.2, the primary vehicle states associated with the lateral stability of articulated heavy vehicle are tractor lateral velocity, tractor yaw rate, articulation rate and articulation angle. In this study, the desired value of the primary vehicle states is considered as the steady state response of vehicle on high friction road to a steering command, which can be derived from Equation (8) below assuming there is no active control input.

$$x_d = [v_{yd} \quad \gamma_d \quad q_d \quad \theta_d]^T = A^{-1}E\delta \tag{9}$$

In the implementation, the desired tractor lateral velocity is set to zero. The desired tractor yaw rate is bounded by a reasonable value using the relation $\gamma_1 \leq \mu g / v_{x1}$ [13]. μ is the friction coefficient.

3.2 *ADP optimal controller*

Rewrite the vehicle system model in Section 2 as the general format as below

$$\dot{x} = f(x) + g(x)u + \xi_1 \tag{10}$$

where $f(x)$ and $g(x)$ are nonlinear functions that are Lipchitz continuous on a given domain that contains a neighborhood, ξ_1 is assumed to the disturbance input related to the driver steering command.

The objective of the optimal tracking control problem is to develop an optimal controller for (10) to make sure that state vector x tracks the specified trajectory x_d. The tracking error is defined as:

$$\begin{aligned} e &= x - x_d \\ &= [v_{y1} - v_{yd} \quad \gamma_1 - \gamma_d \quad q - q_d \quad \theta - \theta_d]^T \end{aligned} \tag{11}$$

To achieve optimal tracking control, the control input u is designed as $u = u_d + u_e$, where u_d is the steady state control which ensures that the tracking error at the steady state, and u_e is the adaptive optimal control which is used to stabilize the tracking error dynamics in an optimal way. u_d aims to retain the steady-state tracking error and thus should be designed to compensate for the nonlinear dynamic in (10). Hence, let u_d be

$$u_d = g^+(x)[\dot{x}_d - f(x_d)] \tag{12}$$

where $g^+(x)$ denotes the generalized inverse of $g(x)$. Based on the Section 3.1, the desired trajectory is defined as

$$\dot{x}_d = h(x_d) \tag{13}$$

where $h(x_d)$ satisfies the locally Lipchitz function and $h(0) = 0$.

Then from Equations (10) and (12), the tracking error dynamics can be written as

$$\dot{e} = \dot{x} - \dot{x}_d = f(x) + g(x)u + \xi_1 - \dot{x}_d \tag{14}$$

In this case, the tracking problem with (10) is reduced to the regulator problem of (13). The adaptive optimal control u_e is designed to stabilize the error dynamics (14) in an optimal manner. Here, the infinite horizon performance cost function as following

$$V(e(t)) = \int_t^{\infty} r(e(\tau), u_e(e(\tau)))d\tau \tag{15}$$

where the utility function with symmetric positive definite matrices Q and R is defined as

$$r(e(t), u(t)) = e^T(t)Qe(t) + u^T(t)Ru(t) \tag{16}$$

According to the optimal regulator problem design in [8], an admissible control policy u_e should be designed to ensure that infinite horizon cost function (15) related to (14) is minimized. So, the Hamiltonian function of (14) is defined as

$$\begin{aligned} H(e, u_e, V) = V_e^T[f(x) - f(x_d) + g(x)u_e + \xi] \\ + e^T Qe + u_e^T Ru_e \end{aligned} \tag{17}$$

where $V_e = \partial V / \partial e$ is the partial derivative of the value function with respect to e.

Define the optimal cost function as

$$V^*(e(t)) = \min_{u_e \in \psi(\Omega)} \left(\int_t^{\infty} r(e(\tau), u_e(e(\tau)))d\tau \right) \tag{18}$$

and it satisfies the following HJB equation

$$\min_{u_e \in \psi(\Omega)} [H(e, u_e^*, V^*)] = 0 \tag{19}$$

By solving Equation (17), the adaptive optimal control u_e^* can be obtained

$$u_e^* = -\frac{1}{2} R^{-1} g^T(x) \frac{\partial V^*(e)}{\partial e} \tag{20}$$

It can be learned from Equation (20) that the optimal control value u_e^* is based the optimal value function $V^*(e)$. However, it is difficult to solve the nonlinear partial differential HJB equation to obtain $V^*(e)$. The commonly used method is to get the approximate solution via a critic NN as [6]. In this study, a single layer critic NN is designed to approximate the optimal value function,

$$V^*(e) = \mathrm{W}_1^{*\mathrm{T}} \phi(e) + \xi_2 \tag{21}$$

and its derivative is

$$\frac{\partial V^*(e)}{\partial e} = \nabla \phi^T(e) \mathrm{W}_1^* + \nabla \xi_2 \tag{22}$$

where $W_1^* \in R^I$ is the nominal weight vector, $\phi(e) \in R^I$ is the critic NN active function and ξ_2 is the approximation error, I is the number of neurons. $\nabla\phi(e) = \partial\phi(e)/\partial e$ and $\nabla\xi_2 = \partial\xi_2/\partial e$ are the partial derivative of $\phi(e)$ and ξ_2 with respect to e respectively. In this study, the critic NN activation function is selected as $\phi(e) = [\, e_1^2 \;\; e_2^2 \;\; e_3^2 \;\; e_4^2 \,]^T$.

Assumption 1: The nominal weight vector W_1^*, the active function $\phi(e)$ and its derivative $\nabla\phi(e)$ are all bounded, i.e. $\left\|\mathrm{W}_1^*\right\| \le \overline{W}_1$, $\|\phi(e)\| \le \bar{\phi}_1$, $\|\nabla\xi_2\| \le \bar{\phi}_2$.

Then substituting (22) into (20), one obtains

$$u_e^* = -\frac{1}{2} R^{-1} g^T(x)(\nabla \phi^T(e) \mathrm{W}_1^* + \nabla \xi_2) \tag{23}$$

In practical implementation, the critic NN is represented as

$$\hat{V}(e) = \hat{\mathrm{W}}_1^T \phi(e) \tag{24}$$

where $\hat{\mathrm{W}}_1$ is the estimation of nominal W_1^*.

Then the adaptive optimal control can be obtained from (23) and (24)

$$u_e = -\frac{1}{2} R^{-1} g^T(x) \nabla \phi^T(e) \hat{\mathrm{W}}_1 \tag{25}$$

Thus, the overall input u for optimal tracking control is given by

$$u = u_d + u_e \tag{26}$$

3.3 *Braking torque distribution*

The desired yaw moments can be generated by appropriately distributing yaw moments to some wheels of the tractor and semitrailer axles. The effective yaw moments generated by the individual wheels, however, tend to differ considerably even when subjected to identical brake torque. The brake torque distribution scheme [13] is employed considering two different situations corresponding to a potential yaw instability, denoted as understeer (yaw rate error <0) and over-steer (yaw rate error >0).

The distribution strategy is designed to limit the yaw rate when the yaw rate errors are positive, and exceed a defined threshold value. A negative yaw moment, thus needs to be applied, which could be realized through braking of outer-track wheels. When the vehicle's or a particular unit's yaw rate is less than the desired value, the control strategy is designed to reduce the error magnitude by applying brake torques to wheels on the inner track. The details of braking torque distribution on each wheel can be referred to [13].

4 RESULTS AND DISCUSSION

In this section, the proposed ADP based optimal tracking control is evaluated using TruckSim and Matlab/Simulink. Lane change maneuver is set in TruckSim. The vehicle initially runs at 100 km/h on a slippery road with friction efficient of 0.4. After 1 s,

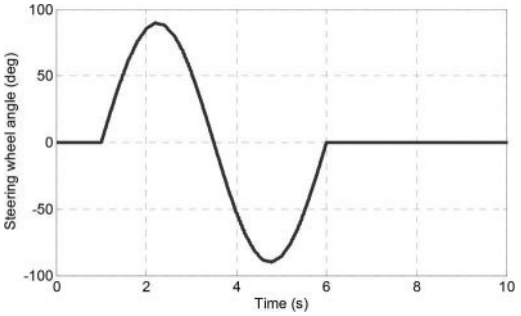


Figure 3. Steering wheel angle.

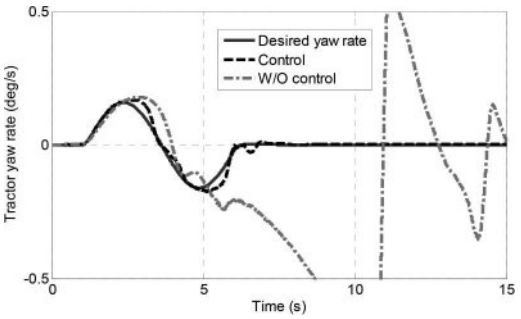


Figure 4. Yaw rate response of tractor.

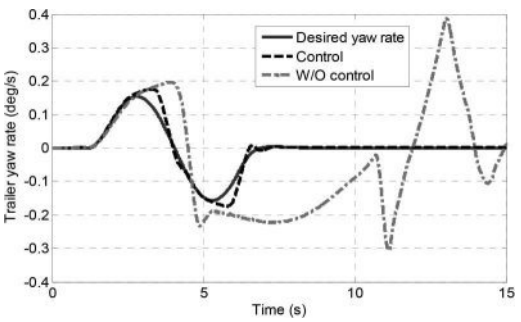


Figure 5. Yaw rate response of semitrailer.

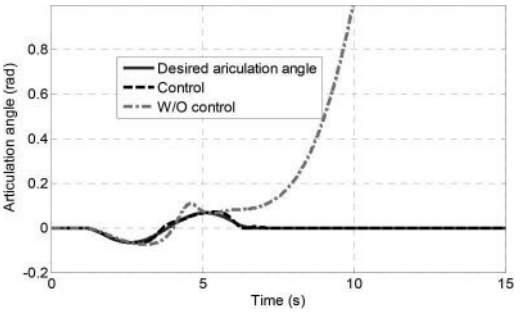


Figure 6. Articulation angle response.

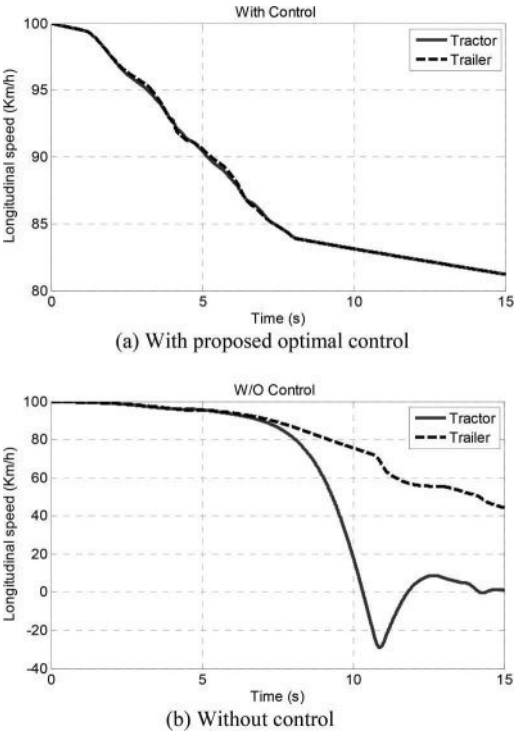


Figure 7. Longitudinal speed response of tractor and semitrailer.

the vehicle is steered with the amplitude of 90 degree and the frequency of 0.2 Hz as shown in Figure 3. The steer gear ratio is 25. The responses are also obtained for the vehicle without control in order to evaluate the potential benefits of the proposed ADP optimal controller.

The state responses of tractor and semitrailer are given and compared in Figure 4 to Figure 8 for the vehicle with proposed ADP optimal controller and the vehicle without control. Figure 4 and 5 show the yaw rate response of tractor and semitrailer, respectively. The articulation angle response is given in Figure 6. It can be seen that, with the proposed control, the actual yaw rate can follow the desired yaw rate while the yaw rate without control increases rapidly after 6s to a large value, which suggests the possible loss of vehicle stability. Similarly, the yaw rate response of semitrailer in Figure 5 also reveals that it cannot follow the desired one if no active control is applied. It is obvious from Figure 6 that jackknifing occurs without control because of the large articulation angle. With the proposed optimal control, the actual articulation angle can follow the desired value well. So, the proposed controller provides a satisfactory tracking performance for vehicle states. Figure 7 compares the longitudinal speed responses of tractor & semitrailer with proposed controller and without control. With proper braking, longitudinal speed of both units decreases slowly and smoothly while, if there is no control applied, the longitudinal speed of tractor decrease rapidly to zero around 10s and the longitudinal speed of semitrailer

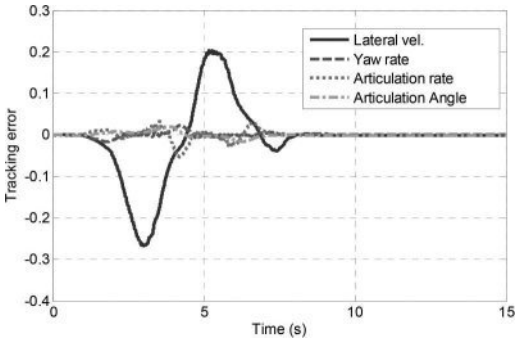


Figure 8. Vehicle state tracking error with control.

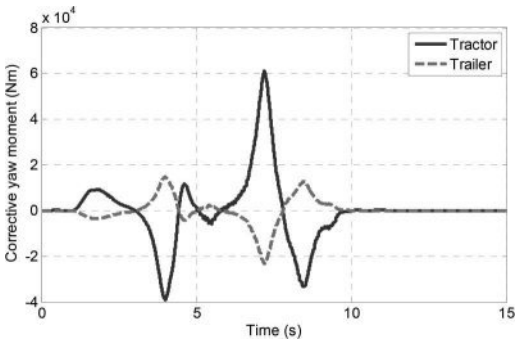


Figure 9. Corrective yaw moments.

is much larger than that of tractor which further cause the vehicle instability.

Figure 8 shows the tracking errors of vehicle states: tractor lateral velocity, tractor yaw rate, articulation rate and articulation angle with the proposed optimal controller. It can be seen that the tracking errors for tractor yaw rate and articulation angle are small while the tracking error for lateral velocity and articulation rate are slightly larger, especially for lateral velocity. A possible reason is that there are two control inputs which could not be enough for controlling four vehicle states simultaneously. The corrective yaw moments obtained from the proposed ADP optimal tracking controller in Figure 9.

5 CONCLUSIONS

The major contribution of this paper is to apply an ADP based optimal control to improve the lateral stability of articulated heavy vehicles. In the controller design, an infinite horizon cost function is defined and a single critic neural network framework is developed to solve the HJB equation and obtain the feedback control inputs. By applying the proposed optimal controller to articulated heavy vehicle, the preliminary simulation results under lane change maneuver show that ADP based optimal control can achieve a satisfactory tracking performance to the desired vehicle response and maintain the vehicle lateral stability. In the future study, the robustness and parameter adaptiveness of ADP based optimal tracking control will be studied and more simulations will be done under different maneuvers to verify the effectiveness of the proposed controller.

REFERENCES

[1] Gerdes, J. C. 2002. Safety performance and robustness of heavy vehicle AVCS. Stanford University: Dept. of Mechanical Engineering-Design Division.

[2] Kharrazi S. and Thomson R. 2007. Study of heavy truck accidents with focus on maneuvers causing loss of control. International Journal of Vehicle safety, 3:32–44.

[3] Palkovics, L. and El-Gindy M. 1995. Design of an active unilateral brake control system for five-axle tractor-semi-trailer based on sensitivity analysis. Vehicle System Dynamics, 24:725–758.

[4] Tabatabaei Oreh S. H., Kazemi R. and Azadi S. 2014. A Sliding-mode Controller for Directional Control of Articulated Heavy Vehicles. Proc IMechE Part D: Journal of Automobile Engineering, 228(3) :245–262.

[5] Chen, L. and Shieh, Y. 2011. Jackknife prevention for articulated vehicles using model reference adaptive control. Proc IMechE Part D: J Automobile Engineering, 225(1):28–42.

[6] Lewis F. L. and Liu D. 2013. Approximate Dynamic Programming and Reinforcement Learning for Feedback Control. Hoboken, NJ: Wiley.

[7] Werbos, P. 1992. Approximate dynamic programming for real-time control and neural modeling. Handbook of Intelligent Control, Neural, Fuzzy, and Adaptive Approaches. Van Nostrand Reinhold, New York.

[8] S. Bhasin, R. Kamalapurkar, M. et al. 2013. A novel actor-critic-identifier architecture for approximate optimal control of uncertain nonlinear systems. Automatica, 49(1):82–92.

[9] Lv Y., Na J., Yang Q., Wu X. and Guo Y. 2016. Online adaptive optimal control for continuous-time nonlinear systems with completely unknown dynamics. International Journal of Control, 89(1):99–112.

[10] Kamalapurkar R., Dinhb H., Bhasin S., Dixona W. E. 2015. Approximate optimal trajectory tracking for continuous-time nonlinear systems. Automatica, 51:40–48.

[11] Sardarmehni T. and Heydari A. 2015. Optimal switching in anti-lock brake systems of ground vehicles based on approximate dynamic programming. Pro. of the ASME Dynamic Systems and Control Conference, Columbus, Ohio, USA.

[12] Hac A., Fulk D. and Chen H. 2008. Stability and control considerations of vehicle-trailer combination. SAE paper 2008-01-1228.

[13] Li B.and Rakheja S. 2015. Jackknifing Prevention of Tractor-semitrailer Combination using Active Braking Control. *SAE Paper* 2015-01-2746.

Advanced Vehicle Control – Edelmann, Plöchl & Pfeffer (Eds)
© 2017 Taylor & Francis Group, London, ISBN 978-1-138-02992-7

MiniMax – a situational and geometrical adaptive chassis: Driving safety and space efficiency

J. Kalbfleisch, P. Wagner & H. Winner
Institute of Automotive Engineering, Technische Universität Darmstadt, Germany

ABSTRACT: The aim of the MiniMax project is the revaluation of conventional chassis designs by combining minimal resource requirements in terms of footprint, energy, and cost while not affecting driving stability and comfort at the same time. The chassis geometries wheelbase, track width, center of gravity height, and roll angle constitute the four degrees of freedom of a situational and geometrical adaptive chassis. Based on a simulation model, the static and transient influences on driving stability were determined. Finally, an elaborated evaluation revealed the most promising adaption concept, taking into account combinations of the aforementioned degrees of freedom and the adaption kinematics as well as actuator requirements and adaption strategies.

1 MOTIVATION FOR A SITUATIONAL AND GEOMETRICAL ADAPTIVE CHASSIS

Current trends in mobility and the way of life – namely motorization and urbanization – require new solutions for future urban mobility. Nowadays about 54% of the world's inhabitants live in urban areas. It is estimated that this rate will increase to 66.4% by the year 2050 (United Nations (UN) 2015). Furthermore, individual mobility is expected to rise from 123 passenger cars per 1,000 world inhabitants in 2014 to 194 passenger cars per 1,000 people in 2035 (Shell 2014). Combining both trends – urbanization and motorization – leads to the conclusion that our cities will get even more congested with passenger cars. This does not only affect available parking space but also the flow of traffic.

Possible approaches to escape this situation include intelligent traffic management systems as well as new concepts for (individual) mobility. Nevertheless, especially individual mobility has to fulfill contemporary requirements like driving safety, driving reward, driving comfort, range, and sustainability. These specifications require a rethinking of today's chassis design and call for a groundbreaking new concept.

2 BUILDING SET FOR A CHASSIS

Since the year 2012 the Institute of Automotive Engineering (FZD) at Technische Universität Darmstadt (TUD) researches an approach for a Personal Electric Vehicle (PEV), which conserves resources in terms of energy and space. The basic idea is to adapt the chassis of the PEV so that it uses just as much space as required by the currently performed driving maneuver and therewith associated driving dynamics.

The foundations for a situational and geometrical adaptive chassis were laid by Wege (Wege 2012) by dividing the chassis design in its basic tasks and subfunctions. On this basis, Schweizerhof (Schweizerhof 2014a,b) analyzed the optimization of a chassis regarding minimum footprint, maximum driving safety, and maximum maneuverability by using a geometrically adaptive chassis concept. Stationary stability was proven and even improved compared to static chassis concepts. This is accomplished by adjusting the chassis geometries wheelbase, track width, center of gravity (CG) height, and roll angle, which constitute the four degrees of freedom (DOF) of the geometrically adaptive chassis.

3 DRIVING STABILITY ANALYSIS FOR A PEV WITH A GEOMETRICALLY ADAPTIVE CHASSIS

3.1 *Basic chassis dimensions*

The definition of the basic chassis dimensions is derived from the minimal anthropometric dimensions (Deutsches Institut für Normung e.V. 2005) and optimal seat height (Figure 1).

3.2 *Methodology for researching transient driving stability*

In order to adapt the chassis geometry without affecting driving stability, Schneider (Schneider 2015a,b) identified the stability effects of the transient adaption process. The driving dynamics study of the adaptive chassis accounts for highly dynamic driving maneuvers with and without adaption. An advanced two-track simulation model was built up in Matlab Simulink

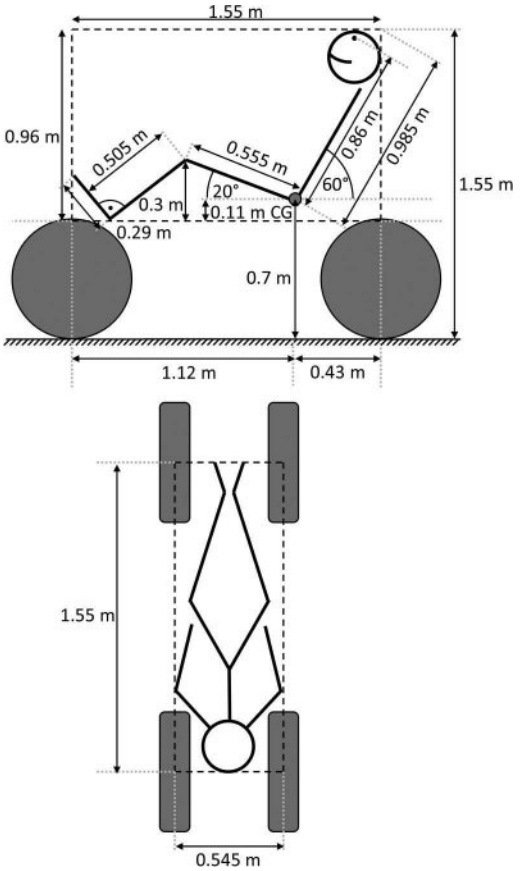


Figure 1. Minimum chassis dimensions (cf. Schweizerhof 2014a).

and extended by the additional chassis DOF. Sensitivity analyses reveal the effects of the transient chassis adaption on driving dynamics.

The results of the study lead to a solution field determining which DOF need to be adaptive to ensure driving stability for longitudinal and lateral dynamics. The aim is to ensure roll-over stability even at the traction limit of the tires. This is derived by the so-called static stability factor (SSF) (Eqn. 1–2):

$$\frac{\ddot{y}_{CG}}{g} \leq \frac{w_{l/r}}{2h_{CG}} = SSF_y \tag{1}$$

$$\frac{\ddot{x}_{CG}}{g} \leq \frac{l_{f/r}}{h_{CG}} = SSF_x \tag{2}$$

The value of the SSF can be compared to the maximum traction limit of the tires. To increase the robustness against disturbance factors, for example fluctuations in friction or aerodynamic forces, a safety factor $S_{x/y} = 1.2$ is introduced, corresponding to a desired SSF in target state. With the desired $SSF_{des} = 1.2$ and the basic layout of the chassis it can be derived which DOF have to be adjustable to ensure driving stability for longitudinal and lateral accelerations. The track width is increased to 0.75 m to enable the deployment of a side airbag and a sufficient thickness of the door body. This emerged from an expert discussion with an OEM's employees working at crash simulations. For the concept selection the chassis dimensions are chosen as described in table 1.

Table 1. Initial chassis dimensions

Parameter	Value	Initial SSF SSF_0
Wheelbase l	1.55 m	–
Wheelbase rear l_r	0.43 m	0.61
Wheelbase front l_f	1.12 m	1.6
Track width w	0.75 m	0.53
CG height h_{CG}	0.7 m	0.53
Tilt angle ϕ	0°	–

3.3 *Results of the transient driving stability analysis*

The chassis dimensions in combination with the driving dynamics study reveal that the chassis only needs to be adaptive for lateral accelerations. When accelerating in negative longitudinal direction (i.e. braking), an SSF of 1.6 (cf. Table 1) is sufficient. When accelerating in positive longitudinal direction, an SSF of 0.61 (cf. Table 1) is deficient. Nevertheless, the driving torque can be electronically limited (also account for road gradient) so that the negative longitudinal acceleration stays below 0.51 g ($=SSF_{0,-x}/S_x = 0.61/1.2$). In addition, the study shows deficient tilt stability characteristics for roll angle adaption with the prescribed chassis parameters. This is partly due to the support torque that is generated by the tilt movement. Depending on the tilt acceleration, the support torque may lead to one-sided wheel lift-off and therefore impairment of driving stability. Thus, the tilt angle DOF is excluded from the solution field. For more detailed results of the driving stability analysis see Schneider (2015a).

An adaption of the wheelbase is not necessary and therefore the wheelbase is set to the required minimum. Furthermore, to achieve maximum acceleration, it is proposed to integrate a drive torque limitation into the vehicle control in order to prevent a lift-off of the front axle or tipping of the vehicle if it accelerates up a slope.

The results of the driving dynamics analysis have been summarized by Wagner & Winner (2016).

4 CONCEPT SELECTION FOR A PEV WITH A SITUATIONAL AND GEOMETRICAL ADAPTIVE CHASSIS (, CF. KALBFLEISCH 2015)

4.1 *Selection of to be adapted DOF*

Section 3.3 deems the track width and CG height adaption as favorable, whereas wheelbase and tilt angle adaption are excluded from the solution field.

Advantageous for a track width adaption is the possibility to take advantage of system immanent forces

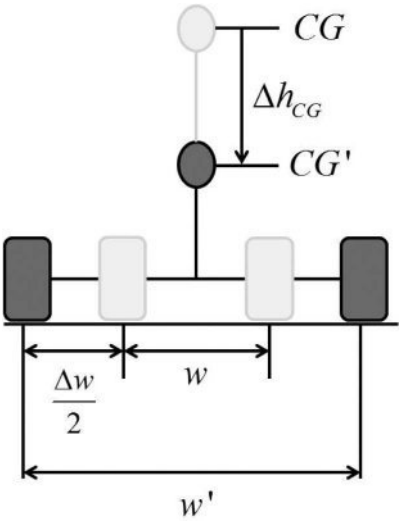


Figure 2. Combined CG height and track width adaption.

for the adaption: An active toe angle adaption would generate lateral wheel forces pushing the wheels to the outside. While cornering, the outer wheels' adaption is supported by the lateral wheel force generated by the slip angle. Nevertheless, it has to be mentioned that the inner wheel has to be adapted against this lateral wheel force. A suitable force transmission mechanism from the outer to the inner wheel could compensate this effect and therefore decrease the actuator requirements.

The CG height adaption is advantageous in matters of energy (the potential energy can be reclaimed and decreases the actuator requirements), driving stability (no influence on maneuverability and straight line driving quality), and footprint (no increase due to adaption).

For the final evaluation of the adaption concept, not only the individual adaptions of the DOF are taken into account for the solution field but also a combined adaption. To find a suitable combined adaption, the evaluation criteria's influence on footprint, energy demand, SSF, technical effort, and influence on yaw velocity gain (YVG) are used. The results of this evaluation show that the adaption of the track width and the CG height is the most promising combined adaption. Therefore, the solution field was expanded by a combined adaption of the track width and CG height, figure 2.

4.2 *Adaption kinematics*

To simulate the transient adaption process, a representation of the dynamic behavior in terms of velocity has to be designed. The variety of kinematic functions has been reduced to three idealized functions describing an adaption from an initial to an end position. The velocity characteristics of the adaption are described by mathematic functions: triangle (TRI), sine half wave (SIN) and $(1-\cos^2)$ (COS) (fig. 3).

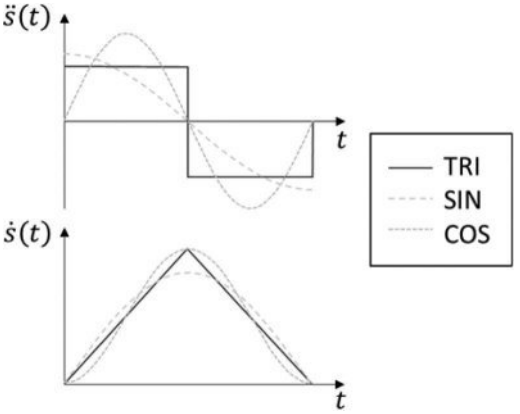


Figure 3. Velocity (bottom) and acceleration (top) characteristics for the three adaption kinematic functions TRI, SIN, and COS (Schneider 2015b).

Comparing the kinematics shows that an adaption with the SIN function is comparatively energy and power efficient. An adaption with the TRI function requires the lowest maximum acceleration for the adaption of the CG height. The smooth COS function has the worst characteristics because it requires the highest maximum acceleration and power in comparison to the other two functions (Kalbfleisch, 2015).

4.3 *Adaption boundaries*

Of particular interest for the adaptation of the individual DOF is the product of speed and acceleration, and the maximum acceleration of the respective adjusting kinematics. The adaption kinematics based on the criteria of minimum speed, acceleration, power, and energy demand were determined for the chassis' DOF. The calculation of the required displacement paths for each adaption concept can be calculated from the desired SSF as follows (Fig. 4 & Eqn. 3–5).

Equilibrium of moments around the outer wheel leads to:

$$\sum M_{W,R} = m \cdot \ddot{y}_{CG} \cdot h_{CG} - m \cdot g \cdot \frac{w}{2} = 0 \tag{3}$$

With a safety factor, it leads to the necessary adaption paths as shown in Table 2:

$$S_y \frac{\ddot{y}_{CG}}{g} \leq \frac{w}{2h_{CG}} = SSF_y \tag{4}$$

$$S_y = 1.2\,;\, \ddot{y}_{CG,\max} = g\,;\, SSF_{des.} = 1.2 \tag{5}$$

4.4 *Adaption strategy*

The solution field was completed by defining a reactive, a passive, and a proactive adaption strategy for each adaption concept. The chassis is adapted reactively to the maximum driving stability setup as a direct

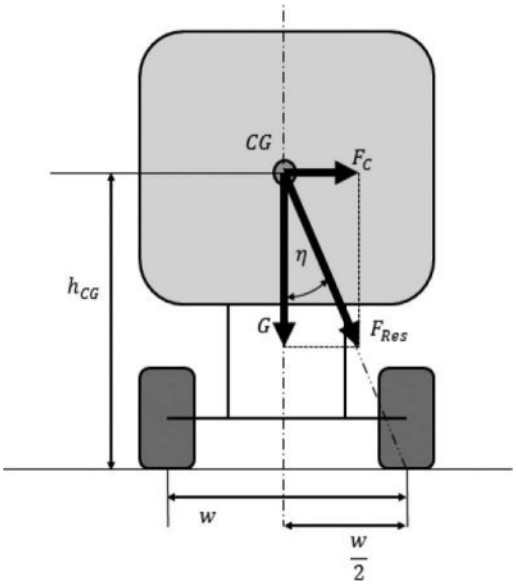


Figure 4. Adaption paths calculation from SSF (Kalbfleisch 2015).

Table 2. CG height and track width adaption displacement.

Parameter	Symbol	Value
Initial track width	w_0	0.75 m
Desired track width		
combined adaption	w_1	1 m
individual adaption	w_2	1.68 m
Track width displacement		
Combined adaption	Δw_1	0.25 m
Individual adaption	Δw_2	0.93 m
Initial CG height	$h_{CG,0}$	0.7 m
Desired CG height		
Combined adaption	$h_{CG,1}$	0.416 m
Individual adaption	$h_{CG,2}$	0.316 m
CG height displacement		
Combined adaption	$\Delta h_{CG,1}$	0.284 m
Individual adaption	$\Delta h_{CG,2}$	0.388 m

result of highly dynamic driving maneuvers where the stationary tilt stability is not sufficient, e.g. during an evasive maneuver in an emergency situation. A passive adaption is done prior to a highly dynamic driving maneuver, e.g. due to travelling speed, traffic environment, or the selected user profile (sporty, moderate, or passive). A proactive adaption adjusts the chassis due to forthcoming highly dynamic driving maneuvers. This adaption is somewhat comparable to the reactive strategy with a certain lead time, thus decreasing the actuator requirements. Nevertheless, this adaption is only possible if dynamic driving maneuvers can be foreseen, as could be with automated vehicles.

Because this technology is not available with a required high degree of reliability, only the reactive and passive adaption strategies are taken into account. Combinations of adaption strategies are possible, but not accounted for in this analysis in order to research the worst case requirements for a geometrical and situational adaptive chassis.

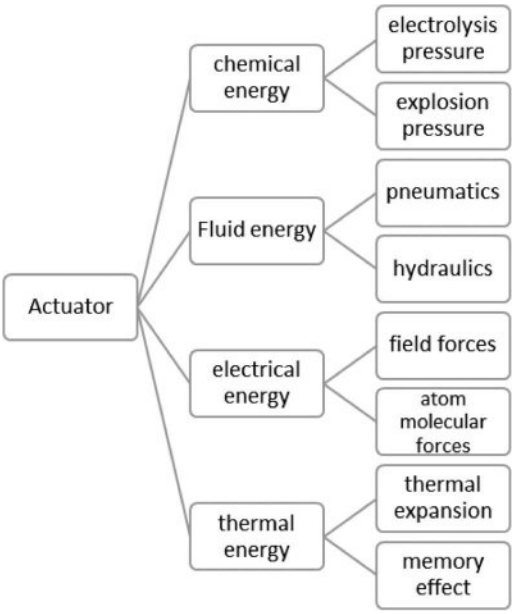


Figure 5. Auxiliary energies and forces for generating mechanical output quantities, cf. Isermann (2008).

4.5 *Actuator selection*

4.5.1 *Actuator selection methodology*

To select proper actuators for a geometrically adaptive chassis, firstly a survey of state-of-the-art actuator technology is conducted. Secondly, the required product features are defined, e.g. the ability to utilize the potential energy of the CG height adaption.

With these information, partial solutions for the product features can be developed. An actuator preselection reduces the solution field to a reasonable number that allows the development and assessment of overall solutions for the geometrically adaptive chassis.

4.5.2 *Actuator preselection*

The actuators can be described by the auxiliary energy they are driven by, Figure 5. Thermal and chemical energy are among the range of unconventional actuators and as using two energy sources in parallel is not suitable for meeting the requirements, they are excluded from further evaluation. Therefore, only actuators driven by electrical and fluid energy are further assessed.

4.5.3 *Final actuator selection*

The remaining two actuator principles are evaluated by the criteria efficiency, energy consumption, dynamics, construction volume, controllability,

wear/maintenance, and environmental friendliness. The criteria are ranked through a paired comparison.

Together with the data available from the state-of-the-art survey, the evaluation yields a weighted score of 1.76 for electric actuators and 1.56 for fluid actuators, where higher scores indicate higher suitability. Therefore, further investigations will be made with electric actuators.

4.5.4 *Modelling of electric actuators*

The dynamic behavior of the actuator was determined through a rough pre-selection of suitable actuators. Preliminary actuator requirements were identified by extending the existing simulation model with dynamic actuator behavior. To simulate real actuator behavior, the actuator-related damping and stiffness are accounted for by a PT2-element. The maximum actuator requirements are thereby determined by simulating a maneuver that exploits the maximum friction coefficient of the tire with a maximum acceleration gradient. This results in a conservative assumption and ensures that the actuator can perform an adaption of the chassis during a highly dynamic driving maneuver.

The wheel load change induced by the maneuver has a direct impact on the actuator requirements because with an increased wheel load a greater force is necessary to adjust the wheels in lateral direction. Furthermore, it should be noted that the necessary forces, power, and energy requirements vary depending on the wheel. Due to the specified geometry of the adaptive chassis (cf. table 1 and fig. 1) a higher wheel load results for the rear wheels. The maximum actuator requirements for a driving maneuver utilizing the maximum friction coefficient of the tires are thus determined by considering of the outside rear wheel. In addition, all values for the actuator requirements are multiplied with a safety factor $S_{Act} = 1.2$ to ensure that the actuator provides sufficient dynamic behavior under any conditions.

4.6 *Final solution field*

The adaption strategies, adaption concepts, and actuator requirements lead to the final possible solution field:

1. Reactive strategy for combined adaption of track width and CG height
2. Reactive strategy for CG height adaption
3. Reactive strategy for track width adaption
4. Passive strategy for combined adaption of track width and CG height
5. Passive strategy for CG height adaption
6. Passive strategy for track width adaption

4.7 *Evaluation criteria*

To find the most suitable adaption concept, an evaluation process is carried out. For the evaluation the criteria

1. Footprint (weighting factor 0.63)
2. Energy demand (weighting factor 0.81)
3. Actuator requirements maximum velocity v, acceleration a, Force F, energy demand E, and power demand P (weighting factor 1)
4. Overview (weighting factor 0.45)
5. Maneuverability/YVG (weighting factor 0.45)
6. Costs (weighting factor 0.09)

are ranked through a paired comparison, from which the weighting factors in parentheses result. Each criterion is made quantifiable by defining a four-level scale that relates the fulfilment of a criterion to a score. With the preliminary actuator requirements and the criteria of the MiniMax project (footprint, energy consumption, costs, comfort, driving stability) the adaption concepts were evaluated.

Table 3. Actuator Requirements for the combined adaption of track width and CG height

Requirement	DOF	
	Track width	CG height
a_{max}	$\geq$4.5 m/s^2	$\geq$13.7 m/s^2
v_{max}	$\geq$0.58 m/s	$\geq$0.58 m/s
F	$\geq$6152 N	$-$1042 N–14,050 N
P	$\geq$3120 W	$\geq -$13,350 W
E	$\geq$518 J	$\geq -$2069 J
Displacement	$\geq$0.125 m	$\geq$0.284 m

4.8 *Evaluation results*

The results of the evaluation show that a **combined reactive adaption of the track width and the CG height** is the most promising concept. Furthermore, the simulation results show that state-of-the-art actuators can fulfill the actuator requirements, which are stated in Table 3.

4.9 *Adaption frequency*

The initial, minimum footprint setup is "safe" in terms of driving stability up to lateral accelerations of 5.3 m/s^2 when neglecting the safety factor S_y (cf. Table 1). For evaluating the overall energy demand, it is of interest how often the chassis has to be adapted to the maximum driving stability setup.

Therefore, preliminary recorded data from a volunteer study conducted at FZD in 2014 has been analyzed. The subject collective consisted of 30 persons. A representative city course was used, which was distinguished by an appropriate selection of everyday urban traffic situations. The city course was created based on a point system taking into account the road density in the previously selected area, the traffic density, and a weighting of the roads to main roads, secondary roads, and roads with increased traffic. The distance of the course is 21 km and the trip took about 1 h to 1.5 h depending on traffic (Graupner 2012).

The analysis revealed that within the whole subject collective a lateral acceleration above 5 m/s^2 was only reached 17 times. Dividing by the overall driving time yields an average rate of 0.57 occurrences per hour. This correlates with found results from literature (e.g. Hackenberg 1982). Conversely, this means that a reactive adaption of the chassis due to lateral accelerations above the adaption threshold occurs every 1 h 45 min on average, which seems reasonable in terms of energy consumption and comfort.

5 CONCLUSION

For the first time, different concepts of a situational and geometrical adaptive chassis have been investigated in terms of driving stability, footprint, maneuverability, and actuator requirements. The results prove that a situational and geometrical adaptive chassis concept is a promising solution for future individual mobility, combining minimal footprint and maximum driving stability. The most promising concept comprises a combined reactive adaption of the track width and the CG height.

6 OUTLOOK

The structural design of the entire MiniMax PEV will be carried out in a follow-up investigation. This includes the final actuators for the adaptive chassis and the final masses and dimensions of each unit. Since the suitability of electrical and fluid energy driven actuators is very similar, a re-evaluation of fluid actuators will be made.

The design process will be completed by a CAD model. In addition, a study for a track width adaption by active toe adaption can be made in order to conserve energy and to downsize the actuators. The potential energy released by the CG height adaption will be used as far as possible for the track width adaption. Because the adaption from the maximum driving stability setup to the minimum footprint setup is not safety critical, the adaption time may be increased, resulting in reduced actuator requirements.

As a completion of the MiniMax project, a scaled prototype (approx. 1:3) will be built in order to compare the simulation results with the real test results and to show what commercial potential a situational and geometrical adaptive chassis can achieve.

REFERENCES

Deutsches Institut für Normung e.V. 2005, *DIN 33402: Ergonomics – Human Body Dimensions – Part 2: Values*, Berlin: Beuth.

Graupner, Maren 2011, *Entwicklung eines repräsentativen Stadtparcours*; Bachelorarbeit, Darmstadt: Technische Universität Darmstadt.

Hackenberg, Ulrich & Heißing, Bernd 1982, Die fahrdynamischen Leistungen des Fahrer-Fahrzeug-Systems im Straßenverkehr; *Automobiltechnische Zeitschrift* 84(7/8): 341–345.

Isermann, Rolf 2008, *Mechatronische Systeme, Grundlagen*: 445, Berlin: Springer.

Kalbfleisch, Jonas 2015, *Concept Selection for a Situational Adaptive Chassis*, Masterthesis, Darmstadt: Technische Universität Darmstadt.

Schneider, Johannes 2015, *Investigation of Driving Dynamics Effects of Situational Adaptive Chassis onto Driving Stability*, Masterthesis, Darmstadt: Technische Universität Darmstadt.

Schneider, Johannes & Wagner, Paul & Winner, Hermann 2015, Situational adaptive chassis: Where are the limits?, *Aachen Colloquium, Aachen, 05–07 October 2015.*

Schweizerhof, Hans 2014, *Design of a Situational Adaptive Chassis with Respect to Maneuverability and Footprint*, Diplomarbeit, Darmstadt: Technische Universität Darmstadt.

Schweizerhof, Hans & Betz, Alexander & Winner, Hermann 2014, Analysis of a Situational Adaptive Chassis with Respect to Maneuverability and Footprint, *ASME International Design Engineering Technical Conferences & Computers and Information in Engineering Conference, Buffalo, New York, USA, 17–20 August 2014*.

Shell 2014, *Shell Pkw-Szenarien bis 2040; Fakten, Trends und Perspektiven für Auto-Mobilität*, Hamburg: Shell Deutschland Oil GmbH.

United Nations (UN), Department of economic and social affairs 2015. "*Population Division (2014). World Urbanization Prospects: The 2014 Revision*", New York: United Nations (UN).

Wagner, Paul & Winner, Hermann 2016, MiniMax-Projekt – Fahrwerkskonzept für urbanen Straßenverkehr. *Automobiltechnische Zeitschrift* 118(6): 26–33.

Wege, Gerrit 2012, *Development of a Building Set for a Functional Broken Down Vehicle Chassis for Urban Personal Transportation*, Studienarbeit, Darmstadt: Technische Universität Darmstadt.

Advanced Vehicle Control – Edelmann, Plöchl & Pfeffer (Eds)
© 2017 Taylor & Francis Group, London, ISBN 978-1-138-02992-7

A cascaded model-predictive approach to motorcycle safety

Stefan Hans
BMW Motorrad

Martin Krehel
RWTH Aachen

Markus Köbe & Günther Prokop
Technische Universität Dresden

ABSTRACT: To reduce the number of accidents and traffic injuries or deaths, the driver of a modern car is assisted by various Advanced Driving Assistance Systems (ADAS). They can interact with the driver as well as independently influence the driving dynamics in case of an imminent accident.

Due to its lack of a passenger cabin, a motorcycle has less potential of passive safety. This leads to a crucial need of active safety systems, but until today only reactive systems are available. They are merely able to react to rider's actions and can for example reduce the rider's brake pressure or throttle demand, but there are no active systems that can e.g. brake autonomously. Active and autonomously acting assistants are still not existent in the world of motorcycle safety.

This paper presents an efficient model-predictive controller for a motorcycle, based upon a hierarchical model of the human steering behavior, that can be used for advanced rider assistance systems (ARAS).

1 INTRODUCTION

The steady decrease of car-related injuries can be affiliated to huge improvements in the field of passive safety as well as active safety systems. A growing number of ADAS is available to assist the driver during various situations on different levels of the driving task. Some run in the background and supply information , others can support the driver by intervening in the driving task when there is a dangerous situation. Even highly automated systems are available, that can take over that complete driving task in simple situations. If an accident is inevitable, an optimized passenger cabin and systems like airbags or seat belts protect the passengers and improve the passive safety.

Only very few of the assistance systems were adapted to motorcycles. Exemplarily, an anti-lock braking system was introduced in a mass-production motorcycle in 1988 – ten years after its launch in passenger cars. Traction control systems even had a longer delay and found their way into motorcycle production in 2006. Both of them are rather *reactive* than *active*, since they need the rider's action (braking or accelerating) and only *react* by reducing the control signal if tires would lose grip.

There is no active safety system for motorcycles on the market capable of noticing dangerous riding-situations and hence influencing the motorcycle's dynamic behavior without any human interaction.

In order to improve motorcycle safety and to develop ARAS, the whole vehicle dynamics needs to be understood first. Only then it is possible to distinguish between a normal riding situation and a dangerous one.

2 MOTIVATION

The amount of traffic fatalities is decreasing steadily, especially the number of car passengers. Figure 1 compares road traffic accident fatalities of car occupants and motorcyclists in Germany (Bundesamt 2016).

The number of killed riders as well as pillions of motorcycles is also decreasing. However, their share of the total amount has been almost doubled in this period (starting at 13 percent up to 24 percent).

In contrast to passenger cars, the potentials for passive safety systems for motorcycles and their users are very limited. Comparing the risk of motorcyclists to the risk of car occupants with respect to their vehicle stock and mileage (Hautzinger, Stock, & Schmidt 2002) leads to:

- a nearly 4 times higher risk of getting involved in an accident,
- a 7 times higher risk of getting injured in an accident,
- a more than 24 times higher risk of getting killed in an accident.

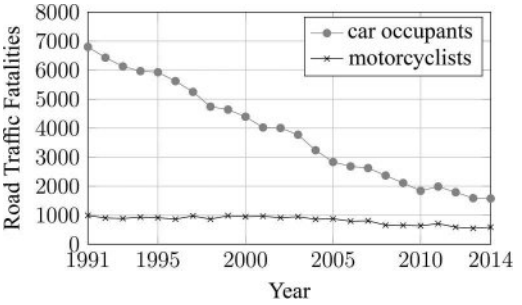


Figure 1. Car occupants and motorcycle rider fatalities in Germany from 1991 to 2014. (Source: DESTATIS).

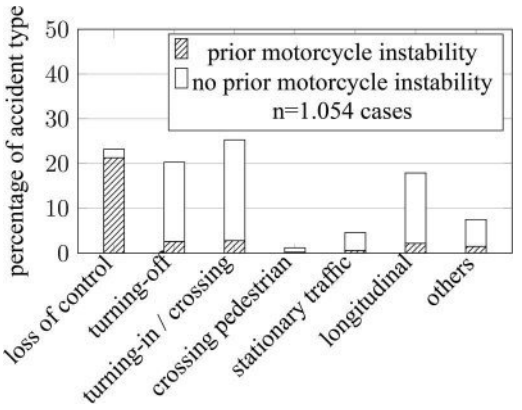


Figure 2. Distribution of different accident types involving a motorcycle and whether the motorcyclist lost control due to a prior instability. (Source: GIDAS).

This increasing relevance justifies special attention and research actions in this field.

2.1 *Accident occurrence of motorcycles*

In contrast to the stabilization task of car drivers, the one of motorcycle riders is more complex due to the unstable and non-minimum-phase vehicle behavior. Considering accidents with motorcycle riders as main perpetrators, every second accident occurred due to a loss of control (Bundesamt 2016).

Based on an analysis of a set of motorcycle accident cases within the German In-Depth Study (GIDAS), figure 2 shows a distribution of types of accidents with motorcycles involved and an estimated influence of a prior instability.

Notwithstanding the accident type, every third case happened with a prior instability on the side of the motorcycle involved (sum of all shaded bars in figure 2). Due to that instability, the rider lost valuable time in which a prevention maneuver or further deceleration could have taken place.

Loss of control accidents in Figure 2 without prior motorcycle instability were caused by another skidding participant.

2.2 *Approach*

To address all accidents two kinds of assistance systems are necessary. Systems supporting motorcycle riders during already present instabilities as well as systems with situation prediction. Latter can be used to avoid instabilities or critical situations with other vehicles before they occur.

Anti-lock braking and traction control systems have been developed to assist the motorcyclist during already existing instabilities. Both systems are well examined and available in series production motorcycles. Therefore they will not be discussed here any further.

This paper covers more complex ARAS with model prediction. Based on knowledge about the motorcycle's surroundings, including the course of the road and other vehicles, these systems can warn or assist the rider before he gets into a critical situation.

In order to perform these tasks a model-predictive approach was chosen with special focus on real-time use. To get a realistic, human-like behavior, the controller concept uses a widespread multilevel structure. Like a virtual rider, this controller can calculate the optimal maneuver under given constraints. If the solution gets close to a critical dynamical state, the motorcyclist can be warned or the dynamics could be influenced directly to mitigate hazards.

In section 3 a simplified common model is used to describe the motorcycle dynamics. It's the basis for the controller design in section 4. The performance of this controller is evaluated by simulating a swerve maneuver. The results are presented in section 5.

3 DYNAMIC MODEL OF THE MOTORCYCLE

In contrast to cars, the dynamics of a bicycle or motorcycle is unstable at low speeds, so the rider has to stabilize it with active control inputs. A dynamic model with a good tradeoff between accuracy and simplicity is the necessary basis for developing an equally working model-predictive controller (MPC). The model used for controller design in this paper is the bicycle model provided by Getz (1995) and Yi, Zhang, & Song (2009)

$$\mathbf{M}(\underline{q})\,\ddot{\underline{q}} = \mathbf{K}(\underline{q},\dot{\underline{q}}) + \mathbf{B}\underbrace{\begin{bmatrix}\omega_\kappa \\ F_{\mathrm{rx}}\end{bmatrix}}_{\underline{u}}, \tag{1}$$

with the Matrices $\mathbf{M} \in \mathbb{R}^{n\times n}$, $\mathbf{K} \in \mathbb{R}^{n\times 1}$ and $\mathbf{B} \in \mathbb{R}^{n\times m}$ as in equations (2a), (2b) and (2c). The state vector $\dot{\underline{q}}$ contains the roll velocity $\dot{\phi}$ and the rear wheel longitudinal velocity v_{rx}. The input vector $\underline{u}$ consists of the time derivative of the path's curvature $\omega_\kappa = \dot{\kappa}$ and a longitudinal force at the rear wheel F_{rx}. All Symbols are denoted in figure 3 and explained in table 1.

$$\mathbf{M}(\underline{q}) = \begin{bmatrix} h^2 & -ch\kappa\cos\phi \\ -ch\kappa\cos\phi & c^2\kappa^2 + h^2\kappa^2\sin^2\phi + 2h\kappa\sin\phi + 1 \end{bmatrix} \tag{2a}$$

$$\mathbf{K}(\underline{q},\dot{\underline{q}}) = \begin{bmatrix} (1+h\kappa\sin\phi)hv_{rx}^2\kappa\cos\phi + \mathrm{g}h\sin\phi - \mathrm{g}ce\kappa\sin\eta\cos\phi \\ -ch\kappa\dot{\phi}^2\sin\phi - 2v_{rx}h^2\kappa^2\dot{\phi}\cos\phi\sin\phi - 2v_{rx}h\kappa\dot{\phi}\cos\phi \end{bmatrix} \tag{2b}$$

$$\mathbf{B}(\underline{q},\dot{\underline{q}}) = \begin{bmatrix} chv_{rx}\cos\phi & 0 \\ -\kappa c^2 v_{rx} - v_{rx}h^2\kappa\sin^2\phi - v_{rx}h\sin\phi & \frac{1}{m} \end{bmatrix} \tag{2c}$$

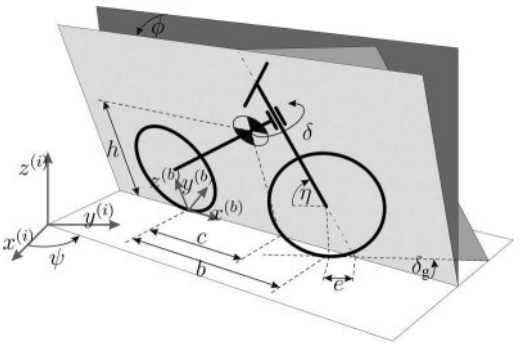


Figure 3. Model of the motorcycle and relevant parameters.

Table 1. List of symbols, descriptions and units.

Symbol	Description	Unit
b	wheelbase	m
c	x-position of COG	m
d	distance orthogonal to reference	m
e	trail	m
g	acceleration due to gravity	m/s^2
h	z-position of COG	m
m	mass	kg
s	arc length along reference	m
v_{rx}	velocity (rear in x-direction)	m/s
ϕ	roll angle	rad
ψ	yaw angle	rad
δ	steering angle	rad
δ_g	effective δ on ground	rad
κ	curvature ($\kappa = \text{radius}^{-1}$)	1/m

4 CONTROLLER CONCEPT

To assess the rider's control inputs on the motorcycle a comparative value has to be generated, assuming we are given the course of a road and a position-dependent velocity target.

There have been numerous approaches to the task of modeling a human as a controller for different systems. One of the first approaches for vehicles was done by Donges (1982). He proposed to divide the whole riding task into three stages: stabilization, guidance and navigation. Rasmussen (1983) presented another multilevel model by dividing human actions into the levels skill-, rule-, and knowledge-based levels. Relating to these hierarchical models, Prokop (2001) proposes a hierarchical controller for a car, that uses constrained nonlinear vector optimization to predict the future movement of the vehicle and an underlying compensatory PID controller for tracking the optimized movement.

In an analogous manner, the controller is cascaded into the following three levels:

1. Low-Level (stabilization/skill-based): This controller tracks a given velocity and roll angle trajectory and prevents the motorcycle from falling over. It uses a robust control method to compensate for disturbances and modeling errors.
2. Medium-Level (guidance/rule-based): This level uses Linear Model Predictive Control (LMPC) to plan a local trajectory. The optimal maneuver for a given period of time is calculated starting at the current state and under the consideration of objectives like comfort or energy consumption. This is handed down to the low-level-controller as reference input for roll angle and velocity.
3. High-Level (navigation/knowledge-based): This level can include strategic decisions, for example which road or lane to use. It will not be presented in further detail here.

4.1 *Low-level-controller*

The input matrix (2c) shows, that the first input ω_κ influences both dynamics whereas the second input F_{rx} only affects the longitudinal system. That is why velocity control is the inner cascaded loop while the roll dynamics is controlled in the outer loop.

4.1.1 *Longitudinal dynamics*

Using the diffeomorphism

$$F_{rx} = B_{22}^{-1}\left(M_{21}\ddot{\phi} + \widehat{F}_{rx}\right) \tag{3}$$

as input substitution, the longitudinal differential equation derived from system (1) leads to the longitudinal subsystem

$$\dot{v}_{rx} = \underbrace{M_{22}^{-1}\left(K_2 + B_{21}\omega_\kappa\right)}_{=:f_v=(\overline{f}_v+\Delta f_v)} + \underbrace{M_{22}^{-1}}_{=:g_v}\widehat{F}_{rx}, \tag{4}$$

which is affine in the dynamics from input $\widehat{F}_{rx}$ to output $\dot{v}_{rx}$.

This is a requirement for the robust sliding mode control. Using this control method, systems with model uncertainties $|\Delta f_v| \leq \delta_v$ can be stabilized (Abel 2006). Choosing the sliding surface as

$$\zeta' = (v_{\mathrm{rx}} - v_{\mathrm{rx,d}}) + k_{v,1}\,(\zeta - \zeta_{\mathrm{d}})\,. \tag{5}$$

leads to the control law

$$\widehat{F}_{\mathrm{rx}} = -\frac{1}{g_v}\left(\overline{f}_v + (k_v + \delta_v)\,\mathrm{sat}(\zeta', \zeta'_{\mathrm{sat}})\right.$$
$$\left. - \dot{v}_{\mathrm{rx,d}} + k_{v,1}\,(v_{\mathrm{rx}} - v_{\mathrm{rx,d}})\right). \tag{6}$$

in which the coefficients k_v, $k_{v,1}$, ζ'_{sat} are design parameters and $k_{v,1}$ can be chosen by specifying an intended error dynamics. The estimation δ_v is application-specific and optional. The real input F_{rx} can be calculated using equation (3).

4.1.2 *Lateral dynamics*

For roll angle tracking a similar controller can be designed for the system

$$\ddot{\phi} = \underbrace{M_{11}^{-1} K_1}_{=:f_\phi=(\overline{f}_\phi+\Delta f_\phi)} + \underbrace{M_{11}^{-1}}_{=:g_\phi}\widehat{\omega}_\kappa \tag{7}$$

by using the substitution

$$\omega_\kappa = B_{11}^{-1}\,(M_{12}\dot{v}_{\mathrm{rx}} + \widehat{\omega}_\kappa) \tag{8}$$

and the sliding surface

$$\zeta = \left(\dot{\phi} - \dot{\phi}_{\mathrm{d}}\right) + k_{\phi,2}\,(\phi - \phi_{\mathrm{d}}) + k_{\phi,1}\int (\phi - \phi_{\mathrm{d}})\,\mathrm{d}t. \tag{9}$$

In an analogous manner, this leads to the control law

$$\widehat{\omega}_\kappa = -\frac{1}{g_\phi}\left(\overline{f}_\phi + (k_\phi + \delta_\phi)\,\mathrm{sat}(\zeta, \zeta_{\mathrm{sat}})\right.$$
$$\left. - \ddot{\phi}_{\mathrm{d}} + k_{\phi,2}\left(\dot{\phi} - \dot{\phi}_{\mathrm{d}}\right) + k_{\phi,1}\,(\phi - \phi_{\mathrm{d}})\right) \tag{10}$$

and the design parameters $k_\phi, k_{\phi,1}, k_{\phi,2}, \zeta_{\mathrm{sat}}$ as well as the optional estimation $\delta_\phi \geq |\Delta f_\phi|$.

4.2 *Medium-level-controller*

Since the motorcycle is a nonlinear system, the obvious approach would be a nonlinear model predictive controller (NMPC), which is a non-convex optimization problem, and therefore very time-consuming and not applicable for real-time use.

A convenient approach to the model predictive goal can be accomplished by formulating it as a linear-quadratic optimization problem. Linearizing the dynamics around the time-invariant upright position of rest would neglect the whole roll dynamics so a better approach is a time-variant linearization around a given desired trajectory.

Taking the lateral component of the dynamic system (1) and solving for $\omega_\kappa = \dot{\kappa}$ leads to the equation

$$f_\kappa(\underline{x}) := \dot{\kappa} = -\left(\frac{1}{h} + \kappa \sin\phi\right)\frac{h}{c}v_{\mathrm{rx}}\kappa - \frac{\mathrm{g}}{c}\frac{\tan\phi}{v_{\mathrm{rx}}}$$
$$+ \frac{ge\sin\eta}{h}\frac{\kappa}{v_{\mathrm{rx}}} - \kappa\frac{\dot{v}_{\mathrm{rx}}}{v_{\mathrm{rx}}} + \frac{h}{c}\frac{\ddot{\phi}}{v_{\mathrm{rx}}\cos\phi}. \tag{11}$$

Not only the dynamics but also the kinematic part is essential for planning a lateral trajectory, so we also have to include those states which can be approximated by

$$\dot{d} = v_{\mathrm{ref}}\Delta\psi \tag{12a}$$

$$\dot{e}_\psi = v_{\mathrm{ref}}(\kappa - \kappa_{\mathrm{ref}}) \tag{12b}$$

where d denotes the lateral offset to a given trajectory (subscript "ref" for reference) and e_ψ is the heading error (Werling 2011).

By linearizing this nonlinear, time-invariant dynamics around the known trajectory $u_{\mathrm{ref}} = \ddot{\phi}_{\mathrm{ref}}$ and $\underline{x}_{\mathrm{ref}} = \left[\, d_{\mathrm{ref}} \;\; \psi_{\mathrm{ref}} \;\; \kappa_{\mathrm{ref}} \;\; \phi_{\mathrm{ref}} \;\; \dot{\phi}_{\mathrm{ref}} \;\; \ddot{\phi}_{\mathrm{ref}} \,\right]^{\mathrm{T}}$ it can be transformed into a linear, time-variant system

$$\Delta\dot{\underline{x}} = \mathbf{A}(t)\Delta\underline{x} + \mathbf{B}\Delta u \tag{13}$$

$$\underline{y} = \mathbf{C}\Delta\underline{x} + \mathbf{W}\underline{d}. \tag{14}$$

To consider constraints for the states, absolute coordinates are generated in the output equation by adding the needed reference states $\underline{d}$ as a known disturbance and using the output $\underline{y}$ for the cost function instead of the states. For a simplified collision check, in this example we approximate the motorcycle by three circles along its axis of symmetry. One at the rear wheel contact point (the local origin) and two further to the front on the same axis with distance l_1 and l_2 to the local origin.

With the batch approach (Borrelli, Bemporad, & Morari 2011), it is possible to express the state-vector's dynamics for the whole time horizon by multiplying backwards the linearized dynamic- and input-matrices to get a single large linear system which describes the relative motion with respect to the reference trajectory. Therefore the equivalent discrete-time dynamic matrices $\mathbf{A}_k$, $\mathbf{B}_k$ are needed, which can be calculated

for example by using the MATLAB *Symbolic Math Toolbox*.

$$\Delta\mathbf{x} = \underbrace{\begin{bmatrix} \mathbf{A}_0 \\ \prod_{q=0}^{1} \mathbf{A}_{1-q} \\ \vdots \\ \prod_{q=0}^{N-1} \mathbf{A}_{N-1-q} \end{bmatrix}}_{\mathcal{A}\in\mathbb{R}^{nN\times n}} \Delta\underline{x}_0 \quad +$$

$$\underbrace{\begin{bmatrix} \mathbf{B}_0 & \mathbf{0} & \cdots & \mathbf{0} \\ \mathbf{A}_1\mathbf{B}_0 & \mathbf{B}_1 & \cdots & \mathbf{0} \\ \vdots & \ddots & \ddots & \vdots \\ \left(\prod_{q=1}^{N-1} \mathbf{A}_{N-q}\right)\mathbf{B}_0 & \cdots & \cdots & \mathbf{B}_{N-1} \end{bmatrix}}_{\mathcal{B}\in\mathbb{R}^{nN\times mN}} \Delta\mathbf{u} \tag{15}$$

$$\mathbf{y} = \mathcal{C}\Delta\mathbf{x} + \mathcal{W}\mathbf{d} \tag{16}$$

whereas each matrix entry can be calculated with $i, j = 1, \ldots, N$

$$\mathcal{A}_i = \prod_{q=0}^{i-1} \mathbf{A}_{i-1-q} = \mathbf{A}_{i-1}\mathbf{A}_{i-2}\cdots\mathbf{A}_1\mathbf{A}_0 \tag{17a}$$

$$\mathcal{B}_{i,j} = \begin{cases} \left(\prod_{q=j}^{i-1} \mathbf{A}_{i+j-q-1}\right)\mathbf{B}_{j-1}, & \text{if } i \geq j+1 \\ 0, & \text{else} \end{cases} \tag{17b}$$

$$\mathcal{C} = \operatorname{diag}(\overbrace{\mathbf{C}, \ldots, \mathbf{C}}^{N \text{ times}}) \quad \text{and} \tag{17c}$$

$$\mathcal{W} = \operatorname{diag}(\underbrace{\mathbf{W}, \ldots, \mathbf{W}}_{N \text{ times}}). \tag{17d}$$

The general quadratic criterion

$$J(\underline{x}_0, \mathbf{u}) = \underline{y}_N^{\mathrm{T}}\mathbf{P}\underline{y}_N + \sum_{k=1}^{N-1} \underline{y}_k^{\mathrm{T}}\mathbf{Q}\underline{y}_k + \sum_{k=0}^{N-1} \underline{u}_k^{\mathrm{T}}\mathbf{R}\underline{u}_k \tag{18}$$

is used as a cost function for an optimal compromise between different states and weighting the controller output with the weighting matrices $\mathbf{Q} \in \mathbb{R}^{n\times n}$ for the output steps 1 to $N-1$, $\mathbf{P} \in \mathbb{R}^{n\times n}$ for the final output step N and $\mathbf{R} \in \mathbb{R}^{m\times m}$ for costs generated by the input. It can be converted to

$$J(\underline{x}_0, \Delta\mathbf{u}) = \Delta\mathbf{u}^{\mathrm{T}}\mathbf{H}\Delta\mathbf{u} + \mathbf{K}\Delta\mathbf{u}, \tag{19}$$

which only depends on the initial state $\Delta\underline{x}_0$ and the controller output $\Delta\mathbf{u}$, through the transformations (Gutjahr & Werling 2015)

$$\mathbf{H} = \mathcal{B}^{\mathrm{T}}\mathcal{Q}\mathcal{B} + \mathcal{R},$$

$$\mathbf{K} = 2\Delta\underline{x}_0^{\mathrm{T}}\mathbf{F} + 2\underline{d}^{\mathrm{T}}\mathbf{M},$$

$$\mathbf{F} = \mathcal{A}^{\mathrm{T}}\mathcal{Q}\mathcal{B}, \quad \mathcal{Q} = \mathcal{C}^{\mathrm{T}}\widehat{\mathcal{Q}}\mathcal{C},$$

$$\mathbf{M} = \mathcal{W}^{\mathrm{T}}\widehat{\mathcal{Q}}\mathcal{C}\mathcal{B},$$

$$\widehat{\mathcal{Q}} = \operatorname{diag}(\underbrace{\mathbf{Q}, \ldots, \mathbf{Q}}_{(N-1) \text{ times}}, \mathbf{P}),$$

$$\mathcal{R} = \operatorname{diag}(\underbrace{\mathbf{R}, \ldots, \mathbf{R}}_{N \text{ times}}).$$

By combining the output equation (16) and replacing $\Delta\mathbf{x}$ by the system dynamic equation (15) the inequality constraints

$$\mathbf{y}_{\min} \leq \mathbf{y} \leq \mathbf{y}_{\max} \tag{20}$$

can be written as

$$\underbrace{\begin{bmatrix} \mathcal{C}\mathcal{B} \\ -\mathcal{C}\mathcal{B} \end{bmatrix}}_{\mathcal{A}_c\in\mathbb{R}^{2pN\times mN}} \Delta\mathbf{u} \leq \underbrace{\begin{bmatrix} \mathbf{y}_{\max} - \mathcal{C}\mathcal{A}\Delta\underline{x}_0 - \mathcal{W}\mathbf{d} \\ -\mathbf{y}_{\min} + \mathcal{C}\mathcal{A}\Delta\underline{x}_0 + \mathcal{W}\mathbf{d} \end{bmatrix}}_{\mathbf{b}_c\in\mathbb{R}^{2pN}}. \tag{21}$$

Altogether this leads to a linear-quadratic optimization

$$\min_{\Delta\mathbf{u}} \quad J(\underline{x}_0, \Delta\mathbf{u}) \tag{22a}$$

$$\text{subject to} \quad \mathcal{A}_c\Delta\mathbf{u} \leq \mathbf{b}_c \tag{22b}$$

$$\Delta\mathbf{u} \leq \mathbf{u}_{\max} - \mathbf{u}_{\text{ref}}, \tag{22c}$$

$$-\Delta\mathbf{u} \leq \mathbf{u}_{\text{ref}} - \mathbf{u}_{\min} \tag{22d}$$

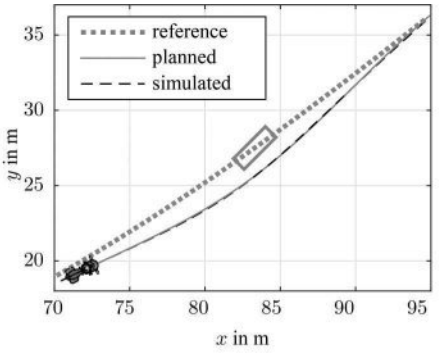
for which very efficient solvers are available. Adding the reference input $\underline{u}_{\text{ref}}$ results in the real system input for each time step

$$u = u_{\text{ref}} + \Delta u. \tag{23}$$

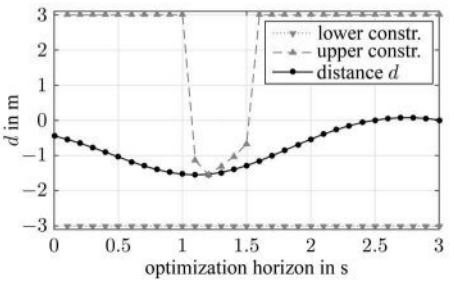
5 RESULTS

Figure 4 shows the results of a swerve maneuver caused by an obstacle on the reference trajectory. In figure 4(a) the bird-view perspective shows the reference as a bold dashed gray line. Once the prediction horizon reaches the obstacle, the swerve maneuver is started.

The optimal maneuver is the one that passes the obstacle with the minimal allowed distance. As



(a) Bird-view of swerve maneuver with the original reference trajectory and the resulting maneuver of the MPC.



(b) Planned lateral distance to the reference and constraints for the optimization step shown in the upper figure.

Figure 4. Swerve maneuver as a combination of low- and medium-level controller.

expected, figure 4b shows that at time step 1.2 s the upper constraint is active.

The same controller can also be used for an ARAS where it runs in the background and supervises a rider's actions. At every time step it calculates the optimal maneuver and can check if it is possible without getting too close to unstable situations.

6 CONCLUSION

As the accident research shows, every third accident involves a motorcycle with a prior instability. Since there are already reactive assistant systems that assist the rider in such a situation, this paper presents a basis for developing advanced rider assistant systems that can prevent critical situations before they occur.

The controller uses a time-efficient formulation of the model predictive control (MPC) by expressing it as a linear-quadratic optimization problem. For this kind of optimization problem very efficient solvers are available.

Safety systems can use this controller as a virtual rider that monitors the riding situation. Its model knowledge can either be used to predict the future movement of the motorcycle, to detect possible collisions with other traffic participants or to plan an optimal maneuver for the motorcycle itself. Based on that maneuver it can compare its command signals to the ones from the real rider to detect a divergence and deduce the best time for warnings or mitigating actions.

REFERENCES

Abel, D. (2006). *Höhere Regelungstechnik*. Aachener Forschungsgesellschaft Regelungstechnik e.V.

Borrelli, F., A. Bemporad, & M. Morari (2011). Predictive control for linear and hybrid systems. *Cambridge February 20*, 2011.

Bundesamt, S. (2016). *Verkehr – Verkehrsunfälle 2015*. Wiesbaden: Statistisches Bundesamt.

Donges, E. (1982). Aspekte der aktiven sicherheit bei der führung von personenkraftwagen. *AUTOMOBIND 27*(2), 183–190.

Getz, N. H. (1995). *Dynamic inversion of nonlinear maps with applications to nonlinear control and robotics*. Ph. D. thesis, University of California at Berkeley.

Gutjahr, B. & M. Werling (2015). Optimale fahrzeugquerführung mittels linearer, zeitvarianter mpc. In *Workshop Fahrerassistenzsysteme*.

Hautzinger, H., W. Stock, & J. Schmidt (2002). *Fahrleistungserhebung 2002 – Inlandsfahrleistung und Unfallrisiko – Berichte der Bundesanstalt für Straßenwesen*. Heilbronn, Mannheim: Institut für angewandte Verkehrs- und Tourismusforschung – IVT – Bundesanstalt für Straßenwesen.

Prokop, G. (2001). Modeling human vehicle driving by model predictive online optimization. *Vehicle System Dynamics 35*(1), 19–53.

Rasmussen, J. (1983). Skills, rules, and knowledge; signals, signs, and symbols, and other distinctions in human performance models. *IEEE transactions on systems, man, and cybernetics 3*, 257–266.

Werling, M. (2011). *Ein neues Konzept für die Trajektoriengenerierung und -stabilisierung in zeitkritischen Verkehrsszenarien*, Volume 34. KIT Scientific Publishing.

Yi, J., Y. Zhang, & D. Song (2009). Autonomous motorcycles for agile maneuvers, part i: Dynamic modeling. In *Decision and Control, 2009 held jointly with the 2009 28th Chinese Control Conference. CDC/CCC 2009. Proceedings of the 48th IEEE Conference on*, pp. 4613–4618. IEEE.

Database

Advanced Vehicle Control – Edelmann, Plöchl & Pfeffer (Eds)
© 2017 Taylor & Francis Group, London, ISBN 978-1-138-02992-7

Geostatistical meta-modeling for a model-based calibration of an adaptive shock absorber

S. Blume & S. Reicherts
University of Duisburg-Essen, Duisburg, Germany

H. Koegeler & N. Didcock
AVL List GmbH, Graz, Austria

T. Henn
Dr. Ing. h.c. F. Porsche AG, Stuttgart, Germany

ABSTRACT: The goal of every calibration is to identify an optimal setup. As modern chassis control systems are influenced by an increasing number of different parameter, the calibration task is getting also more complex. So far, the identification of an optimal parameter setup was done with an iterative attempt. This attempt seems to be overtaken by the fast growing complexity of new systems. In this approach a method is presented to simplify the calibration by techniques of Design of Experiments. Specifically the meta-model for simulation results is discussed in detail. So far, Design of Experiments is used mainly on the basis of measured results in automotive context. This paper presents the differences between interpolating modeling approaches against conventional meta-models and emphasizes on its advantages and borderlines.

1 INTRODUCTION

The present development of automotive systems yields a variety of new challenges in every vehicle component. New combustion engines are required to be powerful as well as economic the same time, while fulfilling new legislation requirements. For modern chassis systems the balancing act between driving performance, comfort and safety has to be managed as well. To ensure future-compliant vehicles for the market, a number of partly contradictory requirements have to be considered and implemented during the development process. The expansion in derivatives makes development even more challenging. Conversely, the massive amount of cross-system requirements leads to a significant increase in complexity, resulting in a blow up of development and coordination task. The global goal, independent of the calibration task itself, is to find an optimal setup for every component and for the complete vehicle as well. In the calibration process of the control unit of combustion engines the methodology of Design of Experiments (abbr. DoE) is well-established. The control of vehicle engines is generally based on thousands of calibration parameter, the complexity is not manageable without detailed system knowledge. As the calibration is done at a test bench, it is not feasible to test every possible combination of parameters. Rather, the statistic methodology of DoE helps the developer to achieve the knowledge about interaction of calibration parameter. Normally an approximation model called meta-model is built, that represents the inherent transfer behavior between the input, output and calibration parameter. The meta-model is based on measurement data from the test bench. It can easily be optimized and the resulting calibration parameter can be applied to the real combustion engine. The development process is called model-based calibration.

A second important pillar in automotive development is the proceeding efforts to transfer as much of the calibration process as possible to a simulation environment as prototype tests are very expensive and only possible in late stages of the development process. In order to guarantee higher accuracy the simulation model complexity is growing constantly. Meantime the model size had grown, so that a direct optimization of those model is not feasible any longer. Rather, a meta-model is build that is limited to the representation of a defined relationship. The optimization of the meta-model is inexpensive.

In principle, it is conceivable to use the established techniques that are used for engine calibration task, for simulation components also. In figure 1 the process of model-based calibration is presented in principal. As it can be seen, the general process for a real component or for a virtual one does not differ.

But the two approaches differ in their inherent characteristics. It is important to consider the general difference between building a meta-model of a simulation model or a real assembly. In real world calibrations task, measurements are done. Measurements signals are always polluted with noise, resulting in variance

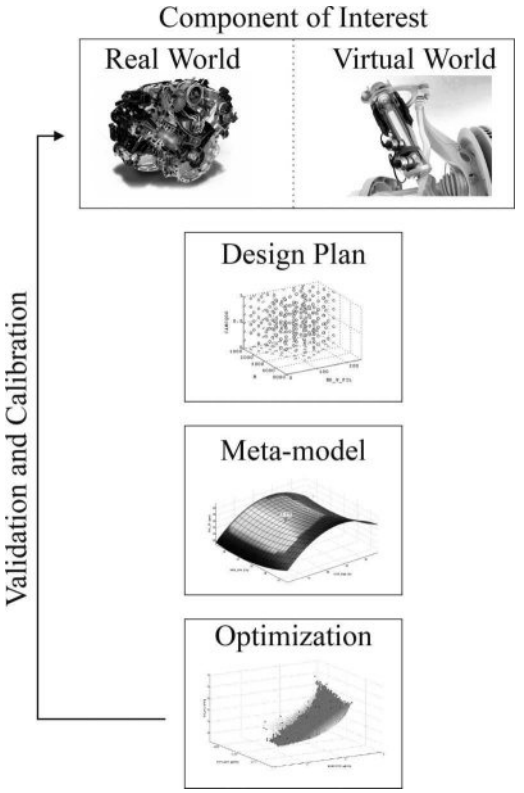


Figure 1. Model-based calibration process.

in the results. A simulation model is deterministic, according to this fact a defined input will always result in the same output, hence it is reasonable to assume that alternative meta-models could be more suitable than the established ones. In this approach an interpolating meta-model shall be discussed as an alternative to conventional models for the calibration of simulation environment.

2 FORMULATION OF THE PROBLEM

The particular properties of the interpolating meta-model compared to conventional meta-models should be demonstrated at the example of the calibration process of an adaptive shock absorber.

The increasing consumer demand for chassis design that offers a large inclination between driving dynamics on the one hand and driving comfort on the other hand, cannot be satisfied by passive chassis systems. Hence, active and semi-active chassis control systems are used. Those chassis control systems enable the developers to design vehicle characteristics that completely fulfill the consumer and market requirements. Yet, the superior driving characteristics of semi-active and active systems come along with rapidly increased complexity in calibration tasks.

In this approach a simulation model of a driving dynamic controller for adaptive shock absorber is used. The different calibration setups are rated by objective criterias regarding driving performance and comfort. For this approach multidimensional functions that represent different criteria will be investigated. The criteria itself will not be presented in more detail, as the focus of this work is on the meta-modeling and not on the calibration task itself. Themodel is very detailed and feasible for virtual parameter calibrations, see (Henn, Eisenbarth, & Schramm 2015). Simultaneously the computational effort is increasing due to the need for increasing accuracy and the accompanying increase in the number of parameters. Consequently, the simulation model has become too expensive for a direct multi-objective optimization.

3 META-MODEL THEORY

With the knowledge of the model's input-output relationship a meta-model is created. Established DoE techniques offers several methods to create such a meta-model, but most calibration areas are nondeterministic and results are varied (Stadlbauer, Didcock, Hametner, Jakubek, Rainer, & H. 2014).

3.1 *Kriging*

As the simulation model is deterministic, an interpolating meta-model method might be more appropriate than a classical stochastic model, which considers scattered data. For this purpose the geostatistical Kriging-method (Matheron 1963) is used to analyze the relationship between calibration parameter and characteristic values of the shock absorber model. The results are compared to the established Robust Neural Network (abbr. RNN). The Ordinary-Kriging method is a form of weighted averaging, such that the predicted value Z^*_{OK} at point $\mathbf{x}_0$ is

$$Z^*_{OK}(\mathbf{x}_0) = \sum_{\alpha=1}^{n} w_\alpha(\mathbf{x}_0) Z(\mathbf{x}_\alpha), \tag{1}$$

where $\mathbf{x}_0$ is the point to be predicted, w_α is the weight of the sample point $\mathbf{x}_\alpha$ and $Z(\mathbf{x}_\alpha)$ is the measurement at sample point $\mathbf{x}_\alpha$.

The weights are chosen such that the error associated with the predictor is less than any other linear sum. This is called best linear unbiased predictor, as the weights add up to one and hence

$$\begin{aligned} & E\left[Z^*(\mathbf{x}_0) - Z(\mathbf{x}_0)\right] \\ = \; & E[\sum_{\alpha=1}^{n} w_\alpha Z(\mathbf{x}_\alpha) - Z(\mathbf{x}_0) \underbrace{\sum_{\alpha=1}^{n} w_\alpha}_{=1}] \\ = \; & \sum_{\alpha=1}^{n} w_\alpha E\left[Z(\mathbf{x}_\alpha) - Z(\mathbf{x}_0)\right] \\ = \; & 0 \end{aligned} \tag{2}$$

is true, where E[·] is the expected value.

The weights depend upon the distance to the sampling points of the prediction process and upon the covariation reflected in the semivariogram. The semivariogram is a function $\gamma(h)$ of the distance h and indicates the theoretical spatial correlation of the observation points. So, the semivariogram only depends on the distance h of two points but not on their position in the domain.

If the estimation variance

$$\begin{aligned}\sigma_E^2 &= E\left[(Z^*(\mathbf{x}_0) - Z(\mathbf{x}_0))^2\right] \\ &= -\gamma(\mathbf{x}_0 - \mathbf{x}_0) - \sum_{\alpha=1}^{n}\sum_{\beta=1}^{n} w_\alpha w_\beta \gamma(\mathbf{x}_\alpha - \mathbf{x}_\beta) \\ &\quad +2\sum_{\alpha=1}^{n} w_\alpha \gamma(\mathbf{x}_\alpha - \mathbf{x}_0), \end{aligned} \tag{3}$$

is minimized, the weights can be calculated by evaluating the system of equations

$$\begin{pmatrix} \gamma(\mathbf{x}_1-\mathbf{x}_1) & \dots & \gamma(\mathbf{x}_1-\mathbf{x}_n) & 1 \\ \vdots & \ddots & \vdots & \vdots \\ \gamma(\mathbf{x}_n-\mathbf{x}_1) & \dots & \gamma(\mathbf{x}_n-\mathbf{x}_n) & 1 \\ 1 & \dots & 1 & 0 \end{pmatrix} \begin{pmatrix} w_1 \\ \vdots \\ w_n \\ \mu \end{pmatrix}$$

$$= \begin{pmatrix} \gamma(\mathbf{x}_1-\mathbf{x}_0) \\ \vdots \\ \gamma(\mathbf{x}_n-\mathbf{x}_0) \\ 1 \end{pmatrix}, \tag{4}$$

where μ is the Lagrange parameter.

Ordinary Kriging is an exact interpolator, such that the predicted output $Z^*(\mathbf{x}_0)$ and the measured output $Z(\mathbf{x}_0)$ are identical if the prediction point $\mathbf{x}_0$ is one of the sample points $\mathbf{x}_\alpha$, $\alpha = 1, \dots, n$. This can easily be seen when $\mathbf{x}_0 = \mathbf{x}_\alpha$, the right hand side of equation (4) is equal to one column of the left hand side. Thus,

$$\exists!\, \alpha \in \{1, ..., n\} : w_\alpha = 1 \wedge w_\beta = 0, \forall \beta \neq \alpha. \tag{5}$$

Since the matrix on the left hand side of equation (4) is regular, this is the only solution of the System of equations (Wackernagel 2003).

3.2 *Robust Neuronal Network*

This section briefly discusses a Robust Neural Network (abbr. RNN) structure implemented in AVL CAMEO^{TM} which was used for comparison with the discussed Kriging interpolation model. These neural networks have the structure of so-called local polynomial models, see e.g. (Nelles 2013). They are characterized by a number of weighted (local), linear regression models, e.g. quadratic polynomials, and demonstratively perform well e.g. for NO_x emission models (Hametner, Mayr, & Jakubek 2014).

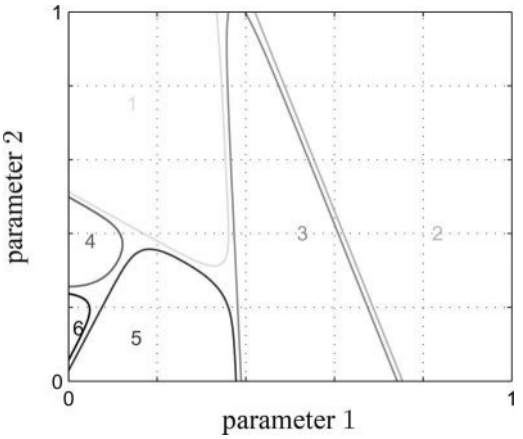


Figure 2. Validity regions: contour plot of possible validity regions after recursive intersection for a local model network with six local polynomials.

A local model network with M local models has the form

$$Z^*_{RNN}(\boldsymbol{x}_0) = \sum_{l=1}^{M} \Phi_l(\boldsymbol{x}_0) \cdot \boldsymbol{p}(\boldsymbol{x}_0)^T \boldsymbol{\beta}_l, \tag{6}$$

where, locally, the model output is approximately of the form $\boldsymbol{p}(\boldsymbol{x})^T \beta_l$ and the regression vector, $\boldsymbol{p}(\boldsymbol{x})$, is of polynomial form. The activation function, $\Phi_l(\boldsymbol{x})$, can be modeled by recursively intersecting the input space and determining the validity of the local polynomials in each region. If, locally, the data is poorly estimated by the local polynomial, the validity region is split by a hyperplane and two separate local regressions are performed. The splitting procedure is depicted in Figure 2, which shows a possible contour plot of the validity regions for six local models.

Let $\boldsymbol{P}$ denote the regressor matrix of the form $\boldsymbol{P} = [\boldsymbol{p}(\boldsymbol{x}_1), \dots, \boldsymbol{p}(\boldsymbol{x}_n)]^T$. The optimal parameter to minimize the sum of the *local costs* (Nelles 2013):

$$\ell(\boldsymbol{\theta}) = \sum_{l=1}^{M} \left(\boldsymbol{Z} - \boldsymbol{P}^T \boldsymbol{\beta}_l\right)^T \boldsymbol{W}_l \left(\boldsymbol{Z} - \boldsymbol{P}^T \boldsymbol{\beta}_l\right) / n \tag{7}$$

$\boldsymbol{W}_l = \mathrm{diag}(\Phi_l(\boldsymbol{x}_1), \dots, \Phi_l(\boldsymbol{x}_n))$. For a detailed discussion on parameter estimation in local model networks see (Jakubek & Hametner 2009).

4 INVESTIGATION

The analyzed shock absorber model consists of different parameters to change the characteristic maps of dampers, springs and other components in the vehicle to manipulate the driving behavior of a sports car. This behavior is classified in characteristic values which describe different kinds of characteristic oscillations of the vehicle like high or low frequency vibrations of the body motion. For example, three parameters and

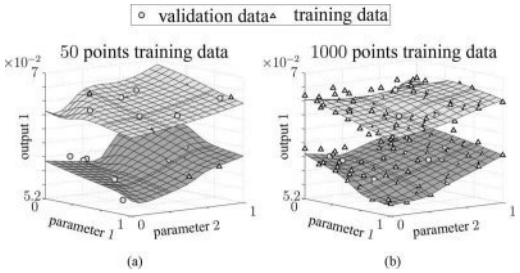


Figure 3. Surfaces Robust Neural Network (a) with 50 Sample Points and (b) with 501 Sample Points.

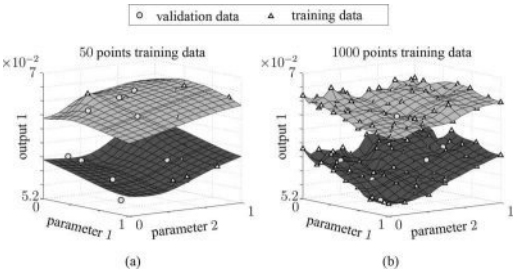


Figure 4. Surfaces Ordinary Kriging (a) with 50 Sample Points and (b) with 501 Sample Points.

ten characteristic values were chosen to compare different types of meta-models, where the first output is investigated in more detail. The parameters of the analyzed shock absorber model are the inputs of the meta-model and the characteristic values are the outputs. Thus, the influence and sensitivity of parameters on characteristic values can be evaluated. Therefore, the shock absorber model is simulated for a vertical maneuver driven at 60 kmph. This simulation is run several times with different parameter setups where the parameter adjustments are determined by a parameter design plan.

The design plan consists of 1000 runs with different parameter combinations, the so-called inputs of the meta-model. For the training task of the metamodel the design plan is split into pieces of ascending size of 50, 100, 200, 500 and 1000 simulation runs. For the simulation design an S-optimal design plan is constructed in AVL CAMEO^{TM}. An S-optimal design plan has the property that it is a space filling test design, taking into account the distance between design and candidate list to optimize different criteria. This optimization ensures that the design is laid out in the test space and nonlinearities can be detected by a model approach. In principle, it maximizes the minimal distance to the next point, like rejecting magnets. It can be split easily into different pieces, which itself is again a space-filling test design.

Figure 3 shows a three dimensional surface for the exemplified first output value of the RNN trained with (a) 50 sample points and (b) 1000 sample points . On the vertical axis the value of the first output is plotted. On the horizontal axes parameters one and two are diagrammed whereas parameter three is fixed to its upper and lower limit respectively. The lower, dark yellow surface is a characteristic value of the shock absorber model if the third parameter is fixed to its lower limit and the upper, bright yellow surface represents the output if the third parameter is fixed to its upper limit. The surface offers the beholder an idea about the design range of the visualized output. The green dots represent the verification points and the white triangles correspond to the sample points used to train the models. The verification points are randomly distributed over the two parameters shown having the third parameter at its lower and upper limit. The same surfaces can be seen in Figure 4 but for Ordinary Kriging. Figure 3 and Figure 4 show the behavior of the two types of meta-models and their development from 50 to 1000 sample points. In fact, both surfaces in Figure 3 are very smooth and simple. However, the disparity in the surface shapes is obvious. The sample points (white triangles) used to construct the models are not part of the surface, as the models assume a variance in the measured data. The green validation points are fitted quite well in the center of the design space, whereas in the border area, especially the RNN with only 50 sample points reveals large deviations.

In comparison to the RNN the Kriging model do not have a smooth surface. The surface is similar to a mountain landscape, particularly the Kriging model with 1000 sample points. However, the sharpness of the surface is not a surprise, as in section 3.1, it was already explained, that Kriging is an exact interpolator. Hence, the surface is forced to fit every sample point, see figure 4. The tendency to show an uneven surface grows with the number of sample points.

5 VALIDATION

The validation of the models are made with independent simulation results which are not used to construct the models. To create such a validation design a space filling plan should be used and the parameter setups should be random. For this task a Sobol design plan with 100 validation points is generated in AVL CAMEO^{TM}. Sobol design, named after the Russian mathematician I.M. Sobol, uses a quasi-randomized algorithm that evenly distributes the design points in the design space of the unit hypercube which belongs to the space filling designs (Sobol 1967).

The quality of the fits can be seen in Figures 5 and 6 where (a) shows the Measured-Predicted plot for the models trained with 50 sample points and and (b) represents the Measured-Predicted plot for the models with 1000 sample points. Both Plots were evaluated for the random Sobol design and hence the validation points are independent of the training data of the S-optimal designs. The Measured-Predicted plot indicates the quality of the fits as the simulated values of the models are plot over the measured values. So, if and only if the calculation of the models and the measured values are equal, the points perfectly fit the diagonal.

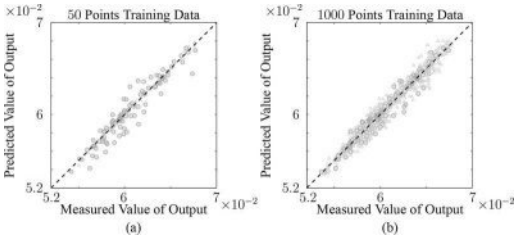


Figure 5. Figure of measured vs. predicted values of RNN models for 50 and 1000 sample points.

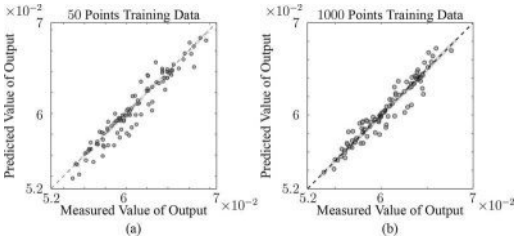


Figure 6. Figure of measured vs. predicted values of Kriging models for 50 and 1000 sample points.

A "lack of fit" is given in case the scattering of the trainings data around the model is significant higher than the scattering of the verification data. For the calibration process of the adaptive shock absorber, the measured values are the outputs of the detailed simulation model and the predicted values are the computed outputs of the meta-models.

The yellow points in Figure 5 and the blue points in Figure 6 represent the measured and predicted points of the validation data. The gray triangles are the sample points used to construct the models with 50 sample points and 1000 sample points.

Figure 5 and Figure 6 show that both models provide good results although the Kriging model is superior for a small data set. By increasing the sample data sets, the RNN gets better and the Kriging method gets worse. This is a result of overfitting since Kriging is an interpolating method, which can bee seen by looking at the sample points plotted in Figure 5 and Figure 6. It is obvious that all sample points predicted by Kriging are exactly the same as the measured data. The sample data simulated by RNN scatters around the diagonal in the same range as the verification data are remaining to do.

This characteristic is more obvious in Figure 7. This figure shows the Normalized Root Mean Squared Error (abbr. NRMSE)

$$\mathrm{NRMSE} = \frac{\sqrt{\frac{1}{m}\sum_{\alpha=1}^{m}(Z(\mathbf{x}_{\alpha,val}) - Z^*(\mathbf{x}_{\alpha,val}))^2}}{Z(\mathbf{x}_{max}) - Z(\mathbf{x}_{min})}, \quad (8)$$

where m is the number of validation points, $Z(\mathbf{x}_{\alpha,val})$ is the measured validation output, $Z^*(\mathbf{x}_{\alpha,val})$ is the simulated output of RNN or Kriging and $Z(\mathbf{x}_{max})$ and

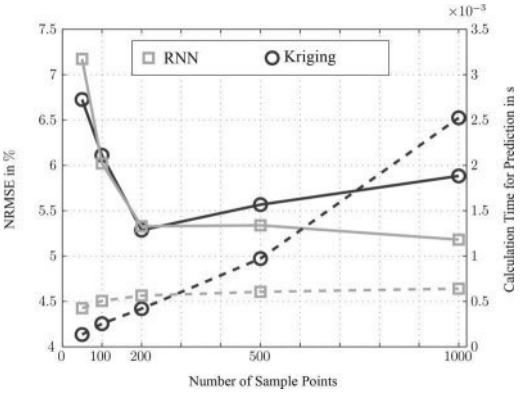


Figure 7. Progression of NRMSE (solid line) and Calculation Time (dashed line) for Prediction over increasing amount of sampling points for Kriging and RNN shown for the first output.

$Z(\mathbf{x}_{min})$ is the maximal and minimal measured output of the sample points. On the other hand, Figure 7 shows the needed time to predict one characteristic value for a parameter set. Both results are plotted over the total number of sample data points used to train the particular models, where the NRMSEs are represented by solid lines and the prediction times are plotted as the dashed lines.

For a small number of data the Kriging method is more appropriate for both error and calculation time. Then the number of points to construct the models is increased, both models are getting better and more equal. Between 200 and 500 sample points both models have nearly the same error and calculation time. The results from RNN get better with higher number of sampling points. In fact, Kriging tends to overfit with sample points greater than 500 and gets worse. Furthermore, the time needed to predict the characteristic values for a parameter set with the Kriging method increases strong by increasing number of sample data, while RNN calculation time just increases a bit, if more local models are used.

The increase in calculation time of Kriging is due to the growing size of the matrix as shown in equation (4). Along with increasing calculation time, the time to construct the models also increases with the number of sample points. In comparison with the RNN, the increase in the construction time of Kriging is more dramatic as the growing covariance matrix has to be inverted. Indeed, for construction task with 1000 sample points the construction time is insignificant small, if considering, that the construction has to be done only once. Hence, a closer look to the construction time is left open. The quality properties of Kriging and RNN demonstrated for the first output can also be seen for the other nine outputs. Figure 8 shows a summary of the comparison of the residua of the two types of meta-models for all ten outputs. Therefore, the NRMSE of the Kriging models is subtracted from the NRMSE of the RNN in order to calculate the residua of both and

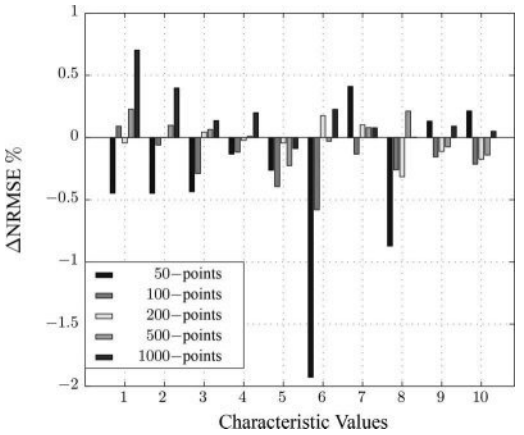


Figure 8. Residua of the NRMSE of Kriging and RNN for varying quantity of sample points.

give a quality statement as to which meta-model performs better. Consequently, if ΔNRMSE is positive, RNN is superior to Kriging. If ΔNRMSE is negative, Kriging is superior to RNN. In this figure no statement regarding the absolute quality of both models is made. Figure 8 shows that for most of the outputs Kriging has its strength for less than 200 sample points. For higher number of sample points, RNN outperforms the Kriging models. Apart from the mentioned tendency, some outputs show a dissenting behavior. For output number five, the Kriging model predicts better than RNN for all numbers of sample points. The contrary outcome can be seen for output number seven. Except for the case of 100 sample points, RNN is always better than Kriging.

6 CONCLUSIONS

In the early stages of a vehicle development project, simulations are used to identify trends and trade offs in system calibration and design. If the goals in system calibration depend on a high amount of parameters, fast and efficient models are necessary. Kriging fulfills those requirements in context of a small number of simulations, given in this early stage of process. The Kriging model shows the property to fit the training data exactly. The expectation, that this property would result in a robust model with small deviations could not be confirmed. The Kriging type models are comparable to the RNN type, and at very low number of points, they represent the verification data better for most cases – for sure on an higher level of absolute error. This trend can also be seen for the calculation time, where Kriging predicts faster in case of very low number of points and needs more time than RNN for a high number of points.

With advanced development process, the simulation models become more detailed and complex based on the increasing information from test experiments and validation. In this case these simulation models get more involved into the development process and support real world testing, e.g. virtual variant coverage. Therefore, accurate meta-models are required which only can be guaranteed by a high number of simulation runs. In case of having many simulation results available, the RNN-type models improve further while the Kriging type models show a tendency to overfit. Despite having no deviation to the training data, the remaining error to the validation points increase more and more. So, for the calibration of the Sky hook damper discussed in (Henn et al. 2015) no significant improvement is expected in the optimization results, when using Kriging instead of Neuronal Networks. In this example of the model based tuning of an adaptive shock absorber with its highly nonlinear responses a range of 100 to 300, simulation runs seems to be appropriate, where both types of models give good results.

REFERENCES

Hametner, C., C. Mayr, & S. Jakubek (2014). Dynamic nox emission modelling using local model networks. *International Journal of Engine Research*, 1468087414523281.

Henn, T., M. Eisenbarth, & D. Schramm (2015). Model-based calibration of an adaptive shock absorber by objective comfort criterions. *Aachener Kolloquium Fahrzeug- und Motorentechnik 24*, 807–818.

Jakubek, S. & C. Hametner (2009). Identification of neurofuzzy models using gtls parameter estimation. *IEEE Transactions on Systems, Man, and Cybernetics, Part B (Cybernetics) 39*(5), 1121–1133.

Matheron, G. (1963). Principles of geostatistics. *Economic Geology 58*(8), 1246–1266.

Nelles, O. (2013). *Nonlinear system identification: from classical approaches to neural networks and fuzzy models*. Springer Science & Business Media.

Sobol, I. (1967). On the distribution of points in a cube and the approximate evaluation of integrals. *USSR Computational Mathematics and Mathematical Physics 7*(4), 86–112.

Stadlbauer, M., N. Didcock, C. Hametner, S. Jakubek, A. Rainer, & K. H. (2014). Online design of experiments in the relevant output range. *Optimization and Optimal Control in Automotive Systems*, 273–289.

Wackernagel, H. (2003). *Multivariate Geostatistics – An Introduction with Applications*. Berlin, Heidelberg: Springer.

Advanced Vehicle Control – Edelmann, Plöchl & Pfeffer (Eds)
© 2017 Taylor & Francis Group, London, ISBN 978-1-138-02992-7

Predictive modeling for vehicle time-series data

J. Wallner & F. Diermeyer
Lehrstuhl für Fahrzeugtechnik, Technische Universität München, Germany

S. Engel
Abteilung für Fahrzeugsicherheit, AUDI AG, Germany

ABSTRACT: The majority of data in current vehicles is evaluated solely in a local manner. The proposed method offers the possibility of using the latest data analysis techniques to develop functions for active safety and driver assistance systems, or vehicle testing of automated driving systems. We show an approach that combines the advantages of machine learning for logged vehicle data with the ability to use the predictive models created online in vehicles. Starting with intelligent data pre-processing, optimal conditions for the analysis step are established. Using machine learning techniques, predictive models are created to estimate various kinds of outcome variables. The concept is shown using the example of estimating the dynamic criticality in vehicles, based on driving dynamics signals and radar data.

1 INTRODUCTION

Connected cars provide an increasing number of safety and comfort functions to the driver. All functions are based on local data analysis. The signals used are delivered by vehicle dynamic sensors, driver input or ambient environment sensors. With the help of algorithms, these functions work well, nevertheless they ignore experience-based data – which would always be used by a human driver. Additionally, local data analysis in vehicles is limited in terms of computing power and available data.

The proposed method will generate a model based on logged and labeled vehicle data, using machine learning algorithms. This modeling step is done offline, which means that hardware is unrestricted. The result, a predictive model, can now be used online in a vehicle. This combines, to some extent, the experience of historical data with real-time data evaluation. The main steps of the approach are shown in Figure 1.

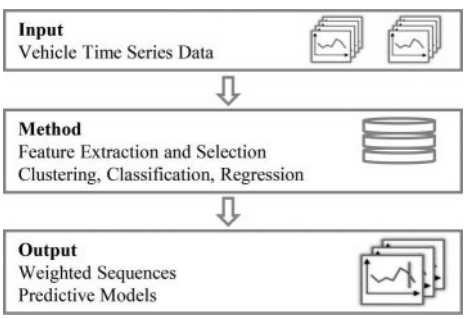


Figure 1. Overview of the Concept.

All steps and methods are explained using the example of estimating the criticality of a driving state in vehicles. This approach is valid without losing generality for other purposes, having a similar database structure with time-series data and well-defined outcome variables. Other areas of application may include maintaining components, optimizing driving dynamics, predicting driver behavior and testing automated driving functions. The latter includes the selection and evaluation of characteristic scenarios.

2 RELATED WORK

Chapter 2 focuses on the example of criticality estimation.

2.1 *Incident database*

There are several approaches to building an incident database. The best opportunities are offered by Field Operational Tests (FOT) or Naturalistic Driving Studies (NDS). In contrast to logged functional testing data, the critical situations are usually generated by normal drivers and have consequently more explanatory power in a safety application for normal drivers.

In (Benmimoun *et al.* 2011), an automated incident detection based on indicator thresholds of CAN data was used to build an incident database out of the large-scale field operational test "euroFOT". Nevertheless, for reliable criticality estimation, the database contains too few crashes. The statistical inference between crashes and incidents is assumed but cannot be verified with this data (Metz *et al.* 2013, p. 74).

Bigger NDS like the "100-car study" (Dingus *et al.* 2006) or the "Strategic Highway Research Program

2 (SHRP2)" (Boyle *et al.* 2012) offer better conditions in terms of reliability and statistical power. In SHRP2, over 1,400 crashes and 2,700 near-crashes were logged and labeled (Virginia Tech Transportation Institute VTTI 2016).

On the basis of these data, database layouts are available to initiate further analysis. (Themann *et al.* 2016) suggests an integrated evaluation of connected and automated driving that combines relevant situations from virtual tests, testing grounds, FOTs and real traffic. The approach seems meaningful for concepts such as the proposed predictive modeling.

A similar method is shown in (Ebner 2014). The frequency of characteristic reference scenarios is used as a basis to develop and evaluate active safety systems. The scenarios were identified from accident data, NDS data and "experiments to analyze driver behavior". They can subsequently be analyzed for active safety systems. Using these scenarios as a database, predictive modeling is also possible here.

2.2 *Definition of a criticality measure*

The criticality is a means of expressing the threat or the danger of a traffic situation (Herrmann *et al.* 2015). For technical purposes an objective measure should be pursued.

A criticality measure can evaluate specific maneuvers. For an example, see (Rodemerk *et al.* 2012), where a general criticality criterion for the risk estimation of driving situations is developed and applied to lane-change maneuvers. This criterion uses the ratio of overlapping areas of predicted locations from the ego vehicle and surrounding objects.

Another way to express the criticality, especially for rear-end collisions, is by calculating the intensity of avoidance maneuvers. This intensity is expressed through an acceleration norm combining the longitudinal and the lateral acceleration of the center of gravity of the vehicle. Calculating the minimally-intense evasion trajectory, which minimizes the norm, results in a quantification of the criticality (Herrmann *et al.* 2015).

Other means of expressing criticality measures involve speed curves. In (Li *et al.* 2014), a surrogate safety measure for evaluating rear-end collision risk related to kinematic waves near recurrent freeway bottlenecks is shown. The measure is derived from the traffic density, occupancy, average vehicle length and average vehicle speed.

Continuous measures of criticality based on the distance to the next target is shown in (Eggert 2014). The proposed measures can generalize time metrics as Time-To-Collision (TTC). They can be used for behavior planning to evaluate trajectories according to their risk.

Another way to define a criticality measure is to integrate human impressions in the risk estimation process. In (Siordia *et al.* 2010), a criticality measure is generated by expert evaluations of drives in a truck cabin simulator. Analogously in (Muehlfeld *et al.* 2011), pre-crash scenarios from a driving simulator are evaluated. The subjective criticality measure of the driver is used and compared with objective features like minimum evasion maneuver.

2.3 *Predictive criticality estimation*

The estimation of criticality is one key task for active safety systems. The higher the quality of estimates for the subsequent time steps, the more potential an active safety system has.

For intelligent Advanced Driver Assistance Systems (ADAS), a predictive risk estimation is shown in (Eggert 2014). This risk estimation can be represented on predictive risk maps and used for a risk sensitive path planning for cognitive vehicles (Damerow and Eggert 2014).

(Wang *et al.* 2015) makes a driving risk assessment using a near-crash database through data mining of a tree-based model. But it is problematic to infer the criticality of real crashes from a near-crash database. The transition from near-crash to crash scenarios still cannot be validated. A significant discrepancy can be seen between the rear-striking crashes and the near-crashes that occurred in the 100-car study (Jonasson and Rootzen 2014).

Another possible means of predicting the crash likelihood is using real-time loop detector data on freeways. In (Xu *et al.* 2013) and (Li *et al.* 2014), crashes are predicted with logistic regression. Similarly, (Yu and Abdel-Aty 2013) use a Support Vector Machine (SVM) for real-time crash risk evaluation, or in (Yu and Abdel-Aty 2014) a hierarchical Bayesian binary probit model is applied in order to analyze crash injury severity. Note that these approaches are not based directly on internal vehicle data, but on loop detector data regarding many vehicles at the same time.

In criticality prediction, a modular concept is also possible: combining a complete driving scene prediction as made in (Jordan *et al.* 2015) with the calculation of a criticality measure presented in section 2.2 allows criticality to also be estimated. In (Jordan *et al.* 2015), a grid-based environment representation is used together with an autoregressive (AR) model that inherently includes the interactions between different vehicles.

It is also possible to use the subjective criticality measure from experts and apply different classification techniques such as Classification and Regression Tree (CART), SVM, K-Nearest Neighbors (KNN) or Artificial Neural Networks (ANN) as shown in (Siordia *et al.* 2010).

To optimize the execution speed, a machine learning approach based on Random Forest classifier with feature selection is adapted in (Herrmann *et al.* 2015) to predict the criticality of combined braking and steering maneuvers.

3 DATABASE

Any kind of time series data is possible as an input. In an automotive context, this may be signals from

Table 1. Overview of possible areas of application.

Areas of application	Types of time-series data	Outcome variable	Goal
Maintenance of components	Monitoring usage data	Probability of failure, remaining usage time	Saving of repair/downtime costs
Optimization of driving dynamics	IMU signals, GPS, chassis signals	Comfort/performance measure	Predictive control of chassis adjustments
Driver behavior	Monitoring driver state	Drowsiness, distraction, state of health	Predictive attention control, driving break recommendation, guaranteed takeover time
Environment perception	Sensor signals	Estimated driving scene	Predictive behavior estimation of road users
Automated driving functions	Sensor signals, signals from vehicle dynamic	System states for automated driving functions	Predictive estimation of system boundaries/critical system states
Testing of highly automated driving	Logged test drive data	Occurrence of characteristic scenarios/situations	Predictive control of test drives to fulfill requirements on functional safety

vehicle dynamics (like velocity, acceleration and yaw rate), ambient environment sensors, component monitoring, driver behavior or system states for automated driving functions. An overview of possible data types with the corresponding outcome variable and the possible goal of a predictive modeling is shown in Table 1.

One sequence consists of n sample points or observations $x_{ij}(t)$, where i is the index for the different sequences and j the index for the signals.

Based on this signals the outcome variable $y_{ik}(t)$ is the goal of the predictive approach. Depending on the application, $y_{ik}(t)$ could be the criticality, the probability or the frequency of an event, for example. Another possible outcome variable could be some kind of classification with the class label c_l. Note that index $l \leq i$ because one class c_l can occur in more sequences. Using the example of criticality this may include classes such as crash, near-crash and non-critical. The structure of the signals is summarized in Table 2.

Table 2. Signal structure of database.

		Outcome	
	Input Signals 1…j	Continuous 1…k	Class label 1…l
Sequences 1…i	$x_{11}(t)\cdots x_{1j}(t)$	$y_{11}(t)\cdots y_{1k}(t)$	c_1
	$\vdots$	$\vdots$	$\vdots$
	$x_{i1}(t)\cdots x_{ij}(t)$	$y_{i1}(t)\cdots y_{ik}(t)$	c_1

3.1 *Data pre-processing*

There are several steps involved in preparing this kind of data for machine learning algorithms. First, all sequences have to be set to the same length, which means that they have the same duration t_{end}.

Ideally, a balanced selection of ground truth and event sequences should be chosen, because most machine learning algorithms work best with equalized quantities. Ground truth is the data occurring during normal driving, in terms of criticality these are sequences without any critical events.

3.2 *Additional labeling*

To include additional information about the outcome, the sequences need to be labeled with the output variable. The goal is that all event sequences contain some kind of an "event", e.g. an exceeded threshold in at least one outcome variable or a characteristic situation in environment perception. In terms of criticality, this is a crash/near-crash for one crash type. There are examples of databases that already contain a normal classification. The NDS data of SHRP2 differentiates in its evaluation between crash, near-crash and non-critical sequences.

For continuous purposes, it may be necessary to add a continuous outcome measure as presented in section 2.2. Additional labeling is possible with some kind of human evaluation, (e.g. (Siordia *et al.* 2010)), or with a continuous rule-based or calculated measure (e.g. (Herrmann *et al.* 2015)).

In the end, the dataset of processing data has i sequences, each with j signals and k output variables or l class labels.

4 METHOD

This chapter shows how the time-series data is processed and evaluated using machine learning techniques.

4.1 *Feature extraction and selection*

The most important features (predictors, variables) of the given time-series data are determined mainly with the following concepts:

A statistical investigation can identify highly correlated variables. This means that they represent the same underlying information. Removing those predictors reduces complexity and computational time. In addition, model performance and stability may improve for some model types (Kuhn and Johnson 2013, p. 35).

In some cases, the creation of new predictor variables as functions of given signals is recommended. These extracted features often contain physical quantities causally connected to the output. Thus the so-called "expert knowledge" can influence the database and the prediction result. Using the example of criticality, this could be the calculation of an objective criticality measure. Depending on the application, a feature generated can also consist of a situation interpretation or a virtual quantity without a physical meaning that describes an effect the developer is expecting. Once this step has been performed, the data has a greater informative value with regard to the objective.

A final step called feature selection can identify the importance of each predictor in choosing the optimal and minimal subset for the modeling process (Kuhn and Johnson 2013, p. 490). There are two possible versions of feature selection (John *et al.* 1994):

On the one hand, Wrapper methods try to find an optimal combination of predictors that maximize the effectiveness of the model. Note that Wrapper methods need a comparatively high computation time. On the other hand, Filter methods analyze the relationship between each predictor and the output. They can be computed more effectively but their selection criterion is not directly related to the model performance. For more details, see (Saeys *et al.* 2007).

In addition, data reduction techniques like Principal Component Analysis (PCA) can trim the number of predictors and therefore the computational effort. PCA combines the former predictors in linear combination to capture the most possible variance. The main disadvantage of this method is that it is no longer possible to interpret the results.

4.2 *Machine learning*

Depending on the characteristics of the given dataset and the algorithms used, a process plan is made. One option would be to split the data into a fixed training and a fixed evaluation set. Another option is to use resampling techniques, which repeat the training and evaluation step several times with changing data sets. The goal here is to have adequate subsets for training end evaluation without the effect of overfitting.

4.2.1 *Clustering*

In order to examine the underlying structure of the sequences, it can be useful to apply clustering algorithms to the processing data. Clustering belongs to the unsupervised types of machine learning where no desired output value is given. In this way, similarities and differences relating to specific signals are visible. For datasets with no labeling, a subsequent categorization and synthetic generation of the output vector would be possible. One instance where clustering makes sense is the testing of highly-automated driving. In this case, the occurrence of characteristic scenarios can be identified in logged test-drive data. Characteristic scenarios may be complex environment interpretations or difficult decisions in behavior generation. If these scenarios can be clustered spatiotemporally, it is possible to decrease the testing effort by choosing optimal routes for optimal scenarios.

4.2.2 *Classification*

Classification algorithms try to generate models that predict a given discrete outcome. The selection of the right algorithm depends strongly on the application and the physical interrelationships between the input and output variables.

When a model type is chosen, the accuracy required and the complexity (which correlates with computing power) must be weighed up against one another. Several statistical methods may be used to compare different methodologies, see (Hothorn *et al.* 2005) (Eugster *et al.* 2008).

During normal driving, critical events are very rare. When the same distribution of critical and non-critical sequences as in reality is used for the classification algorithm, overfitting could occur if the learning dataset does not contain a sufficient number of different crash/critical events. In such a case, all critical events are simply "memorized" by the algorithm and it cannot be generally applied to similar but different events.

4.2.3 *Regression*

The prediction of continuous output signals requires an underlying regression model that contains a functional relationship between the input signals and the outcome. This can be achieved either directly with a function $f(x)$ or, from a probabilistic perspective, with a predictive distribution of the outcome $p(y_{ik}|x_{ij})$that implies the uncertainty about the value of y_{ik} for any new value of x_{ij} (Bishop 2006, p. 138).

With supervised machine learning methods, the relationship is adapted through minimization of the prediction error. As indicated in section 4.2.2, the choice of an optimal method can follow statistical rules derived from benchmark experiments as proposed in (Hothorn *et al.* 2005) and (Eugster *et al.* 2008). However, it is advisable to choose "the simplest model that approximates the performance of more complex models" (Kuhn and Johnson 2013, p. 79).

In general, supervised learning always needs to deal with the bias-variance tradeoff that addresses the problem of simple models having a low variance combined with a high bias, and complex models having high variance with low bias (Geman *et al.* 1992) (Kuhn and Johnson 2013, p. 98) (Bishop 2006, p. 147).

For criticality estimation, different crash or incident types are expected to need their own database subsets and related regression models. Another interesting aspect could be an analysis for the causal chain during critical events.

5 OUTPUT

This chapter describes the expected output of this method.

5.1 *Weighted sequences*

One result is grouped and weighted sequences from clustering. They can be used to see and understand important subsets, explore the likelihood of specific events or start further analysis with a more specialized dataset. Such groups allow a deeper understanding of the origin database.

In terms of criticality, matching with an existing crash database is reasonable. Proving that the ratios of different crash types in the time-series data are comparable to officially-published crash statistics can verify the statistical power of the time-series data (which is always a subset of reality).

5.2 *Predictive models*

The most important result is a predictive model created by machine learning techniques. Assuming that the input dataset was representative, the model can be used online in a vehicle to predict the outcome variables for a larger time horizon, as with local approaches. Besides the root mean squared error (RMSE), such methods as the confusion matrix, Receiver Operating Characteristic (ROC) Curves or Lift charts are used to evaluate the predictive performance of these models (Kuhn and Johnson 2013, 247ff).

For criticality estimation, in the case of class labels the predictive models provide a class probability or at least a discrete category prediction. In the case of a continuous criticality measure, the model estimates the further signal path of the outcome variable.

6 DISCUSSION

It is difficult to test models generated by machine learning. Especially for approaches using artificial neural networks, the model is comparable to a black box with an almost unpredictable outcome. Efforts are currently underway to solve this problem, see (Kurd *et al.* 2006). Nevertheless, the behavior of active safety systems has to be deterministic, so in this case transparent methods like decision trees or SVM are to be preferred.

7 CONCLUSION AND OUTLOOK

This paper has presented a flexible machine learning approach to generating predictive models from vehicle time-series data. A proof of concept for this method seems possible, even for smaller datasets. Nevertheless, the effectiveness of the method correlates strongly with the amount and quality of the input data. This approach does not place any restriction on the technical purpose. It can be used for safety issues, maintenance of components, optimization of driving dynamics, prediction of driver behavior or testing of automated driving functions.

Technical implementation is required before the effectiveness of this concept can be verified. The next research steps will attempt to show the feasibility of this. A combined analysis of time-series data and quasi-static information of the driving state could further improve model performance.

ACKNOWLEDGMENT

The research project is funded and supported by AUDI AG. The authors want to thank Stephan Herrmann for his discussions and ideas.

CONTRIBUTIONS

S. Engel and F. Diermeyer made an essential contribution to the conception of the research project. They revised the paper critically for important intellectual content.

REFERENCES

Benmimoun, M.*, et al.*, 2011. Incident detection based on vehicle CAN-data within the large scale field operational test “euroFOT”. *In: 22nd Enhanced Safety of Vehicles Conference (ESV 2011)*.

Bishop, C.M., 2006. *Pattern recognition and machine learning*. New York: Springer.

Boyle, L.N.*, et al.*, 2012. *Integration of Analysis Methods and Development of Analysis Plan*. SHRP 2 Report S2-S02-RW-1. Washington, D.C.: Transportation Research Board of the National Academies.

Damerow, F. and Eggert, J., 2014. Predictive risk maps. *In: 2014 IEEE 17th International Conference on Intelligent Transportation Systems – (ITSC 2014)*, 703–710.

Dingus, T.A.*, et al.*, 2006. *The 100-Car Naturalistic Driving Study – Phase II – Results of the 100-Car Field Experiment* DOT HS 810 593: U.S. Department of Transportation, National Highway Traffic Safety Administration.

Ebner, A., 2014. *Referenzszenarien als Grundlage für die Entwicklung und Bewertung von Systemen der Aktiven Sicherheit*. Dissertation. Technische Universität Berlin.

Eggert, J., 2014. Predictive risk estimation for intelligent ADAS functions. *In: 2014 IEEE 17th International Conference on Intelligent Transportation Systems (ITSC)*, 711–718.

Eugster, M.J.A., Hothorn, T., and Leisch, F., 2008. *Exploratory and Inferential Analysis of Benchmark Experiments*, 30. Available from: http://nbn-resolving.de/urn/resolver.pl?urn=nbn:de:bvb:19-epub-4134-6.

Geman, S., Bienenstock, E., and Doursat, R., 1992. Neural Networks and the Bias/Variance Dilemma. *Neural Computation*, 4 (1), 1–58.

Herrmann, S.*, et al.*, 2015. Supervised Learning via Optimal Control Labeling for Criticality Classification in

Vehicle Active Safety. *In: 2015 IEEE 18th International Conference on Intelligent Transportation Systems – (ITSC 2015)*, 2024–2031.

Hothorn, T.*, et al.*, 2005. The Design and Analysis of Benchmark Experiments. *Journal of Computational and Graphical Statistics*, 14 (3), 675–699.

John, G.H., Kohavi, R., and Pfleger, K., 1994. *Irrelevant Features and the Subset Selection Problem*.

Jonasson, J.K. and Rootzen, H., 2014. Internal validation of near-crashes in naturalistic driving studies: a continuous and multivariate approach. *Accident Analysis & Prevention*, 62, 102–109.

Jordan, J.*, et al.*, 2015. Learning Driving Scene Prediction from Environmental Perception of Vehicle Fleet Data. *In: 2015 IEEE 18th International Conference on Intelligent Transportation Systems – (ITSC 2015)*, 547–552.

Kuhn, M. and Johnson, K., 2013. *Applied predictive modeling*. New York, NY: Springer.

Kurd, Z., Kelly, T., and Austin, J., 2006. Developing artificial neural networks for safety critical systems. *Neural Computing and Applications*, 16 (1), 11–19.

Li, Z.*, et al.*, 2014. Surrogate safety measure for evaluating rear-end collision risk related to kinematic waves near freeway recurrent bottlenecks. *Accident Analysis & Prevention*, 64, 52–61.

Metz, B.*, et al.*, 2013. *Naturalistic Driving Data – Re-Analyse von Daten aus dem EU-Projekt euroFOT*. FAT – Schriftenreihe 256. Berlin: Würzburger Institut für Verkehrswissenschaften.

Muehlfeld, F.*, et al.*, 2011. Criticality estimation of Pre-Crash scenarios. *In: 2011 14th International IEEE Conference on Intelligent Transportation Systems – (ITSC 2011)*, 1211–1216.

Rodemerk, C.*, et al.*, 2012. Development of a general criticality criterion for the risk estimation of driving situations and its application to a maneuver-based lane change assistance system. *In: 2012 IEEE Intelligent Vehicles Symposium (IV)*, 264–269.

Saeys, Y., Inza, I., and Larranaga, P., 2007. A review of feature selection techniques in bioinformatics. *Bioinformatics (Oxford, England)*, 23 (19), 2507–2517.

Siordia, O.S.*, et al.*, 2010. Driving risk classification based on experts evaluation. *In: 2010 IEEE Intelligent Vehicles Symposium (IV)*, 1098–1103.

Themann, P.*, et al.*, 2016. Ganzheitliche Bewertung des vernetzten und automatisierten Fahrens. *ATZ – Automobiltechnische Zeitschrift*, 118 (01), 26–30.

Virginia Tech Transportation Institute VTTI, 2016. *SHRP2 NDS Data Access* [online]. Available from: https://insight.shrp2nds.us/home [Accessed 7 Jun 2016].

Wang, J.*, et al.*, 2015. Driving risk assessment using near-crash database through data mining of tree-based model. *Accident Analysis & Prevention*, 84, 54–64.

Xu, C.*, et al.*, 2013. Predicting crash likelihood and severity on freeways with real-time loop detector data. *Accident Analysis & Prevention*, 57, 30–39.

Yu, R. and Abdel-Aty, M., 2013. Utilizing support vector machine in real-time crash risk evaluation. *Accident Analysis & Prevention*, 51, 252–259.

Yu, R. and Abdel-Aty, M., 2014. Using hierarchical Bayesian binary probit models to analyze crash injury severity on high speed facilities with real-time traffic data. *Accident Analysis & Prevention*, 62, 161–167.

Advanced Vehicle Control – Edelmann, Plöchl & Pfeffer (Eds)
© 2017 Taylor & Francis Group, London, ISBN 978-1-138-02992-7

Study on cooperative driving of automated driving vehicles via spatial information server

S. Okada, T. Hisamatsu & M. Omae
Graduate School of Media and Governance, Keio University, Kanagawa, Japan

ABSTRACT: This paper proposes a method of cooperative driving of automated driving vehicles. In the proposed method, the vehicles share information of their intention, such as future pathway or velocity, through the spatial information infrastructure by long-period one (server) to N (vehicles) communication. Each vehicle decides on its driving strategy considering the shared information of other vehicle's intention, resulting in smoother flow of traffic than that realized by an automated driving strategy based on sensor information. This paper explains the proposed cooperation method and reports on the evaluation results.

1 INTRODUCTION

In this paper, the effectiveness of cooperation between automated driving vehicles via the spatial information infrastructure used for sharing their information, such as status or future pathway, is evaluated and presented. Specifically, a server acts as the infrastructure for sharing future pathway and status information of client-automated driving vehicles, and a cooperation system has been built for a number of client vehicles to use this shared information to contribute the efficiency of the traffic in complex shaped roads. Finally, an evaluation of the effectiveness of the system was carried out. This system was developed on the basis of the following ideas:

- In spite of a long period of communication between multiple automated driving vehicles and the server, it was thought that the shared information would still be useful because it is used for making decisions in cooperation with other vehicles rather than used for vehicle's motion control.
- Sharing vehicles' future pathway or status using the spatial information may simplify the procedure of obtaining future pathway and status of the other vehicles on the road because the information corresponds to coordinates of real space.

Previously, practical use of automated driving vehicles has been considered difficult because of problems related to technology and laws. However, it is expected that these challenges will be resolved because of structural reform, which was declared by the Japanese government in 2013. This declaration promoted the development of automated driving technology and the goal of realizing the world's safest, most environment-friendly and economical road transportation system by the 2020 Summer Olympics. According to the Japanese government's roadmap on automated driving car technology, it is expected that automated driving will be practically used on highways in the second half of the 2020s.

The majority of automated driving cars being developed use onboard sensors to observe and recognize the environment around the car. This autonomous automated driving technology does not depend on any infrastructure and can be positioned as an enhanced advanced driver-assistance system, which is already in use; hence, it is possible that autonomous automated driving vehicles may be implemented earlier. On the other hand, penetration of the autonomous automated driving vehicle may deteriorate traffic flow because each vehicle cannot obtain information of the others intention, such as future pathway and status, because they keep themselves safe by the use of onboard sensors and independent decision making. For example, it is impossible to change lanes unless there is excessive space, or entering an intersection, or distinguishing a parked vehicle from an idling vehicle because the intention of the other autonomous automated driving vehicle is unknown. However, with an automated driving vehicle, the automated driving system is aware of the vehicle's decision so that it is possible to influence another vehicle's intention, and if this intention and status is clear, resources for decision making are richer, which results in more efficient traffic. Namely, communicating automated driving vehicles' intention and status for cooperation between automated driving vehicles is a highly important technology for improving the efficiency of transportation.

Platoon (Fukao et al. 2014) or cooperative ACC (Mishima et al. 2013) systems are presently in the R&D process as a technology for cooperation; however, these are not able to support all possible situations because they are only intended for longitude control. Therefore, in this study, a mechanism of cooperation between automated driving vehicles for all situations

is proposed and its effectiveness is evaluated. Specifically, an infrastructure of N (vehicles) to one (server) communication, which is used for the automated driving vehicles to share future pathway and status information, and a method of cooperation using this shared information is proposed and evaluated in terms of the effectiveness to improve traffic flow efficiency. Although the communication period is relatively long compared to vehicle-to-vehicle (V2V), sharing information of future pathway and status is considered to be useful for cooperation. In this paper, the method and infrastructure for cooperation is presented and the travel time is evaluated by simulation and experiment to quantitatively clarify its effectiveness.

This study has been conceived independently to studies on dynamic map (Sato et al. 2015a, b Suda & Aoki 2015) or local dynamic map, that are currently in development, though these are similar in terms of sharing, among others, information of objects' coordinates and status for vehicle control. It is considered that the scope of use and content of the shared information are wider in the dynamic map compared to this study. Thus, this study proposed and evaluated a design of future pathway and a cooperative method as a related study to the dynamic map concept.

This paper is presented in the following format. Infrastructure for sharing spatial information is described in Chapter 2. Content of the spatial information for cooperation is described in Chapter 3. Method of cooperation between automated driving vehicles is described in Chapter 4. The results from the experiment and simulation are discussed in Chapter 5. Finally, Chapter 6 presents the conclusions.

2 SPATIAL INFORMATION SERVER

This chapter describes the spatial information server that was proposed.

The spatial information server provides the communication to link N vehicles to one server to realize cooperation between automated driving vehicles.

There was consideration that the spatial information server will be used by various users such as vehicles, pedestrians, and infrastructure. Furthermore, considering the use of mobile communications (like cellular networks), where the clients are served by fixed-location base stations, and in some cases multiple clients connect through one base station, a communication period of approximately 1 second was assumed.

Multiple vehicles access the server through the mobile network to send their own information and receive information of nearby vehicles needed for cooperation.

The spatial information server constructs a virtual space that simulates the real space to visualize vehicles' intentions, driving strategies, and statuses that are invisible in the real world.

An example is shown in Figure 1 of the anticipated effects of this system when a vehicle travels into a nonsignal intersection. When several vehicles approach a nonsignal intersection, an autonomous vehicle ensures there is sufficient safety margin before entering the intersection. In the situation shown in Figure 1, Vehicle 1 must stop at the intersection because the other vehicles intentions are unknown. However, in case that every vehicle shares its status and intention as shown in the upper part of Figure 1, Vehicle 1 can go straight through the intersection without stopping because each vehicle acquires the intention of the nearby vehicles as below.

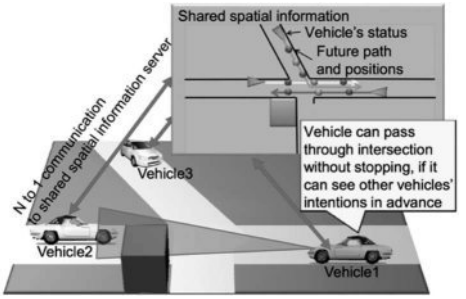


Figure 1. Illustration of cooperative driving control through shared spatial information infrastructure.

- Vehicle 2 intends to go straight on
- Vehicle 3 intends to turn left
- Therefore, no interference occurs.

The objective of this study is that every road user shares its status information and intention through the spatial information server. When a road user does not share its status information and intention through the spatial information server, that vehicle will need to compare vehicle position, as shared through the spatial information server, and vehicle position based on real-world sensing in order to travel safely.

3 PROCEDURE FOR VECHILE TO ACCESS SPATIAL INFORMATION

This chapter describes the spatial information itself and its procedure to write the spatial information to the server. The spatial information for cooperation is managed by the server system for the client-automated driving vehicles to write their information and read each other's information. In each section below, the procedure of writing and reading information is described.

3.1 *Procedure of writing spatial information*

In this section, content of the spatial information for realizing cooperation and its procedure of writing are described.

The server managing the spatial information accepts the request from the client-automated driving vehicles to start communication. After the connection is established, the server receives information from the vehicles. The information consists of the vehicle's ID,

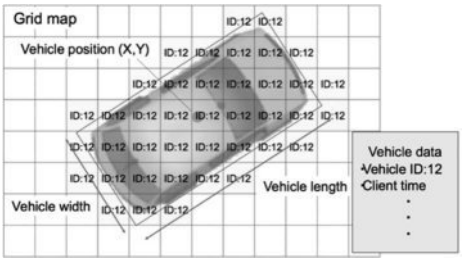


Figure 2. Grid map of spatial information (Current position of one vehicle).

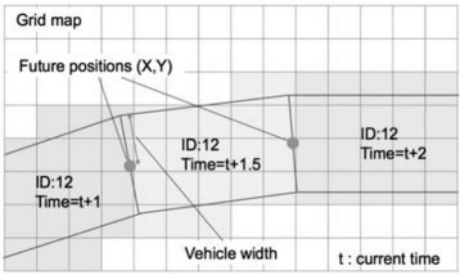


Figure 3. Grid map of spatial information (Future positions of vehicles).

the system time of its computer, its position, yaw angle, velocity, vehicle's width, length and future pathway. The IP address of the vehicle is used as the vehicle's ID in communication. System time of the computer is not used in the server side process. The position of the vehicle is expressed as XY coordinates of the center of the vehicle. The future pathway is a set of future positions of the vehicle for the next 10 seconds where the period is 0.5 seconds and exact position is the center of the vehicle's front end.

The received information is associated with the vehicle's ID and stored into the memory, and the ID is stored in the geometrically corresponding cell of the grid map, which constructs the spatial information. In this study, a grid map was used, which covers the entire area of the experimental site, which has cells of 0.2 m × 0.2 m and an area of 200 m × 200 m. As shown in Figure 2, a vehicle's ID is stored in the cells that are occupied by the vehicle according to its position, width and length. The grid map is geometrically linked to the real space, and each cell has the ability to store a vehicle's ID and time when the vehicle passes there. Moreover, system time of the server is stored along with a vehicle's local system time. The future pathway is written into the grid map as well. As shown in Figure 3, cells that will be occupied in future store a vehicle's ID and estimated time taken by the vehicle to pass. Each cell of the grid map can store information of multiple vehicles, up to a maximum of 10. Figure 4 shows the future pathway of the automated driving vehicles written in the grid map. The server deletes information, which is not refreshed in the past 2 seconds.

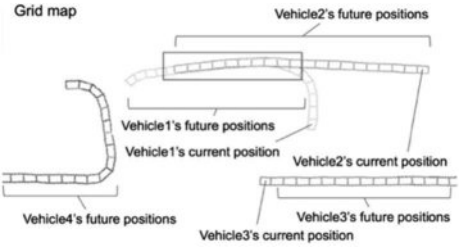


Figure 4. Grid map of spatial information (Multiple vehicles).

3.2 *Procedure of reading information*

This section describes the procedure of reading information.

The spatial information server searches for vehicles that are present or those that intend to enter the area, which is designated by client automated driving vehicle, and responds to the request by that client vehicle. The request is sent by the automated driving vehicle at the same time as its information (future pathway and status) is written. Therefore, the client vehicle can obtain information of vehicles, which are present or intend to present in a designated area.

It is necessary to make corrections using the differential of system time between the server and automated driving vehicles because the information of a vehicles' position is managed with the server's time. The server attaches processing time (in milliseconds) and current system time to the response data that it sends back to the client vehicle. The client vehicle calculates the differential of time by an equation $(T_r - T_s) - T_p$; where T_r is the system time when the request was sent, T_s is the system time when the response data was received, and T_p is the processing time taken by the server.

4 COOPERATIVE DRIVING

This section describes a method for cooperative driving using information from the spatial information server. The method used by the spatial information server is to write self-vehicle's information and to read other vehicle's information, because it is necessary for automated driving vehicles to make independent decisions from data provided by the server. Each section below describes the data reading process, the decision making process using the spatial information, and the vehicle-control algorithm.

4.1 *Procedure to read information and make decisions for cooperative driving*

This section describes a method of data reading and a procedure for cooperation. An automated driving vehicle requires the spatial information server to search other vehicles and read their information. In the proposed cooperative method, vehicles' future position is divided into quadrangles, and a vehicle's information is stored in the quadrangle from the spatial information

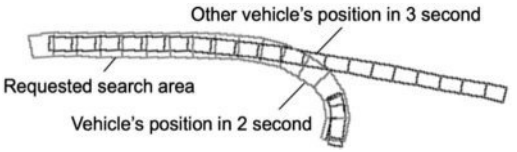


Figure 5. Search of other vehicles on future pathway.

server. As shown in Figure 5, the automated driving vehicle requests the server to search the vehicle in the quadrangle shaped areas every 0.5 second in the trajectory of the next 8 seconds where the target velocity of the self-vehicle is supposed to be same as the designated velocity.

Once the information of the other vehicles in the designated search area is read, the automated driving vehicle decides according to that information. In the proposed cooperative method, the automated driving vehicles avoid interference between each other's trajectory, depending on the level of priority given to the roads, when any other vehicle present on the self-vehicle's trajectory is within t_p seconds (where t_p was defined as 2 seconds in this study). Each road has been given priority, and each vehicle recognizes its own priority by comparing with the other's priority, which is obtained from the spatial information server. The priority of the road was defined based by basic traffic rules. The automated driving vehicles store the information of the trajectory or maps in its onboard computers. Figure 5 shows a deceleration because of a predicted interference, estimated to occur in 2 seconds, between the selfvehicle and another where the road, which the self-vehicle travels along, has a lower priority. After the avoidance, the vehicle travels on at the designated velocity.

4.2 *Vehicle-control algorithm*

This section describes an algorithm for avoiding interference between the trajectory of the self-vehicle, which travels along the lower priority road, and the other vehicle's one in cooperation.

The lower priority vehicle decelerates as defined by equation 1 below, and stops at a desired stop line, which is x m on the self-vehicle's side of the interference position; x was defined as 5 m in this study.

$$a_{des} = K_1 d_{stop} - K_2 v \quad (1)$$

In this formula, a_{des} is the target acceleration (system input) [m/s^2], d_{stop} is the distance to the desired stop line [m], v is velocity [m/s], and K_1 and K_2 are feedback gains. Acceleration was given a range between -2 m/s^2 to 1 m/s^2. The velocity was controlled by a proportional-integral (PI) controller for cruise control while no interference occurred.

5 EVALUATION

This chapter presents and evaluates results from the experiment and simulation.

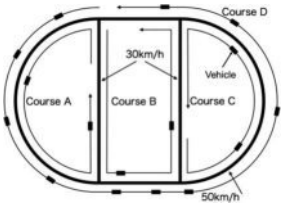


Figure 6. Environment of the simulation.

5.1 *Simulation*

In this study, simulations with a vehicle model, which simulates a typical passenger vehicle, were carried out to evaluate the proposed cooperative method under conditions similar to actual traffic.

The sections below describe the environment of the simulation, and thereafter report and discuss the results from the simulation.

5.1.1 *Condition of simulation*

This section describes the simulation roads and rules in cooperative and noncooperative driving.

The number of the vehicles was set to 16 in the simulation. As shown in Figure 6, four courses and four intersections were provided for the simulation. Courses A and C were a semicircle with the radius of 100 m, and course B was a 100 m by 200 m rectangle. The target velocity of the vehicles was designated as 13.88 m/s (50 km/h) at the peripheral road and 8.33 m/s (30 km/h) at the inside of the peripheral road. In the simulation, two vehicles were set to travel along course A, two vehicles along course B, two vehicles along the course C, and 10 vehicles along course D. All vehicles traveled anti-clockwise.

The quantity of cooperative vehicles was changed one by one through the simulation to clarify the relation between the effectiveness to improve traffic flow efficiency and penetration rate of the proposed cooperative system. At each stage, vehicles are randomly chosen to be cooperative and tested 100 times to determine relevance between penetration rate and effect on traffic flow efficiency.

Rules of a non-cooperative automated driving vehicle are described below. The vehicle starts by traveling at the designated speed. At the intersections, when the vehicle travels onto the higher priority road (the peripheral road) from the lower priority road (inner-branch road of the course A, B, or C), if any vehicle traveling along the higher priority road and arriving at the intersection within t_s second is detected (Yang et al. 2015) by the onboard sensor, the self-vehicle decelerates or stops to give way. The right side of the intersection will be monitored because the flow of vehicles was anticlockwise as shown in the left part of Figure 7; t_s was configured to be 5 seconds in this study.

Rules of a cooperative automated driving vehicle are described as below. Each cooperative vehicle sends the spatial information server their information of future pathway and status, and receives information of

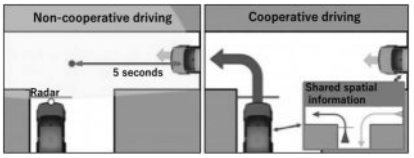


Figure 7. Noncooperative driving and cooperative driving control at intersection.

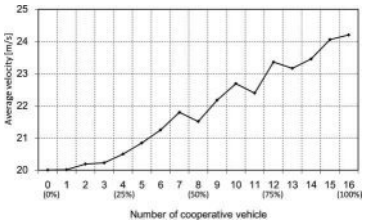


Figure 8. Average velocity of the vehicles that traveled on course A, B, or C.

the others. Interference at the intersections is detected by that information instead of an onboard sensor. As described in section 4.1, the vehicles along the lower prioritized road decelerate or stop to avoid interference if interference is predicted to occur within 2 seconds. As the right side of Figure 7 shows, no deceleration or stopping is necessary if it is certain that another vehicle coming into the intersection from the higher priority road intends to turn left. In both cooperative vehicles and noncooperative vehicles, it is ruled that vehicles moving along the peripheral road have priority to go first at the intersections.

5.1.2 *Result of simulation*

Figure 8 shows the results from the simulation. The X-axis indicates number of the cooperative vehicles. The Y-axis indicates time averaged velocity of the vehicles, which traveled along the lower prioritized roads (course A, B, and C). The vehicles on course A, B, or C took 899.5 seconds on average to travel 5000 m when the number of cooperative vehicle was 1. In contrast, they took 730.2 seconds to travel 5000 m when all of the vehicles were cooperative. As shown in Figure 8, the average velocity does not increase significantly when the penetration rate is under 25%. However, it increases linearly against the number of cooperative vehicle when the penetration rate is $>25\%$.

5.2 *Experiment*

This section describes the environment and preparation of the experiment, and reports and discusses the results from the experiment.

5.2.1 *Experimental conditions*

The experimental site was set in the parking area of the Keio University Shin-Kawasaki Town campus. The experimental roads with four intersections are shown in Figure 9. Moreover, there are four different courses A, B, C, and D.

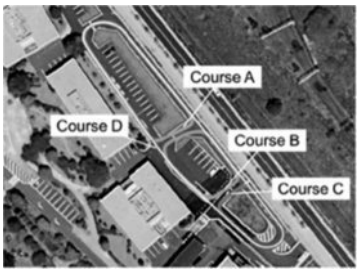


Figure 9. Experimental road and course of vehicles.

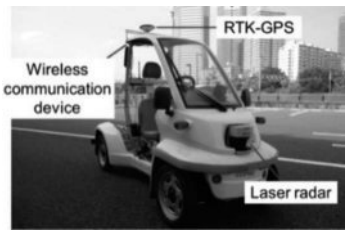


Figure 10. Experimental vehicles.

The experimental vehicle is a small electric vehicle, whose steering, power, and braking are capable of being controlled by a computer, as shown in Figure 10. Lateral motion (steering) of the vehicles was controlled automatically in the experiment to accurately follow each course (Omae et al. 2004). Specifically, vehicles were steered by measuring its relative position to the target trajectory of the course using Real Time Kinematic satellite navigation (RTK-GPS). Wireless LAN was used for communication between vehicles and the spatial information server.

In the experiment, one vehicle was traveling along course A, one vehicle along course B, one vehicle along course C, and two vehicles along course D. The designated velocity of the vehicles was 2.22 m/s (8 km/h). The rules for cooperative and noncooperative driving were the same as in the simulation.

The experiment was carried out in two conditions:

- All automated driving vehicles were cooperating via the proposed spatial information server.
- None of the automated driving vehicles were cooperating.

5.2.2 *Result of experiment*

Figures 11 and 12 show the results of noncooperative driving, and Figures 13 and 14 show the results of cooperative driving. Each set of figures shows a recording of speed and distance traveled for each vehicle. Figures 11 and 13 show that the number of deceleration and stopping events is smaller when the vehicles cooperate compared to noncooperative driving. Furthermore, the cooperative vehicles traveled further, as shown in Figures 12 and 14. Noncooperative vehicles took 283.4 seconds to travel 600 m on average, whereas cooperative vehicles took 270.9 seconds on average to cover the same distance. Because it takes

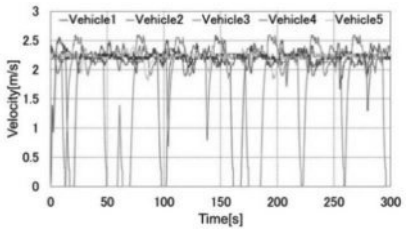


Figure 11. Experimental result of noncooperative driving (Vehicle speed).

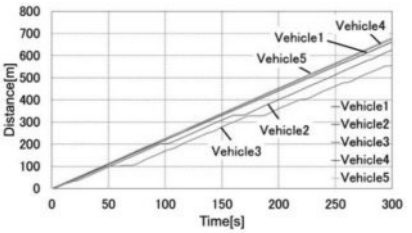


Figure 12. Experimental result of noncooperative driving (Travel distance).

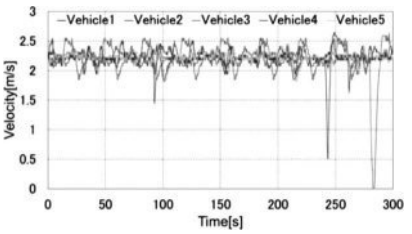


Figure 13. Experimental result of cooperative driving (Vehicle speed).

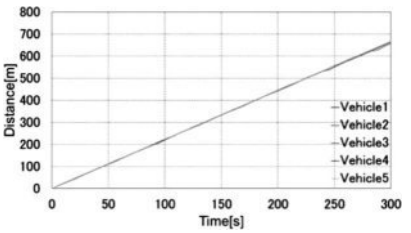


Figure 14. Experimental result of cooperative driving (Travel distance).

270.0 seconds to travel 600 m without deceleration and stopping, the average loss is 13.4 seconds for noncooperative driving and 0.9 seconds for cooperative driving.

5.3 *Summary of evaluation*

It was confirmed both experimentally and through simulation that the proposed method for cooperation between automated driving vehicles decreases the number of deceleration and stopping events, which results in shorter travel time in roads with intersections. Moreover, the simulation ensured that the proposed cooperative system raises the efficiency of traffic flow within the speed range of actual traffic.

Although the experimental environment was limited, the experiment indicates that the proposed method is able to be applied to a real vehicle, and can realize more efficient transportation.

6 CONCLUSIONS

This paper proposed and evaluated a method for cooperation between automated driving vehicles via a spatial information server to realize more efficient and smooth traffic flow under a high penetration rate of automated driving technology. This study proposed a spatial information management server and the procedure of reading and writing of information in one (server) to N (vehicles) communication with a period of 1 second. In spite of this relatively long communication period, time required for decisionmaking at intersections is decreased and improved efficiency of traffic flow was validated through an experiment and simulation.

The evaluation focused on decision-making at intersections; however, the spatial information server can be applied to other scenarios such as, among others, changing lanes or distinguishing a parked vehicle from an idling vehicle. Furthermore, the level of its effectiveness can be maintained by cooperative vehicles sharing information of detected objects when the penetration rate of cooperative vehicles is low to medium. It is recommended to evaluate cooperative driving in other scenarios in future work.

REFERENCES

Fukao, T., Sugimachi, T. 2014. Control Technologies on Platooning of Trucks. *Institute of Systems, Control and information Engineers* 58(5): 175–180. (in Japanese).

Mishima, Y., Konishi, T., Tajika, H., Sato, H., Sakurai, Y., Omae, M., Suganuma, N. 2013. Development of the Cooperative Adaptive Cruise Control System Using four Heavy-Duty Trucks. *Proceedings of JSAE Annual Congress (55–13):* 19–22. (in Japanese).

Omae, M., Hashimoto, N., Shimizu, H., Fujioka, T. 2004. Vehicle Motion Control for Automatic Driving in Local Area with Parking Space. *Transactions of Society of Automotive Engineers of Japan* 35(3): 235–240. (in Japanese).

Sato, K., Hashimoto, M., Suganuma, N., Kato, S., Shiba, N., Hanai, M., Takada, H., Amanuma, M., Ktsuna, M., Oishi, J. 2015. Field Experiment of LDM Global Concept for Cooperative Automated Driving, *Proceedings of 13th ITS symposium* (in Japanese).

Suda, Y., Aoki, K. 2015. Current activities and some issues on the development of automated driving. *Journal of Information Processing and Management* 57(11): 809–817. (in Japanese).

Yang, B., Zheng, R., Shimono, K., Nakano, K. Evaluation of the Method to Assist a Driver by Displaying Traffic Signal in the vehicle. *Proceedings of JSAE Annual Congress* (15–15S): 415–418. (in Japanese).

Advanced Vehicle Control – Edelmann, Plöchl & Pfeffer (Eds)
© 2017 Taylor & Francis Group, London, ISBN 978-1-138-02992-7

Database of relevant traffic scenarios as a tool for the development and validation of automated driving

P. Themann, A. Pütz & A. Zlocki
Forschungsgesellschaft Kraftfahrwesen Aachen mbH, Aachen, Germany

L. Eckstein
Institut für Kraftfahrzeuge, RWTH Aachen University, Aachen, Germany

ABSTRACT: The complexity of automated and connected driving functions increases significantly, which requires higher efforts for a reliable validation and sign-off procedure of these systems. Following conventional methods a very high amount of test kilometers has to be driven in field operational tests in order to approve the safety of an automated driving system. Even small changes of the function require new field tests, which seems not to be appropriate. This paper presents a new method to overcome this test dilemma. This method foresees to store all relevant traffic scenarios in a database. These scenarios are extracted to various validation tools such as simulations, driving simulators or test tracks for specific validation tests along the process engineering model. Therefore the database contributes as a core module in a new method for the validation of automated driving functions with a reduced amount of efforts compared to conventional validation methods.

1 INTRODUCTION

First level 2 automated driving functions are already introduced into the market and are more and more able to handle complex traffic scenarios. The first generation of these functions has been deployed for driving in structured environments such as motorways at low speed ranges. Systems with higher levels of automation that are currently being developed address more complex driving environments and higher vehicle speeds. In complex urban driving environments systems need to consider various impact factors such as the behavior of human drivers or other traffic participants (e.g. cyclists or pedestrians).

While the level of automation increases, at the same time the connectivity of vehicles rises. Several communication technologies are able to provide information on the current driving environment and other traffic participants in the vicinity. There are various technical standards and communication technologies to connect vehicles, resulting in significant differences in the characteristics of the physical transmission of data. This affects the system performance and needs to be considered in validation.

The increase in both automation and in connectivity results in complex system architectures and requires an elaborated methodology for the system validation.

2 VALIDATION OF AUTOMATED DRIVING

For an automated driving function a distance of several million kilometers needs to be travelled in a field operational test in order to validate the safety of the system [1]. As the systems get more and more complex this approach does not seem to be appropriate as every small change requires new field tests.

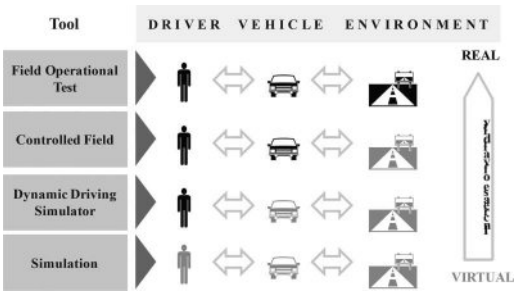


Figure 1. Classification of evaluation methods (grey: virtual elements; black: real elements) [2].

In the validation of advanced driver assistance systems and automated driving systems several tools and evaluation methods are used (see Figure 1). Besides simulations and studies in driving simulators also test drives in the controlled field and field operational tests on public roads are applied methods. To link all relevant validation tools a database is proposed in literature [2, 3] (see Figure 2). This database stores traffic scenarios in an appropriate way and enables the impact analysis for a specific function in traffic scenarios that are relevant for this function. The general approach to use a database of relevant scenarios is described in more detail in the following section.

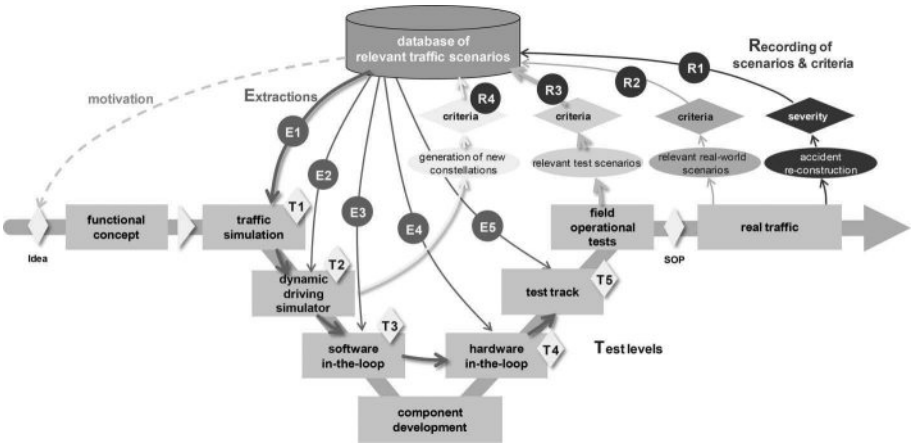


Figure 2. Database of relevant traffic situations connected to different validation tools in the V-model [4].

3 DATABASE APPROACH FOR VALIDATION

The relations between the validation tools (as typically used in the V-model process) and the central database are depicted in Figure 2. The relations are described in more detail in the following sections.

3.1 *Recording of relevant scenarios*

The initial set of scenarios in the database is recorded from real-world traffic by analyzing accident data (R1) e.g. from accident databases and critical traffic scenarios recorded in public traffic (R2). Additionally, the outcome of field operational tests (R3) is fed into the database as well as new relevant driving scenarios resulting from driving simulator studies (R4). Especially in R4 new situations, which cannot be measured in real traffic due to the lack of automated vehicles, are depicted in detail and provide input for future use cases.

3.2 *Extractions of relevant scenarios to simulations*

Extractions (E1 to E5) of traffic scenarios from the database are fed to the different validation test tools (T1 to T5). This allows re-assessing the impact of an automated driving system in a previously recorded traffic scenario that is classified as relevant for the specific system. Traffic simulations (E1) in various standardized software tools are able to analyze a huge amount of scenarios. Virtual variations of the traffic scenarios may be performed in simulations and provided to the database.

Additionally, a dynamic driving simulator (E2) is able to assess if the introduction of innovative functions may result in new relevant driving scenarios to be included in the database (R4).

Traffic scenarios are also extracted to software or hardware-in-the-loop tests (E3 and E4) of components.

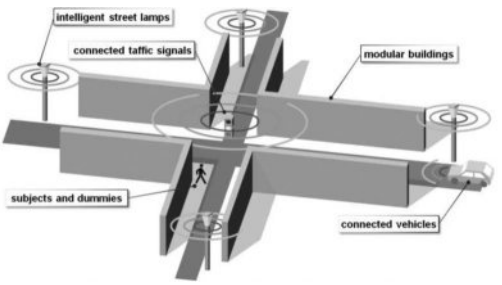


Figure 3. Modular intersection at RWTH Aachen University to test connected and automated driving in urban traffic scenarios [4].

3.3 *Extractions of relevant scenarios to test track*

In order to test a system in real-world driving tests on a test track a scenario recorded in the database is reproduced on a dedicated test facility (E5). The trajectories of all relevant traffic participants are reproduced by e.g. dummy vehicles or pedestrians. Additionally, the driving environment needs to be configured as recorded in the database. This includes the characteristics of the radio environment in order to reliably test the impact of communication technologies. A test site particularly designed for urban traffic scenarios needs to be modular also with respect to the size and position of buildings (Figure 3) [4].

3.4 *Implementation of selected aspects of the holistic approach in different research projects*

The database centered approach as described above is not implemented in a single project. Several research projects aim to implement specific aspects of the approach. The most relevant projects and their respective relation to the aspects of the approach are described in sections 4 and 5.

4 SCALE-UP AND IMPACT ASSESSMENT

Among others the performance of the human driver was examined in the research project UR:BAN (*www.urban-online.org*) in several studies. Especially the results of the subproject *Controllability* are of high relevance since they give insights to the reaction of human drivers to unexpected system intervention, e.g. a system initiated evasive maneuver [5]. But also the mutual interaction behavior between vehicle drivers and pedestrian which has been analyzed in the subproject *Simulation* provides background on the driver performance in highly demanding scenarios [6]. Both inputs may therefore serve as a reference behavior for the evaluating the system performance in scenarios that require fast decisions and comprehensive perception of a complex situational context. Hence, the results are transferred into a format to be fed into a database representing the controllability and the driver perception performance.

Several large research projects on international level such as interactive (*www.interactive-ip.eu*) or AdaptIVe (*www.adaptive-ip.eu*) work on a methodology to assess the impact of advanced driver assistance systems and also the impact of automated driving functions on large scale. These valuable inputs are considered in the design of the holistic impact assessment approach but not elaborated in more detail in this paper.

5 IDENTIFICATION OF CRITICAL SCENARIOS

One of the key data sources to populate a database with relevant traffic scenarios are field operational tests. In addition to providing data on human driver behavior and the usage of driver assistance functions projects like euroFOT (*www.eurofot-ip.eu*) also developed methods to identify critical scenarios. In [7] and [8] the automatic identification of incidents based on CAN-data is described. Main information sources for the detection algorithms are data on the vehicle motion behavior as well as the driver input. By comparing this data to thresholds that have been established based on pilot test incidents of different levels and types were identified for a high mileage.

Besides other important aspects partners in the research project PEGASUS (http://www.bmwi.de/DE/Presse/pressemitteilungen,did=749340.html) also design a process to feed traffic scenario data from various sources into a central database. All scenario data gathered in the project is processed by a coherent set of algorithms in order to identify scenarios relevant for the validation of automated driving systems. All partners need to agree on the same definition of algorithms e.g. defining the criticality of a certain traffic scenario, which is described in the following sections in more detail.

In the research project PEGASUS thus only one specific aspect of the database approach for validation, as described in section 3, is implemented by fka.

5.1 *Aims of the project PEGASUS*

Several partners from the automotive industry and academia join forces in the research project PEGASUS, which aims to address the following general research questions:

- Which safety level is required for automated driving systems?
- Which method needs to be applied in order to validate the safety level of automated driving systems?

In this attempt a database is used to handle different traffic scenarios that are relevant for the validation of automated driving systems. As several partners provide measurement data describing traffic situations, a generalized structure of this input data needs to be defined. Furthermore a standardized process flow to identify critical scenarios has to be designed and applied for all sets of input data. The following sections of this paper elaborate on the last mentioned issues in more detail.

5.2 *Requirements and use cases*

The high level requirements for the approach are outlined in the description in section 3. In the research project PEGASUS functional requirements for a central database are defined:

- Measurement data from different validation tools (e.g. simulations or real-world tests) need to be converted to a standardized data format.
- Measurement data from different validation tools need to be analyzed by the same algorithms in a coherent way to ensure comparability.
- Algorithms to characterize e.g. the criticality of a scenario need to use the standardized data format.
- The generic process needs to be expandable as new algorithms and measurement data will be added over time.
- The process needs to ensure privacy and security of all data provided by different partners.
- Only relevant traffic scenarios need to be shared between partners, if they agree to this.

Besides functional requirements also use cases for the database are formulated to define the process in more detail. Most requirements are included in the following use case:

Several partners provide relevant traffic scenarios from different validation tools (e.g. simulations or real-world tests) to the database. The algorithms implemented in the database analyze these scenarios, apply coherent indicators and cluster the scenarios. When a new automated driving system is developed, boundary conditions for the activation of this (e.g. activation only on motorways etc.) are used to filter relevant traffic scenarios from the database. These relevant traffic scenarios are used to validate the automated driving system in different validation tools.

```
{
"Name":          "SpeedX",
"Class":         "MeasuredSignal",
"Group":         "MotionState",
"Description":   "absolute velocity in direction of x-axis of
                  vehicle centric coordinate system",
"Unit":          "m/s"
}
```

Figure 4. *Json* file for the signal “SpeedX”.

5.3 *General structure and definition of input data*

One of the most important requirements to implement the database approach is the availability of standardized input data (e.g. measurement data from field trials). In order to define a data structure each input measurement signal (e.g. from CAN bus in real-world tests or from simulation tools) is described in a *json* file. These contain the definition of an input signal as given in Figure 4.

Using *json* files allows parsing the information of each standardized input measurement signal in various tools and programming languages. As each signal is described by exactly one single *json* file change requests from different partners can be handled effectively using a repository management tool such as *GitLab* (*https://gitlab.com/*).

5.4 *Generic process flow to identify scenarios*

The most challenging requirement on the process chain is that is has to cope with new algorithms and signals that are introduced later. In order to fulfill this requirement a generic process flow is defined that allows implementing algorithms at certain process steps (see Figure 5).

In the first step of the process the input data is processed in the standardized data format as defined in the *json* files. Users provide either continuously measured signals over time (e.g. velocity of the vehicle), constants (e.g. vehicle mass or age of the driver) or discrete information changing slowly over time (e.g. rain yes or no).

In the second step user defined algorithms are applied in order to calculate derived signals from the input data. If the current velocity of a vehicle and the distance to the front vehicle are provided e.g. the time-to-collision is calculated as a signal over time and added to the set of measurement signals.

A scenario likelihood is calculated in step three based on user defined algorithms. These algorithms may assess all signals available in order to calculate a likelihood (as a percentage) indicating if a certain traffic scenario is depicted by the signals. A traffic scenario in this sense is defined by a maneuver of a vehicle e.g. a lane change or a change in road infrastructure (e.g. end of lane on motorway).

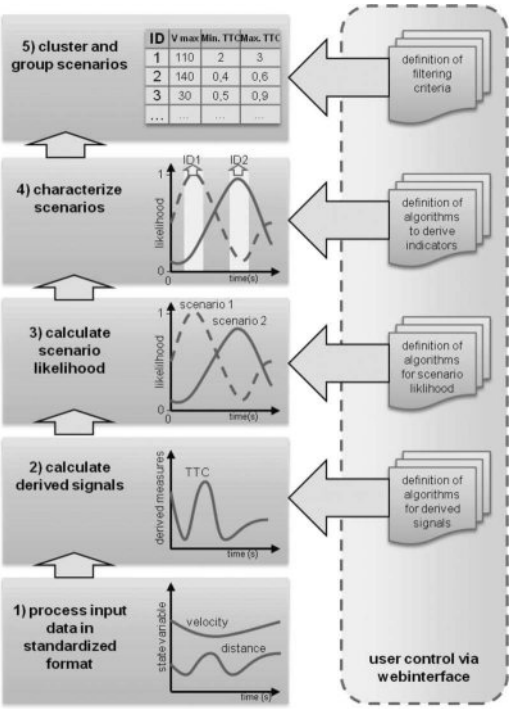


Figure 5. Process flow to identify and characterize relevant traffic scenarios in a coherent way for standardized input data.

In the fourth step periods of time with high likelihoods for a certain scenario are identified and characterized by indicators. Algorithms analyze the period of time and derive scalar values to characterize these e.g. by the minimum time-to-collision or the average velocity. The time based signals are thus transformed into scalar values expressing their characteristics.

The scalar indicators derived in step four are analyzed in the last step five in order to cluster and group similar traffic scenarios. Filter algorithms are applied in order to extract a set of similar scenarios for the validation of an automated driving system

5.5 *Algorithms and metrics*

All algorithms used in the process described above can be exchanged and also extended in future. The general interfaces between all process steps are defined. This guarantees an easy integration of additional indicators, scenario definitions and filtering algorithms in this process. Users of the process can use a web frontend to choose relevant algorithms in order to filter scenarios for their specific purpose.

Algorithms to identify critical scenarios have already been developed in various projects and are described in literature. Most important results from projects such as *euroFOT* or *TeleFOT* are analyzed and respective indicators for critical scenarios are implemented in the framework.

6 CONCLUSION AND OUTLOOK

This work summarizes the database-centered approach for impact assessment of automated driving functions. First of all the general approach is described and relevant development and validation tools as well as their interface to a central database are outlined. The concept of the database to record and analyze relevant traffic scenarios is presented.

The database-centered approach is not implemented in a single project. Several research projects aim to implement specific aspects of the approach. The most relevant projects and their respective relation to the aspects of the approach are described in sections 4 and 5 of this work. Especially the process to identify critical scenarios is described in more detail. The processing frameworks as well as the most important interfaces are described. This paper proposes to use *json* files to standardize the input files for a central database. These files can easily be managed by a repository system such as *GitLab*, which allows different partners and stakeholders to simultaneously work on the format of the measurement data from various sources.

The proposed process of using *json* files to standardize the input data is exemplarily implemented in the research project PEGASUS. In a first step the impact assessment applied in this project is limited to motorway scenarios and the most relevant signals are discussed using a *GitLab* repository. In future the proposed method is to be extended in order to also handle traffic scenarios in urban areas.

The research project PEGASUS first of all aims to gather all scenarios relevant for the highway chauffeur function and later on also addresses other scenario categories. In this project environmental conditions in Germany are considered and scenarios in Europe and from other regions in the world are added later. A first set of simple scenarios is derived from expert knowledge and measurement data from various sources are used to gather more complex scenarios. This way the number of scenarios handled in the database increases in order to consider all relevant test scenarios in the validation of automated driving functions.

REFERENCES

[1] Winner, H. 2015. How to Address the Approval Trap for Autonomous Vehicles. 18th IEEE ITSC, Gran Canaria

[2] Eckstein, L. & Zlocki, A. 2013. Safety Potential of ADAS – Combined Methods for an Effective Evaluation. ESV 2013, Seoul, South-Korea

[3] Zlocki, A.; Fahrenkrog, F. & Eckstein, L. 2014. Effective Evaluation of ADAS and Automated Driving. AVEC, Tokyo, Japan

[4] Themann, P.; Raudszus, D.; Zlocki, A. & Eckstein, L. 2016. Holistic Assessment of Connected Mobility and Automated Driving. ATZ worldwide, Vol. 118, No. 1, pp. 26–31

[5] Pütz, A.; Josten, J.; Zlocki, A. & Eckstein, L. 2014. UR:BAN: controllability evaluation of system interventions of evading assistance, 23rd Aachen Colloquium Automobile and Engine Technology, Aachen, Germany

[6] Kotte, J. & Pütz, A. 2016. Analyse der Interaktion zwischen Fußgängern und Fahrzeugen im Realverkehr und kontrollierten Feld, UR:BAN-Konferenz 18./19.02.2016, Garching, Germany

[7] Benmimoun, M.; Fahrenkrog, F.; Zlocki, A. & Eckstein, L. 2011. Incident detection based on vehicle can-data within the large scale field operational test "euroFOT", 22nd International Technical Conference on the Enhanced Safety of Vehicles, Washington, USA

[8] Benmimoun, M.; Fahrenkrog F. & Benmimoun A. 2010. Automatisierte Situationserkennung zur Bewertung des Potentials von Fahrerassistenzsystemen im Rahmen des Feldversuchs "euroFOT", VDI-Berichte 2104, Wolfsburg, Germany

State estimation

Advanced Vehicle Control – Edelmann, Plöchl & Pfeffer (Eds)
© 2017 Taylor & Francis Group, London, ISBN 978-1-138-02992-7

Full vehicle and tyre identification using unscented and extended identifying Kalman filters

Matthew C. Best & Karol Bogdanski
Loughborough University, Loughborough, UK

ABSTRACT: This paper considers identification of all significant vehicle handling and driveline dynamics of a test vehicle, including identification of a combined-slip tyre model, using only those sensors currently available on most vehicle CAN buses. The method extends previous work using augmented Kalman Filter state estimators to concentrate wholly on parameter identification, and it compares Extended and Unscented Kalman filter algorithms. Using an appropriately simple but efficient model structure, all of the independent parameters are found from test vehicle data, with the resulting model accuracy demonstrated on independent validation data. The method is suited to applications of system identification, but also in on-line model predictive controllers or estimators. It can also operate in real-time, so the model could be continuously identified to maintain accuracy with each new journey.

Keywords: Topics/Vehicle Dynamics, Tyre Model, Modeling and Simulation, State Estimation, System Identification

1 INTRODUCTION

Several previous publications have considered estimation of individual parameters of a vehicle dynamic model, particularly for tyre and friction coefficient estimation [1, 2]. The validity of these (necessarily simplified) models also depends on many other fixed, estimated parameters. Usually, even if these other values are physically accurately set, the simplified model can be made to perform better if they are tuned or also identified.

Here we embark on an ambitious attempt to identify all the independent parameters in a simplified whole vehicle handling model, including yaw and roll freedoms, independent combined-slip load dependent tyres and appropriate drivetrain lags. This is achievable, given recent findings that Kalman filter methods can be applied to identify all parameters in any well-conditioned model structure [3].

In the extended abstract we demonstrated the principle by simulated identification of longitudinal tyre dynamics, including wheel-spin and lock, using an Extended Kalman Filter. In this final paper we consider data collected from a test vehicle carrying out medium to high magnitude manoeuvres including wheel-spin and terminal understeer, in order to build a model which is valid over the whole range of the tyres. We also consider the relative advantages over EKF of using the more computationally efficient, Unscented Kalman Filter for the identification process.

2 IDENTIFYING EXTENDED KALMAN FILTER

The standard Extended Kalman Filter (EKF) operates on nonlinear system and sensor models **f** and **h**, which relate the state vector **x**, measured sensor set **y**, known inputs **u** and model parameters θ through

$$\dot{\mathbf{x}} = \mathbf{f}\left(\mathbf{x},\mathbf{u},\boldsymbol{\theta}\right) + \boldsymbol{\omega} \tag{1}$$

$$\mathbf{y} = \mathbf{h}\left(\mathbf{x},\mathbf{u},\boldsymbol{\theta}\right) + \boldsymbol{\upsilon} \tag{2}$$

$\boldsymbol{\omega}$ represents state propagation and modelling error, $\boldsymbol{\upsilon}$ is the sensor error, and an optimal filter can be derived using estimates or expectations of the error covariance matrices:

$$\mathbf{Q} = E\left(\boldsymbol{\omega}\boldsymbol{\omega}^T\right) \quad \mathbf{R} = E\left(\boldsymbol{\upsilon}\boldsymbol{\upsilon}^T\right) \tag{3}$$

The EKF also requires model Jacobians to be evaluated at each time step, defined

$$\mathbf{F} = \frac{\partial \mathbf{f}\left(\mathbf{x},\mathbf{u},\boldsymbol{\theta}\right)}{\partial \mathbf{x}} \quad \mathbf{H} = \frac{\partial \mathbf{h}\left(\mathbf{x},\mathbf{u},\boldsymbol{\theta}\right)}{\partial \mathbf{x}} \tag{4}$$

For further details of the full EKF see [2].

The Identifying EKF (IEKF) takes advantage of the fact that **f** and **h** are general nonlinear functions of **x** and $\boldsymbol{\theta}$, defining an extended state vector **z** with

extended state derivatives set zero for the parameter states:

$$\dot{\mathbf{z}} = \begin{bmatrix} \dot{\mathbf{x}} \\ \dot{\boldsymbol{\theta}} \end{bmatrix} = \begin{bmatrix} \mathbf{f}(\mathbf{z},\mathbf{u}) \\ \mathbf{0} \end{bmatrix} \tag{5}$$

It is computed using a sequence of equations which develop a time-varying estimate of state error covariance, $\mathbf{P}_k$ and Kalman gain $\mathbf{K}_k$; at each time step of the recorded time histories, compute

$$\begin{aligned} \mathbf{K}_k &= \mathbf{P}_k \mathbf{H}_k^{\mathrm{T}} \left[\mathbf{H}_k \mathbf{P}_k \mathbf{H}_k^{\mathrm{T}} + \mathbf{R} \right]^{-1} \\ \mathbf{P}_k^* &= \left[\mathbf{I} - \mathbf{K}_k \mathbf{H}_k \right] \mathbf{P}_k \\ \mathbf{P}_{k+1} &= \mathbf{P}_k^* + T \left[\mathbf{F}_k \mathbf{P}_k^* + \mathbf{P}_k^* \mathbf{F}_k^{\mathrm{T}} + \mathbf{Q} \right] \\ \hat{\mathbf{z}}_{k+1} &= \hat{\mathbf{z}}_k + T\mathbf{f}_k + \mathbf{K}_k \left(\mathbf{y}_k - \mathbf{h}_k \right) \end{aligned} \tag{6}$$

The final equation in set (6) combines Euler integration of the system using time step T with state and parameter adaptation driven by the output error, (known as the *innovation* sequence).

3 UNSCENTED KALMAN FILTER

The unscented Kalman filter (UKF) identifies its own error statistics at each iteration, and hence avoids the need to use Jacobians. According to [4],[5], a sample of $(2n+1)$ so called sigma points are selected around the nth order state vector, at each instant k in time:

$$\begin{aligned} \boldsymbol{\chi}_{0k} &= \hat{\mathbf{x}}_k \\ \boldsymbol{\chi}_{ik} &= \hat{\mathbf{x}}_k + \left\{ \sqrt{(n+\kappa)\mathbf{P}_k} \right\}_i \\ \boldsymbol{\chi}_{(i+n)k} &= \hat{\mathbf{x}}_k - \left\{ \sqrt{(n+\kappa)\mathbf{P}_k} \right\}_i \end{aligned} \tag{7}$$

where $\left\{ \sqrt{(n+\kappa)\mathbf{P}_k} \right\}_i$ is the ith column of the matrix square root of $(n+\kappa)\mathbf{P}_k$ (obtained here using Cholesky decomposition) and $\mathbf{P}_k$ is the current estimate of state error covariance. These sigma points are propagated by the model, here as for IEKF, using Euler approximation:

$$\boldsymbol{\chi}_{i(k+1)} = T\mathbf{f}(\boldsymbol{\chi}_{ik}, \mathbf{u}_k, \boldsymbol{\theta}) \tag{8}$$

and intermediate estimates for the propagated state and covariance matrix are computed by weighted averages:

$$\begin{aligned} \hat{\mathbf{x}}_{k+1}^* &= \sum_{i=0-2n} W_i \boldsymbol{\chi}_{i(k+1)} \\ \mathbf{P}_{k+1}^* &= \sum_{i=0-2n} W_i \left\{ \boldsymbol{\chi}_{i(k+1)} - \hat{\mathbf{x}}_{(k+1)} \right\} \left\{ \boldsymbol{\chi}_{i(k+1)} - \hat{\mathbf{x}}_{(k+1)} \right\}^T + T\mathbf{Q} \end{aligned} \tag{9}$$

With $W_0 = \frac{\kappa}{n+\kappa}$ and for all other i, $W_i = \frac{1}{2(n+\kappa)}$

Similarly, average outputs are obtained according to the output model:

$$\begin{aligned} \Upsilon_{i(k+1)} &= \mathbf{h}(\boldsymbol{\chi}_{ik}, \mathbf{u}_k, \boldsymbol{\theta}) \\ \hat{\mathbf{y}}_{k+1} &= \sum_{i=0-2n} W_i \Upsilon_{i(k+1)} \end{aligned} \tag{10}$$

The UKF then propagates output error covariance according to the transformed sigma points:

$$\mathbf{P}_{yy} = \sum_{i=0-2n} W_i \left\{ \Upsilon_{i(k+1)} - \hat{\mathbf{y}}_{(k+1)} \right\} \left\{ \Upsilon_{i(k+1)} - \hat{\mathbf{y}}_{(k+1)} \right\}^T + \mathbf{R} \tag{11}$$

and uses this together with a cross correlation estimate

$$\mathbf{P}_{xy} = \sum_{i=0-2n} W_i \left\{ \boldsymbol{\chi}_{i(k+1)} - \hat{\mathbf{x}}_{(k+1)} \right\} \left\{ \Upsilon_{i(k+1)} - \hat{\mathbf{y}}_{(k+1)} \right\}^T \tag{12}$$

to find the Kalman gain by

$$\mathbf{K}_{k+1} = \mathbf{P}_{xy} \mathbf{P}_{yy}^{-1}$$

State and covariance estimates are then updated using the innovation sequence, in a similar way to IEKF:

$$\begin{aligned} \mathbf{P}_{k+1} &= \mathbf{P}_{k+1}^* - \mathbf{K}_{k+1} \mathbf{P}_{yy} \mathbf{K}_{k+1}^T \\ \hat{\mathbf{x}}_{k+1} &= \hat{\mathbf{x}}_{k+1}^* + \mathbf{K}_{k+1} \left(\mathbf{y}_{k+1} - \hat{\mathbf{y}}_{k+1} \right) \end{aligned} \tag{13}$$

The above UKF derivation is common to all implementations of state and parameter estimation, so the simple substitution of $\mathbf{x}$ in the above, with $\mathbf{z}$ from eqn (5) provides the identifying filter.

4 VEHICLE MODEL

The vehicle model is based on the well-known three degree of freedom model, simulating yaw, roll, and sideslip using a load dependent, combined-slip Pacejka tyre model. A fourth, longitudinal degree of freedom is included, so the principal equations of motion are

longitudinal: $$M\dot{U} = \sum_{i=1,4} F_{xi} + MrV + Mhrp \tag{14}$$

lateral: $$M\dot{V} + Mh\dot{p} = \sum_{i=1,4} F_{yi} - MUr \tag{15}$$

yaw:

$$I_{zz}\dot{r} = a\sum_{i=1,2} F_{yi} - b\sum_{i=3,4} F_{yi} + c\sum_{i=1,3} F_{xi} - c\sum_{i=2,4} F_{xi} \tag{16}$$

roll:

$$\begin{aligned} &Mh\dot{V} + I_{xx}\dot{p} = \cdots \\ &-MhUr + Mgh\phi - h_0 \sum_{i=1-4} F_{yi} + c\sum_{i=1,3} F_z - c\sum_{i=2,4} F_z \end{aligned} \tag{17}$$

roll kinematics: $$\dot{\phi} = p \tag{18}$$

Standard SAE axes are used, fixed relative to the vehicle wheelbase, and the wheels are labelled (1–4) in ascending order as (front-left, front-right, rear-left, rear-right). Equal half-track c is assumed, with axles separated distances a and b from the front and rear axles respectively, and vertical suspension geometry

is based on fixed roll centres $h_{R(f,r)}$ and CG height h_G such that

$$h_0 = h_{Rf} + \frac{W_r}{Mg}\left(h_{Rr} - h_{Rf}\right) \qquad h = h_G - h_0 \tag{19}$$

The forces controlling the vehicle body motion (F_{xi}, F_{yi}) allow for large steer angles

$$\begin{aligned} F_{x1,2} &= F^*_{tx1,2}\cos\delta - F^*_{ty1,2}\sin\delta \qquad & F_{x3,4} &= F^*_{tx3,4} \\ F_{y1,2} &= F^*_{ty1,2}\cos\delta - F^*_{tx1,2}\sin\delta \qquad & F_{y3,4} &= F^*_{ty3,4} \end{aligned} \tag{20}$$

based on lagged tyre forces, where each of the 8 elements are lagged to simulate relaxation within the tyre

$$\dot{F}^*_{tx/y,i} = \tau^{-1}(F_{tx/y,i} - F^*_{tx/y,i}) \tag{21}$$

The tyre forces (F_{txi}, F_{tyi}) are modelled according to a slightly simplified Pacejka magic formula

$$P(|\mathbf{k}|) = D\sin\left(C\tan^{-1}\left(\frac{|\mathbf{k}|}{C} - E\left(\frac{|\mathbf{k}|}{C} - \tan^{-1}\frac{|\mathbf{k}|}{C}\right)\right)\right) \tag{22}$$

using normalized slip and isotropic similarity scaling [6], [7]. The normalized slip vector is

$$\mathbf{k} = \begin{pmatrix} k_x \\ k_y \end{pmatrix} = \frac{C_\alpha}{\mu F_z}\begin{pmatrix} K_x S_i \\ \tan\alpha_i \end{pmatrix} \tag{23}$$

where S is the longitudinal slip ratio, and α is the slip angle at each tyre contact patch,

$$S_i = \frac{r_r\omega_i - U_{xi}}{U_{xi}} \qquad \tan\alpha_i = \frac{-U_{yi}}{U_{xi}} \tag{24}$$

based on wheel oriented velocities

$$\begin{aligned} U_{xi} &= U^*_{xi}\cos\delta_i + U^*_{yi}\sin\delta_i \\ U_{yi} &= U^*_{yi}\cos\delta_i - U^*_{xi}\sin\delta_i \end{aligned} \tag{25}$$

and

$$\begin{aligned} U^*_{x1,3} &= U + cr \qquad & U^*_{x2,4} &= U - cr \\ U^*_{y1,2} &= V + ar \qquad & U^*_{y3,4} &= V - br \end{aligned} \tag{26}$$

The resulting tyre force vector is then

$$\begin{pmatrix} F_{tx} \\ F_{ty} \end{pmatrix} = P(|\mathbf{k}|)\frac{\mu F_z}{|\mathbf{k}|}\begin{pmatrix} k_x \\ k_y \end{pmatrix} \tag{27}$$

Vertical tyre loads F_z are calculated from static weight distribution, modified to accommodate lateral load transfer using separate front/rear distributions according to:

$$\Delta_{lat}F_{z(f/r)} = \frac{\sum F_{y(f/r)}h_{R(f/r)} + K_{\phi(f/r)}\phi + B_{\phi(f/r)}p}{2c} \tag{28}$$

and longitudinal load transfer, according to a rigid, zero pitch approximation

$$\Delta_{long}F_z = \frac{\sum_{i=1-4} F_{xi}h_G}{(a+b)} \tag{29}$$

5 IMPLEMENTATION

Test data were obtained from a '08 MY Jaguar XF equipped with an OXTS 3200 inertial navigation (IN) device, driven on a dry proving ground. For the identification, input data is comprised of steer angle and the four wheel speeds, and the outputs are CG longitudinal and lateral accelerations and body roll rate, modeled as

$$\begin{aligned} \mathbf{u} &= [\delta,\ \omega_1,\ \omega_2,\ \omega_3,\ \omega_4]^T \\ \mathbf{y} &= \left[\frac{1}{M}\sum_{i=1-4}F_{xi},\ \frac{1}{M}\sum_{i=1-4}F_{xi},\ p\right]^T \end{aligned} \tag{30}$$

All the above measurements with the exception of body roll rate were taken from the vehicle CAN; although roll was measured using the IN, this sensor may already be available in other CAN sets, or would be cheap to add. IN measured vehicle speed, roll angle, yaw rate and lateral velocity are also used for validation of the identified model.

A range of high and low magnitude, separated and combined slip manoeuvres were conducted, exciting both dynamic and steady-state vehicle responses. One 100 second test covering dynamic, combined excitation of steering, brake and acceleration inputs was used as the identification set, with a variety of other tests used for validation. The CAN data was inter-sampled at a constant 100 Hz to match the IN (setting $T = 0.01$) and all data was then digitally filtered at 10 Hz to remove higher frequency noise; this is necessary to prevent instability in both Kalman filters, as they are propagated by Euler integration. Although here we perform a batch data process, the identifying KFs are designed to work equally well in real-time, and real-time parameter tuning could easily be achieved using a combination of dynamic low pass filters and/or higher sampling rate T.

Identification is achieved iteratively by 'rinsing' the data repeatedly through either Kalman filter, starting with an initial, nominal parameter set. Both filters require covariance estimates and here $\mathbf{Q}$ is fixed throughout as $\mathbf{Q} = \rho\mathbf{I}$, with $\rho = 1\text{e}-7$ (see [3] for more detail). For any given estimate $\hat{\boldsymbol{\theta}}$ of the identified parameters, $\mathbf{R}$ can be obtained numerically from the covariance of υ using eqn (2). Here, $\mathbf{R}$ is recomputed after each iteration. Finally, $\mathbf{P}_0 = \mathbf{Q}$, and for the UKF $\kappa = 1$.

The only difficult task is the decision of which parameters to adapt in the identification, and which to fix. The KFs can identify any number of parameters, but if they are not independent in their influence on the recorded outputs, the parameters will diverge. Following various trials the following identification set was established as the minimum non-divergent set:

$$\begin{aligned} \boldsymbol{\theta}_{\text{id}} = [&h_G, I_{zz}, K_\phi, B_\phi, K_{xf}, K_{xr}, C_{\alpha f}, C_{\alpha r}, \cdots \\ &C_f, D_f, E_f, C_r, D_r, E_r] \end{aligned}$$

This allows full identification of separate front and rear individual tyre-suspension models but with roll

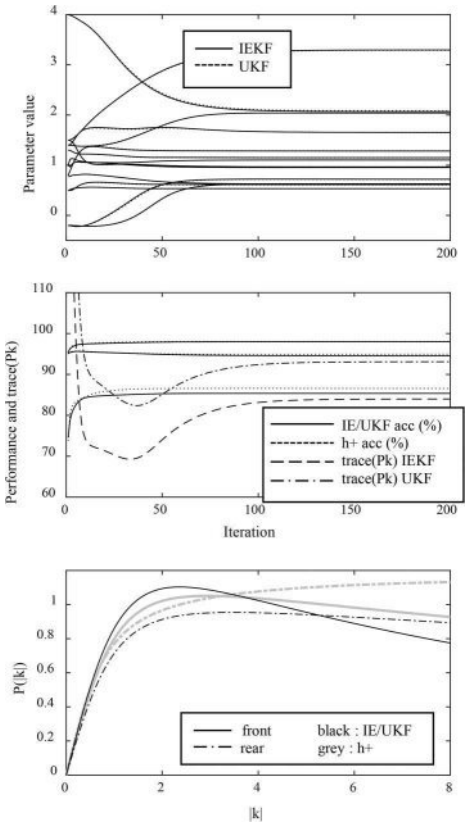


Figure 1. Identification convergence and resulting tyre.

stiffness and damping applied at a constant ratio, known from manufacturer supplied data. The remaining fixed parameters constrain the weight balance, roll inertia and essential geometry ($L =$ wheelbase), and are set

$$\boldsymbol{\theta}_{\text{fix}} = [W_f = 9567, W_r = 8635, I_{xx} = 696, \cdots$$
$$h_{Rf} = 0.08, h_{Rr} = 0.125, c = 0.79, L = 2.91]$$

Friction is identified via the tyre D parameters, so we set $\mu = 1$. To illustrate the effect of identifying too many parameters, we will also consider the case of adding roll centre heights h_{Rf} and h_{Rr} to the identified set; these are referred to below as the h+ case.

6 RESULTS

Fig. 1 and Table 1 illustrate convergence results over 200 passes (iterations) through the 100 seconds of identification data for IEKF, UKF and h+ (IEKF) cases. The resulting parameters are generally in the range expected, with the front tyre having lower stiffness and quicker saturation than the rear; this is consistent with expected front steer compliance seen in an earlier study [8].

Table 1. Parameters identified.

Parameter	IEKF	UKF	h+
h_G (m)	0.533	0.532	0.633
h_{Rf} (m)	(0.08)	(0.08)	−0.344
h_{Rr} (m)	(0.125)	(0.125)	0.223
I_{zz} (×1000 kgm^2)	2.069	2.086	2.214
K_ϕ (×100 kNm/rad)	1.152	1.147	1.692
B_ϕ (×10 kNms/rad)	0.615	0.608	1.010
K_{xf}	3.299	3.291	3.116
K_{xr}	0.966	0.966	1.036
$C_{\alpha f}$ (×100 kN/rad)	0.625	0.627	0.665
$C_{\alpha r}$ (×100 kN/rad)	1.283	1.286	1.311
C_f	2.042	2.043	1.801
D_f	1.103	1.102	1.051
E_f	0.630	0.632	0.724
C_r	1.653	1.652	1.085
D_r	0.954	0.955	1.155
E_r	0.720	0.714	0.711

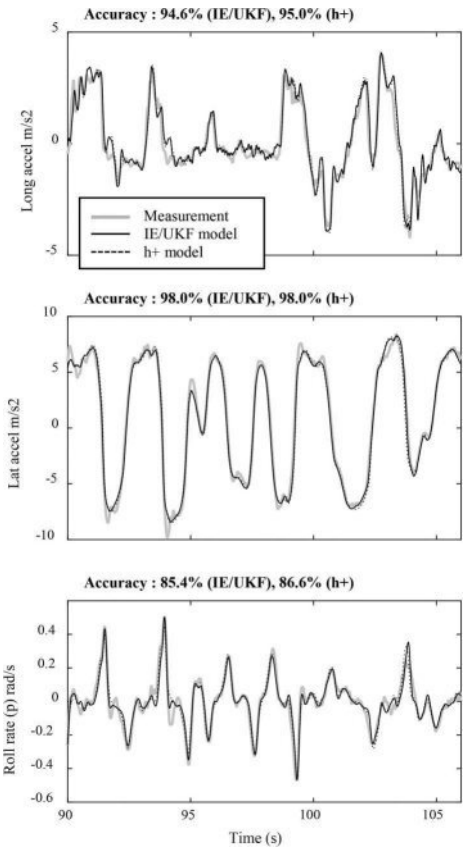


Figure 2. Model fit to measured, fitted output data.

Most striking is that although the methods are very different, the IEKF and UKF results are almost identical, not just in the final model, but throughout the convergence process; only the magnitude of trace ($\mathbf{P}_k$) varies between them.

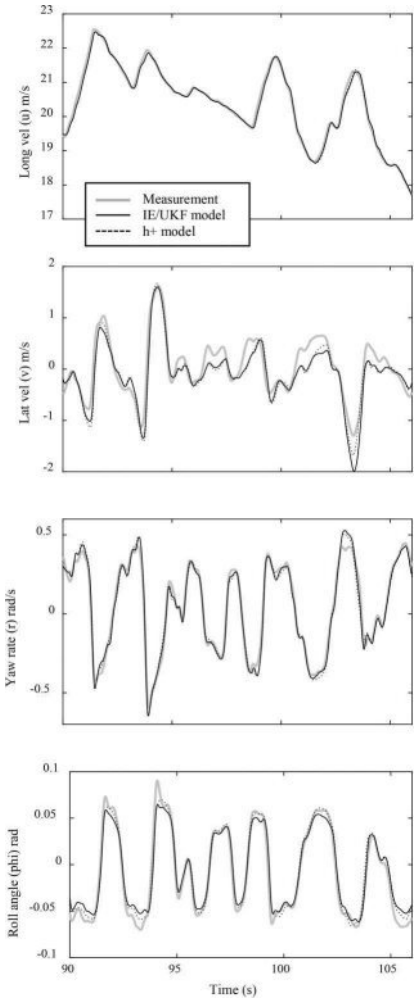


Figure 3. Model fit to unfitted measurements in the identification data.

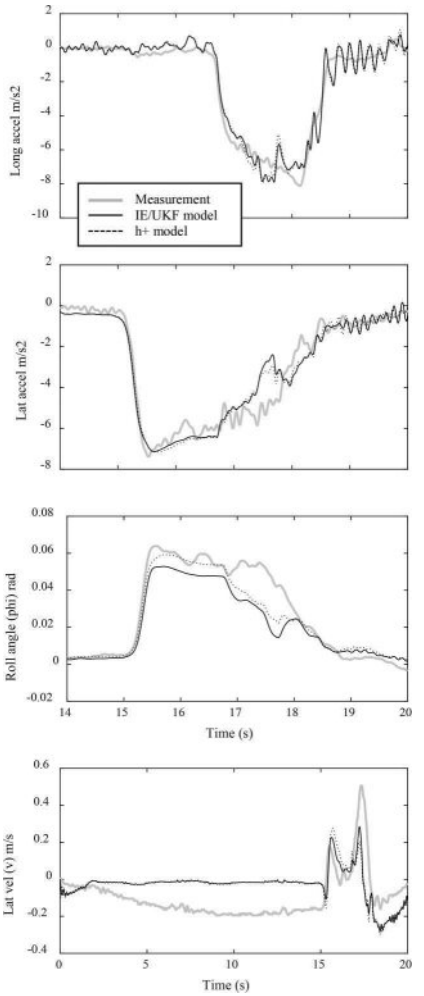


Figure 4. Identified model fit to validation test.

The decision over which of IEKF and UKF is 'better' therefore depends only on computational efficiency and complexity of code. UKF has the advantage that Jacobians are not required, so it is simpler to code, though Matlab's Symbolic toolbox means this overhead in complexity is slight. The CPU time needed to evaluate **F** and **H** might make the UKF preferable, and this is likely to be significant for state estimation applications where the state vector is smaller. Here the long state vector **z** means the UKF computes 55 sigma points at each time step, so it does not operate much quicker than IEKF; for each iteration UKF took 212 seconds, where IEKF took 266. We can therefore conclude UKF is the better method, being simpler and faster, though this may not be the case if the parameter count rose significantly.

The h+ case sees a slight performance advantage in roll rate, but this is at the expense of a converged, physically interpretable model. Note that the result in Table 1 is a snapshot at the 200th iteration, showing unrealistic negative h_{Rf} and high K_ϕ and h_G; the parameters are also divergent, with K_ϕ and h_G both rising. Interestingly, the 'snapshot' h+ model still delivers excellent performance across all outputs (see below).

Fig. 2 shows performance of the identified models on the fitted outputs and Fig. 3 shows good fits to additional unfitted outputs that were also measured.

Validation of the models on an independent test, a step steer followed by combined braking, is presented in Fig. 4. Some error is introduced to lateral acceleration when the brake is applied, at 17–18 seconds, but the model is still acceptable. Sadly there was a problem with calibration of the lateral velocity sensor – Fig. 4 shows that the model matches the essential dynamic behavior, but the measurement shows drift error over the first 10 seconds of this test, where the vehicle actually followed a straight path.

Finally, Figs. 5 and 6 show a very positive result, validating the combined-slip tyre/suspension model in single-slip tests. Here we see very accurate results

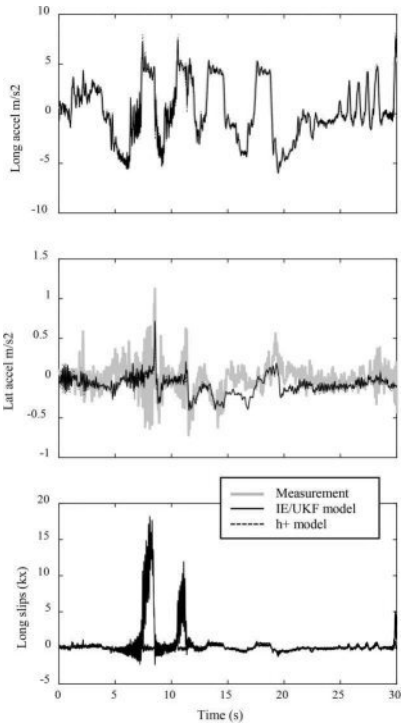


Figure 5. Model fit to straight-line brake/accel test.

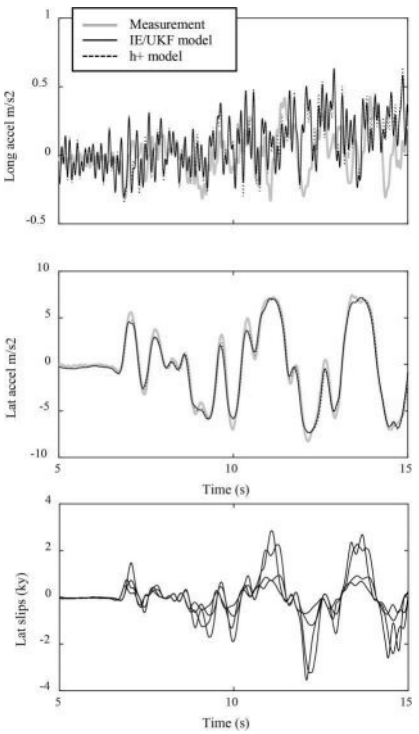


Figure 6. Model fit to constant speed, random steer test.

for a straight line braking and acceleration test under zero steer; the modeled longitudinal acceleration is indistinguishable from the measured data despite the high k_x excursions caused by wheel-spin. And Fig. 6 sees high accuracy for a constant speed, random steer manoeuvre. Both of these tests explore the tyre in low to medium magnitude and also in over-slip saturation conditions.

7 CONCLUSIONS

A full set of the independent parameters of a simplified 4-dof nonlinear handling model has been identified, including combined-slip tyre/suspension characteristics identified over their full range up to and beyond saturation. Results show excellent acceleration fits in both single and combined slip validation tests, and the model also performs well on independent output variables.

Unscented and Extended Kalman Filters have been tested, with the UKF proving slightly easier to implement and faster to run, but with both identifying identical models. The choice of which parameters to identify and which to fix can be critical, but the convergence characteristics of the identified parameters make it easy to determine unphysical and/or under-determined combinations.

ACKNOWLEDGMENT

This work is supported by Jaguar Land Rover and the UK-EPSRC grant EP/K014102/1 as part of the jointly funded Programme for Simulation Innovation (PSi).

REFERENCES

[1] Wenzel, T.A., et al, “Dual Extended Kalman Filter for Vehicle State and Parameter Estimation”, Vehicle System Dynamics, 2006, Vol. 44, No. 2, pp. 153–171.

[2] Best M.C., et al, “An Extended Adaptive Kalman Filter for Real-time State Estimation of Vehicle Handling Dynamics”, Vehicle System Dynamics, 2000, Vol. 34, No. 1, pp. 57–75.

[3] Best, M.C. and Bogdanski, K., “Extending the Kalman Filter for Structured Identification of Linear and Nonlinear Systems”, International Journal of Modelling, Identification and Control. (in press).

[4] Julier, S.J. and Uhlmann, J.K., “A New Extension of the Kalman Filter to Nonlinear Systems”, International Society for Optics and Photonics (AeroSense ’97), 1997, Vol. 7, No. 28, pp. 182–193.

[5] Wu, Y. et al, “Unscented Kalman Filtering for Additive Noise Case: Augmented vs Nonaugmented”, IEEE Signal Processing Letters, 2005, Vol 12, No. 5, pp. 357–360.

[6] Milliken, D.L. and Milliken, W.F., “Race Car Vehicle Dynamics”, SAE International, 1995.

[7] Pacejka, H.B., “Tyre and Vehicle Dynamics”, Butterworth Heinemann, 2002.

[8] Best M.C. and Newton A.P., “Vehicle Tyre and Handling Model Identification using an Extended Kalman Filter”, 9th International Symposium on Advanced Vehicle Control (AVEC ’08), Taipei, Taiwan, 2008.

Advanced Vehicle Control – Edelmann, Plöchl & Pfeffer (Eds)
© 2017 Taylor & Francis Group, London, ISBN 978-1-138-02992-7

Model-based state estimator for an intelligent tire

J. Goos, A.P. Teerhuis & A.J.C. Schmeitz
Integrated Vehicle Safety, TNO, Helmond, The Netherlands

I. Besselink & H. Nijmeijer
Department of Mechanical Engineering, Dynamics and Control, Eindhoven University of Technology, Eindhoven, The Netherlands

ABSTRACT: In this work a Tire State Estimator (TSE) is developed and validated using data from a tri-axial accelerometer, installed at the inner liner of the tire. The Flexible Ring Tire (FRT) model is proposed to calculate the tire deformation. For a rolling tire, this deformation is transformed into tangential and radial accelerations of a point on the inner liner. The results of this model show close correspondence to the experimental data. The FRT model is implemented in the observer of the TSE to estimate the longitudinal and vertical tire forces. Besides the observer, the TSE comprises a peak synchronization (PS) algorithm. Experiments show that the TSE provides accurate estimation of longitudinal and vertical tire forces, even for severe braking conditions. In addition, it shows robustness and fast convergence for large initial estimation errors. Finally, this concept of model-based tire force estimation results in a small estimation time delay.

1 INTRODUCTION

Driving situations become increasingly complex and a growing number of advanced driver assistance and vehicle dynamics control systems are introduced. Nowadays, these technologies become more and more dependent on accurate, real-time state information of the vehicle, driver and its surroundings. A performance gain can be achieved by predicting the tire capabilities and fully utilize these during emergency situations. To achieve this goal, exact and up to date knowledge of the tire-road contact forces and their potential is required, which can be provided by intelligent tire technology. Hence, the objective of this technology is to estimate tire states and force potential and thereby providing and improving key vehicle state information, by monitoring friction, slip and tire-road contact forces where these are generated.

Since many years intelligent tire systems are under development. A comprehensive overview of the state of the art up to 2005 is provided in the deliverables of the European APOLLO project (APOLLO Consortium (2003) and Mäkinen (2005)). Tire states, such as tire forces, can be estimated by measuring the deformation in and near the contact patch. Several methods may be applied to obtain this deformation, e.g. by measuring distance, acceleration or strain. Currently it seems that using an accelerometer mounted on the inner liner of the tire is the most promising solution for series production (Braghin, Brusarosco, Cheli, Cigada, Manzoni, & Mancosu (2006), Morinaga, Wakao, Hanatsuka, & Kobayakawa (2006), Matilainen & Tuononen (2012)). In this study, a mini tri-axial accelerometer is used. An algorithm is developed to transform the measured accelerations into actual tire operating conditions, in this case the vertical and longitudinal tire forces. This method is different compared to feature extraction algorithms found in the literature, such as peak detection algorithms developed by Braghin et al. (2006). The objective is to develop a model-based Tire State Estimator (TSE), which is robust for noisy signals and combined inputs occurring in real vehicles while driving.

In previous work of Teerhuis, Schmeitz, & van de Molengraft-Luijten (2015), a model-based estimator for the vertical force was developed that uses an empirical model for describing the accelerations of the tire inner liner. The estimator comprises a peak synchronization (PS) algorithm and a model-based observer. The empirical model contains several coefficients which are obtained using a least-squares fitting procedure. The TSE showed accurate and fast vertical force estimation. The follow-up paper of Schmeitz & Teerhuis (2015) investigates the robustness of the TSE to additional tire operating conditions. Although the TSE developed by Teerhuis et al. (2015) performs well, an extension of the TSE towards more tire states requires the empirical model to be extended and its complexity rapidly increases. Therefore, the empirical model has been reconsidered, resulting in a physical tire model that can also describe the longitudinal force. The development and validation of this model and the altered TSE are described in this paper. This paper is organised as follows. First, the experimental setup



Figure 1. Experimental setup: (A) Tire Test Trailer, (B) Measurement tower, (C) Accelerometers at the inner liner.

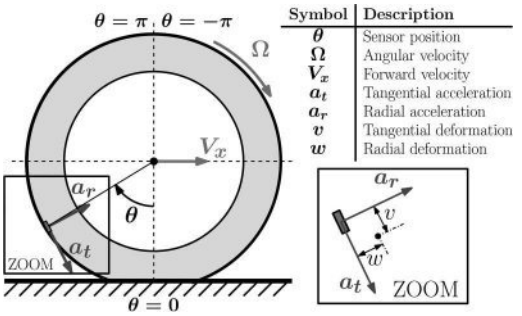


Figure 2. Schematic representation of intelligent tire.

is described. Next, the TSE is explained in Section 3. Afterwards, the results and discussion are provided and eventually the main conclusions are given.

2 EXPERIMENTAL SETUP

An experimental setup using TNO's Tire Test Trailer was developed to obtain the required measurement data for the development and validation of the TSE, see Figure 1. This on-road test laboratory provides accurate and well controlled tire force and moment measurements under realistic operating conditions: various side slip angles, vertical forces, longitudinal slip by braking, camber angles, forward velocities on real road surfaces. Three tri-axial accelerometers are placed on the inner liner of the intelligent tire, see Figure 1 (C). These accelerometers are piezoelectric sensors, which are not capable of measuring constant accelerations. For this reason, constant components in the acceleration signal are not observed. The wheel with the intelligent tire is mounted on a measurement hub, which measures the actual tire forces at the wheel center. These forces will be used as a reference for both model and estimator validation. Moreover, a slip ring assembly and a separate data acquisition system are installed to record the acceleration signals of the intelligent tire.

In this research, the focus is on the *in-plane* tire behaviour. For this reason, only the tangential a_t and radial acceleration a_r signals from the center accelerometer are considered. Figure 2 shows a schematic representation of the intelligent tire and explains the notation used in this paper.

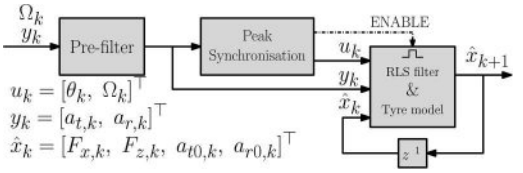


Figure 3. Schematic diagram of the TSE.

3 TIRE STATE ESTIMATOR

The TSE is designed to transform the measured tangential a_t and radial acceleration a_r signal of the inner liner to longitudinal F_x and vertical tire forces F_z estimates. The TSE consists of a PS algorithm and a model-based observer. The observer requires an accurate model for the calculation of the acceleration signals. This model requires the sensor position θ, angular velocity Ω, tire forces and acceleration offsets a_{t0} and a_{r0}. The angular velocity is measured using a wheel speed sensor. The unknowns are the tire forces, acceleration offsets and the sensor position. The tire model is highly nonlinear with respect to the sensor position θ. In most cases, including θ in the vector of estimates of the observer would give poor results due to the high nonlinearity. For this reason, the sensor position is separately estimated using the PS algorithm. When the estimation of the sensor position is within a specified threshold, the model-based observer is enabled. A recursive least-squares (RLS) filter is used to estimate the remaining unknowns. Figure 3 shows a diagram of the TSE.

3.1 *Flexible Ring Tire model*

A model is developed for the calculation of the accelerations of the tire inner liner. The acceleration vector of the sensor is:

$$\vec{a}_S = \ddot{\vec{r}}_S + \vec{g}, \tag{1}$$

where $\vec{g}$ is the gravitational acceleration and $\vec{r}_S$ is the distance from the wheel center to the sensor. The calculation of $\vec{r}_S$ requires the tire belt deformation in tangential and radial direction (v and w). The Flexible Ring Tire (FRT) model is proposed to calculate this deformation. This model has been developed by Gong (1993) and adapted in this research. In this model, the tire comprises three components: the belt, sidewall and the rim. The belt is modelled as an elastic, circular beam that is connected with the rim via the sidewall. The sidewall is represented by an elastic foundation with tangential and radial stiffnesses distributed along the circumference. Figure 4 shows a schematic representation of the FRT model.

According to Gong (1993), the governing equations of the rotating belt are derived using Hamilton's principle. This method requires the strain and kinetic energy of the belt, the elastic energy of the foundation, and external forces. The governing equations of the belt are two partial differential equations for the tangential and radial tire belt deformation v and w. It is assumed that the belt is in-extensible, so the circumferential

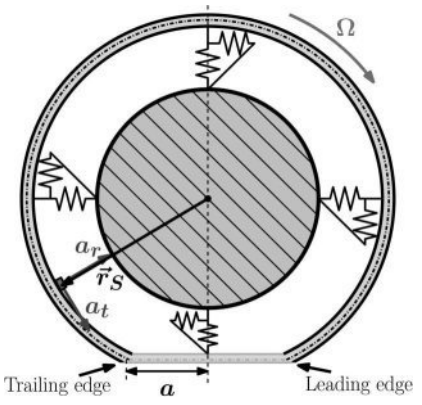


Figure 4. Schematic representation of the FRT model.

length of the belt does not change during deformation. This results in the following relation for the radial belt deformation:

$$w = -\frac{\partial v}{\partial \theta}. \tag{2}$$

Applying this relation, the governing equations are reduced to one partial differential equation for the tangential belt deformation (Gong (1993)):

$$-\frac{EI}{R^4}\left(\frac{\partial^2 v}{\partial \theta^2} + 2\frac{\partial^4 v}{\partial \theta^4} + \frac{\partial^6 v}{\partial \theta^6}\right) + \frac{p_0 b}{R}\left(\frac{\partial^2 v}{\partial \theta^2} + \frac{\partial^4 v}{\partial \theta^4}\right) - k_w \frac{\partial^2 v}{\partial \theta^2} + k_v v = q_v + \frac{\partial q_w}{\partial \theta}, \tag{3}$$

where EI is the bending stiffness of the belt, R is the undeformed belt radius and b is the belt width. Furthermore, k_v and k_w are the tangential and radial stiffnesses of the elastic foundation, and q_v and q_w are the tangential and radial external force distributions per unit of length. The tire inflation pressure is p_0.

In order to solve this sixth order partial differential equation, the contact pressure distribution between the tire and the road is required (q_v and q_w). The calculation of this distribution is complex and often done iteratively. As the forces need to be determined in real-time, an iterative procedure is undesirable. For this reason, the tire model is applied outside the contact patch only and thus the contact pressure distribution is not required ($q_v = q_w = 0$), see Figure 4. The general solution of (3) is:

$$v(\theta) = \sum_{i=1}^{6} C_i e^{z_i \theta}, \tag{4}$$

where z_i are the roots of the characteristic equation of (3) and C_i are constants of integration. In order to calculate C_i, six boundary conditions at the contact patch edges are required. To determine these, the contact patch length must be known. In the model the contact length, which is related to the vertical tire force and inflation pressure, is empirically modelled using measurements from the test trailer. The six boundary conditions are obtained from the tangential and radial deformations at the contact patch edges, which are calculated from the deformed tire geometry.

Summarizing, the longitudinal and vertical tire forces are the inputs of the model. With these forces, the contact patch length and boundary conditions are calculated. This results in the constants of integration. The tire belt deformation is then calculated using (2) and (4). With this deformation, the varying sensor radius along the inner liner circumference is known. Finally, (1) is used to calculate the accelerations at the inner liner. The calculation sequence is listed below:

1. Calculate half of the contact patch length a
2. Calculate boundary conditions using F_x and F_z
3. Calculate constants of integration C_i
4. Calculate tire belt deformation v and w
5. Calculate sensor radius $\vec{r}_S$
6. Calculate inner liner accelerations a_t and a_r

The tire model is validated using data from the Tire Test Trailer. The model results are compared with measurements for various angular velocities, vertical and longitudinal tire forces and tire inflation pressures. Figure 5 provides a comparison of the FRT model results with the measured accelerations for a free-rolling wheel and a braked wheel (left and middle plot). Furthermore, it shows the resulting tire belt deformation in the global coordinate system (right plot). From this figure, it is concluded that the modelled accelerations corresponds well with the measurement data obtained from the intelligent tire. For other operating conditions, the comparison of the model results with the measurements show similar satisfying results, meaning that the tire model is appropriate for implementation in the observer of the TSE.

3.2 *Peak synchronization*

The PS algorithm is used to estimate the sensor position θ and is developed by Teerhuis et al. (2015). The sensor position is calculated via numerical integration of the wheel speed signal. However, due to the unknown initial position, the sensor position in the model must to be synchronized with the acceleration signals of the sensor. The algorithm is based on the definition that $\theta = 0$ corresponds to the sensor being at the contact patch center. The contact patch center corresponds with the center of the negative dip in a_r, which is defined as θ_{peak}. When assuming a free-rolling tire and $\theta_{peak} = 0$, a_r is symmetric around $\theta = 0$, see Figure 5 (left). In this case, the integral of a_r^2 for $\theta < 0$ equals the integral for $\theta > 0$ for an individual revolution. This is formulated by the condition:

$$\int_{-\pi}^{\pi} w_{PS}(\theta)(\theta - \theta_{peak}) a_r(\theta)^2 \mathrm{d}\theta, \text{ for } \theta_{peak} = 0, \tag{5}$$

where w_{PS} is a weighting function which emphasises the negative dip. With this formulation, θ_{peak} can be calculated if the sensor position is not synchronized yet. At the end of each revolution, (5) is used to calculate θ_{peak}:

$$\sum_{i=1}^{N_{rev}} w_{PS,i}\theta_i a_{r,i}^2 - \sum_{i=1}^{N_{rev}} w_{PS,i}\theta_{peak} a_{r,i}^2 \approx 0. \tag{6}$$

Thus:

$$\theta_{peak} \approx \frac{\sum_{i=1}^{N_{rev}} w_{PS,i}\theta_i a_{r,i}^2}{\sum_{i=1}^{N_{rev}} w_{PS,i} a_{r,i}^2}, \tag{7}$$

where N_{rev} is the number of samples within a revolution and $\theta_i \in [-\pi, \pi]$. At the end of the revolution, the sensor position is corrected with θ_{peak} as follows:

$$\theta_k = -\pi - \theta_{peak}. \tag{8}$$

Hence, the integration starts at the corrected position instead of at $\theta_k = -\pi$. Each revolution θ_{peak} is calculated and the sensor position is corrected. When θ_{peak} is within a specified threshold, the sensor position is assumed to be accurate enough and the RLS filter is enabled. Figure 6 shows an example of the estimation of the sensor position when the wheel starts from standstill. Here, the integration starts at $\theta_0 = -\pi$. After 1.7 s, one revolution is completed and $\theta_{peak} \approx -0.46\pi$. The sensor position is corrected: $\theta_k = -\pi - \theta_{peak} \approx -0.54\pi$. The integration continues with the corrected sensor position. After five revolutions, θ_{peak} is within the threshold.

3.3 *Recursive least-squares filter*

After synchronization, the RLS filter is enabled and the tire forces can be estimated. The concept of a directional forgetting factor is used to allow tracking of the time-varying forces and acceleration offsets, which operate with different timescales. The measurement vector, the estimates and input vector are:

$$\begin{aligned} y_k &= [a_{t,k} \quad a_{r,k}]^\top \\ \hat{x}_k &= [F_{x,k} \quad F_{z,k} \quad a_{t0,k} \quad a_{r0,k}]^\top \\ u_k &= [\theta_k \quad \Omega_k]^\top. \end{aligned} \tag{9}$$

Here, $a_{t0,k}$ and $a_{r0,k}$ are tangential and radial acceleration offsets at $\theta_k = \pm\pi$. The measurement vector is modelled as:

$$y_k = h(\hat{x}_k, u_k) + v_k, \tag{10}$$

where $h(\hat{x}_k, u_k)$ is calculated with (1) using the FRT model. Furthermore, v_k is the measurement noise. The measurement error e_k is defined as:

$$e_k = y_k - h(\hat{x}_k, u_k). \tag{11}$$

The sum of the squared error (11) is minimized using the following set RLS equations:

$$\begin{aligned} \hat{x}_k &= \hat{x}_{k-1} + K_k[y_k - h(\hat{x}_k, u_k)] \\ K_k &= \Lambda^{-1} P_{k-1} H_k^\top \left(I + H_k \Lambda^{-1} P_{k-1} H_k^\top\right) \\ P_k &= \Lambda^{-1} P_{k-1} - K_k H_k \Lambda^{-1} P_{k-1}. \end{aligned} \tag{12}$$

Here, K_k is the estimator gain matrix, P_k is the estimation error covariance matrix, H_k is the Jacobian of $h(\hat{x}_k, u_k)$ with respect to $\hat{x}_k$, and Λ is a diagonal matrix with forgetting factors. The full derivation of the RLS filter is provided in Haykin (2008). The filter is tuned by varying the forgetting factors and the initial covariance matrix P_0. In order to estimate abruptly varying tire forces, a change detection algorithm is designed. For each revolution the cumulative sum of the measurement error e_k is calculated. When this value exceeds a specified threshold, the algorithm resets the error covariance matrix P_k to a large value. Thus, the confidence in the estimates is again low which results in a high convergence rate.

4 RESULTS AND DISCUSSION

The TSE is tested offline using data from the TNO tire test trailer. Many experiments have been conducted in which velocity, vertical force, brake force and inflation pressure have been varied. Two interesting cases are discussed in this paper:

1. Free-rolling tire, with varying vertical force F_z and wheel angular velocity Ω.
2. Pure braking with constant vertical force F_z.

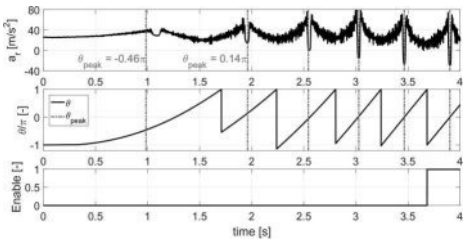


Figure 6. Example of the estimation of the sensor position.

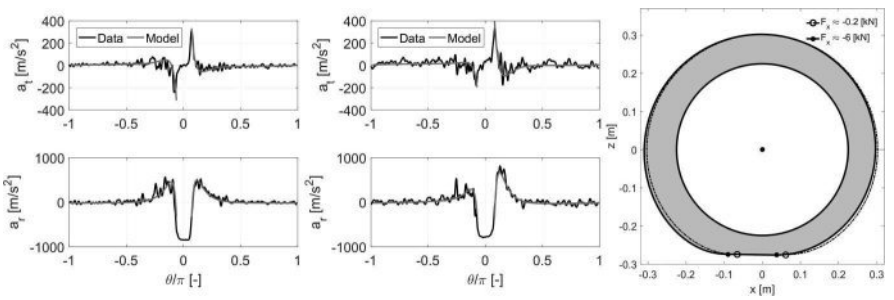


Figure 5. Validation of FRT model. A) Free-rolling tire: $\Omega \approx 50$ [rad/s], $F_z \approx 7.2$ [kN], $F_x \approx -0.2$ [kN]. B) Tire with brake force: $\Omega \approx 50$ [rad/s], $F_z \approx 7.2$ [kN], $F_x \approx -6.0$ [kN]. The deformation is plotted in C) for both conditions.

The TSE model is created in MATLAB/Simulink, running at a sampling frequency of $f_s = 4$ [kHz]. The initial tire force estimations are set to a high value to show the convergence rate ($F_{x,0} = 4$ [kN] and $F_{z,0} = 10$ [kN]). When the sensor is in the contact patch region, the accelerations cannot be calculated due to the limitation of the tire model. In this region, the RLS equations (12) are not updated. In the following figures, the black lines correspond with the measured accelerations from the intelligent tire. The red lines represent the estimated accelerations and tire forces from the TSE. Furthermore, the green lines are the reference tire forces measured with the test trailer.

4.1 *Results free-rolling tire*

The first case is presented in Figure 7 to 10. The angular velocity Ω varies between 20 and 80 [rad/s], see Figure 7. Figure 8 shows the measured and estimated acceleration signals of the start of the experiment. Figure 9 shows the corresponding tire forces at the start. Concluding from Figure 8, the PS algorithm requires two revolutions to obtain the correct sensor position. Now, the RLS filter is enabled and the tire forces are initialized at a high value to show the convergence capabilities. This over-estimation results in a mismatch between the calculated and measured accelerations between 0.18 and 0.23 [s] in Figure 8. This is observed by the filter and causes the tire forces to converge quickly to the reference forces, see Figure 9. Updating the estimates during the revolution is a key advantage of this TSE compared to conventional estimators, which update only after each full revolution. This feature results in a small delay. After around 0.3 [s], the tire forces are already within a margin of 5%. Figure 10 shows the estimated and reference tire forces of the total experiment. The estimated vertical tire force follows the reference measurement closely with a delay of approximately 0.1 [s]. The longitudinal estimation fluctuates and sometimes has a small offset w.r.t. the reference measurement. The average errors are: $\overline{e}_{F_x} = 2.9\%$ and $\overline{e}_{F_z} = 5.5\%$.

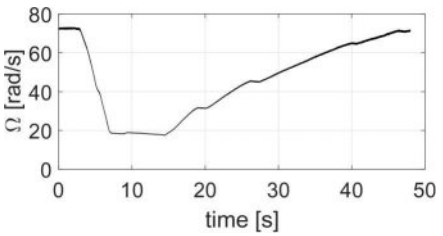


Figure 7. TSE results case 1: angular velocity Ω.

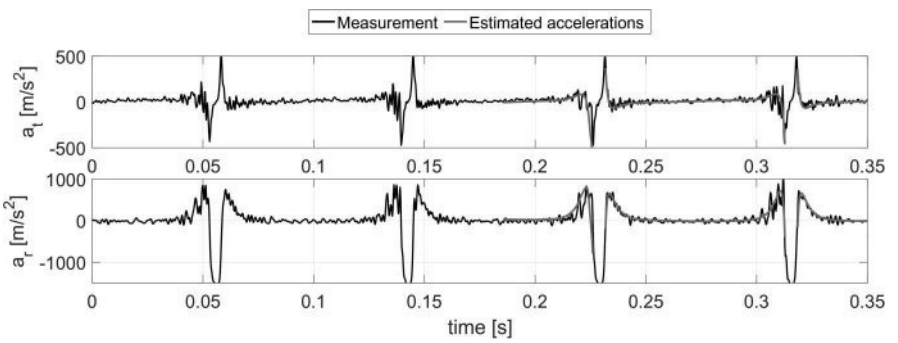


Figure 8. Start of TSE results case 1: accelerations a_t and a_r.

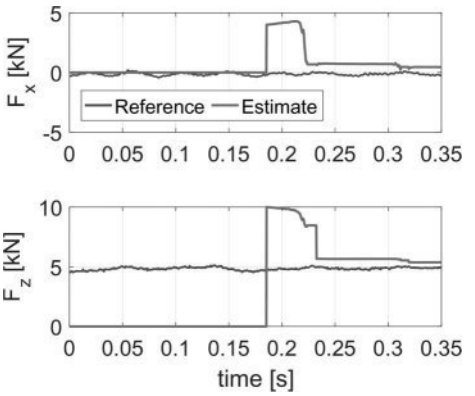


Figure 9. Start of TSE results case 1: tire forces F_x and F_z.

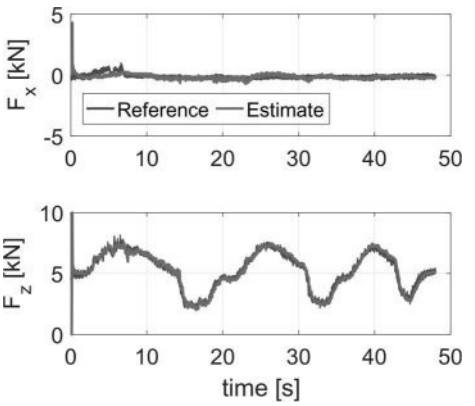


Figure 10. TSE results case 1: tire forces F_x and F_z.

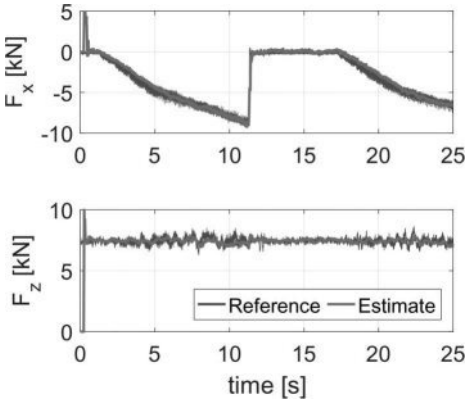


Figure 11. TSE results case 2: tire forces F_x and F_z.

Table 1. Maximum estimation errors of TSE results.

Loadcase	No. exp.	max $\lvert e_{Fx} \rvert$	max $\lvert e_{Fz} \rvert$
Free-rolling tire	23	6.3%	6.2%
Pure braking	11	7.5%	7.0%

4.2 *Results pure braking*

Now a second case will be discussed, where a gradually increasing brake force is applied to the wheel until approximately the maximum brake force. Then, the brake force is released and it increases again. The vertical tire force is approximately constant in this experiment. In Figure 11 the estimated tire forces are compared with the measurements from the test trailer. The first period is required for estimating the sensor position and convergence. In this case, the convergence period is also short. From this figure, it is concluded that the TSE is able to estimate both longitudinal and vertical tire forces, even for severe brake forces. Furthermore, the estimator is able to deal with rapid changes of the tire forces when the brakes are released around 11 [s]. The F_x estimation requires only 0.1 [s] to converge back within a margin of 5%. The average errors are: $\overline{e}_{F_x} = 5.1\%$ and $\overline{e}_{F_z} = 5.2\%$.

4.3 *Overall performance of TSE*

In total 34 experiments have been conducted for free-rolling tire and braking conditions. For each experiment, the average errors are calculated and the maximum error value of these experiments are provided in Table 1. For a free-rolling tire, the errors are lower than 6.3%. In a braking event, the error is somewhat higher, but lower than 7.5%. The vertical force estimation is improved by 7% compared to the existing TSE developed by Teerhuis et al. (2015). The average delay in all experiments is 0.1 [s] or lower. Moreover, in all experiments the TSE requires less than 0.3 [s] to converge back after the release of the brake force. The delays can be reduced by lowering the forgetting factor and by changing the reset values of the covariance matrix of the change detection algorithm. However, this comes at the cost of smoothness of the estimates. If this improvement would be insufficient, additional accelerometer(s) can be installed distributed over the circumference of the inner liner.

5 CONCLUSION

The FRT model is able to accurately calculate the tire belt deformation and acceleration. The model is validated using measurements of TNO's Tire Test Trailer for various tire operating conditions. The physical tire model is implemented in the TSE, which consists of a PS algorithm and an RLS filter. The PS algorithm and the RLS filter are used to estimate the sensor position and the tire forces, respectively. Concluding from the various tests, the TSE provides tracking of both vertical and longitudinal tire forces with a maximum error of 7.5%, even for severe brake forces. The results show good convergence capabilities and a maximum delay of 0.1 [s]. Furthermore, the TSE is able to deal with rapid changes due to the change detection algorithm. In addition, the fast convergence and robustness capability are shown in two test cases.

REFERENCES

APOLLO Consortium (2003). Intelligent tyre systems-state of the art and potential technologies. *Technical Research Centre of Finland (VTT), APOLLO Deliverable D7 for Project IST-2001-34372*.

Braghin, F., M. Brusarosco, F. Cheli, A. Cigada, S. Manzoni, & F. Mancosu (2006). Measurement of contact forces and patch features by means of accelerometers fixed inside the tire to improve future car active control. *Vehicle System Dynamics 44*(sup1), 3–13.

Gong, S. (1993). *A study of in-plane dynamics of tires*. TU Delft, Delft University of Technology.

Haykin, S. S. (2008). *Adaptive filter theory*. Pearson Education India.

Mäkinen, T. (2005). Apollo–final report including technical implementation plan. Deliverable 22/23 for the European commission, Tampere, Finland; 2005.

Matilainen, M. & A. Tuononen (2012). Intelligent tire to measure contact length in dry asphalt and wet concrete conditions. In *Proceedings of the 11th International Symposium on Advanced Vehicle Control, Seoul, Korea*, pp. 9–12.

Morinaga, H., Y. Wakao, Y. Hanatsuka, & A. Kobayakawa (2006). The possibility of intelligent tire (technology of contact area information sensing). *FISITA2006 Trans., F2006V104*.

Schmeitz, A. & A. Teerhuis (2015). Tire state estimator for an intelligent tire, robustness and applicability. In *the thirty-fourth annual meeting and conference on Tire Science and Technology, September 9-10, 2015, Akron, Ohio, USA*.

Teerhuis, A., A. Schmeitz, & L. van de Molengraft-Luijten (2015). Tire state estimation based on measured accelerations at the tire inner liner using an extended kalman filter design. In *International Tyre Colloquium, 4th, 2015, Guildford, United Kingdom*.

Advanced Vehicle Control – Edelmann, Plöchl & Pfeffer (Eds)
© 2017 Taylor & Francis Group, London, ISBN 978-1-138-02992-7

Nonlinear vehicle velocity estimation with friction adaption for four-wheel-independent-drive EVs

X. Xia, L. Xiong, B. Leng & Z. Yu
School of Automotive Studies, Tongji University, Shanghai, China

ABSTRACT: In order to improve the active safety for vehicle, nonlinear real-time observer for estimation of longitudinal velocity with road maximum friction coefficient for four-wheel-independent-drive EVs was proposed. Vehicle longitudinal velocity was estimated using the feedback value of each wheel slip ratio and longitudinal acceleration sensor, and the convergence of estimation error is proved. In order to improve accuracy for calculating slip ratio under different road conditions, the road maximum friction coefficient(RMFC) estimator was proposed based on modified Burckhardt tire model. The amount of computations for this method is small but with high estimation precision. The effectiveness of the algorithm and adaptive law was validated through experiments in various working condition.

1 INTRODUCTION

Accurate estimation of longitudinal velocity is the foundation of those active safety systems such as ABS, ASR and ESP. Sensors that can measure longitudinal velocity directly are too expensive to be promoted. However it is difficult to estimate velocity for four-wheel-independent-drive (FWID) EVs with the characteristic of all wheel independent driving. Based on above, the algorithm in this paper chooses pre-existing sensors in FWID EVs to realize the longitudinal velocity estimation with road maximum friction coefficient adaption.

According to state of the art, major approaches of the longitudinal velocity estimation can be divided into two categories. One called kinematic method is based on the wheel speed and vehicle acceleration signals, calculating the vehicle velocity directly (Gao *et al*., 2013). This kind of method is robust to the vehicle model and road friction coefficient, but sensitive to measurement noise and accuracy and road gradient. The other called dynamics method or observer method is an indirect approach based on the vehicle and tire model (Vietinghoff *et al*., 2007; Hsu *et al*., 2009). Thus the accuracy of this kind of method is determined by the vehicle and tire model including road friction coefficient. The more accurate the model is, the less efficient the algorithm will be. The algorithm which has been used most widely is filter estimation method such as KF(Kobayashi *et al*.,1995), EKF(Cong *et al*., 2007), UKF, PF et al. While this kind of filter method leads to huge calculation quantity and it is hard to work in real time (Sun *et al*., 2015). Compared with the filter estimation method, nonlinear estimation methods reduce the computational complexity as they only need to solve n odes while $3/2n + 1/2n^2$ in EKF.

Based on those above, the novel nonlinear estimation method in this paper fuses the kinematic and dynamics method and makes full use of the merits of each method for high estimation accuracy. In the meantime, the RMFC was estimated using a modified Burckhardt tire model to update the tire model in velocity estimation for RMFC adaption. In the end, the effectiveness of the algorithm and adaptive law was validated through experiments in various working condition.

2 NONLINEAR VELOCITY ESTIMATOR

2.1 *Tire model*

Burckhardt tire model can describe the relationship between the slip ratio and longitudinal force simply containing road maximum friction coefficient explicitly (Burckhardt, 1993). In (Jin *et al.*, 2014), the parameters of the Burckhardt tire model are increased from three to five parameters. The modified Burckhardt tire model is able to describe the real tire longitudinal characteristic more accurately. The modified Burckhardt tire model is shown in Equation (1).

$$\mu(\theta,\lambda) = \theta - \theta e^{-\frac{c_1}{\theta}\left(\lambda + c_2\lambda^2\right)} - c_3\lambda\,\mathrm{sgn}\left(\lambda\right) + c_4\lambda^2 \qquad (1)$$

Here θ is RMFC, μ is normalized longitudinal tire force, λ is slip ratio and c_1–c_4 are constants.

The parameters in Equation (1) play the following distinctive roles: The peak value of normalized tire force in $\mu-\lambda$ curve is mainly determined by θ which is the road maximum friction coefficient. c_1 dominates the longitudinal slip stiffness at the origin of the $\mu-\lambda$

curve. c_2 can be exploited to adjust the general stiffness of the tire without influencing the stiffness at the origin or the maximum tire force. c_3 and c_4 are positive numbers used to make μ descend a little bit after its peak point. If the two parameters are set to be zero, the $\mu-\lambda$ curve is flat at large slip ratio. Usually c_2–c_4 vary a little under different road conditions. Based on the experimental test of the tire, the parameters of c_2–c_4 can be set 8, 0.25, 0.11 respectively.

The influence of θ and c_1 on the shape of the $\mu-\lambda$ curve is shown in Figure 1. The peak value and longitudinal slip stiffness near origin can be adjusted through tuning the values of θ and c_1 respectively.

In Figure 1(a), c_1 is set 18. In Figure 1(b), θ is set 0.8. As is shown in Figure 1(b), c_1 has little influence on the peak value of the curve. Therefore, it is reasonable that c_1–c_4 are set to constant, which means that the tire model is only determined by the road maximum friction coefficient θ.

2.2 *Velocity estimator design*

$$\dot{\hat{v}} = a_x + u \tag{2}$$

$$u = sat[L \cdot (\omega - \hat{\omega})] \tag{3}$$

$$\hat{\omega} = g(\hat{\lambda}, \hat{v}) \tag{4}$$

$$\dot{\hat{\lambda}} = f(\hat{\lambda}, T, \hat{v}, F_z, \hat{\theta}) \tag{5}$$

Where

$$\hat{\omega} = g(\hat{\lambda}, \hat{v}) = \frac{(1+\hat{\lambda})\hat{v}}{R} \tag{6}$$

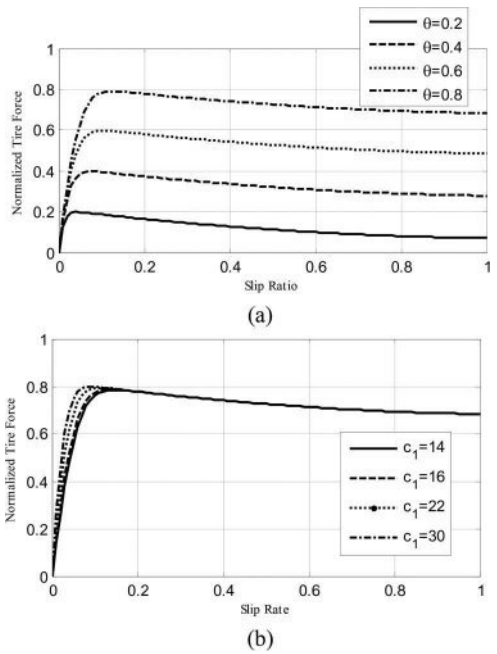


Figure 1. $\mu-\lambda$ curve of modified Burckhardt tire model.

$$\dot{\hat{\lambda}} = \left(\frac{\hat{\omega}R - \hat{v}}{\hat{v}}\right)' = \frac{\dot{\hat{\omega}}}{\hat{v}} R \tag{7}$$

The wheel rotational dynamics can be represented as

$$T = F_x(\hat{\lambda}, F_z) \cdot R - J_w \cdot \dot{\hat{\omega}} \tag{8}$$

Therefore

$$\dot{\hat{\lambda}} = f(\hat{\lambda}, T, \hat{v}, F_z) = \frac{\dot{\hat{\omega}}}{\hat{v}} R = \frac{\frac{T - F_x(\hat{\lambda}, F_z) \cdot R}{J_w}}{\hat{v}} R \tag{9}$$

where $\hat{v}$ is the estimated velocity, a_x longitudinal acceleration, ω wheel rotation speed, R tire rolling radius, J_ω wheel moment of inertia, $\hat{\omega}$ estimation of ω, L a constant, $\hat{\lambda}$ estimated slip ratio, T wheel torque, F_z wheel normal force, $\hat{\theta}$ estimated value of θ, $sat(\cdot)$ saturation function, $g(\cdot)$ and $f(\cdot)$ nonlinear function. $F_x(\cdot)$ is longitudinal tire force calculated by the modified Burckhardt tire model as Equation (1).

In order to prevent the over correction from u to a_x, we use a saturation function to calculate u. In the meantime, we involve the slip ratio of each wheel to obtain the feedback gain as Equation (10) shows.

$$\begin{aligned} k_{fl} &= 1 - |\lambda_{fl}| \\ k_{fr} &= 1 - |\lambda_{fr}| \\ k_{rl} &= 1 - |\lambda_{rl}| \\ k_{rr} &= 1 - |\lambda_{rr}| \\ k_s &= k_{fl} + k_{fr} + k_{rl} + k_{rr} \end{aligned} \tag{10}$$

$$\begin{aligned} \omega - \hat{\omega} = &\frac{k_{fl}}{k_s}(\omega - \hat{\omega})_{fl} + \frac{k_{fr}}{k_s}(\omega - \hat{\omega})_{fr} \\ &+ \frac{k_{rl}}{k_s}(\omega - \hat{\omega})_{rl} + \frac{k_{rr}}{k_s}(\omega - \hat{\omega})_{rr} \end{aligned} \tag{11}$$

fl, *fr*, *rl*, *rr* mean front left wheel, front right wheel, rear left wheel, and rear right wheel respectively.

Considering the load transfer due to the pitch and roll, the wheel normal load is estimated by Equation (12).

$$\begin{aligned} F_z^{fl} &= mg\frac{l_r}{2l} - m\frac{h_g}{2l}a_x - m\frac{h_g l_r}{B_f l}a_y, \\ F_z^{fr} &= mg\frac{l_r}{2l} - m\frac{h_g}{2l}a_x + m\frac{h_g l_r}{B_f l}a_y, \\ F_z^{rl} &= mg\frac{l_f}{2l} + m\frac{h_g}{2l}a_x - m\frac{h_g l_f}{B_r l}a_y, \\ F_z^{rr} &= mg\frac{l_f}{2l} + m\frac{h_g}{2l}a_x + m\frac{h_g l_f}{B_r l}a_y. \end{aligned} \tag{12}$$

where m denotes the vehicle mass, g is the gravity acceleration, l_f and l_r are the distances from the front

axis and the rear axis to center of gravity (COG), l is the wheel base, h_g is the height of the COG, a_y are the longitudinal acceleration and lateral acceleration respectively, and B_f and B_r are the front and rear wheel track respectively.

2.3 *Estimation error analysis*

The estimation error is denoted by

$$\tilde{v} = \hat{v} - v \tag{13}$$

Then we obtain the error dynamics as Equation (14) shown.

$$\begin{aligned}\dot{\tilde{v}} &= \dot{\hat{v}} - \dot{v} \\ &= a + u \\ &= a + sat\left[k(1+\lambda)(\hat{v}-\tilde{v}) - k(1+\hat{\lambda})\hat{v}\right] \\ &= a + sat\left[k(1+\lambda)\hat{v} - k(1+\lambda)\tilde{v} - k(1+\hat{\lambda})\hat{v}\right] \\ &= a + sat\left[-k(1+\lambda)\tilde{v} + k\tilde{\lambda}\hat{v}\right]\end{aligned} \tag{14}$$

where k is defined as $k = L/R$ which is a positive value. $\dot{\tilde{v}}$ is the derivative of $\tilde{v}$. The slip ratio in acceleration situation is defined by $\lambda = \frac{\omega R - v}{v}$, and the derivative of slip ratio is $\dot{\lambda} = (\frac{\omega R - v}{v})' \approx \frac{\dot{\omega}}{v} R$.

Based on Equation (8), Equation (14) is derived

$$\frac{J_w \cdot \dot{\omega} R}{v} = \frac{-F_x(\lambda, F_z) \cdot R + T}{v} \cdot R \tag{15}$$

Then

$$\begin{aligned}J_w \dot{\tilde{\lambda}} = &\left[\frac{-F_x(\hat{\lambda}, F_z)R}{\hat{v}} + \frac{F_x(\lambda, F_z)R}{v} + \frac{T}{\hat{v}} - \frac{T}{v}\right]R = \\ &\left\{-\frac{[F_x(\hat{\lambda}, F_z) - F_x(\lambda, F_z)]}{\hat{v}} R^2\right\} - \frac{\tilde{v}}{\hat{v}} \frac{J_w}{R} \dot{\lambda}\end{aligned} \tag{16}$$

From Equation (16), the item $[F_x(\hat{\lambda}, F_z) - F_x(\lambda, F_z)]$ could be represented by $\phi_x(\tilde{\lambda}, \hat{\lambda}, F_z)$ which is a nonlinear function with respect of $\tilde{\lambda}$ and $\hat{\lambda}$. The second item can be regarded as a disturbance with high frequency and can be ignored.

Therefore we obtain

$$J_w \dot{\tilde{\lambda}} = -\frac{\varphi_x(\tilde{\lambda}, \hat{\lambda}, F_z)}{\hat{v}} \cdot R \tag{17}$$

The nonlinear function $\phi_x(\tilde{\lambda}, \hat{\lambda}, F_z)$ is monotonic increasing with respect of $\tilde{\lambda}$ in the linear region of the tire model and $\varphi_x(0, \hat{\lambda}, F_z) = 0$ which means when $\tilde{\lambda}$ is approach to zero, $\varphi_x(0, \hat{\lambda}, F_z)$ approach to zero too.

Therefore from Equation (14), when $\tilde{v}$ is large the $\dot{\tilde{v}}$ is negative. In addition, the estimation error $\tilde{v}$ is bounded by Equation (18) as long as we choose the appropriate coefficient k and saturation value of the saturation function.

$$|\tilde{v}| < \frac{|\tilde{a}|}{k / R} \tag{18}$$

Based on the above, the estimation error is convergent to a certain value with the assumption that the slip ratio is in the monotonic increasing region of the tire model. When the slip ratio is large in some situation, the estimator may not work well. But we could use a slip ratio controller to maintain the slip ratio in the linear region. With the help of the slip ratio controller, on the one hand we could estimate the longitudinal velocity, on the other hand, we could make full use of the maximum tire force.

3 ROAD MAXIMUM FRICTION COEFFICIENT ADAPTION

With the real time and accurate information of motor torque and rotation speed of the four-in-wheel-motor-drive electric vehicles, based on the Burckhardt tire model, we developed the road friction coefficient estimation method. The estimator is shown from Equation (19) to Equation (21).

$$\dot{y} = -K_\phi \left(\frac{1}{J_\omega} T + \hat{\phi}\right) + \frac{1}{J_\omega} \frac{\partial \mu(\hat{\theta}, \omega)}{\partial \theta} F_z R \mu_\theta(\omega, \hat{\phi}, \hat{\theta}) \tag{19}$$

$$\hat{\phi} = y + K_\phi \omega - \frac{1}{J_\omega} F_z R \mu(\hat{\theta}, \omega) \tag{20}$$

$$\dot{\hat{\theta}} = \mu_\theta\left(\omega, \hat{\phi}, \hat{\theta}\right) = \mathrm{Proj}\left[\gamma\left(\theta^*(\omega, \hat{\phi}) - \hat{\theta}\right)\right] \tag{21}$$

K_ϕ and γ are the observer gains needed to be tuned, and Proj is projection function.

4 ESTIMATION STRUCTURE

Fig. 2 depicts the closed loop estimation structure. The RMFC estimator provides the RMFC for velocity estimator to update the tire model in Equation (5) and

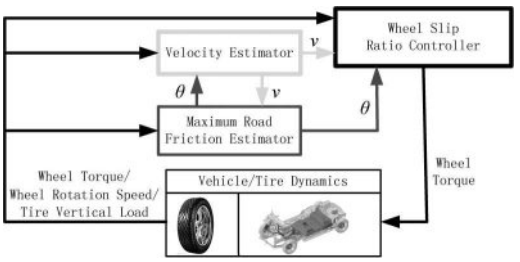


Figure 2. Estimation structure.

the velocity estimator provides the velocity for RMFC estimator to calculate μ.

As it is mentioned on the above, the velocity estimator must work under the assumption that tire works in the region where the force monotonically increasing with slip ratio. However from Fig. 1a we know that it is hard to distinguish the different friction road until the μ–λ curve getting to the peak point or even larger that is to say sufficient excitation is needed to estimate the RMFC which is contradicts to the assumption of the velocity estimator to some degree. In this sense, we expect the slip ratio is near the peak value to guarantee the effect of both the velocity estimator and the RMFC estimator. Therefore the wheel slip ratio controller working together with the estimators is included here to restrict the slip ratio near the peak value (optimal slip ratio) of μ–λ curve.

5 EXPERIMENTAL RESULTS

5.1 *Test vehicle*

The test vehicle is setup from a SAIC Roewe E50 as shown in Figure 3 driven by four motors among which two hub motors are mounted to the rear axle and two motors and gear boxes are mounted to the front axle. The main parameters of the vehicle and powertrain are shown in table 1&2. Figure 4 shows the test system configuration. A MicroAutoBox from dSPACE is used for real time controller and data acquisition. A GPS-INS RT3003 from Oxford Technical Solutions is used to measure longitudinal velocity and acceleration. The original vehicle gateway can provide the acceleration pedal signal. Motor torque and rotational speed are from motor controller. Based on this measurement system, the maximum road friction estimation method is proposed. The acceleration signal is used to calculate the tire vertical load. The longitudinal velocity and the motor rotational speed are used to calculate the slip ratio of the tire.

The tests were conducted in Maxxis tire proving ground. The tire proving ground contains low road maximum friction coefficient road, high-low road maximum friction coefficient joint road and high-low road maximum friction coefficient split road. We take the front left tire to analyze in the low θ road and θ joint road and take the two tires of the front axle to analyze for θ-split road condition.

5.2 *Test results on low friction road*

The vehicle accelerates with full throttle on the slippery wet tile road where the RMFC is 0.3.

5.3 *Test results on joint road*

The vehicle accelerates with full throttle on high-low RMFC joint road. The RMFC before t = 2.2 s is about 0.65. Then vehicle goes into the slippery road where the RMFC is 0.25.

Table 1. Parameters of the test vehicle.

Parameter	Value	Parameter	Value
Mass (kg)	1358	Yaw moment of inertia (kg·m^2)	1835
Wheel base (m)	2.305	Wheel track (mm)	1325 (Front)/ 1390 (Rear)
Distance between COG and front axle (m)	1.117	Distance between COG and front axle (m)	1.188
Height of COG (m)	0.525	Tire rolling radius (m)	0.29
Steering ratio	16.68	Front/Rear axle load	54/46

Table 2. Motor parameters of test vehicle.

Parameter	Front axle motor	Rear axle motor
Rated power (kW)	15	5
Peak power (kW)	25	7.5
Rated torque (Nm)	35.8	100
Peak torque (Nm)	90	150
Rated speed (rpm)	4000	480
Maximum speed (rpm)	9500	1350
Gear ratio	6.2	1



Figure 3. Test vehicle.

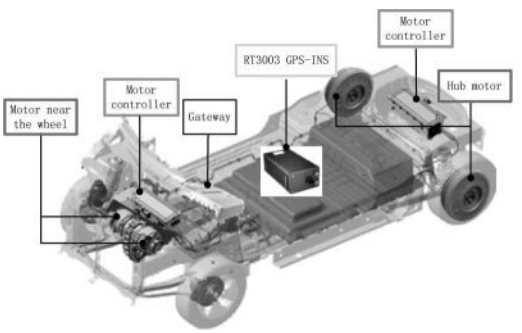


Figure 4. Sensor configuration of test vehicle.

5.4 *Test results on split road*

The vehicle accelerates with full throttle on high-low RMFC joint and split road. The RMFC before t = 2.3 s is about 0.65. After t = 2.3 s, the RMFC of left side is 0.45 higher than right side where the RMFC is 0.25.

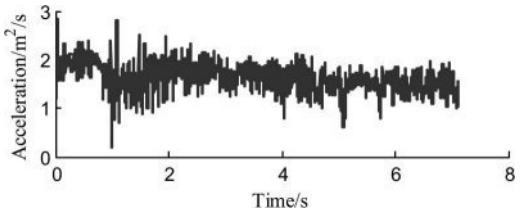


Figure 5. Acceleration on low friction road.

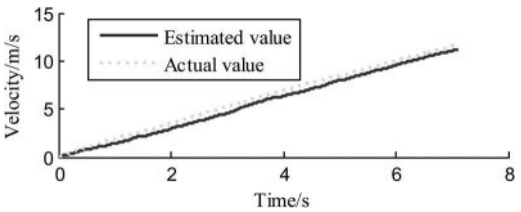


Figure 6. Velocity estimation result on low friction road.

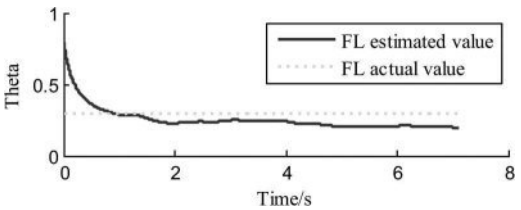


Figure 7. Road maximum friction estimation result on low friction road.

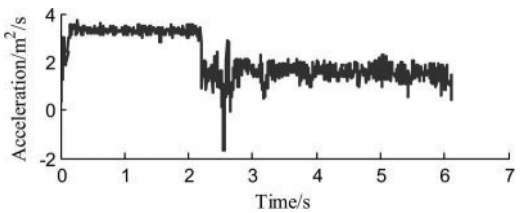


Figure 8. Acceleration on joint road.

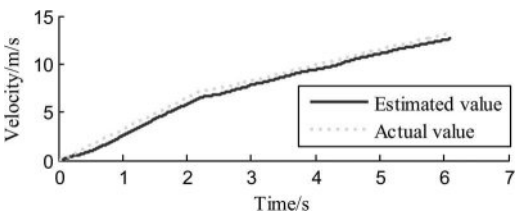


Figure 9. Velocity estimation result on joint road.

5.5 *Discussion*

Figure 5, 8 and 11 show the acceleration information of the three test experiments respectively. Figure 6, 9 and 12 show the velocity estimation results. Figure 7, 10 and 13 show the RMFC estimation results. From Figure 6 and 7, we know that on the low friction road, both the velocity and RMFC estimator work well. RMFC estimation result converges to a certain value a little small than the nominal RMFC and updates the tire model used in the velocity estimator. From Figure 9 we find that when the vehicle gets into the low friction

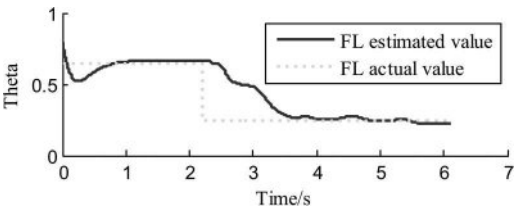


Figure 10. Road maximum friction estimation result on joint road.

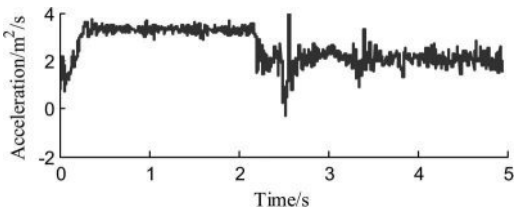


Figure 11. Acceleration on split road.

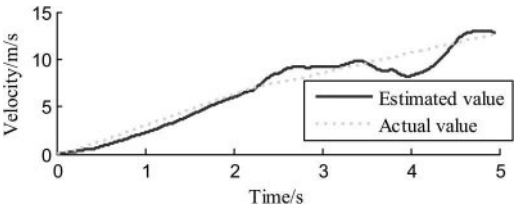


Figure 12. Velocity estimation result on split road.

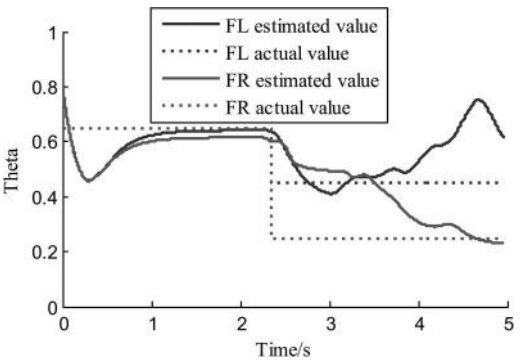


Figure 13. Road maximum friction estimation result on split road.

road at t = 2.2 s, the velocity estimation error becomes a little larger since the estimation of RMFC converges to the actual value slowly. During t = 2.2 s–t = 2.5 s, the tire model is not accurate in the velocity estimator. After t = 3.5 s, the velocity estimation error becomes small apparently. From Figure 12 we can draw the same conclusion that, when the estimation result of RMFC is not accurate, the estimation error of velocity become large at t = 2.7 s and t = 4 s. However when the RMFC estimation result converges the velocity estimation error converges too suddenly. On the split road, the estimation result fluctuates in an acceptable range but doesn't diverge. Because the RMFC is different on different side, the longitudinal tire force is also different. The different tire force will generate yaw moment causing the vehicle to yaw. In the meantime there will be lateral force on the tire. However the modified Burckhardt tire model only focuses on the longitudinal characteristic. When there exists lateral force, the tire model cannot describe the tire longitudinal characteristic accurately. That is why the estimation fluctuates. In addition, it will be our future work to research velocity estimation and the RMFC estimation under longitudinal and lateral force coupling condition.

6 CONCLUSION

In this paper, based on the Burckhardt tire model, we focused on the straight acceleration situation and have developed a nonlinear real-time observer for estimation of longitudinal velocity with road maximum friction coefficient for four-wheel-independent-drive EVs. With the slip ratio controller working together, the effectiveness of the algorithm and adaptive law was validated through experiments in various working condition. On the one hand, when the estimation result of RMFC is accurate, the velocity estimator could provide good estimate result. On the other hand, when the estimation result of RMFC fluctuates on the split road, the velocity estimation error would not diverge.

ACKNOWLEDGEMENT

This research is supported by 'National key research and development plan of China' (Grant No. 2016YFB0100901). 'National Science and Technology Support Program of China' (Grant No. 2015BAG17B01), and 'National Natural Science Foundation of China' (Grant No. U1564207).

REFERENCES

Burckhardt M. (1993). Vehicle chassis technology-wheel sub system. Wurtzburg: Vogel-Verlag.

Geng, Cong, T. Uchida, and Y. Hori. (2007). Body Slip Angle Estimation and Control for Electric Vehicle with In-Wheel Motors. 33rd Annual Conference of the IEEE, Taipei.

Jin C, Xiong L, and Yu Z, et al. (2014). Path Following Control for Skid Steering Vehicles with Vehicle Speed Adaption, *SAE Paper* No. 2014-01-0277.

Kobayashi, K Cheok, KC and Watanabe K. (1995). Estimation of Absolute Vehicle Speed using Fuzzy Logic Rule-Based Kalman filter, Proceeding of American Control Conference, Seattle.

Ling-Yuan Hsu, Tsung-lin Chen. (2009). Vehicle Full-State Estimation and Prediction System Using State Observers. IEEE Transactions on Vehicular Technology. 58, 6, 2651–2662.

Sun F, Huang X, and Rudolph J, et al. (2015). Vehicle state estimation for anti-lock control with nonlinear observer, Control Engineering Practice. 43. 69–84.

Vietinghoff A V, Olbrich S, and Kiencke U. (2007). Extended Kalman filter for vehicle dynamics determination based on a nonlinear model combining longitudinal and lateral dynamics, SAE Paper No.2007-01-0834, 2007.

Yunlong Gao, Yuan Feng and Lu Xiong. (2013). Vehicle Longitudinal Velocity Estimation with Adaptive Kalman Filter, Proceedings of the FISITA 2012 World Automotive Congress, Beijing.

Advanced Vehicle Control – Edelmann, Plöchl & Pfeffer (Eds)
© 2017 Taylor & Francis Group, London, ISBN 978-1-138-02992-7

Unscented Kalman filter for combined longitudinal and lateral vehicle dynamics

M. Wielitzka, S. Eicke, A. Busch, M. Dagen & T. Ortmaier
Institute for Mechatronic Systems, Leibniz Universität Hannover, Hanover, Germany

ABSTRACT: Numerous advanced driver assistance systems rely on parametric models describing the vehicle's behavior and stability. Accurate knowledge about the vehicle's dynamics in terms of specific states has the potential to improve these systems' performance drastically. Since several crucial states, e.g. side slip angle, can not be measured directly, estimation methodologies were developed. In this paper a highly nonlinear model of the vehicle's longitudinal and lateral dynamics, containing 13 states and 8 measurements is used within an unscented Kalman Filter. The estimation results are compared to high precision measurements taken using a Genesys ADMA inertial measurement unit on a Volkswagen Golf GTE Plug-In Hybrid during three different maneuvers.

1 INTRODUCTION

Modern vehicles have become highly complex mechatronic systems within the past few decades. In this regard advanced driver assistance systems (ADAS) achieved enormous improvements concerning safety and comfort, starting with the implementation of the anti-lock braking system (ABS) in the in the 1960s and 70s, leading to the electronic stability program (ESP) in 1995 and further achievements in the past years, e.g. active cruise control (ACC), collision avoidance systems and lane change assistance (Reif 2010). Especially by taking advantage of the proceeding electrification of powertrains, a leap in evolution within assistance systems development can be realized. Following this progress the future goal of autonomous driving can be accomplished within the next years (Winner 2015).

Many of the established systems and future developments rely or will rely on parametric models describing the vehicle's behavior and stability. Therefore, exceeding interest is focused on the development of precise modeling, and thus, detailed knowledge about the vehicle's dynamics (Wielitzka, Dagen, & Ortmaier 2014a, Li, Wang, & Zhou 2006). Furthermore, advanced estimation techniques are utilized to estimate the vehicle's dynamics using a parametric model, e.g a planar two-track model (Figure 1), and additional serial sensor measurements, e.g. using the extended (Dakhlallah, Glaser, Mammar, & Sebsadji 2008, Gadola, Chindamo, Romano, & Padula 2014) or unscented Kalman Filter (Doumiati, Victorino, Charara, & Lechner 2009, Wielitzka, Dagen, & Ortmaier 2014b).

In this paper a methodology for state estimation of the vehicle's longitudinal and lateral dynamics is presented, utilizing an unscented Kalman Filter (UKF). The results are compared considering real measurements on a Volkswagen Golf GTE Plug-In Hybrid.

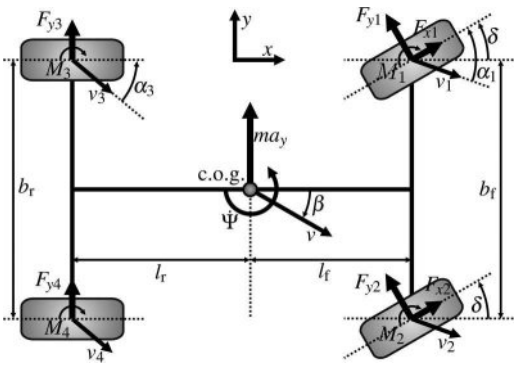
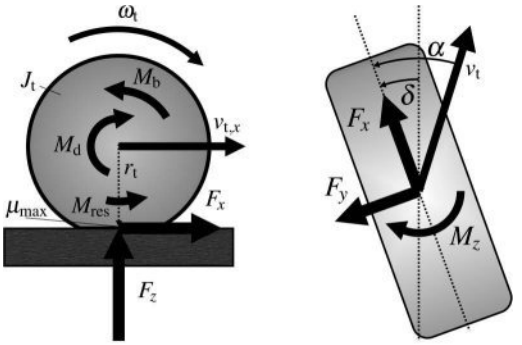


Figure 1. Schematic visualization of the used vehicle dynamics model.

The paper is organized as follows: In section 2 a detailed model of the vehicle's dynamics considering longitudinal and lateral dynamics is presented. In section 3 the UKF for state estimation is introduced. Section 4 and 5 describe the reference measurement setup and present the results of the introduced methodologies, respectively. Finally, a conclusion is given in section 6.

2 VEHICLE DYNAMICS MODELING

In this section a combined model for the vehicle's longitudinal and lateral dynamics is presented. Considering the contact patch between tires and road



(a) lateral view (b) top view

Figure 2. Torques and forces acting on a tire.

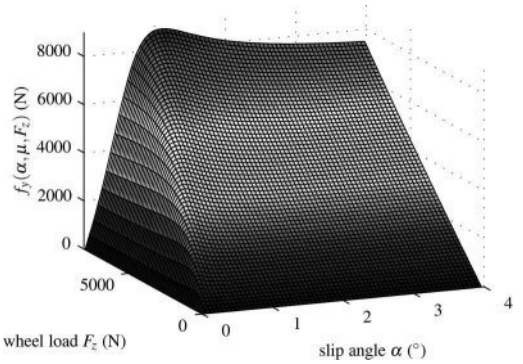


Figure 3. Visualization of the magic formula tire model for lateral forces, depending on sideslip angle α and wheel loads F_z.

as leading influence for the vehicle's dynamics, sub models for the tires and the vehicle body are introduced, separately. Since this model will be implemented in an online estimator, a trade-off between accuracy and computational effort has to be found.

2.1 *Tire model*

First, the vehicle's tires are considered, representing the contact patch between vehicle and road, consequently providing forces substantially influencing the vehicle's dynamics. Regarding this patch as a single point, forces in longitudinal and lateral direction of the tire can arise. These forces result from differences in relative motion between tire and road, leading to tire longitudinal slip

$$\lambda = \frac{|\omega_t r_t - v_{t,x}|}{\max(\omega_t r_t, v_{t,x})} \tag{1}$$

and tire sideslip angle

$$\alpha = \delta - \arctan\left(\frac{v_{t,y}}{v_{t,x}}\right) \tag{2}$$

for longitudinal and lateral motion, respectively (Figure 2). Thus, ω_t represents the rotational velocity, δ the steering angle, $v_{t,x,y}$ the components of the wheel's velocity v_t, and r_t the effective tire radius, which is assumed to be constant. The associated stationary tire forces F_x^s and F_y^s are functions of the longitudinal slip and sideslip angle, respectively:

$$F_x^s = f_x(\lambda, \mu, F_z)\; h(F_y), \tag{3}$$

$$F_y^s = f_y(\alpha, \mu, F_z)\; h(F_x), \tag{4}$$

where μ represents the friction coefficient between tire and road and F_z the wheel load. The nonlinear functions $f_{x,y}$ represent the (side)slip dependency of the tire forces by the magic formula tire model (Pacejka & Bakker 1992) as

$$f_{x,y}(x, \mu, F_z) = D \sin\left(C \arctan\left(Bx - E\left(Bx - \arctan\left(Bx\right)\right)\right)\right), \tag{5}$$

with x representing λ or α for longitudinal or lateral forces, respectively and constants $D = \mu F_z$, $B = C_F/(CD)$ and $C_F = c_1 \sin(2 \arctan(F_z/c_2))$, representing the influence of changing friction coefficient and wheel loads (Figure 3). The function $h(F_{x,y}) = \cos(\arctan(B_{xy} F_{y,x}))$ accounts for reduced forces in presence of both, lateral and longitudinal forces, with scaling factor B_{xy}. Furthermore, the lateral forces F_y are modeled as PT_1-element:

$$F_y + \frac{l_t}{v_t}\dot{F}_y = f_y(\alpha, \mu, F_z)\; h(F_x), \tag{6}$$

with tire-delay constant l_t (Rajamani 2012). Due to different dynamics in longitudinal direction this can be neglected for F_x, leading to $F_x^s = F_x$.

The inputs to the system are the drive and break torques M_d and M_b, and the steering angle δ. This leads to the equation of motion for the rotational velocity of one tire

$$J_t \dot{\omega}_t = M_d - M_b - F_x r_t - M_{res}, \tag{7}$$

with the tire's moment of inertia J_t and rolling resistance M_{res} (Figure 2).

2.2 *Vehicle body dynamics*

Considering a two-track model including roll dynamics as displayed in Figure 1 and 4 the vehicle's dynamics under disregard of vertical dynamics can be described by the vehicle's yaw-rate $\dot{\Psi}$, its sideslip angle β, the roll angle κ, and its center of gravity (c.o.g.) velocity v_{cog}. These quantities represent the angular velocity of rotation around the vertical axis, the angle

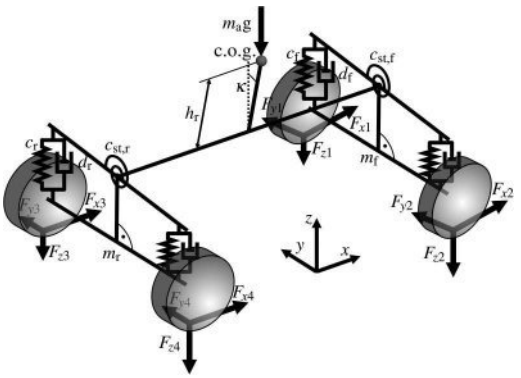


Figure 4. Schematic visualization of the used two-track model including roll dynamics.

between the vehicle's longitudinal axis and its velocity vector, the angle between the vehicle's vertical axis and the stationary vertical axis, and the velocity of the center of gravity, respectively. This leads to the following, slightly simplified equations of motion:

$$J_z \ddot{\Psi} = \tag{8}$$

$$l_\mathrm{f}\left(F_{y1}+F_{y2}\right)\cos\left(\delta\right) - l_\mathrm{r}\left(F_{y3}+F_{y4}\right) - \sum_{i=1}^{4} M_{z,i},$$

$$m v_\mathrm{cog}\left(\dot{\beta}+\dot{\Psi}\right) = \tag{9}$$

$$\left(F_{y1}+F_{y2}\right)\cos\left(\beta-\delta\right) + \left(F_{y3}+F_{y4}\right)\cos\beta,$$

$$m\dot{v}_\mathrm{cog} = \tag{10}$$

$$\left(F_{x1}+F_{x2}\right)\cos(\beta-\delta) + \left(F_{x3}+F_{x4}\right)\cos\beta - F_\mathrm{air},$$

$$m_\mathrm{a} h_\mathrm{r} a_y = J_\kappa \ddot{\kappa} + d_\kappa \dot{\kappa} + c_\kappa \kappa - m_\mathrm{a} g h_\mathrm{r} \sin\kappa, \tag{11}$$

with $l_{\mathrm{f,r}}$ being the distance between front and rear axis to the c.o.g., respectively, mass m, moment of inertia with respect to the vertical axis J_z, velocity and acceleration of the c.o.g. v_cog, $\dot{v}_\mathrm{cog}$, forces due to air resistance F_air, and self-aligning torques $M_{z,i}$. Roll dynamics are represented in analogy to a spring-damper system with gravitational influence with chassis mass m_a, distance between roll axis and c.o.g. h_r, moment of inertia with respect to the roll axis $J_\kappa = J_x + m_\mathrm{a} h_\mathrm{r}^2$, gravitational acceleration g, and nonlinear spring and damper coefficients c_κ and d_κ, respectively, representing progressive and declining characteristics. These constants result from combining suspension constants $c_{\mathrm{f,r}}$, $d_{\mathrm{f,r}}$ and stabilization constant $c_{\mathrm{st,f,r}}$ (Figure 4).

Using the introduced state representations the tire side slip angles α_i and wheel loads $F_{z,i}$ used in (2), (3) and (4) can be expressed as

$$\alpha_{1,2} = \delta - \arctan\left(\frac{l_\mathrm{f}\dot{\Psi} + v\sin\beta + h_\mathrm{r}\dot{\kappa}}{v\cos\beta \pm \frac{b_\mathrm{f}}{2}\dot{\Psi}}\right) \tag{12}$$

and

$$F_{z,1,2} = m\left(\frac{l_\mathrm{r} g - h a_x}{l}\right)\left(\frac{1}{2} \mp \frac{h a_y}{b_\mathrm{f} g}\right) \pm \frac{J_\kappa}{b_\mathrm{f}}\ddot{\kappa} \tag{13}$$

for the front axis, with $l = l_\mathrm{f} + l_\mathrm{r}$ and assuming $h = h_\mathrm{r} + r_\mathrm{rad}$ (Dai 1996). All parameters utilized within the model either have to be measured, e.g. geometrical parameters, or identified using an offline identification algorithm to adapt it to a certain vehicle. Since the model is strongly nonlinear a combination of particle swarm optimization (PSO) and sequential quadratic programming (SQP) was implemented (Wielitzka, Dagen, & Ortmaier 2014a).

2.3 *Measurement model*

For later implementation of the vehicle model into an UKF a measurement model will be introduced. Modern vehicles are equipped with standard sensors measuring the vehicle's yaw rate $\dot{\Psi}$, longitudinal and lateral acceleration, a_x and a_y, and all four tire's rotational velocities ω_i. Furthermore, for single-axle driven vehicles, a pseudo measurement of the vehicle's velocity of the c.o.g. considering tire velocities at the undriven axis can be utilized. Thus, only the accelerations and the pseudo measurement of the vehicle's velocity are measurements which are no states and can be represented by

$$a_x = \dot{v}_\mathrm{cog}\cos\beta - v_\mathrm{cog}\left(\dot{\Psi}+\beta\right)\sin\beta + l_{\ddot{\Psi},x}\ddot{\Psi}, \tag{14}$$

$$a_y = \dot{v}_\mathrm{cog}\sin\beta + v_\mathrm{cog}\left(\dot{\Psi}+\beta\right)\cos\beta + l_{\ddot{\Psi},y}\ddot{\Psi} + l_{\ddot{\kappa}}\ddot{\kappa}, \tag{15}$$

$$v_\mathrm{cog} = \frac{\omega_3+\omega_4}{2} r_\mathrm{t}. \tag{16}$$

The additive correction terms proportional to $\ddot{\Psi}$ and $\ddot{\kappa}$ in (14) and (15) consider sensor positions distant of the c.o.g. with lever arms $l_{\ddot{\Psi},x,y}$ and $l_{\ddot{\kappa}}$, respectively.

3 UNSCENTED KALMAN FILTER

Kalman Filtering is an approach for estimating (hidden) states in dynamic systems by using an underlying parametric model of the system and (noisy) measurements. The Kalman Filter realizes optimal estimation in the sense of minimizing the error covariance. In the following the methodologies for the UKF are introduced.

3.1 *The unscented Kalman filter*

Considering a system modeled by the discretized state and measurement equations

$$\boldsymbol{x}_k = \boldsymbol{F}\left(\boldsymbol{x}_{k-1}, \boldsymbol{u}_{k-1}\right) + \boldsymbol{v}_{k-1}, \tag{17}$$

$$\boldsymbol{y}_k = \boldsymbol{H}\left(\boldsymbol{x}_k, \boldsymbol{u}_k\right) + \boldsymbol{w}_k, \tag{18}$$

with system state $\boldsymbol{x}_k \in \mathbb{R}^{n_x}$ at discrete time k, known input $\boldsymbol{u}_k \in \mathbb{R}^{n_u}$, and measurement $\boldsymbol{y}_k \in \mathbb{R}^{n_y}$, with state, input, and measurement dimensions n_x, n_u, and n_y, respectively. The gaussian random variables $\boldsymbol{v}_{k-1} \in \mathbb{R}^{n_x}$ and $\boldsymbol{w}_k \in \mathbb{R}^{n_y}$ represent additive process and measurement noise, respectively. These are assumed to be independent of each other with normal probability distributions $p(\boldsymbol{v}) \propto \mathcal{N}(\boldsymbol{0}, \boldsymbol{Q})$ and $p(\boldsymbol{w}) \propto \mathcal{N}(\boldsymbol{0}, \boldsymbol{R})$, with $\boldsymbol{Q} \in \mathbb{R}^{n_x \times n_x}$ and $\boldsymbol{R} \in \mathbb{R}^{n_y \times n_y}$ being the process and measurement covariance matrices, respectively.

The Unscented Kalman Filter (Wan & Van der Merwe 2000) utilizes the scaled unscented transform (Julier 2002) to approximate a random variable of dimension n transformed through a nonlinear function. Therefore, a set of $2n+1$ carefully chosen sigma points for time step k is calculated by

$$\begin{aligned}
\boldsymbol{x}_{k,0} &= \hat{\boldsymbol{x}}_k, \\
\boldsymbol{x}_{k,i} &= \hat{\boldsymbol{x}}_k + \left(\sqrt{(n+\lambda_{\text{ukf}})\boldsymbol{P}_k}\right)_i, \quad i = 1, ..., n, \\
\boldsymbol{x}_{k,i} &= \hat{\boldsymbol{x}}_k - \left(\sqrt{(n+\lambda_{\text{ukf}})\boldsymbol{P}_k}\right)_{i-n}, \; i = n+1, ..., 2n,
\end{aligned} \tag{19}$$

with $\hat{\boldsymbol{x}}_k$ representing the state estimate at time k. Thereby holds, $\lambda_{\text{ukf}} = \alpha_{\text{ukf}}^2 n + \kappa_{\text{ukf}} - n$, with scaling parameters, α_{ukf} and κ_{ukf}. Furthermore, $(\sqrt{(n+\lambda_{\text{ukf}})\boldsymbol{P}_k})_i$ is the ith column of the matrix square root, e.g. using Cholesky decomposition. For initialization an initial state and covariance estimate $\hat{x}_0$ and P_0 have to be chosen. Thereafter, the estimation process can repeatedly be expressed in two steps, i.e. the process and the measurement update. For the process update, each sigma point undergoes the real nonlinear transformation (17). Afterwards, the transformed points are used to calculate an a-priori state and covariance estimate $\boldsymbol{x}_k^-$ and $\boldsymbol{P}_k^-$ by

$$\boldsymbol{x}_{k,i} = \boldsymbol{F}\left(\boldsymbol{x}_{k-1,i}, \boldsymbol{u}_{k-1}\right), \tag{20}$$

$$\boldsymbol{x}_k^- = \sum_{i=0}^{2n} W_i^m \boldsymbol{x}_{k,i}^-, \tag{21}$$

$$\boldsymbol{P}_k^- = \sum_{i=0}^{2n} W_i^c \left(\boldsymbol{x}_{k,i}^- - \boldsymbol{x}_k^-\right)\left(\boldsymbol{x}_{k,i}^- - \boldsymbol{x}_k^-\right)^{\mathrm{T}} + \boldsymbol{Q}, \tag{22}$$

with weighting factors $W_0^m = \frac{\lambda_{\text{ukf}}}{n+\lambda_{\text{ukf}}}$, $W_0^c = \frac{\lambda_{\text{ukf}}}{n+\lambda_{\text{ukf}}} + (1 - \alpha_{\text{ukf}} + \beta_{\text{ukf}})$ and $W_i^m = W_i^c = \frac{\lambda_{\text{ukf}}}{2(n+\lambda_{\text{ukf}})}$, using an additional scaling factor β_{ukf}.

During the second step, i.e. the measurement update, an a-priori measurement estimation $\boldsymbol{y}_k^-$ is calculated for each sigma point utilizing (18), followed by the calculation of covariances $\boldsymbol{P}_{yy_k}$ and $\boldsymbol{P}_{xy_k}$, and a Kalman gain $\boldsymbol{K}_k$. After receiving a real measurement $\boldsymbol{y}_k$ from the system a new state and covariance estimate $\hat{\boldsymbol{x}}_k$ and $\boldsymbol{P}_k$ can be calculated by

$$\boldsymbol{y}_{k,i}^- = \boldsymbol{H}\left(\boldsymbol{x}_{k,i}, \boldsymbol{u}_k\right), \tag{23}$$



(a) Golf GTE Plug-In Hybrid (b) Genesys ADMA-G-Eco+

Figure 5. Test vehicle and inertial measurement unit for high precision measurements

$$\boldsymbol{y}_k^- = \sum_{i=0}^{2n} W_i^m \boldsymbol{y}_{k,i}^-, \tag{24}$$

$$\boldsymbol{P}_{xy_k} = \sum_{i=0}^{2n} W_i^c \left(\boldsymbol{x}_{k,i}^- - \boldsymbol{x}_k^-\right)\left(\boldsymbol{y}_{k,i}^- - \boldsymbol{y}_k^-\right)^{\mathrm{T}}, \tag{25}$$

$$\boldsymbol{P}_{yy_k} = \sum_{i=0}^{2n} W_i^c \left(\boldsymbol{y}_{k,i}^- - \boldsymbol{y}_k^-\right)\left(\boldsymbol{y}_{k,i}^- - \boldsymbol{y}_k^-\right)^{\mathrm{T}} + \boldsymbol{R}, \tag{26}$$

$$\boldsymbol{K}_k = \boldsymbol{P}_{xy_k}\boldsymbol{P}_{yy_k}^{-1}, \tag{27}$$

$$\boldsymbol{x}_k = \boldsymbol{x}_k^- + \boldsymbol{K}_k\left(\boldsymbol{y}_k - \boldsymbol{y}_k^-\right), \tag{28}$$

$$\hat{\boldsymbol{P}}_k = \boldsymbol{P}_k^- - \boldsymbol{K}_k\boldsymbol{P}_{yy_k}\boldsymbol{K}_k^{\mathrm{T}}. \tag{29}$$

Thus, an iterative estimation of the vehicle's states can be realized.

4 MEASUREMENT AND ESTIMATION SETUP

In this section the reference measurements setup, including the equipment and the UKF settings are introduced.

4.1 *Measurement setup*

The introduced methodologies are verified taking high precision measurements using a Volkswagen Golf GTE Plug-In Hybrid equipped with a Genesys ADMA-G-Eco+ GPS-based inertial measurement unit (Figure 5). This sensor takes reference measurements of the states yaw rate $\dot{\Psi}$, side slip angle β, velocity of the c.o.g. v_{cog}, and roll angle and rate, κ and $\dot{\kappa}$. Furthermore, measurements of the longitudinal and lateral accelerations a_x and a_y are provided. Additional measurements of the wheel speed and reference velocity of the c.o.g. are taken from the vehicle's bus system.

4.2 *Unscented Kalman filter setup*

The UKF utilizes all 13 states introduced in section 2 to describe the vehicle's dynamics. Additionally,

the measurements are taken according to section 2.3 leading to the estimator's state and measurement

$$\boldsymbol{x} = \left(\dot{\Psi}, \beta, \kappa, \dot{\kappa}, F_{y_i}, \omega_i, v_{\text{cog}}\right)^{\mathrm{T}},$$

$$\boldsymbol{y} = \left(\dot{\Psi}, a_y, a_x, \omega_i, v_{\text{cog}}\right)^{\mathrm{T}}.$$

In the presented methodology the measurements of longitudinal and lateral accelerations are taken from the inertial measurement unit, therefore the lever arms $l_{\ddot{\Psi},y}$, $l_{\ddot{\Psi},x}$ and $l_{\ddot{\kappa}}$ are set to zero, since the measurements are projected into the vehicle's c.o.g. The process and measurement covariances $\boldsymbol{Q}$ and $\boldsymbol{R}$ are empirically found and set to

$$\boldsymbol{Q} = \operatorname{diag}\Big(10^{-5},\ 10^{-9},\ 10^{-8},\ 10^{-8},\ 10^{2},\ 10^{2}$$
$$10^{2},\ 10^{2}, 10^{-1},\ 10^{-1},\ 10^{-1},\ 10^{-1},\ 10^{-8}\Big),$$

$$\boldsymbol{R} = \operatorname{diag}\Big(10^{-4},\ 10^{-1},\ 10^{-1},\ 1,\ 1,\ 1,\ 1,\ 10^{-1}\Big).$$

The UKF's parameters are set to $\alpha_{\text{ukf}} = 1$, $\beta_{\text{ukf}} = 2$ and $\kappa_{\text{ukf}} = 20$.

5 RESULTS

In this section the results of the introduced state estimation is presented. Therefore, three different maneuvers are considered, i.e. a steering sweep, a double lane change and an arbitrary maneuver including longitudinal and lateral excitation. Each maneuver is displayed by eight plots, i.e. yaw rate and side slip angle at the top, representing lateral dynamics, roll angle and rate in the second line, representing roll dynamics, velocity and wheel speeds in the third line, representing longitudinal dynamics and the accelerations in longitudinal and lateral direction at the bottom. The UKF estimations are displayed in blue, while the reference measurements are colored red. Furthermore, for velocity estimation the reference velocity is displayed in green.

In Figure 6 a steering sweep maneuver with periodical steering angle input at nearly constant amplitude and increasing frequency and constant velocity of 8.5 m/s^2 (30 km/h) is displayed. An accurate estimation of all states can be seen during the whole maneuver, especially improved performance of velocity estimation comparing to the reference measurement can be emphasized. In Figure 7 a double lane change maneuver with lateral accelerations up to 10 m/s^2 and velocity of about 16 m/s (58 km/h) is presented. Despite the high lateral acceleration an accurate estimation of sideslip angle can still be realized, again accompanied by improved estimation of the vehicles velocity. Figure 8 demonstrates an arbitrary maneuver over 40 s with velocities from 2 m/s (7 km/h) to 16 m/s (58 km/h) including passages of longitudinal, lateral and combined excitation. Repeatedly, an accurate and robust estimation of all states is noticeable, even during combined excitation.

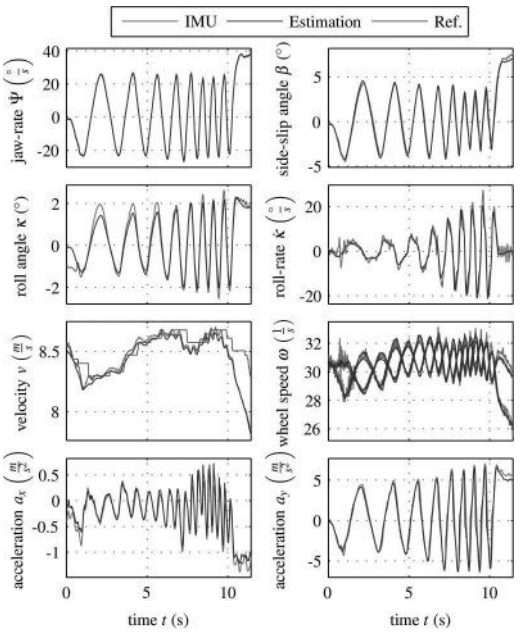


Figure 6. Steering sweep maneuver with lateral accelerations above 6 m/s^2.

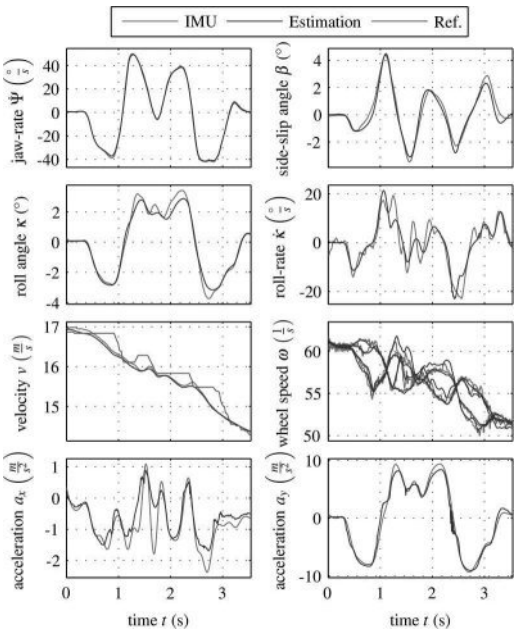


Figure 7. Double lane change maneuver with lateral accelerations of almost 10 m/s^2.

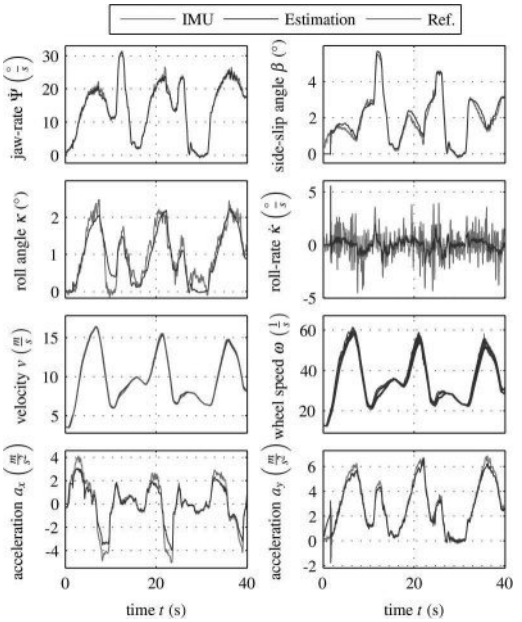


Figure 8. Arbitrary maneuver with longitudinal and lateral acceleration of 4 m/s^2 and 6.5 m/s^2, respectively.

Concluding, a precise and robust estimation of the vehicle's longitudinal and lateral dynamics, represented by specific states can be realized. An improved estimation of the vehicle's velocity, compared to the reference estimation can be emphasized.

6 CONCLUSION AND OUTLOOK

In this paper a highly nonlinear model of the vehicle's longitudinal and lateral dynamics was introduced. Based on this, an unscented Kalman Filter was set up for state estimation considering 13 states and 8 measurements, containing one pseudo measurement. Comparing with high precision measurements taken on a Volkswagen Golf GTE Plug-In Hybrid using a Genesys ADMA inertial measurement unit, accurate and robust performance of the introduced methodology is shown. Especially, the accurate estimation of the sideslip angle and velocity can be emphasized.

In future research activities online estimation of changing parameters can be realized using the presented model and state estimation methodology. Therefore, for example robust online estimation of the friction coefficient between tires and road could be accomplished.

ACKNOWLEDGMENT

The authors would like to thank the "Bundesministerium für Wirtschaft und Energie (BMWi)", Germany, for founding this project.

REFERENCES

Dai, A. (1996). *Beobachtung fahrdynamischer Zustnde und Verbesserung einer ABS- und Fahrdynamikregelung.* Fortschrittberichte VDI. Dsseldorf: VDI Verlag.

Dakhlallah, J., S. Glaser, S. Mammar, & Y. Sebsadji (2008, June). Tire-road forces estimation using extended Kalman filter and sideslip angle evaluation. In *American Control Conference, 2008,* pp. 4597–4602.

Doumiati, M., A. Victorino, A. Charara, & D. Lechner (2009, June). Unscented Kalman filter for real-time vehicle lateral tire forces and sideslip angle estimation. In *2009 IEEE Intelligent Vehicles Symposium,* pp. 901–906.

Gadola, M., D. Chindamo, M. Romano, & F. Padula (2014, January). Development and validation of a Kalman filter-based model for vehicle slip angle estimation. *Vehicle System Dynamics 52*(1), 68–84.

Julier, S. (2002). The scaled unscented transformation. In *American Control Conference, 2002. Proceedings of the 2002,* Volume 6, pp. 4555–4559 vol. 6.

Li, L., F.-Y. Wang, & Q. Zhou (2006, March). Integrated longitudinal and lateral tire/road friction modeling and monitoring for vehicle motion control. *IEEE Transactions on Intelligent Transportation Systems 7*(1), 1–19.

Pacejka, H. B. & E. Bakker (1992). The Magic Formula Tyre Model. *Vehicle System Dynamics 21*(sup001), 1–18.

Rajamani, R. (2012). *Vehicle Dynamics and Control,* Volume 2. New York, USA: Springer.

Reif, K. (2010). *Fahrstabilisierungssysteme und Fahrerassistenzsysteme.* Springer Vieweg.

Wan, E. & R. Van der Merwe (2000). The unscented Kalman filter for nonlinear estimation. In *Adaptive Systems for Signal Processing, Communications, and Control Symposium 2000. AS-SPCC. The IEEE 2000,* pp. 153–158.

Wielitzka, M., M. Dagen, & T. Ortmaier (2014a, September). Nonlinear Modeling and Parameter Identification of Vehicle's Lateral Dynamics. In *12th International Symposium on Advanced Vehicle Control.*

Wielitzka, M., M. Dagen, & T. Ortmaier (2014b, December). State estimation of vehicle's lateral dynamics using unscented Kalman filter. In *2014 IEEE 53rd Annual Conference on Decision and Control (CDC),* pp. 5015–5020.

Winner, H. (2015). *Autonomes Fahren.* Springer Vieweg.

Advanced Vehicle Control – Edelmann, Plöchl & Pfeffer (Eds)
© 2017 Taylor & Francis Group, London, ISBN 978-1-138-02992-7

Vehicle state estimation from a sports-car application point of view focusing on handling dynamics

Martin Haudum, Johannes Edelmann & Manfred Plöchl
Institute of Mechanics and Mechatronics, TU Wien, Austria

Manuel Höll
Dr. Ing. H.C. F. Porsche AG, Germany

ABSTRACT: Consistent vehicle states and parameters will become a requirement for the effective application of integrated vehicle dynamics control and automatic driving. Besides a basic model-based state estimation algorithm, additional modules, e.g. for the estimation of road grade and slope, and maximal longitudinal and lateral friction coefficients may decide on the quality of estimation when focusing on handling dynamics. Both enhanced complexity and inflexibility of a global vehicle state estimator and, alternatively, interdepended individual estimation modules face major drawbacks. This paper addresses a module based estimation approach to guarantee design flexibility, which has been tested with standard vehicle sensors at ordinary and extreme driving manoeuvres and road conditions to discuss benefits and drawbacks of the proposed modular vehicle state estimation approach.

1 INTRODUCTION

Vehicle state estimation has been given continuous interest and a large bulk of scientific papers has been published, e.g. (Wenzel et al. 2006, Antonov et al. 2011, Doumiati et al. 2013), in particular focusing on vehicle handling behaviour which is considered here only as well. A consistent set of vehicle states and parameters may in particular become important when benefits from integrated vehicle dynamics control methods shall be utilized, for either enhanced vehicle performance or active safety. An appropriate knowledge of the actual vehicle states, required to allow controllers for optimal performance and to decide about the best choice of controlled actuation devices, in combination with the estimation of varying parameters of the vehicle, vehicle–road contact and environmental conditions makes the estimation problem a comprehensive challenge. An overview of addressed estimation modules is given in Fig. 1. A focus will be set on "lateral dynamics", in particular on the estimation of the lateral velocities of the tyres, resp. of the centre of gravity of the vehicle. As this representative state variable (which is not sensed at production cars) is not only influenced by the driver's commands, but also derives from lateral road grade and depends on the available friction potential between tyres and road, also the modules "road grade" and "max. friction coefficients" will be addressed. Measurements have been performed with a 4WD sports-car, which is typically able to be vigorously operated at large vehicle accelerations and a large handling envelope can be utilized.

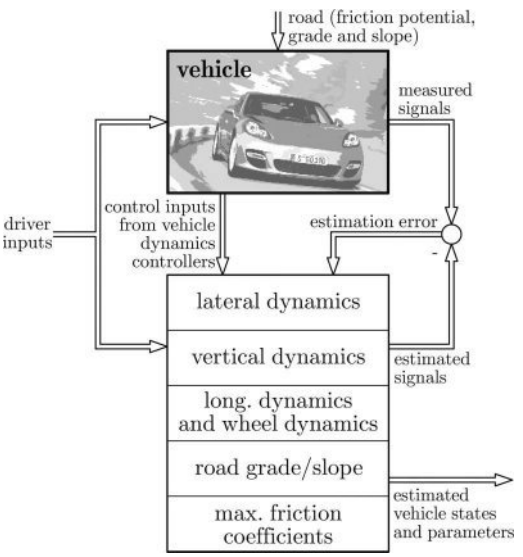


Figure 1. Overview of modular vehicle state/parameter observer.

The quality of estimated vehicle states is assessed w.r.t. the requirement of consistent levels of modelling complexity and demanded effectiveness of mentioned modules in their compound from a sports-car perspective, restricted by available sensors and signal quality, and limiting real-time and precision specifications.

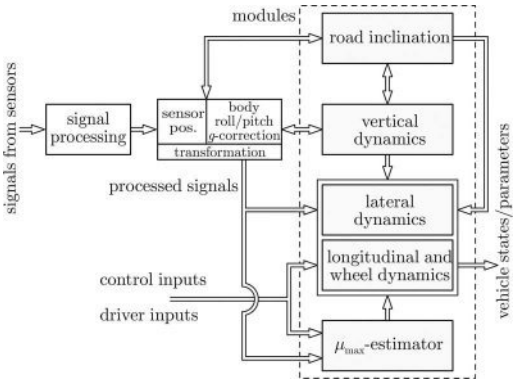


Figure 2. Signal flow corr. to Fig. 1.

The signal flow of the modular vehicle state/parameter observer is presented in Fig. 2 in more detail. Measured signals from CAN, such as steering angle, longitudinal and lateral acceleration, yaw rate, wheel speeds and engine torque, are pre-filtered, scaled, offset-aligned before they are transformed accounting for the sensor positions and portions of the gravitational acceleration g in the measured acceleration signals to finally become inputs to the various observer modules. Using basic CAN-signals only, mapping horizontal vehicle motion, does not allow to uniquely distinct effects from driver steering input, lateral road grade and lateral max. friction coefficient on vehicle side slip angle. For some kind of relief of this conflict, "mathematical" sensors are added to provide the steering rack force and inclination of the vehicle with respect to the inclined road using additional sensor inputs from the EPS and semi-active damping system. However, no roll rate sensor is available. For a stand-alone application of some modules, feedback loops shall be avoided, although only limited feasible.

2 VEHICLE AND TYRE MODEL

The vehicle and tyre model are kept as easy applicable (considering ECU restrictions, parametrization) and effective as possible, however, to account for an integrative vehicle dynamics controller environment, such as semi-active damping, rear wheel steering and active roll stabilization, respective input signals to the state observer need to be considered. Consequently, a 4-wheel vehicle model with respective force or steering angle actuation capabilities at the wheel centres and nonlinear tyre characteristics has been applied to be able to map longitudinal, lateral and vertical vehicle states for manoeuvres with large (combined) accelerations. The road surface may be inclined in longitudinal direction, road slope angle θ_R, and lateral direction, road bank/grade angle φ_R. Fig. 3 denotes main lateral vehicle states and parameters.

As a sports-car stands-out for its enlarged linear handling behaviour, Fig. 4, simplified models, such as the basic linear 2-wheel vehicle model and

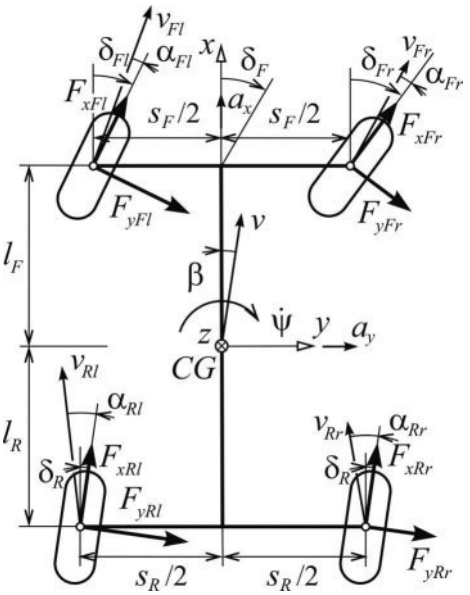


Figure 3. 4-wheel vehicle model (separate longitudinal and vertical model not depicted).

a nonlinear 2-wheel vehicle and tyre model, (1), (2), may be of interest due to its ease of application and parametrization as well. Estimation results derive from a (extended) Kalman filter, KF and EKF, respectively, see section 4. The Kalman filters build on the measured signals of the lateral acceleration and yaw rate (from CAN) in this case.

$$\dot{v}_y = \frac{1}{m}\left(F_{xR}\delta_R + F_{yR} + F_{xF}\sin\delta_F + F_{yF}\cos\delta_F\right) - g\cos\theta_R\sin\varphi_R - \dot{\psi}v_x \quad (1)$$

$$\ddot{\psi} = \frac{1}{I_z}\left(-l_R\left(F_{xR}\delta_R + F_{yR}\right) + l_F\left(F_{yF}\cos\delta_F + F_{xF}\sin\delta_F\right)\right) \quad (2)$$

Tyre models of different complexity have been considered/compared, in particular, a linear, exp-function based, brush and "Magic Formula" tyre model. While for the 4-wheel vehicle model combined longitudinal and lateral slip effects have been accounted for in the tyre model, the nonlinear 2-wheel vehicle model is based on lateral slip only. The following tests have been performed and simulated with a premium-class sports-car (mass about 2100 kg, wheel-base 3 m), here without 4WS. A modified brush tyre model has been applied. All three models have been individually parameterized, and do not descend from each other.

A comparison between the linear and the nonlinear vehicle model and measurements (from optical sensor and IMU) is illustrated in Fig. 5. As speed is usually moderate on an urban road, and steering angles may become quite large (here up to 400°), also side slip angles of the vehicle may reach a high level. Obviously, both vehicle models meet the measured vehicle side

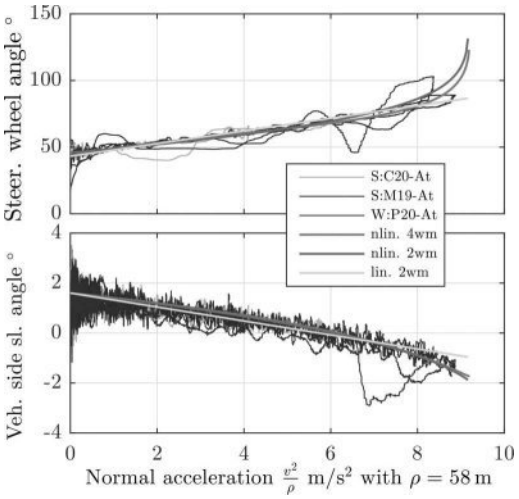


Figure 4. Handling diagram; measurements and model-based.

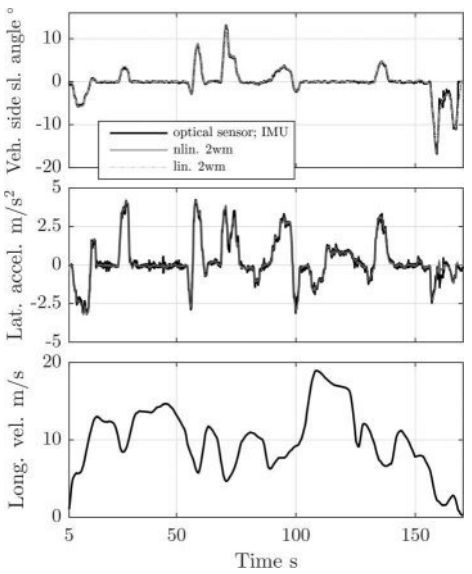


Figure 5. Urban road, model comparison.

slip angle (and lateral acceleration) very well, as lateral accelerations remain small.

Maintained step steer inputs have been carried out at about 50 km/h in Fig. 6. Lateral accelerations reach now a high level close to 10 m/s^2, and lateral tyre forces become saturated. Having the fit of the handling diagram in Fig. 4 in mind, it is no real surprise, that the linear model and the corresponding KF still meet quite well also the very high lateral accelerations. However, the match of the side slip angle of the vehicle becomes worse for increasing lateral accelerations before it completely fails. The results at (short) rather steady-state periods depend also on the fit of the steady-state handling diagram and the compromise between the fit of the lateral acceleration and vehicle

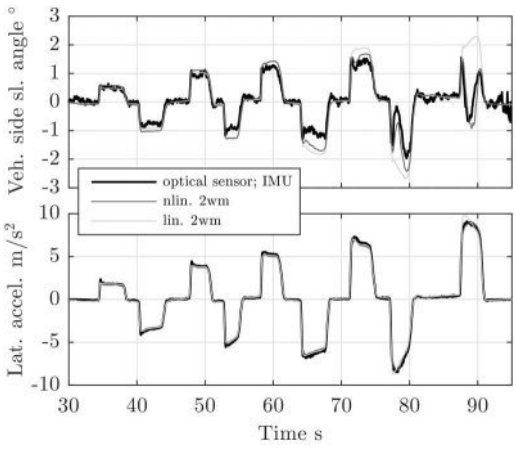


Figure 6. Maintained step steer manoeuvres, model comparison.

side slip angle. Here, the KF remains "inactive" as a good match of measured and estimated lateral accelerations already comes from the model parametrization. The shortcomings of the tyre model cannot be compensated with the KF, and the vehicle side slip angle may not be acceptable at severe driving manoeuvres. The nonlinear 2-wheel vehicle model reveals a less good fit of the vehicle side slip angle already in the handling diagram, Fig. 4, at small accelerations. The change of the vehicle side slip angle with time just before 90 s for constant measured lateral acceleration with constant steering angle but decreasing speed (changing the sign of the vehicle side slip angle), is qualitatively better mapped with the nonlinear tyre characteristics. A more detailed vehicle and tyre model may perform better, which will be addressed next.

A section of a race track is shown in Fig. 7. Pronounced braking and acceleration together with high lateral accelerations characterize this test. Here only the 4-wheel vehicle model including the dynamic change of load distribution and its enhanced tyre model accounts for the inaction between lateral tyre force and longitudinal slip of the 4WD vehicle. Consequently, wheel dynamics need to be included. Then, the match between estimated and measured vehicle states becomes promising up to the limits of tyre adhesion.

3 ROAD GRADE AND MAXIMUM FRICTION COEFFICIENTS ESTIMATION

The influence of lateral road grade and variation of road surface conditions will be discussed with respect to required and achieved accuracy of the parameter estimation module in particular related to resulting effects on the (lateral) state estimation module.

The estimation of the road bank angle φ_R is based on the kinematic relation for the total roll angle $\varphi_G = \varphi_G(\varphi_R, \varphi, \theta, \theta_R)$, for small angles $\varphi_G \approx \varphi_R + \varphi$,

$$a_{yMm} = \hat{\dot{v}}_{yM} + \dot{\psi}_m \hat{v}_{xM} + g \sin \varphi_G \cos \theta_G \,, \qquad (3)$$

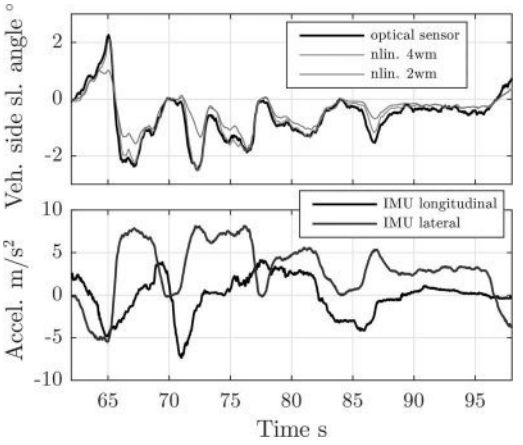


Figure 7. Race track, model comparison.

with measured yaw rate $\dot{\psi}_m$, lateral acceleration a_{yMm} in the vehicle body fixed reference frame at the location M of the sensor, and (small) roll and pitch angles, φ and θ, respectively. The longitudinal velocity $\hat{v}_{xM}$ is estimated independently in the "road slope" module considering a 4WD vehicle.

To avoid a feedback loop, the change of the lateral velocity in (3) with time cannot be used from the "lateral dynamics" module and is in general not available. Therefore, it is often neglected at all, and quasi steady-state manoeuvres are presumed. This assumption may fail when operating a sports-car with high dynamics, or when changing directions at large side slip angles of the vehicle.

A smart method to estimate a dynamic factor (DFC) of the manoeuvre directly related to $\hat{\dot{v}}_{yCG}$ is proposed in (Tseng 2000),

$$DFC = \frac{2\hat{v}_{xCG}^2}{l + \tilde{K}_{US}\hat{v}_{xCG}^2}\left(\tilde{K}_{US}a_{yCGm} + \frac{l}{\hat{v}_{xCG}}\dot{\psi}_m - \delta_F\right), \quad (4)$$

with understeer gradient $\tilde{K}_{US}$. The estimated road grade angle is scaled with $(1 - |DFC|/g)$, passing through the unscaled signal at steady-state, when the term in brackets and thus DFC become zero, which can easily be interpreted. For high dynamics the road grade angle tends to zero, which is correct on a horizontal road surface. The method is practicable if the change in lateral dynamics remains small.

For slowly changing $\hat{\dot{v}}_{yCG} = \hat{\dot{\beta}}\,\hat{v}_{xCG}$ and $\hat{v}_{xCG}$, the approximation

$$\hat{\dot{\beta}} = \frac{1 - \frac{ml_F\hat{v}_{xCG}^2}{C_{\alpha R}l_R l}}{1 + \frac{\hat{v}_{xCG}^2}{v_{\mathrm{ch}}^2}}\frac{l_R}{l}\dot{\delta}_F \quad \text{with} \quad v_{\mathrm{ch}}^2 = \frac{l}{\tilde{K}_{US}} \quad (5)$$

can be used (not considering small body roll and pitch here) to improve the estimation quality of the road grade angle φ_R and subsequently of the lateral vehicle states from the "lateral dynamics" module, although both road grade angle and vehicle side slip angle are

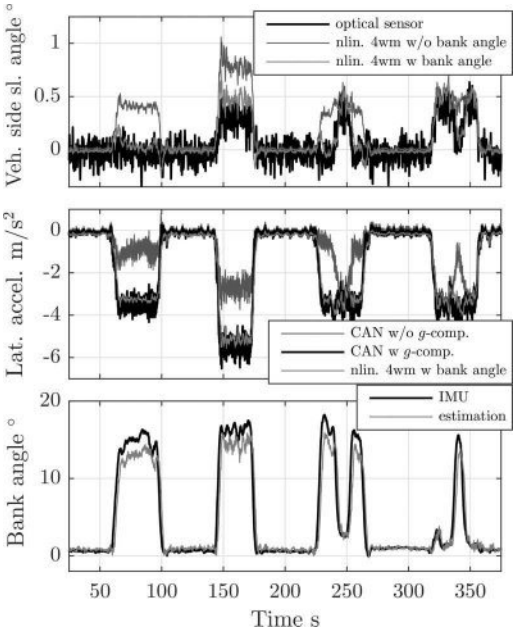


Figure 8. Lane change on banked turn (145 and 180 km/h).

not observable from a linear control theory point of view.

The resulting signal is finally processed by a weighted complementary filter to better separate effects from high-frequency steering inputs from low-frequency road bank angle changes. In this way the bias in the acceleration signal from the gravitational acceleration on inclined roads may be removed to serve as input for the Kalman filter.

As an example, lane change manoeuvres on a banked road are shown in Fig. 8. Note the biased lateral acceleration of the CAN and the acceptable performance of the road bank angle estimator. Only then can reasonable estimates for vehicle states, here the vehicle side slip angle, be derived.

The tyre/road friction estimation module is based on utilizing effects of varied tyre/road friction on vehicle states, and is separated into longitudinal, lateral and combined excitation. Methods proposed in literature have been tested and most effective methods combined. A feedback loop from the "longitudinal and lateral dynamics" module has been avoided, and the module operates mostly autonomously. Here, friction estimation based on the Gough plot will be focussed with more details in e.g. (Pasterkamp and Pacejka 1997, Takagi and Inoue 2010, Matilainen and Tuononen 2011, Edelmann et al. 2015).

In the Gough plot, i.e. lateral tyre force over aligning torque, a pair of values (F_y, M_z) results in a unique pair of values $(\alpha, \mu_{\max})$. However, (F_y, M_z) are not available to directly estimate $\mu_{\max}$. Therefore, (F_y, M_z) derived with the tyre model of the 4-wheel vehicle model are transferred to a combined steering rack force $F_{\mathrm{tr\,sum}}$ incorporating front axle kinematics and load transfer,

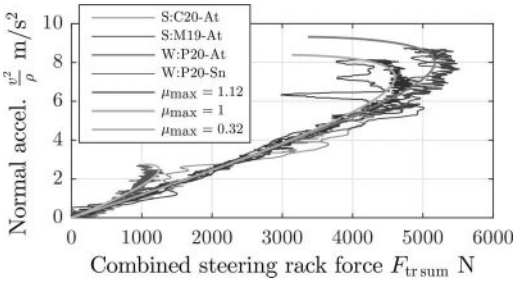


Figure 9. Combined steering rack force at steady-state cornering, corr. to Fig. 4.

see Fig. 9, for different friction levels (dry asphalt and ice). Where $\mu_{\max}$-lines almost coincide, the distinction between various friction levels becomes hard, also sensitivity to unknown or varying tyre/axle parameters is an issue. Nevertheless, the method is appealing due to its immediate guess of $\mu_{\max}$. Only a respective look-up table for $\mu_{\max} = f(|a_y|, |F_{\text{tr sum}}|, |\delta_F|)$ has to be provided.

It is not clear then, how to incorporate $\mu_{\max}$ of the "friction estimator" module to the EKF of the "lateral dynamics" module, where $\hat{\mu}_{\max}$ is considered as a "constant" parameter (state) to be estimated. For example, $\mu_{\max}$ from the friction estimator may be used as a trigger to adapt the covariance matrices of the EKF to allow for other consistent vehicle states. Or, some bounds with respect to $\mu_{\max}$ may be introduced and a mathematical estimate projection ("clipping") method, (Simon 2006) applied to adapt $\hat{\mu}_{\max}$ (and states) of the EKF within these bounds.

Fig. 10 illustrates the results of both methods. Initially $\mu_{\max} = \hat{\mu}_{\max}$ is set to 1 (dry road), then some arbitrary steering excitations on a road with snow on ice ($\mu_{\max} \approx 0.36$) stimulate the friction estimator. Already after the first excitation $\mu_{\max}$ immediately drops, but is "clipped" (close) to the upper bound until the third, litte stronger excitation. The first excitation peak is passed by the robust design of the **Q**-adaptation method, see section 4. When $\hat{\mu}_{\max}$ is close to 0.36, even large vehicle side slip angles are estimated well. For low excitation, the influence of $\mu_{\max}$ is not present, which becomes obvious during the first, and smallest steering excitation peak.

4 ESTIMATION ALGORITHM AND DESIGN

For state estimation a Kalman filter (KF) for the linear model and an extended Kalman filter (EKF) for the nonlinear models is used, (Gelb 1974, Simon 2006). Also an unscented Kalman filter (UKF) has be applied without much difference. Other estimation algorithms, such as a moving horizon estimator or sliding mode observer, have not be considered so far, and for specific manoeuvres some improvement might be expected. But in general, the EKF performs well over a wide range of manoeuvres and excitations.

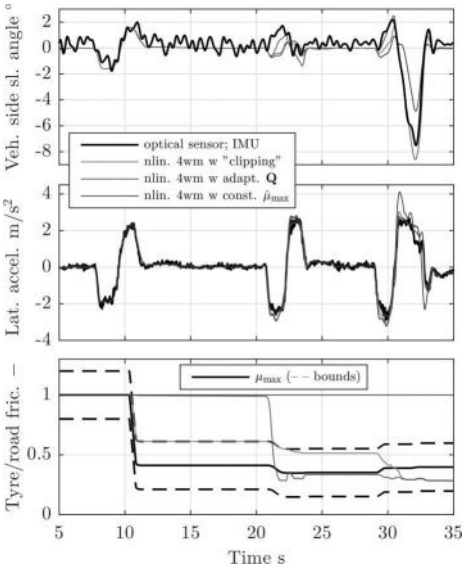


Figure 10. Combined estimation of friction potential and vehicle side slip angle.

Basically the design of a Kalman filter would be a straightforward task, which can be followed in many textbooks, (Gelb 1974, Simon 2006), if the underlying system model (equations, parameters and noise characterization) were exactly known. But in most cases, only the model equations and some of their parameters are available with sufficient accuracy. The characterization of process and measurement noise, more specifically the second order moments of noise – the covariance matrices of the process noise **Q** and measurement noise **R** – are (mostly) unknown. Therefore the elements of **Q** and **R** are often used as kind of tuning parameters in Kalman filter design.

Over five decades many papers have been published on the subject of Kalman filter design. In 1970 Mehra, (Mehra 1970, Mehra 1972), layed the foundation and classified the estimation of covariance matrices **Q** and **R** in four different categories: Bayesian estimation, e.g. (Matisko and Havlena 2013), maximum likelihood estimation, e.g. (Bavdekar et al. 2011), correlation methods, e.g. (Åkesson et al. 2008), and covariance matching methods, e.g. (Mohamed and Schwarz 1999). Further, classical system identification techniques, such as "subspace identification" (SID) or "time series methods", and all kinds of optimization approaches, e.g. (Powell 2002), shall be mentioned as well. Other effective design methods for the process noise covariance matrix, that exploits information about parametric uncertainties in the process model, when these are known, are given e.g. in (Schneider and Georgakis 2013).

However, irrespective of these mathematical approaches, **Q** and **R** are often determined by heuristic approaches, most commonly by "trial and error".

Some of the above approaches have been tested, but are not discussed here. For this paper, an optimization

method, (Powell 2002), applying a genetic algorithm, is applied to determine (only) the diagonal elements of **Q**. The objective function is based on the weighted squared estimation errors $\underline{e}^T\mathbf{W}\underline{e}$, provided that true-states are available (measured) for the tuning process. The problem with measurement noise in the true-states is roughly solved by offline (zero-phase) filtering. For the determination of **R** measured signals of steady-state manoeuvres have been assessed (covariance analysis of the measurement error).

A crucial aspect in KF-tuning is the choice of manoeuvres/input signals. From the mathematical point of view, already Mehra discusses this topic 1974 in (Mehra 1974). From a more practical point of view, a "wide excitation spectrum" shall be used, (Satria and Best 2002). Here measurements on a race track have been used.

5 CONCLUSIONS

It is reasonable to introduce individual modules for vehicle state and parameter estimation having flexibility and ease of design (for production development) in mind. However, adaptation of the modules to each other cannot be avoided, such as coordination of tyre characteristics to give an example. This results in a laborious task and requires a lot of testing to find out possible failures. In the end, a lateral dynamics, road grade and friction estimation module in combination can allow to reliably estimate vehicle states, such as the vehicle side slip angle, also at extreme handling manoeuvres with a sports-car with few failures.

The required model complexity is not as clear as expected. A Kalman filter can compensate deficiencies of the model, often with surprise to a large extent, even sometimes without much care about Kalman filter design parameters, but it can hardly be predicted at which manoeuvres the estimator may fail.

Due to the demanded linearity in the dynamic (handling) behaviour of a sports-car, a Kalman filter with a linear model already works quite well, if parameters are fitted well to steady-state cornering in particular, but may completely fail. The nonlinear 2-wheel vehicle model is effective also for large accelerations, if an appropriate tyre model is applied and reasonably parameterized. Lateral tyre force–side slip angle characteristics based on exp-functions are not appropriate for sports-car tyres, typically showing a long linear increase before a pronounced saturation. A more detailed 4-wheel vehicle model is required, if longitudinal dynamics need to be included, or respective vehicle dynamics control systems have to be mapped in the vehicle model. Additional modelled complexity has to be balanced with appropriate choice of covariance matrices of process (and measurement) noise. Experience in the choice of manoeuvres for Kalman filter design is essential to decide what kind of "wide excitation spectrum" is useful, which finally ends in trial-and-error, even though optimization methods have proven successful in the determination of covariance matrices of the Kalman filter.

To estimate vehicle states of a sports-car with 4WD on a banked race track or on icy roads is a tough challenge, but great to validate.

REFERENCES

Åkesson, B. M., J. B. Jørgensen, N. K. Poulsen, & S. B. Jørgensen (2008). A generalized autocovariance least-squares method for kalman filter tuning. *J. Process Contr. 18*, 769–779.

Antonov, S., A. Fehn, & A. Kugi (2011). Unscented kalman filter for vehicle state estimation. *Vehicle Syst. Dyn. 49*, 1497–1520.

Bavdekar, V. A., A. P. Deshpande, & S. C. Patwardhan (2011). Identification of process and measurement noise covariance for state and parameter estimation using extended kalman filter. *J. Process Contr. 21*, 585–601.

Doumiati, M., A. Charara, A. Victorino, & D. Lechner (2013). *Vehicle dynamics estimation using kalman filtering: experimental validation*. London, UK: John Wiley & Sons, Inc.

Edelmann, J., M. Gobbi, G. Mastinu, M. Plöchl, & G. Previati (2015). Friction estimation at tire–ground contact. *SAE Int. J. Commercial Vehicles 8*, 182–188.

Gelb, A. (1974). *Applied optimal estimation*. Cambridge (Massachusetts), USA: MIT press.

Matilainen, M. J. & A. J. Tuononen (2011). Tire friction potential estimation from measured tie rod forces. In *Intelligent Vehicles Symposium (IV), 2011 IEEE*, 320–325.

Matisko, P. & V. Havlena (2013). Noise covariance estimation for kalman filter tuning using bayesian approach and monte carlo. *Int. J. Adapt. Control 27*, 957–973.

Mehra, R. K. (1974). Optimal input signals for parameter estimation in dynamic systems–survey and new results. *IEEE T. Automat. Contr. 19*, 753–768.

Mehra, R. K. (1970). On the identification of variances and adaptive kalman filtering. *IEEE T. Automat. Contr. 15*, 175–184.

Mehra, R. K. (1972). Approaches to adaptive filtering. *IEEE T. Automat. Contr. 17*, 693–698.

Mohamed, A. H. & K. P. Schwarz (1999). Adaptive kalman filtering for ins/gps. *J. Geodesy 73*, 193–203.

Pasterkamp, W. R. & H. B. Pacejka (1997). The tyre as a sensor to estimate friction. *Vehicle Syst. Dyn. 27*, 409–422.

Powell, T. D. (2002). Automated tuning of an extended kalman filter using the downhill simplex algorithm. *J. Guid. Control Dynam. 25*, 901–908.

Satria, M. & M. C. Best (2002). Comparison between kalman filter and robust filter for vehicle handling dynamics state estimation. In *SAE Technical Paper 2002-01-1185*, 12 p.

Schneider, R. & C. Georgakis (2013). How to not make the extended kalman filter fail. *Ind. Eng. Chem. Res. 52*, 3354–3362.

Simon, D. (2006). *Optimal state estimation: Kalman, H infinity, and nonlinear approaches*. London, UK: John Wiley & Sons.

Takagi, F. & N. Inoue (2010). Estimation of maximum tire–road friction coefficient using electric power assist steering. *Mitsubishi Electric Advance 132*, 3 p.

Tseng, H. E. (2000). Dynamic estimation of road bank angle. In *AVEC'98*, Ann Arbor, USA, 421–428.

Wenzel, T. A., K. J. Burnham, M. V. Blundell, & R. A. Williams (2006). Dual extended kalman filter for vehicle state and parameter estimation. *Vehicle Syst. Dyn. 44*, 153–171.

Advanced Vehicle Control – Edelmann, Plöchl & Pfeffer (Eds)
© 2017 Taylor & Francis Group, London, ISBN 978-1-138-02992-7

Exploring different vehicle model complexity for reference in a sensor signal processing model controller

I. Ramirez Ruiz
Ferrari, Maranello, Politecnico di Milano, Milan, Italy

M. Alirand
SIEMENS, Lyon, France

F. Cheli & E. Sabbioni
Politecnico di Milano, Milan, Italy

ABSTRACT: Vehicle handling and stability performances are of great importance high performance sport cars. To reach these targets, very high standards of performance all the more prestigious vehicle companies have improved a lot the kinematics and compliance of the front and rear suspensions, together with the tire characteristics development. Normally the improvements have been obtained working on existing suspensions without adding any active systems able to change the suspension kinematics and compliances. The only exception has been some suspension rework of 4 wheel steering system studied in the early 80ies years, that is an active system able to change the toe angle of the rear suspension wheels. This solution has not obtained a significant success also in the market of very prestigious cars because could not reach the target performance improvement of driving requested by the customer. The proposed research work is innovative because instead to change actively the wheel toe angle it applies a solution to change the wheel camber angle through the geometry of the rear suspension. The proposed system uses two separated electro mechanical actuators, one per wheel, in place of two existing rear suspension links.

A Sensor Signal Processing Model has been developed to estimate the vehicle states and calculating tire-road contact forces and vehicle sideslip angle. The methodological approach uses the equations of motion of the chassis applying the fundamental principles of classical physics: Newtonian method and Euler angles. In parallel a 15 dof (degrees of freedom) preview vehicle model has been used to achieve a high fidelity simulation vehicle dynamics. The selected software is LMS.Amesim to handle complex real-time 3D-1D mechatronic systems without any simplified conceptual models. The vehicle control logic is based on the continuous updating of the preview vehicle model by the controller sensors information network, which makes the model forecast behaviour closer to the real one and improve comfort and linearity of the vehicle response.

Keywords: Topics/Steering system, Integrated chassis control systems, Advanced concept vehicles

1 INTRODUCTION

In the present paper, a preliminary study concerning the possibility of using a vehicle model in real-time control-oriented applications is described. Final aim of the activity is to use predictions of unmeasured quantities (e.g. sideslip angle, camber angle, etc.) provided by the preview model within a control strategy (e.g. active camber control [1–2]).

Current industry uses reduced degree of freedom models for the design and validation of control and intelligent systems. The on board vehicle control logics require a simplified model which removes bodies and degrees of freedom until the model has been reduced enough to execute real-time. Typically, real time vehicle models contain about 15 independent degrees of freedom. Specifically a 15dof vehicle model of a sport car was implemented, equipped with a front double wishbone suspension and a rear semi virtual suspension. The developed model demonstrated real-time capabilities in performing limit handling manoeuvres.

In parallel certain number of signals are available on board vehicle fusing the multi-rate measurements of the Inertial Navigation System (INS), Global Positioning System (GPS), suspension potentiometers, steering wheel angle and wheels' angular speed. Those are the inputs for the algorithm Sensor Signal Processing Model (SSPM) used to estimate the vehicle state. The equation on motion of the SSPM are based on Newton's Law and the rotational equations of motion using Euler's rotational equations, using elementary

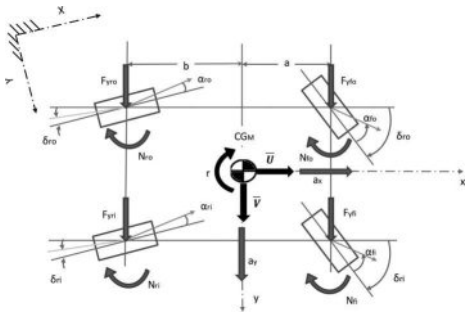


Figure 1. Vehicle orientation and tire forces.

vector calculations and appropriate coordinate transformation matrices in the driving equations of motion.

To make predictions of the preview vehicle model reliable, its parameters should be constantly updated to account for changes in vehicle load, tires (pressure, temperature, wear, etc.), road friction, etc, with the available measurements of the algorithm Sensor Signal Processing Model (SSPM).

2 VEHICLE STATE ESTIMATION

The vehicle state estimation, named sensor signal processing model (SSPM), is based on a Matlab subroutine [3] that calculates in addition to the forces, all the other secondary parameters as camber angle, toe angle to have finally the effective side slip at the four contact patches, in order to identify the tires/ground instant characteristic and update the multibody model.

There is a description of the methodology to calculate the vertical, lateral and longitudinal wheel forces and moments using certain on board vehicle sensors. The approach uses a physical vehicle model as an observer sensitive to changes in the vehicle parameters.

The chassis of the vehicle is assumed to be a rigid body. The equations of motion of the chassis are obtained by applying the fundamental principles of classical physics [4–6]. This leads to three ordinary differential equations for the translational motion of the center of the gravity and three ordinary differential equations for the rotations. Totally, the sprung mass system describes 6 DOFs of the vehicle body. Due to the complexity of the formulas the vehicle model assumed for the presented analysis has three degrees of freedom: lateral displacement, yawing and rolling motions.

The equations of motion of the three-mass vehicle model assumed (Figures 1,2) can be written as follows:

Lateral Force

$$\sum Y = M(\dot{V} + Ur) + M_s h_{RA}\dot{p} + M_{uf} a_F(\dot{p}) + M_{ur} a_R(\dot{p}) \quad (1)$$

Yawing Moment

$$\sum N = I_z\dot{r} - I_{xz_s}\dot{p} - I_{yz_s}pr - I_{xy_s}p^2 + \left(M_s a_s + M_{uf} a - M_{ur} b\right)\left(\dot{V} + U_r\right) \quad (2)$$

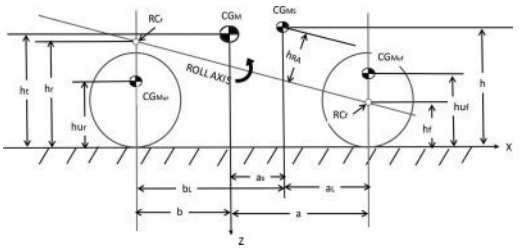


Figure 2. Vehicle roll axis and mass distribution.

Rolling Moment For Sprung Mass

$$\sum L_s = I_{x_s}\dot{p} + M_s h_{RA}\left(\dot{V} + Ur\right) - I_{xz_s}\dot{r} - I_{xy_s}pr + I_{yz_s}r^2 \quad (3)$$

Neglecting the aerodynamic load, the lateral force and yawing moment acting on a vehicle result from tire lateral forces and aligning torques. The rolling motion of the sprung mass about it's roll axis is provided by the spring and damping elements of a vehicle's suspensions:

$$\sum Y = F_{yfo} + F_{yfi} + F_{yro} + F_{yri} \quad (4)$$

$$\sum N = a(F_{yfo} + F_{yfi}) - b\left(F_{yro} + F_{yri}\right) + \frac{\partial N_f}{\partial \alpha_f}\alpha_f + \frac{\partial N_r}{\partial \alpha_r}\alpha_r \quad (5)$$

$$\sum L_s = \left(M_s g h_{RA} - \frac{\partial L_{RA}}{\partial \emptyset}\right)\emptyset - \frac{\partial L_{RA}}{\partial p}\mathrm{p} \quad (6)$$

The normal forces of front and rear wheels are determined from the static load, longitudinal weight transfer due to braking or thrust, and the lateral weight transfer due to cornering:

$$F_{zfo} = \frac{Mgb}{2L} + \frac{M_s a_x g h}{2L} + W_{TF} \quad (7)$$

$$F_{zfi} = \frac{Mgb}{2L} + \frac{M_s a_x g h}{2L} - W_{TF} \quad (8)$$

$$F_{zro} = \frac{Mga}{2L} - \frac{M_s a_x g h}{2L} + W_{TR} \quad (9)$$

$$F_{zri} = \frac{Mga}{2L} - \frac{M_s a_x g h}{2L} - W_{TR} \quad (10)$$

The front and rear lateral weight transfers are determined:

$$W_{TF} = \frac{M_s a_y}{t_f}\left(h_{RA}\cos\emptyset\frac{k_f}{k_{tot}} + \frac{bh_f}{L}\right) + M_{uf} a_y \frac{h_{uf}}{t_f} \quad (11)$$

$$W_{TR} = \frac{M_s a_y}{t_r}\left(h_{RA}\cos\emptyset\frac{k_r}{k_{tot}} + \frac{ah_r}{L}\right) + M_{ur} a_y \frac{h_{ur}}{t_r} \quad (12)$$

A non-linear tire model has been used ready to accept Magic Formula tire data [5]. The tires' cornering stiffness are strongly dependent upon their normal loads, and tires' frictional properties are determined by peak braking and lateral force coefficients.

The tire lateral force is a function of the normal load, the slip angle and the friction coefficient. The influence of wheel normal loads on generated tire forces

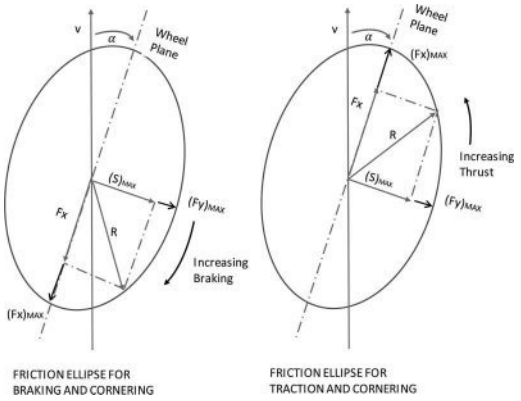


Figure 3. Friction ellipse concept in combined vehicle maneuvers.

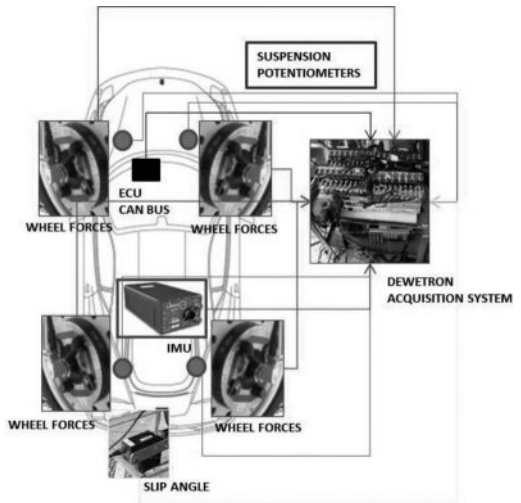


Figure 4. The vehicle-dynamics instrumentation.

is represented both directly and indirectly through the lateral force coefficient:

$$F_{yfo} = SN\mu_{yfo}F_{zfo}f(\bar{\alpha}_{fo}) + \left(\frac{\partial F_y}{\partial \gamma}\right) f \frac{\partial \gamma}{\partial \emptyset} \emptyset \quad (13)$$

$$F_{yfi} = SN\mu_{yfi}F_{zfi}f(\bar{\alpha}_{fi}) + \left(\frac{\partial F_y}{\partial \gamma}\right) f \frac{\partial \gamma}{\partial \emptyset} \emptyset \quad (14)$$

$$F_{yro} = SN\mu_{yro}F_{zro}f(\bar{\alpha}_{ro}) \quad (15)$$

$$F_{yri} = SN\mu_{yri}F_{zri}f(\bar{\alpha}_{ri}) \quad (16)$$

The tire adhesion model utilizes the friction ellipse concept (Figure. 3), where the tires' maximum lateral forces in combined cornering and braking, or cornering and accelerating manoeuvres are, as found from the friction ellipse.

With the intention to offer a precise evaluation a vehicle test has been developed. Figure 4 shows a scheme of the experimental vehicle and of the

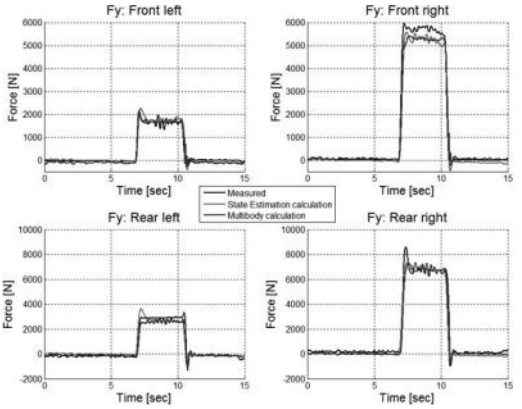


Figure 5. Lateral forces calculation compared with measured data.

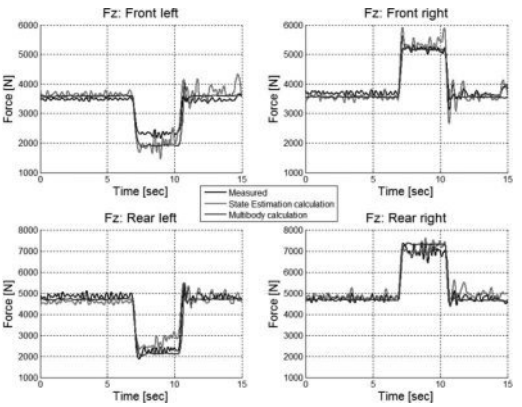


Figure 6. Vertical forces calculation compared with measured data.

installed sensors. Specifically, the vehicle is a sport car, equipped with a set of state-of-the-art sensors, measuring the vehicle sideslip angle (optical sensor), carbody accelerations and angular rates (Inertial Measuring Unit-IMU), suspension stroke, GPS and dynamometric wheels for wheel center forces and moments.

The presented results are the comparison of lateral (Figure 5), and normal forces at the wheel center (Figure 6).

The experimental data (black lines), the vehicle model (blue lines) and the SPPM (red lines) are compared. A step-steer maneuver is considered. The correlation of lateral and vertical forces and lateral dynamics parameters estimated by SSPM is very close to the measured values. The same quantities calculated by the real-time multibody model are also very close to the measured values. As a further development, update of multibody model parameters based on performed measurements and predictions (SPPM) will be investigated, so to further reduce differences between simulation and experimental data.

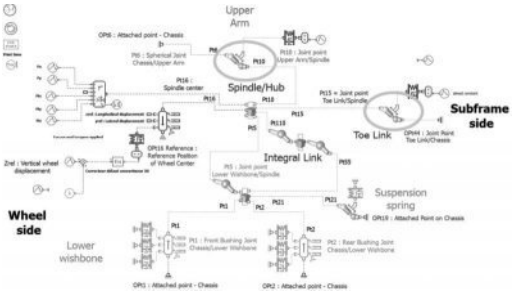


Figure 7. AMESIM 3D mechanical library suspension kinematics model.

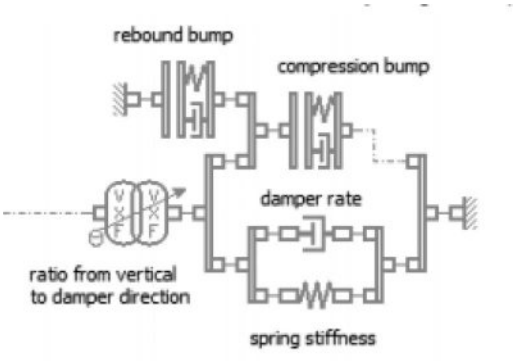


Figure 8. AMESIM spring – damper model.

3 THE DEVELOPED FUNCTIONAL VEHICLE MODEL

To test the controller, a functional vehicle model having 15 dof and using look-up tables for the suspension kinematics and compliances have been introduced in [7].

In order to generate the suspension kinematics for the vehicle functional model, 3D mechanical models of the front and rear (piloted and not piloted) suspensions has been developed and validated for pure kinematics and bushing contributions (Figure 7).

The axle kinematics data is represented by: Z & Zopp current and opposite suspension stroke, Yn steering rack displacement, X and Y longitudinal and lateral wheel displacement, and toe, camber and self rotation wheel angles (Euler ZXY decomposition) due to suspension kinematics.

In the 15dof vehicle model there is a way to manage the force in the suspension Force- Displacement characteristics including the spring, damper and endstops (Figure 8) with the introduction of a ratio between vertical stroke and the stroke in the direction of the spring/damper.

Finally the functional vehicle model being still simple aims to run real time. However the dynamics of the electrical devices limit a bit the performances of the complete vehicle model. Figure 9 describes how the electric motors are connected to the vehicle

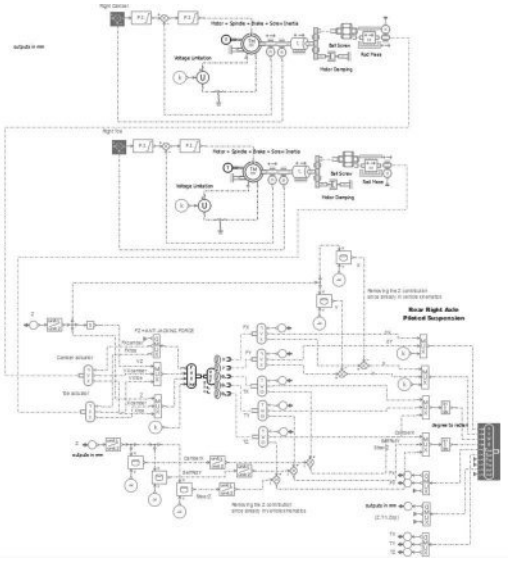


Figure 9. Piloting the rear suspension.

via lookup tables representing the kinematics relationships between the two actuator motion and the rear suspension kinematics changes.

The control logic of the camber system changes the angles of the rear suspensions using the elasto kinematics inputs/outputs as an additional contribution. Consequently the influences of the camber modifications on the tire forces and torques are the correct ones. However the way to bring these efforts on the chassis body using the suspension kinematics continues to use the suspension passive part as an approximation. Consequently the general anti dive effects are not exactly the ones of the vehicle with piloted rear suspensions.

The complete model including the functional vehicle, the electro mechanical actuators and a simplified version of control logic has been tested in [7]. Despite the limitations exposed above, the first results show that the functional vehicle model is finally acceptable for improving and testing the performances of the controller.

4 THE CONTROLLER

The vehicle control logic base on the continuous updating of the preview vehicle model by the controller sensors information network [3] (Figure 10), will make the model forecast behaviour closer to the real one and will improve the comfort and linearity of the vehicle response.

The drive control system will be defined into three phases:

- 1° phase:
  - Learning
  - Comparing results from sensors to the results from vehicle model. Correction of the vehicle model parameters (shock absorbers, tires, bushings).

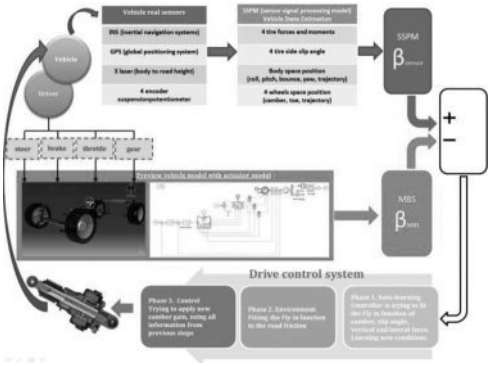


Figure 10. Final view of the controller.

- 2° phase:
  - Environment
  - Update the vehicle model to the current environmental condition (ground friction, temperature effect…).
- 3° phase:
  - Control
  - Applying results to the control systems (ABS, ESP…) of the vehicle.

The drive control logic is integrated into a single high level vehicle dynamics controller which also controls all the active systems of the vehicle [8][9].

5 CONCLUSION

In the present paper, a preliminary study concerning the possibility of using a vehicle preview model in real-time control-oriented applications is presented. Final aim of the activity is to use predictions of unmeasured quantities (e.g. sideslip angle, camber angle, etc.) provided by the multibody model within a control strategy (e.g. active camber control).

Specifically a 15dof vehicle model of a sport car was implemented, equipped with a front double wishbone suspension and a rear semi virtual suspension. The developed model demonstrated real-time capabilities in performing limit handling manoeuvres.

To make predictions of the preview model reliable, its parameters should be constantly updated to account for changes in vehicle load, tires (pressure, temperature, wear, etc.), road friction, etc. On the purpose, a Sensor Signal Processing Model (SSPM) based on available measurements was developed.

The vehicle control logic increases the performance and drive ability of the vehicle interacting with all the active systems. One demonstration will be with the active system moving rear wheel camber.

REFERENCES

[1] Ramirez Ruiz I. “High performance electro mechanical actuator for active rear axle kinematics of a sport car”, SAE Paper n° 2012-01-0974, 2012, pp. 1–14.

[2] Braghin.F., Pnada.A., Sabbioni.E, “Potentialities of Active Suspension for the Improvements of Handling Performances”, ASME – ESDA, Istanbul, 2010

[3] Ramirez Ruiz I., Cheli F., “Vehicle dynamics, stability and control”, SAE Paper n° 2014-01-0134, pp. 1–6.

[4] Alamdari, A., Sovizi, J., Krovi, V., “Enhanced Full-State Estimation and Dynamic-Model-Based Prediction for Road-Vehicles,” *ASME IDETC/CIE DETC2014-34453*

[5] Zewari, S., Bayard, E., “Theorical Model of a Vehicle Using Vector Analysis and Eurler’s Rigid Body Dynamics,” *SAE paper No. 820762*

[6] Nalecz, A., “ Investigation into the Effects of Suspension Design on Stability of Light Vehicles,” *SAE Paper No.870497*

[7] Ramirez Ruiz I., Alirand M., Kieny N. Cheli F. “Smart Electro mechanical system to improve vehicle handling and stability by toe and camber control on the rear wheel”, 6th Int. Munich Chassis Symposium Chassis Tech, June 2015, Munich, Germany.

[8] Kuwayama.I, Baldoni.F., Cheli.F., “Development of a Control Strategy for a Variable Camber Suspension”, Int. Journal of Mechanics and Control, 8(1), pp. 38–52

[9] Zewari, S., Bayard, E., “Theorical Model of a Vehicle Using Vector Analysis and Eurler’s Rigid Body Dynamics,” *SAE paper No. 820762*

NOMENCLATURE

a	– distance from sprung mass CG to front axle
aF(p·)	– acceleration of CG of front unsprung mass due to sprung mass roll
ax	– longitudinal acceleration
ay	– lateral acceleration
aR(p·)	– acceleration of CG of rear unsprung mass due to sprung mass roll
as	– distance from sprung mass CG to total mass CG (measured along x)
b	– distance from sprung mass CG to rear axle
Fyfo	– lateral force on front outside wheel
Fyfi	– lateral force on front internal wheel
Fyro	– lateral force on rear outside wheel
Fyri	– lateral force on rear inside wheel
Fzfo	– normal force on front outside wheel
Fzfi	– normal force on front internal wheel
Fzro	– normal force on rear outside wheel
Fzri	– normal force on rear inside wheel
g	– gravitational acceleration
h	– height of sprung mass CG
hf	– height of front suspension roll center
hr	– height of rear suspension roll center
hRA	– distance from roll axis to sprung mass CG
ht	– height of vehicle CG
huf	– height of front unsprung mass CG
hur	– height of rear unsprung mass CG
IXs	– mass moment of inertia about the roll axis
IZ	– mass moment of inertia about the yaw axis
kf	– roll stiffness of front suspension
kr	– roll stiffness of rear suspension
ktot	– total roll stiffness of suspension
L	– wheelbase
M	– total mass of vehicle

Ms – sprung mass of vehicle
Muf – unsprung mass of front suspension
Mur – unsprung mass of rear suspension
p – sprung mass roll angular velocity
r – yaw angular velocity
SN – tire skid number
tf – front track width
tr – rear track width
U – vehicle forward velocity
V – vehicle lateral velocity
wTF – total front lateral weight transfer
wTR – total rear lateral weight transfer
α f – front tire slip angle
α r – rear tire slip angle
$\dot{\alpha}_{fo}$, $\bar{\alpha}_{fi}$ – outside and inside front tires slip angles variables
$\bar{\alpha}_{ro}$, $\bar{\alpha}_{ri}$ – outside and inside rear tires slip angles variables

δ – steering angle of front wheels
$\left(\frac{\partial F_y}{\partial y}\right) f$ – inclination stiffness of front tires
$\frac{\partial y}{\partial \rho}$ – roll axis torsional stiffness
$\frac{\partial L_{RA}}{\partial \theta}$ – roll axis damping
$\frac{\partial \gamma}{\partial \theta}$ – rate of change of front wheel inclination with roll of sprung mass
$\mu_{yf\alpha}$, μ_{yfi} – peak lateral force coefficient of front tires
μ_{yro}, μ_{yri} – peak lateral force coefficient of rear tires
ϕ – sprung mass roll angle
y – vehicle yaw angle

Advanced Vehicle Control – Edelmann, Plöchl & Pfeffer (Eds)
© 2017 Taylor & Francis Group, London, ISBN 978-1-138-02992-7

Articulation angle estimation and control for reversing articulated vehicles

S. Kim, J. Yang & K. Huh
Department of Automotive Engineering, Hanyang University, Korea

ABSTRACT: The ADAS (Advanced Driver Assistance System) and Autonomous Vehicle technologies can offer the convenience and safety to many drivers. While passenger vehicles have been adopting various versions of driving assistance, the tractor-trailer vehicles are being driven manually. Especially, backward motion of tractor-trailer vehicle is a burden to the driver. This paper considers the steering controller design applied to a backward motion assistance system for tractor-trailer vehicles. The proposed algorithm is evaluated in simulations and the results show that the proposed algorithm can effectively control the tractor-trailer vehicle in the case of backward driving.

1 INTRODUCTION

The commercial semi-trailer truck combines tractor and semi-trailer units to carry freight, and the each unit travels in a different trajectory when the vehicle drives on curved road. Accordingly, a semi-trailer truck driver should consider the trajectories of not only the7 tractor but also the trailer. In particular, when the semi-trailer truck moves backward, the driver of this vehicle undergoes a great difficulty in controlling the pose of the trailer because of an unstable characteristics of the articulation angle.

Recently, researches on ADAS (Advanced Driver Assistance System) have provided convenience for drivers in various driving conditions, but, most applications are mainly focused on general passenger vehicles. ADAS for commercial semi-trailer truck vehicle has not been investigated actively. There were some studies about controlling reverse motion of semi-trailer tractor vehicles. González-Cantos et al. proposed a reversing steering control algorithm using a kinematic model of tractor-trailer vehicle (González-Cantos et al. 2009). In this research, controllability minimum principle is introduced to avoid jackknife of semi-trailer truck vehicles and the steering control law is suggested which makes the trailer unit to follow the reference path. Yoshimoto et al. proposed a control algorithm of the articulated vehicle based on Lyapunov stability theory (Yoshimoto et al. 2013). They introduced an error dynamics model representing the error between the articulated vehicle and the reference paths, and the Lyapunov based controller was designed to calculate the proper steering angle for trailer unit to track the reference path. Werling et al. proposed a semi-trailer truck vehicle controller by converting the reference path to a modified curvature which allows the driving of the semi-trailer truck vehicle (Werling et al. 2014). However, the above studies suggested the control methods where only the trailer unit follows the reference path and the difference between the tractor and trailer paths is not considered. In addition, the hitch angle is often used in the control methods, but its real-time information is not available in semi-trailer trucks.

In this paper, a steering control system is proposed for reversing semi-trailer trucks without using the articulation angle sensor. The proposed system consists of two main algorithms. First, the articulation angle estimation algorithm is designed based on the articulation dynamics model and the Kalman filter is applied to obtain the accurate articulation angle information. Secondly, the steering angle control algorithm for the semi-trailer tractor is designed based on the articulated vehicle kinematic model. The MPC (Model Predictive Control) method is utilized to calculate the proper steer angle such that both the tractor and the trailer follow the given path without departing from the road boundary. The structure of the proposed control system is illustrated in Figure 1.

This paper is organized as follows. Section 2 explains a mathematical model of semi-trailer truck

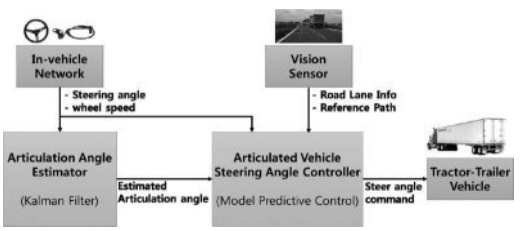


Figure 1. Proposed tractor-trailer control system architecture.

vehicle. Section 3 describes a designing process of the articulation angle estimation algorithm. The steering angle control is designed in Section 4 based on the semi-trailer truck vehicle model. The performance of the proposed control system is evaluated in Section 5. Finally, Section 6 presents the conclusion of this research.

2 MODELING OF THE ARTICULATED VEHICLE

In general, the semi-trailer truck vehicle moves backward at low speed and the slip angle at each wheel is very small. Thus, the slip angle of each wheel is assumed zero in this study and Figure 2 shows the relationship between the steering angle and the lateral movement of semi-trailer truck vehicle.

2.1 *Kinematic motion of the articulated vehicle*

The lateral movement of the tractor unit is described by the 'Ackermann geometry' when the slip angle of each tire is zero. Using the Ackermann geometry properties, the lateral movement of the tractor is described as,

$$\begin{aligned} \dot{y}_1 &= v_{x1} \cdot \psi_1 \\ \dot{\psi}_1 &= \frac{v_{x1}}{L_1} \tan\delta \end{aligned} \tag{1}$$

where y_1 and ψ_1 represent the lateral position and the heading angle of the tractor unit, respectively. v_{x1} is the longitudinal velocity of the tractor vehicle, and L_1 is the wheel base of the tractor. δ represents the front steering angle of the tractor.

Because typical semi-trailer unit does not have the front axle, the lateral movement of the trailer unit depends on the articulation angle. Assuming the articulation angle as the steering angle of the trailer part, the yaw-rate of the trailer is described as follows:

$$\dot{\psi}_2 = \frac{v_{x2}}{L_2} \tan\phi \tag{2}$$

where ψ_1 and v_{x2} represent the heading angle and the longitudinal velocity of the trailer, respectively, L_2 is the wheel base of the trailer and ϕ is the articulation angle of the semi-trailer truck vehicle.

The longitudinal velocities of the tractor and the trailer have the following relationship based on the articulation angle.

$$v_{x2} = v_{x1} \cdot \cos\phi \tag{3}$$

By applying equation (3) to equation (2), the yaw-rate of the trailer unit is derived as:

$$\dot{\psi}_2 = \frac{v_{x1} \cdot \cos\phi}{L_2} \tan\phi = \frac{v_{x1}}{L_2} \sin\phi \tag{4}$$

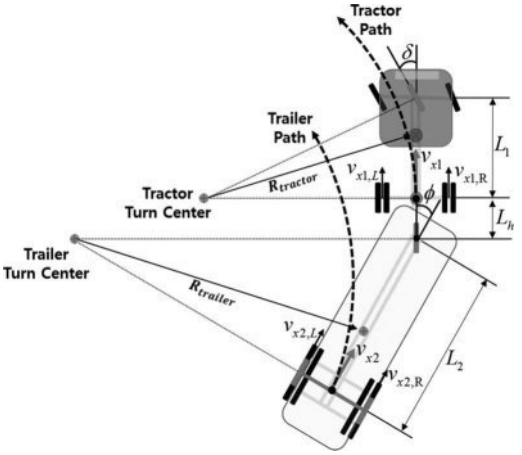


Figure 2. Kinematic motion of the articulated vehicle.

Note that the articulation angle is caused by the heading angle difference between the tractor and the trailer. The difference in heading angles is also generated by the difference of yaw-rate between the tractor and trailer. Therefore, by substituting equations (1) and (4), the articulation angle dynamics is expressed into the following form.

$$\begin{aligned} \dot{\phi} &= \dot{\psi}_1 - \dot{\psi}_2 \\ \dot{\phi} &= -\frac{v_{x1}}{L_2} \sin\phi + \frac{v_{x1}}{L_1} \tan\delta \end{aligned} \tag{5}$$

2.2 *State-space equation of the articulated vehicle*

From equation (1) and (5), a kinematic model can be derived representing the lateral position, heading angle and articulation angle of the semi-trailer truck.

$$\begin{aligned} \dot{y} &= v_{x1} \cdot \psi_1 \\ \dot{\psi}_1 &= \frac{v_{x1}}{L_1} \tan\delta \\ \dot{\phi} &= -\frac{v_{x1}}{L_2} \sin\phi + \frac{v_{x1}}{L_1} \tan\delta \end{aligned} \tag{6}$$

Because, it is difficult to apply linear control or estimation theory to the nonlinear terms in equation (6), a linearized lateral kinematic model is derived into the following state-space from.

$$\begin{bmatrix} \dot{\underline{y}} \\ \dot{\underline{\psi}}_1 \\ \dot{\underline{\phi}} \end{bmatrix} = \begin{bmatrix} 0 & v_{x1} & 0 \\ 0 & 0 & 0 \\ 0 & 0 & -\frac{v_{x1}\cos\phi_{eq}}{L_2} \end{bmatrix} \begin{bmatrix} \underline{y} \\ \underline{\psi}_1 \\ \underline{\phi} \end{bmatrix} + \begin{bmatrix} 0 \\ \frac{v_{x1}}{L_1\cos^2\delta_{eq}} \\ \frac{v_{x1}}{L_1\cos^2\delta_{eq}} \end{bmatrix} \underline{\delta} \tag{7}$$

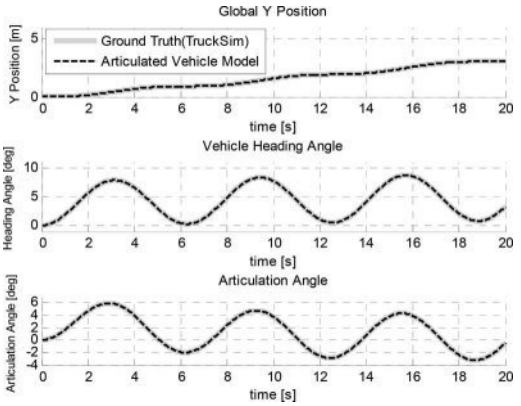


Figure 3. Validation results of the articulated vehicle model.

where the subscript *eq* represents the equilibrium point of the states and underline – represents the linearized states ($\underline{x} = x - x_{eq}$).

Finally, the discrete-time model based on equation (6) is expressed to design estimation and control algorithms.

$$\begin{bmatrix} \overline{y} \\ \overline{\psi}_1 \\ \overline{\phi} \end{bmatrix}_{k+1} = \begin{bmatrix} 1 & dt \cdot v_{x1} & 0 \\ 0 & 1 & 0 \\ 0 & 0 & 1 - dt \cdot \frac{v_{x1}}{L_2} \cos\phi_{eq} \end{bmatrix} \begin{bmatrix} \overline{y} \\ \overline{\psi}_1 \\ \overline{\phi} \end{bmatrix}_k + \begin{bmatrix} 0 \\ \frac{dt \cdot v_{x1}}{L_1 \cos^2 \delta_{eq}} \\ \frac{dt \cdot v_{x1}}{L_1 \cos^2 \delta_{eq}} \end{bmatrix} \overline{\delta} \tag{8}$$

where *dt* is the sampling period of the estimation and control algorithm.

The proposed articulated vehicle model is verified in simulations using a commercial software, the TruckSim. As shown in Figure 3, by applying the sine wave steering input the kinematic model of equation (7) provides very close results to those from the TruckSim.

3 ESTIMATION OF THE ARTICULATION ANGLE

Recently, in order to improve the stability of the semi-trailer truck vehicle, trailer-mountable ABS (Anti-lock Brake System) is developed and applied (Chandrasekharan et al. 2009). Because the ABS contains the wheel speed sensors, the wheel speed information of both tractor and trailer unit is assumed available in this study.

3.1 *Calculation of the articulation angle*

When the speed of the tractor and the trailer can be measured independently, the articulation angle can be calculated using equation (3).

$$\begin{aligned} & v_{x1} = \frac{1}{2}\left(v_{x1,L} + v_{x1,R}\right), \quad v_{x2} = \frac{1}{2}\left(v_{x2,L} + v_{x2,R}\right) \\ & \Rightarrow \phi = \cos^{-1}\left(\frac{v_{x2}}{v_{x1}}\right) = \cos^{-1}\left(\frac{v_{x2,L} + v_{x2,R}}{v_{x1,L} + v_{x1,R}}\right) \end{aligned} \tag{9}$$

where $v_{x1,L}/v_{x1,R}$ and $v_{x2,L}/v_{x2,R}$ represent left/right wheel speeds of the tractor unit and trailer unit, respectively. In addition, left/right wheel speeds of the trailer are compared to determine the sign of the calculated articulation angle.

$$\phi = sign\left(\frac{v_{x2,\mathrm{R}} - v_{x2,L}}{v_{x2,\mathrm{R}} + v_{x2,L}}\right) \cdot \cos^{-1}\left(\frac{v_{x2,L} + v_{x2,R}}{v_{x1,L} + v_{x1,R}}\right) \tag{10}$$

3.2 *Articulation angle estimator design*

Even though the articulation angle can be calculated using equation (10), resolution of the speed sensors and road bumps can deteriorate the reliability of wheel speed data. Thus, in this study, Kalman filter (Grewal. 2011) based estimation algorithm is proposed using the semi-trailer truck model of equation (5) and the calculated articulation angle from equation (10). The articulation angle dynamics model of equation (5) is described into a linearized state-space form.

$$\phi_{k+1} = a \cdot \phi_k + b \cdot \delta_k + w_k \tag{11}$$

where

$$a = 1 - \frac{dt \cdot v_{x1}}{L_2} \cos\phi_{k-1}, \quad b = \frac{dt \cdot v_{x1}}{L_1 \cdot \cos^2 \delta_{k-1}},$$
$$w_k \sim N(0, Q)$$

The calculated articulation angle from equation (10) is utilized in the measurement equation.

$$z_k = h \cdot \phi_k + v_k \tag{12}$$

where $h = 1, \quad z_k = \phi_{cal}, \quad v_k \sim N(0, R)$

and ϕ_{cal} represents the articulation angle information calculated in equation (10).

Based on equation (11), the state vector and the error covariance matrix are calculated first at the prediction stage.

$$\tilde{\phi}_k = a \cdot \hat{\phi}_{k-1} + b \cdot u_{k-1} \tag{13}$$

$$\tilde{P}_k = a\hat{P}_{k-1}a^T + Q \tag{14}$$

where superscripts of ˆ and ~ represent the estimated and predicted values, respectively.

The state variables are estimated at the correction stage using the predicted and the measured values. The Kalman filter gain, K_k, is determined as follows.

$$K_k = \tilde{P}_k h^T \left(h\tilde{P}_k h^T + R \right)^{-1} \tag{15}$$

and the estimated state vector and the error covariance are updated using the following equations.

$$P_k = \tilde{P}_k - K_k h\tilde{P}_k \tag{16}$$

$$\hat{\phi}_k = \tilde{\phi}_k + K_k \left(z_k - h\tilde{\phi}_k \right) \tag{17}$$

4 STEERING ANGLE CONTROL ALGORITHM FOR THE ARTICULATED VEHICLE

In this study, it is assumed that the road lane data from the vision sensor is available and the reference path inside the lane boundary can be obtained. Besides, this road information is assumed to be expressed in a 2-D vehicle coordinate. Figure 4 shows the obtained road information based on vehicle coordinate.

The requirements of the steering controller for reversing semi-trailer truck vehicle is determined as follows: When the reference path was determined, the steering controller should calculate appropriate steering input such that both the tractor and the trailer units follow the reference path. At the same time, in order to avoid a collision with the obstacles or vehicles outside the lane, the tractor and the trailer should be controlled not to depart the road boundary.

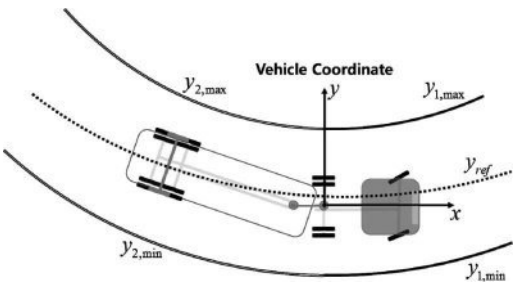


Figure 4. Road lane and reference path information.

In order to satisfy these requirements, MPC (Model Predictive Control) method is applied in designing the steering control algorithm (Camacho et al. 2013). The optimal steering angle can be determined by using the MPC method with a proper object function. In addition, by setting the road boundary as the constraints of the MPC method, it is possible to control the vehicle not to depart road boundary.

4.1 *Object function of the controller*

In order to calculate the MPC based optimal control input, the articulated vehicle model in equation (7) is utilized as a prediction model.

$$\begin{aligned} \mathbf{x}_{k+1} &= A\mathbf{x}_k + B\mathbf{u}_k \\ \mathbf{y}_k &= C\mathbf{x}_k \end{aligned} \tag{18}$$

where

$$\mathbf{x}_k = \begin{bmatrix} y_1 & \psi_1 & \phi \end{bmatrix}_k^T, \quad \mathbf{y}_k = \begin{bmatrix} y_1 & y_2 \end{bmatrix}_k, \quad \mathbf{u}_k = \delta_k$$

$$A = \begin{bmatrix} 1 & dt \cdot v_{x1} & 0 \\ 0 & 1 & 0 \\ 0 & 0 & 1 - \dfrac{dt \cdot v_{x1}}{L_2} \cos\phi_{eq} \end{bmatrix}, B = \begin{bmatrix} 0 \\ \dfrac{dt \cdot v_{x1}}{L_1 \cos^2 \delta_{eq}} \\ \dfrac{dt \cdot v_{x1}}{L_1 \cos^2 \delta_{eq}} \end{bmatrix},$$

$$C = \begin{bmatrix} 1 & 0 & 0 \\ 1 & -(L_h + L_2) & L_2 \end{bmatrix}$$

y_1 and y_2 is lateral positions of the tractor and the trailer respectively. L_h is the distance between the tractor's rear axle and the hitch point. As illustrated in Figure 1, the lateral position of the tractor and the trailer satisfies the relationship $y_2 = y_1 - (L_h + L_2)\psi_1 + L_2\phi$ by the geometric correlation.

A quadratic object function for the reference path tracking is formulated as follows:

$$\begin{aligned} J_k = &\sum_{i=k+1}^{k+N_p} \frac{1}{2} \left(\mathbf{y}_i - \mathbf{w}_i \right)^T Q_e \left(\mathbf{y}_i - \mathbf{w}_i \right) + \sum_{i=k}^{k+N_p-1} \frac{1}{2} \mathbf{u}_i{}^T R_u \mathbf{u}_i \\ &+ \sum_{i=k}^{k+N_p-1} \frac{1}{2} \Delta\mathbf{u}_i{}^T R_{\Delta u} \Delta\mathbf{u}_i \end{aligned} \tag{19}$$

where N_p is the prediction horizon. Q_e, R_u and $R_{\Delta u}$ represent weights of control error, control input and control input rate, respectively. **w** is the control target of the tractor and trailer lateral positions to follow the reference path.

4.2 *Constraints of the controller*

The control requirements contain the condition that the tractor and the trailer should be controlled inside the lane all the time. Accordingly, the constraints about

the lateral position of the semi-trailer truck vehicle are represented as follows:

$$\begin{aligned} y^j_{1,\min}(i) \le y^j_1(k+i+1|k) \le y^j_{1,\max}(i) \\ y^j_{2,\min}(i) \le y^j_2(k+i+1|k) \le y^j_{2,\max}(i) \\ i = 0, \cdots, p-1 \end{aligned} \tag{20}$$

where $y^j_{n,min}$ and $y^j_{n,max}$ represent right and left boundaries of the driving road, respectively. The superscript, j, represents the j-th component of a vector, k represents the current time, and $(k+i|k)$ represents the i-th predicted value from the current states.

In addition, the physical limits of the steering angle and angular speed are formulated as constraints of the steering actuator.

$$\begin{aligned} \mathbf{u}^j_{\min}(i) \le \mathbf{u}^j(k+i+1|\mathrm{k}) \le \mathbf{u}^j_{\max}(i) \\ \Delta\mathbf{u}^j_{\min}(i) \le \Delta\mathbf{u}^j(k+i+1|\mathrm{k}) \le \Delta\mathbf{u}^j_{\max}(i) \end{aligned} \tag{21}$$

where $\mathbf{u}^j_{\min}$ and $\mathbf{u}^j_{\max}$ represent the minimum/maximum steering angle, ranges and their values are set to -30 deg and $+30$ deg, respectively, in this study. Similarly, $\Delta\mathbf{u}^j_{\min}$ and $\Delta\mathbf{u}^j_{\max}$ represent the minimum/maximum steering rate, respectively, and their values set to ± 15 deg/s.

5 EVALUATIONS

The proposed articulation angle estimation and steering control algorithms are validated in the co-simulation environment with the commercial software. Figure 5 shows the tractor-trailer vehicle model and the road shape used in TruckSim. The proposed estimation and control algorithms are implemented in the MATLAB/Simulink environment. A resolution of the wheel speed sensor is assumed to be 0.05 km/h. The articulation angle is estimated based on the wheel speed signals and the steering angle is controlled for the semi-trailer truck to follow the reference path.

Figure 6 compares the estimated articulation angle with the calculated articulation angle and the ground truth. In spite of the inaccurate wheel speed data, the estimation errors are within ± 1.2 deg and demonstrate the effectiveness of the proposed algorithm.

The top graph in Figure 7 illustrates the optimal steering angle input determined from proposed control algorithm and the bottom graph shows path tracking errors of the tractor and trailer. The maximum path tracking errors of the tractor and trailer are 1.3 m and 0.7 m, respectively. Even if the maximum tracking error of the tractor is larger than that of the trailer, the steering angle is determined so that both the tractor and trailer in reverse motion are controlled within the left and right road boundaries.

Figure 8 shows the situation where the tractor-trailer vehicle is turning the corner in reverse. The trailer is driving on inside, and the tractor is driving on outside of the road center. It is demonstrated that both tractor

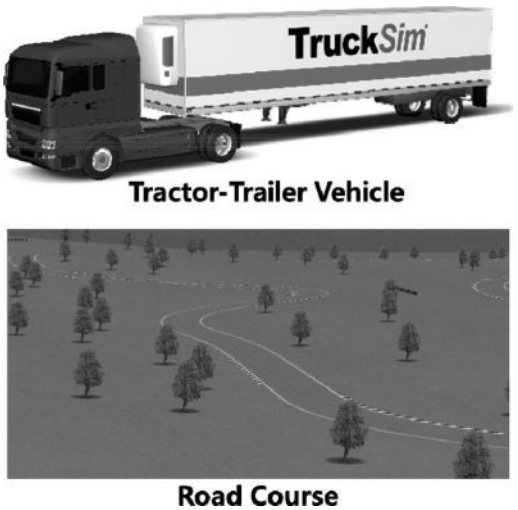


Figure 5. Validation results of the articulated vehicle model.

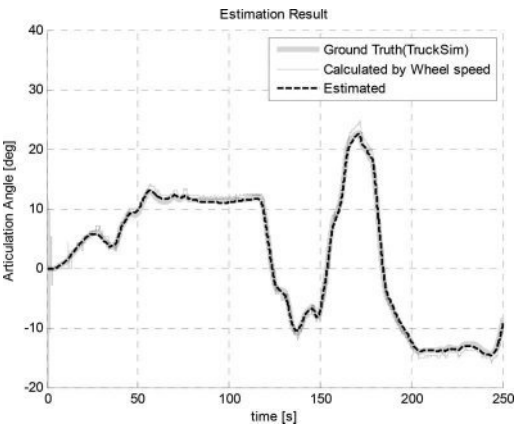


Figure 6. Validation results of the articulated vehicle model.

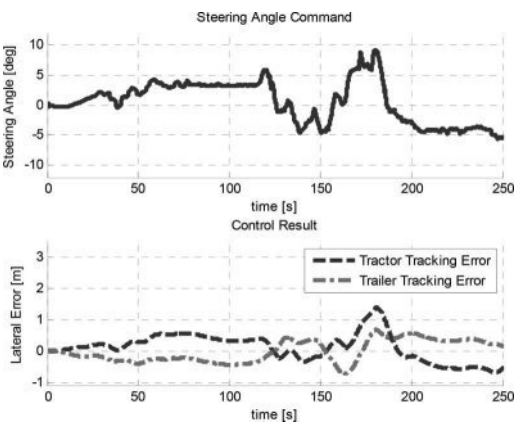


Figure 7. Validation results of the articulated vehicle model.

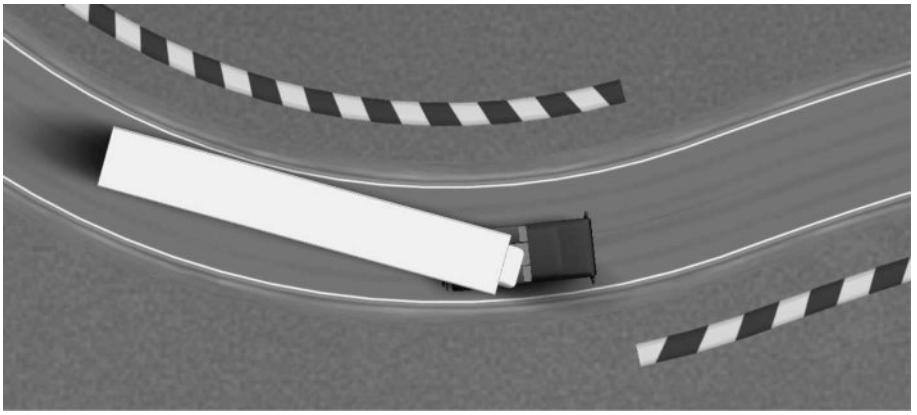


Figure 8. Validation results of the articulated vehicle model.

and trailer are following the reference path well, and that an adequate steering angle is provided to avoid the lane departure or collision.

6 CONCLUSIONS

The steering control system is investigated for reversing the articulated vehicle. The proposed system is composed of two parts. First, the articulation angle is estimated in real time for the semi-trailer truck vehicles without articulation angle sensor. Second, the steering control algorithm of the articulated vehicle is designed for path tracking and lane keeping. The proposed system is verified in co-simulation of the commercial software, MATLAB/Simulink and TruckSim. The simulation results show that the estimation error of the articulation angle is within ± 1.2 deg and the path tracking error of the vehicle is within ± 1.3 m. It is demonstrated that the proposed system can effectively estimate the articulation angle and control the reversing semi-trailer truck vehicle and that the proposed system can be utilized in steering angle control of ADAS or autonomous driving for commercial truck vehicles.

REFERENCES

Camacho, E. F., & Alba, C. B. (2nd) 2013. *Model predictive control.* Berlin Heidelberg: Springer Science & Business Media.

Chandrasekharan, S., Guenther, D. A., Heydinger, G. J., Salaani, M. K., & Zagorski, S. B. 2009. Development of a roll stability control model for a tractor trailer vehicle. *SAE International Journal of Passenger Cars-Mechanical Systems*, 2(2009-01-0451): 670–679.

González-Cantos, A., & Ollero, A. 2009. Backing-up maneuvers of autonomous tractor-trailer vehicles using the qualitative theory of nonlinear dynamical systems. *The International Journal of Robotics Research*, 28(1): 49–65.

Grewal, M. S. 2011. *Kalman filtering*. Berlin Heidelberg: Springer Science & Business Media.

Werling, M., Reinisch, P., Heidingsfeld, M., & Gresser, K. 2014. Reversing the general one-trailer system: Asymptotic curvature stabilization and path tracking. *IEEE Transactions on Intelligent Transportation Systems*, 15(2): 627–636.

Yoshimoto, T., Kaida, K., Fukao, T., Ishiyama, K., Kamiya, T., & Murakami, N. 2013. Backward path following control of an articulated vehicle. *In System Integration (SII), 2013 IEEE/SICE International Symposium on.* IEEE: pp. 48–53

Tyre and friction

Advanced Vehicle Control – Edelmann, Plöchl & Pfeffer (Eds)
© 2017 Taylor & Francis Group, London, ISBN 978-1-138-02992-7

Friction utilization for tyre-road friction estimation on snow: An experimental study

A. Albinsson, F. Bruzelius & B. Jacobson
Department of Applied Mechanics, Chalmers University of Technology, Gothenburg, Sweden

ABSTRACT: Friction estimation using effect-based approaches are challenging during normal driving due to the large tyre excitation needed for an accurate estimate. The required excitation level varies for different tyres, road surfaces, road conditions and tyre models used in the estimator. Previous research has investigated the required friction utilization on different surfaces but due to the small sample sizes it is hard to draw any general conclusions. This paper investigates the tyre excitation required to estimate the tyre-road friction coefficient with a generic estimator for 76 different tyres on snow for five different tyre models and for different levels of measurement noise.

1 INTRODUCTION

The maximum tyre-road friction limits the horizontal forces that the tyres can generate. Knowledge about the tyre-road friction coefficient is thus useful for active safety and driver assistance systems where the appropriate intervention is dependent on the maximum available road grip. Vehicles with increasing levels of autonomous functions, such as autonomous emergency braking or, in the future, fully autonomous vehicle, can use this information to adapt the intervention thresholds or vehicle velocity based on the prevailing road conditions. The information can also be shared with other drivers or vehicles to warn them of an approaching area with low friction.

The tyre-road friction coefficient is difficult to estimate during normal driving, mainly due to the limited information about the maximum achievable tyre forces in the linear tyre region, see (Lex, 2015) and (Ray, 1997). Previous research have attempted to correlate the slip stiffness to the maximum road friction coefficient to remove the need for large tyre excitation (Gustafsson, 1997). However, the relation between the friction coefficient and the slip stiffness relies on empirical data. A-priori information about the tyres that are currently fitted to the vehicle is thus required. Another approach was evaluated experimentally in (Albinsson et al., 2015). Opposite wheel torques were added to the front and the rear axle to achieve large tyre excitation during normal driving, see also (Chen and Wang, 2011). This method, active tyre force excitation, makes it possible to achieve large tyre forces during normal driving and thus to estimate the friction coefficient.

The required utilization, i.e. here defined as the ratio of the required and maximum normalized longitudinal force, to estimate the friction coefficient within an accuracy of $\pm 15\%$ for different tyres and road surfaces is investigated in (Svendenius, 2007). However, only a few different tyres were evaluated using the brush model and it is therefore difficult to draw any general conclusions.

This study investigates how well the tyre-road friction coefficient can be estimated by fitting a non-linear tyre model to measurements on a snow surface for 76 different tyres. The estimation error that can be expected without any a-priori information about the tyre can thus be evaluated with a large sample size. Furthermore, the estimation error for different tyre models are evaluated and compared, thus indicating which tyre models that are more suitable for friction estimation on snow. Noise was added to the measurements signals to investigate how different fitting error cost functions influence the estimation accuracy.

2 METHOD

The measurements were performed for another study with the BV12 measurement vehicle from VTI (The Swedish National Road and Transport Research Institute), (Hjort and Eriksson, 2015). Four to six slip ratio sweeps up to a fully locked wheel was done in each test run. The data was filtered and the offset at zero slip was removed so that the tyre force is zero at zero longitudinal slip. The data was used as the reference tyre characteristics when evaluating the different tyre models. These tyre models assumes steady-state conditions and the slip ratio gradient should thus be kept small.

During the measurements, the maximum slip ratio gradient was around $0.2\,[(\mathrm{ms}^{-1})/(\mathrm{ms}^{-1})1/\mathrm{s}]$ at small tyre forces. With a first order relaxation model,

Equation 1, the difference between the nominal $\delta_{x,nom}$ and the actual slip ratio δ_x can be calculated as,

$$\dot{\sigma_x} = \left(\sigma_{x,nom} - \sigma_x\right)\frac{v_x}{r_{lx}} \tag{1}$$

$$\left(\sigma_{x,nom} - \sigma_x\right) = \dot{\sigma_x}\frac{r_{lx}}{v_x} \tag{2}$$

where r_{lx} is the relaxation length and v_x is the longitudinal velocity of the vehicle. Assuming that the relaxation length is 0.1 and with the longitudinal velocity of 8.33 m/s the difference between the nominal and the actual slip ratio is 0.0024 [$(ms^{-1})/(ms^{-1})$]. At a slip level of 0.05 [$(ms^{-1})/(ms^{-1})$] this corresponds to a 5% error.

The tyre relaxation will hence have an influence on the tyre characteristics and so will other measurement errors. However, the characteristics of specific road-tyre combinations are not interesting in themselves for the purpose of this study but rather the variation in the tyre-road characteristics represented by these different tyres.

The tested tyres were 9 new and 17 used studded tyres, 9 new and 16 used Nordic non-studded winter tyres, and 9 new and 16 used European non-studded winter tyres.

2.1 *Tyre models and tyre parameter fitting*

Four different tyre models are evaluated, the brush model with parabolic pressure distribution, the magic tyre formula with 4 parameters (Bakker et al., 1987), Burckhardt tyre model and Dugoff tyre model (Dugoff et al., 1969), see Equation 3–6. These tyre models are commonly used for online friction estimation, where the number of parameters is a concern due to the limited number of measurement points and since the estimation is normally done recursively.

$$f(\sigma_x) = \begin{cases} -C\sigma_x + \frac{C^2\sigma_x|\sigma_x|}{3\mu_{max}} - \frac{C^3\sigma_x^3}{27\mu_{max}^2} \; for \; |\sigma_x| \leq \frac{3\mu_{max}}{C} \\ -sign(\sigma_x)\mu F_z \; else \end{cases} \tag{3}$$

$$f(\sigma_x) = D\sin(C_m\tan^{-1}(B\sigma_x - E\left(B\sigma_x - \tan^{-1}(B\sigma_x)\right))) \tag{4}$$

$$f(\sigma_x) = c_1(1 - e^{c_2\sigma_x} - c_3\sigma_x) \tag{5}$$

$$f(\sigma_x) = \begin{cases} C\sigma_x(2-\lambda)\lambda \; for \; |\lambda| < 1 \\ C\sigma_x \; else \end{cases} \qquad \lambda = \frac{\mu_{max}}{2|C\sigma_x|} \tag{6}$$

The tyre model parameters are fitted to the measurements to minimize two different cost functions,

$$J_f = \sum_{i=1}^{N}(f_m[i] - f_d[i])^2 \tag{7}$$

Table 1. Tyre parameter constraints.

C	[2, 100]	B	[1, 100]
μ_{max}	[0.05, 1.5]	c_1	[0.05, 1.5]
D	[0.05, 1.5]	c_2	[0, 50]
E	[−1.5, 1]	c_3	[−0.01, 0.01]
C_m	[1, 1], [1, 1.6]		

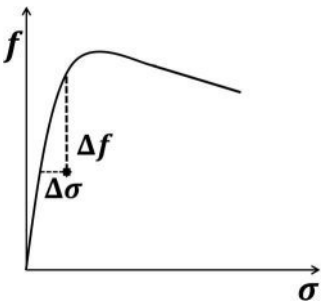


Figure 1. Cost function illustration.

$$J_s = \sum_{i=1}^{N}(f_m[i] - f_d[i])^2) + (\frac{\partial f}{\partial \sigma_d}|_{\sigma_d[i]}(\sigma_m[i] - \sigma_d[i]))^2 \tag{8}$$

f_m is the normalized force from the tyre model at the measured slip ratio, f_d is the measured normalized force, σ_d is the measured slip ratio and σ_m is the slip ratio at the measured normalized force obtained from the inverse tyre model. The cost function J_f in Equation 7 does not penalize the slip ratio error and should thus reasonably make the tyre parameter estimates more sensitive to measurement noise in the slip measurements. Equation 8 is inspired by the total least square approach but has been simplified so that the terms in the cost function is available directly from the tyre model. Figure 1 illustrates the different components in the cost functions, J_f penalizes Δf, J_s penalizes Δf and $\Delta\sigma$.

By using the cost function in Equation 8 rather than the total least square method the evaluation of the cost function is made computationally more efficient. A total-least square approach use the perpendicular distance between the measurement point and the model. However, the expressions for finding the corresponding model point σ_m,f_m are nonlinear and not easily solved analytically which results in the high computational cost. The cost function J_s is hence a compromise to get an expression that penalizes both the slip and force error that is easily obtained from the tyre models and which is easy implement online.

The parameters of the tyre models were found using the gradient based optimization function fmincon with the interior-point algorithm in Matlab. The parameters of the tyre models were constrained to obtain reasonable tyre characteristics, Table 1. The gradient based

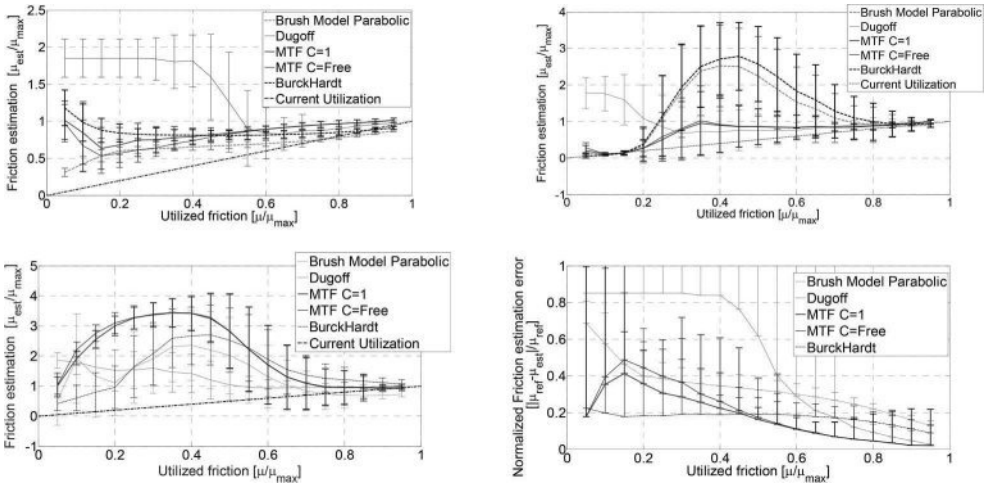


Figure 2. Mean normalized friction estimation of the measurements for the 76 tyres as a function of utilized friction with standard deviation shown as error bars. The current friction utilization is plotted as a dotted black line. Top left) Noise free input signals and minimizing force error. Top right) White Gaussian measurement noise ($\sigma^2 = 0.05^2$) added to the slip and force and minimizing force error. Bottom left) noise added to the slip and force and minimizing force & slip error (Equation 2). Bottom right) Mean and maximum friction estimation error, noise-free environment, force error minimization.

optimization approach can in some circumstances converge to a local minimum. The cost function should hence preferably have one distinct minimum and not be too flat.

2.2 *Evaluation procedure*

By using the reference tyre data from the measurements as a lookup table, an arbitrary excitation can be used to evaluate the different tyre models. However, it has to be ensured that the time derivative of the slip ratio is kept small enough to keep the tyre relaxation negligible. The excitation levels are described by the friction utilization μ_{util}, defined here as the ratio between the normalized force μ and the maximum friction coefficient $\mu_{\max}$.

The normalized estimated friction coefficient $\hat{\mu}_{norm}$ and the normalized friction estimation error $\tilde{\mu}_{norm}$ are defined as,

$$\hat{\mu}_{norm} = \frac{\hat{\mu}_{max}}{\mu_{max}} \tag{9}$$

$$\tilde{\mu}_{norm} = \frac{\hat{\mu}_{max} - \mu_{max}}{\mu_{max}} \tag{10}$$

These measures can be used to compare the results from different tyres since they are normalized with the maximum friction coefficient. The evaluations are done for different levels of white Gaussian noise added to the slip ratio and force signal. The noisy environment highlights the differences between the two different cost functions. The added noise signals are uncorrelated but has the same variance σ^2. The lower noise level, $\sigma^2 = 0.003^2$, approximately corresponds to the noise levels found for the force and slip estimates during active tyre force excitation but with a lower variance for the force estimation (Albinsson et al., 2015). Other disturbances, due to for instance suspension compliance or uneven road surfaces, are not represented by the added noise. These disturbances will influence the measurements in reality but experience a behaviour that is hard to model and analyse.

3 RESULTS

The mean of the tyre-road friction coefficient estimate, normalized with the measured maximum friction coefficient, for the different tyre models as a function of the utilized friction are shown in Figure 2. The standard deviation of the estimate is shown with an error bar.

The level of utilization required to obtain a friction estimation error of below 10% and 20% for two different noise level is presented in Figure 3–6. The noise level is the same on both the force and the slip ratio signal. Note that the limit of 10% and 20% is strict. The Dugoff model with noise std = 0.005 and using the force cost function J_f is close to the 10% error limit already from 75% utilization, see Figure 3.

The value of the cost functions for different tyre parameters has been plotted for one of the tyres with noise for the Dugoff model, see Figure 8. Different noise levels are used on the force and the slip ratio signals to more closely represent the noise found in previous work, see (Albinsson et al., 2015). Note that the cost function values has been limited to have the same scale in the different figures. The cost function J_{f}, which only penalizes the force error, does not have as distinct boundary at the lower friction values as the cost function J_{s}. The cost function J_{s} thus penalizes low friction estimates more than the cost function J_{f}. This

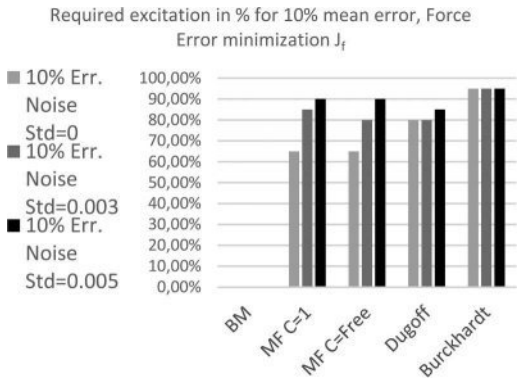


Figure 3. Required excitation in % for 10% mean error, Force Error minimization J_f.

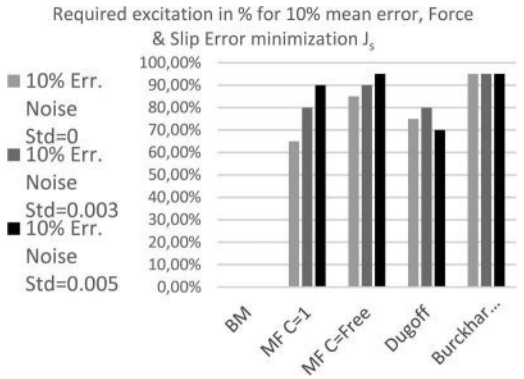


Figure 4. Required excitation in % for 10% mean error, Force and Slip Error minimization J_s.

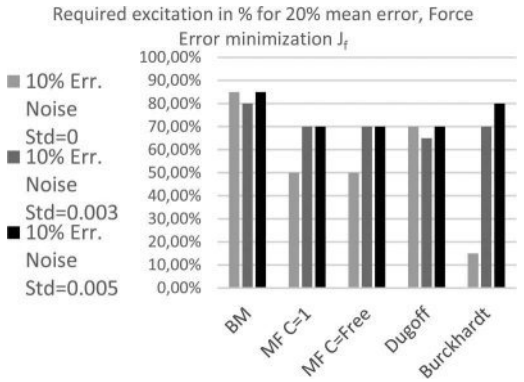


Figure 5. Required excitation in % for 20% mean error, Force Error minimization J_f.

means that the friction is more likely to be underestimated at low friction utilization when the cost function J_f is used compared to using the cost function J_s.

The reason for this can be understood by looking at Figure 1. If noise is present on both the slip signals and the force signal and only penalizes deviations in the force, measurement points as indicated in

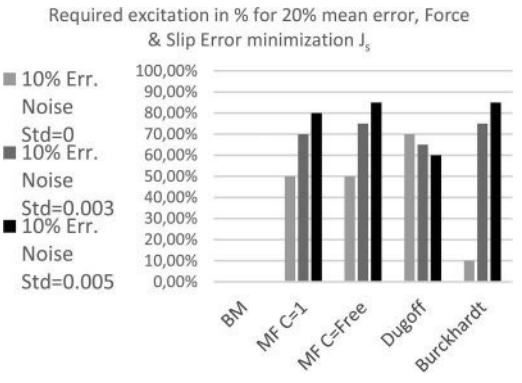


Figure 6. Required excitation in % for 20% mean error, Force and Slip Error minimization J_s.

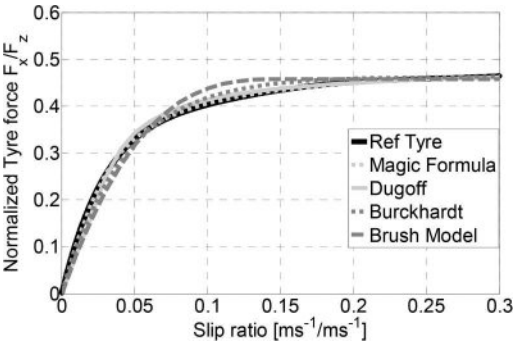


Figure 7. Example of brush model modelling error.

Figure 2 must be fitted by changing the friction coefficient. However, if the slip error is penalized as well the influence of these measurement points on the friction estimation is smaller. The tendency to underestimate the friction coefficient when only penalizing the force estimation can be seen in Figure 9 where the distribution of the normalized friction estimation error for low utilization is plotted.

4 DISCUSSION

The brush model with parabolic pressure distribution does not perform as well as the other tyre models. The mean friction estimate is lower than the current utilization even at high utilization levels. This is due to the poor fit that the brush model has for tyre characteristics on snow, see Figure 7. The difference in shape between the data and the tyre model makes it difficult to find tyre parameters that provides a good fit.

The Dugoff model fits the snow measurements better than the brush model. The models are based on the same basic assumptions but with different vertical pressure distribution in the contact patch. Both these models have only two parameters and have therefore

difficulty to fit the data when the curvature of the non-linear tyre region does not match the one described by the model.

The Magic formula and the Burckhardt model have more than two parameters and can fit the snow measurements better. As seen from Figure 3–6, the magic tyre formula has the lowest required utilization for a 10% error in the friction estimate without any measurement noise.

When adding noise, the performance of the Dugoff model does not decrease much in terms of required utilization. This makes it one of the models which require the lowest excitation levels in a noisy environment. With measurement noise, the Dugoff tyre model has lower required utilization than the magic formula. Both the Magic tyre formula together with the Dugoff tyre model shows good promise to separate between low and high friction at low excitation and to achieve accurate friction estimation at larger excitation. The tyre model of choice should thus depend on the expected noise levels. However, it is important to note that these results are only valid for one road surface. On other road surfaces the tyre models may not perform as well. Similar studies should thus be performed on other road surfaces to investigate the change in friction estimation error for the different road surfaces. The Burckhardt model maintains the same performance in terms of required utilization (for ten percent error) when adding noise, however the Burckhardt model seems to require a larger excitation level compared to the magic formula and the Dugoff model.

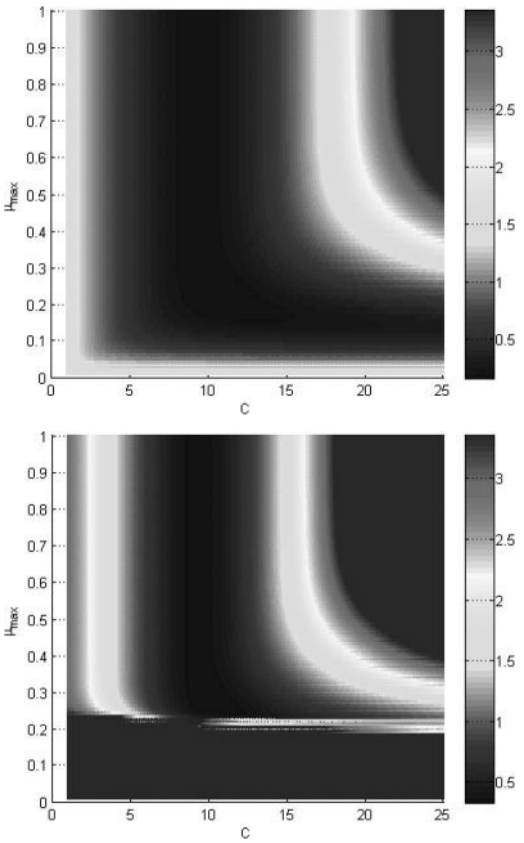


Figure 8. Cost function value for Dugoff tyre model for one of the tyres, with added noise on the force signal $\sigma_f^2 = 0.03^2$ and the slip signal $\sigma_{\sigma_x}^2 = 0.003^2$. Right plot for J_s, left plot for J_f. All plots at 30% friction utilization with $\mu_{ref} = 0.54$.

4.1 *Cost function and measurement noise*

When noise is present on both the force and the wheel speed signal, only minimizing the force error can provide poor estimates since the friction coefficient estimate tends to follow the current utilization at low tyre utilizations.

The additional slip term in the alternative cost function, Equation 2, creates a more distinguished separation between low and high friction at low tyre utilizations, see Figure 2. It penalizes low friction estimates more compared to only minimizing the force error, see Figure 10. Although the actual friction coefficient is unknown, the separation makes it possible to distinguish between high- and low-friction surfaces at low excitation levels. The Dugoff model is not as sensitive to measurement noise as the other models at

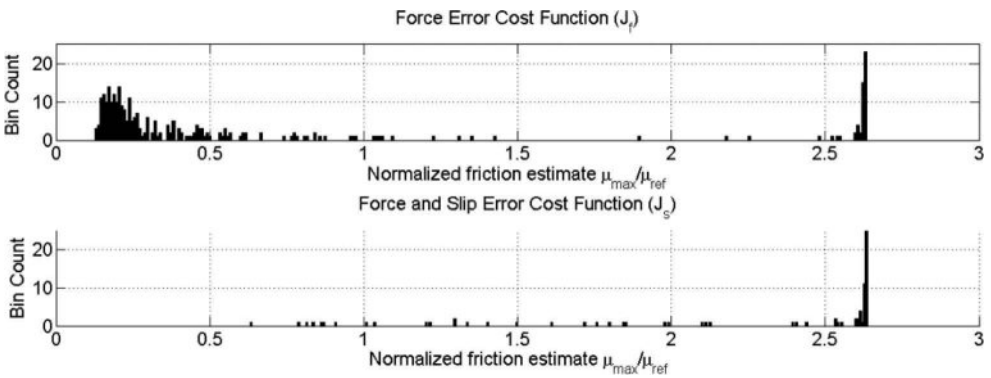


Figure 9. Normalized Friction estimation distribution μ_{max}/μ_{ref} for the brush model at 20% friction utilization and for 300 noise realizations. Force noise variance $\sigma_f^2 = 0.03^2$ and slip noise variance $\sigma_{\sigma_x}^2 = 0.003$.

low excitation. This is likely due to the fact that the Dugoff model is exactly linear at low tyre excitations. The cost function should thus be chosen depending on the noise level and the chosen tyre model.

4.2 *Required tyre excitation*

The required tyre excitation to estimate the friction coefficient with an average error of less than 10% and 20% is presented in Figure 3–6. As seen from the figures, the lowest required excitation can be found for the magic tyre formula (both with locked and estimated C_m parameter) that has a required excitation of 65% (for 10% error) in a noise free environment. As expected the required excitation increases for increasing noise levels and with a white Gaussian noise with a standard deviation of 0.005 the required excitation has increased to 90% for the magic formula. This trend is similar for both cost functions.

Naturally, noise and disturbances cannot be avoided in the real-world application where compliances in the suspension, uneven road surfaces, varying pitch angle all affect the measurement signals. These disturbance are most likely not zero mean white Gaussian noise as used in this study and may further increase the need for large excitations. Nevertheless, the results illustrates the importance of actively working towards minimizing any noise and disturbances.

It should also be noted that this is the excitation required to reach a mean error of below 10%. The error distribution is not shown here. However, it was found that at the excitation level required for 10% mean error in a noise free environment the maximum error was within 15% for all tyre models.

In this study, 200 samples were used for friction estimation. This corresponds to 2 s in a system with 100 Hz sampling time. With the vehicle used in previous studies, see (Albinsson et al., 2015), which had a maximum torque gradient of 1200 Nm/s the maximum front axle torque that can be reached is 2400 Nm or approximately 7500 N. For the vehicle in question it is enough to reach a normalized force of 0.92 [N/N] and thus enough to achieve 100% friction utilization on snow. Naturally the required torque may not be reached at higher velocities for vehicles with less powerful engines.

5 CONCLUSION AND FUTURE WORK

The brush model is not suitable for friction estimation on snow. The friction estimation error never goes below 10% and it has large modelling errors, see Figure 3–6 and Figure 7. The Dugoff model and the Magic formula on the other hand performs better with a lower required excitation. The Magic Formula requires lower excitation levels in a noise free environment. However, when adding noise to the slip and force signal the difference between the Dugoff Model and the Magic Formula in terms of required excitation is smaller. With noise added to the slip and force signals, the required excitation generally increase. In order to increase the performance of the estimator the noise and disturbance should hence be reduced as much as possible.

Similar measurements have been performed on wet asphalt and a similar study should be performed for these measurements as well. It is expected that the relative performance of some tyre models will change when the surface is changed from snow to wet asphalt due to modelling errors which favours one of the surfaces.

REFERENCES

Albinsson, A., Bruzelius, F., Gustafsson, T., Jonasson, M. & Jacobson, B. Identification of tyre characteristics using active force excitation. 24th International Symposium on Dynamics of Vehicles on Roads and Tracks, 2015 Graz, Austria.

Bakker, E., Nyborg, L. & Pacejka, H. B. 1987. Tyre modelling for use in vehicle dynamics studies. SAE Technical Paper.

Chen, Y. & Wang, J. 2011. Adaptive vehicle speed control with input injections for longitudinal motion independent road frictional condition estimation. *Vehicular Technology, IEEE Transactions on*, 60, 839–848.

Dugoff, H., Fancher, P. S. & Segel, L. 1969. Tire performance characteristics affecting vehicle response to steering and braking control inputs. Ann Arbor, Michigan: Highway Safety Research Institute.

Gustafsson, F. 1997. Slip-based tire-road friction estimation. *Automatica*, 33, 1087–1099.

Hjort, M. & Eriksson, O. 2015. Test av is- och snögrepp för slitna vinterdäck. Jämförelse av olika kategorier av vinterdäck. www.vti.se Swedish National Road and Transport Research Institute (VTI).

Lex, C. 2015. *Estimation of the Maximum Coefficient of Friction between Tire and Road Based on Vehicle State Measurements.* PhD dissertation, Graz University of Technology.

Ray, L. R. 1997. Nonlinear tire force estimation and road friction identification: simulation and experiments. *Automatica*, 33, 1819–1833.

Svendenius, J. 2007. *Tire modeling and friction estimation.* Lund University.

Advanced Vehicle Control – Edelmann, Plöchl & Pfeffer (Eds)
© 2017 Taylor & Francis Group, London, ISBN 978-1-138-02992-7

Wheel force measurement for vehicle dynamics control using an intelligent bearing

S.M.A.A. Kerst, B. Shyrokau & E.G.M. Holweg
Delft University of Technology, Delft, The Netherlands

ABSTRACT: The measurement and estimation of wheel loads is an interesting and complex topic relevant for vehicle dynamics control. Accurate wheel load information allows for more straight-forward, more robust and more efficient control. In this paper a novel model based wheel load reconstruction approach is presented. An Unscented Kalman Filter is used to reconstruct the unknown wheel loads by analysis of the deformation of the bearing outer-ring. The performance of the approach is demonstrated by field tests using an instrumented passenger car. Results show that the proposed approach is well able to reconstruct both tilting and self-aligning moments as well as lateral and vertical wheel forces during various steering maneuvers.

1 INTRODUCTION

Accurate information of the forces and moments generated at the tire-road contact is important for active vehicle safety and driving assistance systems. For control of the vehicle accurate knowledge of these loads is paramount. While currently indirect estimation approaches are used, an accurate high bandwidth direct measurement could result in more straight-forward, more robust and more efficient control approaches. It is mainly due that it is an active field of research, which has resulted in numerous measurement approaches.

These load measurement approaches vary significantly in terms as components used, methodologies applied and number of reconstructed loads, accuracy and bandwidth. Examples of some load measurement approaches are tire inner-liner acceleration based (Cheli et al., 2015), tire sidewall deformation based (Suzuki et al., 2007), wheel rim deformation based (Rupp et al., 1993), suspension bushing deformation based (Chae et al., 2000) and bearing displacement (Nam, 2015) or deformation based (Mol, 2004) approaches.

The current unavailability of any commercial feasible wheel load measurement approach reflects the difficulty in generating an accurate, robust, durable as well as inexpensive load measurement for passenger vehicles.

In this study focus is put on upgrading the bearing to a load measurement device. Usage of the bearing has considerable advantages as it (i) usually serves the entire lifetime of the vehicle; (ii) allows for straightforward data acquisition; (iii) allows for the measurement of brake forces and (iv) has low impact on the dynamic behavior of the vehicle (Kerst et al., 2016).

After an introduction to the concept of bearing load measurement (section 2), this paper presents a novel model based reconstruction approach based on bearing deformation (section 3). A basic description of the used models is provided and the reconstruction concept, using an Unscented Kalman Filter, is presented. The experimental setup is discussed in section 4, after which in section 5 results are presented and discussed. The final section will draw conclusions and discuss the future work.

2 BEARING LOAD MEASUREMENT

All loads generated at the wheel level, either originating from the tire-road contact patch of friction brakes, are transmitted towards the vehicle via the wheel bearing, knuckle, suspension linkages and strut. These components therefore allow for the reconstruction of some or all of the wheel loads using various methodologies (Kerst et al., 2016). For the bearing level the load path is visualized in figure 1. The wheel loads are applied to the bearing system at the inner-ring via a rigid connection with the wheel. This load is transferred via the rolling elements of the double-row ball bearing towards the non-rotating outer-ring. Finally the connection with four bolts to the knuckle provides the load equilibrium for the bearing system.

The transfer of wheel loads towards the knuckle naturally causes deformation and stresses in the bearing components, which on its turn results in relative rotation and translation between inner- and outer-ring.

2.1 *Bearing load measurement approaches*

Based on the previous one can identify two principally different sources for bearing load measurement,

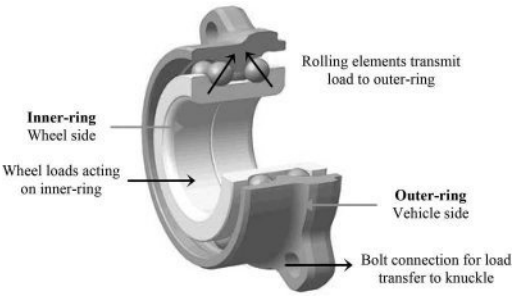


Figure 1. A CAD model of the HUB3 bearing unit of a BMW 5-series passenger car providing a general idea of the load path.

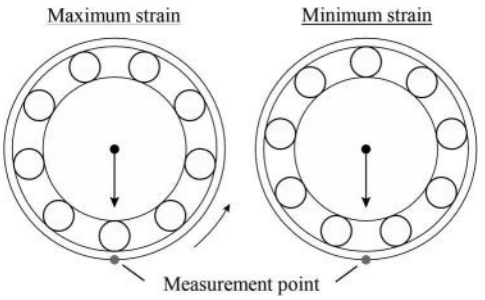


Figure 2. Movement of rolling elements causes the measurement point to register fluctuating deformation/strain even at constant loading.

namely displacements and deformations. Displacement based approaches focus on the relative translations and/or rotations of the inner-ring with respect to the outer-ring as measurement input (Nam, 2015). Deformation based approaches on the other hand focus on the resultant strain at the surface of the stationary outer-ring as a consequence of the applied loading. This latter is further discussed and extended in this paper.

2.2 *Deformation based bearing load measurement*

The deformation of the stationary outer-ring is captured using strain gauges. Placement of several gauges at different azimuth rotations on the outer ring allows for the reconstruction of direction and magnitude of the bearing load. An important bearing related aspect, visualized in figure 2, also plays an important role in the load reconstruction.

As generally understood, the rotational degree of freedom of the bearing is obtained by the movement of rolling elements. This rotational degree of freedom causes significant variation in the arrangement and deformation of the bearing. Any strain measurement therefore always captures varying strains even when the applied load is constant.

Furthermore, an even more challenging effect arises due to the close proximity of in- and outboard rows of

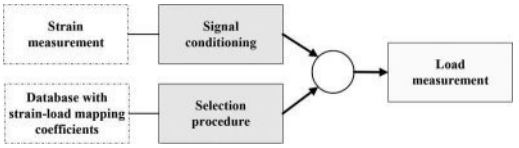


Figure 3. Schematic overview of current deformation based bearing load sensing approaches.

the vehicle wheel double row ball bearings. This results in a strain measurement that comprises a superposition of varying strains from both in- and outboard element rows. This is more thoroughly discussed in a previous publication (Kerst et al., 2016).

In order to accommodate accurate load reconstruction any bearing load measurement approach or algorithm should be able to cope with these latter non-linearities appropriately. Especially the last aspect of strain superposition is a challenging task.

2.3 *State of the art*

Current approaches found in literature (Nishikawa, 2011; Kerst et al, 2015) cope with the previously introduced characteristics in a similar way. The methodologies can be best explained using the scheme as presented in figure 3.

Although using a different implementation, the signal conditioning of both approaches is similar as the variation due to passing elements is filtered. However, by doing so the in- and outboard strain contributions are lumped in a single measurement, which leads to a high non-linear relationship with respect to the input loads. Now in order to produce a correct estimate the non-linear relationship is linearized at numerous loading conditions resulting in a database of strain-load mapping coefficients. A selection procedure is employed for coefficient selection to determine the wheel load at different loading conditions.

Although results of both approaches seem interesting the solutions are suboptimal (due to lumping of in- and outboard contributions) and may lack robustness due to the necessity of coefficient selection depending on the maneuver.

3 PROPOSED MODEL BASED APPROACH

Instead of strain filtering and in-situ mapping of the strains to loads, in this paper a bottom-up model based reconstruction approach is proposed. Based on modeling of two fundamental parts of the relevant physics the in- and outboard strain contribution can be distinguished. This results in a generally valid approach producing accurate load measurements without the need of different mapping coefficients for different loading conditions.

In the following first a brief description of the relevant physical models will be presented, after which the model implementation using an Unscented Kalman Filtering (UKF) approach is discussed. Note that

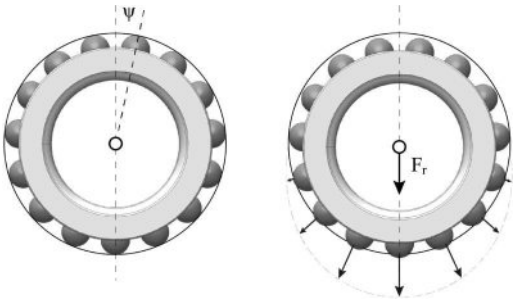


Figure 4. Single degree of freedom example of the element force distribution when a single load is applied.

although the description is considerably simplified due to page limitations, most relevant aspects regarding the approach are presented.

3.1 *Internal load distribution*

The normal load of a single element in a roller bearing can be described by (Harris and Kotzalas, 2006):

$$Q = K_n \delta^{\frac{3}{2}} \tag{1}$$

where Q = the element normal load; K_n = combined raceway-element load-deflection factor; and δ = the normal approach of both raceways. Factor K_n is dependent on the contact curvatures, rolling element radius and the moduli of elasticity of rollers, inner- and outer-ring.

With the assumption of a rigid rings, the normal approach at each element azimuth rotation ψ is fully defined by the relative displacement and rotations of inner- and outer-ring (Harris and Kotzalas, 2006). For example, consider the bearing of figure 4, which has only a single degree of freedom, being the displacement in vertical direction.

In this case, considering zero radial clearance, the relative normal approach for each rolling element azimuth rotation ψ can be described by:

$$\delta(\psi) = \Delta_r \cos(\psi) \tag{2}$$

where Δ_r = the vertical displacement of the bearing inner-ring with respect to the outer-ring; and ψ = the azimuth rotation. All rolling element forces can now be fully described by combining equations 1 and 2.

3.2 *Relation between element and bearing forces*

The most heavily loaded rolling element can be related to the bearing radial, axial and moment loads using the load-integrals J_r, J_a and J_m respectively (Harris and Kotzalas, 2006). In fact, any loaded element at any azimuth rotation ψ can be related to the bearing loads when the appropriate load-integral J is known.

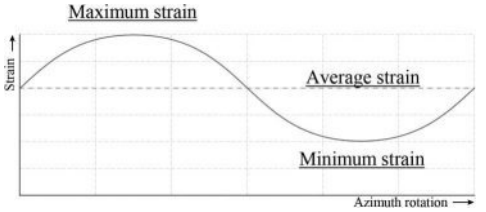


Figure 5. Observed strain when a single rolling element passes the measurement point at constant loading.

Considering the example of figure 4, any loaded element can be related to the bearing force using:

$$F_r = Q(\psi) J_r(\psi) \tag{3}$$

where F_r = the force in vertical direction; $Q(\psi)$ = the element force in azimuth direction ψ; and $J_r(\psi)$ = the load integral for vertical direction at the corresponding azimuth rotation.

3.3 *Relation between strain and element forces*

As described in section 2, the reallocation of rolling elements results in a varying strain pattern at the outer circumference of the bearing. For a constant loading case, this results in a (close-to) sinusoidal strain pattern as presented in figure 5.

Both average and strain amplitude of this measured signal relate to the local element loading. Although previous approaches focus on the average strain, in this study the strain amplitude is considered. It is found that, at constant approaching angles, the strain amplitude is (close to) linearly related to the local rolling element force. The sensitivity of strain amplitude to the element force is dependent on the outer-ring geometry, material and boundary conditions but in a general sense can be described as follows:

$$\varepsilon = Q G_{\varepsilon Q}(\psi \cdot n) \tag{4}$$

where ε = the measured strain; $G_{\varepsilon Q}$ = the periodic transfer function of Q to ε; and n = the number of rolling elements. As all rolling elements are identical n periods of $G_{\varepsilon Q}$ are encountered per full rotation of the bearing cage.

3.4 *UKF load reconstruction approach*

Based on the previously introduced analytical description the bearing state can be related to the outer circumferential bearing strain by combining the internal load distribution formulae with the element force to strain relationship. Using an UKF approach the internal states and element forces can be determined by minimization of the modeled strain with respect to the measured outer-circumferential bearing strain. The wheel loads can be reconstructed by multiplication of the UKF determined element forces with the appropriate load-integrals.

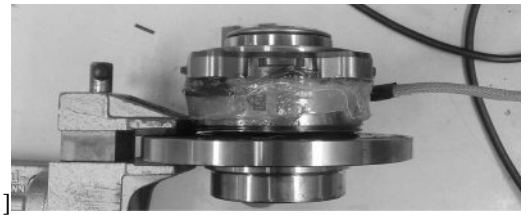


Figure 6. The prototype Intelligent Bearing.

Based on the described analytical model, the proposed load reconstruction UKF model includes:

- A five degrees of freedom bearing model containing 3 displacements Δ_x, Δ_y and Δ_z and 2 rotations θ_x and θ_y of inner- to outer-ring;
- An accurate model of $G_{\varepsilon Q}(\psi)$ for each element row at each measurement location based on a FEM study;
- Load-integrals determined by a multi-variable regression analysis using a calibration dataset (as discussed in the experimental setup section).

Within the UKF furthermore additional states are added to (i) cope with slowly varying strain variations (i.e. temperature related deformation) and (ii) capture global deformation of the bearing such to capture effects arising due to non-rigidness of the outer-ring. The latter two aspects are not discussed due to page limitations, and will be more thoroughly discussed in future publications.

4 EXPERIMENTAL SETUP

4.1 *Intelligent Bearing prototype and test vehicle*

For experimental testing and validation of the approach a BMW 5-series test vehicle is equipped with four prototype Intelligent Bearings (figure 6). The update considers placement of strain gauges on the bearing outer-ring and additional signal conditioning electronics. Furthermore, the vehicle is equipped with a RaceLogic GPS speed sensor (VBSS100SL) for vehicle speed and location logging and VELOS wheel force transducer (Rupp et al., 1993) for determination of reference wheel loads. A dSpace AutoBox is used for data acquisition.

As only one measurement rim is available, mounted on the front right as visible in figure 7, the results section only focusses on the load reconstruction at a single corner of the vehicle.

4.2 *Test procedure*

Driving tests were performed during two two-day test sessions in June and July 2016 at the former military air base Valkenburg. Although various tests were performed, current focus lies on steering maneuvers: left/right cornering with constant radius at both constant and increasing speeds and step steer maneuvers.



Figure 7. The test vehicle at the test site (Valkenburg Airstrip).

As steering maneuvers are at interest, it is chosen to focus on the reconstruction ability of tilting moment (M_x), self-aligning moment (M_z) and lateral (F_y) and vertical force (F_z).

4.3 *Determination of load-integrals*

The load-integrals, used to reconstruct the wheel forces based on rolling element forces, are determined using a multi-variable regression analysis based on numerous driving tests. As the integrals are determined using the measurement rim as reference all results are in the VELOS local coordinate system. Furthermore note that the results presented are not in the calibration set and that for all presented tests the same load-integrals are used.

5 RESULTS AND DISCUSSION

In this section the results of the load reconstruction approach during 3 steering maneuvers are presented and discussed.

5.1 *Cornering with increasing speed (left)*

In this first validation experiment during a left cornering maneuver an approximately constant radius is tracked while increasing vehicle speed. A slow speed increase is chosen, such to show the load estimation performance over a large excitation range at near steady state cornering conditions. The driving trajectory and vehicle speed during the experiment are presented in figure 8.

Within the figure the starting point, loss of control and vehicle stopping point are indicated. Figure 9 shows the vehicle lateral acceleration and relevant wheel loads during the maneuver.

From the figure it can be clearly seen that all reconstructed loads being reconstructed accurately. Only the self-aligning moment (M_z) shows significant error when the friction limits are reached. This latter is most probably related to the calibration set being too focused on the stable region.

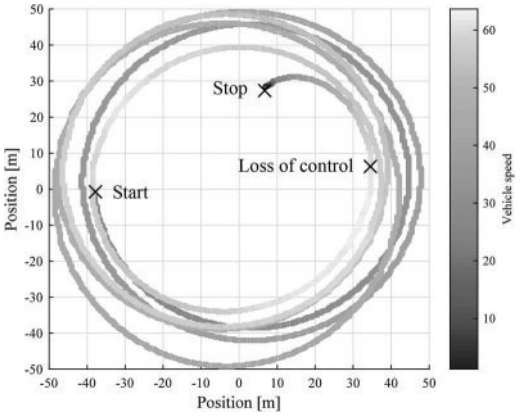


Figure 8. Top view plot of the trajectory and speed of the vehicle during experiment 1.

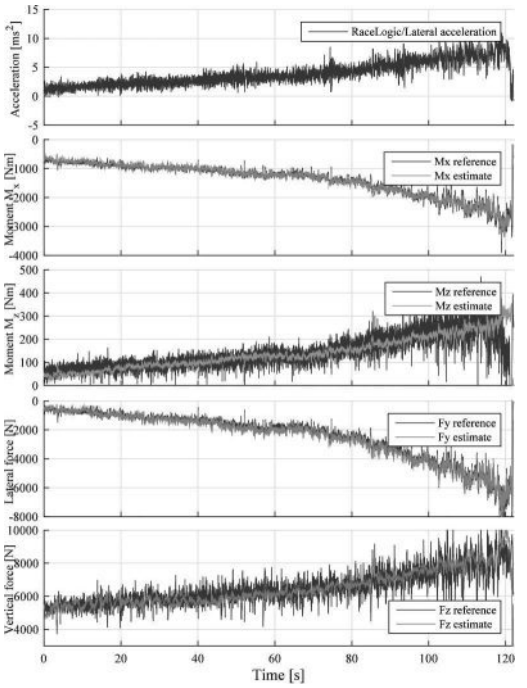


Figure 9. a 120 second capture of the load reconstruction during a cornering maneuver at increasing vehicle speed tracking an approximately constant radius. (Captured on June 9th 2016).

5.2 *Step steer (left)*

This second validation experiment is focused on load reconstruction during a more dynamic driving situation. An aggressive left turn cornering maneuver is initiated at a vehicle speed of approximately 75 km/h. Figure 10 shows the results of this test.

From the results several observations can be made. First of all, during the initial straight driving, offsets in all estimates can be observed. This is mainly due to the

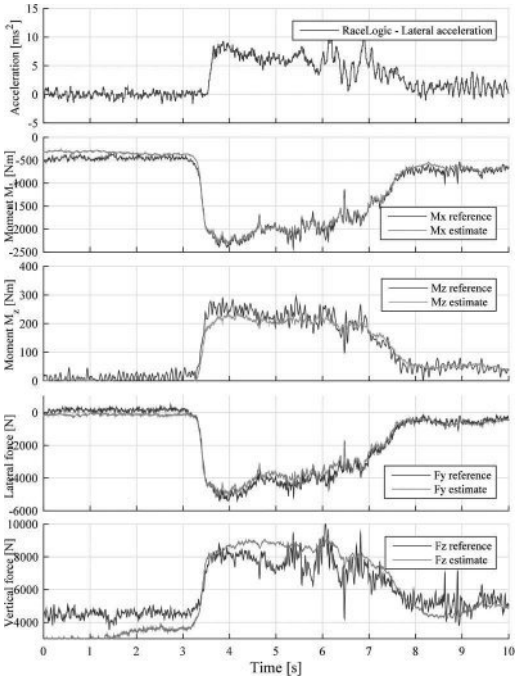


Figure 10. An aggressive left corner step steer maneuver, starting at an initial speed of 75 km/h. (Captured on July 21st 2016).

low signal to noise ratio of the strain measurements as the bearing is only moderately excited. The aggressive load increase due to the step steer input is accurately captured with minimal delay. During the steering maneuver tilting moment (M_x), self-aligning moment (M_z) as well as lateral force (F_y) are reconstructed well. The algorithm however has difficulties reconstructing the vertical load (F_z), due to the aggressive dynamics of the maneuver.

5.3 *Steady state cornering (right)*

The last validation experiment treats steady state cornering at constant speed. During the experiment at a vehicle velocity of 50 km/h a circle with a radius of approximately 25 m is tracked in clockwise direction. In figure 11, a 5 second capture is presented allowing for a more close analysis of the reconstruction ability at higher frequencies.

Analyzing the results, it can be observed that the closely related tilting moment (M_x) as well as lateral force (F_y) are tracked well with considerable bandwidth. The self-aligning moment (M_z) does not reconstruct the heavily oscillating reference. However, this could also be related due to the inaccuracy of the reference itself. Furthermore, it is again observed that the high frequency content of vertical load (F_z) is not captured well, although over time the estimate seems to converges towards the actual average vertical load.

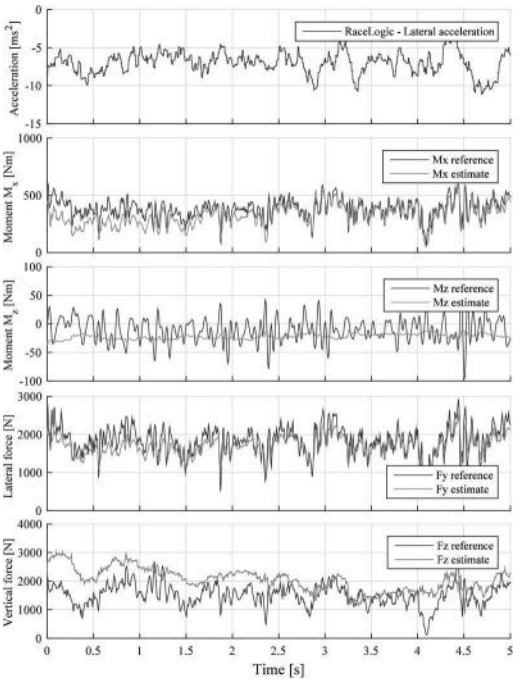


Figure 11. Steady state clockwise cornering at a constant vehicle velocity of 50 km/h. (Captured on June 9th 2016).

6 CONCLUSIONS AND FUTURE WORK

Overall it can be stated that the novel model based bearing load measurement approach is well able to reconstruct the wheel loading during various steering maneuvers. Both tilting moment (M_x) as well as lateral force (F_y) are reconstructed accurately up to considerable bandwidth in all cases. Self-aligning moment (M_z) is also well representative, although lacking high frequency content. However, the accuracy of the reference M_z is also debatable. The measurement ability regarding the vertical force (F_z) is good at low dynamical loading but lacks accurate tracking ability in more dynamic conditions.

An important facet of the results is that all loads were accurately reconstructed with identical filter model settings and without any form of re-calibration, this whilst the two test sessions were dated more than one month apart. This in contrary to the reference measurement rim, which was bound to re-calibration and alignment every two hours.

The accurate reconstruction results and stability with respect to calibration are encouraging and future work will focus on further testing and validation of the approach in additional driving situations. For these future tests a more reliable reference measurement rim will be used. Furthermore, the foundation of the approach, namely the bearing model, is still under development in order to improve robustness and accuracy during more dynamic situations.

REFERENCES

Chae, C.-K., Bae, B.-K., Kim, K.-J., Park, J.-H. & Choe, N.-C. 2000. A Feasibility Study on Indirect Identification of Transmission Forces through Rubber Bushing in Vehicle Suspension System by Using Vibration Signals Measured on Links. *Vehicle System Dynamics*, 33: 327–349.

Cheli, F., Ivone, D. & Sabbioni, E. 2015. Smart Tyre Induced Benefits in Sideslip Angle and Friction Coefficient Estimation. *Sensors and Instrumentation*, 5: 73–83.

Harris, T. A. & Kotzalas, M. N. 2006. Essential concepts of bearing technology, *CRC press*.

Kerst, S., Shyrokau, B. & Holweg E. 2015. "Anti-lock Braking Control based on Bearing Load Sensing," *Proc. of EuroBrake 2015,* Dresden, Germany

Kerst, S., Shyrokau, B. & Holweg, E. 2016. Reconstruction of Wheel Forces Using an Intelligent Bearing. SAE Int. J. *Passeng. Cars – Electron. Electr. Syst.*, 9: 196–203.

Nam, K. 2015. Application of Novel Lateral Tire Force Sensors to Vehicle Parameter Estimation of Electric Vehicles. *Sensors*, 15: 385–401.

Mol, H. Method and sensor arrangement for load measurement on rolling element bearing based on model deformation, *patent No. PCT/NL2004/000641*.

Nishikawa, K. 2011. "Hub Bearing with Integrated Multi-axis Load Sensor," *Technical Review, no.77*.

Rupp, A., Grubisic, V. & Neugebauer, J. 1993. Development of a Multi-Component Wheel Force Transducer – A Tool to Support Vehicle Design and Validation, *SAE Technical Paper*, 930258.

Suzuki, M., Nakano, K., Miyoshi, A., Katagiri, A. & Kunii, M. 2007. Method for sensing tire force in three directional components and vehicle control using this method. *SAE Technical Paper*, 2007-01-0830.

Advanced Vehicle Control – Edelmann, Plöchl & Pfeffer (Eds)
© 2017 Taylor & Francis Group, London, ISBN 978-1-138-02992-7

The influence of tire transient property on vehicle behavior

T. Takahashi
Toyota Central Research and Development Laboratories, Inc., Nagakute, Aichi, Japan

ABSTRACT: The formerly developed tire model which describes the tire transient response of side force and aligning moment under the time-varying vertical load was implemented to the vehicle dynamics simulation software (IPG CarMaker) and the influence of tire side force transient property on the vehicle behavior was investigated. The vehicle responses with/without tire transient property on sinusoidally undulated road surfaces were simulated and compared. It was seen that the average lateral acceleration of the vehicle to the sinusoidal steering wheel angle input decreases on undulated roads of rather long wavelength (3m) for both cases, but when the wavelength becomes shorter (1m), the average lateral acceleration increases only in the case that the transient property is considered. Also the steady state turning behavior of the vehicle on undulated roads was shown.

1 INTRODUCTION

In the analysis of vehicle handling behavior, the road surface is assumed as flat and even in most cases. On the other hand, the road unevenness is considered in the analysis of riding comfort, but the vehicle straight running is assumed mostly. It is needless to say that the actual roads on which the vehicles are driven are undulated more or less.

So, the author et al. studied the tire cornering characteristics under the time-varying vertical load considering the road undulation. In this paper, those studies are summarized briefly at first. Then the developed tire response model will be implemented in the vehicle dynamics simulation software to study the influence of tire transient characteristics on the vehicle handling behavior. As the first step of this study, some simulated results will be presented and discussed here.

2 FORMER STUDIES

2.1 *Responses at small slip angles*

Because the tire contact area with the road surface can be assumed as the complete adhesion at small slip angle range, the simple pragmatic tire model of side force and aligning moment under time-varying vertical load was developed by introducing the nonlinear properties of model parameters based on so-called stretched string concept (Pacejka 2012). The calculated results by the model were compared with the experiments which were performed by the special test rig on which the tire vertical load was excited by various frequencies to change the wavelengths under the constant slip angle and the speed. It was found that the average values decrease when the wavelength becomes shorter. The loss is composed of 'static loss' and 'dynamic loss' and the latter is caused from the variation of the relaxation length. It was concluded that the developed tire model agrees well with the experiments in the range of wavelengths not less than about two meters (Takahashi & Pacejka 1988).

2.2 *Extension to large slip angle range*

When the slip angle becomes larger, the assumption of complete adhesion in the tire-road contact area cannot hold any more, because the partial sliding occurs. As the result, the linear relation of side force and aligning moment against slip angle at steady state conditions cannot be used. For the expression of those characteristics, the Magic Formula tire model was introduced. After some improvements of the tire model (Takahashi & Pacejka 1992), finally the following tire model was newly developed (Takahashi & Hoshino 1996, Takahashi 2008).

$$\sigma^* \frac{dv_1}{dx} + v_1 = \sigma^* \tan(\alpha) \tag{1}$$

$$\alpha_1 = \tan^{-1}\left(\frac{v_1}{\sigma^*}\right) \tag{2}$$

$$F_y = F_{y,stat}(\alpha_1,\ F_z) \tag{3}$$

$$M_z' = M_{z,stat}(\alpha_1,\ F_z) \tag{4}$$

$$M_{zgyr} = C_{gyr} V^2 \frac{dF_y}{dx} \tag{5}$$

$$M_z = M_z' + M_{zgyr} \tag{6}$$

$$\sigma^* = \sigma^*(\alpha_1,\ F_z) = \sigma_0(F_z) \frac{\sin\left\{\tan^{-1}(C_\sigma \alpha_1)\right\}}{C_\sigma \alpha_1} \tag{7}$$

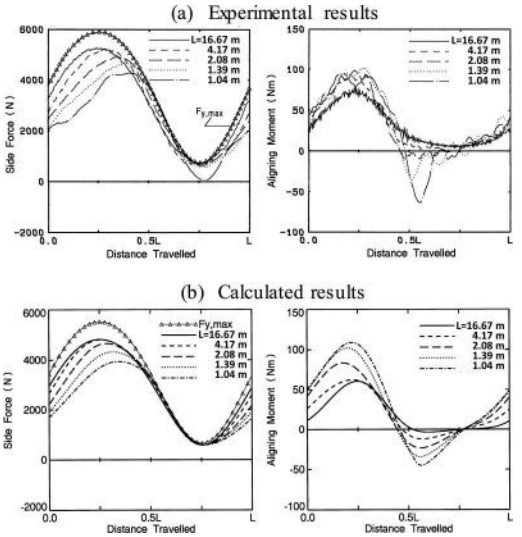


Figure 1. Side force and aligning moment under time-varying vertical load (V = 30 km/h, $\alpha = 6$ degrees).

Here,
C_σ: coefficient of σ^*
C_{gyr}: gyroscopic coefficient
F_y: side force
$F_{y,stat}$: side force described by Magic Formula
F_z: vertical load
M_z: total aligning moment
$M_{z,stat}$: aligning moment described by Magic Formula
M_z': aligning moment due to tire lateral distortion
M_{zgyr}: gyroscopic couple
V: forward speed
v_1: lateral deflection at leading edge of tire string model
x: distance travelled
α: slip angle
α_1: equivalent slip angle
σ_0: relaxation length at slip angle 0
σ^*: intersection length

The concepts of this model are, 1) to calculate the lateral deflection at the leading edge of tire string model by solving the differential equation 1(Pacejka 2012, 336–338), 2) to define the equivalent slip angle by that deflection and the intersection length (Equation 2), 3) to introduce the intersection length dependency on the equivalent slip angle and the relaxation length at slip angle 0 (Equation 7). Finally, the side force and the aligning moment due to lateral deflection are calculated by using the Magic Formula (Equation 3, 4). The gyroscopic couple due to the tire lateral deformation (Equation 5) is added to the total aligning moment (Equation 6). In the numerical calculation of Equation 1 and 5, the state variable x (distance travelled) will be transformed by using the relation, $dx = Vdt$.

The experimental and calculated results are shown in Figure 1, in which the slip angle and the forward speed were set to constant values, 6 degrees and 30 km/h, whereas the vertical load was fluctuated sinusoidally at various frequencies (wavelengths). The mean value of vertical load was 3 kN and the amplitude of fluctuation was 2.5 kN. Figure 2 shows the experimental (plots) and the calculated results of dynamic loss of side force. It seems that the model agrees well with the experiments in the range of wavelengths less than 1 meter, but more experiments are needed for the confirmation (Takahashi & Hoshino 1996).

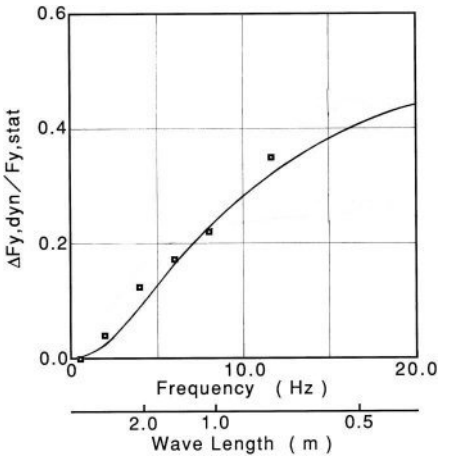


Figure 2. Comparison of dynamic loss of side force between calculation and experiments (V = 30 km/h, $\alpha = 6$ degrees).

3 SIMULATION ENVIRONMENT AND VEHICLE/TIRE MODELS

3.1 *Simulation environment*

The tire model explained above was newly implemented to the vehicle dynamics simulation software, CarMaker which has been distributed by IPG Automotive GmbH. In the simulation, both of the original tire model (Magic Formula) and the new model can be used.

3.2 *Vehicle model*

The model of front-wheel-drive vehicle with diesel engine of 1400 cc displacement was developed in CarMaker environment. The main specifications are below.

- Total vehicle mass: 1460 kg
- Load distribution: Front/Rear = 60/40%
- Wheel base: 2510 mm
- Tread base: Front/Rear = 1460/1445 mm
- Tire size: 195/50R16 (Air pressure: Front/Rear = 220/200 kPa).

3.3 *Tire model*

The Magic Formula (abbreviated as MF) tire model of side force and aligning moment are shown in

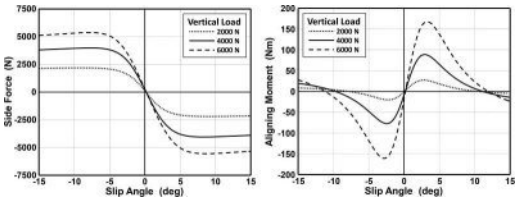


Figure 3. Magic Formula tire model of side force and aligning moment of front tire (air pressure = 2.2 kPa).

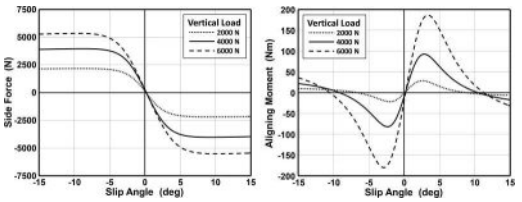


Figure 4. Magic Formula tire model of side force and aligning moment of rear tire (air pressure = 2.0 kPa).

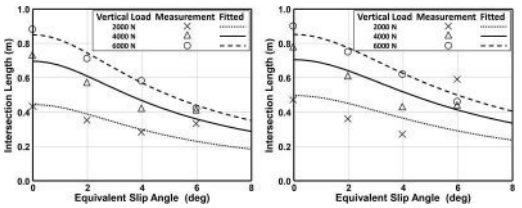


Figure 5. Relation of intersection length and equivalent slip angle of front and rear tires.

Figure 3 and 4, which are used in the original and in the new transient tire model. As known well, MF is the measured-data-based identification tire model. Although the front and rear tires are same, the air pressure is different.

Figure 5 shows the relation of the intersection length and the equivalent slip angle which is used only in the new model. For the measuring method, refer to Takahashi & Hoshino (1996). In the figure, plots are measured data and the curves show the calculated results from Equation 7 (C_σ was obtained by fitting to measured data).

4 RESPONSE AT SINUSOIDAL STEERING ANGLE INPUT

4.1 *Condition of simulation*

The purpose of this study is to investigate the influence of tire transient properties on the vehicle handling behavior under time-varying vertical load. To do so, the undulated roads were defined in CarMaker simulation environment. The road is undulated sinusoidally

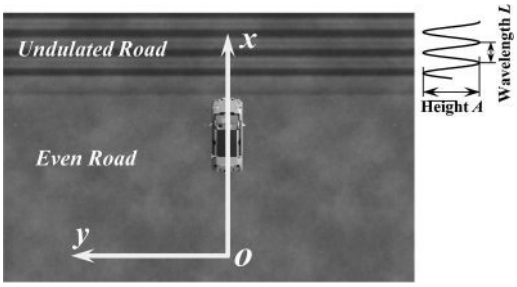


Figure 6. Definition of undulated roads in CarMaker.

only in the x direction (global coordinate) of the wavelength (notated as L) and the height (peak-to-peak value of sine wave, notated as A), whereas the height is constant in the y direction (see Fig. 6). As mentioned in the former chapter, the new tire transient model may agree with measurements in the range of wavelength longer than 1 m or so, L was changed variously longer than 1 m. The height A was changed in the range that 4 tires keep in contact with the road.

In this chapter, the simulated results of vehicle response will be shown at constant running speed of 60 km/h and at sinusoidal steering wheel angle input of ±60 degrees, 3 seconds period.

4.2 *Results and discussion*

Figure 7 shows the results at $L = 3$ m, $A = 6$ cm and Figure 8 shows the results at $L = 1$ m, $A = 0.8$ cm. In the figures, the wave forms of exact 1 period after several periods from the start of sinusoidal steering are cut and shown. Also in the figures, the results of 3 conditions below have been compared.

1) On even road (no undulation)
2) On undulated road with original MF tire model
3) On undulated road with transient tire model

"On even road" is added as the reference and their results were the same, when "original MF tire model" was employed and when "transient tire model" was employed.

It seems from those figures that the mean lateral acceleration of 3) near the peaks is smaller than 1) and 2) when the wavelength is large ($L = 3$ m, Fig. 7(b)), to which the decrease of side force is mainly contributing when the tire is inside of cornering. But the mean lateral acceleration of 3) is larger when the wavelength is small ($L = 1$ m, Fig. 8(b)), to which the increase of side force (absolute value) is mainly contributing when the tire is outside of cornering. To understand the reason, the time histories of 2) and 3) of 1 period of the wavelength of road undulation are shown in Figure 9 and 10 by expanding the part of Figure 7 and 8. In the figures, the slip angle of "MF model" and the equivalent slip angle of "transient model" are added. Although the vertical loads of 2) and 3) are almost same, the slip angles are different, which corresponds to the difference of side force.

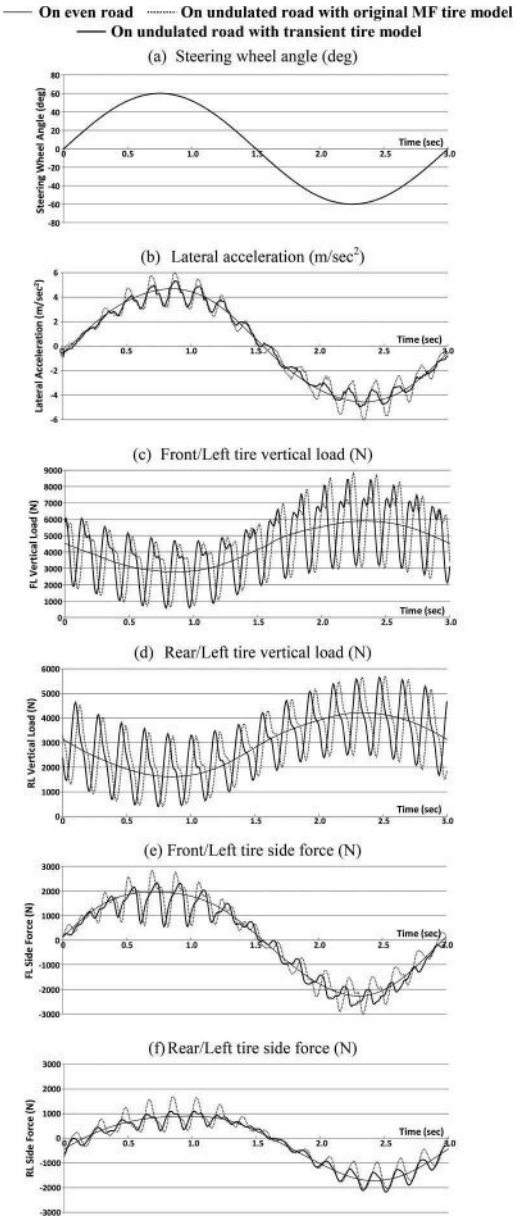


Figure 7. Vehicle and tire responses at sinusoidal steering wheel angle input ($L = 3$ m, $A = 6$ cm, running speed = 60 km/h, steering wheel angle input = ± 60 degrees).

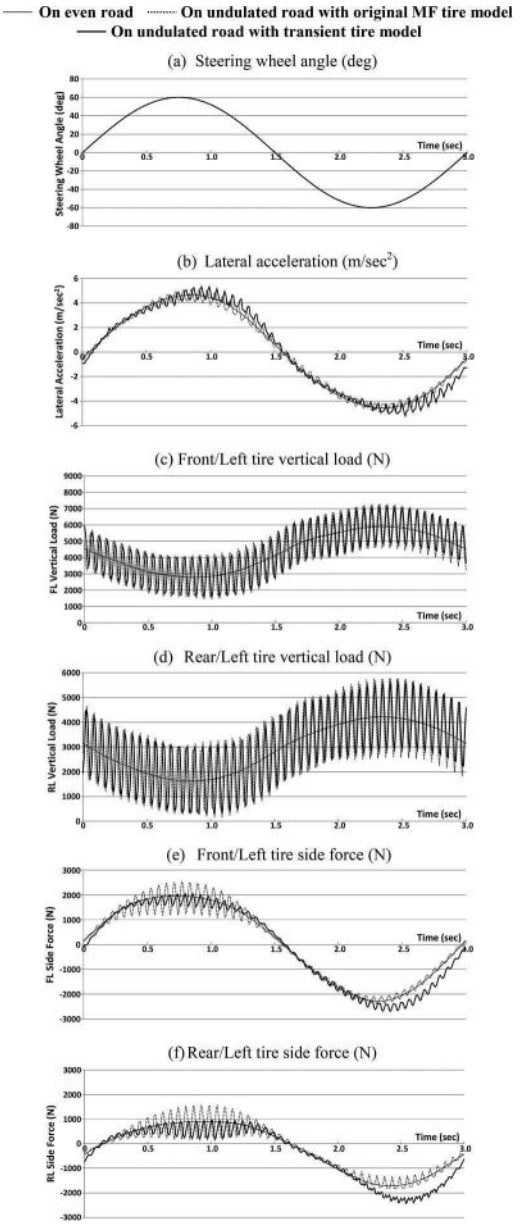


Figure 8. Vehicle and tire responses at sinusoidal steering wheel angle input ($L = 1$ m, $A = 0.8$ cm, running speed = 60 km/h, steering wheel angle input = ± 60 degrees).

To see the change of mean lateral acceleration more clearly, the simulations on various undulations were performed and the results are shown in Figure 11. The horizontal axis is the height of undulation and the vertical axis is the average lateral acceleration which is the average value of absolute values of lateral acceleration in 1 period of sinusoidal steering. Another vertical axis shows the ratio in % to the value of 1). It is understood that the average lateral acceleration of 2) is smaller than that of 1) for all the cases, which causes from the static loss of side force. But in the case that the tire transient properties is considered, the average value decreases or increases depending on L and A. When the tire is considered in the vehicle system, both of the slip angle and the vertical load are always changing complicatedly, which is different from the analysis in Chapter 2.

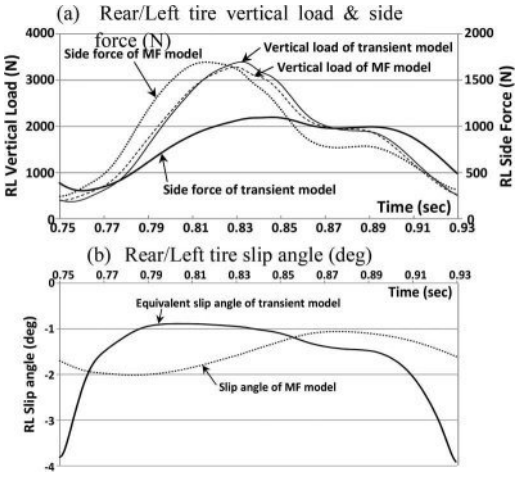


Figure 9. Comparison of Rear/Left tire-related variables between "with original MF tire model" and "with transient tire model" for 1 period of road undulation ($L = 3$ m, $A = 6$ cm).

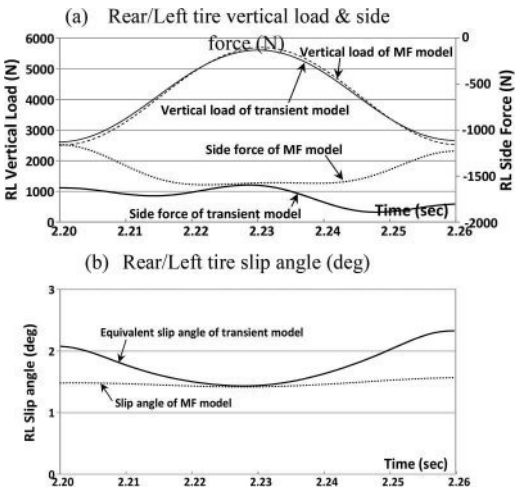


Figure 10. Comparison of Rear/Left tire-related variables between "with original MF tire model" and "with transient tire model" for 1 period of road undulation ($L = 1$ m, $A = 0.8$ cm).

5 STEADY STATE TURNING BEHAVIOR

5.1 *Condition of simulation*

The same undulated roads were defined as in the former chapter. Here the simulated results of vehicle steady state turning behavior will be shown. The vehicle is running straight at constant speed of 60 km/h on the undulated road and the steering wheel is steered in stepwise to the angle of 25 degrees which correspond to the lateral acceleration of 2 m/sec^2 at steady state turning on "even road". The schematic sketch of the

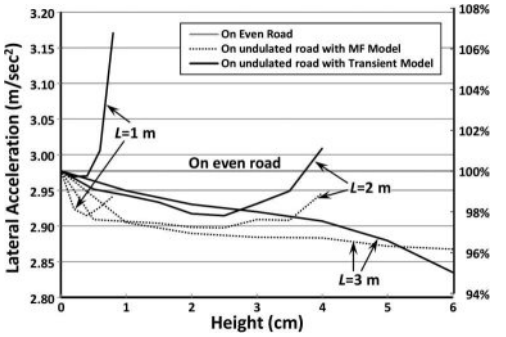


Figure 11. Relation of average lateral acceleration with wavelengths and heights of road undulation.

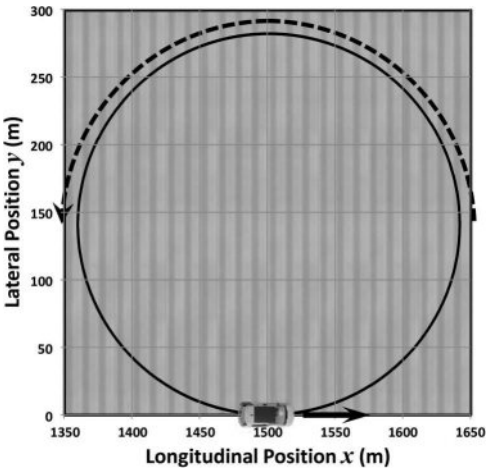


Figure 12. Schematic sketch of steady state turning.

vehicle trajectory is shown in Figure 12. The calculated results shown below are the part of the dotted arrow (half of turn).

5.2 *Results and discussion*

By the limitation of number of pages of the paper, only the results at $L = 1$ m, $A = 1.1$ cm are shown in Figure 13. In the figure, the results of 3 conditions are compared as same as former chapter.

In case of sinusoidal steering angle input, the frequency of vertical load oscillation was almost constant, if the wavelength of undulation is decided. But in this case, the frequency changes continuously from very low to the maximum (16.7 Hz), as seen in Figure 13. The tendency of the change of lateral acceleration of "with transient tire model" shows the same tendency as the results of sinusoidal steering wheel angle input, that is, the side force of outside of cornering (Fig. 13(e)) becomes large at the range of short wavelength, which causes the increase of lateral acceleration (also yaw rate).

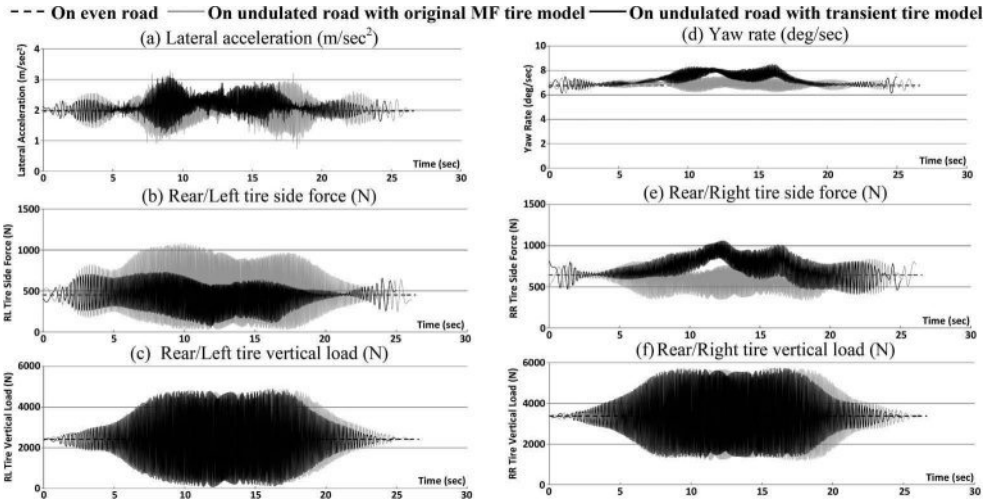


Figure 13. Vehicle and tire responses at steady state turning ($L = 1$ m, $A = 1.1$ cm, running speed $= 60$ km/h).

6 CONCLUSION

1) The formerly developed tire transient model of side force and aligning moment was implemented to the vehicle dynamics software. For the simulation, the vehicle and the tire model were developed.
2) From the analysis of vehicle behavior on undulated roads at sinusoidal steering wheel angle input, it was found that the change of vehicle behavior can be explained from the static loss when only the tire steady state characteristics are considered, but that the vehicle behavior changes complicatedly when the tire transient properties are considered. The average lateral acceleration decreases when the wavelength is large, but it increases when that is small.
3) The change of lateral acceleration at steady state turning shows the same tendency as the sinusoidal steering angle input in the case that the tire transient property is considered.
4) Further study:

   In this paper, only the transient property of side force was investigated. The further study is needed also for the transient property of aligning moment and for its influence on vehicle closed loop behavior.

ACKNOWLEDGEMENTS

The author expresses his deep thankfulness to IPG Automotive GmbH and IPG Automotive K.K. for their great help to implement the new tire model to CarMaker.

REFERENCES

Pacejka, H.B. 2012. *Tire and Vehicle Dynamics, Third Edition,* Elsevier.

Takahashi, T. & Pacejka, H.B. 1988. Cornering on Uneven Roads, *Supplement to Vehicle System Dynamics Vol. 17*: 469–480.

Takahashi, T. & Pacejka, H.B. 1992. Pure Slip Characteristics of Tyres on Flat and on Undulated Road Surfaces; *Proc. intern. symp. AVEC '92, Yokohama, 14–17 September 1992*: 360–365.

Takahashi, T. & Hoshino, M. 1996. The Tyre Cornering Model on Uneven Road Surfaces for Vehicle Dynamics Studies; *Proc. intern. symp. AVEC '96, Aachen, 24–28 June 1996*: 941–953.

Takahashi, T. 2008. The Modeling of Tire Cornering Characteristics Considering the Transient Vertical Load Change (in Japanese), *Trans. JSME, Vol. 74, No. 745*: 2221–2228.

Advanced Vehicle Control – Edelmann, Plöchl & Pfeffer (Eds)
© 2017 Taylor & Francis Group, London, ISBN 978-1-138-02992-7

Estimation of tire road friction during vehicle steering

L. Shao, C. Lex, A. Hackl & A. Eichberger
Institute of Automotive Engineering, Technical University of Graz, Graz, Austria

ABSTRACT: Automated vehicles require information on the current road condition, i.e. the tire-road friction coefficient for trajectory planning and braking or steering interventions. In this paper an adaptive observer to estimate tire-road friction only utilizing the information from Electric Power System (EPS) and other sensors installed in production vehicles is applied. A new state, the front wheel slip angle divided by tire-road friction coefficient, is introduced for friction estimation and to judge when the estimated result is reliable. The algorithm is verified in IPG-Carmaker.

1 INTRODUCTION

Tire-road friction coefficient estimation is critical for designing control systems in highly automated and autonomous vehicles for vehicle safety and performance, since the responsibility to adapt the driving style to the road condition is transferred from the driver to the automated system. Approaches to determine $\mu_{\max}$ on-board a vehicle during driving can be mainly divided into cause-based methods, i.e. methods that measure parameters influencing the road condition like precipitation, or effect-based methods, e.g. like measuring parameters influenced by the road condition like the vehicle's dynamic response. In this article, an effect based method during steering is presented which considers vehicle dynamics related information, namely lateral tire force F_y and the self-aligning torque M_z. Related approaches presented in the literature fitting these specifications show several shortcomings. For example, in (Hsu & Gerdes 2008), a nonlinear observer is designed which is only guaranteed to be stable when the front wheel slip angle α_f and the tire-road friction coefficient $\mu_{\max}$ are both over- or underestimated. In (Ahn, Peng, & Tseng, a recursive nonlinear least squares method is proposed, where the global minimum depends highly on the initial guess of $\mu_{\max}$ and α_f, which are usually not known very accurately. In (Ahn, Peng, & Tseng 2013), a nonlinear robust observer is designed which is only proven to be locally stable, and the attraction domain cannot cover the whole working area of the tires. In (Matsuda, Jo, Nishira, & Deguchi 2013), an Extended Kalman Filter (EKF) to estimate the $\mu_{\max}$ and α_f is applied which cannot ensure the stability of the system. All of the above methods cannot solve or prove the stability or convergence problem well. In addition, no knowledge on the required dynamical excitation to deliver reliable estimates of $\mu_{\max}$ are given. This is required because the slope in the quasi-linear region of the lateral tire forces vs. the wheel slip angle is nearly independent of $\mu_{\max}$.

The present work tries to solve the stability problem by implementing an adaptive observer with the state variable $\frac{\alpha_f}{\mu_{\max}}$, with which it is possible to detect whether the steering excitation is large enough to make the estimation of $\mu_{\max}$ reliable regardless of the present road condition.

To achieve this, at first an observer is used to estimate the front axle lateral force F_{yf}, see Section 3.1, and total-aligning torque τ_{zf} is obtained indirectly from Electric Power System (EPS), see Section 2.3. Then, $\frac{\alpha_f}{\mu_{\max}}$ is calculated algebraically with F_{yf} and τ_{zf}, see Section 3.2. Finally, the adaptive observer is used to estimate $\mu_{\max}$ based on $\frac{\alpha_f}{\mu_{\max}}$ as a measurement and detection threshold, see Section 3.3. The approach is verified in IPG-Carmaker, see Section 4.

2 TIRE AND VEHICLE MODEL

2.1 *Tire model*

Two related tire models are used. For F_y, "TMsimple" is implemented due to its simplicity (Hirschberg 2014), but does not give a formula for M_z. Therefore, for M_z, the tire model "TMeasy" is used (Rill 2012). These models finally describe F_y and M_z as functions of wheel slip angle α and road friction $\mu_{\max}$:

$$\begin{cases} F_y = -K\mu_{\max}\sin[B(1-e^{\frac{-|\alpha|}{\lambda\mu_{\max}}})]\mathbf{sign}(\alpha)] \\ M_z = F_y \cdot n \end{cases} \tag{1}$$

and term n is computed using the following relation

$$\begin{cases} \frac{n}{L} = (\frac{n}{L})_0[(1-w)(1-s) \\ \qquad +w(1-(3-2s)s^2)] & |\frac{\alpha}{\mu_{\max}}| \le s_y^0 \\ \frac{n}{L} = (\frac{n}{L})_0[-(1-w)(s-1) \\ \qquad (\frac{1-ws}{1-w})^2] & s_y^0 \le |\frac{\alpha}{\mu_{\max}}| \le s_y^E \\ \frac{n}{L} = 0 & |\frac{\alpha}{\mu_{\max}}| > s_y^E, \end{cases} \tag{2}$$

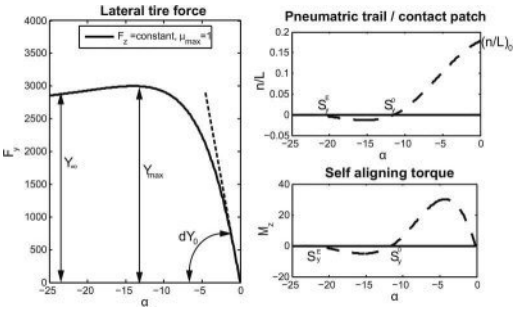


Figure 1. Example of a passenger car tire characteristics.

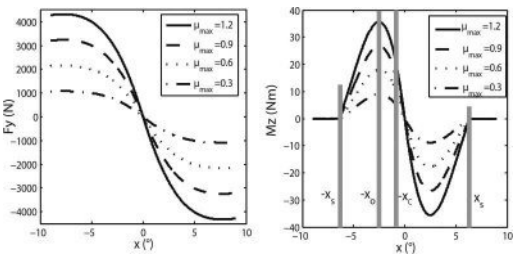


Figure 2. F_y and M_z varies with x in different $\mu_{\max}$ for a constant normal force based on (Takagi 2010).

where $K = Y_{\max}$, $B = \pi - \arcsin(Y_\infty / Y_{\max})$ $(Y_\infty \leq Y_{\max})$, $A = (1/dY_0)KB$ are all constant and only determined by normal force F_z, see Figure 1; L denotes the tire road contact length, n the pneumatic trail, $(\frac{n}{L})_0$ the initial value of the pneumatic trail divided by the contact length, $s = \frac{\alpha}{s_y^0 \mu_{\max}}$, $w = \frac{s_y^0}{s_y^E}$, and s_y^0 and s_y^E are both constant independent of $\mu_{\max}$ and are identified using experimental data.

Define $x = \alpha / \mu_{\max}$, (1) can be written as

$$\begin{cases} F_y = \mu_{\max} \cdot f(x) \\ M_z = \mu_{\max} \cdot g(x), \end{cases} \tag{3}$$

which decouples x and $\mu_{\max}$ in the expression of F_y and M_z. Then tire characteristics in Figure 2 are obtained under a constant normal force with new abscissa x. In Figure 2 (right), it can be deduced that the peak of M_z is at the same value of $x = x_o$ independent of $\mu_{\max}$. In addition, the smaller $|x|$ is, the closer the relationship of $|x|$ to M_z is to a linear one, making a possible estimation of $\mu_{\max}$ in this area less accurate. In this article, $|x| \leq x_c$ is used to indicate the quasi-linear region. Although the values of x for the peak and the end of the linear region differ, this assumption for the linear region also holds for F_y over x . For different tire normal forces, the values of x_c and x_o vary, however, if we assume the longitudinal velocity changes slowly or is a constant, leading to negligible longitudinal load transfer, both x_c and x_o vary little for the overall front lateral force and self-aligning torque in the front axle(especially for low

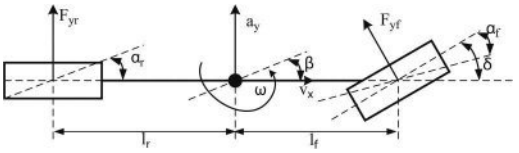


Figure 3. Single track model.

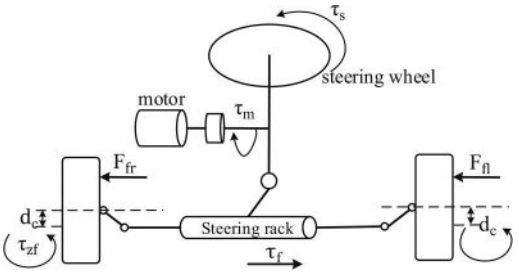


Figure 4. Steering system with EPS.

road friction coefficient) and can be assumed constant for application (Shao, Lex, Hackl, & Eichberger 2016).

2.2 *Vehicle model*

A nonlinear single track model shown in Figure 3 is used to express lateral dynamics of the vehicle. It considers lateral load transfer and assumes $\mu_{\max}$ to be piecewise constant, and can be written as

$$\dot{\omega} = \frac{l_f F_{yf} \cos\delta}{I_z} - \frac{l_r F_{yr}}{I_z}, \tag{4}$$

$$\dot{\beta} = \frac{a_y}{v_x} - \omega, \tag{5}$$

where l_f is the distance between front axle to center of Gravity, l_r the distance between rear axle to center of gravity, δ the front wheel steering angle, F_{yf} the front axle lateral force, F_{yr} rear axle lateral force, v_x the slow varying or constant longitudinal velocity, ω the yaw rate, β the side slip angle, a_y the lateral acceleration and I_z the moment of inertia of the vehicle.

2.3 *Steering system*

The steering system with EPS in Figure 4 can be described by

$$J_{eff}\ddot{\delta} + b_{eff}\dot{\delta} + k\delta = \tau_{zf} + \tau_m + \tau_s + \tau_f, \tag{6}$$

where J_{eff} is the front axle effective steering inertial moment, b_{eff} the effective damping, k the jack up moment coefficient, τ_{zf} the front axle total aligning torque, τ_m the motor torque, τ_s the steering torque and τ_f the steering friction torque which can be predetermined using a coulomb friction model (Ahn, Peng, & Tseng 2009). Using (6), τ_{zf} can be obtained from EPS

sensor signals and the relevant steering parameters using a disturbance observer (Hsu & Gerdes 2008). Another way to estimate τ_{zf} is to use tie-rod force model and EPS output torque model from (Matsuda, Jo, Nishira, & Deguchi 2013). Finally, with τ_{zf}, a relation for M_{zf} and the front lateral forces can be given by

$$\tau_{zf} = M_{zf} + (F_{yfl} + F_{yfr})d_c, \tag{7}$$

where F_{yfl} is the front left lateral force, F_{yfr} the front right lateral force, d_c the front tires mechanical trail and M_{zf} the front axle self-aligning torque. For simplicity, it is assumed that the mechanical trail is the same for both the front left and the front right tire.

3 ROAD FRICTION ESTIMATION

3.1 *Front axle lateral force*

From (4), it is easy to deduce that

$$\dot{\omega} = \frac{lF_{yf}\cos\delta}{I_z} - \frac{l_r m a_y}{I_z}, \tag{8}$$

due to

$$F_{yr} = ma_y - F_{yf}\cos\delta, \tag{9}$$

where l is the wheel base. Using a super-twisting algorithm based on sliding mode techniques as implemented by (Tafner 2014), the estimation of F_{yf} can be written as

$$\begin{cases} \dot{\hat{\omega}} = -\frac{l_r m a_y}{I_z} + \hat{\eta} + k_1|\omega - \hat{\omega}|^{0.5}\mathbf{sign}(\omega - \hat{\omega}) \\ \dot{\hat{\eta}} = k_2\mathbf{sign}(\omega - \hat{\omega}), \end{cases} \tag{10}$$

where k_1 and k_2 are tuning parameters which are positive constant. Then estimation can be written as

$$\hat{F}_{yf} = \frac{\hat{\eta} I_z}{l\cos\delta}. \tag{11}$$

3.2 x_f *estimation*

After obtaining F_{yf}, and τ_{zf} from EPS, according to (3) and (7), they can be both written as

$$\begin{cases} F_{zf} = \mu_{\max}(f_{yfl}(x_f) + f_{yfr}(x_f)) \\ \tau_{zf} = \mu_{\max}(g_{fl}(x_f) + g_{fr}(x_f)) \\ \qquad +\mu_{\max}(f_{yfl}(x_f) + f_{yfr}(x_f))d_c, \end{cases} \tag{12}$$

where *fl*: front left and *fr*: front right. $x_f = \frac{\alpha_f}{\mu_{\max}}$, where α_f is front wheel slip angle. $x_f \in \Theta$, where $\Theta := \{x_f | -x_s \le x_f \le x_s\}$, see Figure 2.

This leads to

$$\frac{\tau_{zf}}{F_{yf}} = \frac{(g_{fl}(x_f) + g_{fr}(x_f))}{(f_{yfl}(x_f) + f_{yfr}(x_f))} + d_c, \tag{13}$$

The value $\frac{\tau_{zf}}{F_{yf}}$ is always positive, which can also be deduced when comparing the characteristics shown in Figure 2. Therefore, one way to obtain $|x_f|$ is numerically calculating it due to the monotonicity of $\frac{\tau_{zf}}{F_{yf}}$ with respect to $|x_f|$ within $(0, x_s)$. Using this way, the sign of x_f is the opposite of τ_{zf}. Another way to acquire x_f is to implement a pre-defined look-up table, in which a given $\frac{\tau_{zf}}{F_{yf}}$ at a certain a_y have a corresponding $|x_f|$.

3.3 *Adaptive observer for road friction estimation*

Using the approach of (Hsu & Gerdes 2008), the formulation in (5) can be transformed to a state equation with front wheel slip angle as state:

$$\dot{\alpha}_f = aF_{yf}\cos\delta + bF_{yr} - \omega - \dot{\delta}, \tag{14}$$

where $a = \frac{1}{mv_x} + \frac{l_f^2}{I_z v_x}$ and $b = \frac{1}{mv_x} - \frac{l_f l_r}{I_z v_x}$. With (9) and (12), (14) can be written as

$$\begin{aligned} \dot{x}_f = {} & (a-b)(f_{yfl}(x_f) + f_{yfr}(x_f))\cos\delta \\ & + \frac{(bma_y - \omega - \dot{\delta})}{\mu_{max}}, \end{aligned} \tag{15}$$

which is a linear time varying system with an unknown parameter $\mu_{\max}$. For solving such a problem, there is a traditional method in adaptive observer design which needs the condition of uniform complete observability (Ioannou & Sun 1996), but this method does not give explicit bounds for the convergence rates which does not offer a guideline to tune parameters (Loria & Panteley 2002), therefore, another adaptive observer is implemented which is easy to handle and tune the convergence rate of unknown parameters (Grip, Johansen, Imsland, & Kaasa 2010).

In order to implement this parameter estimator, (15) is written as

$$\dot{x}_f = p(\delta) f_{yf}(x_f) + q(t)\theta, \tag{16}$$

where $p(\delta) = (a-b)\cos\delta$, $f_{yf}(x_f) = f_{yfl}(x_f) + f_{yfr}(x_f)$, $q(t) = (bma_y - \omega - \dot{\delta})$, $\theta = \frac{1}{\mu_{\max}}$.

With x_f as measurement, the adaptive observer is then written as

$$\begin{cases} \dot{z} = -k_\varphi(p(\delta)f_{yf} + \hat{\varphi}) - q(t)u_\theta \\ \hat{\varphi} = z + k_\varphi x_f + q(t)\hat{\theta} \\ \dot{\hat{\theta}} = k_\theta \mathbf{sign}(q(t))(\hat{\varphi} - q(t)\hat{\theta}) = u_\theta, \end{cases} \tag{17}$$

where k_φ and k_θ are both positive constants. Besides, convergence rate of $\hat{\theta}$ is proportional to the value of k_θ when k_φ is fixed.

When the following two assumptions are satisfied, (17) is exponentially stable:

Assumption 1: There exist $T > 0$, positive ε_1 and ε_2, such that for all $t \in R_{\ge 0}$,

$$\varepsilon_1 \le \int_t^{t+T} |q(t)| d\tau \le \varepsilon_2, \tag{18}$$

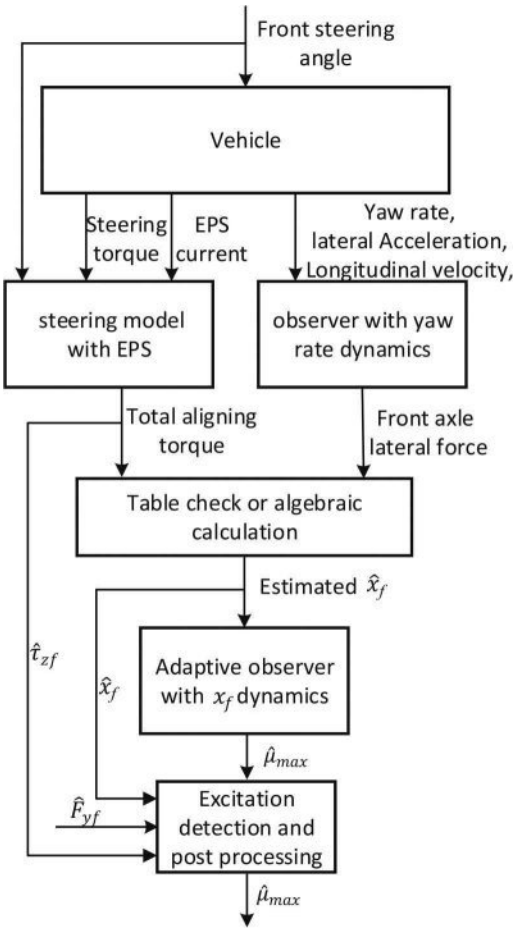


Figure 5. Overall structure of the estimation system.

Assumption 2: $|q(t)|$ and $|\dot{q}_(t)|$ are bounded for all $t \in R_{\geq 0}$.

For an exponentially stable observer, the property of input state stability can be deduced within Θ, guaranteeing strong robustness of the road friction estimation. For detailed proof, refer to (Grip, Johansen, Imsland, & Kaasa 2010).

3.4 *Overall structure of the friction estimation*

For better understanding the above description, the overall structure of the friction estimation is presented, see in Figure 5. It is noticeable that there is a block — Excitation detection and post processing, which is used to process the road friction estimation result, since in the real road condition, there is a region of x_f, where both M_{zf} and F_{yf} are nearly linear, and no reliable information on $\mu_{\max}$ can be delivered. So, only when M_{zf} comes into the nonlinear region as indicated by x_c, which means τ_{zf} also comes into the nonlinear region, estimation of $\mu_{\max}$ is reliable. However, due to noise or model uncertainty, estimated x_f may have some errors which cause the misuse of the threshold. When x_f is overestimated, it is possible to activate the threshold though there is no reliable information of $\mu_{\max}$. On the other hand, when x_f is underestimated, the updated road friction is not updated since the threshold is still deactivated, and the valuable excitation is squandered. To compensate this to some extent, $|\tau_{zf}|$ and $|F_{yf}|$ are also introduced as thresholds, and the overall rules are as follows:

$$\begin{cases} \mu_{max} \text{ frozen, if} |\tau_{zf}| < \tau_{zf}^0 \text{or} |F_{yf}| < F_{yf}^0 \text{or} |x_f| < x_c \\ \mu_{max} \text{ updated, otherwise} \end{cases} \tag{19}$$

where τ_{zf}^0 and F_{yf}^0 are thresholds to detect whether the steering excitation is high enough. In this way, only when $|\tau_{zf}|$, $|F_{yf}|$ and $|x_f|$ are all over the threshold, the road friction estimation will be updated, which increases the robustness of the estimation result.

Table 1. Table of maneuver.

Maneuvers	Road condition	Longitudinal velocity (km/h)
sinus (0.25 Hz, 0.7 rad)	0.4	40
sinus (0.25 Hz, 0.7 rad)	0.7	60
sinus (0.25 Hz, 0.7 rad)	1	72
sinus (0.25 Hz, 0.7 rad)	1-0.7-0.4	60

4 SIMULATION RESULT

To verify the algorithm, simulations are conducted in IPG CarMaker. Three sinusoidal excitations in three different constant road conditions with different velocities and one sinusoidal excitation in varying road conditions are investigated and can be seen in Table 1. For all simulations, the threshold $|x_c|$ for the update of $\mu_{\max}$ is chosen to be 1.4°, all sinusoidal steering maneuvers have the same frequency (0.25 Hz) and amplitude (0.7 rad). It has to be noted that within the reference simulation in IPG CarMaker, the vehicle behavior used as input for the observer is simulated using the tire model Magic Formula. However, the observer considers the tire models described in Section 2. In addition, the influence of mechanical trail is not simulated and the corresponding self-aligning torque is directly obtained from IPG Carmaker, but the overall structure as described in Section 3.4 still holds.

The results for the sinusoidal maneuvers on three different constant road conditions are shown in Figure 6, Figure 7, Figure 8, respectively. For x_f estimation, it can be seen that though there is noise in yaw rate and lateral acceleration, the estimated x_f can still well

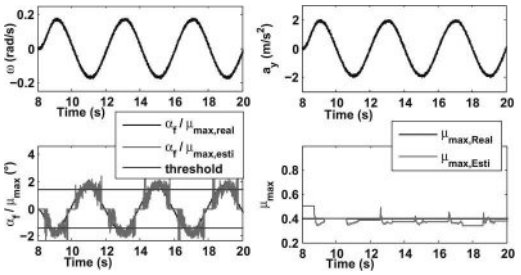


Figure 6. Road friction estimation on low friction.

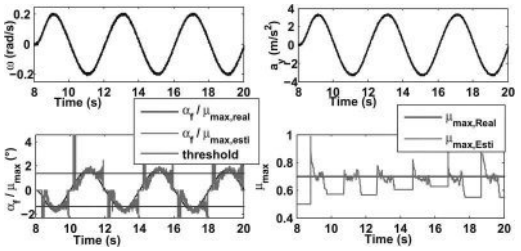


Figure 7. Road friction estimation on moderate friction.

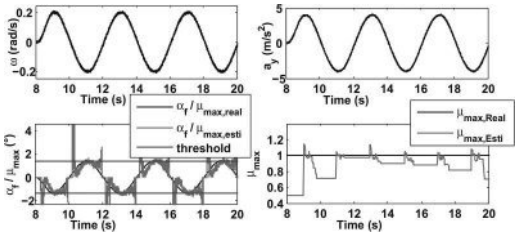


Figure 8. Road friction estimation on high friction.

follow the real x_f in all three different road conditions. Besides, in Figure 6, Figure 7 and Figure 8, estimated x_f is set to 0 when F_{yf} and τ_{zf} are close to zero in x_f calculation part (e.g., at 10 second), and there are jump (e.g., around 10 second) due to the singularity in the $\frac{\tau_{zf}}{F_{yf}}$, but the $\mu_{\max}$ estimation is not activated because of the rule in (19). For $\mu_{\max}$ estimation, it is demonstrated that, the lower the road friction is, the more accurate the estimation result is. This is because the threshold set for different road conditions are the same in (19), therefore, the thresholds τ_{zf}^0 and a_y^0 play more important role in low friction condition. This can be explained since for lower road friction condition, τ_{zf}^0 and F_{yf}^0 result in higher values of x_f. These x_f are then closer to the nonlinear region of tire characteristics, which guarantees more reliable estimation results. This behavior is wanted for the application of friction estimation, because it is more important to accurately detect low friction condition than high friction conditions.

The result for the friction estimation in varying road conditions are shown in Figure 9. At $\mu_{\max}$ being 1, the steering excitation is not high enough to activate the threshold x_c , so the estimation of $\mu_{\max}$ does not update

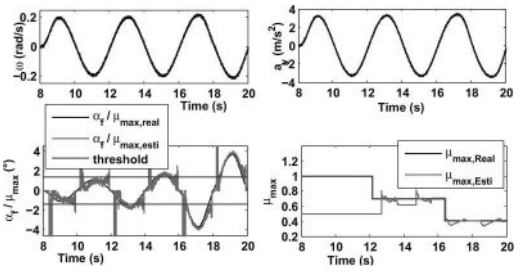


Figure 9. Road friction estimation on varying road condition.

and the initial value of 0.5 is kept constant (see Figure 9, right below). When the road condition suddenly decreases to 0.7, $\mu_{\max}$ estimation doesn't update until x_f reaches the threshold. Afterwards, $\mu_{\max}$ is estimated with a small error. This also holds for the situation when the road condition declines from 0.7 to 0.4.

In summary, the estimation performs well both in constant road friction and varying road friction. With the combination of thresholds for $|\tau_{zf}|$, $|F_{yf}|$ and $|x_f|$, the estimation result is more robust, especially in low friction condition, which is useful in real application.

5 CONCLUSION

With increasing automation of vehicles, reliable estimates of the road condition are required to plan and control vehicle interventions. An estimation structure is presented to solve the stability problem of tire road friction estimation during steering, and introduces a threshold $\frac{\alpha_f}{\mu_{\max}}$ to judge when the dynamical excitation is sufficient to obtain a reliable estimate of $\mu_{\max}$.

The results show high potential for the proposed tire-road friction estimation structure by using simulation data. Especially low friction conditions can be estimated accurately, which is in general desirable for the application in vehicle control systems. In the future, road tests will be conducted to further verify the algorithm.

REFERENCES

Ahn, C., H. Peng, & H. E. Tseng (2009). Estimation of road friction for enhanced active safety systems: Algebraic approach. In *ACC'09*, pp. 1104–1109.

Ahn, C., H. Peng, & H. E. Tseng (2013). Robust estimation of road frictional coefficient. *IEEE Transactions On Control Systems Technology 21*, 1–13.

Grip, H. F., T. A. Johansen, L. Imsland, & G. Kaasa (2010). Parameter estimation and compensation in systems with nonlinearly parameterized perturbations. *Automatica 46*, 19–28.

Hirschberg, W. (2014). Fahrzeugdynamik. Skript, Austria, Tu Graz, FTG.

Hsu, Y.-J. & J. C. Gerdes (2008). The predictive nature of pneumatic trail: Tire slip angle and peak force estimation using steering torque. In *AVEC'08*, pp. 80–85.

Ioannou, A. P. & J. Sun (1996). *Robust adaptive control*. Prentice Hall.

Loria, A. & E. Panteley (2002). Uniformly exponential stability of linear time-varying systems: revisited. *Systems & Control Letters 47*, 13–24.

Matsuda, T., S. Jo, h. Nishira, & Y. Deguchi (2013). Instantaneous estimation of road friction based on front tire sat using kalman filter. *SAE Int. J. Passeng. Cars – Mech. Syst. 6*, 147–153.

Rill, G. (2012). *Road vehicle dynamics, fundamentals and modeling*. Boca Raton: Taylor & Francis Group.

Shao, L., C. Lex, A. Hackl, & A. Eichberger (2016). Road friction estimation using recursive total least squares. In *IEEE intelligent Vehicle Symposium*.

Tafner, R. e. a. (2014). Estimation of tire parameters via second-order sliding mode observers with unknown inputs. In *Variable Structure Systems (VSS)*.

Takagi, F. (2010). An estimation method of the maximum tire road friction coefficient using an electric power assist steering. In *AVEC'10*, pp. 13–15.

Longitudinal dynamics

Advanced Vehicle Control – Edelmann, Plöchl & Pfeffer (Eds)
© 2017 Taylor & Francis Group, London, ISBN 978-1-138-02992-7

Adaptive anti-slip regulation method for distributed drive electric vehicle

K. Sun, Z. Yu, L. Xiong & R. Zhang
School of Automotive Studies, Tongji University, Shanghai, China
Clean Energy Automotive Engineering Center, Tongji University, Shanghai, China

ABSTRACT: A robust anti-slip regulation method adaptive to different road-tire conditions is proposed for distributed drive electric vehicles. The controller is robust to wheel parameter uncertainty and takes wheel speed as control variable, avoiding the disadvantage at low vehicle speed when slip ratio is taken as control variable. A non-affine parameter estimator is adopted to estimate road condition using improved Burckhardt model, the reference slip ratio is set according to the estimated road condition. Hence the realization of adaptive anti-slip regulation. Multi-condition experiments show that the controller is adaptive to road change, can improve vehicle driving efficiency and ensure wheel and vehicle stability.

1 INTRODUCTION

Anti-slip regulation (ASR) is part of vehicle's active safety system and has gained increasing attention lately. The essential problem is to control the slip ratio to a target optimum value. Based on this, typical ASR algorithms can be divided into two categories, one that only controls the slip ratio to a certain constant value and the other controls the slip ratio to a value varying according to road condition. The latter kind is the so called adaptive slip control, which requires an additional road estimator to provide road information. For slip control, typical controller designs include MFC, PID, SMC, etc. Each has its merits and flaws. For road estimation schemes, there are methods like slip stiffness method, model based method, polynomial fitting method, etc. Among them the model based method is mostly used, and most research is based on tire model that is affine to peak road adhesion coefficient. In this paper, an adaptive anti-slip regulation method using a non-affine road estimator is proposed. The slip controller derives from SMC with boundary layer to avoid chattering. Inside the boundary layer is a conditional integrator, eliminating the steady state error and improving system's transient behavior (Kay & Khalil, 2002). To avoid deterioration of slip control quality when the vehicle's velocity is low, the proposed controller takes wheel angular velocity as control variable. System's stability is studied and various experiments verify the proposed ASR controller.

2 SYSTEM ARCHITECTURE

System architecture of the proposed adaptive ASR controller is shown in Figure 1.

The ASR controller consists of two components, the wheel speed controller and the road estimator.

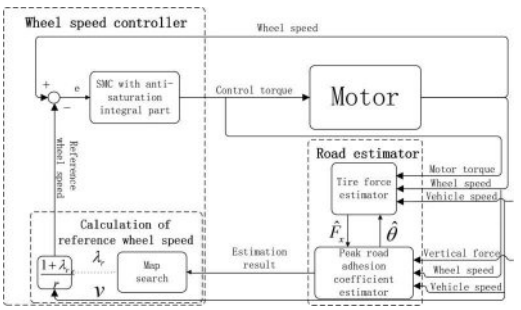


Figure 1. System architecture.

The wheel speed controller also has two parts, one searches for the optimum slip ratio and calculates corresponding reference wheel speed according to the result from the road estimator. The other controls the actual wheel speed converging to the reference value, which employs a SMC with conditional integrator. The road estimator consists of two estimators as well, one is the longitudinal force estimator, the other is the peak road cohesion coefficient estimator, the two estimators disturb with each other and have global asymptotic Lyapunov stability (Grip, 2010). In the following analysis, we assume that the vehicle velocity is known whether by measurement or estimation.

3 WHEEL DYNAMICS CONTROLLER

3.1 *Quarter car model and control variable*

Motor torques of distributed drive electric vehicles can be controlled independently so the torque of each wheel won't disturb with each other. Therefore, the slip

ratio controller is devised based on the 2-DOF single wheel model,

$$\begin{aligned} I\dot{\omega} &= T_m - rF_d \\ F_d &= F_z\mu(\lambda) \end{aligned} \tag{1}$$

where F_d is the longitudinal force, ω is the wheel angular speed, I is the moment of inertia of a single wheel, r is the rolling radius of tire, T_m is the motor torque, μ is the nonlinear relationship between wheel slip λ and normalized longitudinal force. In driving condition, wheel slip is defined as,

$$\lambda = \frac{\omega r - v}{\omega r} \tag{2}$$

where v is vehicle longitudinal speed.

According to the definition of slip ratio in (2), it can be seen that when the vehicle is at low speed, the slip ratio is sensitive to vehicle speed so speed estimation or measurement error causes a large disturbance to slip ratio calculation. To avoid this problem, this paper takes wheel speed as the control variable.

According to the definition of slip ratio, the reference wheel speed is

$$\omega_r = v/(1-\lambda_r)r \tag{3}$$

where λ_r is reference slip ratio and ω_r is the corresponding reference wheel speed.

Besides, in order to prevent impact to reference wheel speed at low speed caused by vehicle speed error, a minimum speed strategy is devised, that is, when the estimated speed is less than a certain value, the reference wheel speed is calculated via this preset speed

$$\omega_r = (1+\lambda_r)\max(v, v_{\min})/r \tag{4}$$

where $v_{\min}$ is the preset minimum speed.

3.2 *ASR control law*

According to (1), dynamic of the wheel can be obtained,

$$I\dot{\omega} = -rF_z\mu(1-\frac{v}{\omega r}) + T_m \tag{5}$$

Define wheel speed error as $e = \omega - \omega_r$, then its dynamic is,

$$I\dot{e} = \varphi(e,t) + b(\lambda_r, t) + T_m - \bar{T}/2 \tag{6}$$

where $\bar{T}$ represents the maximum motor toque and

$$\varphi(e,t) = rF_z\left(-\mu(1-\frac{v}{(\omega_r+e)r}) + \mu(1-\frac{v}{\omega_r r})\right) \tag{7}$$

$$b(\lambda_r, t) = -rF_z\mu(\lambda_r) + \bar{T}/2 \tag{8}$$

obviously we have $\varphi(0,t) \equiv 0$.

The sliding mode control has been an effective solution to nonlinear control problem due to its robustness to model uncertainty and system disturbance. And its drawback of chattering in control input can be suppressed by employing continuous boundary layer near the sliding face. Enlightened by a kind of conditional integrator design (Kay & Khalil, 2002), we propose the SMC with conditional integrator (9) as ASR controller. Within the boundary layer, it has the advantage of low feedback gain of conditional PI controller. At the same time, it will prevent the integral part from being too large to deteriorate system's dynamic response by suppressing overshoot.

$$\begin{aligned} \dot{\rho} &= -k_0\rho + \theta sat\left(\frac{e+k_0\rho}{\theta}\right), |\rho(0)| \le \frac{\theta}{k_0} \\ T_m &= -\frac{1}{2}\bar{T}sat\left(\frac{e+k_0\rho}{\theta}\right) + \frac{1}{2}\bar{T} \end{aligned} \tag{9}$$

Where k_0 and θ are controller design parameters. Applying control law (9) under the premises of (10), it can be proved that the system has an equilibrium and the equilibrium is globally asymptotically stable, locally exponentially stable.

$$rF_z\mu(\lambda_r) + Ik_0\theta, \forall\lambda + \lambda_r$$

$$\begin{aligned} &\bar{T} > rF_z\mu(\lambda_r) + 2k_0\theta, \\ &\frac{\bar{T}}{\theta} + \frac{\varphi(e,t)}{e} \ge c_p > 0, \forall e \end{aligned} \tag{10}$$

where c_p is a positive constant.

Case 1. If b is a constant, then system (6) has equilibrium $e=0$, $\rho = \frac{2\theta b}{k_0\bar{T}}$, the equilibrium is globally asymptotically stable, and locally exponentially stable.

Case 2, if b varies with time and the derivative of b is bounded, then tracking error e is bounded.

Proof:

First we prove that $|\rho| \le \frac{\theta}{k_0}$ is an invariant set. Let $V(\rho) = \frac{1}{2}\rho^2$, when $|\rho| \ge \frac{\theta}{k_0}$, its derivative $\dot{V}(\rho) = \rho\dot{\rho} = -k_0\rho^2 + \theta\rho sat\left(\frac{e+k_0\rho}{\theta}\right) \le -k_0\rho^2 + \theta\rho \le 0$ equal sign is valid only when $\rho = \pm\frac{\theta}{k_0}$, thus $|\rho| \le \frac{\theta}{k_0}$ is an invariant set.

Then, there exist time t_1, when $\forall t > t_1$, $|s| \le \theta$, where $s \triangleq \Delta = e + k_0\rho$. Let us consider two cases,

a) when $s > \theta$, $s\dot{s} = s(\dot{e} + k_0\dot{\rho})$, taking (6) and (9) into consideration,

$$s\dot{s} = s(-\frac{rF_z}{I}\mu(\lambda) - k_0^2\rho + k_0\theta) \le s(-\frac{rF_z}{I}\mu(\lambda) + k_0\theta) < 0$$

The last inequality comes from the first premise in (10).

b) when $s < -\theta$,

$$s\dot{s} = s(\frac{\varphi(e,t)+b(\lambda_r,t)}{I} + \frac{\overline{T}}{2I} - k_0^2\rho - k_0\theta)$$
$$= s[\frac{(b(\lambda_r,t)+\overline{T}/2-2Ik_0\theta)+\varphi(e,t)}{I} - k_0^2\rho + k_0\theta]$$
$$< s\frac{\varphi(e,t)}{I} < 0$$

the first inequality comes from the second premise in (10).

Hence the existence of t_1. When $t > t_1$, define a new integral variable

$$\rho_e = \rho - \frac{2\theta}{k_0\overline{T}}b$$

the wheel dynamic function turns into

$$\begin{aligned}\dot{\rho}_e &= e + \dot{g}(t)\\ \dot{e} &= -k_p e - k_I \rho_e\end{aligned} \tag{11}$$

where

$$g(t) = -\frac{2\theta}{k_0\overline{T}}b(\lambda_r,t)$$
$$k_p = \frac{\overline{T}}{2\theta} - \frac{\varphi(e,t)}{e} > 0$$
$$k_I = \frac{k_0\overline{T}}{2\theta} > 0$$

system (11) is equivalent to a two order nonlinear mass-spring system disturbed by $\dot{g}(t)$. This kind of system has been studied in detail in nonlinear system theory (Khalil, 2002). It is easy to prove that there exists a positive quadratic Lyapunov function V which satisfies $\exists P > 0$, $Q > 0$ and $\forall t \geq t_2$, s. t.

$$\begin{aligned}V &= x^T Px\\ \dot{V} &\leq -x^T Qx + c_1\|x\|_2|\dot{g}|\end{aligned} \tag{12}$$

we can conclude from (12) that, x is ISS to $\dot{g}(t)$ (Khalil, 2002), a bounded $\dot{g}(t)$ results to a bounded error of x. When $\dot{g}(t) \equiv 0$, system's equilibrium is globally asymptotically stable, and locally exponentially stable.

4 ROAD ESTIMATOR

4.1 *Estimation principle*

The process of estimating the road condition by wheel dynamic can split into two steps, to estimate the longitudinal force first, and then use certain tire model to get the peak road adhesion coefficient. Therefore, the estimator devised in this paper consists of two components, one is the longitudinal force estimator, and the other is the peak road adhesion coefficient estimator. The two estimators disturb with each other and have global asymptotic Lyapunov stability (Grip, 2010). The structure of the estimator is shown in figure 2.

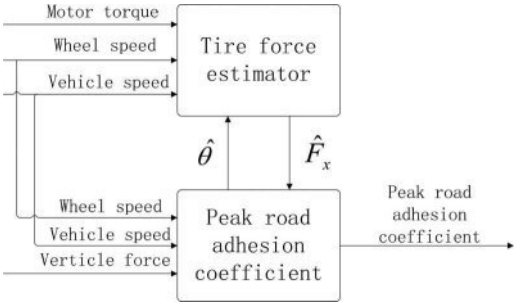


Figure 2. Structure of road estimator.

4.2 *Tire model*

Since Burckhardt tire model can describe the relationship between the tire slip ratio and the longitudinal force clearly, when longitudinal force and tire slip ratio information is known, peak road adhesion coefficient can be calculated. In order to better describe the curve shape in large slip ratio region, the model arguments are increased from three to five (Jin et al, 2014):

$$\begin{aligned}\mu(\lambda,\theta) = \theta_1 - \theta_1\exp[-\frac{\theta_2}{\theta_1}(\lambda+\theta_5\lambda^2)]\\ -\theta_3\lambda\,\mathrm{sgn}(\lambda) + \theta_4\lambda^2\end{aligned} \tag{13}$$

θ_1 denotes the peak road adhesion coefficient, which is referred to as θ in later text. θ_2 is the longitudinal stiffness, which is the slope of $\mu - s$ curve at origin. $\theta_3 - \theta_5$ are arguments used to describe large slip ratio region of $\mu - s$ curve.

4.3 *Parameter estimator*

The wheel model can be described as

$$\hat{F}_x = \frac{I}{r}(y + K_i\omega) - F_z\mu(t,\omega,\hat{\theta}) \tag{14}$$

where y can be deemed as observation of wheel angular acceleration $\dot{\omega}$ and K_i is observer parameter. Here we define ϕ as

$$\phi = \frac{r}{I}F_x = \frac{1}{I}rF_z\mu(\theta,\omega) \tag{15}$$

its observation is

$$\hat{\phi} = y + K_i\omega - \frac{1}{I_\omega}rF_z\mu(\hat{\theta},\omega) \tag{16}$$

where $\hat{\phi}$ is the estimation of longitudinal force F_x but with different dimension. Then peak road adhesion coefficient θ then can be achieved by the tire model given the longitudinal force. Here we design the update law of $\hat{\theta}$ as

$$\dot{\hat{\theta}} = f(t,\omega,\hat{\phi},\hat{\theta}) = \gamma[\theta^*(t,\omega,\hat{F}_x) - \hat{\theta}] \tag{17}$$

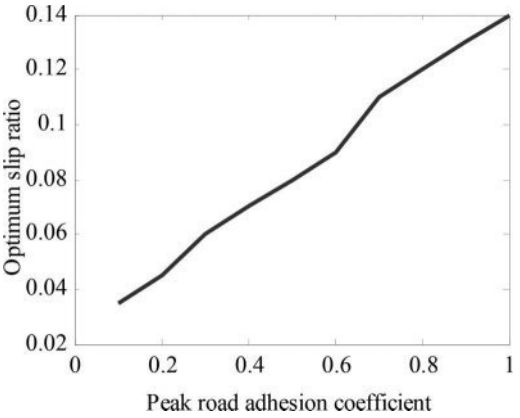


Figure 3. Map of optimum slip ratio.

where θ^* is the numerical solution of function $\phi(t,\omega,\theta)=\hat{\varphi}$.

Based on the above analysis, peak road adhesion coefficient estimator is designed as

$$\begin{aligned}
&\dot{y}=-\frac{K_i}{I}(T_m+r\hat{F}_x)\\
&+\frac{rF_z}{I}f(t,\omega,\hat{\phi},\hat{\theta})\frac{\partial\mu(t,\omega,\hat{\theta})}{\partial\hat{\theta}}\\
&\hat{F}_x=\frac{I}{r}(y+K_i\omega)-F_z\mu(t,\omega,\hat{\theta})\\
&\dot{\hat{\theta}}=\gamma[\theta^*(t,\omega,\hat{F}_x)-\hat{\theta}]=f(t,\omega,\hat{\phi},\hat{\theta})
\end{aligned}\tag{18}$$

5 ADAPTIVE CONTROL OF WHEEL SPEED

There is a one to one mapping relationship between peak road adhesion coefficient and optimum slip ratio. The algorithm proposed in this paper adjusts the reference slip ratio based on the estimation of peak road adhesion coefficient. Then the adaptive control of slip ratio under different road conditions is realized.

Based on Carsim Tiretest module and tire characteristic simulations under different peak road adhesion coefficient, a diagram of optimal slip ratio is acquired and shown in Figure 3.

The online peak road adhesion coefficient estimator estimates the current road and then sends the result to the wheel speed controller, the controller searches for the corresponding optimum slip ratio to calculate the reference wheel speed.

6 EXPERIMENTAL RESULTS

6.1 *Test vehicle*

The test vehicle is a distributed drive electric vehicle shown in Figure 4. The vehicle's front axle is driven by two 25 kW wheel-side motors with reduction gear, the rear axle is driven by two 7.5 kW in-wheel motors.



Figure 4. Test vehicle.

Table 1. Parameters of the test vehicle.

Parameter	Value	Parameter	Value
Mass (kg)	1358	Yaw moment of inertia (kg·m^2)	1835
Wheel base (m)	2.305	Wheel track (mm)	1325 (Front)/ 1390 (Rear)
Distance between COG and front axle (m)	1.117	Distance between COG and front axle (m)	1.188
Height of COG (m)	0.525	Tire rolling radius (m)	0.29
Steering ratio	16.68	Front/Rear axle load	54/46

Table 2. Motor parameters of test vehicle.

Parameter	Front axle motor	Rear axle motor
Rated power (kW)	15	5
Peak power (kW)	25	7.5
Rated torque (Nm)	35.8	100
Peak torque (Nm)	90	150
Rated speed (rpm)	4000	480
Maximum speed (rpm)	9500	1350
Gear ratio	6.2	1

Parameters of the vehicle and motors are listed in table 1 and table 2.

6.2 *Test results on low friction road*

The test condition of experiment is set as follows: the vehicle drives from stationary on a wet slippery tile pavement (peak road adhesion coefficient to be 0.3) with full throttle. The experiment results of left front wheel are shown in Figures 5–7.

It can be seen from the test result that with the control algorithm's involvement, the vehicle's driving efficiency improves significantly, with a final speed

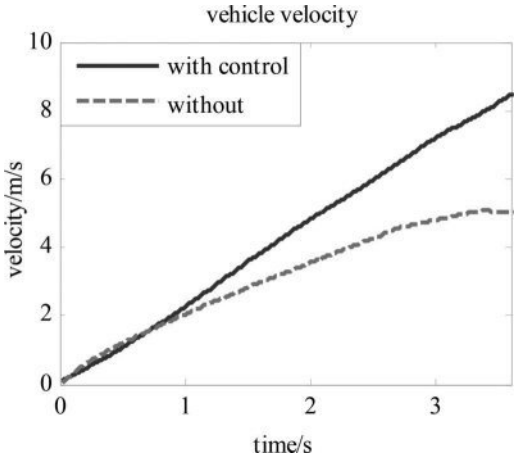


Figure 5. Vehicle velocity versus time.

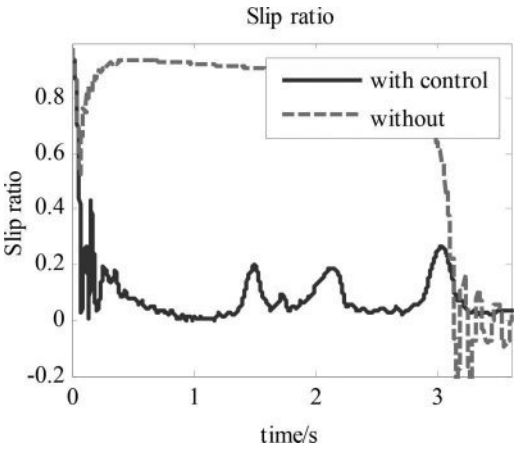


Figure 6. Slip ratio versus time.

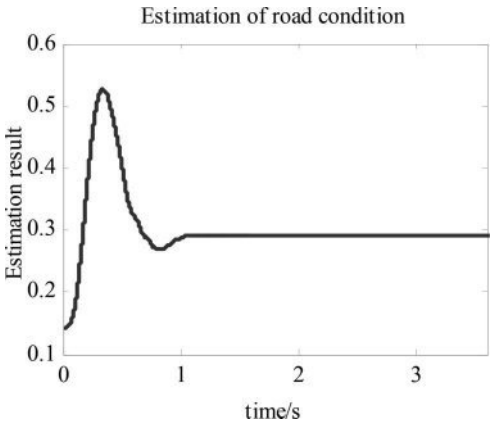


Figure 7. Estimation of road condition versus time.

of 8.3 m/s comparing to 5.1 m/s, which is a 65% improvement in longitudinal acceleration. From the wheel speed and slip ratio diagram, it is clear that the algorithm prevents the wheel speed from surging

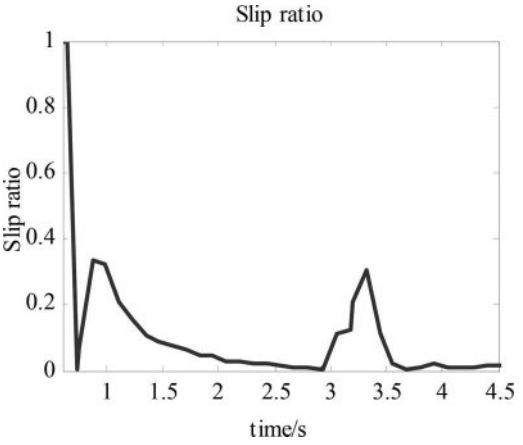


Figure 8. Slip ratio versus time.

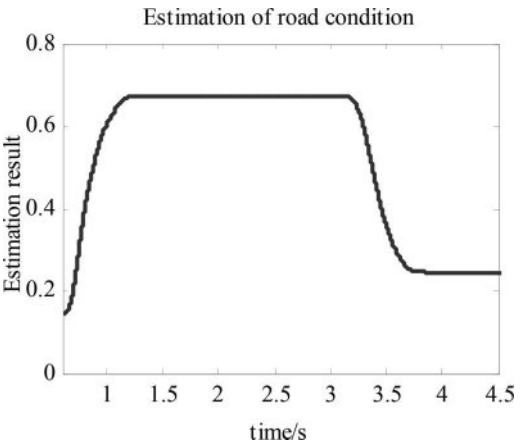


Figure 9. Estimation of road condition versus time.

and increases the usage of the motor torque. Road estimator converges to the real value in 0.5 s.

6.3 *Test results on joint road*

The test condition of experiment is set as follows: the vehicle starts on an asphalt road (peak road adhesion coefficient to be 0.6) to a wet slippery tile pavement, with full throttle. The experiment results of left front wheel are shown in Figure 8–10.

It can be seen from the test result that during the first 3 s, the vehicle is on the high friction road and there is no obvious slippage of wheel. After 3 s when the vehicle enters into the low friction road, there is a sudden rise in slip ratio. But after a short regulation, the controller successfully tracks the reference wheel speed and avoids the slipping trend. The road estimator can estimate the road change and the slip ratio is controlled around the reference value. There is no obvious chattering in driving torque either.

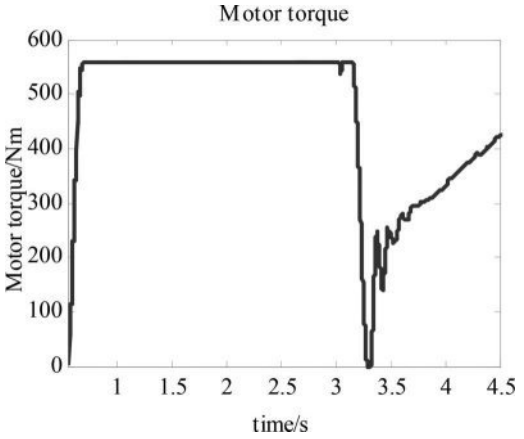


Figure 10. Motor torque versus time.

7 CONCLUSION

In this paper, an adaptive slip ratio control algorithm is proposed for distributed drive electric vehicles. The slip ratio controller is a SMC with conditional integrator, wheel speed is taken as control variable to avoid disturbance of slip ratio at low speed. The algorithm, combined with the road estimator, is robust to the change of road conditions. Experiments show that the algorithm can effectively control the slip ratio converging to the reference slip ratio, and there is a more than 65% improvement of driving efficiency on low tire-road friction road. The road estimator can estimate the real peak road adhesion coefficient in 0.5s after wheel slips.

ACKNOWLEDGEMENT

This research is supported by 'National key research and development plan of China'(Grant No. 2016YFB0100901). 'National Science and Technology Support Program of China' (Grant No. 2015BAG17B01), and 'National Natural Science Foundation of China' (Grant No. U1564207). And the International Exchange Program for Graduate Students, Tongji University.

REFERENCES

Grip, H. F. 2010, Topics in State and Parameter Estimation for Nonlinear and Uncertain Systems. Ph.D Dissertation. Norwegian University of Science and Technology.

Jin C, Xiong L, Yu Z, et al. 2014. Path Following Control for Skid Steering Vehicles with Vehicle Speed Adaption, SAE Paper No. 2014-01-0277.

Khalil H K. 2002. Nonlinear Systems Third Edition. Upper Saddle River, NJ: Prentice-Hall, Inc.

Kay H S, Khalil H K. 2002. Universal controllers with nonlinear integrators. Proceedings of the American Control Conference. Vol. 1, p.116–121.

Advanced Vehicle Control – Edelmann, Plöchl & Pfeffer (Eds)
© 2017 Taylor & Francis Group, London, ISBN 978-1-138-02992-7

Perceptible changes in driving dynamics due to regenerative braking: Analysis and reduction through active chassis systems

T. Helfrich & M. Lienkamp
Department of Mechanical Engineering, Institute of Automotive Engineering, Technical University of Munich, Munich, Germany

ABSTRACT: The changes of vehicle behavior when using regenerative braking compared to braking with the hydraulic brake force distribution are investigated by comparing them to thresholds representing driver-perceivable changes in yaw, pitch, and roll in real driving conditions. Active chassis systems are then investigated to reduce these changes and therefore allow for higher regenerative braking at the rear axle. This illustrates the potential usage of active chassis systems to achieve higher energy efficiency without undesired feedback to the driver.

1 INTRODUCTION

The vehicle dynamics of agile and sporty cars is a well-established topic. The current state-of-the-art in braking behavior may be considered near-optimal for average drivers and even for most drivers with higher than usual demands on driving behavior. The introduction of regenerative braking in electric vehicles may cause deviations from this target behavior, especially when regenerative braking is suddenly switched on or off. This may cause safety concerns and owner dissatisfaction with their vehicle. Perceivable deviations while yawing may occur well below stability limits, especially in vehicles with rear-wheel drive (Helfrich and Lienkamp 2015, Dahlke et al. 2016).

According to Crolla and Cao (2012), vehicles with regenerative braking may have a different behavior not only in yaw, but in pitch and roll as well. They ascribe these mostly to changes in center of gravity or mass caused by the electric drivetrain. In this paper, it will be investigated, if changes can be caused by regenerative braking alone and not only due to varying vehicle properties. Differences in all three spatial dimensions will be analyzed using a multi-body simulation (MBS) model and compared to well-founded thresholds of driver-acceptable changes in yaw, pitch, and roll.

Active chassis systems have become more and more common in recent years. Therefore, after analyzing the occuring differences, the potential of different active chassis control systems to reduce them is studied. The target behavior matches the behavior under braking with the installed brake force distribution, as this is a sensible safe operating mode. Active chasssis systems have already been investigated for their possible influence on yaw control under regenerative braking, but without considering driver perception, pitch, or roll (Shyrokau et al. 2014).

2 THRESHOLDS FOR ACCEPTABLE CHANGES

Thresholds for human perception of rotational motion have been researched since at least the 1960s (Guedry and Lauver 1961). Most studies in cognitive science have limited applicability to real driving conditions, which are the focus of this paper. This is due to their experimental setup, which often includes repeated oscillations around a single axis of motion while the subjects are blindfolded, e.g. (Benson et al. 1989, Grabherr et al. 2008). In contrast, motions in vehicles are often superimposed with simultaneous visual inputs and cognitive load for performing the driving task. There is no consensus in literature if this may lead to an increase or decrease of thresholds.

For this paper, the values are therefore taken from sources that match real driving conditions more closely, i.e. real driving tests and tests in high-quality driving simulators. Most of the selected publications utilize an evaluation system correlating the objective differences in yaw, pitch, or roll with a rating provided by subjects on a scale, e.g. 1–10. The thresholds of the identified and pertinent sources are given in table 1. Thresholds are determined by the needed value for a rating change on the respective scale, which yields the discernible difference.

The values are irregularly scattered with some very small or large outliers. To obtain single values for the dimensions, the median of these values is taken. For pitch and roll, both an angle and an angular velocity value are provided. The final values for this paper are $\dot{\psi}_{\text{thresh}} = 0.54^\circ\,\text{s}^{-1}$ for yaw, $\Theta_{\text{thresh}} = 0.33^\circ$ and $\dot{\Theta}_{\text{thresh}} = 0.24^\circ\,\text{s}^{-1}$ for pitch, $\varphi_{\text{thresh}} = 0.51^\circ$ and $\dot{\varphi}_{\text{thresh}} = 0.62^\circ\,\text{s}^{-1}$ for roll, and $\beta_{\text{thresh}} = 0.5^\circ$ for the side-slip angle.

Table 1. Thresholds for detectable differences in behavior.

Reference	Yaw rate	Pitch angle and rate	Roll angle and rate	Side-slip angle
Matsushita et al. (1980)	2.5° s^{-1}	–	–	–
Ash (2002)	1.5° s^{-1}	–	–	–
Muragishi et al. (2006)	0.08–0.58° s^{-1}	0.08–0.4° s^{-1}	0.2–0.24° s^{-1}	–
Schmidt et al. (2006)	2.0° s^{-1}	0.5°	1.0°	–
Neukum et al. (2008)	0.5° s^{-1}	–	1.0° s^{-1}	–
Neukum et al. (2010b)	0.5° s^{-1}	–	–	–
Kraft et al. (2011)	–	0.18–0.33°	–	–
Stock et al. (2011)	2.17° s^{-1}	–	–	0.5°
Nesti et al. (2012)	–	–	6.3° s^{-1}	–
Simmermacher et al. (2013)	0.4° s^{-1}	–	–	0.73°
Tosolin et al. (2013)	0.3° s^{-1}	–	–	–
Gutjahr et al. (2014)	–	–	0.02°	0.01°

3 TEST VEHICLE AND MANEUVERS

The studied vehicle is the research vehicle *Visio.M* which was built during a joint research project at the Technical University of Munich (Riederer and Lienkamp 2014). It is modeled in the MBS-tool SIMPACK. The model has been validated with Kinematics & Compliance measurement data. Validation of the model with real driving tests is ongoing. The vehicle model consists of McPherson struts at the front and rear, steering and anti-roll bar at the front and a simplified drivetrain with a differential at the rear wheels.

The Visio.M is a full-electric two-seater for urban environments developed with a focus on high energy efficiency while offering satisfying and enjoyable driving dynamics (Schultze et al. 2014, Schultze et al. 2015). The high efficiency is achieved by low weight, aerodynamic drag, and rolling resistance. The concept includes a torque vectoring differential at the driven rear axle. Some key facts are compiled in table 2.

Simulations of braking maneuvers from 80 km h^{-1} with lateral accelerations ranging from 0–6 m s^{-2} are conducted on a high-μ surface. This range exemplifies the use-case of sporty driving as detailed in section 1. The mechanical brake force, regenerative braking torque and active systems are all applied as a ramp within 0.1 s. Available power for regenerative braking from the electric motor is not considered as a limiting factor.

Table 2. Vehicle parameters.

Body mass with driver	720 kg
Wheel base	2.1 m
Track width front/rear	1.45/1.55 m
Continuous/peak power	15/45 kW
Wheel dimensions front and rear	115/70 R16
Weight distribution front:rear	43:57
Brake force distribution front:rear	62.5:37.5

Table 3. Modeling approach for active systems.

Torque vectoring	additional torque between left and right output shaft of differential
Brake torque vectoring	additional pressure acting between brake disks and pads
Active springs	additional forces proportional to spring travel
Active dampers	additional forces proportional to damper velocity
Active anti-roll bar	additional torque between left and right halves of torsion bar
Active front/rear steering	added movement around the wheels' z-axes
Active camber	added movement around the wheels' x-axes

4 INVESTIGATED ACTIVE CHASSIS SYSTEMS

According to preliminary results (Helfrich and Lienkamp 2015), brake torque vectoring, torque vectoring and active front and rear steering are most promising to influence yaw behavior. Active anti-roll bars, dampers and springs are additionally considered for affecting pitch and roll dynamics. Active camber is investigated, as well.

The multi-body modeling of the systems happened in a simplified way, either through additional forces or torques applied to the model or, in case of the active steering and camber systems, through added, artificially moved bodies which act between the wheel and wheel hub, see table 3. The investigated actions for each system cover a realistic range adapted to the vehicle.

5 METHODOLOGY

A corridor constituting the acceptable region for vehicle behavior around the time-dependent target behavior is defined using the thresholds determined in section 2. An optimizing function representing this corridor is defined (Helfrich & Lienkamp 2015,

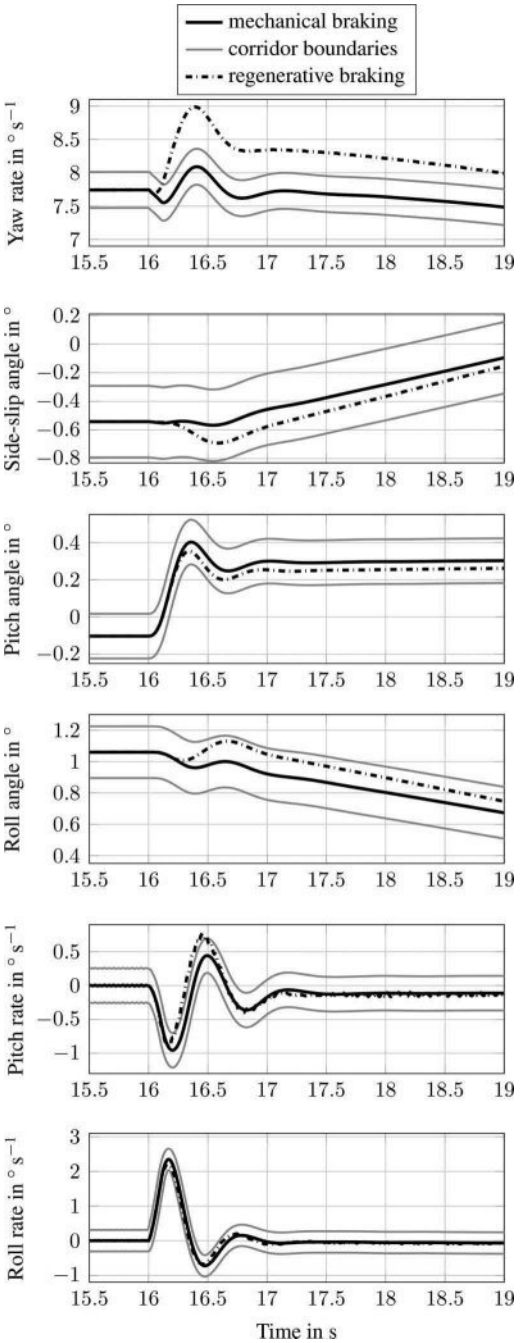


Figure 1. Exemplary plot comparing mechanical braking and its corridor with regenerative braking.

Murmann, Harzheim, & Dominico 2014). This is implemented as a Co-Simulation between SIMPACK and MATLAB.

At first, without applying an active chassis system, limits for pure regenerative braking are determined by comparing the corridor to the vehicles' behavior under regenerative braking. These results are presented and discussed in section 6.1.

Figure 1 shows an exemplary plot of the differences in yaw, pitch, and roll during a braking in corner maneuver at a lateral acceleration of $3\,\mathrm{m\,s^{-2}}$ and a deceleration of $1.5\,\mathrm{m\,s^{-2}}$. The deceleration starts at $t = 16\,\mathrm{s}$ from steady-state cornering. The thresholds for yaw and pitch rate are exceeded, while roll angle also approaches its threshold.

The construction of the corridors allows for differences in time and the threshold of the respective dimension. In each iteration of the optimization it is used to check for exceedance of the thresholds by comparing the regenerative braking to mechanical braking of the same deceleration. Thereby, the maximum amount of regenerative braking can be optimized for each single threshold by checking against the respective corridor.

Afterwards, the optimization is used to determine the necessary intensity of intervention of the active chassis systems to keep the vehicle within the acceptable region for an increased amount of regenerative braking. This results in a maximum attainable deceleration by regenerative braking within the boundaries of the corridors for single active chassis system. These results are presented in section 6.2 and compared with results without active systems. This shows their respective potential for improving vehicle dynamics under regenerative braking.

6 RESULTS

6.1 *Differences between normal and regenerative braking*

For straight-line braking, the maximum achievable deceleration through regenerative braking at the rear axle is between 4–$4.5\,\mathrm{m\,s^{-2}}$. When braking harder, excessive wheel-slip occurs. These simulations have been discarded for straight line braking and braking while cornering.

Figure 2 shows the maximum deceleration by regenerative braking until the thresholds are exceeded for the whole range of initial lateral accelerations. The threshold for pitch angle is never exceeded for these situations, therefore it is not diagramed. The driving situation displayed in figure 1 is marked by the asterisk ($*$).

The differences in pitch rate are most noticeable already for straight-line braking and up to $1.3\,\mathrm{m\,s^{-2}}$ lateral acceleration. Pitch rate is also the most noticeable for lateral accelerations ranging from around 2.4–$3.9\,\mathrm{m\,s^{-2}}$. The second most noticable effect is the difference in yaw rate, which is also crucial for vehicle stability while cornering. The results for side-slip angle and roll angle are similarly shaped and much higher than for the yaw rate. The roll rate threshold is close to the yaw rate threshold for low lateral accelerations. If yaw behavior were less noticable, and thus shifted to higher decelerations, changes in roll

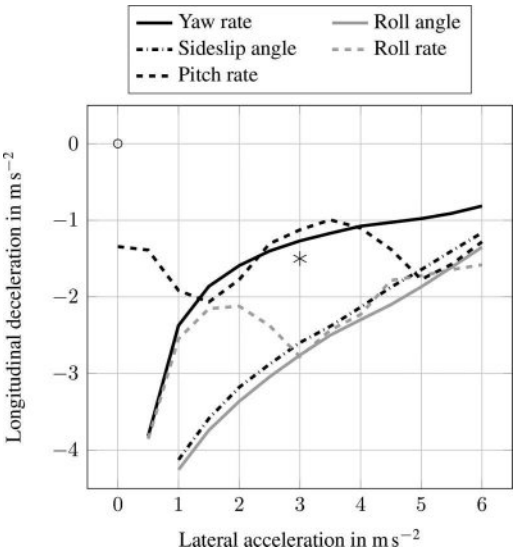


Figure 2. Limits for decelerations for different thresholds.

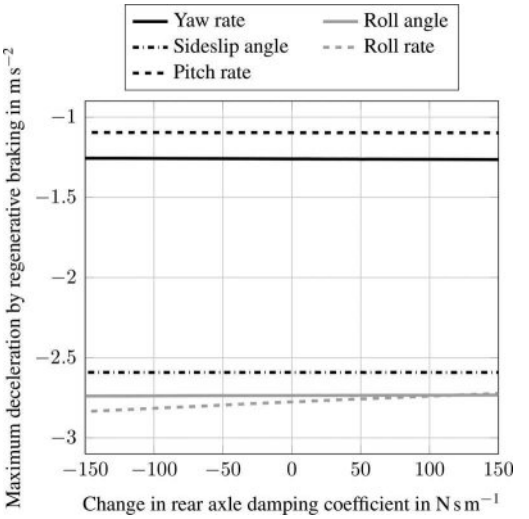


Figure 3. Results for all dimensions over the range of action for the rear dampers for 3 m s^{-2} of lateral acceleration.

rate might be noticable first. The trend of roll and pitch rates is non-monotonous, because their responses over time are not monotonically increasing with lateral acceleration for each time step, but are also phase-shifting compared mechanical braking.

6.2 *Possible increases by use of active chassis systems*

The potential of the active systems is now determined according to section 5. A lateral acceleration of 3 m s^{-2}, as displayed in figure 1, is selected for this investigation, as this exemplifies an agile driving situation. For each active system and all six corridors, the required amount of action from the system for a maximization of regenerative braking torque is determined. The results for increases of more than 1% are compiled in table 4. They will now be discussed by system in detail.

Pitch-angle is not shown, because the threshold is never exceeded for regenerative braking. The cross-domain column shows the maximum relative decleration in relation to the lowest passive value (pitch-rate).

Torque vectoring allows for much higher regenerative braking for the yaw rate and pitch rate thresholds. The necessary differential torques for these two optima also lie together closely allowing near optimal control for both dimensions. Influences in side-slip angle and roll angle dimensions are moderate, influence on roll rate is small.

Brake torque vectoring considerably increases the possible amount of regenerative braking until yaw rate and pitch rate limits are exceeded. Modest gains are achieved for side-slip angle and roll dimensions. Brake torque vectoring in this case acts on the front right wheel to decrease the oversteer reaction in left turns. It naturally increases the vehicle's deceleration further than pure regenerative braking, dissipating a substantial amount of kinetic energy in the process, but still allows for a large increase in regenerative braking.

Active springs can moderately influence all dimensions, yet very high actions are required to influence yaw behavior. Influencing pitch rates by softening the springs is much more effective on the front axle than on the rear axle.

Variable dampers at the front and rear axle are only able to influence the limit set by the roll-rate threshold and only at a low level. The necessary change in damping coefficient is very high. Figure 3 shows the results over the whole range of action from −150–150 N s m^{-1} for the rear dampers. Results for all dimensions but roll rate are virtually constant, for roll rate a linear trend appears. Not considered are side-effects on comfort.

Active anti-roll bars at the front and rear can have a distinct influence on the yaw rate results, but require very high actions. The effect of roll-steer on yaw behavior seems to dominate for this vehicle, as the applied torque at the front and rear axle have the same negative sign resulting in more roll angle. A positive sign of torque leads to higher yaw reactions and might even destabilize the vehicle leading to discarding of the simulation runs, which happens for the roll angle simulations explaining the low impact of the anti-roll bars here.

Active steering is very effective for both front and rear axles, leading to good yaw and pitch behavior. Side-slip and roll angles can be influenced moderately.

Active camber can moderately improve yaw and pitch behavior at the front axle, but only for high values of 4.5°, the maximum allowed value, as displayed in figure 4. Improvements in yaw pitch rate and roll angle can already be shown for more feasible lower angles.

Table 4. Ratio of relative increases ($\frac{\text{Increased regenerative deceleration}}{\text{Original regenerative deceleration}}$, each first row) and necessary action (each second row) per dimension and system. ∗: value limited by the investigated range of action, ∗∗: value limited by the investigated range of regenerative braking.

System	Yaw rate	Side-slip angle	Pitch rate	Roll angle	Roll rate	Cross-domain
Torque vectoring	3.01	1.52	3.33	1.38	1.05	1.95
at value, N m	−97.69	−71.43	−101.92	−56.57	−21.37	−60.26
Brake torque vectoring, front right	2.98	1.27	2.49	1.20	1.03	2.49
at value, bar	8.63	3.75	5.25	2.81	2.63	5.25
Active springs, front	1.52	1.11	1.51	–	1.05	1.46
at value, N mm^{-1}	−26.00∗	−26.00∗	−7.22	–	−3.32	−7.35
Active springs, rear	1.60	1.17	1.35	1.06	–	1.16
at value, N mm^{-1}	−26.13	−29.00	−29.50	29.88	–	−13.85
Active dampers, front	–	–	–	–	1.03	–
at value, N s m^{-1}	–	–	–	–	150.00∗	–
Active dampers, rear	–	–	–	–	1.02	–
at value, N s m^{-1}	–	–	–	–	−150.00∗	–
Active anti-roll bar, front	1.67	1.08	1.53	1.09	1.05	1.49
at value, N m	−75.00∗	−75.00∗	−49.31	40.78	−9.53	−95.39
Active anti-roll bar, rear	1.84	1.16	–	1.02	1.04	–
at value, N m	−75.00∗	−75.00∗	–	12.94	−10.40	–
Active steering, front	3.28	1.44	2.85	1.73∗∗	1.09	1.89
at value, °	−0.99	−0.76	−0.97	−0.40	−0.34	0.12
Active steering, rear	2.40	1.27	2.52	1.22	1.06	2.03
at value, °	0.46	0.30	0.39	0.28	0.15	0.20
Active camber, front	1.43	1.05	1.24	1.08	–	1.21
at value, °	4.05∗	4.50∗	4.50∗	4.50∗	–	−3.49
Active camber, rear	1.10	1.02	1.12	–	–	1.12
at value, °	0.59	0.44	0.65	–	–	0.65

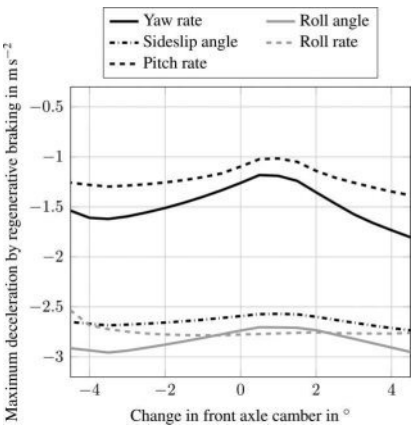


Figure 4. Results for all dimensions over the range of action for front camber for 3 m s^{-2} of lateral acceleration.

The cross-domain-column shows the necessary action by the respective active systems, which allows for the highest increase when considering all dimensions at the same time.

6.3 *Summary*

It has been shown, that differences in perceptible vehicle behavior not only can occur in yaw, but, depending on situation, also in pitch and roll. Active chassis systems allow for higher regenerative braking levels by reducing these differences and, therefore, their impact on the driver.

For yaw motions, side-slip angles, and pitch rates, torque vectoring, brake torque vectoring and active steering systems are most effective. Roll behavior is closely coupled to yaw behavior leading to similar, yet lower results.

7 CONCLUSION

Having highlighted the occurring differences induced by regenerative braking, multi-body simulations were used to determine the potential of active chassis systems to reduce these differences to levels below thresholds for perceivable changes in driving dynamics. Thereby, vehicle behavior is more consistent for the driver, while allowing for higher amounts of regenerative braking and, thus, a higher overall energy efficiency.

8 OUTLOOK

In future work, the quality of modeling of the vehicle and active chassis systems will be increased. Furthermore, energy costs and weight increases can be monitored and compared to increases in regenerative braking. Therefore, reults presented here might not be energy optimal for the full vehicle. Additionally, behavior on low-μ-surfaces and for all lateral accelerations needs to be considered.

This paper shows, which systems might be used to influence behavior under regenerative braking. While the influences are too low to justify installing an additional active system, already present systems can be accordingly utilized to improve driving impression.

CONTRIBUTIONS AND ACKNOWLEDGMENTS

T. Helfrich (corresponding author) initiated the idea of the paper, defined the conditions under which the study was conducted, provided the simulation model and optimization framework, and executed the simulations and post-processing.

M. Lienkamp made an essential contribution to the conception of the research project. He revised the paper critically for important intellectual content. He gave final approval of the version to be published and agrees to all aspects of the work. As a guarantor, he accepts responsibility for the overall integrity of the paper.

The project Visio.M was funded under the priority program "Key Technologies for Electric Mobility – STROM" of the Federal Ministry for Education and Research (BMBF).

REFERENCES

Ash, H. A. S. (2002). *Correlation of Subjective and Objective Handling of Vehicle Behaviour*. Dissertation, University of Leeds, Leeds.

Benson, A. J., E. C. Hutt, & S. F. Brown (1989). Thresholds for the perception of whole body angular movement about a vertical axis. *Aviation, space, and environmental medicine 60*(3), 205–213.

Crolla, D. A. & D. Cao (2012). The impact of hybrid and electric powertrains on vehicle dynamics, control systems and energy regeneration. *Vehicle System Dynamics 50*(sup1), 95–109.

Dahlke, F., P. Bortolussi, & D. Schramm (2016). Maximization of electric brake torquethrough hybrid adaptive model control. In P. Pfeffer (Ed.), *7th International Munich Chassis Symposium 2016*, Proceedings, pp. 777–795. Wiesbaden: Springer Fachmedien Wiesbaden GmbH and Springer Vieweg.

Grabherr, L., K. Nicoucar, F. W. Mast, & D. M. Merfeld (2008). Vestibular thresholds for yaw rotation about an earth-vertical axis as a function of frequency. *Experimental brain research 186*(4), 677–681.

Guedry, F. E. & L. S. Lauver (1961). Vestibular reactions during prolonged constant angular acceleration. *Journal of Applied Physiology 16*(2), 215–220.

Gutjahr, D. (2014). *Objektive Bewertung querdynamischer Reifeneigenschaften im Gesamtfahrzeugversuch: KIT, Diss.–Karlsruhe, 2013*, Volume 20 of *Karlsruher Schriftenreihe Fahrzeugsystemtechnik*. Karlsruhe and Hannover: KIT Scientific Publishing and Technische Informationsbibliothek u. Universitätsbibliothek.

Helfrich, T. & M. Lienkamp (2015). Potentiale zur Steigerung der Rekuperation durch aktive Fahrwerkssysteme. In *Reifen-Fahrwerk-Fahrbahn 2015*, Volume 2241 of *VDI-Berichte*. Düsseldorf: VDI-Verlag.

Kraft, C. (2011). *Gezielte Variation und Analyse des Fahrverhaltens von Kraftfahrzeugen mittels elektrischer Linearaktuatoren im Fahrwerksbereich: KIT, Diss.–Karlsruhe, 2010* (Print on demand ed.), Volume 5 of *Karlsruher Schriftenreihe Fahrzeugsystemtechnik*. Karlsruhe and Hannover: KIT Scientific Publishing and Technische Informationsbibliothek u. Universitätsbibliothek.

Matsushita, A., K. Takanami, N. Takeda, & M. Takahashi (1980). Subjective Evaluation and Vehicle Behavior in Lane-Change Maneuvers. In SAE International (Ed.), *Passenger Car Meeting & Exposition*, SAE Technical Paper Series. SAE International400 Commonwealth Drive, Warrendale, PA, United States.

Muragishi, Y., K. Fukui, Y. Asaga, E. Ono, Y. Yamamoto, E. Katsuyama, & H. Sakai (2006). Enhancement of Vehicle Dynamic Behavior Based on Visual and Motion Sensitivity (First Report): Development of Human Sensitivity Evaluation System. In Advanced Vehicle Control (Ed.), *Proceedings of the International Symposium on Advanced Vehicle Control 2006*, Hsinchu. National Tsing Hua Univ.

Murmann, R., L. Harzheim, & S. Dominico (2014). Neuartige Methode zur Bewertung von Versuchs- und Simulationsergebnissen. In VDI (Ed.), *17. Kongress SIMVEC – Simulation und Erprobung in der Fahrzeugentwicklung 2014*, Volume 2224 of *VDI-Berichte*, pp. 71–84. Düsseldorf: VDI-Verlag.

Nesti, A., C. Masone, M. Barnett-Cowan, P. R. Giordano, H. H. Bülthoff, & P. Pretto (2012). Roll rate thresholds and perceived realism in driving simulation. *Actes INRETS*, 23–31.

Neukum, A. (2010). Controllability of erroneous steering torque interventions: Driver reactions and influencing factors. In P. Pfeffer (Ed.), *1st International Munich Chassis Symposium 2010*, Proceedings.

Neukum, A., E. Ufer, J. Paulig, & H.-P. Krüger (2008). Controllability of superposition steering system failures. *Steering tech*, 1–12.

Riederer, S. & M. Lienkamp (Eds.) (2014). *Forschungsprojekt Visio.M: ATZextra Oktober 2014*. Springer Verlag.

Schmidt, G., S. Scholz, A. Neukum, & H.-P. Krüger (2006). *Fahrer-Fahrzeug-Wechselwirkungen bei Fahrmanövern mit Querdynamikbeanspruchungen und zusätzlichen Vertikaldynamikstörungen*, Volume 208 of *FAT-Schriftenreihe*. FAT.

Schultze, A., T. Helfrich, & M. Lienkamp (2014). Effiziente Fahrdynamik. In S. Riederer and M. Lienkamp (Eds.), *Forschungsprojekt Visio.M*. Springer Verlag.

Schultze, A., T. Helfrich, & M. Lienkamp (2015). Suspension design of the Visio.M electric research vehicle. In P. Pfeffer (Ed.), *6th International Munich Chassis Symposium 2015*, Proceedings, pp. 79–94. Wiesbaden: Springer Fachmedien Wiesbaden.

Shyrokau, B., D. Savitski, & D. Wang (2014). Influence of Active Subsystems on Electric Vehicle Behavior and Energy Characteristics.

Simmermacher, D. (2013). *Objektive Beherrschbarkeit von Gierstörungen in Bremsmanövern* (Als Ms. gedr ed.), Volume 771 of *Fahrzeugtechnik TU Darmstadt*. Düsseldorf: VDI-Verlag.

Stock, G. (2011). *Handlingpotentialbewertung aktiver Fahrwerkregelsysteme: Techn. Univ., Diss.–Braunschweig, 2010*, Volume 25 of *Schriftenreihe des Instituts für Fahrzeugtechnik, TU Braunschweig*. Aachen: Shaker Verlag.

Tosolin, G., J. Webb, A. Català, A. Escuer, & Y. J. Hyun (2013). Development of Methodologies for Evaluation, Simulation and Improvement of Cross-Wind Sensitivity. In *Proceedings of the FISITA 2012 World Automotive Congress*, Volume 195 of *Lecture Notes in Electrical Engineering*, pp. 23–33. Berlin and Heidelberg: Springer Verlag.

Advanced Vehicle Control – Edelmann, Plöchl & Pfeffer (Eds)
© 2017 Taylor & Francis Group, London, ISBN 978-1-138-02992-7

A development of nonlinear adaptive ABS control using optimal slip tracker

S. Lee, B. Yang & J. Jeon
Hyundai Motor Company R&D Division, Hwaseong-si, Gyeonggi-do, Republic of Korea

ABSTRACT: ABS control strategies can be classified mainly according to its control patterns, deceleration control and slip control. Deceleration control is noisy but robust while slip control is smoother but has robustness issues because the real optimal slip, the target of control, is unknown itself. In this research, adaptive nonlinear sliding control was designed for main slip controller to give NVH advantage with optimal slip tracker to give robustness. Controller was designed based on nonlinear wheel dynamics and stability and convergence were proved by Lyapunov method. Augmented control architecture with simple estimation of normal forces and friction coefficients was implemented in MATLAB-CarSim Simulation environment with CarSim-default vehicle and the good performance of the designed whole control law was demonstrated for high friction, low friction and high to low friction jump situation with ideal and real actuators showing the importance of actuator model accuracy for the real system.

1 INTRODUCTION

In 1945, after being developed to avoid spin-out of an airplane and puncture of tire (Petersen 2003), Anti-lock Brake System (ABS) started to be installed on vehicles in the 1960s and has been widely and deeply researched (Aly et al. 2011) so that is essential safety system which is indispensable for all the vehicle in these days.

The strategy of ABS control can be classified to 2 types. The first one is deceleration-based control which controls wheel based on the rate of wheel speed, that is, deceleration of the wheel that can be noisy because of calculation of the derivative of wheel speed which is the only information of the wheel when we design the controller of ABS. This method has been produced for many vehicles by many companies and has high robustness with loss of NVH because of the noisy characteristics. Otherwise, the other control strategy, slip-based control regulates the wheel based on slip amount so that has profits on NVH aspect because the magnitude of oscillation of the wheel speed can be reduced, but the optimal slip point itself can't be known by this control and this can makes the control performance be suboptimal which is followed by increase of braking distance that means the loss of braking. Therefore to secure deceleration which is related to the braking performance, a number of tuning is necessary and still having the issue with robustness.

Also, the controller has been developed by linear controller with gain-scheduling in many times. To respond the nonlinearity of wheel dynamics enough, therefore, developer should tune case by case for all of the road condition and weather and so on and this results in the full of man hours of the developer.

For this, in this paper, slip-based nonlinear adaptive ABS control law with optimal slip tracker based for longitudinal direction is proposed. Inner loop controller of adaptive sliding mode control adapts matched, unmatched uncertainties and carries out tracking of the target slip command from outer loop controller which tracks the optimal slip point based on simple estimation of road-wheel friction coefficients and normal forces of each wheel to integrate the profits of the two methods in control architecture.

At first, sliding mode controller will be designed based on the nonlinear wheel slip dynamics and the adaptive controller to overcome the uncertainties will be designed. In addition to this, the optimal slip tracker which will be designed after this will be integrated in the numerical simulation environment of MATLAB-CarSim simulation environment with CarSim-default vehicle to show the performance and robustness of proposed controller with various road conditions. Here, one can see the importance of the enough consideration of actuator dynamics for real system which has the real actuator with time delay and some response.

2 NONLINEAR WHEEL SLIP DYNAMICS

To design ABS controller for longitudinal direction, first, nonlinear wheel dynamics should be considered. Figure 1 shows the free body diagram of a wheel braking and the variables used here were arranged in Table 1, where T_o indicates sum of all the other torques exerting on the wheel except braking torque, T_b.

The nonlinear dynamics of a wheel can be described with Equation 1. With the definition of wheel slip (Eq. 2), wheel slip dynamics can be derived as (Eq. 3)

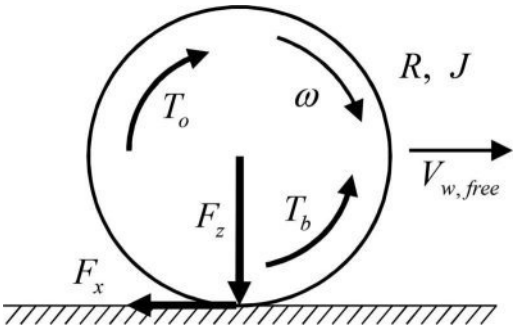


Figure 1. Free body diagram for wheel dynamics.

Table 1. Nomenclature.

Variables	Meanings
J	Wheel moment of inertia
ω	Wheel angular speed
R	Radius of wheel
F_z	Normal force
F_x	Longitudinal force
μ	Longitudinal friction coefficient
T_b	Braking torque
T_o	Other torque exerted
$V_{w,free}$	Free rolling wheel speed
λ	Wheel slip

(Savaresi & Tanelli 2010). Here, $1/V_{w,free}$ multiplied to every term in this equation implies that even with the same net torque and braking deceleration exerted on the wheel, the rate of slip change increase more and more with respect to the vehicle speed decreasing, which is the exact situation to overcome by ABS controller. And this makes that a real actuator with some response characteristics or time delay get increase the instability of the wheel dynamics for low speed.

$$J\dot{\omega} = RF_z\mu + T_o - T_b \tag{1}$$

$$\lambda = \frac{V_{w,free} - R\omega}{V_{w,free}} \tag{2}$$

$$\begin{aligned}\dot{\lambda} &= -\frac{R\dot{\omega}V_{w,free} - R\omega\dot{V}_{w,free}}{V_{w,free}^{\ 2}} \\ &= -\frac{R}{JV_{w,free}}\left(RF_z\mu + T_o - T_b\right) + \frac{1-\lambda}{V_{w,free}}\dot{V}_{w,free}\end{aligned} \tag{3}$$

T_o is matched to the braking torque, T_b, including driving torque on each situation with various gear transmission position and rolling resistance and so on, therefore was defined as matched uncertainty, σ_m. And the model errors which is realized by the estimation performance of normal forces and friction coefficients can be defined as unmatched uncertainty σ'_{um} at the outside of the matching. Then, the slip dynamics can be derived as Equation 4. Note that, in control phase, the uncertainties will have constant nominal values in steady state.

$$\begin{aligned}\dot{\lambda} &= -\frac{R}{JV_{w,free}}\left(RF_z\mu + \sigma_m - T_b\right) \\ &\quad + \frac{1-\lambda}{V_{w,free}}\dot{V}_{w,free} + \sigma'_{um}\end{aligned} \tag{4}$$

3 CONTROLLER DESIGN

3.1 *Inner loop: Nonlinear adaptive slip controller*

ABS control architecture suggested in this paper is composed of optimal slip tracker generating target slip command in outer loop and nonlinear adaptive slip controller getting and tracking this command in inner loop. In this research, nonlinear adaptive sliding mode controller was used for the inner loop slip tracking controller.

Let's define sliding variable. The relative order in wheel dynamics in Equation 4 is unity therefore the sliding variable can be defined as the slip error, $S = \lambda - \lambda_{des}$. Then the rate of change of the sliding variable can be derived as following.

$$\begin{aligned}\dot{S} = \dot{\lambda} - \dot{\lambda}_{des} &= -\frac{R}{JV_{w,free}}\left(RF_z\mu + \sigma_m - T_b\right) \\ &\quad + \frac{1-\lambda}{V_{w,free}}\dot{V}_{w,free} + \sigma_{um}\end{aligned} \tag{5}$$

Here, $\sigma_{um} = \sigma'_{um}$ – derivative of λ_{des} which means the unmatched uncertainty we will adapt includes the change of the desired slip from outer loop controller.

Sliding manifold of derivative of $S = -KS$ for smooth convergence without chattering was introduced and the target braking torque command with estimates for normal forces, friction coefficients and adaptive parameters was derived as Equation 6. Here, as we mentioned, the estimates of unmatched uncertainty, σ_{um}, adapts the real unmatched uncertainty with change rate of desired slip command from outer loop controller.

$$\begin{aligned}T_{b,CMD} &= \hat{C}^{-1}(s)\Big(RF_z\mu + \hat{\sigma}_m \\ &\quad - \frac{JV_{w,free}}{R}\left(\frac{1-\lambda}{V_{w,free}}\dot{V}_{w,free} + \hat{\sigma}_{um} + KS\right)\Big)\end{aligned} \tag{6}$$

Here, C(s) is for actuator model ($T_b = C(s)\ T_{b,CMD}$) with Laplace variable, s. Therefore, the proposed braking torque command above has the estimate of actuator dynamics. In this research, the other estimations were abbreviated, in other words, the estimation of speed was assumed to be exact enough.

The error dynamics of the sliding mode was shown in Equation 7. In steady state, the multiplication of actuator dynamics modeled and inverse of the real actuator dynamics converges to unity. Therefore, Equation 8 shows the sliding variable in steady state and this means with no adaptive errors the sliding variable converges to the origin in phase plane.

$$\begin{aligned}\dot{S} &= -\frac{R}{JV_{w,free}}\left(RF_z\mu + \sigma_m - C(s)T_{b,CMD}\right) \\ &+ \frac{1-\lambda}{V_{w,free}}\dot{V}_{w,free} + \sigma_{um} \\ &= -KS - \frac{R}{JV_{w,free}}\left(\left(1 - C(s)\hat{C}^{-1}(s)\right)RF_z\mu\right. \\ &\left. + \sigma_m - C(s)\hat{C}^{-1}(s)\hat{\sigma}_m\right) \\ &+ \left(1 - C(s)\hat{C}^{-1}(s)\right)\left(\frac{1-\lambda}{V_{w,free}}\dot{V}_{w,free} + KS\right) \\ &+ \sigma_{um} - C(s)\hat{C}^{-1}(s)\hat{\sigma}_{um}\end{aligned} \tag{7}$$

$$S = \frac{1}{K}\left(-\frac{R}{JV_{w,free}}\tilde{\sigma}_m + \tilde{\sigma}_{um}\right) \tag{8}$$

where the uncertainty variables with wave representation above it means adaptive errors of real values minus estimates.

To get rid of the errors of adaptation, adaptive law was designed by Lyapunov method. First, with the Lyapunov candidate, $L = 1/2\ S^2$, can make the rate of change of Lyapunov candidate as following.

$$\begin{aligned}\dot{L} &= S\dot{S} = -KS^2 \\ &- S\frac{R}{JV_{w,free}}\left(\left(1 - C(s)\hat{C}^{-1}(s)\right)\left(RF_z\mu + \hat{\sigma}_m\right) + \tilde{\sigma}_m\right) \\ &+ S\left(1 - C(s)\hat{C}^{-1}(s)\right)\left(\frac{1-\lambda}{V_{w,free}}\dot{V}_{w,free} + KS\right) \\ &+ S\left(\tilde{\sigma}_{um} + \left(1 - C(s)\hat{C}^{-1}(s)\right)\hat{\sigma}_{um}\right)\end{aligned} \tag{9}$$

With the definition of the whole augmented Lyapunov candidate as Equation 10, the rate of change of the Lyapunov candidate can be derived as Equation 11.

$$L = \frac{1}{2}S^2 + \frac{1}{2K_{\sigma m}}\tilde{\sigma}_m^{\ 2} + \frac{1}{2K_{\sigma um}}\tilde{\sigma}_{um}^{\ 2} \tag{10}$$

$$\begin{aligned}\dot{L} &= S\dot{S} + \frac{1}{K_{\sigma m}}\tilde{\sigma}_m\dot{\tilde{\sigma}}_m + \frac{1}{K_{\sigma um}}\tilde{\sigma}_{um}\dot{\tilde{\sigma}}_{um} \\ &= -KS^2 - S\frac{R}{JV_{w,free}}\left(d(s)\left(RF_z\mu + \hat{\sigma}_m\right) + \tilde{\sigma}_m\right) \\ &+ Sd(s)\left(\frac{1-\lambda}{V_{w,free}}\dot{V}_{w,free} + KS\right) \\ &+ S\left(\tilde{\sigma}_{um} + d(s)\hat{\sigma}_{um}\right) \\ &+ \frac{1}{K_{\sigma m}}\tilde{\sigma}_m\dot{\tilde{\sigma}}_m + \frac{1}{K_{\sigma um}}\tilde{\sigma}_{um}\dot{\tilde{\sigma}}_{um} \\ &= -KS^2 + \tilde{\sigma}_m\left(-S\frac{R}{JV_{w,free}} + \frac{1}{K_{\sigma m}}\dot{\tilde{\sigma}}_m\right) \\ &+ \tilde{\sigma}_{um}\left(S + \frac{1}{K_{\sigma m}}\dot{\tilde{\sigma}}_{um}\right) - Sd(s)\frac{R}{JV_{w,free}}\hat{C}(s)T_{b,CMD}\end{aligned} \tag{11}$$

where d(s) is one minus C(s) multiplied by the inverse of estimate of C(s). Introducing adaptive law in Equation 12, this makes the Lyapunov candidate of Equation 10 have the derivative of the Lyapunov function like Equation 13. Here, the $\sigma^*_{m/um}$ is the nominal function of the $\sigma_{m/um}$ in ABS control phase.

$$\begin{aligned}-\dot{\tilde{\sigma}}_m &= -\dot{\sigma}^*_m + \dot{\hat{\sigma}}_m = \dot{\hat{\sigma}}_m = -K_{\sigma m}S\frac{R}{JV_{w,free}} \\ -\dot{\tilde{\sigma}}_{um} &= -\dot{\sigma}^*_{um} + \dot{\hat{\sigma}}_{um} = \dot{\hat{\sigma}}_{um} = K_{\sigma um}S\end{aligned} \tag{12}$$

$$\begin{aligned}\dot{L} &= -KS^2 - Sd(s)\frac{R}{JV_{w,free}}\hat{C}(s)T_{b,CMD} \\ &\le -KS^2 - Sd(s)\frac{R}{JV_{w,free}}\hat{T}_b \\ &= -KS^2 - S\frac{R}{JV_{w,free}}\left(\hat{T}_b - T_b\right)\end{aligned} \tag{13}$$

ABS control system is turned off at low speed before vehicle stops. Therefore $1/V_{w,free}$ of the second term doesn't go to infinity in ABS control phase. And in steady state, the difference between estimate and the real value of braking torque is zero with appropriate actuator modeling and even in transient phase the value is bounded. Also, one can easily derive that the double derivative of the Lyapunov candidate is bounded as well from this.

The error between estimate and the real value of braking torque, T_b, can be described as the difference made by the modeling error of actuator dynamics. In that the actuator model will be designed to be close to the real one, the sign of the error of the braking torques will have similar pattern to the sign of sliding variable except some points. Note that the situation the braking torque increases implies the sign of braking torque error is constant except some points because of good modeling of actuator. And this is made by the slip increasing to desired value so that S is negative and vice versa.

Therefore even in transient phase, except some points, we can find the positive k in Equation 14.

Therefore, sliding gain K which has the under limit of Equation 15 makes the rate of Lyapunov candidate become Equation 16.

$$\left|\frac{R}{JV_{w,free}}\left(\hat{T}_b - T_b\right)\right| \le \left|\frac{R}{JV_{\min}}\left(\hat{T}_b - T_b\right)\right| \le k|S| \tag{14}$$

$$K \ge \kappa + k \tag{15}$$

$$\begin{aligned}\dot{L} &\le -KS^2 + k\,\mathrm{sgn}(S)S^2 \\ &= -(K - k\,\mathrm{sgn}(S))S^2 \\ &\le -(K-k)S^2 \\ &\le -\kappa S^2 \le 0\end{aligned} \tag{16}$$

The positive definite function L with the under limit of zero has negative semi-definite function of the derivative of L and, as mentioned above, one can easily derive the double derivative of L is bounded so that the derivative of L is uniformly continuous function with respect to time. By Barbarat's lemma or Lyapunov-like theorem, the derivative of L converges to zero as $t \to \infty$ which means the sliding variable converges to the origin as time passes and the adaptive parameters also converge to the origin (Khalil 2008, Slotine & Li 1991).

As a result, stability and convergence of the sliding mode and adaptive parameters were proved and, because the whole augmented system has radially unbounded positive definite Lyapunov function with negative semi-definite rate of it, the augmented system is globally asymptotically stable in so called global state space in ABS phase. The global state space means all the state space physically reachable.

3.2 *Outer loop: Optimal slip tracker*

Outer loop gives target slip command which tracks the optimal slip ratio having maximum potential to use friction for inner loop to track it with simple estimation for normal forces and friction coefficients. Equation 17 shows the simple estimation of the normal force used in this research where it is assumed that the lateral behavior of the vehicle is very small so that is negligible ($r \ll 1, V_y \ll 1$).

$$\begin{aligned}F_{z,FRONT} &= \frac{L_r}{2L}mg - \frac{mh_G}{2L}\dot{V}_x \\ F_{z,REAR} &= \frac{L_f}{2L}mg + \frac{mh_G}{2L}\dot{V}_x\end{aligned} \tag{17}$$

For longitudinal direction, simple friction estimation of Equation 18 was used in this research. It is self-evident that the more accuracy one gives in estimation, the better the performance is.

$$\mu_w = \frac{F_{x,w}}{F_{z,w}} = \frac{m_w A_{x,w}}{m_w g} = \frac{A_x}{g} \tag{18}$$

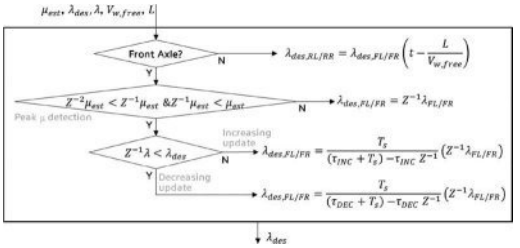


Figure 2. Discrete optimal slip tracker.

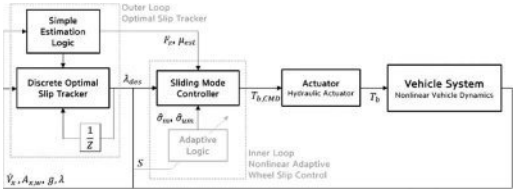


Figure 3. Whole augmented control system architecture.

where m_w is the mass which the wheel is in charge in an instant. The estimation is same for all the wheel to give more robustness in various road-tire condition because even when the friction coefficient of front wheel changes in locally uniform road the friction coefficient of front and rear wheel will be identical again right after the transient phase until the instant friction coefficient of rear wheel follows the friction coefficient of front wheel.

Discrete optimal slip tracker proposed in this research was demonstrated in Figure 2. For front wheel, when the tracker detects the local maximum friction coefficient the target slip is updated to the slip point in that instant. To reduce noise and to give smooth convergence, low pass filter was implemented before this tracker transmits the final command of target slip.

In the case of having to decrease target slip, which means the present is a state of over slip so that the wheel tends to unstable, faster convergence should be done. Therefore $\tau_{inc} > \tau_{dec}$. The target slip of rear wheel updates to front target slip of each direction after time delay which is needed for rear wheel to be reached in the μ jump point.

Consequential whole augmented control system was demonstrated in Figure 3.

4 NUMERICAL SIMULATION RESULT

Numerical simulation of the whole control system was integrated to MATLAB-CarSim simulation environment with CarSim-default vehicle.

4.1 *With ideal actuator*

At first, the simulation was performed with ideal actuator and the result was demonstrated in Figure 4–6. As in Figure 4–5, ABS control starts with assumed target slip, adapts target slip to track local pick μ

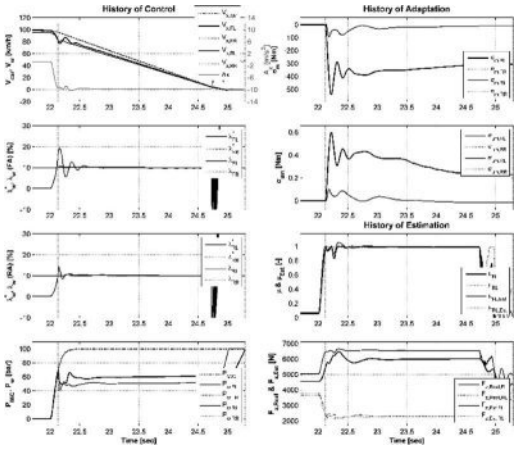


Figure 4. Simulation result for dry asphalt ($\mu = 1.0$) with ideal actuator.

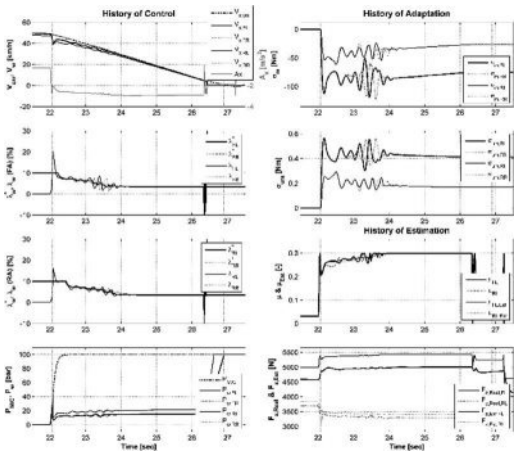


Figure 5. Simulation result for snow ($\mu = 0.3$) with ideal actuator.

and finally vehicle brakes with maximum deceleration which means good performance of ABS control with good adaptation. The control performance is good even for the case of negative μ jump as in Figure 6.

4.2 *With real actuator*

The Real actuator model with time delay and some physical response like the real system was introduced to the simulation setup. The result was demonstrated in Figure 8–10. As expected, instability was increased in low speed but the nonlinear adaptive controller braked the vehicle well with high friction showing good performance. Note that more precise actuator model in braking torque command makes the control performance be higher. In addition, because the inverse of time delay can't be realized in physically, to reduce the time delay from hardware communication, etc. is needed for good braking performance in real vehicle environment.

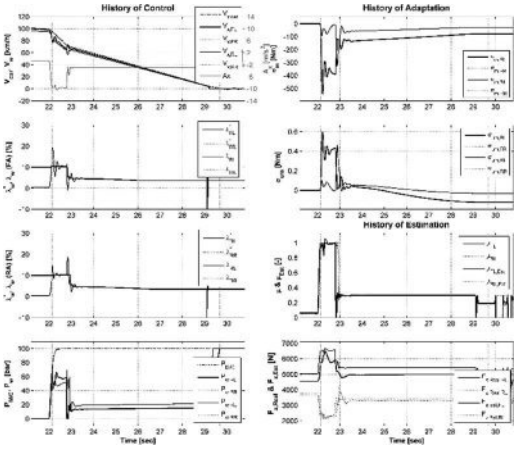


Figure 6. Simulation result for H2L μ Jump ($\mu = 1.0 \rightarrow 0.3$) with ideal actuator.

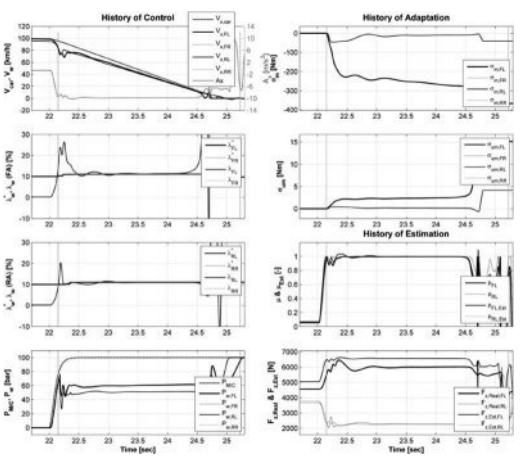


Figure 7. Simulation result for dry asphalt ($\mu = 1.0$) with real actuator.

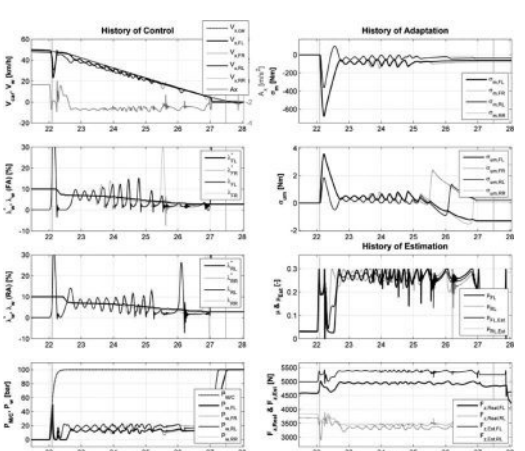


Figure 8. Simulation result for snow ($\mu = 0.3$) with real actuator.

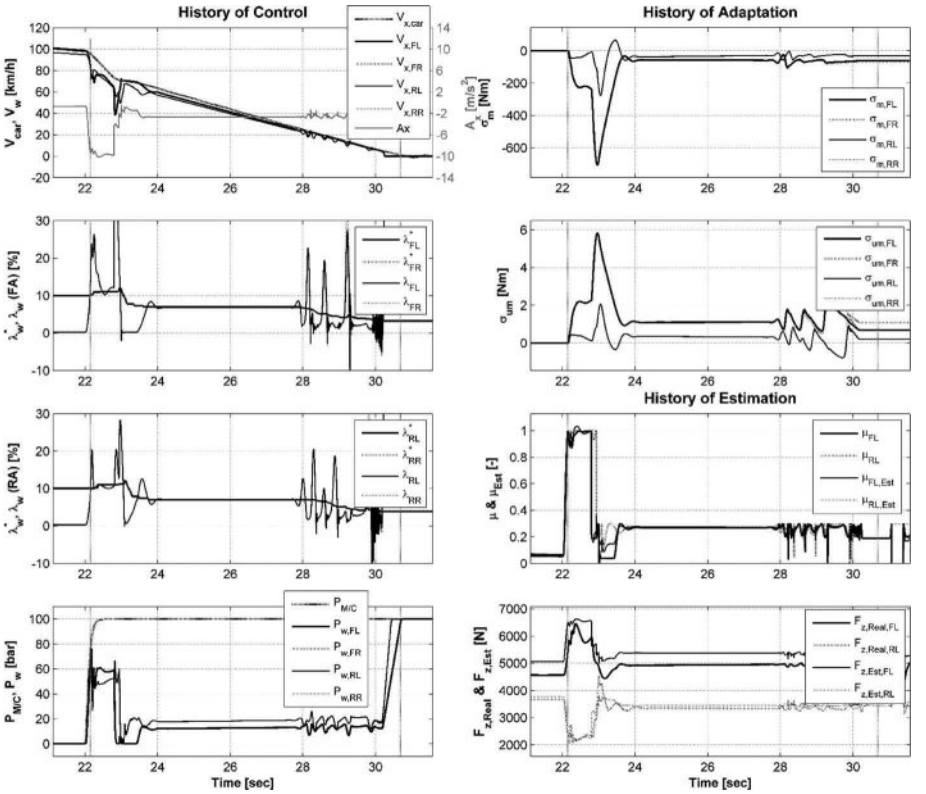


Figure 9. Simulation result for H2L μ Jump ($\mu = 1.0 \rightarrow 0.3$) with real actuator.

5 CONCLUSION

Nonlinear adaptive ABS controller which uses adaptive sliding mode control with optimal slip tracker was designed to combine NVH advantage and robustness. The adaptive sliding mode control regulates matched and unmatched uncertainties with adaptive parameters to track the slip target command exactly. And optimal slip tracker tracks the optimal slip to get the maximum friction potential for high braking performance. The designed control law was proved to have enough stability and convergence by Lyapunov method and we could see the importance of actuator modeling. Finally several numerical simulations with MATLAB-CarSim environment were performed to show the good performance of the proposed controller and importance of actuator modeling. Further vehicle test in various road condition would complete this research in the future.

REFERENCES

Aly, A.A., Zeidan, E.S., Hamed, A. & Salem, F. 2011. An Antilock-Braking Systems (ABS) Control: A Technical Review. *Intelligent Control and Automation* 2(3): 186–195.

Khalil, H. K. 2008. *Nonlinear Systems* (3rd ed.). New Jersey: Prentice-Hall International.

Petersen, I. 2003. Wheel Slip Control in ABS Brakes using Gain Scheduled Optimal Control with Constraints. *Thesis*. Norway: NUST.

Savaresi, S.M. & Tanelli, M. 2010. *Active Braking Control Systems Design for Vehicles*. Springer.

Slotine, E. & Li, W. 1991. *Applied Nonlinear Control*. New Jersey: Prentice-Hall International.

Advanced Vehicle Control – Edelmann, Plöchl & Pfeffer (Eds)
© 2017 Taylor & Francis Group, London, ISBN 978-1-138-02992-7

Integration of torque blending and slip control using real-time nonlinear model predictive control

M. Sofian Basrah, E. Siampis, E. Velenis, D. Cao & S. Longo
Cranfield University, Bedford, UK

ABSTRACT: Antilock Braking System (ABS) is a crucial active vehicle safety feature in preventing accidents during emergency braking. Electrified vehicles which include both hydraulic and regenerative braking systems provide the opportunity to implement brake torque blending during slip control operation. Nevertheless, ABS is still employed by the conventional friction brakes. Existing Hybrid Electric Vehicles (HEV) have low deceleration threshold to deactivate regenerative brakes. Main benefits of ABS torque blending is to increase the regenerative braking activation window and take advantage of the electric motor's (EM) high bandwidth. This study evaluates the design and implementation of a new torque allocation algorithm using a Nonlinear Model Predictive Control (NMPC) strategy that can run in real-time, with results showing that wheel-locking can be prevented while also permitting energy recuperation. Simulation using high fidelity model is used to validate the proposed NMPC strategy.

1 INTRODUCTION

Vehicle electrification is part of the major initiative by automotive manufacturers as solution to emission issues and the diminishment of the fossil fuel resources (Chan 2007). Electrified vehicles are equipped with redundant braking actuators, namely hydraulic brakes and a regenerative braking system using electric motors (EMs). This creates the opportunity for research into brake torque blending for Anti-lock Braking System (ABS) in a hybrid braking system. The existence of the new actuator creates the opportunity not only to increase energy efficiency but to enhance the performance of the safety aspect of the vehicle (Crolla & Cao 2012). ABS is an important feature of active vehicle safety to avoid wheel locking while maintaining vehicle steerability and stability during panic braking. The ABS controls the braking torque when the system identifies incipient wheel lock, since the driver will be unable to steer the vehicle as it continues to slide if the front wheels are locked, while the vehicle is prone to spin out of control when the rear wheels lock. Regenerative braking can be deployed to support hydraulic friction braking system during braking event to recuperate energy for future use and also during emergency situation such as to avoid wheel locking. Presently, only conservative strategies have been applied for the deployment of EM during braking, which is disabled if any risk of emergency situation emerges and the friction brakes are prioritised (Bayar et al. 2012, Crolla & Cao 2012).

This work concentrates on enabling the integration of the slip control and torque blending between the braking actuators being hydraulic friction brake and regenerative braking. The main motivation is to allow for a wider window of regenerative braking activation which mostly using conservative strategy to cut-off the electric motor braking during high deceleration or emergency braking. Additionally, the distinct advantage of using an electric motor such as accurate and fast control can be utilized in improving the slip control operation. Murata (2012) claims that electric machines have limited torque range for braking but have very quick and precise response, and the applied torque can be measured easily. On the other hand, HFB is capable of delivering high retarding torque but is limited by high delay of response (de Castro et al. 2012, Murata 2012). With the combination of the two actuators, ABS performance can be improved and the energy regeneration can have a wider activation window to increase efficiency.

Several articles report torque blending algorithms using optimization methods. De Castro et al. (2012) proposed an adaptive slip controller and the brake torque allocation is designed using Control Allocation (CA). Satzger et al. (2014) presented a linear slip controller and a linear Model Predictive Control (MPC) strategy is employed to allocate the brake torque between the two actuators. The cascaded strategy is replaced with a combined strategy for slip control and torque blending using linear MPC (Satzger et al. 2014). Static brake torque allocation by Daisy Chain (DC) which requires less computational effort

as compared to optimization methods is proposed and tested on a hardware-in-the-loop simulator (Basrah et al. 2015). Yuan et al. (2015) propose a slip control using nonlinear model predictive control (NMPC) for EV using in-wheel motor (IWM). However, there is no real time implementation and there is no brake torque blending considered. Furthermore, results shown indicate the wheel slip achieved is much smaller than the desired slip.

The problem of integrating slip control and brake torque allocation includes important nonlinearities in both the system dynamics and constraints. The emergence of real time nonlinear optimization solvers make it possible to treat the optimization as a constrained nonlinear problem instead of using linear approximations. To the authors' best knowledge, there is currently no work on integrated slip control and brake torque allocation using Nonlinear Model Predictive Control (NMPC) with real time implementation capability. This work therefore presents a slip control and torque blending strategy incorporated in single NMPC formulation. The model of single wheel vehicle and braking actuators are presented next, followed by the NMPC strategy proposed. Simulation results using single wheel model and high fidelity model are then presented in section 4 and 5 respectively. Finally, we summarise our work and propose future work.

2 MODELLING

2.1 *Vehicle and wheel dynamics*

For the NMPC formulation a single-wheel model is employed. Assume that the continuous-time model is

$$\dot{V}_x = \frac{F_x}{m}, \tag{1}$$

$$\dot{\omega}_x = \frac{T_{total} - F_x R_w}{J_w}, \tag{2}$$

$$s_x = \frac{\omega_x R_w - V_x}{V_x}, \tag{3}$$

with V_x the wheel's forward velocity, ω_x the angular wheel speed, F_x the tyre's longitudinal force, T_{total} the total torque applied on the wheel and R_w, J_w and m the wheel's radius, moment of inertia and mass respectively. In the above model, F_x is set as a function of longitudinal wheel slip, s_x through a simplified version of Pacejka's Magic Formula (MF) (Bakker et al. 1987):

$$F_x = F_z D \sin\left(C \tan^{-1}\left(B s_x\right)\right), \tag{4}$$

where B, C and D are the MF's factors and F_z the vertical force on the tyre. For our blending strategy, the T_{total} is the summation of the torque from the electric motor T_e and the torque from the hydraulic brake T_h.

$$T_{total} = T_e + T_h, \tag{5}$$

2.2 *Braking actuator dynamics*

There are two braking actuators available in vehicle model in this work being hydraulic friction brake system and regenerative braking system via EM.

To represent the actuator dynamics of the friction braking and the EM we implement a first order system with delay (de Castro et al. 2012)

$$\frac{T_i}{T_i^*} = \frac{1}{\tau_i s + 1}, \tag{6}$$

where $i \in \{hydraulic, electric\}$, T_i the applied brake torque, T_i^* the reference brake torque and τ_i the time constant for the delay.

3 NONLINEAR MODEL PREDICTIVE CONTROL STRATEGY

For the nonlinear discrete-time system

$$x(k+1) = f(x(k), u(k)), \tag{7}$$

with $x = [V_x \quad \omega]^T$ and $u = [T_e \quad T_h]^T$, if we assume that the input only changes at times $k, k+1, \ldots, k+N-1$ where N is the prediction horizon, we can augment the state vector with the trivial equalities

$$\begin{aligned} \Delta T_e(k+1) &= T_e(k+1) - T_e(k), \\ \Delta T_h(k+1) &= T_h(k+1) - T_h(k), \end{aligned} \tag{8}$$

to obtain

$$\hat{x}(k+1) = g(\hat{x}(k), \hat{u}(k)),$$

with $\hat{x} = [V_x \quad \omega_x \quad T_e \quad T_h]^T$ and $\hat{u} = [\Delta T_e \quad \Delta T_h]^T$. Using system (8) the NMPC problem with sampling time T_s is then

$$\begin{aligned} \min_{x,u} \sum_{k=0}^{N-1} [\; & q_s \left(s_x(k) - s_{ref}\right)^2 + q_T T_h^2(k) + \\ & + q_e \Delta T_e^2(k) + q_h \Delta T_h^2(k) \;], \end{aligned}$$

$$s.t. \quad \hat{x}(0) = \hat{x}_{init},$$

$$\hat{x}(k+1) = g(\hat{x}(k), \hat{u}(k)), \quad k = 0, \ldots, N-1,$$

$$\underline{x} \le \hat{x}(k) \le \overline{x}, \qquad k = 0, \ldots, N-1,$$

$$\underline{u} \le \hat{u}(k) \le \overline{u}, \qquad k = 0, \ldots, N-1,$$

where we choose to penalize the s_x from a given reference through its definition (3), the control effort in the form of a penalty on the torque rates ΔT_e and ΔT_h, along with an extra penalty on the T_h to avoid using the hydraulic brakes when possible. In this way we do

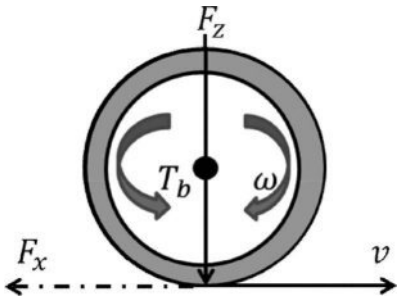


Figure 1. Forces acting on wheel.

not explicitly set references for the electric motor and hydraulic brake torques, but rather leave the NMPC to find the appropriate values according to the given longitudinal slip reference, the torque and torque rate constraints, and the chosen weight $q_s, q_e, q_h, q_T > 0$.

To solve the NMPC problem in real time the Primal Dual Interior Point (PDIP) method as available in Forces Pro (Dohamidi & Jerez 2014) is employed, where the discrete-time system dynamics (2) are derived from the continuous-time system using 5 steps of the fourth order Runge-Kutta scheme.

4 SIMULATION STUDY

In this section we present preliminary results using the NMPC strategy from section 3 on a single-wheel model in Simulink, with the motor and hydraulic brake modelled as simple first order delays (time constants of $\tau_e = 0.0015$ and $\tau_h = 0.016$ respectively) (de Castro et al. 2012). The wheel and tyre parameters used can be found in Table 1.

For the NMPC we set $T_s = 5$ ms and $N = 20$. The rate limits for the motor and the hydraulic brake are set to 7500 Nm/s and 3000 Nm/s respectively and the weights in the cost function are chosen such that we penalize large longitudinal slip errors, while also we give priority to the use of the electric motor for the torque delivery.

$$T_e^{\min} \le T_e \le T_e^{\max}, \qquad T_h^{\min} \le T_h \le T_h^{\max}, \tag{9}$$

$$T_e^{\min} = -750Nm, \qquad T_e^{\max} = 750Nm$$

$$T_h^{\min} = -3000Nm, \qquad T_h^{\max} = 0Nm$$

$$\Delta T_e \le \Delta T_e^{\lim it}, \qquad \Delta T_h \le \Delta T_h^{\lim it}, \tag{10}$$

$$\Delta T_e^{\lim it} = 7500Nm/s$$

$$\Delta T_h^{\lim it} = 3000Nm/s$$

Table 1. Vehicle and tyre parameters.

wheel total mass	m	362.5 kg
wheel moment of inertia	J_w	1.04 kgm^2
wheel radius	R_w	0.3 m
MF's stiffness factor	B	7
MF's shape factor	C	1.6
MF's peak value	D	0.3, 1

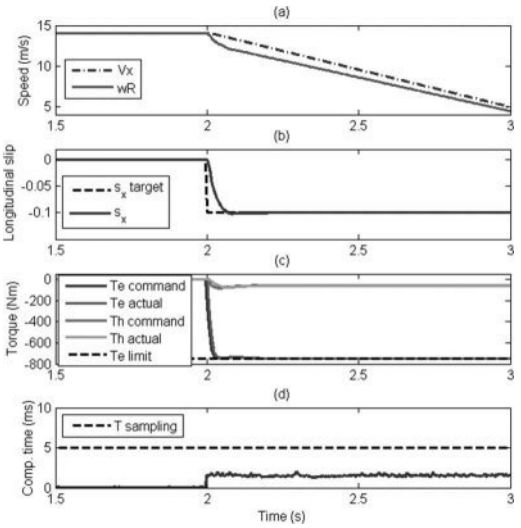


Figure 2. Braking on road $\mu = 1$ for single wheel model.

In the presented scenario the wheel is initially free-rolling with initial speed of 50 km/h on a dry road ($\mu = 1$ and $D = 1$) and after 2s a slip target of $s_x = -0.1$ is demanded. As we can see from figure 2, the NMPC strategy successfully regulates the longitudinal slip (figure 2(b)) by distributing the T_e and T_h torques (figure 2(c)), with an obvious preference for the electric motor. It is also worth noting at this point that the commanded torques from the controller are very close to the actual torques as delivered by the actuators, a result of including the torque rate constraints in the NMPC formulation. Finally, as we can see from figure 2(d), the time to compute the solution using a rather standard desktop (i7-4790 M at 3.60 GHz with 16 GB of memory) takes an average of 1.8 ms with maximum of 2.2 ms, which is much lower than the sampling time of 5 ms.

The second simulation shows the performance of the NMPC strategy on a packed snow road ($\mu = 0.3$ and $D = 0.3$). We can observe from figure 3(b) that the wheel slip reference can be achieved without any risk of wheel locking. Interestingly, only electric braking torque is deployed without the need of friction brake as illustrated in figure 3(c).

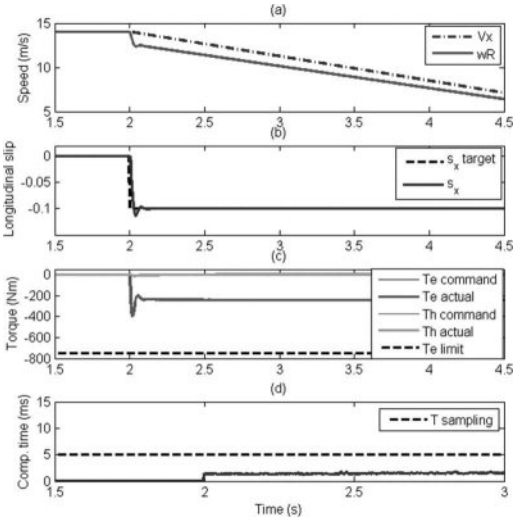


Figure 3. Braking on road $\mu = 0.3$ for single wheel model.

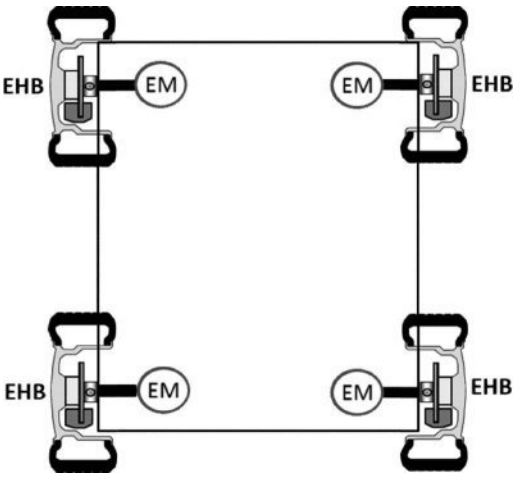


Figure 4. Four-wheel BEV model configuration.

5 VALIDATION USING HIGH FIDELITY MODEL

The proposed NMPC strategy is evaluated in this section using high fidelity model which includes Simulink for the controller deployment and vehicle dynamics simulation environment in IPG CarMaker. We also injected noise in input signals which we assume measured using modern vehicle sensors. Mass of the vehicle used in simulation is 1137 kg. Vehicle configuration chosen in this work is a four wheel drive battery electric vehicle (BEV) using four near-wheel motors with brake-by-wire capability as shown in figure 4.

Straight line braking on a μ-split road is suitable to evaluate the performance of slip controller. We assume the vehicle is travelling with left wheels on dry asphalt ($\mu = 1$ and $D = 1$) and right wheels on snow ($\mu = 0.3$ and $D = 0.3$). The main objectives are to stop the vehicle as quickly as possible without any wheel locking and to maintain steerability and stability of the vehicle. Similar to test pattern in section 4, brake is applied at initial speed of 50 km/h.

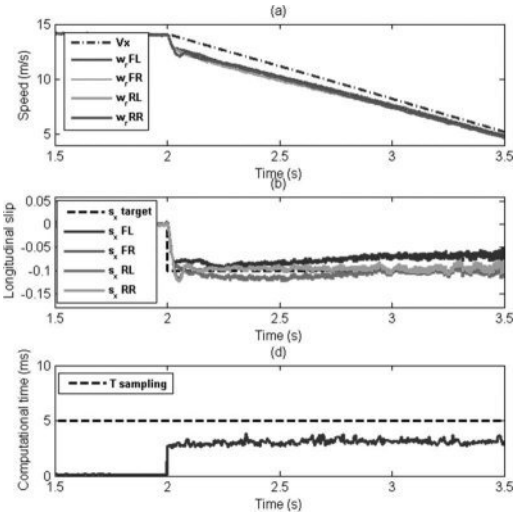


Figure 5. Speed for braking on μ split road.

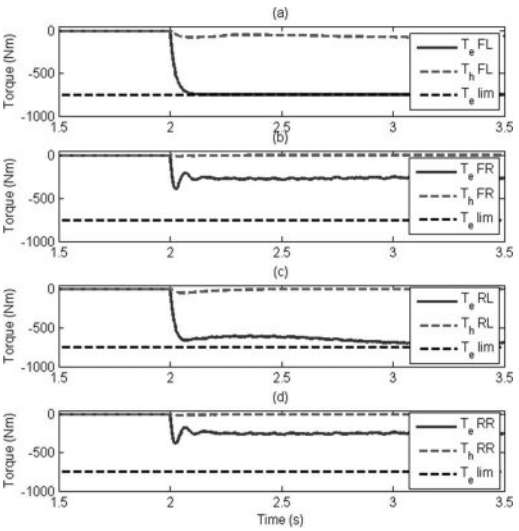


Figure 6. Brake torque for μ split road braking.

We can see in figure 5 that the vehicle is stopped in a safe manner without locking any of the wheels. The NMPC strategy proposed managed to maintain the wheel slip on each wheels close to the desired value with the capability to integrate both brake actuators accordingly. There is a yaw moment created towards the high μ road and the vehicle will be pulled to the high friction side during the braking. Vehicle can be unstable if equal braking torque applied on both right and left sides of the vehicle. Figure 6 shows that lower brake torque is required for the wheels on snow road

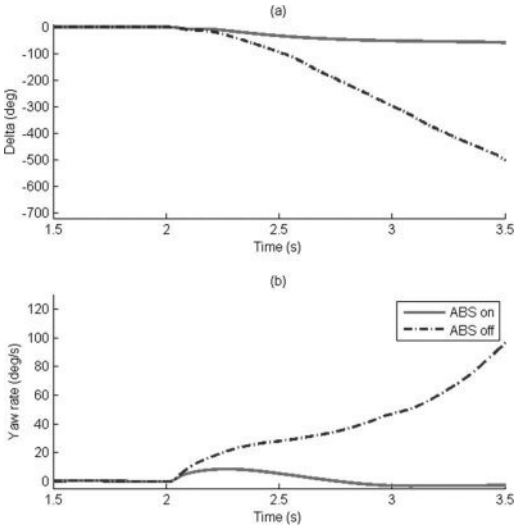


Figure 7. Stability performance for braking on μ split road.

compared to the side on dry road in order to achieve similar longitudinal wheel slip.

We use IPG driver model in CarMaker which controls the brake pedal and steering wheel to ensure best repeatability and consistency for closed loop test simulation. To prove the steerability and stability aspects of our proposed strategy we can see in figure 7 the maximum yaw rate achieved by the vehicle is at an acceptable value of 8 deg/s in comparison to 119 deg/s when the wheels are locked. In addition, the maximum steering wheel angle correction required by the driver in order to maintain the vehicle path during emergency braking is just 95 deg (clockwise direction) compared to 610 deg without slip control activated.

An important contribution of this work can be clearly described in terms of the real time implementation capability of the NMPC strategy which opens up the possibility to deploy the controller using hardware-in-the-loop simulation testing as well as vehicle testing. The optimization problem is solved with mean time value of 2.9 ms and maximum of 3.5 ms and this proves the capability to deploy the NMPC formulation online.

6 CONCLUSION

In this work we have demonstrated that nonlinear MPC can be implemented in real time to optimally coordinate hydraulic and electric brake actuators during ABS interventions. In addition to the optimality of the controller, the proposed method allows us to explicitly incorporate state (torque) and control input (torque rate) constraints in the control problem formulation. The proposed MPC control design was performed using a simple longitudinal single wheel vehicle model and successfully implemented on a high fidelity vehicle dynamics model, where the lateral stability of the vehicle can be assessed. Ongoing work includes validation using hardware-in-the-loop simulation testing and the inclusion of state estimation to allow for real vehicle testing.

REFERENCES

Bakker, E., L. Nyborg, & H. Pacejka (1987). Tyre modelling for use in vehicle dynamics studies. *SAE Technical Paper 870421*.

Basrah, M. S., E. Velenis & D. Cao (2015). Four wheel torque blending for slip control in a hybrid electric vehicle with a single electric machine. *International Conference on Sustainable Energy Engineering and Application*, 19–24.

Bayar, K., J. Wang & G. Rizzoni (2012). Development of a vehicle stability control strategy for a hybrid electric vehicle equipped with axle motors. *Proc. Inst. Mech. Eng. Part J. Automob. Eng.* 226, no. 6, 795–814.

Chan, C. C. (2007). The state of the art of electric, hybrid, and fuel cell vehicles. *Proceedings of the IEEE*. 95, no. 4, 704–718.

Crolla, D. & D. Cao (2012). The impact of hybrid and electric powertrains on vehicle dynamics, control systems and energy regeneration. *Vehicle System Dynamics*, 50, supp. 1, 95–109.

de Castro, R., R. E. Araujo, M. Tanelli, S. M. Savaresi & D. Freitas (2012). Torque blending and wheel slip control in EVs with in-wheel motors. *Vehicle System Dynamics*, 50, supp. 1, 71–94.

Dohamidi, A. & J. Jerez (2014). FORCES Professional. *Embotech GmbH*, (http://embotech.com/FORCES-Pro).

Murata, S. (2012). Innovation by in-wheel-motor drive unit. *Vehicle System Dynamics*, 50, issue 6, 807–830.

Satzger, C., R. de Castro & T. Bunte (2014). A model predictive control allocation approach to hybrid braking of electric vehicles. *IEEE Intelligent Vehicles Symposium Proceedings*, 286–292.

Satzger, C. & R. de Castro (2014). Combined wheel-slip control and torque blending using MPC. *International Conference on Connected Vehicles and Expo*, 618–624.

Yuan, L., H. Chen, B. Ren & H. Zhao (2015). Model predictive slip control for electric vehicle with four in-wheel motors. Chinese Control Conference (CCC), 7895–7900.

Torque/G-Vectoring

Advanced Vehicle Control – Edelmann, Plöchl & Pfeffer (Eds)
© 2017 Taylor & Francis Group, London, ISBN 978-1-138-02992-7

Study of mechanism improving target course traceability in G-Vectoring Control

M. Yamakado, M. Abe & Y. Kano
Kanagawa Institute of Technology, Kanagawa, Japan

D. Umetsu & T. Yoshioka
Mazda Motor Corporation, Hiroshima, Japan

ABSTRACT: Production-type G-Vectoring Control vehicles are now being put on the market. Reviewers have praised the handling quality and course traceability of these vehicles. This paper clarifies the mechanism behind this improvement in handling quality using a simple bicycle model and driver model analysis. It focuses on the residual yaw angular acceleration when the steering speed is zero and shows that G-Vectoring Control reduces its value. This result provides evidence for improved handling quality in G-Vectoring Control vehicles.

1 INTRODUCTION

We have been researching and developing G-Vectoring Control (GVC) for almost ten years as a means of controlling acceleration and deceleration in coordination with the vehicle's lateral motion. In this research, we have been closely examining the driving operation of expert drivers and extracting a control algorithm based on the vehicle's lateral jerk.

Production-type GVC vehicles having high-response engines have recently been developed and put on the market. This type of vehicle uses a high-response internal combustion engine (gasoline or diesel) and reduces engine torque based on the value of a GVC deceleration command. Such controlled deceleration is extremely small and essentially unnoticeable. Many drivers including journalists have evaluated these vehicles. Though not academic in nature, some of their comments are listed below.

- Completely different from past control. I'm not talking in low-dimensional terms about sharp or hard/soft motions, but rather about advanced control of the texture of motion. The feeling is that motions and changes in the behavior of an automobile have been infinitely reduced.
- Overshoot in steering is common in ordinary cars, but no such behavior here. "Steering is set with one attempt!"

The above evaluations were performed with a vehicle having a function for turning GVC ON/OFF as desired, and it was found that "texture, transient motions, and connections between motions differed" by simply turning GVC ON or OFF.

To turn such subjective evaluations of drivers into useful engineering knowledge, it is necessary to combine existing engineering approaches and establish evaluation indices from a new perspective.

In this report, we first calculate steering input and motion using both a "two-degree-of-freedom bicycle model" extended for representing GVC vehicle characteristics and the "preview-follower driver model" described by a transfer function. and evaluate steering input and motion as "target course traceability performance." Specifically, we evaluate the degree of correction steering required to stay on the course, overshoot of the vehicle's yaw angular acceleration (residual yaw angular acceleration) when steering is stopped (steering speed is zero), etc. We also report on the results of a driving simulator test and vehicle test to corroborate the results.

2 OVERVIEW AND ROLE OF GVC

In research to date, we proposed the following equation called G-Vectoring Control (GVC) (Yamakado et al. 2008, 2010) as a basic control principle for coordinating longitudinal motion with lateral motion.

$$G_{xc} = -\mathrm{sgn}\left(G_y \cdot \dot{G}_y\right) \frac{C_{xy}}{1+Ts} \left|\dot{G}_y\right| \tag{1}$$

G_{xc} is the longitudinal acceleration command, G_y is lateral acceleration, and G_{y_dot} is lateral jerk, that is, the first-order derivative of the lateral acceleration.

From the viewpoint of recently developed production-type GVC vehicles, it would be more meaningful to treat GVC as "cooperative control" that aims to get the engine and steering equipment, which have been separately developed since the dawn of the automobile age, to work together to achieve "ideal motion" using this control rule as an intermediary.

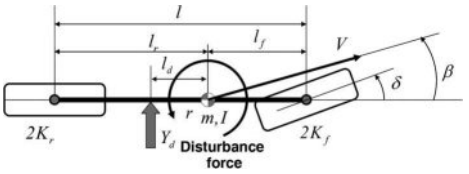


Figure 1. Two-degree-of-freedom bicycle model.

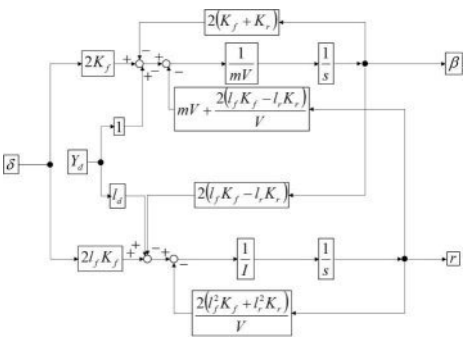


Figure 2. Integration-type block diagram of bicycle model.

In the following sections, we construct a bicycle model assuming GVC operation and combine this with a driver model to perform an orthodox analysis.

3 BICYCLE MODEL IN GVC OPERATION

We substitute a four-wheel vehicle with the two-degree-of-freedom bicycle model shown in Figure 1.

Here, m, I are vehicle mass and vehicle yaw moment of inertia, V is vehicle velocity, β, r are the vehicle slip angle and yaw rate, δ is the steering angle, $2K_f$, $2K_r$ are the front-wheel and rear-wheel cornering stiffness (two wheels' worth), and l, l_f, l_r are wheel base, distance from front wheel to vehicle center of gravity, and distance from rear wheel to vehicle center of gravity. In Figure 1, it can be seen that a lateral disturbance force is being applied at the coordinates corresponding to a distance l_d from the center of gravity (in this figure, $l_d < 0$). In the vehicle model, input to the vehicle is taken to be steering angle δ and disturbance Y_d. The equations of motion for this bicycle model are expressed as follows and its integration-type block diagram is shown in Figure 2.

$$\begin{bmatrix} mVs+2(K_f+K_r) & mV+\frac{2}{V}(l_fK_f-l_rK_r) \\ 2(l_fK_f-l_rK_r) & I_zs+\frac{2}{V}(l_f^2K_f+l_r^2K_r) \end{bmatrix} \begin{bmatrix} \beta(s) \\ r(s) \end{bmatrix} = \begin{bmatrix} 2K_f \\ 2l_fK_f \end{bmatrix} \delta(s) + \begin{bmatrix} 1 \\ l_d \end{bmatrix} Y_d(s) \quad (2)$$

On accelerating or decelerating, the tire vertical load moves between the front and rear wheels. At the same time, it is well known that cornering force is load dependent. Here, denoting cornering stiffness as K_{iw} ($i = f, r$; f: front, r: rear) and assuming it to have

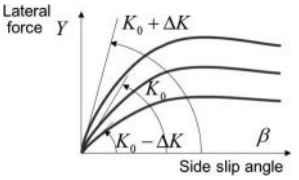


Figure 3. Controlled cornering stiffness.

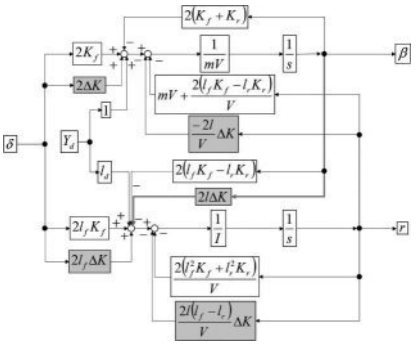


Figure 4. Block diagram of bicycle model with GVC.

first-order load dependency with respect to tire vertical load W_i (coefficient C_1), we express it as follows:

$$K_{iw} = C_1 W_i \quad (3)$$

Furthermore, denoting the height of vehicle center of gravity as h and given that the vehicle is accelerating or decelerating by G_x, we get the following expressions for front-wheel load W_f and rear-wheel load W_r (one axle's worth):

$$W_f = \frac{ml_rg}{2l}\left(1-\frac{h}{l_rg}G_x\right) \quad W_r = \frac{ml_fg}{2l}\left(1+\frac{h}{l_fg}G_x\right) \quad (4), (5)$$

Front-wheel and rear-wheel cornering stiffness can now be expressed as follows:

$$K_{fw} = C_1W_f = K_{f0}\left(1-\frac{h}{l_rg}G_x\right) \approx K_{f0} + \Delta K \quad (6)$$

$$K_{rw} = C_1W_r = K_{r0}\left(1+\frac{h}{l_fg}G_x\right) \approx K_{r0} - \Delta K \quad (7)$$

Here, we make the approximation $l_f = l_r$ for the sake of simplicity and describe acceleration/deceleration as deceleration by GVC ($G_x < 0$). In the above equations, G_x is substituted by the value of the GVC deceleration control command of Equation (1).

Now, in the case of very small deceleration by GVC, change in speed can be ignored, and if we consider the effects of front and rear forces to be small, the effect of GVC turns out to be nothing other than change ΔK of this cornering stiffness. The plots of Figure 3 show the conditions for change in ΔK.

The block diagram in GVC operation is shown in Figure 4. Here, the slip angle, coefficient of the

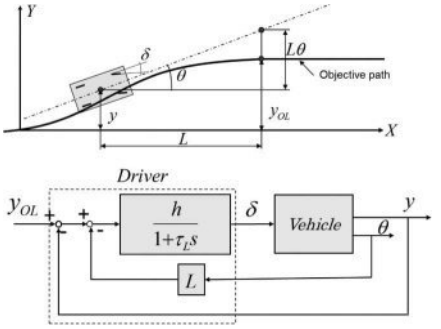


Figure 5. Preview-follower driver model.

yaw-rate feedback term, and coefficient of the cross-coupling term change actively according to lateral motion. This is the simplest model of a GVC vehicle having very small acceleration and deceleration.

4 PREVIEW-FOLLOWER DRIVER MODEL

The driver model to be combined with the GVC vehicle model described above need not be specifically for GVC use. Accordingly, we assume a nearly linear target course and a simple preview-follower driver model (Abe, 2015) as shown in Figure 5.

Using vehicle velocity V and slip angle β and yaw rate r calculated by the GVC-operated vehicle model of Figure 4, we apply the following equations to calculate yaw angle θ and position x, y. Then, using look-ahead distance L, we calculate steering angle δ.

$$\theta = \theta_0 + \int_0^t r dt \tag{8}$$

$$x = x_0 + V\int_0^t \cos(\beta+\theta)dt \quad y = y_0 + V\int_0^t \sin(\beta+\theta)dt \tag{9), (10}$$

Here, y_{OL} is the lateral displacement of the target course at the look-ahead point. Letting input to the driver transfer function be ε (error), we have:

$$\varepsilon = y + L\theta - y_{OL} \tag{11}$$

The driver transfer function is expressed by gain h having a first-order delay indicated by time constant τ_L. Steering angle δ to be input to the vehicle model is consequently as follows:

$$\delta = \frac{h}{1+\tau_L}\{(y - y_{OL}) + L\theta\} \tag{12}$$

It can be seen from Equation (12) that a steering angle will be calculated even if the vehicle is on the target course as long as the yaw angle is not zero.

5 REQUIREMENTS SOUGHT BY DRIVERS

How could we achieve an evaluation of handling quality with small overshoot in the manner of "Steering is set with one attempt!" as shown before?

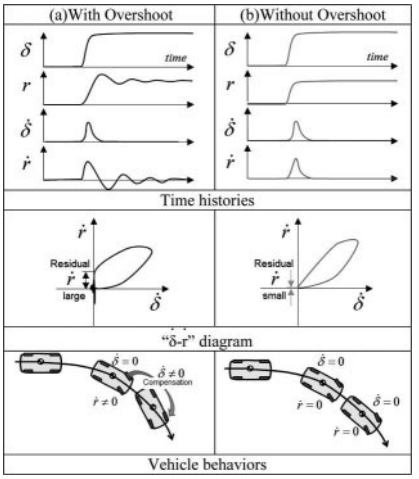


Figure 6. Conceptual diagram of handling quality evaluation.

Conditions under which the error of Equation (11) becomes zero can be treated as those for determining steering. If this error should stay at zero when steering is stopped, maintaining that steering angle is fine. (However, in the driver model of section 4, steering angle returns to zero if error is zero, so there is no function for maintaining steering angle.) However, if error arises on the vehicle side with a time delay after steering stops on the driver side, the driver will again perform a steering action for correction purposes. This corrected steering angle will result in another change in motion.

A conceptual diagram of these handling conditions is shown in Figure 6. Here, Figure 6 (a) shows handling conditions with overshoot in yaw motion with respect to steering angle and Figure 6 (b) shows handling conditions without overshoot. The top portion of the figure shows time histories of the waveforms for steering angle δ, yaw rate r, steering angular speed δ_{dot}, and yaw angular acceleration r_{dot}. The middle portion of the figure, meanwhile, shows a "$\delta_{dot} - r_{dot}$" diagram consisting of a Lissajous curve for steering angular speed and yaw angular acceleration. Finally, the bottom portion of the figure shows vehicle behavior and conditions for maintaining steering angle without correction steering.

Referring again to the "$\delta_{dot} - r_{dot}$" diagram, if overshoot of the vehicle's yaw angular acceleration (referred to below as residual yaw angular acceleration) is large when steering is stopped (steering speed is zero), the yaw rate will not be constant. As a result, vehicle motion will be inward with respect to the target course. In terms of the driver model shown in Fig. 5, this corresponds to conditions in which yaw angle is not zero. (Note: Figure 6 shows conditions that include prediction of future vehicle position based on an arc that considers turning radius based on the current steering angle.) Of course, a driver model adds correction steering meaning that steering angle is not set. As shown in Figure 6 (b), it is essential that error

Table 1. Simulation specifications.



	Definition	Value	Item	Definition	Value
m	Vehicle Mass	1444 kg	hg	Height of C.G	0.600 m
I	Moment of inertia	2242 kgm^2	l_f	C.G to front axle	1.100 m
l_r	C.G to rear axle	1.600 m	K_f	Cornering Stiff. F	55000 N/rad
K_r	Cornering Stiff. R	60000 N/rad	V	Vehicle speed	Variable
τ_L	Driver delay time	0.2s	L	Look ahead dist.	V m
h	Proportional gain	0.02 rad/s	μ	Road friction	1.0
T	GVC delay time	0.05 s	C_{xy}	GVC gain	0.05∼0.2

be at the least near zero when steering is stopped to achieve conditions reflected by "Steering is set with one attempt!" The model presented in section 4 is sufficient to understand such transient conditions in the simplest way possible, despite the lack of a function for maintaining steering angle.

6 SIMULATION STUDY

6.1 *Residual yaw angular acceleration*

Replacing the vehicle model of Fig. 5 with the vehicle model with GVC of Figure 4, we performed a simulation. The task here was to perform S-shaped driving (smooth lane change) to reproduce "Steering is set with one attempt!" conditions when "entering a corner" and "switching lanes." Simulation requirements and constants are listed in Table 1.

Here, to make it easier to observe control effects, we made GVC gain C_{xy} slightly larger than that of a production-type vehicle. This gain takes on a form incorporating "speed – gain characteristics," which is a unique element based on model-specific steering characteristics applied to production-type vehicles.

Figure 7 (a)–(d) show "$\delta_{dot}-r_{dot}$" diagrams of yaw angular acceleration versus steering speed for different vehicle velocities and GVC ON/OFF.

For a velocity of 36 km/h, the lowest of the velocities shown here, the task could be completed even within a small range of steering speed. Here, yaw angular acceleration is nearly zero and the difference between GVC ON and OFF is extremely small. In this speed domain, we consider that "Steering is set with one attempt!" conditions can be naturally achieved regardless of control or no control.

As speed increases, yaw angular acceleration r ($\delta = 0$) becomes larger for GVC OFF. We note here that, while not shown, speed has an effect on the steady-state slip angle: in case (a) in Figure 7, slip angle is positive, in case (b) it is nearly zero, and in cases (c) and (d), it is negative.

Regardless of change in sign of the slip angle, yaw angular acceleration approached zero for all speed domains with GVC ON. Based on the above results, it

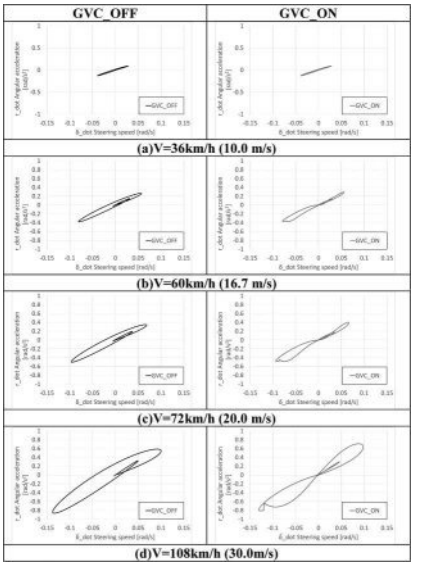


Figure 7. "δ−r" diagrams.

can be said that GVC has a clear effect on decreasing residual yaw angular acceleration and that "Steering is set with one attempt!" conditions can be achieved by GVC.

(Note: The third quadrant edge generated as a result of sign reversal in GVC operation does not occur in a production-type vehicle because filter processing.)

Next, we consider the reasons for this mechanism. The right side of the upper portion of Figure 8 shows time-history data for cases (b) and (d) above. The black broken line in the figure represents steering speed δ_{dot}. Here, it can be seen that yaw angular acceleration with GVC shown by the red line converges to zero at a point near 1.63 [s] where $\delta_{dot} = 0$ after making an unnatural turn (control effect) compared with no control. The results of this calculation example relate to cutting of the steering wheel, but if steering is made to stop near 1.63 [s], the vehicle can enter a steady circular turn under "Steering is set with one attempt!" conditions.

Thus, to orient yaw angular acceleration that has been excited in the positive direction toward zero timed with the stopping of steering, a total yaw moment must be zero. Since vehicle jerk normally becomes zero near the time that steering speed becomes zero, GVC would terminate at this time (Equations (6) and (7), $\Delta K = 0$ in Fig. 4). We here return to the two-degree-of-freedom bicycle model of Figure 1 and take another look at the equation for the yaw motion.

$$\begin{aligned} I\cdot\dot{r} = &-2\left(l_f K_f - l_r K_r + l\Delta K\right)\beta \\ &-\frac{2}{V}\left(l_f^2 K_f + l_r^2 K_r - l\left(l_f - l_r\right)\Delta K\right)r \\ &+2l_f\left(K_f + \Delta K\right)\delta(s) \end{aligned} \tag{13}$$

From Equation (13), it can be seen that the yaw moment consists of a (a) cross-coupling term with side-slip β, (b) yaw damping term, and (c) steer-input term. As described earlier, (a) side-slip β in (a)

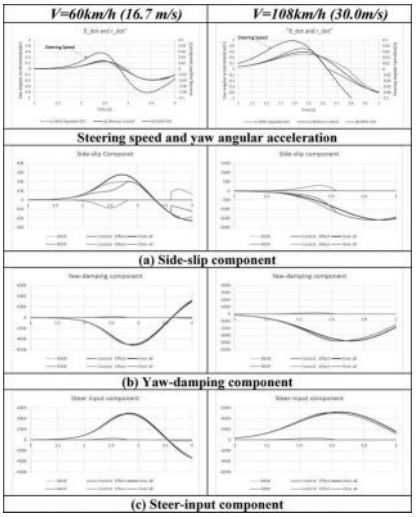


Figure 8. Components of yaw moment.

above includes a sign reversal and has vehicle speed dependency. In the following, we investigate these components at various vehicle velocities. We note, however, that near a velocity of 30 km/h, though the steady-state side-slip gain is positive, the yaw angular acceleration is inherently very small even in the case of no control. Jerk is also small, so the value of the control command is small as well. For these reasons, we omit this velocity from our study.

Simulation results for a velocity of 60 km/h (slip angle near zero) and 108 km/h (slip angle is large and negative) are shown in Figure 8. The horizontal and vertical axes in Figure 8 (a), (b), and (c) represent yaw moment [N·m] and time [s], respectively. Each set of results includes those for GVC ON and OFF for comparison purposes.

In the figure, BASE indicates the original moment configured by cornering stiffness. Since side-slip motion and yaw motion change by GVC, it should be noted that this BASE component itself changes in accordance with GVC operation. Next, Control Effect indicates the effect by GVC. Its value is zero when GVC is OFF or when the control command vanishes. Finally, Overall (red and black lines) indicates the overall moment component, which directly affects residual yaw angular acceleration.

First, for high velocity on the right side of Figure 8, we consider that the slip angle is in a negative state.

Among the side-slip components of (a) with GVC ON, the Control Effect component (orange line) caused by ΔK in Eq. (13) is positive resulting in control that promotes yaw motion. Furthermore, while not shown here, rise in the slip angle improves and becomes larger by GVC. Thus, among the components in (a), the BASE restoring moment (blue line) configured with the original cornering stiffness has a large negative value compared with GVC OFF. In the vicinity of 1.6 [s], if steering speed drops and jerk becomes small, the component arising from ΔK vanishes. At this time, Overall with GVC operation (red

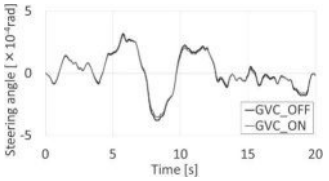


Figure 9. Steering angle with high-frequency disturbance.

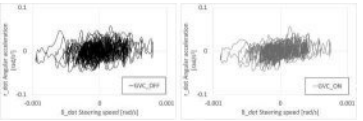


Figure 10. "$\dot{\delta}-\dot{r}$" diagram with high-frequency disturbance.

line) surpasses Overall with no GVC operation (black line) in the negative direction and quickly converges with BASE (blue line). In this way, yaw motion decelerates just as if the brake was suddenly applied with the result that residual yaw angular acceleration when steering is stopped decreases.

Additionally, since yaw motion is being promoted as described above, yaw rate is also increasing compared with GVC OFF. It must therefore be kept in mind that the yaw damping component in (b) is larger under GVC operation and that the component decelerating yaw motion is large. Furthermore, while ΔK exists, the positive input terms in (c) become slightly larger, but when ΔK vanishes, this component likewise vanishes (positive components decline overall), which also leads to a deceleration in yaw motion.

Next, for speeds near 60 km/h on the left side of Fig. 8, we consider that the slip angle is near zero. In the figure, a slip angle slightly arises in the positive direction, and when ΔK exists, a moment is applied in the direction of decelerating yaw motion as a control effect with GVC ON in contrast to the case of high velocity. Near 2.8 [s] where control stops, the restoring moment (on the side of yaw motion deceleration) is small. The moment created by the side-slip component in (a) is on the side of yaw motion promotion as an Overall component. It can be said that its amplitude is reduced by control. The reduction effect for residual yaw angular acceleration is small (amplitude is small to begin with).

The effects in (b) and (c), show a trend similar to that of 108 km/h. These components mainly serve to reduce the residual yaw angular acceleration.

We can summarize the above reduction of residual yaw angular acceleration by GVC, that is, the "Steering is set with one attempt!" effect, from the viewpoint of control gain at various speeds. That is, the desired reduction effect in residual yaw angular acceleration can be obtained in the following ways. (1) At low speeds with the slip angle in a positive range, gain may be made relatively small since residual yaw angular acceleration is small to begin with. (2) With the slip angle in a range near zero, gain is made large since the reduction effect in residual yaw angular acceleration

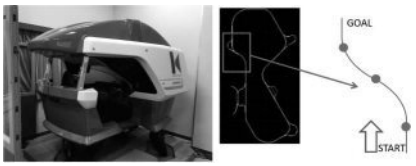


Figure 11. Driving simulator and evaluation course.

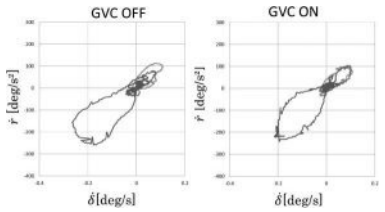


Figure 12. Evaluation results of "$\dot{\delta}-\dot{r}$" diagram.

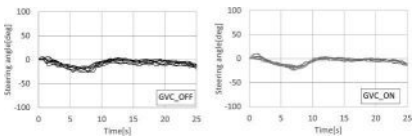


Figure 13. Steering angle of urban road driving.

due to the slip angle is small. (3) With the slip angle negative and large in value, gain is made small.

To discuss vehicle motion control on the level of "texture, transient motions, and motion connections," control tuning from the point in time that the control command value ends until the vehicle responds as performed here should become increasingly important going forward.

6.2 *Against high-frequency disturbance*

Given a vehicle traveling at a velocity of 36 km/h (10 m/s) with the model configuration of section 6.1, the results of evaluating steering angle and "$\delta_{dot}-r_{dot}$" diagrams when adding lateral disturbance Y_d of Equation (2) are shown in Figures 9 and 10, respectively. To make these results easy to understand, Y_d is given a maximum amplitude of 3000 [N] and multiplied by a random value normalized within the range of ±1 at sampling intervals of 1 [ms]. Here, we set l_d in Figure 1 to zero so that the disturbance is applied to the vehicle's center of gravity. This, in effect, meant a 1 kHz input. This disturbance results in extremely small vehicle motion and a very small amount of steering based on the driver model (motion differs according to control ON/OFF).

Examining the results of Figure 9 and 10, it can be seen that GVC has the effect, though only slight, of decreasing the correction steering angle.

7 STUDY BY DRIVING SIMULATOR

Using the driving simulator shown in Figure 11, we conducted an S-shaped driving test at a velocity of 100 km/h on a simulated expressway course. Results revealed "$\delta_{dot}-r_{dot}$" diagrams similar to those of the simulation of section 6 for GVC ON/OFF.

8 STUDY BY ACTUAL VEHICLE TEST

Finally, Figure 13 shows steering angle when driving a production-type GVC vehicle having a high-response engine and a GVC ON/OFF function over a nearly straight, ordinary road with an uneven surface. Ten test runs were made with GVC ON and nine with GVC OFF. Each run was conducted without the driver knowing which mode was set. Similar to the results of section 6, these results show that steering angles under control match those without control well even for steering angles with a small absolute value. This outcome demonstrates that stable driving can be performed even with the input of a high-frequency disturbance other than steering such as unevenness on the road surface. In essence, this means an improvement in straight-ahead stability, which should help reduce driver fatigue.

9 CONCLUSION

In this report, we evaluated "target course traceability performance" in terms of steering input and vehicle motion calculated by a "two-degree-of-freedom bicycle model" extended for representing GVC vehicle characteristics and a "preview-follower driver model" described by a transfer function. This evaluation produced the following findings:

1. GVC has the effect of reducing overshoot of the vehicle's yaw angular acceleration (residual yaw angular acceleration) when steering stops (steering speed is zero).
2. GVC has the effect of minimizing correction steering with respect to input of a high-frequency disturbance.
3. The results of a driving simulator test and actual vehicle test corroborated the above findings.

REFERENCES

Abe, M. 2015. *Vehicle Handling Dynamics, Theory and application -second edition-*, Butterworth–Heinemman, Elsevier.

Takahashi, J., Yamakado, M., Saito, S. and Yokoyama, A. 2012. A hybrid stability-control system: combining direct yaw-moment control and G-Vectoring Control, *Vehicle System Dynamics, Volume 50, Issue 6*, June 2012, pp. 847–859.

Yamakado, M., Abe, M. 2008. An experimentally confirmed driver longitudinal acceleration control model combined with vehicle lateral motion, *Vehicle System Dynamics Volume 46, Supplement 1*, September 2008, pp. 129–149.

Yamakado, M., Takahashi, J., Saito, S., Yokoyama, A., and Abe, M. 2010. Improvement in Vehicle Agility and Stability by G-Vectoring Control, *Vehicle System Dynamics, Volume 48, Supplement 1*, December 2010, pp. 231–254.

Advanced Vehicle Control – Edelmann, Plöchl & Pfeffer (Eds)
© 2017 Taylor & Francis Group, London, ISBN 978-1-138-02992-7

Development of G-Vectoring Control system based on engine torque control

T. Yoshioka, Y. Takahara, F. Kato, O. Sunahara, T. Tsukano, Y. Takeda, K. Takemura & D. Umetsu
Mazda Motor Corporation, Hiroshima, Japan

M. Yamakado, Y. Kano & M. Abe
Kanagawa Institute of Technology, Atsugi, Kanagawa, Japan

J. Takahashi
Hitachi, Ltd., Hitachinaka, Ibaraki, Japan

ABSTRACT: For the enhanced driving quality for human drivers, it is crucial to realize the harmonious transition between lateral and longitudinal motions. We have focused on G-Vectoring Control (GVC) which controls longitudinal acceleration in coordination with lateral acceleration. While the past researches applied brake control or electric motor control to decelerate the vehicle, the significance of the newly developed GVC is to use the high-response internal combustion engine to improve vehicle dynamics. Though the amount of engine torque reduction with the system is smaller than the engine brake, the system's benefits were confirmed in various driving situations such as cornering and straight ahead driving. In this paper, after the system configuration is described, its control effects are evaluated through the field tests in objective and subjective aspects. Finally, it is emphasized that the GVC improves vehicle dynamics performance as human-vehicle closed loop system by modifying driver's operation.

1 INTRODUCTION

It is important to achieve harmonious g transition among deceleration, cornering and acceleration to enhance the driving quality for human drivers. The smooth g transition in cornering can be shown with the "g-g" diagram (Milliken, W. et al. 1995) in Figure 1. We have pursued the sense of unity of vehicle dynamics by coordinating the transient vehicle responses and feedback to the driver. It, however, is difficult to ensure the smooth g transition under various road conditions such as road undulations.

GVC controls the longitudinal acceleration in coordination with lateral motion. Its concept has been verified through field tests with brake control and electric motor control at the deceleration which is larger than the engine brake (Yamakado, M. et al. 2010). We have developed a new GVC system which employs engine torque control based on high response internal combustion engines. Though the amount of engine torque reduction is much smaller than the past researches, we confirmed that the system improves the vehicle dynamics in various driving situations such as cornering, lane following and straight ahead driving especially from the viewpoint of human-vehicle closed loop system.

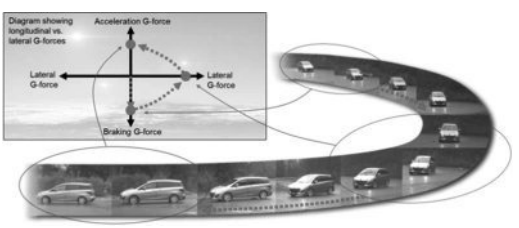


Figure 1. Concept of harmonized dynamic feel.

2 CONCEPT OF GVC

Experienced drivers achieve harmonious transition in lateral and longitudinal accelerations. Their typical operation in cornering is illustrated in Figure 2. They decelerate vehicles when they turn the steering wheel increasingly where the lateral jerk is positive and accelerate when they turn the steering wheel back to the neutral position where the lateral jerk is negative. This implies that they intend to increase the front vertical

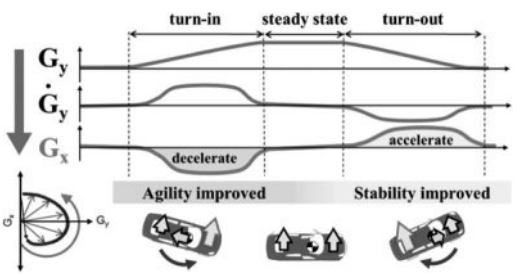


Figure 2. Experienced drivers' operation in cornering.

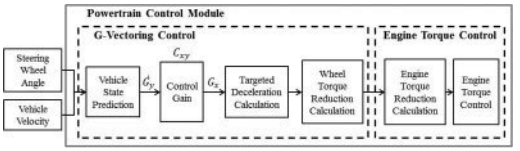


Figure 3. System configuration of new GVC.



Figure 4. Test vehicle.

load to improve agility when entering a corner and to increase the rear vertical load to improve stability when exiting a corner.

The basic formula of GVC can be expressed in Equation 1 (Yamakado, M. et al. 2008).

$$G_{xc} = -\operatorname{sgn}\left(G_y \cdot \dot{G}_y\right)\frac{C_{xy}}{1+Ts}\left|\dot{G}_y\right| \quad (1)$$

where G_{xc} = targeted deceleration; G_y = lateral acceleration; G_y_dot = lateral jerk; C_{xy} = control gain; and T = time constant.

In the past researches, the effects of GVC have been verified with prototype vehicles in emergency maneuvers and limit handling on low-mu surface using brake control or electric motor control with the deceleration of 1–3 m/s^2, larger than the engine brake. By carefully applying the GVC concept to the vehicles, we found that very subtle control of deceleration which is less than engine brake, at most 0.5 m/s^2, greatly improves the driving quality for human drivers in the daily driving situations including straight ahead driving.

3 SYSTEM CONFIGURATION OF GVC BY ENGINE TORQUE CONTROL

To widely apply the GVC concept to the market, we decided to use high-response internal combustion engines for the precise deceleration control. The sys-tem configuration is outlined in Figure 3.

The G-Vectoring Control module embedded in Powertrain Control Module (PCM) predicts the lateral jerk from steering wheel angle (SWA) and vehicle velocity. The lateral jerk is converted to targeted deceleration based on Equation 1, from which the necessary torque reduction at driving wheels is de-rived. The Engine Torque Control module converts it to the targeted engine torque reduction and reduces the engine torque by considering current engine status. Since all the process is integrated in the PCM, the delay time for the control is minimized.

Table 1. Specifications of test vehicle.

Length	4805 mm
Width	1840 mm
Height	1480 mm
Wheelbase	2750 mm
Weight	1520 kg

4 EVALUATION OF GVC

4.1 *Specifications of test vehicle*

The test vehicle is a front-engine and front-driven car of CD segment shown in Figure 4. Its specifications are shown in Table 1. The function of the GVC is turned on and off when necessary.

4.2 *System activation of GVC function*

The GVC function was confirmed with the test vehicle equipped with the measurement facilities such as steering robot and six-axis wheel force transducers. Figure 5 shows the result of a J-turn at the vehicle velocity of about 11 m/s. The SWA input is about 1.9 rad in 3 seconds (Fig. 5(a)). The targeted deceleration is at most 0.08 m/s^2 (Fig. 5(b)). The drive torque at front wheels reduces immediately, and the maximum torque reduction is 40–50 Nm (Fig. 5(c)). The torque reduction results in the vertical load transfer from the rear to the front of about 30 N in transient response (Fig. 5(d)). As the result, the GVC controls the transient vertical load in response to the SWA input effectively and subtly.

4.3 *Open loop evaluation of GVC*

4.3.1 *Influence on vehicle velocity*

Vehicle velocity which the GVC may affect is an important vehicle state to discuss the vehicle dynamics. The decrease of longitudinal vehicle velocity in the J-turn (Fig. 5) due to GVC activation is negligible as shown in Figure 6.

4.3.2 *Influence on vehicle planar motion*

The GVC improves the "g-g" diagram. Figure 7 shows the influence of the GVC on the lateral and longitudinal jerk. While there is a slight phase lead in lateral jerk with GVC (Fig. 7(a)) due to the transient vertical load change shown in Figure 5(d), the longitudinal jerk is significantly modified depending on steering operation (Fig. 7(b)). By shifting the peak of longitudinal jerk forward, the GVC shortens the delay time of the longitudinal acceleration against the lateral acceleration. The resulting "g-g" diagram is shown in Figure 8. The transition of longitudinal and lateral accelerations becomes more harmonious from the beginning of cornering.

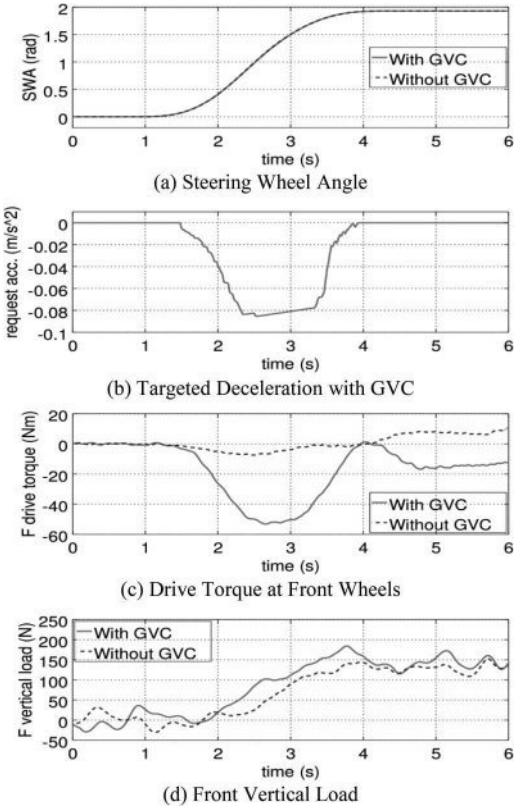


Figure 5. Activation of GVC at J-turn.

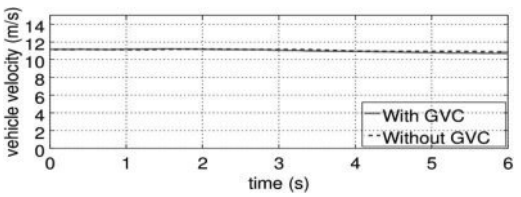


Figure 6. Longitudinal vehicle velocity.

The phase lead of lateral jerk in Figure 7(a) also induces better lateral motion. Figure 9 shows the vehicle lateral jerk with respect to steering wheel angular velocity (SWV). The hysteresis of lateral jerk is suppressed with GVC which results in the better vehicle transient response in the planar motion.

4.3.3 *Influence on vehicle attitude*

The vehicle attitude is another important aspect to evaluate vehicle dynamics. Figure 10 shows the relation between SWV and roll rate, and the hysteresis of roll rate with respect to SWV is reduced with GVC which results in better damped roll motion.

Figure 11 shows the relation between roll angle and pitch angle. The vehicle noses down in response to the roll motion with GVC while it noses up without GVC. The roll mode at the lateral acceleration of 2.5 m/s^2 in a right turn is illustrated in Figure 12. The four apexes of each rhombus correspond to the suspension positions

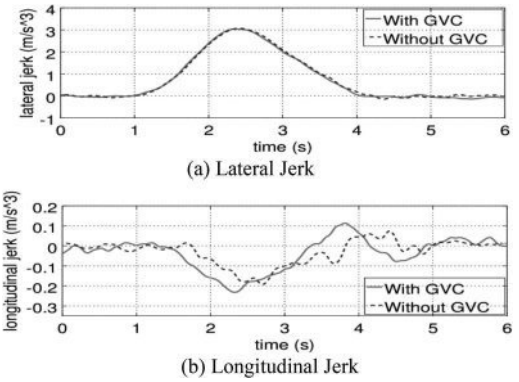


Figure 7. Lateral jerk and longitudinal jerk.

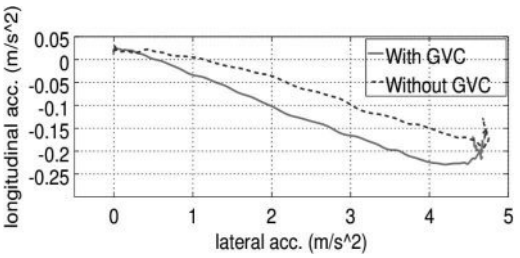


Figure 8. "g-g" Diagram.

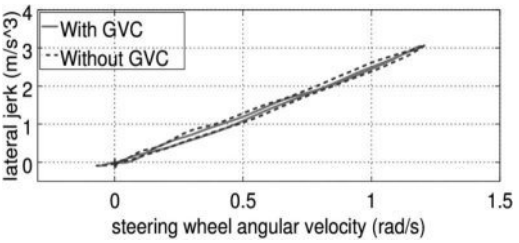


Figure 9. Lateral jerk against SWV.

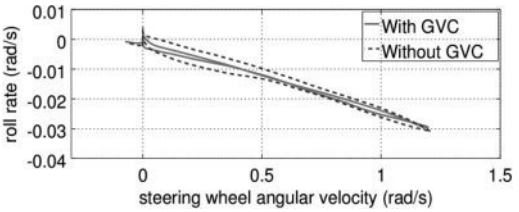


Figure 10. Roll rate against SWV.

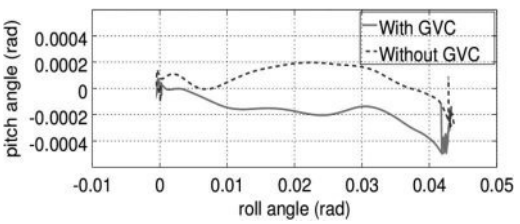


Figure 11. Pitch angle against roll angle.

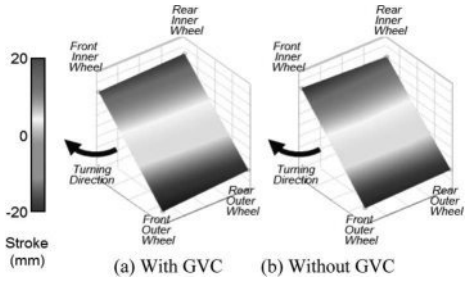


Figure 12. Comparison of suspension stroke mode.

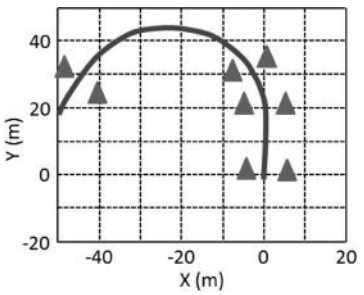


Figure 13. Pylon layout for J-Turn.

such as front outer wheel and rear inner wheel. The vehicle with GVC noses down clearly while rolling, which is called as diagonal roll and is expected to match the human sensitivity (Kodaira, T. et al. 2007).

4.4 *Closed loop evaluation of GVC*

4.4.1 *Steering operation in J-turn*

The GVC improves the line trace capability in human-vehicle closed loop system which can be evaluated with driver's steering operation. The pylon lay-out for J-turn is defined in Figure 13 where the driver is directed to pass through the pylons at the vehicle velocity of about 11 m/s.

In Figure 14, the driver turns the steering wheel more smoothly with GVC so that the maximum SWV decreases by about 7%.

4.4.2 *Steering operation in lane change*

The pylon layout for the lane change is defined in Figure 15 where the vehicle velocity is about 17 m/s. In Figure 16, the driver turns the steering wheel back to the neutral position earlier with GVC, decreases the amount of SWA and SWV by half especially at the latter part of the maneuver and suppresses the overshoot of SWA and yaw rate as the result. In short, the driver controls the vehicle more effectively and adequately with GVC.

4.4.3 *Steering operation on winding road*

The GVC improves the line trace capability in more general driving situations such as winding road. The outline of the track is shown in Figure 17 which comprises of road curvatures of 200 m and 100 m.

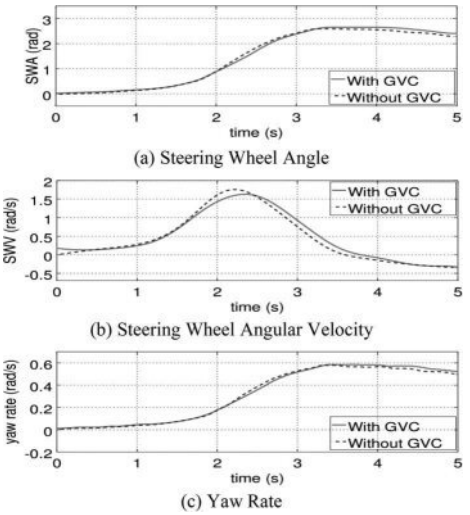


Figure 14. Steering operation in J-turn.

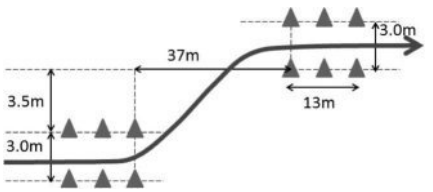


Figure 15. Pylon layout for lane change.

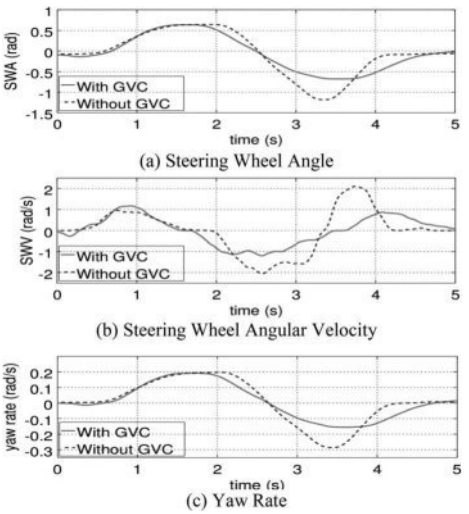


Figure 16. Steering operation in lane change.

The driver's steering operation at the vehicle velocity of about 17 m/s is shown in Figure 18. The overall profile of SWA and yaw rate with and without GVC resembles to each other, because the driver traces the designated track, but the deviations of SWV is clearly suppressed with GVC which implies that the driver controls the vehicle with less steering corrections.

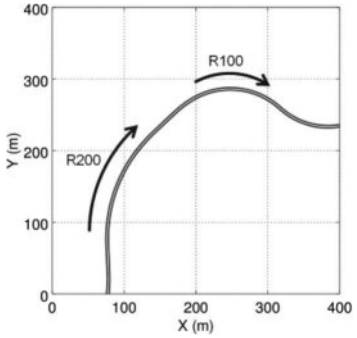


Figure 17. Winding road.

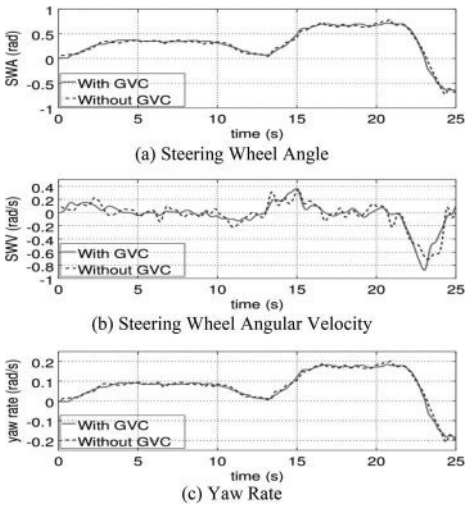


Figure 18. Steering operation on winding road.

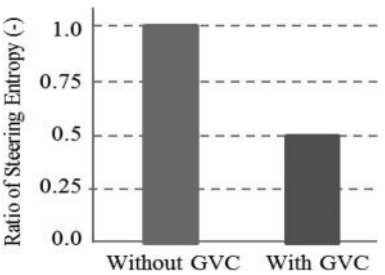


Figure 19. Steering entropy on winding road.

The steering entropy, an index to evaluate the smoothness of steering operation (Nakayama, O. et al. 1999), decreases by half as shown in Figure 19. As a result, the GVC improves the driver's steering operation and realizes better driving quality for human drivers in various driving situations.

4.5 *Subjective evaluation of GVC*

Experienced and non-experienced drivers highly evaluate the GVC system in various driving situations such as proving grounds and public roads, high and low road friction, high and low speed, with and without road undulations. Their comments are all positive, and some of them are listed below:

- Drivers can feel more agility and stability.
- The system improves driver's capability of driving.
- Every driver enjoys benefits of the system regardless of their driving skills.

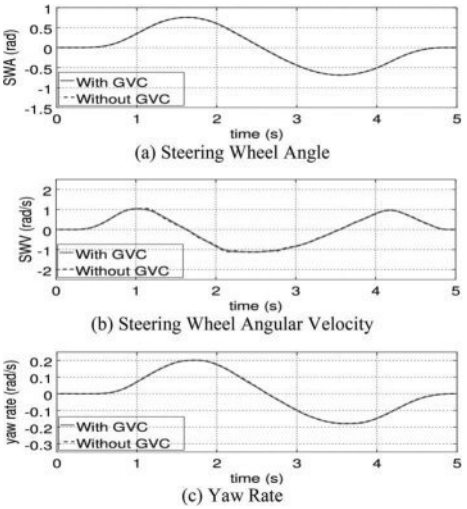


Figure 20. Lane change with steering robot.

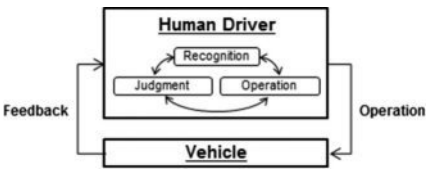


Figure 21. Human vehicle closed loop system.

5 ANALYSIS OF GVC PERFORMANCE FROM HUMAN ASPECTS

The GVC improves the vehicle dynamics as the performance of human-vehicle closed loop system. Figure 20 shows the results of lane change maneuver with the steering robot which emulates the driver's steering operation with GVC in Figure 16. Though there is a significant difference between the cases with and without GVC when the driver controls the vehicle (Fig. 16), the difference is very small with the steering robot operation (Fig. 20). This infers that the GVC improves human driver's operation itself better than vehicle's mechanical responses.

Figure 21 shows the schematics of human-vehicle closed loop system. Though the human driver's operation has been largely modified due to GVC, it is not clear how the modification is realized since the mechanism of the driver's operation in the human-vehicle closed loop has not been fully understood.

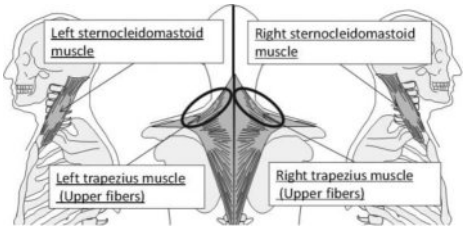


Figure 22. Location of muscles for measurement.

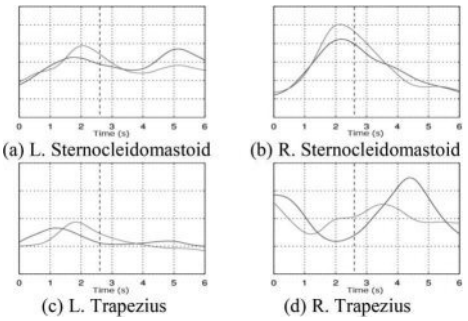


Figure 23. Electromyogram with GVC.

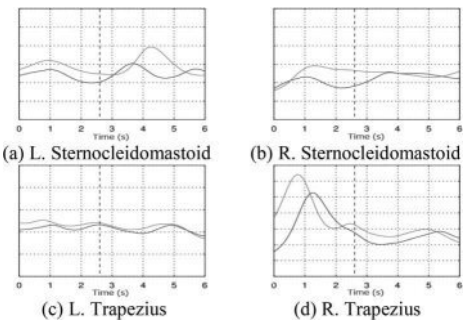


Figure 24. Electromyogram without GVC.

We evaluated the muscle activities of a driver to observe his or her changes. Figure 22 shows the muscle locations we measured. They are sternocleidomastoid muscles and upper trapezius muscles which are supposed to sustain the driver's head against the external forces such as inertial force during driving. The data of electromyogram with and without GVC in a left J-turn are shown in Figures 23 and 24. In each chart, two samples of electromyogram of each muscle are plotted, and the vertical dotted line represents the time when the vehicle lateral jerk is biggest.

In a left turn, the left and right sternocleidomastoid muscles and the left upper trapezius muscle are expected to sustain the driver's head against the inertial force to the right. In Figure 23, the electromyograms of these muscles reach the peak value prior to the maximum lateral jerk with GVC, but they don't without GVC (Fig. 24). The muscles to sustain the driver's head seem to work more effectively with GVC.

We also evaluated the driver's motion on the seat in a J-turn which is measured with seat pressure sensor.

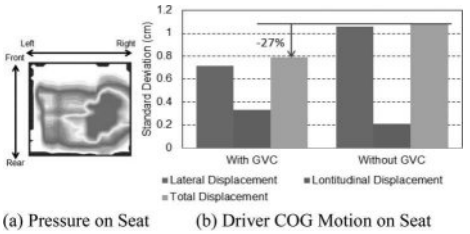


Figure 25. COG of driver on seat.

An example of measurement of pressure distribution is illustrated in Figure 25(a), and the standard deviations of the center of gravity of the driver are shown in Figure 25(b). The driver's COG motion is reduced by 27% in total with GVC.

These facts infer that the GVC enhances the driver's postural adjustments in driving. The relation among vehicle behaviors, driver's postural adjustments and his or her driving operation has not been fully clarified, but the better postural adjustment may contribute to the better vehicle dynamics of the human-vehicle closed loop system.

6 CONCLUSIONS

We developed the new GVC system for mass production by using engine torque control. It is the result of elaborate collaboration between vehicle dynamics development and high-response powertrain control.

We confirmed that the drivers enjoy the better driving quality with the system regardless of their driving skills. While the system realizes the better mechanical characteristics of the vehicle such as reduced response delay and diagonal roll, it greatly improves the driver's steering operation as the vehicle dynamics performance of the human-vehicle closed loop system.

We still need to understand the mechanism of the human driver's role in the human-vehicle closed loop system so that we can adapt the vehicle to human drivers and passengers more adequately in the future. This aspect must be important even in the case of autonomous driving as well.

REFERENCES

Kodaira, T. et al. 2007. Improvement of Vehicle Dynamics Based on Human Sensitivity (Second Report) – A Study of Cornering Feel-, *SAE Technical Paper,* 2007-01-0447.

Milliken, W. & Milliken, D. 1995. Race Car Vehicle Dynamics. *SAE International*.

Nakayama, O. et al. 1999. Development of a Steering Entropy Method for Evaluating Driver Workload, *SAE Technical Paper,* 1999-01-0892.

Yamakado, M. et al. 2008. An experimentally confirmed driver longitudinal acceleration control model combined with vehicle lateral motion, *Vehicle System Dynamics*, Vol. 46: pp. 129–149.

Yamakado, M. et al. 2010. Improvement in vehicle agility and stability by G-Vectoring control, *Vehicle System Dynamics*, Vol. 48: pp 231–254.

Advanced Vehicle Control – Edelmann, Plöchl & Pfeffer (Eds)
© 2017 Taylor & Francis Group, London, ISBN 978-1-138-02992-7

Effect of yaw-moment control based on lateral jerk information on lane change task

Junya Takahashi
Hitachi Ltd., Hitachinaka, Japan

Makoto Yamakado
Kanagawa Institute of Technology, Atsugi, Japan

Keiichiro Nagatsuka
Hitachi Automotive Systems Europe, Paris, France

Seichi Sato & Naoki Hiraga
Hitachi Automotive Systems Ltd., Hitachinaka, Japan

Daisuke Umetsu & Yasunori Takahara
Mazda Motor Corporation, Hiroshima, Japan

ABSTRACT: "Moment Plus (M+)" is the yaw-moment control based on lateral jerk information, and the effect of M+ on lane change maneuver was studied from driver's controllability point of view. The relation between steering speed and yaw angler acceleration was used as the index to evaluate the controllability of the vehicle. It was confirmed that M+ can improve the linearity of this index by combining with G-Vectoring Control, which is the longitudinal-acceleration control based on lateral jerk. This result indicates that M+ can be an useful application to reduce the steering control effort for lane change.

1 INTRODUCTION

Automated driving system is one of the solutions to reduce the traffic accidents and provide a new transportation system to the people who cannot drive a vehicle. However, it will take a long time to replace the all current vehicle to the automated one and even though the number of automated driving vehicle is increased on a road, the vehicle controlled by a human driver will still remain on a road. To improve the safety of a vehicle controlled by a human driver, many driver assistance systems are provided in a vehicle (e.g. Electronic Stability Control (ESC), Automatic Emergency Braking (AEB), Lane Keeping Assist System (LKAS) etc.) and these systems are useful to prevent the accidents caused by human error. However, most of these systems are designed to activate after a driver makes mistakes to put the vehicle motion into a serious unstable motion.

Authors are studying about the driving assistance system which works during daily driving scenario (that is, not only urgent case) to reduce the driver's work-load and human error itself. Some assistance systems were proposed based on the control algorism derived from a skilled driver's driving named "G-Vectoring Control (GVC)", which is a longitudinal motion (acceleration) control for coordination with lateral motion (jerk) (Yamakado et al. 2010, Takahashi et al. 2012).

"Moment Plus (M+)" is one of the proposed systems to control the yaw-moment directly based on G-Vectoring Control algorism and it was reported that M+ can improve the stability for cornering by combining with GVC and ESC (Yamakado et al. 2014a. A yaw-moment. . .). In this study, it was studied how GVC and M+ affects a driver's steering maneuver for the lane change task.

2 OVERVIEW OF MOMENT PLUS

2.1 *Basic principle of Moment Plus*

In a previous works, the authors proposed the following formula shown in Equation (1) as a basic control policy for linking a vehicle's longitudinal motion according to its lateral motion. This technique is named G-Vectoring Control (GVC). G_{xt} is a longitudinal acceleration command of GVC, G_y is the lateral acceleration, and $\dot{G}_y$ is the vehicle's lateral jerk (the first derivative of the lateral acceleration). Basically, this is a simple control law whereby the lateral jerk

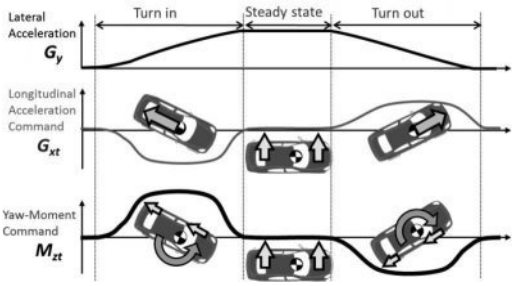


Figure 1. Activation image of G-Vectoring and Moment Plus control.

$\dot{G}_y$ is multiplied by a gain C_{xy} and subjected to a first-order delay to produce the longitudinal acceleration command.

$$G_{xt} = -\mathrm{sgn}\left(G_y \cdot \dot{G}_y\right)\frac{C_{xy}}{1+Ts}\left|\dot{G}_y\right| \quad (1)$$

As shown in Eq. (1), GVC decelerates the vehicle as the lateral jerk increases when the vehicle starts turning a corner. After that, no deceleration/acceleration is applied during steady-state cornering, because the lateral jerk becomes zero. The vehicle begins to accelerate when it begins to return to straight-ahead driving. This deceleration/acceleration of GVC effects on yaw motion of the vehicle during cornering because of the shift in vertical load between the front and rear wheels; GVC controls the yaw motion by indirect way.

Moment Plus (M+) is the direct yaw-moment control based on the G-Vectoring theory. Considering an analogy with the GVC command value in Eq. (1), the yaw-moment command of M+ (M_{zt}) is defined as shown in Equation (2); C_{mn} is a proportional constant, and T_{mn} is a first-order lag time constant.

$$M_{zt} = -\mathrm{sgn}\left(G_y \cdot \dot{G}_y\right)\frac{-C_{mn}}{1+T_{mn}s}\left|\dot{G}_y\right| \quad (2)$$

Figure 1 shows the activation image of GVC and M+. As shown in Figure 1, M+ applies the different braking/driving forces on the left and right side wheels to enhance the yaw motion at the turn in phase and stabilize the motion at the turn out phase. The waveform of M_{zt} can be similar with longitudinal acceleration command of GVC (G_{xt}), because the moment instruction value and the acceleration/deceleration instruction values are all based on the lateral jerk, selection of equal first-order delay time constants for Eq. (1) and Eq. (2).

2.2 *System layout of G-Vectoring and Moment Plus combined system with ESC*

Availability of GVC and M+ for cornering depends on the installed actuators in a vehicle. In GVC case, it is necessary to control both driving and braking force acting on wheels, but no need to make a difference between driving/braking force acting on left side and right side. On the other hands, in M+ case,

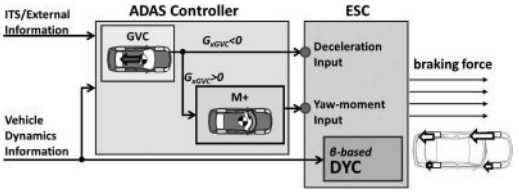


Figure 2. System layout of GVC M+ combined system using ESC.

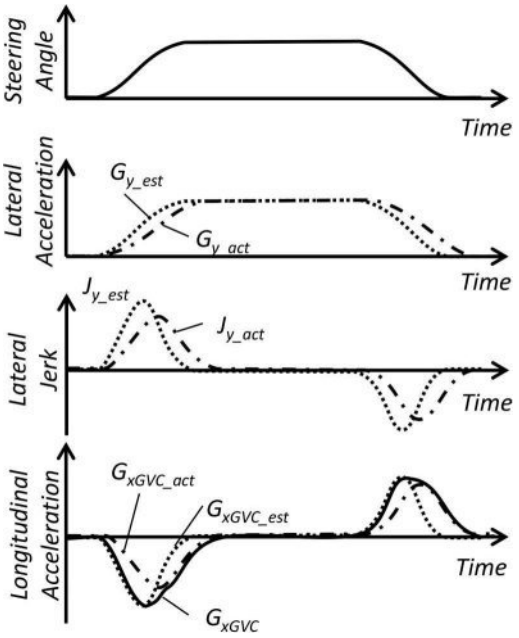


Figure 3. Longitudinal acceleration command image of G-Vectoring Control.

it is necessary to control driving or braking force acting on wheels individually to make a difference between driving/braking force acting on left side and right side. There are several combination of actuator to achieve both GVC and M+ (e.g. single electric motor & ESC unit, combustion engine & ESC unit, combustion engine & ESC unit & DYC unit, In-wheel-motor etc.). In this study, ESC unit, which can control both deceleration and direct yaw-moment, is used as the actuator for GVC and M+. Figure 2 shows the system layout of GVC M+ combined system using ESC.

As shown in Figure 2, GVC and M+ are installed in the ADAS (Advanced Driver Assistance System) controller and this controller sends deceleration command calculated by GVC and yaw-moment command calculated by M+ to ESC controller. ESC controller sends the braking force command based on these deceleration and yaw-moment commands and DYC command of ESC, which is based on a slip angle and deviation between actual yaw-rate and target yaw-rate calculated by steering angle and vehicle speed.

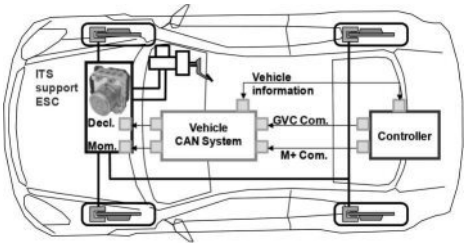


Figure 4. Configuration of test vehicle.

Figure 3 shows the longitudinal acceleration command image of G-Vectoring Control. As shown in Figure 3, GVC command is calculated based on two lateral acceleration/jerk signals; one is G_{y_est}/J_{y_est}, and the other is G_{y_act}/J_{y_act}. G_{y_est} is calculated using vehicle model with steering angle and vehicle speed and G_{y_act} is calculated using an acceleration sensor data.

G_{xGVC_est}, which is calculated based on G_{y_est}/J_{y_est}, works to compensate the control delay caused by signal filtering and the actuator response. G_{xGVC_act}, which is calculated, based on G_{y_act}/J_{y_act}, works to reflect the actual vehicle motion on the longitudinal acceleration command; it is useful especially on a slippery road condition case, which has a big difference between estimated motion by vehicle model and actual motion. Longitudinal acceleration command of GVC (G_{xGVC}) is calculated by combining these two acceleration commands (G_{xGVC_est}, G_{xGVC_act}) as shown in Figure 3 (solid line).

In the previous works (Yamakado et al. 2014b. Comparison. . .), it was reported that the deceleration control by GVC is more effective than yaw-moment control by M+ at the beginning of cornering (turn-in phase). Therefore deceleration command is calculated by GVC. On the other hand, it is difficult to apply the positive longitudinal acceleration by GVC to stabilize the yaw motion at the end of cornering in this system, and yaw-moment control using braking force is quite effective to stabilize the yaw motion. Therefore, yaw-moment command for stability is calculated by M+ based on the positive longitudinal acceleration command of GVC.

2.3 *The effect of GVC, M+ combined system on Lane change*

Before the discussion about the M+ effect on lane change task, the driving test results on a slippery road condition (packed snow) were reprinted. Figure 4 shows the configuration of the test vehicle and figure 5 shows the course layout of the driving test.

The test vehicle shown in Figure 4 was a 2500 cc FR (front engine, rear drive) car with five-speed automatic transmission. The ESC unit was an ITS-compatible model using a gear pump. GVC and M+ are installed in an additional rapid prototyping controller, and the deceleration command and yaw-moment command are sent to the ESC. No hardware modifications for actuator are performed in these tests.

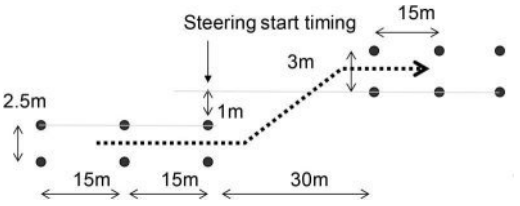


Figure 5. Course layouts for lane change.

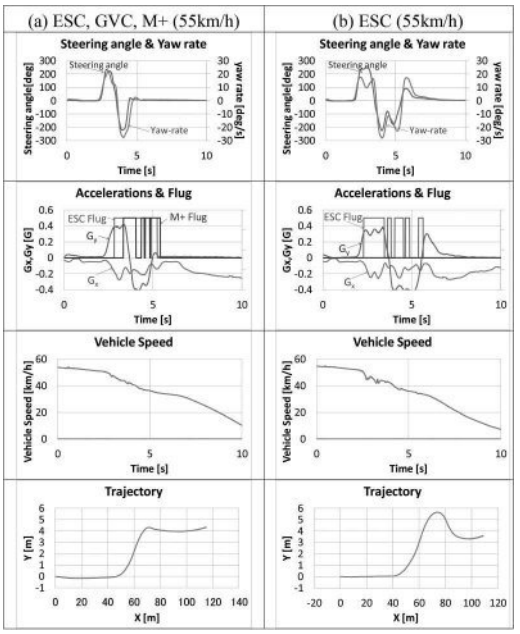


Figure 6. Single lane change test results on a slippery road.

The driving tests were performed with full control condition (GVC, ESC, M+) and only ESC condition (corresponding to a normal vehicle). Assuming a single lane change as an emergency avoidance maneuver, the vehicle's ability to follow the driver's operations (trace performance) and handling stability (convergence) were evaluated by comparison of the different control setting (full control case and only ESC case). Figure 6 shows the driving test results.

As shown in Figure 6, the lane change task was completed without oscillatory steering with GVC, M+ and ESC case (Fig. 6(a)), even though heavy oscillatory steering behavior is observed with only ESC case (Fig. 6(b)). In case (a), it is considered that yaw-motion enhancement by GVC deceleration reduces the steering angle on the primary steering phase and yaw-moment control by M+ and ESC helps to stabilize the yaw motion on the reverse steering phase. Compared with case (a), the lateral movement performance seems to be lower and a large steering angle and unstable yaw motion was observed in case (b).

To observe the effect of additional control (GVC, M+) on lane change task, the relation between steering behaviour and yaw motion was observed using $\dot{\delta}$

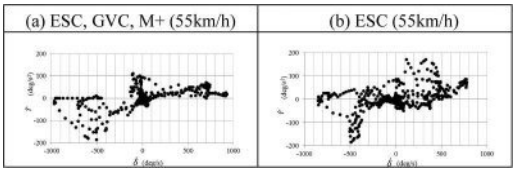


Figure 7. $\dot{\delta}-\dot{r}$ diagram of single lane change.

(steering speed) – $\dot{r}$ (yaw angler acceleration) diagram. Figure 7 shows the $\dot{\delta}-\dot{r}$ diagram of lane change tests on packed snow road with all control (ESC, GVC and M+: case (a)) and only ESC (case (b)).

As shown in Figure 7, case (a) show more linearity (Fig. 7(a)) compared with case (b) (Fig. 7(b)), especially on the second and third quadrants. In case (b), there are many plots on second quadrant in wide area. On the other hands, the plots on second quadrant are limited in case (a) and these plots are closed to the x-axis (and origin). The plots on second quadrants mean yaw-rate increases even though steering angle decreases. In such situation, normal driver increases the steering angle/speed more and this behaviour would be one of the reasons to cause oscillatory steering during lane change task.

These driving test results indicate that GVC and M+ can reduce the oscillatory steering and improve the lane change performance. However this is the combined control (ESC, GVC and M+) effects on lane change task, and it is still unclear how M+ contributes on this phenomenon. In this study, the effect of M+ on this phenomenon is analyzed using full vehicle simulation.

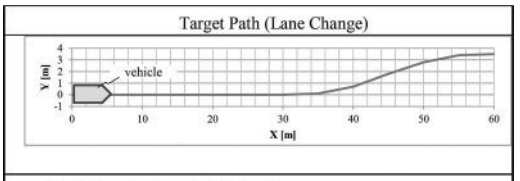
3 EVALUATION OF MOMENT PLUS EFFECT ON LANE CHANGE TASK BY SIMULATION

3.1 *Overview of the simulation*

To analyse the effect of M+ on lane change task, full-vehicle simulations are performed with the simulation condition shown in Table 1; target path, initial speed, and brake, steer, acceleration control setting. The steering control is performed by a driver model (Abe. 2009) using a preview point following (preview time: 0.5 s, driver time lag: 0 s) and the initial speed was set based on a preliminary simulation using this driver model without brake control condition; initial speed is increased by 5 km/h from 50 km/h until the unstable motion was observed (75 km/h in this case).

As the brake control, two settings were prepared; (a) GVC & M+, (b) GVC & ESC. Figure 8 shows the block diagram of setting (a) and (b). In setting (a) case, the longitudinal acceleration command of GVC (G_{xt}) is used as a deceleration command if $G_{xt} < 0$, and as an input signal of M+. M+ calculates yaw-moment command (M_{zt}) based on G_{xt} and vehicle dynamics information (vehicle speed, steering angle and lateral acceleration). On the other hands, in setting (b) case, GVC command is used only as a deceleration

Table 1. Simulation conditions of lane change test.



Initial Speed : 75km/h (20.8m/s)

Road	friction 0.5	Tire	Magic Formula
Brake Control	(a) GVC & M+ (b) GVC & ESC	Steering Control	Preview follower (Preview time 0.5s, Driver Time Lag 0s)
		Accel. Control	None

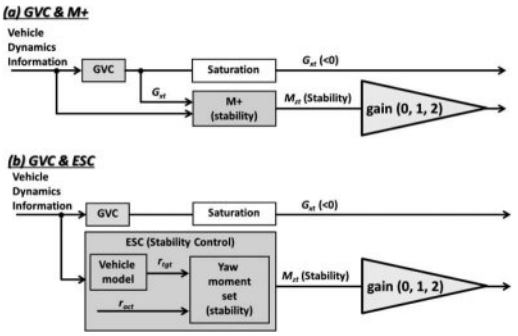


Figure 8. Brake Control by (a) GVC & M+ and (b) GVC & ESC.

command and ESC calculates yaw moment command based on a simple yaw-rate feedback control: yaw moment of ESC is calculated based on the deviation between target yaw-rate (r_{tgt}) using vehicle model and actual yaw-rate (r_{act}). Here, ESC works only to prevent spinning and no yaw moment control to enhance the yaw motion. Each yaw moment command (M_{zt}) has a gain and it is changed from 0 to 2 in this simulation to analyse the effect of M_{zt}.

3.2 *Analysis of M+ effect on lane change task*

Figure 9 shows the simulation results of lane change with (a) GVC & M+ / (b) GVC & ESC; vehicle speed, yaw angle, steering angle, yaw-rate, side slip angle, lateral- and longitudinal-acceleration (G_y, G_x), and braking force of Front Left (FL) and Front right (FR) tires.

In both cases, "gain 0" (dashed-dotted line) is no yaw-moment command condition, that is, only GVC case. "gain 1" (dash line) is a base setting, which were set to make the steering angle half at the straight part of second lane (X > 60 m) compared with "gain 0" case. "gain 2" (solid line) is the case that the yaw moment command is twice of "gain 1" case.

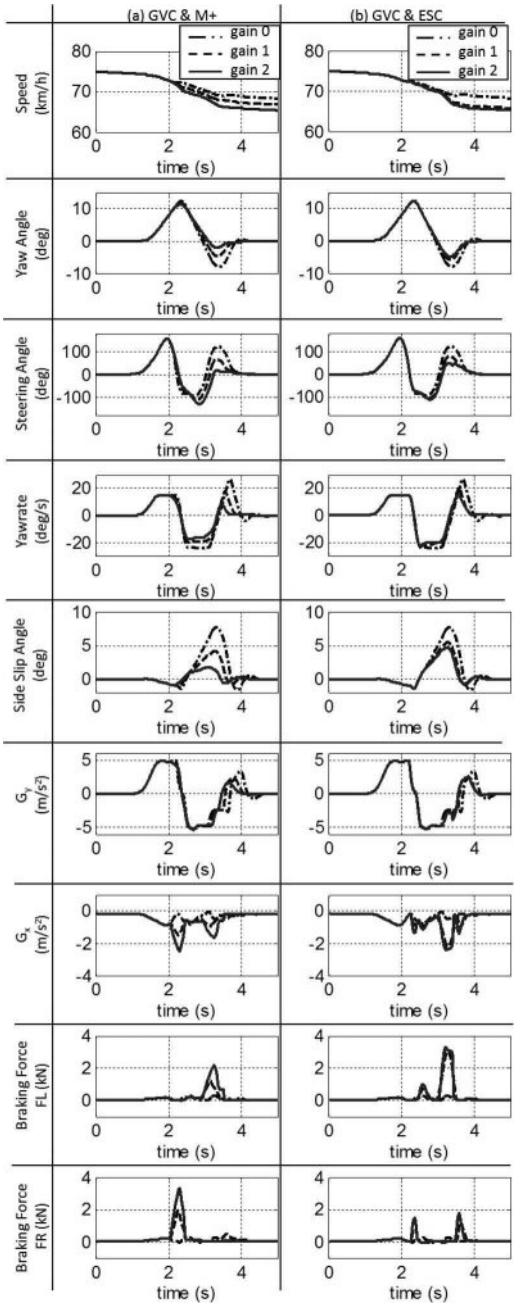


Figure 9. Simulation result of single lane change with (a) GVC & M+, (b) GVC & ESC.

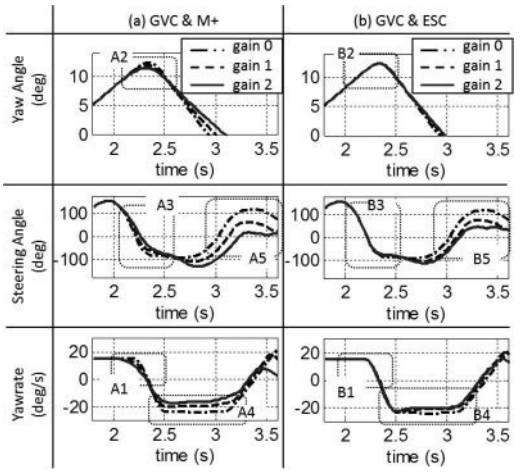


Figure 10. Simulation result of single lane change with (a) GVC & M+, (b) GVC & ESC (1.8 s–3.6 s).

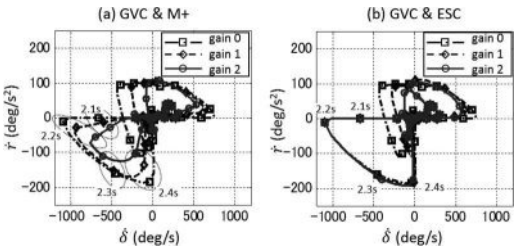


Figure 11. $\dot{\delta}-\dot{r}$ diagram of single lane change simulation.

As shown in Figure 9, the braking force increases after steering angle increases in both cases by GVC. After that, ESC and M+ control the braking force of FR and FL in a different way. In case (b), ESC applies strongest braking force after the side slip angle becomes larger (around 3.2 second). On the other hand, in case (a) M+ applies the strongest braking force after the first deceleration control by GVC (around 2.2 second), even though the side slip angle is still small at this moment. This early timing of yaw moment control by M+ affects steering maneuver more than ESC case during lane change. Figure 10 shows a closed-up image of Figure 9 from 1.8 to 3.6 second, and Figure 11 shows $\dot{\delta}-\dot{r}$ diagram.

In (a) GVC & M+ case, the timing when yaw-rate start decreasing becomes earlier (Fig.10A1) with the increasing of gain (0 to 2) after 2 second because of the yaw-moment control by M+. This reduction of yaw-rate decreases the peak of yaw angle (Fig. 10A2), and it changes the steering maneuver controlled by a preview point following driver model; the steering speed from the one side (left side in this simulation) to the other side (right side) is slower with the increasing of gain (Fig. 10A3).

On the other hand, in (b) GVC & ESC case, there is no big difference with the increasing of gain until 2.5 second (Fig. 10B1, 2, 3), because the yaw-moment control by ESC is smaller and later than M+ at this moment. In (b) case, yaw-moment control is mainly performed after 2.5 second when the side slip angle is larger as shown in Figure 9. However, the effect to reduce the yaw-rate and side slip angle during the turn-back phase is less than M+ case (Fig. 10A4, B4). As the result, the effect to reduce the steering angle at

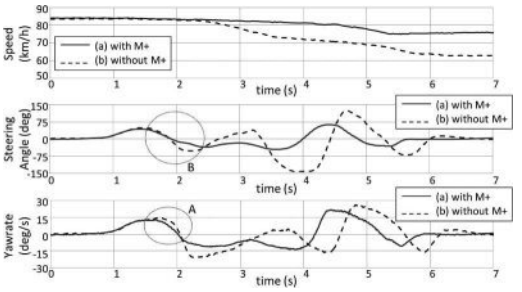


Figure 12. Driving test result of double lane change on a slippery road.

the end of lane change task (after 3 second) is less than M+ case (Fig.10A5, B5)

This difference between (a) and (b) is also appeared on $\dot{\delta}-\dot{r}$ diagram clearly. As shown in Figure 11, in (a) case, the relation between $\dot{\delta}$ and $\dot{r}$ in third quadrants becomes more linear with the increasing of gain (0 to 2), but no difference in (b) case. This tendency is similar with the driving test results shown Figure 7.

These simulation results indicates that the reduction of the steering speed form the one side the other side could be one of the effective points of M+ to reduce the oscillatory steering by driver and improve the stability for lane change. Figure 12 shows the one driving test result of double lane change on a slippery road as a reference.

As shown in Figure 12, the steering manoeuvre of the case (a) with M+ (solid line) is smoother than the case (b) without M+ (dash line); the strong oscillatory steering manoeuvre is observed in the case (b). Focusing on the early stage of double lane change, it is observed in the case (a) that the reduction of yaw-rate is earlier (Fig. 12A), and the steering speed from one side to the other side is slower (Fig. 12B) compared with the case (b).

Further investigation is still necessary to clarify the relation between driver's steering manoeuvre and control (GVC, M+ and ESC), but these results indicate that the reduction of the secondary steering speed could be one of the M+ effects on lane change task to prevent oscillatory steering by driver.

4 CONCLUCSION

The effect of Moment Plus (M+) on single lane change task is analyzed by full-vehicle simulation. The results are as following;

(1) The simulation results indicated that M+ can reduce the peak of yaw angle during single lane change and this reduction have an effect to decrease the steering speed from the one side to the other side.
(2) It was confirmed by full-vehicle simulation that the relation between steering speed ($\dot{\delta}$) and yaw angler acceleration ($\dot{r}$) becomes more linear on the third quadrants of $\dot{\delta}-\dot{r}$ diagram by using M+ for lane change task.
(3) The reduction of the steering speed and improvement of the linearity between $\dot{\delta}-\dot{r}$ by M+ could be one of the reasons to prevent the oscillatory steering during lane change task.

REFERENCES

Abe, M. (2009). *Vehicle Handling Dynamics, Butterworth-Heinemman*.

Takahashi, J., Yamakado, M., Saito, S. and Yokoyama, A. (2012). A hybrid stability-control system: combining direct-yaw-moment control and G-Vectoring Control *Vehicle System Dynamics*, **50**, **6**, 847–859.

Yamakado, M., Takahashi, J., Saito, S., Yokoyama, A., and Abe, M. (2010). Improvement in Vehicle Agility and Stability by G-Vectoring Control, *Vehicle System Dynamics*, **48**, 231–254

Yamakado, M., Nagatsuka, K., and Takahashi, J. (2014). A yaw-moment control method based on a vehicle's lateral jerk information, *Vehicle System Dynamics*, **52**, 1233–1253

Yamakado, M., Nagatsuka, K., and Takahashi, J. (2014). Comparison of Deceleration Control and Yaw-moment Control Applied in the Early Stage of Cornering, *Proc. AVEC'14, Tokyo, 22–26 September 2014*.

Advanced Vehicle Control – Edelmann, Plöchl & Pfeffer (Eds)
© 2017 Taylor & Francis Group, London, ISBN 978-1-138-02992-7

Model predictive control for active drive-torque distribution during a slalom manouevre

J.S. Hellewell, A.A. Popov, G.E. Burnett & J.W. Griffin
Faculty of Engineering, University of Nottingham, University Park, Nottingham, UK

ABSTRACT: Model Predictive Control (MPC) is an increasingly popular research area for active torque distribution. Previous predictive methods have utilised non-linear models with online partial differentiation to obtain state space matrices. This is computationally expensive and can limit how quickly the controller operates. A two-degree-of-freedom (DOF) state space controller is developed to control the vehicle's yaw rate and lateral acceleration. The controller was evaluated using a 7DOF vehicle model and a sinusoidal steering input. The control algorithm improved the vehicle performance and does not show obvious limitations due to its lower model complexity.

1 INTRODUCTION

Chassis control systems have increased in popularity over the past 20 years, the focus being on controlling dynamic behaviour in the lateral, longitudinal and vertical directions (Yu et al. 2008). Traditional safety systems, such as an Electronic Stability Program (ESP), only come into effect during extreme conditions or emergency situations. Torque vectoring control however actively manages the driveline torque; providing similar effects to the lateral dynamic behaviour of these traditional systems without the reduction in vehicle acceleration (Osborn & Shim 2006).

Current control strategies often implement proportional and integral (PI) control. Derivative action is not used within an automotive dynamic control system due to the presence of high frequency noise in the signal and the inconsistent effect it has on system stability in practical applications (Ang et al. 2005).

PI systems only provide reactive control as it is a feedback mechanism and so it rarely provides optimal control; Model predictive control (MPC) however, calculates the future plant state in real-time and compares this to a reference trajectory to calculate an error term. Numerical optimisation is then used to minimise the error term utilising the control inputs (Camacho & Bordons 1999).

The application of MPC to enhance wheel torque distribution has been considered before (Ghike et al. 2009), utilising an 8 degree-of-freedom (DOF) model, with online partial differentiation of the model output. These computationally intensive tasks require powerful hardware for the controller, limiting the minimum discrete time-step of the controller.

In this paper, it is proposed that a simple discrete state space model shall be used to model the lateral acceleration and yaw rate of the vehicle. By reducing the complexity of the control model, a small time step can be used.

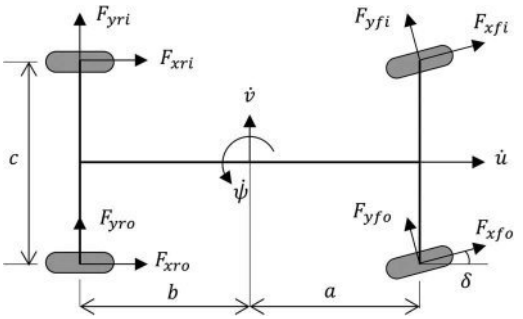


Figure 1. Vehicle model.

In Section 2, the simulation model used is described; Section 3 outlines the design of the MPC torque-vectoring controller. Numerical results for the effect on vehicle behaviour during a slalom manoeuvre are presented in Section 4.

2 SIMULATION MODEL

The vehicle model presented in this section is the same used by Osborn & Shim (2006) for the independent control of torque distribution. The vehicle is modelled with seven degrees-of-freedom, with the roll, pitch and heave motions of the vehicle body not modelled as the model has no suspension system. The longitudinal and lateral acceleration, along with the yaw acceleration of the vehicle body is simulated, along with the rotational acceleration of each wheel.

The vehicle's equations of motion are obtained by summing the forces and moments about the vehicle's Centre of Mass (CoM):

$$m(\dot{u} - \psi v) = \left(F_{xfi} + F_{xfo}\right)\cos\delta + F_{xri} + F_{xro} - \left(F_{yfi} + F_{yfo}\right)\sin\delta \quad (1)$$

$$m(\dot{v} + \psi u) = \left(F_{yfi} + F_{yfo}\right)\cos\delta + F_{yri} + F_{yro} + \left(F_{xfi} + F_{xfo}\right)\sin\delta \quad (2)$$

$$I\dot{\psi} = a\Big(\left(F_{yfi} + F_{yfo}\right)\cos\delta + \left(F_{xfi} + F_{xfo}\right)\sin\delta\Big) - b\left(F_{yri} + F_{yro}\right) + \frac{c}{2}\Big(\left(F_{yfi} - F_{yfo}\right)\sin\delta + \left(F_{xfo} - F_{xfi}\right)\cos\delta + F_{xro} - F_{xri}\Big) \quad (3)$$

The terms F_x and F_y are the longitudinal and lateral forces with respect to the orientation of the respective tyre. The subscripts refer to the tyres with '*fi*' being the front inner tyre and '*ro*' being the rear outer for a positive steering angle.

With the suspension being omitted from the model, an alternate method is requiring to calculate the vehicle's normal forces. The static weight distribution of the vehicle was used, along with the longitudinal and lateral acceleration to calculate the tyre normal forces:

$$F_{zfi} = \frac{mb}{2(a+b)}g - \frac{mh}{2(a+b)}a_x - \frac{mh}{2c}a_y$$

$$F_{zfo} = \frac{mb}{2(a+b)}g - \frac{mh}{2(a+b)}a_x + \frac{mh}{2c}a_y \quad (4)$$

$$F_{zri} = \frac{ma}{2(a+b)}g + \frac{mh}{2(a+b)}a_x - \frac{mh}{2c}a_y$$

$$F_{zro} = \frac{ma}{2(a+b)}g + \frac{mh}{2(a+b)}a_x + \frac{mh}{2c}a_y$$

For the tyre forces, the longitudinal and lateral velocities at each wheel centre are required to calculate the slip terms. They are obtained by transforming the yaw rate, longitudinal and lateral velocities of the vehicle to the longitudinal and lateral axes of the wheel. For the longitudinal wheel velocities:

$$u_{fi} = (v + a\psi)\sin\delta + \left(u - \frac{t}{2}\psi\right)\cos\delta$$

$$u_{fo} = (v + a\psi)\sin\delta + \left(u + \frac{t}{2}\psi\right)\cos\delta \quad (5)$$

$$u_{ri} = u - \frac{t}{2}\psi, \qquad u_{ro} = u + \frac{t}{2}\psi$$

and for the lateral velocities:

$$v_{fi} = (v + a\psi)\cos\delta - \left(u - \frac{t}{2}\psi\right)\sin\delta$$

$$v_{fo} = (v + a\psi)\cos\delta - \left(u + \frac{t}{2}\psi\right)\sin\delta \quad (6)$$

$$v_{ri} = v - b\psi, \qquad v_{ro} = v - b\psi$$

The acceleration of a driven wheel is given by:

$$I_w\dot{\omega} = T - R_w F_x \quad (7)$$

R_w is the effective tyre radius, assumed constant and I_w is the inertia of the wheel and tyre about its axis of rotation.

2.1 *Tyre model*

The Dugoff Tyre model is used to calculate the longitudinal and lateral tyre forces (Rajamani 2012). The Dugoff model depends on the wheel slip for calculating the longitudinal and lateral tyre forces.

The wheel slip angle is given by:

$$\tan\alpha_{fi} = \frac{v_{fi}}{u_{fi}} \quad (8)$$

with the longitudinal tyre slip:

$$\kappa_{fi} = \frac{R_w\omega_{fi} - u_{fi}}{R_w\omega_{fi}} \quad (9)$$

and the tyre forces defined as:

$$f_y = -\frac{C_y\tan\alpha}{1+\kappa}f(\lambda), \qquad f_x = \frac{C_x\kappa}{1+\kappa}f(\lambda) \quad (10)$$

where C_y and C_x are the lateral and longitudinal tyre stiffness values respectively. λ is given by:

$$\lambda = \frac{\mu F_z(1+\kappa)}{2\sqrt{(C_x\kappa)^2 + \left(C_y\tan\alpha\right)^2}} \quad (11)$$

and

$$f(\lambda) = \begin{cases}(2-\lambda)\lambda, & \lambda < 1\\ 1, & \lambda \geq 1\end{cases} \quad (12)$$

μ is the coefficient of friction between the tyre and the road surface, a dynamic value which depends on the sliding velocity, V_s, of the contact patch (Dugoff et al. 1969):

$$\mu = \mu_0(1 - AV_s), \qquad V_s = |u|\sqrt{\kappa^2 + \tan^2\alpha} \quad (13)$$

where μ_0 is the static coefficient of friction and A is a shape factor.

2.2 *Driveline model*

The torque distribution assumes that the torque split between the inside and outside of the vehicle is the same for the front and rear axles. The torque supplied to each individual wheel is given by:

$$\begin{aligned} T_{fi} &= T_T r_{FR} r_{IO} \\ T_{fo} &= T_T r_{FR}(1 - r_{IO}) \\ T_{ri} &= T_T(1 - r_{FR}) r_{IO} \\ T_{ro} &= T_T(1 - r_{FR})(1 - r_{IO}) \end{aligned} \tag{14}$$

r_{FR} and r_{IO} are the front/rear and inner/outer torque distributions respectively. Both are dimensionless values between zero and one.

T_T is given by:

$$T_T = \begin{cases} T_{max} \dfrac{\sqrt{(\mu g)^2 - {a_y}^2}}{\mu g}, & a_y < \mu g \\ 0, & a_y \geq \mu g \end{cases} \tag{15}$$

so that T_T takes a value equal to the maximum torque provided by the powertrain when the vehicle is travelling in the forward direction and a value of zero when the vehicle is cornering at the limit of grip.

3 CONTROLLER DESIGN

A two degree of freedom model is proposed, using an extended bicycle model. The longitudinal tyre force is considered to be directly proportional to the drive torque of the wheel. This allows the drive torque and control inputs, r_{FR} and r_{IO}, which control the front/rear and inner/outer torque distributions, respectively, to be represented in state-space form.

The controller assumes a constant forward velocity and that the lateral tyre force is linearly dependant on the tyre slip and the lateral tyre stiffness. The error term is then calculated by comparing this prediction against a neutral steering vehicle.

The control limits are set at different levels for r_{FR} and r_{IO} to show the flexibility of the controller.

3.1 *Reduced vehicle model*

The lateral acceleration and yaw rate of the reduced vehicle model is given by:

$$\dot{v} = -\frac{C_f + C_r}{mu} v - \left(\frac{aC_f - bC_r}{mu} + u\right)\psi + \frac{C_f}{m}\delta + \frac{F_{xf}}{m}\delta \tag{16}$$

$$\dot{\psi} = -\frac{aC_f - bC_r}{Iu} v - \frac{a^2 C_f + b^2 C_r}{Iu}\psi + \frac{aC_f}{I}\delta - \frac{c}{2I}(\Delta F_{xf} + \Delta F_{xr}) \tag{17}$$

ΔF_{xf} and ΔF_{xr} are the differences in longitudinal force between the inner and outer wheel on the front and rear axles respectively. Assuming low slip angles, the difference is given by:

$$\Delta F_{xf} = \frac{T_{fi} - T_{fo}}{R_w}, \quad \Delta F_{xr} = \frac{T_{ri} - T_{ro}}{R_w} \tag{18}$$

By extending this logic, the total longitudinal force generated by the rear wheels is:

$$F_{xf} = \frac{T_{fi} + T_{fo}}{R_w} \tag{19}$$

Written in state-space form this becomes:

$$\dot{\mathbf{x}} = \mathbf{A}\mathbf{x} + \mathbf{B}\mathbf{u} + \mathbf{v} \tag{20}$$

where $\mathbf{x} = (u\psi)^T$ is the state vector and $\mathrm{u} = (r_{FR} r_{IO})^T$ is the control vector, **A**, **B** and **v** are given by:

$$\mathbf{A}_c = \begin{bmatrix} -\dfrac{C_{yf} + C_{yr}}{mu} & -\dfrac{aC_{yf} - bC_{yr}}{mu} - u \\ -\dfrac{aC_{yf} - bC_{yr}}{Iu} & -\dfrac{a^2 C_{yf} + b^2 C_{yr}}{Iu} \end{bmatrix} \tag{21}$$

$$\mathbf{B}_c = \begin{bmatrix} \dfrac{T_T \delta}{R_w m} & 0 \\ \dfrac{aT_T \delta}{R_w I} & -\dfrac{cT_T}{R_w I} \end{bmatrix}, \quad \mathbf{v} = \begin{bmatrix} \dfrac{C_f \delta}{m} \\ \dfrac{cT_T}{2R_w I} \end{bmatrix} \tag{22}$$

3.2 *MPC algorithm formulation*

In order to minimise the complexity of the model and therefore reduce the computation time of the control output only the present control action is calculated. This section is based on the work described in (Rusico 2013), adapted to suit the torque vectoring application.

A and **B** are approximated to discrete time zero-order hold form by:

$$\mathbf{A} = \mathbf{I} + T_s \mathbf{A}_c, \qquad \mathbf{B} = T_s \mathbf{B}_c \tag{23}$$

A discrete-time, state space model for the controller is then:

$$\Delta\mathbf{x}_{k+1} = \mathbf{A}\Delta\mathbf{x}_k + \mathbf{B}\Delta\mathbf{u}_k \tag{24}$$

$$\mathbf{y}_k = \mathbf{y}_{k-1} + \mathbf{C}\Delta\mathbf{x}_k \tag{25}$$

with $\Delta\mathbf{x}_k = \mathbf{x}_k - \mathbf{x}_{k-1}$, $\Delta\mathbf{u}_k = \mathbf{u}_k - \mathbf{u}_{k-1}$ and $\mathbf{y}_1 = \mathbf{CA}\Delta\mathbf{x}_1 + \mathbf{CB}\Delta\mathbf{u}_1 + \mathbf{Cv}$. This state space model, can be used to define the following Prediction Model (PM):

$$\mathbf{y}_{k+1|N_p} = \mathbf{p}_{N_p} + \mathbf{F}\Delta\mathbf{u}_k \tag{26}$$

where

$$\mathbf{p}_{N_p} = \mathbf{O}_{N_p}\mathbf{A}\Delta\mathbf{x}_k, \qquad \mathbf{F} = \mathbf{O}_{N_p}\mathbf{B} \tag{27}$$

The subscript '$k+1|N_p$' denotes that the PM predicts the future states of the vehicle from time-step $k+1$ to the preview horizon, $k+N_p$.

$\mathbf{O}_{Np} \in \mathbb{R}^{2Np\times 2}$ is the extended observability matrix of the pair ($\mathbf{C}$, $\mathbf{A}$):

$$\mathbf{O}_{N_p} = [\mathbf{C} \quad \mathbf{CA} \quad \cdots \quad \mathbf{CA}^{N_p-1}]^T \tag{28}$$

which leads to a control objective as a function of the control increment only:

$$J_k = \frac{1}{2}\,\Delta\mathbf{u}_k{}^T\mathbf{H}\Delta\mathbf{u}_k + \mathbf{f}_k{}^T\Delta\mathbf{u}_k \tag{29}$$

with

$$\mathbf{H} = \mathbf{F}^T\mathbf{Q}\mathbf{F} + \mathbf{P}_1 \tag{30}$$

$$\mathbf{f_k} = \mathbf{F}^T\mathbf{Q}\left(\mathbf{p}_{N_p} - \mathbf{r}_{k+1|N_p}\right) \tag{31}$$

where $\mathbf{r}_{k+1|Np}$ is the reference trajectory for the controller and $\mathbf{P}_1 \in \mathrm{R}^{2\times 2}$ and $\mathbf{Q} \in \mathrm{R}^{2Np\times 2Np}$ are weighting matrices of appropriate dimensions for the controller states:

$$\mathbf{f_k} = \mathbf{F}^T\mathbf{Q}\left(\mathbf{p}_{N_p} - \mathbf{r}_{k+1|N_p}\right) \tag{32}$$

$$\mathbf{Q} = \begin{bmatrix} \boldsymbol{Q_1} & & \\ & \ddots & \\ & & \boldsymbol{Q_1} \end{bmatrix} \tag{33}$$

The reference trajectory of the controller is the steady-state cornering behaviour of the vehicle and is assumed constant throughout the prediction mode. Due to the linear assumptions made in the controller design, only the longitudinal velocity is used in the calculation of the reference yaw rate, rather than the resultant of the lateral and longitudinal velocities. The reference trajectories up to the preview horizon is given by:

$$\mathbf{r}_{k+1|N_p} = \begin{bmatrix} \mathbf{r} \\ \vdots \\ \mathbf{r} \end{bmatrix} \tag{34}$$

where

$$\mathbf{r} = \begin{bmatrix} \dfrac{u\delta}{a+b} \\ 0 \end{bmatrix} \tag{35}$$

The constraints on the controller output and slew rate can be written as a linear inequality:

$$\boldsymbol{\mathcal{A}} = \begin{bmatrix} \boldsymbol{I}_{r\times r} \\ -\boldsymbol{I}_{r\times r} \\ \boldsymbol{I}_{r\times r} \\ -\boldsymbol{I}_{r\times r} \end{bmatrix}, \qquad \mathbf{b}_k = \begin{bmatrix} \Delta\mathbf{u}_{max} \\ -\Delta\mathbf{u}_{min} \\ \mathbf{u}_{\max} - \mathbf{u}_{k-1} \\ -\mathbf{u}_{min} + \boldsymbol{u}_{k-1} \end{bmatrix} \tag{36}$$

The optimal torque distribution increment is then the solution of the following Quadratic Programming (QP) problem:

$$\Delta\mathbf{u}_k{}^* = \arg\min_{\boldsymbol{\mathcal{A}}\Delta\mathbf{u_k}\le\boldsymbol{b_k}} J_k \tag{37}$$

The control action is then:

$$\mathbf{u}_k = \mathbf{u}_{k-1} + \Delta\mathbf{u}_k{}^* \tag{38}$$

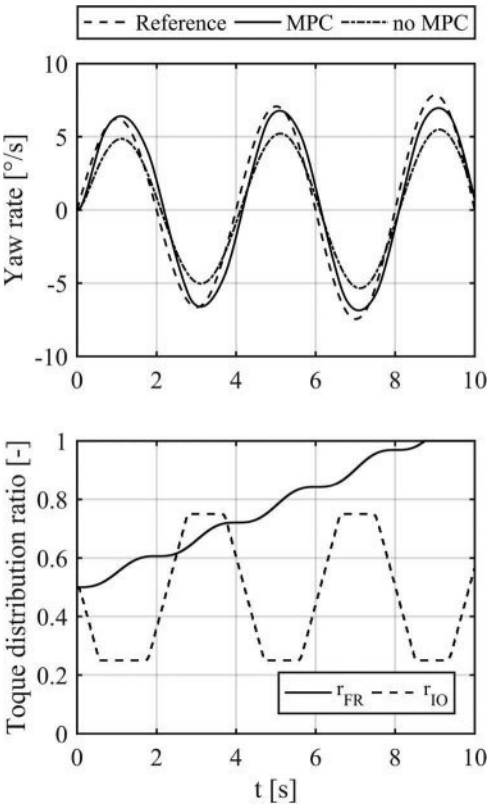


Figure 2. (a) Comparison of yaw rate for the controlled and passive vehicle with an initial speed of 15 m/s, a maximum steering angle of 1° and a steering frequency of 0.25 Hz. (b) The torque distribution ratios of the controlled vehicle.

4 RESULTS

The performance of the model predictive controller is analysed in simulation using the 7DOF model with a sinusoidal steering input. The controlled vehicle is presented alongside a passive vehicle with constant torque distribution ($r_{FR} = r_{IO} = 0.5$). The limits placed upon the torque distribution ratios allow up to 75% of the total driveline torque to be sent to an individual wheel, with the remaining 25% then being directed to the other wheel on the same axle.

Figure 2a shows the yaw rate of both vehicles during a slalom manoeuvre with a 1° steering angle applied to the front wheels. The controlled vehicle's yaw rate rises quickly to track the reference yaw rate. The controller overshoots the reference yaw rate early in the simulation (t = 1 s, t = 3 s).

As the longitudinal velocity of the vehicle increases, the controller can no longer provide the required yaw moment to match the reference values; however, it still tracks the reference yaw rate much more closely than the passive vehicle.

Figure 2b shows the torque distribution values for the controlled vehicle during the 1° slalom manoeuvre;

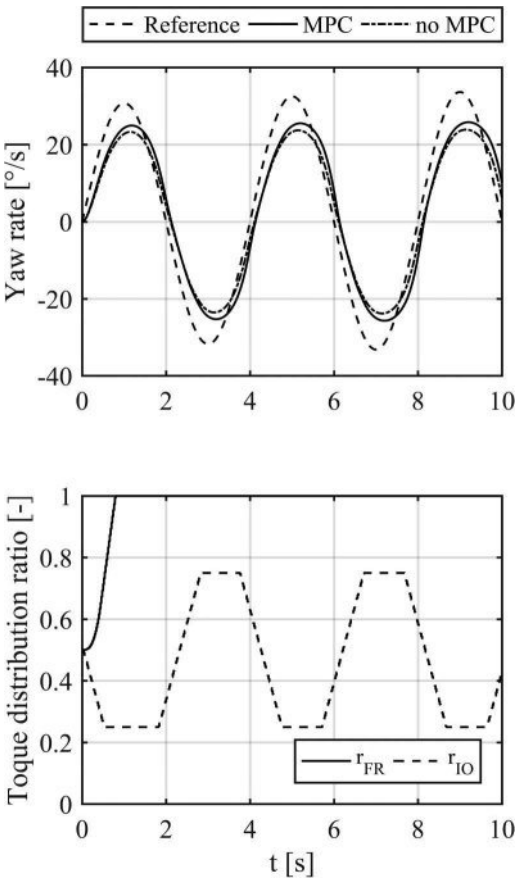


Figure 3. (a) Comparison of yaw rate for the controlled and passive vehicle with an initial speed of 15 m/s, a maximum steering angle of 5° and a steering frequency of 0.25 Hz. (b) The torque distribution ratios of the controlled vehicle.

Table 1. Vehicle parameters used for numerical simulation.

vehicle mass	m	1500 kg
vehicle yaw moment of inertia	I	2000 kg m^2
wheel moment of inertia	I_w	1 kg m^2
distance from CoM to front axle	a	1.1 m
distance from CoM to rear axle	b	1.4 m
distance from road plane to CoM	h	0.5 m
vehicle track	h	1.5 m
wheel radius	R_w	0.25 m
longitudinal rear tyre stiffness	C_{xf}	54 kN
longitudinal front tyre stiffness	C_{xr}	57 kN
lateral rear tyre stiffness	C_{yf}	36 kN/rad
lateral front tyre stiffness	C_{yr}	38 kN/rad
static coefficient of friction	μ_0	0.95
shape factor	A	0.03
maximum torque provided to wheel	T_{max}	300 Nm

Table 2. Controller parameters.

controller time step	T_s	0.02 s
preview horizon	N_p	10
state weighting matrix	$\mathbf{Q}_1$	$\begin{bmatrix} 250 & 0 \\ 0 & 500 \end{bmatrix}$
control weighting matrix	$\mathbf{P}_1$	$\begin{bmatrix} 25 & 0 \\ 0 & 50 \end{bmatrix}$
maximum slew-rate vector	$\Delta\mathbf{u}_{max}$	$\begin{bmatrix} 0.02 \\ 0.01 \end{bmatrix}$
minimum slew-rate vector	$\Delta\mathbf{u}_{min}$	$\begin{bmatrix} -0.02 \\ -0.01 \end{bmatrix}$
maximum control vector	$\mathbf{u}_{max}$	$\begin{bmatrix} 1 \\ 0.75 \end{bmatrix}$
minimum control vector	$\mathbf{u}_{min}$	$\begin{bmatrix} 0 \\ 0.25 \end{bmatrix}$

the torque distribution between the inside and outside of the vehicle moves its upper and lower limit.

The front-rear torque distribution, r_{FR} increases over time, meaning that more of the drive torque transfers to the front two wheels. Throughout the slalom manoeuvre, as the reference and controlled vehicle yaw rates coincide, r_{FR} levels off and stops increasing. As the steering angle begins to increase again in the opposite direction and the magnitude of the reference yaw rate increases, r_{FR} begins to increase once again to try to match the yaw rate.

The simulation was then repeated with the amplitude of the steering input increased to 5°. The controlled vehicle can no longer track match the maximum reference yaw rate (Fig. 3a), even during the early stages of the manoeuvre as it no longer has the yaw authority required; it still has improved cornering performance over the passive vehicle.

Figure 3b shows the corresponding torque distribution ratios during the 5° slalom. The inner-outer torque distribution behaves similarly to the previous manoeuvre, but the front-rear distribution now behaves differently; r_{FR} rapidly rises to its maximum value of one after approximately 1s into the slalom manoeuvre. After reaching this maximum value, it remains saturated to maximise the yaw rate.

5 CONCLUSION

In this paper, the effect of a simple Model Predictive controller on a vehicle during a slalom manoeuvre has been presented. The model is able to manipulate the torque distribution between the front and rear axles along with the inside-outside balance of the four-wheel drive vehicle to minimise the error term, with constraints on both the limits and slew-rate of the control. Only the present control action is calculated to minimise the computational complexity of the model.

While this control has a beneficial effect on the yaw rate of the vehicle, the distribution of drive-torque alone will not be sufficient to create the necessary yaw moment to remove yaw rate error.

Despite the fact that the control model is a simple 2DOF model that assumes constant driver inputs,

the controller demonstrates that low complexity MPC controllers could be used to improve the handling behaviour of four-wheel drive vehicles.

The controller is stable even without the use of a stabilising terminal state weighting matrix.

REFERENCES

Ang, K. H., Chong, G. & Li, Y. 2005. PID Control System Analysis, Design and Technology. *IEEE Transactions on Control Systems Technology* 13(4): 559–576.

Camacho, E. F. & Bordons, C. 1999. *Model Predictive Control.* London: Springer-Verlag.

Dugoff, H., Fancher, P.S. & Leonard, S. 1969. *Tire Performance Characteristics Affecting Vehicle Response to Steering and Braking Control Inputs.*

Ghike, C., Shim, T & Asgari, J. 2009. Integrated Control of Wheel Drive-Brake Torque for Vehicle-Handling Enhancement. *Proc. IMechE Part D: J Automobile Engineering* 223(4): 439–457.

Osborn, R. P. & Shim, T. 2006. Independent control of all-wheel drive torque distribution. *Vehicle System Dynamics* 44(7): 529–546.

Rajamani, R. 2012. *Vehicle Dynamics and control*. 2nd ed. New York: Springer.

Rusico, D.D. 2013. Model Predictive Control with Integral Action: A simple MPC algorithm. *Modeling, Identification and Control* 34(3): 119–129.

Yu, F., Li, D.-F. & Crolla, D.A. 2008. Integrated Vehicle Dynamics Control – State-of the Art Review. In, *IEEE Vehicle Power and Propulsion Conference, Harbin, 3–5 October 2008*.

Torque vectoring

Advanced Vehicle Control – Edelmann, Plöchl & Pfeffer (Eds)
© 2017 Taylor & Francis Group, London, ISBN 978-1-138-02992-7

Evaluation of optimal yaw rate reference for electric vehicle torque vectoring

E.N. Smith, E. Velenis & D. Cao
Advanced Vehicle Engineering Centre, Cranfield University, Bedford, UK

D. Tavernini
Centre for Automotive Engineering, University of Surrey, Guildford, UK

ABSTRACT: This work evaluates the intrinsic contribution of the yaw rate reference to the overall handling performance of an electric vehicle with torque vectoring in terms of minimum-time manoeuvring. A 'Time-Optimal' Yaw rate reference (TOY) derived from optimal control problems was generated which coincides exactly with the analytical steady-state single-track expression for yaw rate gain. Alternative yaw rate references are compared with TOY through closed-loop optimal control simulations. Results show that when yaw rate reference, parameterised by understeer gradient, is set away from the 'time-optimal' value, performance is degraded at a rate of 0.65 s/deg/g.

1 INTRODUCTION

Active yaw control systems for improved performance and safety have been commonplace on passenger vehicles for the past two decades. Modern all-wheel-drive electrified vehicles (EVs) offer substantial opportunities for active control of yaw dynamics by over-actuation, namely torque vectoring (TV); the distribution of wheel torques between multiple wheels. TV extends the maximum cornering force by superior distribution of yaw moment, making better use of friction availability [1].

With reference to Figure 1, TV systems typically follow a yaw rate reference, achieved by tuning of a Controller and a subsequent Control Allocation (CA) for torque arbitration between individual wheels. Advanced techniques using mathematical analysis and simulation tools have been used to optimise both controller [2] and CA [3, 4] performance, yet very little rigorous work has been undertaken into research of the optimal yaw rate reference. The majority of yaw rate references have been derived from the steady-state single-track linear-tyre equations, modifying the handling for stability or agility by selecting an appropriate understeer gradient, K.

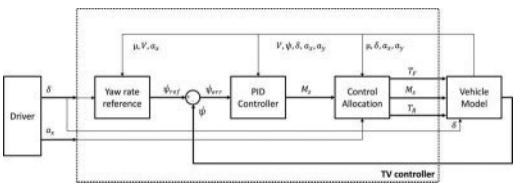


Figure 1. Torque vectoring controller schematic.

De Novellis et al. [3] chose a reference heuristically between achievable limits on the dynamic steer-lateral acceleration 'handling diagram', such that responsiveness is maximised in the linear region, the linear region is extended and lateral acceleration boundary maximised. Limits are calculated by steady-state analysis of a single-track model with nonlinear tyres, taking into account a direct yaw moment term. Wheals et al. [5] constructed a yaw rate map by interrogation of a high-fidelity model at steady-state considering equal wheel torques, and noted significant differences to the single-track model map attributed to roll and nonlinear tyres. This was not trialled within a controller; they went on to use a linearised two-track model considering nonlinear tyres and aerodynamic forces in which sideslip and velocity derivatives are decoupled and the reference set presuming zero sideslip and no longitudinal acceleration. No evaluation of the reference *per se* was made.

A first-order delay to account for the yaw inertia of the vehicle has been incorporated by [5, 6], however Bünte et al. [7] proposed a yaw rate reference considering fully-dynamic elements, combining steady-state and lateral dynamics transfer functions from the single-track model, tuned heuristically to modify the transient response.

The aim of this research is to evaluate the contribution of the yaw rate reference to overall vehicle performance within a closed-loop TV control system. This work presents 'TOY', a mathematically 'Time-Optimal' Yaw rate reference for an electric sportscar with 4-wheel torque vectoring capability.

The performance of TOY over a U-turn manoeuvre is then compared against two *K*-parameterised references.

2 VEHICLE SYSTEM MODELLING

This study uses a three degree of freedom single-track model with linear tyres (equations (1–3)), parameterised to represent a high-performance EV with an electric motor powering each wheel independently. To emulate left-right torque vectoring, a direct yaw moment, M_z, is included in the yaw acceleration equation (3). Lateral load transfer is neglected, along with roll and pitch dynamics.

$$m\dot{V}_x = m\left(a_x + V_y\dot{\psi}\right) \tag{1}$$

$$m\dot{V}_y = -\frac{C_f C_r}{V_x}V_y + \left(-mV_x + \frac{(-l_f C_f + l_r C_r)}{V_x}\right)\dot{\psi} + C_f\delta \tag{2}$$

$$I_z\ddot{\psi} = -\frac{(l_f C_f + l_r C_r)}{V_x}V_y - \frac{(l_f^2 C_f + l_r^2 C_r)}{V_x}\dot{\psi} + l_f C_f\delta + M_z \tag{3}$$

where a_x is the longitudinal acceleration, considered as an input to the system, m is the vehicle mass; $\dot{\psi}$ is the yaw rate; I_z is the yaw moment of inertia about the vertical axis; l_f and l_r are the distances of the front and rear axles to the centre of gravity (CG); C_f and C_r and the front and rear tyre cornering stiffnesses; V_x and V_y are the longitudinal and lateral vehicle velocities respectively. Retarding torque is provided exclusively by regenerative braking.

A linear tyre model with cornering stiffness dependent on normal load is used, considering a quasi-steady-state approximation to normal load.

$$F_{yj} = -C_j\alpha = -\eta_j F_{zj}\alpha_j \tag{4}$$

where $$C_j = \eta_j F_{zj} \tag{5}$$

$$F_{zf} = \frac{mg\ell_r}{L} - \frac{h}{L}ma_x, \quad F_{zr} = \frac{mg\ell_f}{L} + \frac{h}{L}ma_x \tag{6}$$

where for each $j \in [f, r]$, η_j is the tyre cornering coefficient, α_j is the tyre slip angle, F_{zj} is the axle normal load and F_{yj} is the axle lateral force on front and rear. g is the gravitational acceleration constant, L is the wheelbase, h is the height of the CG. The natural (uncontrolled), steady-state understeer gradient of the vehicle is defined as [8]:

$$K_{nat}^{SS} = \left(\frac{1}{\eta_f} - \frac{1}{\eta_r}\right)/g, \tag{7}$$

and modified by selecting cornering coefficient values η_f and η_r, assuming that the cornering coefficient is constant. A 50:50 static distribution is used for the vehicle without TV control. For TV, front-rear torque vectoring is modelled by distributing torques front-rear by a CA that allocates longitudinal forces in proportion to the normal load on the axle (8), found to be the optimal distribution [4]:

$$F_{xj} = ma_x\frac{F_{zj}}{F_{zf} + F_{zr}}. \tag{8}$$

Neglecting wheel spin axis rotational inertia, wheel torques become

$$T_{xj} = F_{xj}R_w, \tag{9}$$

where R_w is the rolling radius of the tyres. Longitudinal and lateral forces are coupled and saturated at the limit by friction circle constraints (10):

$$\left(\frac{F_{xj}}{F_j}\right)^2 + \left(\frac{F_{yj}}{F_j}\right)^2 \leq \bar{\mu}_{max}^2, \tag{10}$$

where $$F_j = \bar{\mu}F_{zj}, \tag{11}$$

with $\bar{\mu}$ is tyre-road friction coefficient.

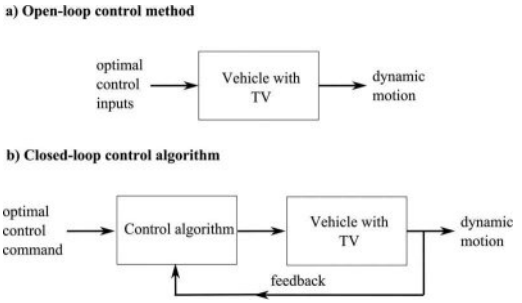


Figure 2. *Open-loop control method* and *closed-loop control algorithm* after [9].

3 OPTIMAL CONTROL FORMULATIONS

To determine the 'time-optimal' yaw rate reference and hence evaluate it within a TV control system, two different optimal control problem (OCP) formulations are required, as shown in Figure 2. Figure 2a shows the *open-loop control method* (after [9]), which permits the maximum performance potential of TV to be determined, considering optimal control inputs from a 'perfect' driver, including M_z, applied to the vehicle directly and is used to generate the 'Time-optimal' yaw rate reference in section 4. In reality optimal open-loop control defined in this way is unrealisable in the real world. Figure 1 shows a TV control system that determines torques that must be applied at each wheel, via a controller, from a desired yaw rate reference. As shown in figure 2b, this is defined as a *closed-loop control algorithm*. This *closed-loop control algorithm*

is incorporated into an OCP in section 5 to evaluate the relative performance of different yaw rate references. The optimal control problems may be mathematically formulated as follows. Consider a dynamic system in the form:

$$\dot{\mathbf{x}} = \mathbf{f}[\mathbf{x}(t), \mathbf{u}(t)]; \tag{12}$$

subject to initial and final conditions:

$$\mathbf{x}(t_0) = \mathbf{x}_0, \qquad \mathbf{x}(t_f) = \mathbf{x}_f. \tag{13}$$

An OCP seeks to find the control vector sequence $\mathbf{u}$ to minimise a certain cost function, subject to equality and inequality constraints:

$$J = \phi[\mathbf{x}(t_f)] + \int_{t_0}^{t_f} L[\mathbf{x}(t), \mathbf{u}(t)], \tag{14}$$

$$\mathbf{p}[\mathbf{x}(t), \mathbf{u}(t)] = 0, \qquad \mathbf{g}[\mathbf{x}(t), \mathbf{u}(t)] \leq 0. \tag{15}$$

Road boundary constraints are simplified by a change of coordinate reference frame from vehicle-centred to road-centred 'curvilinear' coordinates:

$$w_{R,l} \leq s_n \leq w_{R,r}, \tag{16}$$

where $w_{R,l}$ and $w_{R,r}$ denote the left and right road widths. By changing the independent variable from time to distance travelled along the road centreline, s, vehicle dynamics may be expressed in terms of lateral position, s_n, and the angle of the vehicle, χ, relative to the road centreline. Dynamic system equations (12)–(15) are transformed from a time-base to s as follows:

$$\frac{dx}{ds} = x' = \frac{dx}{dt}\frac{dt}{ds} = \dot{x}\dot{s}^{-1}, \tag{17}$$

where x is any state variable. Other constraints include steering control bandwidth (limited to 1 Hz), imposition of a maximum steer angle and motor power/torques constrained according to a power curve:

$$|\delta| \leq \delta_{max}, \qquad |\dot{\delta}| \leq \dot{\delta}_{max}, \tag{18}$$

$$F_{xj}V_x \leq P_{max,j}, \tag{19}$$

where $P_{max,j}$ is the maximum power of the motors. To seek to minimise time of travel, the cost function becomes:

$$J(t) = \int_{t_0}^{t_f} dt \qquad \mapsto \qquad J(s) = \int_{s_0}^{s_f} \frac{1}{\dot{s}}\, ds. \tag{20}$$

The state and control vectors are

$$\mathbf{x} = \{V_x, V_y, \dot{\psi}, x_R, y_R, \theta_R, s_n, \chi, \delta, t\}^T, \tag{21}$$

$$\mathbf{u} = \{a_x, \dot{\delta}\}^T, \tag{22}$$

where x_R, y_R & θ_R are position and heading of the road centreline respectively, t is elapsed time. For the *Open-loop control method* (TV active), the control vector includes yaw moment: $\mathbf{u} = \{a_x, M_z, \dot{\delta}\}^T$. *GPOPS-II* [10], was used to transcribe the continuous-time OCP into a discrete nonlinear programming problem (NLP), and solved using sequential quadratic programming.

4 OPEN-LOOP CONTROL

This section will determine the *open-loop control method* performance used to identify the 'time-optimal' yaw rate reference that the closed-loop TV controller should follow. A left-hand U-Turn manoeuvre consisting of two 30 m straights joined by a bend of tightening radius of curvature, up to an apex radius of 35 m is used. Straight-line running conditions were enforced at the start of the maneouvre. Figure 3 overlays states, controls and calculated quantities for the vehicle with TV active (*TV*) and TV inactive (*Unctrl*).

Manoeuvre time is 0.374 s faster with *TV* than *Unctrl*. This is a significant time improvement for just one corner, and shows the performance of the 4-motor topology. With reference to figures 3a & 3g, it is clear that *TV* is able to sustain a greater level of drive/brake torque and hence can both start and exit the manoeuvre at higher speeds. *Unctrl* is able to maintain higher speed over $s \in [90, 120]$ and thus gains time back during this portion of the manoeuvre. It exhibits steady-state behaviour here; maintaining constant yaw rate, sideslip and vehicle speed. *TV* is able to accelerate and brake much more aggressively than *Unctrl*, which is forced to coast during the constant radius section.

A dynamic scenario is considered, yet the steady-state (instantaneous) understeer gradient is still useful in giving an indication of vehicle handling behaviour, defined as follows:

$$K_{inst}^{SS} = \frac{\frac{V\delta}{\dot{\psi}} - L}{V^2}. \tag{23}$$

K_{inst}^{SS} is plotted in figure 3e: the key finding is that *TV* is able to achieve the natural steady-state understeer gradient, K_{nat}^{SS}, throughout the manoeuvre whereas *Unctrl* handling exhibits oversteer relative to K_{nat}^{SS} under braking and understeer relative to K_{nat}^{SS} during acceleration, an effect well-known due to longitudinal load transfer effects.

Friction utilisation is defined as the axle lateral/longitudinal or total force divided by the axle normal load and plotted in figures 3d (front) & 3i (rear). Examination of slip angles in figure 3j is another useful tool for understanding the dynamic handling balance. It is useful also to consider how understeer gradient is related to slip angles [8]:

$$K_{inst}^{SS} = (\alpha_f - \alpha_r)/a_y. \tag{24}$$

Referring to figures 3i & 3j, under braking, *Unctrl* has a reduced rear lateral friction capability due to longitudinal load transfer. Hence α_r is increased and α_f reduced, resulting in a oversteer balance relative to K_{nat}^{SS} (0.5deg/g). The opposite is true during acceleration. *TV* yaw moment, M_z, shown in figure 3h, is stabilising under braking and destabilising during acceleration in order to counteract load transfer effects and achieve a constant K_{inst}^{SS} equal to K_{nat}^{SS}. Figure 4 shows how yaw moment affects lateral force and slip angle for the left turn. Under braking (fig. 4a), stabilising M_z is applied clockwise, such that larger lateral

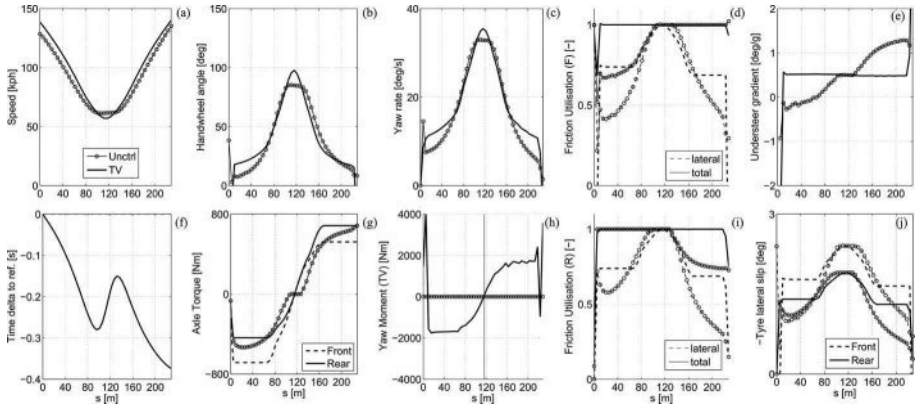


Figure 3. Comparison of *Open-loop control method*: TV inactive (*Unctrl*) (o) against TV active (*TV*) (no marker).

force from the front tyres can be applied in the direction of the turn to maintain yaw dynamic equilibrium. As a result, figures 3j,d,i & e respectively show larger front slip angles are developed, tyre friction availability maximised, and K_{inst}^{SS} exhibits a greater degree of understeer with respect to *Unctrl*. Figure 4b shows the acceleration case. Figure 3j shows that *Unctrl* develops larger slip angles at the front than rear due to load transfer (understeer relative to K_{nat}^{SS}). *TV*, however, is able to develop greater slip angle at the rear than *Unctrl* to balance the destabilising yaw moment and hence make full use of the friction available, counteracting the tendency to understeer. Observation of figure 3h shows that magnitude of yaw moment is proportional to a_x. This trend of direct yaw control effecting a stabilising yaw moment under deceleration and a destabilising yaw moment under acceleration is confirmed by [4] for a similar topology and by [3] where a nonlinear yaw rate reference independent of a_x is used.

A 'time-optimal' yaw rate reference was derived from analysis of the OCPs described, repeated for U-turns with turn radius $R \in [10{:}10{:}80]$ m. Figure 5 shows yaw rate gain as a function of longitudinal acceleration and speed for *TV* and *Unctrl*. The grey surface are the results from optimisations and the mesh is the steady-state analytical definition [8]:

$$\frac{\dot{\psi}}{\delta} = \frac{V}{K_{nat}^{SS} V^2 + L}, \tag{25}$$

Figure 5b shows the *Unctrl* result. Under braking, yaw rate gain oversteers the natural characteristic (yaw rate gain tending to infinity at critical speed); under acceleration the yaw rate gain tends towards an understeer response. Where $a_x = 0\,\mathrm{m/s^2}$, the numerical fit from OCPs intersects the analytical solution. Figure 5b generalises the specific solution for *TV*: that for all dynamic manouevres in this range, *TV* is able to negate load transfer effects such that the yaw rate gain response is identical to the steady-state response. Therefore, the analytical definition is adopted as the benchmark 'Time-Optimal' Yaw rate reference (TOY) against which to compare other references.

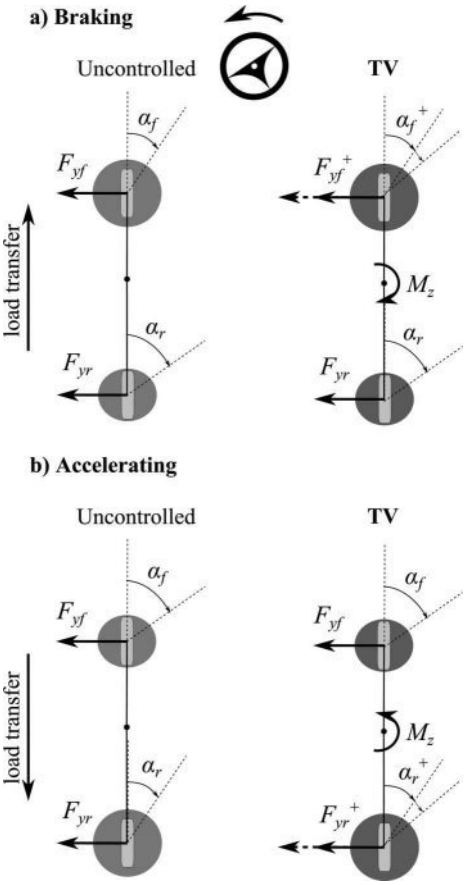


Figure 4. Analysis: TV yaw moment effect on lateral force potential and slip angles and therefore understeer gradient.

5 CLOSED-LOOP CONTROL

This section includes closed-loop control in the OCP to determine the relative performance of references: the major contribution of this work. Small modifications are made to the optimal control formulation used

to generate the TOY in section 4. The OCP is now used to find the optimal control history of a 'perfect' driver's steering and accelerator/brake inputs. Figure 1 shows this OCP formulation. It consists of a simplified TV controller (based on an experimentally-validated version [6]) which converts the driver inputs and vehicle states into a reference yaw rate. Yaw moment demand, M_z is output by a PID controller with yaw rate error input. Recall (8) for the CA.

The ability of this *closed-loop control algorithm* to convert the theoretical maximum performance into actuality may be determined. Three variations of the steady-state single-track yaw rate reference—where K_{nat}^{SS} is replaced by K_{tar} in (25)–are compared by setting the TOY reference $K_{tar} = K_{nat}^{SS} = 0.5$ deg/g and then $K_{tar} = K_{nat}^{SS} \pm 0.5$ deg/g, i.e. $K = K_{tar} \in [0{:}0.5{:}1.0]$ deg/g.

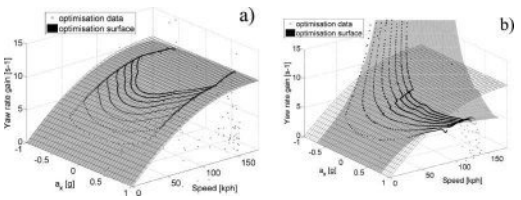


Figure 5. Yaw rate gain surfaces as a function of speed and longitudinal acceleration dynamic OCP results (grey surface) overlaid on steady-state analytic (mesh) for a) TV and b) uncontrolled.

Table 1. Effect of yaw rate target (TV), $K_{nat}^{SS} = 0.5$deg/g.

Simulation	K_{tar} (deg/g)	Time (s)	Δt (s)
OL Baseline	n/a	8.8269	−0.0176
CL $K_{nat}^{SS} + 0.5$	+1.0	9.1597	+0.3152
CL K_{nat}^{SS} (TOY)	+0.5	8.8445	+0.0000
CL $K_{nat}^{SS} - 0.5$	+0.0	9.1974	+0.3529

Referring to Table 1, the closed-loop (CL) controller including the TOY as reference is 0.0176 s slower than the open-loop (OL) baseline. Since the controller is well tuned for a realistic real-world implementation and the CA is a good compromise between optimality and simplicity for practical implementation, these elements are not modified and therefore all differences in performance between CL optimisations will be a result of the contribution of the yaw rate reference only. Inspection of the time deltas, Δt, reveals approximately equal time loss of ∼0.3 s for both comparison references, the mean rate of time loss is 0.67 s/deg/g as K_{tar} moves away from TOY (K_{nat}^{SS}), 7.5% of the TOY maneouvre time. This is a clear demonstration not only that the optimal yaw rate reference should follow the natural, uncontrolled, steady-state behaviour of the vehicle but that selection of a sub-optimal yaw rate reference has a highly negative effect on manoeuvre time and therefore the selection of the reference is crucial. Figure 6 overlays states, controls and calculated quantities for the CL results for each yaw rate reference. In figure 6h, TOY ($K_{tar} = 0.5$ deg/g) yaw moment transitions from stabilising under braking to destabilising under acceleration to overcome load transfer effects, as in section 4. Figure 6a shows that TOY achieves highest minimum speed by some margin, which corresponds, in figure 6f, with the greatest change in Δt during $s \in [90{,}140]$ m, at which point, in figure 6c, the difference in yaw rate is greatest. TOY achieves the highest yaw rate and correspondingly, the lowest manouevre time. Figures 6d, i & figure j plot front and rear friction utilisation and tyre lateral slip respectively. The comparion reference cannot match TOY due to a reduction in total friction utilisation at the unsaturated tyre. Taking the $K_{tar} = 0$ deg/g case as an exemplar, in figure 6d, front friction utilisation drops from 80% under maximum braking to a 60% minimum at the apex, at which point lateral friction utilisation increases. Total utilisation decreases since longitudinal acceleration reduces to zero. Overall friction utilisation cannot be increased, since front friction

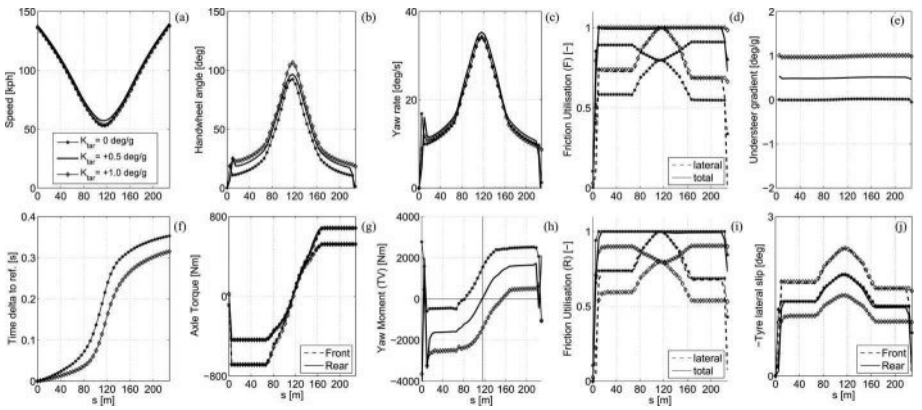


Figure 6. *Closed-loop control algorithm*: comparison of yaw rate reference. 0 deg/g (*), TOY 0.5 deg/g (no marker), 1 deg/g (◇).

utilisation cannot be increased. This would require an increase in front lateral force and therefore slip angle and hence alter the balance too far towards understeer, away from the target $K_{tar} = 0$ deg/g balance. The total friction capability and therefore performance, then, is limited by K_{tar}, which requires a certain difference between front and rear slip angles which in turn dictates the permissible lateral force at front or rear. Only by following TOY ($K_{tar} = 0.5$ deg/g) can friction be fully utilised and manoeuvre time minimised.

6 CONCLUSIONS

This work found that the 'Time-Optimal' Yaw rate reference (TOY) derived from optimal control for a sportscar with 4-wheel independent torque vectoring coincides exactly with the analytical steady-state single-track expression for yaw rate gain. The unique contribution of this research was the inclusion of a closed-loop controller within an optimal control problem; results found that setting yaw rate reference away from natural understeer gradient degrades performance at a rate of 0.65 s/deg/g, which equates to 7.3%/deg/g of the TOY manoeuvre time. TOY achieves the highest minimum speed of the references compared and the greatest yaw rate. TOY is able to use all the available friction at all times by optimising front and rear lateral forces. This study has contributed a rational, mathematical approach to determining optimal yaw rate references and a method by which to objectively compare yaw rate reference performance.

FUNDING

The lead author gratefully acknowledges the support of an ESPRC iCASE industrial studentship with Jaguar Land Rover.

REFERENCES

[1] Crolla DA, Cao D. The impact of hybrid and electric powertrains on vehicle dynamics, control systems and energy regeneration. VSD. 2012 Jan; 50(sup1): 95–109.
[2] Siampis E, Velenis E, Longo S. Rear wheel torque vectoring model predictive control with velocity regulation for electric vehicles. VSD. 2015; 53(11): 1555–1579.
[3] De Novellis L, Sorniotti A, Gruber P. Wheel torque distribution criteria for electric vehicles with torque-vectoring differentials. IEEE Transactions on Vehicular Technology. 2014; 63(4): 1593–1602.
[4] de Castro R, Tanelli M, Araujo RE, Savaresi SM. Minimum-time manoeuvring in electric vehicles with four wheel-individualmotors. VSD. 2014 Jun; 52(6): 824-846.
[5] Wheals JC, Baker H, Ramsey K, Turner W. Torque vectoring AWD driveline: Design, simulation, capabilities and control. 2004; SAE Technical Paper 2004-01-0863.
[6] Smith E, Tavernini D, Claret C, Velenis E, Cao D. Optimal yaw-rate target for electric vehicle torque vectoring system. In: IAVSD 2015, Graz. CRC Press; 2016. p. 107.
[7] Bünte T, Kaspar S, Hohmann S, Brembeck J. Inverse model based torque vectoring control for a rear wheel driven battery electric vehicle. In: IFAC World Congress; 2014.
[8] Wong JY. Theory of ground vehicles. John Wiley & Sons; 2001.
[9] Horiuchi S. Evaluation of chassis control algorithms using controllability region analysis. In: IAVSD 2015, Graz. CRC Press; 2016. p. 35.
[10] Patterson MA, Rao AV. Gpops-II: A matlab software for solving multiple-phase optimal control problems using hp–adaptive gaussian quadrature collocation methods and sparse nonlinear programming. ACM TOMS. 2013; 39(3): 1–41.

Advanced Vehicle Control – Edelmann, Plöchl & Pfeffer (Eds)
© 2017 Taylor & Francis Group, London, ISBN 978-1-138-02992-7

Inversion based feedforward design to improve the lateral dynamics of high performance sports cars

S. Rahimi Fetrati & C. Kandler
Dr. Ing. h. c. F. Porsche AG, Weissach, Germany

C. Kärcher
Karlsruhe Institute of Technology, Karlsruhe, Germany

D. Schramm
Chair of Mechatronics, University of Duisburg-Essen, Duisburg, Germany

ABSTRACT: This paper presents a control concept for an electromechanical Torque Vectoring system, installed at the driven rear axle of a vehicle. Asymmetric torque distribution enables active manipulation of the vehicles yaw dynamics. Appropriate controller design implements the desired agility without compromising the stability goals, which is of special interest for high performance vehicles. The controller structure consists of an inversion based feedforward. To this end, well known key variables, which define controllability and stability of the vehicle, are derived from a linear single track model. The calibration parameters are modified to deal with the reduced stability potential at high lateral acceleration domain during critical maneuvers. The verification of the proposed method is carried out using a high dimensional nonlinear simulation environment.

1 INTRODUCTION

The aim of a torque vectoring (TV)-system is to vary the distribution of wheel torque at the driven axle based on driving situation, to enhance the required driving performance and prevent loss of traction. Asymmetric distribution of torque between wheels generates a corrective yaw torque around the vertical axis, which can improve the handling response of the vehicle. The torque distribution should keep the tires in their optimal longitudinal slip. In this paper we propose a control concept, to use the benefits of TV particularly in the lateral domain. This controller considers the tire potential defined as lateral and longitudinal forces, which form kamms circle. During the design process of chassis control systems, great attention should be paid to performance and handling characteristics of the vehicle. According to Milliken (Milliken & Milliken 1995) acceleration limit in both longitudinal and lateral direction can be defined as a performance criteria. Moreover, he emphasizes that a vehicle should present a good degree of controllability and stability that allows a driver to exploit the performance potential of the vehicle. Isermann (Isermann 2006) describes performance as a measure of responsiveness of a vehicle to driver inputs and stability as a remain potential of longitudinal, lateral and vertical forces to their physical limits in a driving situation. The longitudinal performance is usually limited due to the engine power and tire maximal longitudinal forces. However, the lateral performance depends on the optimal and individual utilization of tire lateral forces.

In this paper we propose an inversion based feedforward for the TV-system to increase the lateral performance and handling behavior of the vehicle. In order to have a concept, which results into a reproducible and reliable vehicle behavior. A high dimensional nonlinear simulation model of a Porsche Macan has been used to validate the performance of our proposed concept. This paper is structured as follow. A brief description of the considered TV unit and fundamental equations of vehicle dynamics can be found in section 2. Section 3 introduces the design concept of an inversion based feedforward method including calibration parameters. After that the simulation validation is presented in 4. Finally, the main discussion points of this paper are summarized in section 5.

2 TORQUE VECTORING

This section introduces the principal of torque distribution by use of an electromechanical TV-system. Moreover, the necessary equations of a simplified vehicle model are derived.

2.1 *Electromechanical TV-system*

Electrification of drivetrain can be seen as an additional degree of freedom. In comparison to clutch-based systems, electric motors benefit from lower wear

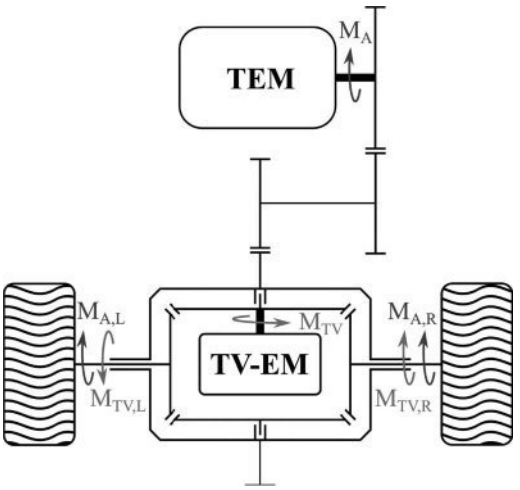


Figure 1. Schematic presentation of an electromechanical TV-system. TEM and EM, are respectively traction motor and electric motor.

along with higher energy efficiency. Moreover, the application of electrical drives offers a more precise torque distribution. An innovative possibility to benefit from the mentioned advantages is shown in Figure 1. As it can be seen an electric motor (EM) is integrated in the differential. Thus, it is possible to distribute the torque M_{TV} between wheels of an axle. As long as the EM is not actuated, the TV-system works as a conventional differential and the driving torque M_A is divided identically between the left and right wheels.

If the control motor generates torque then the superimposing stage between electric motor and the differential will be actuated, which results in differential wheel torque. The resultant wheel torque for the right wheel ($M_{w,R}$) and left wheel ($M_{w,L}$) can be calculated as $M_{w,R} = M_{A,R} + M_{TV,R}$ and $M_{w,L} = M_{A,L} - M_{TV,L}$. The torque wheel has a positive sign for a left curve. The wheel torque difference ΔM_w considering the wheel torque of each wheel is $\Delta M_w = M_{w,R} + M_{w,L}$. This asymmetric distribution of torque results into a yaw moment M_z around the vertical axis of the vehicle. The yaw moment can be calculated from the wheel difference torque and geometric transformation depending on the vehicle track width S and dynamic wheel radius r_{dyn} as

$$M_z = \frac{S}{2r_{dyn}} \Delta M_w \tag{1}$$

Figure 2 depicts a TV-system installed at the rear axle. It can be seen from Figure 2(a) that the vehicle equipped with TV is pushed into the curve and has to drive a tighter curve radius (trajectory curve in red). Moreover, as Figure 2(b) illustrates by use of vector superposition the resultant force F_{Res} does not change, which implies that the TV does not effect the longitudinal dynamics. More details about the mechanical design of TV can be found in (Rohe 2014) and (Hoehn, Stahl, Wirth, Lienkamp, Kurth, & Wiesbeck 2011).

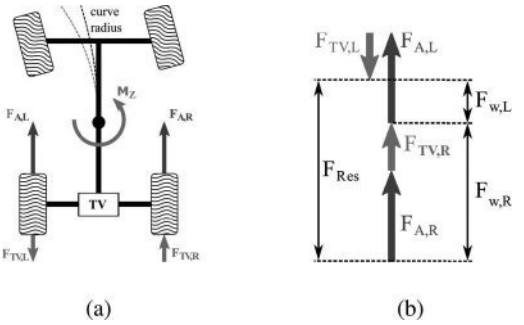


Figure 2. The resultant forces with TV.

2.2 *Dynamic modeling of the vehicle*

A two degree of freedom single track model (STM) as in Figure 3 is used to describe the lateral dynamics of the vehicle. Detailed information can be found in literature (Schramm, Hiller, & Bardini 2014). The vehicle's planar dynamics can be defined with respect to two translation (longitudinal v_x and lateral v_y – velocity) and one rotational motion (yaw motion $\dot{\psi}$)

$$a_y = \dot{v_y} + v_x \dot{\psi}. \tag{2}$$

As this paper is focused on lateral behavior of the vehicle, the equations describing longitudinal dynamics are neglected. Equations of motion based on Newton second law can be expressed as:

$$\dot{\beta} = \sum_{i_A} F_{y,i_A}/mv_x - \dot{\psi}, \qquad i_A = [F, R] \tag{3}$$

$$\ddot{\psi} = \sum M_z/J_z. \tag{4}$$

In (3) the vehicle slip angle is defined as β, ΣF_y denotes the sum of cornering forces at front and rear axle and mass of the vehicle is given by m. In (4) ΣM_z and J_z, are respectively, yaw motion of the vehicle and the moment of inertia around the vehicle's z-axis. The lateral forces by considering small tire slip angle, α are defined by

$$F_{y,f} = C_{\alpha,f} \underbrace{(\delta_f - \beta - l_f \dot{\psi}/v_x)}_{\alpha_f}, \tag{5}$$

$$F_{y,r} = C_{\alpha,r} \underbrace{(-\beta + l_r \dot{\psi}/v_x)}_{\alpha_r}. \tag{6}$$

The cornering stiffness coefficients for the front and rear axle are $C_{\alpha,f}$ and $C_{\alpha,r}$. The distance of the mass center from front and rear axle are assumed by l_f and l_r. The vehicle is assumed to travel with constant speed of v_x and small vehicle's slip angle. Eqs. (3)–(6) can be summarized in a state space representation with vehicle side slip angle and yaw rate as system states

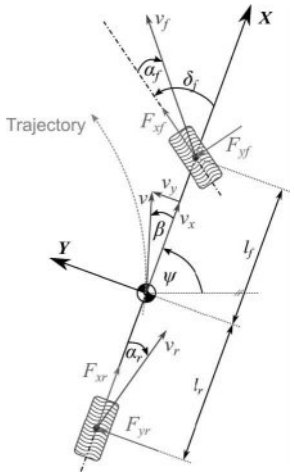


Figure 3. Kinematic representation of linear STM.

and front steering angle and yaw moment as control inputs, as follow

$$\begin{bmatrix}\dot{\beta}\\ \ddot{\psi}\end{bmatrix} = \underbrace{\begin{bmatrix}a_{11} & a_{12}\\ a_{21} & a_{22}\end{bmatrix}}_{A}\begin{bmatrix}\beta\\ \dot{\psi}\end{bmatrix} + \underbrace{\begin{bmatrix}b_{11} & b_{12}\\ b_{21} & b_{22}\end{bmatrix}}_{B}\begin{bmatrix}\delta_f\\ M_z\end{bmatrix} \tag{7}$$

The coefficients of matrices A and B can be found in Appendix A. By solving (7) in the Laplace domain a transfer function which describes the relation between the inputs and the yaw rate can be derived be written

$$\dot{\psi} = \left(\frac{\dot{\psi}}{\delta_f}\right)_{stat} \frac{1+T_{\dot{\psi},z}s}{1+\frac{2D}{w_e}s+\frac{1}{w_e^2}s^2}\delta_f + \left(\frac{\dot{\psi}}{M_z}\right)_{stat} \frac{1+T_{M,z}s}{1+\frac{2D}{w_e}s+\frac{1}{w_e^2}s^2}M_z \tag{8}$$

A set of parameters derived from (8) is used to describe the vehicle behavior. It will be seen in 3.1 that these parameters are related to the vehicle behavior and are used as the basis of our calibration strategy. The complete set of parameters for (8) can be found in Appendix A.

3 FEEDFORWARD CONTROL BASED ON AN INVERSE MODEL

The objective of this section is to find a control law that make use of TV in order to improve the yaw motion of the vehicle. Figure 4 depicts the so-called two degree of freedom control structure (Lunze 2010). A pure feedforward control can be obtained by removing the feedback control path. Thereby, the control input u does not depend on the controlled variable y itself, but only reacts to changes in the desired trajectory w. On the other hand, feedback control responds to deviation between the plant and the desired trajectory

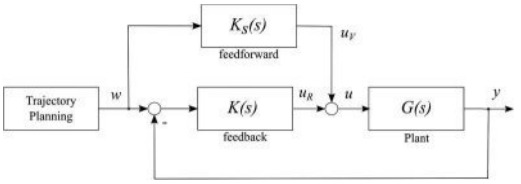


Figure 4. A two-degree of freedom control structure.

and tries to minimize the difference. Thus, any time the deviation of the trajectory and the plant exceeds a pre-defined threshold, the feedback control varies the control input to compensate the occurred deviation and stabilize the system. In the real driving situations, particularity skilled drivers of high performance vehicles, try to stabilize the vehicle by applying very rapid inputs changes to steering wheel angle, braking or gas pedal changes. In order to ensure a reproducible and reliable driving behavior and to preserve a natural driving feeling a pure feedforward control concept is selected.

The core of feedforward design is to define a desire vehicle behavior and to find an appropriate inverse model to realize the desired driving behavior.

3.1 *Reference vehicle parameter design*

The aim of reference parameter design is to correlate the driver's desired with the actual vehicle motion by means of the yaw rate dynamic parameters. In different contributions such as (Koenig, Walter, Gutmayer, & Merlein 2014) the correlation between driving impression and physical vehicle parameters has been investigated and a calibration procedure based on these parameters has been introduced. (Buente, Kaspar, Hohmann, & Brembeck 2014) examine the velocity dependent yaw transfer function parameter and describe how tuning the feedforward controller based on these parameters implies a natural driving behavior. In this paper a detailed parameter study is introduced, which use the yaw transfer function parameters (steady-state yaw rate gain $\left(\frac{\dot{\psi}}{\delta_f}\right)_{stat}$, damping D, frequency coefficient w_e and time response $T_{\dot{\psi},z}$) to determine a parameter set with the following TV goals

- increasing lateral acceleration and reducing the understeer behavior,
- improvement of vehicle reaction by decreasing the rise time and oscillation,
- decreasing the delay between driver input and the vehicles yaw motion.

To understand the effect of each parameter on vehicle behavior, each parameter is varied alone and its time response to a steer step ($\delta_f = 25°$ and $v_x = 100$ km/h) has been investigated. The step steer response of the second-order transfer function is already known (Mitschke & Wallentowitz 2014). The parameter are varied to a degree which results into an unstable driving situation (refer to Figure 5). The same procedure has been done for the other three parameters

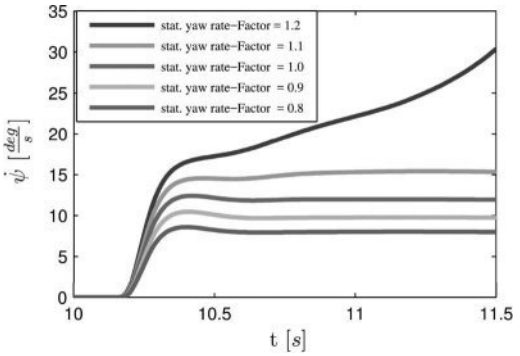


Figure 5. Influence of variation of stationary yaw rate gain on yaw rate behavior.

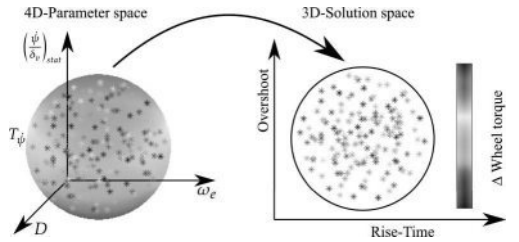


Figure 6. An approach used to study the effect of parameter variation on vehicle behavior.

to determine an acceptable parameter variation range. In the next step values of calibration parameters are varied systematically to generate a parameter space, see Figure 6. To simplify the optimization problem the parameter space is transformed to a three dimensional solution space with following boundary conditions

- overshoot and settling time should be within a specified velocity dependent band,
- allowable deviation from the steady state value is less than 1%,
- maximum wheel torque, due to hardware safety<= 1500 Nm.

Figure 8 presents a parameter variation for constant velocity 80 km/h. Each point corresponds to a valid parameter combination, which fulfills the above goals. It should be noted that for each point, the stationary yaw gain is constant. The color of each point reflects the requested wheel torque. As it can be seen in Figure 8 the parameter variation forms a pareto front which implies that, this problem doesn't have a global optimum. The arrows in Figure 8 indicate a direction in which just one parameter is increased, whereas the other parameters are kept constant. This information can be useful for further calibration. For instance, it can be concluded that increasing the frequency does not effect the overshoot, as raising the time constant does. The group of parameters which presented in Figure 8 by a circle, suggest that it is possible to reach a special amount of overshoot and rise time with different combinations of parameter variation. However,

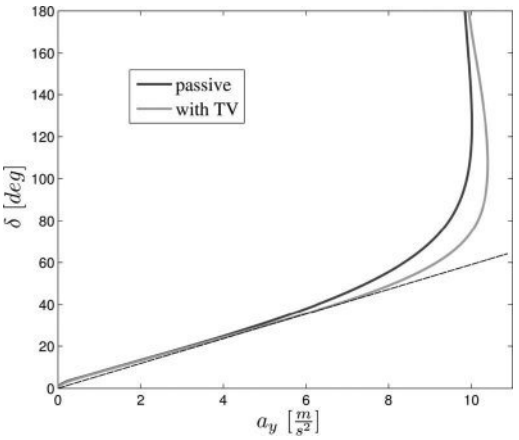


Figure 7. Example of decreasing understeer behavior by calibration the stationary yaw rate gain for a slow ramp maneuver at 100 km/h.

they differ in their required manipulation of wheel torque. After carrying this procedure for a range of different velocities it is possible to schedule each of the calibration parameters for different velocity. The calibration parameters D, w_e and $T_{\dot{\psi},z}$ effect the transient behavior of the yaw motion. The effect of stationary yaw gain can be examined by use of stationary and quasi-stationary maneuvers as slow ramp steer. A slow ramp steer is a good measure for understeer behavior of the vehicle. This maneuver can indicate how the gradient of steering wheel angle changes regarding to lateral acceleration (Bergman 1965). A linear relation between steering wheel angle and lateral acceleration is considers as a neutral driving behavior, which is particularity desirable for sports cars drivers. The calibration of the stationary yaw gain should meet following goals

- extending the linear driving domain and decreasing the understeer behavior,
- decreasing overshoot and rise time,
- reaching higher lateral acceleration without compromising the stability of the vehicle.

In this work the yaw rate gain has been scheduled with respect to velocity and lateral acceleration. This method results into a more predictable vehicle behavior, especially in higher lateral acceleration domain. The magnitude of understeer is a design parameter, which should be determined during the chassis development (Bortolussi, Pascali, & Castrup 2014). Thus, for each lateral acceleration, actual steering wheel angle is compare to a desire one $\delta_{f,des}$. Moreover, to ensure the fast response time and avoid overshoot, response of a step steer with magnitude equal to $\delta_{f,des}$ is investigated. The result of this calibration can be seen in Figure 7 which is a confirmation for fulfillment of above goals. The reference trajectory planning of the proposed control scheme is summarized in Figure 9. The first block calculates the transient and stationary second order system in response to inputs. The

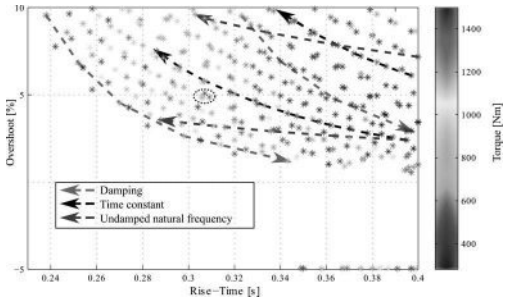


Figure 8. Pareto front optimization for velocity dependent application parameters at constant velocity 80 km/h.

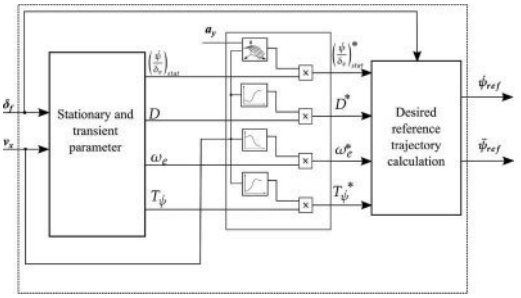


Figure 9. Reference vehicle model structure.

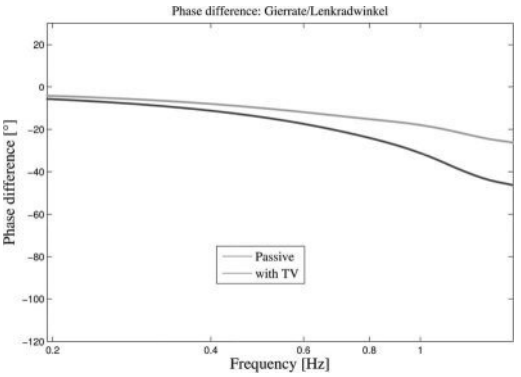


Figure 10. Frequency response of feedforward control.

calibration block is separated to make a transparent interface for driver and calibration engineers. Finally, the desired yaw motion in terms of ($\dot{\psi}_{ref}$ and $\ddot{\psi}_{ref}$) are calculated by solving an algebraic second order differential equation. The quality of reference model strongly depends on good knowledge about the vehicle itself. In order to consider the nonlinear (NL) region, yet use the benefits of introduced structure in Figure 9, the driver steering input is reduced by a coefficient. This coefficient is calculated as a deviation between cornering forces in linear and nonlinear region, which damp the transient parameter in nonlinear region. This coefficient improves the stability of the vehicle in critical driving situations, particularly when the driver tries to stabilize the vehicle by rapid steering changes. The result of this section has been used as a basis for further calibration procedures, which has been done during various test drives.

3.2 *Inversion based feedforward control*

In order to solve the exact tracking problem an inverse model is created. Thus, from Figure 4 it can be concluded that $k_s(s) = G^{-1}(s)$. The problem of finding an inverse has been solved by algebraic calculation of feedforward control output $u_v(t)$ depending on the desired input w(t). In this paper $u_v(t)$ can be interpreted as TV torque and the $w(t)$ as the vehicle's desired yaw motion. The desired trajectory $w(t)$ is defined by a second order polynomial, which is a good approximation of a linear vehicle model. Solving (7) for yaw acceleration and after some modification the TV torque can be calculated depending on the tuned yaw motion as $M_z = J_z\ddot{\psi}_{ref} - C_{\alpha,f}(\delta_f - \beta - lf\dot{\psi}_{ref}/v_x)l_f + C_{\alpha,r}(-\beta + lr\dot{\psi}_{ref}/v_x)l_r$. The vehicle slip angle is calculated according to (3) to compensate the yaw motion changes. From the yaw torque M_z the allocated wheel torque difference between the left and right wheel ΔM_w can be calculated, see (1).

4 SIMULATION RESULTS

To evaluate the performance of the proposed method a simulation model of a Porsche Macan is modified. It is assumed that a rear axle wheel torque is being distributed by use of a previously described TV-system. The actuator limits are considered and the calibration parameters are adapted respectively.

The response of a vehicle equipped with TV to a predefined dynamic maneuver such as sweep is investigated. The steering wheel excitation is between 0–1.5 Hz. The driver tries to keep the vehicle speed constant throughout the maneuver (in this simulation the initial velocity is 100 km/h). By analyzing the behavior of a vehicle in the frequency domain it is possible to estimate the phase difference between driver input and vehicle's response in terms of yaw motion. To have a direct driving feeling it is preferable to have a small phase difference. Figure 10 presents the phase shift between passive and TV-system. It can be seen that the vehicle with TV shows a faster response to the driver steering. To sum up the difference between the passive vehicle and the one with TV, the key performance parameters which represent handling and performance are plotted on a radar chart. As mentioned in (He, Hori, Kamachi,Walters, & Yoshida 2005) a vehicle with a better driving handling and stability has a larger surface. In this chart we summarized the improvement of the vehicle after applying TV. The five parameter have been derived using the optimization goals described in 3.1. As it can be seen from Figure 11 the defined goals of TV-system (refer to section 3.1) are achieved by use of the proposed controller.

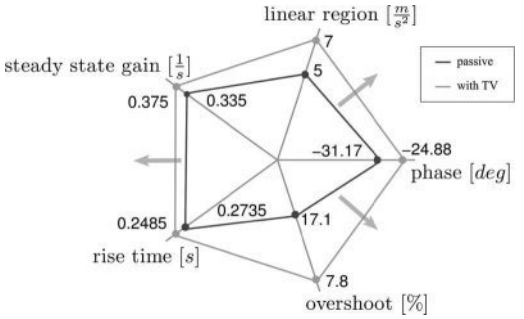


Figure 11. Radar chart to compare between passive and active vehicle.

5 CONCLUSION

In this paper a control concept for an electromechanical TV-system aimed at high performance vehicle is proposed. The proposed control concept is realized by means of an inversion based feedforward control scheme. Adequate calibration has been done to meet sports cars performance requirements in higher lateral acceleration domain. Improvement of the vehicles lateral performance and yaw stability as a result of the proposed control concept can be observed from the simulation results. More tests especially for vehicle behavior on low friction surface are planned. Moreover, consideration of force allocation and stability potential of tires within the feedforward is being investigated.

REFERENCES

Bergman, W. (1965). The basic nature of vehicle understeeroversteer. *SAE Technical Paper 650085*.

Bortolussi, P., L. Pascali, & N. Castrup (2014). An effective process for trackside vehicle development.Wiesbaden. Springer Fachmedien.

Buente, T., S. Kaspar, S. Hohmann, & J. Brembeck (2014). Inverse model based torque vectoring control for a rear wheel driven battery electric vehicle. *19th IFAC World Congress*, 12016–12022.

He, H. P., Y. Hori, M. Kamachi, K. Walters, & H. Yoshida (2005). Future motion control to be realized by in-wheel motored electric vehicle. *Industrial Electronics Society, 2005. IECON 2005. 31st Annual Conference of IEEE*, 6–10.

Hoehn, B., K. Stahl, C. Wirth, M. Lienkamp, F. Kurth, & F. Wiesbeck (2011). Elektromechanisches torque-vectoring mit aktivem differential zur maximierung der rekuperationsfhigkeit.

Isermann, R. (2006). *Fahrdynamik-Regelung Modellbildung, Fahrerassistenzsysteme, Mechatronik*.

Koenig, L., T. Walter, B. Gutmayer, & D. Merlein (2014). Integrated vehicle dynamics control – an optimized approach for linking multiple chassis actuators. Wiesbaden. Springer Fachmedien.

Lunze, J. (2010). *Regelungstechnik 1: Systemtheoretische Grundlagen, Analyse und Entwurf einschleifiger Regelungen*. Springer-Verlag Berlin Heidelberg.

Milliken, W. & D. Milliken (1995). *Race Car Vehicle Dynamics*, Volume 146. Society of Automotive Engineers.

Mitschke, M. & H. Wallentowitz (2014). *Dynamik der Kraftfahrzeuge* (5 ed.). Wiesbaden: Springer Vieweg.

Rohe, M. (2014). The electrification of the power train makes it possible – realization of electric concept vehicles as source of innovations. Wiesbaden. Springer Fachmedien.

Schramm, D., M. Hiller, & R. Bardini (2014). *Vehicle Dynamics Modeling and Simulation*. Berlin Heidelberg: Springer Vieweg.

A SINGLE TRACK MODEL STATE SPACE REPRESENTATION

$$A = \begin{bmatrix} \frac{C_{\alpha f}+C_{\alpha r}}{mv_x} & \frac{l_f C_{\alpha f}-l_r C_{\alpha r}}{mv_x^2} \\ \frac{l_f C_{\alpha f}-l_r C_{\alpha r}}{J_z} & \frac{l_f^2 C_{\alpha f}+l_r^2 C_{\alpha r}}{J_z v_x} \end{bmatrix} \tag{9}$$

$$B = \begin{bmatrix} \frac{C_{\alpha f}}{mv_x} & 0 \\ \frac{l_f C_{\alpha f}}{J_z} & \frac{1}{J_z} \end{bmatrix} \tag{10}$$

$$T_z = \frac{mv_x l_f}{C_{\alpha f} l} \tag{11}$$

$$w_e = \sqrt{\frac{C_{\alpha r} l_r - C_{\alpha f} l_f}{J_z} + \frac{C_{\alpha r} C_{\alpha f} l^2}{J_z m v_x^2}} \tag{12}$$

$$D = \frac{\frac{C_{\alpha f}+C_{\alpha r}}{mv_x} + \frac{C_{\alpha f} l_f^2 + C_{\alpha r} l_r^2}{J_z v_x}}{2w_e} \tag{13}$$

$$T_z = \frac{mv_x l_f}{C_{\alpha f} l} \tag{14}$$

$$\left(\frac{\dot{\psi}}{\delta_f}\right)_{stat} = \frac{v_x}{l(1+\frac{v_x^2}{v_{char}^2})} \tag{15}$$

$$v_{char}^2 = \frac{C_{\alpha f} C_{\alpha r} l^2}{m(C_{\alpha f} l_f - C_{\alpha r} l_r)} \tag{16}$$

$$T_{M_z} = \frac{mv_x}{C_{\alpha f} + C_{\alpha r}} \tag{17}$$

$$\left(\frac{\dot{\psi}}{M_z}\right)_{stat} = \frac{v_x}{l(1+\frac{v_x^2}{v_{char}^2})} \frac{C_{\alpha f} + C_{\alpha r}}{C_{\alpha f} C_{\alpha r} l} \tag{18}$$

Advanced Vehicle Control – Edelmann, Plöchl & Pfeffer (Eds)
© 2017 Taylor & Francis Group, London, ISBN 978-1-138-02992-7

Efficient direct yaw moment control of in-wheel motor vehicle

T. Kobayashi, H. Sugiura & E. Ono
Toyota Central R&D Labs., Inc.

E. Katsuyama & M. Yamamoto
Toyota Motor Corporation

ABSTRACT: This paper proposes an efficient direct yaw moment control (DYC) capable of minimizing tyre slip loss on contact patches in an electric vehicle equipped with four-independently driven in-wheel motors (IWMs). Simulations identified a significant loss reduction due to a change in steer characteristics during acceleration or deceleration while turning. Simultaneously, the vehicle motion is also stabilized. As a result, the proposed control method can ensure compatibility between vehicle dynamics performance and energy efficiency. This paper also describes the results of a full-vehicle simulation that was conducted to examine the effectiveness of the proposed DYC.

1 INTRODUCTION

In-wheel motors (IWMs) are regarded as a promising and innovative type of electric powertrain. In addition to high efficiency, IWMs enable less restrictive vehicle packaging and driving force distribution control than electric vehicles equipped with a single motor. Various kinds of driving force distribution controls have been developed in the past decades to improve the manoeuvrability (Osborn, 2006 & Shibahata, 1993) and ride comfort (Katsuyama, 2013) of vehicles equipped with IWMs. In contrast, one issue that remains to be solved is the low mileage per charge due to the limited battery capacity of these vehicles. To help address this issue, some studies (Abe, 2012 & Nishihara, 2013) have examined driving force distribution controls that reduce tyre slip loss while turning. Increases in tyre slip loss raise the temperature of the tyre at higher acceleration. Although the proposed controls have a certain effect, it is necessary to explore the detailed mechanism of the loss and to identify suitable driving conditions and vehicle specifications to maximize the advantages of these controls.

This paper describes the development of an efficient direct yaw moment control (DYC) based on an analytical approach. By incorporating the equation of vehicle motion into the equation of energy, the vehicle loss due to the tyre slip can be defined as a convex function of direct yaw moment. Based on the loss mechanism, an optimization problem can be conducted to obtain the efficient direct yaw moment. This paper also examines the vehicle dynamics performance using the control, and the effect of tyre non-linearity on direct yaw moment. Finally, a full-vehicle simulation is described that demonstrates the effect of the proposed DYC.

2 TYRE SLIP LOSS MODELING

2.1 *Equation of motion*

This paper uses a vehicle dynamics model as shown in Fig. 1. Since the actual steer angle is important for cornering resistance, this paper considers the rear steer angle that is changed due to the suspension compliance. In this paper, the steer angles and body slip angle are assumed to be small. The equation of motion can be expressed as follows.

$$m(\dot{u}-vr)=F_d-F_{rr}-F_{ar}-(F_{y1}+F_{y2})\delta_f-(F_{y3}+F_{y4})\delta_r \tag{1}$$

$$m(\dot{v}+ur)=F_{y1}+F_{y2}+F_{y3}+F_{y4} \tag{2}$$

$$I_z\dot{r}=l_f(F_{y1}+F_{y2})-l_r(F_{y3}+F_{y4})+M_z \tag{3}$$

where, m is the vehicle mass, F_d is the total driving force, F_{rr} is the rolling resistance of the tyres, F_{ar} is the aerodynamic resistance, M_z is the direct yaw moment due to the driving force distribution, u is the longitudinal velocity, v is the lateral velocity, r is the yaw rate, l_f and l_r are the distances from the centre of gravity to the front and rear axles, and δ_f and δ_r are the front and rear steer angles, respectively. F_{yj} is the lateral force. The subscript j indicates each wheel position ($j=1$: front left, 2: front right, 3: rear left, 4: rear right). The total driving and direct yaw moment are defined as follows.

$$F_d=F_{x1}+F_{x2}+F_{x3}+F_{x4} \tag{4}$$

$$M_z=(-F_{x1}+F_{x2})\frac{t_f}{2}+(-F_{x3}+F_{x4})\frac{t_r}{2} \tag{5}$$

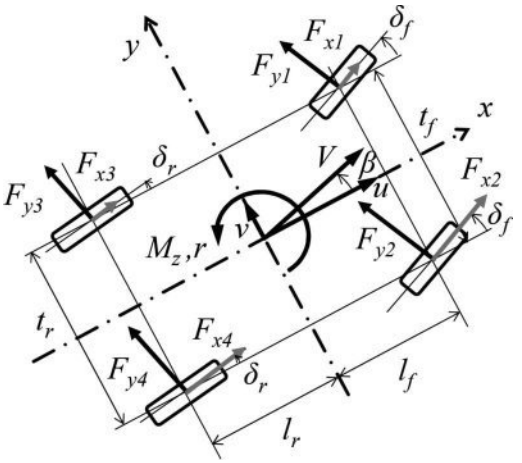


Figure 1. Vehicle dynamics model.

The rolling resistance of the tyres and the aerodynamic resistance can be calculated by the following general definition.

$$F_{rr} = \mu_r mg \tag{6}$$

$$F_{ar} = \rho A C_D V^2 / 2 \tag{7}$$

where, μ_r is the rolling resistance of the tyres, g is the gravitational acceleration, ρ is the air density, C_D is the aerodynamic resistance coefficient, and V is the vehicle speed. This paper disregards the effect of the body slip angle β on the aerodynamic resistance.

Since Equations 1–3 are intricately interrelated, the so-called quasi steady state cornering (Abe, 2009) analysis method was applied to simplify them in this paper. Under this approach, transitional changes in vehicle speed and yaw motion can be disregarded. As a result, even the vehicle motion during acceleration and deceleration while turning can be formulated analytically.

$$\dot{u} = A_x, \quad \dot{r} = 0, \quad \dot{\beta} = 0 \tag{8}$$

Using the above assumption and linearizing the Equations 1–3, the total driving force can be expressed as follows.

$$F_d = mA_x + F_{rr} + F_{ar} + F_{cr} \tag{9}$$

$$F_{cr} \equiv \left(F_{y1} + F_{y2}\right)\left(\delta_f - \beta\right) + \left(F_{y3} + F_{y4}\right)\left(\delta_r - \beta\right) \tag{10}$$

Equation 10 indicates that the cornering resistance F_{cr} is the sum of the lateral forces projected to the body slip angle, and can be explained as driving resistance that interferes with longitudinal motion due to lateral force. Generally, the longitudinal and lateral forces of the tyres become saturated at high slip magnitudes and couple with each other. Although the tyre force characteristics are non-linear due to vertical load, the characteristics were linearized as follows to facilitate the analytical consideration.

$$F_{y1} + F_{y2} = 2F_{yf} = -2K_{yf}\alpha_f, \quad F_{y3} + F_{y4} = 2F_{yr} = -2K_{yr}\alpha_r \tag{11}$$

where, F_{yj} is the lateral force, K_{yj} is the cornering stiffness of the tyres, and α_j is the slip angle. The subscripts f and r refer to the front and rear wheels.

Based on these assumptions, the steer angles and body slip angle can be expressed as follows.

$$\delta_f - \delta_r = \left(1 - \frac{m}{2l^2}\frac{l_f K_{yf} - l_r K_{yr}}{K_{yf} K_{yr}} V^2\right)\frac{l}{R} - \frac{K_{yf} + K_{yr}}{2lK_{yf}K_{yr}} M_z \tag{12}$$

$$\beta = \frac{1}{1 - \frac{m}{2l^2}\frac{l_f K_{yf} - l_r K_{yr}}{K_{yf} K_{yr}} V^2} \cdot \left[\left(1 - \frac{m}{2l}\frac{l_f V^2}{l_r K_{yr}}\right)\frac{l_r}{l}\delta_f + \left(1 + \frac{m}{2l}\frac{l_r V^2}{l_f K_{yf}}\right)\frac{l_f}{l}\delta_r - \frac{mV^2 + 2\left(l_f K_{yf} - l_r K_{yr}\right)}{4l^2 K_{yf} K_{yr}} M_z\right] \tag{13}$$

where, l is the wheelbase. The cornering resistance can be expressed as a quadratic function of the direct yaw moment.

$$F_{cr} = \left(\frac{l_r^2}{K_{yf}} + \frac{l_f^2}{K_{yr}}\right)\frac{\left(mA_y\right)^2}{2l^2} - \left[\frac{1}{R} + \left(\frac{l_r}{K_{yf}} - \frac{l_f}{K_{yr}}\right)\frac{mA_y}{l^2}\right] M_z + \left(\frac{1}{K_{yf}} + \frac{1}{K_{yr}}\right)\frac{M_z^2}{2l^2} \tag{14}$$

where, A_y is the lateral acceleration. In particular, the first term is the cornering resistance of conventional vehicles without DYC. A higher cornering stiffness is desirable for cornering efficiency. The second term, which plays an important role in this paper, is discussed in the next section.

2.2 *Equation of energy*

The total mechanical power P_v can be expressed as shown in the following equation. Here, the driving torque and angular velocity at each wheel are represented as τ_j and ω_j, respectively.

$$P_v = \sum_{j=1}^{4} \tau_j \omega_j \tag{15}$$

$$\tau_j = r_t F_{xj}, \quad \omega_j = \left(1 + s_j\right)\frac{V_j}{r_t} \tag{16}$$

where, r_t is the tyre radius and s_j is the longitudinal slip ratio. V_j is the vehicle speed at each wheel position and can be expressed as follows.

$$V_1 = V - \frac{t_f}{2}r, V_2 = V + \frac{t_f}{2}r, V_3 = V - \frac{t_r}{2}r, V_4 = V + \frac{t_r}{2}r \tag{17}$$

As a result, the total mechanical power P_v can be expressed as follows.

$$\begin{aligned} P_v &= F_d V + M_z r + \sum_{j=1}^{4}\left(s_j V_j F_{xj}\right) \\ &= mA_x V + F_{rr} V + F_{ar} V + \sum_{j=1}^{4}\left(s_j V_j F_{xj}\right) + \left(F_{cr} + \frac{M_z}{R}\right) V \end{aligned} \tag{18}$$

The first term is the acceleration power that converts effectively to kinetic energy. The second and third terms are the rolling resistance loss and aerodynamic loss, respectively. The fourth and fifth terms are the longitudinal and lateral slip losses of the tyres.

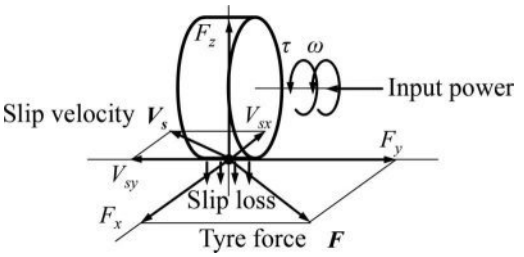


Figure 2. Tyre slip loss on contact patch.

In particular, the lateral slip loss can be represented by substituting Equation 14 into the fifth term of Equation 18.

$$\left(F_{cr}+\frac{M_z}{R}\right)V=\left[\left(\frac{l_r^2}{K_{yf}}+\frac{l_f^2}{K_{yr}}\right)\frac{(mA_y)^2}{2l^2}-\left(\frac{l_r}{K_{yf}}-\frac{l_f}{K_{yr}}\right)\frac{mA_z}{l^2}M_z+\left(\frac{1}{K_{yf}}+\frac{1}{K_{yr}}\right)\frac{M_z^2}{2l^2}\right]V \quad (19)$$

The second term indicates the slip loss reduction effect by direct yaw moment. To explore the possibility of maximizing this effect, a coefficient was examined based on an assumption that the cornering stiffness is proportional to the vertical load.

$$\lambda=\frac{l_r}{K_{yf}}-\frac{l_f}{K_{yr}}\propto\frac{1}{C_{yf}}\left(\frac{F_{zf0}}{F_{zf}}\right)-\frac{1}{C_{yr}}\left(\frac{F_{zr0}}{F_{zr}}\right) \quad (20)$$

where, C_{yj} is the normalized cornering stiffness by the vertical load, F_{zj0} is the initial vertical load, and F_{zj} is the vertical load including the load shift. Given that the front and rear tyres are the same, λ is zero in steady state cornering. However, λ becomes a positive value during acceleration, resulting in a positive direct yaw moment that can reduce the loss. In contrast, λ becomes a negative value during deceleration, resulting in a negative direct yaw moment that can reduce the loss.

The lateral slip loss can be represented in another way.

$$\left(F_{cr}+\frac{M_z}{R}\right)V=\sum_{j=1}^{4}\left(K_j\alpha_j{}^2\right)V \quad (21)$$

As a result, the total slip loss can be expressed as follows by representing V_{sx} and V_{sy} as the tyre longitudinal and lateral slip velocities.

$$\begin{aligned}P_s&=\sum_{j=1}^{4}\left(s_jV_jF_{zj}\right)+\left(F_{cr}+\frac{M_z}{R}\right)V\\&=-\sum_{j=1}^{4}\left(F_{xj}V_{sxj}+F_{yj}V_{syj}\right)\\&=-\sum_{j=1}^{4}\vec{F}_j\cdot\vec{V}_{sj}\end{aligned} \quad (22)$$

The total loss can be calculated as the scalar product of the tyre force vectors and tyre slip velocity vectors. The definition of loss is consistent with the amount of heat generation in tyre thermal models (Kelly, 2012, Hancock, 2005, Mizuno, 2005 & Sorniotti, 2009) that are capable of predicting tyre loss and warming. In other words, a direct yaw moment control that avoids warming the tyres improves the cornering efficiency.

The result of the above equations was validated in an actual vehicle test in the previous report (Kobayashi, 2014).

Table 1. Major specifications.

Specification	Unit	Value
Vehicle mass	kg	2195
Wheelbase	m	2.85
Track front/rear	m	1.54/1.55
Weight distribution	–	50:50
Load shift distribution	–	53:47
Normalized driving stiffness	–	28.2
Normalized cornering stiffness	–	25.4
Nominal load of tyre	N	5000
Load non-linear parameter	N^{-1}	0.0001

3 TYRE SLIP LOSS CHARACTERISTICS

The tyre slip loss reduction effect was examined using the formulated model. First, the load shift due to the longitudinal and lateral acceleration can be calculated as follows.

$$\begin{aligned}F_{z1}&=\frac{F_{zf0}}{2}-\frac{\rho_f mA_yh}{t_f}-\frac{mA_xh}{2l},F_{z2}=\frac{F_{zf0}}{2}+\frac{\rho_f mA_yh}{t_f}-\frac{mA_xh}{2l}\\F_{z3}&=\frac{F_{zr0}}{2}-\frac{\rho_r mA_yh}{t_r}+\frac{mA_xh}{2l},F_{z4}=\frac{F_{zr0}}{2}+\frac{\rho_r mA_yh}{t_r}+\frac{mA_xh}{2l}\end{aligned} \quad (23)$$

where, ρ_f and ρ_r are the load shift distribution ratio of the front and rear wheels, and h is the height of the centre of gravity. Additionally, since the tyre slip state is influenced significantly by the non-linear tyre load characteristics, this paper compares the effect as shown below.

$$K_{xj}=C_x\left[1-\varepsilon\left(F_{zj}-F_{zn}\right)\right]F_{zj} \quad (24)$$

$$K_{yj}=C_y\left[1-\varepsilon\left(F_{zj}-F_{zn}\right)\right]F_{zj} \quad (25)$$

where, C_x is driving stiffness normalized by the vertical load, ε is the load non-linear parameter, and F_{zn} is the nominal load, respectively. When the load non-linearity is disregarded, the parameter is set to zero. Moreover, the brush model in this paper considers the saturation and combined slip. Table 1 shows the major specifications used in this paper.

Figures 3 and 4 depict the tyre slip loss characteristics during acceleration and deceleration, respectively. As an example, Figure 3 shows the characteristics at a longitudinal acceleration of 2 m/s^2 in a left turn at 80 km/h and lateral acceleration of 2 m/s^2. The direct yaw moment distribution ratio between the front and rear wheels is set to be proportional to the longitudinal load shift. Also, the figure depicts the characteristics of steady-state cornering as a reference. Compared to steady-state cornering, the overall tyre slip loss increases during acceleration. This is because the driving force required to accelerate the vehicle increases the longitudinal slip. This overall increase in tyre slip loss can be minimized by a positive direct yaw moment capable of modifying understeer. At a longitudinal acceleration of 2 m/s^2, the maximum reduction

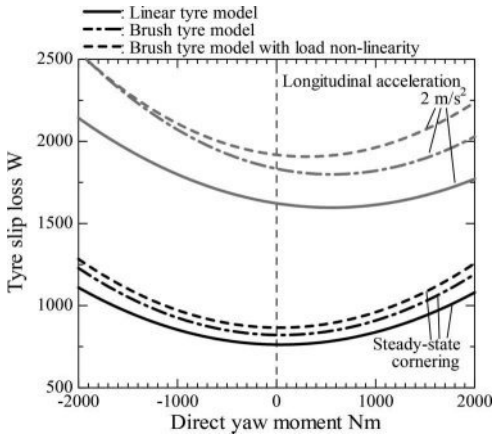


Figure 3. Tyre slip loss characteristics during acceleration.

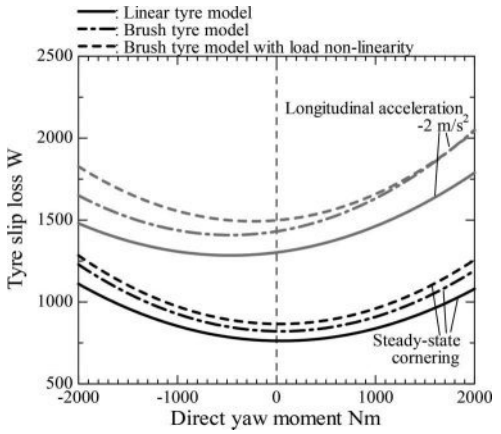


Figure 4. Tyre slip loss characteristics during deceleration.

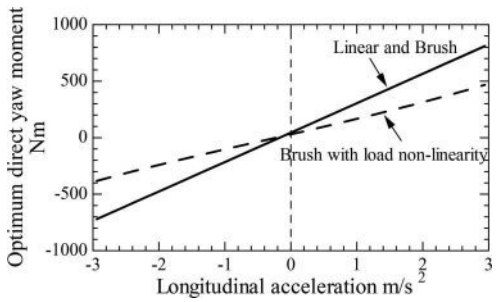


Figure 5. Optimum direct yaw moment during acceleration and deceleration (2 m/s^2 left turn).

is approximately 1.6%. The mechanism of this minimization effect can be explained by the change in steer characteristics due to the longitudinal load shift. The direct yaw moment that acts in the same direction as the turning direction increases the proportion of the rear lateral force. The tyre slip loss is minimized by suppressing the lateral tyre slip of the front wheels with less vertical load.

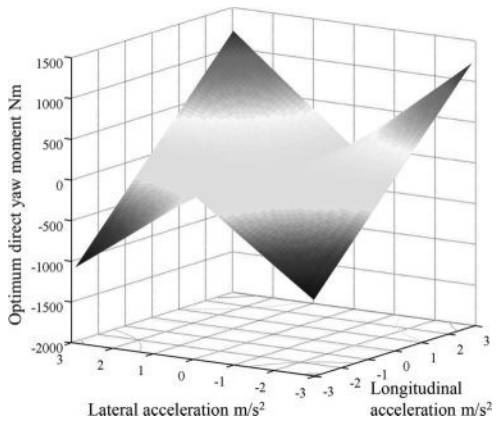


Figure 6. Optimum direct yaw moment contour map (without load non-linearity).

Figure 4 shows the tyre slip loss characteristics at a longitudinal deceleration of 2 m/s^2 in a left turn at 80 km/h and lateral acceleration of 2 m/s^2. In contrast, here, the tyre slip loss can be minimized by a negative direct yaw moment capable of modifying oversteer. The direct yaw moment that acts in the opposite direction increases the proportion of the front lateral force. As a result, the lateral tyre slip of the rear wheels is suppressed. Using the optimum direct yaw moment, the vehicle can regenerate the kinetic energy with minimal loss.

Both figures show the effects of tyre non-linearity on tyre slip loss. Compared to the linear tyre model, slip losses increase in both tyre models. This is because the non-linearity lowers the tyre grip, resulting in an increase in loss. In addition, as shown in Fig. 5, although the optimum direct yaw moment is almost the same in the linear and brush tyre models, the optimum direct yaw moment decreases by approximately half in the case of a tyre with a non-linear load. This is because the non-linear load stabilizes the steer characteristics to a certain extent.

Figure 6 shows the contour plot of the optimum direct yaw moment that minimizes the tyre slip loss under each turning condition. When the sign of the direct yaw moment is positive, it acts in the same direction as the turning direction. In contrast, when the sign is negative, it acts in the opposite direction as the turning direction. In particular, the optimum direct yaw moment is required when the longitudinal and lateral accelerations are coupled.

4 CONSIDERATIONS ABOUT EFFICIENT DYC

4.1 *Minimization of tyre slip loss*

An optimization problem was conducted as follows to construct an efficient DYC capable of minimizing tyre slip loss.

Constraint condition:

$$K_{x1}s_1 + K_{x2}s_2 + K_{x3}s_3 + K_{x4}s_4 = F_x \tag{26}$$

$$-K_{y1}\alpha_1 - K_{y2}\alpha_2 - K_{y3}\alpha_3 - K_{y4}\alpha_4 = F_y \tag{27}$$

Evaluation function:

$$\begin{aligned} J &= -\sum_{j=1}^{4} \boldsymbol{F}_j \cdot \boldsymbol{V}_{sj} \\ &= \left(K_{x1}s_1^{\,2} + K_{y1}\alpha_1^{\,2}\right)V_1 + \left(K_{x2}s_2^{\,2} + K_{y2}\alpha_2^{\,2}\right)V_2 \\ &\quad + \left(K_{x3}s_3^{\,2} + K_{y3}\alpha_3^{\,2}\right)V_3 + \left(K_{x4}s_4^{\,2} + K_{y4}\alpha_4^{\,2}\right)V_4 \end{aligned} \tag{28}$$

To obtain the least-norm solution using the Moore-Penrose pseudoinverse, the tyre slip vector $\boldsymbol{q}$ is transformed as follows.

$$\boldsymbol{q} = \begin{pmatrix} s_1 & s_2 & s_3 & s_4 & \alpha_1 & \alpha_2 & \alpha_3 & \alpha_4 \end{pmatrix}^T \tag{29}$$

$$\begin{aligned} \boldsymbol{p} = diag\Big(&\sqrt{K_{x1}V_1} \quad \sqrt{K_{x2}V_2} \quad \sqrt{K_{x3}V_3} \quad \sqrt{K_{x4}V_4} \\ &\sqrt{K_{y1}V_1} \quad \sqrt{K_{y2}V_2} \quad \sqrt{K_{y3}V_3} \quad \sqrt{K_{y4}V_4}\Big) \cdot \boldsymbol{q} \end{aligned} \tag{30}$$

The optimization problem can be redefined as follows.

Constraint condition:

$$\begin{pmatrix} \sqrt{\frac{K_{x1}}{V_1}} & \sqrt{\frac{K_{x2}}{V_2}} & \sqrt{\frac{K_{x3}}{V_3}} & \sqrt{\frac{K_{x4}}{V_4}} & 0 & 0 & 0 & 0 \\ 0 & 0 & 0 & 0 & -\sqrt{\frac{K_{y1}}{V_1}} & -\sqrt{\frac{K_{y2}}{V_2}} & -\sqrt{\frac{K_{y3}}{V_3}} & -\sqrt{\frac{K_{y4}}{V_4}} \end{pmatrix} \cdot \boldsymbol{p} = \begin{pmatrix} F_x \\ F_y \end{pmatrix} \tag{31}$$

Evaluation function:

$$J = \|\boldsymbol{p}\|^2 \tag{32}$$

Accordingly, $\boldsymbol{p}$ that minimizes Equation 32 can be expressed as follows.

$$\boldsymbol{p} = \begin{pmatrix} \sqrt{\frac{K_{x1}}{V_1}} & \sqrt{\frac{K_{x2}}{V_2}} & \sqrt{\frac{K_{x3}}{V_3}} & \sqrt{\frac{K_{x4}}{V_4}} & 0 & 0 & 0 & 0 \\ 0 & 0 & 0 & 0 & -\sqrt{\frac{K_{y1}}{V_1}} & -\sqrt{\frac{K_{y2}}{V_2}} & -\sqrt{\frac{K_{y3}}{V_3}} & -\sqrt{\frac{K_{y4}}{V_4}} \end{pmatrix}^+ \cdot \begin{pmatrix} F_x \\ F_y \end{pmatrix} \tag{33}$$

where, the subscript + of the coefficient matrix on the right side indicates the pseudoinverse matrix. Finally, $\boldsymbol{q}$ can be expressed as follows.

$$\begin{aligned} \boldsymbol{q} &= \begin{pmatrix} s_1 & s_2 & s_3 & s_4 & \alpha_1 & \alpha_2 & \alpha_3 & \alpha_4 \end{pmatrix}^T \\ &= \begin{pmatrix} \frac{d^{-1}F_x}{V_1} & \frac{d^{-1}F_x}{V_2} & \frac{d^{-1}F_x}{V_3} & \frac{d^{-1}F_x}{V_4} & -\frac{a^{-1}F_y}{V_1} & -\frac{a^{-1}F_y}{V_2} & -\frac{a^{-1}F_y}{V_3} & -\frac{a^{-1}F_y}{V_4} \end{pmatrix}^T \end{aligned} \tag{34}$$

where, the parameters d and a are defined as follows.

$$d = \sum_{j=1}^{4} \frac{K_{xj}}{V_j} = \left(\sum_{j=1}^{4} \frac{F_{zj}}{V_j}\right) C_x, a = \sum_{j=1}^{4} \frac{K_{yj}}{V_j} = \left(\sum_{j=1}^{4} \frac{F_{zj}}{V_j}\right) C_y \tag{35}$$

By extracting the slip ratio and slip angle of each wheel, the optimum side slip state can be expressed as follows.

$$\boldsymbol{s}_{sj} = \begin{pmatrix} s_j & \alpha_j \end{pmatrix}^T = \begin{pmatrix} \frac{F_x}{dV_j} & -\frac{F_y}{aV_j} \end{pmatrix}^T \tag{36}$$

According to Equation 36, the optimum slip state of each wheel depends on the vehicle velocity at the tyre position. By multiplying the velocity, Equation 36 can be newly expressed as follows.

$$\boldsymbol{V}_{sj} = \begin{pmatrix} V_j s_j & V_j \alpha_j \end{pmatrix}^T = \begin{pmatrix} \frac{F_x}{d} & -\frac{F_y}{a} \end{pmatrix}^T \tag{37}$$

The left side of Equation 37 is the slip velocity vector consisting of the longitudinal and lateral slip velocity. The right side is consistent for all wheels. The minimization of the tyre slip loss requires the equalization of the tyre slip velocity vector.

4.2 *Vehicle dynamics performance*

In terms of saving energy, the previous section proved that it is necessary to equalize the tyre slip vector for all wheels. This section discusses the relationship between the equalized slip vector and vehicle dynamics performance. To analyse the vehicle motion, the optimized state as shown in Equation 37 was approximated to a two-wheel model. In other words, the wheel speed difference between the inner and outer wheels was disregarded.

$$V_1 = V_2 = V_3 = V_4 = V \tag{38}$$

The slip state of each wheel can be expressed as follows.

$$\boldsymbol{s}_{sj} = \begin{pmatrix} s_j & \alpha_j \end{pmatrix}^T = \begin{pmatrix} \frac{F_x}{dV} & -\frac{F_y}{aV} \end{pmatrix}^T \tag{39}$$

The driving force can be expressed as the product of the slip ratio and driving stiffness. Here, tyre nonlinearity was also disregarded for simplicity.

$$F_{xj} = K_{xj}s_j = \left(\frac{F_x}{F_z}\right) F_{zj} \tag{40}$$

Therefore, the optimum solution is to distribute the driving force proportionally to the vertical load. The direct yaw moment obtained from Equation 40 can cancel out the yaw moment change due to acceleration and deceleration (Shibahata, 1993). Consequently, the steer characteristics can be stabilized, when the vehicle accelerates or decelerates while turning as shown in Figure 7. Additionally, the lateral force can be obtained from the product of the slip angle and cornering stiffness.

$$F_{yj} = -K_{yj}\alpha_j = \left(\frac{F_y}{F_z}\right) F_{zj} \tag{41}$$

The lateral force is also generated proportionally to the vertical load. As a result, the maximum tyre work load is reduced under the control. As an example, Figure 8 shows the proposed control effect under the same conditions as Fig. 3. In particular, the work load at the front left tyre is reduced. Therefore, this research revealed that an efficient DYC that enhances cornering efficiency involves conventional control laws capable of stabilizing vehicle motion in the linear vehicle dynamics region.

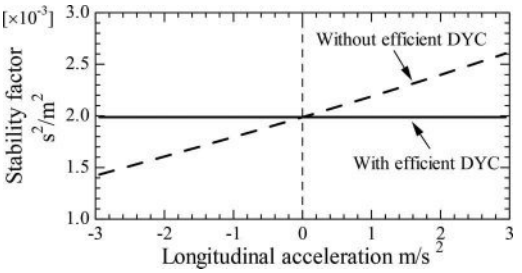


Figure 7. Stability factor during acceleration and deceleration (2 m/s^2 left turn at 80 km/h).

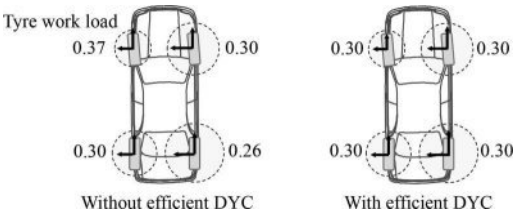


Figure 8. Comparison of tyre work load (2 m/s^2 accelerating while 2 m/s^{2}left turning at 80 km/h).

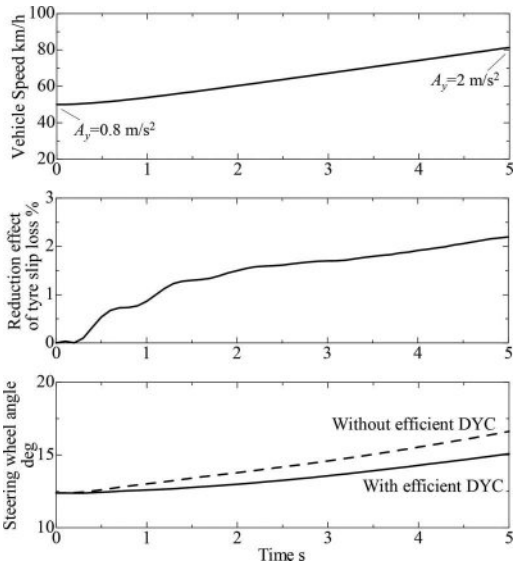


Figure 9. Full vehicle simulation result (accelerating while turning).

5 FULL VEHICLE SIMULATION

A full vehicle simulation was conducted to examine the effectiveness of the proposed control. In addition to yaw and lateral motions, this model can also calculate pitch and roll motions. The tyre force was calculated based on Magic Formula model. A linear load was assumed. A look-ahead driver model is employed to control the steering angle.

As an example, this paper compares the tyre slip loss during acceleration ($A_x = 2$ m/s^2) while turning in a R250 m circle. Figure 9 shows that the proposed control reduces the slip loss by approximately 2%. Additionally, the understeer caused by acceleration was also improved as described above. The proposed control can enhance both cornering efficiency and drivability.

6 CONCLUSIONS

This paper has described the development of an efficient DYC capable of minimizing tyre longitudinal and lateral slip losses. An analytical approach to formulate cornering resistance revealed that slip loss can be reduced using direct yaw moment because of the change in steering characteristics during acceleration and deceleration. An optimization problem was conducted to construct the DYC. As a result, it was found that an equalized tyre slip velocity vector was required to minimize the tyre slip loss. Moreover, the proposed control can also stabilize vehicle motion during acceleration and deceleration while turning.

REFERENCES

Abe, M. 2009. *Vehicle Handling Dynamics, Theory and Application*. Butterworth-Heinemann.

Abe, M. 2012. Evaluation of Active Vehicle Motion Controls from Tire Energy Dissipation Points of View. *AVEC 2012*.

Hancock, M. J., Williams, R. A., Gordon, T. J., & Best, M. C. 2005. A comparison of braking and differential control of road vehicle yaw-sideslip dynamics. *Proc. of IMechE* D(219): 309–327.

Katsuyama, E. 2013. Decoupled 3D Moment Control for Vehicle Motion Using In-Wheel Motors. *SAE Technical Paper* 2013-01-0679.

Kelly, D. P. & Sharp, R. S. 2012. Time-optimal control of the race car: influence of a thermodynamics tyre model. *Vehicle System Dynamics* 50(4): 641–662.

Kobayashi, T., Katsuyama, E., Sugiura, H., Ono, E., & Yamamoto, M. 2014. Direct Yaw Moment Control and Power Consumption of In-wheel Motor Vehicle. *AVEC '14*.

Mizuno, M., Sakai, H., Oyama, K., & Isomura, Y. 2005. Development of a tyre force model incorporating the influence of the tyre surface temperature. *Vehicle System Dynamics* 43: sup1. 395–402.

Nishihara, O. & Higashino, S. Optimum Distribution of Lateral and Traction/braking Forces for Energy Conservation. *IFAC AAC 2013*.

Osborn, R.P. & Shim, T. 2006. Independent control of all-wheel-drive torque distribution. *Vehicle System Dynamics* 44(7): 529–546.

Shibahata, Y., Shimada, K., & Tomari, T.. 1993. Improvement of Vehicle Maneuverability by Direct Yaw Moment Control. *Vehicle System Dynamics* 22(5): 465–481.

Sorniotti, A. 2009. Tire Thermal Model for Enhanced Vehicle Dynamics Simulation. *SAE Technical Paper* 2009-01-0441.

Advanced Vehicle Control – Edelmann, Plöchl & Pfeffer (Eds)
© 2017 Taylor & Francis Group, London, ISBN 978-1-138-02992-7

Torque vectoring control for different powertrain layouts of hybrid and electric vehicles

M. Vignati & E. Sabbioni
Department of Mechanical Engineering, Politecnico di Milano, Milan, Italy

ABSTRACT: In recent years the need in energy saving in transportation raised the attention on alternative powertrain. The main competitor of ICE become electric motors. With this type of powertrain it is possible to drastically change the power train layout of a vehicle. It is in fact possible to equip the vehicle with more than one single motor. In this paper the author analyses the effectiveness of a control strategy for lateral dynamics applied on different powertrain layouts comparing the performance of each layout with respect to others and with respect to the passive equivalent vehicle.

1 INTRODUCTION

Hybrid and electric vehicles (HEV) technology is developing really fast in last years, pushed by the need of energy saving for pollution reduction. The simplest way of designing an hybrid/electric vehicle with pure electric powertrain is to substitute the internal combustion engine (ICE) with and electric motor (EM). This solution, despite its simplicity, may not be the best solution in terms of efficiency and, moreover, it cannot exploit all the characteristics of an EM.

Consider in fact that an EM can easily drive or brake a wheel passing from one condition to the other with a really short delay. If more than one motor is mounted on the vehicle, e.g. one per each wheel, it is possible to design high level control strategies that can both increase energy efficiency in straightforward driving and vehicle safety and performance in lateral dynamics. Several examples are available in literature like (Sakai, Sado, & Hori 1999), (Osborn & Shim 2006), (Klomp, Lidberg, & Gordon 2014) and (De Novellis, Sorniotti, Gruber, Shead, Ivanov, & Hoepping 2012).

In this paper a newly designed control strategy for hybrid and electric vehicle with more than one EM is applied to different powertrain layouts.

2 DIFFERENT POWERTRAIN LAYOUTS FOR HEV

In figure 1 are reported some possible powertrain layouts for HEV; they can be summarized as follow:

layout A consist of four independent EM, one per each wheel. This solution has been studied by many authors since it seems the one that better allows to exploit all EM capabilities;

layout B consist of two independent EM on the rear axle;

layout C consist of two independent EM on the front axle;

layout D consist of one motor in the front axle, which can either be a conventional ICE or an EM, and two independent EM on the rear axle;

layout E is similar to layout B but the reversed. Two independent EM on front axle and one EM or ICE on rear axle.

3 VEHICLE MODEL

In order to evaluate the vehicle response in several manoeuvres, a 14 dofs model of the vehicle has been developed based on a segment D passengers car. It account for three displacement of vehicle cog, three rotation about cog, four vertical displacement of wheels and four angular velocity of wheels about hub axis. Main vehicle data are reported in table 1. Steer is accounted as a given input to the system.

In order to account for EM characteristics, the torque-speed curve is considered; also motor dynamics

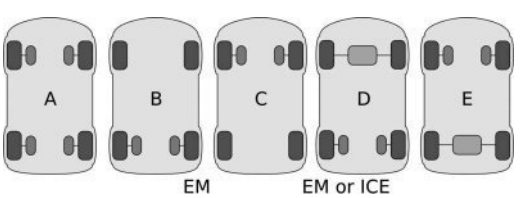


Figure 1. Powertrain layouts: A) 4 independent motors; B) 1 motor front 2 motors rear; C) 2 motors front 1 motor rear; D) 2 motors rear; E) 2 motors front.

Table 1. Main vehicle data.

description	symbol	unit	value
overall vehicle mass	m	kg	1580
wheel base length	l	m	2.7
weight distribution front/rear			62/38
front track width	c_f	m	1.54
rear track width	c_r	m	1.54
cog height from ground	h_G	m	0.58

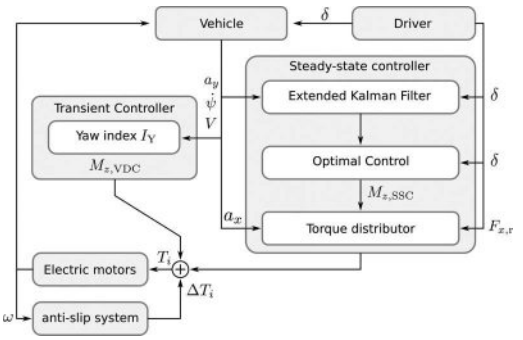


Figure 2. Main scheme of the controller.

is accounted by means of first order time lag transfer function that considers both motor and motor drive latency.

In order to better compare different layout, no change in weight distribution of the vehicle is considered.

4 CONTROL STRATEGY

The control strategy main scheme is reported in figure 2. For detailed description of the control strategy see (Vignati, Sabbioni, & Tarsitano ress). The controller is divided in two main contribution:

- the Vehicle Dynamics Controller (VDC) that increases vehicle lateral stability mainly in transient conditions;
- the Steady-State Controller (SSC) that increases vehicle cornering performances mainly in steady-state manoeuvres.

The two contributions generate a desired set of torques on wheels which are then summed according to the following equation

$$T_i = T_{i,VDC} + \zeta_{YI} T_{i,SSC} \tag{1}$$

where ζ_{YI} is a weight coefficient that ranges from 1 to zero in order to reduce the SSC contribution in transient critical manoeuvres where SSC contribution could be opposite to VDC contribution. To smooth transition, ζ_{YI} is a sigmoid function of $\left|\frac{a_y}{v_x}\right| - |\dot{\psi}|$.

4.1 *Vehicle dynamics controller*

VDC generate a yaw moment proportional to yaw index

$$M_{z,VDC} = k_{YI} I_Y = k_{YI} \left(\frac{a_y}{v_x} - \dot{\psi} \right) \tag{2}$$

which is related to transient over/understeering condition of the vehicle. Torques are distributed among wheels according to yaw index absolute value

$$T_{FR} = -T_{FL} = \begin{cases} \frac{M_{z,VDC}}{2 c_f R_r} & \left|\frac{a_y}{v_x}\right| < |\dot{\psi}| \\ 0 & \frac{a_y}{v_x} > |\dot{\psi}| \end{cases} \tag{3}$$

$$T_{RR} = -T_{RL} = \begin{cases} 0 & \left|\frac{a_y}{v_x}\right| < |\dot{\psi}| \\ \frac{M_{z,VDC}}{2 c_r R_r} & \frac{a_y}{v_x} > |\dot{\psi}| \end{cases} \tag{4}$$

where c_f and c_r are the front and rear track half width respectively and R_r is the rolling radius. If the i-th wheel doesn't have an independent motor, only braking torques are applied on it through the braking system. This results in a speed reduction but it can be accepted to avoid vehicle spin.

4.2 *Steady-state controller*

SSC is based on Optimal Control theory and it is coupled with Extended Kalman Filter for friction and sideslip angle estimation Optimal control theory is applied to a non linear single track vehicle model

$$\begin{Bmatrix} mV\dot{\beta} \\ J\ddot{\psi} \end{Bmatrix} = \begin{Bmatrix} F_{y,f} + F_{y,r} - V\dot{\psi} - a_x\beta \\ F_{y,f} l_f - F_{y,r} l_r + M_{z,SSC} \end{Bmatrix} \tag{5}$$

where m and J are respectively the mass and the yaw moment of inertia of the vehicle, a and b are the distance of the vehicle centre of mass from the front and rear axle respectively, M_z is the control action, i.e. the yaw moment generated by the controller. $F_{y,f}$ and $F_{y,r}$ are the cornering contact forces of the front and rear axle which are calculated according to MF-Tyre by Pacejka

$$F_{y,i} = \mu F_{z,i} d_i \sin[C_i \arctan(B_i \alpha_i)] \tag{6}$$

where μ is the mean friction coefficient between tyres and road, $F_{z,i}$ is the static load on the i-th axle, d_i is the ratio between the maximum lateral force $F_{y,\max}$ and the vertical load on the axle F_z.

Being x_r the reference state, the state deviation from reference is then

$$\Delta \boldsymbol{x} = \boldsymbol{x}_r - \boldsymbol{x} \tag{7}$$

which is supposed to be constant, the quadratic cost function for controller synthesis can be written as

$$J(\boldsymbol{x}, t) = \int_t^{t_f} (\Delta \boldsymbol{x}^T [Q] \Delta \boldsymbol{x} + \boldsymbol{u}^T [R]) \boldsymbol{u} dt \tag{8}$$

where $[Q] = [Q]^T \geq 0$ is a symmetric and positive semi-definite matrix and $[R] = [R]^T > 0$ is a symmetric and positive definite matrix.

In order to estimate the sideslip angle β and the friction coefficient μ, an Extended Kalman Filter has been designed based on vehicle non linear model equations (5). The state of the system is extended in order to account for friction contribution on vehicle dynamics. The friction coefficient is modelled as white Gaussian noise.

4.2.1 *Torque distribution strategy*

Once the Optimal Controller has generated a desired yaw moment M_z, torques have to be applied on wheels in order to generate this yaw moment. It has also to be considered that also the total driving/braking force required by the driver has to be satisfied:

$$F_{xFR} + F_{xFL} + F_{xRR} + F_{xRL} = F_x \tag{9}$$

$$(F_{xFR} - F_{xFL})c_f + (F_{xRR} - F_{xRL})c_r = M_z \tag{10}$$

also vertical load distribution among front and rear axle is considered

$$\frac{|F_{xFR}| + |F_{xFL}|}{|F_{xRR}| + |F_{xRL}|} = \frac{l_r - \frac{a_x}{g} h_G}{l_f + \frac{a_x}{g} h_G} \tag{11}$$

where l_f and l_r are the distance of the vehicle cog from front and rear axle respectively, h_G is the height of vehicle cog, g is gravity and a_x is the longitudinal acceleration of the vehicle.

When applying the torque distribution equation (9), (10) and (11) to the layouts of figure 1, some other constraints have to added:

Layout B $F_{xFR}, F_{xFL} \leq 0$ it means that on front axle only braking torques can be developed;
Layout C $F_{xRR}, F_{xRL} \leq 0$ it means that on rear axle only braking torques can be developed;
Layout D $F_{xFR} = F_{xFL}$ it means that on front axle driving torques are the same due to differential;
Layout E $F_{xRR} = F_{xRL}$ it means that on rear axle driving torques are the same due to differential.

5 RESULTS

In order to assess the control performances associated to each powertrain layout, several standard manoeuvres for vehicle dynamics evaluation have been simulated.

5.1 *Steady-state circular driving behaviour*

Steady state performances are evaluated by means of steering pad constant radius manoeuvre. In figure 3 results of the simulation are reported. In particular for each layout the active vehicle is compared with the corresponding passive vehicle. Table 2 reports instead the

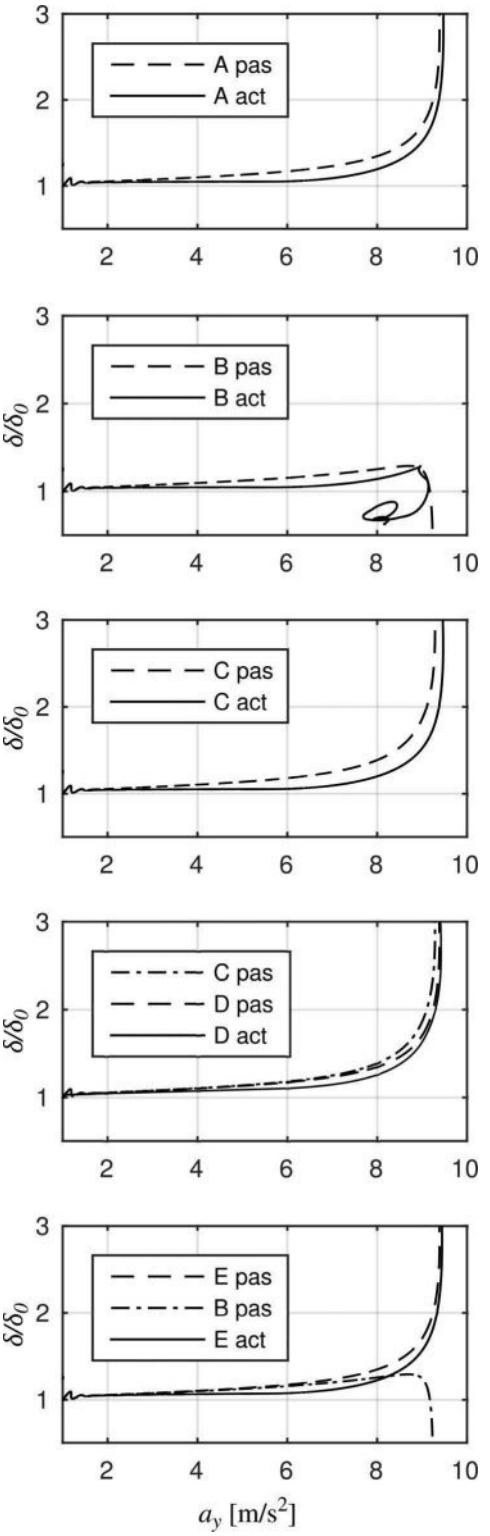


Figure 3. Steering Pad Constant Radius manoeuvre. Comparison of different layout with corresponding passive vehicle.

numerical values of normalized steering angle for different values of lateral acceleration for active vehicles in order to compare active layouts with each other.

In general it can be observed that the active vehicle presents higher linear behaviour and an higher value of maximum lateral acceleration is achieved.

Layout B is unstable in passive configuration while active configuration is stable, in fact the active vehicle, when its becomes oversteering, presents a cut off of the longitudinal force required by the transient controller which allows to maintain the vehicle on the desired path with a constant longitudinal speed and a limited sideslip angle despite the request of the driver to accelerate.

Layout C presents the best improvement with respect to its corresponding passive vehicle. In fact linear behaviour is largely increased and the maximum lateral acceleration achieved is increased of about 2%.

Layout D is compared both with layout D passive and with layout C passive. This is done in order to evaluate the effect of adding an independently wheel driven rear axle to a front wheel driven vehicle (passive layout C is in fact equivalent to a FWD vehicle with one motor and a differential, longitudinal forces on the front axle are the same due to differential). Layout D active vehicle presents an increase in linearity with respect to passive 4WD vehicle and a little increase in maximum lateral acceleration. Instead higher improvement are obtained with respect to FWD passive vehicle where the maximum lateral acceleration is increased of about 1.4%.

Layout E is compared, as done for layout D, with both E passive layout and B passive layout. Like layout D, little improvement are obtained with respect to 4WD passive vehicle while high improvement are obtained with respect to passive RWD vehicle. In particular the oversteering behaviour is cancelled and the maximum lateral acceleration is increased of about 2.3%.

Comparing the active layouts, the one which presents better performances in terms of linearity is layout B but it presents the worse value of maximum lateral acceleration and the abrupt intervention of transient controller is not so indicated for commercial vehicles. The layout which instead presents the higher value of lateral acceleration is layout A. The small advantage obtained with respect to layout C makes this second layout preferable for its lower complexity. For sure layout A remains preferable when accelerating the vehicle in straightaway.

It is to point out that the passive vehicle is an understeering vehicle and the controller reference is generated in order to reduce this understeering behaviour. If the passive vehicle presents different under/oversteer behaviour the intervention of the control can change and may be tuned properly.

5.2 *Transient cornering behaviour*

Transient behaviour of the vehicle is evaluated through simulation of ATI90-90 manoeuvre. The vehicle at the beginning of the manoeuvre has a speed of 75 km/h and no intervention is made on brakes and accelerator pedal. The steer is applied in open loop.

In figure 4 steering wheel angle δ_{SW}, yaw rate $\dot{\psi}$, longitudinal speed v_x, sideslip angle β and lateral acceleration a_y are reported. The passive vehicle is the same for all layouts since no torques on wheels are applied. Considering this condition layout B and D are equivalent since torque vectoring is fully exploited only by independent wheel driven axles, on other axle only braking torques are applied through hydraulic brakes; the same consideration is done for layout C and E.

Layout B (same as D) is the less suitable for damping vehicle oscillations in particular when the vehicle is spinning. This can be easily explained by considering the friction limit of tyre in combined slip condition. This configuration can be useful when reducing understeer and in sub-limit driving conditions ((Pinto, Aldworth, Watkinson, Jeary, & Franco-Jorge 2010) reports same results). Layout C (same as E) presents comparable results with layout A which is the most performing. Both layout reduce oscillations of yaw rate, sideslip angle and lateral acceleration, this results in an increase of vehicle damping. Also, the vehicle promptness is increased, the delay between the steer input and the vehicle response in terms of yaw rate and lateral acceleration is increase with respect to passive vehicle. At the end of the manoeuvre layout A presents the top longitudinal speed, this is due to the higher effectiveness of the controller which is capable of increasing vehicle stability without reducing longitudinal speed.

Table 2. Steering pad constant radius. δ/δ_0 for different value of lateral acceleration and maximum lateral acceleration value. Comparison between active layouts.

	A	B	C	D	E
a_y [m/s^2]			δ/δ_0		
3	1.044	1.042	1.045	1.061	1.054
5	1.049	1.045	1.050	1.083	1.064
7	1.089	1.073	1.091	1.144	1.111
9	1.516	1.285	1.520	1.627	1.526
a_y max	9.476	9.141	9.470	9.416	9.445

Table 3. ATI9090.

	A	B	C	pas
$\dot{\psi}_{\max}$ [deg/s]	30.98	31.78	35.05	36.96
$\dot{\psi}_{\max}/\dot{\psi}_{ss}$	1.079	1.107	1.221	1.287
$t(\dot{\psi}_{\max})$ [s]	1.37	1.37	1.37	1.49
$\beta_{\max}$ [deg]	2.00	2.07	7.47	5.15
$v_x(t_{\text{end}})$ [km/h]	58.83	58.44	52.53	56.92

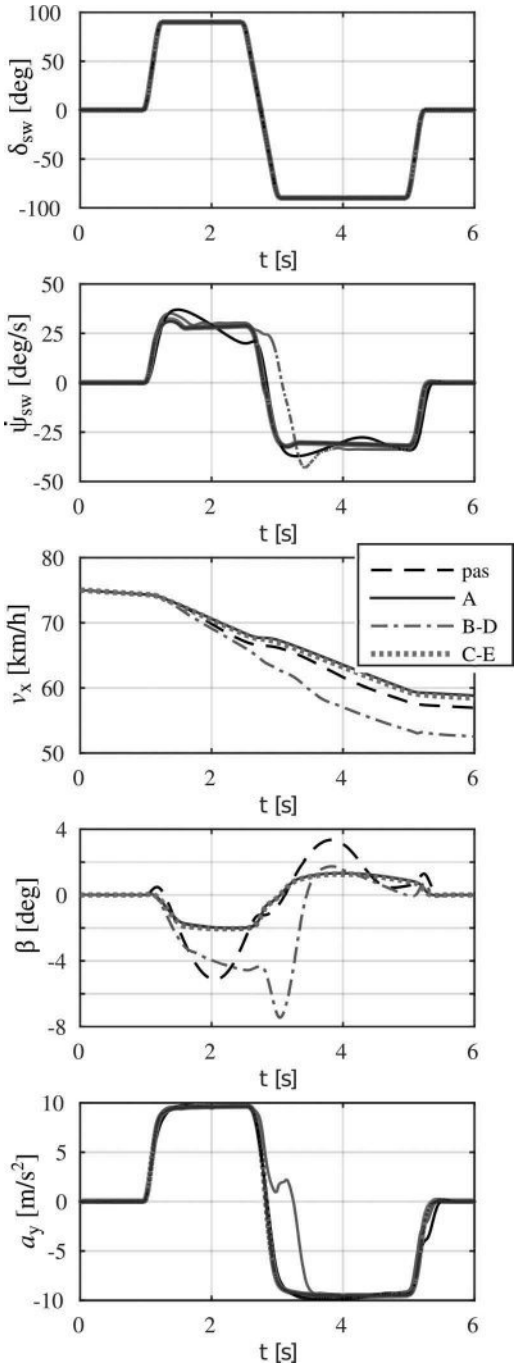


Figure 4. ATI 90-90 manoeuvre. Comparison of different powertrain layout and with passive vehicle.

6 CONCLUSIONS

Several layout for HEV have been compared by means of numerical simulations. Considered layouts are compared with their corresponding passive vehicle in terms of lateral dynamics behaviour in steady-state and in transient conditions. Four independent wheel driven vehicle (layout A) seams to be the most performing both in steady-state and in transient conditions. Rear independent wheel driven vehicle (layout B) presents an increase in steady-state performances with respect to passive vehicle but is not so effective in damping oscillation in transient, in fact hydraulic brakes intervention on the front axle is needed. Front independent wheel driven vehicle (layout C) is the most improving layout with respect to the corresponding passive vehicle; the only concern related to this layout is the performance comparison in pure longitudinal acceleration with respect to other layouts which was not enquired in this paper. Layout D and E can be an optimal solution for expanding performances of existing vehicle with a plug-in solution on front/rear axle. In particular the plug-in solution of a front axle with independent motors allows to obtain high benefits for rear wheel drive conventional sport cars in particular in cornering promptness and moreover in stability enhancing. The presented control strategy is applied to an understeering passive vehicle, effectiveness of the controller can change if applied to a passive vehicle with difference steady-state behaviour.

REFERENCES

De Novellis, L., A. Sorniotti, P. Gruber, L. Shead, V. Ivanov, & K. Hoepping (2012). Torque vectoring for electric vehicles with individually controlled motors: state-of-the-art and future developments. In *26th Electric Vehicle Symposium 2012.*

Klomp, M., M. Lidberg, & T. Gordon (2014). On optimal recovery from terminal understeer. *Proceedings of the Institution ofMechanical Engineers, Part D: Journal of Automobile Engineering 228*(4), 412–425. cited By 2.

Osborn, R. P. & T. Shim (2006). Independent control of all-wheel-drive torque distribution. *Vehicle system dynamics 44*(7), 529–546.

Pinto, L., S. Aldworth, M. Watkinson, P. Jeary, & M. Franco-Jorge (2010). Advanced yaw motion control of a hybrid vehicle using twin rear electric motors. In *Advanced Vehicle Control*, Volume 4, pp. 640–645.

Sakai, S.-i., H. Sado, & Y. Hori (1999). Motion control in an electric vehicle with four independently driven in-wheel motors. *Mechatronics, IEEE/ASME Transactions on 4*(1), 9–16.

Vignati, M., E. Sabbioni, & D. Tarsitano (in press). Torque vectoring control for iwm vehicles. *International Journal of Vehicle Performance.*

Vertical dynamics

Advanced Vehicle Control – Edelmann, Plöchl & Pfeffer (Eds)
© 2017 Taylor & Francis Group, London, ISBN 978-1-138-02992-7

A study on invariant points of semi-active suspension

Ye Zhuang, Shida Nie, Fan Chen & Jie Xie
State Key Laboratory of Automotive Simulation and Control, Jilin University, Changchun, Jilin, China

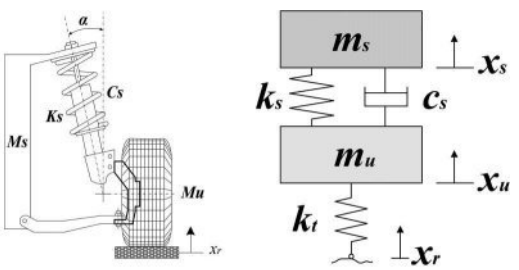
ABSTRACT: The invariant points of the quarter vehicle 2-DOF model shape many properties that concerned in vehicle suspension design. According to their traits, the invariant points are sorted into three categories in this paper. Then, the invariant points of semi-active suspension are proposed, which were not ever mentioned in the past. An equivalent linear approximate model is derived from the transformation of the sky-hook semi-active suspension model, which is utilized to analyze the invariant points of semi-active suspension. Finally, the effects of invariant points on suspension design and control are discussed.

1 INTRODUCTION

Usually, two kind of quarter vehicle model are utilized to deal with the suspension analysis and design, which are shown in Figure 1. The multi-body suspension model, as in Figure 1(a), could describe the suspension in more detail and express the nonlinear geometry and dynamics well. While, the 2-DOF system, as in Figure 1(b) simplify the suspension into the upper sprung mass and unsprung mass which are connected by linearized suspension spring and damper. Simplification of the suspension model brings the following advantages to suspension study (Karnopp, 2009).

- Less parameters are needed to complete analysis, and valid results can be easily obtained;
- High efficiency in controllable suspension study, such as semi-active and active suspension;
- Good generality of different suspension structure.

The invariant point is a typical phenomenon that only suit for the simplified suspension model neglecting tire damping (Hrovat, 1997; Karnopp, 2009; Savaresi et al., 2010).

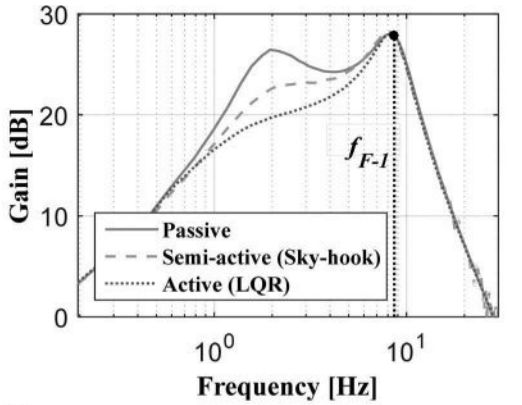


(a) Multi-body model (b) Simplified Model

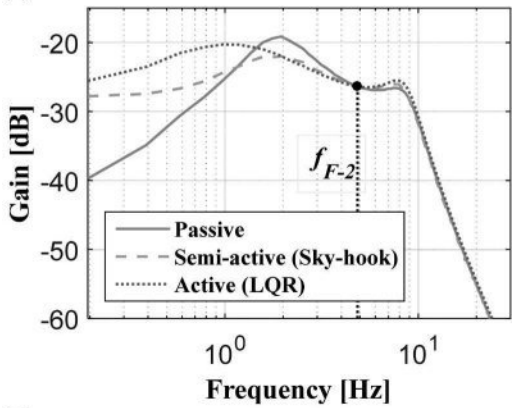
Figure 1. Quarter vehicle model.

Invariant points are some special points in frequency response curve of vehicle body acceleration, tire relative vertical load, suspension deflection, or other associated frequency response. These special points have certain response at certain excited frequencies. Karl. Hedrick derived invariant points through studying three transfer function of interest (acceleration, suspension deflection and tire deflection) and made an investigation of suspension improvement limits (Hedrick and Butsuen, 1990). R. Rajamani studied the invariant points of a vibration system that has the same 2-DOF structure and an opposite vibration transfer path compared with the quarter vehicle (Rajamani and Larparisudthi, 2004). This study analyses the invariant points' existence with two kinds of input applied to the machine, force and displacement. And the influence of invariant points on active vibration isolation was also thoroughly researched. D. Karnopp considered the invariant points as the 'fruit on an oversimplified tree' (Karnopp, 2009) which is much in line with the study of Levitt and Zorka (Levitt and Zorka, 1991), that even a small amount of tire damping could alter the above invariance and lead to a significant change in body acceleration around the wheel-hop frequency. This left suspension designers with hope that better suspension can be designed despite the strong limitations implied by the simple linear quarter car model.

All the invariant points mentioned above depend only on tire stiffness, sprung mass and unsprung mass, but not on suspension stiffness, damping or active actuator force. Furthermore, they are suit for passive, semi-active and active suspension. S.M. Savaresi derived several invariant points that only suit for passive quarter vehicle model (Savaresi et al., 2010). These invariant points depend on tire stiffness, sprung mass, unsprung mass and suspension stiffness, not on suspension damping. Although suit only for passive quarter vehicle, they are of particular interest for the semi-active suspension application.



(a)



(b)

Figure 2. FIPs of the concerned transfer functions (a) sprung mass acceleration; (b) suspension deflection.

The invariant properties of the suspension have been studied for decades. Various invariant points were presented. Yet, classification of them is in need to clearly understand the usage and limitations among different kind of invariant points. In this paper, the invariant points presented in the literatures are reviewed and sorted. The properties of them are summarized. Then, the invariant points of semi-active suspension are proposed. An equivalent linear approximate model (ELAM) is proposed to analyze the invariant points of semi-active suspension. At last, the effects and inspirations of invariant points on suspension design and control are summarized.

2 SIMPLIFIED SUSPENSION MODEL

The simplified suspension model shown in Figure 1(b) is studied by many researchers. The two DOFs of this model are vehicle wheel displacement x_u and body bounce x_s that are both in vertical direction. The road vertical excitation is signified by x_r. In this model, sprung mass and unsprung mass are expressed by m_s and m_u respectively. The suspension system is modeled by a linear spring k_s and damper c_s. As for active suspension, the damper can be replaced by an actuator. The tire is simplified by a linear spring k_t. Damping of the tire is often neglected in this model to approximate to the reality (Karnopp, 2009).

Table 1. Frequencies of the FIPs.

Transfer function	Frequency
$H_a(s)$	$2\pi f_{F-1} = \omega_{F-1} = \omega_u$
$H_d(s)$	$2\pi f_{F-2} = \omega_{F-2} = \sqrt{k_t/(m_s + m_u)}$

3 FIXED INVARIANT POINTS (FIPs)

As introduced above, a kind of invariant points depend only on tire stiffness, sprung mass and unsprung mass, but not on suspension stiffness, damping or active actuator force. In other word, only if the simplified quarter vehicle model is used, this kind of invariant points always exist, no matter passive, semi-active or active suspension, which is defined as Fixed Invariant Points (FIPs).

Transfer functions from road velocity to sprung mass acceleration $H_a(s)$, tire relative dynamic load $H_{TDL}(s)$ and suspension deflection $H_d(s)$ are usually related to ride comfort, road-holding and suspension limitation. Hence, the invariant points of the three concerned transfer functions have great effects on suspension designing and tuning.

FIPs could be observed only in the two transfer functions shown in Figure 2. The frequencies of the FIPs are presented in Table 1.

In which, $\omega_u = \sqrt{k_t/m_u}$ is the second order resonance frequency.

4 INVARIANT POINTS OF LINEAR-TIME-INVARIANT MODEL (LIPs)

This kind of invariant points are unique to linear-time-invariant suspension model, i.e. linear passive suspension model. LIPs reflect the effect of damping on suspension performance, which could be helpful to control designing of semi-active suspension. The LIPs of the two concerned transfer functions are shown in Figure 3.

In suspension designing, the key goal is to improve ride qualities and road-holding. Some concerned properties of invariant points are concluded in Figure 4:

- Soft damping is needed to reduce *vehicle body acceleration* after f_{L-1} except the frequency range between f_{F-1} and f_{L-2} (Refer to Figure 3(a)).
- Soft damping is needed to reduce *tire relative vertical load* between f_{L-3} and f_{L-4}. Hard damping is needed in other frequencies (Refer to Figure 3(b)).

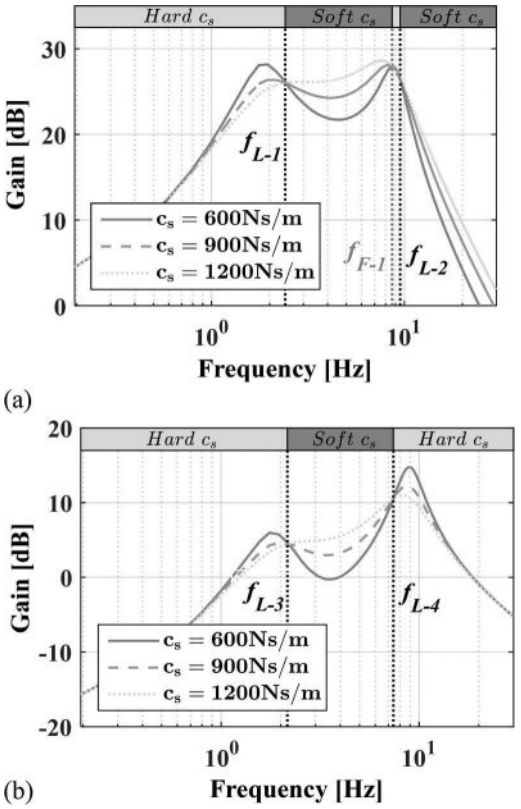


Figure 3. LIPs of the concerned transfer functions (a) sprung mass acceleration; (b) tire relative dynamic load.

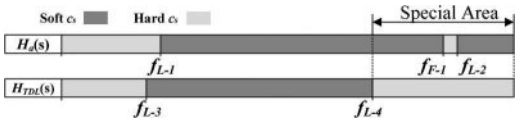


Figure 4. Influence of suspension damping value c_s on suspension performance.

As shown in Figure 4, it is still a problem to balance ride-qualities and road-holding, especially in the frequency range after f_{L-4}. In this area, the needed damping of ride-qualities contradicts that of road-holding. This explains the dilemma of passive suspension design to balance ride-qualities and road-holding. In terms of the semi-active suspension, even without the LIPs, the effect of damping on ride-qualities and road-holding still follows this law (Hedrick and Butsuen, 1990). Hence, it is clear that semi-active suspension has the same special range of frequencies to balance ride-qualities and road-holding.

The frequencies of LIPs are presented in Table 2.

In which,

$$\alpha = \omega_s^2 + \omega_{su}^2 + \frac{\omega_u^2}{2}, \quad \beta = \frac{m_u + m_s}{2m_u}\omega_s^2 + \frac{m_s + 2m_u}{4(m_s + m_u)}\omega_u^2,$$
$$\omega_s = \sqrt{k_s/m_s}, \quad \omega_{su} = \sqrt{k_s/m_u}$$

Table 2. Frequencies of the LIPs.

Transfer function	Frequency
$H_a(s)$	$2\pi f_{L-1} = \omega_{L-1} = \sqrt{\alpha - \sqrt{\alpha^2 - 2\omega_s^2\omega_u^2}}$
	$2\pi f_{L-2} = \omega_{L-2} = \sqrt{\alpha + \sqrt{\alpha^2 - 2\omega_s^2\omega_u^2}}$
$H_{TDL}(s)$	$2\pi f_{L-3} = \omega_{L-3} = \sqrt{\beta - \sqrt{\beta^2 - \omega_s^2\omega_u^2}}$
	$2\pi f_{L-4} = \omega_{L-4} = \sqrt{\beta + \sqrt{\beta^2 - \omega_s^2\omega_u^2}}$

The frequencies of LIPs on each transfer functions have the properties as follows:

$$\text{On } H_a(s), \ \omega_{L-1}\omega_{L-2} = \sqrt{2}\omega_s\omega_u \tag{1}$$

$$\text{On } H_{TDL}(s), \ \omega_{L-3}\omega_{L-4} = \omega_s\omega_u \tag{2}$$

5 INVARIANT POINTS OF SEMI-ACTIVE SUSPENSION (SIPs)

5.1 *Semi-active suspension modelling*

The sky-hook semi-active suspension model can be written as follows:

$$\begin{aligned} m_s\ddot{x}_s + k_s(x_s - x_u) + c_s(\dot{x}_s - \dot{x}_u) &= 0 \\ m_u\ddot{x}_u + k_t(x_u - x_r) - k_s(x_s - x_u) - c_s(\dot{x}_s - \dot{x}_u) &= 0 \end{aligned} \tag{3}$$

$$c_s = \left(\frac{\Lambda c}{2} + \frac{\Delta c}{2}\mathbf{sgn}(\dot{x}_s\dot{x}_{def})\right) \tag{4}$$

In which, $\Lambda c = c_{\max} + c_{\min}$, $\Delta c = c_{\max} - c_{\min}$. $c_{\max}$ signifies the maximum damping of a semi-active controlled damper; $c_{\min}$ signifies the minimum damping of a semi-active controlled damper. $\dot{x}_{def} = \dot{x}_s - \dot{x}_u$ signifies the differential of suspension deflection. Sign function $\mathbf{sgn}(x)$ extracts the sign of a real number x to realize the control switching.

$$\mathbf{sgn}(x) = \begin{cases} 1 & x \geq 0 \\ -1 & x < 0 \end{cases} \tag{5}$$

Figure 5 shows the frequency responses of two concerned transfer functions $H_a(s)$, $H_{TDL}(s)$. Different dampers are adopted in semi-active suspension. The Δc of different dampers have the same value 300 N·s/m. The Λc value of the dampers is an arithmetic progression. In Figure 5, it is easy to be found that the frequency response curves intersect in some points. The number of the points is equal to LIPs and the positions are similar to LIPs. They are named as SIPs in this paper.

The frequency response of sky-hook semi-active suspension with different dampers present similar properties to passive suspensions. Large or small Λc is needed in different frequency range for good vehicle

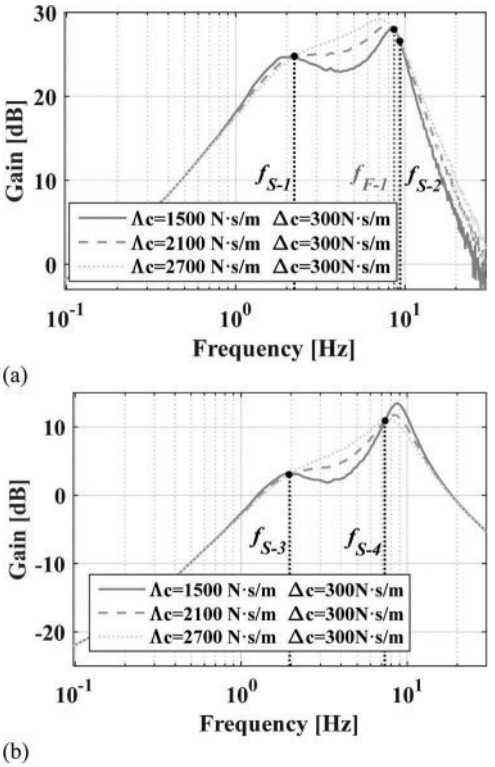


Figure 5. SIPs of the concerned transfer functions (a) sprung mass acceleration; (b) tire relative dynamic load.

performance. But it is not obvious before f_{s-1} in Figure 5(a) and before f_{s-3} in Figure 5(b), i.e. the first order resonance in both frequency responses. This property is attributed to the better performance of sky-hook suspension around first order resonance.

5.2 *Derivation of SIPs*

Since semi-active control algorithms, such as that in equation 4, are nonlinear, the close-loop system also behaves nonlinear (Poussot-Vassal et al., 2008). Hence, it is hard to derive analytical expressions of the concerned transfer characteristics. It is also difficult to derive the invariant points. To deduce the expression of SIPs, linear approximation of sky-hook semi-active suspension is proposed in this paper. As shown in Figure 6, the semi-active suspension is approximately equivalent to a passive suspension. The passive suspension has a constant damping of $\Lambda c/2$. The stiffness is also constant, the value of which will be determined in the following.

In equivalent linear approximate model, it is assumed that the total suspension force generated by spring and damper remains the same. So, we can get,

$$\begin{aligned} &k_s\left(x_s-x_u\right)+c_s\left(\dot{x}_s-\dot{x}_u\right) \\ &=\tilde{k}_s\left(x_s-x_u\right)+\frac{\Lambda c}{2}\left(\dot{x}_s-\dot{x}_u\right) \end{aligned} \tag{6}$$

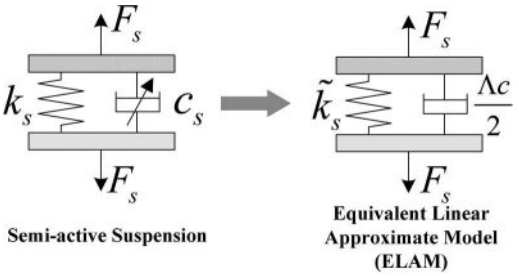


Figure 6. Linear approximation of semi-active suspension.

Substitute Equation (4) into Equation (6), and simplify it, we can get,

$$\tilde{k}_s=k_s+\frac{\Delta c}{2}\left|\dot{x}_{def}\right|\frac{\mathbf{sgn}\left(\dot{x}_s\right)}{x_{def}} \tag{7}$$

With suspension model (3), it is easy to get the transfer function from $\dot{x}_s$ to x_{def}.

$$H_m\left(s\right)=-\frac{m_s s}{c_s s+k_s} \tag{8}$$

Hence, the phase angle between $\dot{x}_s$ and x_{def} can be expressed as:

$$\underline{\left|H_m\left(s\right)\right.}=180°+\underline{\left|\frac{m_s s}{c_s s+k_s}\right.}=180°+\arctan\left(\frac{k_s}{c_s\omega}\right) \tag{9}$$

In which, $\omega\in\mathbb{R}^+$ is the frequency range involved in the vibration of vehicle. Therefore, the phase angle $\underline{\left|H_m(s)\right.}\in(180°,270°)$. With the increase of frequency ω, the phase angle tends to 180°, which means the directions of $\dot{x}_s$ and x_{def} are almost opposite. Hence, equation (7) can be approximately equivalent to the following.

$$\tilde{k}_s\approx k_s-\frac{\Delta c}{2}\left|\frac{\dot{x}_{def}}{x_{def}}\right| \tag{10}$$

$\left|\frac{\dot{x}_{def}}{x_{def}}\right|\in\mathbb{R}^+$ is a variable which related to vehicle parameters including Δc. Since the ELAM is a time-invariant system, the suspension stiffness $\tilde{k}_s$ should also be time-invariant. Therefore, it is assumed that:

$$\frac{1}{2}\left|\frac{\dot{x}_{def}}{x_{def}}\right|\approx\lambda\Delta c \tag{11}$$

In which, $\lambda\in\mathbb{R}^+$ is a constant which is related to quarter vehicle parameters. Combining equation (10) with (11), the stiffness of ELAM can be expressed as:

$$\tilde{k}_s=k_s-\lambda\Delta c^2 \tag{12}$$

Table 3. Frequencies of the SIPs.

Transfer function	Frequency
$H_a(s)$	$2\pi f_{S-1}=\omega_{S-1}=\sqrt{\tilde{\alpha}-\sqrt{\tilde{\alpha}^2-2\tilde{\omega}_s^2\omega_u^2}}$
	$2\pi f_{S-2}=\omega_{S-2}=\sqrt{\tilde{\alpha}+\sqrt{\tilde{\alpha}^2-2\tilde{\omega}_s^2\omega_u^2}}$
$H_{TDL}(s)$	$2\pi f_{S-3}=\omega_{S-3}=\sqrt{\tilde{\beta}-\sqrt{\tilde{\beta}^2-\tilde{\omega}_s^2\omega_u^2}}$
	$2\pi f_{S-4}=\omega_{S-4}=\sqrt{\tilde{\beta}+\sqrt{\tilde{\beta}^2-\tilde{\omega}_s^2\omega_u^2}}$

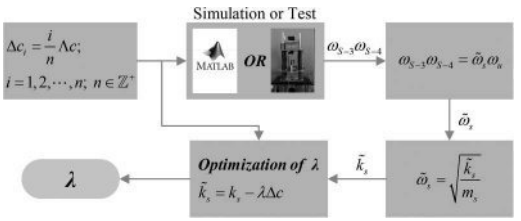


Figure 7. Identification procedure of λ.

In which, $\lambda\in\mathbb{R}^+$ is a constant which is related to quarter vehicle parameters.

After linear approximation of sky-hook semi-active suspension, the frequency of SIPs can be derived in the same way with LIPs, which is presented in (Savaresi et al., 2010).

In which,

$$\tilde{\alpha}=\tilde{\omega}_s^2+\tilde{\omega}_{su}^2+\frac{\omega_u^2}{2},\quad \tilde{\beta}=\frac{m_u+m_s}{2m_u}\tilde{\omega}_s^2+\frac{m_s+2m_u}{4(m_s+m_u)}\omega_u^2,$$
$$\tilde{\omega}_s=\sqrt{\tilde{k}_s/m_s},\quad \tilde{\omega}_{su}=\sqrt{\tilde{k}_s/m_u},\quad \tilde{k}_s=k_s-\lambda\Delta c^2$$

5.3 *Identification of* λ

As introduced above, λ is a constant related to vehicle parameters. Therefore, a certain vehicle has specific λ. With the expression shown in Table 3, the following properties can be obtained easily to identify the value of λ.

$$\omega_{S-1}\omega_{S-2}=\sqrt{2}\tilde{\omega}_s\omega_u \tag{13}$$

$$\omega_{S-3}\omega_{S-4}=\tilde{\omega}_s\omega_u \tag{14}$$

The identification procedure of λ is shown in Figure 7. Simulation or test is conducted with a set of Δc to calculate the product of ω_{S-3} and ω_{S-4}. Then, the value of $\tilde{k}_s$ can be calculated with equation (14) and the expression of $\tilde{\omega}_s$. At last, the value of λ is identified with a set of Δc and $\tilde{k}_s$.

5.4 *Example study*

The parameters of the studied quarter vehicle are given in Table 4.

Table 4. Parameters of the studied quarter vehicle.

Parameter	Value
m_s [kg]	86
m_u [kg]	40
k_s [N/m]	12060
k_t [N/m]	117000
Λc [N·s/m]	[1200, 3000]
Δc [N·s/m]	[0, Λc]

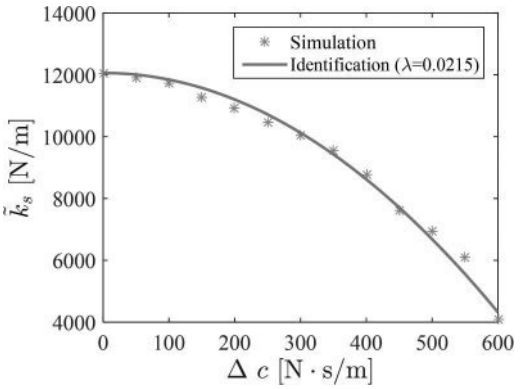


Figure 8. Relationship between equivalent stiffness $\tilde{k}_s$ and damping difference Δc.

Simulation is adopted in the identification process. As shown in Figure 8, the equivalent stiffness $\tilde{k}_s$ and damping difference Δc present a quadratic relationship. The identified value of λ is 0.0215. The identification result fits the simulation well.

To validate the effect of equivalent linear approximation, simulation is conducted to compare the frequencies of SIPs and invariant points of the proposed model. The damping difference Δc is selected as 500 N·s/m. With the identified λ, the equivalent stiffness $\tilde{k}_s$ can be easily calculated as 6932.6 N/m. Two sets of Λc, 1800 and 2400 N·s/m, are adopted in the simulation.

Figure 9 shows the frequency responses of two concerned transfer functions $H_a(s)$, $H_{TDL}(s)$. The two frequency responses of ELAM have a similar trend to semi-active suspension as a whole. As shown in magnified figures of SIPs, the curves of ELAM cross at the SIPs. In conclusion, ELAM can behave similar to a semi-active suspension.

6 SUMMARY AND PROSPECT

As the invariant points being independent of suspension force, FIPs appear in all kinds of suspensions, including passive, semi-active and active suspensions. The FIPs give insights into the suspension design limitations. However, these limitations suit only for simplified vehicle model. When tire damping or nonlinear properties of suspension structure is considered, the

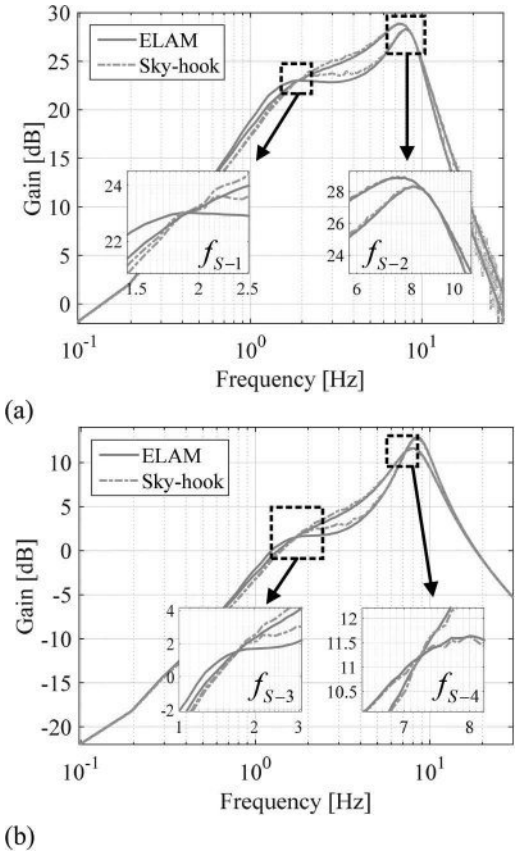


Figure 9. SIPs of the concerned transfer functions (a) sprung mass acceleration; (b) tire relative dynamic load.

FIPs will disappear. Hence, vehicle performance still has potential to be improved in actual development.

In passive suspensions, the LIPs give insights into the effects of damping on vehicle performance. LIPs are critical points across which a certain damping has opposite effects on vehicle. This characteristics of LIPs are helpful to develop semi-active control algorithms.

The invariant points in semi-active suspension which have similar properties to LIPs are named SIPs. Due to nonlinear properties of semi-active suspension, it is not easy to derive their expressions. Hence, ELAM is proposed to obtain the frequency expressions of SIPs. As shown in Figure 10, the frequencies of SIPs derived with ELAM (analytic solution) fit the simulation results of semi-active suspension (numerical solution) well. Due to the limitation on suspension static deflection in vehicle design, ELAM with a small stiffness is suitable for theoretical analysis, not for actual suspension design.

Around the first resonance frequency, the SIPs limit the control effect of sky-hook algorithm. However, the

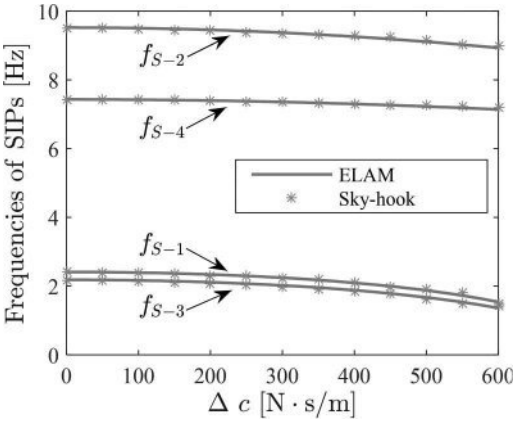


Figure 10. Influence of Δc on frequencies of SIPs.

frequencies of SIPs decrease as the damping difference Δc increasing (see Figure 10). This characteristic suggests that a large damping difference could help the sky-hook suspension to perform better.

In this paper, the invariant points from the literature are reviewed and sorted. An equivalent linear approximate model of semi-active suspension is introduced to analyze the properties of SIPs, which is proved to be effective. Up to now, the equivalent linear approximate model is built based on the sky-hook suspension. Later on, this method could be applied to more semi-active suspensions control algorithms.

REFERENCES

Hedrick JK & Butsuen T 1990 Invariant properties of automotive suspensions. *ARCHIVE: Proceedings of the Institution of Mechanical Engineers, Part D: Journal of Automobile Engineering 1989–1996 (vols 203–210)* 204(14): 21–27.

Hrovat D 1997 Survey of Advanced Suspension Developments and Related Optimal Control Applications. *Automatica* 33(10): 1781–1817.

Karnopp D 2009 How significant are transfer function relations and invariant points for a quarter car suspension model? *Vehicle System Dynamics* 47(4): 457–464.

Levitt JA & Zorka NG 1991 The Influence of Tire Damping in Quarter Car Active Suspension Models. *Journal of Dynamic Systems, Measurement, and Control* 113(March 1991): 134.

Poussot-Vassal C, Sename O, Dugard L, et al. 2008 A new semi-active suspension control strategy through LPV technique. *Control Engineering Practice* 16(12): 1519–1534.

Rajamani R & Larparisudthi S 2004 On invariant points and their influence on active vibration isolation. *Mechatronics* 14: 175–198.

Savaresi SM, Poussot-Vassal C, Spelta C, et al. (2010) *Semi-Active Suspension Control Design for Vehicles*. Elsevier.

Advanced Vehicle Control – Edelmann, Plöchl & Pfeffer (Eds)
© 2017 Taylor & Francis Group, London, ISBN 978-1-138-02992-7

Dynamic sensitivity analysis of a suspension model

S. Hamza & F. Anstett-Collin
Centre de Recherche en Automatique de Nancy (UMR 7039), Université de Lorraine, France

Q. Li & L. Denis-Vidal
Laboratoire de Mathématiques Appliquées de Compiègne (EA 2222), Sorbonne Universités, Université de Technologie de Compiègne, France

A. Birouche & M. Basset
Laboratoire Modélisation, Intelligence, Processus, Systèmes (EA 2332), Université de Haute-Alsace, France

ABSTRACT: A sensitivity analysis of a suspension model has been performed in order to highlight the most influential parameters on the sprung mass displacement. To analyse this dynamical model, a new global and bounded dynamic method is investigated. This method, based on the interval analysis, consists in determining lower and upper bounds including the dynamic sensitivity indices. It requires only the knowledge of the parameter variation ranges and not the joint probability density function of the parameters which is hard to estimate. The advantage of the proposed approach is that it takes into account the recursive behavior of the system dynamics.

1 INTRODUCTION

Suspension plays an important role in vehicle safety and road holding. In general, the suspension system behavior is described by dynamical models depending on parameters that are subject to uncertainty due to insufficient knowledge, measurement error or imprecision, etc. Sensitivity analysis can help to evaluate the impact of this lack of knowledge on the model response, which here is the displacement of the sprung mass.

Numerous studies have focused on the sensitivity analysis for static models (Saltelli, Ratto, Andres, Campolongo, Cariboni, Gatelli, Saisana, & Tarantola 2008). In the case of dynamical models, local approaches based on partial derivatives are often used. However, in the automotive field, it can be of great importance to consider the entire uncertainty range of parameters since they can vary within large intervals depending on their meaning. Few global approaches have been proposed for dynamical models. In general, these methods are statistical and are based on the analysis of the output variance. In the case of dynamical model, they consist in computing the sensitivity indices at each time instant (Haro Sandoval, Anstett-Collin, & Basset 2012). This can lead to an important amount of informations, not easy to analyse. Moreover, these approaches require the knowledge of the joint probability density function of the parameters which is hard to estimate. In this work, a new sensitivity analysis method based on interval analysis is provided.

The key idea is to determine upper and lower bounds including the sensitivity functions, based on the knowledge of the parameter variation ranges. If they exist, these bounds are guaranteed (Lin & Stadtherr 2008). Unlike the statistical methods, the proposed approach does not require the knowledge of the joint probability density function of the parameter. Furthermore, the approach takes into account the recursive behavior of the system dynamics. This paper is organized as follows: in section 2 problem statement is introduced. In section 3, partial derivative based sensitivity analysis method is described. In section 4, the principle of interval analysis technique is introduced. An illustrative example, is presented in the end of section 3 and 4. In section 5, an application of the method on a quarter vehicle model is presented. Conclusion is given in section 6.

2 PROBLEM STATEMENT

Consider a linear dynamic model represented in the state space form as:

$$\begin{cases} \dot{x}(t) = A(\theta)\,x(t) + B(\theta)\,u(t) \\ y(t) = C(\theta)\,x(t) + D(\theta)\,u(t) \\ x(t_0) = x_0 \end{cases} \quad (1)$$

where $x(t) \in \mathbb{R}^n$ is the state vector, $u(t) \in \mathbb{R}^m$ is the input vector, $y(t) \in \mathbb{R}^l$ is the output vector, $A(\cdot) \in \mathbb{R}^{n\times n}$, $B(\cdot) \in \mathbb{R}^{n\times m}$, $C(\cdot) \in \mathbb{R}^{l\times n}$ and $D(\cdot) \in \mathbb{R}^{l\times m}$.

$\theta = [\theta_1, \ldots, \theta_p]$ is the uncertain parameter vector, where p is the parameters number, $\theta_i \in \mathbb{R}$.

In order to study parameters variation impact on the output model, classically, local sensitivity analysis is applied. This method consists of computing parameter effect around a nominal value. The influence of parameter θ_i is defined by the partial derivative of the output $y(t)$ with respect to the parameter θ_i and is given by:

$$S_i(t) = \frac{\partial y(t)}{\partial \theta_i} \tag{2}$$

Assuming that $\theta_i \in [\theta_{i_{min}}, \theta_{i_{max}}]$, local sensitivity analysis application can lead to erroneous results and fault index interpretation. Consequently, it cannot be efficient to measure the influence of each parameter on the model output.

To overcome this problem and those ones given in the introduction, a new methodology is presented. The method consists of determining an upper and lower bound, ensuring the existence of sensitivity function inside, using interval analysis technique.

In the next section, the sensitivity analysis method based on partial derivative, is explained.

3 PARTIAL DERIVATIVE-BASED SENSITIVITY ANALYSIS

Consider the model representation given by (1).

The objective of this section is to determine a system of sensitivity functions describing the dynamic behavior of sensitivity functions which measure the influence of each model parameter. This system is linear and can be written in a state space form (see figure 1). It is determined using available informations such as: the output measurements y and the model input u.

The objective of the following paragraph is to determine the system of sensitivity functions.

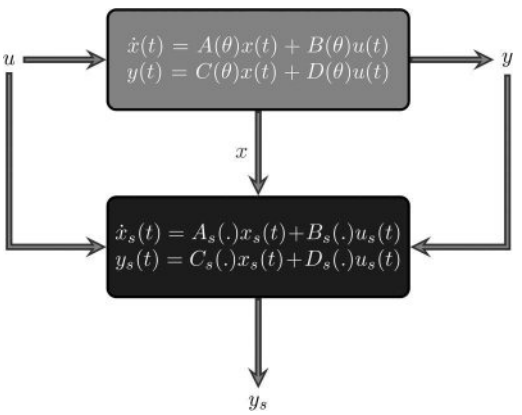


Figure 1. Principle of sensitivity functions system.

3.1 *Sensitivity functions representation*

The partial derivative of the state vector $x(t)$ given by (1) is:

$$\begin{aligned}\frac{\partial \dot{x}(t)}{\partial \theta_i} &= A(\theta)\frac{\partial x(t)}{\partial \theta_i} + \frac{\partial A(\theta)}{\partial \theta_i}x(t) + \frac{\partial B(\theta)}{\partial \theta_i}u(t) \\ &\quad + B(\theta)\frac{\partial u(t)}{\partial \theta_i}\end{aligned} \tag{3}$$

Assuming u is a function of time which does not depend on parameter θ_i, $\frac{\partial}{\partial \theta_i}\left(\frac{\partial x(t)}{\partial t}\right) = \frac{\partial}{\partial t}\left(\frac{\partial x(t)}{\partial \theta_i}\right)$ as θ_i is a constant, not varying with time. We assume also there is no dependence between these parameters: $\frac{\partial \theta_j}{\partial \theta_i} = 0$ for $i \neq j$.

Let define two sensitivity matrices of the model output $S_y(t)$ and of the state vector $S_x(t)$ given by:

$$S_y(t) = \frac{\partial y(t)}{\partial \theta} \qquad S_x(t) = \frac{\partial x(t)}{\partial \theta} \tag{4}$$

For each parameter θ_i, the following subsystem is defined:

$$\begin{cases} \dot{S}_x^i(t) = A(\theta)\, S_x^i(t) + \frac{\partial A(\theta)}{\partial \theta_i}\, x(t) + \frac{\partial B(\theta(t))}{\partial \theta_i}\, u(t) \\ S_y^i(t) = C(\theta)\, S_x^i(t) + \frac{\partial C(\theta)}{\partial \theta_i}\, x(t) + \frac{\partial D(\theta)}{\partial \theta_i}\, u(t) \\ S_x(t_0) = S_{x_0} \end{cases} \tag{5}$$

Grouped all subsystems together, the sensitivity of the state vector is defined by $x_s(t) = [S_x^1(t), S_x^2(t), \ldots, S_x^p(t)]^T$ which contains the sensitivity functions and the sensitivity functions of the output model define $y_s(t) = [S_y^1(t), S_y^2(t), \ldots, S_y^p(t)]^T$.

The whole system of sensitivity functions is given finally as:

$$\begin{cases} \dot{x}_s(t) = \begin{pmatrix} A(\theta)\, S_x^1(t) + \frac{\partial A(\theta)}{\partial \theta_1}\, x(t) + \frac{\partial B(\theta)}{\partial \theta_1}\, u(t) \\ A(\theta)\, S_x^2(t) + \frac{\partial A(\theta)}{\partial \theta_2}\, x(t) + \frac{\partial B(\theta)}{\partial \theta_2}\, u(t) \\ \vdots \\ A(\theta)\, S_x^p(t) + \frac{\partial A(\theta)}{\partial \theta_p}\, x(t) + \frac{\partial B(\theta)}{\partial \theta_p}\, u(t) \end{pmatrix} \\ y_s(t) = \begin{pmatrix} C(\theta)\, S_x^1(t) + \frac{\partial C(\theta)}{\partial \theta_1}\, x(t) + \frac{\partial D(\theta)}{\partial \theta_1}\, u(t) \\ C(\theta)\, S_x^2(t) + \frac{\partial C(\theta)}{\partial \theta_2}\, x(t) + \frac{\partial D(\theta)}{\partial \theta_2}\, u(t) \\ \vdots \\ C(\theta)\, S_x^p(t) + \frac{\partial C(\theta)}{\partial \theta_p}\, x(t) + \frac{\partial D(\theta)}{\partial \theta_p}\, u(t) \end{pmatrix} \end{cases} \tag{6}$$

Thus, the sensitivity system can be written in a state space system form as:

$$\begin{cases} \dot{x}_s(t) = A_s(\theta)\, x_s(t) + B_s(\theta)\, u_s(t) \\ y_s(t) = C_s(\theta)\, x_s(t) + D_s(\theta)\, u_s(t) \end{cases} \tag{7}$$

where:

$$A_s(\theta) = \begin{pmatrix} A(\theta) & 0_{n\times n} & \cdots & 0_{n\times n} \\ 0_{n\times n} & A(\theta) & \ddots & \vdots \\ \vdots & \ddots & \ddots & 0_{n\times n} \\ 0_{n\times n} & \cdots & 0_{n\times n} & A(\theta) \end{pmatrix} \tag{8}$$

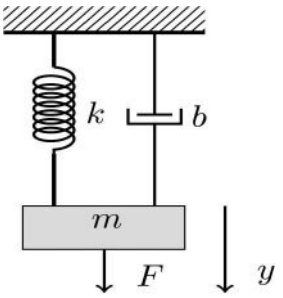


Figure 2. Schematic representation of a mass-spring-damper model.

$$B_s(\theta) = \begin{pmatrix} \frac{\partial A(\theta)}{\partial \theta_1} & \frac{\partial B(\theta)}{\partial \theta_1} \\ \frac{\partial A(\theta)}{\partial \theta_2} & \frac{\partial B(\theta)}{\partial \theta_2} \\ \vdots & \vdots \\ \frac{\partial A(\theta)}{\partial \theta_p} & \frac{\partial B(\theta)}{\partial \theta_p} \end{pmatrix} \tag{9}$$

$$C_s(\theta) = \begin{pmatrix} C(\theta) & 0_{l\times n} & \cdots & 0_{l\times n} \\ 0_{l\times n} & C(\theta) & \ddots & \vdots \\ \vdots & \ddots & \ddots & 0_{l\times n} \\ 0_{l\times n} & \cdots & 0_{l\times n} & C(\theta) \end{pmatrix} \tag{10}$$

$$D_s(\theta) = \begin{pmatrix} \frac{\partial C(\theta)}{\partial \theta_1} & \frac{\partial D(\theta)}{\partial \theta_1} \\ \frac{\partial C(\theta)}{\partial \theta_2} & \frac{\partial D(\theta)}{\partial \theta_2} \\ \vdots & \vdots \\ \frac{\partial C(\theta)}{\partial \theta_p} & \frac{\partial D(\theta)}{\partial \theta_p} \end{pmatrix} \tag{11}$$

$$u_s(t) = \begin{pmatrix} x(t) \\ u(t) \end{pmatrix} \tag{12}$$

with $x_s(t_0) = 0_{n\times 1}$. $0_{l\times k}$ is a $l \times k$ zero matrix.

In the next paragraph, a test example is considered and sensitivity analysis functions, computed using method previous described, are determined.

3.2 *Illustrative example*

3.2.1 *System description*

Consider a mass-spring-damper system given in figure 2.

As a mechanical system, the dynamics of a mass-spring-damper system can be described by the following 2nd-order differential equation:

$$m\ddot{y}(t) + b\dot{y}(t) + ky(t) = F(t) \tag{13}$$

where m is the mass, b is the damping coefficient, k is the stiffness coefficient and F is the force acting on the mass.

We introduce the state vector $\dot{x} = \begin{bmatrix} x_1(t) \\ x_2(t) \end{bmatrix}$.

where x_1 and x_2 are respectively the mass displacement and velocity.

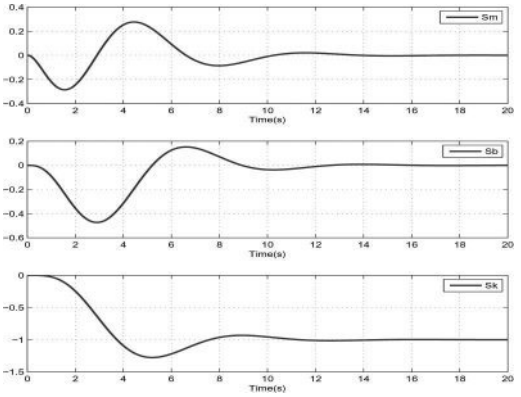


Figure 3. Sensitivity analysis functions.

The system (13) can be then written in a state space form as follows:

$$\begin{bmatrix} \dot{x}_1(t) \\ \dot{x}_2(t) \end{bmatrix} = \begin{bmatrix} 0 & 1 \\ -\frac{k}{m} & -\frac{b}{m} \end{bmatrix} \begin{bmatrix} x_1(t) \\ x_2(t) \end{bmatrix} + \begin{bmatrix} 0 \\ \frac{1}{m} \end{bmatrix} F(t)$$
$$y(t) = \begin{bmatrix} 1 & 0 \end{bmatrix} \begin{bmatrix} x_1(t) \\ x_2(t) \end{bmatrix} \tag{14}$$

The objective is to study the influence of parameters variation of m, b and k on the mass position x_1.

3.2.2 *Partial derivative-based sensitivity analysis*

Firstly, let us study the influence of parameters m, b and k around their nominal values which are fixed to 1. A constant integration step size is chosen with $h = 0.1$ m and the step signal is applied on F. Figure 3 represents the sensitivity function of each parameter. These functions have been determined using (7).

We can see that all parameters are influent on the mass displacement until $t = 10$ s. After this transient time, only the stiffness coefficient k dominates the mass position variation. In fact, the mass and the damping coefficient depend on the velocity and the acceleration, thus, they are influent in the transient region. When the velocity and the acceleration tend to zero, only the stiffness coefficient is influent. Its influence can be seen in the steady state. In the next section, interval analysis method is introduced.

4 INTERVAL ANALYSIS METHOD

Here, the principle of interval analysis for linear and nonlinear model is explained. The objective is to find a validated enclosure of all solutions of parametric autonomous system:

$$\dot{x}_s(t) = f(x_s(t), \theta), \quad x_s(t_0) = x_{s_0} \in X_{s_0}, \quad \theta \in \Theta. \tag{15}$$

where $t \in [t_0, t_m]$. θ is a p-dimensional parameter vector, x_s is the n-dimensional vector of state variables and x_{s_0} is the n-dimensional vector of initial values. The interval vectors Θ and X_{s_0} represent enclosures of the uncertainties in θ and x_{s_0}, respectively.

$f : \mathbb{R}^n \times \mathbb{R}^p \longrightarrow \mathbb{R}^n$ is $(k-1)$ times continuously differentiable with respect to the parameter θ on $\mathbb{R}^n$.

VSPODE tool (Lin & Stadtherr 2007) is used to compute a rigorously guaranteed enclosure on the trajectories of a linear or nonlinear ODE system with interval-valued initial values or parameters. This enclosure is computed by using an interval Taylor series method, combined with Taylor models to overcome the dependency of each uncertain quantities and wrapping effect. The use of Taylor models leads to a considerable large reduction of the overestimation which is often associated with interval methods. Before describing how this method works, a convenient notation for Taylor Coefficients (TC) should be introduced.

$$\begin{aligned} f^{[0]}(x_s) &= x_s \\ f^{[1]}(x_s) &= f \\ f^{[i]}(x_s) &= \frac{1}{i}\left(\frac{\partial f^{[i-1]}}{\partial x_s} f\right)(x_s) \quad \text{for i} \geq 2 \end{aligned} \tag{16}$$

This interval method consists of two algorithms applied at each integration step. In the first step, existence and uniqueness of the solution are proved using the Picard-Lindelöf operator. In the second step, a tighter enclosure of the solution is computed.

4.1 *Validating existence and uniqueness*

To get a priori bounds of an ordinary differential equation, we use an interval evaluated Taylor series with respect to time. Suppose that at t_j we have an enclosure $[y_{s_j}]$ of $y_s(t; t_0, [y_{s_0}], \theta)$. By using the Picard-Lindelöf operator and the Banach fixed-point theorem, one can show that if a stepsize h_j and a priori enclosure $[\tilde{y}_j]$ satisfy:

$$[y_{s_j}] + [0, h_j] f([\tilde{y}_{s_j}], \theta) \subseteq [\tilde{y}_{s_j}] \tag{17}$$

then (15) has a unique solution $y_s(t; t_j, y_{s_j}, \theta) \in [\tilde{y}_{s_j}]$.

4.2 *Computing a tighter enclosure*

A basic instinct to obtain the tighter enclosure $[y_{s_{j+1}}]$ will be by using the interval Taylor series with the following form:

$$[y_{s_{j+1}}] = [y_{s_j}] + \sum_{i=1}^{k-1} h_j^i f^{[i]}(y_{s_j}, \theta) + h_j^k f^{[k]}(y_s; t_j, t_{j+1}, \theta) \tag{18}$$

This basic first order interval evaluation form will lead sooner the sets $[y_{s_{j+1}}]$ be overestimated as the intrinsic wrapping problem. Without applying the Taylor model directly on the inclusion function f, VSPODE using a mean-value form to reduce the propagation of wrapping effect which results big overestimation, the limitation of the use of this approach has been discussed by Neumaier (Neumaier 2002). By projecting the original domain sets to an orthogonal domain with the help of parallelepiped or QR-factorization methods (Nedialkov, Jackson, & Corliss 1999), the wrapping effect in the polynomial part of Taylor model could be relatively reduced but it still propagates in the reminder part due to the intrinsic dependency problem of interval analysis.

In the next paragraph, method described above is applied on mass-spring-damper system considered on previous section.

4.3 *Illustrative example*

Now, let us consider the parameters m, b and k varying within the range of 0.9 to 1.1. Like the previous case, a constant integration step size is chosen with $h = 0.1m$ and the step signal is applied on F.

Consider the initial state of $x(0) = [0, 0]^T$, we use VSPODE to determine a verified state enclosure for $t \in [0; 20]$. The order of the Taylor model and the interval Taylor series were chosen as 17 and 20, respectively, which are aimed to avoid the overestimation during calculation.

Figure 4 shows the curves representing the upper and lower bounds and the sensitivity functions corresponding on the influence of m, b and k on the mass displacement.

Bounds are obtained using VSPODE. Several points are chosen from parameters interval and sensitivity functions have been determined by a validated integrator VNODE (Validated Numerical ODE). Sensitivity functions are guaranteed within the bounds. A large interval has been obtained in the transient regime until $t = 12$ s. m, b and k are influential on the mass position. However, in the static regime we can observe that

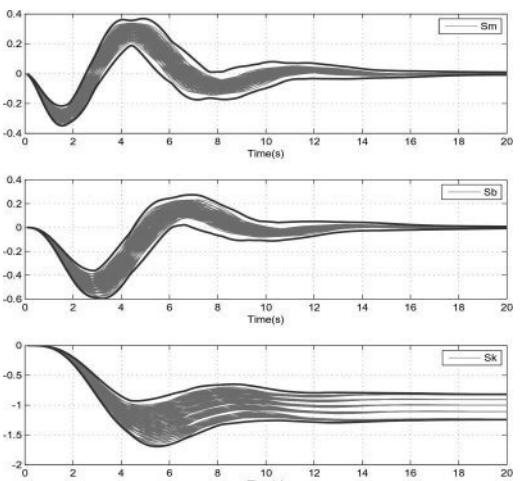


Figure 4. Interval enclosure for sensitivity functions.

the enclosure is tightest so for any value of parameter in this regime and only k is influential. In order to show the effectiveness of this method, it is applied to study the sensitivity analysis of quarter vehicle model parameters.

5 SENSITIVITY ANALYSIS OF A SUSPENSION SYSTEM

5.1 *System description*

Consider a simple quarter vehicle model given in figure 5. This model is often used in studies dealing with suspensions.

The model is composed of a sprung mass m and an unsprung mass m_r connected by a spring with the stiffness coefficient k_s and a damper with the damping coefficient f. The tire is modeled by a spring with the stiffness coefficient k_t. Distances z_c, z_r and z_v are, respectively, the road profile, the vertical displacements of unsprung and sprung masses.

The vertical dynamics of the quarter vehicle is governed by the following equations:

$$\begin{cases} m_s\ddot{z}_v(t) = -k_s\left(z_v(t) - z_r(t)\right) - b\left(\dot{z}_v(t) - \dot{z}_r(t)\right) \\ m_r\ddot{z}_r(t) = -k_s\left(z_r(t) - z_v(t)\right) - b\left(\dot{z}_r(t) - \dot{z}_v(t)\right) \\ -k_r\left(z_r(t) - z_c(t)\right) \end{cases} \tag{19}$$

The system (19) can be written in a state space form as follows:

$$\begin{bmatrix} \dot{z}_v(t) \\ \ddot{z}_v(t) \\ \dot{z}_r(t) \\ \ddot{z}_r(t) \end{bmatrix} = \begin{bmatrix} 0 & 1 & 0 & 0 \\ -\frac{k_s}{m_s} & -\frac{b}{m_s} & \frac{k_s}{m_s} & \frac{b}{m_s} \\ 0 & 0 & 0 & 1 \\ \frac{k_s}{m_r} & \frac{b}{m_r} & \frac{-k_r-k_s}{m_r} & -\frac{b}{m_r} \end{bmatrix} \begin{bmatrix} z_v(t) \\ \dot{z}_v(t) \\ z_r(t) \\ \dot{z}_r(t) \end{bmatrix} + \begin{bmatrix} 0 \\ 0 \\ 0 \\ \frac{k_r}{m_r} \end{bmatrix} z_c(t)$$

$$y(t) = \begin{bmatrix} 1 & 0 & 0 & 0 \end{bmatrix} \begin{bmatrix} z_v(t) \\ \dot{z}_v(t) \\ z_r(t) \\ \dot{z}_r(t) \end{bmatrix} \tag{20}$$

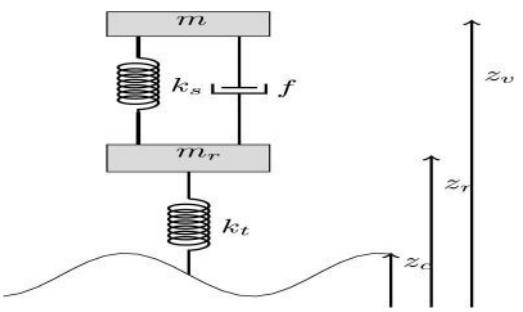


Figure 5. Model of quarter vehicle.

The objective here is to study the influence of parameters k_s, m, f, m_r and k_t on the vertical displacement of the sprung mass. We determine then sensitivity functions as defined in (7).

5.2 *Results*

Firstly, sensitivity functions have been determined, using (7), around the nominal values of parameters k_s, m, f, m_r and k_t which are fixed respectively to 29500 N·m^{-1}, 450 kg, 2000 Ns·m^{-1}, 40 kg and 210000 N·m^{-1}. Figure 6 shows the sensitivity functions, considering a step road profile (the amplitude is 0.1 m).

One can observe that in the transient region, the most important parameter is the unsprung mass m_r. When the system has passed its transient phase, all sensitivity functions converge to zero. Thus parameters become not influent. In fact, this result depends on road profile applied which corresponds to a situation where a vehicle goes up on a sidewalk. When the road profile changes, the sprung mass is the most influent. Once the vehicle is on the sidewalk, the vertical displacement of the unsprung mass z_v returns to its first state.

We assume now that parameters k_s, m, f, m_r and k_r vary in the interval [265500 N·m^{-1}; 32450 N·m^{-1}], [260 kg; 540 kg], [1800 Ns·m^{-1}; 2200 Ns·m^{-1}], [36 kg; 44 kg] and [189000 N·m^{-1}; 231000 N·m^{-1}].

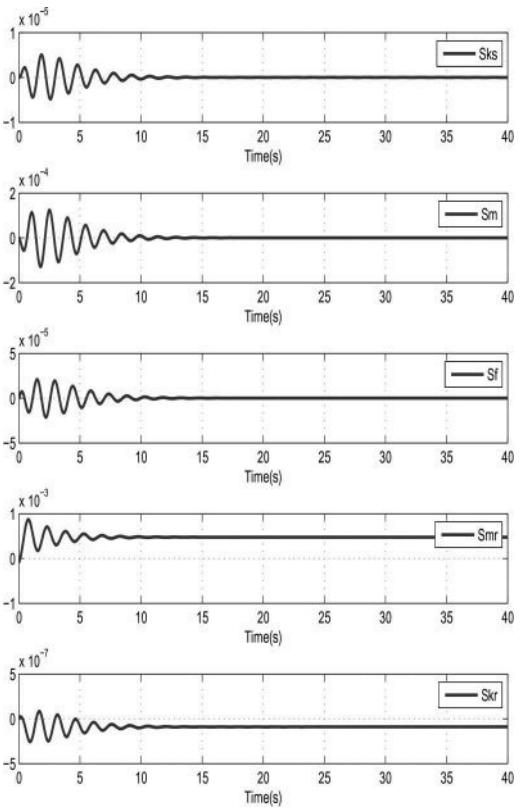


Figure 6. Sensitivity analysis functions.

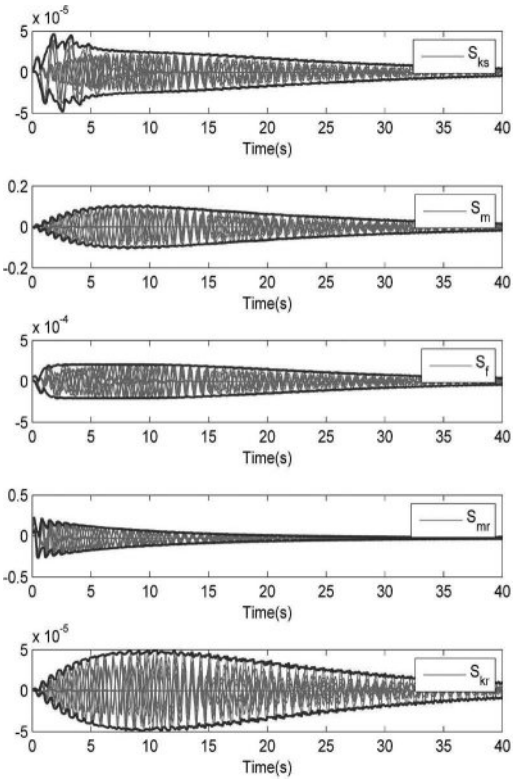


Figure 7. Interval enclosure for sensitivity functions.

Figure 7 shows the curves representing the upper and lower bounds obtained using VSPODE. Figure 7 gives also sensitivity functions computed around different values of parameters in their interval variation in order to verify the determined bounds.

It is clearly observed that upper and lower bounds have ensured the existence of sensitivity functions inside. In this interval of variation, unsprung mass m_r is the most influential. The sprung mass m follows. Other parameters appear of less impact, compared to m_r and m, on the displacement of the sprung mass.

6 CONCLUSION

In this paper, global and dynamic sensitivity analysis method have been presented. Sensitivity functions are firstly computed using the partial derivative then interval enclosure ensuring the existence of sensitivity function inside is determined. The upper and lower interval enclosure are computed using VSPODE solver. The effectiveness of the proposed approach has been demonstrated through an illustrative example and an application on a quarter vehicle model. Consistent results have been shown. However, it is necessary to note that interval enclosure depends on the initial condition of the states and the parameters. When dealing with large intervals, possibly, this interval approach produces the overestimation of the reachable sets. One can divide the initial sets with several small sets to reduce the overestimation, or try to take all the parameter around 1 will also release the pessimism. For near future, it will be interesting to consider a more complex model.

REFERENCES

Haro Sandoval, E., F. Anstett-Collin, & M. Basset (2012). Sensitivity study of dynamic systems using polynomial chaos. *Reliability Engineering System Safety 104*(0), 15–26.

Lin, Y. & M. Stadtherr (2007). Guaranteed state and parameter estimation for nonlinear continuous-time systems with bounded-error measurements. *Industrial and Engineering Chemistry Research*, 7198–7207.

Lin, Y. & M. Stadtherr (2008). Validated solutions of initial value problems for parametric odes. *Applied Numerical Mathematics 57*(10), 1145–1162.

Nedialkov, N., K. Jackson, & G. Corliss (1999). Validated solutions of initial value problems for ordinary differential equations. *Applied Mathematical Computing 105*, 21–68.

Neumaier, A. (2002). Taylor forms – use and limits. *Reliable computing*.

Saltelli, A., M. Ratto, T. Andres, F. Campolongo, J. Cariboni, D. Gatelli, M. Saisana, & S. Tarantola (2008). *Global Sensitivity Analysis. The Primer*. Wiley.

Advanced Vehicle Control – Edelmann, Plöchl & Pfeffer (Eds)
© 2017 Taylor & Francis Group, London, ISBN 978-1-138-02992-7

Improvement of ride comfort by unsprung negative skyhook damper control using in-wheel motors

E. Katsuyama & A. Omae
Toyota Motor Corporation, Susono, Shizuoka, Japan

ABSTRACT: Vehicles equipped with in-wheel motors (IWMs) are capable of independent control of the driving force at each wheel. These vehicles can also control the motion of the sprung mass by driving force distribution. However, one disadvantage of IWMs is an increase in unsprung mass, which may result in an uncomfortable ride. This research aimed to improve ride comfort through driving force control. As a result, a method was derived by analysis that reduced uncomfortable vibration through a control that applies unsprung vertical velocity in the direction that enhances that velocity. The improvement effect on ride comfort of this control was then verified.

1 INTRODUCTION

Vehicles equipped with in-wheel motors (IWMs) are capable of independently controlling the driving force at each wheel. Therefore, in addition to yaw control, IWMs can also control the motion of the sprung mass using the vertical suspension reaction force generated by driving (Katsuyama, 2013). For this reason, IWMs are regarded as a highly promising technology from the standpoint of controlling vehicle motion. However, the increased sprung mass of IWMs is generally regarded as disadvantageous for ensuring ride comfort on rough roads. This paper examines a method of reducing uncomfortable vibrations caused by this increased unsprung mass through a ride comfort control that uses driving force distribution.

2 RIDE COMFORT CONTROL IN RESPONSE TO ROAD SURFACE DISTURBANCES

2.1 *Conventional control*

First, this research confirmed the effects of the unsprung mass on ride comfort performance. This was accomplished by carrying out a full-vehicle simulation at 60 km/h on an uneven road after increasing the unsprung mass at each wheel by 25% compared to a baseline vehicle (same total weight). Figure 1 shows the resulting power spectral density (PSD) of vertical acceleration of the vehicle body. The increase in unsprung mass resulted in higher vibration, particularly in the 3 to 9 Hz frequency range. Since ISO Standard 2631-1 (1997) regards the frequency range between 4 and 8 Hz as uncomfortable for vehicle occupants, a heavy unsprung mass is not desirable from the standpoint of ride comfort.

Before being applied to vehicles, active suspension controls originated from rail vehicle engineering

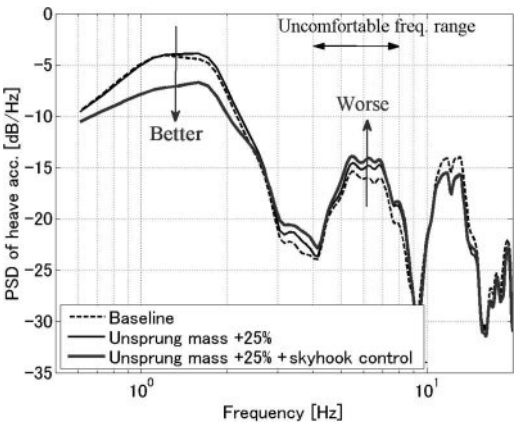


Figure 1. Effect of increased unsprung mass and skyhook damper control on vertical acceleration of vehicle body (simulation).

(Hedrick, 1981). Although various types of automotive active suspension controls have been developed (Tseng, 2015), skyhook damper control is a simple and highly effective method that has been widely adopted in the past (Karnopp, 1983). First, to confirm the effect of skyhook damper control, the same simulation was carried out using skyhook damper control (Katsuyama, 2013) to distribute the driving force of IWMs. These results are also shown in Fig. 1. Although the control was effective in reducing vibration around the sprung mass resonance frequency (1 to 2 Hz), it had an adverse effect in the uncomfortable 4 to 8 Hz range (vibration in this frequency range is referred to as "mid-frequency vibration" in this paper).

The reasons for the adverse effect of the skyhook damper control on mid-frequency vibration were examined theoretically. Figure 2 defines the quarter-car 2-degree-of-freedom (DOF) model used for this

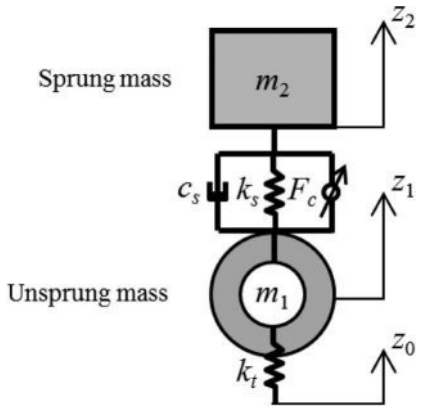


Figure 2. Quarter-car 2-DOF model.

Table 1. Parameters for calculation.

Parameters	Symbol	Unit	Value
Sprung mass	m_2	kg	500
Unsprung mass	m_1	kg	80
Spring stiffness	k_s	N/m	30e3
Damping factor	c_s	N/(m/s)	2000
Tire stiffness	k_t	N/m	300e3

purpose. Equations 1 and 2 show the equations of motion for the sprung and unsprung mass, respectively. Here, m_1 and m_2 are the unsprung and sprung mass, k_s and c_s are the spring constant and damping factor of the suspension, and k_t is the spring constant of the tires. F_c is the acting force of the suspension due to the control and is a positive value in the rebound direction. z_0, z_1, and z_2 are the vertical displacements of the road surface, unsprung mass, and sprung mass, respectively. s is the Laplace operator. c_{sh} in Equation 3 is the damping factor of the skyhook damper control, which is multiplied by the control lag transfer function $D(s)$. Table 1 shows the values used for calculation in this model.

$$m_2 z_2 s^2 = c_s(z_1 - z_2)s + k_s(z_1 - z_2) + F_c \quad (1)$$

$$m_1 z_1 s^2 = c_s(z_2 - z_1)s + k_s(z_2 - z_1) + k_t(z_0 - z_1) - F_c \quad (2)$$

$$F_c = -c_{sh} z_2 s D(s) \quad (3)$$

Figure 3 shows a Bode plot of the sprung mass acceleration that occurs in response to road surface displacement input, as calculated by the model. The first order lag shown in Equation 4 was substituted for $D(s)$, 30 msec was set for the time constant t_c, and $0.4 \times c_s$ was substituted into the control damping factor c_{sh}. In addition, the input amplitude was multiplied by $1/f$, which is the reciprocal of the input frequency f. As a result, applying the skyhook damper control reduced vibration around the sprung mass resonance frequency and slightly worsened mid-frequency vibration due to the effect of the control lag. These results reproduce the same trends calculated using the full-vehicle model.

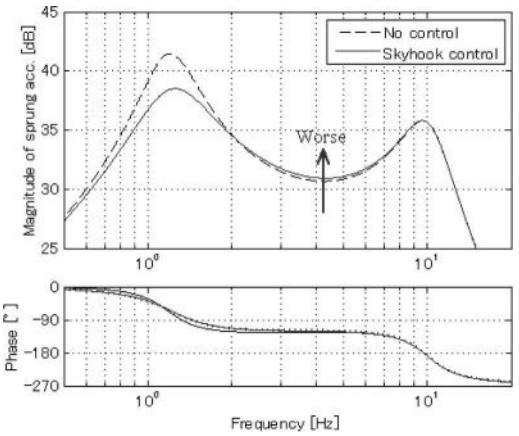


Figure 3. Effect of skyhook damper control on sprung mass vertical acceleration.

$$D(s) = 1/(t_c s + 1) \quad (4)$$

The mechanism by which the control worsened mid-frequency vibration was analyzed more simply by calculating the transfer function for sprung mass displacement z_2 with respect to unsprung mass displacement z_1. Equation 5 was used for this purpose.

$$\frac{z_2}{z_1} = \frac{c_s s + k_s}{m_2 s^2 + (c_s + c_{sh} D(s))s + k_s} \quad (5)$$

This equation can be understood as follows by regarding $D(s)$ as a coefficient. The suspension damping factor c_s is contained in the damping terms of both the numerator and denominator of the transfer function shown in Equation 5. Therefore, although convergence improves as the suspension damping factor increases, it also increases the input force from the unsprung mass. In contrast, since the skyhook damper coefficient c_{sh} is only included in the denominator, it improves the convergence of the sprung mass without changing the input from the unsprung mass. However, since a control lag is applied to c_{sh}, the equation can be used to understand the effects on the motion of the sprung mass as the speed of the frequency inputs increases.

2.2 *Factor analysis of adverse effect of conventional control on mid-frequency vibration*

Returning to basics, this research then investigated the relationship between the damping factor and the sprung mass acceleration. Figure 4 shows the magnitude of the Bode plot of the sprung mass acceleration when the damping terms c_s in the numerator and denominator are increased respectively by between 0.4 and 2.0 times in a conventional state in which c_{sh} in Equation 5 is 0. The figure indicates that the damping factor of the denominator mainly has an effect around the sprung mass resonance frequency. Because

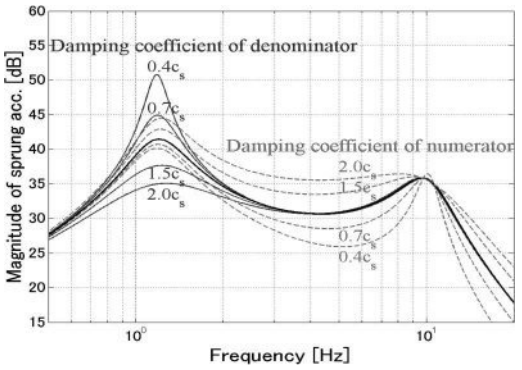


Figure 4. Effect of damping factor of numerator and denominator on sprung mass vertical acceleration.

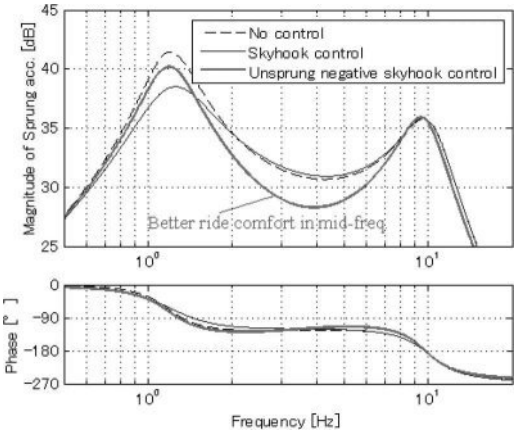


Figure 5. Effect of unsprung negative skyhook damper control on sprung mass vertical acceleration.

the damping factor of the denominator is proportional to the sprung mass velocity, the response of the sprung mass decreases as the frequency increases. In contrast, the damping factor of the numerator has an effect over a wide frequency range. Because the damping factor of the numerator is proportional to the unsprung mass velocity, the unsprung mass velocity responds to road surface displacement up to higher frequencies. Therefore, the adverse effect of the sprung mass skyhook damper control on mid-frequency vibration is because the control contains components that increase both the damping factors of the denominator and numerator due to the control lag.

2.3 *Proposed control*

According to the previous section, it should be possible to improve mid-frequency vibration by reducing the damping term of the numerator. Using this principle, an effective approach would be to control the sprung mass displacement with respect to unsprung mass displacement based on Equation 6. The command values for this control can be calculated from Equations 6 and 1. The calculated results can be shown by Equation 7, which expresses the application of a proportional control force to the unsprung vertical velocity.

$$\frac{z_2}{z_1} = \frac{(c_s - c_{sh}D(s))s + k_s}{m_2 s^2 + c_s s + k_s} \tag{6}$$

$$F_c = -c_{sh} z_1 s D(s) \tag{7}$$

As shown in Equation 7, one distinguishing feature of the proposed control is that it does not require information about the sprung mass, and that the control is performed using only information about the unsprung mass. Since the direction of this control force is opposite to the skyhook damper, it enhances the absolute vertical velocity of the unsprung mass. Therefore, this control is called the unsprung negative skyhook damper control. This control can be explained in physical terms as follows. When a wheel travels over a bump, the unsprung mass possesses velocity in the upward direction. This control raises the unsprung mass and, simultaneously, the reaction force lowers the sprung mass. Therefore, although the sprung mass should inherently rise up, this has the effect of holding down the sprung mass at an early stage, while restricting an increase in the contact load. When the wheel moves down after the bump, the opposite action occurs and the same sprung mass motion suppression effect occurs. Ultimately, this control acts to actively move the tires to follow the road surface profile.

The effect of the proposed controls was confirmed using the quarter-car model simulation. Figure 5 shows the results. Although the conventional sprung skyhook damper control increased the mid-frequency vibration, the proposed control enabled a substantial improvement in the simulation. However, Equation 6 contains a lag term in the numerator. Since the effect of this control lag on sprung motion could not be explained, this research focused on examining this phenomenon.

3 CONSIDERATIONS

3.1 *Effect of control lag on ride comfort control*

Equation 8 defines the sprung mass displacement with respect to the unsprung mass displacement. To perform unsprung negative skyhook damper control that contains no lag using c_{sh} as the control damping factor, $w_1 = -1$ and $w_2 = 0$ should be substituted into the equation. However, as described in the previous section, these values cannot be achieved for w_1 and w_2 due to the control lag. Therefore, the quarter-car model was used to examine how the control lag changes damping factors of numerator and denominator.

$$\frac{z_2}{z_1} = \frac{(c_s + w_1 c_{sh})s + k_s}{m_2 s^2 + (c_s + w_2 c_{sh})s + k_s} \tag{8}$$

The command waveform F_c of the control with lag is expressed by a composition of both the unsprung vertical velocity $\dot{z}_1$ and the sprung vertical velocity $\dot{z}_2$. First, each vertical velocity was defined as the sine

functions shown in Equations 9 to 11. Here, ω is the input frequency.

$$F_c \stackrel{\text{def}}{=} g_c \sin(\omega t + \theta_c) \tag{9}$$

$$\dot{z}_1 \stackrel{\text{def}}{=} g_1 \sin(\omega t + \theta_1) \tag{10}$$

$$\dot{z}_2 \stackrel{\text{def}}{=} g_2 \sin(\omega t + \theta_2) \tag{11}$$

Equation 12 is obtained by calculating F_c from Equations 8 and 1.

$$F_c = w_1 c_{sh} \dot{z}_1 - w_2 c_{sh} \dot{z}_2 \tag{12}$$

After substituting Equations 10 and 11 into Equation 12 and applying the addition theorem of sine waves, the right side of Equation 12 can be converted as shown in Equation 13. A part of the right side of the equation is defined as a and b.

$$F_c = c_{sh}[g_1 \quad g_2]\begin{bmatrix} w_1 & 0 \\ 0 & -w_2 \end{bmatrix}\begin{bmatrix} \cos\theta_1 & \sin\theta_1 \\ \cos\theta_2 & \sin\theta_2 \end{bmatrix}\begin{bmatrix} \sin\omega t \\ \cos\omega t \end{bmatrix}$$

$$\stackrel{\text{def}}{=} [a \quad b]\begin{bmatrix} \sin\omega t \\ \cos\omega t \end{bmatrix} \tag{13}$$

In addition, using the definition of r shown in Equation 14, Equation 13 can be converted into Equation 15.

$$r \stackrel{\text{def}}{=} \sqrt{a^2 + b^2} \tag{14}$$

$$F_c = r\begin{bmatrix} \frac{a}{r} & \frac{b}{r} \end{bmatrix}\begin{bmatrix} \sin\omega t \\ \cos\omega t \end{bmatrix} \tag{15}$$

Here, since Equation 16 is true, θ_d that satisfies Equation 17 exists.

$$\begin{bmatrix} \frac{a}{r} & \frac{b}{r} \end{bmatrix}\begin{bmatrix} \frac{a}{r} & \frac{b}{r} \end{bmatrix}^T = 1 \tag{16}$$

$$\begin{bmatrix} \frac{a}{r} \\ \frac{b}{r} \end{bmatrix} = \begin{bmatrix} \cos\theta_d \\ \sin\theta_d \end{bmatrix} \tag{17}$$

Therefore, Equation 15 can be converted into Equation 18.

$$F_c = r[\cos\theta_d \quad \sin\theta_d]\begin{bmatrix} \sin\omega t \\ \cos\omega t \end{bmatrix} \tag{18}$$

Further in accordance with the addition theorem, Equation 18 becomes Equation 19 and r and θ_d correspond to g_c and θ_c in Equation 9.

$$F_c = r\sin(\omega t + \theta_d) \tag{19}$$

Based on the calculations described above, w_1 and w_2 can be calculated as shown in Equation 20.

$$\begin{bmatrix} w_1 \\ w_2 \end{bmatrix} = \frac{1}{c_{sh}}\begin{bmatrix} \frac{g_c}{g_1}\frac{\sin(\theta_2-\theta_c)}{\sin(\theta_2-\theta_1)} \\ \frac{g_c}{g_2}\frac{\sin(\theta_1-\theta_c)}{\sin(\theta_2-\theta_1)} \end{bmatrix} \tag{20}$$

The frequency transfer functions of the sprung and unsprung velocities $\dot{z}_1$ and $\dot{z}_2$ with respect to the road surface input z_0 as calculated by the quarter-car 2-DOF model simulation are defined as $G_1(j\omega)$ and $G_2(j\omega)$, respectively. As shown in Equation 21, the magnitudes of $G_1(j\omega)$ and $G_2(j\omega)$ are defined as g_1 and g_2, and the phase angles are defined as θ_1 and θ_2. In addition, the value obtained by multiplying the unsprung velocity magnitude with the control lag magnitude and the control damping factor is defined as g_c, and the value obtained by adding the control lag phase angle to the phase angle of the unsprung velocity is defined as θ_c. These values are substituted into Equation 20. Additionally, as the control lag, $D(j\omega)$ was defined with first order lag characteristics as shown in Equation 22 and a comparative calculation was performed with a total of three values for time constant t_c (0 msec, 15 msec, and 30 msec).

$$\left.\begin{array}{c} g_1 = |G_1(j\omega)|,\ \theta_1 = \angle G_1(j\omega) \\ g_2 = |G_2(j\omega)|, \theta_2 = \angle G_2(j\omega) \\ g_c = -g_1 c_{sh}|D(j\omega)|, \theta_c = \theta_1 + \angle D(j\omega) \end{array}\right\} \tag{21}$$

$$D(j\omega) = 1/(j\omega t_c + 1) \tag{22}$$

Figure 6 shows the results for the damping factors of the numerator and denominator of Equation 8, which were calculated from the weighting functions w_1 and w_2 with respect to the input frequency ω obtained above. In the unsprung negative skyhook damper control, if there is no control lag, the numerator would maintain the $c_s - c_{sh}$ value and the denominator would maintain the c_s value. However, the control lag lowers the numerator damping factor reduction effect in the mid-frequency vibration range, while simultaneously increasing the damping factor of the denominator. Therefore, it can be seen that the proposed control has the additional effect of reducing low-frequency vibration due to the control lag.

3.2 *Comparison of conventional and proposed controls*

The differences between the conventional and proposed controls were compared based on Equation 7, which expresses the control force of the proposed unsprung negative skyhook damper control. Equation 7 can be converted as shown in Equation 23. In addition to the conventional skyhook control, this equation also contains the shock absorber damping reduction term multiplied by the control lag $D(s)$.

$$F_c = -c_{sh} z_2 s D(s) - c_{sh}(z_1 - z_2) s D(s) \tag{23}$$

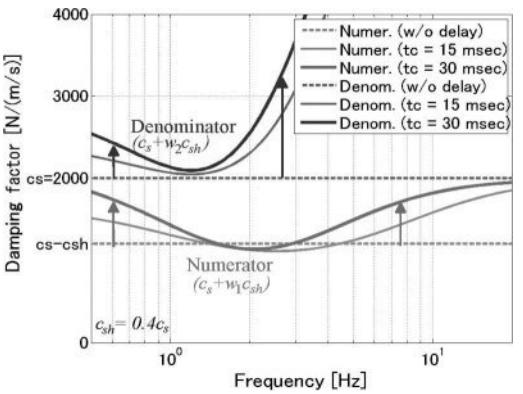


Figure 6. Weighting shift of unsprung negative skyhook damper control due to lag.

In other words, the proposed control obtains a state close to one in which the conventional control is applied to a vehicle installed with low damping mechanical shock absorbers. This state can be expressed by substituting Equation 24 into F_c.

$$F_c = -c_{sh} z_2 s D(s) - c_{sh}(z_1 - z_2)s \tag{24}$$

These differences can be explained as follows. The magnitude of the control lag $D(s)$ approaches 1 below the cutoff frequency and approaches 0 above the cutoff frequency. If these values are substituted into Equations 23 and 24, both controls have the same characteristics at low frequencies where the effect of the lag can be disregarded. However, at high frequencies where the control does not respond, the shock absorber damping reduction term remains only in Equation 24. Therefore, it can be assumed that mechanical damping is insufficient at high frequencies in the case of the conventional control.

The frequency response of the sprung mass acceleration and contact load fluctuations for both controls was calculated using the quarter-car 2-DOF model. Figure 7 shows the results. As described in the previous section, mid-frequency sprung mass acceleration improves in the same way for both controls. In addition, the contact load fluctuations at the unsprung resonance frequency worsen in the case of the conventional control with a low damping shock absorber. In contrast, the proposed control can reduce mid-frequency vibration while restricting the adverse effects at high frequencies by setting a time constant (i.e., a cutoff frequency) for $D(s)$ that allows mid-frequency vibration to pass and shuts off the unsprung mass resonance frequency. In general terms, although the sprung vibration and the contact load fluctuations have a trade-off relationship (Hrovat, 1997), the proposed control improves both sides of the relationship at the same time and has no negative effects on handling performance.

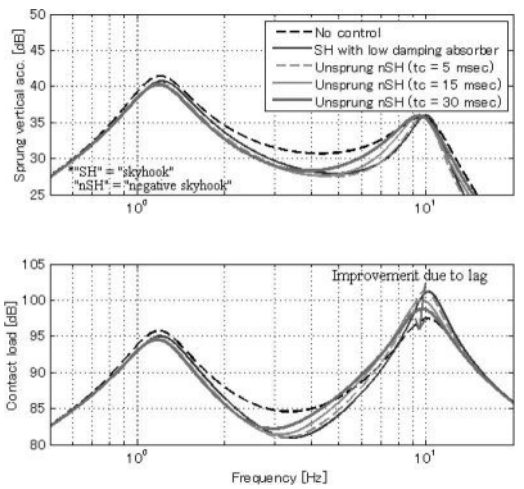


Figure 7. Comparison of unsprung negative skyhook damper control with skyhook damper control on contact load.

4 APPLICATION OF CONTROL TO VEHICLE EQUIPPED WITH IWMS AND VERIFICATION OF EFFECT

This paper has described the verification of the proposed control using a quarter-car model. This section describes its application to a vehicle with 4 IWMs. In this test, the value obtained by multiplying the unsprung vertical velocity $\boldsymbol{V}$ at each wheel by the control damping factor $-c_{sh}$ was the command value for the unsprung negative skyhook damper control at each wheel. Equation 25 converts these values to control command value $\boldsymbol{F}$ that acts in the longitudinal, heave, roll, pitch, and yaw directions of the sprung mass, after applying coefficient matrix $\boldsymbol{L}$. In this equation, l_f and l_r are the distance from the center of gravity to the front and rear axles, and t_f and t_r are the track of the front and rear wheels.

$$\boldsymbol{F} = -c_{sh}\boldsymbol{L}\boldsymbol{V} \tag{25}$$

$$\left.\begin{aligned} \boldsymbol{F} &= [F_x \quad F_z \quad M_x \quad M_y \quad M_z]^T \\ \boldsymbol{L} &= \begin{bmatrix} 0 & 0 & 0 & 0 \\ 1 & 1 & 1 & 1 \\ \frac{t_f}{2} & -\frac{t_f}{2} & \frac{t_r}{2} & -\frac{t_r}{2} \\ -l_f & -l_f & l_r & l_r \\ 0 & 0 & 0 & 0 \end{bmatrix} \\ \boldsymbol{V} &= [v_{zfl} \quad v_{zfr} \quad v_{zrl} \quad v_{zrr}]^T \end{aligned}\right\} \tag{26}$$

Equation 27 shows the relationship between the IWM driving force and the force acting on the sprung mass. $\boldsymbol{X}$ is the control driving force at each wheel, and $\boldsymbol{C}$ is the coefficient matrix that converts $\boldsymbol{X}$ to the $\boldsymbol{F}$ direction. θ_f and θ_r are the angles of the lines drawn from the contact point of the front or rear wheels to the instantaneous center of the front or rear suspension with respect to the horizontal plane, when the vehicle is viewed from the side.

$$\boldsymbol{F} = \boldsymbol{C}\boldsymbol{X} \tag{27}$$

$$\left.\begin{aligned} \boldsymbol{C} &= \begin{bmatrix} 1 & 1 & 1 & 1 \\ -\tan\theta_f & -\tan\theta_f & \tan\theta_r & \tan\theta_r \\ -\frac{t_f}{2}\tan\theta_f & \frac{t_f}{2}\tan\theta_f & \frac{t_r}{2}\tan\theta_r & -\frac{t_r}{2}\tan\theta_r \\ l_f\tan\theta_f & l_f\tan\theta_f & l_r\tan\theta_r & l_r\tan\theta_r \\ -\frac{t_f}{2} & \frac{t_f}{2} & -\frac{t_r}{2} & \frac{t_r}{2} \end{bmatrix} \\ \boldsymbol{X} &= [F_{xfl} \quad F_{xfr} \quad F_{xrl} \quad F_{xrr}]^T \end{aligned}\right\} \tag{28}$$

Control driving force $\boldsymbol{X}$ with respect to unsprung velocity $\boldsymbol{V}$ is calculated after defining Equations 25 and 27 as equal. Because there are more control objects than actuators (motors), $\boldsymbol{X}$ can be solved by Equation 29 using a pseudo-inverse matrix.

$$\boldsymbol{X} = -c_{sh}(\boldsymbol{C}^T\boldsymbol{C})^{-1}\boldsymbol{C}^T\boldsymbol{L}\boldsymbol{V} \tag{29}$$

Solving Equation 29 is somewhat complicated. To understand the structure of this equation, the following approximation is used: $l_f = l_r$ and $t_f = t_r$. In addition, since suspension designs generally use a setting whereby $\theta_f << \theta_r$, approximating θ_f as 0 means that Equation 29 can be expressed as Equation 30.

This equation indicates that a vehicle equipped with IWMs can apply negative skyhook damper control to each wheel while controlling the vertical force

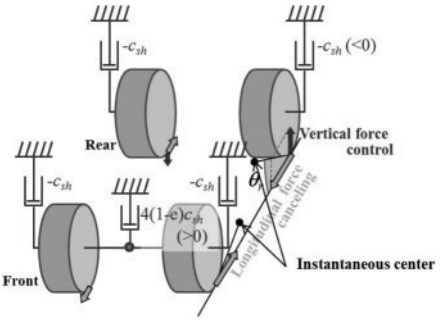


Figure 8. Application of unsprung negative skyhook damper control to vehicle equipped with IWMs.

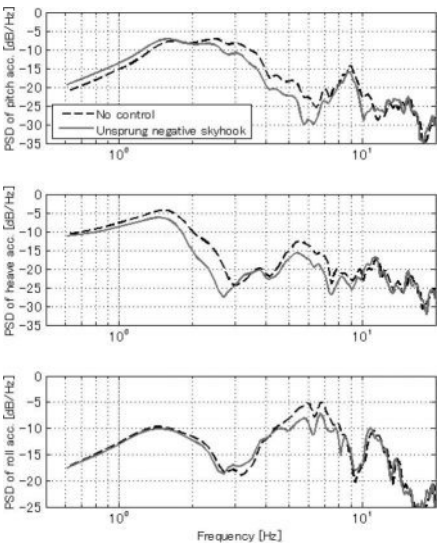


Figure 9. Effects of unsprung negative skyhook damper control on pitch, heave, and roll acceleration (actual vehicle data).

generated by the same-phase positive skyhook damper control of the front left and right wheels at the rear wheels. In addition, coefficient e is the weighting for the heave and pitch that cannot be controlled independently of each other. Coefficient e can be calculated by solving Equation 29, and the calculated results can be expressed by Equation 31. However, it is sufficient to determine coefficient e by evaluating occupant comfort in an actual vehicle. When $e = 1$, only the heave control is applied and, when $e = 0$, only the pitch control is applied. Furthermore, since the front wheels generate virtually no vertical force due to driving, the front wheels are used to offset the longitudinal force of the rear wheels.

$$\begin{bmatrix} F_{xrl} \\ F_{xrr} \end{bmatrix} \approx -\frac{c_{sh}}{\tan\theta_r} \left\{ \begin{bmatrix} v_{zfl} + v_{zrl} - 2(1-e)\dfrac{v_{zfl}+v_{zfr}}{2} \\ v_{zfr} + v_{zrr} - 2(1-e)\dfrac{v_{zfl}+v_{zfr}}{2} \end{bmatrix} \right\} \quad (30)$$

$$[F_{xfl} \quad F_{xfr}]^T = -[F_{xrl} \quad F_{xrr}]^T$$

$$e = 1/[1 + (l/2)^2] \quad (31)$$

Figure 8 visualizes the vertical forces applied by this control to the unsprung mass in terms of dampers. The vertical force that acts on the front and rear wheels on the left is generated by the rear-left wheel, and the vertical force that acts on the front and rear wheels on the right is generates by the rear-right wheel. The vertical reaction force that acts on the sprung mass plays an important role in the control.

This control was installed in an actual vehicle and the behavior of the vehicle was measured on an uneven road at 60 km/h. The specifications of the test vehicle were, weight: 1,950 kg, wheelbase: 2.7 m, front/rear track: 1.54/1.55 m, and tires: 235/45R18. Figure 9 shows the results. The targeted mid-frequency reductions in sprung pitch, heave, and roll were achieved.

It should be noted that this control method can be applied to any vehicle that adopts active suspension controls, as well as to vehicles equipped with IWMs. Providing that independent force control is possible for each wheel, the control effect of the front wheels can be applied to provide further improved control effects.

5 CONCLUSIONS

A theory was derived that mid-frequency vibration could be reduced through driving force control that applies force proportionally to the vertical velocity of the unsprung mass and in the direction that enhances that velocity (i.e., unsprung negative skyhook damper control). In addition, compared to the conventional control, the proposed control is also capable of suppressing the adverse effect on contact load fluctuations.

The proposed control was adopted in a test vehicle equipped with IWMs. Tests confirmed that the control reduced sprung mid-frequency vibration and improved ride comfort performance.

One of the distinguishing characteristics of this control is that it functions using the unsprung vertical velocity only, without requiring detection or estimation of sprung mass movement. It can also be applied to suspension controllers other than IWMs and further control effects can be expected provided that the vertical force can be controlled independently for all four wheels.

REFERENCES

Hedrick, J.K. 1981. Railway vehicle active suspensions. *Vehicle System Dynamics* 10(4–5): 267–283.

Hrovat, D. 1997. Survey of advanced suspension developments and related optimal control applications. *Automatica* 33(10): 1781–1817.

Karnopp, D. 1983. Active damping in road vehicle suspension system. *Vehicle System Dynamics* 12(6).

Katsuyama, E. 2013. Decoupled 3D moment control using in-wheel motors. *Vehicle System Dynamics* 51(1): 18–31.

Tseng, H. & Hrovat, D. 2015. State of the art survey: active and semi-active suspension control. *Vehicle System Dynamics* 53(7): 1034–1062.

Advanced Vehicle Control – Edelmann, Plöchl & Pfeffer (Eds)
© 2017 Taylor & Francis Group, London, ISBN 978-1-138-02992-7

Nonlinear $\mathcal{H}_2$ control of a low-bandwidth active vehicle suspension system using Takagi-Sugeno methods

Nils Pletschen
Institute of Automatic Control (Prof. Dr.-Ing. B. Lohmann), Technische Universität München, Garching, Germany

ABSTRACT: In this contribution, we make use of the Takagi-Sugeno (TS) system representation of a mechatronic vehicle suspension to design an overall nonlinear controller based on linear control methods. Linear-quadratic regulator (LQR) design is employed to derive the feedback gains of a parallel distributed compensator (PDC). The $\mathcal{H}_2$ controller synthesis problem is formulated in terms of linear matrix inequalities (LMI), which are successfully numerically solved. Using stochastic disturbance inputs, the concept is studied in comparison to benchmark controllers in simulations and experiments on a quarter-vehicle test rig, which features semi-active and low-bandwidth active force actuators.

1 INTRODUCTION

Much effort has been spent on research and development of mechatronic vehicle suspension systems during the last decades. However, new kinds of suspension configurations and advanced control algorithms are still a central subject for both the automotive industry and research institutions (Tseng & Hrovat 2015). This is because the conflicting tasks of increasing ride comfort and ride safety, while simultaneously meeting constructional constraints, has not yet been solved satisfactorily. Though the integration of active and semi-active components into the suspension mitigates the aforementioned conflict, it cannot be completely resolved. In fact, to which extent the performance potential of the available hardware set-up can be exploited in operation, highly depends on the suspension control algorithms applied. In series production, mostly approaches based on the famous skyhook algorithm (Karnopp et al. 1974) or combined skyhook-groundhook concepts (Novák & Valášek 1996) prevail. These control schemes are not only well-studied, but they are also characterized by a transparent behavior and ease of implementation. Yet, as computational restrictions become less important, advanced controller schemes are able to take increased advantage of controllable suspension components. This allows for the design of even more energy-efficient and effective suspension systems. Hence, other controller approaches have been studied that ground on the solution to a linear-quadratic (LQ) optimization problem. Thereby, the objective function corresponds to the variances of the suspension-related performance criteria, i.e. body acceleration (ride comfort) and dynamic tire load (road-holding), see e.g. (Venhovens 1994; Hrovat 1997; Unger 2012).

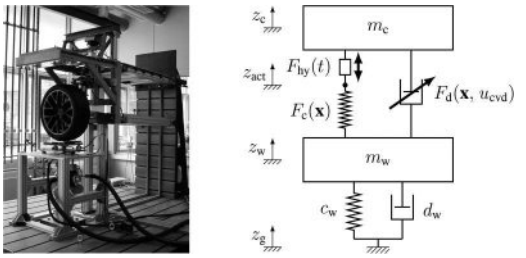


Figure 1. Test stand (left) and model (right) of the hybrid quarter-car configuration with two control inputs.

1.1 *Problem definition*

When the focus is on the vertical motion of vehicle body and wheel mass m_c and m_w, quarter-car models can be used to study the major dynamic effects in the frequency range below 25 Hz (Mitschke & Wallentowitz 2004). In order to analyze existing and new control concepts in a realistic setting, a quarter-car test stand has been constructed and put into operation at the author's institution, see Figure 1 (left). It features the mass ratio and the kinematics of a current upper class sedan and only actuators available from production vehicles are used. In fact, a combination of a slow-active actuator (featuring a bandwidth of up to 5 Hz) in series to a passive spring and a semi-active continuously variable damper (CVD) is integrated into the experimental suspension set-up, see Figure 1 (right). For more details about this so-called *hybrid suspension configuration*, the interested reader is referred to (Koch et al. 2011).

A major challenge in the design of suspension controllers is related to the nonlinear characteristics of

components that are usually used in practice. Degressive and asymmetric damper characteristics which depend on the electrical current applied to the controlled damper valves, progressive spring characteristics due to additional compression and rebound buffers, as well as dry friction effects need to be considered for the controller design. However, nonlinear control schemes are often complicated to design and—with only few exceptions—rather intransparent to tune. Moreover, the nonlinear effects are often rather available in terms of identified look-up tables than by means of analytic relationships. This property renders some known control approaches impractical.

Thus, in this paper, we present a nonlinear control approach that builds upon linear controller methods and is still able to *exactly* cope with all major nonlinearities of the hardware configuration on the basis of their characteristic maps.

The remainder of the paper is organized as follows: In Section 2, we give a short introduction to the Takagi-Sugeno system representation and the corresponding controller design. Based on the actual situation at the quarter-car test stand, we derive a TS model of the hybrid suspension set-up in Section 3. In Section 4, we then focus on the suspension controller design, before the results achieved by the controller in simulation and experiment are discussed in Section 5. We finally draw conclusions in Section 6.

2 TAKAGI-SUGENO CONTROLLER DESIGN

2.1 *TS system representation*

In the framework of *Takagi-Sugeno (TS) models* (Takagi & Sugeno 1985), nonlinear system dynamics are represented by a smooth interpolation of l linear state space models. By making use of the so-called *sector nonlinearity transformation* (Tanaka & Wang 2001), a quite general class of nonlinear systems of the form

$$\begin{aligned}\dot{\mathbf{x}}(t) &= \mathbf{A}(\mathbf{x},\mathbf{u})\mathbf{x}(t) + \mathbf{B}(\mathbf{x},\mathbf{u})\mathbf{u}(t) + \mathbf{E}(\mathbf{x},\mathbf{u})\mathbf{d}(t)\\ \mathbf{y}(t) &= \mathbf{C}(\mathbf{x},\mathbf{u})\mathbf{x}(t) + \mathbf{D}(\mathbf{x},\mathbf{u})\mathbf{u}(t) + \mathbf{F}(\mathbf{x},\mathbf{u})\mathbf{d}(t)\end{aligned} \tag{1}$$

can be *exactly* rewritten in the TS representation as

$$\begin{aligned}\dot{\mathbf{x}}(t) &= \sum_{i=1}^{l} h_i(\boldsymbol{\theta}(t))\left[\mathbf{A}_i\mathbf{x}(t) + \mathbf{B}_i\mathbf{u}(t) + \mathbf{E}_i\mathbf{d}(t)\right]\\ \mathbf{y}(t) &= \sum_{i=1}^{l} h_i(\boldsymbol{\theta}(t))\left[\mathbf{C}_i\mathbf{x}(t) + \mathbf{D}_i\mathbf{u}(t) + \mathbf{F}_i\mathbf{d}(t)\right]\end{aligned} \tag{2}$$

at least on a compact region of interest including the origin. Therein, $\mathbf{x} \in \mathbb{R}^n$ refers to the system state and $\mathbf{u} \in \mathbb{R}^m$ and $\mathbf{d} \in \mathbb{R}^p$ are the control input and the disturbance input, respectively; $\mathbf{y} \in \mathbb{R}^q$ indicates the controlled output. In (2), $h_i(\boldsymbol{\theta}(t))$ denotes the weighting function determining the share by which the ith linear subsystem $(\mathbf{A}_i, \mathbf{B}_i, \mathbf{E}_i, \mathbf{C}_i, \mathbf{D}_i, \mathbf{F}_i)$ contributes to the overall system dynamics at current time t. These weighting functions satisfy the *convex sum property*

$$\sum_{i=1}^{l} h_i(\boldsymbol{\theta}(t)) = 1 \quad \text{and} \quad 0 \le h_i(\boldsymbol{\theta}(t)) \le 1, \quad \forall i. \tag{3}$$

The argument $\boldsymbol{\theta}(t)$ is called the vector of premise variables, which incorporates all the quantities the nonlinear functions depend on. Each nonlinear relationship of system (1) is separately dealt with. Thereby, each nonlinearity $f_k(\boldsymbol{\theta}(t)), k \in \{1, \ldots, n_l\}$, multiplying a state or an input variable, must be bounded from above and below—if not globally on $\mathbb{R}^{n+m}$, then at least locally on the so-called *universe of discourse* $\Omega \subset \mathbb{R}^{n+m}$. This allows to replace the nonlinearity $f_k(\boldsymbol{\theta}(t))$ by its minimum $\underline{f}_k$ and its maximum $\overline{f}_k$ in the linear subsystems and represent it through convex interpolation according to the weighting functions $h_i(\boldsymbol{\theta}(t))$.

2.2 *TS controller design*

As the underlying subsystems of the TS model are linear, we may apply linear control methods upon each of the models before constructing a global controller

$$\mathbf{u}(t) = -\sum_{i=1}^{l} h_i(\boldsymbol{\theta}(t))\, \mathbf{K}_i\mathbf{x}(t), \tag{4}$$

i.e. a *parallel distributed compensator* (PDC), for the overall nonlinear system. Thereby, the total controller gain is assembled according to the weighting functions of the system model. Each $\mathbf{K}_i$ is designed on the basis of classical LQR methodology, such that stable linear controllers result and the individual performance index functions

$$J_i = \frac{1}{2}\int_0^\infty \left(\mathbf{y}^T\mathbf{Q}_{\mathbf{y},i}\mathbf{y} + \mathbf{u}^T\mathbf{R}_i\mathbf{u}\right) \mathrm{d}t, \quad \forall i, \tag{5}$$

are minimized based on the positive definite weighting matrices $\mathbf{Q}_{\mathbf{y},i}$ and $\mathbf{R}_i$. This $\mathcal{H}_2$ performance index minimization problem can also be expressed in terms of LMI conditions, cf. (Scherer & Weiland 2015). However, as the convex interpolation of individual stabilizing controllers not necessarily leads to an overall stable closed-loop behavior of the nonlinear plant

$$\dot{\mathbf{x}} = \sum_{i=1}^{l}\sum_{j=1}^{l} h_i(\boldsymbol{\theta}(t))h_j(\boldsymbol{\theta}(t))\left[\mathbf{A}_i - \mathbf{B}_i\mathbf{K}_j\right]\mathbf{x}, \tag{6}$$

stability needs subsequently to be ensured. This can be done by providing evidence that a common Lyapunov function (CLF) exists for the l linear subsystems. Here, we restrict ourselves to quadratic Lyapunov function candidates $V = \mathbf{x}^T\overline{\mathbf{P}}\mathbf{x}$, such that the search for a common positive definite matrix $\overline{\mathbf{P}} = \overline{\mathbf{P}}^T > 0$ can again be

posed as a LMI problem, which can then efficiently be solved numerically. With $\mathbf{X} = \overline{\mathbf{P}}^{-1}$, stability is assured by the constraints

$$\mathbf{X}\frac{(\mathbf{H}_{ij}+\mathbf{H}_{ji})^T}{2}+\frac{(\mathbf{H}_{ij}+\mathbf{H}_{ji})}{2}\mathbf{X} \prec 0, \quad \forall i \le j \le l, \quad (7)$$

where $\mathbf{H}_{ij} = (\mathbf{A}_i - \mathbf{B}_i\mathbf{K}_j)$ and $i, j \in \{1, \ldots, l\}$.

3 HYBRID SUSPENSION CONFIGURATION

3.1 *Quarter-vehicle test rig*

As already introduced in Section 1.1, we use a quarter-vehicle test stand to develop, analyze, and validate novel suspension control and estimation concepts at our institute. The included suspension strut resembles the aforementioned hybrid suspension configuration such that two separate control inputs are available to ease the well-known conflict of goals. However, for benchmark comparisons a constant setting can be assigned to the hydraulic spring mount adjustment (SMA), i.e. the slow-active actuator, and/or the CVD. Thereby, a conventional passive or a mere semi-active suspension configuration can be emulated, respectively. In doing so, an undamped natural frequency and a damping ratio of the body mass of

$$f_{\mathrm{c,p}} = \frac{1}{2\pi}\sqrt{\frac{c_{\mathrm{c}}}{m_{\mathrm{c}}}} \approx 1.1\,\mathrm{Hz} \quad \text{and} \quad D_{\mathrm{c,p}} = \frac{d_{\mathrm{c}}}{2\sqrt{c_{\mathrm{c}} m_{\mathrm{c}}}} \approx 0.21$$

are attained for the passive set-up.

Based on the conditions at the test rig, all relevant vehicle parameters and major nonlinear characteristics have been identified to form an accurate physical suspension model. This full-scale model includes

- a progressive spring characteristic due to the included compression and tension end stops,
- a CVD with degressive force-velocity characteristics as well as an asymmetric behavior in the compression and the tension direction,
- Coulomb friction within the damper,
- due to the inclined position, a kinematic transmission factor (Matschinsky 1998)

$$i_{\mathrm{dyn}}(\mathbf{x}) = \frac{(\dot{z}_{\mathrm{c}}-\dot{z}_{\mathrm{w}})^{(\mathrm{strut})}}{(\dot{z}_{\mathrm{c}}-\dot{z}_{\mathrm{w}})} = i_0 - i_1\,(z_{\mathrm{c}} - z_{\mathrm{w}}) \quad (8)$$

  between the suspension strut plane and the wheel plane that changes linearly with the suspension deflection, as well as
- a linear-quadratic stiffness and a frequency-dependent damping behavior of the rubber tire including potential wheel lift-off, which is reproduced by the so-called Gehmann model, see Mitschke & Wallentowitz (2004).

On the basis of the quarter-vehicle model in Figure 1 (right) and with the state vector $\mathbf{x}(t) = \left[z_{\mathrm{c}} - z_{\mathrm{w}},\ \dot{z}_{\mathrm{c}},\ z_{\mathrm{w}} - z_{\mathrm{g}},\ \dot{z}_{\mathrm{w}}\right]^T$, the control input vector $\mathbf{u}(t) = \left[u_{\mathrm{hy}},\ u_{\mathrm{cvd}}\right]^T$, and the road-induced disturbance input $d(t) = \dot{z}_{\mathrm{g}}(t)$, we derived a fourth-order nonlinear state space description. While the deflection of the hydraulic actuator $u_{\mathrm{hy}}(t)$ manipulates the spring mount according to $z_{\mathrm{act}}(t) = z_{\mathrm{c}}(t) - \frac{u_{\mathrm{hy}}(t)}{i_{\mathrm{dyn}}(\mathbf{x})}$, $u_{\mathrm{cvd}}(t) = I_{\mathrm{d}}(t)$ adjusts the valve current of the semi-active damper.

The signals measured at the test rig resemble a typical sensor configuration of current production vehicles equipped with mechatronic suspension systems: For suspension control purposes, the chassis and the wheel acceleration $\ddot{z}_{\mathrm{c}}$ and $\ddot{z}_{\mathrm{w}}$, and also the suspension travel $z_{\mathrm{cw}} = z_{\mathrm{c}} - z_{\mathrm{w}}$ are available. These quantities are summarized in the measurement output vector $\mathbf{y}_{\mathrm{m}}(t) = [\ddot{z}_{\mathrm{c}},\ \ddot{z}_{\mathrm{w}},\ z_{\mathrm{cw}}]^T$. However, the damper relative velocity $\dot{z}_{\mathrm{cw}} = \dot{z}_{\mathrm{c}} - \dot{z}_{\mathrm{w}}$ is usually needed for the actuator control of the semi-active damper and, thus, is frequently generated from the available measurement signals by applying a complementary filtering approach described in detail e.g. by Koch et al. (2010). The resulting velocity estimate has no phase delay and is of high estimation accuracy, such that the extended measurement vector $\tilde{\mathbf{y}}_{\mathrm{m}}(t) = [\ddot{z}_{\mathrm{c}},\ \ddot{z}_{\mathrm{w}},\ z_{\mathrm{cw}},\ \dot{z}_{\mathrm{cw}}]^T$ is obtained. Moreover, the low-level actuator controller uses measurements of the damper valve current and the displacement of the spring mount actuator.

For reasons of performance evaluation at the test rig only, force sensors additionally log the dynamic tire load F_{dyn} between the tire and the virtual "road".

However, in order to employ state feedback control laws, the whole state information $\mathbf{x}(t)$ is needed on-line. Therefore, we use a state estimation approach recently proposed in Pletschen & Badur (2014) and Pletschen & Diepold (2016), which is based on a combination of conventional (linear) Kalman filtering and the TS modeling concept introduced in Section 2.1. Through this method, a highly accurate estimation $\hat{\mathbf{x}}(t)$ of the complete vehicle suspension state is available in the experimental set-up at comparatively little numerical cost with regard to the well-known EKF and UKF variants for nonlinear systems.

3.2 *Suspension model in TS representation*

Out of the major nonlinear effects that have been specified in Section 3.1 all effects that operate within the suspension strut between the vehicle body and the wheel may be summarized in the nonlinear spring and damping force maps $F_{\mathrm{c}}(\mathbf{x})$ and $F_{\mathrm{d}}(\mathbf{x},\ u_{\mathrm{cvd}})$. Note that these force characteristics are rather given in terms of identified look-up tables than by analytic relationships. Transforming the force maps into state- and input-affine nonlinearities, the nonlinear stiffness coefficient map $f_1(\boldsymbol{\theta}(t)) \triangleq \tilde{c}_{\mathrm{c}}(\mathbf{x})$ and the nonlinear damping coefficient map $f_2(\boldsymbol{\theta}(t)) \triangleq \tilde{d}_{\mathrm{c}}(\mathbf{x}, u_{\mathrm{cvd}})$ result. These are shown in Figure 2, where a selection of constant valve current settings u_{cvd} are depicted for the semi-active damping device. The passive damping coefficient is shown by the solid black line and the damping coefficients of the softest and the hardest damper characteristic are illustrated by dashed black

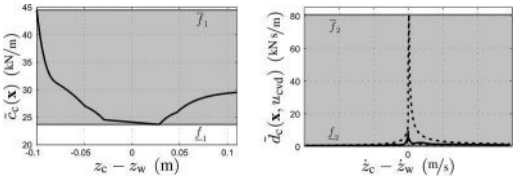


Figure 2. Nonlinear stiffness (left) and damping coefficient map (right) with their sector bounds.

Table 1. Parameters of TS suspension model.

Parameter	Symbol	Value	Unit
Sprung mass	m_c	≈ 500	kg
Unsprung mass	m_w	≈ 70	kg
Tire stiffness	c_w	≈ 380	kN/m
Tire damping	d_w	$= 0$	N s/m
Sector bounds:			
Stiffness coefficient	$\tilde{c}_c \in \left[\underline{f}_1, \bar{f}_1\right]$	$\approx [23, 45]$	kN/m
Damping coefficient	$\tilde{d}_c \in \left[\underline{f}_2, \bar{f}_2\right]$	$\approx [0.4, 81]$	kN s/m

lines. Thus, the nonlinearities used in the TS model of the controlled suspension have a clear physical interpretation. To keep the number l of linear subsystems small, the nonlinear tire characteristics from Section 3.1 are neglected in the TS model and a linearized tire stiffness is assumed. As a result, $\boldsymbol{\theta}(t) = [z_{cw},\ \dot{z}_{cw},\ u_{cvd}]^T$ holds for the premise vector. A state space model of the hybrid vehicle suspension based on the nonlinearities $\tilde{c}_c(\mathbf{x})$ and $\tilde{d}_c(\mathbf{x}, u_{cvd})$ is explicitly given in Pletschen & Diepold (2016).

As a set of two sector bounds $\underline{f}_k$ and $\bar{f}_k$ is needed to describe each of the two nonlinearities, a number of $l = 4$ linear subsystems results. The ith linear subsystem in (2) is then constructed by employing one specific combination of minimum and maximum sector bounds instead of using the nonlinearities themselves and, thus, represents the nonlinear system at a vertex. The TS suspension model parameters and the sector bounds of the TS nonlinearities are given in Table 1.

4 SUSPENSION CONTROLLER DESIGN

4.1 *Performance objectives*

Traveling on a road, the wheel mass of the vehicle is excited by the road irregularities, which has a negative impact on both ride comfort and road holding performance. Here, we consider the vertical road profile velocity as disturbance input to the system, i.e. $d(t) = \dot{z}_g(t)$. In general, occupants rate *ride comfort* to a large extent by the amount of acceleration that they are exposed to. Hence, the vertical acceleration $\ddot{z}_c(t)$ of the vehicle body is taken as a measure. The application of a comfort-weighting filter (ISO 1997) results in the quantity $\ddot{z}_{c,iso}(t)$ and accentuates the comfort-relevant frequency range between 4–8 Hz, where the human body is most sensitive to vertical vibration. In order to account for the development over time, the root mean square (rms) average of both signals $\|\ddot{z}_c(t)\|_{rms}$ and $\|\ddot{z}_{c,iso}(t)\|_{rms}$ is used as a comfort measure. However, also the maximum acceleration experienced $\max(|\ddot{z}_c|)$ is crucial.

On the other hand, *road holding* properties immediately depend on the variations of the force between the tire and the ground, i.e. the dynamic tire load F_{dyn}. Hence, for good tire-road contact, $\|F_{dyn}(t)\|_{rms}$ should be as small as possible and $F_{dyn}(t)$ should never exceed the negative value of the static tire load $F_{stat} = (m_c + m_w) \cdot g$ to avoid wheel lift-off.

At the same time, the *suspension deflection* z_{cw} must stay within the constructional suspension travel limits, i.e. $-0.10\,\text{m} = \underline{z}_{cw} \le z_{cw}(t) \le \bar{z}_{cw} = 0.11\,\text{m}$. The relevant performance quantities are summarized in the controlled output vector $\mathbf{y}(t) = [\ddot{z}_c,\ F_{dyn},\ z_{cw}]^T$.

However, while the adjustable, but ultimately passive damping device only consumes a negligible amount of auxiliary power by its varying valve current u_{cvd}, the demand of the low-bandwidth active actuator needs explicitly to be taken into account. It is quantified by the average of the positive mechanical actuator power as defined in Koch et al. (2011)

$$\overline{P^+} = \frac{1}{T}\int_0^T P^+(\tau)\mathrm{d}\tau, \quad \text{where} \tag{9}$$

$$P^+(t) = \begin{cases} F_{hy}(t)\Delta\dot{z}_{hy}(t) & \text{for} \quad F_{hy}(t)\Delta\dot{z}_{hy} > 0 \\ 0 & \text{else.} \end{cases} \tag{10}$$

Therein, $F_{hy}(t)$ and $\Delta\dot{z}_{hy}(t)$ represent the actuator force and the relative actuator velocity, respectively.

4.2 *$\mathcal{H}_2$-optimal TS suspension control*

With the hybrid suspension configuration, we have two separate control inputs at our disposal: we can choose an adequate damping characteristic through the choice of the damper valve current $u_{cvd}(t)$ and, in addition, we can specify a desired deflection $u_{hy}(t)$ of the hydraulic SMA. However, while the valve current of the CVD does not enter the system in an affine manner—it rather changes a major characteristic within the dynamic matrix $\mathbf{A}(\mathbf{x}, \mathbf{u})$ of the system, namely the damping—the deflection of the hydraulic actuator can be considered as an affine control input. As a result, the information how the valve current influences the damping coefficient and, thus, the suspension dynamics is not included in the structure of the system matrices $(\mathbf{A}_i, \mathbf{B}_i, \mathbf{C}_i, \mathbf{D}_i)$. In fact, it is incorporated in the nonlinear weighting functions $h_i(\boldsymbol{\theta}(t))$. As TS controller design is based on these matrices of the linear subsystems, this relation is not apparent to a TS controller. Moreover, the control of the SMA should match with the amount of damping realized by the variable damper. Therefore, we employ a

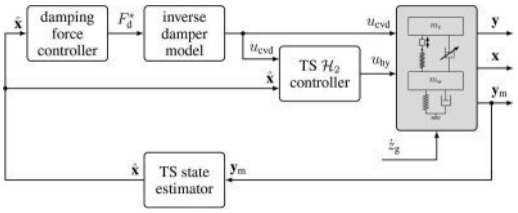


Figure 3. TS PDC controller structure for the hybrid suspension configuration where the desired damper force F_{d}^* is calculated from a skyhook or a LQ control law, respectively.

parallel approach, which is illustrated in Figure 3: A damping force controller specifies a desired force F_{d}^* as a virtual, affine control input, which is then turned into a desired damper valve current u_{cvd} by means of an inverse damper model based on the static damping characteristics. Depending on the controller variant chosen, the valve current $u_{\mathrm{cvd}}(t)$ of the CVD is either kept constant at a medium level, i.e. the passive setting of the damper, or the desired damping force is determined by means of a skyhook or a linear-quadratic control law. Subsequently, the $\mathcal{H}_2$ TS PDC controller calculates an adequate deflection $u_{\mathrm{hy}}(t)$ of the low-bandwidth hydraulic actuator and thereby accounts for the present damping.

4.2.1 *Spring mount deflection controller*

We want to design the control law $u_{\mathrm{hy}}(t)$ for the spring mount adjustment such that the controller takes into account all major nonlinearities of the suspension. Therefore, we apply the TS PDC framework as introduced in Section 2.2. The weighting matrices $\mathbf{Q}_{\mathbf{y},i}$ and R_i in (5) are the tuning knobs of the LQ-based PDC controller. For the sake of transparent controller parametrization, we choose the weights identical for all linear subsystems, i.e. $\mathbf{Q}_{\mathbf{y},i} \equiv \mathbf{Q}_{\mathbf{y}}$ and $R_i \equiv R$ holds. A diagonal structure is specified for the weighting matrices, such that $\mathbf{Q}_{\mathbf{y}} = \mathrm{diag}\left(q_{\dot{z}_{\mathrm{c}}},\ q_{F_{\mathrm{dyn}}},\ q_{z_{\mathrm{cw}}}\right)$ and $R = r_{u_{\mathrm{hy}}}$ weight the controlled output $\mathbf{y} = [\dot{z}_{\mathrm{c}},\ F_{\mathrm{dyn}},\ z_{\mathrm{cw}}]^T$ and the control input u_{hy}, respectively. As the choice of these weights is crucial for the control performance, we determine them by means of a Pareto optimization using a numerical multi-objective optimization framework, (Deb et al. 2002). In the process, one simulation of the nonlinear full-scale model as introduced in Section 3.1 traveling on a road profile, which has been artificially generated from white noise, is conducted for each controller parametrization. Based on the performance numbers of each configuration, a suitable set of controller weights that results in a Pareto-optimal performance of the controlled suspension can be selected. Thereby, normalized weights $\tilde{q}_{\dot{z}_{\mathrm{c}}}$, $\tilde{q}_{F_{\mathrm{dyn}}}$, $\tilde{q}_{z_{\mathrm{cw}}}$, and $\tilde{r}_{u_{\mathrm{hy}}}$ allow to put physical insight into the tuning process. Based on the rms-value $\|\xi(t)\|_{\mathrm{rms}}^{\mathrm{passive}}$ of the to-be-weighted quantity $\xi(t)$ resulting from a simulation of the passive configuration on the same excitation, the absolute weights q_ξ and r_ξ are calculated by $q_\xi = \tilde{q}_\xi / \|\xi(t)\|_{\mathrm{rms}}^{\mathrm{passive}}$ and $r_\xi = \tilde{r}_\xi / \|\xi(t)\|_{\mathrm{rms}}^{\mathrm{passive}}$, respectively. Since essentially only the relative weighting of variables decides on the feedback law, we fix $\tilde{r}_{u_{\mathrm{hy}}} = 1$ and alter only the remaining normalized weights. Out of the resulting Pareto front, we choose a set of normalized weights $\tilde{q}_\xi$ corresponding to an intermediate controller, which reduces both body acceleration and dynamic tire load without producing excessive suspension travel. The values of the chosen weights are specified in Table 2.

Table 2. Normalized output and input weights of TS PDC controller resulting from numerical Pareto optimization.

	$\tilde{q}_{\dot{z}_{\mathrm{c}}}$	$\tilde{q}_{F_{\mathrm{dyn}}}$	$\tilde{q}_{z_{\mathrm{cw}}}$	$\tilde{r}_{u_{\mathrm{hy}}}$
Value	$2.5 \cdot 10^5$	$1 \cdot 10^5$	$1 \cdot 10^5$	1

4.2.2 *Damping force controller*

The TS PDC controller as designed in Section 4.2.1 is applied to the SMA in combination with different damper settings: A configuration that omits the variable damper and instead uses a conventional, passive one is synthesized by applying a constant medium valve current $I_{\mathrm{d,p}}$ to the damper (PDC + passive).

In the case of the skyhook controlled damper (PDC + SH), the desired force F_{d}^* is calculated from a combination of the nonlinear, passive damping characteristic and an additional skyhook component as

$$F_{\mathrm{d,sky}}^* = -\tilde{d}_{\mathrm{c}}(\mathbf{x}, I_{\mathrm{d,p}}) \cdot \dot{z}_{\mathrm{cw}} - d_{\mathrm{sky}} \cdot \dot{z}_{\mathrm{c}}. \tag{11}$$

Therein, the virtual skyhook damping coefficient which damps the absolute vehicle body velocity is chosen to $d_{\mathrm{sky}} = 2000\,\mathrm{N\,s/m}$ (Koch et al. 2011).

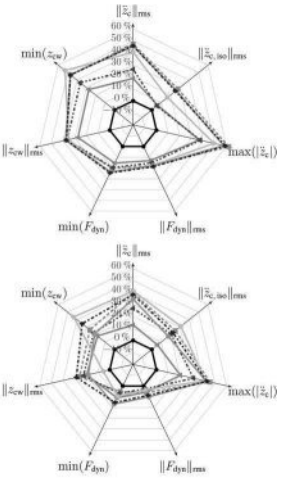
On the other hand, the LQ damping force controller (PDC + LQR) is designed on the basis of the quarter-vehicle model from Section 3 linearized at its static equilibrium position. The linearized model incorporates a minimum passive damping coefficient $\underline{f}_2 = 400\,\mathrm{N\,s/m}$ adopted from the TS representation of the suspension model, see Table 1, and assumes an additional controllable force $F_{\mathrm{add}}(t)$ in parallel to the linear spring and the linear minimum damper as control input. In the LQ design for the CVD, the controlled output variables $\mathbf{y}$ as well as the force control input F_{add} are weighted in the cost function J_{cvd}. The normalized output weights $\tilde{q}_{\dot{z}_{\mathrm{c}}}$, $\tilde{q}_{F_{\mathrm{dyn}}}$, and $\tilde{q}_{z_{\mathrm{cw}}}$ are chosen consistent with the TS PDC controller, see Table 2, and are together with the normalized input weight $\tilde{r}_{F_{\mathrm{add}}} = 1$ the result of a numerical optimization, see Section 4.2.1. The resulting feedback law $F_{\mathrm{add}}(t) = -\mathbf{k}_{\mathrm{cvd}}^T \mathbf{x}$ is added to the minimum damping force, such that the overall desired damping force is calculated by

$$F_{\mathrm{d,lqr}}^* = -\underline{f}_2 \cdot \dot{z}_{\mathrm{cw}} - \mathbf{k}_{\mathrm{cvd}}^T \mathbf{x}. \tag{12}$$

Restricted by the available damper characteristics, the desired damping force is realized up to the available limit, leading to a *clipped-optimal* damper force.

Table 3. Controller performance on country road profile of bad quality ($v_{\text{veh}} = 50\,\text{km/h}$) in the simulation (left). Spider charts illustrate the benefit relative to the passive configuration in simulations (upper right) and experiments (lower right).

SMA: / CVD:	passive	fixed SH	SH	LQR	PDC passive	PDC SH	PDC LQR
Quantity	—●—	—▲—	--▲--	—●—	—●—	--◆--	--■--
$\|\ddot{z}_c\|_{\text{rms}}$ (m/s^2)	1.71	1.39	1.26	1.01	0.93	0.92	0.90
Benefit vs. passive	–	18.8 %	26.4 %	40.7 %	45.7 %	46.1 %	47.5 %
$\|\ddot{z}_{c,\text{iso}}\|_{\text{rms}}$ (m/s^2)	1.05	0.98	0.99	0.87	0.78	0.78	0.76
Benefit vs. passive	–	6.2 %	5.4 %	16.8 %	26.0 %	25.3 %	27.9 %
$\max(\|\ddot{z}_c\|)$ (m/s^2)	6.75	4.27	4.20	3.42	2.85	2.76	2.57
Benefit vs. passive	–	36.8 %	37.7 %	49.3 %	57.7 %	59.0 %	61.9 %
$\|F_{\text{dyn}}\|_{\text{rms}}$ (N)	1127	980	955	929	924	916	927
Benefit vs. passive	–	13.1 %	15.3 %	17.6 %	18.0 %	18.7 %	17.8 %
$\min(F_{\text{dyn}})$ (N)	−3475	−2939	−2794	−2638	−2656	−2625	−2778
Benefit vs. passive	–	15.4 %	19.6 %	24.1 %	23.6 %	24.5 %	20.1 %
$\|z_{\text{cw}}\|_{\text{rms}}$ (cm)	2.8	2.0	1.7	1.8	1.7	1.7	1.7
Benefit vs. passive	–	27.3 %	36.5 %	35.2 %	37.8 %	37.3 %	36.8 %
$\min(z_{\text{cw}})$ (cm)	−9.1	−6.6	−5.8	−4.3	−4.8	−4.8	−4.8
Benefit vs. passive	–	27.3 %	36.5 %	52.8 %	47.1 %	46.9 %	46.9 %
$\overline{P^+}$ (W)	0	0	123	188	154	163	140



4.3 *Benchmark controllers*

In order to assess the effectiveness of the proposed control approach, we compare the TS PDC controller variants introduced in Section 4 with well-known controller configurations from the literature. The state-of-the-art approach is resembled by controlling only the CVD via the skyhook force in (11), but keeping the spring mount actuator fixed at a constant level (fixed + SH). Thereby, a semi-active suspension configuration is reproduced.

An active skyhook configuration (SH) is achieved by distributing the skyhook force in (11) in a dynamic-optimal manner to the two separate control inputs u_{cvd} and u_{hy}. This control allocation approach splits the overall desired suspension force across the two controllable force devices such that—besides the restricted damper characteristics and the limited active actuator bandwidth—as much of the reference force can be realized as possible, see (Spirk et al. 2011). This allocation method promises the highest possible performance with respect to the underlying overall suspension force control concept.

Finally, also the LQ-based damper force in (12) is employed as an overall desired suspension force reference. This configuration (LQR) also makes use of the dynamic-optimal control allocation approach described before to split the overall desired force across the two control input variables.

5 RESULTS: SIMULATION AND EXPERIMENT

The validation of the TS PDC control approach is conducted by means of simulations of the full-scale suspension model and experiments at the hybrid quarter-vehicle test stand, see Section 3.1. In the simulation, now also simple actuator models are incorporated to approximately reflect the force generation dynamics of the CVD and the SMA. Other than in the parameter optimization in Section 4, a measurement of a real country road profile traveled at a vehicle speed of $v_{\text{veh}} = 50\,\text{km/h}$ is used as excitation.

While we directly use the state variables $\mathbf{x}(t)$ for the controller feedback in the simulation, in the experiments we employ the TS Kalman filtering approach from Pletschen & Diepold (2016) to generate and feedback the estimated state vector $\hat{\mathbf{x}}(t)$.

Table 3 lists the performance values of the various controller configurations in comparison with the passive setting for the simulation results. Spider charts in Table 3 (right) visualize the performance gain

$$\Gamma\left(\|\cdot\|\right) = 1 - \frac{\|\cdot\|_{\text{controlled}}}{\|\cdot\|_{\text{passive}}} \tag{13}$$

for each relevant quantity $\|\cdot\|$ with regard to the passive configuration (black solid line) for the simulation (upper chart) and the experiment (lower chart). All controlled set-ups show superior performance over the conventional, passive suspension configuration. The ride comfort measures can be improved by just under 20% by the semi-active skyhook-controlled configuration, up to just under 50% by the combination of the TS PDC-controlled active actuator and the LQ-controlled damper. Also in the maximum absolute body acceleration the TS PDC controller variants show the highest benefit of about 60%, when compared to the passive numbers. With respect to road holding, the performance increase amounts to 15–20% in the rms-values and up to 25% for the most critical tire-road contact. The capability of the TS PDC control

is confirmed by the fact that the PDC + passive variant, where the damper characteristic is not altered at all, almost reaches the same high performance gains as the PDC + LQR alternative at a slightly higher power demand. Although the profile is challenging with respect to suspension travel, see the minimum suspension deflection of the passive configuration in Table 3, all controlled settings securely meet the constructional constraints. This gain in performance comes along with a significant power demand of the SMA in the active set-ups of up to $\overline{P^+} = 188$ W for the solely LQ-controlled suspension. However, with power savings of $\Delta\overline{P^+} = 25$–$48$ W, the TS PDC controller variants act considerably more efficient, especially in view of the higher capability.

The experimental validation confirms the efficiency of the TS PDC control. Though the performance benefit decreases overall by 5–15 % in comparison to the simulation, ride comfort can still be improved by 20–45%. Despite the additional comfort gain, all the active configurations feature road holding abilities that are comparable or even outperform the semi-active state-of-the-art solution. The remarkable performance of the purely LQ-controlled hybrid suspension is alleviated by its additional power demand of $\Delta\overline{P^+} = 70$–$100$ W with respect to the TS PDC controllers. The performance loss in the experiments for almost all numbers can mainly be explained by two facts: first, the controlled suspensions depend on estimated states and, second, the complex force dynamics including hysteresis of the real CVD cannot be reproduced by the simple actuator model in the simulation.

6 CONCLUSION

Making use of the TS representation of a mechatronic vehicle suspension, we designed a parallel distributed compensator, which generates the nonlinear control for a low-bandwidth active spring mount actuator. Thereby, the PDC is constructed on the basis of well-known linear-quadratic control theory, while simultaneously taking into account the nonlinear behavior of the variable damper and other nonlinear effects. The combination of the TS PDC control with three adequate strategies to control the semi-active damper and a comparison with various benchmark active and semi-active control approaches have shown the capability of the method when employed on measurements of real road profiles. In fact, even in the experiments at the quarter-vehicle test stand, ride comfort improvements of up to 45% can be realized by the TS controllers, yet maintaining a superior road holding ability over the passive and the skyhook-controlled benchmark suspension configurations.

REFERENCES

Deb, K., A. Pratap, S. Agarwal, & T. Meyarivan (2002). A fast and elitist multiobjective genetic algorithm: NSGA-II. *IEEE Transactions on Evolutionary Computation* 6 (2): 182–197.

Hrovat, D. (1997). Survey of advanced suspension developments and related optimal control applications. *Automatica* 33 (10): 1781–1817.

ISO (1997). *ISO 2631-1: Mechanical vibration and shock – Evaluation of human exposure to whole-body vibration*.

Karnopp, D., M. J. Crosby, & R. A. Harwood (1974). Vibration control using semi-active force generators. *Transactions of the ASME – Journal of Engineering for Industry* 96 (2): 619–626.

Koch, G., T. Kloiber, & B. Lohmann (2010). Nonlinear and filter based estimation for vehicle suspension control. *Proc. 49th IEEE CDC*, 5592–5597.

Koch, G., S. Spirk, E. Pellegrini, N. Pletschen, & B. Lohmann (2011). Experimental validation of a new adaptive control approach for a hybrid suspension system. *Proc. 2011 ACC*, 4580–4585.

Matschinsky, W. (1998). *Road Vehicle Suspensions*. John Wiley & Sons, Inc.

Mitschke, M. & H. Wallentowitz (2004). *Dynamik der Kraftfahrzeuge.* 4th. Springer-Verlag Berlin.

Novák, M. & M. Valášek (1996). A new concept of semi-active control of truck's suspension. *Proceedings of the International Symposium on Advanced Vehicle Control* (AVEC'96), 141–152.

Pletschen, N. & P. Badur (2014). Nonlinear state estimation in suspension control based on Takagi-Sugeno model. *Proc. 19th IFAC World Congress*, 11231–11237.

Pletschen, N. & K. J. Diepold (2016). Nonlinear state estimation for suspension control applications: a Takagi-Sugeno Kalman filtering approach. *Control Engineering Practice*.

Scherer, C. & S. Weiland (2015). *Linear Matrix Inequalities in Control*. Jan.

Spirk, S., G. Koch, E. Pellegrini, & B. Lohmann (2011). *Dynamik- und energieoptimale Stellgrößenaufteilung für die Regelung eines hybriden Fahrwerks. Intelligente Technische Systeme – Entwurf mechatronischer Systeme*. Ed. by J. Gausemeier et al. Vol. 294, 107–119.

Takagi, T. & M. Sugeno (1985). Fuzzy identification of systems and its applications to modeling and control. *IEEE Transactions on Systems, Man and Cybernetics* 15 (1): 116–132.

Tanaka, K. & H. O. Wang (2001). *Fuzzy Control Systems Design and Analysis: A Linear Matrix Inequality Approach*. JohnWiley & Sons, Inc.

Tseng, H. E. & D. Hrovat (2015). State of the art survey: active and semi-active suspension control. *Vehicle System Dynamics* 53 (7): 1034–1062.

Unger, A. (2012). *Quadratic Optimal Control Suitable for Series Production for Semi-Active Car Suspensions*. (in German). Dissertation. Technische Universität München.

Venhovens, P. J. T. (1994). *Optimal Control of Vehicle Suspensions.* Dissertation. Delft University of Technology.

Powertrain

Advanced Vehicle Control – Edelmann, Plöchl & Pfeffer (Eds)
© 2017 Taylor & Francis Group, London, ISBN 978-1-138-02992-7

Optimal design of hybrid track-type dozers with two-planetary gear sets and clutches

Z. Qin, Y. Luo & K. Li
State Key Laboratory of Automotive Safety and Energy, Tsinghua University, Beijing, China

Z. Pan & H. Peng
Department of Mechanical Engineering, University of Michigan, Ann Arbor, MI, USA

ABSTRACT: Series hybrid electric systems for track-type dozers (TTD) have been applied now. This paper provides a new type of design with multi-modes based on two-planetary gear sets. The track on each side can be controlled independently, which can realize central steering and precise control. A systematic methodology is developed to screen out optimal designs which can ensure the driving attributes such as steering and going backwards. The fuel economy of the feasible designs is then compared with the series hybrid TTD under typical conditions using optimal control. The results show that hybrid systems with planetary gear sets have developmental potential for TTD, which can be used for future application.

1 INTRODUCTION

The hybrid electric powertrain based on planetary gear (PG) sets has been used widely on passenger cars, such as Toyota Prius or Chevy Volt. The powertrain based on PG sets is very compact which can realize a continuously variable transmission. With different components or connections to the node, different kinds of powertrain can be found, which may be fit for different types of cars.

The research of the drive system for the track-type dozer (TTD) which is widely used for construction or agriculture is important. For crawler dozer which is used for construction, traditional transmissions using directly internal combustion engine (ICE) are always adopted, with high towing power, which costs lots of fuel consumption and has low energy efficiency. Hybrid power is an effective way to save the energy and reduce the emission. Hybrid electric crawler dozer has been researched for long time, while Caterpillar firstly made out the hybrid track-type dozer called D7E that has been proved with good performance using the electric generator, power inverter and propulsion module in the electric drive system to replace the traditional mechanical components. The system adopts a series hybrid powertrain. The engine and the generator work together to give the power to the two motors connected to the differential steering system to drive the dozer. D7E works without the traditional mechanical gearbox and can reduce the fuel economy by 20% compared with D7 which has same size while driven by traditional ICE transmission (Kwak, S. et al. 2010).

Many researches have been done base on power-split hybrid vehicles using planetary gear sets which are widely used due to the higher operation efficiency compared with the series or parallel hybrid powertrain. Besides, nearly 82% of the market share of hybrid passenger cars are power-split ones in 2013 in the USA (Online, 2014). The optimal design of power-split hybrid vehicles was firstly proposed by Jinming Liu who establishes a systematic design approach for two planetary gear power-split passenger cars with two modes (Liu J. et al. 2010). Many researches analyse different possible configurations using clutches and have come up with better designs compared with existing ones. However, the research mainly focuses on one-output planetary gear sets with one drive shaft. Few researches have been done using two outputs. Yoshimura from Toyota firstly gives a drive system using two planetary gear sets which has two outputs to control the front and rear drive shaft respectively (Yoshimura, T. 2013). Ziheng Pan proposes the optimal design of hybrid pick-up trucks which adopts two-output shafts to realize all-wheel-drive (Pan Z. et al. 2015).

As for the track-type dozer (TTD), no one has done a research about a hybrid power drive system based on planetary gear sets. In this paper, we give the optimal configuration design method about the drive system of TTD with planetary gear sets, which have two outputs to drive the left and right track independently.

Prior studies have shown that there exists a large number of possible configurations using two planetary gear sets (Zhang X. 2014). Considering about the towing capacity, the steering performance and fuel economy, the design method is proposed based on the configuration mentioned in the existing Toyota pattern, which can find the optimal design for TTD.

The main contributions of this paper can be listed as follows. 1) The drive system with two outputs to control the left and right tracks respectively using planetary gear sets is firstly proposed. 2) The optimal design method for the TTD is established to screen out the large number of configurations and designs. 3) The optimal design can both realize the towing capacity and steering without extra steering system which can make it more compact and reduce the complexity. The paper is organized as follows. Section 2 presents the research object and describe the design process based on the reference patent. Section 3 shows the automated modelling method for all the designs. Section 4 presents the screening conditions for the TTD. Section 5 shows the advantages of the proposed design compared with conventional and series hybrid ones. Section 6 gives the conclusion of this paper.

2 ESEARCH OBJECT AND DESIGN PROCESS

The referred patented Toyota design has two outputs, the front and the rear driving output shown in Fig. 1.

The system has one engine, two motors and two outputs, which are connected by six nodes in two planetary gear (PG) sets. The PG sets are connected by a clutch.

There are three nodes in a single PG set, namely the ring gear, the sun gear and the carrier gear. The kinematics of the PG can be shown as follows using the lever diagram.

$$\omega_R \cdot R + \omega_S \cdot S = \omega_C \cdot (R+S) \tag{1}$$

where ω_R, ω_S, ω_C represent the speed of the ring, sun and carrier gear respectively. R and S are the radius of the ring and sun gear.

Using the lever diagram (H. Benford. et al. 1981), the dynamic equations of the Toyota patent can be written as follows.

$$\begin{aligned}
&(I_e + I_{c1})\dot{\omega}_e = T_e + F_1(R_1 + S_1)\\
&(I_{V_r} + I_{r2} + I_{mg2})\dot{\omega}_R = -T_r + T_{mg2} - F_2 S_2\\
&(I_{mg1} + I_{s1})\dot{\omega}_{mg1} = T_{mg1} - F_1 S_1\\
&(I_{V_f} + I_{c2})\dot{\omega}_F = -T_f + F_2(R_2 + S_2)\\
&I_{r1}\dot{\omega}_{r1} = T_{c1} - F_1 R_1\\
&I_{r2}\dot{\omega}_{r2} = -T_{c1} - F_2 R_2\\
&(R_1 + S_1)\dot{\omega}_e = R_1\dot{\omega}_{r1} + S_1\dot{\omega}_{mg1}\\
&(R_2 + S_2)\dot{\omega}_{V_f} = R_2\dot{\omega}_{r2} + S_2\dot{\omega}_{mg2}
\end{aligned} \tag{2}$$

In this article, we adopt this kind of configuration to realize the hybrid system of TTD. The components are one engine, two motors and two outputs. The two outputs control the left and right side of the track respectively. One motor is directly connected to one output. To describe clearly for our design, we name several terms as follows: Configuration shows how the components connect to the nodes of PG. Design means that the clutches have been placed into the configurations. Mode means that the status of all clutches in one design has been firmed, engaged or disengaged.

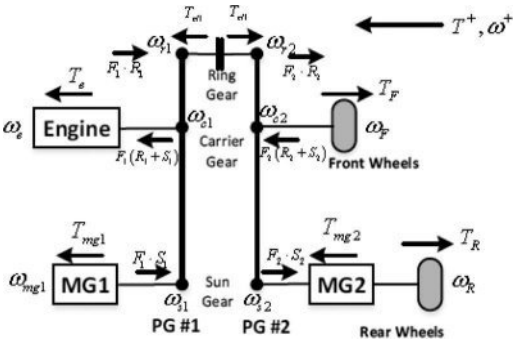


Figure 1. Toyota patent with two outputs.

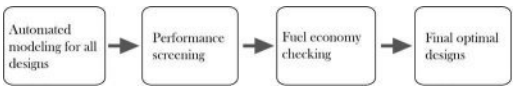


Figure 2. The whole design process.

To make the TTD controllable and drivable, we choose to use 3 clutches in our design to get 8 modes. But actually, 6 modes are finally used to get 2 or 3 degree of freedom, which means that the mode with all clutches engaged or disengaged is considered infeasible.

All designs should be searched to find the feasible ones for TTD. The process can be summarized into three main steps for our research object in Fig. 2. The process will be described in detail in the sections below.

3 AUTOMATED MODELING WITH CLUTCHES

The dynamic equation of the patent can be written into a matrix in Equation (3). The square matrix can be decomposed into four parts in Equation (4). D matrix represents the connection between the components and the nodes, which can be called the feature matrix. A certain D matrix corresponds to a unique design.

$$\begin{bmatrix}
I_e+I_{c1} & 0 & 0 & 0 & 0 & 0 & R_1+S_1 & 0 \\
0 & I_{V_r}+I_{r2}+I_{mg2} & 0 & 0 & 0 & 0 & 0 & -S_2 \\
0 & 0 & I_{mg1}+I_{s1} & 0 & 0 & 0 & -S_1 & 0 \\
0 & 0 & 0 & I_{c2}+I_{V_f} & 0 & 0 & 0 & R_2+S_2 \\
0 & 0 & 0 & 0 & I_{r1} & 0 & -R_1 & 0 \\
0 & 0 & 0 & 0 & 0 & I_{r2} & 0 & -R_2 \\
R_1+S_1 & 0 & -S_1 & 0 & -R_1 & 0 & 0 & 0 \\
0 & -S_2 & 0 & R_2+S_2 & 0 & -R_2 & 0 & 0
\end{bmatrix}
\begin{bmatrix} \dot{\omega}_e \\ \dot{\omega}_{V_r} \\ \dot{\omega}_{mg1} \\ \dot{\omega}_{V_f} \\ \dot{\omega}_{r1} \\ \dot{\omega}_{r2} \\ F \\ F_2 \end{bmatrix}
=
\begin{bmatrix} T_e \\ T_{V_r}+T_{mg2} \\ T_{mg1} \\ T_{V_f} \\ 0 \\ 0 \\ 0 \\ 0 \end{bmatrix} \tag{3}$$

$$\begin{bmatrix} J & D \\ D^T & 0 \end{bmatrix}\begin{bmatrix} \dot{\Omega} \\ F \end{bmatrix} = \begin{bmatrix} T \\ 0 \end{bmatrix} \tag{4}$$

3 clutches are added to each configuration, the clutch can be connected to two nodes in one PG, or to different PG, or the grounding clutch of one node. As the two outputs cannot be grounded and only one clutch is needed which locks any two nodes of one PG, the placement number of one

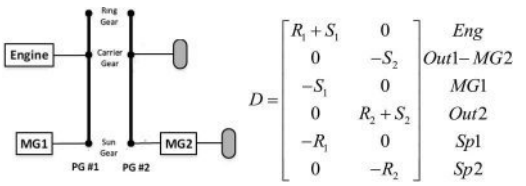


Figure 3. The matrix of configuration.

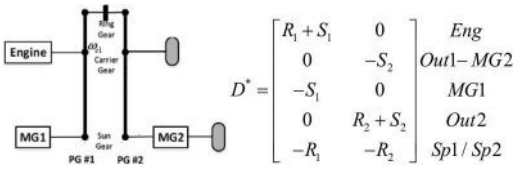


Figure 4. The matrix of design with clutches.

clutch is $C_6^2+6-4-2=15$ (Zhang X. et al. 2015). So all designs are got with the total number of $A_6^4 \cdot C_{15}^3/2=81900$. Assume that the gear ratio of each PG is 2.5 and the final drive ratio for each output is between 50:1 to 80:1 according to real application.

As described before, through D matrix, we can know how the components are connected to PG sets. First, all the D matrixes for all configurations can be written automatically by the following rules.

Rule 1. The D matrix has six rows which represents the six nodes, and two columns which represents the number of PG sets. In our design, the six rows represent the engine, motor 1, motor 2 and output 1, output2, spare 1 (unconnected with any component) and spare 2 respectively.

Rule 2. For all components, the node coefficient should be entered, $-S_i$ means the component is connected to the sun gear of the ith PG. $-R_i$ means the component is connected to the ring gear of the ith PG. R_i+S_i means the component is connected to the carrier gear of the ith PG.

Rule 3. The other elements should be filled with zeros.

Take the Toyota patent as an example, the configuration and the D matrix can be established below in Fig. 3.

The next step is to add clutches to the configuration which forms the design. Transition should be defined as clutch engagement changes.

Rule: When the ath node is connected to the bth node, assuming that $a<b$, then add the bth row of D to ath row while elimate the ath row. When the ath node is connected to the ground, elimate the ath row directly. Then the new transited matrix D* can be got.

For example, the Toyota patent structure has one clutch, and the D* is as follows.

After these two steps, the dynamic equations for all designs can be written for future use. Besides, all modes in a design can be represented by a unique D*.

4 PERFORMANCE SCREENING

To design the TTD which can satisfy the necessary features, the performances below should be checked to find the feasible designs in all design pool.

To provide large driving power, the positive torque at both outputs should be controlled independently by the components, which also ensures that TTD can steer at different velocity.

Besides, TTD can drive backwards with engine on or by pure electricity.

In order to realize central steering, the two outputs should have same output power but opposite operating speed, which can be controlled by the components.

The three attributes above should be checked for all designs and all modes. If all three attributes can be realized by any mode in a design, the design can be proved feasible. This process can be tested by a deduced matrix.

Through automated modelling, the speed and torque relations of each node and component can be obtained by the dynamics and the matrix D*. However, the relations are still hard to obtain because of other variables such as F. So A* is constructed to obtain a final matrix which can easily calculate the speed and torque relations between components as shown in Equation (5).

$$\begin{bmatrix} \omega_{eng} \\ \omega_{out1-mg2} \\ \omega_{mg1} \\ \omega_{out2} \end{bmatrix} = A^* \begin{bmatrix} T_{eng} \\ T_{out1}+T_{mg1} \\ T_{mg1} \\ T_{out2} \end{bmatrix} \tag{5}$$

To obtain the A*, define a matrix E:

$$E = J^{-1/2} D^* \tag{6}$$

Then after some manipulations, the results can be shown below:

$$\dot{\Omega} = J^{-1/2}(I - E(E^T E)^{-1} E^T) J^{-1/2} T \tag{7}$$

Then we get A*,

$$A^* = J^{-1/2}(I - E(E^T E)^{-1} E^T) J^{-1/2} \tag{8}$$

If the inertias of the components are ignored, then A* can be simplified to:

$$A^* = (D^{*T} D^*)^{-1}(I - D^*(D^{*T} D^*)^{-1} D^{*T}) \tag{9}$$

If A* is equal to the following matrix.

$$A^* = \begin{bmatrix} A^*_{11} & A^*_{12} & A^*_{13} & A^*_{14} \\ A^*_{21} & A^*_{22} & A^*_{23} & A^*_{24} \\ A^*_{31} & A^*_{32} & A^*_{33} & A^*_{34} \\ A^*_{41} & A^*_{42} & A^*_{43} & A^*_{44} \end{bmatrix} \tag{10}$$

Then all the three attributes can be tested by the conditions in Table 1.

After the performance screening, totally 20 designs among 8 configurations are feasible. The fuel economy of the survived designs will be further analyzed as follows.

Table 1. Performance screening conditions.

Performance	Screening conditions
Two output controlled independently	$rank(A^* \geq 2), \frac{A^*_{21}}{A^*_{22}} > 0, \frac{A^*_{41}}{A^*_{44}} > 0$
Driving backwards	$\frac{A^*_{21}}{A^*_{22}} < 0, \frac{A^*_{41}}{A^*_{44}} < 0$ *or* $\frac{A^*_{23}}{A^*_{22}} \cdot \frac{A^*_{43}}{A^*_{44}} > 0$
Central steering	$\frac{A^*_{21}}{A^*_{22}} \cdot \frac{A^*_{41}}{A^*_{44}} < 0$ *or* $\frac{A^*_{23}}{A^*_{22}} \cdot \frac{A^*_{43}}{A^*_{44}} < 0$

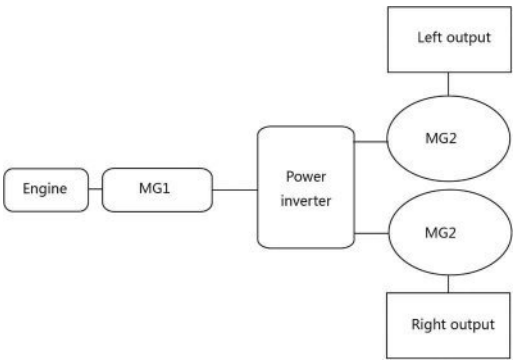


Figure 5. Series dual-motor-drive hybrid dozer.

5 OPTIMAL CONTROL AND SIMULATION RESULTS

After verifying the features that can satisfy the dozer's working conditions, 20 designs can be obtained. For the TTD, customers may also focus on the fuel consumption. In this section, the fuel consumption of the survived 20 designs is compared with the conventional engine-drive and series dual-mode-drive dozers.

We choose the conventional engine powered dozer and the series dual-motor-drive hybrid dozer as comparison to vertify the advantages of the power-split structure based on two planetary gear sets. The powertrain of the series hybrid dozer is shown in Fig. 5.

The parameters of the TTD for simulation are listed as follows (Online. 2013).

The driving cycle is established on the basis of a real TTD's working velocities shown as Fig. 6, which can be used for following simulations (Wang H, et al. 2015). The working stages in the cycle can be described as follows: 1–4 s traveling stage; 4–16 s soil-cutting stage; 16–31 s soil-transportation stage; 31–33 s unloading soil stage; and 33–50 s no-load stage.

The operating torque can be calculated through the speed and the soil-cutting depth, which is given in (G. Bekker. 1956). Using the operating torque and speed, simulations can be done.

For the surviving 20 designs, optimal control results are used for comparison of the fuel consumption. As

Table 2. Main vehicle parameters of the HEB.

	Parameter	Value
Vehicle	Vehicle mass (kg)	26055
	Track length (m)	3.016
	Track gauge (m)	1.981
Engine	Engine displacement (L)	9.3
	Max. power (kW)	198
	Max. drag torque (N·m)	1180
Motor	Rated Power (kW)	160
	Max. driving torque (N·m)	1270
	Max. working speed (rpm)	6000

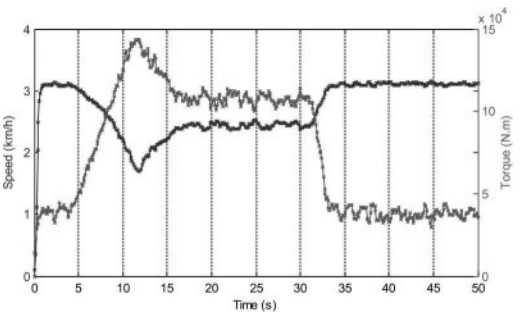


Figure 6. Driving cycle of TTD.

Table 3. States and control variables for PG designs.

States and controls	PG designs
State 1	State of charge (SOC)
State 2	Engine speed
State 3	Clutch state
Control 1	Engine torque
Control 2	Clutch state

the design candidates are not so much, we choose the dynamic programming (DP) to guarantee the global optimality (Bertsekas D P. 1995).

The conventional engine powered dozer and the series dual-motor-drive hybrid dozer are used as the comparison. In DP problems, control decisions are given by DP through the cost function shown in the Equation (11). The states and control variables are listed as the following. Without loss of generality, the two outputs on both sides have the same driving torque while straight driving. DP ensures that the end value of state of charge (SOC) will remain almost the same as the initial value.

$$J = \alpha(SOC_{desired} - SOC_N)^2 + \sum_{k=0}^{N-1}(fuel_k + \beta\Delta\omega^2_e + \gamma\Delta\omega^2_{MG1} + \delta\Delta\omega^2_{MG2}) \quad (11)$$

After vertifying the fuel econemy, 3 designs have better fuel econemy than the series hybrid TTD, the results can be found in Table 4.

Table 4. Comparison results of fuel economy.

TTD	Fuel economy (mpg)
Conventional	0.759
Series	0.928
PG Winning design 1	1.047
PG Winning design 2	1.025
PG Winning design 3	1.214

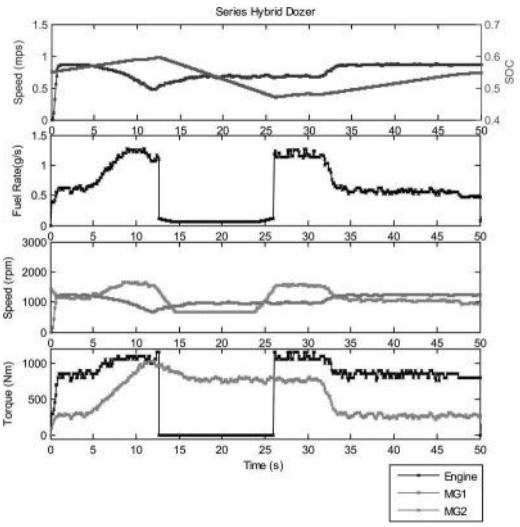


Figure 7. Simulation results of series hybrid TTD.

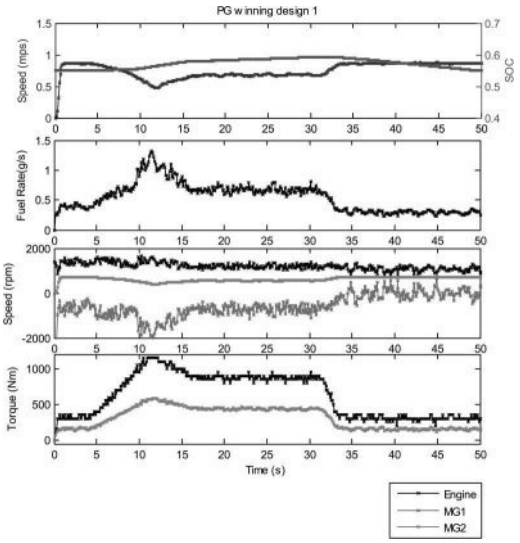


Figure 8. Simulation results of PG winning plan 1.

The speed and torque listed as below in Fig. 7 is the DP results for the series hybrid DDP, while Fig. 8 is the DP results for the PG winning design 1. Besides, the structures of the 3 winning designs are also given as Fig. 9.

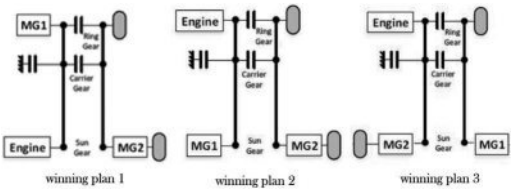


Figure 9. Three PG winning plans.

6 CONCLUSION

In this paper, the optimal design of the hybrid systems for TTD based on PG sets and clutches has been developed. The design approach has been established to find out the feasible designs that can realize the features of TTD. The selected optimal design can ensure the steering, driving backwards and central steering. The simulation results show that the PG winning plans achieve average 35% and 15% better fuel economy compared with the conventional and series hybrid TTD. The paper has proposed a new kind of hybrid power system based on 2 PG sets and 3 clutches, with two outputs controlled independently. Such kinds of design based on PG sets and clutches can be further researched, which can bring new design ideas for track-type vehicles.

ACKNOWLEDGMENTS

The authors are grateful for the sponsorship from the State Key Laboratory of Fluid Power and Mechatronic Systems (Grant No. GZKF—201410) and the National Key Research and Development Program of China (2016YFB0100905).

REFERENCES

Kwak S, et al. “Phase-redundant-based reliable direct AC/AC converter drive for series hybrid off-highway heavy electric vehicles”. *Vehicular Technology, IEEE Transactions on*, 2010, 59(6): 2674–2688.

Alternative fuels and advanced vehicles data center,” 2014. [Online]. http://www.afdc.energy.gov/data/.

Liu J, Peng H. “A systematic design approach for two planetary gear split hybrid vehicles”. *Vehicle System Dynamics*, 2010, 48(11): 1395–1412.

T. Yoshimura, “Vehicle power transmission,” US Patent 8535189 B2, 2013.

Pan Z, Zhang X, Silvas E, et al. Optimal design of all-wheel-drive hybrid pick-up trucks[C]//*ASME 2015 Dynamic Systems and Control Conference*. American Society of Mechanical Engineers, 2015: V001T10A002-V001T10A002.

X. Zhang, H. Peng, J. Sun, and S. Li, “Automated Modeling and Mode Screening for Exhaustive Search of Double-Planetary-Gear Power Split Hybrid Powertrains,” in *ASME 2014 Dynamic Systems and Control Conference*, 2014.

H. Benford and M. Leising. “The lever analogy: a new tool in transmission analysis,” *SAE Paper*, 810102, 1981.

Zhang X, et al. “Efficient Exhaustive Search of Power-Split Hybrid Powertrains With Multiple Planetary Gears and Clutches”. *Journal of Dynamic Systems, Measurement, and Control*, 2015, 137(12): 121006.

Cat | D7E Track-Type Tractor | Caterpillar. [Online]. http://www.cat.com

Wang H, et al. “Dynamic Modeling and Control Strategy Optimization for a Hybrid Electric Tracked Vehicle”. *Mathematical Problems in Engineering*, 2015.

G. Bekker M, Theory of Land Locomotion, *The University of Michigan Press*, Ann Arbor, Mich, USA, 1956.

Bertsekas D P. “Dynamic programming and optimal control”. Belmont, MA: Athena Scientific, 1995.

Advanced Vehicle Control – Edelmann, Plöchl & Pfeffer (Eds)
© 2017 Taylor & Francis Group, London, ISBN 978-1-138-02992-7

Upshift control strategy for dual clutch transmission with single clutch's slipping

J. Liu
School of Mechanical Engineering, Beijing Institute of Technology, Beijing, China
Department of Mechanical Engineering, University of California Berkeley, California, USA

B. Ma & H. Li
School of Mechanical Engineering, Beijing Institute of Technology, Beijing, China
Collaborative Innovation Center of Electric Vehicles in Beijing, Beijing, China

G. Li
Department of Mechanical and Process Engineering, Technische Universität Kaiserslautern, Kaiserslautern, Germany

ABSTRACT: This paper focuses on the control strategy for the upshifting process of Dual Clutch Transmission (DCT). To obtain the weakness of the conventional control strategy, different stages of the upshifting process are analyzed in detail. According to the results, the optimized releasing pressure that changes along with the charging pressure is obtained. Then, the upshift control strategy, characterized by accomplishing the upshift process with single clutch slippage during the torque phase, is proposed. To validate the effectiveness of the proposed control strategy, the simulation model is established on the Matlab/Simulink platform and simulation results show that, compared with conventional control strategies, the proposed one can not only avoid the torque hole and power circulation, but reduce the friction work. Meanwhile, for different charging pressure profiles and different external loads, the control strategy also performs well.

1 INTRODUCTION

Combining the advantages of manual transmission (MT) and conventional automatic transmission (AT), DCT has spread worldwide in the automotive industry. As a power transmission unit, associated technologies should be developed when fitted into a vehicle. Shift control strategy, which has a great influence on the shift quality and lifetime of clutch discs, is of vital importance for DCT. One of critical points of gearshift control is to arrange the timing of the engagement and disengagement clutches, so that the engine torque can be transferred from one clutch to the another without engine flare and clutch tie-up. To address this problem, various formulation methods and programming techniques have been developed to model the dynamics of vehicle powertrain equipped with DCT and simulate the performance of transmission control.

To achieve synchronization during the transfer of engine torque from clutch-to-clutch through clutch slip control, a detailed powertrain model of a front wheel drive vehicle with a DCT is applied (Gortz et al 2004) and a gearshift control strategy is proposed (Gortz et al 2005). In order to reduce the effect of engine, Walker et al (2011) and Liu et al (2014) proposed control strategies to combine speed and torque control of both the engine and clutches in reducing shift transient for DCT. And the control strategies are validated to be able to satisfy the shift requirement in terms of shift response and smoothness. As for the internal work conditions when DCT works, methods to identify clutch torque while two clutches are slipping are developed by Liu et al (2014) and Oh et al (2014). For analyzing and predicting DCT dynamic characteristics and performance metrics, more detailed models are developed (Kulkarni et al 2007, Galvagno et al 2011, Walker & Zhang 2013).

In control area, various theories are adopted to solve the problems resulted from different uncertainties and nonlinearities during the vehicle shifting process. Fuzzy control strategies that use throttle opening and the relative deviation between actual and target engine speeds as the main control variables are proposed by Tanaka & Wada (1995) and Zhao et al (2014). These methods can not only satisfy the shifting quality requirements, but adapt to the various shifting intentions, having a strong robustness. As to model-based clutch starting optimal control, linear quadratic optimal control has been used to obtain the clutch dynamic optimal engagement curves (Wu et al 2010, Gu & Cheng 2011, Meng et al 2015), and the results show that the method reduces the level of jerk and

frictional energy loss, also satisfies different starting intentions of the driver. In recent paper (Zhao et al 2016), a self-adaptive optimal control method based on the minimum principle is proposed for the dry DCT. The research work obtains the optimal clutch and engine torques and rotating speed, with the minimum jerk intensity and friction work. For the wet DCT, a model-based nonlinear gearshift controller is designed by the back-stepping method and the effectiveness of the designed controller is validated (Hu et al 2014).

Owing to the considerable work, starting and shifting quality of DCT has been improved significantly. However, there are still some weaknesses in the research about the cooperation mode between the engagement clutch and the disengagement clutch which is crucial to avoid torque hole and power circulation, especially for the relationship between two pressure profiles for wet DCT. For most control strategies, the pressure applied on the off-going clutch is usually controlled by simple ways or released to zero directly and, meanwhile, two clutches slip together during the torque phase. Nevertheless, from another point of view, the slippages of two clutches can be considered as the generation of the torque hole, as the system inertia torque that should be transferred exceeds the torque capacity of the off-going clutch. And, of course, the shift quality will suffer a certain influence, including the shift time and system efficiency etc.

Hence, in order to solve this problem, an in-depth analysis of the upshifting process for a powertrain equipped with DCT is provided firstly. Then the optimized pressure applied on the off-going clutch is deduced to achieve the upshifting process with only one clutch slippage during the torque phase. After that, a novel control strategy is proposed. Furthermore, Matlab/Simulink is used to develop the dynamic model for the vehicle powertrain. According to the analysis about the simulation results, the effectiveness of the proposed control strategy is validated.

2 DCT UPSHIFTING PROCESS DESCRIPTION

This study focuses on the upshifting process of the clutch rather than the synchronizer. Thus, it's assumed that the synchronizer is already engaged before the upshifting process starts.

Kinematically, gearshifts in a DCT are similar to clutch-to-clutch shifts in an AT, with one providing odd gears and the other even gears. As shown in Figure 1, clutch L(CL) connects to the first gear while clutch H (CH) connects to the second gear. When in first gear, CL is engaged and torque is transferred from the engine through CL to the output shaft. CH remains open. To upshift, CL is released slowly and CH engaged simultaneously. Then power form the engine can be transferred between two clutches uninterruptedly during a gearshift.

The shifting process of DCT consists of two phases: the torque phase and the inertia phase. Without losing generality, system equations for 1-2 shift are presented, which can be easily extended to the other gearshifts. Figure 2 shows the different stages of a 1-2 upshift.

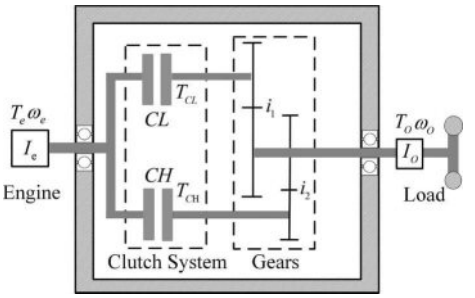


Figure 1. Dynamic Model.

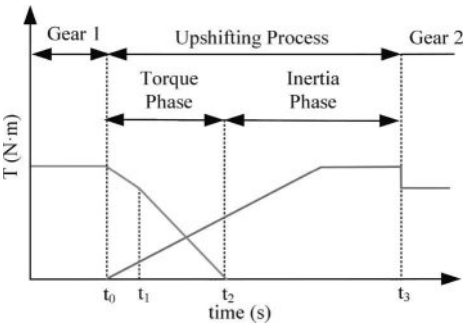


Figure 2. Different stages of upshifting process.

2.1 *Torque phase*

The DCT upshifting process begins with the torque phase. During this phase, the pressure applied on CL is gradually released, resulting in the decrease of the torque capacity of CL. At the same time, the charging pressure is applied and CH begins to slip. When the system inertia torque that should be transferred is less than the torque capacity of CL, CL maintains the original status. However, when it exceeds, CL begins to slip and, meanwhile, the gear ratio varies. Hence, this phase can be divided into two stages.

The first stage is $t_0 \le t \le t_1$. System equations of the motion are presented as follows:

$$T_e - T_{CLi} - T_{CH} = I_e\dot{\omega}_e \tag{1}$$

$$T_{CLi}i_1 + T_{CH}i_2 - T_o = I_o\dot{\omega}_o \tag{2}$$

where i_1 and i_2 = gear ratios; I_e = mass moment of inertia of engine; I_o = mass moment of the inertia of the vehicle; ω_e, ω_o = angular velocities; T_{CLi} = system inertia torque; T_o = output shaft torque.

The CH friction torque can be calculated based on the geometry and friction characteristics.

$$T_{CH} = sign(\Delta\omega_{CH})\mu PAn\left(\frac{2}{3}\right)\left(\frac{R_o^3 - R_i^3}{R_o^2 - R_i^2}\right) \tag{3}$$

where $\Delta\omega_{CH}$ = the relative angular velocity between CH driving and driven discs; P = the normal effective pressure; A = the interface area between friction discs; n = the number of friction pairs; R_o = outside radius of friction disc; R_i = inside radius of friction disc.

Friction coefficient μ is modeled as a function of relative angular speed.

$$\mu = \mu_k + (\mu_s - \mu_k) e^{-d_c \Delta\omega} \tag{4}$$

where μ_s = the static friction coefficient; μ_k = the kinetic friction coefficient; d_c = the decay coefficient.

According to equations (1) and (2), the system inertia torque transferred by CL is expressed as follows.

$$T_{CLi} = \frac{T_e I_R - T_{CH}(I_R + I_e i_2 i_1) + I_e T_o i_1}{I_e i_1^2 + I_o} \tag{5}$$

When the stage two $t_1 \le t \le t_2$ comes, two clutches slip together. Equations (1) and (2) should be changed due to the slippage of CL.

$$T_e - T_{CL} - T_{CH} = I_e \dot{\omega}_e \tag{6}$$

$$T_{CL} i_1 + T_{CH} i_2 - T_o = I_o \dot{\omega}_o \tag{7}$$

Similar to the expression of friction torque of CH, the friction torque of CL can be expressed as follows.

$$T_{CL} = sign(\Delta\omega_{CL}) \mu P A n \left(\frac{2}{3}\right)\left(\frac{R_o^3 - R_i^3}{R_o^2 - R_i^2}\right) \tag{8}$$

2.2 *Inertia phase*

After the pressure applied on CL decreases to zero, the following stage is the inertia phase. During this phase, the pressure applied on CH continues to rise. Torque is transferred by the slippage of CH. Correspondingly, equations (1) and (2) should be changed into equations (9) and (10) due to the disengagement of CL.

$$T_e - T_{CH} = I_e \dot{\omega}_e \tag{9}$$

$$T_{CH} i_2 - T_o = I_o \dot{\omega}_o \tag{10}$$

When there is no relative angular velocity between two discs of CH, the gear ratio changes to the second gear. Then, CH begins to transfer the system inertia torque, and the pressure applied on CH increases to system oil pressure rapidly. The entire upshifting process ends.

3 UPSHIFT CONTROL STRATEGY

From the above analysis, during the stage ($t_1 \le t \le t_2$), the torque transfer process is accomplished by two clutches concurrent slippages. For most control strategies, two clutches are always under this status. However, it also can be considered as torque hole as the system inertia torque exceeds the torque capacity of the off-going clutch. To avoid this condition, the releasing pressure applied on the off-going clutch is optimized to provide CL enough torque capacity to transmit the system inertia torque. According to equations (5) and (8), the optimized pressure applied on CL is presented as follows.

$$P_{CL} = \frac{\dfrac{T_e I_o - T_{CH}(I_o + I_e i_2 i_1) + I_e T_o i_1}{I_e i_1^2 + I_o}}{\dfrac{2}{3}\mu_s A n \left(\dfrac{R_o^3 - R_i^3}{R_o^2 - R_i^2}\right)} \tag{11}$$

Based on the optimized releasing pressure, a control strategy can be proposed for the DCT upshifting process.

Before the torque phase, the pressure applied on the off-going clutch is quickly released to the critical value that the torque capacity of CL equals to the system inertia torque. Meanwhile the pressure on the oncoming clutch is quickly ramped up to eliminate clutch free travel. This stage of the torque phase is the preparation of the shifting process. During this stage, both off-going and the oncoming clutches have little effect on the shift quality.

After that, the torque phase starts and the engine torque transfers from the off-going clutch to the oncoming clutch gradually. The pressure applied on the oncoming clutch is usually decided by the driver's attention (Liu et al 2014, Zhao et al 2016) or calculated by the linear quadratic optimal control theory (Zhao et al 2015, Wu et al 2010, Meng et al 2015, Gu & Cheng 2011). However, no matter how the effective pressure applied on the oncoming clutch varies, the pressure applied on the off-going clutch can be calculated according to the equation (11). With the increase of the effective pressure applied on the oncoming clutch, friction torque transferred by CH increases. Meanwhile, the system inertia torque transferred by CL varies. Until the pressure applied on CL decreases to zero. The torque phase ends and the inertia phase starts. With the increase of the pressure applied on CH, the status of CH changes from slippage to engagement. And then the entire upshift process ends.

The control strategy is shown in Figure 3. What deserves to be mentioned is, during the entire torque phase, the relative angular velocity between the driving and driven discs of CL is zero as the application of the optimized releasing pressure. Consequently, the DCT upshifting process is achieved by the single slippage of CH.

4 SIMULATION RELUSTS

To validate the effectiveness of the proposed control strategy, the simulation model of powertrain system is established on Matlab/Simulink. As shown in the engine map (Fig. 4), the throttle angle varies from 5% to 100% and the simulation is conducted under 40%

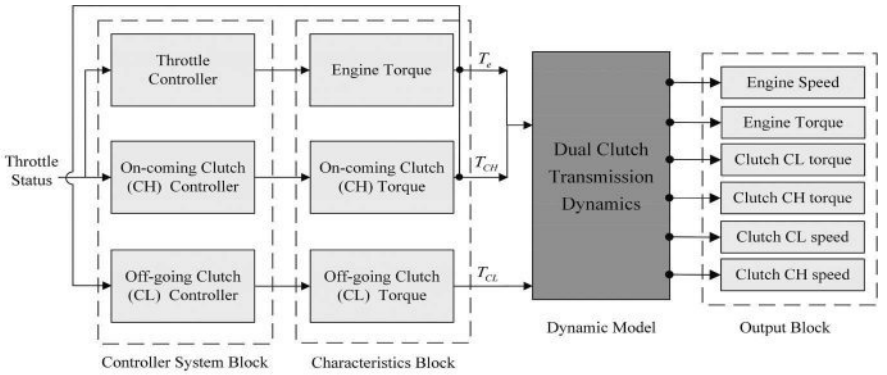


Figure 3. Control architecture for upshifting process.

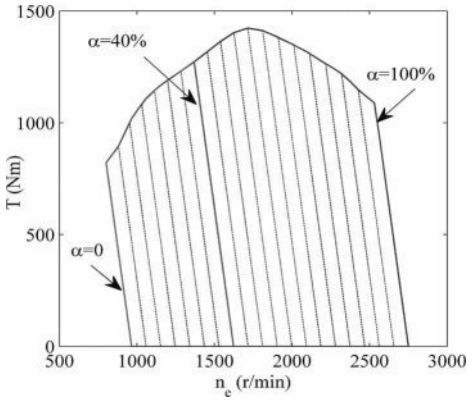


Figure 4. Diesel engine torque output.

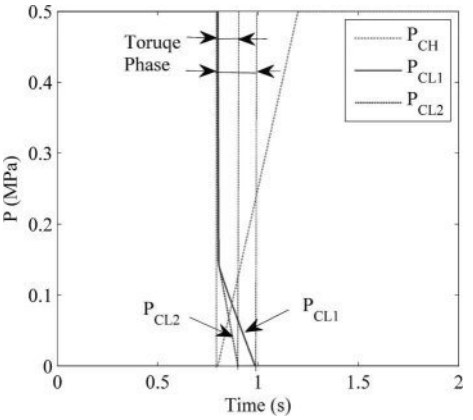


Figure 5. Pressure profiles under different control strategies.

Table 1. Main parameters of DCT.

Parameters	Value	Parameters	Value
i_1	1.29	i_2	0.775
Ro	0.093m	Ri	0.069 m
I_e	3.65 kg·m^2	I_o	5 kg·m^2
n	6		

accelerator opening. Main parameters of the DCT are shown in Table 1.

4.1 *Compare with conventional control strategy*

The charging pressure applied on CH is set as slope pressure (Kulkarni et al 2007). Releasing pressure profiles obtained according to the proposed control strategy(P_{CL1}) and conventional control strategy(P_{CL2}) are shown in Figure 5.

Simulation results of the upshifting process based on the proposed control strategy are shown in Figure 6. Obviously, during the torque phase, T_o nearly has no change, which means the torque hole and circulating power is avoided. Also during the inertia phase, both T_e and T_o vary smoothly. In terms of gear ratio, it

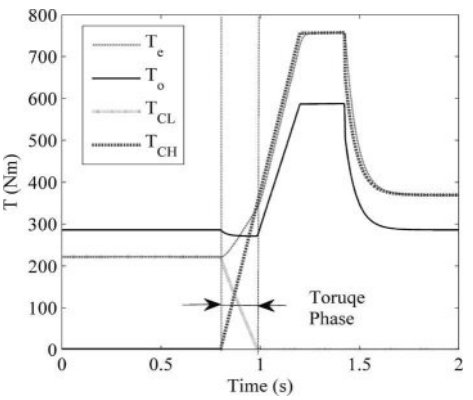


Figure 6a. Torque of clutches, engine and output.

maintains 1.29 during the torque phase and then varies to 0.775 slowly which can be seen from Figure 6b.

When DCT upshifts with P_{CL2}, the results are show in Figure 7. During the torque phase, T_o has an interruption, resulting in a slight increase of n_o and decrease of gear ratio as shown in Figure 7b. Compared with the conventional control strategy, the proposed

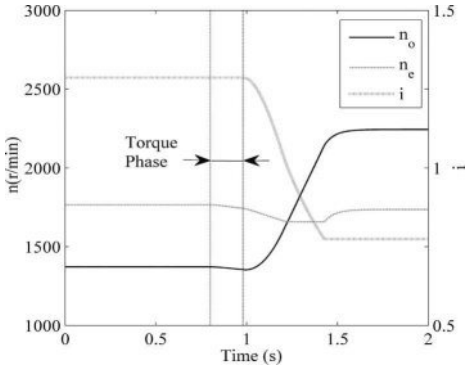


Figure 6b. Gear ratio and speed.

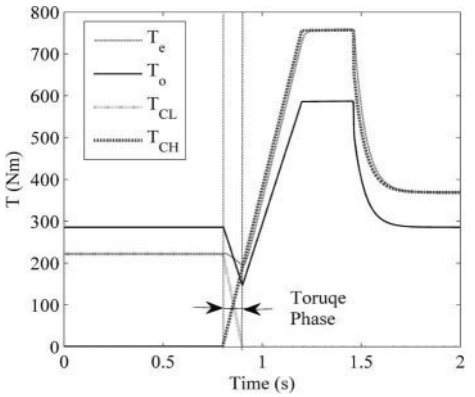


Figure 7a. Torque of clutches, engine and output.

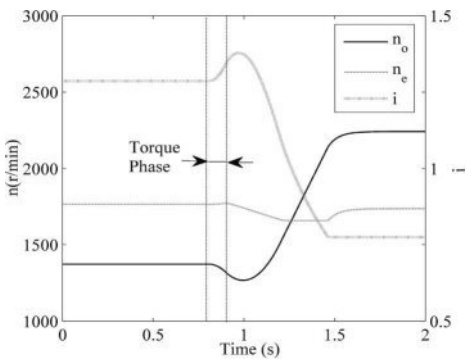


Figure 7b. Gear ratio and speed.

one reduces the friction work by 1250J (Fig. 8). The relative angular velocity between the driving and driven parts of CL maintains zero during the torque phase which means the upshifting process is achieved by the single slippage of CH (Fig. 8).

4.2 *Different charging pressure profiles*

As the pressure applied on CH is always calculated by different ways, different charging pressure profiles are

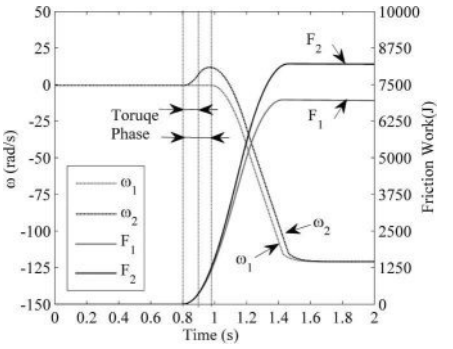


Figure 8. Friction work and relative angular velocity.

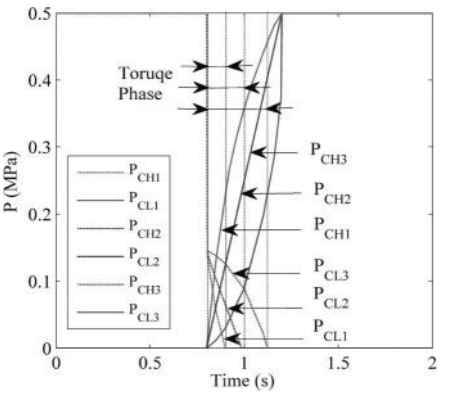


Figure 9. Different P_{CL} and P_{CH} profiles.

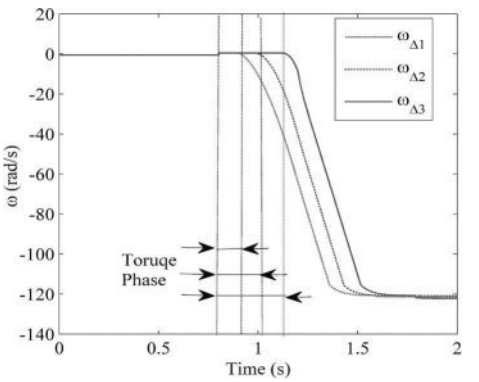


Figure 10. Relative angular velocity.

simulated to verify the effectiveness of the proposed control strategy and simulation results are shown in Figure 9. With the variation of P_{CH}, P_{CL} also shows different changing trends. However, the relative angular velocity maintains zero (Fig. 10).

4.3 *Different external loads*

As to different external loads, corresponding simulations are also carried out. With the increase of the external load, the duration of the torque phase

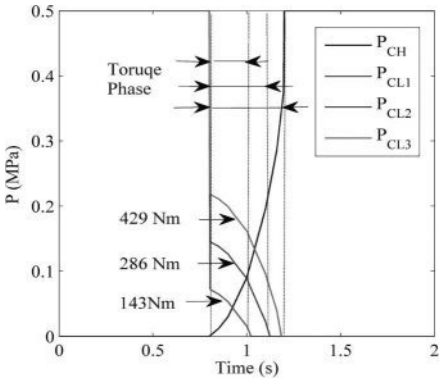


Figure 11. Different external loads.

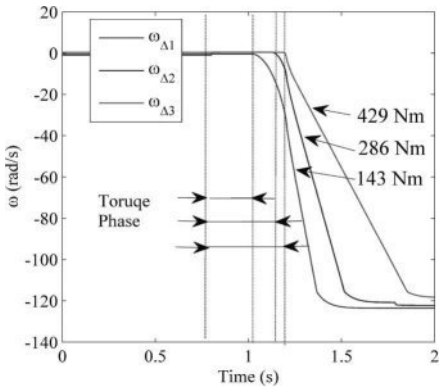


Figure 12. Relative angular velocity.

increases (Fig. 11). And the relative angular velocity is still zero as shown in Figure 12.

5 CONCLUSION

By investigating the working principle of the DCT upshifting process, the weakness of the conventional control strategy is provided. To avoid it, the releasing pressure is optimized to achieve the upshift task with only the oncoming clutch slippage during the torque phase. Then, a novel control strategy is proposed based on the optimized pressure profiles.

Dynamic model integrating the engine and DCT has been established on the Matlab/Simulink platform. From the obtained results, the control strategy can not only avoid the torque hole and power circulation, but reduce the friction work. Also, when the charging pressure and the external load change, the control strategy also performs well.

ACKNOWLEDGMENT

This work was supported by the National Natural Science Foundation of China (No. 51175042 and No. 51575042) and Ministry of Industry and Information Technology of China (No. VTDP3203).

REFERENCES

Galvagno, E., Velardocchia, M., & Vigliani, A. 2011. Dynamic and kinematic model of a dual clutch transmission. *Mechanism and Machine Theory* 46(6): 794–805.

Goetz, M., Levesley, M. C., & Crolla, D. A. 2004. Integrated powertrain control of gearshifts on twin clutch transmissions (No. 2004-01-1637). SAE Technical Paper.

Goetz, M., Levesley, M. C., & Crolla, D. A. 2005. Dynamics and control of gearshifts on twin-clutch transmissions. *Proceedings of the institution of mechanical engineers, Part D: Journal of Automobile Engineering* 219(8): 951–963.

Gu, Q. & Cheng, X.S. 2011. Study on double-clutch transmission gear shift control based on optimal control theory. *In Industrial Engineering and Engineering Management (IE&EM), 2011 IEEE 18Th International Conference* on (pp. 629–634). IEEE.

Hu, Y., Tian, L., Gao, B., & Chen, H. 2014. Nonlinear gearshifts control of dual-clutch transmissions during inertia phase. *ISA transactions* 53(4): 1320–1331.

Kulkarni, M., Shim, T., & Zhang, Y. 2007. Shift dynamics and control of dual-clutch transmissions. *Mechanism and Machine Theory* 42(2): 168–182.

Liu, Y., Qin, D., Jiang, H., Liu, C., & Zhang, Y. 2011. Clutch torque formulation and calibration for dry dual clutch transmissions. *Mechanism and Machine Theory* 46(2):218–227.

Liu, Y., Qin, D., Jiang, H., & Zhang, Y. 2014. Shift control strategy and experimental validation for dry dual clutch transmissions. *Mechanism and Machine Theory* 75: 41–53.

Meng, F., Tao, G., Zhang, T., Hu, Y., & Geng, P. 2015. Optimal shifting control strategy in inertia phase of an automatic transmission for automotive applications. *Mechanical Systems and Signal Processing* 60: 742–752.

Oh, J. J., Choi, S. B., & Kim, J. 2014. Driveline modeling and estimation of individual clutch torque during gear shifts for dual clutch transmission. *Mechatronics* 24(5): 449–463.

Tanaka, H., & Wada, H. 1995. Fuzzy control of clutch engagement for automated manual transmission. *Vehicle system dynamics* 24(4–5): 365–376.

Walker, P. D., & Zhang, N. 2013. Modelling of dual clutch transmission equipped powertrains for shift transient simulations. *Mechanism and Machine Theory* 60: 47–59.

Walker, P. D., Zhang, N., & Tamba, R. 2011. Control of gear shifts in dual clutch transmission powertrains. *Mechanical Systems and Signal Processing* 25(6): 1923–1936.

Wu, M. X., Zhang, J. W., Lu, T. L., & Ni, C. S. 2010. Research on optimal control for dry dual-clutch engagement during launch. *Proceedings of the Institution of Mechanical Engineers, Part D: Journal of Automobile Engineering* 224(6): 749–763.

Zhao, Z., Chen, H., & Yang, Y. 2014. Fuzzy determination of target shifting time and torque control of shifting phase for dry dual clutch transmission. *Mathematical Problems in Engineering* 2014.

Zhao, Z., He, L., Zheng, Z., Yang, Y., & Wu, C. 2016. Self-adaptive optimal control of dry dual clutch transmission (DCT) during starting process. *Mechanical Systems and Signal Processing* 68: 504–522.

Advanced Vehicle Control – Edelmann, Plöchl & Pfeffer (Eds)
© 2017 Taylor & Francis Group, London, ISBN 978-1-138-02992-7

Predictive energy management of hybrid powertrains using deterministic and Markov chain predictions

R.S. Vadamalu & C. Beidl
Institute for Internal Combustion Engines and Powertrain Systems,
Technische Universität Darmstadt, Darmstadt, Germany

ABSTRACT: Hybridized powertrains with multiple onboard energy converters offer an additional degree of freedom to fulfill the propulsion power demand. This degree of freedom coupled with increased vehicle connectivity, provide opportunities to improve powertrain efficiency along with reduction in pollutant emissions. Powertrain Energy Management (EM) coordinates these different objectives and decides on coordination between the power sources to meet the motive power demand. This paper presents an online optimizing EM controller, which solves the optimal power split among the energy converters. The controller thereby uses acausal data from predicted driving conditions in a receding horizon fashion. The proposed framework can operate with information resulting from vehicle connectivity under autonomous vehicle guidance. In case of driver-aware scenario, it operates using non-deterministic/stochastic predictions resulting from stochastic modeling of driving characteristics using finite Markov Chain. The receding horizon control problem is transcribed as finite dimensional constrained optimization problem, which can be solved using nonlinear optimization methods. Simulation analysis of the proposed approach is used to demonstrate the functionality of the controller.

1 INTRODUCTION

Development of automotive powertrains faces challenges to achieve better powertrain efficiency along with emission reductions to reduce emissions due to stringent regulatory environment. Further, customer demand for vehicles with better drivability along with reduced fuel consumption is on the rise. Binding regualtory limits such as the one from European Union restricts fleet level CO_2 emissions to 95 g per driven kilometer. According to (Wirth et al. (2015)), to reach such a target using combustion engine powertrains, the average efficiency of the engine shall be 40% or more. This clearly emphasises the need for electrification measures.

Powertrain hybridization presents a viable alternative to reduce fuel consumption and associated CO_2 emissions along with avoiding range anxiety. Such a hybridized powertrain offers operational modes such as electric traction, recuperation and load point shift of internal combustion engine (ICE), thanks to the multiple on-board energy converters. Plug-in Hybrid Electric Vehicle (PHEV), with a combination of ICE and eletric traction machine (ETM) together with high energy capacity battery, which can be charged externally, offers reasonable electric range. The operational degree-of-freedom (DOF) and coordination of the different operational modes is handled by a supervisory controller known as the energy management (EM) (Sciarretta and Guzzella (2007)).

Vehicle certification process evaluates fuel consumption and emissions using synthetic driving profiles. Currently, the New European Driving Cycle (NEDC) is used with proposed introduction of Worldwide harmonized Light vehicles Test Cycle (WLTC) between 2017 and 2020. Deviations of fuel consumption and emission measurements between certification values and real driving values have attracted a lot of attention recently (Wirth et al. (2015)). As a consequence, EM functionality of hybridized powertrains which have been validated using synthetic certification cycles would have to show same or better performance in the future in real world testing scenarios. One possibility to achieve this goal is to exploit predicted data about future trajectories/events. This paper presents such an EM controller which uses prediction information to reduce fuel consumption, respecting battery state of charge (SOC) limits under deterministic and stochastic prediction framework.

Under nominal driving conditions, both driver and traffic management systems show potential to reduce fuel consumption to levels that could be achieved by the "perfect eco-driver" along with "perfectly eco-managed" transport infrastructure (Benz et al. (2012)). Reports (ECOMOVE (2010)) show due to inefficient braking or non-optimal driver reaction lead to 22% of wasted fuel. In order to take advantage of such situations, driver assistance systems operating on the powertrain level, facilitate optimal velocity planning on vehicle level or optimal power demand split on the powertrain level. Such systems operating under nominal driving conditions with predicted data, such as road topography, have demonstrated advantages (Radke (2013)). Recently, development and integration of

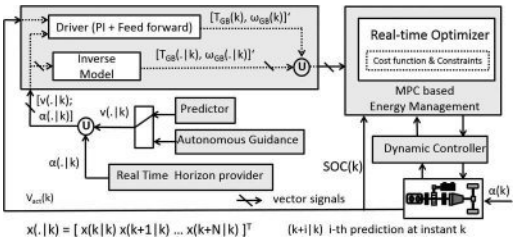


Figure 1. Structure of MPC based EM.

such systems received regulatory stimulus in the name of Eco-Innovations (in the EU) and Off-Cycle Credits (in the USA).

2 MODELING AND THEORY

This section briefly summarises the theoretical aspects of the publication along with the models employed for investigation.

2.1 *Modeling*

Model predictive control (MPC) uses model of the process to pre-compute state trajectories to determine the control policy optimizing given cost function with constraints. This model that is used as part of MPC framework shall be termed as the control oriented model (COM). Since COM is calculated in every sampling instant for the length of prediction horizon, this model shall be simple and fidel enough to maintain the relevant dynamics. In case of EM, the dynamics are governed by the battery SOC evolution (Sciarretta and Guzzella (2007)), hence the battery energy conversion dynamics shall be modelled in COM. ICE fuel consumption is used as optimization criteria and hence has to be approximated for computation in the MPC. Both these effects, ICE fuel consumption and energy conversion efficiency of eletrical path has been modelled using polynomial approximations (Vadamalu et al. (2015), Vadamalu and Beidl (2016a)).

As depicted in Figure 1, the development of MPC EM is performed using non-linear vehicle and driver model, termed Nonlinear Model (NM). Nevertheless, the validation environment is not restricted to simulations (real-/non real-time). Using In-The-Loop methodolgy, validation environment can be extended to include real components ranging from engines (Engine-In-The-Loop), drivelines (Driveline-In-The-Loop) to vehicle (Chassis Dynamometer-In-The-Loop) (Vadamalu and Beidl (2016a), Bier (), Weber (2016)). NM models the longitudinal dynamics of the vehicle along with the powertrain dynamics. The powertrain components are represented with their respective look-up tables along with their dynamic effects modelled using time-delay and first order lag dynamics. The Clutches in the parallel P2 powertrain configuration are modelled using Karnopp approach, without switching between stick and slip states. The battery model computes decrease and increase of SOC based on the power demand/input. Sample time of 1 ms with RK4 solver was chosen by linearized analysis of the system dynamics. A detailed exposition of the NM can be found in (Vadamalu and Beidl (2016a), Vadamalu et al. (2015)).

2.2 *Theory*

The generic EM problem of hybridized powertrains can be expressed as continuous time fuel consumption minimisation problem over the driving profile, constrained by the limits on battery state of charge (SOC) (Sciarretta and Guzzella (2007)). Using the method of direct optimal control and sequential discretization, the problem is formulated as a finite horizon MPC problem. The prediction data used for computation by MPC EM results from deterministic or Markov Chain based prediction methods.

2.2.1 *PHEV EM as economic MPC problem*

MPC is a control methodology that evaluates online control action by solving a finite horizon optimization problem using forecasted system behaviour by using current measurements. MPC easily scales to multi-dimensional problems and can handle state and input constraints directly. With the availability of fast computing resources and efficient algorithms, the computational complexity of MPC is not a bottleneck for its application. There are different variants of MPC such as regulation/stabilizing MPC, economic MPC. In constrast to regulation or tracking MPC which penalize the distance of the current state to some desired state considering process dynamics and input constraints, economic MPC uses a stage cost that reflects the process economics (Rawlings and Mayne (2009)). The generic form of an economic MPC problem is presented in equation (1). The goal is to find the control input that minimises the cost function V_N defined over the finite horizon without violating the constraints.

$$\min_u V_N(x,u) \quad (1)$$

$$\text{s. t. } x^+ = f(x,u), \qquad x(0) = x, \qquad x(N)\,\epsilon\,\mathcal{X}_N$$

$$(x(k),u(k))\,\epsilon\,\mathcal{F}, \qquad k\epsilon\{0:N-1\}$$

Objective of PHEV EM is to minimize the fuel consumption maintaining the battery SOC within prescribed limits. This has been formulated as an economic MPC problem with the fuel consumption serving as the economic objective. The infinite-dimensional finite time horizon problem is approximated as finite dimensional problem using discretization and approximation of the objective function and system dynamics using polynomials. The SOC dynamics is approximated using an affine function, whereas ICE fuel consumption is represented as a quadratic function. The quantities x_{min} and x_{max} are

the opertional limits on SOC over the prediction horizon. The quantity x_{ref} expresses the desired value of SOC at the end of the prediction horizon. This terminal state constraint, forcing the SOC to lie above a certain reference level x_{ref}, ensures stability of the closed loop system enforcing terminal regional constraint. The resulting finite horizon optimization problem can be expressed as below:

$$\begin{bmatrix} T_{ETM}^{opt}(.|k) \\ s_{ICE}^{opt}(.|k) \end{bmatrix} = \text{argmin} \sum_{i=0}^{N} \dot{m_f} \cdot T_s \tag{2}$$

$$\text{s. t. } x(k) + T_s \cdot \sum_{i=0}^{N} \dot{x}(k+i|k) \geq x_{ref} \tag{3}$$

$$x_{min} \leq x(k) + T_s \cdot \sum_{i=0}^{N-1} \dot{x}(k+i|k) \leq x_{max} \tag{4}$$

$$\dot{m_f} = a_0 + a_1 \cdot (T_{ICE}) + a_2 \cdot (T_{ICE})^2 \tag{5}$$

$$\dot{SOC} = -\frac{b_1(\omega_{ETM})T_{ETM} + b_0(\omega_{ETM})}{Q_{max}} \tag{6}$$

$$\widetilde{T}_{ETM,min} \leq T_{ETM} \leq \widetilde{T}_{ETM,max} \tag{7}$$

The goal is to compute the ICE On/Off state, s_{ICE}^{opt} (boolean variable) and torque split, T_{ETM}^{opt} (owing to parallel powertrain topology) between the energy converters. The resulting mixed boolean optimization problem can be viewed as a combination of a convex quadratic optimization problem, to compute the torque set-point to the energy converters and a boolen optimization problem, to determine the current state of engine. The convex QP sub-problem can be solved using nonlinear optimization methods such as Active-Set based methods (Vadamalu et al. (2015)), Primal-Dual Interior point methods (Vadamalu and Beidl (2016b)). The boolean sub-problem of finding the state of the engine is solved by exploiting proper initialization (warm-start) and heuristics conditions on the value function. ICE state is initialized with a turned on engine, only if the motive torque demand is positive and the speed at gearbox input is above the ICE idling speed. During iterations, heurisitics on the value function $V(i)$, as in the equation 8 is used as stopping criterion. If the stopping criterion is not met, the iterations are continued with ICE switched off at low torque regimes, thereby using the electric traction and later charging the battery by ICE load-point shift towards higher ICE loads.

$$\mathcal{H}(V_i) \stackrel{\text{def}}{=} |V(i) - V(i-1)| \leq \epsilon \tag{8}$$

As shown in Figure 1, MPC computes torque set point values which is realized by component-level dynamic controllers. MPC EM operates on the predicted velocity corridor constituted by the future vehicle velocity and road gradient over a predefined horizon. In driver-aware scenario, predictions of velocity and hence power demand result from the Markov Chain (MC) predictions.

2.2.2 *Deterministic prediction*

The deterministic prediction framework does not account for model uncertainities and accuracy of both the static and dynamic data used for predictive control. As explained, the predictive data used by MPC EM are prediction of torque T_{GB} and speed ω_{GB} values at gearbox input over the prediction horizon. These values are obtained from the predicted velocities and road grade values as shown below:

$$\omega_{GB}(.|k) = v(.|k)(i_G(.|k)i_D))/r_w \tag{9}$$

$$T_{GB}(.|k) = r_w(0.5\rho_{air}c_wAv^2(.|k) + c_rmg\gamma cos(\alpha(.|k)) \tag{10}$$
$$+mg\gamma sin(\alpha(.|k)) + \gamma m\dot{v}(.|k))/(i_G(.|k)i_D))$$

where the r_w denotes radius of wheel, c_r coefficient of rolling resistance, A front area of vehicle, γ factor for rotational interia of vehicle, η_{GB} efficiency of gearbox, c_w coefficient of wind resistance, ρ_{air} density of air, T_{GB} torque at gearbox input, T_w wheel torque and α road grade. During execution, the prediction window of length N is moved forward in a receding horizon fashion.

2.3 *Markov Chain prediction*

This section presents the Markov Chain based prediction of the future motive power demand. The vehicle and driveline parameters in the equations (9) and (10) are assumed to be known and deterministic. Stochasticity in the predicted power demand results only from the uncertainity in velocity and acceleration. Further, as the predictive EM problem deals with longitudinal dynamics, the relevant states are the vehicle velocity and acceleration. The prediction of future value of these states is done employing a stationary Markov Process. Stationarity assumption implies that the moments are not affected by a time shift. If a stochastic process $\{X_m : m \geq 0\}$ is stationary for time instants $k_1, \ldots, k_m$ with $k \geq 0$, the joint probability of $(X_{k_1}, \ldots, X_{k_m})$ is shift invariant with respect to time/time-invariant. Discretization in the time and state space results in a finite dimensional Markov Chain. The stochastic prediction is carried out in two steps: learning step and prediction step. Prediction step is realized using three methods, P_1, P_2 and P_3.

2.3.1 *Learning step for TPM*

The learning step involves computing the transition probabilites for the various transitions and using entries of Transition Probability Matrix (TPM) to compute the change in velocity ΔV_k and acceleration ΔA_k corresponding to the transition with the maximum occurence likelihood. This modularization of learning and prediction also enables offline generation of TPM using measured driving profiles. Learning process uses categorization of driving profiles using driving and traffic conditions prevailing during measurements such as urban, country or highway driving. Online update of the TPM can be performed iteratively

Algorithm 1 Generation of Markov Chain

procedure MARKOV CHAIN GENERATION
  Input 1 : Drive cycle velocity and acceleration
  Input 2: N **step to learn**
  Generate sample space $s \in \Omega : (v_p, a_q)$ for all possible
combinations of $v_{p\in P}$ and $a_{q\in Q}$ and $sizeof\,(\Omega) = P * Q$
  for each n in $Nstep$ **do**
    Sample every n data from Input 1
    Use sampled data to Compute TPM π (See Algorithm 2)
    find $j^* \leftarrow \text{argmax}_{i\in K}\pi(i,j)$ for each i
    $\Delta V(i, j*, n) = (v_m \in \Omega(j*)) - (v_m \in \Omega(i))$
    $\Delta A(i, j*, n) = (a_m \in \Omega(j*)) - (a_m \in \Omega(i))$
  end for
  Output : Matrices $\pi, \Delta V, \Delta A$
end procedure

computing TPM using blocks of observed data. The iteratively computed TPM is combined with the offline TPM using weights depending on the driving conditions. Further, selection of used TPM category is based on prelevant driving and traffic conditions.

Let a sequence of random variables and their realisations be represented as $X_1, X_2, X_3, \ldots, X_k$ and $x_1, x_2, x_3, \ldots, x_k$. Each realisation is an outcome corresponding to velocity and acceleration from a driving cycle $x_k = (v_x, a_x)$. Markov chain modelling involves generation of transition probability matrix, which is called a learning step. This transition probability matrix (TPM) is used to predict in the prediction step. Transition matrix π_{ij} is generated using the driving cycle data and it is defined as $\pi_{ij} := \Pi(X_{k+1} = j | X_k = i)$. This definition of TPM considers continuous samples from the driving cycle data, which here we refer to as *1-step* learning. Similarly, for a sample x_k, x_{k+2} can also be used to generate TPM, which we refer to as *2-step* learning. In general, several TPM are generated using definition $\pi_{ij} := \Pi(X_{k+n} = j | X_k = i)$, where n corresponds to *n-step* learning. This generation procedure is represented as state diagram in Figures 2 & 3 and elaborated in Algorithm 1 & 2.

Algorithm 1 lays down the steps to compute ΔV and ΔA while Algorithm 2 details the steps to compute TPM. Ω is the sample space which contains all possible cases $x_k = (v_x, a_x)$. Three prediction methods, namely P_1, P_2 and P_3 are employed to predict future velocity and acceleration from TPM Data.

2.3.2 *Stochastic prediction:* P_1

In this prediction method, based on the current velocity and acceleration, values for the change in velocity and acceleration are computed. This value is used to compute future velocities and accelerations. The method is summarized in the equations (11) and (12). As the

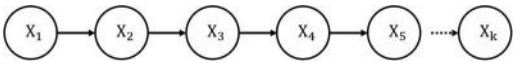


Figure 2. Schematic of single step MC learning.

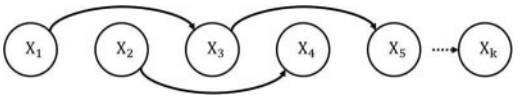


Figure 3. Schematic of two step MC learning.

Algorithm 2 Generation of TPM

procedure TPM COMPUTATION
  Input 1: Under sampled data $x(k)$ **for** $k \in K$
  Input 2: Sample space $s \in \Omega$
  init: $\pi \leftarrow$zeros(size(Ω),size(Ω)) $x_s : (v_p, a_q)$
  for each k in K **do**
    $s_1^* = index$ of outcome $x(k) \in \Omega$
    $s_2^* = index$ of outcome $x(k+1) \in \Omega$
    $\pi(s_1^*, s_2^*) \leftarrow \pi(s_1^*, s_2^*) + 1$
  end for
  Normalise TPM such that $\Sigma_j \pi(i,j) = 1$
  Output : Matrix π
end procedure

lookup operation (access of TPM) is performed only once, this method is rather fast but not suitable for longer prediction horizons.

$$(\Delta V_k, \Delta A_k) = f(v_k, a_k) \tag{11}$$

$$v_{k+1} = v_k + \Delta V_k, a_{k+1} = a_k + \Delta A_k \tag{12}$$

2.3.3 *Stochastic prediction:* P_2

This method computes iteratively the values of future velocities and acceleration by corresponding lookup operations. As the process is recursive it can capture dynamic driving involving rapid changes in velocity and acceleration in a better way. The below equations present the implementation of the method.

$$(\Delta V_{k+1}, \Delta A_{k+1}) = g(v_k, a_k) \tag{13}$$

$$v_{k+2} = v_{k+1} + \Delta V_{k+1}, a_{k+2} = a_{k+1} + \Delta A_{k+1} \tag{14}$$

2.3.4 *Stochastic prediction:* P_3

Using the learning of multi-step Markov jumps, the corresponding lookup table can be used to compute the transitions from the current state. Hence, learning of multi-step Markov transitions can speed up the prediction process, which can be parallelized by using simultaneous access, based on the current state vector. The below equations summarize the method.

$$(\Delta V_k, \Delta A_k) = f_1(v_k, a_k) \tag{15}$$

$$v_{k+1} = v_k + \Delta V_k, a_{k+1} = a_k + \Delta A_k \tag{16}$$

$$(\Delta V_{k+1}, \Delta A_{k+1}) = f_2(v_k, a_k) \tag{17}$$

$$v_{k+2} = v_{k+1} + \Delta V_{k+1}, a_{k+2} = a_{k+1} + \Delta A_{k+1} \tag{18}$$

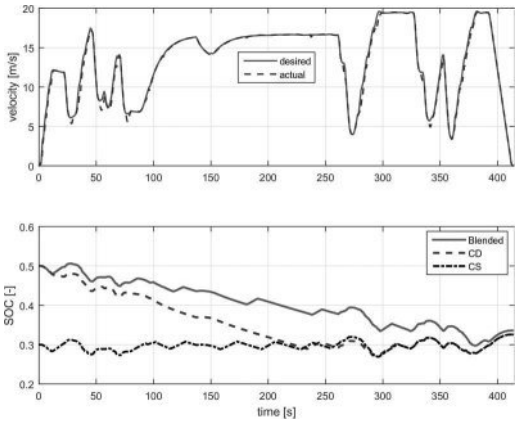


Figure 4. Velocity and SOC profiles for non-synthetic driving profile.

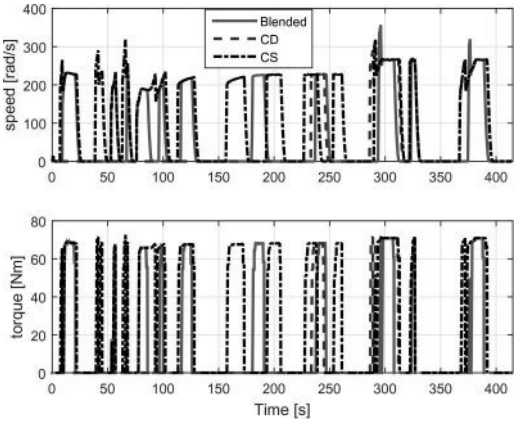


Figure 5. ICE torque and speed profiles for non-synthetic driving profile.

3 RESULTS

This section presents the results of the EM operation using deterministic (prediction horizon of length 50) and stochastic prediction information. Both non-synthetic driving profile data and regulatory evaluation velocity profiles shall be used for evaluation.

3.1 *Deterministic prediction scenario*

Figure 4 depicts the EM operation in different PHEV operation modes, namely Charge Sustaining (CS), Charge Depleting (CD) and Blended operation mode. The realization of these mode for an arbitrary deterministic velocity profile is done by online tuning of the parameter x_{ref}. Battery SOC, represented as x at the beginnning of the cycle is 0.3 in case of CD and blended mode, for CS operation an initial SOC value of 0.3 has been used. In case of CS and CD modes, x_{ref} is fixed at 0.3, whereas blended operation mode tunes online the value of x_{ref} based on prediction data. The resulting ICE operation is shown in Figure 5. It can be observed that despite beginning with the same initial SOC value, in the blended mode, ICE is switched on more often than the CD mode. In case of CD mode, energy stored in the battery is depleted and then the ICE is used depending on the motive power demand and prediction data. In all the three modes, MPC operates the ICE at high torque operation, ensuring efficient operation of ICE.

3.2 *Stochastic prediction scenario*

Figure 7 depicts the predicted velocities for 5 step prediction for the stochastic prediction methods P_1, P_2 and P_3 respectively. The use of WLTC cycle is only to aid the understanding of the prediction methods. As discussed in 2.3, prediction methods P_2 and P_3 better capture dynamics of the driving profile. Results from the EM operation using the different prediction methods has been displayed in the Figure 6. The SOC

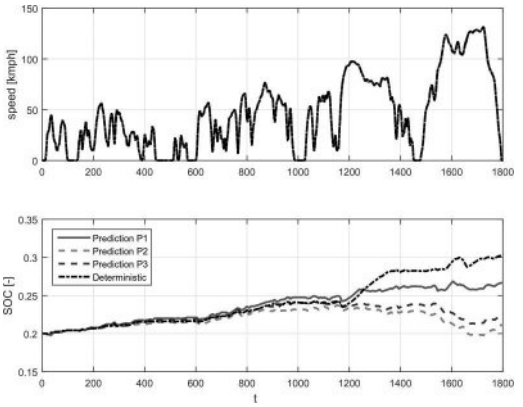


Figure 6. WLTC SOC Comparison.

terminal constraint and initial value of 0.3 and 0.2 were used respectively. As it can be seen the EM strategy under deterministic prediction data was able to satisfy the SOC terminal constraint. However the increase of the stored energy in the battery has been achieved at the expense of higher fuel consumption as it can be observed from the Table 1. Further it can be observed that the nominal MPC EM was not able to satisfy the SOC terminal constraints, in presence of uncertain prediction data. This motivates the need for investigation of robust or stochastic MPC controllers. Further as the level of stochastic in the prediction increases, the deviation of terminal SOC to the terminal constraint setting also increases, which is also reflected in the values of fuel consumption for the different prediction scenarios.

4 CONCLUSIONS

A self-optimizing EM controller was developed by solving online a quadratic optimization problem with linear constraints. It can operate using deterministic

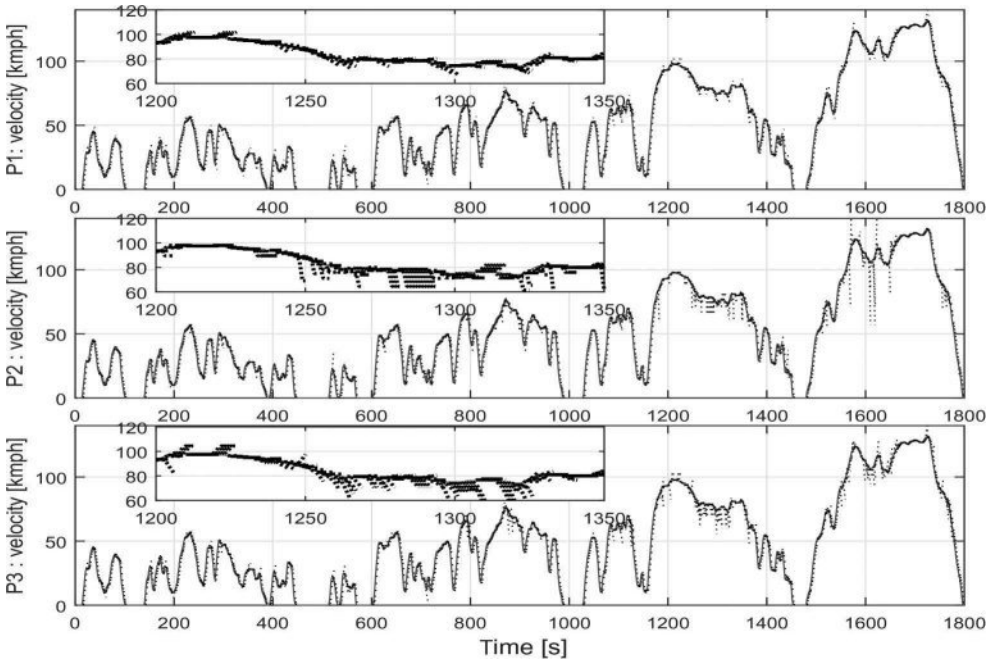


Figure 7. Comparison of stochastic predictions for WLTC driving cycle.

Table 1. EM operation with different prediction framework.

Method of prediction	ΔSOC	Fuel Consumption (g)
Stochastic, P_1	0.0664	1134
Stochastic, P_2	0.011	934
Stochastic, P_3	0.0224	970
Deterministic	0.1022	1228

predictions in case of autonomous driving and stochastic predictions in case of driver-aware scenario. The EM controller is real-time capable and has fewer number of parameters in comparison to the rule-based EM controller. The performance of the EM controller was demonstrated using driving profile with standardized characteristics and realistic/random driving profiles. Analysis reveal the sub-optimal performance of the nominal MPC scheme. Future work would focus on making the MPC EM strategies robust to deal with uncertainty in both prediction information and model uncertainty.

REFERENCES

Benz, T., N. El Ghouti, F. Krietsch, P. Matthias, F. Peyeron, & Themann (2012). The eCoMove Simulation Test Bed. *Procedia – Social and Behavioral Sciences 48*.

Bier, M. Hardware-In-the-Loop-Motorpruefstand zur Entwicklung hybrider Antriebsstraenge. *Dissertation, TU Darmstadt*.

ECOMOVE, C. (2010). eComove: eCoMove – Description of Work.

Radke, T. (2013). Energieoptimale Laẗngsfuẗhrung von Kraftfahrzeugen durch Einsatz vorausschauender Fahrstrategien. *Dissertation, KIT*.

Rawlings, J. & D. Mayne (2009). Model Predictive Control: Theory and Design. *Nob Hill Publishing*.

Sciarretta, A. & L. Guzzella (2007). Control of Hybrid Electric Vehicles. *IEEE Control Systems Magazine*.

Vadamalu, R. & C. Beidl (2016a). Explicit MPC PHEV Energy Management using Markov chain based predictor: Development and Validation at Engine-In-The-Loop testbed. *European Control Conference*.

Vadamalu, R. & C. Beidl (2016b). Online MPC based PHEV Energy Management using Conic Interior-point Methods. *IEEE Intelligent Vehicles Symposium*.

Vadamalu, R., D. Buch, & C. Xiao, H. and; Beidl (2015). Energy Management of Hybrid Electric Powertrain using Predictive Trajectory Planning Based on Direct Optimal Control. *IFAC workshop on control applications of optimization*.

Weber, T. (2016). Beitrag zum Uẗbertrag von Straenfahrten auf den Rollenprfstand mittels Echtzeitsimulation. *Dissertation, TU Darmstadt*.

Wirth, M., L. Bartsch, S. Ploumen, & C. Weber (2015). In a Hybridized Future with Alternative Fuels: Is the SI Engine the Winning Concept? *SIA POWERTRAIN*.

Advanced Vehicle Control – Edelmann, Plöchl & Pfeffer (Eds)
© 2017 Taylor & Francis Group, London, ISBN 978-1-138-02992-7

Adaptive power management strategy for a four-mode plug-in hybrid electric vehicle

J.-C. Guan & B.-C. Chen
National Taipei University of Technology, Taipei, Taiwan

L.-K. Chen
National Taiwan University of Science and Technology, Taipei, Taiwan

ABSTRACT: An adaptive power management strategy (PMS) based on the equivalent fuel consumption minimization strategy (ECMS) is developed for a four-mode PHEV in this paper. The four-mode PHEV which consists of an internal combustion engine (ICE) and two motors provides four modes of operation, including electric vehicle mode, range extended mode, parallel mode and power split mode. A self-organizing fuzzy controller is employed to adaptively adjust the equivalence factor of electric energy consumption based on the SOC deviation and the change of SOC deviation. A cost function of instantaneous fuel consumption is minimized to obtain the optimum power distributions of the ICE and motors. Simulation results show that the adaptive PMS can effectively improve the fuel economy for different driving cycles and reduce the average charging/discharging power for extending the battery life.

1 INTRODUCTION

Hybrid electric vehicles (HEVs) and plug-in hybrid electric vehicles (PHEVs) have been acknowledged as promising solutions to reduce exhaust emissions and fuel consumptions. HEVs and PHEVs which consist of an internal combustion engine (ICE), one or multple electric motors, and a battery pack. But PHEVs differ from the HEVs due to a larger battery pack which can be recharged from an external power source.

Powertrain electrification can reduce the fuel consumption by operating ICE in the high efficiency region. However, the increased configuration complexity poses a challenge for efficiently controling the power flow between multiple power sources. Various control methods have been investigated to provide better fuel consumption performances in HEVs.

The power management strategies (PMS) of PHEV can be classified into three types. Type I employs rule-based control technologies. A charge depleting-charge sustaining (CD-CS) strategy is implemented in the Chevrolet Volt (Matthé & Eberle 2014). The PHEV is driven in all-electric mode (CD mode) until a low battery state of charge SOC bound is achieved. Then the SOC is sustained (CS mode) until the end of the driving event. Type II employs static optimization methods to minimize the instantaneous total equivalent fuel consumption based on the equivalent consumption minimization strategy (ECMS) (Kim et al. 2011). Yan et al. (2012) employed model predictive control (MPC) to design PMS. Borhan et al. (2012) formulated a nonlinear and constrained optimal control problem for the PMS design. MPC is then utilized to obtain the power split between the ICE and electrical motors. Vajedi et al. (2014) designed a new real-time route-based PMS for PHEVs based on the adaptive ECMS (A-ECMS). A-ECMS takes advantage of preview trip information to achieve even higher efficiencies. Manzie et al. (2015) presented a PMS to track the proposed state of charge trajectory using the A-ECMS. Sun et al. (2016) proposed an adaptive-ECMS combined with a velocity predictor to provide temporary driving information for real-time adaptation of the equivalence factor (EF). Type III employs dynamic optimization methods to obtain the global minimization of the fuel consumption over a time horizon based on dynamic programming (DP) (Liu et al. 2008, Kum et al. 2013). Due to the computational complexity, DP cannot be implmemented in real time. However, DP can offer the performance upper bound to benchmark other control strategies for a specific driving cycle.

In this paper, we design an adaptive PMS of PHEV based on ECMS. A self-organizing fuzzy controller is employed to adaptively adjust the equivalence factor of electric energy consumption based on the SOC deviation and the change of SOC deviation. A cost function of instantaneous fuel consumption is minimized to obtain the optimum power distributions of the ICE and motors.

The remainder of the paper is organized as follows. In Section 2, the configuration of a four-mode PHEV is introduced. The proposed adaptive PMS is presented in Section 3. Simulation results are illustrated

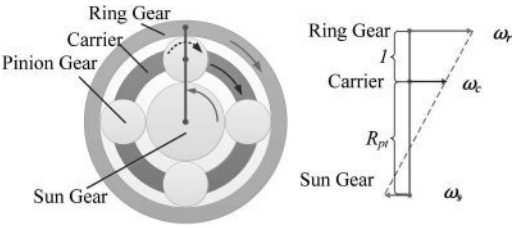


Figure 1. Planetary gear and its level diagram analogy.

in Section 4, and conclusions are presented in Section 5.

2 MODELING

The four-mode PHEV uses a planetary gear (PG) as its power-split device. The PG consists of a ring gear, a sun gear, and a carrier with several pinion gears. The two degrees of freedom dynamics of the PG system is shown in Figure 1. The rotational speeds of the sun gear ω_s ring gear ω_r and carrier ω_c in a PG system must satisfy the constraint as shown below.

$$\omega_s + \omega_r R_{pt} = \omega_c(1 + R_{pt}) \tag{1}$$

where R_{pt} is the basic gear ratio of the PG set between the number of teeth of the sun gear and the ring gear.

The system configuration of the four-mode PHEV (Lin 2012) is shown in Figure 2. An ICE, an internal starter generator (ISG), and a traction motor (TM) are connected via a planetary gear (PG). Table 1 shows the operating modes of the four mode PHEV. The EV mode includes EV1 and EV2. In EV1, TM is connected to the sun gear and the ground brake B is engaged. In EV2, sun gear and carrier are connected with the clutch C_1 engaged and TM transmits power to the final drive directly. The range extended (RE) mode includes RE1 and RE2 which using ICE and ISG as a genset with the clutch C_2 open and TM propels the vehicle the same way as the EV mode. The parallel mode uses ICE and ISG with C_1 and C_2 engaged. The power-split mode with the electronic continuously variable transmission (eCVT) function uses ICE, ISG and TM with C_2 engaged. The engine of the four-mode HEV is a 2.0 liter ICE with turbo charger. The rated powers of the TM and ISG are 50 kW and 25 kW, respectively.

According to speed constraint of PG system, the dynamic model for the power-split mode is shown in

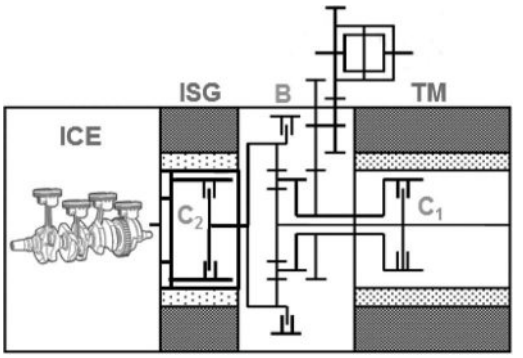


Figure 2. Configuration of the four-mode PHEV.

Table 1. Operating modes of the four mode PHEV.

	Component operation*			Clutch operation*		
Mode	ICE	ISG	TM	C_2	C_1	B
EV1	–	–	√	0	0	1
EV2	–	–	√	0	1	0
RE1	√	√	√	0	0	1
RE2	√	√	√	0	1	0
Parallel	√	√	–	1	1	0
Power-Split	√	√	√	1	0	0

*√: component is on; –: component is off; 1: clutch is engaged; 0: clutch is open

Equation 2. T is the torque output; I is the inertia; b is the rotational damping coefficient of crankshaft bearing; ω is the rotational speed; F_x is the longitudinal tire force; r_w is the wheel radius; n_{fd} is the final drive gear ratio. The torque constraint of PG system at steady state can be expressed as follows.

$$T_{TM} R_{pt} = (T_{ICE} + T_{ISG}) \tag{3}$$

3 POWER MANAGEMENT STRATEGY

A charge depleting according to the energy-to-distance ratio problem (Kum et al. 2013) is formulated as shown in Figure 3. A self-organizing fuzzy control (SOFC) is employed to adjust the equivalence factor according to the SOC deviation. An instantaneous cost function which consists of the total equivalent fuel consumption is then minimized to obtain the optimal power

$$\begin{bmatrix} T_{TM}(1+R_{pt})n_{fd} - F_x r_w \\ (T_{ICE}+T_{ISG})\left(\frac{1+R_{pt}}{R_{pt}}\right)n_{fd} - F_x r_w \\ 0 \end{bmatrix} = \begin{bmatrix} I_{TM}(1+R_{pt})n_{fd} & 0 & I_{fd} \\ 0 & (I_{ICE}+I_{ISG})\left(\frac{1+R_{pt}}{R_{pt}}\right)n_{fd} & I_{fd} \\ -1 & -R_{pt} & (1+R_{pt})n_{fd} \end{bmatrix} \begin{bmatrix} \dot{\omega}_{TM} \\ \dot{\omega}_{ICE} \\ \dot{\omega}_{fd} \end{bmatrix}$$

$$+ \begin{bmatrix} 0 & 0 & b_{TM}+b_{fd} \\ 0 & 0 & b_{ICE}+b_{ISG}+b_{fd} \\ 0 & 0 & 0 \end{bmatrix} \begin{bmatrix} \omega_{TM} \\ \omega_{ICE} \\ \omega_{fd} \end{bmatrix} \tag{2}$$

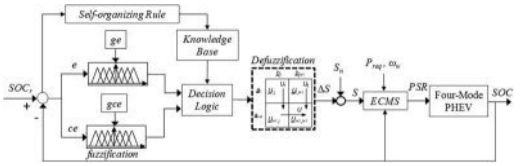


Figure 3. Proposed adaptive power management strategy.

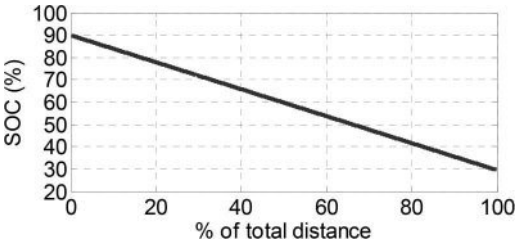


Figure 4. The SOC-distance curve.

split ratios of ICE, ISG and TM based on the ECMS concept.

3.1 *Equivalent consumption ninimization strategy*

For PHEV, the battery is required to work under a charge-depleting mode (Wirasingha & Emadi 2011), for the optimal solution. The SOC-distance curve behaves like a straight line with a constant slope as shown in Figure 4. The driver only needs to provide the approximate estimation of traveling distance to plan the reference trajectory of SOC for discharging the battery. After obtaining the power request P_{req} from the driver, the power outputs of ICE, ISG and TM should satisfy the following equation.

$$P_{req} = P_{ICE} + P_{ISG} + P_{TM} \tag{4}$$

An instantaneous cost function which consists of the total equivalent fuel consumption is then minimized to obtain the optimal power distributions of the ICE, ISG and TM based on the ECMS concept. The instantaneous cost function is established as follows.

$$J_{ECMS,mode} = \dot{m}_{ICE}(P_{ICE}) + \dot{m}_{batt}(P_{batt}) \tag{5}$$

where the subscript mode is defined in Table 1; $\dot{m}_{ICE}$ is the fuel consumption rate of P_{ICE}; $\dot{m}_{batt}$ is the equivalent fuel consumption rate of the battery power $P_{batt} = P_{ISG} + P_{TM}$. $\dot{m}_{batt}$ can be obtained from the following equation.

$$\dot{m}_{batt} = \gamma \frac{SP_{batt} g_{ICE}}{\eta_{batt}} + (1-\gamma) SP_{batt} g_{ICE} \eta_{batt} \tag{6}$$

where η_{batt} is the efficiency of the battery which is function of P_{batt} and SOC; g_{ICE} is the minimum brake specific fuel consumption (BSFC) of the engine; $\gamma = 0.5(1 + \text{sign}(P_{batt}))$ is equal to 1 and 0 for discharging and charging, respectively. The equivalent factor S is used to obtain the equivalent fuel consumption of the electric power consumption. If the equivalence factor is large, using electric power is more expensive than using ICE. And vice versa.

Since the minimization of J_{ECMS} is subject to the power constraint in Equation 4, we can transform the four-dimensional problem into the following three-dimensional problem as follows.

$$(PSR^*_{ICE}, PSR^*_{TM}, mode^*) = \underset{PSR_{ICE}, PSR_{TM}, mode}{\arg\min} J_{ECMS} \tag{7}$$

where $PSR_{ICE} = P_{ICE}/P_{req}$ is the power split ratio of ICE and $PSR_{TM} = P_{TM}/P_{req}$ is the power split ratio of TM. The power split ratio of ISG can then be obtained as $PSR_{ISG} = 1 - PSR_{ICE} - PSR_{TM}$. Various methods for two-dimensional optimization (Schilling & Harris 2000) can be applied to solve the minimization problem.

In this paper, the ICE is designed to operate on the optimum operating curve. The optimum engine speed and torque are determined for a given P_{ICE}. According to speed constraint in Equation 1 and torque constraint in Equation 3, three-dimensional optimization problem can be further simplified to two-dimensional optimization problem as follows.

$$(PSR^*_{ICE}, mode^*) = \underset{PSR_{ICE}, mode}{\arg\min} J_{ECMS} \tag{8}$$

The golden section search method is employed to find the optimal PSR_{ICE} at each mode. $mode^*$ is selected to be the mode with the lowest J_{ECMS}. We can then determine the globa optimal PSR_{ICE} at $mode^*$.

3.2 *Adaptive power management strategy*

If the SOC is decreasing, the equivalence factor should be increased to represent a more expensive cost of electric power. Thus prevent over discharging the battery. On the other hand, if the SOC is increasing, the equivalence factor should be reduced to represent a cheaper cost of electric energy. Thus encourage the usage of electric power to prevent over charging the battery. The nominal equivalence factor S_n is optimized to obtain the lowest fuel consumption with respect to the given driving cycle. SOFC is used to generate the correction of the equivalence factor ΔS according to the SOC deviation $e = SOCr - SOC$ and the change of SOC deviation between sample time $ce_k = e_k - e_{k-1}$. Genetic algorithm is used optimize the gains of SOC error and the change of SOC error. The subscript k denotes for the kth sample time. SOC_r is the reference SOC. ΔS is derived from the fuzzy inference decision and defuzzification operation. The overall equivalence factor S used for ECMS can be expressed as

$$S = S_n + \Delta S \tag{9}$$

where S_n is the nominal equivalence factor optimized for the lowest fuel consumption with respect to the

given driving cycle; ΔS is derived from the fuzzy inference decision and defuzzification operation. If the equivalence factor S is large, the electric energy consumption is more expensive than the fuel consumption. If S is small, the electrical energy consumption is cheaper than the fuel consumption.

The parameters of the membership functions and fuzzy rules are often designed by trial and error to obtain an appropriate performance. SOFC is employed to modify these rules automatically. The self-organizing rule consists of performance measure, model estimation, and rule modification. The control correction of the ith fuzzy rule can be expressed as follows

$$\Delta u_{i,k} = w_{e,i} w_{ce,i} \gamma [(1-\zeta) e_k + \zeta ce_k] \tag{10}$$

where γ indicates the correction rate. A large value of γ results in a large correction of fuzzy rules and system output oscillation. The correction value of each fuzzy rule is proportional to its excitation strength. ζ is the performance weighting between e and ce. Excitation strengths w_e and w_{ce} for the ith rule, which can be obtained from the membership functions, are used as the correction weightings for the activated rules. Thus the resulting fuzzy control value of the ith rule can be expressed as

$$u_{i,k+1} = u_{i,k} + \Delta u_{i,k} \tag{11}$$

According to Equation 10, Δu_i is zero only when $e = ce = 0$ or $(1-\zeta)e_k + \zeta ce_k = 0$. In order to prevent unnecessary correction around the zero point, the rule is not updated when the absolute values of e and ce are less than the threshold values.

In order to reduce frequent mode shifting, the penalty of mode switching is added to J_{ECMS} at the kth sample as follows.

$$J_{mode,k} = J_{ECMS,k} + \beta shift_k \tag{12}$$

$$shift_k = \begin{cases} 0, if \;\; mode_{k+1} = mode_k \\ 1, if \;\; mode_{k+1} \neq mode_k \end{cases} \tag{13}$$

where β is a positive weighting factor.

4 SIMULATION RESULT

One NEDC cycle is used for optimizing the proposed adaptive PMS. 10 NEDC cycles are used to evaluate the proposed adaptive PMS. The desired SOC trajectory is designed with the initial SOC equal to 90% and the energy-to-distance ratio equal to 0.55% for reaching the final SOC at 30%. The results of the 6th NEDC cycle is discussed in this paper. The operating points of ICE, ISG and TM at each mode of the proposed adaptive PMS are shown in Figures 5–7. In the RE mode, both ICE and ISG are operated around the optimal operating curve. For the power split mode, the ISG is used to adjust the ICE speed such that the ICE can be operated around the optimal operating curve. The TM can provide additional power when necessary. The TM is operated at vehicle speeds below 40 km/hr for the EV and RE modes.

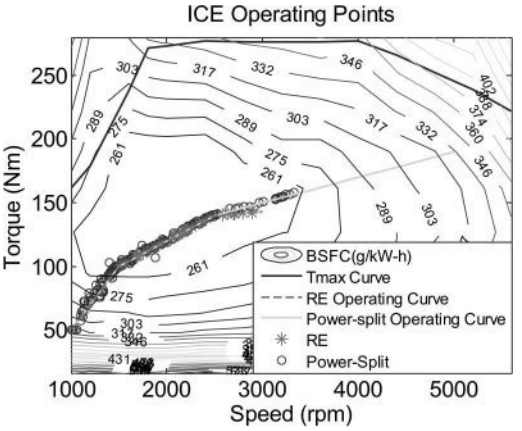


Figure 5. ICE operating points for the 6th NEDC.

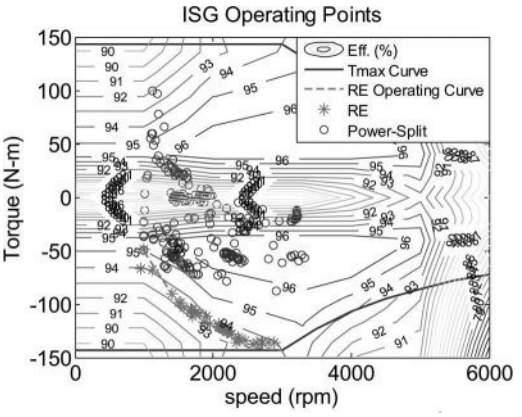


Figure 6. ISG operating points for the 6th NEDC.

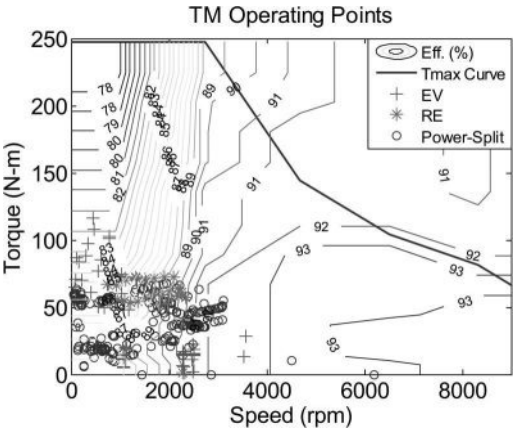


Figure 7. TM operating points for the 6th NEDC.

Mode switching results of the 6th NEDC cycle are shown in Figure 8. From 6718 sec to 6795 sec, the PHEV is operated in the power split mode. The proposed adaptive PMS can track the desired SOC within an acceptable deviation. According to the optimal power distributions of the ICE and motors, the power-split mode can also achieve the eCVT function.

In the simulation, regenerative braking works for vehicle speed above 15 km/hr, and the regenerated power is limited by the battery charging specification. The responses of battery SOC for running 10 NEDC cycles with total distance of 109 km are shown in Figure 9. The initial SOC and terminal SOC are set to be 90% and 30%, respectively. The CD-CS method operates the PHEV in all-electric mode until the SOC is below 30%. Then the SOC is sustained in the CS mode until the end of the driving event. The proposed adaptive PMS method can gradually discharge the battery such that the final SOC is approximately equal to 30%.

Standard driving cycles of FTP75 and HWFET are employed to evaluate the adaptiveness of the proposed adaptive PMS. Simulation results of 10 NEDC cycles,

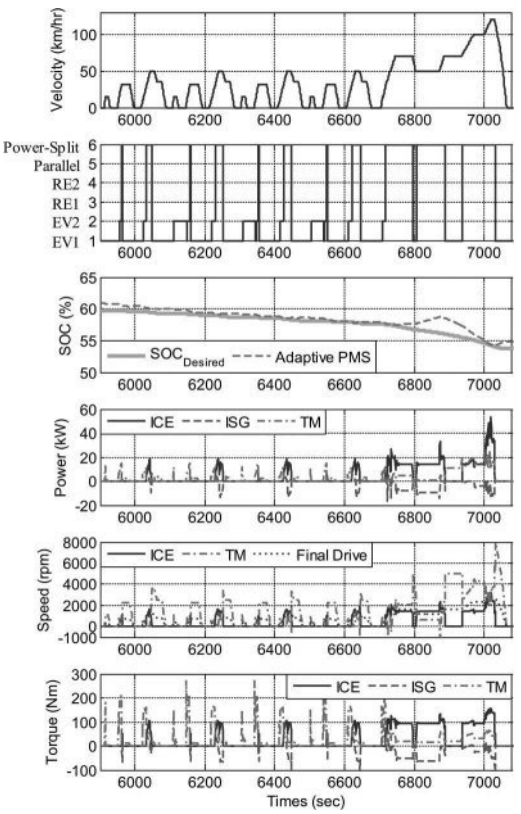


Figure 8. Simulation results for the 6th NEDC.

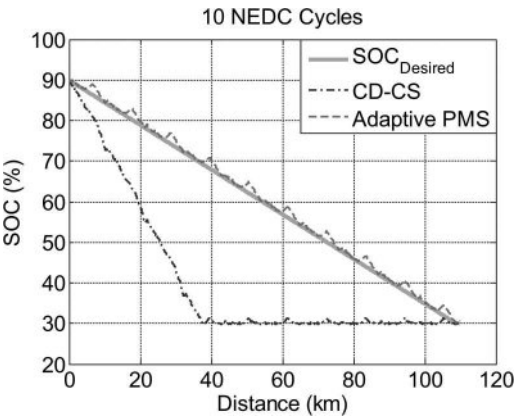


Figure 9. SOC responses for 10 NEDC cycles.

Table 2. Fuel economies of the CD-CS and proposed adaptive PMS.

		CD-CS		Adaptive PMS		
Driving cycle	Distance (km)	Final SOC (%)	Fuel economy (km/L) (SOC corrected)	Final SOC (%)	Fuel economy (km/L) (SOC corrected)	Improvement (%)
10 NEDC	109	30.6	19.7	30.7	20.3	3.0
6 FTP75	106	30.4	20.5	30.7	21.4	4.5
7 HWFET	114	30.5	17.2	30.6	18.1	5.0

Table 3. Averaged battery charge/discharge powers of the CD-CS and proposed adaptive PMS.

		CD-CS		Adaptive PMS	
Driving cycle	Distance (km)	Averaged charge (kW)	Averaged discharge (kW)	Averaged charge (kW)	Averaged discharge (kW)
10 NEDC	109	5.3	9.7	5.0	8.4
6 FTP75	106	5.3	11.0	4.6	9.2
7 HWFET	114	3.6	10.7	3.4	7.0

6 FTP75 cycles, and 7 HWFET cycles based on different methods are presented in Tables 2 and 3. The associated fuel consumptions in Table 2 are all corrected using the SAE standard J1711 (1999). For 10 NEDC cycles, the four-mode PHEV with the proposed adaptive PMS method can improve the fuel economy of CD-CS method by 3.0%. For 6 FTP75 cycles and 7 HWFET cycles, the four-mode PHEV with the proposed adaptive PMS method can improve the fuel economy of CD-CS method by 4.5% and 5.0%, respectively. Meanwhile, the averaged battery charge and discharge powers of adaptive PMS method are less than those of the CD-CS method for each driving cycle. If the battery power usages are reduced for the same given driving cycle, it is possible to extend the battery life (Gao 2009).

5 CONCLUSION

An adaptive PMS is designed based on ECMS with the equivalent factor adjusted using SOFC for a four-mode PHEV. SOFC can achieve SOC tracking control via adjusting the equivalence factor according to the SOC deviation. Genetic algorithm is used optimize the gains of SOC error and the change of SOC error. A cost function of instantaneous fuel consumption is minimized to obtain the optimum power distributions of ICE, ISG, and TM. In order to reduce frequent mode shifting, the penalty of mode switching is added to the instantaneous cost function. Simulation results show that the proposed adaptive PMS has superior fuel economy than the CD-CS method for different driving cycles. Meanwhile, the adaptive PMS method can reduce the average charging/discharging power for extending the battery life.

ACKNOWLEDGEMENTS

This project was supported by the Ministry of Science and Technology in Taiwan under the contract No. of MOST 105-3113-E-027-003-CC2.

REFERENCES

Borhan, H., Vahidi, A., Phillips, A.M., Kuang, M.L., Kolmanovsky, I.V. & Cairano, S.D. 2012. MPC-Based energy management of a power-split hybrid electric vehicle. *IEEE Transactions on Control Systems Technology*. 20, 593–603.

Gao, J.P., Zhu, G.M.G., Strangas, E.G. & Sun, F.C. 2009. Equivalent fuel consumption optimal control of a series hybrid electric vehicle. *Proceedings of the Institution of Mechanical Engineers, Part D: Journal of Automobile Engineering.* 223, 1003–1018.

Kim, N., Cha, S. & Peng, H. 2011. Optimal Control of Hybrid Electric Vehicles Based on Pontryagin's Minimum Principle. *IEEE Transactions on Control Systems Technology*. 19, 1279–1287.

Kum, D., Peng, H., & Bucknor, N.K. 2013. Optimal energy and catalyst temperature management of plug-in hybrid electric vehicles for minimum fuel consumption and tailpipe emissions. *IEEE Transactions on*. 21, 14–26.

Liu, J. & Peng, H. 2008. Modeling and control of a power-split hybrid vehicle. *IEEE Transactions on*. 16, 1242–1251.

Lin, S.S. 2012. Trend and challenge of technology development for powertrain electrification. *Modern Engineering and Technology Seminar*, Taipei, Taiwan.

Manzie, C., Dewangan, P., Corde, G., Grondin, O., & Sciarretta, A. 2015. State of charge management for plug-in hybrid vehicles with uncertain trip information. *Journal of Dynamic Systems, Measurement, and Control*. 137, 1–7.

Matthé, R. & Ulrich Eberle, U. 2014. The voltec system—energy storage and electric propulsion. Lithium-ion batteries: advances and applications. Chapter 8, 151–176

SAE. 1999. Recommended practice for measuring the exhaust emissions and fuel economy of hybrid-electric vehicles. *SAE J1711*.

Schilling, R. J. & Harris, S. L. 2000. Applied numerical methods for engineers using matlab and C. *Pacific Grove.* CA: Brooks/Cole.

Sun, C., Sun, F.C. & He, H.W. 2016. Investigating adaptive-ECMS with velocity forecast ability for hybrid electric vehicles. *Applied Energy*.

Vajedi, M., Chehrehsaz, M. & Azad, N.L. 2014. Intelligent power management of plug-in hybrid electric vehicles, part II: real-time route based power management. *Int. J. Electric and Hybrid Vehicles*. 6, 68–86.

Wirasingha, S.G., & Emadi, A. 2011. Classification and review of control strategies for plug-in hybrid electric vehicles. *IEEE Transactions on Vehicular Technology*. 60, 111–122.

Yan, F., Wang, J. & Huang, K. 2012. Hybrid electric vehicle model predictive control torque-split strategy incorporating engine transient characteristic. *IEEE Transactions on Vehicular Technology*. 61, 2458–2467.

Advanced Vehicle Control – Edelmann, Plöchl & Pfeffer (Eds)
© 2017 Taylor & Francis Group, London, ISBN 978-1-138-02992-7

Reduced order propulsion models for vehicle control and energy management

Kazuhide Togai
Osaka Sangyo University, Japan

Naoto Fujinaga
Mitsubishi Motors Corporation, Japan

Hiroki Yamaura
Mitsubishi Automotive Engineering Ltd., Japan

ABSTRACT: Engine output torque models have been applied to engine control, energy management and NVH development. Engine torque profile in a cycle is fixed after intake valves closing, so that a mean value engine model is suitable for those purposes considering accuracy and convenience. One of factors to affect model complexity is required cutoff frequency. Relationship between the frequency and engine cycle frequency is to be explained. An engine torque modeling methodology is to be proposed including a modeling approach applicable to a turbocharged engine in which a positive feedback loop exists in air intake process.

1 INTRODUCTION

Engine output torque models have been applied to engine control, energy management and NVH development. Engine torque profile in a cycle is fixed after intake valves closing, so that a mean value engine model is suitable for those purposes considering accuracy and convenience if combustion variation is not considered.

One of factors to affect model complexity is required cutoff frequency. Relationship between the frequency and engine cycle frequency is to be explained. An engine torque modeling methodology is to be proposed including a modeling approach applicable to a turbocharged engine in which a positive feedback loop exists in air intake process.

Engine torque is generated in an energy conversion process in a combustion chamber. This process is described as a gain. Then air transfer process is added. This may be described with a first order delay. Engine torque in a cycle contains ignition frequency and harmonics.

Required cut off frequency in vehicle control and energy management purposes is lower than that of ICE control. Time constants of a NA (naturally aspirated) engine model can be ignored for those purposes.

2 ENGINE MODEL CLASSIFICATION BASED ON CUTOFF FREQUENCY

2.1 *Quasi-stationary – DC*

For speed tracking application, e.g. emission test cycle simulation, sometimes A DC engine model is applicable without any compromise of accuracy. For energy management purpose, quasi-stationary model is applied. And fuel mass flow based torque calculation is more convenient for relative fuel economy prediction and energy management.

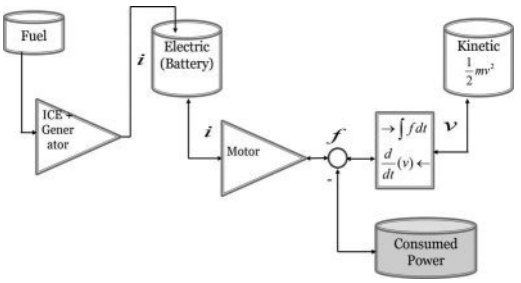


Figure 1. Energy flow and storage in a HEV system.

2.2 *Air transfer into a combustion cylinder – up to 10 Hz*

As well-known or sometimes experienced, engine torque is delayed to accelerator operation. The delay consists of air transportation delay from the throttle to the combustion chamber and engine cycle delay, e.g. intake and combustion strokes. Further delay is added if turbocharger equipped.

Those delay is not significant for emission test cycle simulations, however those effect on vehicle acceleration performance including driver's acceptance. And also lower frequency vibration may be caused depending on the time constant of torque response.

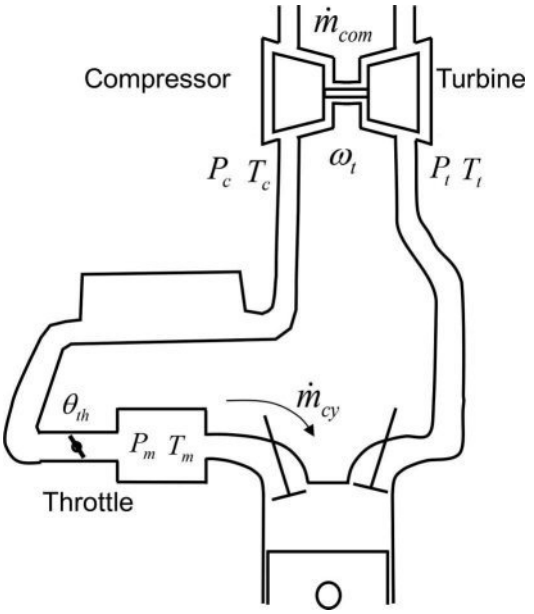


Figure 2. Air mass storage & boost in a turbocharger system.

2.3 *Engine cycle proportional – ignition frequency & harmonics*

Required model properties are frequency of up to crank angle 1 degree Frequency and one dimension.

Torque profile in a cycle can be generated using an amplitude modulation based on a mean value engine model without difficulty. Authors have been proposed amplitude modulation method to generate torque profile in a cycle. Required parameters are 8 if the torque is approximated up to 8th order.

3 QUASI-STATIONARY MODEL (DC)

3.1 *Energy conversion to mechanical power*

Mechanical power is converted from fuel in a combustion chamber. The energy is described as equation (1).

$$E_{fuel} = M_{fuel} Q_{fuel} \tag{1}$$

where, E_{fuel}: energy in a combustion chamber in a cycle [J], M_{fuel}: fuel mass [kg], Q_{fuel}: heat released from the fuel [J/kg].

Mechanical power is calculated with energy conversion efficiency as equation (2).

$$P_{mech} = \eta_i m_{fuel} Q_{fuel} \tag{2}$$

where, P_{mech}: converted mechanical power in a combustion chamber [J/s], η_i: conversion efficiency, m_{fuel}: fuel mass flow [kg/s], Q_{fuel}: heat released from the fuel [J/kg].

The conversion efficient is indicated power based and can be assumed constant at an engine speed range.

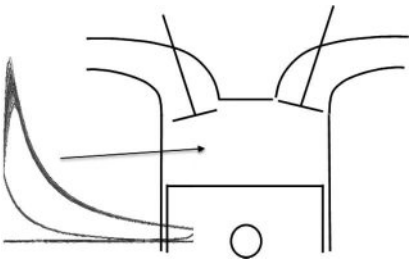


Figure 3. Energy combustion in a combustion cylinder.

Output torque approximated with fuel mass in a cycle and friction as the following section.

3.2 *Engine torque model*

As explained, dynamic behavior from the control mean (a throttle) to output torque is not required to be considered. Danno & Togai (1989) proposed that output torque of an ICE is proportional to air mass taken in to a combustion chamber. Maximum brake mean effective pressure (BMEP) of a typical naturally aspirated engine is approximately 10 bar. An ICE for electric generation is mainly operated at stoichiometric air fuel ratio. That means that amount of fuel injected is proportional to amount of air taken to combustion chambers. The following equations show the relationship between injected fuel and output torque of an ICE.

$$T_e = Af_t - T_l$$

where, T_e: ICE torque, A: torque conversion coefficient, T_l: friction torque of an ICE.

Equation (3) indicate that required fuel rate can be calculated form required power. The friction torque of an ICE is depending on engine speed. However, that may be considered constant for smaller operating speed range for generation. Enrichment to raise maximum torque and to cool intake ports may be avoided and ignition timing delay strategy for knocking suppression may not be taken for generation ICEs. Maximum energy efficiency is obtained at the torque maximum line.

4 ENGINE TORQUE MODEL BASED ON AIR TRANSFER PROCESS

4.1 *Naturally aspirated engine model*

Mean value engine torque in a stroke is proportional to fuel mass injected in a cycle and the fuel mass is proportional to air mass flow in a cycle in a gasoline engine. The air intake process from the throttle to the combustion chambers is described with the following equations.

$$\dot{m}_{th} = A_{th} k \sqrt{P_a - P_m} \tag{3}$$

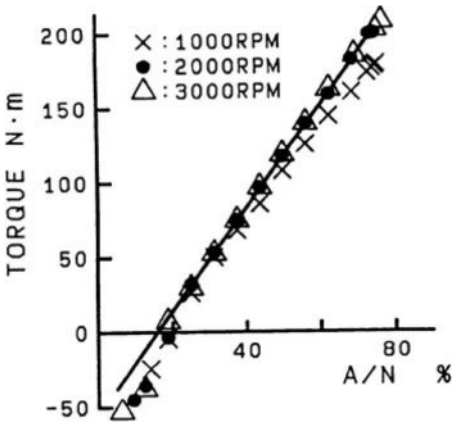


Figure 4. Relationship between torque and intake air.

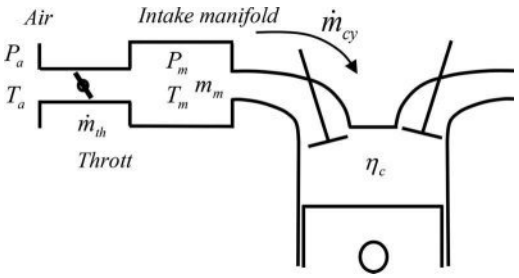


Figure 5. Air intake system for a NA engine.

$$m_m = \int (\dot{m}_{th} - \dot{m}_{cy})dt \tag{4}$$

$$P_m = \frac{m_m R T_m}{V_m} \tag{5}$$

where, m_{th}: air mass through throttle, P_a: upper stream pressure of the throttle, P_m: MAP, A_{th}: throttle opening area, k: throttle flow coefficient, m_{cy}: air taken into a combustion cylinder.

A first order delay system transfer function is derived from equations above directly. The transfer function Gth(s) is described as equation (6)

$$G_{th}(s) = \frac{1}{1+Ts} \tag{6}$$

where, T: time constant depending on the ratio of the cylinder displacement over the plenum chamber multiplied by the engine speed, s: Laplace operator.

4.2 *Positive feedback system model for a turbocharger*

Intake air pressure increases as exhaust pressure increases with a turbocharger. That leads to increase the exhaust pressure.

The system shown above is assumed as a first order delay with time constant of T without loss of generality. Also the controller and the gain can be assumed as gain 1.0 and K respectively.

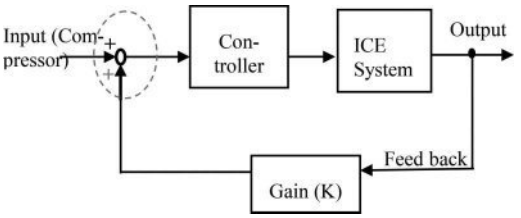


Figure 6. Air intake system for a NA engine.

If the feedback gain $K < 1.0$, then the system is stable. Time constant is $T/(1-K)$ and the system gain is $1/(1-K)$.

4.3 *A transfer function model for a turbo charger system*

A model with positive feedback loop is derived and property of the model related to gains will be shown.

4.3.1 *Model reduction: Assumption*

Dynamic response property related to throttle opening change in a NA engine is only mass reservation at the intake manifold and cylinder intake air mass flow is not larger than that of initially pass thorough the throttle. In contrast, cylinder intake air after throttle opening raise is larger than that of the initial throttle opening due to amplifying mechanism with the turbocharger. Efficiencies of the turbine and the compressor is less than 1.0. Then, driving force of the compressor is saturated at a steady state. Initial throttle operation is amplified with the turbine – compressor mechanism that is one of differences from a NA engine. Non-linear models have been applied for engine controls. Theoretical equations and experiments indicate the followings.

- Compressor pressure ratio may be proportional to turbine speed square.
- Turbine speed may be a first order delay to air mass flow through the throttle.

4.3.2 *Thermal dynamic process combining a turbine and a compressor*

Main operation measure to control the mass airflow is the throttle and the waste gate is used to limit the throttle upper stream pressure. That can be used for a control measure.

4.3.2.1 Turbine thermal dynamics power

Adiabatic expansion work is described for 1.0 kg/s mixture mass flow as equation (7).

$$W_t = RT_t \frac{\kappa_g}{\kappa_g - 1}\left(1 - \left(\frac{p_{t2}}{p_{t1}}\right)^{\frac{\kappa_g - 1}{\kappa_g}}\right) \tag{7}$$

where, W_t: work to drive the turbine, T_t: turbine entrance temperature, P_{t1}, P_{t2}: turbine entrance and exit pressure respectively, R: gas constant, κ_g: specific heat ratio of the mixture.

4.3.2.2 Compressor thermal dynamics power

Adiabatic compression work is described for 1.0 kg/s air mass flow as equation (8).

$$W_c = RT_c \frac{\kappa}{\kappa - 1}\left(\left(\frac{p_{c2}}{p_{c1}}\right)^{\frac{\kappa-1}{\kappa}} - 1\right) \tag{8}$$

where, W_c: work to drive the compressor, T_c: compressor entrance temperature, p_{c1}, p_{c2}: compressor entrance and exit pressure respectively, κ: specific heat ratio of air.

4.3.2.3 Relationship between compressor power and turbine speed

Work to accelerate air is described as the following equation (9).

$$W_a = \psi\sigma(r\omega)^2 \tag{9}$$

where, W_a: work to accelerate air, Ψ: work coefficient, σ: slippage, r: impeller radius, ω: turbine speed.

4.3.2.4 Turbine motion equation

The turbine is accelerated by the torque difference between the turbine drive torque and compressor load torque as described in equation (10).

$$I_t\dot{\omega} = T_{rqt} - T_{rqc} = \eta_t \frac{W_t}{\omega} - \eta_c \frac{W_c}{\omega} \tag{10}$$

where, I_t: turbine inertia, T_{rqt}: turbine torque, T_{rqc}: compressor torque, η_t: turbine efficiency, η_c: compressor efficiency.

4.3.2.5 Turbine speed model

A turbine speed equation is described with turbine inertia, drive torque and load. Equation (10) is written in other form as equation (11)

$$I_t\dot{\omega} = T_{rqt} - \eta_c \frac{W_c}{\omega} \tag{11}$$

The compressor power is proportional to turbine speed square. Then, Turbine speed response is approximated as a first order delay to turbine drive torque. That is obtained turbine input power divided by the turbine speed. Once Map is raised above 1.0 bar, the power can be approximated with the air mass flow in to combustion cylinders

$$I_t\dot{\omega} = T_{rqt} - k_c\omega \tag{12}$$

4.3.3 *Transfer functions based on theoretical equations*

4.3.3.1 Model block diagram

The time constant of a turbine – compressor system T_{tc} is derived from equation (12).

$$T_{tc} = \frac{I_t}{k_c} \tag{13}$$

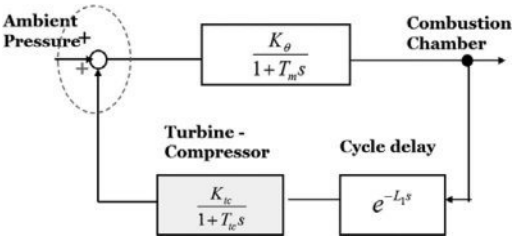


Figure 7. A block diagram for intake air boosting process with a turbo-charger.

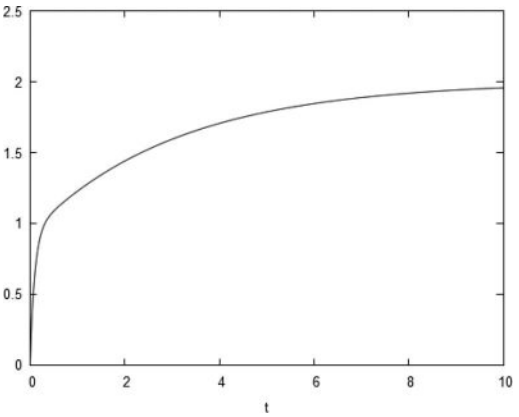


Figure 8. Step response of the reduced order model.

A block diagram is constructed based on an air transfer process described with equations (3)–(6) and an air compression process, i.e. a positive feedback, in a turbo charger system described with equations (7)–(13).

The closed loop transfer function of the system shown in Figure 7 can be calculated systematically with a computer algebra system (CAS), e.g. Maxima, and is described as equation (14).

$$G(s) = \frac{(1+T_{tc}s)K_\theta}{(1-K_\theta K_{tc}+T_{tc}s)(1+T_m s)} \tag{14}$$

Response to a step input, e.g. throttle opening change from idle to WOT, is calculated with the CAS and is shown in Figure 7. The horizontal axis is time in second and the vertical axis is normalized response.

The first quicker response to 1.0 until 0.2 seconds represents air transfer from a throttle to a combustion chamber and next slow response represents compressor pressure rise with the positive feedback.

4.3.3.2 Model prameters estimation and model validation with engine tests

A passenger car engine with a turbocharger was tested and parameters of the proposed model were derived with the measurement.

A coefficient of turbine speed to compressor work described in equation (9) cannot be derived from theoretical equations without detail properties of a turbocharger. The coefficient can be estimated with the

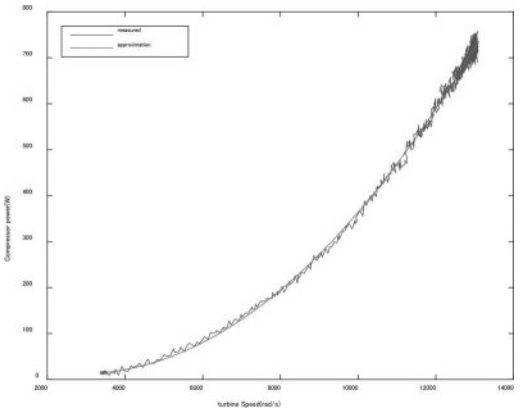


Figure 9. Compressor power is proportional to turbine speed square.

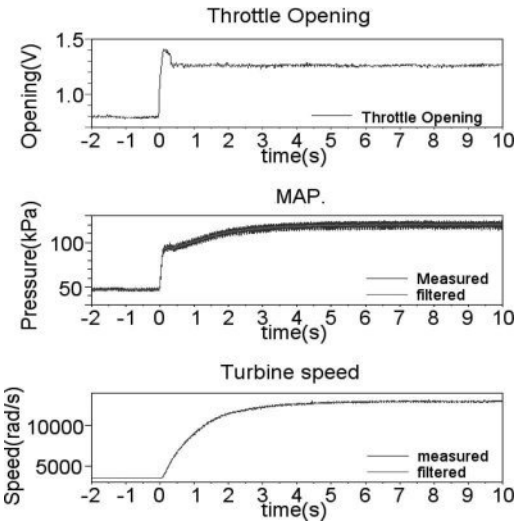


Figure 10. Measured data: step response at 1500 rpm.

measured data. Compressor work calculated with measured pressures and temperatures is proportional to turbine speed square as shown in Figure 9.

Turbine speed and MAP was measured at engine speed 1500 rpm. Behavior of turbine speed, the bottom graph, is that of first order delay system as modeled. MAP that is proportional to the compressor work is increasing as described in the previous chapter as shown in the second row graph of Figure 7.

5 TORQUE MODEL BASED ON ENGINE CYCLE

Combustion pressure profile at a certain operating condition is consistent once an engine management system calibrated. Combustion pressure was measured on a gasoline engine for various operating conditions. Combustion derived torque contains ignition frequency and its harmonics. Amplitude of each harmonics was normalized by the DC amplitude (mean torque) (Togai & Tamaki, 2012).

The normalized amplitude ratio for each harmonics is nearly constant over the operating range. Based on the fact, torque profile during one stroke can be generated only with the mean torque. Reverse Fourier transfer is one of applicable methods to generate the torque profile. Truncation up to eighth order is suggested for a reduced model without deteriorating accuracy significantly. Torque profile in a cycle can be generated with the cycle mean torque or the brake mean effective pressure. The equation is shown below.

$$T_e = T_{e0} + T_f + T_{e0}\sum_{1}^{n}\{(a_{cn}\cos(n\omega t) + b_{cn}\sin(n\omega t))\} + b_{i2}\sin(2\omega t) \quad (15)$$

where, T_e: engine torque (Nm), T_{e0}: stroke mean torque (Nm), T_f: friction torque (Nm), b_{i2}: inertia torque coefficient, a_{cn}: combustion torque coefficient for n-th order, b_{cn}: combustion torque coefficient for n-th order, ω: engine speed (rad/s), t: time (s)

6 CONCLUSIONS

A reduced order ICE torque model is required for engine management and vehicle control. An ICE model in time domain is more convenient and sufficient for those purposes comparing with a model in crank angle domain.

Mean value engine torque in a stroke is proportional to fuel injected in a cycle. This is described as a gain model. This model is very simple and useful for emission test cycle simulation and vehicle energy management particularly in HEV.

The fuel mass in a combustion chamber needs equivalent air mass. So, air transportation process should be considered for the engine response. Torque response delay to throttle valve opening is mainly depending on air transfer path in a gasoline engine.

In a NA engine, the air transfer path consists of intake manifold volume and cylinder volume. Time constant of response delay is reversely proportional to engine speed. More simplified model, i.e. gain only, may be applicable.

In a Turbocharged engine, the air transfer path consists of a positive feedback system of a turbocharger in addition to that of a NA engine. That leads to longer time constant of the torque response that may not be ignored for some application.

REFERENCES

Danno, Y., Togai, K. et al. 1989. Powertrain Control by DBW System – Strategy and Modeling, *SAE Technical Paper 890760*

Dickinson, P. Glover, K. Collings, N. et al. 2015. Transient Evaluation of Two-Stage Turbocharger Configurations using Model Predictive Control, *SAE Technical Paper 2015-01-1980*

Hendrics, E. 1991. SI Engine Controls and Mean Value Engine Modeling, *SAE Technical Paper 910258*

Saravanamutoo, H., Rogers, G., Cohen, H., Straznicky, P. 2009. *Gas turbine theory (6th Edition)*, Pearson Education Ltd.

Togai, K., Yamaura, H., Ishihama, M. 2013. Output profile shaping of an internal combustion engine for noise & vibration improvement, *JSAE20135626*

Togai, K., Tamaki, H. 2012. A Reduced Order Powertrain Model Concept for Model Based Development Process with a Driver Agent, SAE International, *SAE Technical Paper 2012-01-1628*

Advanced Vehicle Control – Edelmann, Plöchl & Pfeffer (Eds)
© 2017 Taylor & Francis Group, London, ISBN 978-1-138-02992-7

Modeling hydro mounts in vehicles for durability load analyses, ride comfort and vehicle dynamics simulation

Christian Scheiblegger
CSC Vehicle Dynamics

Nantu Roy
Fiat-Chrysler-Automobiles

Peter E. Pfeffer
Munich University of Applied Sciences, Munich, Germany

Andrew Hillis
University of Bath, Bath, UK

ABSTRACT: Hydraulically damped mounts and bushings are crucial for vehicle handling, ride comfort and noise vibration and harshness (NVH). Multi-body simulation (MBS) software is used to calculate loads and vibrations; where simple mount models lead to trade-offs in the overall vehicle simulation accuracy.

A model for many sorts of hydro mounts is presented. Accurate results are reached by correctly implementing the amplitude dependence of the mount's underlying rubber parts.

The model is evaluated with experiments from a component test rig; with transient test signals from on-road durability events. Accuracy of full-vehicle simulation improves significantly, so that physical vehicle tests can be reduced to save costs and development time.

Keywords: Modeling and Simulation/Vehicle Dynamics, Suspension/Integrated chassis control systems

1 INTRODUCTION

For heavy duty and light duty trucks reliability and robustness are key requirements and therefore the accurate prediction of durability load is crucial during development process. Multi body simulation tools are used to simulate the impact of different stiffness and position of the mounts and bushings in the early phase of development [1]. Prediction of road load using full-vehicle simulation is described in [2], where the tyre model has been validated and the excitation at wheel carrier/spindle loads proved to be correct. For further analyses along the load-path over suspension, frame into the body the level of details for all bushing elements needs to be increased. Fig. 1 shows the model of the pick-up truck used for this survey with several elastomer mounts and a hydro cab mount (C-pillar) being marked.

Elastomer mounts are widely used in automotive and railway applications [3]. Such parts exhibit amplitude dependent behavior due to the Payne effect [4]. The mounts stiffness and damping characteristics are sensitive to the excitation amplitude and frequency as well as preload conditions. This non-linear behavior also affects hydraulically damped mounts due to their underlying rubber parts.

In the standard development process, the amplitude dependence of rubber parts is not considered within the MBS environment but simple spring-damper models are used for cab mounts, suspension bushings and jounce bumpers. In [5] new amplitude-dependent bushing models were used for all cab mounts within the ADAMS/Car environment to improve full-vehicle simulation for durability loads. [6] discusses the overall improvement of full-vehicle simulation due to improved models for elastomer cab mounts and flexible car body structures, for a truck without hydro mounts. This paper presents a practical approach to model different sorts of hydro mounts in full-vehicle simulation.

2 HYDRO MOUNT BEHAVIOUR

Fig. 2 shows photograph and scheme of the hydraulically damped cab mount that has been used for this survey. This cab mount is divided into the main rubber carrier on top and the hydraulic section with its fluid filled rubber chambers and the fluid channel.

Static stiffness k_{stat}, dynamic stiffness k_{dyn}, and loss angle δ are widely used to characterise mounts and bushings. This experimental data is used to derive

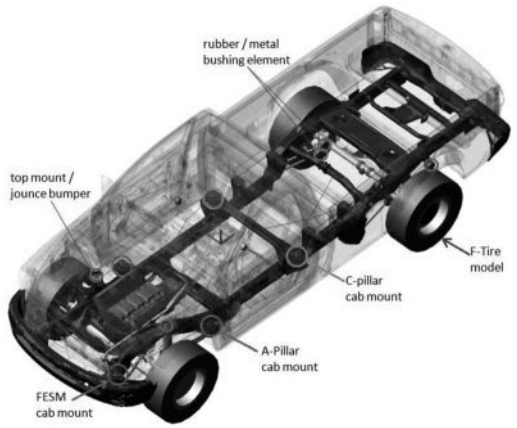


Figure 1. The ADAMS model of a full-size pickup truck with a hydro cab mount (C-pillar) and several elastomer mounts.

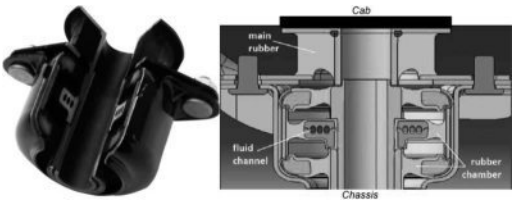


Figure 2. Hydraulically damped cab mount with its main components.

model parameters for mount models within full-vehicle simulation. [7–9]. The mount's static stiffness k_{stat} depends on the loading conditions. Therefore, the following characteristics may depend on the preload.

The main rubber part carries the gravitational load of the cab and offers some damping. Under dynamic excitation a pressure difference from upper to lower chamber forces the fluid to pulsate with the spiral-formed fluid channel. A water-glycerin mix or oils are used as liquid.

Hydraulically damped mounts and bushings use the tuned mass damping effect (TMD) and additional fluid damping to generate high dynamic stiffness and high damping around the tuned resonance frequency. Hydro mounts changes dynamic stiffness and damping properties very significantly over frequency and over amplitude as shown in Fig. 3.

Measurement data at low frequency (A) already shows relevant difference in stiffness, due to amplitude dependence of main rubber. Fluid damping in the orifice and fluid friction lead to additional damping in the resonance frequency range (B). The internal damping also restricts the fluid flow at high frequencies (C). At high frequency fluid pulsation stops, so that the overall stiffness can be assumed to be main rubber stiffness plus stiffness against chamber compliance.

The hydro mount's typical resonance peak goes back to the tuned mass damping effect. Under certain operating conditions, the fluid inside the channel

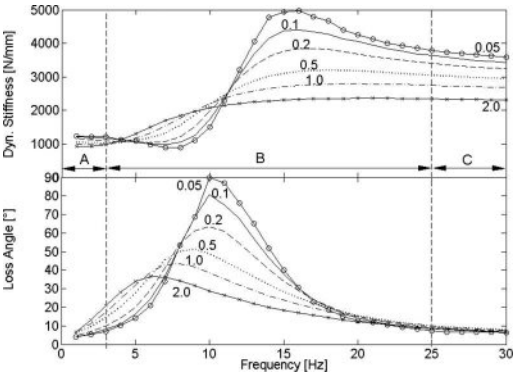


Figure 3. Measured dynamic stiffness and loss angle of hydro cab mount for amplitude 0.05 mm–2.0 mm.

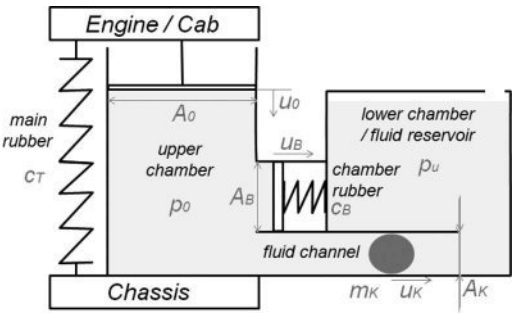


Figure 4. Simple hydro mount model for principal investigations.* Springs represent complete nonlinear amplitude-dependent elastomer sub-models.

pulsates counter-phase-wise to the excitation. The rubber chambers act as a spring with volumetric stiffness to restrict chamber compliance. The fluid mass inside the channel is amplified by the hydraulic lever arm and acts as TMD mass. At high excitation the movement of the cab or powertrain is limited and damped at the same time. The fluid mass inside the channel, the rubber stiffness and chamber compliance are tuned to give high damping at certain resonance frequency. To study these underlying phenomena, a basic model is presented. The level of details will then be continuously increased to cover all effects.

3 HYDRO MOUNT MODEL

3.1 *Model structure*

The principal hydro mount phenomena are discussed with the model approach as shown in Fig. 4. The presented model is of a modular structure where hydro mount model behavior is a superposition of:

– *Elastomer behavior* of its underlying rubber parts where c_T represents the main rubber stiffness (in vertical direction). The chamber stiffness c_B represents the resistance against puffing of chamber

when pressure increases (chamber compliance, volumetric stiffness). Both springs for main rubber c_T and chamber rubber c_B are to be calculated from a sub-model for elastomer that takes into account amplitude dependence due to the Payne effects. c_T and c_B are to be regarded as complex stiffness and depend on the current preload, frequency, amplitude.

– *Tuned mass damping effect* with chamber compliance c_B, main rubber stiffness c_T and fluid mass m_K as main factors of impact. The virtual fluid mass m_K is known from channel length l_K, channel area A_K and fluid density ρ_F. The pulsation in the fluid channel is amplified over hydraulic lever arm, where the areas of the main spring A_0, the chamber A_B and fluid channel area A_K are relevant.
– Additional *fluid damping* in the channel and orifice depending on the velocity of fluid flow; damping coefficients $d$and β for linear or non-linear fluid damping.

Physically meaningful parameters are used to model the mount. A force on top of the hydro mount due to gravitational load leads to deflection u_0 of the main rubber spring c_T and increase of pressure in upper chamber p_0:

$$F = c_T \cdot u_0 + p_0 \cdot A_B \tag{1}$$

When pressure p_0 increases due to the force F the chamber displacement (deflection) u_B results from the pressure in the upper chamber p_o.

$$p_0 \cdot A_B = u_B \cdot c_B \tag{2}$$

The fluid (mass m_K and displacement u_K) flows through the channel with length l_K and cross sectional area A_K while d and β are damping coefficients for linear and non-linear fluid damping in the channel, respectively:

$$m_K \cdot \ddot{u}_K = p_0 \cdot A_K - d \cdot \dot{u}_K - d \cdot \beta \cdot \dot{u}_K{}^2 \cdot sign(\dot{u}_K) \tag{3}$$

In simple passive engine mounts the lower chamber consists of a flexible rubber diaphragm membrane and acts as fluid reservoir with atmospheric pressure $p_u = 0$. Even if the lower chamber is physically closed and under pressure, this assumption $p_u = 0$ still gives a good agreement to experimental data, as will be discussed, later on.

For further simplification it is assumed that the main rubber area is the same as chamber area.

$$A_0 \approx A_B \tag{4}$$

*German notation for springs has been kept with cT for the dynamic stiffness of main rubber (top mount/Tragfeder) and cB of chamber rubber (bulge stiffness/Blähfeder) because earlier model versions are still in use that refer to cT and cB as model parameters in the user interfaces.

A change of input displacement at slow excitation does not affect the pressure p_0 inside the mount because fluid flows freely through the channel without relevant damping and mass inertia. Therefore, input displacement u_0 only goes into the calculation of F_T due to the rubber spring c_T. Chamber deflection of u_B is calculated from the integral of velocity du_0 over time; thereby eliminating a constant displacement offset due to static gravitational load onto the mount.

$$u_B = \int \left(\dot{u}_0 - \dot{u}_K \frac{A_K}{A_B} \right) \tag{5}$$

Pressure can be calculated as:

$$p_0 = \frac{u_B \cdot c_B}{A_B} = \int \left(\dot{u}_0 - \dot{u}_K \frac{A_K}{A_B} \right) \cdot \frac{c_B}{A_B} \tag{6}$$

The model approach shown in Fig. 4 has been implemented into MBS environment, a software plug-in for MSC.Adams/Car is available from VI-grade [10-13]. Furthermore, sophisticated graphical user interfaces have been developed for import of measurement data, parameter estimation and export into parameter files. These tools include a virtual mount test rig and have been used for the following hydro mount design analyses. All sub-functionalities of the hydro mount model can be deactivated.

3.2 *Non-linear fluid damping*

Beside the fluid mass' inertia, a velocity-proportional term with damping coefficient d and an additional non-linear damping term with coefficient β contribute to the damping in the fluid channel. It may be suggested that linear and non-linear parts should be regarded entirely separated, so that:

$$p_0 \cdot A_K = m_K \cdot \ddot{u}_K + d \cdot \dot{u}_K + \beta \cdot \dot{u}_K{}^2 \cdot sign(\dot{u}_K) \tag{7}$$

However, numerous tests where the mount model parameters were identified for different sorts of hydro mounts (and hydro bushings) proved that it is beneficial to assume the main damping coefficient d has impact on the non-linear damping term ß, also.

$$p_0 \cdot A_K = m_K \cdot \ddot{u}_K + d \cdot \left(\dot{u}_K + \beta \cdot \dot{u}_K{}^2 \cdot sign(\dot{u}_K) \right) \tag{8}$$

This way the main characteristics can be estimated easily and fast via the damping coefficient d. Parameter variation for β then gives fine-tuning of the behaviour. This coupling of linear and non-linear damping leads to significant simplifications and improved stability for a semi-automatic parameter estimation process where many model internal parameters are varied for a good fit to experimental data.

For model implementation into a practical tool for hydro mount simulation and design studies, several

options for fluid damping are useful. So, a more general formulation is used, where:

$$F_{fluid} = p_0 \cdot A_K = F_{TMD} + F_{damp1} + F_{damp2} \quad (9)$$

With

$$F_{TMD} = m_K \cdot \ddot{u}_K \text{ and } F_{damp1} = d \cdot \dot{u}_K \quad (10)$$

Plus additional non-linear damping

$$F_{damp2} = \beta \cdot \dot{u}_K{}^2 \cdot sign(\dot{u}_K) \quad (11)$$

Or alternatively

$$F_{damp2} = \beta \cdot \dot{u}_K{}^3 \quad (12)$$

For the final model implementation the grade of nonlinearity can be changed via exponential coefficient n_{POW}. where $n_{POW} = 1$, 2 or 3. A continuous formulation for changing signs for velocity is needed to ensure low computing times when variable time step solvers are used. The sign of velocity is therefore calculated using a tangens-hyperbolicus-function with gradient factor k_{SingD}. The discontinuous sign function and its derivative is thereby replaced with continuous function.

$$F_{damp2} = \beta \cdot \dot{u}_K{}^{n_{POW}} \cdot \tanh(k_{SignD} \cdot \dot{u}_K) \quad (13)$$

3.3 *Elastomer model*

For hydro mount models it is often assumed that main rubber stiffness and chamber stiffness are constant. In reality main rubber stiffness c_T and chamber rubber stiffness c_B change over frequency and over amplitude.

Table 1 shows model parameters for the cab mount for the basic model approach when main rubber *cT* and chamber compliance *cB* are assumed to be constant springs and fluid damping is non-linear. With this simplification underlying effects can already be studied. Due to such simplifications the table values may but must not be equal to physical part's geometry. Instead, model parameters are estimated first and then automatically tuned for a good fit to experimental data.

Fig. 6 gives measurement for three amplitudes (markers) and simulation results (in solid lines) using the table values below derived from automatic parameter optimisation.

Simulation results look good at first glance, but such a simplified model reveals the following drawbacks because stiffness for main rubber c_T and chamber rubber c_B are considered to be constant:

– Stiffness of main rubber is constant so that static and dynamic stiffness are the same. The static stiffness is estimated too high if c_T is tuned for good results under dynamic excitation; the static equilibrium of the full-vehicle model will be inaccurate, leading to severe drawbacks if the simulation runs for complex 3D excitation.

Table 1. incenter Table 1. Model parameters for basic hydro mount model with constant stiffness for main rubber and chamber rubber.

Parameter	Symbol	Value
Stiffness top mount (main rubber)	c_T	1e3 kN/m
Effective piston area chamber	A_B	8.586e-3 m^2
Area of fluid channel	A_K	8.191e-5m^2
Length of fluid channel	l_K	0.248428 m
Fluid damping coefficient linear	D	0.333 Ns/m
Non-linear fluid damping coeff.	β	1.393 Ns^2/m^2
Effective channel fluid mass	m_K	0.019333 kg
Chamber stiffness	c_B	1643e3 N/m

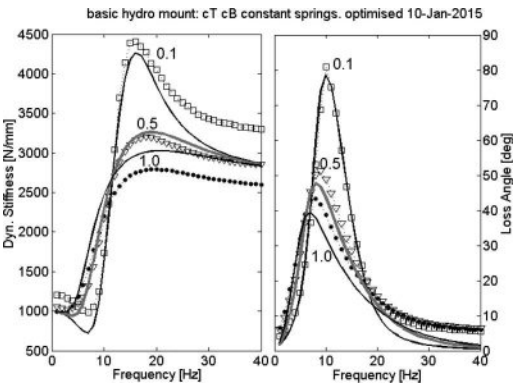


Figure 5. Simulation (solid lines) assuming constant springs for main rubber and chamber rubber.

– The calculated stiffness is the same for all amplitudes at low frequency (1Hz) and at high frequency (>30Hz). In contrast, measurement shows relevant differences due to the elastomer behavior.
– The simulation behavior at transient excitation might be different to the real parts, due to simplifications.

For better results and to make the hydro mount model flexible for all sorts of different hydro mounts and hydro bushings, it is vital to accurately model the elastomer's amplitude dependence and frequency dependence.

Standard bushing models in MBS environments do not take the elastomer amplitude dependence due to the Payne effect into account. For accurate results, it is crucial that the hydro mount's elastomer parts are modeled in details. For the simulation of durability loads high amplitudes and changing preloads are of interest, so that special care has to be taken in terms of modeling the elastomer parts of a hydro mount. [5] describe a new non-linear model for elastomer mounts that is used as sub-module for the elastomeric parts (main rubber c_T and chamber rubber c_B) within the hydro mount model in Fig. 4.

Similar non-linear models for conventional rubber mounts and bushings that take into account amplitude dependence are presented in [23–28]. There are many papers onto the topic but only few models have been implemented into MBS environment with full functionality to prove practical use and numerical stability. Others lack easy to use tools for fast parameter identification.

Main outcome of this research is that all sorts of (passively) hydraulically damped mounts and bushings can be simulated equally well, (only) if the underlying model approaches for the elastomer parts are accurate.

3.4 *Optional hydro mount features*

Beside the simple hydro cab mount the presented mount model is also able to accurately map different sorts of hydro mounts and hydraulic suspension bushings. A decoupling functionality and bypass valve for hydro suspension bushings are also implemented in the model, but not discussed herein. A linearized model version for high frequencies and its specific extension for active hydraulic engine mounts is discussed in [33].

3.5 *Parameter identification process*

The parameter estimation process is performed semi-automatically with the help of sophisticated graphical user-interfaces. The following work steps are recommended:

A) Load measurement data for static and dynamic experiments
B) Define preloading conditions for static stiffness
C) Automatically set initial values for the parameter optimization to commence on.
D) Decide for the level of details of the model. Depending on existing measurement data and physical mount properties, certain nonlinearities are taken into account or can be neglected for simplification. E.g. if the mount is decoupled at small amplitudes or has additional bypass valve more parameters need to be varied.
E) Run automatic parameter optimization program.
F) Calculation of damping coefficients, for fluid pressure in the upper chamber and elastomer properties are automatically carried out.
G) Export model parameters to property file

The automatic parameter optimisation process takes in average 5–15 minutes, depending on the given measured amplitudes and frequency steps and how many model internal parameters are varied. Due to the complexity of the programming it is not further discribed, herein.

4 MODEL EVALUATION

4.1 *Sinusoidal excitation*

The cab mount shown in Fig. 1 is used for further validation. Fig. 6 presents actual simulation results for the full non-linear model including amplitude dependence for elastomer parts.

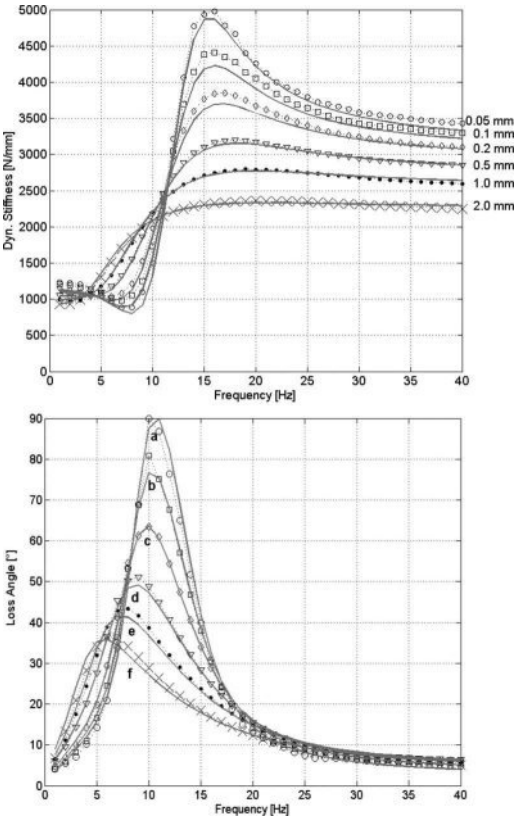


Figure 6. Hydro mount model evaluation under sinusoidal excitation: Simulation (solid lines) and measurement for amplitudes 0.05 mm (a) 0.1 mm (b) 0.2 mm (c) 0.5 mm (d) 1.0 mm (e) and 2.0 mm (f).

The springs for c_T and c_B in the principal model scheme (Fig. 4) are represented by a full non-linear elastomer model including amplitude dependence.

All measured amplitudes 0.05 mm, 0.1 mm, 0.2 mm, 0.5 mm, 1.0 mm and 2.0 mm have been used during the automatic parameter optimisation routine.

Error values are calculated for each amplitude and frequency for loss angle as well as frequency during parameter optimization. In this case, the error sums for dynamic stiffness and loss angle have been weighted equally important.

Results at sinusoidal excitation are very accurate over the whole amplitude range if amplitude dependent effects due to the underlying rubber parts are taken into account. This type of mount has no decoupler or bypass valve, so that it can be compared with most passive hydraulic engine mounts.

Transient behavior/reaching steady state

At most tests on the component test rig, transient phenomena are neglected because the mount is fixed onto the test rig on both sides. Per test definition, the

mount is allowed to reach steady state before force-displacement loops are recorded and dynamic stiffness and loss angle are calculated thereof.

In contrast, for real world excitation the behavior before reaching steady-state is crucial to tune the mounts and bushings. Additional to the dynamic stiffness and loss angle (or other parameters to characterize the damping properties) the actual transient response at freely damped vibration is relevant. [14, 16, 19] discuss some limitations of similar modeling approaches for the prediction of transient excitations.

For model evaluation in this study, transient test rig signals have been derived from real on-road tests as input on the mount test rig. Moreover, the improvement of such hydro mount model into full-vehicle simulation had been briefly studied in [5, 20].

In this paper, the dynamic characteristics are mainly studied from dyn. stiffness and loss angle because these are the most commonly used parameters for standard dynamic measurement data. [14] suggest to use complex imaginary stiffness instead of loss angle for the hydro mount characterization. In any case, the calculation of complex stiffness is based on the assumption of elliptical hysteresis loops but that is not always the case. Therefore, transient signals have also been used for the model evaluation.

Hydro mount behavior at transient excitation and limitations of modeling approaches are discussed in [15–19]. [21] studies the transient response of hydro mounts and also revealed that the force during expansion is significantly lower than under compression, due to limited pressure. Measurement data for pressure inside the mount has not been available for our studies, because the parts would have to be destroyed.

[22] discuss the scattering of measurement data within the samples of a batch of hydraulic engine mounts and found the characteristics can highly vary over the production range. In order to eliminate this influence, on-road vehicle tests have been performed with the specific mounts after they had been tested on the test rig.

4.2 *Durability loads from experiment*

Model parameter identification is based only on quasi-static and sinusoidal excitation after the bushing has reached a steady-state. However, it is known that elastomeric parts exhibit different behavior under transient excitation. Here, the mount will vibrate mainly at a certain resonance frequency but the excitation amplitude is declining from its maximum value to zero after each single obstacle or input.

To evaluate the accuracy of the full-vehicle model using the new non-linear bushing models under transient excitation, the mount loads have been measured during on-road tests for durability. Based on these data a transient displacement signal has been generated as input for the mount test rig. The measured resulting forces from the test rig are qualitatively very similar to the loads during on-road tests.

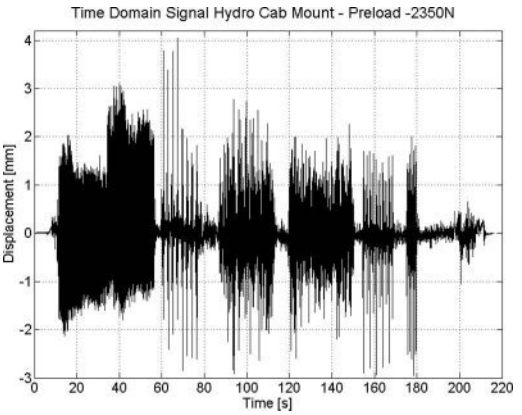


Figure 7. Input of transient durability load signal without offset due to preload.

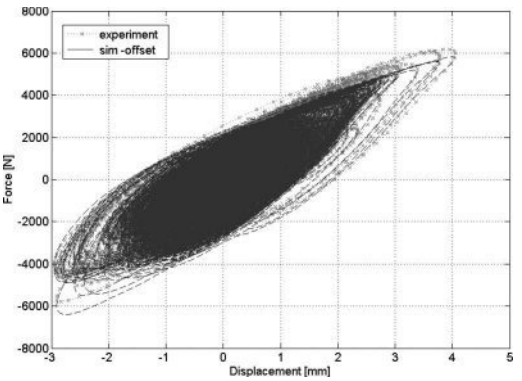


Figure 8. Model validation: Force-displacement loop of transient durability load signal.

Fig. 7 presents the transient input displacement signal with high deflections. The road contained in-phase bumps, out-of phase bumps, diagonal trenches, random potholes, cobblestones, alternating potholes, and transverse trenches. The following model evaluation shows results for the hydraulically damped cab mount.

Fig. 9 gives the resulting simulated and measured force over the displacement. The resulting force offset due to preload has been terminated for the following plots. The preload for parameter identification was significantly lower than during the durability load signal for model validation. Nevertheless, simulation results are very accurate. Please note that the overall force-displacement loops are not purely elliptical because the internal pressure inside the mount's chamber is limited during decompression after high deflections; damping is much higher under compression. The good results prove that the pressure inside the upper chamber was modeled correctly and accurately.

Figs. 10 and 11 present the mounts load over time and details thereof. Overall, the simulation results for the mounts are very accurate.

The model evaluation under sinusoidal excitation already proved a very high model performance over a

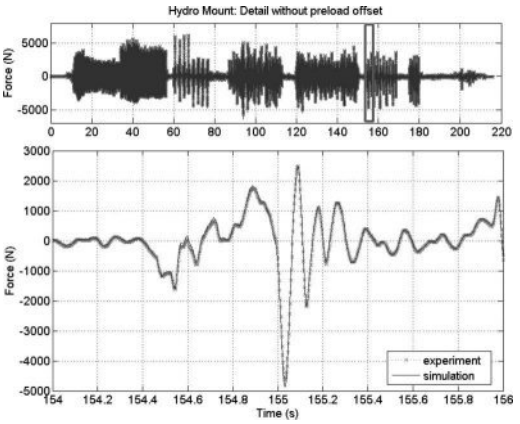


Figure 9. Model validation at transient input signal.

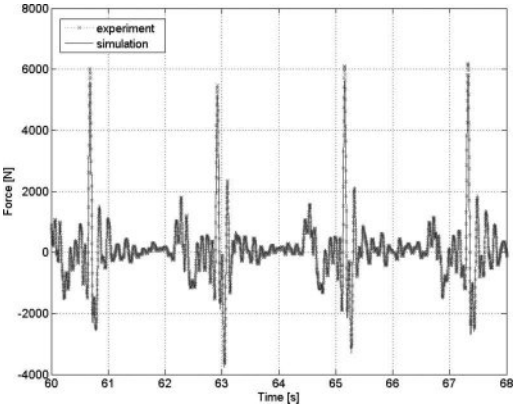


Figure 10. Model validation at transient input signal: Detail.

wide amplitude range. The evaluation with a transient time signal on the mount test rig also confirms a very high level of accuracy.

SUMMARY/CONCLUSIONS

MBS simulations are vital for the vehicle development process and the bushing elements along the load path are crucial for the overall accuracy of the full vehicle model. Elastomer parts exhibit significant dynamic hardening ratios that depend on excitation amplitude and preload. This behavior also highly affects hydro mounts due to its underlying rubber parts.

A non-linear hydro mount model for MBS full-vehicle simulation was presented and validated on the example of durability load analyses for a light duty truck with hydro cab mounts. Starting from a simple modeling approach with constant stiffness for main rubber and chamber rubber, the principal phenomena of hydro mount behavior have been studied. Similar models exist for simple passively damped hydro engine mounts but there is no such flexible modeling approach for different types of mounts: simple passive hydro engine mounts as well as partially or fully decoupled hydro engine mounts can be covered and results are also accurate for hydro suspension bushings.

Main conclusion of this investigation is that hydro mount behavior is only mapped accurately, if the amplitude dependence of the underlying elastomer parts is taken into account. To improve accuracy of other existing mount models in MBS it is recommended to implement the amplitude dependent characteristic of the underlying elastomer parts.

The model evaluation under transient excitations has covered a wider amplitude range; simulation showed very good agreement to measured loads. With the presented model for the hydro cab mount the full-vehicle simulation accuracy improved significantly. Testing times and prototypes can therefore be reduced, to save cost and development time.

ACKNOWLEDGEMENTS

All experiments for mount characterization were carried out at Conti Tech Vibration and Control, Hanover. The Authors would like to thank the dept. of product testing development for consultancy and the valuable discussions regarding mount testing in general. Further thank goes to VI-grade for providing a customer tailored test version of user plug-in for Adams/Car and the support and advice for this study.

REFERENCES

[1] Yang X and Xu P. “Road Load Analysis Techniques in Automotive Engineering,” Metal Fatigue Analysis Handbook 2012. p. 1–60.

[2] Roy, N. and Villaire, M., “Virtual Road Load Data Acquisition using Full Vehicle Simulations,” SAE Technical Paper 2013-01-1189, 2013, doi: 10.4271/2013-01-1189

[3] Yu, Y., Naganathan, N. G., and Dukkipati, R. V., “A literature review of automotive vehicle engine mounting systems,” Mechanism and Machine Theory, 2001, Vol. 36, 123–142.

[4] Payne, A. R., “The Dynamic Properties of Carbon Black-Loaded Natural Rubber Vulcanizates Part I,” Journal of Applied Polymer Science, 1962, 6(19): 57–63.

[5] Scheiblegger, C., Roy, N., Silva Parez, O., Hillis, A. et al., “Non-Linear Modeling of Bushings and Cab Mounts for Calculation of Durability Loads,” SAE Technical Paper 2014-01-0880, 2014, doi: 10.4271/2014-01-0880

[6] Roy, N., Scheiblegger, C., Darling, J. et al., “Durability Loads Prediction of Body-on-Frame Vehicles using Full Vehicle Simulation,” Int. Journal of Passenger Cars, forthcoming

[7] VDI standard, “VDI 3880: Damping of Materials and Members: Damping of Solids,” ed, 2004.

[8] DIN standard 53 535, “Grundlagen für dynamische Prüfverfahren,” ed. Berlin: Beuth Verlag, 1982.

[9] Cardillo, R.M., “Dynamic testing of elastomer mountings,” *Journal of Applied Polymer Science,* vol. 8, pp. 53–71, 1964.

[10] www.vi-grade.com.

[11] Pfeffer, P., “Modelling and Simulation of the Elastomer and Hydromount Models (Generation 2) and their implementation in ADAMS,” 3rd VI-grade Users Conference, 13th–14th October 2010, Bad Nauheim, Germany

[12] Buechler, H.-J., “Application of a new elastomer and hydromount model integrated in the full vehicle simulation process at Porsche: analysis of drive train vibrations on the example of the Panamera Diesel,” 4th VI-grade Users Conference, 18th-19th October 2011, Udine, Italy

[13] Pfeffer P., Scheiblegger, C., Roy, N., Ortmann, C. “Models for elastomeric and hydraulically damped vibration isolators within full vehicle simulation” 2014 VI-grade Users Conference, 11th–12th April 2014, Pollenzo – Bra (CN), Italy

[14] Barker, M., “The Behaviour of Non-Linear Hydraulic Isolators” In: Engineering Integrity, 2004, Vol. 15, No. 1, pp.28–42.

[15] Singh, R., Tiwari, M., Adiguna, H., Hrovat, D. et al. “Transient Response Evaluation of a Hydraulic Engine Mount,” In: Sound and vibration, 2002, Vol. 36, No.7, pp.30–35.

[16] Lee, J.-H.; Bae, M.-S.; Kim, K.-J., “Limitations of Mechanical Model With Lumped Mass in Representing Dynamic Characteristics of Hydraulic Mount,” (SAE 2003-01-1466) In: SAE Transactions; Journal of Passenger Cars – Mechanical Systems, Vol. 112, No. 1, pp.1679–1683, doi: 10.4271/2003-01-1466

[17] Lee, J.-H. and Kim, K.-J., “An Efficient Technique for Design of Hydraulic Engine Mount via Design Variable-Embedded Damping Modeling,” In: Journal of Vibration and Acoustics, 2005, Vol. 127, No. 1, pp.93–99

[18] He, S., Singh, R., “Discontinuous compliance nonlinearities in the hydraulic engine mount,” In: Journal of Sound and Vibration, 2007, Vol. 307, pp.545–563

[19] Lee, J.H., Singh, R., “Critical analysis of analogous mechanical models used to describe hydraulic engine mounts,” In: Journal of Sound and Vibration, 2008, Vol. 311, pp.1457–1464. doi: 10.1016/j.jsv.2007.10.021.

[20] Scheiblegger, C., Pfeffer, P. E., Karrer, H., Geiger, N., “Modelling of Elastomer and Hydro Mounts for Ride Comfort and Handling Simulation,” 13th International VDI Congress Tires-Chassis-Road, 25th–26th October 2011; VDI Berichte, 2137; 247–268

[21] Adiguna, H., Tiwari, M., Singh, R., Tseng, H. E. et al., “Transient response of a hydraulic engine mount,” *Journal of Sound and Vibration*. 2003, 268 (2):217–248, doi: 10.1016/s0022-460x(03)00076-2.

[22] Mitsch, M., Mack, W. and Falkner, A., “On the scattering of test data and the significance of the standard coefficients ‘dynamic stiffness’ and ‘loss angle’ for hydraulic engine mounts,” *Vehicle System Dynamics,* vol. 48: 387–403, 2010, doi: 10.1080/00423110902898077.

[23] Sjøberg, M., “On Dynamic Properties of Rubber Isolators”, PhD Thesis, KTH Stockholm, 2002.

[24] Berg, M., “A model for rubber springs in the dynamic analysis of rail vehicles,” In: Proceedings of the Institution of Mechanical Engineers, Part F: Journal of Rail and Rapid Transit, 1997, Vol. 211.

[25] Berg, M., “A Non-Linear Rubber Spring Model for Rail Vehicle Dynamics Analysis,” Vehicle System Dynamics, 1998, 30: 197–212

[26] Dronka, S., Rauh, J., “Modell zur Simulation von Fahrwerks-Gummilagern. Eigenschaften – Modellstruktur – Parametrierung,” In: VDI-Berichte, 2007, Vol. 2003, pp.371–390

[27] Sedlaczek, K. Dronka, S. and Rauh, J., “Advanced modular modelling of rubber bushings for vehicle simulations,” Vehicle System Dynamics, 2011, 49(5): 741–759.

[28] Williams, H. T., Whear, R., “Elastomer Models for Virtual Mounting Systems,” SAE Technical Paper 2005-01-1075, 2005, doi: 10.4271/2005-01-1075

[29] Pfeffer, P. E. and Hofer, K., “Simple Non-Linear Model for Elastomer and Hydro-Mountings,” *to Optimise Overall Vehicle Simulation,* 2002., ATZ worldwide, 2002, 2002-05

[30] Lambertz, S., “Nichtlineares Materialgesetz für technische Gummiwerkstoffe mit deformationsabhängigen Eigenschaften und seine experimentelle Überprüfung an Gummifederelementen,” Berichte aus der Werkstofftechnik,. PhD Thesis, Aachen: Shaker, 1993.

[31] Peeken, H., Lambertz, S. (1994): Nichtlineares Materialmodell zur Beschreibung des Spannungs-Dehnungsverhaltens gefuellter Kautschuk-Vulkanisate. In: Konstruktion: Organ Der VDI Gesellschaft Konstruktion und Entwicklung, Vol. 46, No. 1, pp.9–15.

[32] Scheiblegger, C., Lin, J. and Karrer, H., “New nonlinear bushing model for ride comfort and handling simulation: Focussing on linearization and the implementation into MBS environment,” Proceedings of the FISITA 2012 World Automotive Congress, 2013, Volume 10: Chassis Systems and Integration Technology; doi: 10.1007/978-3-642-33795-6_38

[33] Hausberg, F., Scheiblegger, C., Pfeffer, P., Plöchl, M., Hecker, S., Rupp, S., “Experimental and analytical study of secondary path variations in active engine mounts,” Journal of Sound and Vibration, 340 (2015), 22–38.

[34] Whear, R., Williams, H. T., ”Advanced Hydraulically Damped Elastomeric Component Models,” In: SAE Transactions; Journal of Passenger Cars - Mechanical Systems, 2005, Vol. 114,

[35] Sauer, W., Guy, Y., ”Hydro Bushings – Innovative NVH Solutions in Chassis Technology,” SAE Technical Paper 2003-01-1475, 2003, doi: 10.4271/2003-01-1475

Energy efficiency

Advanced Vehicle Control – Edelmann, Plöchl & Pfeffer (Eds)
© 2017 Taylor & Francis Group, London, ISBN 978-1-138-02992-7

Rolling loss analysis of combined camber and slip angle control

M.M. Davari
KTH Vehicle Dynamics, Department of Aeronautical and Vehicle Engineering, Royal Institute of Technology, Stockholm, Sweden

M. Jonasson
KTH Vehicle Dynamics, Department of Aeronautical and Vehicle Engineering, Royal Institute of Technology, Stockholm, Sweden
Active Safety & Vehicle Dynamic Functions, Volvo Cars Group, Gothenburg, Sweden

J. Jerrelind, A. Stensson Trigell & L. Drugge
KTH Vehicle Dynamics, Department of Aeronautical and Vehicle Engineering, Royal Institute of Technology, Stockholm, Sweden

ABSTRACT: The objective of this work is to present a new functionality of over-actuated systems, such as Wheel Corner Modules, to reduce the rolling loss in vehicles. The findings are based on numerical simulations using a bicycle model coupled with a newly proposed tyre model which is capable of simulating the tyre losses during vehicle motions. The results show that for the considered vehicle in the considered manoeuvre the rolling loss can be reduced about 25–40% by proper control of camber and slip angle combinations, while still maintaining the vehicle performance.

1 INTRODUCTION

The growing concerns about −the environmental problems of conventional vehicles speeds up the development of new vehicles with alternative power solutions, like hybrid and electric vehicles. These types of vehicles provide various opportunities in terms of vehicle motion control with for example use of in-wheel motors or control by wire systems, see Figure 1 (Wallmark 2014). This led to extensive research into the application of such systems and the opportunities that they could bring to the vehicle dynamic behaviour (Edrén 2014). A wide range of research has been performed to improve the vehicle motion control from safety and performance points of view (e.g. Furukawa 1997, Parker et al. 2015). However, employing these systems to influence the energy consumption in vehicles still needs to be explored and scrutinised more, though interesting works are going on in this regard (e.g. Abe 2012, Fujimoto et al. 2011, Pennycott et al. 2013).

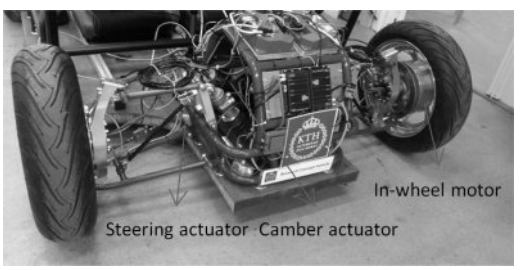


Figure 1. Example of an active chassis.

Respecting the capabilities of active and semi-active systems in vehicles from handling and safety points of view, the focus of this paper is on the capabilities of these systems to reduce the energy loss using active control of camber and slip angles. The considered components of the rolling loss in this work are the rolling resistance, cornering resistance, sliding and internal losses of the tyre (Davari 2015).

2 MOTIVATION

The generated lateral force due to the inclination of the tyre plane (camber angle) is referred to as camber thrust. This force will always be applied in the direction which the tyre is inclined, where a positive camber angle will generate a positive camber thrust and vice versa.

The physical behaviour of the tyre under combined conditions, shown in Figure 2(a), demonstrates how different combinations of side slip (α) and camber (γ) angles can result in same lateral forces (F_y), see Figure 2(b) (The results in Figure 2 are generated with the Extended Brush tyre Model (EBM) (Davari 2015)).

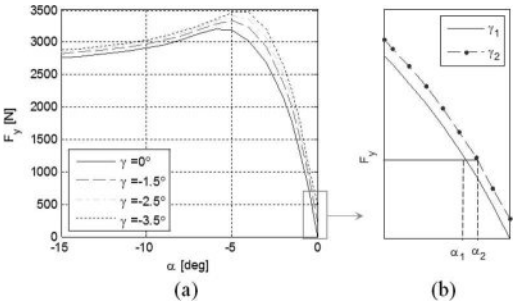


Figure 2. Tyre lateral force characteristics from the EBM model.

Considering that one of the influential components of rolling loss is the cornering resistance which is directly produced by the slip angle of the tyre, a first approach of how reducing the side slip while applying camber can reduce the cornering resistance is obtained.

3 CONTROL LOGIC

The obtained knowledge about the tyre performance under combined conditions and their relation to rolling loss, describes how same lateral force can be obtained during a manoeuvre by simultaneous control of tyre side slip angle and camber angle, see Figure 2(b), in which the γ_1 is zero and γ_2 represent a non-zero camber angle (in this case negative). Therefore, it can be concluded that the total lateral force, F_y, produced by the tyre is a combination of the lateral force due to tyre side slip, F_y^{α}, and the lateral force due to camber thrust, F_y^{γ}.

$$F_y = F_y^{\alpha_1} \quad , \quad (\gamma_1 = 0) \tag{1}$$

$$F_y = F_y^{\alpha_2} + F_y^{\gamma_2} \tag{2}$$

In this regard, through a mapping process, the possible combination of the side slips and camber angles which can generate same lateral force are calculated for the chosen tyre using the tyre model, see Figure 3.

As shown in Figure 3, the reference plane (Ref. Plane) is the required lateral force to fulfil a turn. The intersection points of the reference plane with the tyre map, $F_y(\alpha, \gamma)$, show the acceptable coordinates (wheel sets) which can achieve same lateral forces. These wheel sets will later be used for controlling the tyre behaviour during the manoeuvre. The assigned number to the reference wheel set (Ref. Set.) is 17 for later investigation of the simulations.

It should be noted that the wheel sets required to fulfil a turn are unique and are determined based on the individual manoeuvre, wheel load, vehicle speed etc. Therefore, the sets are subjected to change when either the curvature or vehicle conditions differ during the manoeuvre, see Figure 4. In this work the focus is on the car tyres. Nevertheless, the strategy can further be developed for truck tyres.

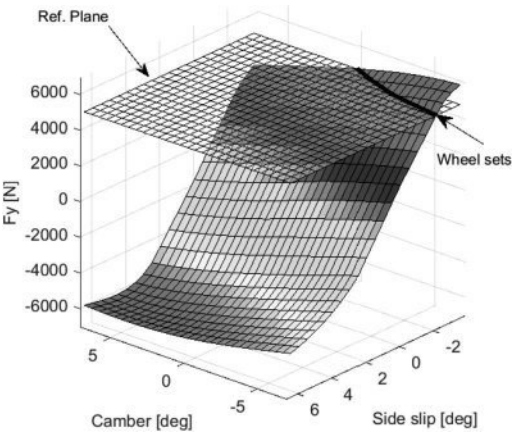


Figure 3. Example of tyre mapping for the chosen tyre with reference plane at R = 30 m and V = 22 m/s.

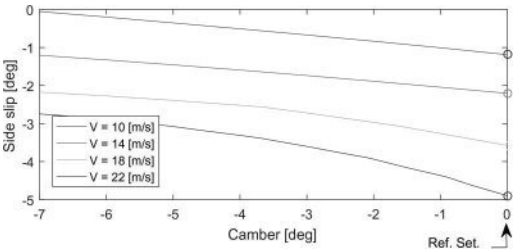


Figure 4. Wheel sets at different curving speeds.

3.1 *Control architecture*

The path curvature (ρ) and the reference speed (v^{ref}) define the driver commands for the vehicle movement to follow the path in the plane. These conditions are then provided to a reference vehicle in order to translate the global vehicle force and moments into the local coordinates of the tyre contact patch for both front and rear axles. The camber angles of the tyres in the reference vehicle are set to zero. Having the slip angles of both axles, the tyre model provides the reference forces of the tyres.

Finally, the alternative wheel settings to fulfil the desired vehicle motion in the reference path are estimated inside the camber and slip angle control algorithm, see Figure 5.

4 SIMULATION

The tyre model used in this study is a semi-physical non-linear tyre model (Davari et al. in press), which enables studies of rolling loss within vehicle dynamic simulations. In this work the losses due to air resistance and road slop are not considered. The proposed model, named Extended Brush tyre Model (EBM) is coupled with a bicycle model with vehicle parameter settings according to Table 1.

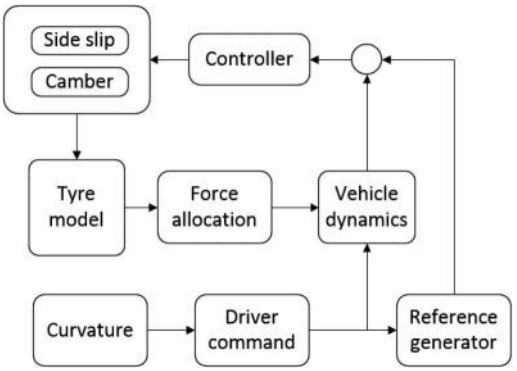


Figure 5. Illustration of the closed loop camber-slip controller (CSC function).

Table 1. Vehicle parameters.

Vehicle mass	m	1435	kg
Yaw moment of inertia	J_z	2380	kgm^2
CoG distance to front axle	f	1.04	m
CoG distance to rear axle	b	1.50	m

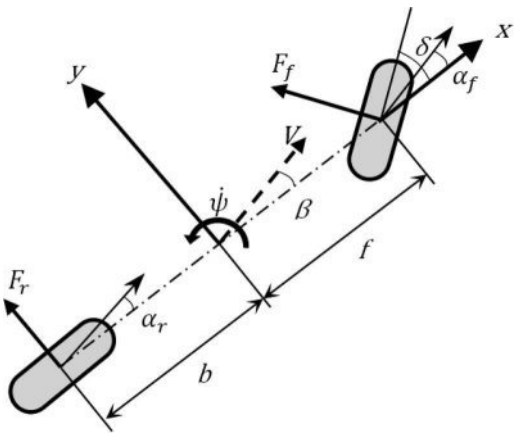


Figure 6. Vehicle model.

The model is validated using measurement data of a Volvo V40. The tyre spin as well the small offset in the lateral force generated due to the tyre asymmetry caused by conicity and ply steer are neglected. In this study a constant radius manoeuvre ($R = 30$ m) under steady-state conditions including various speeds and constant tyre load was performed. The applicable camber angle was limited to -7 to 7 degrees.

Considering the vehicle model with two states while the longitudinal speed is constant, the equations of motion are formulated as;

$$\dot{v}_y = \frac{1}{m}(F_r + F_f \cdot \cos\delta - v_x \cdot \dot{\psi}) \tag{3}$$

$$\ddot{\psi} = \frac{1}{J_z}(F_f \cdot \cos\delta \cdot f - F_r \cdot b) \tag{4}$$

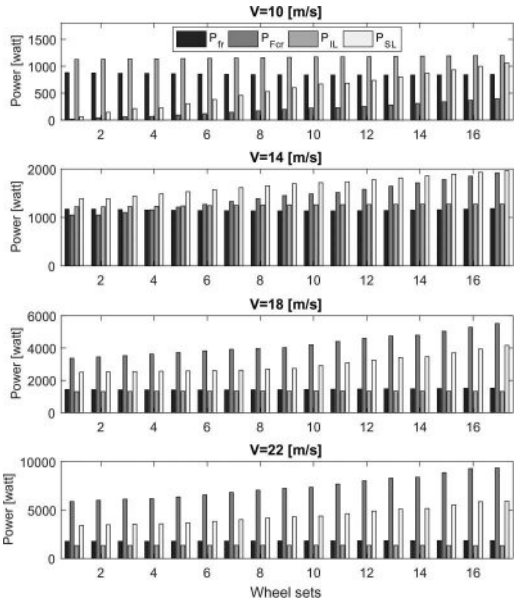


Figure 7. Rolling loss components in different wheel sets for different velocities.

with the side slip angles calculated as;

$$\alpha_f = tan^{-1}(\frac{v_y + \dot{\psi} \cdot f}{v_x}) - \delta \tag{5}$$

$$\alpha_r = tan^{-1}(\frac{v_y - \dot{\psi} \cdot b}{v_x}) \tag{6}$$

5 RESULTS

Different components of rolling loss are investigated for the feasible combinations of wheel sets, which result in the same vehicle motion and are compared with the reference wheel set (wheel set #17), see Figure 7. The considered loss elements are rolling resistance, P_{fr}, cornering resistance, P_{Fcr}, internal loss, P_{IL} and sliding loss, P_{SL}. The results show the influence of each wheel set on respective loss elements.

As shown in Figure 7, in low lateral acceleration the internal loss is dominant. It is also clear that the internal loss remains almost intact during the wheel control process while the rolling resistance slightly increases. However, both the cornering resistance and sliding loss are considerably influenced by employing different wheel sets. For instance at the extreme control point where the maximum camber is exploited, the cornering resistance and sliding losses are nearly zero. From this and refereeing to Figure 4, it can be comprehended that at low lateral accelerations where the tyre is in its linear range and the slip angle is small, a turn can be achieved with only pure camber control of the wheels.

Investigating the losses at higher speeds clarifies that the behaviour of loss components are not unique

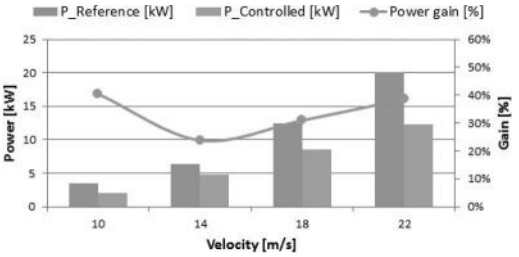


Figure 8. Rolling loss analysis and achieved gains in different manoeuvres.

during different manoeuvres, i.e. for higher speeds the dominant loss component are the cornering resistance and the sliding loss. However, for the studied case it is only at speeds 18 m/s and 22 m/s that the cornering resistance is the dominant part of the loss. This perception gives an insight to build a more efficient and realistic control strategy when it comes to energy optimisation.

An analysis of the rolling loss in the accomplished manoeuvres is shown in Figure 8. The comparison is based on the calculated rolling loss of a reference vehicle without control and the minimum possible rolling loss achieved by the controlled vehicle. The results suggest that the proposed control strategy can theoretically achieve about 25–40% reduction of the considered rolling loss.

Though the maximum gain is shown to be achieved in low lateral acceleration, by increasing the speed there is also an increasing potential in reducing the loss by applying the camber-slip control (CSC). However, it doesn't necessarily means that the total loss is lower since at higher lateral acceleration contribution of sliding and cornering resistance losses are higher which makes the overall losses higher than those of the low speed manoeuvres.

6 CONCLUSION

To conclude, in this study the potential of combining camber and slip angle control for reducing the rolling loss during a manoeuvre is presented. The proposed strategy adds a new dimension to active control of chassis for more energy efficient driving. These results clarify that in low lateral acceleration the turning manoeuvre can be performed by only cambering the wheels which will considerably reduce the rolling loss. The proposed control logic can be used for both the linear and non-linear range of tyre. However, finding an optimum control for each of those ranges needs further investigations.

Considering the physical phenomenon behind the control logic, mentioned in Section 2, the proposed strategy can be used in both conventional vehicles as well in electric vehicles. In both cases the energy consumption will be reduced. Using special tyre construction with higher camber range and greater camber thrust as well as specific type of vehicles such as innovative concepts with over-actuated systems, where the range of applied camber can be wider, the application of using the CSC function can be extended to more transient manoeuvres.

Considering the dependency of wheel sets to the requested manoeuvre, the optimum wheel set in a full vehicle model can be obtained by high level optimisation methods which will be the subject of future work.

Though the proposed control algorithm is still not optimized for online implementation due to its computational effort, it represents promising results in terms of energy optimization which can be used as a platform for further development of optimal control strategies. However, further studies are necessary to evaluate the camber control strategy in the transient conditions with higher lateral accelerations where tyre transient situations during the manoeuvres are inevitable. The findings will further be evaluated for different driving conditions using a research vehicle.

REFERENCES

Abe, M. (2012). Evaluation of active vehicle motion controls from tire energy dissipation points of view. In *Proc. 11th AVEC*, Seoul, Korea.

Davari, M. M. (2015). *A tyre model for energy studies in vehicle dynamics simulations*. Licentiate Thesis in Vehicle Engineering, KTH Royal Institute of Technology, Stockholm, Sweden, TRITA-AVE 2015:15, ISSN 1651-7660.

Davari, M. M., Jerrelind, J., Stensson Trigell, A., & Drugge, L. (in press). Extended brush tyre model to study rolling loss in vehicle dynamics simulations. *International Journal of Vehicle Design*.

Edren, J. (2014). *Motion modelling and control strategies of over-actuated vehicles*. Ph.D. thesis, in Vehicle Engineering, KTH Royal Institute of Technology, Stockholm, Sweden, TRITA-AVE 2014:75, ISSN 1651-7660.

Fujimoto, H. & H. Sumiya (2011). Range extension control system of electric vehicle based on optimal torque distribution and cornering resistance minimization. In *IECON 2011-37th Annual Conference on IEEE Industrial Electronics Society*, Melbourne, VIC, Australia.

Furukawa, Y. & M. Abe (1997). Advanced chassis control systems for vehicle handling and active safety. *Vehicle System Dynamics: International Journal of Vehicle Mechanics and Mobility 28*, 59–86.

Parker, G., J. Griffin, & A. Popov (2015). The effect on power consumption & handling of efficiency-driven active torque distribution in a four wheeled vehicle. In *Proc. 24th IAVSD*, Graz, Austria.

Pennycott, A., L. De Novellis, P. Gruber, A. Sorniotti, & T. Goggia (2013). Enhancing the energy efficiency of fully electric vehicles via the minimization of motor power losses. In *IEEE International Conference on Systems, Man, and Cybernetics*, Manchester, UK.

Wallmark, O., M. Nybacka, D. Malmquist, M. Burman, P. Wennhage, & P. Georen (2014). Design and implementation of an experimental research and concept demonstration vehicle. In *IEEE Vehicle Power and Propulsion Conference*.

Advanced Vehicle Control – Edelmann, Plöchl & Pfeffer (Eds)
© 2017 Taylor & Francis Group, London, ISBN 978-1-138-02992-7

Integrated traction control strategy for 4-motorized-wheels electric vehicles with improvement of economy and longitudinal driving stability

Xudong Zhang & Dietmar Göhlich
Product Development Methods and Mechatronics, Technical University of Berlin, Germany

ABSTRACT: This paper presents an integrated traction control strategy (ITCS) for 4-motorized-wheels electric vehicles. The purpose of this proposed strategy is to improve vehicle economy and longitudinal stability. On high adhesion roads, economy optimization algorithm is applied to maximize motors efficiency by means of the optimized torque distribution. On low adhesion roads, sliding mode control (SMC) algorithm is implemented to guarantee the wheel slip ratio under the target slip ratio to make full use of road driving capacity. Since the optimal slip ratio on different road conditions varies a lot, a quasi-optimal slip ratio is introduced and set as the target value. The integrated traction control strategy is designed for combining the vehicle economy and longitudinal stability via three torque allocation cases: economy-based torque allocation, pedal self-correcting torque allocation and inter-axle torque allocation. Finally, simulation results show that the proposed strategy effectively reduces vehicle energy consumption, suppresses wheel skid and enhances the vehicle longitudinal driving performance.

1 INTRODUCTION

During the past years, due to the energy crisis and environmental concerns, electric vehicles have become a fast-growing hotspot [1]. With the improvements on the electric motor and motor controller technology, many possibilities of the power train configurations are proposed [2]. One of the latest configurations is known as 4-motorized-wheels EVs, which employs four motors that are integrated to each wheel and controlled independently. This configuration has many advantages such as quick and accurate torque response, easier torque and RPM measurement, independent control for one single motor, which provides a broad prospect for vehicle dynamic improvement.

Traction control is a very significant aspect of vehicle dynamic control, which greatly influences the vehicle stability, safety and even economy. Therefore, lots of studies have been carried out so far focusing on this area. Due to its robustness sliding mode control has more and more applied in vehicle traction control. H. Wen et al. presented an acceleration slip regulation strategy based on sliding mode control [4]. In his research slip ratio calculation formula in the form of a state equation is used for solving the numerical problem caused by the traditional way. In purely economy terms, Nam, K. proposed a traction-ability and energy efficiency improvement method using wheel slip control. However the energy consumption only led by unnecessary wheel spin can be reduced [5]. X. Yuan utilized the independent characteristics of traction motors to develop a torque distribution method for decreasing EV energy [6]. In spite of this, most of the control strategies are incomplete, for they only put the focus on either stability or energy saving, while taking insufficient account of different road conditions.

In the presented strategy, vehicle efficiency is optimized through rational distribution of total driving torque between front and rear wheels. Sliding mode control is used to calculate the torque which can make the tire reach the quasi-optimal slip ratio point. The quasi-optimal slip ratio is proposed to avoid the error during the identification of road friction level. Finally, the effectiveness of the proposed integrated traction control strategy (ITCS) for both energy saving performance and longitudinal stability is validated in Matlab/Simulink.

2 VEHICLE MODELING

A detailed and comprehensive vehicle model must be used in order to accurately simulate the vehicle response under various maneuvers. Here the vehicle model developed and verified by Dirk E. Smith et al. [7] is utilized as the full vehicle model. The longitudinal velocity, lateral velocity, yaw rate, roll rate and four tire rotations lead to 8-DOF. The effects of tire force saturation, tire side force lag, tire normal load transfer etc. are all included. Besides, each wheel of the vehicle is individually driven by a DC motor through a fixed reduction gear. The motor torque external characteristics and efficiency map are shown in Figure 1. For calculation simplification, it is assumed that the motor efficiency of regenerative braking condition is identical with that of driving condition.

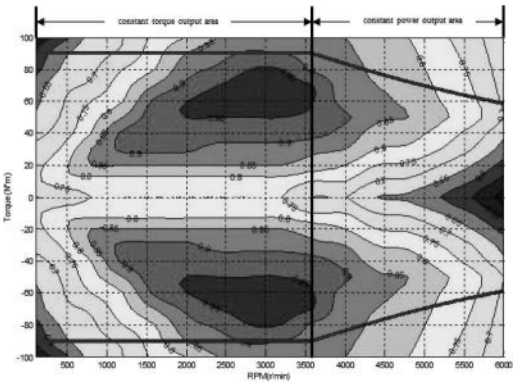


Figure 1. Motor external characteristics and efficiency map.

The motor's torque response can be simplified as first-order inertia as the following equation

$$T_i = \frac{T_{cmdi}}{\tau \cdot s + 1} \tag{1}$$

where T_i is the motor's torque output, T_{cmdi} is the torque command signal and τ is the time constant.

Since motor power is the function of motor efficiency, rotational speed and torque output, based on the efficiency map in Figure 1, the motor power can be easily calculated as

$$P_i = \begin{cases} \dfrac{n_i \cdot T_i}{\eta_i(T_i,\ n_i)}, & \text{Driving condition} \\ n_i \cdot T \cdot \eta_i(T_i,\ n_i), & \text{Regeneration condition} \end{cases} \tag{2}$$

where P_i and n_i denote the motor power and rotational speed; η_i is the motor efficiency.

3 INTEGRATED CONTROL STRATEGY

3.1 *Economy-based control*

3.1.1 *Objective functions establishment*

The relationship among the motor's torque, RPM and efficiency is shown in Figure 1. The motor efficiency is quite distinguishing in different working regions and especially when it works in the low speed or low torque output region, the motor has poor efficiency. If the driving torque can be in real-time distributed among four motors according to motor operating conditions, then motors efficiency will be improved [8]. Taking regenerative braking into consideration, the following economy objective functions are established,

$$\min J_d = \sum_{i=1-4}^{4} P_i = \sum_{i=1-4}^{4} \frac{n_i \cdot T_i}{\eta_i(T_i, n_i)} \tag{3}$$

$$\max J_r = \sum_{i=1-4}^{4} P_i = \sum_{i=1-4}^{4} n_i \cdot T_i \cdot \eta_i(T_i, n_i) \tag{4}$$

The objective functions should satisfy the following equality constraints and inequality constraints, such as the desired driving torque T_d, the motor properties and a few assumptions.

$$\begin{cases} \sum_{i=1-4}^{4} T_i = T_d \\ T_1 + T_3 \geq T_2 + T \\ |T_i| \leq |T_{motor}| \end{cases} \tag{5}$$

where T_{motor} is the motor maximum torque output.

For the sake of simplicity, a few assumptions are listed:

(1) The slip ratio and rotational speed difference of each wheel is quite small and hence, the motor rotational speed n equals *beta·u/r*.
(2) The torque output is identical if the motors are on the same axle.

Despite its simplification, these assumptions are still justified, since only longitudinal dynamic is discussed here and economy control will be activated only when the controller is fully sure that the car runs stable. The assumptions can be formulated as,

$$\begin{cases} T_1 = T_3 = T_f / 2 = p \cdot T_d / 2 \\ T_2 = T_4 = T_r / 2 = (1-p) \cdot T_d / 2 \\ n = beta \cdot \dfrac{u}{r} \end{cases}$$

where $p \in [0.5, 1]$ is economy distribution coefficient; T_f is the front axle driving torque; T_r is the rear axle driving torque. Then the final economy objective function is obtained,

$$J_d = n\left\{\frac{p \cdot T_d}{\eta[0.5p \cdot T_d, n]} + \frac{(1-p) \cdot T_d}{\eta[0.5(1-p) \cdot T_d, n]}\right\} \tag{6}$$

$$J_r = n\left\{pT_d\eta\left[\frac{pT_d}{2}, n\right] + (1-p)T_d\eta\left[\frac{(1-p)T_d}{2}, n\right]\right\} \tag{7}$$

3.1.2 *Solutions to objective functions*

In this paper, genetic algorithm is applied to solve these discontinuous objective functions. It can effectively prevent local optimization and find the solutions accurately and rapidly.

The objective functions solution p, is given as a two dimensional lookup table with current desired driving torque and motor rotational speed, which can avoid numerous online calculations and meet system real-time requirements. The economy-based distribution coefficient p is shown in Figure 2.

3.2 *Stability-based control*

3.2.1 *Quasi-optimal slip ratio*

The so-called "optimal slip ratio" λ_{opt} is the slip ratio value that can produce the maximum longitudinal traction force. However, for actual vehicles and roads,

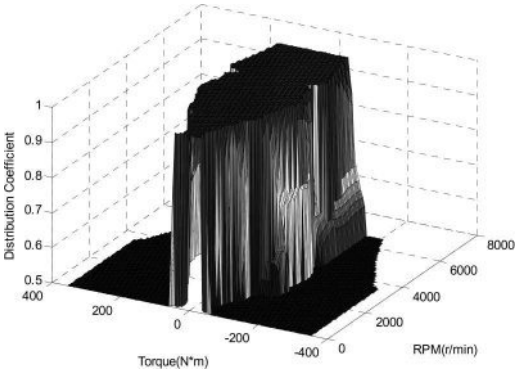


Figure 2. Economy-based distribution coefficient map.

Table 1. Burckhardt friction model parameters.

Roads	c_1	c_2	c_3	λ_{opt}	$\mu(\lambda_{opt})$
Dry asphalt	1.280	23.99	0.52	0.17	1.17
Wet asphalt	0.857	33.82	0.347	0.13	0.80
Dry concrete	1.197	25.16	0.537	0.16	1.09
Snow	0.194	94.12	0.065	0.06	0.19
Ice	0.05	306.3	0	0.03	0.05

optimal slip ratio is not a constant value. It changes due to the road conditions and its variation range is as much as 20%. Typical methods to estimate the friction coefficient is to use the information of the slip ratio and normalized driving force F_t/F_z to match the standard $\mu-\lambda$ curves. However, it is not easy to obtain the slip ratio and F_t/F_z signals accurately especially on the low slip ratio condition. Therefore, to avoid the error during the road identification the quasi-optimal slip ratio λ_{qo} is proposed based on Burckhardt friction model

$$\mu(\lambda) = c_1(1 - e^{-c_2\lambda}) - c_3\lambda \tag{8}$$

The friction model parameters of typical road surfaces, and corresponding optimal slip ratios λ_{opt} and maximum normalized driving forces are given in Table 1.

The fixed quasi-optimal slip ratio λ_{qo} is not the optimal choice for one particular road condition. However $\mu(\lambda_{qo})$ is most close to $\mu(\lambda_{opt})$ on all road conditions. The objective function and inequality constraints for solving this quasi-optimal slip ratio are expressed as Equation (9).

$$\min f(\lambda) = \sum \frac{\mu_i(\lambda_{opt}) - \mu_i(\lambda_{qo})}{\mu_i(\lambda_{opt})} \tag{9}$$

S.T. $\mu_i(\lambda_{qo})/\mu_i(\lambda_{opt}) \geq 90\%$ the solution of which is 14.3% easily obtained by solving nonlinear programming problem. In Table 2, it can be seen that the normalized driving force achieved under the proposed quasi-optimal slip ratio is almost as same as the one under optimal slip ratio.

Table 2. Normalized driving force comparison.

Roads	Dry asphalt	Wet asphalt	Dry concrete	Snow	Ice
$\frac{\mu_i(\lambda_{qo})}{\mu_i(\lambda_{opt})}$	99.7%	99.8%	99.9%	97.0%	99.7%

3.2.2 *Slip ratio control algorithm*

In this section, a sliding mode controller is developed to make the actual wheel slip ratio track the quasi-optimal slip ratio described above. Then the track error is defined as

$$e = \lambda - \lambda_{qo} \tag{10}$$

where the slip ratio λ is calculated as the following equation.

$$\lambda = \frac{\omega \cdot r - u}{u} = \frac{\omega}{\omega_0} - 1 \tag{11}$$

where u means the wheel's center velocity that equals to the vehicle body velocity since this article focuses on the longitudinal dynamics.

Then define a switching function s as follows

$$s = e + c\int e\, dt \tag{12}$$

which represents the designed sliding surface. In this paper, exponential reaching law is selected and given as

$$\dot{s} = -ks - \varepsilon\,\mathrm{sgn}(s) \tag{13}$$

where c is the strictly positive constant gain and ε is reaching velocity factor.

Taking the derivative of Equation (12), and substituting into Equation (13) gives

$$-\varepsilon\,\mathrm{sgn}(s) = \dot{e} + ce = \dot{\lambda} + e\left(\lambda - \lambda_{qo}\right) \tag{14}$$

Since for 4-motorized-wheels EVs each wheel is independently controlled by a motor, we have the wheel torque balance equation as

$$J_w\dot{w} = T_q \cdot beta - F_t \cdot r \tag{15}$$

where T_q is defined as the torque which can make tires reach the quasi-optimal slip ratio.

Taking derivative of the wheel slip ratio that is Equation (11) and substituting it into (15), the wheel slip ratio dynamic equation is obtained,

$$\dot{\lambda} = \frac{u}{J_w\omega^2 r}(T_o \cdot beta - F_t \cdot r) + \frac{\dot{u}}{\omega \cdot r} \tag{16}$$

The sliding mode control law is derived by substituting Equation (16) into Equation (14),

$$T_q = -[\varepsilon \operatorname{sgn}(s) + ks + c(\lambda - \lambda_{qo})]\frac{J_w \omega^2 u}{u \cdot beta} + \frac{J_w \omega \cdot \dot{u}}{u \cdot beta} + \frac{F_f \cdot r}{beta} \quad (17)$$

Finally, to reduce high-frequency chattering due to the non-deterministic switching control, a saturation function sat(s/Φ) is applied instead of sgn(s), where Φ is a positive constant which determines the thickness of the saturation boundary layer.

3.3 *Integrated control strategy design*

The integrated control strategy aiming at the economy optimization and stability control is proposed based on the analysis of the driver desired torque, motor output and road driving capability. Driver desired torque is denoted by T_d and is proportional to accelerator pedal position.

As shown in Figure 3, the control system diagram includes *control input* and *control case selection*. The latter is the main part of the proposed strategy. Three cases are designed and given as follows:

Case 1: economy-based torque allocation:

It corresponds to high adhesion road. When a vehicle is traveling on this kind of surface, the traction for each tire offered by the road is greater than the actual motor output, which means in this situation no tire skid issues exists for this vehicle. Therefore, economy-based torque allocation is activated preferentially.

Case 2: pedal self-correcting torque allocation:

It corresponds to low adhesion road. When a vehicle is driving on a low adhesion road like snow road or even quick starts and stops on wet cement road, sometimes the road adhesion capacity cannot meet the driver's torque request, which will lead to tire's unstable skid. In order to avoid this situation, the acceleration pedal coefficient must be adjusted to a reasonable region to guarantee vehicle stability. Pedal self-correcting torque allocation is designed to keep actual wheel slip ratio at the quasi-optimal slip ratio point, to make the most of the road friction and to meet the driver desired torque as far as possible.

Case 3: inter-axles torque allocation:

It corresponds to intermediate adhesion road. In addition to high and low adhesion road, sometimes despite the total road adhesion is more than the driver desired torque, however, if the car is running on a joint road, the friction coefficient for front and rear wheels will be different. Or due to the vehicle load distribution, the wheel with lower vertical load can only be applied with relatively small traction. Otherwise, it may lead to a seriously tire skid. Conversely, for the wheel with larger vertical load, it is necessary to moderately increase its motor torque output to make full use of the road capacity.

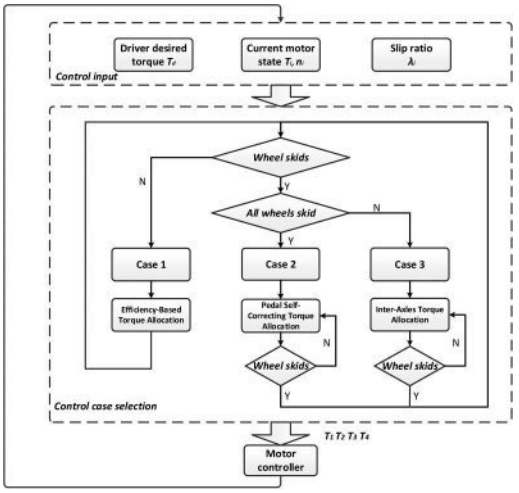


Figure 3. Integrated traction control strategy diagram.

Table 3. Vehicle parameters.

Parameters	Values
Vehicle mass	1280 kg
Vehicle inertia about Z axis	2460 kg·m^2
Distance of c.g. from front axle	1.2 m
Distance of c.g. from rear axle	1.3 m
Wheels track	1.5 m
Air resistance coefficient	0.35
Reducer ratio	3.5
Reducer efficiency	0.9
Tire effective rolling radius	0.3 m
Height of the sprung mass c.g.	0.5 m
Wheel rotational inertia	2.22 kg·m^2

By comparing different torque signals including driver desired torque, current motor torque output and quasi-optimal slip ratio torque, a suitable control case will be activated and kept operating until the vehicle running condition changes. Then the system needs to reselect the corresponding control case constantly to guarantee the control strategy's adaptability under different conditions.

4 SIMULATION RRESULTS AND ANALYSIS

The purpose of this section is to verify the proposed integrated control strategy using computer simulations. The vehicle parameters are listed in the Table 3.

4.1 *Simulation for economy-based control*

This economy evaluation is carried out according to the New European Driving Cycle (NEDC). The 4-wheel even torque drive (4WETD) and front-wheel-drive (FWD) are chosen to compare with the proposed integrated traction control strategy (ITCS). Figure 5 and Figure 6 show the simulation results.

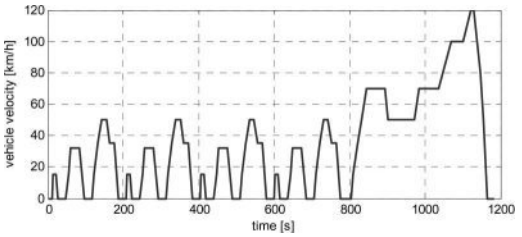


Figure 4. New European driving cycle.

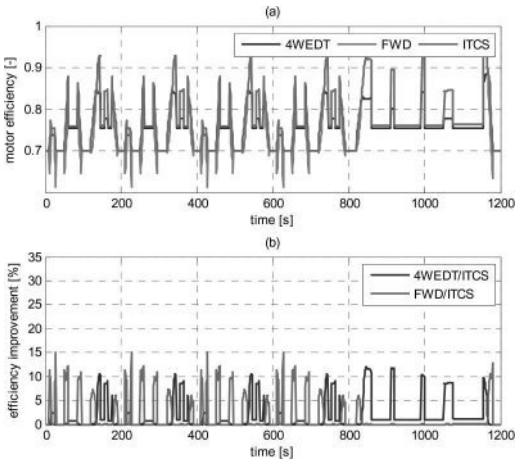


Figure 5. Working efficiency and improvement.

Figure 5 illustrates that vehicle working efficiency is significantly improved after adopting economy-based torque allocation. In some conditions, the improvement rate even reaches around 15%. Besides, as Figure 6 shows, the economy-based torque allocation also achieves lower thermal loss than the others, which can reduce motor's heat load and prolong its service life.

Table 4 lists the simulation results of economy improvement and equivalent weight reduction in each driving cycle stage. The highest energy saving occurs in high speed stage. Economy-based torque allocation decreases 8.06% energy consumption compared with 4WETD. Lowest energy saving, 0.46%, also occurs in high speed stage but it's relative to FWD. As for the whole driving cycle, economy-based torque allocation can decrease 6.88% and 4.00% energy consumption respectively, by comparison to 4WETD and FWD. If we use weight to measure the energy saving effect, it means 75.43 kg and 51.22 kg weight reduction equivalently, which is difficult to achieve in engineering design phase.

4.2 *Simulation for stability-based control*

In order to test the validity and robustness of the stability performance of the proposed control strategy, a compressive simulation experiment is additionally carried out under strongly varying conditions, which

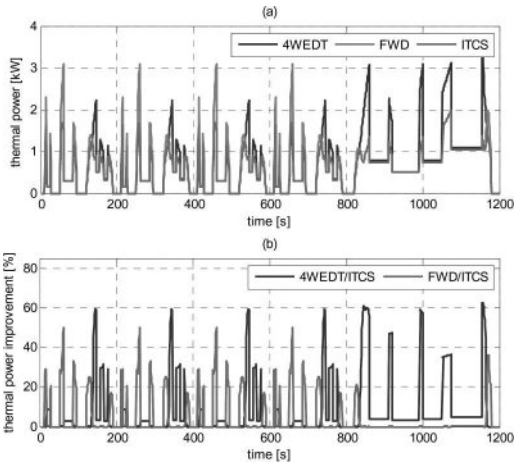


Figure 6. Thermal power and improvement.

Table 4. Improvement results analysis.

Cycle Stage	Energy Consumption (kJ)		ITCS	Energy Saving	Equivalent Weight Reduction
Low Speed	4WETD	919.2	870.9	5.26%	65.21 kg
	FWD	947.1		8.04%	96.34 kg
High Speed	4WETD	1267.0	1164	8.06%	97.54 kg
	FWD	1173.4		0.46%	17.65 kg
Whole Cycle	4WETD	2186.2	2036	6.88%	75.43 kg
	FWD	2120.4		4.00%	51.22 kg

Table 5. Road surface input for front wheels.

Distance (m)	Tire/Road Friction Coefficient
0–10	0.8
10–50	0.1
50–80	0.2
80–end	0.9

contains the switching of different road conditions and driver desired torque. The road surface input for front tires in this simulation is listed in Table 5. The time delay of the road switching for front and rear tires is also taken into consideration. In this simulation, the accelerator pedal position is set at 85%. After 9 s, the vehicle velocity reaches 60 km/h and then the accelerator pedal is released to 28% opening.

As shown in Figure 7, in the first 2.3 seconds, the car is running on a high adhesion road. The traction capacity provided by the road is much greater the driver desired torque. Therefore, Case 1 economy-based torque allocation is activated as shown in Figure 7(d). According to current torque and RPM signals, the economy coefficient p is set as 0.5, which means even torque allocation is applied. And then, the front wheels move into the low adhesion area firstly and the rear wheels are still in the high adhesion area. The control

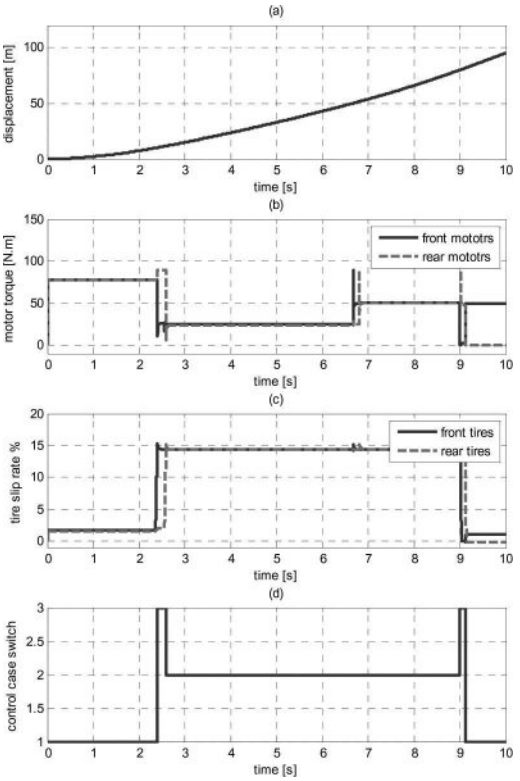


Figure 7. Simulation results on variable conditions: (a) Vehicle displacement; (b) motor torque output; (c) actual slip ratio; (d) control case switch.

case switches from Case 1 to Case 3 inter-axles torque allocation as shown in Figure 7(d). Based on sliding mode control, the torque output of front motors should be reduced to prevent the slip ratio from skidding. At the same time, the controller raises the rear motors output to ensure the vehicle dynamic performance to meet the driver's demand as shown in Figure 7(b). When all the four wheels move into the low adhesion road, Case 2 pedal self-correcting torque allocation is activated. At about 6.4 seconds, the friction coefficient changes from 0.1 to 0.2, however the Case 2 keeps running, since its condition is still satisfied. Furthermore, it should be noted that after the accelerator pedal position decreases from 85% to 28% at the 9th second, Case 1 starts running, however the front and rear motors' outputs are different the torque outputs from before. That is because through analysis of desired torque and RPM information, economy coefficient p is reset as 1, front-wheel-drive mode, to make the vehicle achieve the optimal economy performance.

5 CONCLUSIONS

In this paper, a novel integrated control strategy for 4-motorized-wheels electric vehicles is proposed, aiming at improving economy and longitudinal driving stability. According to the economy-based distribution coefficient, driver desired torque is allocated reasonably among four driving motors, which maximizes the motor driving efficiency and improves overall vehicle economy. Meanwhile, pedal self-correcting torque allocation and inter-axle torque allocation are moreover designed to overcome vehicle stability problems on low adhesion road. By means of solving nonlinear programming problem, the quasi-optimal slip ratio on different road surfaces is obtained as a fixed value. Based on sliding mode control, the torque output of each motor is adjusted to keep the wheel slip ratio under the target slip ratio rapidly and stably. It can be concluded that the proposed ITCS is able to balance the relationship between road/tire friction conditions, motor efficiency and driver desired torque; achieve vehicle economy and longitudinal stability optimization.

ACKNOWLEDGMENTS

The work is supported by the BCV project (Berlin City Vehicle Project) in Technical University of Berlin. And the authors would like to thank China Scholarship Council (CSC) for providing a scholarship as the financial support for the first author to pursue his Ph.D. degree at TU Berlin.

REFERENCES

[1] Hori, Y., Toyoda, Y., & Tsuruoka, Y. (1998). Traction control of electric vehicle: Basic experimental results using the test EV "UOT Electric March". Industry Applications, IEEE Transactions on, 34(5), 1131–1138.

[2] Esmailzadeh, E., Vossoughi, G. R., & Goodarzi, A. (2001). Dynamic modelling and analysis of a four motorized wheels electric vehicle. Vehicle System Dynamics, 35(3), 163–194.

[3] Yin, D., Oh, S., & Hori, Y. (2009). A novel traction control for EV based on maximum transmissible torque estimation. Industrial Electronics, IEEE Transactions on, 56(6), 2086–2094.

[4] He, H., Peng, J., Xiong, R., & Fan, H. (2014). An acceleration slip regulation strategy for four-wheel drive electric vehicles based on sliding mode control. Energies, 7(6), 3748–3763.

[5] Nam, K., Hori, Y., & Lee, C. (2015). Wheel Slip Control for Improving Traction-Ability and Energy Efficiency of a Personal Electric Vehicle. Energies, 8(7), 6820–6840.

[6] Yuan, X., & Wang, J. (2012). Torque distribution strategy for a front-and rear-wheel-driven electric vehicle. Vehicular Technology, IEEE Transactions on, 61(8), 3365–3374.

[7] Smith DE, Starkey JM. Effects of Model Complexity on the Performance of Automated Vehicle Steering Controllers: Model Development, Validation and Comparison. Vehicle System Dynamics. 1995 Mar;24(2):163–81.

[8] X. Zhang, D. Göhlich, X.L. Wu. (2015). Optimal torque distribution strategy for a four motorized wheels electric vehicle. EVS28 International Electric Vehicle Symposium and Exhibition.

Advanced Vehicle Control – Edelmann, Plöchl & Pfeffer (Eds)
© 2017 Taylor & Francis Group, London, ISBN 978-1-138-02992-7

Author index

Abe, M. 593, 599
Adomat, R. 31
Akamatsu, Y. 31
Albinsson, A. 541
Alirand, M. 527
Alirezaei, M. 119, 127
Andersson Eurenius, C. 431
Anstett-Collin, F. 651
Araújo, R.E. 417
Arikere, A. 37

Bakker, E. 431
Basrah, M.S. 585
Basset, M. 651
Beidl, C. 685
Beitelschmidt, D. 275
Besselink, I. 359, 405, 503
Best, M.C. 497
Bian, M. 397
Bian, Y. 111
Birouche, A. 651
Blume, S. 471
Bogdanski, K. 497
Boisdequin, G. 3
Borrelli, F. 43, 93, 133
Braghieri, G. 345
Brembeck, J. 105
Bremmer, P. 437
Brissard, A. 79
Bruzelius, F. 541
Burnett, G.E. 611
Busch, A. 515
Büyükyildiz, G. 73

Cao, D. 585, 619
Cao, Y. 61
Carvalho, A. 43, 93
Cheli, F. 527
Chen, B.-C. 163, 691
Chen, F. 645
Chen, L. 397
Chen, L.-K. 691
Chucholowski, F. 85
Chung, R. 365
Cole, D. 317, 329, 345
Contini, A. 269
Čorić, M. 9

Dagen, M. 515
Davari, M.M. 713
de Castro, R. 105
De Filippis, G. 17
Della Rossa, F. 243
Deng, W. 371
Denis-Vidal, L. 651
Deur, J. 9
Didcock, N. 471
Diermeyer, F. 477
Diskett, D. 445
Donnay Cortiñas, J. 431
dos Santos, B. 417
Drugge, L. 431, 713
Dubois-Lounis, M. 209

Eckstein, L. 489
Economou, J.T. 445
Edelmann, J. 521
Ehira, T. 189
Eichberger, A. 559
Eicke, S. 515
Engel, S. 477
Ercan, Z. 43
Ernst, S. 275

Fallah, S. 17
Fan, C. 67
Fényes, D. 261
Fournier, J.-Y. 209
Frerichs, D. 423
Fu, Z. 451
Fujimori, S. 177
Fujinaga, N. 697
Fujinami, Y. 31
Fukumori, Y. 285
Furusho, H. 293

Galvão Wall, D. 445
Gao, Y. 157, 203
Gáspár, P. 261
Gil Gómez, G.L. 431
Gnandt, C. 85
Göhlich, D. 717
Gokasan, M. 43
Gonzales, J. 133
Goos, J. 503
Gordon, T. 157, 203
Griffin, J.W. 611
Gruber, P. 17
Guan, J.-C. 691

Hackl, A. 559
Hafner, A. 73
Hafner, S. 85
Halleröd, T. 55
Hamza, S. 651
Hans, S. 463
Harada, M. 145
Hata, H. 411
Haudum, M. 521
Hayashi, R. 177, 285
Helfrich, T. 573
Hellewell, J.S. 611
Henn, T. 471
Henze, R. 73
Heo, J. 365
Hepperle, C. 85
Hillis, A. 703
Hiraga, N. 605
Hisamatsu, T. 483
Höll, M. 521
Holweg, E.G.M. 547
Honjo, T. 341
Hosono, T. 281
Hrovat, D. 9
Huh, K. 533

Imai, Y. 285
Imanaga, H. 311
Inoue, H. 49
Inoue, S. 49
Ishikura, T. 335
Ishizaki, R. 411
Iwaki, R. 311
Iwata, H. 177

Jacobson, B. 431, 541
Jansen, S.T.H. 127
Jeng, L.-W. 67
Jeon, J. 579
Jerrelind, J. 713
Jiang, Y. 371
Jin, Z. 235
Johansson, R. 55
Johnsson, A. 255
Jonasson, M. 23, 55, 713
Jung, J. 365

Kageyama, I. 323
Kalbfleisch, J. 457
Kandler, C. 625
Kaneko, T. 151
Kano, Y. 593, 599
Kärcher, C. 625
Kato, F. 599
Katsuyama, E. 631, 657
Kawaguchi, S. 281
Kerst, S.M.A.A. 547

Khajepour, A. 235
Kim, B. 183
Kim, S. 533
Kim, T. 215
Kitazawa, S. 151
Klomp, M. 37, 255
Kobayashi, T. 631
Köbe, M. 463
Koegeler, H. 471
Koenig, D. 385
Krehel, M. 463
Küçükay, F. 73
Kuriyagawa, Y. 323

Ledoux, V. 209
Lee, J. 365
Lee, K. 163
Lee, S. 579
Lefèvre, S. 43, 93
Leng, B. 509
Lenzo, B. 17
Lex, C. 559
Li, B. 451
Li, G. 679
Li, H. 679
Li, K. 67, 111, 133, 397, 673
Li, Q. 651
Li, S.E. 111
Li, X.H. 299
Lidberg, M. 37, 157, 203
Lienkamp, M. 573
Lin, Y.-M. 163
Liu, J. 679
Longo, S. 585
Loof, J. 359
Lopes, A. 417
Louis, L. 305
Lu, H. 249
Luo, Y. 397, 673

Ma, B. 679
Madhusudhanan, A.K. 127
Mastinu, G. 243
Matsumoto, T. 351
Maulick, Th. 3
Min, K. 215
Monsma, S. 437
Moulaire, P. 385
Mouri, H. 293, 377
Muenst, W. 305
Müller, S. 195

Nagai, M. 49
Nagatsuka, K. 605
Nakano, K. 285
Nakatsuji, T. 335
Nash, C.J. 317
Naude, C. 209
Németh, B. 261
Nie, S. 645
Niegl, M. 269
Nijmeijer, H. 99, 359, 405, 503
Nishizaki, K. 293
Nybacka, M. 431

Oh, J. 365
Ohno, A. 351
Ohno, S. 391
Okada, S. 483
Omae, A. 657
Omae, M. 483
Ono, E. 631
Ortmaier, T. 515
Ozawa, T. 49

Pan, Z. 673
Park, K. 215
Peng, H. 673
Pfeffer, P.E. 269, 703
Pletschen, N. 663
Plöchl, M. 521
Ploeg, J. 99, 119
Popov, A.A. 611
Prokop, G. 275, 463
Purdy, D.J. 445
Pütz, A. 489

Qin, Z. 397, 673

Rahimi Fetrati, S. 625
Rakheja, S. 451
Raksincharoensak, P. 49, 293, 377
Ramirez Ruiz, I. 527
Raste, T. 423
Rehder, T. 305
Reicherts, S. 471
Rosier, C.W. 329
Rötting, M. 299
Roy, N. 703

Sabath, St. 3
Sabbioni, E. 527, 637
Sato, K. 377
Sato, S. 605
Satzger, C. 105
Schaub, A. 105
Scheiblegger, C. 703
Schildbach, G. 139
Schmeitz, A.J.C. 127, 503
Schramm, D. 229, 305, 625
Schyr, C. 79
Semsar-Kazerooni, E. 119
Sename, O. 385
Serre, T. 209
Shao, L. 559
Shi, Y. 249
Shiiba, T. 281, 411
Shimono, K. 189
Shyrokau, B. 547
Siampis, E. 585
Simner, D. 445
Smith, E.N. 619
Sorniotti, A. 17
Srivastava, D. 223
Stensson Trigell, A. 713
Suda, Y. 285
Sugiura, H. 631
Suh, J. 183
Sukharev, O. 243
Sun, K. 567
Sunahara, O. 599
Sundström, P. 255
Suzuki, H. 335

Tagawa, Y. 189
Takagi, F. 411
Takahara, Y. 599, 605
Takahashi, J. 599, 605
Takahashi, T. 553
Takeda, Y. 599
Takemura, K. 599
Tamakawa, S. 377
Tamaki, H. 351
Tamura, K. 411
Tanabe, H. 377
Tavernini, D. 619
Teerhuis, A.P. 503
Themann, P. 489
Thor, M. 23
Tischer, W. 275
Togai, K. 351, 697
Tsai, C.-T. 163
Tseng, H.E. 9, 43
Tsukano, T. 599
Tüschen, T. 275

Uchida, N. 311
Udagawa, Y. 281
Ulbricht, D. 31
Umetsu, D. 593, 599, 605

Vadamalu, R.S. 685
van der Sande, T. 405
van Oort, M. 437
Velenis, E. 585, 619
Vignati, M. 637
Vollrath, M. 73

Wada, T. 169
Wagner, P. 457
Wahle, M. 229
Wallner, J. 477
Wang, C. 235
Wang, E. 67
Wang, Q. 195
Wang, W.S. 299
Wang, Y. 323
Watanabe, S. 145
Wielitzka, M. 515
Williams, A. 93
Wimmler, J. 229
Winner, H. 457
Wu, J. 371

Xia, X. 509
Xie, J. 645
Xing, H. 99
Xiong, L. 509, 567
Xu, L. 9

Yamaguchi, I. 311
Yamakado, M. 593, 599, 605
Yamakawa, J. 341
Yamamoto, K. 385
Yamamoto, M. 631
Yamaura, H. 697
Yang, B. 579
Yang, D. 55
Yang, J. 533
Yi, K. 183, 215
Yoneda, A. 391
Yoshida, H. 341
Yoshioka, T. 593, 599
Yu, F. 61, 249
Yu, Z. 509, 567

Zegelaar, P. 405
Zhang, D. 203
Zhang, F. 133
Zhang, K. 371
Zhang, L. 235
Zhang, R. 567
Zhang, S. 371
Zhang, X. 717
Zheng, Y. 111
Zhuang, Y. 645
Zimmermann, M. 229
Zlocki, A. 489
Zong, C. 203